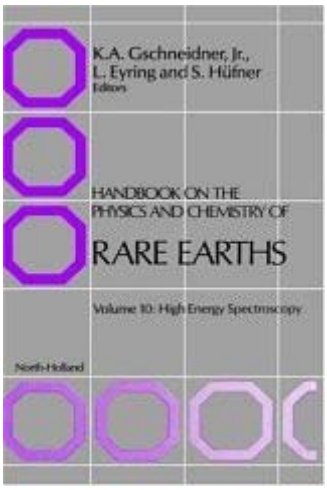

Handbook on the Physics and Chemistry of Rare Earths volume 10

High Energy Spectroscopy

Elsevier, 1987

Edited by: K.A. Gschneidner, L. Eyring, S. Hüfner

ISBN: 978-0-444-87063-6

Handbook on the Physics and Chemistry of Rare Earths, Vol. 10
edited by K.A. Gschneidner, Jr., L. Eyring and S. Hüfner

PREFACE

Karl A. GSCHNEIDNER, Jr., LeRoy EYRING and Stefan HÜFNER

These elements perplex us in our rearches [sic], *baffle us in our speculations, and haunt us in our very dreams. They stretch like an unknown sea before us – mocking, mystifying, and murmuring strange revelations and possibilities.*

Sir William Crookes (February 16, 1887)

As part of the world-wide celebration of the 200th anniversary of the discovery of the rare earths by Lieutenant Carl Axel Arrhenius, the editors and publishers of this Handbook series are pleased to dedicate this volume to the scientists, engineers, technologists, industrialists, and others who have contributed to discoveries, advancements, knowledge and applications of these materials since 1787, and have brought the rare earths to their imposing present-day position.

This coherent volume on "High Energy Spectroscopy" returns to a more focused content as found in the first four volumes of the Handbook. The plans for this volume started in early 1983 as a result of a suggestion from our editorial board who recommended that a thorough discussion of a currently topical aspect of the physics and chemistry of the rare earths should occasionally be assembled as the need arose. This volume is the first of these volumes. Over the next six months the contents of this volume began to take shape, especially with the help of Professor S. Hüfner, who was invited to serve as a special co-editor for this volume.

It is appropriate to point out one special feature that is important in understanding the application of high energy probes to lanthanide compounds. The experimental techniques, which are described in this volume, change (because of the nature of the measuring process) the electron number of the ion. This holds even to some degree for X-ray absorption (near the edge), which is the least perturbing experiment because it places a localized core electron into the delocalized conduction orbital. In materials such as the free electron-like simple metals the conduction electrons quite effectively screen out the perturbation produced by such a measuring process. In the lanthanides, the 4f electrons are highly localized and thus they participate much less effectively in the screening process. Actually only in metallic Ce and, to a lesser degree, in Pr and Nd and their compounds can one observe some itineracy of the 4f electrons via the techniques described in this volume. Therefore the ejection of a core electron in lanthanide compounds generally leaves the 4f count intact (with the notable exception of Ce, and Pr and Nd). While on the other hand the ejection of a 4f electron leads to a state differing in 4f count from the initial state (again with the exception of Ce, and Pr and Nd). This behavior is a distinct

departure from that observed in the main group elements and transition metals, and accounts for some of the interest in studying the lanthanides and their compounds by high energy probes.

The experimental study of H.G.J. Moseley in the early 1910s on the X-ray spectra of the elements clearly showed for the first time that only 14 4f elements could exist and that one element still remained to be discovered. Furthermore, the anomaly that 14 elements with properties similar to lanthanum proved to be an extremely important clue in aiding Bohr and other theorists in developing our present theory of atomic structure. This work was probably the greatest contribution to the field of the rare earths (lanthanides) since their discovery in 1787.

As pointed out in J. Röhler's chapter (71) high energy spectroscopy has been used as a research tool to understand the chemical and physical nature of materials since the early years of this century. Its application, other than as an analytical tool for detecting and measuring the concentrations of these elements in a substance, in studying the electronic nature the rare earths is of relatively recent origin ($\sim$the last ten years). There are several reasons for this long hiatus – the need for the modern high precision instruments required to obtain reliable spectra, and reliable theories and powerful computational techniques to calculate the electronic structures needed by the experimentalists to aid in the interpretation of the measured spectra. The strong interaction between theorists and experimentalists is also evident in the content of this volume. Four of the eleven papers of volume 10 deal with various theoretical aspects: from the band and electronic structure calculations presented by Freeman, Min and Norman (chapter 65) and Herbst and Wilkins (chapter 68) to the approach of Gunnarsson and Schönhammer employing the Anderson Hamiltonian (chapter 64) and the thermodynamic techniques of Johansson and Mårtensson (chapter 69).

The experimental papers cover the various spectroscopic techniques and a few deal with special materials. The introductory chapter (62) by Baer and Schneider presents an overview of this field and helps tie the various aspects together that are reviewed in detail in the remaining chapters of the volume. Photoemission studies (UPS – ultraviolet photoemission spectroscopy, and XPS – X-ray photoemission spectroscopy) on various materials are discussed by Campagna and Hillebrecht (chapter 63) – intermetallic compounds, by Lynch and Weaver (chapter 66) – cerium and its compounds, and by Hüfner (chapter 67) – chalcogenides. Other experimental techniques covered include BIS (bremsstrahlung isochromat spectroscopy) by Hillebrecht and Campagna (chapter 70), X-ray absorption and X-ray emission by Röhler (chapter 71) and inelastic electron scattering by Netzer and Matthew (chapter 72).

July 24, 1987

CONTENTS

CONTENTS OF VOLUMES 1–9

VOLUME 1: METALS

VOLUME 2: ALLOYS AND INTERMETALLICS

VOLUME 3: NON-METALLIC COMPOUNDS – I

VOLUME 4: NON-METALLIC COMPOUNDS – II

VOLUME 5

VOLUME 6

VOLUME 7

VOLUME 8

VOLUME 9

Handbook on the Physics and Chemistry of Rare Earths, Vol. 10
edited by K.A. Gschneidner, Jr., L. Eyring and S. Hüfner

Chapter 62

HIGH-ENERGY SPECTROSCOPY OF LANTHANIDE MATERIALS – AN OVERVIEW

Y. BAER and W.-D. SCHNEIDER
Institut de Physique, Université de Neuchâtel, CH-2000 Neuchâtel, Switzerland

Contents

List of symbols

B	Bandwidth	E_i, E_g	Eigenvalues for photoemission 4f final states
δ	Total energy gain by the hybridization between f and band states ('Kondo energy')	$E_i^c = E_i - E_c$	Eigenvalues for photoemission 3d final states
Δ	Coupling parameter between f and band states	$E_t(N)$	Total energy of the N-electron system
Δ_-, Δ_+	Minimum many-electron energies required to modify the population of the f shell	n_f	Occupancy of the f shell in the ground state
		N_f	Degeneracy of the f orbital
$\Delta_{s,b}$	Difference in core-level binding energies between bulk and surface atoms	$P(r)$	Radial charge density
		$\rho_c(\varepsilon)$	Core-level spectrum
		$\rho_s^f(\varepsilon)$	Spectrum of the split-off states
Δ_{so}	Spin–orbit splitting	r_a	Atomic radii
ε_c	Core-level energy	r_m^{4f}	4f radial wave function maxima
ε_k	Energy of a band electron		
ε_f, (ε_f^c)	Total energy difference (in the presence of a core hole) between consecutive f populations when hybridization and f Coulomb energy are not considered	$S(E_t)$	Density of outer level excitations on a total energy scale
		$T_K = \delta/k_B$	Kondo temperature
		U_{fc}	Core-hole 4f Coulomb energy
		U_{ff}	f–f Coulomb energy
		V_{mk}, $V(\varepsilon)$	Hopping matrix elements between f and band states
E_F	Fermi energy		
E_i^B	Adiabatic binding energy of the level i		

1. Introduction

In the periodic table of the elements, the delayed occupation onset of the shells with an orbital quantum number $l \geqslant 2$ is a well-known consequence of the centrifugal term of the effective potential in the radial Schrödinger equation. In the lanthanides, this term is responsible for the 4f localization which is the most pronounced among the partly occupied shells since the 4f wave functions have no node and correspond to the highest angular momentum. Already in the early Thomas–Fermi model of the atom it has been shown (Goeppert–Mayer 1941) that the spatial extension of the 4f wave functions drops suddenly at the beginning of the lanthanide series. More recent calculations (Freeman 1980) confirm that these states can approximately be considered to belong to an open inner shell with respect to the 5s, 5p, 5d and 6s states. This situation is illustrated in fig. 1 by the radial charge density of these states in Gd.

Fascinating problems are raised by the lanthanide elements when they form solids since their 4f states keep largely their atomic character while their binding energies become comparable to the band widths as a consequence of the screening by the extended states in which they are embedded. Smith and Kmetko (1983) have proposed the very useful arrangement of the 3d, 4d, 5d, 4f and 5f series shown in fig. 2, where the localized character of these shells increases systematically upward and from the left to the right. The shaded area represents the border region separating the elements where the considered states have a predominant atomic character from those where they participate to the bands. The lanthanides occupy the top of this

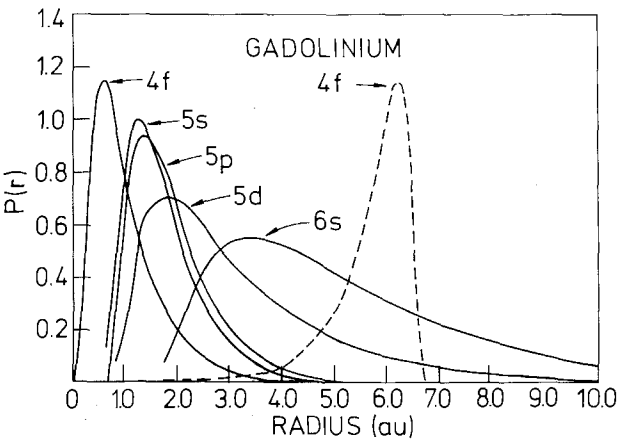

Fig. 1. Radial charge density of the outer orbitals of a neutral Gd atom (after Freeman 1980). The dashed curve represents the 4f charge of a Gd atom located at the nearest-neighbour distance in the metal.

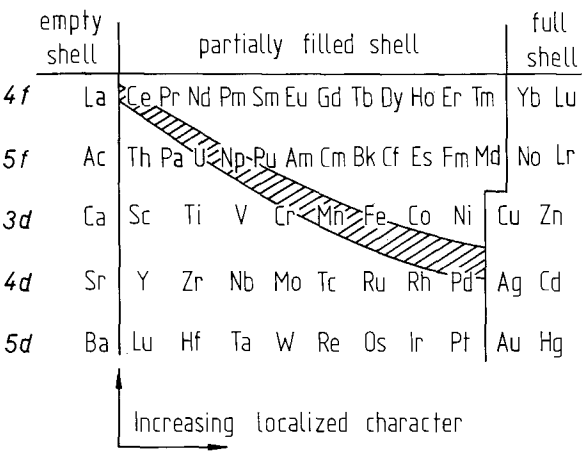

Fig. 2. Table of the elements of the 3d, 4d, 5d, 4f and 5f series disposed in an order showing the systematic variation of the localized character among the partly filled d and f shells (after Smith and Kmetko 1983).

table so that the 4f states of the light elements in this series have the most pronounced tendency to contribute to the bond by hybridization with neighbour atoms. The intermediate situation between localization and delocalization corresponds to a rather unstable balance giving rise to spectacular manifestations which are the subject of intensive investigations at the present time.

This book is devoted to lanthanide studies using high-energy spectroscopies. The concept of high energy is only relevant for the fact that the induced transitions can be assumed to occur instantaneously. The ultimate resolution of these methods is determined by the lifetimes of the states which are involved but is not affected by the high energy of the transitions, as commonly believed. In contrast to optical spectroscopies, in most of these methods the energy of the different electronic final states can be selected and for this reason they are commonly considered as very direct tools for probing the electronic states in solids. The spectra are implicitly analyzed in terms of transitions between single-particle eigenstates of a system containing a very large number of interacting electrons. This approach is quite satisfactory for describing the ionization of deep core levels or transitions involving only extended states, but it breaks down completely for the 4f states which belong to

the outermost levels by their binding energies and to the core levels by their orbital dimensions. In the case of a clear-cut localization of the 4f states, this difficulty can be easily overcome if the single-particle energy is replaced by the screened energy difference between initial and final states of an atomic-like excitation. The situation remains very confusing for an intermediate behaviour between localization and delocalization and in this case the conventional interpretations of spectroscopic data have led to unfounded and whimsical conclusions which have been for many years the subject of numerous debates in the literature. It is a very important achievement of recent theories to have allowed the development of model calculations predicting correctly all kinds of excitation spectra in such systems. They yield an unified and simple analysis of the data from which the numerical values of the relevant parameters characterizing the electronic ground state can be extracted.

Already in the early days of the electron spectroscopies, these techniques have often been exploited to investigate the intriguing electronic structure of the lanthanides. Since the last general review on this subject (Campagna et al. 1979), a tremendous number of experimental results has been accumulated, new spectroscopies have been developed and decisive theoretical progress has been made in the interpretation of the data. The first aim of this overview is to provide to scientists which are not familiar with the high-energy spectroscopies, the general principles of these techniques and the basic concepts used to analyze the spectra. Then, an attempt will be made to account systematically for the different aspects of the electronic structure resulting from the presence of the 4f states, as revealed by spectroscopic techniques. The conventional and established 4f manifestations which are commonly quoted as fingerprints of the initial state will also be briefly reviewed. The physical concepts will be used to guide the presentation of the various subjects which will be only illustrated by some relevant examples. A particular effort will be made to find out the merit and complementarity of the different spectroscopies applied to the elucidation of specific problems and the emphasis will be put on the fact that a credible interpretation can only result from an unified model accounting for all observations. In this respect Ce plays a central role since, together with Yb, it offers the simplest initial situation but displays many unconventional manifestations which have been carefully investigated and can be accounted for by many-body calculations. On the other hand, it is not the purpose of this overview to sketch all systematic behaviours of sequences of compounds nor to cover thoroughly the results obtained by each technique and each theoretical approach. As often as possible, reference will be made to the following chapters of this book where these topics are reviewed separately.

2. The basic concepts of high-energy spectroscopies

The principle of the spectroscopies considered here is to expose a solid to an electron or photon beam of known high-energy which interacts with the N electrons of the system and to select the type and the energy of the emitted particles resulting from the transitions induced in the solid (see figs. 3 and 4). Depending upon the

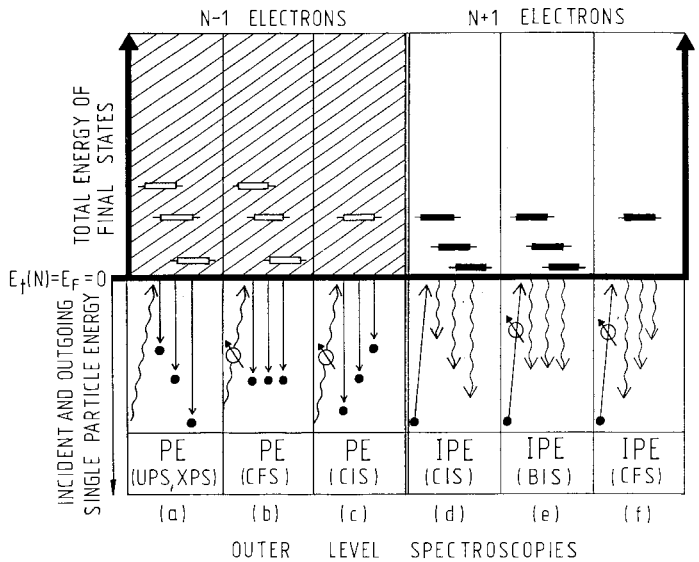

Fig. 3. Schematic representation of the principle of the different outer level spectroscopies. *Lower part*: Incident and emitted particles outside the sample. The experiment gives access only to these single-particle energies. (a) PE, UPS, XPS: photoemission, UV-photoemission spectroscopy, X-ray photoemission spectroscopy. (b) PE, CFS: photoemission measured at constant final state. (c) PE, CIS: photoemission measured at constant initial state. (d) IPE, CIS: inverse photoemission measured at constant initial state. (e) IPE, BIS: inverse photoemission, bremsstrahlung isochromat spectroscopy. (f) IPE, CFS: inverse photoemission measured at constant final state. *Upper part*: Total energy difference between the ground state of the N-electron system and the final states after electron subtraction (open rectangles) or electron addition (filled rectangles) processes. The origin of the total energy scale is fixed at the Fermi energy (see also figs. 7 and 19a).

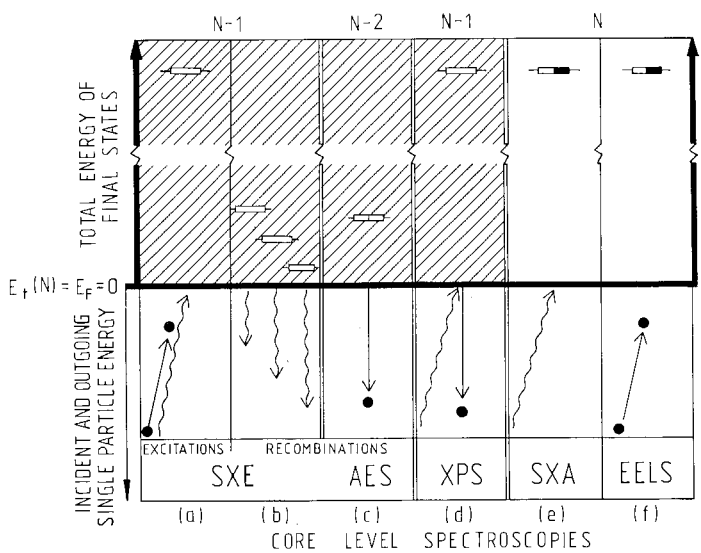

Fig. 4. Schematic representation of the principle of the different core level spectroscopies. *Lower part*: (See caption of fig. 3.) (a) and (b) SXE: soft X-ray emission. (a) and (c) AES: Auger electron spectroscopy. (d) XPS: X-ray photoemission spectroscopy. (e) SXA: soft X-ray absorption. (f) EELS: electron energy loss spectroscopy. *Upper part*: (See caption of fig. 3.) Half-filled rectangle: excited final state with the same electron count as in the initial state, (e), (f). Divided rectangle: final state with two electrons less than in the initial state (see also fig. 19b).

choice of the particles and of the energy range, one can define many different spectroscopies which will be presented in section 3. For the moment we shall simply consider that a given spectrum represents the probability distribution of the energy gains of the system left after a particular type of process. The essential problem is then to relate the measured spectra to the most suitable quantities obtained from theoretical descriptions of the N-electron system.

2.1. *The adiabatic energies*

The most common approaches to the electronic structure in solids are the mean-field theories which reduce the N-electron problem to the calculation of N single-particle states in the self-consistent field of the $N-1$ other electrons. For the sake of simplicity we will adopt here the Hartree–Fock (HF) formalism, despite the fact that it is a very poor approximation for the highly correlated systems we are interested in. It yields for the ground state (G) N occupied single-particle eigenstates with energies ε_i. The Slater determinant composed of these orbitals represents within this approach the best many-electron wave function $\Psi^{\mathrm{G}}_{\mathrm{HF}}(N)$ corresponding to the total energy $E^{\mathrm{G}}_{\mathrm{HF}}(N)$. With the help of such a calculation, the situation can be simply described by the population n_i of the single-particle levels and their energy distribution is called density of states (DOS). The same calculation can be repeated for any other state where the population of the levels has been modified in some arbitrary way. One has to anticipate that in the considered system this modification has only a minor influence on the single-particle eigenstates so that their initial labelling can be maintained to identify them in the modified state. For the simplest cases one obtains the energy differences:

$$E_i^{\mathrm{B}} = E(N-1) - E^{\mathrm{G}}(N) = E_{\mathrm{HF}}(\ldots(n_i-1)\ldots n_j\ldots) - E^{\mathrm{G}}_{\mathrm{HF}}(\ldots n_i\ldots n_j\ldots), \tag{1}$$

$$E_j^{\mathrm{A}} = E(N+1) - E^{\mathrm{G}}(N) = E_{\mathrm{HF}}(\ldots n_i\ldots(n_j+1)\ldots) - E^{\mathrm{G}}_{\mathrm{HF}}(\ldots n_i\ldots n_j\ldots), \tag{2}$$

$$E_{ij}^{\mathrm{T}} = E^*(N) - E^{\mathrm{G}}(N) = E_{\mathrm{HF}}(\ldots(n_i-1)\ldots(n_j+1)\ldots) - E^{\mathrm{G}}_{\mathrm{HF}}(\ldots n_i\ldots n_j\ldots), \tag{3}$$

which are respectively the adiabatic expressions for the binding energy of the level i, the addition energy to the level j and the transition energy between these two levels. These energies are interpreted as resulting from adiabatic transitions in the sense that the hypothetical processes can only lead to the lowest final states. If the correlation is so strong that the HF or any more realistic mean-field theory is no longer appropriate, only the first part of these three equations remains valid.

2.2. *The Koopmans approximation*

One can take advantage of the fact that the system contains a very large number N of electrons if each of them is really in instantaneous interaction with many other electrons. In this case, the emission of one electron for example induces only a very small change of the self-consistent field experienced by the $N-1$ electrons occupying the 'passive' orbitals not directly involved in the emission process. In first

approximation one can 'freeze' (fr) these $N-1$ orbitals in their initial states for the calculation of the final state energy:

$$E_i^B \lesssim E^{fr}(\ldots(n_i-1)\ldots) - E_{HF}^G(\ldots n_i\ldots) = -\varepsilon_i. \tag{4}$$

In the HF formalism this energy difference corresponds precisely to the eigenvalue of the electron which has been eliminated from the system (Madelung 1978). Since the frozen final state energy is not correctly minimized, the eigenvalue $-\varepsilon_i$ always overestimates somewhat the HF binding energy. The first part of eq. (4) is the Koopmans approximation (Koopmans 1934) which is well satisfied for nearly-free band states and deep core levels. Extensions of this formalism to correlated states have been proposed (Phillips 1961, Smith and Day 1975). Strictly speaking, a single-particle eigenvalue can never be directly observed in any experiment, at least not in the usual sense, and the energy excess when compared to the exact binding energy E_i^B is commonly visualized as a relaxation energy $\Delta E_{rel}^i > 0$ so that

$$E_i^B \equiv -\varepsilon_i - \Delta E_{rel}^i. \tag{5}$$

The validity of the Koopmans approximation is then simply expressed by the condition:

$$\Delta E_{rel}^i \ll -\varepsilon_i. \tag{6}$$

An elegant language for describing the physical meaning of the Koopmans approximation is provided by the density-functional formalism which shows that the partial derivatives of the total energy with respect to the occupation numbers are rigorously given by orbital eigenvalues (Janak 1978, Williams and Lang 1978). This allows us to write the adiabatic binding energy as a Taylor expansion:

$$E_i^B = E(\ldots(n_i-1)\ldots) - E^G(\ldots n_i\ldots) = -\frac{\partial E^G}{\partial n_i} + \frac{1}{2}\frac{\partial^2 E^G}{\partial n_i^2} - \cdots$$

$$= -\varepsilon_i + \frac{1}{2}\frac{\partial \varepsilon_i}{\partial n_i} - \cdots = -\varepsilon_i - \Delta E_{rel}^i. \tag{7}$$

The Koopmans approximation is equivalent to a limitation of this expansion to the first term by assuming that it is sufficient to linearize the function $E^G(\ldots n_i\ldots)$ around the population corresponding to the ground state. An approximate linear dependence of the energy on a small charge variation means that the mean-field produced by $N-1$ 'passive' electrons on one particular electron which is emitted is rather correctly simulated by a fixed potential, or, in other words, that the self-consistency can be considered as switched off in the ground state. This is precisely the assumption made in the Koopmans final state used in eq. (4). It is a simple matter to express in the same language the other transitions defined by eqs. (2) and (3). The accuracy of this type of calculation can be improved by using the transition state technique (Slater 1974).

2.3. *The sudden approximation of electronic processes*

In the high-energy transitions considered here, the impinging or emitted electrons

have a high speed. In a classical language one can say that the time interval τ during which they interact with the system when a transition takes place is very short (Fano and Cooper 1968, Meldner and Perez 1971, Gadzuk and Sunjic 1975). Let us consider the most familiar photoemission process of an electron occupying in the initial state the orbital ϕ_i. The lifetimes of the excited final states resulting from this process are much longer than τ and for the moment we assume stationary final states. In the limit of $\tau \to 0$, one can schematically describe the emission event as the sudden disappearance from the system of the electron populating the state ϕ_i (Manne and Åberg 1970). If now our attention is focussed exclusively on the $N-1$ passive electrons, their final state is just described by their initial orbitals as a consequence of the wave function continuity as a function of time. We notice that it corresponds to the final state $\Psi_G^{fr}(N-1)$ assumed in the Koopmans approximation (eq. (4)) and that it is not an eigenstate of $H(N-1)$. Such a final state has to be expressed as linear combination of the eigenstates $\Psi_m(N-1)$ of $H(N-1)$ with energies $E_m(N-1)$:

$$\Psi_G^{fr}(N-1) = \sum_m b_m \Psi_m(N-1), \qquad b_m = \langle \Psi_G^{fr}(N-1) | \Psi_m(N-1) \rangle. \tag{8}$$

The weights of the different observable final eigenstates are given by $|b_m|^2$ which obey the sum rule $\Sigma_m |b_m|^2 = 1$. The condition ensuring the validity of the sudden approximation can be easily derived (Schiff 1955) and it appears to be satisfied in all practical situations (Meldner and Perez 1971, Gadzuk and Sunjic 1975).

In order to describe now a real photoemission process, one has to calculate the matrix elements resulting from the presence of a perturbing radiation field A. The most important term which has to be considered in the new single-particle Hamiltonian is $h = (e/mc)\boldsymbol{A}(\boldsymbol{r})\boldsymbol{p}$. For a particular transition in which an electron occupying the orbital ϕ_i is emitted into a continuum state ϕ_ε of energy ε, we shall retain from the general expression for the transition probability (Martin and Shirley 1976) only the leading term:

$$P_{i\varepsilon} \propto |\langle \Psi_m(N-1) | \Psi^{fr}(N-1) \rangle \langle \phi_\varepsilon | h | \phi_i \rangle|^2 \delta(\Omega) = |b_m|^2 |M_{i\varepsilon}|^2 \delta(\Omega) \tag{9}$$

with

$$\Omega = h\omega - \varepsilon - (E_m(N-1) - E_G(N)).$$

$M_{i\varepsilon}$ is the usual single-particle matrix element. The sudden approximation applied to the photoemission process shows that as a function of ε the ionization spectrum of the state ϕ_i contains an infinity of lines reflecting the final states of the passive $N-1$ electrons. In conventional systems containing no localized outer levels, the largest overlap integral (eq. (8)) is b_0 corresponding to the adiabatic final state, so that in the sudden limit the spectra display mainly the adiabatic component. The mean-field approach is no longer suitable for describing f systems but the sudden approximation remains valid and the overlap integrals are simply expressed as $\langle \Phi(N-1) | a | \Phi_0(N) \rangle$ where a is the annihilation operator for an electron of the symmetry determined by the single-particle selection rules.

Finally, within the HF approximation, one can easily show that the mean energy

of the complete set of final states observed for the ionization of the level ϕ_i is given by

$$\bar{E}(\ldots(n_i-1)\ldots)=\sum_m |b_m^i|^2 E_m(\ldots(n_i-1)\ldots)=E^{\mathrm{fr}}(\ldots(n_i-1)\ldots). \tag{10}$$

If this result is combined with eq. (4) one obtains

$$\bar{E}(\ldots(n_i-1)\ldots)-E_{\mathrm{HF}}^{\mathrm{G}}(\ldots n_i\ldots)=-\varepsilon_i. \tag{11}$$

The center of gravity of the complete emission spectrum for the level ϕ_i determines precisely its eigenvalue. This result is sometimes referred to as Koopmans' theorem and it should be noticed that it is not equivalent to the Koopmans approximation (eq. (4)).

2.4. *General situation*

The HF formalism has been chosen for this preliminary discussion since it is tractable but it provides such a restricted set of basis functions that it yields even not always a realistic approach to the low correlation limit of electron gases (Hedin and Johansson 1969). However, it has the didactical virtue to indicate the evolution trend of the spectra for increasing correlation. The discussion will also be limited here to photoemission, its extension to other processes is rather straightforward. In a nearly-free electron system, the photoemission spectrum of the band can be considered to reflect correctly the distribution of the ground-state eigenvalues (DOS) modulated by the single-particle matrix elements. When the localized character becomes more pronounced, as for example in the 3d metals, the relaxation energy which is always infinitesimal at E_{F} (Janak 1978), increases markedly towards the bottom of the band. For this reason, when compared to a calculated DOS, the band-like part of the photoemission spectrum corresponding to the adiabatic final states is narrower and loses gradually its intensity. On the other hand, the center of gravity of the band excitations has to remain at its frozen energy (eq. (10)) so that new final states of higher energy are formed in order to satisfy this requirement. They can no longer be derived from the ground state by the Koopmans approximation, in broad-band metals they involve many low-energy electron–hole pairs and plasmons whereas in narrow-band metals they reflect mainly excitations with enhanced atomic character commonly called satellites. The origin and importance of such satellites have been first discovered in Ni and suitable formalisms have been developed to account for them (Treglia et al. 1980a,b). The same kind of excitations occurs in the sudden emission of a core electron (Kotani and Toyozawa 1974) but the final state hole can deeply modify the relative energies of the outer levels.

One can now anticipate the qualitative evolution of metallic spectra when the character of the considered outer states is approaching very close to a complete localization. The band-like contribution to the spectrum remains pinned at E_{F} but its width and intensity becomes very small while the main weight of the spectrum is transferred to more complex final states containing increasingly localized excitations. When this stage is reached, the usual and straightforward interpretation of

the spectra in terms of ground-state DOS becomes completely erroneous. The spectral function given by eq. (9) in our simple approach must be now calculated in a formalism where a suitable and realistic set of basis functions is chosen in order to account for the peculiarities of the considered system. For the 4f states this critical situation is met at the beginning of the lanthanide series and it will be discussed in sections 6 and 7.2. In the heavy lanthanides, the limit is reached where the local character of the 4f states dominates completely. Despite the definitive validity loss of the Koopmans approximation, the situation is again tractable. The reason is simply that, when the expression (9) is applied to describe the emission from a localized 4f shell, the huge total number of electrons which has to be taken into account in general, can be reduced to the 4f electrons of a single atom. It is sufficient to consider the well-known atomic behaviour of the 4f shell and to account for the solid in which it is embedded by a renormalization of the excitation energies resulting from the band state screening (section 4.2). Finally, the simple approach presented in this section cannot account for the particular regime where two nearly localized f-configurations show at finite temperature many aspects of a f-count fluctuation. This situation will be tentatively discussed in section 7.3.

3. Review of the electron spectroscopies

3.1. *Classification*

Electron spectroscopic methods offer many different tools for investigating the electronic properties of solids. They are all based on an external excitation inducing transitions between an initial state (which is not necessarily the ground state) and the accessible final states compatible with the conservation and selection laws. The aim of this section is to remind the reader of the different types of transitions which are involved in these spectroscopies and which cover the whole energy range up to 10^4 eV. The resolution of the different techniques lies generally between 0.1 and 1 eV, only recently the range below 100 meV has become accessible. It has to be noted here that optical methods (Travaglini and Wachter 1984) and point contact spectroscopy (Bussian et al. 1982, Frankowski and Wachter 1982, Moser et al. 1985) represent powerful alternative tools for probing the low-energy excitations in solids.

Depending upon the choice of the excitation and detection mode, and of the parameters which are varied in the experiment, the different methods can be classified into outer level and core level spectroscopies. A schematic representation of the different principles of the measurements and of the electronic transitions involved in these spectroscopies is depicted in figs. 3 and 4. The lower part of figs. 3 and 4 displays schematically the incident and emitted particles outside the sample. The experiment gives access only to these single-particle energies which allow us to determine the total energy difference between the ground state of the N-electron system and the excited states left in this system after a particular process. In addition to this total energy difference shown in the upper part of figs. 3 and 4, we know also

the induced population changes which are indicated by different symbols. It is convenient in such a representation to fix the origin of the total energy scale and the Fermi level E_F (chemical potential) at the same position. This definition is very useful in metals since, when a single particle approach of the excitation is valid, the total final state energy represents also the single-particle eigenvalue from which the population has been modified (eq. (4)). The fact that the Fermi energy is the origin of the excitation spectrum in an extended metallic system has been proved by Janak (1978). This means that the relaxation energy is infinitesimal at E_F.

This definition of a common origin of single-particle and total energy scales can be in principle maintained in insulators. However, the Fermi level is no longer a meaningful reference for discussing the influence of the chemical bond on the different excitation energies observed in series of compounds. We shall discuss in section 6.2.1 the different problems related to the choice of the origin of excitation spectra in metals and insulators.

Photoemission (PE) and inverse photoemission (IPE) play a central role in the study of the outermost states because the corresponding transitions induce the lowest possible population change among these states only (fig. 3). In all other methods (fig. 4) the information about outer states extracted from the spectra accounts for a local DOS around atoms with an effective nuclear charge $Z + 1$ rather than for the unperturbed DOS. This difference increases when the states forming the considered band approach the localization limit.

The following review of the different methods will be limited to a short presentation of the phenomena, more detailed information about these techniques and further references can be found in several reviews of different authors which have contributed to the following books classified according to their editors: Fabian and Watson (1973), Azaroff (1974), Brundle and Baker (1977, 1978, 1979), Ibach (1977), Feuerbacher et al. (1978), Cardona and Ley (1978), Ley and Cardona (1979), Day (1981), Freeman and Lander (1984). Further review articles have been devoted to XPS (Watson and Perlman 1975), UPS (Bradshaw et al. 1975), IPE (low energy) (Dose 1983), surface-specific spin-sensitive spectroscopies (Dunning et al. 1985) and to surface studies (Netzer and Matthew 1986).

3.2. *Outer level spectroscopies: photoemission and inverse photoemission*

The photoemission techniques (PE: fig. 3a, b, c,) are based on the observation of the energy and intensity distribution of the electrons emitted by a sample irradiated by a monochromatic photon source. The spectra are then interpreted in terms of electronic transitions resulting from the annihilation of these photons of known energy. The photoemission methods can be devided into two broad categories defined by the photon energy range: ultraviolet photoemission (UPS) for $h\nu < 100\,\text{eV}$ and X-ray photoemission spectroscopy (XPS) for $h\nu \approx 1200$–$1500\,\text{eV}$.

This division has been historically determined by the existing photon sources but meanwhile the access to synchroton light sources has filled the gap between these two ranges. It is still meaningful within a single-particle approach to consider separately the situations encountered for high and low photon energies. In addition

to the energy conservation, the photoemission process in solids must obey k-vector conservation, which means that only vertical transitions are allowed in a reduced Brillouin zone scheme. The important consequence in the low-energy limit is that UPS probes restricted regions of the Brillouin zone determined by energy and momentum conservation. In the most common UPS experiment (fig. 3a), the sample is exposed to monoenergetic photon sources and the energy distribution curves (EDC's) of the emitted electrons are recorded. These are clearly related to the joint density of states where initial and final states are on an equal footing and both contribute to the observed spectral feature. The continuous nature of synchrotron radiation allows a decoupling of initial and final density of states and a determination of the symmetries of the investigated DOS. These spectroscopies can be conveniently described in the language of fig. 3: if the free electron final state is kept constant (PE(CFS): fig. 3b) and the photon energy is varied, this technique probes essentially the excited many-body states, whereas if both, photon energies and energies of the emitted electrons are varied simultaneously by the same amount (PE(CIS): fig. 3c) the spectrum reflects the single-particle DOS above the vacuum level E_V. In particular situations, when the photon energy is swept through the threshold excitation energy of a core level, the observed intensity of the outermost states may show a resonant behaviour (resonant photoemission) which can be used to determine the symmetry character of these states (see section 4.5.).

The k-vector orientation of the emitted electron in vacuum can also be measured (angle resolved photoemission). For a single crystal of known orientation, the total momentum conservation determines, inside the solid, the final-state k vector which cannot be extracted completely unambiguously from the measurement as a consequence of the escape process at the surface.

The use of polarized light allows one to determine the polarity of the states with respect to a mirror plane by exploiting the symmetry selection rules for different polarizations. Moreover atomic-like symmetry (l) of band states can be identified by typical cross-section dependences (see fig. 6, section 4) as a function of the photon energy and polarization.

In addition to the energy, symmetry and momentum, the spin orientation of the initial states from which the electrons are excited can also be measured in a photoemission experiment (Siegmann 1975, Celotta et al. 1979, Kisker et al. 1980). Spin-polarized angle resolved UPS spectra allow one to determine the spin-dependent energy dispersion relations which are the most detailed information about the electronic states that one can hope to obtain by this technique.

The photon energy has to be increased, probably to as high as 100 eV, to be sure that the final state is correctly approximated by free-electron state with a smooth DOS no longer contributing to the structures in the photoemission spectra. With increasing photon energy the accessible final states are distributed rather homogeneously in the reciprocal space so that the influence of the k-vector conservation is weaker and gradually the whole Brillouin zone contributes to the observed intensity. In X-ray photoemission spectroscopy (XPS, $h\nu \approx 1500$ eV) a high-energy regime is undoubtedly reached allowing us to simply interpret the valence band spectra as a superposition of the different l-projected DOS, weighted by the appropriate cross sections. It must be emphasized, however, that increasing correlation of the outer

electrons up to the localization limit leads to a breakdown of this simple one-electron picture (see section 2).

When the electrons of a monoenergetic external beam penetrate into a sample, their interaction with the potential of the solid induces decay transitions to lower unoccupied states with emission of photons which are analyzed (fig. 3d, e, f, single-particle energy), the system being left in an excited state (fig. 3d, e, f, total energy). This type of spectrosocpy is called inverse photoemission (IPE), also bremsstrahlung isochromat spectroscopy (BIS) or short wavelength limit (SWL) (fig. 3e). It represents the most direct method for probing the empty states straight above the Fermi energy. Excepting the usual screening mechanism of the additional charge, the rest of the electronic system remains passive in such processes. The most important factors determining the probability of this type of transitions are the density of the low-lying empty states and the corresponding matrix elements. The intensity of the emitted bremsstrahlung can be considered as a measure of the final states above E_F. The interpretation of this process as an inverse photoemission process is obvious (compare figs. 3a and 3e) and at E_F these two transitions are even perfectly identical. The analogy between PE and IPE can be pursued further. At high energies the corresponding techniques are XPS and BIS. In the UV range the choice of the parameters becomes as important as in UPS, making possible the use of CIS and CFS techniques. If the direction and spin polarization of the incident electrons are well defined, the investigation of spin-dependent dispersions of unoccupied bands becomes accessible (Unguris et al. 1982, Scheidt et al. 1983).

3.3. *Core level spectroscopies*

Any technique based on transitions involving core levels (figs. 4a–f) will be considered here as a core level spectroscopy even if the emphasis of the interpretation is not on the core levels. In principle all these methods allow one to determine the binding energies of the deep levels or energy differences between them. Since these quantities are characteristic for all atoms in the periodic table, their measurement yields a straightforward chemical analysis of the sample region probed by the considered technique. Beyond the simplest analytical aspect of core level spectroscopies, the chemical shifts of the binding energies associated with the reorganization of the outer charges in the solid offer a powerful tool for investigating the nature of bonds.

In figs. 4a–f the excitation of the deep core level is depicted by the corresponding total energy of the hole state. The total energies of the final states resulting from recombination processes involving the outer occupied states are indicated schematically for soft-X-ray emission and Auger electron emission (SXE: figs. 4a, b; AES: figs. 4a, c) where in the latter the sum of the two-hole final state has to be considered. The total energies involved in the population increase in the outer unoccupied levels in the presence of a core hole are symbolically indicated for soft-X-ray absorption and electron energy loss spectroscopy (SXA: fig. 4e; EELS: fig. 4f). X-ray photoemission of core levels (XPS: fig. 4d) is the most direct technique to specifically probe deep levels, since the high-energy final state (single-particle energy in fig. 4) far above E_F can be considered as free-electron like.

Only in the simplest case, when the outermost states form broad bands, the threshold energies of X-ray emission and absorption bands can be identified with core level binding energies. In these situations the overall band shapes are usually interpreted as *l*-projected densities of the occupied (fig. 4b) or empty (fig. 4e) states selected by the dipole matrix elements compatible with the core level symmetry. In fact, EELS (fig. 4f) at very high energy (of the order of 100 keV) and very low momentum transfer is equivalent to SXA and obeys the same selection rules. The variation of the momentum transfer and/or the decrease of the primary electrons energy remove this limitation to the dipole selection rules (see section 4.4). In general, EELS core excitation spectra are expected to reflect aspects of the unoccupied DOS and in simple cases the threshold energies yield in principle the corresponding core level binding energies.

However, the identification of the observed threshold energies with the core level binding energies is not always unambiguous. Only an adiabatic transition would yield the energy corresponding to the definition of the binding energy (eq. (3)). Undoubtedly the transitions considered here have a sudden character constraining the final state to be a combination of all eigenstates and, for example, XPS core excitations in heavy lanthanides do not display at all adiabatic transitions. In many cases the adiabatic limit is still observed, since the lowest final states have a dominant weight in the spectra. A typical example of this situation is given by the XPS core level lines of simple metals, which reveal the electron–hole pair density of the extended states excited in the screening mechanism of the core holes. The resulting asymmetric lineshapes are very accurately described by the Doniach–Sunjic (Doniach and Sunjic 1970) analytic form (Wertheim and Citrin 1978). The adiabatic limit can be extracted by analyzing the Lorentzian shape of the low-binding energy flank of these lines.

Beyond these simple manifestations of many-body excitations of the extended states, the strong interaction between deep holes and open and highly correlated outer shells gives rise to complex multiplet (see section 4) and satellite structure in the spectra. So far only in the simple cases of the light lanthanide solids detailed many-body formalisms yield a full understanding of these phenomena (see section 6).

Finally one should be aware that the interpretation of electron spectroscopic results for insulating samples raises the very difficult question of the nature of the screening. Our ignorance of the exact screening mechanism in insulators should make us cautious in the analysis of binding energies and chemical shifts, particularly when metallic and insulating systems are compared (see section 6.2.1).

3.4. *Surface sensitivity and experimental conditions*

In the electron spectroscopies it is the moderate kinetic energy of the incident or emitted electrons involved in the transitions which determines the surface sensitivity of the method. The important parameter is the inelastic mean free path which for many different materials has the same order of magnitude and a similar energy dependence (Ertl and Küppers 1974). At the vacuum level it is of the order of 50 Å, it

decreases abruptly down to a minimum value of less than 10 Å somewhere between 50 and 200 eV and increases then slowly towards higher energies. The important consequence is that the PE and IPE spectra recorded at moderate energies account only for a few atomic layers at the sample surface (see section 5).

SXE can also be excited by photons (fig. 4a), in which case the thickness of the investigated surface depth is increased by a few orders of magnitude. Conventional SXA of thin samples has in practice no surface sensitivity when compared to the other methods. The detection of the photon absorption can also be performed by measuring the yield of the emitted electrons so that the surface sensitivity may even be very high if the electrons are selected in a narrow energy window at low kinetic energy (partial yield spectroscopy).

The high surface sensitivity of the electron spectroscopies requires preparation of atomically clean sample surfaces in situ, i.e. in the vacuum vessel where the spectroscopic measurement is performed. Ultra-high vacuum better than 10^{-10} Torr is a further condition which must be satisfied in order to keep the contamination below the limit of detection during the data accumulation. Very thin polycrystalline films deposited by evaporation on conducting substrates are suitable for many electron spectroscopies. The surface of bulk samples introduced in the instruments from a poor vacuum or an inert atmosphere needs to be cleaned. The easiest and most common method is to produce in situ by some mechanical action (scraping, filing, cutting, fracturing) a new surface. These methods obviously disturb deeply the crystalline state of the sample surface and are only suitable for spectroscopies which do not depend on the crystalline orientation. For techniques requiring oriented crystal faces (e.g. angle resolved photoemission) single crystals are usually cleaved, but this is only possible for particular planes of crystals in which the bond has a sufficiently high ionic character. Since single crystals of good metals cannot be cleaved, they are usually cut parallel to a particular plane, electropolished and then cycles of ion bombardment and heat treatments are performed in order to get rid of the contamination and to restore the crystalline state at the surface.

4. Atomic aspects of the 4f states in solids

4.1. *Characterization of the 4f states in solids*

The striking properties observed in many solids containing lanthanide elements originate always from the presence of an open 4f shell keeping largely its atomic character. The localization of the 4f charge inside the mean orbit of the 5s, 5p, 5d and 6s shells is pronounced as illustrated in fig. 1 of section 1, but as a consequence of their very low binding energies, the 4f states remain in principle available for the formation of bonds. It is the key problem in lanthanide studies to investigate which one of the atomic or bonding character dominates and how far they can coexist. In solids the 5d states are forming bands and they determine the atomic radii r_a which remain constant within a few per cent for all trivalent lanthanides. Since one of the important factors determining the strength of a bond is the wave function overlap of

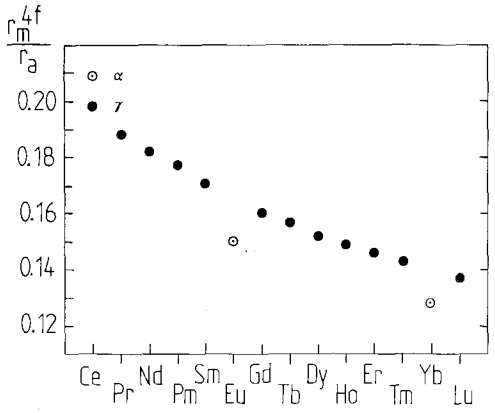

Fig. 5. Systematic behaviour (Hill plot) of the 4f radial wave function maxima r_m^{4f} interpolated from the tables of Herman and Skillmann (1963) and normalized to their atomic radii r_a.

neighbour atoms, in fig. 1 the 4f radial charge of a nearest neighbour in Gd metal has been sketched. It appears clearly that the 4f–4f overlap is practically negligible when compared to the 4f–5d overlap (the smooth spherical distribution of the s states makes them not suitable for hybridization with 4f states). The well-known decrease of the 4f-orbit dimensions (lanthanide contraction) along the lanthanide series results from the inefficiency of the mutual screening of the atomic potential among electrons belonging to the same shell. This systematic contraction in the pure metals is shown in fig. 5 as a plot of the ratio r_m^{4f}/r_a (Hill plot) which scales the 4f wave function extension to the typical radii of the lanthanide atoms in solids. From Ce to Lu this ratio decreases by 30% so that one has to look for sizable hybridization effects mainly in the light elements. The hybridization strength between 4f and band states varies very fast with this ratio but it needs to be calculated for each case since it depends also on the symmetry of the available states and on the arrangement and number of the neighbour atoms. As a first approximation one can assume that in solids the energy eigenvalues of the atomic 4f states are only shifted by their Coulomb interaction with the band states. This approach neglects completely any mixing of the 4f wave function with states of other symmetries so that the concomitant charge reorganization minimizing the total energy of the system is ignored. For a band calculation this approximation means that the presence of the 4f electrons is accounted for by including them in the construction of the ionic potential. The drawback of this simplification is that no information concerning their energy can be obtained. If one is mainly interested in the 4f states, one can take advantage of their localized character by using the renormalized atom scheme involving simply one Wigner–Seitz cell. This will be the point of view adopted in this section which has the aim to describe only situations where the hybridization effects can be neglected. The spectroscopic manifestations of the 4f states are then expected to reflect the purely atomic-like character of a f shell occupied by an integral number of electrons.

4.2. *Population changes within an atomic-like 4f shell*

The most straightforward method of studying the 4f states of an open shell

consists in inducing directly a 4f population increase or decrease by photoemission or inverse photoemission, respectively. In the spectra, the structures originating from 4f and band states appear often in the same energy range and it is not always easy to make the distinction between these two types of excitation. Localized states have a negligible dispersion and yield generally narrow peaks, unless the final-state lifetime becomes too important or close multiplet structures cannot be resolved. On the other hand, the band spectra contain also sharp structures so that one needs some other characteristic behaviour to separate these two contributions. The simplest symptom commonly invoked to recognize transitions involving direct 4f population changes in photoemission and inverse photoemission is based on the energy dependence of the single-particle photoelectric cross-sections for the different symmetries. For a qualitative discussion, the atomic cross-sections calculated in the dipole approximation are usually considered. This is certainly correct for 4f states but may become questionable at low energy for Bloch states. As an example, fig. 6 shows the atomic cross-section ratios $\sigma(\mathrm{Ce}\,4f^1)/\sigma(\mathrm{Sb}\,5p^6)$ and $\sigma(\mathrm{Ce}\,4f^1)/\sigma(\mathrm{Ta}\,5d^1)$ taken from the calculations of Goldberg et al. (1981). These two typical cases illustrate the quite general fact that at low photon energies the 4f cross-section increases much faster than those for other symmetries. The origin of the delayed 4f cross-section onset can be simply explained: for $l \to l+1$ transitions the 4f wave function has a very weak overlap with the ε_g wave function which is pushed away from the atom by the very high effective potential, for $l \to l-1$ transitions the

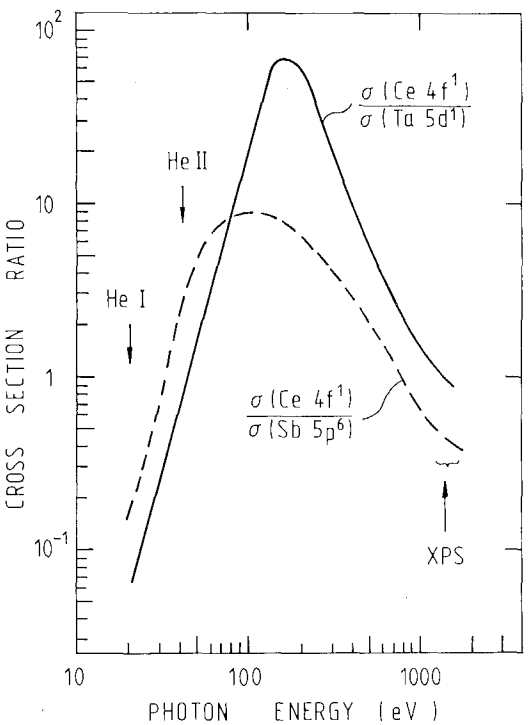

Fig. 6. Energy dependence of two typical atomic cross-section ratios calculated from the tabulated values of Goldberg et al. (1981).

already fast oscillations of the ε_d wave function give rise to an important cancellation of the matrix element (Fano and Cooper 1968, Brodén et al. 1973). The exceptionally steep increase of $\sigma(\mathrm{Ce}\,4f^1)$ with photon energy is due to the penetration of the ε_g wave function closer to the nucleus until its nodes set a limit to the overlap integral of the matrix element. Already by measuring with the two commonly available resonance lines He I and He II, the variation of the cross-section ratios is sufficiently large to allow a straightforward identification of the 4f character (fig. 6). When synchrotron radiation is used it is possible to follow continuously the intensity ratio of the structures originating from states with different symmetries. However, the single-particle cross-sections considered here cannot account for the huge resonances observed when the photons reach the threshold energies for core level excitations. These phenomena are discussed in section 4.5.

In order to sort out the different problems encountered in excitations of atomic-like 4f states, we shall assume at first that the intra-atomic couplings originating from the angular dependence of the 4f charge distribution and from the electron spin are not taken into consideration. With this simplification, all electrons of this shell are equivalent and each population gives rise only to a single total energy. Even in this atomic approach of 4f shells in solids, the energy required for a population change is deeply influenced by the band states in which they are embedded. The renormalized-atom scheme has been developed to account for this situation (Herbst et al. 1972, 1976, 1978, and chapter 68 of this book). In this approximation the problem is limited to the Wigner–Seitz cell where the 4f wave functions are renormalized and an atomic-like calculation is performed. Changes in correlation and exchange energies are taken into account on passing from free to renormalized atom. The decisive advantage of this scheme is that its local character offers a simple possibility to simulate the final states resulting from any 4f population change. The basic assumption which need to be made in metals is that a complete screening of the induced 4f charge occurs at E_F inside the Wigner–Seitz cell. The important achievements of this scheme are to demonstrate the complete breakdown of the Koopmans approximation for 4f excitations and to provide for them reliable computed values. The relevant quantities extracted from the photoemission and inverse photoemission spectra $S(E)$ are the energies $\Delta_-(f^n \rightarrow f^{n-1})$ and $\Delta_+(f^n \rightarrow f^{n+1})$ which are visualized in fig. 7. The same spectra display also the usual band state excitations which can be interpreted as single-particle DOS. The assumption of the screening of the f^{n+1} and f^{n-1} final states by a charge transfer at E_F allows us to decompose the processes into two steps showing that the positions of the f peaks referenced to E_F are the minimum many-electron energies Δ_- and Δ_+ required to modify the population of the atomic like shell. This picture is in fact a simple specialisation of the general processes shown in fig. 3, the only difference is that the total energy scales of XPS and BIS have opposite directions in order to be consistent with the traditional single-particle DOS which is continuous across the Fermi energy (see also fig. 19 in section 6.1.). It is important to keep in mind that Δ_- and Δ_+ are total energy differences which have no meaning in the single-particle language. Finally the intra-atomic Coulomb energy U_{ff}, defined as the minimum energy difference involved in the population change $4f^n + 4f^n \rightarrow 4f^{n-1} + 4f^{n+1}$ of

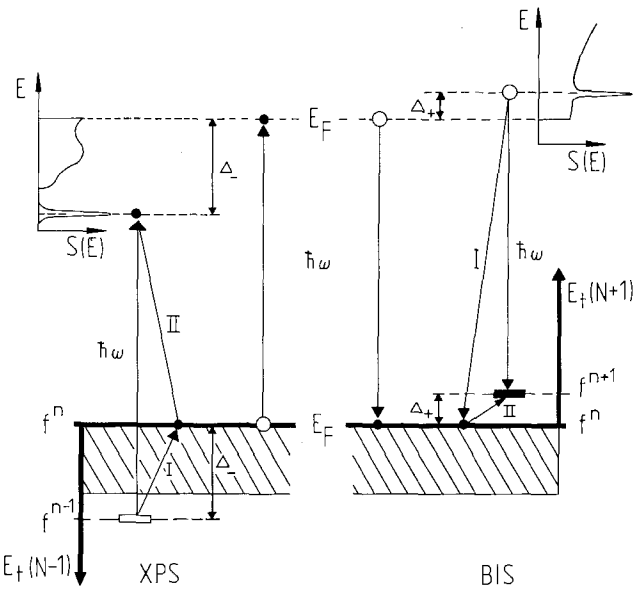

Fig. 7. Schematic representation of XPS and BIS processes in a metal containing an open and atomic-like $4f^n$ shell. The decompositions of the 4f excitations into two steps show how the corresponding energies Δ_- and Δ_+ are related to the position of E_F observed in the experimental spectra $S(E)$. This representation is equivalent to the one given in fig. 3a and e but it provides more details. The total energy scales $E_t(n+1)$ and $E_t(n-1)$ have opposite directions as illustrated more explicitely in fig. 19a.

two non-interacting atoms, can just be obtained from the representation of fig. 7 as $U_{ff} = \Delta_+ + \Delta_-$. In insulators the absence of free charge carriers for the final state screening obscures somewhat the interpretation of these different excitation energies. This problem will be discussed in section 6.2.1 (Baer et al. 1987).

When our unrealistic assumption of spherical symmetry for the charge distribution of 4f electrons without spin is removed, each population of this open shell gives rise to a large number of nonequivalent states with different total energies (multiplets). This is a classical problem of atomic physics which will only be sketched here in order to define the concepts used in the analysis of the spectra. The different quantum number sets characterizing the states of f^N, f^{N-1} and f^1 will be simply labelled Ω^N, Ω^{N-1} and Ω^1, respectively. Any state of a population N and in particular the ground state $|\Omega^N\rangle$ can be expressed in a unique manner on a basis set of wave functions having the correct spin and symmetry properties by choosing suitable linear combinations of $|f^{N-1}\rangle|f^1\rangle$ wave functions. For the sake of simplicity we shall write symbolically this development as

$$|\Omega^N\rangle = \sum_{\Omega^{N-1},\Omega^1} Q(\Omega^N,\Omega^{N-1},\Omega^1)|\Omega^{N-1}\rangle|\Omega^1\rangle. \tag{12}$$

The weight of the different parent terms $|\Omega^{N-1}\rangle$ in the ground state wave function is given by the coefficients of fractional parentage (cfp) Q. When the sudden approx-

imation (section 2.3) is applied to describe the photoemission of an atomic-like 4f shell, it appears immediately that the parent terms are the symmetry-allowed final states and that their intensities in a spectrum are given by the squared cfp (Cox 1975). These coefficients calculated in the *LS* coupling scheme have been tabulated by Nielson and Koster (1964) and they have been used with success to analyze the 4f spectra of the metals (Lang et al. 1981). However, in the second half of the lanthanide series, the spin–orbit interaction becomes more important and the cfp calculated with the intermediate coupling scheme (Gerken 1983) provide a better fit to the data. Figure 8 shows this type of analysis for the XPS spectra of all the pure metals. In order to display also the configurations $4f^6$ and $4f^{13}$ the spectra of Eu^{3+} (only theory) and YbP (Wuilloud et al. 1986) have been added to this collection. The *LS* coupling scheme used in the original analysis has been replaced by the intermediate coupling scheme for f^8 to f^{12}, further details on the fitting procedure and adjustments necessary in solids can be found in the papers quoted previously.

The BIS process is very similar to the XPS process when it is expressed in the language of holes in an atomic shell. Taking advantage of this analogy, it is a simple matter to transform the previous formalism and to calculate the cfp for 4f inverse photoemission (Cox et al. 1981). This work has only been performed within the *LS* coupling scheme but it is not a serious drawback since the experimental peaks are broader in BIS than in XPS as a consequence of the shorter lifetime and the more important instrumental broadening. Figure 8 demonstrates the success of this approach for BIS (Lang et al. 1981, Laubschat et al. 1984). Since these cfp have never been listed in previous publications, we give them in table 1. Once the validity of this approach to atomic 4f excitations in solids is established, it becomes a very useful tool for identifying the ground state population of 4f shells.

When the multiplets are taken into account, one has to refine the previous definitions of Δ_-, Δ_+ and U_{ff} which are now the energy differences between the lowest states of the relevant 4f populations. For this reason a careful analysis of the spectra with the cfp is important in order to extract accurately these quantities from the experimental data. Their systematic behaviour in the pure metals is represented in fig. 9 together with the renormalized-atom predictions which trace faithfully the experimental values. Born–Haber cycles have also been used to derive these promotion energies in solids from thermochemical and optical data (see chapter 69 in this volume). As shown in fig. 9 the agreement between these different values is quite satisfactory. The stability of half-filled and full shells is the mechanism responsible for the divalence of Eu and Yb metals. For the trivalent metals the jump of Δ_- and Δ_+ reflects the large increase of the exchange energy from the $4f^7$ to the $4f^8$ configuration. The 4f states of Ce which can no longer be considered as atomic-like will be the main subject of sections 6 and 7. In compounds, the chemical bond can stabilize another configuration in elements like Sm, Eu, Tm and Yb where a population change requires only a modest energy increase. As discussed in section 5, the perturbation associated with the surface can also be responsible for such population modifications.

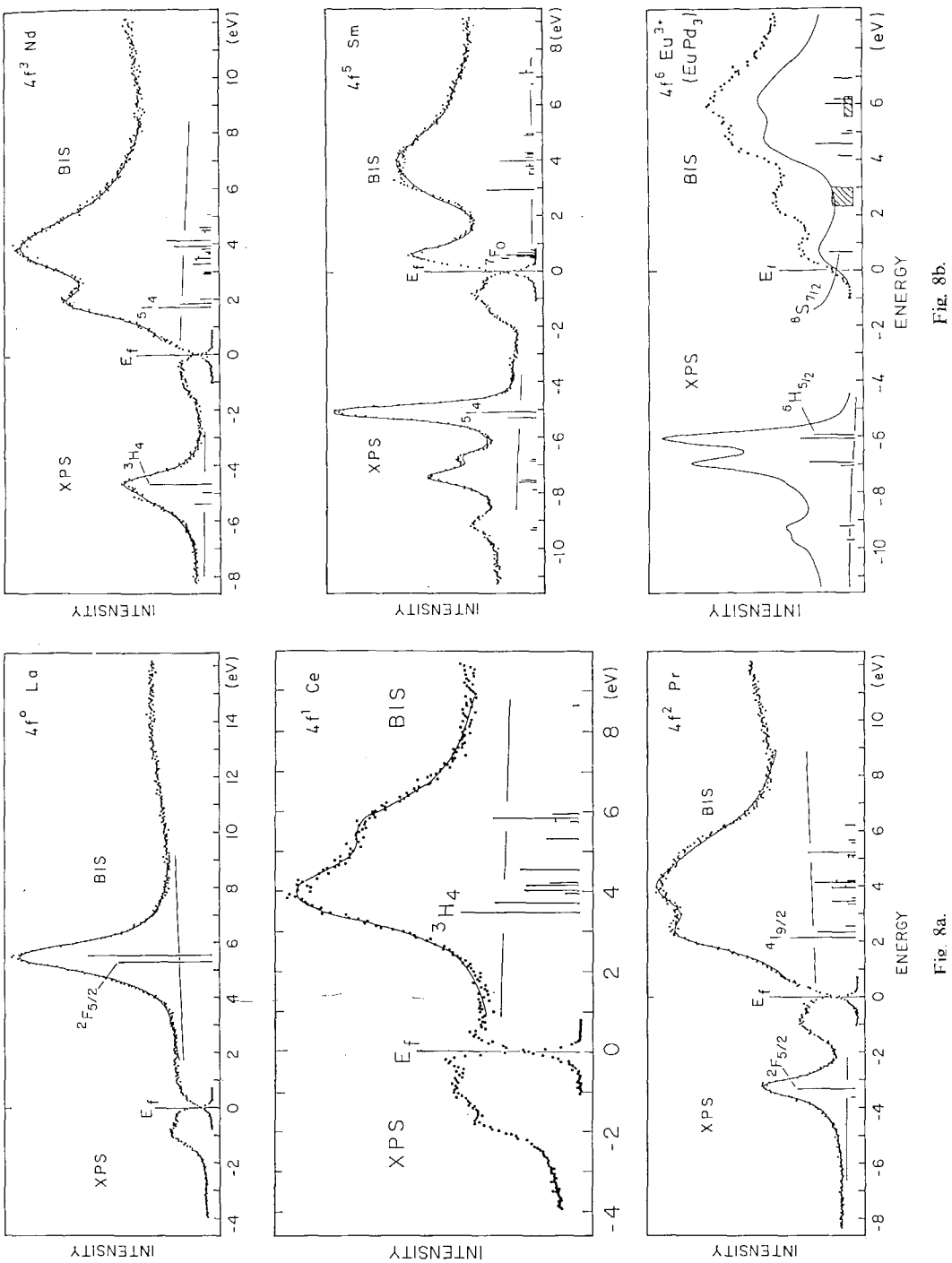
4f⁰ La
4f¹ Ce
4f² Pr
4f³ Nd
4f⁵ Sm
4f⁶ Eu³⁺ (EuPd₃)
XPS
BIS
E_f
²F5/2
³H4
⁴I9/2
⁵I4
⁷F0
⁶H5/2
⁸S7/2
INTENSITY
ENERGY
(eV)

Fig. 8a.

Fig. 8b.

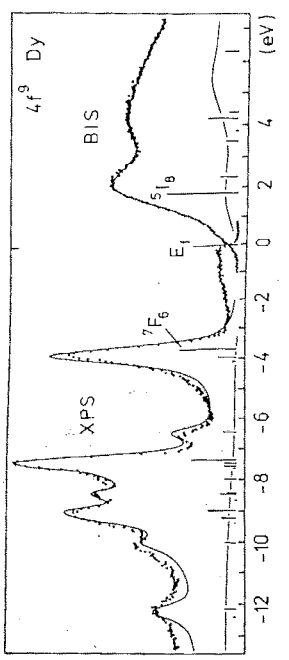
4f9 Dy
XPS
BIS
7F6
5I8
Ef
INTENSITY
(eV)

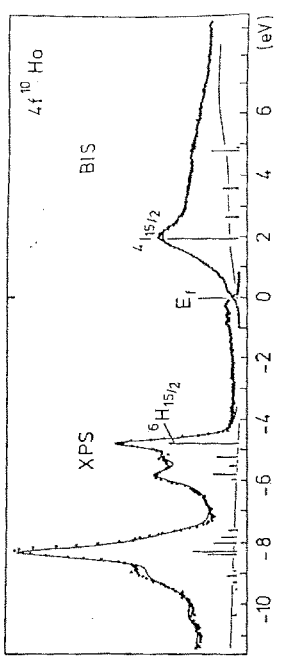
4f10 Ho
XPS
BIS
6H15/2
4I15/2
Ef
INTENSITY
(eV)

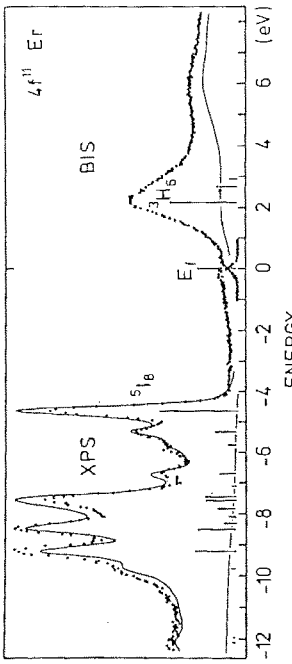
4f11 Er
XPS
BIS
5I8
3H6
Ef
INTENSITY
ENERGY
(eV)

Fig. 8d.

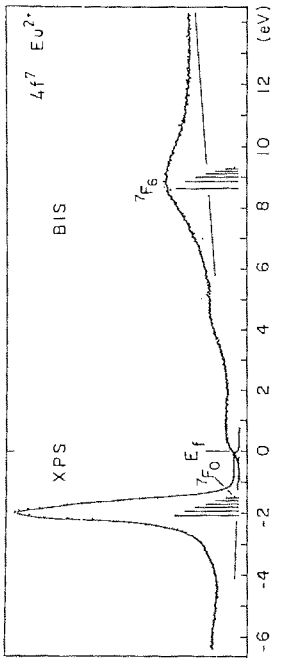
4f7 Eu2+
XPS
BIS
7F6
7F0
Ef
INTENSITY
(eV)

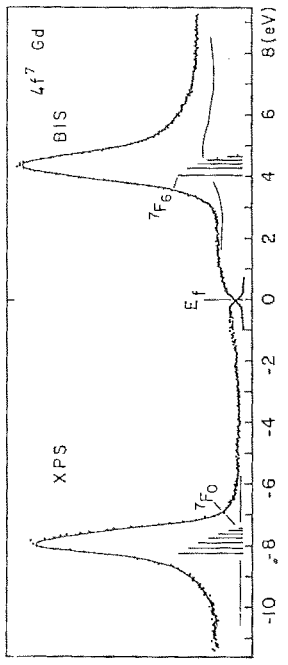
4f7 Gd
XPS
BIS
7F6
7F0
Ef
INTENSITY
8(eV)

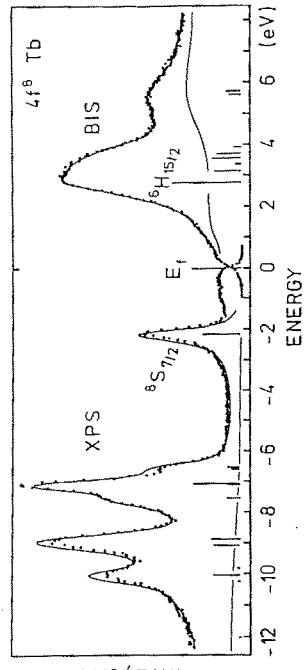
4f8 Tb
XPS
BIS
8S7/2
6H15/2
Ef
INTENSITY
ENERGY
(eV)

Fig. 8c.

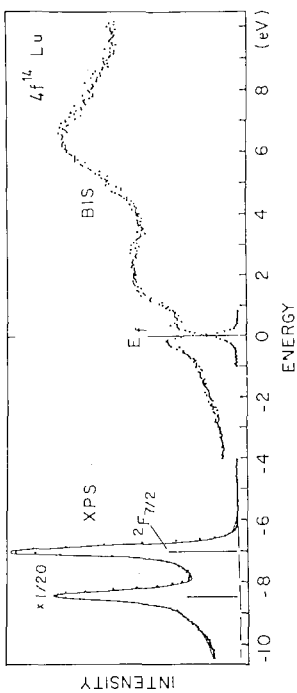

Fig. f.

Fig. 8. Atomic-like analysis of XPS and BIS spectra for all $4f^n$ initial states. The spectra of the pure metals are taken from Lang et al. (1981), the spectra of YbP from Wuilloud et al. (1986) and the BIS spectrum of $EuPd_3$ from Laubschat et al. (1984). The coefficients of fractional parentage shown as vertical bars have been calculated in the *LS* coupling scheme (Nielson and Koster 1964, Cox et al. 1981), except for the XPS process from the initial configurations f^8 to f^{13} where the intermediate coupling scheme has been used (Gerken 1983). The particular situation met in Ce is discussed in sections 6 and 7.

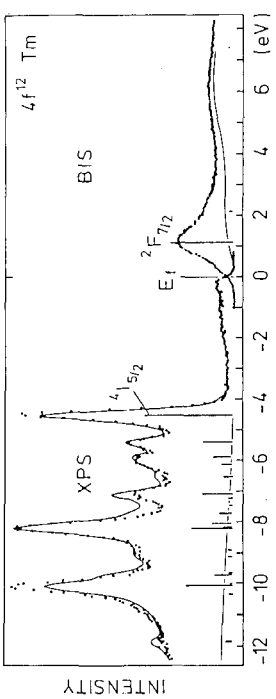

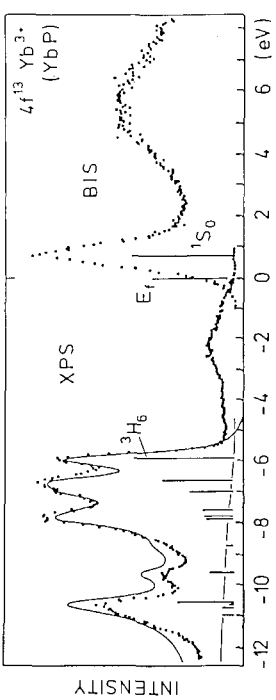

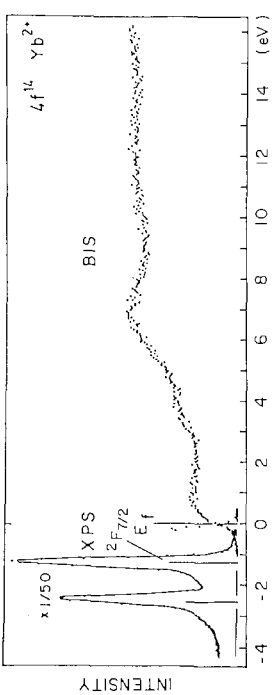

Fig. 8e.

4.3. *Reaction of an atomic-like 4f shell to the creation of a core hole*

When a deep core electron is emitted from a lanthanide atom in a XPS process, the 4f shell, assumed to remain purely atomic-like, suffers a nearly instantaneous potential change. As a consequence of the sudden approximation, the integral 4f population cannot be modified in this transition. The final state must be expressed as a distribution of eigenstates resulting from the coupling of the hole with the incomplete 4f shell. This mechanism gives rise to complicated multiplet structures in XPS core level spectra. The most spectacular examples are observed for the emission of 4d states which have orbit dimensions similar to those of the 4f states. Figure 10 shows the 4d XPS spectrum of Eu offering a nontrivial but sufficiently simple situation to be analyzed on the basis of a calculation (Kowalczyk et al. 1974). For

TABLE 1

Intensities (Intens.) of the final states ($S'L'J'$) of the configuration $4f^{n+1}$ arising from electron addition to the initial state (SLJ) of $4f^n$, normalized to $(14 - n)$. The intensities of the multiplets J' are calculated within the Russel–Saunders (LS) coupling scheme. Only multiplet components with normalized intensity $\geqslant 0.1$ are listed. The relative energies E are obtained from UV-absorption data (Carnall et al. 1968, Crosswhite et al. 1969). The states are listed in the order of increasing energy.

Transition from $4f^0$ to $4f^1$

La^{3+}: Initial state $^1S_0$

Final states				
$S'L'$	Intens.	J'	E(eV)	Intens.
^2F	14	5/2	0.0	6
		7/2	0.282	8

Transition from $4f^1$ to $4f^2$

Ce^{3+}: Initial state $^2F_{5/2}$

Final states				
$S'L'$	Intens.	J'	E(eV)	Intens.
^3H	4.714	4	0.0	2.571
		5	0.258	1.833
		6	0.527	0.310
^3F	3.000	2	0.608	1.190
		3	0.780	1.167
		4	0.834	0.643
^1G	1.286	4	1.195	1.286
^1D	0.714	2	2.057	0.714
^3P	1.286	0	2.537	0.191
		1	2.614	0.500
^1I	1.857	6	2.635	1.857
^3P		2	2.764	0.595
^1S	0.143	0	5.784	0.143

Transition from $4f^2$ to $4f^3$

Pr^{3+}: Initial state $^3H_4$

Final states				
$S'L'$	Intens.	J'	E(eV)	Intens.
^4I	3.677	9/2	0.0	2.100
		11/2	0.232	1.227
		13/2	0.480	0.339
^4F	0.667	3/2	1.413	0.280
		5/2	1.543	0.253
^2H	1.000	9/2	1.563	0.757
^4F		7/2	1.653	0.122
^4G	1.688	5/2	2.112	0.784
^2G	0.396	7/2	2.133	0.316
^2K	1.364	13/2	2.342	1.309
^4G		7/2	2.352	0.606
		9/2	2.407	0.274
^4D	0.635	3/2	3.494	0.279
		5/2	3.514	0.111
^2I	0.263	11/2	3.533	0.243
^4D		1/2	3.566	0.233
^2L	1.545	15/2	3.612	1.545
^2H		9/2	4.022	0.134
^2D	0.296	3/2	4.135	0.221
^2F	0.470	5/2	4.758	0.347

TABLE 1 (cont.)

Transition from $4f^3$ to $4f^4$

Nd^{3+}: Initial state $^4I_{9/2}$

		Final states		
$S'L'$	Intens.	J'	E(eV)	Intens.
^5I	3.182	4	0.0	1.713
		5	0.183	1.041
		6	0.383	0.391
^5F	0.625	1	1.525	0.279
		2	1.576	0.243
^3K	1.154	6	1.956	0.619
^3H	0.846	4	2.136	0.507
^5G	1.193	2	2.202	0.548
		3	2.251	0.422
^3H		5	2.420	0.114
^5G		4	2.490	0.192
^3G	0.454	3	2.604	0.340
^3L	1.307	7	2.761	1.225
^3M	1.462	8	3.021	1.462
^3I	0.364	5	3.449	0.222
^3F	0.414	2	3.483	0.330
^3K		6	3.633	0.400
^3H		4	4.196	0.113

Transition from $4f^4$ to $4f^5$

Pm^{3+}: Initial state $^5I_4$

		Final states		
$S'L'$	Intens.	J'	E(eV)	Intens.
^6H	2.800	5/2	0.0	1.170
		7/2	0.128	0.978
		9/2	0.278	0.535
		11/2	0.444	0.111
^6F	0.800	1/2	0.787	0.275
		3/2	0.818	0.319
		5/2	0.878	0.164
^4G	0.692	5/2	2.217	0.347
^4F	0.405	3/2	2.329	0.288
^4G		7/2	2.476	0.139
^4I	1.000	9/2	2.539	0.390
^4M	1.462	15/2	2.552	1.462
^4I		11/2	2.610	0.123
^4L	1.307	13/2	3.039	1.176
^4K	1.154	11/2	3.116	0.781
^4L		15/2	3.173	0.131
^4K		13/2	3.338	0.171
^4G		5/2	3.742	0.103
^4I		9/2	4.393	0.194
^4H	0.379	7/2	5.164	0.199
^4K		11/2	5.460	0.160
^4I		9/2	7.686	0.163

Transition from $4f^5$ to $4f^6$

Sm^{3+}: Initial state $^6H_{5/2}$

		Final states		
$S'L'$	Intens.	J'	E(eV)	Intens.
^7F	2.333	0	0.0	0.150
		1	0.047	0.589
		2	0.130	0.909
		3	0.237	0.553
		4	0.359	0.123
^5L	1.545	6	3.150	1.545
^5H	1.000	3	3.830	0.180
		4	3.882	0.148
^5F	0.303	2	4.111	0.126
^5I	1.182	4	4.202	0.280
		5	4.265	0.147
^5K	1.364	5	4.496	1.091
		6	4.647	0.273
^5G	0.817	2	4.802	0.241
		3	4.869	0.271
^5H		3	5.671	0.325
		4	5.723	0.266
^5D	0.454	1	8.036	0.116
^5I		4	8.538	0.472
		5	8.601	0.247

Transition from $4f^6$ to $4f^7$

Eu^{3+}: Initial state $^7F_0$

		Final states		
$S'L'$	Intens.	J'	E(eV)	Intens.
^8S	1.143	7/2	0.0	1.143
^6P	0.429	5/2	4.065	0.409
^6I	1.857	7/2	4.454	1.857
^6D	0.714	7/2	5.054	0.102
		5/2	5.095	0.612
^6G	1.286	7/2	6.103	0.612
		5/2	6.172	0.674
^6F	1.000	5/2	6.798	0.714
		7/2	6.812	0.286
^6H	1.571	5/2	7.106	0.449
		7/2	7.228	1.122

TABLE 1 (cont.)

Transition from $4f^7$ to $4f^8$

Gd^{3+}: Initial state $^8S_{7/2}$

	Final states			
$S'L'$	Intens.	J'	E(eV)	Intens.
^7F	7.000	6	0.0	1.857
		5	0.253	1.571
		4	0.409	1.286
		3	0.529	1.000
		2	0.614	0.714
		1	0.670	0.429
		0	0.698	0.143

Transition from $4f^8$ to $4f^9$

Tb^{3+}: Initial state $^7F_6$

	Final states			
$S'L'$	Intens.	J'	E(eV)	Intens.
^6H	3.143	15/2	0.0	2.061
		13/2	0.430	0.849
		11/2	0.718	0.202
^6F	2.000	11/2	0.953	0.919
		9/2	1.122	0.766
		7/2	1.362	0.275
^6P	0.857	7/2	3.405	0.398
		5/2	3.535	0.459

Transition from $4f^9$ to $4f^{10}$

Dy^{3+}: Initial state $^6H_{15/2}$

	Final states			
$S'L'$	Intens.	J'	E(eV)	Intens.
^5I	2.758	8	0.0	2.130
		7	0.624	0.561
^5F	0.500	5	1.914	0.400
		4	2.298	0.100
^5G	1.266	6	2.729	0.936
		5	2.952	0.303
^5D	0.476	4	5.139	0.476

Transition from $4f^{10}$ to $4f^{11}$

Ho^{3+}: Initial state $^5I_8$

	Final states			
$S'L'$	Intens.	J'	E(eV)	Intens.
^4I	2.545	15/2	0.0	2.129
		13/2	0.805	0.329
^4F	0.500	9/2	1.877	0.500
^4G	0.955	11/2	3.271	0.843
		9/2	3.393	0.112

Transition from $4f^{11}$ to $4f^{12}$

Er^{3+}: Initial state $^4I_{15/2}$

	Final states			
$S'L'$	Intens.	J'	E(eV)	Intens.
^3H	2.333	6	0.0	2.060
^3F	0.667	4	0.695	0.667
^3H		5	1.015	0.267

Transition from $4f^{12}$ to $4f^{13}$

Tm^{3+}: Initial state $^3H_6$

	Final states			
$S'L'$	Intens.	J'	E(eV)	Intens.
^2F	2.000	7/2	0.0	1.857
		5/2	1.234	0.143

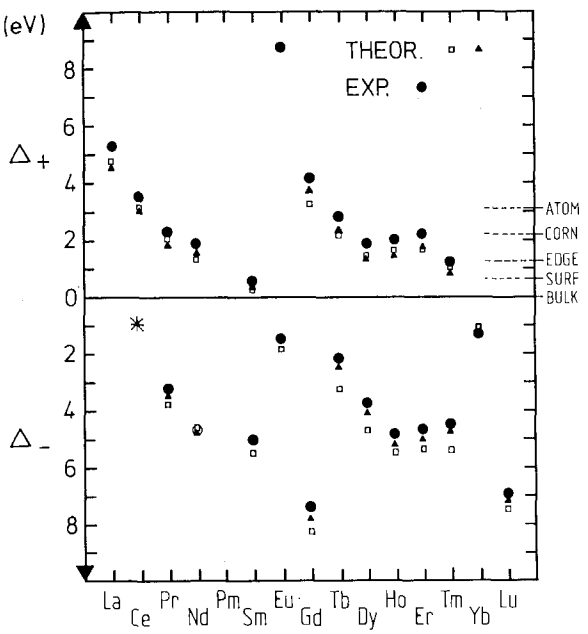

Fig. 9. Comparison of experimental and calculated minimum energies Δ_- and Δ_+ required to modify the 4f population in the pure lanthanide metals. *Circles*: values from combined XPS–BIS spectra (Lang et al. 1981). *Squares*: renormalized atom calculations (Herbst et al. 1976, 1978). *Triangles*: Born–Haber cycles (Johansson 1979b). Since the $4f^1$ state of Ce is not atomic-like, instead of Δ_- the fitted value of ε_f (star) has been plotted (see section 6). The dashed horizontal lines on the right-hand side indicate approximately where the ground state line is shifted for atoms in the indicated situations (see section 5).

deeper shells the energy separation between the different terms decreases whereas the lifetime broadening increases, so that they are not favourable for studying multiplet effects. A particularly simple situation occurs for the excitation of the s core states which are only affected by the exchange splitting due to the unpaired 4f electrons and which can be used to investigate the total atomic spin (Campagna et al. 1979).

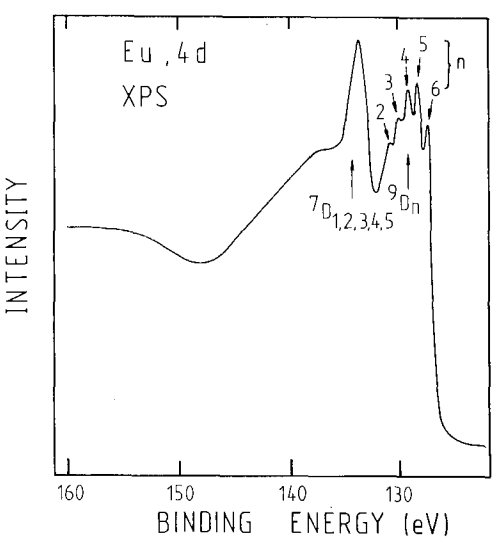

Fig. 10. XPS spectrum of the 4d level in Eu metal with assignment of the $4d^94f^7$ multiplet final states (after Kowalczyk et al. 1974).

The X-ray absorption edges (XAS) corresponding to core shells for which a transition to the empty f states (always assumed to be purely atomic-like) is dipole forbidden, reflect processes very similar to those observed in XPS. The excited electron can only occupy an empty band state of the symmetry required by the selection rules so that the final state is simply a screened impurity and an occupied Bloch state above E_F. This description implies the questionable assumption that no peculiar bound state is formed around the ion. The XPS transitions are selected according to the kinetic energy of the emitted electron whereas the XAS intensity accounts for all transitions induced by each photon energy. An explicit relation between these two kinds of spectra can be found in section 6.2.6. In the atomic limit the population of the 4f states is not modified but multiplets are formed by the coupling with the core hole. As mentioned previously for XPS, the existence of this multiplet splitting is barely discerned in such XAS spectra of deep shells. This situation is well illustrated by the impressive similarity of the L_{III} absorption edges of the metals Sm to Lu (Materlik et al. 1983a) shown in fig. 11. These spectra could be successfully analysed within a one-electron approach of the empty 5d states. However, the leading peak called white line, is attributed to the occupation of 5d states by the excited electron. These states are rather localized around the ion since they participate in the core hole screening. Therefore this white line cannot be interpreted simply in terms of unperturbed DOS.

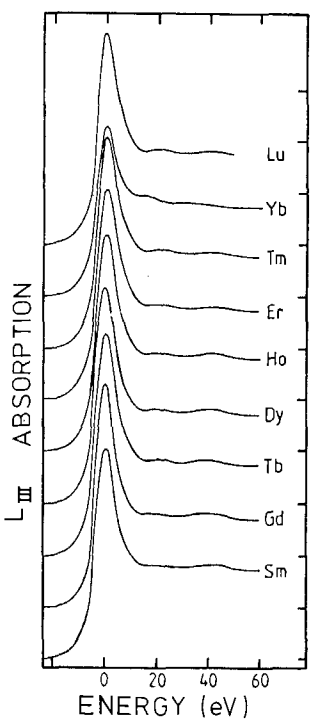

Fig. 11. Systematic behaviour of the L_{III} absorption edges in the metals Sm to Lu (after Materlik et al. 1983a).

4.4. *Transitions from a core level to an atomic-like f shell*

Excited states with one core hole and one additional electron in the 4f shell can be easily studied by threshold spectroscopies like XAS and EELS. As an example, the simplest case of La will be briefly considered here, a more complete presentation of this subject can be found in chapters 71 and 72 of this volume and in the recent papers of Thole et al. (1985). In La the 4f wave functions have the largest extension of the whole lanthanide series but in the pure metal considered here the small hybridization parameter and the important energy separation of the relevant 4f populations prevent them from a sizable mixing (see section 6.2.2). Only for this reason the spectra discussed below account mainly for nearly pure $f^0 \rightarrow f^1$ transitions. In order to populate by an X-ray absorption the initially empty 4f shell of La, the single-particle dipole selection rules require to promote an electron from a d-symmetry core level whereas the EELS processes are not constrained by stringent selection rules. Figure 12 shows a collection of three different types of 3d core level spectra (Moser et al. 1984, Esteva et al. 1983) plotted on a common energy scale (Baer et al. 1987 and section 6.2.1). The calculated positions of the different $3d^94f^1$ levels are given by the vertical bars with lengths proportional to their

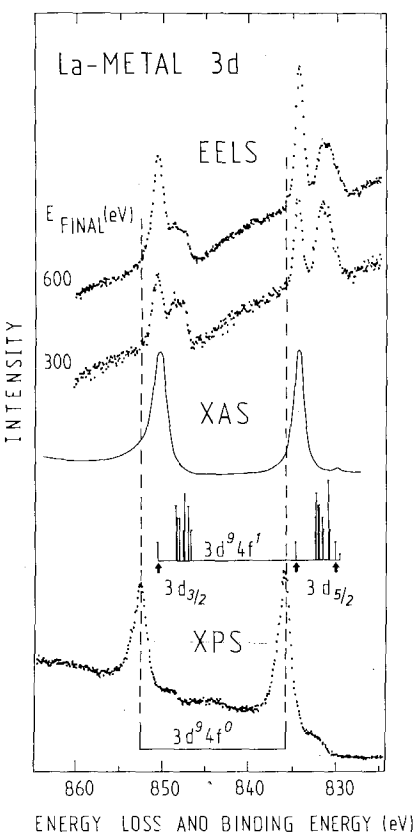

Fig. 12. Comparison of different 3d spectra of La plotted on a common energy scale. The EELS and XPS spectra and the calculated $3d^94f^1$ multiplets are taken from Moser et al. (1984), the XAS spectrum from Esteva et al. (1983). The arrows mark the $3d^94f^1$ final states accessible by dipole allowed transitions. The vertical dashed lines indicate the positions of the two spin–orbit-split components $4f^03d_{3/2,5/2}$ which are only observed in the XPS spectrum.

multiplicity. The three arrows locate the final states accessible by dipole allowed optical transitions. The intensity of the XAS is dominated by the two states at about 834 and 850 eV and a weak indication of the third one can be discerned at 830 eV. The occupation of a 4f orbital localized on the ionized atom is confirmed by the observation of the radiative recombination process yielding emission lines at the same energies (Motais et al. 1984). EELS allows a more detailed analysis of these multiplets since the cross-section for the different symmetries can be varied by the choice of the experimental conditions. In the limit of small momentum transfer, the transition probability becomes proportional to the squared dipole matrix element. In the reflexion geometry used for recording the spectra of fig. 12, the momentum transfer is poorly defined but it remains generally true that the relative weight of the dipole allowed transitions increases with the final kinetic energy of the free electron. This trend is clearly verified in the two EELS spectra which are well predicted by the multiplet calculation. Finally the 3d XPS spectrum has been plotted at the bottom of fig. 12, in order to demonstrate that it corresponds essentially to the $3d^9 4f^0$ final states as explained in section 4.3. However, the existence of a very weak $4f^1$ admixture to the valence band of La metal is revealed by the small $4f^1$ signal in the XPS spectrum, which is best seen as a shoulder on the low-energy side of the $3d_{5/2}$ component (see section 6.2.2).

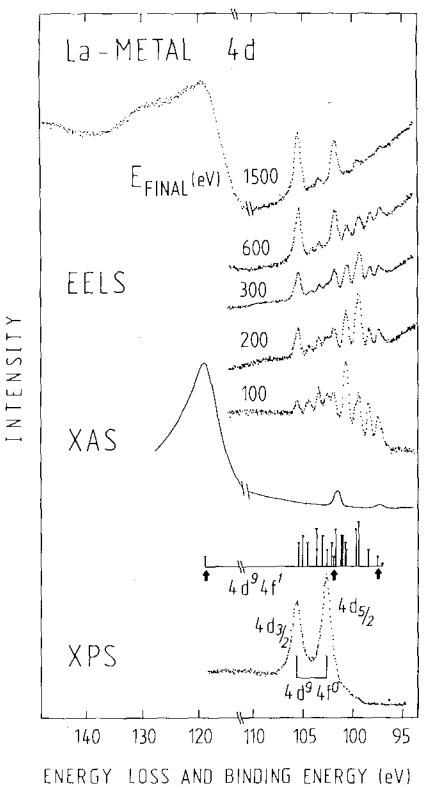

Fig. 13. Comparison of different 4d spectra of La plotted on a common energy scale. The EELS and XPS spectra and the calculated multiplets are taken from Moser et al. (1984), the XAS spectrum from Rabe (1974). The arrows mark the $3d^9 4f^1$ final states accessible by dipole-allowed transitions.

Figure 13 shows the same types of spectra as those of fig. 12, but now for the 4d threshold excitations in La metal (Moser et al. 1984, Rabe 1974). Their interpretation is also based on the same arguments which need not to be repeated. As expected for excited states involving populations changes within the same shell, the spread of the multiplets is much larger and many lines can be resolved by EELS. However, the evolution of their intensities as a function of the free electron kinetic energy in the final state shows an erratic behaviour which so far cannot be predicted. The new aspect of the 4d spectra originates from the fact that the highest $4d^9 4f^1$ final state is only resonantly bound. This means that it decays very fast by autoionization to the states of the continuum $5d^9 \varepsilon f^1$, where εf^1 is outside the potential barrier of the ionized atom. This type of process drags a huge intensity which is spread over a large energy range as a consequence of the very short lifetime of the localized state (Dehmer et al. 1971, Starace 1972). This effect is observed in the 4d spectra of all lanthanides (see chapter 72) and the analogous situation occurs also in the 5d spectra of the actinides (Baer 1984).

4.5. *Resonance phenomena in the atomic limit*

Resonance phenomena are observed when a particular excitation mode of a system opens two distinct channels leading to the same final state. This situation is particularly interesting and has marked consequences on the spectra when one of the channels is discrete and the other one continuous as a function of the excitation energy. In photoemission of lanthanides, this condition is fulfilled in the photon energy range of the dipole allowed transitions from 3d and 4d core levels to the 4f shell. The discrete excited state which is formed can decay by an Auger-type process involving two 4f electrons, the one filling the deep hole, the other one being emitted, so that the same final state can be directly produced by the usual photoemission process of a 4f electron. The competition of these two processes gives rise to a typical Fano profile of the 4f cross-section (Fano 1961) where the intensity is suppressed (anti-resonance) before a resonance. This many-body effect is not included in the single-particle cross-sections displayed in fig. 6. Since a tunable light source is required for observing these resonances, this type of measurement can be exclusively performed with synchrotron radiation giving access to the 4d and 3d thresholds which increase respectively from 100 to 200 eV and from 900 to 1600 eV along the lanthanide series. Even in the quasi atomic approach which has been most often used, the calculation of resonant photoemission in solids is a difficult task (Feldkamp and Davis 1979, Girvin and Penn 1980, Yafet 1980, Davis and Feldkamp 1981). Zangwill and Soven (1980) have given maybe the simplest interpretation of these phenomena in their calculation of the 4d ionization threshold of atomic Ba and Ce. They discuss the response of the electronic charge density to the external perturbation in terms of an effective local field for the different shells. Near the threshold, the situation is entirely controlled by the ten 4d electrons which react to the external oscillating radiation field as a simple damped harmonic oscillator. Among the outer levels the strongest enhancement of the photoionization cross-section near the 4d threshold is obtained for the 4f states and the Fano profile can

be explained by the phase shift between external and induced dipolar fields. It is important to notice that the other outer levels and in particular the 5d and 6s states forming valence bands in solids show also a resonance which is weaker and shifted towards lower photon energy. This qualitative discussion shows that even in the atomic limit this phenomenon can only provide a very approximate method for isolating the 4f signal in photoemission spectra. The common rules used for subtracting anti-resonant spectra from those at resonance have no rigorous foundation and cannot be expected to eliminate completely the intensity originating from states of other symmetries. The situation becomes even more uncertain in the light lanthanides where the atomic-like approach is no longer valid. The hybridization between band and 4f states becomes sizable (see section 6) so that a sound interpretation of spectra could only rely on calculations of resonant photoemission where this mixing is taken into account.

A simple example of a Fano resonance is provided by a study of clean and oxidized Yb (Johansson et al. 1980). In fig. 14, the photoemission spectrum of the clean metal which is divalent ($4f^{14}$) contains only the two lines $^2F_{5/2}$ and $^2F_{7/2}$ whereas the spectrum of the trivalent oxide Yb_2O_3 displays the typical multiplets resulting from a $4f^{13}$ initial configuration (see fig. 8e). Resonant photoemission near the 4d threshold can only occur in the oxide since the metal does not allow the formation of an intermediate state containing an additional 4f electron. In both cases the intensity of a particular region of the 4f spectra indicated by arrows in fig. 14 has been measured as a function of the photon energy (fig. 3c, PE(CIS)). The ratio of these intensities in the oxide and in the metal shown in fig. 15 has been fitted to the equation derived by Fano (1961) for this situation. The pronounced asymmetry of the line profile demonstrates that the process is not a simple resonance but has the character of an interference.

The condition for Fano resonances can also be fulfilled in other spectroscopies

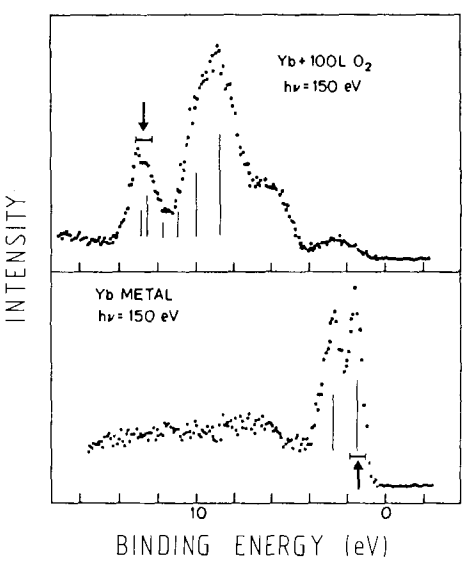

Fig. 14. Photoemission spectra of oxidized (Yb_2O_3) and metallic Yb (after Johansson et al. 1980). The vertical bars represent fractional parentage coefficients of f^{13} and f^{14} ground states (see fig. 8e), the arrows mark the states recorded as a function of photon energy for obtaining the Fano profile shown in fig. 15.

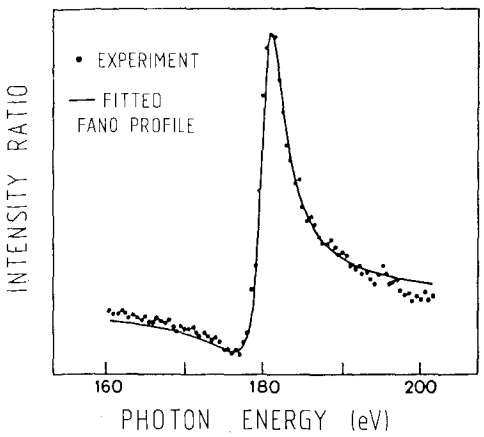

Fig. 15. Intensity ratio of the states marked with arrows in fig. 14 as a function of photon energy (after Johansson et al. 1980) (see text).

and an impressive example is given by the BIS spectra of La in the photon energy range of the 3d threshold (Riehle 1978). In this case the continuous channel is the normal BIS process to a $4f^1$ final state while the discrete channel is the threshold electron energy loss creating a $3d^9 4f^2$ intermediate state which decays by a radiative process in the $3d^{10}4f^1$ final state. When the energy of the incident electron beam is clearly larger than the threshold energy for the creation of a localized intermediate state, the radiative decay appears simply as a Lorentzian emission line. It accounts for the inverse transition of the X-ray absorption at the 3d threshold and consequently has the same energy (Bonnelle 1982, Motais et al. 1984). This type of process is sometimes called resonant X-ray emission but it has not the character of a Fano resonance. Very recently an interesting interference phenomenon of Fano-type has been observed in the excitation of spin-forbidden 4f multiplets by low-energy EELS near the 4d threshold (Modesti et al. 1985).

5. Surface phenomena

5.1. *Binding energy shifts and 4f-configuration stability*

The surface of solids induces severe perturbations of the bulk electronic structure. The reduced coordination at the surface leads to dehybridization of the outermost states and to band narrowing. In order to maintain charge neutrality a redistribution of charge for the surface atoms is necessary, producing a coordination-dependent surface atom core-level energy shift (SCS) of typically 0.1–1 eV. Its sign is determined by the population of the outermost states involved in the surface bond. For the 5d transition metals the SCS is positive (towards higher binding energy) up to Ta and becomes negative from W onwards (Citrin et al. 1978, Desjonqueres et al. 1980, Citrin and Wertheim 1983). This picture has been supported by thermochemical considerations, where the SCS is shown to represent the surface segregation energy of an inpurity (Johansson 1979b, Johansson and Mårtensson 1980,

Rosengren and Johansson 1980, Johansson and Mårtensson 1983, see chapter 69 of this volume) and it has been confirmed by one-electron local density theory (Delley et al. 1983).

The SCS $\Delta_{s,b}$ between bulk and surface atoms can be written in analogy with the atom-to-metal shifts as the difference of two binding energies (Williams and Lang 1978):

$$\Delta_{s,b} = \{E^b(n_c - 1) - E^b(n_c)\} - \{E^s(n_c - 1) - E^s(n_c)\} \tag{13}$$

where $E(n_c)$ is the total energy of the system as a function of the number of electrons in a particular core level. The first term with the superscript b denotes the core-level binding energy for the bulk atom, the second term is the one for the surface. The total surface shift can be decomposed into contributions from configuration changes, surface shifts and relaxation shifts:

$$\Delta_{s,b} = \Delta_{conf} + \Delta_{surf} + \Delta_{relax}. \tag{14}$$

The configuration shift Δ_{conf} results from a configuration change from G^b, the real bulk configuration, to G^{b*}, the configuration supposed to occur at the surface. The two remaining contributions can be evaluated within the density functional formalism.

The binding energies are expanded as Taylor series where the partial derivatives of the total energy with respect to occupation are given by their orbital eigenvalues ε_c (see eq. (7)). Using this fact, term-by-term subtraction of the series representing $E^s(n_c - 1) - E^s(n)$ from that representing $E^{b*}(n_c - 1) - E^{b*}(n_c)$ leads to a definition of the surface and relaxations shifts $\Delta_{surf} = \varepsilon_c^s - \varepsilon_c^{b*}$ and

$$\Delta_{relax} = -\tfrac{1}{2}(\partial\varepsilon_c^s/\partial n_c - \partial\varepsilon_c^{b*}/\partial n_c) + \cdots.$$

It is obvious that the total SCS $\Delta_{s,b}$ contains contributions from both the ground state (configuration changes Δ_{conf} and changes in the environment Δ_{surf}) and final state (screening Δ_{relax}).

In the lanthanides, for the purpose of the present discussion, the 4f states can be considered as core-states (see section 5.2). Their binding energies (which are the total energy differences Δ_- (see section 4)) undergo positive surface shifts ($\approx$0.6 eV) in agreement with the expectation for the low population of the extended 5d states (Gerken et al. 1985). For a few lanthanide metals, however, surface shifts of this order of magnitude can induce 4f population changes in surface atoms. In fact fig. 9 (section 4) shows that for Sm, where the minimum energy Δ_+ to modify the valence of a single bulk atom from 3^+ to 2^+ is only $\approx$0.5 eV, a valence change at the surface is very likely (Johansson 1979a, Johansson and Mårtensson 1983). On the other hand this effect is not too surprising since surface atoms are in an intermediate situation between bulk and free atoms and can be expected to display features reminiscent of their free atom character. In the free atom, except the elements Ce, Gd and Lu, all lanthanides have a divalent configuration. In the pure metals they prefer the trivalent configuration and only Eu and Yb with their stable half-filled and filled 4f shells remain divalent. Materlik et al. (1983b) confirmed this valence change for Sm and Er by a measurement of the L-absorption edges in the gas and

solid phase. The atom-to-solid shifts for these elements were found to be 6 eV larger than for Ce and Gd which have the same configuration in both phases. The origin of the valence change lies in the fact that an electron is promoted from the 4f shell to the 5d6s valence states if the cohesive energy gain on solidification exceeds the 4f promotion energy (Johansson 1979a). At the surface of solids the broken bonds lead to a cohesive energy decrease so that the atomic configuration might still be favoured. This behaviour is illustrated in fig. 9, where the energy difference Δ_+ between the divalent and trivalent states is plotted. As indicated by the horizontal lines, the energy difference between the two configurations will be changed by an amount corresponding to a SCS for atoms in different coordinations. For an atom embedded in a close packed surface layer the line labelled 'surf' indicates that only Sm will have a divalent configuration at the surface. For an edge or corner atom the energy difference will be changed even more, favouring Tm and probably a few other lanthanides to become divalent (Johansson 1979a). Finally, in the free atom only Ce, Gd and Lu maintain their trivalent configuration.

The formation of a lanthanide compound adds the heat of compound formation to the cohesive energy of the metal, inducing a change of the energy difference between the di- and trivalent configurations (Laubschat et al. 1986). Consequently for compounds containing elements like Sm, Eu, Tm and Yb, 4f population changes at the compound surface should occur and in fact, have been observed quite frequently. It is important to notice that the surface induced 4f population change driven by Δ_{conf} (eq. (14)) represents a true ground state property (Schneider et al. 1983b) while the measured SCS $\Delta_{\text{s,b}}$ contains contributions from both, the initial and final state (eq. (14)) (see also Johansson and Mårtensson 1983).

5.2. *Pure metals*

The first indication of a surface effect on the 4f binding energy in a lanthanide metal is contained in photoemission spectra of Yb (Brodén et al. 1973), recorded at low photon energies ($h\nu \leqslant 21$ eV). At these energies an additional doublet, shifted by 0.6 eV, appears at the high-binding-energy side of the $4f^{13}$ spin–orbit split final states. It is not observed at high photon energy (fig. 8e section 4). Using tunable synchrotron radiation allowing a continuous variation of the surface sensitivity of the photoemission experiment (see section 3.4), Alvarado et al. (1980) demonstrated the surface origin of the additional spectral feature. Nowadays this 4f-binding-energy shift is well established as an intrinsic property of a clean Yb surface (Johansson and Mårtensson 1980, Gerken et al. 1982, Takakuwa et al. 1982). In the work by Kaindl et al. (1983) shifts of both, 4f and 5p binding energies were determined and, within the experimental accuracy, they were found to be identical. This result demonstrates that both shells can be considered as core levels with respect to the outer d states participating in the surface bond.

A systematic photoemission study of the SCS for the 4f states in the lanthanide metals (Gerken et al. 1985) shows fairly good agreement with calculated values based on thermochemical considerations (Johansson and Mårtensson 1983). The systematic deviations observed for the heavier trivalent elements have been attri-

buted to the Z-dependent change of the outer-level d population responsible for the surface cohesive energies.

In the course of these investigations the linewidth of the surface emission feature has been found to be considerably larger than those of the bulk emission lines (Alvarado et al. 1980, Gerken et al. 1985). The hypothesis has been put forward that the surface related structures represent a superposition of emission lines originating from different geometrical sites, i.e. from surface atoms with different binding energies. Experimental evidence for this effect has been obtained in a photoemission study of Yb metal, where the influence of the substrate temperature on the microstructure of evaporated thin films was investigated (Schneider et al. 1983a). Representative outer level spectra are shown in fig. 16. They are characterized by $4f^{13}$ doublets originating from bulk atoms (dotted bars) and, at higher binding energies, from surface atoms with lower average coordination numbers. The SCS reflects the microstructure of the film formed by evaporation. At low temperatures, due to the low mobility

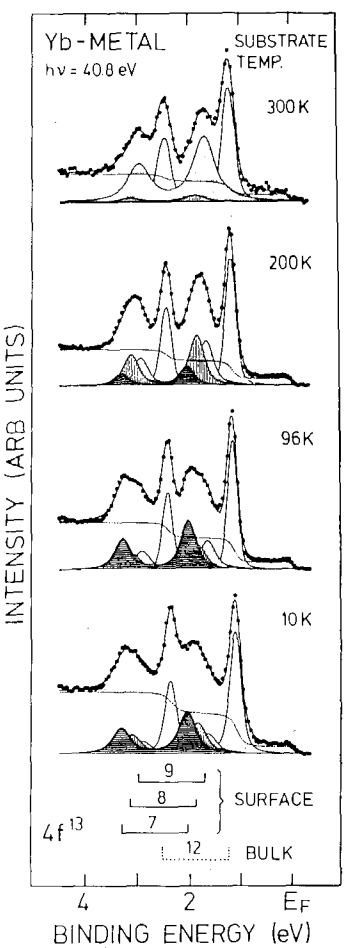

Fig. 16. Outer level photoemission spectra of Yb films grown at different substrate temperatures. The solid line connecting the data points represents the result of a least-squares-fit analysis with four $4f^{13}$ final-state multiplets originating from bulk [light solid curve (dotted bar diagram)] and surface [shaded curve areas (solid bar diagrams)] atoms at the indicated coordinations. The dotted curve denotes the background (Schneider et al. 1983a).

of the Yb atoms impinging on the cold substrate, crystallization is practically inhibited, leading to amorphous films (coordination 7). With increasing substrate temperature the mobility increases producing finally at room temperature predominantly close-packed (111)-surfaces of the Yb fcc-lattice (coordination 9). In this way photoemission can be used as a structural surface tool opening the possibility to investigate the properties of crystal growth and epitaxy.

For Sm and Tm metal a surface shift may stabilize the divalent configuration at the surface (see fig. 9, section 4). In fact, surface sensitive photoemission experiments have shown that Sm surface atoms are in a different 4f-configuration than bulk atoms (Wertheim and Crecelius 1978, Allen et al. 1978, Lang and Baer 1979, Allen et al. 1980, Gerken et al. 1985). Combined XPS and BIS measurements (Lang and Baer 1979) revealed that the valence change was driven by a surface shift of at least 0.46 eV of the occupied $4f^6$ state. The sizable energies involved in the transition were taken as experimental evidence for a completely divalent $4f^6(5d6s)^2$ Sm surface and a completely trivalent $4f^5(5d6s)^3$ bulk, in contrast to earlier interpretations. The study of Gerken et al. (1985) strongly supports the view of a single valency for Sm surface atoms. Figure 17 displays the outer-level spectra of the Sm metal, obtained by these authors. The spectra are characterized by two multiplet structures originating from bulk and surface atoms, respectively. There is no evidence for a surface shifted $4f^4$ final state indicating the absence of trivalent Sm atoms in the divalent Sm surface layer. Independent evidence for a divalent surface layer on the trivalent Sm bulk was found in low-energy EELS by Bertel et al. (1982) who observed different plasmon excitation energies for Sm and trivalent Er.

Tm metal is expected to undergo a 4f-population change to the divalent state at least at edge and corner sites (confer fig. 9, section 4). In fact, photoemission spectra of Tm metal films grown on low-temperature substrates known to favour low coordinations of surface atoms (see Yb, above) or of Ar-sputtered films at room temperature contain emission features from divalent surface sites (Domke et al. 1986). Figure 18 shows outer level spectra of Tm metal obtained after sublimation

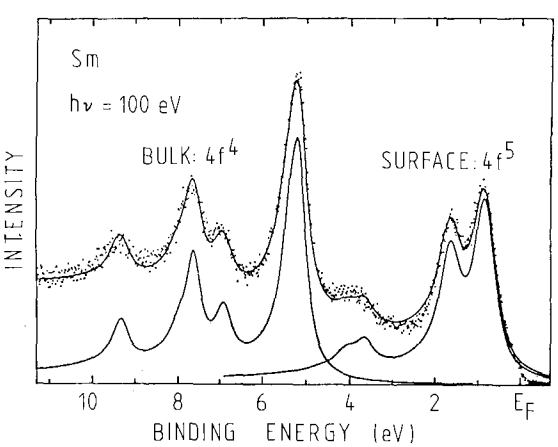

Fig. 17. Fit of the Sm experimental spectrum (dots) by a superposition of $4f^4$ and $4f^5$ multiplets originating from bulk and surface atoms, respectively. After Gerken et al. (1985).

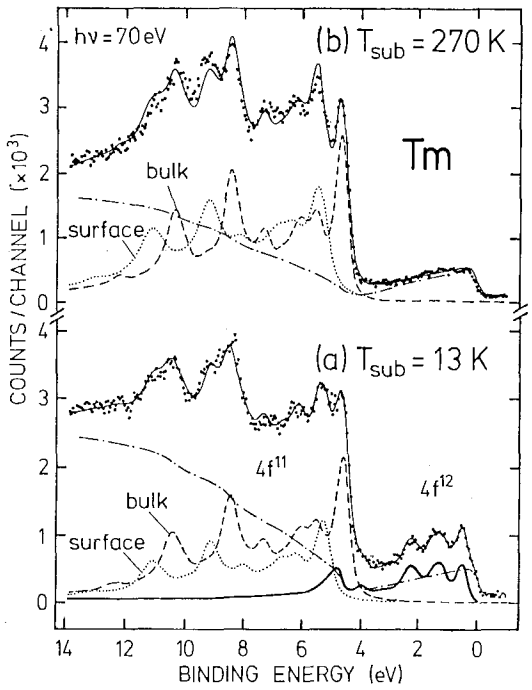

Fig. 18. Photoemission spectra of an ≅1000 Å thick Tm metal film grown on a copper substrate at two different temperatures: (a) 13 K and (b) 270 K. The thin solid line through the data points represents the results of a least-squares-fit analysis. Also shown are the subspectra for trivalent bulk (dashed), trivalent surface (dotted), and divalent surface (thick solid) Tm atoms, including the Tm 5d band, and the integral background of inelastically scattered electrons (dashed-dotted).

on the substrate at the indicated temperatures. In addition to the multiplet pattern between 4 and 11 eV characteristic for the trivalent Tm configuration (see fig. 8e) a triplet of peaks is observed near the Fermi energy only on the low-temperature surface indicating the presence of divalent Tm surface atoms. As opposed to the situation for Sm, where the entire surface layer undergoes the 4f-population change, the divalent state for Tm is restricted to low-coordinated atoms, since also trivalent Tm surface atoms are identified by their SCS in the spectra.

The 4f-population change for both Sm and Tm metal surfaces is expected to influence the physical and chemical properties of these metals in situations where a surface roughening may occur. In fact, among the trivalent lanthanide metals, the boiling points of both metals are exceptionally low, and also the melting points are slightly lower than expected (Gerken et al. 1985, Domke et al. 1986).

5.3. *Compounds, alloys, clusters, layered systems*

Surface effects on core-level binding energies and/or on 4f populations are frequently encountered in lanthanide materials. For a number of lanthanide intermetallics, a linear relation between surface and bulk core-level binding energy shifts relative to the elemental metals was observed, where the surface shifts amount to only ≈70% of the bulk chemical shifts. This behaviour reflects directly the reduction in cohesive energy at the surface (Murgai et al. 1982, Kaindl et al. 1983, Laubschat et al. 1986). Also the larger heat of formation for compounds containing

trivalent lanthanide elements as compared to divalent ones clearly shows up on the magnitude of the shifts (Laubschat et al. 1986).

The surface-to-bulk emission intensity ratios in the photoemission spectra of compounds with divalent or so called 'mixed-valent' lanthanide elements (see section 7) were found to be drastically higher than those with trivalent ones. For Au alloys with divalent Yb or Eu constituents this effect was interpreted in terms of possible surface segregation of the lanthanide elements (Johansson et al. 1982). For the lanthanide dialuminides an alternative explanation, also applicable to the Au alloys, has been proposed (Laubschat et al. 1986). The scattering probability of photoexcited bulk 4f electrons increases with decreasing binding energy leading to a reduction of their mean free path.

The systematic behaviour of the energies Δ_+ and Δ_- in lanthanide metals (fig. 9, section 4) has been exploited for predicting the 4f-configurational stability in a whole compound series when at least two of them have been studied spectroscopically (Mårtensson et al. 1982b, Laubschat et al. 1986). In agreement with this prediction based only on the measurement of the lowest 4f excitation energies for bulk and surface atoms, a divalent surface layer was observed for bulk trivalent $SmAl_2$ and TmS but not for $SmPd_3$ and $TmAl_2$.

Since the electronic structure of surface atoms is expected to be intermediate between that of free and bulk atoms, investigations which can vary in a controlled manner the interatomic distances between surface atoms represent a promising approach to the 4f-stability problem (moreover such experiments should contribute to a better understanding of hybridization between the 4f states and states of other symmetries). An XPS and UPS study of Sm clusters formed on amorphous carbon substrates (Mason et al. 1981) showed that Sm is primarily divalent in particles of small size (measured as coverages of $\approx 10^{15}$ atoms/cm^2) and is becoming progressively trivalent with increasing cluster size (10^{16} atoms/cm^2). This behaviour is consistent with the formation of bulk like Sm^{3+} states and a remaining contribution from divalent Sm surface atoms. Fäldt and Myers (1984a) studied ordered overlayers of Sm on Cu single crystal faces by LEED and XPS core level spectroscopy. The Sm 3d core spectra revealing two signals for each spin–orbit component were taken as an indication for an 'intermediate valence' state. Similar spectra have been obtained from disordered monolayers of Sm deposited on Al (001). Heat treatment however, produces an ordered Sm overstructure which is found to be trivalent (Fäldt and Myers 1983, 1984b, 1985). The different behaviour of Sm on both substrates is ascribed to different overlayer–substrate interaction. Clearly, these studies call for further detailed investigations of the 4f states in order to allow firm conclusions regarding the 4f-stability of Sm on solid surfaces.

Finally the exciting area of surface magnetism (Dunning et al. 1985) in lanthanide systems will be touched on very briefly. The existence of a magnetically nonsatured layer at the surface of EuO was early detected by spin-polarized photoemission (Campagna et al. 1973, Meier and Ruprecht 1976). The interaction of the escaping polarized electrons with a paramagnetic surface layer of Ni, Gd, Ce and Au of variable thickness was investigated by the same technique. From the depolarization of the photoelectrons the exchange constant between them and the paramagnetic

moments was obtained (Meier et al. 1984). Surface-enhanced magnetic order and magnetic surface reconstruction of the 4f spins were detected on a Gd (0001) crystal surface using spin-polarized LEED and spin-polarized photoemission. The observation of magnetic surface reconstruction has become possible by exploiting the SCS of the Gd 4f-final-state multiplets (Weller et al. 1985).

6. Beyond the atomic aspects of the 4f states in lanthanide materials

6.1. *Description of high-energy excitations within the Anderson single-impurity model*

When atoms are brought close together their outer wave functions will overlap and if their energy and symmetry is appropriate they will give rise to hybridization which is essential for the bond and band formation of condensed matter. The unique situation in the lanthanides and their compounds arises from the presence of the atomic-like 4f states with ionization energies comparable to the band width of the extended states. Their core-like orbitals show negligible direct f–f overlap between neighbouring atoms but their hybridization with the extended states of other symmetries can become significant (see fig. 1). Depending on the radial extension of the 4f wave function (see fig. 5), this hybridization will be most important for the light lanthanides, especially for Ce, and it will decrease towards the heavy lanthanides. The hybridized states resulting from the coupling between these states of completely different character can hardly be described in the pure atomic or in the pure band picture.

The most natural description of such a situation is provided by the Anderson single-impurity model which treats localized and extended states on an equal footing. In the formulation of Gunnarsson and Schönhammer (1983a,b, and chapter 64 of this volume), it contains a conduction band with energy dispersion $\varepsilon(\boldsymbol{k})$ and an impurity atom level of degeneracy N_f, characterized by the energy ε_f corresponding to the total energy difference between consecutive f-occupations when hybridization and f-Coulomb correlation energies are discarded:

$$H = \sum_k \varepsilon_k n_k + \varepsilon_f \sum_m n_m + U_{ff} \sum_{m'>m} n_{m'} n_m + n_c \varepsilon_c$$

$$+ (1 - n_c) U_{fc} \sum_m n_m + \sum_{km} (V_{mk} a_k^+ c_m + \text{h.c.}). \tag{15}$$

U_{ff} is the f–f Coulomb repulsion energy (section 4.2) and U_{fc} the Coulomb attraction energy between a core hole and an f state. These two energies are essentially atomic quantities renormalized by the screening mechanisms in solids. The terms responsible for the important and new aspects described in this section are the matrix elements V_{mk} that couple the f level to the conduction states. The orbital indices m and k for the 4f and conduction states implicitly include the spin; c_m and a_k^+ are the annihilation and creation operators for an f electron in the state m

and for a band electron in the state k, respectively. The task is now to choose an appropriate set of basis functions for a given type of excitation allowing us to calculate correctly the initial and final eigenstates. Then, the spectral intensities for the various excitation spectra can be computed within the sudden approximation. Assuming for the moment that all parameters entering the Anderson Hamiltonian have been determined, their influence on the behaviour of high-energy spectra can be simply understood intuitively with the help of a simplified Hamiltonian (15) containing no hopping terms V_{km} (Schneider et al. 1985). In fact it corresponds exactly to the atomic-like approximation adopted in section 4.

For the discussion of the excitation spectra it is convenient to choose as origin of the total energy scale the total electronic energy of the ground state configuration (see figs. 3, 4, 7), which for metals is at the Fermi energy. Within the simple framework without hopping terms, the density of the outer level excitations induced in these spectroscopies will be called 'uncoupled $S(E_t)$'. This quantity is composed of the weighted density of the band states (see section 6.2) and of the discrete excitation spectrum of the uncoupled f states. As shown in fig. 19a the uncoupled $S(E_t)$ can be split into electron-addition and electron-subtraction processes which must be represented on a common total-energy scale in order to be consistent with the Hamiltonian. It is more usual to represent these two types of excitations on a single particle energy scale where the excitation energy is given as the energy required to modify the population of the considered level with one electron taken or added at E_F. This representation is simply obtained from the previous one by a 180° rotation of the electron-addition spectrum. Within the uncoupled scheme, for two atoms in a $4f^n$ ground state configuration one can verify in the single-particle or total-energy representation that U_{ff} corresponds to the common definition of the Coulomb correlation energy involved in the formation of the two non-interacting polar states $4f^{n-1}$ and $4f^{n+1}$. When only f states are considered, their energy is given by $E_n(f^n) = n\varepsilon_f + \frac{1}{2}n(n-1)U_{ff}$, where n is the occupation number. This is just the parabolic behaviour of the total energy as a function of the f population.

For the description of core excitations it is convenient (but not absolutely necessary) to start from the total energy of the initial configuration f^0 even if it is not the ground state configuration. In the presence of a core hole ($n_c = 0$), this energy is simply raised by ε_c as shown in fig. 19b. In the uncoupled scheme it is then rather straightforward to calculate the relative positions of the other final state f populations by inserting the suitable numbers in the simplified Hamiltonian (15). Typical values for the parameters obtained from a many-body calculation of excitation spectra in light lanthanide solids will be discussed later (section 6.2, table 2). The simultaneous excitations of band states created in the core ionization should be represented in fig. 19b as continua extending from each f^n level towards higher total energies.

6.1.1. *A 'poor man's calculation'*

Having established the relationship between the parameters entering the Anderson Hamiltonian and high-energy excitations it is very instructive to illustrate the physical message delivered by this Hamiltonian within the simplest model which

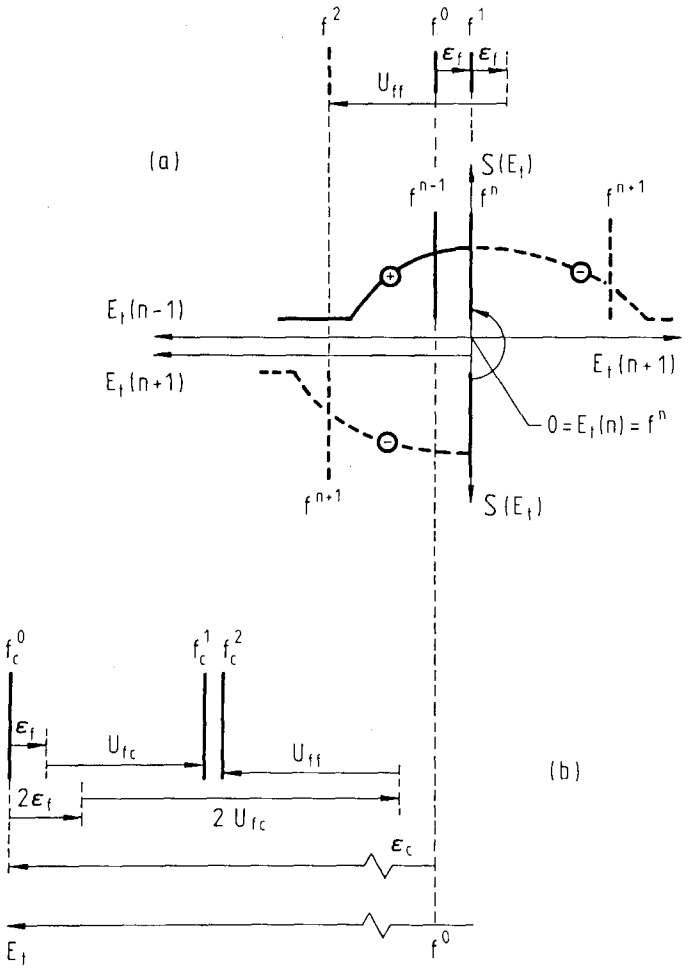

Fig. 19. (a) Screened single-particle excitations of the extended and localized outer levels without coupling as a function of the total electronic energy E_t of the final state: uncoupled $S(E_t)$. *Left part*: Uncoupled $S(E_t)$ resulting from the addition (thick dashed lines) and subtraction (solid lines) of one electron represented separately on a common total energy scale. The position of f^n represents the total energy of the ground state and does not belong to the excitation spectrum. The parameters linking the different 4f populations shown in the top of the figure are correct only for an uncoupled $4f^1$ ground state. *Right part*: The uncoupled $S(E_t)$ for electron addition rotated by 180° around the origin in order to make it consistent with the usual single-particle representation of the excitation spectra (XPS + BIS) (see also figs. 7 and 3). (b) Lowest total energies of the different uncoupled final states in the presence of a core hole for an f^1 ground state. This diagram is most conveniently constructed by starting from the total energy of an initial $4f^0$ configuration. The creation of a core hole raises this energy by ε_c. In addition to the other parameters one has now to take into account the core hole attraction U_{fc}. The relative positions of the different final-state populations can be easily calculated from the simplified Hamiltonian eq. (15) without coupling terms (see also fig. 4) (Schneider et al. 1985).

still accounts for the consequences of the mixing terms (Imer and Wuilloud 1987). It is based on the following assumptions:

(i) The band states are all degenerate (zero-bandwidth limit) so that the term $\Sigma_k \varepsilon_k n_k$ in eq. (15) transforms into $\varepsilon_0 \Sigma_k n_k$ which even disappears since ε_0 is placed at the origin of the total energy scale.

(ii) The eigenstates $|\Phi^i\rangle = \Sigma_{n=0}^{2} c_n^i |\mathrm{f}^n\rangle$ are expressed on a wave function basis limited to the three states $|\mathrm{f}^0\rangle$, $|\mathrm{f}^1\rangle$, $|\mathrm{f}^2\rangle$ with integral f-counts. The coefficients c_n^i are constrained to fulfil the normalization condition $((c_0^i)^2 + (c_1^i)^2 + (c_2^i)^2)^{1/2} = 1$. The f occupation in the ground state $|\Phi^{\mathrm{g}}\rangle$ is simply given by $(c_1^{\mathrm{g}})^2 + 2(c_2^{\mathrm{g}})^2 = n_{\mathrm{f}}$.

(iii) All matrix elements are assumed to be identical so that the coupling parameter $V^2 = V_{mk} V_{mk}^*$ is constant (this mechanism can only couple states with a f-population difference of one electron).

(iv) The degeneracy of the f states is assumed to be $\gg 1$.

The eigenenergies of the system are given by $\langle \Phi^i | H | \Phi^i \rangle$ where H is the expression (15) which has been simplified according to the previous discussion. In our simple basis one obtains

$$H = \begin{pmatrix} 0 & V & 0 \\ V & \varepsilon_{\mathrm{f}} & \sqrt{2V} \\ 0 & \sqrt{2V} & 2\varepsilon_{\mathrm{f}} + U_{\mathrm{ff}} \end{pmatrix}. \tag{16}$$

The diagonal terms represent the energies of the pure configruations. The solutions of the secular equation yield three eigenstates $|\Phi^i\rangle$ $(i = 0, 1, 2)$ with coefficients c_j^i $(j = 0, 1, 2)$, the one with the lowest eigenvalue $(i = 0)$ being the ground state $|\Phi^{\mathrm{g}}\rangle = |\Phi^0\rangle (c_j^0 = c_j^{\mathrm{g}})$. In the sudden approximation (section 2.3), the final state produced by the emission of an electron out of the 4f shell is obtained by applying an annihilation operator to the initial state: $a|\Phi^{\mathrm{g}}\rangle = c_1^{\mathrm{g}} |\mathrm{f}^0\rangle + \sqrt{2} c_3^{\mathrm{g}} |\mathrm{f}^1\rangle$. It does not belong to the eigenstates which are still the $|\Phi^i\rangle$ in the photoemission final state since the Hamiltonian (16) is not modified by the process. The 4f-photoemission intensity for each energy increase of the system $\varepsilon_i = E_i - E_{\mathrm{g}}$ is given (eq. (9)) by

$$I(\varepsilon_i) = |\langle \Phi^i | a | \Phi^{\mathrm{g}} \rangle|^2 = (c_0^i c_1^{\mathrm{g}} + \sqrt{2} c_1^i c_2^{\mathrm{g}})^2. \tag{17}$$

It appears that always one of the final state energies corresponds to the ground-state energy. This indicates that a fraction of the f-excitation spectrum has a metallic character (see section 7.2).

In deep core level spectroscopies of lanthanides, e.g. 3d photoemission, a hole is created which lowers the 4f shell by the Coulomb energy U_{fc}. The final eigenstates $|\Phi^i\rangle$ $(i = 0, 1, 2)$ with coefficients $c_j^i (j = 0, 1, 2)$ are obtained from an appropriate Hamiltonian, where ε_{f} in eq. (16) is replaced by $\varepsilon_{\mathrm{f}}^{\mathrm{c}} = \varepsilon_{\mathrm{f}} - U_{\mathrm{fc}}$. The photoemission intensity at the excitation energy $\varepsilon_i^{\mathrm{c}} = E_i^{\mathrm{c}} - E_{\mathrm{g}}$ (with $E_i^{\mathrm{c}} = E_i - \varepsilon_{\mathrm{c}}$) is given by

$$I(\varepsilon_i^{\mathrm{c}}) = |\langle \Phi^i | a_{\mathrm{c}} | \Phi^{\mathrm{g}} \rangle|^2 = \left(\sum_{j=0}^{2} c_j^i c_j^{\mathrm{g}} \right)^2, \tag{18}$$

where a_{c} is the annihilation operator of the core electron.

In processes like BIS and EELS one electron is added to the f shell (if transitions to other states are neglected). Consequently the resulting final eigenstates have to be expressed in the basis $|f^1\rangle$, $|f^2\rangle$, $|f^3\rangle$. The intensity at the energy $\varepsilon_i = E_i - E_g$ is given by

$$I(\varepsilon_i) = |\langle \Phi^i | a^+ [a_c] | \Phi^g \rangle|^2 = \left(\sum_{j=0}^{2} c_{j+1}^i c_j^g \right)^2, \tag{19}$$

where the annihilation operator a_c has only to be considered in EELS.

Within this simple model the influence of the different parameters (ε_f, V, U_{fc}, U_{ff}) on high-energy spectra of light lanthanide solids can be easily illustrated. The discussion will be restricted to the evolution of the spectra as a function of the energy difference ε_f, while the other parameters are held fixed. More details can be found in the work of Imer and Wuilloud (1987).

Figure 20 displays the behaviour of the eigenvalues $E_i(\varepsilon_f)$ for 4f excitations and $E_i^c(\varepsilon_f^c)$ for 3d excitations as obtained from the simple calculation. The dashed lines describe the energies of the pure configurations $|f^n\rangle$ in the uncoupled case ($V = 0$). They obey the relation $E_i(\varepsilon_f) = n\varepsilon_f + \frac{1}{2}n(n-1)U_{ff}$, where for core excitations $E_i(\varepsilon_f)$ is replaced by $E_i^c(\varepsilon_f^c)$ and U_{ff} is chosen to be 7 eV. For a finite coupling $V = 1.5$ eV the configuration mixing gives rise to the full curves $E_i(\varepsilon_f)$ and $E_i^c(\varepsilon_f^c)$. At large energy separation between the configurations the influence of the coupling is negligible and the energy eigenvalues approach asymptotically the straight lines representing the uncoupled configurations. When approaching the crossing points of

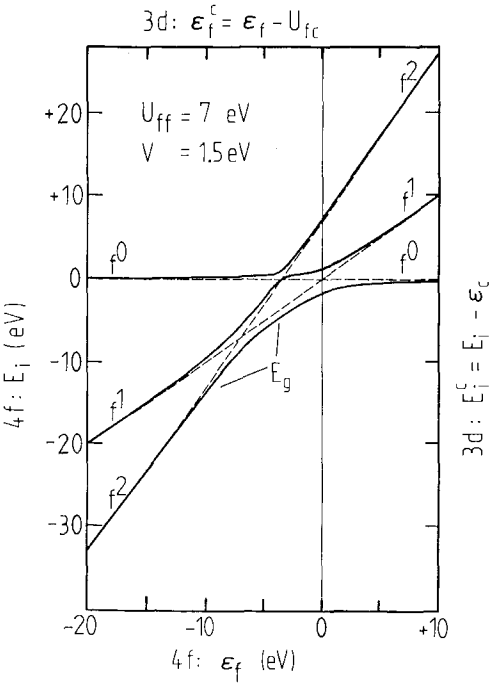

Fig. 20. *Left and bottom scale*: Eigenvalues E_i ($i = 0, 1, 2$) as a function of ε_f for PE 4f final states. The lowest lying curve E_g describes also the dependence of the ground state on ε_f. *Right and top scale*: Eigenvalues E_i^c ($i = 0, 1, 2$) as a function of $\varepsilon_f^c = \varepsilon_f - U_{fc}$ for PE 3d final states. The total energy of the core hole ε_c has been subtracted. The dashed lines correspond to the uncoupled situation ($V = 0$) (Imer and Wuilloud 1987).

the uncoupled configurations ($\varepsilon_f = 0$, $-\frac{1}{2}U_{ff}$, $-U_{ff}$), the hybridization becomes so strong that the weights of the two pure configurations in the eigenstates become equivalent and the degeneracy is avoided. This is a well-known problem of elementary quantum mechanics which is, for example, elegantly described for two levels in the textbook of Cohen-Tannoudji et al. (1973). The result of this simple calculation displayed in fig. 20 illustrates the general rule that the lowest eigenstate (ground state) formed by hybridization has always a smaller energy than the uncoupled states; it is the fundamental mechanism of the chemical bond. This total energy lowering δ which is usually very small when f states are involved in the hybridization will be discussed in section 7.2 for the more realistic model introduced in the next section.

Since the lowest curve in fig. 20 describes the ground state energy of the system, it defines the origin of the total energy scale (E_F in a metal) in excitation spectra (see section 3.1 and figs. 3, 7, 19) and the excitation energy above the ground state is $\varepsilon_i = E_i - E_g$. This situation is illustrated in the perspective representation of fig. 21 (XPS), but now the lowest energy curve $E_g(\varepsilon_f)$ of fig. 20 becomes the straight dashed line denoting the position of the Fermi energy E_F. The relation between the excitation energies ε_i and ε_f is indicated by the dashed curves. Similarly, the right hand part of fig. 21 describes the excitation energies in BIS processes (Imer and Wuilloud 1987). Along the vertical axis of fig. 21 the spectral intensities calculated within the sudden approximation by eqs. (17) and (19) can only be represented by bars standing on the $\varepsilon_i(\varepsilon_f)$ curves, since the unrealistic zero-bandwidth limit has been used in the calculation. In order to allow an easy comparison with experiment a Lorentzian broadening of 1 eV FWHM is introduced leading to the 4f-excitation spectra for XPS and BIS displayed in fig. 21.

The evolution of the spectra is presented as a function of ε_f, which is varied between -3 eV and 12 eV. For large positive ε_f only one structure, located at ε_f and corresponding to the BIS $4f^1$ final state is visible. With decreasing ε_f, the BIS structure approaches E_F while a second BIS structure emerges, representing

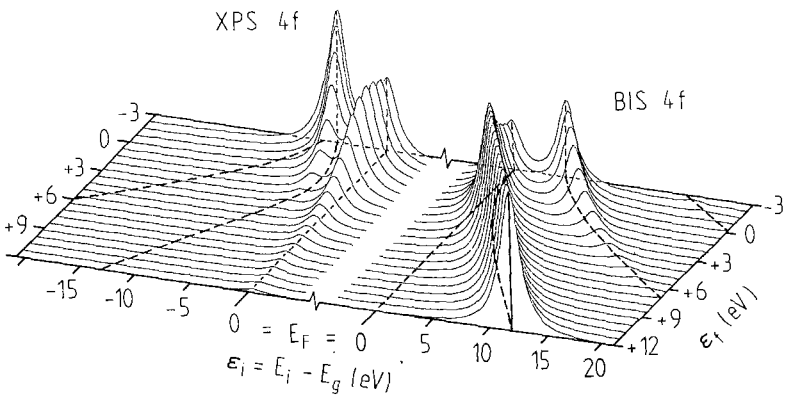

Fig. 21. *Full curves*: 4f-contribution to the XPS and BIS spectra as a function of ε_f. A Lorentzian broadening of 1 eV FWHM is used. *Dashed curves*: Total energy difference ε_i between the ground state E_g and the final eigenstates as a function of ε_f (see fig. 20) (Imer and Wuilloud 1987).

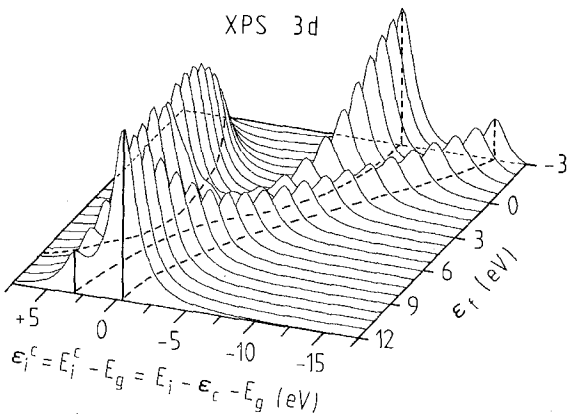

Fig. 22. *Full curves*: 3d contribution to the XPS spectra as a function of ε_f. $U_{fc} = 10\,eV$ and a Lorentzian broadening of 1 eV FWHM are used. *Dashed curves*: Total energy difference ε_i^c between the ground state E_g and the final eigenstates $E_i = E_i^c - \varepsilon_c$ as a function of ε_f (see fig. 20) (Imer and Wuilloud 1987).

essentially the $4f^2$ configuration. Their mutual mixing is small since their energy separation is large compared to the hybridization energy V. When ε_f approaches zero, in the XPS spectra a characteristic double peak structure is growing formed by substantial f^0–f^1 mixing (confer fig. 20, $3\,eV > \varepsilon_f > -3\,eV$).

The evolution of the calculated XPS 3d core level spectra as a function of ε_f^c for the parameters $V = 1.5\,eV$, $U_{ff} = 7\,eV$ (as above) and $U_{fc} = 10\,eV$ is displayed in fig. 22. The connection between the eigenvalues E_i without core hole and E_i^c with a core hole in fig. 20 and the excitation energy ε_i^c observed in the spectra of fig. 22 is easily made transparent. For example, for $\varepsilon_f = 0\,eV$ in fig. 20, the strongly mixed ground state of the system is found at $E_g = -2\,eV$. After the creation of the core hole the eigenvalues E_i^c of the final hole state have to be looked for at $\varepsilon_f^c = \varepsilon_f - U_{fc} = -10\,eV$ yielding $E_i^c = E_i - \varepsilon_c \approx -14\,eV$ for the lowest one. The corresponding transition in the core spectra of fig. 22 is found at the total energy difference $\varepsilon_i^c = E_i^c - E_g = -14 - (-2) = -12\,eV$, indicated by the lowest lying peak of the intensity distribution curve for $\varepsilon_f = 0\,eV$. Each of the low-lying structures is composed of mixed f^1 and f^2 configurations while the f^0 peak at about 10 eV higher total energy remains essentially pure in the final state.

We shall see in section 6.2 that this extremely simple model provides a qualitatively correct picture of high-energy spectra of light lanthanide solids. Similar approaches to excitation spectra of lanthanides have been introduced for clusters (Fujimori 1983, Fujimori and Weaver 1985) and have been considered for solids (Kotani et al. 1985). It must be emphazised, however, that the use of a few molecular orbitals in these simplified models of the Anderson impurity Hamiltonian leads to spectra where the excitations appear necessarily as discrete lines. This approach to a solid is missing irremediably the continuum aspects of the band states interacting with the f state. For example, one unrealistic consequence of a cluster model is the fact that the lowest excitation energies are typically of the order of the hybridization energy for both, metals and insulators. This implies zero specific heat and too small susceptibilities for metallic systems (Fujimori et al. 1984). Nevertheless, such models

are very useful for understanding the basic mechanisms giving rise to the different spectra but they cannot be considered to be realistic. For this reason it is important to perform within the impurity model more complete calculations, where the interaction of an impurity state with a continuum of states is taken into account properly.

6.1.2. *The Gunnarsson–Schönhammer approach*

The simplest conditions for studying high-energy spectra within the Anderson impurity model are offered by Ce, since its low 4f population is not involved in complex multiplet structures. Taking advantage of the large orbital degeneracy N_f of the f state, Gunnarsson and Schönhammer (GS) (1983a,b) solved this problem in metallic Ce systems for a limited number of basis states with integral f-occupation. In the first order calculation, the ground state is expressed as a linear combination of a filled band and empty f states ($|f^0\rangle$) and of a band with one hole and one f state occupied ($|f^1\rangle$) (see eq. (21)). The coefficients determining the weight of these basis states in the ground state are calculated in a variational procedure minimizing the total energy (see preceding section). Then, within the sudden approximation, the excited eigenstates observed in high-energy spectroscopies are computed (see chapter 64 of this volume). It has to be noted that the hybridization V_{mk} is treated as a constant. Consequently the resulting hybridization strength $\Delta = \pi \max(V^2(\varepsilon))$ becomes the main adjustable parameter of the model (Lee et al. 1986).

The achievements of the GS model are the following:

(i) A single set of parameters (see section 6.1) characterizing the electronic structure of a solid, yields correctly all kinds of excitation spectra. This allows one to reconcile the contradictory pictures of the 4f state deduced from the different experimental techniques (XPS, BIS, EELS, XAS, susceptibilities and lattice constants) (Fuggle et al. 1983a,b, Hillebrecht et al. 1984, Wuilloud et al. 1983, Wuilloud et al. 1984a, Delley and Beck 1985, Schneider et al. 1985).

(ii) The correct width of the bands included into the model allows one to predict the spread and shape of the 4f and core spectra in a more realistic way than in any cluster – or zero-bandwidth calculation (see preceding section).

(iii) Mixing in initial and final states is taken into account. In both states the 4f population is found to be integral only in extreme situations. This invalidates the purely atomic-like description and calls in question the use of deep core-level spectroscopy for valence determinations (see also section 7.1).

(iv) Insulating lanthanide compounds can also be analyzed if separate valence and conduction bands are included into the model calculation (Wuilloud et al. 1984b).

These achievements will be discussed in the following sections for a particular sequence of solids where the consequences of 4f admixture to the band states appear in a systematic manner. Despite the hidden aspects of the theoretical GS-computation of the spectra, the simple model presented in section 6.1.1 allows one to understand intuitively how the parameters used to characterize the electronic structure determine the observed excitations.

6.2. *Analysis of selected spectra of light lanthanide materials*

6.2.1. *Choice of the parameters in metals and insulators*

The XPS, BIS, EELS, and L_{III} absorption spectra presented in this section (Schneider et al. 1985) are analyzed within the GS approach using basis states up to double f-occupation (second-order calculation). The first-order approximation is sufficient for Ba and La compounds. The large f-degeneracy N_f is much less important for insulators than for metals since no low-lying band-like excitations lead to divergencies. For each material, the heights, widths, and positions of bands with semi-elliptical shape have been chosen in such a way that the model can account correctly for the mixing of the 4f states with the extended states. The schematic densities of states represented in the figures of this section have been weighted by the coupling strength Δ. They need not to be more realistic since the aim of the model calculation is exclusively the description of the 4f contribution to the different excitations. The computed spectra have been compared to all experimental spectra and the parameters have been varied until the best general agreement is found. This procedure represents a stringent test of the model and in this way more reliable parameters are obtained than from a fit to only one type of experimental spectrum. As shown in table 2, the values of the atomic-like parameters U_{ff} and U_{fc} do not scatter very much among the different types of solids considered. Only Δ and ε_f remain free parameters in the fitting procedure. The values of the initial 4f population n_f, also given in table 2, are a result of the model calculation.

Calculated and measured spectra of metallic and insulating materials are presented on a common energy scale. Its origin is identified with the Fermi energy in metals (see section 3.1) and with the upper valence band edge in insulators. This choice is convenient but it is in fact arbitrary. In EELS and XAS where the total number N of electrons belonging to the solid is not modified, the transition energies do not depend on this origin. They are total-energy differences between the initial and the final states of the N electrons of the solid. In photoemission the analyzed electron is missing in all final states so that one has to choose a transition from some

TABLE 2
Relevant energies (eV) and populations obtained from the fit of the many-body calculations to the experimental spectra.

Material	Δ_{fp}	$\Delta_{f\,cond}$	ε_f	U_{ff}	U_{fc}	n_f
Ba	—	0.1	14.0	8	−12	0.003
LaF_3	0.6	0.06	14.5	8	−13.5	0.002
La_2O_3	0.6	0.06	10.7	8	−12	0.04
La	—	0.08	5.5	8	− 9	0.01
CeO_2	0.6	0.06	0.5	8	−12	0.45
$CeCo_2$	—	0.3	−1.2	5.5	−10	0.76
CeN	0.2	0.1	−0.8	7	−11	0.80
α-Ce	—	0.08	−1.2	6	−10	0.88
γ-Ce	—	0.03	−1.5	6	−10	0.98
$CeSi_2$	0.1	0.05	−1.2	7	−10	0.99

arbitrary level ε_k^r (usually in the band) as reference. The measured energies are total-energy differences between the state with the hole at ε_k^r and the $(N-1)$-electron final states. This shows that XPS and EELS (XAS) spectra of the same core level account for different types of final states which can be compared only in the limit of very small hybridization. Furthermore, the relative position of EELS and XPS spectra is arbitrarily defined by the choice of the level ε_k^r which must be the same in the experiment and the calculation. These considerations apply equally to metals and insulators (Baer et al. 1987) and the characteristics of each solid are expressed by the coupling strength Δ and the energies $\varepsilon_c, \varepsilon_f, U_{ff}$ and U_{fc} which include the screening of impurity charges by the band states.

6.2.2. *Materials with $4f^0$ ground-state configuration in the uncoupled scheme*

The materials selected and discussed in this section have in common the fact that in the uncoupled scheme ($\Delta = 0$) the total energy is larger in the $4f^1$ configuration than in the $4f^0$ configuration ($\varepsilon_f > 0$). This means that without hybridization they would all be in a pure $4f^0$ ground state. In fig. 23 these systems have been disposed vertically in a sequence where the energy difference ε_f decreases gradually. At first we will consider the outer level excitations together with the corresponding uncoupled $S(E_t)$ (see section 6.1) and the model calculations (fig. 23a). Except for CeO_2, the influence of the hybridization remains negligible in the direct population changes induced in XPS and BIS. This is an obvious consequence of the large energy (compared to Δ) separating the $4f^0$ and $4f^1$ configurations as it is already correctly predicted by the simple model (see figs. 20 and 21). Even in LaF_3 and La_2O_3 with larger Δ values, the initial $4f^1$ population n_f is well below 0.1 and in the model calculation of the photoemission spectra its contribution can be barely discerned. The f-structures observed in the BIS spectra have been shaded in order to distinguish them from the population of extended states. Besides strong variations of the width, attributable to the lifetime broadening and to the different instrumental resolutions, the model calculation traces the f-contributions of the BIS spectra very well.

The situation becomes more interesting in CeO_2, where the uncoupled f^0 and f^1 energies are very close (see figs. 20 and 21 for the simple model around $\varepsilon_f = 0$). This proximity and the large value of Δ give rise to a sizable mixing of f^1 with f^0 states responsible for the important initial 4f population $n_f \approx 0.5$. This $4f^1$ admixture to the valence band cannot be distinguished in the total XPS spectrum, but will be reflected in the core spectra. The BIS spectrum is dominated by the $4f^1$ peak, whereas the broad $4f^2$ final states mixed with conduction band states, are embedded into the signal originating from extended states and the background. A more detailed discussion can be found in section 6.2.4.

The XPS 3d core-level excitations displayed in fig. 23b contain many unconventional aspects. They can be easily understood by considering the initial-state situation described previously, the uncoupled final-state positions obtained with the parameters given in table 2 (fig. 19b) and the evolution of the spectra as a function of ε_f in the 'poor man's calculation' (figs. 20 and 22). From Ba to La, the initial-state mixing is negligible and the ground state configuration is nearly pure $4f^0$. The

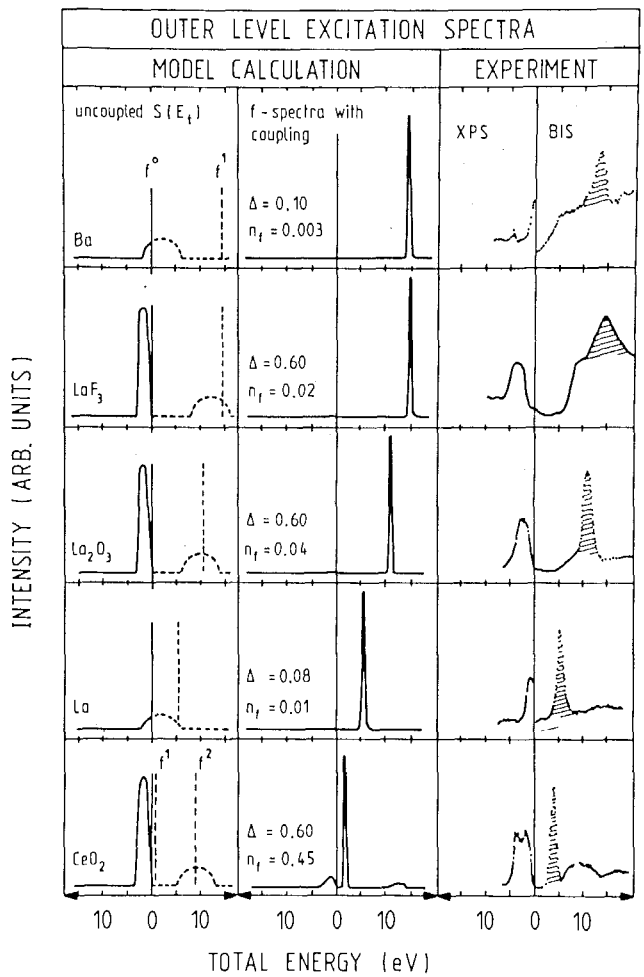

Fig. 23a. Calculated and measured outer-level excitation spectra. In the uncoupled $S(E_f)$ (see fig. 19), the amplitude of the valence and conduction bands is chosen proportional to the hybridization parameters. In the calculation of the f-spectra with coupling, a Gaussian instrumental broadening of 0.4eV FWHM has been included. The experimental spectra have been taken from the following works. XPS: Ba (Hüfner and Steiner 1985); LaF_3 (Sato 1976); La_2O_3, La (Schneider et al. 1985); CeO_2 (Wuilloud et al. 1984b). BIS: Ba (Riehle 1978); LaF_3 (Motais et al. 1984); La_2O_3, La (Schneider et al. 1985); CeO_2 (Wuilloud et al. 1984b). The origin of the total-energy scale is the Fermi energy in metals and the upper valence band edge in insulators. The f contribution corresponds to the hatched areas.

presence of a core hole decreases dramatically the total-energy difference between the $4f^1$ and $4f^0$ configurations so that a final-state mixing becomes possible. In Ba metal the value of Δ is still too small to induce a detectable hybridization and the model predicts a simple Lorentzian shape. The XPS 3d lines confirm this expectation since the pronounced asymmetry is due to electron–hole pair excitations not included in the model and the small satellite can be identified with a plasmon

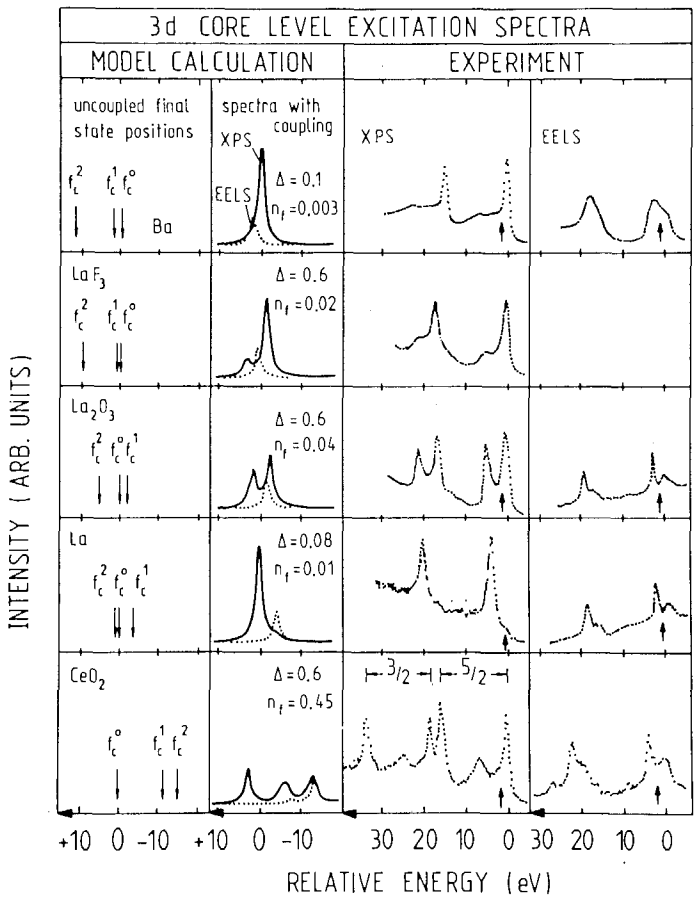

Fig. 23b. Calculated and measured 3d core-excitation spectra. In the spectra with coupling the solid curves correspond to XPS and the dotted curves to EELS. The calculated spectra have been convoluted by a Lorentzian of 1.2 eV FWHM to include lifetime broadening. The total energy of the core hole ε_c has been subtracted. The experimental spectra have been taken from the following works. XPS: Ba (Hüfner and Steiner 1985); LaF_3 (Suzuki et al. 1974); La_2O_3, La (Schneider et al. 1985); CeO_2 (Wuilloud et al. 1984b). EELS: Ba (Kanski and Wendin 1981); La_2O_3, La (Schneider et al. 1985); CeO_2 (Wuilloud et al. 1984b). The XPS and EELS spectra have a common energy scale and the centers of gravity of the EELS final states are indicated by arrows in the corresponding XPS and EELS spectra (Schneider et al. 1985).

excitation (Ley et al. 1980). In the insulator LaF_3, the value of the hybridization parameter Δ is now 0.6 eV and the resultant final state mixing is responsible for the two peaks predicted and observed in the 3d core-level spectrum. In this case an identification of the two structures with different integral 4f populations is dubious and only the more intense one has a clearly dominant $4f_c^0$ component. In La_2O_3, the order of the f_c^1 and f_c^0 uncoupled final-state positions is inverted (for the simple model in fig. 20: $\varepsilon_f^c = \varepsilon_f + U_{fc} \approx 1\,\text{eV}$ (LaF_3) and $\varepsilon_f^c = \varepsilon_f + U_{fc} \approx -1.3\,\text{eV}$ (La_2O_3)) and the value of Δ is large again. The consequence is a splitting of the core–hole final state into two components of nearly equal intensities (see also fig. 22 between

$10\,\text{eV} > \varepsilon_f > 6\,\text{eV}$) as observed in many studies (Jørgensen and Berthou 1972, Signorelli and Hayes 1973, Suzuki et al. 1974, Burroughs et al. 1976, Fuggle et al. 1980, Mullica et al. 1985). Each of them is formed by a mixing of the two configurations f_c^0 and f_c^1 in a ratio of approximately one to one and their separation is mainly determined by Δ. Furthermore, the analysis of the model calculation shows that in fact the excitation spectrum does not consist of two neighbour peaks, but corresponds to a continuous intensity distribution reflecting excitations through the whole bandwidth. La_2O_3 provides one typical example demonstrating that the traditional interpretation of each peak in terms of pure atomic configurations is completely in error.

It is gratifying to note that the evolution of the different excitation spectra of the La compounds with F, O, Cl and Br (Signorelli and Hayes 1973, Suzuki et al. 1974) is also well accounted for by the model calculation which appears to provide a sound and unified description of the La 'satellites'.

In La metal, the f_c^0 and f_c^1 energies are not quite as close and Δ is small. Since the initial $4f^1$ population is negligible ($n_f = 0.01$) and the conditions for a final-state mixing are not favourable, the excitation spectrum contains essentially a leading f_c^0 peak accompanied by a weak f_c^1 satellite. In this case nearly pure final-state configurations are realized. It is interesting to notice that from the f^0 initial state, the matrix element obtained in the sudden approximation for a core electron photoemission provides practically no intensity to the f_c^2 final state. Despite the fact that two configurations f_c^2 and f_c^0 are nearly degenerate, no direct hybridization between states with f-count differences larger than one can take place.

Finally, in CeO_2 the relative positions of the uncoupled energies of the different f^n configurations in the ground state are drastically modified when a core hole is created. f_c^0 has now the highest energy and is well separated from f_c^1 and f_c^2 (see also fig. 20 for $\varepsilon_f^c = \varepsilon_f - U_{fc} \approx -10\,\text{eV}$ and fig. 22 for $\varepsilon_f \approx 0\,\text{eV}$). For this reason it cannot hybridize and consequently appears as a simple isolated peak with a large intensity accounting for the important f^0 character of the initial state. The two close f_c^1 and f_c^2 configurations together with band excitations form a strongly mixed final state continuum dominated by two leading peaks. The observation of a large intensity for states of this nature is a consequence of the initial $4f^1$-character of the valence states which is in this way indirectly demonstrated. For all these 3d core-level spectra, the agreement between the model calculation and each spin–orbit split component of the XPS spectra is striking.

6.2.3. *Materials with $4f^1$ ground-state configuration in the uncoupled scheme*

In figs. 24a and b the outer and core level excitation spectra for $CeCo_2$, CeN, α-Ce and γ-Ce are presented, respectively. They have been selected and displayed vertically according to increasing f-occupation n_f in the ground state. The common property of these materials is the $4f^1$ configuration of their uncoupled ground state, obtained from the best fit of the model calculation to the experimental spectra. For these materials, the total energy is larger in both the $4f^0$ (electron subtraction) and in the $4f^2$ (electron addition) configuration. The uncoupled f^0 and f^1 total energy positions are not far from degeneracy allowing for a mixing of these two con-

figurations when the coupling strength Δ becomes sizable (see also fig. 20, $\varepsilon_f \approx 0$). The XPS excitations are a mixture of f^0 and f^1 configurations producing a continuum of states with a characteristic two-peak intensity distribution (α- and γ-Ce: (Mårtensson et al. 1982a, Wieliczka et al. 1982)). In an early study these two peaks have been identified with f^0 and f^1 configurations (Hüfner and Steiner 1982), an intuitive assignment which ignores the mixing. The BIS excitations show essentially two peaks corresponding roughly to the energy positions of the f^1 and f^2 configurations in the uncoupled $S(E_t)$. With decreasing coupling strength Δ or/and increasing total energy separation between f^0 and f^1 configurations, the limit of a localized $4f^1$ state ($n_f \approx 1$) is approached and the outer level spectra are expected to become more atomic-like (see section 4). This trend is illustrated by the combined XPS–BIS spectrum of γ-Ce where most of the spectral weight is found at the uncoupled f^0 and f^2 energy positions. The interesting case of CeN will be discussed in section 6.2.4.

The creation of a core hole in these materials raises the total energy of the initial $4f^0$ state by ε_c. Then, for the values of U_{fc} and U_{ff} given in table 2, one can find easily with the help of fig. 19b the uncoupled final-state positions of the relevant 4f configurations displayed in fig. 24b (see also fig. 20, $\varepsilon_f^c \approx -10\,\text{eV}$ and fig. 22 ($0 < \varepsilon_f < -2\,\text{eV}$)). This situation is essentially similar to the one in CeO_2 (section 6.2.2). With decreasing hybridization the mixing between f_c^1 and f_c^2 final states becomes weaker and the intensity of the structure at lowest total energy decreases. As a consequence of the large energy separation (compared to Δ), the f_c^0 final state remains essentially pure and its intensity evolution reflects rather well the f^0 population ($1 - n_f$) of the different ground states. On the other hand, one should notice that the intensities of the two structures resulting from the f_c^1–f_c^2 mixing in core level spectra are by no means representative of f^1 and f^2 ground state populations.

The outer and core level excitations for these materials with uncoupled $4f^1$ ground state configurations are very well described by the GS model. The two conditions necessary for the observation of unconventional excitation spectra are encountered: two nearly degenerate configurations and a sizable coupling of the f with the band states.

6.2.4. *Band gap shrinking and f–p hybridization*

It is interesting to compare GS-model calculations with spectroscopic results of materials where the 4f state interacts with a band originating from p states (Croft et al. 1981a, Franciosi et al. 1981). This symmetry offers more freedom than d states to vary strongly the density of the extended states in the energy range of the 4f excitations. Wuilloud et al. (1985) have investigated the sequence CeO_2, CeN and $CeSi_2$, where the band gap shrinks from 6 eV to ≈0 eV. The joined XPS and BIS spectra shown in fig. 25 display the outer level excitations of these materials. For CeO_2 the spectra have been analyzed with a GS model which has been adapted to insulators (see section 6.2.1) (Wuilloud et al. 1984b). This study has provided an unquestionable demonstration that an important participation of f-character ($n_f \approx 0.5$) is involved in the extended states of predominantly p-symmetry. The fact

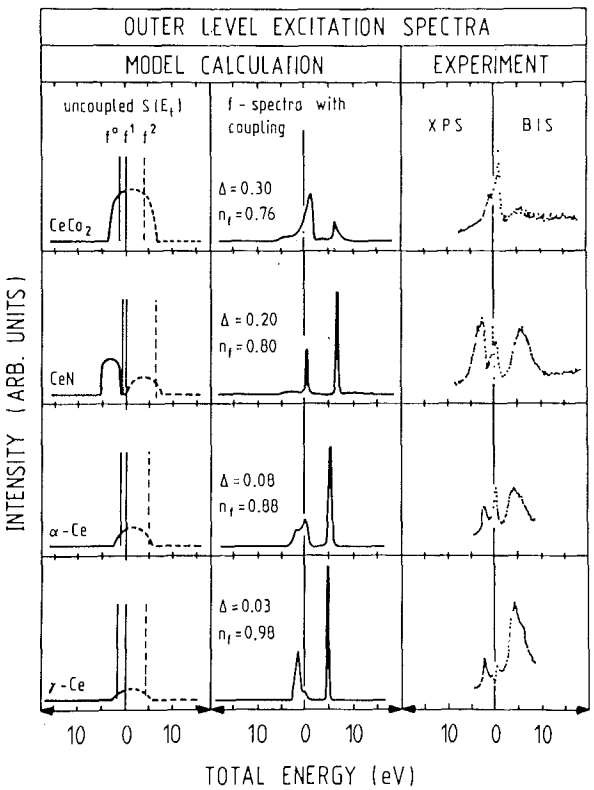

Fig. 24a. Calculated and measured outer-level excitation spectra (see caption of fig. 23a). The experimental spectra have been taken from the following works. XPS: $CeCo_2$ (Schneider et al. 1985); CeN (Wuilloud et al. 1985); α- and γ-Ce (Mårtensson et al. 1982a); BIS: $CeCo_2$ (Schneider et al. 1985); CeN (Wuilloud et al. 1985); α- and γ-Ce (Wuilloud et al. 1983).

that CeO_2 is an insulator constrains this ground state mixing to occur within the full valence band, which must accomodate this f-admixture of extended nature. This contribution does not exhaust all the available $4f^1$ states so that another type of $4f^1$ states is found at higher single-particle energies, in the range where the extended states are forbidden (band gap of the extended states). For this reason the p–f mixing remains small in the gap where nearly pure $4f^1$ states are formed. The agreement of this description resulting from the impurity calculation with a band calculation (Koelling et al. 1983) is gratifying. These results settle a long standing controversy regarding the Ce valence in CeO_2 (Bauchspiess et al. 1981, Wachter 1982, Fujimori 1983). In terms of the valence definition given in section 7.1 the Ce atoms in CeO_2 are tetravalent, since no atomic-like localized 4f state is occupied and the four outer electrons are involved in the chemical bond resulting from an admixture of hybridized p–f and p–d states. Also see comments in chapter 71, section 14 of this volume.

In CeN only three electrons of the Ce atoms are necessary to complete the p-band of N. For this reason the p–f mixing remains small, despite the rather important

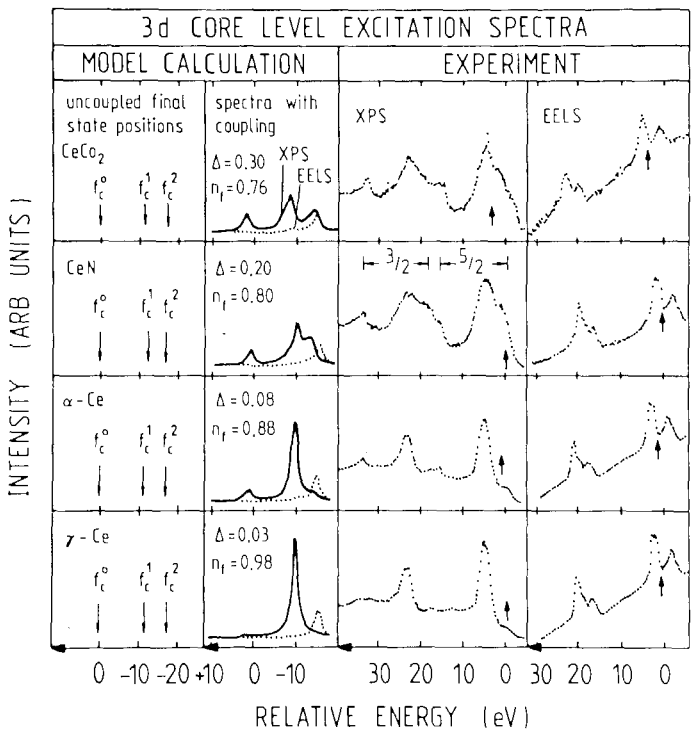

Fig. 24b. Calculated and measured 3d core-excitation spectra (see caption of fig. 23b). The experimental spectra have been taken from the following works. XPS: $CeCo_2$ (Schneider et al. 1985); CeN (Baer and Zürcher 1977); α- and γ-Ce (Wuilloud et al. 1983). EELS: $CeCo_2$ (Schneider et al. 1985); CeN (Wuilloud et al. 1985); α- and γ-Ce (Wuilloud et al. 1983); (Schneider et al. 1985).

coupling parameter $\Delta_{fp} = 0.2\,eV$ (see fig. 24a and table 2) and the small energy difference between the uncoupled f^0 and f^1 configurations. This situation is reflected in the calculated spectra by the fact that only little f-intensity is spread over the p band. In the XPS spectra of fig. 25, by extrapolation the upper valence band edge is found to be located about 1.5 eV below E_F, so that a narrower band gap than in CeO_2 is formed. In the uncoupled scheme the f^1 total energy is about at the bottom of the conduction band (labelled 'cond') so that the coupling $\Delta_{f,cond} = 0.1\,eV$ produces the metallic state. This description is dictated by the choice of parameters producing the best agreement of the many-body calculation with the 4f and core excitations. In fact, recent high-resolution UPS spectra (20 meV) (Patthey et al. 1986a) reveal a narrow band in the immediate vicinity of E_F (see section 7.2). This result is in agreement with an ab initio supercell band-structure calculation for CeN (Norman et al. 1985a,b), where also an f-occupancy $n_f \approx 0.8$ is obtained. Moreover, it is concluded from this calculation that the additional peak observed at 1 eV in an earlier work (Gudat et al. 1981) and interpreted as a surface-shifted 4f peak is a consequence of surface substoichiometry and not of a surface shift. The measurements of Patthey et al. (1986a) fully confirm this prediction.

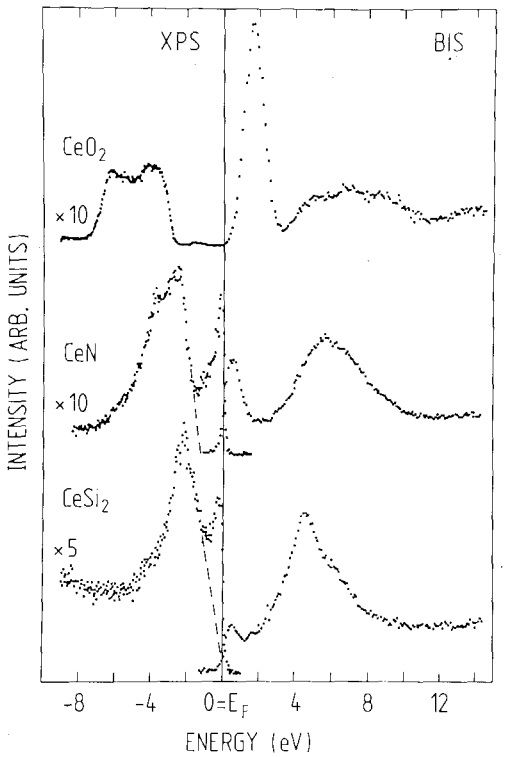

Fig. 25. Combined XPS–BIS spectra of CeO_2, CeN and $CeSi_2$. The extrapolated upper valence band edges are indicated by the dashed lines (Wuilloud et al. 1985).

In $CeSi_2$ the estimation of the upper p-band edge (dashed line in fig. 25) indicates that this compound looks rather like a semimetal with the $4f^1$ state squeezed in the DOS minimum between the conduction and the valence band. The fit of the many-body calculation to the spectra (Wuilloud et al. 1985) (see table 2) yields practically the same coupling energies between 4f and band states as those found for CeN. However, in this case ε_f is found to be located at higher total energy than in CeN. It results that besides the high $4f^1$ intensity at E_F a sizable f-admixture spread through the p band is predicted by the calculation. The measured and computed spectra corresponding to the addition of a 4f electron (BIS) reflect also clearly that Ce in $CeSi_2$ is not far from the trivalence. This conclusion is confirmed by the occurrence of magnetic transitions for compositions with Si deficiency (Satoh et al. 1981, Dijkman et al. 1982). In this respect the situation is very similar to the observations made in the $CePd_3B_x$ series, where increasing boron concentration produces the appearance of magnetic moments (Dhar et al. 1981, Wuilloud et al. 1984a).

The spectra analysis within a single-impurity approach including in separate terms the f-mixing with valence and conduction bands appears to be very successful for these materials.

6.2.5. *EELS versus XPS core level spectra*

For EELS processes in the intermediate energy range it is established that the $3d \rightarrow 5d$ single particle matrix elements are negligible when compared to those determining the intensity of the $3d \rightarrow 4f$ transitions (see section 4.4). For this reason within the sudden approximation, the EELS many-body matrix element corresponds to the BIS matrix element (eq. (19)) in which an annihilation operator for a core state has been inserted. This is quite different from the XPS transitions where a high-energy free electron is created. The important consequences of this difference in the core level spectra can be easily understood schematically by considering the two types of transitions within the simplified framework of the Hamiltonian without hopping terms: a f^n initial state is projected only on a f_c^n final state in XPS and only on a f_c^{n+1} final state in EELS. The introduction of the coupling terms does not change very much from this situation for EELS processes where the initial configuration has a nearly integral population f^n: this $3d \rightarrow 4f$ electron transition between atomic orbitals leaves the valence electrons practically undisturbed so that a nearly pure f_c^{n+1} state having approximately the correct frozen energy (eq. (10)) is formed. On the other hand, for fractional f-occupations, final-state mixing will necessarily take place in EELS. The situation is quite different for XPS processes where the frozen final state energy usually does not correspond to any eigenenergy in the presence of a core hole. In this case, different final eigenstates must be realized in order to produce the correct mean energy required by the sudden approximation (eq. (10)).

The EELS spectra referenced to the primary beam energy provide a straightforward measure of the energy involved in the transitions. As discussed in section 6.2.1, a common total energy scale for XPS and EELS is simply obtained by a calibration. The computed XPS (full line) and EELS (dotted line) spectra are shown together with the measured ones in figs. 23b and 24b. The multiplet splitting, particularly important in EELS (Netzer et al. 1983, Matthew et al. 1983, Moser et al. 1984) (chapter 72 of this volume) has not been incorporated into the calculation. In order to make the comparison easier, the centers of gravity of the EELS final states have been calculated and their positions are indicated by arrows in the corresponding XPS and EELS spectra.

The agreement between calculated and measured relative energy positions is striking. It is particularly enjoyable to observe that the calculated crossing of f_c^1 and f_c^0 uncoupled positions in the sequence Ba, La_2O_3, La is fully confirmed by the experiment. The fact that the EELS final-state position in La_2O_3 is near the center of gravity of the XPS excitations demonstrates the different character of the corresponding final states.

A weak satellite present in the calculated spectra for fractional occupation in EELS is also clearly visible in CeO_2 and (less prominent) in $CeCo_2$. In addition, the observed EELS structures for these systems differ from the characteristic multiplets corresponding to nearly integral f^1 or f^2 final-state populations (Matthew et al. 1983, Moser et al. 1984, Kaindl et al. 1985). These facts reflect in the final state the consequences of the initial-state mixing. However, in order to analyze this mixing quantitatively a GS calculation including multiplet splitting is needed.

6.2.6. *$L_{II,III}$ absorption edges versus XPS core levels*

In first approximation, the 2p → 5d photoabsorption processes involved in $L_{II,III}$ absorption edges can be considered as identical to those occurring in the XPS ionization of any deep core level (see section 4.3). The dipole selection rules offer to the excited electron only the possibility to occupy an extended εd band state. As the Hamiltonian considered for such processes does not contain Coulomb correlation energies between band and localized electrons, the excitation process is the same as the one for XPS core spectroscopy (Delley and Beck 1985). The analogy with a XPS process becomes obvious: for one particular transition the sudden approximation matrix element is identical to the one for the XPS transition of energy $(h\nu - \varepsilon)$ and spectral weight $\rho_c^{XPS}(h\nu - \varepsilon)$. This is precisely the intensity of deep core level spectra, e.g. 3d excitations, computed with the model calculation and shown in figs. 24b and 25b. Then, the total absorption for all possible transitions at the photon energy $h\nu$ is given by the convolution (Delley and Beck 1985, Schneider et al. 1985)

$$\rho_{p\to d}^{XAS}(h\nu) = \int d\varepsilon\, W^2(\varepsilon)\, \rho_c^{XPS}(h\nu - \varepsilon). \tag{20}$$

In order to define the XAS spectra on the common energy scale of the other core level spectroscopies, it has to be represented as a function of $h\nu - \varepsilon_c$. This expression obtained for the $L_{II,III}$ edges is nothing else than a XPS core level spectrum washed out by the convolution with the function $W^2(\varepsilon)$ taking into account the dipole matrix element for absorption and the single-particle density of states. For the calculation, the details of the energy dependence of W^2 are ignored and a smooth form $W^2(\varepsilon) = \sqrt{\varepsilon} e^{-\varepsilon/\lambda}$, with an adjustable parameter λ is assumed.

Figure 26 shows a comparison between the measured (Rao et al. 1981) and calculated L_{III} edge of $CeCo_2$. The model calculation of the 3d XPS core level spectrum presented in fig. 24b and the function $W^2(\varepsilon)$ with $\lambda = 7$ eV have been used for this computation. The three distinct peaks in the XPS spectrum can be recognized as attenuated and broadened structures in the L-edge spectrum. In view of the approximations made in the model, the overall agreement in positions and intensities between the calculated and measured spectral features is surprisingly good. Similar comparisons attempted for La_2O_3, CeO_2, α-Ce and γ-Ce are less satisfactory but they still confirm that this model is a correct first approximation. Obviously the real form of $W^2(\varepsilon)$ and other possible interactions of the excited electrons with the ionized atom have to be taken into account.

Quite often in such systems (for example, Wohlleben and Röhler (1984), and see chapter 71), the $L_{II,III}$ edges have been analyzed as if they were formed of overlapping Lorentzian lines and their intensity ratios were considered to reflect directly the configuration mixing in the initial state. Within the GS formalism discussed in this section, it is not possible to find any sound foundation for such an analysis.

6.3. *Heavy lanthanide materials*

With increasing atomic number the maximum of the 4f radial charge density

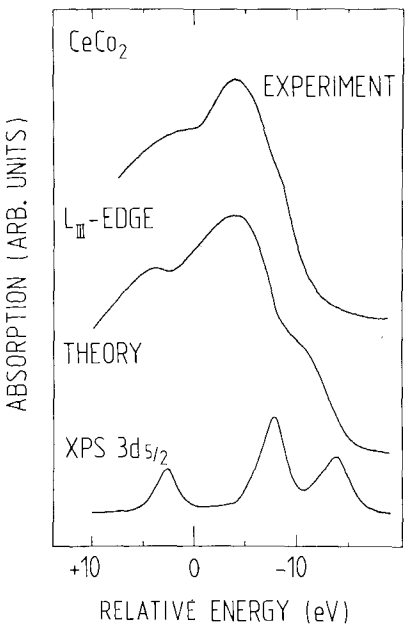

Fig. 26. Calculated and measured L_{III} absorption edge for $CeCo_2$. The calculated edge is obtained by convolution of the XPS $3d_{5/2}$ core spectrum shown in fig. 24b with the function $W^2(\varepsilon) = \sqrt{\varepsilon}\, e^{-\varepsilon/\lambda}$. The total energy of the core hole ε_c has been subtracted. The experimental spectrum was taken from the work of Rao et al. (1981) (Schneider et al. 1985).

moves closer to the nucleus (see fig. 5) reducing the overlap with the outer electron states of neighbour atoms (figs. 1 and 2). For this reason hybridization effects between f and band states are expected to become progressively weaker when proceeding from Ce to Yb. These considerations appear to favour a purely atomic description of the 4f states at least in Yb and its compounds. Trivalent Yb, with its $4f^{13}$ configuration corresponding to one hole in the f shell has a remarkable symmetry with trivalent Ce where one electron occupies the f shell. This situation has been analyzed within the single-impurity Anderson model by Bickers et al. (1985). Assuming a 30% smaller hybridization parameter than for γ-Ce they obtain outer level excitation spectra for Yb which, apart from the larger 4f-spin-orbit splitting, show a striking symmetry to those of γ-Ce. This remarkable prediction of hybridization effects in Yb systems needs to be confirmed experimentally. For the remaining lanthanides, excepted $4f^7$ systems like Eu^{2+} (Andrei and Destri 1984, Tsvelick and Wiegmann 1984), many-body calculations are presently not available This situation is certainly due to the fact that such computations would have to include the complex multiplet structure of the 4f states.

At the present time the electron-spectroscopic manifestations of 4f-hybridization in heavy lanthanide materials are scarce. (The so-called valence fluctuating compounds containing the elements Sm, Eu, Tm or Yb are discarded here (see section 7.3).) Nevertheless, indications for a coupling of the f states with band states have been found in materials where the Eu atoms, according to Mössbauer spectroscopy and the magnetic susceptibility, are in the divalent $4f^7$ configuration. The XPS 3d core level spectra of a few systems, like Eu metal, $EuAl_2$, $EuCu_5$, $EuAg_5$ (Schneider

et al. 1981, Laubschat et al. 1983) and $EuPd_2P_2$ (Wertheim et al. 1985) exhibit a splitting of each spin-orbit component quite similar to the one found in La compounds. Also the L_{III} edges in $EuPd_2P_2$ (Sampathkumaran et al. 1985) and in $Eu(Pd_{1-x}Au_x)_2Si_2$ (Abd-Elmeguid et al. 1985) display an edge structure reminiscent of the one observed for $CeCo_2$. Clearly, these experimental findings call for a thorough theoretical analysis within the impurity model in order to quantify the mixing of the different f configurations involved. In particular situations it appears that the 4f states of the heavy lanthanides require a description going beyond the atomic-like approach.

7. Unconventional behaviour induced by the 4f-hybridization

7.1. *Breakdown of the conventional concept of valence*

Hybridization is one of the most important mechanisms responsible for the stability of solids and molecules. The cohesion of lanthanide atoms in solids is mainly determined by the 5d and 6s states while the 4f states play essentially the role of core states but also contribute very weakly to the stability of the bond by the overlap of their wave function tails with the band wave functions of neighbour atoms. This situation cannot be classified according to the conventional chemical concepts, even if one could find a rigorous and unique definition of the valence (Coulson 1961). This fact is the origin of a dramatically confusing situation in the field of the spectroscopies since often the authors choose a particular name like fractional valence, intermediate valence, mixed valence, valence fluctuation, ambivalence, etc., to characterize unconventional situations without attempting to describe the nature of the observed states. For the purpose of clarifying the following discussion we define the valence of a lanthanide atom as the number of electrons supplied by this atom to the bond. In the atomic limit (section 4), the 4f electrons have clearly not to be considered and the valence is an integral number. The difficulty arises when a small but sizable hybridization involves the 4f states into a metallic bond (section 6). In order to be consistent with our previous definition of the valence, one should include them in the valence electron count. This is not satisfactory since in first approximation they can be considered as core states in valence band calculations. For this reason the valence is no longer a meaningful quantitative concept for characterizing a weak hybridization and it is wise to refrain from assigning to it any precise numerical value. At the present time we believe that the best description of such a situation is provided by the parameters entering the Anderson impurity model used to analyze the spectroscopic results. One must be aware that for a finite hybridization, the initial 4f population n_f obtained from the GS model does not open the possibility to introduce some new concept of valence. On the other hand, insulators yield a clear-cut situation where the projected f-symmetry states of the full valence band with integral population are separated by an energy gap from the atomic-like 4f states. In the example of CeO_2 presented in section 6.2.4, the Ce atoms are tetravalent according to our definition. Finally in

metals an extreme situation can occur in the 4f localization limit when two nearly degenerate configurations with integral f-counts are so weakly coupled that the characteristic probing time of different methods appears to be an important factor determining the aspect of the electronic structure which is revealed (Gonçalves da Silva and Falicov 1976, section 7.3).

The incredible accumulation of experimental and theoretical studies devoted to the elucidation of this weak hybridization problem demonstrates the complexity and diversity of the resulting manifestations. Most recent experimental facts and developments on the subject can be found in the reviews of Lawrence et al. (1981) and Stewart (1984) and a comprehensive sketch of the theoretical issues has been given by Varma (1985). It is not the purpose of the following sections to discuss thoroughly these many-body effects but just to investigate which aspects can be revealed by high-energy spectroscopies. No attempt will be made in the data analysis to go beyond the Anderson single-impurity model which neglects the interaction between 4f states on neighbour atoms and the influence of finite temperatures. It appears that even when it is used abusively, this model has the virtue to simulate correctly the intensity distribution observed in the different types of spectra.

7.2. *The induced metallic 4f-character*

The strongest 4f-hybridization effects occur in the light lanthanides and so far the GS analysis of the electron spectroscopy excitations could only be performed in La and Ce systems. The parameters characterizing the electronic structure in the single-impurity model are extracted rather safely from comparison with experimental spectra (section 6.2) and in a sense one can consider that the problem has been completely solved within this framework. Despite the many-body nature of this approach, it is worth to proceed to a more detailed analysis of the basis states used in this model. In metallic systems it appears that the low-energy excitations in a very narrow energy range above the ground state have a behaviour reminiscent of extended single-particle states. This fact can be intuitively anticipated from the hybridization of band states with the f states which consequently have no longer an integral occupation and have acquired some itinerant character weakening their atomic nature.

In the GS model, the first order N-electron ground state of energy E_0 is of the form given by Varma and Yafet (1976):

$$|\Phi_0\rangle = a_0|0\rangle + \int_{-B}^{0} \mathrm{d}\varepsilon'\, a_0(\varepsilon')|\varepsilon'\rangle. \tag{21}$$

It is an expansion in the basis function $|0\rangle$ formed of all occupied band states and in the continuum of basis functions $|\varepsilon'\rangle$ formed of the occupied band with one hole and one 4f electron. From the parameters entering the GS model, one can calculate the energy lowering δ which results from the hybridization of the 4f states with

band states (Gunnarsson and Schönhammer 1983b, appendix c). We shall see that δ defines the relevant energy scale for the metallic-like f excitations of the system.

The final state of energy E created by the photoemission process can be written in a similar form:

$$|\Phi_E^{\varepsilon}\mu\rangle = a_E(\varepsilon)|\varepsilon\mu\rangle + \int_{-B}^{0} \mathrm{d}\varepsilon'\, a_E(\varepsilon'\varepsilon)|\varepsilon'\varepsilon\mu\rangle. \tag{22}$$

It is again an expansion in two types of basis functions: (i) the function $|\varepsilon\mu\rangle$, characterized by the quantum number μ, represents the band with one hole at ε and no f electron; (ii) the continuous set of functions $|\varepsilon'\varepsilon\mu\rangle$, each of them representing the band with two holes at ε' and ε and one f electron. For fixed values of μ and ε, all sets of final eigenstates have the same structure as a function of E: they contain a lowest state (split-off state, labelled s) separated from a continuum of states by an energy gap of width equal to the energy lowering δ introduced previously. The f-dipole matrix element of the photoemission process couples exclusively $|\varepsilon\rangle$ with $|\varepsilon\mu\rangle$. If only the split-off final states are considered, the coefficients $a_E^{\mathrm{s}}(\varepsilon)$ are constant so that the corresponding f-spectral density $\rho_{\mathrm{s}}^{\mathrm{f}}(E)$ is simply proportional $a_0^2(\varepsilon)$. As already mentioned in section 2.4, for metals the ground-state energy coincides with the origin of the excitation spectrum which is also the Fermi energy ($E_0 = E_{\mathrm{F}} = 0$) (see figs. 3, 7, 19). The lowest photoemission final state corresponds to one hole at E_{F} ($\varepsilon = 0$) and therefore is identical to the initial ground state. For the other split-off states it can be shown that $\varepsilon = E$. Within the narrow energy range $0 \leqslant \varepsilon \leqslant \delta$ above E_{F}, only transitions to the split-off final state can occur and the corresponding f-spectral density is given by $\rho_{\mathrm{s}}^{\mathrm{f}} = (1 - n_{\mathrm{f}})a_0^2(\varepsilon)$. It reflects directly the weight of the basis states $|\varepsilon\rangle$ in the ground state or, in other words, the weight of the f-character mixed to the band states as a function of the energy ε. This quantity can be anticipated to be related to the f-projected DOS which would result from a ground state calculation including f-symmetry states. It can be identified with the adiabatic band-like part of the f-photoemission spectrum as discussed in section 2.4. The f-photoemission spectrum formed exclusively of the split-off states within δ has a metallic character in the sense that, as in a single particle approach to metallic band excitations, a population variation is possible at E_{F} for an infinitesimal total energy variation (Janak 1978) and all final states contain the same f population as the initial state. The shape of $\rho_{\mathrm{s}}^{\mathrm{f}}(\varepsilon) \approx a_0^2(\varepsilon)$ which is pinned at E_{F} can be simply understood when starting from the uncoupled situation represented in fig. 19 (section 6.1). In addition to the energy increase resulting from the decrease of the f-count, the hybridization requires the energy involved in the formation of a band hole in the basis states $|\varepsilon\rangle$ containing one f electron (eq. (21)). The variational calculation of the ground state shows that the total energy lowering resulting from the mixing terms overcomes these two penalties. It is obvious that this is only possible if the weight $a_0^2(\varepsilon)$ of $|\varepsilon\rangle$ is maximum at $\varepsilon = E_{\mathrm{F}} = 0$ and decreases very rapidly within δ towards higher energies. If the total f-spectral density is normalized to n_{f}, the calculation yields for the maximum value of $\rho_{\mathrm{s}}^{\mathrm{f}}(\varepsilon)$: $\rho_{\mathrm{s}}^{\mathrm{f}}(E_{\mathrm{F}}) = (n_{\mathrm{f}}^2\pi)/(N_{\mathrm{f}}\Delta)$ and for its weight: $n_{\mathrm{f}}(1 - n_{\mathrm{f}})$, which is mainly confined within δ.

The final states different from the split-off states have no close relationship to the initial state, they form a continuum starting at the energy δ above the ground state. They result from the high f correlation and for increasing energy they contain a lower f population, i.e., a more pronounced f-hole character (Allen 1985). In the limit of $\Delta \to 0$ ($n_f \to 1$) this continuum of excited states transforms into the single peak $4f^0$ and the metallic peak ($\rho_f^s(\varepsilon)$) located at E_F vanishes, as expected in the atomic-like situation. It is interesting to notice that this description of the f-excitation spectra makes conspicious striking similarities with the photoemission spectra of correlated band states (see section 2.4) as for example in Ni (Treglia et al. 1980a), despite the different nature of these two systems.

The existence of two types of excited final states in photoemission spectra of Ce systems has been often identified as two peaks. However, the current resolution of photoemission (≈ 100 meV) is at least a factor 10 too large to allow a valuable test of the low-energy metallic excitations of f-character which are responsible for unconventional manifestations in the quasi ground state properties of such systems at low temperatures (specific heat, magnetic properties, transport properties). It is a fundamental challenge for the electron spectroscopies to resolve the details of the fine structures near E_F predicted by the GS model. In a recent photoemission study of α- and γ-Ce devoted to this problem with an insufficient resolution (Wieliczka et al. 1984), the situation has not been appreciated correctly and the conclusions of this work appear to be not reliable. With the He I and He II resonance lines produced in a commercial discharge lamp and an electron spectrometer carefully tuned, a total instrumental resolution of 20 meV could be recently achieved (Patthey et al. 1985). With these improved experimental conditions the α- and γ-phases of Ce have been investigated at low temperature. Figure 27 shows in the energy range of 600 meV below E_F for each phase the two photoemission spectra recorded with 40.8 eV and 21.1 eV photon energy. They have been weighted and subtracted from each other in order to isolate as well as possible the f contribution. The new feature observed at high resolution is the existence of two closely spaced peaks, one at E_F, the other one at 280 meV. This is precisely the energy separation of the $4f_{7/2}$ and $4f_{5/2}$ levels in atomic Ce. In fact these states are not resulting from the same excitation mechanism (section 4.2) as the multiplets observed in the atomic limit. They account for the f^1 screened many-body response of the hybridized states to the emission of one electron from the metallic f-peak. A first order GS model calculation has been performed (Patthey et al. 1985) where the spin–orbit interaction is included and the parameters are chosen in order to obtain the best agreement with many different spectroscopic results (Schneider et al. 1985). The essential result is that a modest 30% increase of Δ from 82 meV to 105 meV accounts correctly for all changes observed in the different spectra upon the $\gamma \to \alpha$ transition. The calculation yields for δ the values of 5 meV for γ-Ce and 26 meV for α-Ce. The contribution $\rho_s^f(\varepsilon)$ of the split-off final states has been extracted from the calculation and convoluted with a Lorentzian in order to simulate the instrumental broadening and to account tentatively for the influence of the temperature. It is represented in fig. 27 by the curves defining the hatched area which are 2% and 12% of the total f-spectral weight in γ-Ce and α-Ce respectively. The good agreement between experimental and calculated f contributions to the photoemission spectra shown in fig. 27 establishes

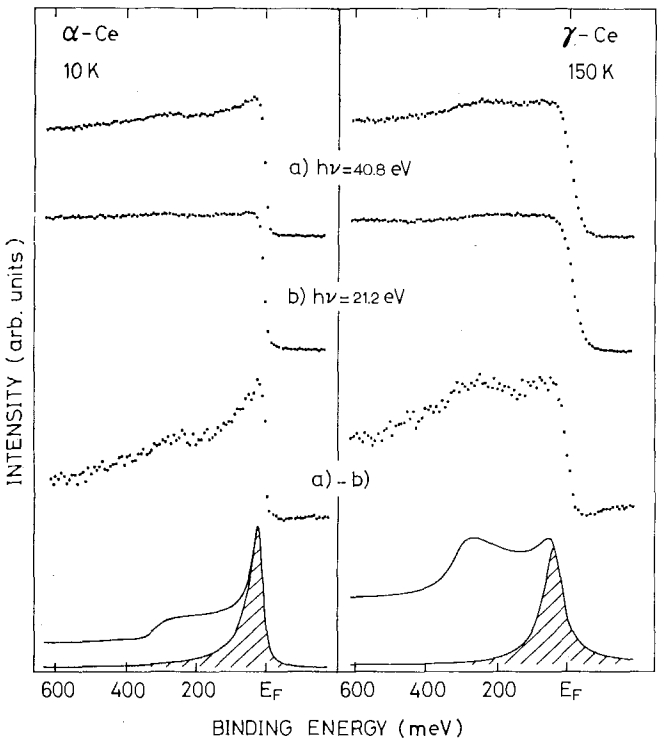

Fig. 27. Curves (a) and (b): Photoemission spectra of α- and γ-Ce within 600 meV below E_F. Curve (a) – (b): difference of weighted spectra (a) and (b) for the same phase. Full curve: GS calculation. The curves defining the hatched areas correspond to $\rho_s^f(\varepsilon)$ convoluted with a Lorentzian (see text), (Patthey et al. 1985).

the validity of this approach and demonstrates that high-energy photoemission is adapted to probe the crucial low-energy range of excitations closely related to the ground state.

When the initial f population n_f is very close to one in Ce systems (spin-fluctuation limit), $\delta/k_B = T_K$ is called Kondo temperature and $\rho_s^f(\varepsilon)$ within δ Kondo peak (Gunnarsson and Schönhammer 1983a,b). Early attempts have been made to estimate the Kondo temperature by using the parameters of the Anderson Hamiltonian extracted from photoemission data (Allen et al. 1981, Croft et al. 1981b). The situation is particularly interesting in metallic Ce systems where $n_f \approx 1$ when a weak hybridization produces a sufficiently small value of δ so that at E_F the maximum of the f-excitation spectrum $\rho_s^f(E_F) = (n_f^2 \pi / N_f \Delta)$ dominates largely the intensity originating from states of other symmetries, while the relative weight $(1 - n_f)$ of the split-off final states confined within δ remains sizable in photoemission spectra. The approach of this problem within the GS model has the drawback to be only valid at $T = 0$ and no attempt has been made to include in it the temperature. However, one can anticipate that when T increases and becomes larger than T_K, the population of the singlet ground state (eq. (21)) decreases to the benefit of the triplet excited states. For this reason the Kondo peak intensity is

expected to be gradually transferred to the more atomic-like final states. A confirmation of this behaviour is given by calculations performed within other formalisms which are also based on the Anderson impurity model (Grewe 1984, Schlottmann 1984, chapter 64). For the analysis of the photoemission spectrum of α-Ce (fig. 27) obtained at 10 K, this is not a problem since $T \ll T_K$ but the measurement of γ-Ce had to be performed at 150 K which is clearly larger than the deduced $T_K = 60$ K. In this case, the excellent simulation of the spectra by the GS model is surprising and one should be able to show that it still provides approximately a correct description of the spectra for effective parameters depending on the temperature.

It is very interesting to investigate with electron spectroscopies the consequences of the extreme conditions $\Delta \ll \varepsilon_f$ in other Ce systems like $CeAl_3$, $CeCu_2Si_2$ or $CeCu_6$ for which the low temperature range is accessible. These compounds show dramatically large values of the magnetic susceptibility and of the linear coefficient of the specific heat. These exotic properties can be accounted for formally by using free-electron expressions with masses which need to be renormalized by factors which can exceed 100. No attempt will be made here to describe the excitement that this discovery of heavy-fermion systems has raised in the scientific community. We shall simply remain within the single-impurity model yielding already a qualitative prediction for the extremely high density of low-energy excitations which are responsible for the anomalous single-particle-like behaviour.

An electron spectroscopy study of $CeCu_6$ has been recently performed (Patthey et al. 1986b) in order to characterize the states responsible for the heavy-electron manifestations observed in this compound. At first sight the different types of spectra show the purest feature of a $4f^1$ ground state ever observed in Ce systems. In fig. 28 the high-resolution (20 meV) UPS spectrum excited with He II radiation at 15 K reveals no intensity enhancement in the 100 meV below E_F and only the $4f_{7/2}$ final-state excitation is observed. The GS analysis has been performed for the different types of spectra and in this extreme situation it allows us only to obtain the limit $(1 - n_f) < 0.005$, corresponding to the energy lowering $\delta \approx 1$ meV. The relative weight of the Kondo peak in the total 4f-photoemission spectrum is therefore of the order of 0.5% and, even if it is not already washed out at a temperature of the order of T_K (Grewe 1984, chapter 64 of this volume), it cannot show up in a measurement performed with a resolution of 20 meV. In fig. 28b, this situation is clearly illustrated by the GS calculation convoluted with a Lorentzian line of width corresponding to the instrumental broadening and superimposed on a constant intensity (dashed line) assumed to account for the other states forming the bands in $CeCu_6$. As shown in the inset of fig. 28, even if it is recorded with the extreme resolution of 12 meV, the UPS spectrum does not contain the weakest indication of an intensity enhancement at E_F attributable to the Kondo peak. In the BIS spectrum (not shown here) the relative intensity of the Kondo peak probed by electron addition is expected to be roughly 13 times stronger than in the photoemission spectrum. Since the rather pure f^2 final states are observed in the experimental spectrum, the Kondo peak intensity can be easily estimated from the GS prediction. It appears that with the BIS instrumental resolution of 0.5 eV achieved at the present time, it is not possible to discern this peak in the spectrum of $CeCu_6$ (Patthey et al. 1986b).

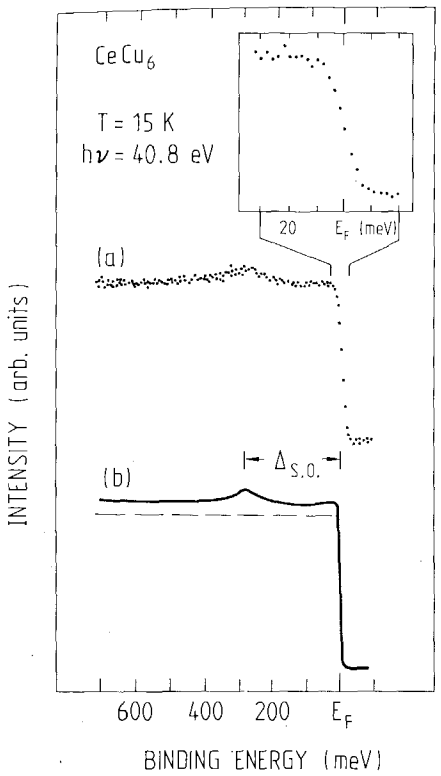

Fig. 28. (a): UPS spectrum of $CeCu_6$ within 700 meV below E_F measured at low temperature with a resolution of 20 meV. (b): Simulation of the measured spectrum (a) by a GS-type calculation including the spin–orbit interaction (Δ_{so} = 280 meV). A Lorentzian broadening (FWHM = 20 meV) has been included by convolution. A constant intensity (dashed line) originating from the states of Cu and Ce with $l \leqslant 2$ has been assumed in this calculation. Inset: Indicated energy range around E_F measured with an ultra-high resolution of 12 meV (Patthey et al. 1986b).

Despite the fact that the GS model ignores the influence of the thermal broadening and of the coherence between the neighbour f states, the message of this study is that the weight of the Kondo peak in the spectra of heavy-fermion systems is too weak to be detected directly with the resolution and low temperatures which could be reached until now. In the light of this conclusion, the interpretation of recent spectroscopic studies devoted to the heavy-fermion problem in Ce and U systems (Parks et al. 1984, Arko et al. 1984, Allen et al. 1985) has to be reconsidered critically.

7.3. *Hybridization in the 4f-localization limit*

An intuitive approach will be adopted to describe the peculiar lanthanide systems showing manifestations suggesting a fluctuation of the 4f population. At first we shall assume that the 4f shell remains purely atomic-like and that at $T = 0$ two degenerate ground states of the whole solid exist, which correspond to two neighbour f-occupations, for example $4f^n$ and $4f^{n+1}$ ($\Delta_+ = 0$ in fig. 9). In this hypothetical situation one would have the choice between two stable ground states with different valences, according to our previous definition (section 7.1), and an infinitely weak external action can induce the transition of the system from one state to the other one. The occurrence of such a situation can be only completely

fortuitous. The contribution of the valence electrons to the total energy is large and its modification upon a transition between the two degenerate states is very important since the band population varies by one electron per lanthanide atom. It is very unlikely that the lowest total energy of this solid could be obtained for these two states where in each of them all lanthanide atoms have the same integral f population (n or $n+1$) (Varma 1985).

Let us release the condition that the average f-count per lanthanide atom needs to be integral so that the lowest total energy determined by the band occupation can be achieved for a fractional population of the atomic-like f levels. We face a difficult situation which can no longer be described with a simple homogeneous model where all lanthanide atoms are equivalent at the same time. At $T = 0$, one can imagine that the two kinds of atoms with f^n and f^{n+1} configurations will form a lattice determined by the most favourable mean f population and lattice constants. In this limit of complete f localization, the situation at $T > 0$ can be visualized as a fluctuating state in the sense that the long-range order of the ion lattice is destroyed by a configuration fluctuation mediated on each lanthanide site by phonon breathing modes. One has to assume that the fluctuation frequency is low enough to allow a local description of the two configurations with well-defined energies. This phenomenon must remain highly correlated in space in order to maintain locally the proportion of the two configurations delivering to the band the number of electrons required for achieving the minimum total energy. Within the sudden approximation, the 4f photoemission spectrum is then expected to display the two transitions $4f^{n+1} \rightarrow 4f^n$ and $4f^n \rightarrow 4f^{n-1}$ with intensities which are proportional to the initial occupation probabilities in this 4f-localization limit. In the first type of transition, the final state achieved on a particular atom is very close to the initial state of the other transition. The only difference is that a $4f^n$ state is suddenly created on a site where a $4f^{n+1}$ configuration was stable in the ground state at this precise moment. If the small energy required in this transformation breaking the correlation is neglected, the lowest term of the $4f^n$ multiplet excitations is observed at E_F in a photoemission spectrum. For the other type of transitions, the $4f^{n-1}$ final state multiplets are usually well separated by Δ_- (fig. 9) in the spectra. This situation is clearly illustrated in fig. 29 by the XPS spectrum of TmSe (Campagna et al. 1976)

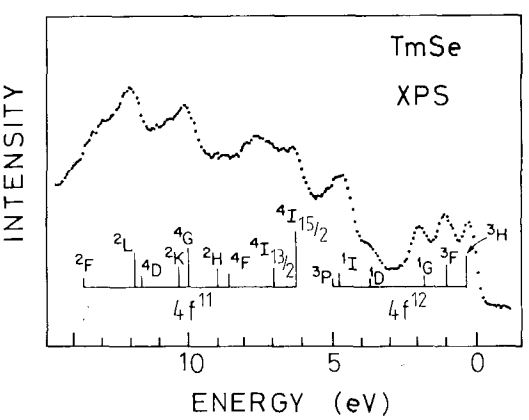

Fig. 29. XPS spectrum of TmSe analyzed with the intensities of the f^{11} and f^{12} final state multiplets (vertical bars) predicted by the fractional parentage coefficients (see fig. 8d,e) (after Campagna et al. 1976).

which displays the multiplet final states of $4f^{11}$ and $4f^{12}$ (see fig. 8e). It is a simple matter to show that it is the lowest $4f^{n+1}$ final state which is located at E_F in BIS spectra. The success of the atomic interpretation of the spectra based on the coefficients of fractional parentage (section 4.2) has strongly contributed to establish this simple concept of homogeneous configuration fluctuation. Since the early observations of such 4f spectra (Campagna et al. 1976), their interpretation has not markedly evoluted but they have been confronted to quantities reflecting stationary aspects of the ground state (lattice parameters) or averaging the response of the whole system (magnetic susceptibility) or averaging the electronic behaviour of a single atom on a limited period of time (Mössbauer effect). It appears that the nature of the information obtained in an experiment depends critically upon the time interval during which the system is probed (Gonçalves da Silva and Falicov 1976). One can naively assume that at finite temperature the configuration fluctuation frequency on one lanthanide atom defines the relevant time scale for the average obtained in a particular measurement. At the present time it is difficult to find a simple theoretical foundation to these intuitive ideas because the many-body calculations of the stationary eigenstates of the whole system are only valid on a time scale much longer than the fluctuations. For this reason it is somewhat hazardous to interpret the fractional expectation value of the 4f population simply in terms of the fraction of times during which the two integral populations are really existing on one atom in the ground state. However, it remains that this problem can certainly be considered as a particular hybridization in the 4f-localization limit.

One can attempt to go beyond the pure atomic-like description and to release somewhat the stringent 4f-localization condition assumed previously. Within the single-impurity model of Anderson, a configuration fluctuation can only be compatible with a very small energy difference between two consecutive f-counts (Δ_+ or Δ_-) and with a total energy lowering δ resulting from their mixing with band states which is of the same order of magnitude or even smaller. There is little doubt that a GS-type calculation could synthetize correctly all observed spectra for a rather correct value of n_f. However, in this case the stability of the configuration ratio in the solid is likely to be determined by the short-range order of the different ions yielding the most favourable filling of the band. A single-impurity model is obviously not adapted to describe this complex situation which is the subject of intensive theoretical efforts at the present time.

8. Recent developments

An important issue for the low-temperature properties of hybridized f systems, which has been recognized and taken into account only recently in the analysis of electron spectroscopic data, is the influence of the crystalline electric field (CEF). Depending on the crystal symmetry, the degeneracy $N_f = 6$ of the $4f^1_{5/2}$ spin–orbit component of Ce is lowered to 4 or 2 in the lowest crystal state. Consequently a GS-type many-body calculation, when performed only to the lowest order in $1/N_f$, certainly does not yield a well-converged ground state. Moreover, the low-energy

parameter δ, representing the energy lowering of the ground state due to hybridization, is reduced with decreasing degeneracy (Hewson et al. 1985, Gunnarsson and Schönhammer 1985, Patthey et al. 1987a). When the splitting Δ_{CEF} between the two lowest crystal-field levels exceeds δ, these levels become apparent in sufficiently well-resolved spectra (Patthey et al. 1987b), opening the possibility to use high-resolution photoemission as a complementary tool to inelastic neutron and light scattering in the study of CEF levels. It has been confirmed that the low-energy parameter δ, extracted from the spectra analysis, is consistent with the analysis of the specific heat and the magnetic susceptibility performed within the same formalism (Patthey et al. 1987a,b, Allen et al. 1986). The analysis of the low-lying excitations, observed with photoemission, yields an undisputable demonstration that already the single-impurity model at $T = 0$ contains the relevant mechanisms allowing us to simulate the spectra. Most recently, this type of spectra analysis has been extended to finite temperatures, enabling a detailed study of the high-temperature collapse of the Kondo resonance in $CeSi_2$ (Patthey et al. 1987b). This investigation confirmed the many-body nature of the low-energy excitations around E_F.

In Ce systems, the many-body parameters deduced from the spectroscopic analysis, are always characteristic for the Kondo regime ($\varepsilon_f \gg \Delta$, $n_f \approx 1$) (Allen et al. 1986). In heavier rare earths, the single-impurity parameters are likely to become different and other regimes are conceivable (Kojima et al. 1984, Coleman 1984). This is the case for $YbAl_3$, which has been found to belong to the mixed valence regime ($\varepsilon_f \approx \Delta$, $n_f \approx 0.5$) (Patthey et al. 1987c), where the ground state consists of a mixing of $4f^{13}$ and $4f^{14}$ wavefunctions with approximatively equal weight.

All these recent data have provided new evidence that the single-impurity model is well adapted to describe the fundamental mechanisms governing the 4f-conduction-band hybridization in rare earth materials.

Acknowledgements

We wish to thank H. Beck, B. Delley, J.-M. Imer, H.R. Moser, F. Patthey and E. Wuilloud for a fruitful collaboration and for stimulating discussions. The financial support from the Swiss National Science Foundation is gratefully appreciated.

References

Abd-Elmeguid, M.M., Ch. Sauer, U. Köbler, W. Zinn, J. Röhler and K. Keulerz, 1985, J. Magn. & Magn. Mater. **47&48**, 417.

Allen, J.W., 1985, J. Magn. & Magn. Mater. **52**, 135.

Allen, J.W., L.I. Johansson, R.S. Bauer and I. Lindau, 1978, Phys. Rev. Lett. **41**, 1499.

Allen, J.W., L.I. Johansson, I. Lindau and S.B. Hagström, 1980, Phys. Rev. B **21**, 1335.

Allen, J.W., S.-J. Oh, I. Lindau, J.M. Lawrence, L.I. Johansson and S.B. Hagström, 1981, Phys. Rev. Lett. **46**, 1100.

Allen, J.W., S.-J. Oh, L.E. Cox, W.P. Ellis, M.S. Wire, Z. Fisk, J.L. Smith, B.B. Pate, I. Lindau and A.J. Arko, 1985, Phys. Rev. Lett. **54**, 2635.

Allen, J.W., S.J. Oh, O. Gunnarsson, K. Schönhammer, M.B. Maple, M.S. Torikachvili and I. Lindau, 1986, Adv. Phys. **35**, 275.

Alvarado, S.F., M. Campagna and W. Gudat, 1980, J. Electron Spectrosc. & Relat. Phenom. **18**, 43.
Andrei, N., and C. Destri, 1984, Phys. Rev. Lett. **52**, 364.
Arko, A.J., C.G. Olson, D.M. Wieliczka, Z. Fisk and J.L. Smith, 1984, Phys. Rev. Lett. **53**, 2050.
Azaroff, L.V., ed., 1974, X-Ray Spectroscopy (McGraw-Hill, New York).
Baer, Y., 1984, Electron spectroscopy studies, in: Handbook on the Physics and Chemistry of the Actinides, Vol. I, eds A.J. Freeman and G.H. Lander (North-Holland, Amsterdam) ch. 4 and refs. therein.
Baer, Y., and P. Zürcher, 1977, Phys. Rev. Lett. **39**, 956.
Baer, Y., F. Patthey, J.-M. Imer and W.-D. Schneider, 1987, J. Electron Spectrosc. & Relat. Phenom. (to appear).
Bauchspiess, K.R., W. Boksch, E. Holland-Moritz, H. Launois, R. Pott and D. Wohlleben, 1981, in: Valence Fluctuations in Solids, eds L.M. Falicov, W. Hanke and M.B. Maple (North-Holland, Amsterdam) p. 417.
Bertel, E., G. Strasser, F.P. Netzer and J.A.D. Matthew, 1982, Phys. Rev. B **25**, 3374.
Bickers, N.E., D.L. Cox and J.W. Wilkins, 1985, Phys. Rev. Lett. **54**, 230.
Bonnelle, C., 1982, Resonant X-ray emission spectroscopy in solids, in: Advances in X-Ray Spectroscopy, eds C. Bonnelle and C. Mandé (Pergamon Press, London) ch. 6.
Bradshaw, A.M., L.S. Cederbaum and W. Domcke, 1975, Structure and Bonding **24**, 133.
Brodén, G., S.B.M. Hagström and C. Norris, 1973, Phys. Kondens. Materie **15**, 327.
Brundle, C.R., and A.D. Baker, eds, 1977, Electron Spectroscopy: Theory, Techniques and Applications, Vol. I (Academic Press, London).
Brundle, C.R., and A.D. Baker, eds, 1978, Electron Spectroscopy: Theory, Techniques and Applications, Vol. II (Academic Press, London).
Brundle, C.R., and A.D. Baker, eds, 1979, Electron Spectroscopy: Theory, Techniques and Applications, Vol. III (Academic Press, London).
Burroughs, P., A. Hamnett, A.F. Orchard and G. Thornton, 1976, J. Chem. Soc. Dalton Trans. **17**, 1686.
Bussian, B., I. Frankowski and D. Wohlleben, 1982, Phys. Rev. Lett. **49**, 1026.
Campagna, M., R. Sattler and H.C. Siegmann, 1973, AIP Conf. Proc. **18**, 1388.
Campagna, M., G.K. Wertheim and E. Bucher, 1976, Structure and Bonding **30**, 99.
Campagna, M., G.K. Wertheim and Y. Baer, 1979, Topics in Appl. Phys. **27** (Springer, Berlin) p. 217 and refs. therein. .
Cardona, M., and L. Ley, eds, 1978, Photoemission in Solids I, Topics in Applied Physics, Vol. 26 (Springer, Berlin).
Carnall, W.T., P.R. Fields and K. Rajnak, 1968, J. Chem. Phys. **49**, 4424.
Celotta, R.J., D.T. Pierce, G.L. Wang, S.D. Bader and G.P. Felcher, 1979, Phys. Rev. Lett. **43**, 728.
Citrin, P.H., and G.K. Wertheim, 1982, Phys. Rev. B **27**, 3176.
Citrin, P.H., G.K. Wertheim and Y. Baer, 1978, Phys. Rev. Lett. **44**, 1425.
Cohen-Tannoudji, C., B. Diu, F. Laloë, 1973, Mécanique Quantique (Hermann, Paris).
Coleman, P., 1984, Phys. Rev. B **29**, 3035.
Coulson, C.A., 1961, Valence (Oxford University Press, Oxford) second edition.
Cox, P.A., 1975, Structure and Bonding **24**, 59.
Cox, P.A., J.K. Lang and Y. Baer, 1981, J. Phys. F **11**, 113.
Croft, M., A. Franciosi, J.H. Weaver and A. Jayaraman, 1981a, Phys. Rev. B **24**, 544.
Croft, M., J.H. Weaver, D.J. Peterman and A. Franciosi, 1981b, Phys. Rev. Lett. **46**, 1104.
Crosswhite, H.M., R.L. Schwiesow and W.T. Carnall, 1969, J. Chem. Phys. **50**, 5032.
Dahr, S.K., S.K. Malik and R. Vijayaraghavan, 1981, Phys. Rev. B **24**, 6182.
Davis, L.C., and L.A. Feldkamp, 1981, Phys. Rev. B **23**, 6239.
Day, P., ed., 1981, Emission and Scattering Techniques (Reidel, Dordrecht).
Dehmer, J.L., A.F. Starace, U. Fano, J. Sugar and J.W. Cooper, 1971, Phys. Rev. Lett. **26**, 1521.
Delley, B., and H. Beck, 1985, J. Magn. & Magn. Mater. **47&48**, 269.
Delley, B., D.E. Ellis, A.J. Freeman, E.J. Baerends and D. Post, 1983, Phys. Rev. B **27**, 2132.
Desjonqueres, M.C., D. Spanjaard, Y. Lassailly and C. Guillot, 1980, Solid State Commun. **34**, 807.
Dijkman, W.H., A.C. Moleman, E. Kesseler, F.R. de Boer and P.F. de Châtel, 1982, in: Valence Instabilities, eds P. Wachter and H. Boppart (North-Holland, Amsterdam) p. 515.
Domke, M., C. Laubschat, M. Prietsch, T. Mandel, G. Kaindl and W.-D. Schneider, 1986, Phys. Rev. Lett. **56**, 1287.
Doniach, S., and M. Sunjic, 1970, J. Phys. C **3**, 285.
Dose, V., 1983, Prog. Surf. Sci. **13**, 225.
Dunning, F.B., C. Rau and G.K. Walters, 1985, Comments Solid State Phys. **12**, 17.
Ertl, G., and J. Küppers, 1974, Low Energy Electrons and Surface Chemistry (Verlag Chemie, Weinheim).
Esteva, J.-M., R.C. Karnatak, J.C. Fuggle and G.A. Sawatzky, 1983, Phys. Rev. Lett. **50**, 910.
Fabian, D.J., and L.M. Watson, eds, 1973, Band Structure Spectroscopy of Metals and Alloys (Academic Press, London).
Fäldt, A., and H.P. Myers, 1983, Solid State Commun. **48**, 253.
Fäldt, A., and H.P. Myers, 1984a, Phys. Rev. Lett. **52**, 1315.

Fäldt, A., and H.P. Myers, 1984b, Phys. Rev. B **30**, 5481.
Fäldt, A., and H.P. Myers, 1985, J. Magn. & Magn. Mater. **47&48**, 225.
Fano, U., 1961, Phys. Rev. **124**, 1866.
Fano, U., and J.W. Cooper, 1968, Rev. Mod. Phys. **40**, 441.
Feldkamp, L.A., and L.C. Davis, 1979, Phys. Rev. Lett. **43**, 151.
Feuerbacher, B., B. Fitton and R.E. Willis, eds, 1978, Photoemission and the Electronic Properties of Surfaces (Wiley, Chichester).
Franciosi, A., J.H. Weaver, N. Mårtensson and M. Croft, 1981, Phys. Rev. B **24**, 3651.
Frankowski, I., and P. Wachter, 1982, J. Appl. Phys. **53**, 7887.
Freeman, A.J., 1980, Physica **102B**, 3.
Freeman, A.J., and G.H. Lander, eds, 1984, Handbook on the Physics and Chemistry of the Actinides (North-Holland, Amsterdam).
Fuggle, J.C., M. Campagna, Z. Zolnierek, R. Lässer and A. Platau, 1980, Phys. Rev. Lett. **45**, 1597.
Fuggle, J.C., F.U. Hillebrecht, J.-M. Esteva, R.C. Karnatak, O. Gunnarsson and K. Schönhammer, 1983a, Phys. Rev. B **27**, 4637.
Fuggle, J.C., F.U. Hillebrecht, Z. Zolnierek, R. Lässer, Ch. Freiburg, O. Gunnarsson and K. Schönhammer, 1983b, Phys. Rev. B **27**, 7330.
Fujimori, A., 1983, Phys. Rev. B **28**, 2281.
Fujimori, A., and J.H. Weaver, 1985, Phys. Rev. B **32**, 3422.
Fujimori, A., E. Wuilloud, B. Delley, W.-D. Schneider and Y. Baer, 1984, Phys. Rev. Lett. **53**, 2518 (Comment and Reply).
Gadzuk, J.W., and M. Sunjic, 1975, Phys. Rev. B **12**, 524.
Gerken, F., 1983, J. Phys. F **13**, 703.
Gerken, F., J. Barth, R. Kammerer, L.I. Johansson and A. Flodström, 1982, Surf. Sci. **117**, 486.
Gerken, F., A.S. Flodström, J. Barth, L.I. Johansson and C. Kunz, 1985, Physica Scripta **32**, 43.
Girvin, S.M., and D.R. Penn, 1980, Phys. Rev. B **22**, 4081.
Goeppert-Mayer, M., 1941, Phys. Rev. **60**, 184.
Goldberg, S.M., C.S. Fadley and S. Kono, 1981, J. Electron Spectrosc. & Relat. Phenom. **21**, 285.
Gonçalves da Silva, C.E.T., and L.M. Falicov, 1976, Phys. Rev. B **13**, 3948.
Grewe, N., 1984, Solid State Commun. **50**, 19.
Gudat, W., M. Campagna, R. Rosei, J.H. Weaver, W. Eberhardt, F. Hulliger and E. Kaldis, 1981, J. Appl. Phys. **52**, 2123.
Gunnarsson, O., and K. Schönhammer, 1983a, Phys. Rev. Lett. **50**, 604.
Gunnarsson, O., and K. Schönhammer, 1983b, Phys. Rev. B **28**, 4315.
Gunnarsson, O., and K. Schönhammer, 1985, in: Theory of Heavy-Fermions and Valence Fluctuations, Springer Series in Solid State Sciences, Vol. 62, eds T. Kasuya and T. Saso (Springer, Berlin) p. 100.
Hedin, L., and A. Johansson, 1969, J. Phys. B **2**, 1336.
Herbst, J.F., D.N. Lowy and R.E. Watson, 1972, Phys. Rev. B **6**, 1913.
Herbst, J.F., R.E. Watson and J.W. Wilkins, 1976, Phys. Rev. B **13**, 1439.
Herbst, J.F., R.E. Watson and J.W. Wilkins, 1978, Phys. Rev. B **17**, 3089.
Herman, F., and S. Skillman, 1963, Atomic Structure Calculation (Prentice-Hall, Englewood Cliffs).
Hewson, A.C., D.M. Newns, J.W. Rasul, N. Read, H.U. Desgranges, P. Strange, 1985, in: Theory of Heavy-Fermions and Valence Fluctuations, Springer Series in Solid State Sciences, Vol. 62, eds T. Kasuya and T. Saso (Springer, Berlin) p. 134.
Hillebrecht, F.U., J.C. Fuggle, G.A. Sawatzky, M. Campagna, O. Gunnarsson and K. Schönhammer, 1984, Phys. Rev. B **30**, 1777.
Hüfner, S., and P. Steiner, 1982, in: Valence Instabilities, eds P. Wachter and H. Boppart (North-Holland, Amsterdam) p. 263.
Hüfner, S., and P. Steiner, 1985, private communication.
Ibach, H., ed., 1977, Electron Spectroscopy for Surface Analysis, Topics in Current Physics, Vol. IV (Springer, Berlin).
Imer, J.-M., and E. Wuilloud, 1987, Z. Phys. B **66**, 153.
Janak, J.F., 1978, Phys. Rev. B **18**, 7165.
Johansson, B., 1979a, Phys. Rev. B **19**, 6615.
Johansson, B., 1979b, Phys. Rev. B **20**, 1315.
Johansson, B., and N. Mårtensson, 1980, Phys. Rev. B **21**, 4427.
Johansson, B., and N. Mårtensson, 1983, Helv. Phys. Acta **56**, 405.
Johansson, L.I., J.W. Allen, I. Lindau, M.M. Hecht and S.B.M. Hagström, 1980, Phys. Rev. B **21**, 1408.
Johansson, L.I., A. Flodström, S.E. Hörnström, B. Johansson, J. Barth and F. Gerken, 1982, Solid State Commun. **41**, 427.
Jørgensen, C.K., and H. Berthou, 1972, Chem. Phys. Lett. **13**, 186.
Kaindl, G., W.-D. Schneider, C. Laubschat, B. Reihl and N. Mårtensson, 1983, Surf. Sci. **126**, 105.
Kaindl, G., G. Kalkowski, W.D. Brewer, E.V. Sampathkumaran, F. Holtzberg and A. Schach v. Wittenau, 1985, J. Magn. & Magn. Mater. **47&48**, 181.
Kanski, J., and G. Wendin, 1981, Phys. Rev. B. **24**, 4977.
Kisker, E., W. Gudat, E. Kuhlmann, R. Clauberg and M. Campagna, 1980, Phys. Rev. Lett. **45**, 2053.
Koelling, D.D., A.M. Boring and J.H. Wood, 1983, Solid State Commun. **47**, 227.
Kojima, H., Y. Kuramoto and M. Tachiki, 1984, Z. Phys. B **54**, 293.
Koopmans, T., 1934, Physica **1**, 104.
Kotani, A., and Y. Toyozawa, 1974, J. Phys. Soc.

Jpn. **37**, 912.
Kotani, A., H. Mizuta, T. Jo and J.C. Parlebas, 1985, Solid State Commun. **53**, 805.
Kowalczyk, S.P., N. Edelstein, F.R. McFeely, L. Ley and D.A. Shirley, 1974, Chem. Phys. Lett. **29**, 491.
Lang, J.K., and Y. Baer, 1979, Solid State Commun. **31**, 945.
Lang, J.K., Y. Baer and P.A. Cox, 1981, J. Phys. F **11**, 121.
Laubschat, C., B. Perscheid and W.-D. Schneider, 1983, Phys. Rev. B **28**, 4342.
Laubschat, C., G. Kaindl, E.V. Sampathkumaran and W.-D. Schneider, 1984, Solid State Commun. **49**, 339.
Laubschat, C., G. Kaindl, W.-D. Schneider, B. Reihl and N. Mårtensson, 1986, Phys. Rev. B **33**, 6675.
Lawrence, J.M., P.S. Riseborough and R.D. Parks, 1981, Rep. Prog. Phys. **44**, 1.
Lee, P.A., T.M. Rice, J.W. Serene, L.J. Sham and J.W. Wilkins, 1986, Comments Cond. Mat. Phys. **12**, 99.
Ley, L., and M. Cardona, eds, 1979, Photoemission in Solids II, Topics in Applied Physics, Vol. **27** (Springer, Berlin).
Ley, L., N. Mårtensson and J. Azoulay, 1980, Phys. Rev. Lett. **45**, 1516.
Madelung, O., 1978, Introduction to solid-state theory, Springer Series in Solid-State Sciences, Vol. II (Springer, Berlin) ch. 1.
Manne, R., and T. Åberg, 1970, Chem. Phys. Lett. 7, 282.
Mårtensson, N., B. Reihl and R.D. Parks, 1982a, Solid State Commun. **41**, 573.
Mårtensson, N., B. Reihl, A. Pollak, F. Holtzberg and G. Kaindl, 1982b, Phys. Rev. B **25**, 6522.
Martin, R.L., and D.A. Shirley, 1976, J. Chem. Phys. **64**, 3685.
Mason, M.G., S.-T. Lee, G. Apai, R.F. Davis, D.A. Shirley, A. Franciosi and J.H. Weaver, 1981, Phys. Rev. Lett. **47**, 730.
Materlik, G., J.E. Müller and J.W. Wilkins, 1983a, Phys. Rev. Lett. **50**, 267.
Materlik, G., B. Sonntag and M. Tausch, 1983b, Phys. Rev. Lett. **51**, 1300.
Matthew, J.A.D., G. Strasser and F.P. Netzer, 1983, Phys. Rev. B **27**, 5839.
Meier, F., and H. Ruprecht, 1976, Comm. Phys. **1**, 137.
Meier, F., G.L. Bona and S. Hüfner, 1984, Phys. Rev. Lett. **52**, 1152.
Meldner, H.W., and J.D. Perez, 1971, Phys. Rev. A **4**, 1388.
Modesti, S., G. Paolucci and E. Tosatti, 1985, Phys. Rev. Lett. **55**, 2995.
Moser, H.R., B. Delley, W.-D. Schneider and Y. Baer, 1984, Phys. Rev. B **29**, 2947.
Moser, M., P. Wachter, F. Hulliger and J.R. Etourneau, 1985, Solid State Commun. **54**, 241.
Motais, P., E. Belin and C. Bonnelle, 1984, Phys. Rev. B **30**, 4399.
Mullica, D.F., C.K.C. Lak, H.O. Perkins and V. Young, 1985, Phys. Rev. B **31**, 4039.
Murgai, L.C., L.C. Gupta, R.D. Parks, N. Mårtensson and B. Reihl, 1982, in: Valence Instabilities, eds P. Wachter and H. Boppart (North-Holland, Amsterdam) p. 299.
Netzer, F.P., and J.A.D. Matthew, 1986, Rep. Prog. Phys. **49**, 621.
Netzer, F.P., G. Strasser and J.A.D. Matthew, 1983, Phys. Rev. Lett. **51**, 211.
Nielson, C.W., and G.F. Koster, 1964, Spectroscopic Coefficients for p^n, d^n and f^n configurations (M.I.T. Press, Cambridge, Mass.).
Norman, M.R., D.D. Koelling and A.J. Freeman, 1985a, Phys. Rev. B **31**, 6251.
Norman, M.R., E. Wimmer and A.J. Freeman, 1985b, Phys. Rev. B **32**, 7830.
Parks, R.D., M.L. denBoer, S. Raaen, J.L. Smith and G.P. Williams, 1984, Phys. Rev. B **30**, 1580.
Patthey, F., B. Delley, W.-D. Schneider and Y. Baer, 1985, Phys. Rev. Lett. **55**, 1518.
Patthey, F., S. Cattarinussi, W.-D. Schneider, Y. Baer and B. Delley, 1986a, Europhys. Lett. **2**, 883.
Patthey, F., W.-D. Schneider, Y. Baer and B. Delley, 1986b, Phys. Rev. B **34**, 2967.
Patthey, F., W.-D. Schneider, Y. Baer and B. Delley, 1987a, Phys. Rev. B **35**, 5903.
Patthey, F., W.-D. Schneider, Y. Baer and B. Delley, 1987b, Phys. Rev. Lett. **58**, 2810.
Patthey, F., J.-M. Imer, W.-D. Schneider, Y. Baer, B. Delley and F. Hulliger, 1987c, submitted to Phys. Rev. Lett.
Phillips, J.C., 1961, Phys. Rev. **123**, 420.
Rabe, P., 1974, Doctoral Thesis, University of Hamburg.
Rao, C.N.R., D.D. Sarma, P.R. Sarode, R. Vijayaraghavan, S.K. Dhar and S.K. Malik, 1981, J. Phys. C **14**, 451.
Riehle, F., 1978, Jpn. J. Appl. Phys. **17**, Suppl. 17-2, 314.
Rosengren, A., and B. Johansson, 1980, Phys. Rev. B **22**, 3706.
Sampathkumaran, E.V., G. Kaindl, W. Krone, B. Perscheid and R. Vijayaraghavan, 1985, Phys. Rev. Lett. **54**, 1067.
Sato, S., 1976, J. Phys. Soc. Jpn. **41**, 913.
Satoh, T., H. Yashima and H. Mori, 1981, in: Valence Fluctuations in Solids, eds L.M. Falicov, W. Hanke and M.B. Maple (North-Holland, Amsterdam) p. 553.
Scheidt, H., M. Glöbl, V. Dose and J. Kirschner, 1983, Phys. Rev. Lett. **51**, 1688.
Schiff, L.I., 1955, Quantum Mechanics (McGraw-Hill, New York) p. 217.
Schlottmann, P., 1984, Z. Phys. B **56**, 127.
Schneider, W.-D., C. Laubschat, I. Nowik and G. Kaindl, 1981, Phys. Rev. B **24**, 5422.
Schneider, W.-D., C. Laubschat, and B. Reihl,

1983a, Phys. Rev. B **27**, 6538.
Schneider, W.-D., C. Laubschat, G. Kalkowski, J. Haase and A. Puschmann, 1983b, Phys. Rev. B **28**, 2017.
Schneider, W.-D., B. Delley, E. Wuilloud, J.-M. Imer and Y. Baer, 1985, Phys. Rev. B **32**, 6819.
Siegmann, H.-C., 1975, Phys. Rep. **17**, 37.
Signorelli, A., and R.G. Hayes, 1973, Phys. Rev. B **8**, 81.
Slater, J.C., 1974, The Self-Consistent Field Theory for Molecules and Solids: Quantum Theory of Molecules and Solids, Vol. IV (McGraw-Hill, New York).
Smith, D., and O.W. Day, 1975, J. Chem. Phys. **63**, 113.
Smith, J.L., and E.A. Kmetko, 1983, J. Less-Common Met. **90**, 83.
Starace, A.F., 1972, Phys. Rev. B **5**, 1773.
Stewart, G.R., 1984, Rev. Mod. Phys. **56**, 755.
Suzuki, S., T. Ishii and T. Sagawa, 1974, J. Phys. Soc. Jpn. **37**, 1334.
Takakuwa, Y., S. Takahashi, S. Suzuki, S. Kono, T. Yokutsuka, T. Takahashi and T. Sagawa, 1982, J. Phys. Soc. Jpn. **51**, 2045.
Thole, B.T., G. van der Laan, J.C. Fuggle, G.A. Sawatzky, R.C. Karnatak and J.-M. Esteva, 1985, Phys. Rev. B **32**, 5107.
Travaglini, G., and P. Wachter, 1984, Phys. Rev. B **29**, 893.
Treglia, G., F. Ducastelle and D. Spanjaard, 1980a, J. Phys. (France) **41**, 281.
Treglia, G., F. Ducastelle and D. Spanjaard, 1980b, Phys. Rev. B **21**, 3729 and refs. therein.
Tsvelick, A.M., and P.B. Wiegmann, 1984, Z. Phys. B **54**, 201.
Unguris, J., A. Seiler, R.J. Celotta, D.T. Pierce, P.D. Johnson and N.V. Smith, 1982, Phys. Rev. Lett. **49**, 1047.
Varma, C.M., 1985, Comments Solid State Phys. **11**, 221.
Varma, C.M., and Y. Yafet, 1976, Phys. Rev. B **13**, 2950.
Wachter, P., 1982, in: Valence Instabilities, eds P. Wachter and H. Boppart (North-Holland, Amsterdam) p. 145.
Watson, R.E., and M.L. Perlman, 1975, Structure and Bonding **24**, 83.
Weller, D., S.F. Alvarado, W. Gudat, K. Schröder and M. Campagna, 1985, Phys. Rev. Lett. **54**, 1555.
Wertheim, G.K., and P.H. Citrin, 1978, Fermi surface excitations in X-ray photoemission line shapes from metals, in: Photoemission in Solids I, Topics in Applied Physics, Vol. 26, eds M. Cardona and L. Ley (Springer, Berlin) ch. 5.
Wertheim, G.K., and G. Crecelius, 1978, Phys. Rev. Lett. **40**, 813.
Wertheim, G.K., E.V. Sampathkumaran, C. Laubschat and G. Kaindl, 1985, Phys. Rev. B **31**, 6836.
Wieliczka, D.M., J.H. Weaver, D.W. Lynch and C.G. Olson, 1982, Phys. Rev. B **26**, 7056.
Wieliczka, D.M., C.G. Olson and D.W. Lynch, 1984, Phys. Rev. B **29**, 3028.
Williams, A.R., and N.D. Lang, 1978, Phys. Rev. Lett. **40**, 954.
Wohlleben, D., and J. Röhler, 1984, J. Appl. Phys. **55**, 1904.
Wuilloud, E., H.R. Moser, W.-D. Schneider and Y. Baer, 1983, Phys. Rev. B **28**, 7354.
Wuilloud, E., W.-D. Schneider, B. Delley, Y. Baer and F. Hulliger, 1984a, J. Phys. C **17**, 4799.
Wuilloud, E., B. Delley, W.-D. Schneider and Y. Baer, 1984b, Phys. Rev. Lett. **53** 202.
Wuilloud, E., B. Delley, W.-D. Schneider and Y. Baer, 1985, J. Magn. & Magn. Mater. **47&48**, 197.
Wuilloud, E., Y. Baer and H.R. Ott, 1986, private communication.
Yafet, Y., 1980, Phys. Rev. B **21**, 5023.
Zangwill, A., and P. Soven, 1980, Phys. Rev. Lett. **45**, 204.

Handbook on the Physics and Chemistry of Rare Earths, Vol. 10
edited by K.A. Gschneidner, Jr., L. Eyring and S. Hüfner

Chapter 63

f-ELECTRON HYBRIDIZATION AND DYNAMICAL SCREENING OF CORE HOLES IN INTERMETALLIC COMPOUNDS

M. CAMPAGNA
Istitut für Festkörperforschung der KFA Jülich, D-5170 Jülich, Fed. Rep. Germany

and

II. Physikalisches Institut der Universität zu Köln, D-5000 Köln 41, Fed. Rep. Germany

F.U. HILLEBRECHT*
Institut für Festkörperforschung der KFA Jülich, D-5170 Jülich, Fed. Rep. Germany

Contents

*Present address: Max-Planck Institut für Festkörperforschung, 7000 Stuttgart 80, Fed. Rep. Germany

List of symbols

c_0	amplitude of f^0 contribution in ground state		fects of hybridization Δ.
c_1	amplitude of f^1 contribution in ground state	$E_m(n-1)$	energy after core hole creation
c_2	amplitude of f^2 contribution in ground state	n_f	occupancy of 4f level
Δ	hybridization between 4f and conduction states	N_f	degeneracy of 4f level
Δ_+	electron affinity of 4f state	ρ_{max}	maximum of the density of conduction states
E_F	Fermi level	U	average Coulomb correlation between two 4f electrons
ε_f	energy of 4f state	U_{fc}	Coulomb interaction between core hole and 4f state
$E_0(N)$	ground state energy of N-electron system, i.e. before creation of a core hole, taking into account ef-	UPS	ultraviolet photoemission spectroscopy
		V	hopping matrix element between 4f and conduction states

1. Introduction: Mixed valence and dynamical screening of core holes in solids

By 1978 we had reached a quantitative understanding of the 4f-electron binding energies, multiplet position and intensities in conducting, '*normal*' compounds of all lanthanides except Ce. Apart from the case of the Ce compounds, 4f photoemission spectra even seemed to allow a direct determination of the most desired quantity, the 4f occupancy n_f – the so-called f count – also in the case of '*anomalous*', mixed valent systems involving Sm, Eu, Tm and Yb (Campagna et al. 1976, 1979, 1981). It was clear that a better agreement between the determination of the 4f occupancy by spectroscopic methods and other low or high energy measurements could be obtained only by a better characterization of the *atomic structure* near the surface.

As an alternative to the 4f electrons, the 4d and especially 3d core levels, with large cross sections for the excitation with laboratory sources such as AlKα radiation (photon energy 1.486 keV), were very appealing to the experimentalist as possible signals for obtaining, in a fast way, a picture of the underlying electronic structure of the lanthanides. This was especially true for Ce, where – without synchrotron radiation – it was clearly very difficult with X-ray Photoemission Spectroscopy (XPS) to detect the 4f-related intensity (Baer et al. 1978).

The motivation for a systematic investigation of the core level XPS spectra of lanthanides in solids and surfaces therefore arose in 1978 from the following needs:

(1) To understand the origin of low-energy satellites in the 3d spectra of *light* lanthanides, their implication for a *dynamical* picture of core level photoionization in the presence of semilocalized screening orbitals; to establish their relation to the ground state electronic structure, see fig. 1 (Wertheim and Campagna 1978).

(2) To determine the relationship which exists between core level lineshape in photoelectron spectroscopy in general and the hybridization (localization) of screening orbitals. This would provide us with a systematic experimental test of ideas put forward by Kotani and Toyozawa (1974), Schönhammer and Gunnarsson (1977a,b,c) and Gunnarsson and Schönhammer (1978a,b) relating the lineshapes of core level

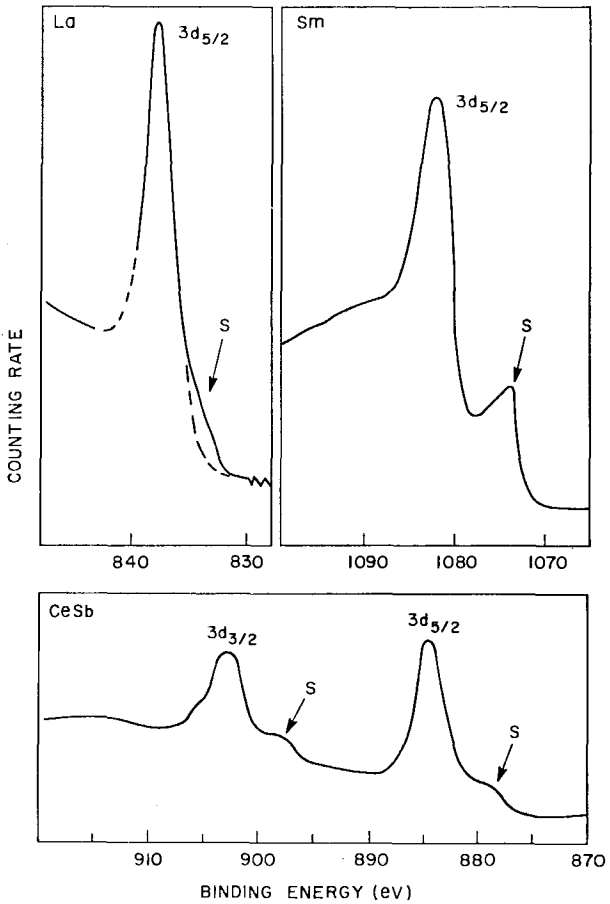

Fig. 1. Low-energy satellite structures (indicated by S) in the region of the 3d XPS spectra of La and Sm metal and of Ce in CeSb, pointing to the need of a *dynamical* description of the core hole screening mechanism (Wertheim and Campagna 1978).

spectra in *adsorbates* to their electronic structure on the surface, see fig. 2 (Fuggle et al. 1978).

As recently as 1977, because of the above unanswered questions, 3d or 4d spectra of Sm metal, shown in fig. 3, could not be used to establish unambiguously whether the 4f electronic configuration near the surface of Sm metal is different from that of the bulk (initial state effect). Alternatively it was suggested that it could be a signature of a new final state configuration generated by the presence of the core hole potential, and therefore due to a dynamical screening mechanism.

2. The surface of Sm metal

Wertheim and Crecelius (1978) and Crecelius et al. (1978) conducted the most systematic investigation of the 3d satellite structure of the light lanthanide elements in the late 70's. Their conclusion, obtained from data as shown in the case of Sm in fig. 4, was that the first atomic layer of trivalent ($4f^5$) metallic Sm has a large

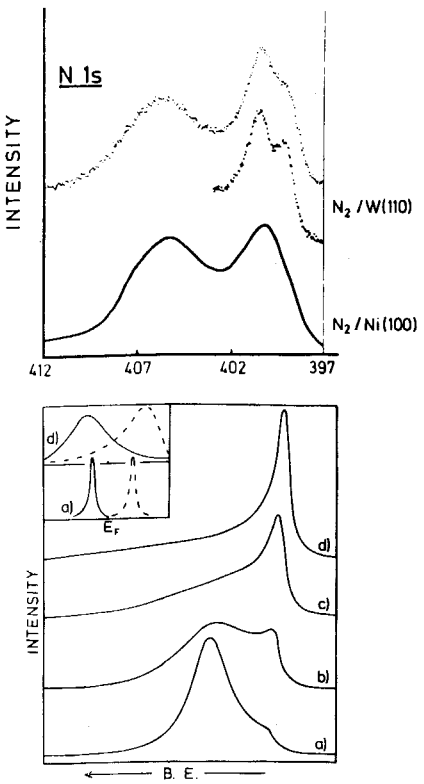

Fig. 2. Upper part: XPS spectra of the N(1s) level of chemisorbed N_2 on W(110) and Ni(100). Lower part: screening model of Schönhammer and Gunnarsson (1977a,b, 1978) and its prediction for the shape of the core level of *adsorbates* (Fuggle et al. 1978).

divalent ($4f^6$) component. The valence transition is due to a narrowing of the 5d band at the surface which populates the low-lying $4f^6$ state. Their conclusion was based on measurements of the photoelectron intensity as a function of the take-off angle. This measurement enhances the surface sensitivity for large take-off angles away from the surface normal. The results shown in fig. 4 demonstrate that indeed the divalent signal increases relative to the trivalent bulk signal with increasing take-off angle.

In the lanthanides from La to Nd two competing screening mechanisms were suggested: the main component of the 3d line is obtained when the core hole is screened by 5d conduction electrons; the low energy satellite due to a $4f^n \rightarrow 4f^{n+1}$ transition during the photoemission process. The satellites in the case of metallic La, Ce, Pr and Nd occur at lower binding energies because the empty 4f level falls below the Fermi energy upon creation of a 3d core hole, and screens the $3d^9$ hole state most effectively. The screening mechanism by semilocalized levels was suggested earlier in another context by Kotani and Toyozawa (1974).

The use of *resonant photoemission* with synchrotron radiation at Hasylab in Hamburg allowed W. Gudat et al. (1981) the direct observation of the divalent surface signal in the valence band of Sm. This observation was made possible by the enhanced surface sensitivity of the photoemission experiment using synchrotron

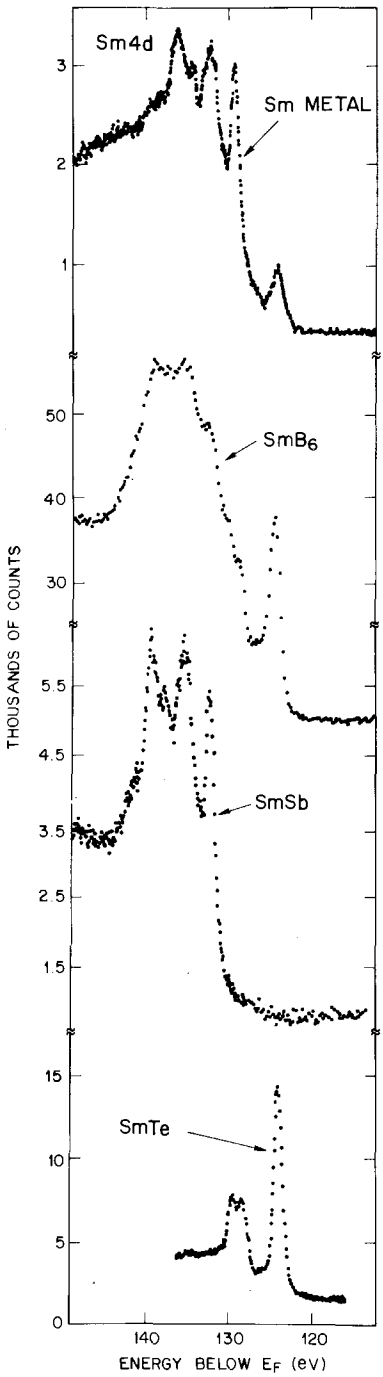

Fig. 3. Comparison of XPS spectra of the 4d levels of Sm metal, mixed-valent SmB_6, trivalent SmSb ($4f^5$), and divalent SmTe ($4f^6$) indicating the existence of a divalent signal in Sm metal whose origin in 1978 was unclear (divalent state confined to a surface layer?) (Wertheim and Campagna 1977).

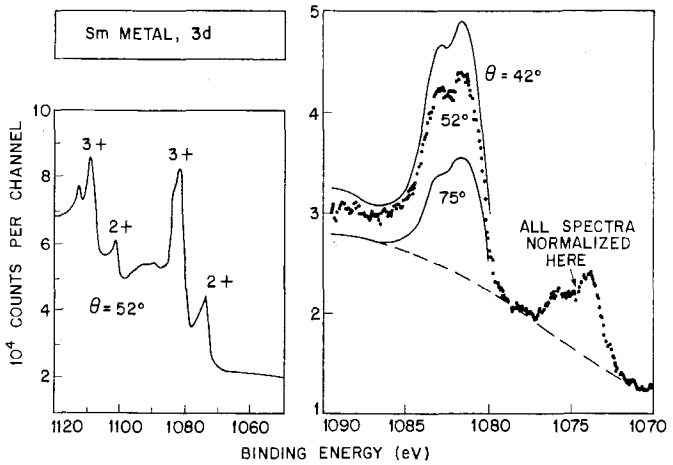

Fig. 4. XPS spectra of the 3d region of Sm metal. The left side indicates the wide scan showing the complete spin–orbit structures $3d_{5/2-3/2}$ corresponding to the divalent ($4f^6$) and trivalent ($4f^5$) signal. The right side of the figure indicates the $3d_{5/2}$ region for three different orientations of the sample allowing different take-off angle of the photoelectrons (increased surface sensitivity) (Wertheim and Crecelius 1978).

radiation of photon energy 99.7 eV as well as the improved total energy resolution (280 meV) compared to the XPS experiment (650 meV), see fig. 5. As we see from fig. 5, the ^{6}H multiplet is not located at E_F. This allows one to conclude that Sm metal, at the surface, is not mixed valent but in a stable $4f^6$ configuration.

The puzzle of the extra structure in the Sm valence band (0–3 eV below E_F) when compared to other lanthanide metals like for example Dy (see fig. 5) was therefore fully resolved by 1980. Even more important, a new way of quantitatively studying *dynamical* screening effects in core level spectroscopy, as we shall illustrate, emerged.

3. Resonant photoemission spectroscopy with synchrotron radiation and surface core level shifts

Resonant photoemission spectroscopy using synchrotron radiation has since then been used to gain a better understanding of both the surface properties of well-characterized lanthanide materials as well as of the mechanism of the resonant photoemission process itself. Using a large number of single crystals of lanthanide chalcogenides grown at ETH-Zürich by F. Hulliger and E. Kaldis, W. Gudat et al. (1978, 1980, 1981), among other investigators, conducted systematic studies, primarily at the Tantalus storage ring in Wisconsin, at the LURE laboratory in Orsay as well as at the DORIS storage ring (Hasylab) in Hamburg. These studies and the work of Lenth et al. (1978, Allen et al. (1978) and Johansson et al. (1978, 1980), demonstrated in addition that the Fano theory of the interaction of a discrete level with the continuum accounts reasonably well for the observed behaviour of the 4f cross section for photoemission near the 4d ionization threshold.

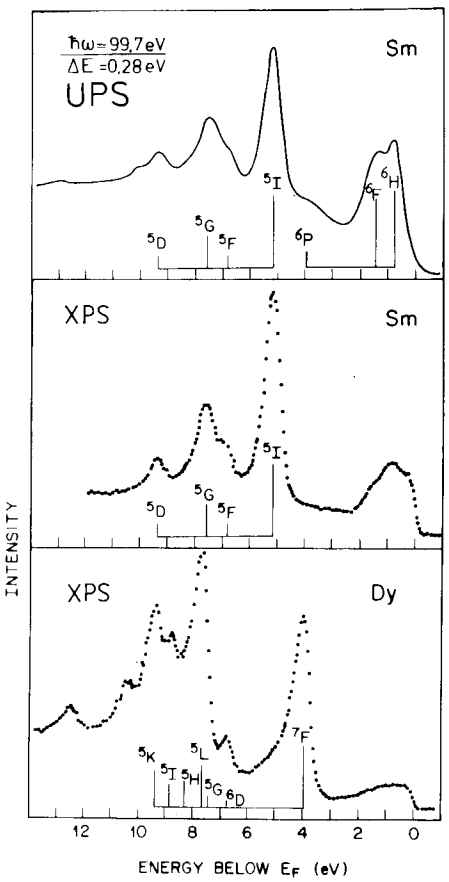

Fig. 5. Comparison of the XPS spectra of the 4f region of Sm and Dy metal and synchrotron radiation spectra of Sm metal (UPS). In the upper part of the figure the divalent $4f^6$ Sm component is clearly seen in the synchrotron radiation data (Gudat et al. 1981).

The improved resolution provided by the synchrotron radiation also allowed the identification of the previously unknown quadruplet structure of the Yb $4f^{14}$ photoemission spectra near the surface (Alvarado et al. 1980). One of the $4f_{7/2}$–$4f_{5/2}$ doublet was observed to have a very asymmetric lineshape and an extremely narrow linewidth (13 meV). It was attributed to bulk 4f emission. The other, the surface doublets, was found to exhibit almost symmetric lines but with a much larger linewidth (430 meV). It was also located at a binding energy larger by 0.6 + 0.03 eV, see fig. 6. The finding of such a large surface shift for stable 4f levels had obviously important *implications* in the quantitative determination of the electronic structure of mixed-valent materials using direct 4f photoemission with synchrotron radiation because of the large *surface sensitivity* of this technique.

4. From mixed valence in heavy lanthanide compounds to Sm clusters

By 1980 we had therefore learned that mixed valence in *heavy* lanthanides systems can be best viewed by direct 4f photoemission at high energy (XPS) (see fig. 7). By

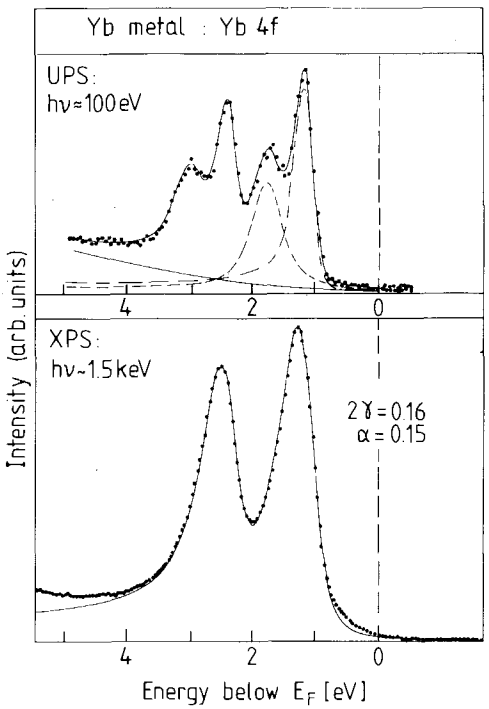

Fig. 6. Comparison of 4fXPS and synchrotron radiation ultraviolet photoemission spectra (UPS) of Yb metal. Only UPS allows the identification of the surface 4f levels shifted to higher binding energy relative to the bulk 4f levels.

using this technique it is also possible to study variations of the valence upon stoichiometry, as demonstrated by Wertheim et al. (1980). However, because of surface effects, the estimates of the average valence (the f count) as deduced from XPS data is different – by about 10% in TmSe – from the one obtained via susceptibility measurements, lattice constant systematics or Mössbauer effect data. We discuss this point also at the end of chapter 70 of this volume.

Although it is possible to use XPS to distinguish between homogeneous and inhomogeneous mixed valence (Wertheim et al. 1978, 1980), when quoting average valences one has always to take into account that the electronic properties of the surface of both stable and mixed valence intermetallic compounds may differ from the bulk especially whenever the 4f level lies close to the Fermi level. The role of the escape depth, i.e. dependence of the mean-free-path of the photoelectrons from their kinetic energy, must be taken into account.

At this point we would like to recall that the systematic spectroscopic investigation of Sm metal allowed also the pioneering data of Mason et al. (1981) on *Sm clusters* to be meaningfully interpreted. Using XPS and UPS data they showed that at small particle sizes Sm has the tendency to be divalent ($4f^6$). Band narrowing due to the reduced surface coordination was found thereby to be more dominant than surface tension effects in establishing the valence of a small Sm cluster, because the trivalent state becomes progressively more abundant only with increasing sizes.

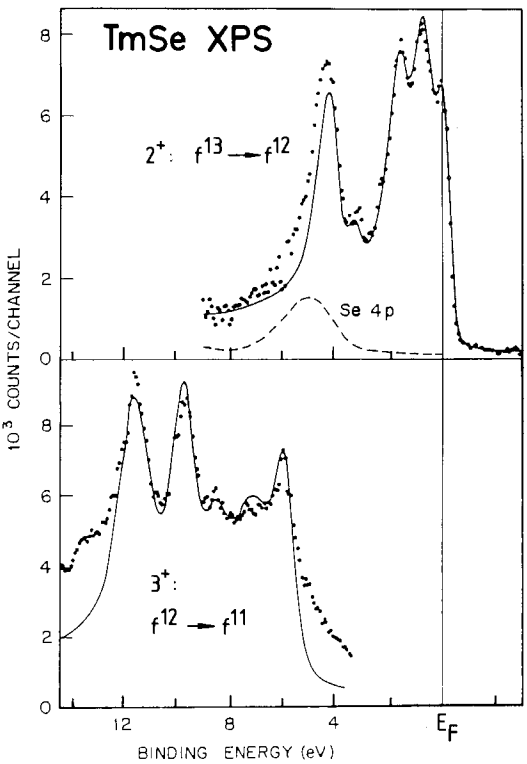

Fig. 7. Divalent and trivalent parts (upper and lower part of the figure) of the 4f XPS spectrum of TmSe. The solid lines indicate optical multiplet energies and fractional parentage intensities. The homogeneous mixed-valence character of TmSe is thereby well illustrated by pinning of the divalent signal at the Fermi energy $E_F = 0$, which was determined by in situ coating with a metal overlayer (Wertheim et al. 1980).

5. Systematics of the La and Ce 3d XPS core levels

5.1. *From chemisorption to the impurity problem*

As discussed by Gunnarsson and Schönhammer in chapter 64 of this book, the parameters relevant to the *extended Anderson single impurity model*, originally proposed in 1977 for the description of the core level lineshapes of adsorbates (see scheme in fig. 2), and now to be used to describe core level XPS data of f-electron systems, are:

(1) attractive core hole potential U_{ac}: for f systems the interaction U_{fc} between f electrons and core hole;

(2) distance Δ_+ of the screening level from the Fermi level E_F, its correlation energy U_{eff}; for f systems: the energy ε_f of the f levels and their Coulomb correlation U;

(3) width Δ of the screening level due to hybridization; for f systems: generally $\Delta = \pi V^2 \rho_{max}$, where V is the hopping between the f levels and the conduction states and ρ_{max} is the maximum of the density of conduction states.

The experimental test of this model requires a systematic investigation of the dependence core level lineshapes on the above parameters U_{ac}, Δ and Δ_+, and a

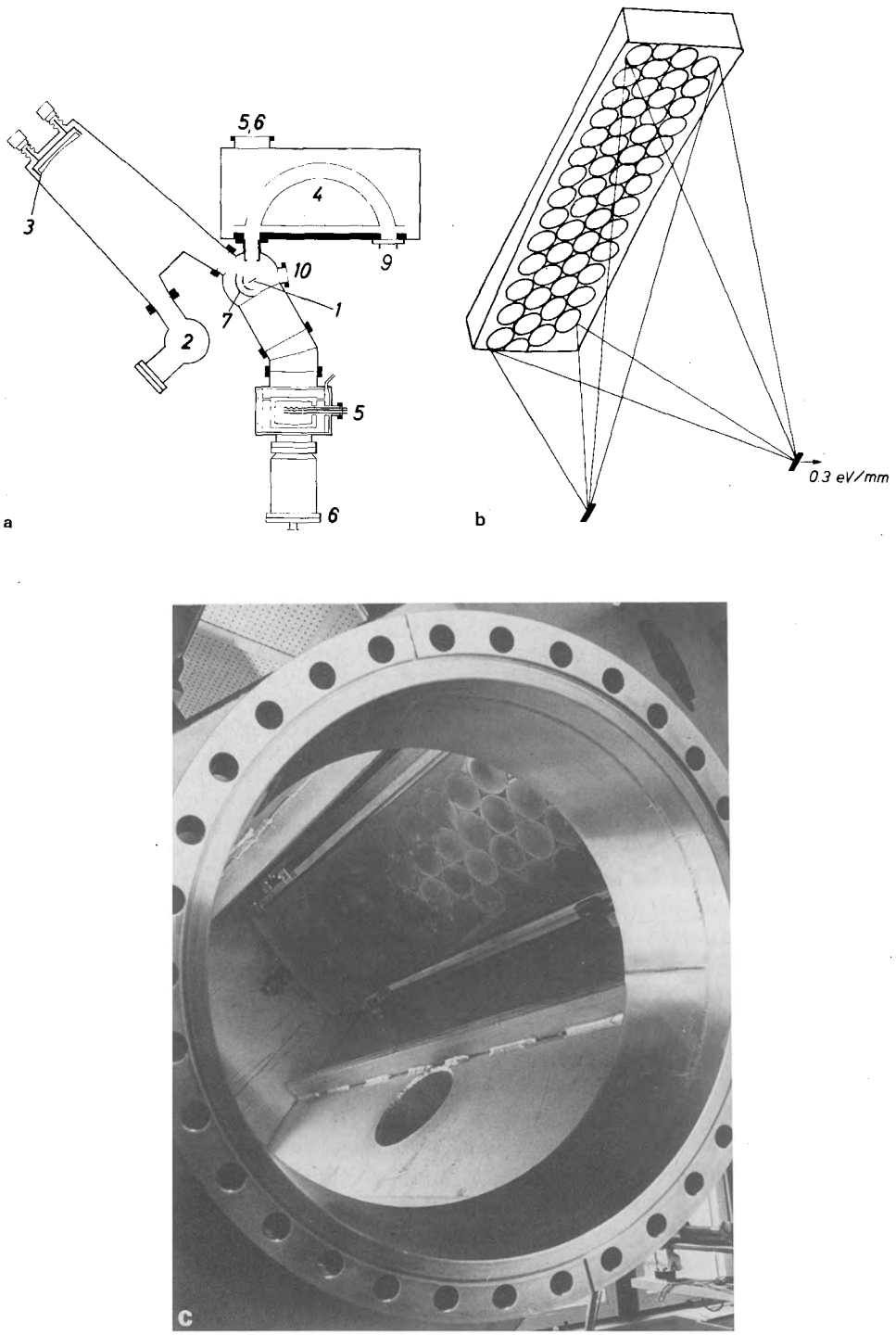

Fig. 8. (a): Scheme of the high resolution, high intensity X-ray photoelectron spectrometer. (b) and (c): Principle and view of the toroidal glass plate with the 54 quarz single crystals acting as large solid angle monochromator for the Al Kα radiation.

detailed *comparison* with calculations. This is experimentally difficult to realize with chemisorption systems, i.e. with *adsorbates*, for obvious reasons. It can however be easily realized with a series of 4f *impurities* with different couplings in rare earth solids. For such an investigation to be successful a highly efficient electron spectrometer is needed as well as many well-characterized samples. This led us, in collaboration with J.C. Fuggle, to the construction of a custom designed spectrometer, whose heart was a large solid angle monochromator with 54 quartz single crystals mounted on a toroidal glass plate (see fig. 8). The instrument was typically operating at a base pressure of 10^{-11} Torr in both measurement and sample preparation chambers. In order to increase the intensity, the slits in the electron optics were opened, which gave 550 meV total instrumental resolution (Hillebrecht 1984).

5.2. *Sample preparation and characterization*

The samples used in these studies were prepared by melting the components together in the required proportion using rf heating in cold crucibles (Hillebrecht 1984). The metals used were of 99.9% purity or better as specified by the procedures of Johnson and Matthey and/or Heraeus. The samples were brittle and mostly air sensitive. They were typically cut to two millimeter slices by spark erosion and checked for second phases by metallography and X-ray diffraction. They were annealed for up to a week in vacuum to reduce the concentration of peritectic precipitates. Clean surfaces were prepared in ultrahigh vacuum by scraping the samples with an Al_2O_3 file. The levels of O and C contamination, as judged by the usual O(1s) and C(1s) XPS peak intensities were usually below detectability.

5.3. *Dynamical screening of core holes in solids*

Conventional, delocalized Friedel–Mahan screening as known for simple or noble metals has been extensively investigated in the 70's (Hüfner et al. 1975, Hüfner 1979, and Wertheim and Citrin 1978). The next step required an understanding of the effect of increasing the screening orbital localization. It has long been known that in going from the 3d (Ti) to the 5f (Th) to the 4f orbitals ($CePd_3$ and γ-Ce) localization increases. Results obtained by bremsstrahlung isochromat spectroscopy (BIS) a few years later, and therefore not yet available at that time, experimentally confirmed and quantified this educated guess concerning the electronic structure of these materials above E_F. From those data, which we discuss in chapter 70 of this volume, one can deduce that the screening orbitals of Ti are the strongly hybridized 3d levels with negligible interatomic Coulomb correlation, located 5 eV above the Fermi level E_F. In Th the semilocalized screening orbitals are the 5f levels, centered at about 5 eV ($=\Delta_+$) and with a width Δ of about 2 to 3 eV due to the 5f–6d hybridization. By comparison with $LaPd_3$ the empty 4f states in $CePd_3$ can be identified; the f^1 state lies at E_F, the other about 5 eV above E_F. In γ-Ce only the f^2 multiplet structure is clearly visible in BIS centered at about 4 eV above E_F. The so-called 'well-screened' XPS peaks of fig. 9, in going from the Ti($2p_{3/2}$) to Th($4f_{7/2}$)

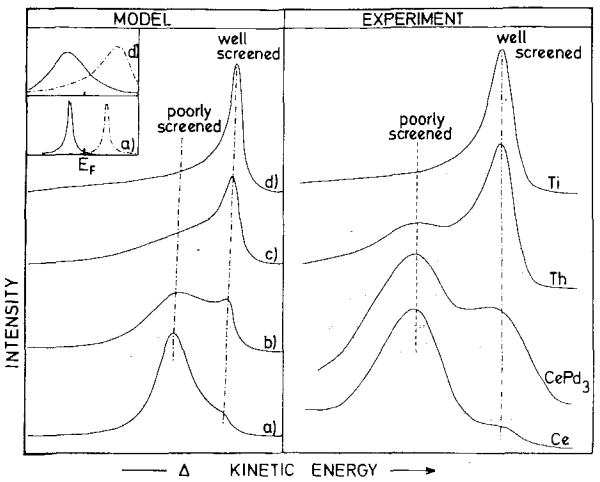

Fig. 9. Left: Illustration of the Schönhammer–Gunnarsson model of screening and its implications for the core level lineshapes in solids. Values of the ratio of the width Δ of the screening levels to Δ_+ are (d) = 0.94, (c) = 0.75, (b) = 0.56, (a) = 0.38 and U_{ac} was $1.5\Delta_+$. Right: $Ce(3d_{5/2})$, $Th(4f_{7/2})$, and $Ti(2p_{3/2})$ XPS peaks from γ-Ce, $CePd_3$, Th and Ti. The peak binding energies are 883, 333 and 454eV for Ce, Th and Ti levels, respectively (Fuggle et al. 1980).

and $Ce(3d_{5/2})$ corresponds to a final state with increased screening orbital localization, leading to a decreased probability (amplitude) of being occupied in the XPS final state (Fuggle et al. 1980). The case of the $CePd_3$ 3d XPS core level peaks, which contain further structure at higher binding energy due to the $3d^9 4f^0$ final state configuration, will be discussed more in detail below.

The relatively large separation between the final state configurations with different f counts, especially in La and Ce, allows one to speak of well-defined configurations in the final state itself. (The notation 'well' and 'poorly' screened states is misleading

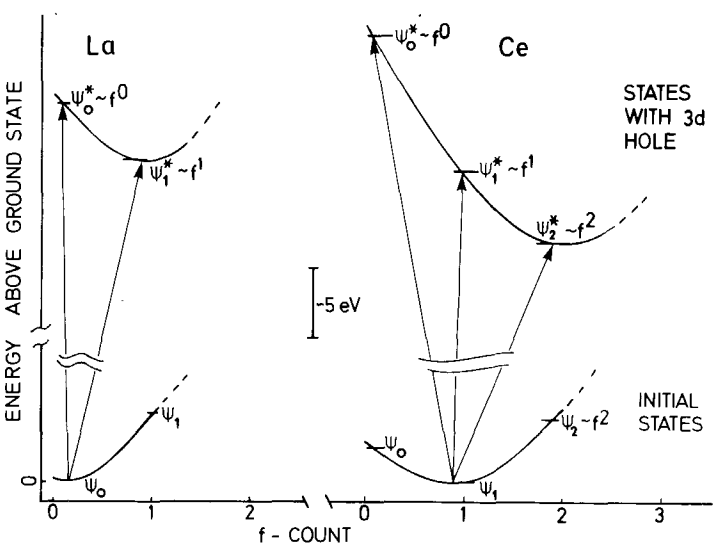

Fig. 10. Schematic diagram of 3d core hole excitation of La and Ce compounds. The transitions leading to the lowest binding energy takes place from an initial state into final states whose approximate configurations are $3d^9 4f^1$ and $3d^9 4f^2$ for La and Ce, respectively (Hillebrecht and Fuggle 1982).

in the sense that both final states are fully screened, but with different relaxation energies.) This is illustrated in fig. 10. In this diagram we show schematically the 3d XPS transitions in La and Ce and their compounds. The excitations leading to the lowest 3d binding energies take place from an initial state into final states whose approximate configurations are $3d^9 4f^1$ (La) and $3d^9 4f^2$ (Ce) (Fuggle et al. 1980), in accordance to the suggestion of Crecelius et al. (1978) for the pure elements.

5.4. *Hybridization of f levels in RPd_3 compounds*

The observation of the close relationship between experiment and theory documented by the data of fig. 9 provided motivation for a subsequent test involving the RPd_3 series of the light lanthanides from La to Sm. The hybridization Δ was expected to decrease in going from La to Sm, also because of the contraction of the 4f wavefunctions. The results of these investigations are shown in fig. 11a,b. The weight of the final state $3d^9 4f^{n+1}$ (from $n = 0$ for La to $n = 5$ for Sm) decreases monotonically and is for practical purposes negligible ($< 5\%$) in $SmPd_3$. The mixing of 4f and conduction electrons cannot, however, be completely neglected for Pr and

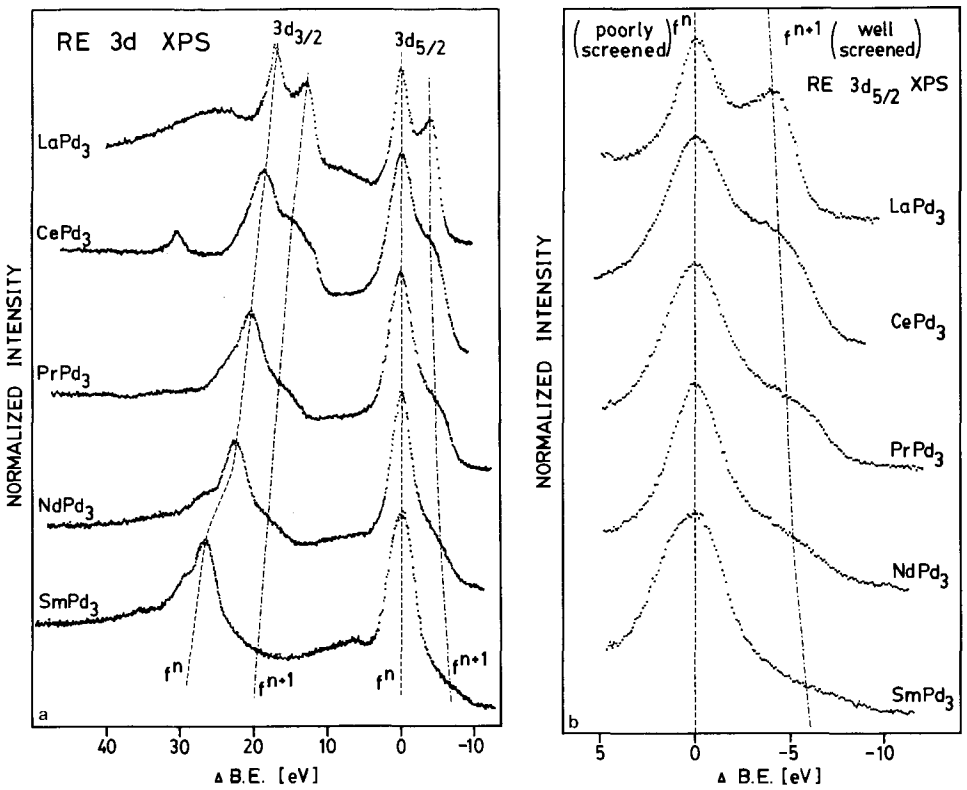

Fig. 11. (a) XPS spectra in the region of the lanthanide $3d_{5/2-3/2}$ for Ln-Pd_3 alloys (Ln = La, Ce, Pr, Nd and Sm). The spectra have been normalized to the height of the $3d_{5/2}$ peaks. (b) Details of the $3d_{5/2}$ XPS peaks for Ln-Pd_3 alloys (Hillebrecht and Fuggle 1982).

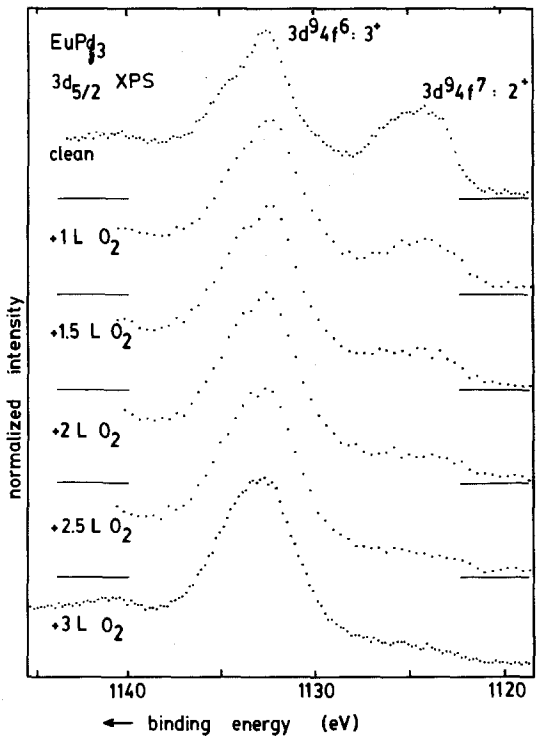

Fig. 12. $3d_{5/2}$ XPS spectra of $EuPd_3$ upon O_2 exposure. The divalent signal $3d^9\ 4f^7$ disappears upon O_2 adsorption demonstrating that this spectral feature is due to a static surface effect.

Nd. On the other hand we can deduce that mixing of initial and final state configurations will be negligible for heavier lanthanides. This implies, for example, that the structure observed in the low-energy region of the 3d XPS spectra of trivalent ($4f^6$) Eu compounds is not, as originally proposed by Schneider et al. (1981) and Laubschat et al. (1983), partly due to dynamical effects as in the case of La or Ce. Rather it is due to a *surface* electronic phase transition like in Sm metal, as demonstrated by Mårtensson et al. (1985), see fig. 12.

In order to further *quantify* the meaning of configuration mixing in initial and/or final states it was clear since 1979 (Campagna et al. 1976, 1979) that a systematic XPS investigation, concentrating on many La and Ce intermetallic compounds, was necessary. The corresponding experimental work also provided the motivation for extensive numerical calculations by Gunnarsson and Schönhammer (1983a,b), made possible by an extension of an idea of Anderson (1981). He had recognized that the large degeneracy N_f of the f orbitals of Ce could be used to develop a mathematical expression for the properties in terms of an expansion in inverse powers of N_f.

The comparison between theory and experiment was extended to various spectroscopies besides XPS, i.e. resonant photoemission spectroscopy. X-ray absorption spectroscopy (XAS) and, as we shall see in chapter 70 of this volume, also to bremsstrahlung isochromat spectroscopy (BIS). With one set of parameters it became possible to describe many experimental results, which in turn made it possible to extract new values of Δ and n_f. These values turned out to be quite

different from the traditional ones (Fuggle et al. 1983a,b, Gunnarsson et al. 1983). Oh and Doniach (1982) has also pointed out that the spectra can be explained by a hybridization significantly larger than the formerly accepted ~ 10 meV. However their model only permitted qualitative conclusions about the hybridization.

5.5. *Quantifying dynamical screening in La–Ni, Ce–Ni, La–Pd, and Ce–Pd compounds*

A prototype or classical set of 3d XPS core level spectra of La and Ce intermetallic compounds is shown in figs. 13 through 20. In all these compounds one can see from the XPS spectra that the f^1 (for La) or the f^2 (for Ce) final-state amplitude increases with the Ni (Pd) concentration. This can best be seen in the close-up view of fig. 15 and fig. 20. In all cases this increase of the f^1 (La) or of the f^2 (Ce) amplitude indicates increased f hybridization. The evidence for the assignment to a $3d^9 4f^0$ final state in the case of the Ce compounds is contained in the 4d XPS spectra shown in fig. 16. Two weak peaks are seen to grow at 120 eV BE with increasing Ni concentration. The splitting of these two peaks is almost equal to the 4d spin–orbit splitting in La so that they can clearly be attributed to $4d^9 4f^0$ final states. The growth of the 3d peaks at 914 eV parallels the growth of the $4d^9 4f^0$ peaks at 120 eV and their separation from the main $4d^9 4f^1$ peaks is similar. This is why the peaks located at 914 eV can be assigned to excitations to final states mainly

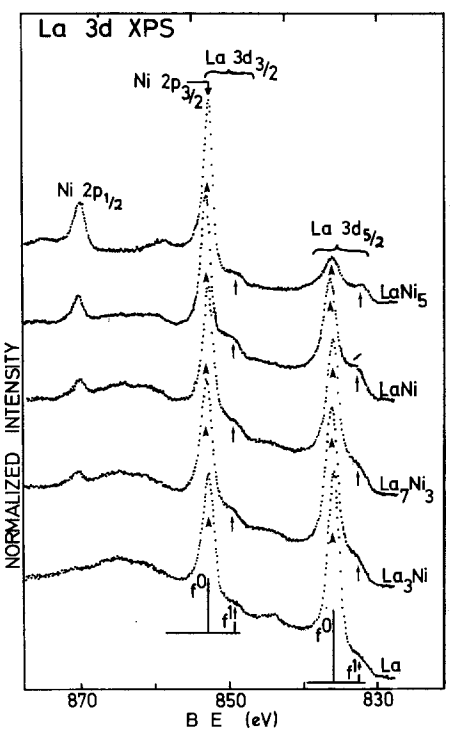

Fig. 13. La 3d XPS core level spectra of La–Ni compounds (Fuggle et al. 1983a,b).

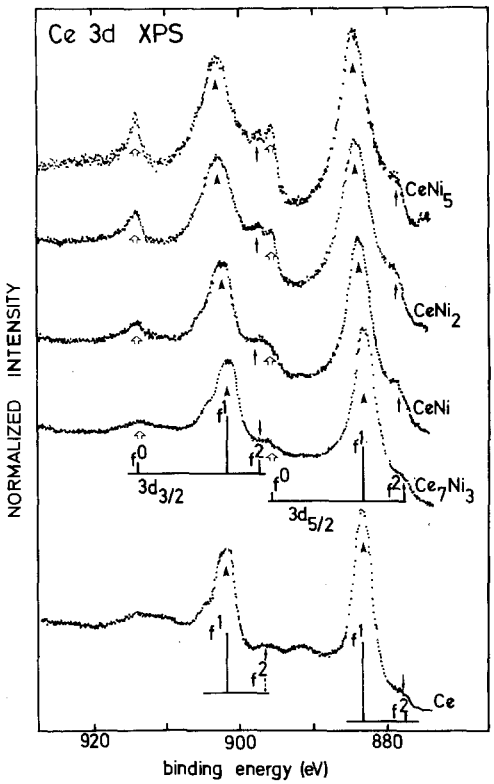

Fig. 14. Ce 3d XPS core level spectra of Ce–Ni compounds (Fuggle et al. 1983a,b).

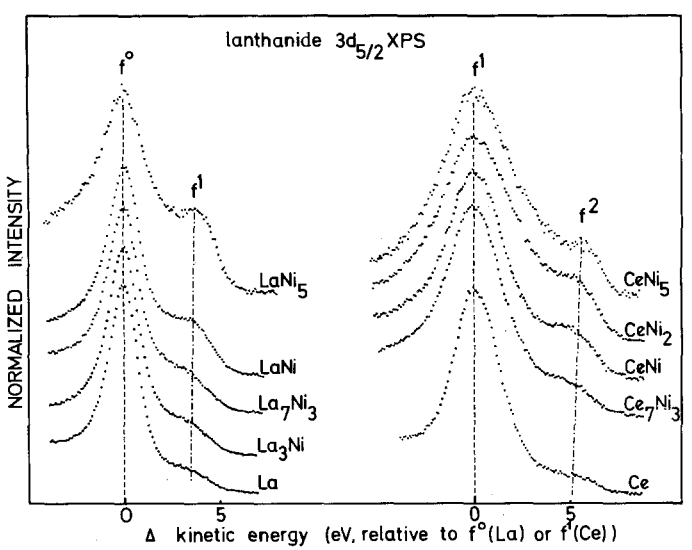

Fig. 15. Main $3d_{5/2}$XPS peak from LaNi and Ce–Ni compounds (Fuggle et al 1983a,b).

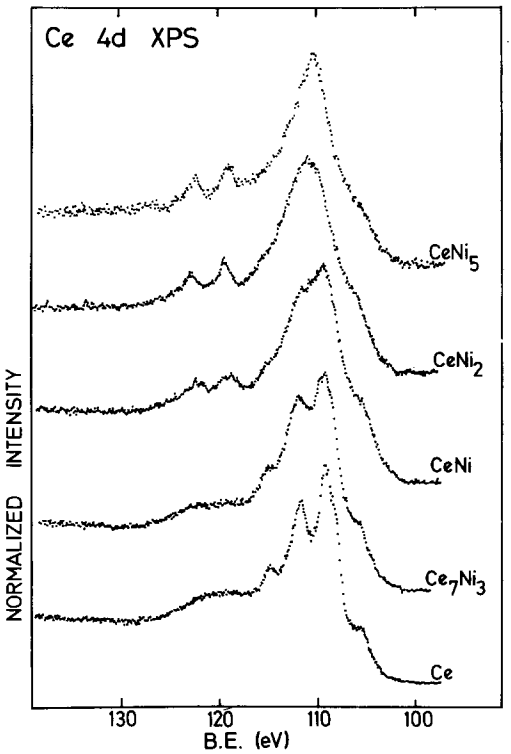

Fig. 16. Ce 4d XPS core level spectra of Ce–Ni compounds allowing the separate observation of the $4d^9 4f^0$ final state at a binding energy (BE) of ≈ 120 eV (Fuggle et al. 1983a,b).

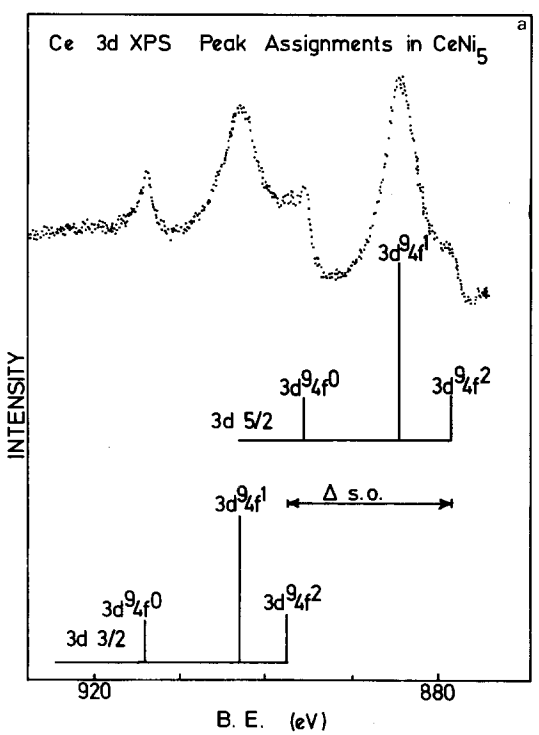

Fig. 17a. Peak assignments for the XPS spectrum of Ce in the region of the 3d peaks for $CeNi_5$. The peaks are labeled according to their approximate final state configuration, i.e. the f counts are not exactly integral (Fuggle et al. 1983a,b).

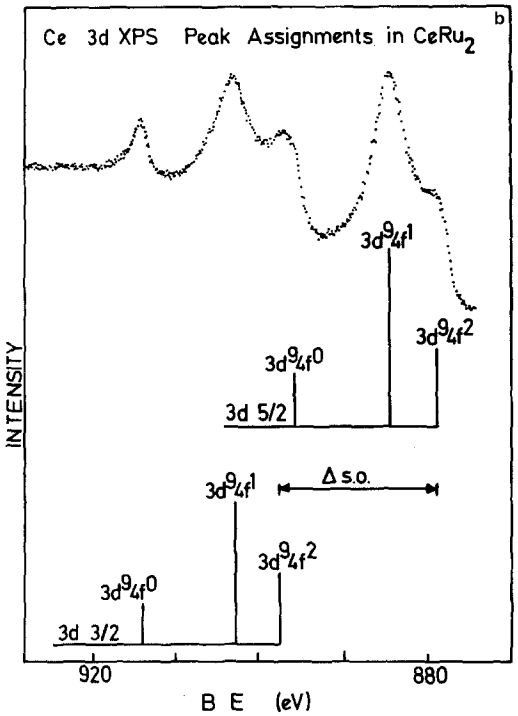

Fig. 17b. The same as in fig. 17a for $CeRu_2$.

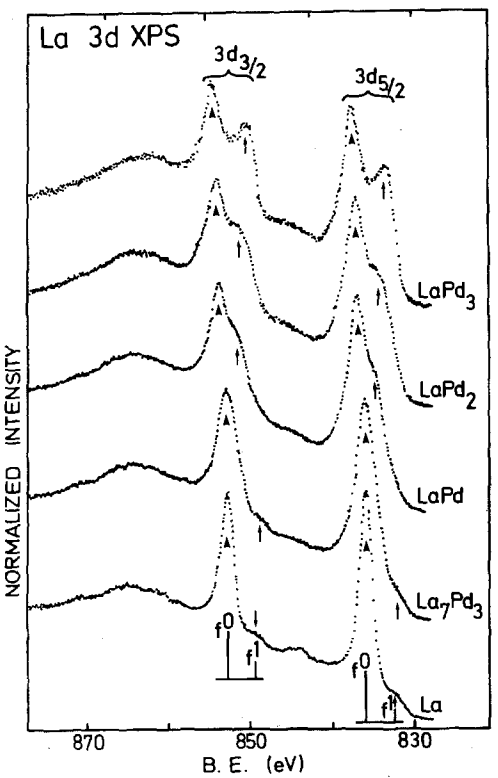

Fig. 18. 3d XPS spectrum of ordered La–Pd intermetallic compounds.

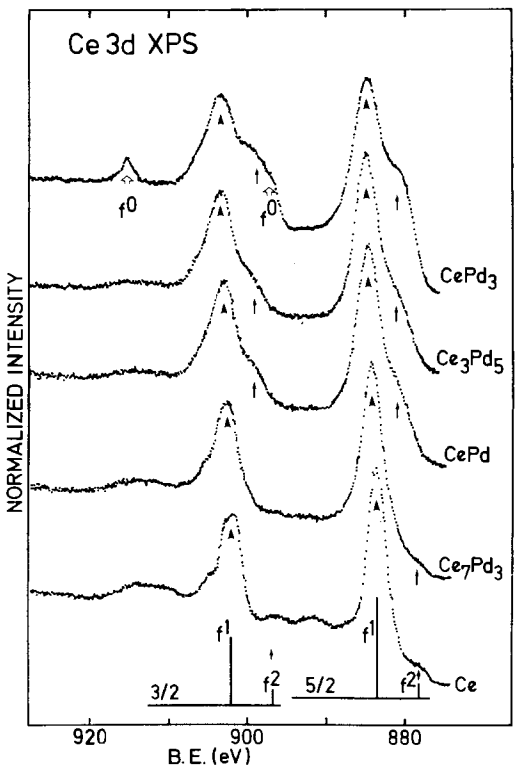

Fig. 19. Same as fig. 18, but for Ce–Pd intermetallic compounds.

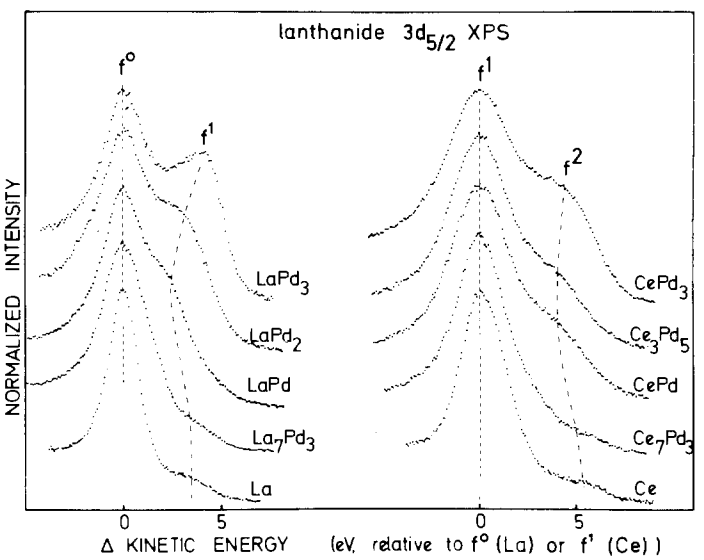

Fig. 20. Main $3d_{5/2}$ XPS peak from La–Pd and Ce–Pd intermetallic compounds.

of $3d^9 4f^0$ character. The shape of the $4d^9 4f^1$ and $4d^9 4f^2$ region cannot be interpreted in detail because the 4d–4f interaction is strong enough to introduce multiplet effects in the 4d XPS peaks which complicate peak shapes and must be treated in intermediate coupling.

For completeness a 3d XPS spectrum of $CeNi_5$ and $CeRu_2$ with the corresponding peak assignment is shown in figs. 17a and b. The spin–orbit splitting of about 18 eV of the 3d levels produces six features, three due to the $3d_{5/2}$ and three due to the $3d_{3/2}$ final state.

At this point, after a qualitative discussion of the 3d XPS results, it is appropriate to illustrate the results of model calculations for the XPS case so as to be able to understand how, by comparison with the experimental results, one can extract numerical values for Δ and n_f. These are shown in the case of Ce in figs. 21 and 22; again we refer the reader to the article of Gunnarsson and Schönhammer, chapter 64 of this book, for details of the calculation. Here we would just like to remember that in the sudden approximation the XPS current is directly related to the core spectral function:

$$\rho_c(\varepsilon) = \sum_n |\langle E_n(N-1)|\psi_c|\phi_0\rangle|^2 \cdot \delta[\varepsilon - E_0(N) + E_n(N-1)], \tag{1}$$

where

$$|\phi_0\rangle = c_0|f^0\rangle + c_1|f^1\rangle + c_2|f^2\rangle \tag{2}$$

is the ground state, $|E_n(N-1)\rangle$ are the excited final states in the presence of a core hole and $E_0(N)$ and $E_n(N-1)$ are the corresponding energies. The annihilation operator of the core level is ψ_c. To evaluate expression (1) Gunnarsson and Schönhammer write the initial ground state of fig. 10 for non-zero Δ as eq. (2). At this point we can understand why the central part of the physics is contained in the so-called low-energy satellite due to the final state of mainly f^2 character in the 3d XPS spectra. This spectral feature can in fact only occur if there is a mixing of the f^1 and f^2 configurations in the initial and/or final states so that f^2-like final state couples into the initial state. A mixing of the final state configurations means that calculations are needed to quantitatively determine to what extent n_f can be obtained from a core spectrum. The weight of the f^2 shoulder in the 3d XPS spectra provides therefore a measure of the mixing, from which one can deduce the size of the hybridization Δ. While Δ is large enough to couple the f^1 and f^2 configurations, the calculations show that the mixing of the final f^0 and f^1 configurations, which have a larger energy separation, is fairly small. The weight of the f^0 peak therefore provides a semi-quantitative measure of n_f via $c_0^2 = 1 - n_f$. Quantitative estimates can be obtained from the calculations. Figure 23 shows the comparison between experiment and calculations. $CeRu_2$ is especially interesting since it has traditionally been thought to be a so-called tetravalent Ce compound, primarily because of its superconductivity. This would have therefore implied $n_f = 0$ for $CeRu_2$. The experimental curve is well reproduced for $n_f = 0.85$ and $\Delta \approx 100$ meV, while we see that $n_f \approx 0.54$ is too much weight for the f^0 peak and $\Delta = 0.05$ eV leads to a very weak f^2 shoulder. The calculated f^1 peak is somewhat too narrow because of the neglect

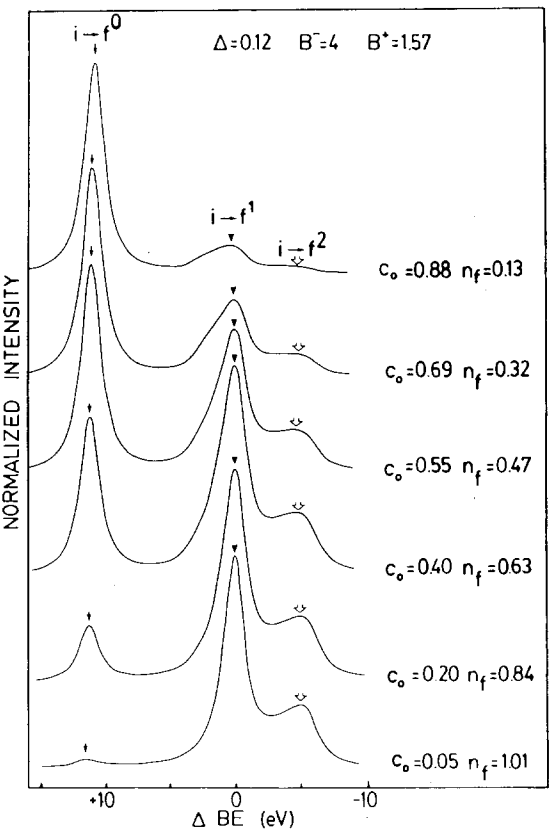

Fig. 21. Calculated Ce 3d XPS spectra (e.g. main line $3d_{5/2}$) with the ground state weight of the f^0 configuration c_0 being varied parametrically. Values of the parameters: $U = 6.4$ eV, $U_{fc} = 9.6$ eV, $\Delta = 120$ meV. A semi-elliptical band with lower edge B^- and upper edge B^+ with respect to E_F is used (Fuggle et al. 1983a,b).

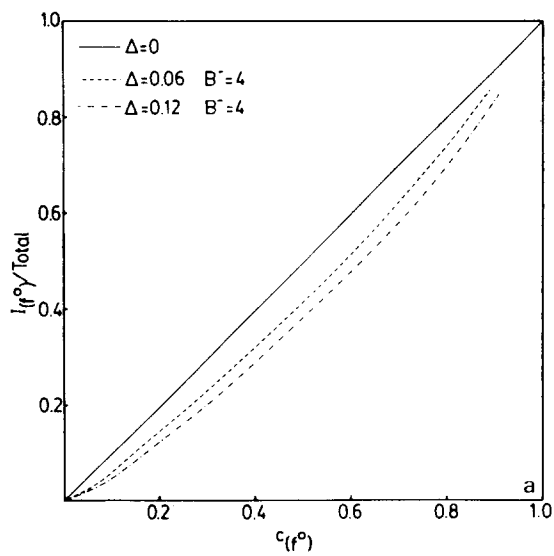

Fig. 22a. Relative intensity of the f^0 peak in the calculated spectra as a function of the ground state weight c_0 for three different values of the hybridization between the f levels and the conduction electron states (given in eV).

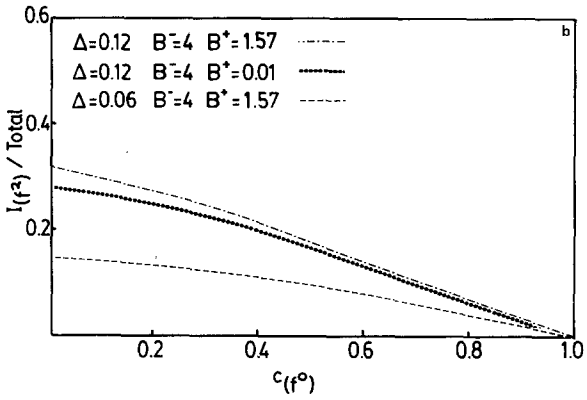

Fig. 22b. Relative intensity of the f^2 peak as a function of c_0 for different values of Δ and different band parameters (all given in eV). A semielliptical band with lower edge B^- and upper edge B^+ with respect to E_F is used.

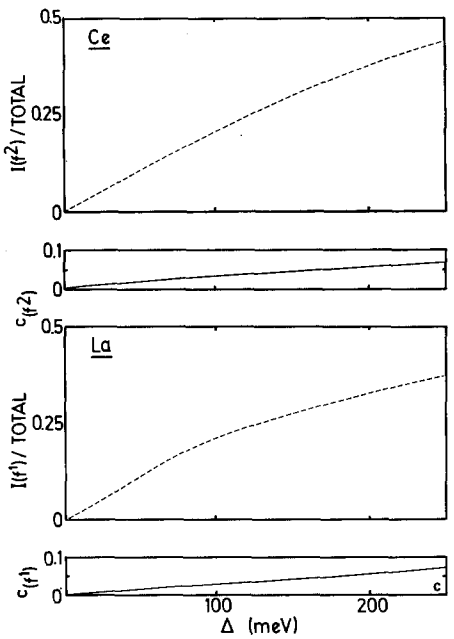

Fig. 22c. Calculated variation of the weight of the f^{n+1} peaks as a function of Δ for La and Ce, also shown is the variation of c_1 and c_2. The semielliptical conduction band has $B^- = 4$ eV, $B^+ = 1.57$ eV (Fuggle et al. 1983).

of multiplet effects. As mentioned above the values of Δ and n_f deduced from this comparison are very different from the traditional ones (Gunnarsson et al. 1983). The superconducting behavior of $CeRu_2$ cannot be explained on the basis of the absence of f electrons (i.e. $c_0 \approx 1$). Similar conclusions regarding Δ and c_0, in disagreement with traditional ones, have been obtained for most of the 'anomalous' Ce compounds (see table 1).

5.6. *Heavy fermion systems: $CeCu_2Si_2$, $CeAl_3$ and $CeCu_6$*

Steglich et al. (1979) first suggested that $CeCu_2Si_2$ is a mixed-valent superconducting Ce compound. Already in 1980 it was demonstrated empirically on the basis of a systematics of 3d XPS spectra that n_f should be rather close to 1 in this

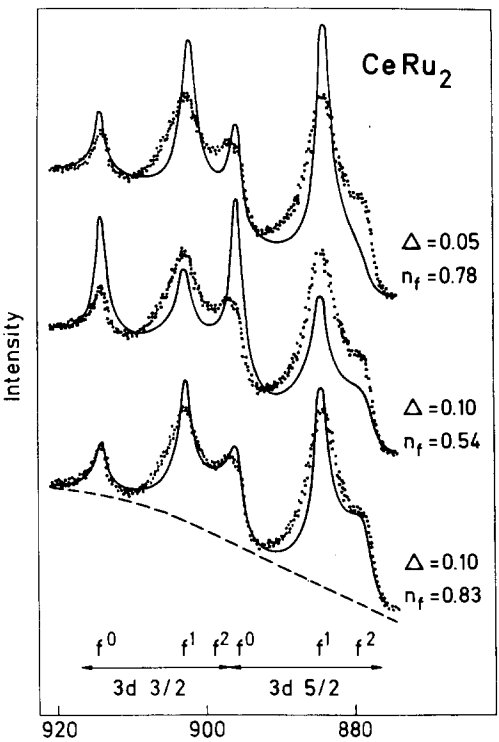

Fig. 23. Comparison between experimental (dots) and theoretical (full curve) 3d XPS spectrum for $CeRu_2$. To describe the spin–orbit splitting of the 3d level in the calculated spectra, the appropriate energy separation and weights have been superimposed. An inelastic background (dashed curve) was also added as well as broadening (Lorentzian) of one 1.8 eV (full width at half maximum, FWHM).

material (Lässer et al. 1980, Fuggle et al. 1982). Comparison with theoretical spectra would lead to $\Delta \approx 35$ meV and $n_f \approx 0.95$, see table 1.

The first known heavy fermion system, $CeAl_3$, was originally also thought to be a mixed-valent Ce compound (Andres et al. 1975). By 1981 it was clear from XPS that here too $n_f \approx 1$ (Baer et al. 1981). Again comparison with calculations would lead us to $\Delta \approx 30$ meV and $n_f \approx 0.95$. On the basis of this spectroscopic evidence it was concluded that $CeCu_2Si_2$ and $CeAl_3$ are so-called Kondo lattice systems. An understanding of their properties should take into account that the f level in the ground state is located well below E_F, i.e. ≈ 2 eV with $n_f \approx 0.95$. This made possible the development of a Fermi liquid theory of the Kondo lattice, explaining especially the heavy (effective) electron masses (Razafimandimby et al. 1984, Grewe 1984). Later, another heavy fermion Ce compound, $CeCu_6$, was discovered (Stewart et al. 1984). Also in this case, from 3d XPS spectra, shown in fig. 24, one can deduce $\Delta \approx 30$ meV and $n_f \approx 0.95$, in accordance with the earlier results for the other Ce heavy fermion systems. As we now know, the anomalous but universal low-temperature properties of these exotic but interesting f electron compounds are a result of the Kondo or Abrikosov–Suhl resonance near the Fermi energy (d'Ambrumenil and Fulde 1985, Bickers et al. 1985). In addition to the singly filled f^1 level below E_F and to the f^2 levels far above E_F there is a sharp resonance of f character just near E_F, which is the topic of current spectroscopic investigations (Patthey et al. 1985).

TABLE 1
4f Hybridization widths in meV and c_0 coefficients for La and Ce compounds.

Compounds	Δ_{4f}(La) from XPS	Δ_{4f}(Ce) from XPS	c_0(Ce) from XPS
R	70	30	<0.05
α-Ce			≈0.05
$CeCo_2$		120	≈0.18
$CeCo_5$		110	≈0.13
La_3Ni	80		
R_7Ni_3	90	60	<0.05
RNi	120	70	≈0.05
$CeNi_2$		100	≈0.12
RNi_5	160	70	≈0.16
$CeRh_3$		160	≈0.26
$CeRu_2$		120	≈0.20
R_7Pd_3	50	30	<0.05
RPd	140	90	<0.05
Ce_3Pd_5		120	<0.05
$LaPd_2$	160		
RPd_3	250	150	≈0.10
RSn_3	70	50	<0.05
$CePt_3$		150	≈0.14
RAu	30	25	<0.05
RAu_2	25	15	<0.05
$CeAl_2$		30	<0.05
RPdAl	70	35	<0.05
$CeCu_2Si_2$		35	<0.05
CeN			≈0.2
CeSb		60	<0.05
CeSe		140	<0.05

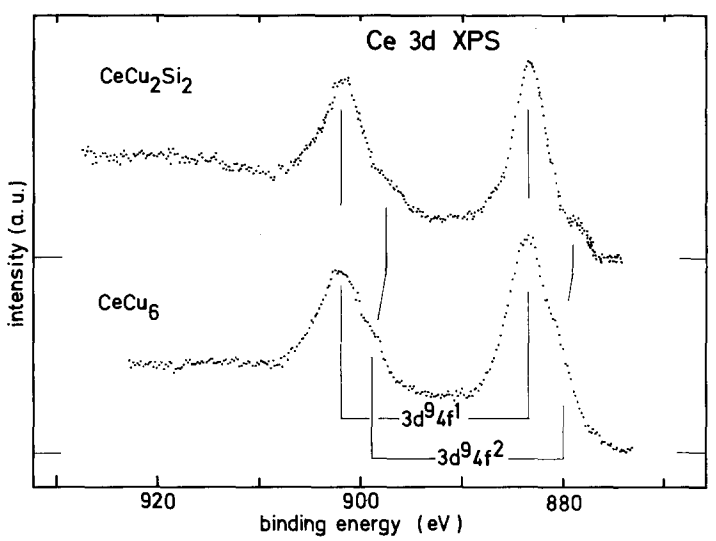

Fig. 24. Comparison of 3d XPS peaks of the heavy fermion system $CeCu_2Si_2$ (Lässer et al. 1980) and $CeCu_6$ (Sarma and Hillebrecht 1986).

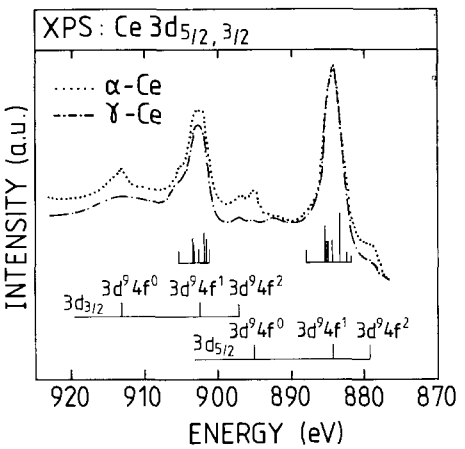

Fig. 25. New assignment of the 3d XPS peaks of γ- and α-Ce (Wuilloud et al. 1983).

Clearly these advances also allowed a re-interpretation of pioneering data of Baer and Zürcher (1977) of 'golden' CeN and α-Ce. For γ- and α-Ce we show the correct peak assignment in fig. 25. The γ–α phase transition can therefore be seen as a dramatic increase of the hybridization Δ, i.e. as a so-called 'Kondo collapse' (Allen and Martin 1982). The nature of the 4f states in Ce, topic of so many investigations (Hüfner 1982) is finally being unraveled!

6. Hydrogen storage materials and epitaxial layers

XPS investigations of hydride formation in La and Ce and in intermetallic compounds known as hydrogen storage materials were initiated by Siegmann et al. (1978). They were followed by extensive investigation by Schlapbach (1981) and Schlapbach and Scheerer (1982), Schlaplach and Osterwalder (1982) and Osterwalder (1985). A number of interesting and intriguing surface segregation phenomena were observed upon exposure to O_2 or water. Especially in going from γ-Ce to $CeH_{2.9}$ a dramatic increase of the f^2 signal in the 3dXPS spectrum was observed. This can be taken as an indication for a dramatic increase of the hybridization of the f level upon hydrogen absorption. Alternatively an increased occupancy of the metal derived conduction electron states should be taken into account. This is an experimental fact which is not yet understood, but would be worth following up in greater detail, especially with investigations at low temperatures. Especially appealing is the simplicity of the electronic structure of such high hydrides.

Epitaxial growth under clean conditions in ultra high vacuum is increasingly used in the field of metal physics as a way of preparing new materials in form of thin films or superlattices. Because of interdiffusion at the metal–metal interface, the control of the structural properties is at least as difficult as in the case of semiconductor–metal interfaces. Some initial, but very interesting steps have, however, recently been reported, also with epitaxial lanthanides. Fäldt and Myers (1985) have prepared and

investigated epitaxial Sm layers on Al(100) and Cu(100). From 3d XPS core level spectra and LEED they concluded that Sm on a Cu substrate makes a transition to an intermediate valence ($n_f \approx 5.3$), starting from divalent ($4f^6$) isolated Sm atoms. It is conceivable that Sm atoms in the oligatomic regime on a metallic substrate could show a mixed-valent behavior. This could however be unambiguously established by photoemission with synchrotron radiation to determine the position of the ^{6}H-multiplet relative to the Fermi level E_F, as was done for the surface of bulk Sm (see fig. 5). Mixed valence would imply pinning of this final state level at E_F.

Weller et al. (1985a,b) have reported the observation of surface enhanced magnetic order on hcp epitaxial Gd on W(110). This observation was possible via a simultaneous use of the magneto-optic Kerr effect (bulk sensitive measurement) and spin-polarized low-energy electron diffraction (a surface sensitive magnetic measurement) as well as analysis of the spin polarization of energy-resolved 4f photoemission with synchrotron radiation at the storage ring BESSY in Berlin. These are rather difficult measurements, which however will receive increased interest by experimentalists because of the availability in a foreseeable future of high brilliance photon sources at dedicated storage rings. The questions related to the nature of the atomic and electronic structure of epitaxial lanthanides down to the monolayer region are indeed very challenging ones.

7. Need for a systematic study of empty states at high photon energy

From the many results shown in the preceding sections we have to conclude that core level XPS investigations since 1978 have provided crucial input for revealing the exciting physics responsible for the 'anomalous' physical properties of many Ce compounds. These extensive systematic investigations have had profound effect in changing our traditional view of such fascinating intermetallic compounds. Most illustrative, in this respect, is the resulting nonlinear relation between lattice constant and so-called f count n_f, due to the significant hybridization of the f electrons with the conduction electrons. This must be contrasted to the behavior of the heavy lanthanides.

The picture of the occupied and empty valence level structure indirectly inferred from core level XPS must be complemented by a direct investigation of this important region of the electronic structure. This can be best performed either by resonant photoemission spectroscopy using synchrotron radiation for the occupied levels or by inverse photoemission spectroscopy using high-energy electrons, by the so-called *bremsstrahlung isochromat spectroscopy* for the empty levels. The results of these new investigations are the topic of chapter 70 of this book.

Acknowledgements

The extensive core level XPS investigations performed at our laboratory as well as the synchrotron radiation experiments performed at Hasylab-Hamburg, LURE-

Orsay, Madison-Wisconsin and SSRL-Stanford would not have been possible without the enjoyable collaboration and support of many colleagues and friends. We acknowledge especially the support of the director Prof. Dr. H. Wenzl and of the members of the Institute for Materials Development of the Solid State Physics Institute (IFF) of KFA, as well as the invaluable help of members of the 'Zentralabteilung für Chemische Analyse' of KFA Jülich in sample characterization.

We thank G.K. Wertheim for a critical reading of the manuscript.

References

Allen, J.W., and R. Martin, 1982, Phys. Rev. Lett. **49**, 1106.

Allen, J.W., L.I. Johansson, R.S. Bauer, I. Lindau and S.B.M. Hagström, 1978, Phys. Rev. Lett. **41**, 1499.

Alvarado, S.F., M. Campagna and W. Gudat, 1980, J. Electron Spectrosc. & Relat. Phenom. **18**, 43.

Anderson, P.W., 1981, in: Valence Fluctuations in Solids, eds L.M. Falicov, W. Hanke and M.B. Maple (North-Holland, Amsterdam) p. 451.

Andres, K., J.E. Graebner and H.R. Ott, 1975, Phys. Rev. Lett. **35**, 1979.

Baer, Y., and Ch. Zürcher, 1977, Phys. Rev. Lett. **39**, 956.

Baer, Y., R. Hauger, Ch. Zürcher, M. Campagna and G.K. Wertheim, 1978, Phys. Rev. B **18**, 4433.

Baer, Y., H.R. Ott, J.C. Fuggle and L.E. de Long, 1981, Phys. Rev. B **24**, 5384.

Bickers, N.E., D.L. Cox and J.W. Wilkins, 1985, Phys. Rev. Lett. **54**, 230.

Campagna, M., 1981, in: Valence Fluctuations in Solids, eds L.M. Falicov, W. Hanke and M.B. Maple (North-Holland, Amsterdam) p. 23.

Campagna, M., G.K. Wertheim and E. Bucher, 1976, Structure and Bonding **30**, 99.

Campagna, M., G.K. Wertheim and Y. Baer, 1979, in: Photoemission in Solids II, Topics in Applied Physics, Vol. 27, eds L. Ley and M. Cardona (Springer, Berlin) p. 218.

Crecelius, G., G.K. Wertheim and D.N.E. Buchanan, 1978, Phys. Rev. B **18**, 6519.

d'Ambrumenil, N., and P. Fulde, 1985, in: Proc. Int. Conf. Valence Fluctuations, Cologne 27–30.08.84, eds E. Müller-Hartmann, B. Roden and D.K. Wohlleben (North-Holland, Amsterdam) J. Magn. & Magn. Mater. **47&48**, 1.

Fäldt, A., and H.P. Myers, 1985, in: Proc. Int. Conf. Valence Fluctuations, Cologne 27–30.08.84, eds E. Müller-Hartmann, B. Roden and D.K. Wohlleben (North-Holland, Amsterdam) J. Magn. & Magn. Mater. **47&48**, 225.

Fuggle, J.C., E. Umbach, D. Menzel, K. Wandelt and C.R. Brundle, 1978, Solid State Commun. **27**, 65.

Fuggle, J.C., M. Campagna, Z. Zolnierek, R. Lässer and A. Platau, 1980, Phys. Rev. Lett. **19**, 1597.

Fuggle, J.C., F.U. Hillebrecht, Z. Zolnierek, Ch. Freiburg and M. Campagna, 1982, in: Valence Instabilities, eds P. Wachter and H. Boppart (North-Holland, Amsterdam) p. 267.

Fuggle, J.C., F.U. Hillebrecht, Z. Zolnierek, R. Lässer and Ch. Freiburg, 1983a, Jül-Report 1824.

Fuggle, J.C., F.U. Hillebrecht, Z. Zolnierek, R. Lässer, Ch. Freiburg, O. Gunnarsson and K. Schönhammer, 1983b, Phys. Rev. B **27**, 7330.

Grewe, N., 1984, Z. Phys. B **56**, 111.

Gudat, W., S.F. Alvarado and M. Campagna, 1978, Solid State Commun. **28**, 943.

Gudat, W., S.F. Alvarado, M. Campagna and Y. Petroff, 1980, J. Phys. Colloq. (France) **C5**, Suppl. 6, Tome 411, p. C5-1.

Gudat, W., M. Campagna, R. Rosei, J.H. Weaver, W. Eberhardt, F. Hulliger and E. Kaldis, 1981, J. Appl. Phys. **52**, 2123.

Gunnarsson, O., and K. Schönhammer, 1978a, Solid State Commun. **26**, 147.

Gunnarsson, O., and K. Schönhammer, 1978b, Phys. Rev. Lett. **41**, 1608.

Gunnarsson, O., and K. Schönhammer, 1983a, Phys. Rev. Lett. **50**, 604.

Gunnarsson, O., and K. Schönhammer, 1983b, Phys. Rev. B **28**, 4315.

Gunnarsson, O., K. Schönhammer, J.C. Fuggle, F.U. Hillebrecht, J.-M. Esteva, R.C. Karnatak and B. Hillebrand, 1983, Phys. Rev. B **28**, 7330.

Hillebrecht, F.U., 1984, Ph.D. Köln; Jül-Bericht KFA, Nr. 1928.

Hillebrecht, F.U., and J.C. Fuggle, 1982, Phys. Rev. B **25**, 3550.

Hüfner, S., 1979, in: Photoemission in Solids II, Topics in Applied Physics, Vol. 27, eds L. Ley and M. Cardona (Springer, Berlin) p. 173.

Hüfner, S., 1982, Z. Phys. B **46**, 37.

Hüfner, S., G.K. Wertheim and J.H. Wernik, 1975, Solid State Commun. **17**, 417.

Johansson, L.I., J.W. Allen, T. Gustafsson, I. Lindau and S.B.M. Hagström, 1978, Solid State Commun. **28**, 53.

Johansson, L.I., J.W. Allen, I. Lindau, M.H. Hecht and S.B.M. Hagström, 1980, Phys. Rev. B **21**, 1408.
Kotani, A., and T. Toyozawa, 1974, J. Phys. Soc. Jpn. **37**, 912.
Krill, G., J.P. Kappler, A. Meyer, L. Abadli and M.F. Ravet, 1981, J. Phys. F **11**, 1713.
Lässer, R., J.C. Fuggle, M. Beyss, M. Campagna, F. Steglich and F. Hulliger, 1980, in: Proc. Int. Conf. on The Physics of Actinides and Related 4f Materials, April 1980, ed. P. Wachter (North-Holland, Amsterdam) Physica **102B**, 360.
Laubschat, C., B. Perscheid and W.-D. Schneider, 1983, Phys. Rev. B **28**, 4342.
Lenth, W., F. Lutz, J. Barth, G. Kalkoffen and C. Kunz, 1978, Phys. Rev. Lett. **41**, 1185.
Mårtensson, N., F.U. Hillebrecht and D.D. Sarma, 1985, Surf. Sci. **152/153**, 733.
Mason, M.G., S.T. Lee, G. Apai, R.F. Davis, D.A. Shirley, A. Franciosi and J.H. Weaver, 1981, Phys. Rev. Lett. **47**, 730.
Oh, S.-J., and S. Doniach, 1982, Phys. Rev. B **26**, 2085.
Osterwalder, J., 1985, Z. Phys. B **61**, 113.
Patthey, F., B. Delley, W.-D. Schneider and Y. Baer, 1985, Phys. Rev. Lett. **55**, 1518.
Razafimandimby, H., P. Fulde, J. Keller, 1984, Z. Phys. B **54**, 111.
Sarma, D.D., and F.U. Hillebrecht, 1986, unpublished.
Schlapbach, L., 1981, Solid State Commun. **38**, 117.
Schlapbach, L., and J. Osterwalder, 1982, Solid State Commun. **42**, 271.
Schlapbach, L., and H.R. Scheerer, 1982, Solid State Commun. **41**, 893.
Schneider, W.-D., C. Laubschat, I. Nowik and G. Kaindl, 1981, Phys. Rev. B. **24**, 5422.
Schönhammer, K., and O. Gunnarsson, 1977a, Solid State Commun. **23**, 691.
Schönhammer, K., and O. Gunnarsson, 1977b, Phys. Rev. Lett. **41**, 1608.
Schönhammer, K., and O. Gunnarsson, 1977c, Z. Phys. B **30**, 297.
Siegmann, H.C., L. Schlapbach and C.R. Brundle, 1978, Phys. Rev. Lett. **40**, 972.
Steglich, F., J. Aarts, C.D. Bredl, W. Lieke, D. Meschede, W. Franz and J. Schäfer, 1979, Phys. Rev. Lett. **43**, 1892.
Stewart, G.R., Z. Fisk and M.S. Wire, 1984, Phys. Rev. B **30**, 482.
Weller, D., S.F. Alvarado, W. Gudat, K. Schröder and M. Campagna, 1985a, Phys. Rev. Lett. **54**, 1555.
Weller, D., S.F. Alvarado, M. Campagna, W. Gudat and D.D. Sarma, 1985b, in: Proc. Int. Rare Earth Conf., Zürich, March 1985, ed. J. Hulliger, J. Less-Comm. Met. **111**, 277.
Wertheim, G.K., and M. Campagna, 1977, Chem. Phys. Lett. **47**, 182.
Wertheim, G.K., and M. Campagna, 1978, Solid State Commun. **26**, 553.
Wertheim, G.K., and P.H. Citrin, 1978, in: Photoemission in Solids I, Topics in Applied Physics, Vol. 26, eds M. Cardona and L. Ley (Springer, Berlin) p. 197.
Wertheim, G.K., and G. Crecelius, 1978, Phys. Rev. Lett. **40**, 813.
Wertheim, G.K., J.H. Wernick and G. Crecelius, 1978, Phys. Rev. B **18**, 875.
Wertheim, G.K., W. Eib, E. Kaldis and M. Campagna, 1980, Phys. Rev. B **22**, 6240.
Wuilloud, E., H.R. Moser, W.-D. Schneider and Y. Baer, 1983, Phys. Rev. B **28**, 7354.

Handbook on the Physics and Chemistry of Rare Earths, Vol. 10
edited by K.A. Gschneidner, Jr., L. Eyring and S. Hüfner

Chapter 64

MANY-BODY FORMULATION OF SPECTRA OF MIXED VALENCE SYSTEMS

O. GUNNARSSON
Max-Planck Institut für Festkörperforschung, D-7000 Stuttgart 80, Fed. Rep. Germany

K. SCHÖNHAMMER
Institut für Theoretische Physik, Universität Göttingen, D-3400 Göttingen, Fed. Rep. Germany

Contents

List of symbols

B	width of the occupied part of the conduction band	Δ_{av}	average over the occupied band of $\Delta(\varepsilon)$
δ	'Kondo' energy	Δ_{so}	spin-orbit splitting
Δ	coupling between the f-level and the conduction band	ε_c	core level energy
$\tilde{\Delta}$	$N_f\Delta$	ε_f	f-level energy
		ε_F	Fermi energy

$E_0(N)$	ground-state energy of N-electron system	N_f	f-level degeneracy
		$\rho_c(\varepsilon)$	core level spectrum
$\|E_0(N)\rangle$	ground-state of N-electron system	$\rho_f^<(\varepsilon)$	total f-electron PES spectrum
		$\rho_f^>(\varepsilon)$	total f-electron BIS spectrum
$\|E_n(N-1)\rangle$	nth excited state of $(N-1)$-electron system	T	temperature
		U	f–f Coulomb interaction
$f(\varepsilon)$	Fermi function	U_{fc}	core level–4f Coulomb interaction
$g_c(z)$	core level PES Green's function		
$g_f^<(z)$	PES f-electron Green's function	U_{fd}	conduction band–4f Coulomb interaction
$g_f^>(z)$	BIS f-electron Green's function		
$g_\nu(z)$	Green's function for f-electron with quantum number ν	μ	chemical potential
		ν	combined spin and angular momentum index
H	Hamiltonian		
$\hbar\omega$	photon energy	$V(\varepsilon)$	hopping matrix element
k_B	Boltzmann's constant	$\tilde{V}(\varepsilon)$	$\sqrt{N_f}V(\varepsilon)$
n_f	f-level occupancy	χ	static, $T=0$ susceptibility

1. Introduction

There have been numerous studies of thermodynamic and transport properties of mixed valence Ce systems (Lawrence et al. 1981). These measurements have been interpreted in terms of a large density of states at the Fermi energy ε_F. Studies of the lattice parameter for Ce mixed valence systems have suggested that the f-occupancy n_f depends sensitively on the chemical environment and that n_f can vary between 0 and 1, depending on the system (Iandelli and Palenzona 1979). These properties have often been interpreted in a promotional model, where the f-level ε_f is very close to $\varepsilon_F = 0$ ($|\varepsilon_f - \varepsilon_F| \leqslant 0.1$ eV) and where its coupling $\Delta \sim 0.01$ eV is very weak so that the f-resonance is very narrow. This model explains the large density of states at ε_F. Furthermore, it could explain the assumed sensitivity of n_f to the chemical environment, since the closeness of the f-level to ε_F could easily lead to the 'promotion' of an f-electron into the conduction band if the chemical situation is changed. This picture was questioned by Johansson (1974), who deduced $|\varepsilon_f - \varepsilon_F| \sim 2.5$ eV from thermodynamic data.

During the last 5 to 10 years there has been much interest in electron spectroscopies (Hüfner and Steiner 1982), since it was realized that these also suggest a very different picture of mixed valence Ce compounds. Valence photoemission spectroscopy (PES) studies showed that the f-spectrum of Ce has weight at ($\varepsilon_f \approx$) -2 eV below ε_F (Platau and Karlsson 1978, Johansson et al. 1978). It was further found that core level X-ray photoemission spectroscopy (XPS) measurements were hard to understand unless Δ (Fuggle et al. 1980b) is much larger than previously assumed. This discrepancy between the interpretations of spectroscopic and thermodynamic data showed the need for a theoretical analysis, based on a microscopic model, of what kind of information can be extracted from different experiments. This was further emphasized when PES studies showed f-character in the spectrum both at -2 eV and close to $\varepsilon_F = 0$ (Mårtensson et al. 1982). This observation created a lively debate about how to interpret the PES spectra.

The mixed valence systems are often discussed in terms of an Anderson (1961) impurity model. The f-electron spectral function of this model has therefore been a long-standing issue. If the coupling Δ is very weak, it follows immediately that the spectrum has two peaks at ε_f (seen in PES) and at $\varepsilon_f + U$ (seen in bremsstrahlung isochromat spectroscopy (BIS)), where U is the f–f Coulomb interaction. It was further realized that the spectrum has a 'Kondo' resonance close to $\varepsilon_F = 0$ (Abrikosov 1965, Suhl 1965). Except for some special cases (Yamada 1975) it was, however, hard to determine even the qualitative properties of the Kondo resonance.

An important progress in the treatment of the Anderson model is the realization that one can treat $1/N_f$ as a small parameter, where N_f is the degeneracy of the f level (Ramakrishnan 1982, Anderson 1982, Ramakrishnan and Sur 1982). Using this idea, we have developed a method for calculating electron spectra, which becomes exact as $N_f \to \infty$ (Gunnarsson and Schönhammer 1983a,b, 1985a). In particular, this method makes it possible to study the Kondo peak quantitatively for a large value of N_f.

This approach demonstrates that the core level XPS spectrum (Oh and Doniach 1982) gives information about n_f, ε_f and Δ (Gunnarsson and Schönhammer 1983b). Typical values for Ce compounds are $n_f \geqslant 0.7$, $\varepsilon_f \sim -2\,\text{eV}$ and $\Delta \sim 0.1\,\text{eV}$ (Fuggle et al. 1983b). When such parameters are used, the calculations of the f-spectrum predict a Kondo peak with enough intensity to be seen in PES for mixed valence Ce compounds (Gunnarsson and Schönhammer 1983a, b, Schneider et al. 1985). If one further takes into account some effects related to the finite value of U, these calculations give a fair description of the f-spectra of many Ce compounds (Gunnarsson and Schönhammer 1985, Allen et al. 1986). Furthermore the Kondo resonance close to ε_F leads to a large density of states at ε_F, which is needed to understand the magnitude of some thermodynamic properties (Allen et al. 1981, Croft et al. 1981, Allen and Martin 1982, Gunnarsson and Schönhammer 1983b, Gunnarsson et al. 1983).

The main aim of this chapter is threefold. First we discuss methods for calculating electron spectra for the Anderson model. Secondly we study to what extent the Anderson model can produce spectra similar to the results obtained from different electron spectroscopies applied to Ce compounds. Thirdly we study to what extent we can use one single set of parameters for each compound to describe many different spectroscopies. Our discussion will be focussed on Ce compounds, in particular mixed valence systems, but other lanthanide compounds will also be considered.

2. Models

In this section we discuss the choice of model for Ce compounds. For the mixed valence Ce compounds the configurations $4f^0C^4$ and $4f^1C^3$ play an important role, where C stands for conduction electrons (5d, 6s, 6p). In fig. 1 we show some of the wavefunctions for a Ce atom according to a calculation (Jones 1985) in the local density approximation (Kohn and Sham 1965). The conduction states 5d and 6s are

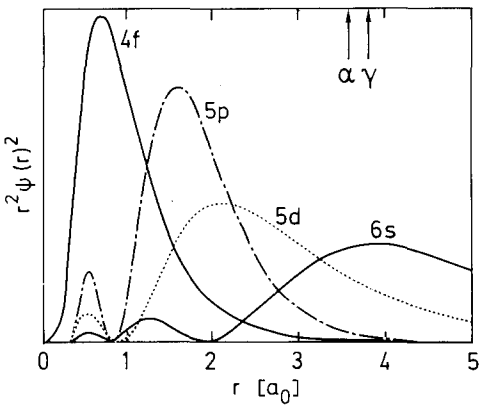

Fig. 1. The atomic wavefunctions of Ce in a LSD calculation using a Ceperly–Alder potential (Vosko et al. 1980) in the configuration $4f^1 5d^1 6s^2$. The arrows show the Wigner–Seitz radii of α- and γ-Ce. In the region $r < 0.3$ the nodes of the functions are not shown.

rather extended and have a substantial weight at the Wigner–Seitz radius. The states 5s (not shown) and 5p belong to the Ce core and are located inside the conduction states. The 4f-states are even more localized and mainly inside the 5s, 5p core. This suggests that the Coulomb interaction U between two 4f-electrons is large, and that it is essential to include this interaction in a model of a Ce compound.

Since the 4f-orbital has a different angular character than the conduction states (5d, 6s, 6p), the matrix element of the Hamiltonian between a 4f-orbital and a conduction orbital on the same site obtains a contribution only from the fairly small nonspherical part of the potential. Furthermore, the overlap between an f-orbital and a conduction orbital on another site is small because of the localized nature of the 4f-orbital. The hopping matrix element between a 4f-orbital and a conduction state is therefore rather small. To describe mixed valence behaviour it is nevertheless essential to include these matrix elements, since they couple different f-configurations.

These arguments suggest the Anderson (1961) lattice model

$$H = \sum_{k\alpha\sigma} \varepsilon_{k\alpha\sigma} n_{k\alpha\sigma} + \varepsilon_f \sum_{im\sigma} n^i_{m\sigma} + \sum_{k\alpha im} (V^i_{k\alpha m} \psi^+_{im\sigma} \psi_{k\alpha\sigma} + \text{h.c.}) + \tfrac{1}{2} U \sum_i \sum_{(m\sigma)\neq(m'\sigma')} n^i_{m\sigma} n^i_{m'\sigma'}, \tag{1}$$

where $\varepsilon_{k\alpha\sigma}$ refers to a conduction state with the wave vector $\boldsymbol{k}$, band index α and spin σ. The energy of the 4f-level is ε_f, i is a site index and m is an orbital index. $V^i_{k\alpha m}$ is a hopping matrix element between the f-orbital $(im\sigma)$ and a conduction state $(\boldsymbol{k}\alpha\sigma)$. The last term describes the Coulomb interaction U between two 4f-electrons on the same site.

Since the model (1) is very difficult to solve, most work has been limited to the Anderson impurity model, where only the f-level on one site is considered. This is perhaps the simplest model of a mixed valence system, since the model only contains the hopping term necessary to couple different f-configurations and the important f–f Coulomb interaction. Variations of this model have been very widely used to describe transport, thermodynamic and spectroscopic properties of mixed valence

systems. The broad use of this model has the advantage that it may enable us to relate different experiments to each other. It will be shown in the following that the impurity model works surprisingly well for the description of Ce mixed valence compounds. Some justification for the impurity model has been given by the observation that the impurity–impurity interaction is of order $1/N_f$ (Read and Newns 1984, Read et al. 1984), where N_f is the degeneracy of the f level.

It is interesting to discuss this model in terms of a one-particle basis set. Such a basis set can be obtained from a band calculation in which the f-electrons are treated as core electrons. Thus the f-level is filled by the appropriate number n_f of f-electrons, which contribute to the effective potential of the conduction electrons, but which do not hybridize with the conduction states. The conduction states and the localized f-orbital can now be used as a one-particle basis set. From this set a Hamiltonian can be derived, which contains terms of the same type as in (1) but in addition many other terms. Many of the additional terms are not small, and the justification for their neglect is a complicated issue.

In (1) the Coulomb interaction between the conduction states is neglected. These states are rather extended (see fig. 1) and the Coulomb integrals are not very large. For such states the local spin density (LSD) approximation of the spin density functional formalism (Kohn and Sham 1965) has been rather successful (von Barth and Williams 1983). In this scheme the electrons are formally treated as independent and correlation effects are included in an effective one-particle potential. By using $\varepsilon_{k\alpha}$'s in (1) which are obtained from a LSD approximation or deduced from experiment, we may incorporate some interaction effects implicitly in the Hamiltonian (1). In this way chemical information about the compound considered may also be incorporated. Relativistic effects on the band structure are also included in this approach.

The Coulomb interaction U_{fd} between a conduction electron and an f-electron on the same site is neglected in (1). The effect of this term is approximately included as a renormalization of U. We want to discuss this renormalization in more detail, since it illustrates the nature of the approximations involved in the use of a model Hamiltonian like (1). According to (1) the energy cost of putting two f-electrons on the same site is U. An estimate of U is given by the Slater Coulomb integral F_0, which is of the order 25 eV (Herbst et al. 1978). In the real system this energy cost is smaller due to the relaxation of the f-orbital and the screening by the conduction electrons. The screening takes place as a reduction in the number n_d of conduction electrons on an atom as the number n_f of f-electrons on the same atom is increased. Due to the interaction U_{fd} this decrease in n_d leads to a reduction in the energy cost for double occupancy of the f-orbital. Herbst et al. (1978) calculated this reduction under the assumption that $n_d + n_f = \text{const.}$ for each atom. Including this and some other effects, they found that the energy cost is reduced from $F_0 \sim 25\,\text{eV}$ to about 5 eV for Ce. We take these effects implicitly into account in (1) by assuming that $U \sim 5\,\text{eV}$.

A Hamiltonian like (1) with an effective U can be used if in the real system the number of conduction electrons can always adjust to the number of f-electrons. This assumption breaks down in, for instance, photoemission spectroscopy, if U_{fd} is

larger than the width of the conduction band. In such a case there are important final states, where an f-electron has been removed but the number of conduction electrons has not been increased correspondingly. These states can lead to an extra peak in the spectrum, which is entirely missing unless U_{fd} is included explicitly (Kotani and Toyozawa, 1974a,b, Schönhammer and Gunnarsson 1977, 1978a).

In a similar way other terms, which are not included explicitly in (1), may be included implicitly. It is therefore hard to judge a priori the accuracy of the model (1) for a certain class of systems and properties. To determine this we have to rely on a comparison of experiments with calculations for this model. For the cases where the model gives a good description, the determination of the parameters from first principles requires an understanding of the types of renormalizations involved. For U and ε_f Herbst et al. (1978) have made important progress in this respect, while the hopping parameters $V_{k\alpha m}$ are much less well understood.

To be able to describe core level spectroscopies, we add to the Hamiltonian (1) a term (Kotani and Toyozawa 1974a,b, Lang and Williams 1977)

$$H_c = \varepsilon_c n_c - U_{fc}(1 - n_c)\sum_{m\sigma} n_{m\sigma}, \tag{2}$$

where ε_c describes a structureless core level. Since the 4f-level is very compact, it feels the core hole attraction more strongly than the conduction electrons. The energetic ordering of the configurations is therefore changed when a core hole is created. In the absence of a core hole the f^2 configuration is a few eV above the f^1 configuration, while in the presence of a core hole it is about 5 eV below. This effect is incorporated in the term containing U_{fc}. The value of U_{fc} is strongly renormalized by, for instance, the core hole–conduction electron Coulomb interaction (Herbst and Wilkins 1979).

In the calculations for the impurity Anderson model, the information about the $V_{k\alpha m}$'s enters in the form

$$\sum_{k\alpha} V^*_{k\alpha m} V_{k\alpha m'} \delta(\varepsilon - \varepsilon_{k\alpha}), \tag{3}$$

where the index i has been suppressed since there is only one impurity. In the following we make the assumption

$$\sum_{k\alpha} V^*_{k\alpha m} V_{k\alpha m'} \delta(\varepsilon - \varepsilon_{k\alpha}) = \bar{V}_m(\varepsilon)^* \rho_{mm'} \bar{V}_{m'}(\varepsilon), \tag{4}$$

where $\rho_{mm'} = \rho^*_{m'm}$ is energy independent. For a cubic system this result immediately follows, if we let m refer to cubic harmonics. Using symmetry arguments one then finds that $\rho_{mm'}$ is diagonal. Even in cases where (4) is not exact, we expect it to be a good approximation. Since the phase of $V_{k\alpha m}$ in general varies rapidly with $\boldsymbol{k}$, the result of the $\boldsymbol{k}$-summation should be small unless $m = m'$.

It is now useful to transform the conduction states to the same symmetry representation as the f-states

$$|\varepsilon, m\sigma\rangle = \bar{V}_m(\varepsilon)^{-1} \sum_{k\alpha} V_{k\alpha m} \delta(\varepsilon - \varepsilon_k) |\boldsymbol{k}\alpha\sigma\rangle, \tag{5}$$

where $|\boldsymbol{k}\alpha\sigma\rangle$ is a conduction state. We then have

$$\langle \varepsilon', m'\sigma' | \varepsilon m\sigma \rangle = \rho_{mm'} \delta(\varepsilon - \varepsilon') \delta_{\sigma\sigma'}. \tag{6}$$

Since $\rho_{m'm}$ is Hermitian it can be diagonalized. This defines an energy-independent unitary transformation and we transform the conduction states to new orthogonal states $|\varepsilon,\gamma\sigma\rangle$, with the normalization

$$\langle\varepsilon',\gamma'\sigma'|\varepsilon,\gamma\sigma\rangle = \delta(\varepsilon-\varepsilon')\delta_{\gamma\gamma'}\delta_{\sigma\sigma'}. \tag{7}$$

The same transformation is used for the f-states. This leads to the Hamiltonian

$$\begin{aligned} H = \sum_{\nu=1}^{N_f} \Big\{ & \int \varepsilon \psi_{\varepsilon\nu}^{+} \psi_{\varepsilon\nu} \mathrm{d}\varepsilon + \varepsilon_f \psi_\nu^{+} \psi_\nu \\ & + \int \mathrm{d}\varepsilon [V_\nu(\varepsilon)\psi_\nu^{+} \psi_{\varepsilon\nu} + \mathrm{h.c.}] \Big\} + U \sum_{\nu<\mu} n_\nu n_\mu + \tilde{H}_0 \\ \equiv & H_0 + \hat{V} + \hat{U} + \tilde{H}_0, \end{aligned} \tag{8}$$

where we have introduced $\nu = (\gamma,\sigma)$ as a combined index for the orbital and spin degeneracies. The f-level degeneracy is $N_f\,(=14)$. $\tilde{H}_0$ contains linear combinations of conduction states, which are orthogonal to the states (5) and therefore do not couple to the f-level. We can therefore neglect $\tilde{H}_0$ for most of the properties studied here. In the following we also assume that $V_\nu(\varepsilon)$ is independent of ν,

$$V_\nu(\varepsilon) \equiv V(\varepsilon). \tag{9}$$

With our normalization of the conduction states, the conduction density of states has been absorbed in $V(\varepsilon)^2$. We put the Fermi energy $\varepsilon_F = 0$, and assume that the conduction band extends between $-B$ and B'.

The Hamiltonian (8) represents the simplest starting point for the discussion of mixed valence systems. It is straight forward to take the spin-orbit splitting of the f-level into account. The 14-fold degenerate f-level is then split into a 6-fold and an 8-fold degenerate level. This has been done in most of the calculations described in section 5. In the same way crystal field splitting can be included as a further splitting of the f-level. In the models (8) and (2) multiplet effects are entirely neglected. Experimentally these effects show up particularly clearly in the core spectroscopies and in bremsstrahlung isochromat spectroscopies (BIS). It should be possible to introduce such effects in the formalism below, but because of the many different multiplet states this is a substantial complication.

As discussed above it would be interesting to introduce the Coulomb interaction between the f-electrons and the conduction electrons and between the conduction electrons themselves. One could then study the renormalization of the parameters in the model (8) as well as the new dynamical effects, such as extra satellites, which appear in the appropriate parameter range. The inclusion of terms containing $\psi_{\varepsilon\nu}^{+}$ $\psi_{\varepsilon'\nu'}^{+}\psi_{\varepsilon''\nu''}\psi_{\nu'''}$ would allow the study of some lifetime effects. Such interactions are, however, a great complication, and it is then a very difficult problem to find an accurate solution.

The model (8) can be generalized to include the coupling of the f-level to a localized phonon mode. In the limit $U\to\infty$, $N_f\to\infty$ exact results for the PES f-level spectrum and some ground-state properties have been obtained (Schönhammer and Gunnarsson 1984).

An alternative to the model Hamiltonian approach discussed above is the use of the LSD approximation (Kohn and Sham 1965) for the description of the f-electron system. A study of the pressure–volume relation for α-Ce and α′-Ce gave a reasonably good agreement with experiment (Glötzel 1978). It was found that the LSD approximation predicts an f-contribution to the pressure which is needed to understand the experiment. At a volume corresponding to γ-Ce, on the other hand, the calculated f-pressure was much too negative. This type of results were also found for Pr (Skriver 1981). The LSD approximation is claimed to give a good Fermi surface for $CeSn_3$, a system where the f-electrons are of importance for the Fermi surface (Koelling 1982). On the other hand the specific heat is an order of magnitude too small for $CeSn_3$ in the LSD approximation (Koelling 1982). Although the energy eigenvalues in this approach have not been shown to give excitation energies (Kohn and Sham 1965) it is standard practice to assume that this is the case. The f-band width is of the order 1 eV (Podloucky and Glötzel 1983), while the experimental f-spectrum is spread over about 8 eV (Lang et al. 1981). This large energy spread can not be described by the LSD approximation, unless the standard procedure for performing band calculations is modified (Norman et al. 1985, Norman 1985). An advantage of the density functional formalism is its first principle nature, i.e. the lack of adjustable parameters of the type ε_f or $V(\varepsilon)$ in the model Hamiltonian approach. As indicated above, however, the presently available approximations, e.g. the LSD or Xα approximations, are not accurate enough to describe many properties of Ce compounds, which are changed qualitatively by the large correlation effects.

3. Methods for calculating spectra

In this section we first demonstrate how various spectroscopies can be related to one-electron Green's functions by using the so-called sudden approximation. Then methods for calculating these Green's functions are reviewed. As discussed in section 2, the Anderson impurity model (AIM) is believed to contain the most important mechanisms for the systems studied here. We therefore focus on the AIM with special emphasis on the limit where correlation effects are important. In the nondegenerate case $N_f = 1$ the interaction term involving the Coulomb interaction U between two electrons in different f-channels does not appear and the resulting problem of noninteracting electrons can be solved exactly (see below). The 'spin-degenerate' case $N_f = 2$ has also been given special attention. The exact solution for ground-state and thermodynamic properties has been found using the Bethe- ansatz (Wiegmann 1980, Kawakami and Okiji 1981, Schlottmann 1983), but spectral functions have not been obtained by this method.

3.1. *One-electron Green's function*

As an example we consider photoemission and we essentially follow Hedin and Lundqvist (1969). The system is assumed to be described by a Hamiltonian H in the absence of any external fields. We introduce an operator τ, which describes

transitions induced by the photons perturbing the system

$$\tau = \sum_{\kappa i} \tau_{\kappa i} \psi_\kappa^+ \psi_i, \tag{10}$$

where $\tau_{\kappa i}$ is a matrix element of the dipole operator between the one-particle states $|i\rangle$ and $|\kappa\rangle$. The N-electron system is assumed to make transitions to final states of the type

$$\psi_\kappa^+ |E_n(N-1)\rangle, \tag{11}$$

where $|E_n(N-1)\rangle$ is an $(N-1)$-electron eigenstate of the Hamiltonian H. Thus the emitted electron in the state $|\kappa\rangle$ is assumed to have no interaction with the remaining $(N-1)$ electrons. This 'sudden' approximation becomes increasingly accurate as the kinetic energy of the emitted electron is increased. For the cases we are interested in, the kinetic energy is typically 50–1000 eV. The sudden approximation is then generally assumed to be a good starting point, although the corrections can be substantial (Fuggle et al. 1980a). According to the golden rule, the number of emitted electrons with the energy ε is then proportional to

$$P(\varepsilon) = \sum_\kappa \sum_n |\langle E_n(N-1)|\psi_\kappa \tau |E_0(N)\rangle|^2 \times \delta(\varepsilon - \varepsilon_\kappa)\, \delta(\varepsilon + E_n(N-1) - \hbar\omega - E_0(N)), \tag{12}$$

where $\hbar\omega$ is the energy of the photon causing the transition. The last δ-function follows from energy conservation.

One now makes the further assumption

$$\psi_\kappa |E_0(N)\rangle = 0. \tag{13}$$

If $|\kappa\rangle$ refers to a high-lying scattering state, this state has a small weight in the initial state $|E_0(N)\rangle$, and (13) is a good approximation. The closely related approximations (11) and (13) therefore both become accurate as $\hbar\omega$ is increased. Equation (13) leads to

$$P(\varepsilon) = \frac{1}{\pi} \sum_\kappa \delta(\varepsilon - \varepsilon_\kappa)\, \mathrm{Im} \langle E_0(N)|\tau_\kappa^+ \frac{1}{\varepsilon - \hbar\omega + H - E_0(N)} \tau_\kappa |E_0(N)\rangle, \tag{14}$$

where

$$\tau_\kappa = \sum_i \tau_{\kappa i} \psi_i. \tag{15}$$

It is now assumed that the interference between different values of i in the two τ_κ in eq. (14) can be neglected. Although this assumption is not necessary, it leads to simpler expressions. This should be a good approximation for the emission from a (core) level which is well separated in energy from the other levels. For valence photoemission for Ce compounds, the interference between the f-level and the conduction band emission may be of importance (Gunnarsson and Schönhammer,

1985a). The neglect of interference leads to

$$P(\varepsilon) \equiv \sum_i P_i(\varepsilon) = \sum_i \frac{1}{\pi} \sum_\kappa |\tau_{\kappa i}|^2 \delta(\varepsilon - \varepsilon_\kappa) \operatorname{Im} g_i^<(\varepsilon - \hbar\omega - \mathrm{i}0), \tag{16}$$

where

$$g_i^<(z) = \langle E_0(N)|\psi_i^+ \frac{1}{z + H - E_0(N)} \psi_i |E_0(N)\rangle. \tag{17}$$

Since we are usually interested in values of ε, the kinetic energy of the emitted electrons, which are not very small, we further assume that

$$\sum_\kappa |\tau_{\kappa i}|^2 \delta(\varepsilon - \varepsilon_\kappa)$$

has a negligible energy dependence. This should be a reasonable approximation if the width of the spectrum (~ 10 eV) is much smaller than ε. Then each contribution $P_i(\varepsilon)$ to $P(\varepsilon)$ is proportional to

$$\rho_i^<(\varepsilon - \hbar\omega) = \frac{1}{\pi} \operatorname{Im} g_i^<(\varepsilon - \hbar\omega - \mathrm{i}0). \tag{18}$$

Thus the main remaining problem is the calculation of $g_i^<(z)$.

In bremsstrahlung isochromat spectroscopy (BIS) the system is exposed to an electron beam and the transitions of the incoming electrons under the emission of photons are studied. In this case it is assumed that the initial state is of the form

$$\psi_\kappa^+ |E_0(N)\rangle, \tag{19}$$

and transitions to final states $|E_n(N+1)\rangle$ are studied. With similar approximations as for PES, the energy distribution of the photons is related to

$$\rho_i^>(E - \hbar\omega) = \frac{1}{\pi} \operatorname{Im} g_i^>(E - \hbar\omega - \mathrm{i}0), \tag{20}$$

where

$$g_i^>(z) = \langle E_0(N)|\psi_i \frac{1}{z - H + E_0(N)} \psi_i^+ |E_0(N)\rangle,$$

and E is the energy of the incoming electron.

The functions $g_i^<(z)$ and $g_i^>(z)$ are directly related to the $T = 0$ limit of the retarded Green's function (Zubarev 1960) (with $A = \psi_i^+$ and $B = \psi_i$)

$$\langle\langle A; B\rangle\rangle_z \equiv -\mathrm{i} \int_0^\infty \langle [A(t), B]_\pm \rangle \mathrm{e}^{\mathrm{i}zt} \, \mathrm{d}t, \tag{21}$$

where $A(t) = \mathrm{e}^{\mathrm{i}Ht} A \, \mathrm{e}^{-\mathrm{i}Ht}$ is the operator A in the Heisenberg picture, $\langle\ \rangle$ denotes the average over the grand canonical ensemble, and z is a complex variable with $\operatorname{Im} z > 0$ to ensure convergence of the time integral. For operators A involving

products of an *odd* (even) number of Fermion field operators the anticommutator $[,]_+$ (commutator $[,]_-$) is chosen.

We define

$$g_\nu(z) \equiv \langle\langle \psi_\nu ; \psi_\nu^+ \rangle\rangle, \tag{22}$$

where ψ_ν annihilates an f-electron with the quantum number ν. At $T = 0$, $g_\nu(z)$ can be written as

$$\begin{aligned} g_\nu(z) &= \langle E_0(N)|\psi_\nu \frac{1}{z - H + E_0(N)} \psi_\nu^+ |E_0(N)\rangle \\ &\quad + \langle E_0(N)|\psi_\nu^+ \frac{1}{z + H - E_0(N)} \psi_\nu |E_0(N)\rangle \\ &\equiv g_\nu^>(z) + g_\nu^<(z). \end{aligned} \tag{23}$$

The relation of the photoemission and BIS spectra to one-electron Green's functions as presented above can be generalized to finite temperatures by averaging over initial eigenstates of the system with the appropriate Boltzmann factors. This leads to

$$\rho_\nu^<(\varepsilon) = \frac{1}{\pi} f(\varepsilon) \operatorname{Im} g_\nu(\varepsilon - \mathrm{i}0), \tag{24}$$

where $f(\varepsilon) = 1 + \exp[(\varepsilon - \mu)/k_B T]^{-1}$ is the Fermi function and μ is the chemical potential. The BIS spectrum is given by

$$\rho_\nu^>(\varepsilon) = \frac{1}{\pi}(1 - f(\varepsilon)) \operatorname{Im} g_\nu(\varepsilon - \mathrm{i}0). \tag{25}$$

Due to the 'rotational invariance' of the Hamiltonian (8) $g_\nu(z)$ is independent of ν and due to the conservation of the electron number in each 'channel ν' $\langle\langle \psi_\nu ; \psi_{\nu'}^+ \rangle\rangle = 0$ for $\nu \neq \nu'$.

The Heisenberg equation of motion (EOM) for $A(t)$ and a partial integration gives the EOM for $\langle\langle A; B \rangle\rangle$

$$z\langle\langle A; B\rangle\rangle - \langle\langle [A, H]; B\rangle\rangle = \langle [A, B]_\pm \rangle. \tag{26}$$

This EOM is very useful for discussing the exactly solvable limits of the AIM. In section 3.2.1 we discuss the 'atomic limit and in section 3.2.2 the 'noninteracting case' $U = 0$.

3.2. *Exactly solvable limits*

To discuss the exactly soluble limits one needs various commutators. With the abbreviation

$$\begin{aligned} \bar{N}_n^{(\nu)} &\equiv \sum_{\nu_1 \neq \nu_2 \neq \cdots \neq \nu_n}{}' n_{\nu_1} n_{\nu_2} \cdots n_{\nu_n}, \qquad n = 1, \ldots, N_f - 1; \\ \bar{N}_0^{(\nu)} &\equiv 1; \qquad \bar{N}_{N_f}^{(\nu)} \equiv 0, \end{aligned} \tag{27}$$

where the prime indicates that the summation over ν is excluded, one obtains

$$[\psi_\nu, H] = \varepsilon_f \psi_\nu + U\psi_\nu \bar{N}_1^{(\nu)} + \int d\varepsilon V(\varepsilon)\psi_{\varepsilon\nu}, \tag{28a}$$

$$[\psi_{\varepsilon\nu}, H] = \varepsilon\psi_{\varepsilon\nu} + V(\varepsilon)\psi_\nu, \tag{28b}$$

and using $\bar{N}_1^{(\nu)}\bar{N}_m^{(\nu)} = m\bar{N}_m^{(\nu)} + \bar{N}_{m+1}^{(\nu)}$ for $m = 1, \ldots, N_f - 1$,

$$[\psi_\nu \bar{N}_m^{(\nu)}, H] = (\varepsilon_f + mU)\psi_\nu \bar{N}_m^{(\nu)} + U\psi_\nu \bar{N}_{m+1}^{(\nu)} + [\psi_\nu \bar{N}_m^{(\nu)}, \hat{V}], \tag{28c}$$

where $\hat{V}$ is the mixing term defined in (8).

3.2.1. *Atomic limit*

Using (28) we obtain for $\hat{V} = 0$ the following closed set of equations

$$(z - \varepsilon_f - mU)\langle\langle \psi_\nu \bar{N}_m^{(\nu)}; \psi_\nu^+ \rangle\rangle^{(0)} - U\langle\langle \psi_\nu \bar{N}_{m+1}^{(\nu)}; \psi_\nu^+ \rangle\rangle^{(0)} = \langle \bar{N}_m^{(\nu)} \rangle^{(0)}, \tag{29}$$

where $m = 0, 1, \ldots, N_f - 1$. The matrix of this linear set of equations has upper diagonal form and can easily be inverted. This yields

$$\langle\langle \psi_\nu \bar{N}_m^{(\nu)}; \psi_\nu \rangle\rangle^{(0)} = \sum_{i=m}^{N_f - 1} \langle \bar{N}_i^{(\nu)} \rangle^{(0)} U^{i-m} \prod_{n=0}^{i-m} \frac{1}{z - \varepsilon_f - (m+n)U}. \tag{30}$$

In the following we are only interested in the case $\varepsilon_f + U > \mu$ where μ is the chemical potential. For temperatures $k_B T \ln N_f \ll \varepsilon_f + U - \mu$ double and higher occupancy of the f-level can then be neglected and for $m = 0$ only the first two terms in the sum in (30) contribute to $g_\nu^{(0)}(z)$. After decomposing the second term into partial fractions one obtains

$$g_\nu^{(0)}(z) = \frac{1 - n_f^0(1 - 1/N_f)}{z - \varepsilon_f} + \frac{n_f^0(1 - 1/N_f)}{z - \varepsilon_f - U}. \tag{31}$$

The total f-occupancy n_f^0 in the atomic limit follows from the 'fluctuation-dissipation theorem' (Zubarev 1960)

$$n_f^0 = -\frac{1}{\pi} N_f \int_{-\infty}^{\infty} \mathrm{Im} g_\nu^{(0)}(\varepsilon + i0) f(\varepsilon)\, d\varepsilon, \tag{32}$$

as

$$n_f^0 = \frac{f(\varepsilon_f)}{f(\varepsilon_f) + (1 - f(\varepsilon_f))/N_f}. \tag{33}$$

For $T = 0$ one obtains $n_f^0 = 1$ for $\varepsilon_f < \mu$ and $n_f^0 = 0$ for $\varepsilon_f > \mu$. For finite temperatures a large degeneracy N_f can lead to an f-occupancy close to one even if ε_f is above the Fermi level. The entropy gain from occupying the f-level can lower the free energy sufficiently to compensate the concomitant energy loss. As shown here for the atomic limit, the limits $T \to 0$ and $N_f \to \infty$ are not interchangeable (Brandt et al. 1985). If one really wanted to study the mathematical limit $N_f \to \infty$ for finite temperatures then the neglect of higher f-occupancy is not justified. For large but

finite N_f this effect is completely unimportant for all relevant temperatures, when $\varepsilon_f + U$ is well above the Fermi level, because the degeneracy enters via its logarithm for the estimate of the temperature range.

For $T = 0$ and $\varepsilon_f < \mu$ the spectral function $\rho_f^{(0)}(\varepsilon) \equiv N_f \mathrm{Im} g_\nu^{(0)}(\varepsilon + \mathrm{i}0)/(-\pi)$ reads

$$\rho_f^{(0)}(\varepsilon) = \delta(\varepsilon - \varepsilon_f) + (N_f - 1)\delta(\varepsilon - \varepsilon_f - U). \tag{34}$$

The delta peak at ε_f describes the photoemission from the f-level, while the peak at $\varepsilon_f + U$ corresponds to the BIS experiment where an electron is added to the system. The probability to find a certain ν-channel occupied in the initial state is $1/N_f$ which leads to a total photoemission 'intensity' $N_f(1/N_f) = 1$.

The probability for the channel to be empty in the initial state is $1 - 1/N_f$ which leads to the total BIS intensity $N_f(1 - 1/N_f) = N_f - 1$. Note that the ratio of the BIS weight and the photoemission weight diverges in the limit $N_f \to \infty$ (Gunnarsson and Schönhammer 1983a,b). The spectral function (34) consists of sharp delta peaks. The broadening of these peaks is one of the effects of the hybridization term $\hat{V}$. To obtain an understanding how a broadening of discrete levels is accomplished by $\hat{V}$ we study the noninteracting limit $U = 0$.

3.2.2. *Noninteracting limit*

Using (28a) and (28b) for $U = 0$ one obtains again a closed set of equations

$$(z - \varepsilon_f)\langle\langle \psi_\nu; \psi_\nu^+ \rangle\rangle - \int \mathrm{d}\varepsilon\, V(\varepsilon)\langle\langle \psi_{\varepsilon\nu}; \psi_\nu^+ \rangle\rangle = 1, \tag{35}$$

$$(z - \varepsilon)\langle\langle \psi_{\varepsilon\nu}; \psi_\nu^+ \rangle\rangle - V(\varepsilon)\langle\langle \psi_\nu; \psi_\nu^+ \rangle\rangle = 0, \tag{36}$$

with the solution for $g_\nu(z)$

$$g_\nu^{U=0}(z) = \frac{1}{z - \varepsilon_f - \Gamma(z)}, \tag{37}$$

with

$$\Gamma(z) = \int_{-\infty}^{\infty} \frac{|V(\varepsilon)|^2}{z - \varepsilon}\, \mathrm{d}\varepsilon. \tag{38}$$

The spectral function $\rho_f^{U=0}(\varepsilon)$ is therefore determined by the strength and the energy dependence of $|V(\varepsilon)|^2$

$$\rho_f^{U=0}(\varepsilon) = \frac{N_f |V(\varepsilon)|^2}{(\varepsilon - \varepsilon_f - \mathrm{Re}\,\Gamma(\varepsilon))^2 + (\pi V(\varepsilon)^2)^2}. \tag{39}$$

In addition to this continuous part, $\rho_f^{U=0}(\varepsilon)$ can have delta contributions at energies ε_i for which $V(\varepsilon_i) = 0$ and $\varepsilon_i - \varepsilon_f - \Gamma(\varepsilon_i) = 0$. In the simplest case of a constant $V(\varepsilon)$, $\rho_f^{U=0}(\varepsilon)$ consists of an unshifted Lorentzian peak whose width is $\pi|V(\varepsilon)|^2$. In section 5 we will discuss systems where $V(\varepsilon)$ is such that $\rho_f^{U=0}(\varepsilon)$ shows additional structure due to the energy dependence of $V(\varepsilon)$.

The result (37) shows that for $U = 0$ the degeneracy does not even enter the result for $g_\nu(z)$. This is very different from the general case which we will discuss next.

3.3. *Expansion in U*

In the general case the EOM approach yields an infinite hierarchy of coupled Green's functions with increasing number of Fermion operators involved. As in the diagrammatic approach discussed below it is useful to incorporate all many-body effects by defining the 'selfenergy' $\Sigma_\nu(z)$ by

$$g_\nu(z) = \frac{1}{z - \varepsilon_f - \Gamma(z) - \Sigma_\nu(z)}. \tag{40}$$

Like $g_\nu(z)$, $\Sigma_\nu(z)$ is an analytic function off the real axis. Without a magnetic field Σ_ν is independent of ν due to the 'rotational' invariance of (8). A comparison of (40) with the general EOM for $g_\nu(z)$ as follows from (28) leads to the relation

$$\Sigma_\nu(z)\langle\langle \psi_\nu; \psi_\nu^+ \rangle\rangle = U\langle\langle \psi_\nu \bar{N}_1^{(\nu)}; \psi_\nu^+ \rangle\rangle. \tag{41}$$

As both Green's functions in (41) vanish as $1/z$ in the limit $z \to \infty$, the selfenergy goes to a constant in that limit. One can therefore separate a constant term in the selfenergy

$$\Sigma_\nu(z) = \Sigma_\nu^\infty + \tilde{\Sigma}_\nu(z). \tag{42}$$

From $\langle\langle A; B\rangle\rangle_z \to \langle [A, B]_\pm \rangle / z$ in the limit $z \to \infty$, we obtain from (41)

$$\Sigma_\nu^\infty = U\langle \bar{N}_1^{(\nu)} \rangle = U \sum_{\nu'}{}' \langle n_{\nu'} \rangle. \tag{43}$$

The approximation of neglecting the frequency-dependent part completely, is just the *Hartree–Fock approximation* (HF)

$$g_\nu^{\mathrm{HF}}(z) = \frac{1}{z - \varepsilon_f - n_f^{\mathrm{HF}} \tilde{U} - \Gamma(z)}, \tag{44}$$

where $\tilde{U} \equiv U(1 - 1/N_f)$ and the Hartree–Fock f-occupancy n_f^{HF} has to be determined selfconsistently by the relation analogous to (32). In the limit of *large U* (and fixed ε_f) which is our main interest, this is a very poor approximation. This can be seen rather easily for a constant $V(\varepsilon)$ i.e. $\Gamma(z) = -i\Delta \mathrm{sign}(\mathrm{Im}(z))$ at $T = 0$. To keep the Coulomb interaction in the HF ground state low, the f-occupancy n_f^{HF} has to decrease with increasing U. Therefore only the tail of the Lorentzian peak resulting from (44) has to be integrated in (32) ($\mu = 0$)

$$n_f^{\mathrm{HF}} \approx N_f \int_{-\infty}^{0} \frac{\Delta/\pi}{(\varepsilon - \varepsilon_f - n_f^{\mathrm{HF}} \tilde{U})^2} \, \mathrm{d}\varepsilon = \frac{N_f \Delta/\pi}{\varepsilon_f + n_f^{\mathrm{HF}} \tilde{U}}. \tag{45}$$

The selfconsistency equation is now a quadratic equation which shows that n_f^{HF} vanishes as $U^{-1/2}$ for $U \to \infty$, while the peak position of the Lorentzian moves to

infinity like $U^{1/2}$. As we will see later this behaviour of the (restricted) HF solution is very unphysical. We will not discuss here the improvements that can be obtained by allowing for different HF occupations in the different f-channels (unrestricted HF).

For *small* U the (restricted) HF solution is the first step in an expansion of the selfenergy in powers of U (Yamada 1975, Yoshida and Yamada 1975, Schönhammer 1977, Zlatic et al. 1985). For the spin degenerate case $N_f = 2$ this expansion has been studied in great detail by Yoshida and Yamada (1975) using Wick's theorem. The selfenergy contribution to second order in U can also be rather easily obtained using the equations of motion,

$$\tilde{\Sigma}_\nu^{(2)}(z) = U^2 \sum_{\nu'}{}' \int d\varepsilon_1\, d\varepsilon_2\, d\varepsilon_3 \frac{\rho_\nu(\varepsilon_1)\rho_{\nu'}(\varepsilon_2)\rho_{\nu'}(\varepsilon_3)}{z - (\varepsilon_1 + \varepsilon_2 - \varepsilon_3)} \times \{f(\varepsilon_1)f(\varepsilon_2)(1 - f(\varepsilon_3)) + (1 - f(\varepsilon_1))(1 - f(\varepsilon_2))f(\varepsilon_3)\}. \tag{46}$$

The spectral densities $\rho_\nu(\varepsilon) = (-1/\pi)\,\mathrm{Im} g_\nu(\varepsilon + \mathrm{i}0)$ which appear in the integrand are those for $U = 0$. An improvement is usually obtained if the HF spectral densities $\rho_\nu^{\mathrm{HF}}(\varepsilon)$ are used, or if the ρ_ν are determined selfconsistently. Such a procedure can be justified by 'diagramatic' arguments.

The result for $\tilde{\Sigma}_\nu^{(2)}(z)$ shares an important property with the exact $\tilde{\Sigma}_\nu(z)$. *For* $T = 0$ the 'phase space' of the energy integrations is such that $\mathrm{Im}\tilde{\Sigma}_\nu(\varepsilon + \mathrm{i}0)$ *vanishes like* $(\varepsilon - \mu)^2$ *near the Fermi energy*. This can be proven to all orders in perturbation theory (Luttinger 1961). The systematic study of the perturbation expansion to all order in U has been very useful for obtaining relations between different physical quantities (Yosida and Yamada 1975, Yoshimori 1976). The magnitude of the selfenergy contributions of higher order than second have been estimated for the spin-degenerate model $N_f = 2$ in the symmetric case, $2\varepsilon_f + U = 2\mu$ and $V(\varepsilon)$ symmetric in $(\varepsilon - \mu)$. Then the HF f-occupancy n_f^{HF} equals the exact value $n_f = 1$ and because of electron-hole symmetry all odd order contributions in U to the selfenergy vanish. The imaginary part of Σ is in this case an even function in $(\varepsilon - \mu)$ while the real part of Σ is an odd function. For a constant $V(\varepsilon)$ the spectral density then has the form ($\nu = 1, 2$) (s: 'symmetric')

$$\rho_\nu^{(\mathrm{s})}(\varepsilon) = \frac{1}{\pi} \frac{\Delta - \mathrm{Im}\,\tilde{\Sigma}_\nu(\varepsilon + \mathrm{i}0)}{(\varepsilon - \mathrm{Re}\,\tilde{\Sigma}_\nu(\varepsilon))^2 + (\Delta - \mathrm{Im}\,\tilde{\Sigma}_\nu(\varepsilon + \mathrm{i}0))^2}. \tag{47}$$

For $\varepsilon = \mu \equiv 0$, i.e., at the Fermi level the *exact* spectral density $\rho_\nu^{(\mathrm{s})}(\varepsilon)$ coincides with the HF spectral density $\rho_\nu^{\mathrm{HF(s)}}(\varepsilon) = (\Delta/\pi)/(\varepsilon^2 + \Delta^2)$ because of the 'Fermi liquid property' $\mathrm{Im}\tilde{\Sigma}_\nu(\mathrm{i}0) = 0$ and because the particle–hole symmetry leads to $\mathrm{Re}\,\tilde{\Sigma}_\nu(0) = 0$. The HF spectral density consists of a Lorentzian peak of width Δ centered at $\varepsilon = 0$. The effect of the selfenergy is to remove spectral weight from the central region near $\varepsilon = 0$ to a region of larger $|\varepsilon|$. For large enough U, i.e. $U/\Delta \gg 1$, the effect of the hybridization Δ should be small and most of the spectral weight is expected near $\varepsilon = \varepsilon_f = -U/2$ and $\varepsilon = \varepsilon_f + U = U/2$ as in the atomic limit (34). As shown by Yamada (1975) the second-order selfenergy has the amazing property of yielding the atomic peaks in the limit $U \gg \Delta$ which carry almost all spectral weight, while the so-called 'Kondo peak' at $\varepsilon = 0$ becomes very narrow and loses its spectral

weight. To understand this behaviour we evaluate $\tilde{\Sigma}_\nu^{(2)}(z)$ in the limit $z \to \infty$. Then the energy variable in the denominator in (46) can be neglected compared with z and one obtains for $z \to \infty$

$$\tilde{\Sigma}_\nu^{(2)}(z) \to \frac{U^2}{z}(N_f - 1)\frac{n_f}{N_f}\left(1 - \frac{n_f}{N_f}\right). \tag{48}$$

For the 'symmetric case' with $N_f = 2$ and $n_f = 1$ and for $U \gg \Delta$ this leads to Lorentzian peaks of width $\Delta/2$ at energies $\varepsilon_{1,2} = \pm U/2$, i.e. the peak positions in the 'atomic limit' are recovered. But as can be seen from (48) this is an artefact of the 'symmetric case'. For nonsymmetrical parameters or even for symmetrical parameters but $N_f > 2$ this is no longer the case. It is surprising that in the 'symmetric case' even for $U = \pi\Delta$ the fourth-order selfenergy is still a factor hundred smaller than the second-order contribution (Yamada 1975). For the parameters we are interested in, the '$\tilde{\Sigma}_\nu^{(2)}$ approach' is, however, not a good approximation.

3.4. *Expansion around the atomic limit*

The perturbation expansion in U is an expansion around a noninteracting system and all 'usual' many-body techniques can be used. It is less straightforward to obtain systematic expansions around the atomic limit, which seems to be the more appropriate starting point for the systems we want to discuss. The problem is that if operators A_i are introduced which bring $H_0 + U$ into the 'standard form' $H_0 + U = \Sigma_i E_i A_i^+ A_i$ these operators A_i do *not* obey the usual fermion anticommutation relations and therefore Wick's theorem cannot be used in a straightforward way to produce a systematic perturbation expansion in V. The more recent attempts to tackle the problem will be discussed later in this section. Here we want to mention that an expansion to order V^2 can be rather easily obtained using the equation of motion method. For $N_f = 2$ Brenig and Schönhammer (1974) have written the frequency-dependent part of the selfenergy $\tilde{\Sigma}_\nu(z)$ as

$$\tilde{\Sigma}_\nu(z) = \frac{U^2 n(1-n)}{z - \varepsilon_f - U(1-n) - \Gamma(z) - m(z)/n(n-1)}, \tag{49}$$

where $n \equiv \langle n_\nu \rangle = n_f/N_f$. Using the EOM techniques it has been shown, that for small V, $m(z)$ vanishes like V^2. An explicit expression for $m(z)$ has been given to second order in V^2 (Brenig and Schönhammer 1974).

For $\varepsilon_f < 0$ and $\varepsilon_f + U > 0$ the peaks of the atomic limit (31) obtain a shift $\sim V^2$ and a half-width $2\,\mathrm{Im}\Gamma(\varepsilon_f)$ and $2\,\mathrm{Im}\Gamma(\varepsilon_f + U)$. This is *twice* the one-particle half-width $\mathrm{Im}\Gamma$. This factor has a very simple explanation, which for the 'photoemission' peak at $z \approx \varepsilon_f$ is as follows. After the ionization the f-level is empty and for the case $N_f = 2$, which was considered, this state can decay by the hopping of a spin-up *or* spin-down ($\nu = 1$ or $\nu = 2$) electron into the f-level. A straightforward generalization of this result to arbitrary N_f leads to the expectation that the photoemission peak has a half-width $N_f\,\mathrm{Im}\Gamma(\varepsilon_f)$ and the 'f_2'-BIS peak at $z \approx \varepsilon_f + U$ obtains a half-width $2\,\mathrm{Im}(\varepsilon_f + U)$ because there are N_f different channels to fill the empty f-level, and either of the two electrons in the f^2-state can tunnel back into the band states. A

shortcoming of this 'second-order selfenergy in V' approach (Brenig and Schönhammer 1974) is, that no 'Kondo peak' is produced. As mentioned earlier the weight of this peak vanishes with V, and is small but finite for small $V \neq 0$.

There have been various attempts to obtain approximations for the f Green's functions by factorizing higher-order Green's functions. Work along this line, which also mainly concentrated on the spin degenerate ($N_f = 2$) case, will be reviewed later in this section. The case of degeneracy $N_f > 2$ was for a long time considered to be more complicated than the $N_f = 2$ case. It was not realized until recently that the limit of large degeneracy N_f is actually easier amenable to approximations. Developments along this line are the main topic of this review. An overview is given in section 3.5 below.

3.5. *Large N_f methods*

An important progress in the treatment of the Anderson model was the realization by Ramakrishnan (1982) and Anderson (1982) that for the calculation of thermodynamic properties $1/N_f$ can be used as a small parameter. We have shown (Gunnarsson and Schönhammer 1983a,b) that similar ideas can be used for spectroscopies. In our method, which in the following will be called the 'intermediate state' method, spectral functions at $T = 0$ are calculated using a set of many-electron states.

Using the $(N+1)$- and $(N-1)$-electron eigenstates of the system, spectral representations can be obtained for $g_v^>(z)$ and $g_v^<(z)$. For $g_v^<(z)$ this reads

$$g_v^<(z) = \int \frac{\rho_v^<(\varepsilon)}{z - \varepsilon} \mathrm{d}\varepsilon,$$

$$\rho_v^<(\varepsilon) = \sum_m |\langle E_m(N-1)|\psi_v|E_0(N)\rangle|^2 \delta(\varepsilon - [E_0(N) - E_m(N-1)]). \tag{50}$$

The total spectral weight $\int \rho_v^<(\varepsilon)\,\mathrm{d}\varepsilon$ of this photoemission part is given by $\langle n_v\rangle = n_f/N_f$. The corresponding formulas for $g_v^>(z)$ lead to a total spectral weight $1 - \langle n_v\rangle = 1 - n_f/N_f$ for the BIS spectral function $\rho_v^>(\varepsilon)$. In the limit $N_f \to \infty$ the ratio $\int \rho^> \,\mathrm{d}\varepsilon / \int \rho^< \,\mathrm{d}\varepsilon$ goes to infinity and we therefore proceed to calculate $g^>$ and $g^<$ *separately*.

In the first step we calculate the ground state variationally using a set of N-electron basis states $\{|\alpha\rangle\}$

$$|E_0(N)\rangle = \sum_\alpha C_\alpha |\alpha\rangle. \tag{51}$$

The choice of the set $\{|\alpha\rangle\}$ is discussed in section 4.1. An important point is that the contributions of the states $|\alpha\rangle$ can be classified in orders of $1/N_f$, if $V(\varepsilon)$ is assumed to *decrease* with increasing degeneracy like $N_f^{-1/2}$, i.e., $V(\varepsilon) = \tilde{V}(\varepsilon)/\sqrt{N_f}$ with $\tilde{V}(\varepsilon)$ *independent* of N_f. If N_f is not very small, a practicable size basis set can therefore give a good description of the ground-state energy and the local properties of the

ground state. In particular exact ground-state properties can be obtained in the limit $N_f \to \infty$ (Gunnarsson and Schönhammer 1983b, 1985a).

Our general method to calculate spectral functions is presented in this section using $g_\nu^<$ as an example

$$g_\nu^<(z) = \langle E_0(N)|\psi_\nu^+ \frac{1}{z - E_0(N) + H}\psi_\nu|E_0(N)\rangle$$

$$= \sum_{ij} \langle E_0(N)|\psi_\nu^+|i\rangle \left\langle i\left|\frac{1}{z - E_0(N) + H}\right|j\right\rangle \langle j|\psi_\nu|E_0(N)\rangle, \tag{52}$$

where a complete set $\{|i\rangle\}$ of $(N-1)$-electron *basis states* has been introduced. Inversion of the matrix

$$(\tilde{H}(z))_{ij} \equiv \langle i|(z - E_0(N) + H)|j\rangle \tag{53}$$

would lead to the exact result for $g_\nu^<(z)$

$$g_\nu^<(z) = \sum_{i,j} \langle E_0(N)|\psi_\nu^+|i\rangle (\tilde{H}(z)^{-1})_{ij} \langle j|\psi_\nu|E_0(N)\rangle \tag{54}$$

if the procedure could be actually carried out for a complete set of states $|i\rangle$. Our approximation consists in truncating the set $\{|i\rangle\}$, again using a classification of states according to their contribution in orders of $1/N_f$.

If such a truncated basis set $\{|i\rangle\}$ is used in the actual calculations, the resulting spectral function $\tilde{\rho}_\nu(\varepsilon)$ has a 'Lehmann representation' similar to (50) but with exact $(N-1)$-electron eigenstates and eigenvalues replaced by the approximate eigenstates $|\tilde{E}_m(N-1)\rangle$ and eigenvalues $\tilde{E}_m(N-1)$ obtained by diagonalizing H in the truncated space $\{|i\rangle\}$. This representation shows that independently of the quality of the basis set $\tilde{\rho}_\nu(\varepsilon)$ is nonnegative for all energies. This is a property which in, for instance, a Green's function decoupling method does not follow automatically. Since it is possible to relate peaks in the spectrum to the corresponding final states and since the character of these final states can be studied, the physical meaning of the structures in the spectrum can be understood in a simple way.

As discussed in more detail in section 4 the exact result for $g_\nu^<(z)$ to leading order in $1/N_f$ can be calculated *analytically* for the case $U = \infty$. In the 'spin fluctuation limit' $-\varepsilon_f \gg N_f\Delta$ the corresponding spectral function has a Lorentzian peak of half-width $N_f\Delta$ near $z = \varepsilon_f$ and sharp rise near the Fermi energy, which corresponds to the onset of the Kondo peak, which has most of its weight in the BIS spectrum slightly above ε_F. An analogous calculation can be carried out for $g_\nu^>(z)$. This shows in addition to the f^2-peak near $\varepsilon_f + U$ a sharp 'f^1-peak' just above the Fermi level. The position $k_B T_K$ and width $\pi k_B T_K/N_f$ of this 'Kondo' or 'Abrikosov–Suhl' resonance is determined by the 'Kondo temperature' T_K for which an explicit expression is given in section 4.

The extension of the large N_f approach to finite temperatures has been carried out by various authors (Kuramoto 1983, Keiter and Czycholl 1983, Grewe 1983b, Zhang and Lee 1983, 1984, Keiter and Morandi 1984, Coleman 1984, Kojima et al. 1984, Kuramoto and Kojima 1984). Some of the ideas in these papers can be traced

back to earlier work (Keiter and Kimball 1971, Grewe and Keiter 1981, Grewe 1982, 1983a, Abrikosov 1965, Barnes 1976). All these approaches, though using different many-body techniques, lead to the same set of integral equations in the so-called 'noncrossing approximation' (NCA). A corresponding approximation for the ground state had earlier been proposed by Inagaki (1979). Only the case $U = \infty$ is treated by these methods, i.e., double and higher occupancy of the f-level is explicitly excluded.

We present a short derivation of these integral equations using Colemans 'slave boson' (sb) approach. In this approach an auxiliary boson is introduced as a bookkeeping device for the number of f-electrons (Barnes 1976), and the Hamiltonian is written as

$$H_{sb} = H_0 + \varepsilon_B b^+ b + V_{sb}, \tag{55}$$

with H_0 defined in (8), b^+ (b) the boson creation (annihilation) operator and V_{sb} the modified mixing term

$$V_{sb} = \int d\varepsilon [V(\varepsilon)\psi_\nu^+ \psi_{\varepsilon\nu} b + V(\varepsilon)^* b^+ \psi_{\varepsilon\nu}^+ \psi_\nu]. \tag{56}$$

This mixing term converts bosons into f-electrons and vice versa, conserving the 'charge' Q defined as

$$Q \equiv b^+ b + \sum_\nu \psi_\nu^+ \psi_\nu. \tag{57}$$

Therefore H_{sb} commutes with Q, and the subspaces F_Q with definite Q are disjoint. The following identification is now made

$$|\rangle \longleftrightarrow |\rangle|1\rangle_B; \qquad \psi_\nu^+ |\rangle \longleftrightarrow \psi_\nu^+ |\rangle|0\rangle_B, \tag{58}$$

where $|\rangle$ is an arbitrary state of band electrons, and $|n\rangle_B$ denotes the state with n bosons present. The states introduced in (58) are eigenstates of Q with eigenvalue $Q = 1$. The relevant subspace is therefore F_1, and in this subspace H_{sb} is equivalent to the original Hamiltonian H (8) under the mapping (58), if $\varepsilon_B = 0$ is chosen.

In the calculation of the f Green's function as defined in (22) one has to make sure that the intermediate $(N-1)$- and $(N+1)$-electron states are in the $Q = 1$ subspace as well. This can be achieved by creating (annihilating) a boson when the f-electron is removed (added). The 'true' f-propagator in the slave boson approach is therefore given by G_ν^{true} defined as

$$G_\nu^{true}(z) \equiv \langle\langle \psi_\nu b^+ ; b\psi_\nu^+ \rangle\rangle^{Q=1} = g_\nu(z). \tag{59}$$

Apart from the necessity to project onto the 'physical' subspace F_1, the form of the slave boson Hamiltonian H_{sb} has the advantage that usual many-body techniques, like the generalization of Wick's theorem to finite temperatures, can be used to produce a systematic perturbation expansion in the mixing term. Coleman performs such an expansion neglecting the restriction on Q and carries out the projection onto the $Q = 1$ subspace in the end of the calculation. For that purpose he extended Abrikosov's scheme (Abrikosov 1965, Barnes 1976) of weighting the $Q > 1$ states by

exp $[-\lambda(Q-1)]$ and letting the Lagrangian multiplier λ tend to infinity. Technically this is achieved by replacing H_{sb} by $H_{sb}+\lambda Q$ in the diagramatic calculations. To calculate G_ν^{true} Coleman introduces the boson propagator $D_\lambda(z) \equiv \langle\langle b; b^+ \rangle\rangle^{(\lambda)}$ and the 'pseudo'-f-propagator $G_\nu^{ps}(z) \equiv \langle\langle \psi_\nu; \psi_\nu^+ \rangle\rangle^{(\lambda)}$, which enter the skeleton diagrams at the Matsubara frequencies. The selfenergies for these propagators are then classified in powers of $1/N_f$

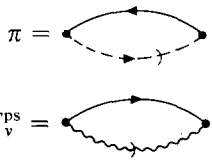

$$\pi = \quad + O(1/N_f^2),$$

$$\Sigma_\nu^{ps} = \quad + O(1/N_f^3), \tag{60}$$

where π denotes the boson selfenergy, Σ_ν^{ps} the pseudo-f-selfenergy, the dots the matrix elements $V(\varepsilon) \sim 1/\sqrt{N_f}$, the full line the band propagators $\langle\langle \psi_{\varepsilon\nu}; \psi_{\varepsilon\nu}^+ \rangle\rangle^{(\lambda)}$, the broken line the pseudo f-propagator $G_{\nu,\lambda}^{ps}$ and the wiggly line the boson propagator D_λ. The arrows $\rightarrow$ and $\twoheadrightarrow$ indicate electron and 'charge Q' flow. The selfenergy diagram shown for π is of order $(1/N_f)^0$ because it involves a summation over the degeneracy variable ν. The diagram shown for $\Sigma_{\nu,\lambda}^{ps}$ is proportional to $1/N_f$. The selfenergy for the band propagators is not shown, as it vanishes in the limit $\lambda \to \infty$. In this limit the diagrams in (60) are equivalent to the coupled integral equations

$$D(z) = \left(z - N_f \int |V(\varepsilon)|^2 \, G_\nu^{ps}(z+\varepsilon) \, f(\varepsilon) \, d\varepsilon \right)^{-1},$$

$$G_\nu^{ps}(z) = \left(z - \varepsilon_f - \int |V(\varepsilon)|^2 \, D(z-\varepsilon)(1-f(\varepsilon)) \, d\varepsilon \right)^{-1}, \tag{61}$$

with $D(z) = \lim_{\lambda\to\infty} D_\lambda(z-\lambda)$ and $G_\nu^{ps}(z) \equiv \lim_{\lambda\to\infty} G_{\nu,\lambda}^{ps}(z-\lambda)$. As already mentioned these functions have no direct physical meaning for the original Anderson model. The true f-propagator as defined in (59) is a 'four-point function'. As shown by Coleman the corresponding vertex corrections vanish like $1/N_f^2$ and the (true) spectral function $\rho_\nu(\varepsilon) = -\mathrm{Im} G_\nu^{true}(\varepsilon + i0)/\pi$ can be expressed as a convolution of the spectral functions of D and G_ν^{ps}.

$$\rho_\nu^{NCA}(\varepsilon) = \frac{Z_B^0}{Z_{MV}} \int A_\nu(\varepsilon+\varepsilon') \, B(\varepsilon) (e^{-\beta(\varepsilon+\varepsilon')} + e^{-\beta\varepsilon'}) \, d\varepsilon', \tag{62}$$

where $A_\nu(\varepsilon) = -\mathrm{Im}\, G_\nu^{ps}(\varepsilon + i0)/\pi$, $B(\varepsilon) = -\mathrm{Im}\, D(\varepsilon + i0)/\pi$ and Z_{MV} and Z_B^0 are the exact and the band (grand) partition functions. The exact partition function Z_{MV} can also be expressed in terms of the spectral functions A_ν and B. The results (61), (62) constitute the so-called *noncrossing approximation* (NCA).

The integral equations (61) have to be solved numerically. In addition to the f-spectral function the temperature dependence of the specific heat and the magnetic susceptibility (Kojima et al. 1984, Bickers et al. 1985, Cox 1985) have been calculated. In the spin-fluctuation limit the f-spectral functions show the Kondo

resonance with a small spectral weight slightly above the Fermi level. At temperatures much smaller than the Kondo temperature spurious nonanalyticities show up in the small frequency range. For $T = 0$ this nonphysical behaviour has been discussed carefully (Müller-Hartmann 1984, Kuramoto and Müller-Hartmann 1985): If an order by order in $1/N_f$ calculation is carried out for $g_\nu^>$ and $g_\nu^<$ separately, instead of the selfconsistent solution of the integral equations, our exact results (Gunnarsson and Schönhammer 1983a,b) are recovered to leading order in $1/N_f$. The mismatch of the total spectral weight in $\rho_\nu^<$ and $\rho_\nu^>$ in the limit $N_f \to \infty$ is probably the reason for the problems in a combined treatment of both. An attempt to overcome these 'low-energy' problems has been carried out with a functional integral method (Read and Newns 1983, Read 1985, Coleman 1985). The starting point for approximations is the mean field solution obtained by replacing b in (56) by a c-number. Coleman has argued that the mean field theory, which corresponds to the saddle point approximation for the functional integral, is *exact* in the limit $N_f \to \infty$, if the limit is taken in such a way that Q also tends to infinity with $q \equiv Q/N_f$ constant. Fluctuations about the mean field solutions have then to be included to remove the spurious phase transition occurring for the boson field at a special finite temperature. It has been claimed that in this approach the low-temperature, low-frequency anomalies can be avoided (Coleman 1985). We present a comparison of results in the NCA with results of our approach in section 4.2.

To end up the discussion of the attempts to calculate spectral functions for the Anderson impurity model we shortly mention decoupling schemes for higher-order Green's functions (Hewson 1966, Theumann 1969, Lacroix 1981, Oh and Doniach 1982, Czycholl 1985). The approximations in this method consist of replacements of the type $\langle\langle \psi_\nu \psi^+_{\varepsilon\nu'} \psi_{\varepsilon'\nu'}; \psi^+_\nu \rangle\rangle \to \langle \psi^+_{\varepsilon\nu'} \psi_{\varepsilon'\nu'} \rangle \langle\langle \psi_\nu; \psi^+_\nu \rangle\rangle$. Apart from the fact that the quality of the results for g_ν is generally hard to judge, the spectral functions obtained this way can have frequency regions with *negative* spectral weight (Oh and Doniach 1982). Special attention to the large N_f limit has been given by Czycholl (1985). To leading order in $1/N_f$ he obtains at $T = 0$ a sharp Kondo peak at the correct Kondo temperature. The exact leading order result for the photoemission part $\lim_{N_f \to \infty} N_f \rho_\nu^<(\varepsilon)$ discussed in section 4 has not yet been obtained by this technique.

4. Spectroscopies

In this section we discuss various spectroscopies, treating a specific spectroscopy in each subsection. We first present the formalism for calculating spectra, and then some typical features and results are given. The discussion of results for specific systems is postponed to section 5. We focus on the 'intermediate state' method presented in section 3.4. Since the calculation of the ground state plays an important role in this method, we present the ground-state calculation in section 4.1. Generally we first give calculations for $U = \infty$ and to lowest order in $1/N_f$. These calculations are very simple and the reader can easily reproduce them to see the general structure of the results. We then discuss the effects of taking into account that U is finite, or of

working to higher order in $1/N_f$. Such calculations usually require computer calculations and we therefore only show some typical results.

4.1. *Ground-state calculation*

The ground-state calculation is performed variationally, which requires the introduction of a many-electron basis set. It turns out that the size of this basis set can be kept 'manageable' by a classification of states in orders of $1/N_f$. For that purpose we let N_f become large. This is a mathematical trick, which means that the parameter N_f in the Hamiltonian (8) becomes large. Thus $N_f = 18$, for instance, is not supposed to simulate g-states, which apart from having a different degeneracy also differ greatly from f-states in many other respects. Instead we want to choose the limit $N_f \to \infty$ so that this limit is similar to, e.g., the case $N_f = 14$ and gives a good but simple starting point for the treatment of the $N_f = 14$ case. In the calculation presented below $V(\varepsilon)$ enters in the combinations $N_f V(\varepsilon)^2$ and $V(\varepsilon)^2$. We therefore define

$$\tilde{V}(\varepsilon) = \sqrt{N_f}\, V(\varepsilon), \tag{63}$$

and require that $\tilde{V}(\varepsilon)$ is independent of N_f (Gunnarsson and Schönhammer 1983a,b). This condition allows us to study the limit $N_f \to \infty$ and to classify the basis states in orders of $1/N_f$. To lowest order in $(1/N_f)$ the $T = 0$ ground-state properties are then independent of N_f (or have a trivial dependence on N_f as, for instance, the susceptibility). The $N_f = 14$ case differs from the $N_f = \infty$ limit through higher-order corrections in $1/N_f$.

To obtain the singlet ground state, we introduce the singlet state

$$|0\rangle = \left(\prod_{\nu=1}^{N_f} \prod_{\varepsilon \leqslant \varepsilon_F} \psi^+_{\varepsilon\nu} \right) \psi^+_c |\text{vacuum}\rangle, \tag{64}$$

where the f-level is empty and the conduction states below the Fermi energy are filled. The core level $|c\rangle$ is also filled. This state is indicated by 0 in fig. 2. It couples via H to the states a in the figure

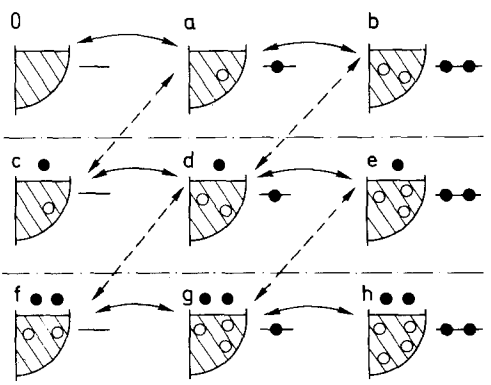

Fig. 2. Schematic representation of the basis states. Solid circles show electrons and open circles show holes. The hatched part indicates the filled conduction band and the horizontal line the f-level. The arrows show which states couple to each other. A solid line indicates the strength $\tilde{V}$ and a dashed line the strength $\tilde{V}/\sqrt{N_f}$.

$$|\varepsilon\rangle = \frac{1}{\sqrt{N_f}} \sum_{\nu} \psi_{\nu}^{+} \psi_{\varepsilon\nu} |0\rangle, \tag{65}$$

in which a conduction electron has hopped into the f-level. These states couple to states with two f-electrons (states b in fig. 2)

$$|\varepsilon\varepsilon'\rangle = \frac{1}{\sqrt{N_f(N_f-1)}} \sum_{\nu \neq \nu'} \psi_{\nu}^{+} \psi_{\varepsilon\nu} \psi_{\nu'}^{+} \psi_{\varepsilon'\nu'} |0\rangle \tag{66}$$

and to states with a conduction electron–conduction hole pair (states c in fig. 2)

$$|E\varepsilon\rangle = \frac{1}{\sqrt{N_f}} \sum_{\nu} \psi_{E\nu}^{+} \psi_{\varepsilon\nu} |0\rangle, \tag{67}$$

where E refers to a state above the Fermi energy ($E > \varepsilon_F$). We assume that states with three or more f-electrons have such a high energy that they can be neglected. The states $|E\varepsilon\rangle$ couple to states with an f-electron, a conduction electron and two holes (states d in fig. 2). We distinguish between states where the holes have the same or different quantum numbers ν and ν':

$$|E\varepsilon\varepsilon', 1\rangle = \frac{1}{\sqrt{N_f(N_f-1)}} \sum_{\nu \neq \nu'} \psi_{E\nu}^{+} \psi_{\varepsilon\nu} \psi_{\nu'}^{+} \psi_{\varepsilon'\nu'} |0\rangle, \tag{68}$$

$$|E\varepsilon\varepsilon', 2\rangle = \frac{1}{\sqrt{N_f}} \sum_{\nu} \psi_{E\nu}^{+} \psi_{\varepsilon\nu} \psi_{\nu}^{+} \psi_{\varepsilon'\nu} |0\rangle. \tag{69}$$

In this way an infinite sequence of basis states can be generated. Some further states are indicated in fig. 2. To avoid linear dependencies, we require $\varepsilon > \varepsilon'$ for the states (66) and (69). The states $|0\rangle$ and $|\varepsilon\rangle$ were used by Varma and Yafet (1976) in a calculation for $N_f = 2$, before the $1/N_f$ ideas had been introduced.

To perform the ground-state calculation, the matrix elements of H are needed. We obtain

$$\langle \varepsilon | H | 0 \rangle = \tilde{V}(\varepsilon), \tag{70}$$

$$\langle \varepsilon\varepsilon' | H | \varepsilon'' \rangle = \sqrt{1 - 1/N_f}\, [\tilde{V}(\varepsilon')\delta(\varepsilon - \varepsilon'') + \tilde{V}(\varepsilon)\delta(\varepsilon' - \varepsilon'')], \tag{71}$$

$$\langle E\varepsilon | H | \varepsilon' \rangle = \tilde{V}(E)/\sqrt{N_f}\,\delta(\varepsilon - \varepsilon'), \tag{72}$$

$$\langle E\varepsilon\varepsilon', 1 | H | E'\varepsilon'' \rangle = \sqrt{1 - 1/N_f}\,\tilde{V}(\varepsilon')\delta(E - E')\delta(\varepsilon - \varepsilon''), \tag{73}$$

$$\langle E\varepsilon\varepsilon'; 2 | H | E'\varepsilon'' \rangle = [\tilde{V}(\varepsilon')\delta(\varepsilon - \varepsilon'') - \tilde{V}(\varepsilon)\delta(\varepsilon' - \varepsilon'')]\delta(E - E')/\sqrt{N_f}. \tag{74}$$

These calculations illustrate the general result that within each row in fig. 2 there are states which couple with the strength $\tilde{V}(\varepsilon)$, while states in different rows at most couple with a strength $\tilde{V}(\varepsilon)/\sqrt{N_f}$. This allows us to classify the states in orders of $1/N_f$ according to their contribution to the total energy. Thus the states in the first, second and third row are of the orders $(1/N_f)^0$, $(1/N_f)^1$ and $(1/N_f)^2$, respectively.

As an illustration we now calculate the ground state for $U = \infty$ and to lowest

order in $1/N_f$. The ground state is written as (Varma and Yafet 1976)

$$|E_0(N)\rangle = A\left[|0\rangle + \int_{-B}^{0} d\varepsilon\, a(\varepsilon)|\varepsilon\rangle\right]. \tag{75}$$

We define ΔE and δ as

$$\Delta E \equiv \varepsilon_f - \delta \equiv E_0(N) - \langle 0|H|0\rangle. \tag{76}$$

From the Schrödinger equation

$$H|E_0(N)\rangle = E_0(N)|E_0(N)\rangle \tag{77}$$

we obtain

$$\Delta E = \int \tilde{V}(\varepsilon)\, a(\varepsilon)\, d\varepsilon, \tag{78}$$

$$(\Delta E - \varepsilon_f + \varepsilon)\, a(\varepsilon) = \tilde{V}(\varepsilon), \tag{79}$$

by applying $\langle 0|$ and $\langle \varepsilon|$, respectively, from the left. This gives an implicit equation for ΔE

$$\Delta E = \int_{-B}^{0} \frac{\tilde{V}(\varepsilon)^2}{\Delta E - \varepsilon_f + \varepsilon}\, d\varepsilon. \tag{80}$$

The f-occupancy n_f is given by

$$n_f = A^2 \int_{-B}^{0} a(\varepsilon)^2\, d\varepsilon = C/(1 + C), \tag{81}$$

where

$$C = \int_{-B}^{0} \frac{\tilde{V}(\varepsilon)^2}{(\Delta E - \varepsilon_f + \varepsilon)^2}\, d\varepsilon, \tag{82}$$

and

$$A^2 = 1 - n_f = 1/(1 + C). \tag{83}$$

If $\tilde{V}(\varepsilon)^2 \equiv \tilde{V}^2 = \tilde{\Delta}/\pi$ is a constant and $\delta \ll B$ one finds

$$\Delta E \approx \frac{\tilde{\Delta}}{\pi} \ln(\delta/B), \tag{84}$$

$$C = \frac{n_f}{1 - n_f} \approx \frac{\tilde{\Delta}}{\pi\delta}. \tag{85}$$

For $\delta \ll \tilde{\Delta}/\pi$ this leads to

$$\delta = B\exp(\pi\Delta E/\tilde{\Delta}) \approx B\exp(\pi\varepsilon_f/\tilde{\Delta}). \tag{86}$$

The coefficient

$$a(\varepsilon)^2 = (\tilde{\Delta}/\pi)/(\delta - \varepsilon)^2 \tag{87}$$

grows on the energy scale δ as the Fermi energy is approached from below. The energy δ depends exponentially on $\pi\varepsilon_f/\tilde{\Delta}$, which suggests that we can interpret δ as a Kondo temperature. This interpretation is supported by the observation that to this order in $1/N_f$ the static, $T = 0$ susceptibility is given by (Gunnarsson and Schönhammer 1983b)

$$\chi = \tfrac{1}{12}(N_f^2 - 1)n_f/\delta. \tag{88}$$

The energy δ is later shown to play an important role for the f-electron spectrum.

The ground-state calculation can easily be extended to include the states $|E\varepsilon\rangle$ and $|E\varepsilon\varepsilon', 1\rangle$ of order $(1/N_f)^1$. The energy ΔE can even in this case be obtained from an implicit equation. The inclusion of the states $|E\varepsilon\varepsilon', 2\rangle$ requires the solution of an integral equation. The matrix element (74) is, however, of the order $1/\sqrt{N_f}$ and this state therefore gives a contribution of the order $(1/N_f)^2$ although it belongs to the second row. To accuracy $(1/N_f)^1$ the complications arising from the states $|E\varepsilon\varepsilon', 2\rangle$ can therefore be avoided. For $U < \infty$ we must include the states $|\varepsilon\varepsilon'\rangle$, which also leads to an integral equation, for $U \gg B'$ the equation becomes separable and it can be solved analytically (Gunnarsson and Schönhammer 1985a).

The accuracy of the $1/N_f$ treatment is an important issue. The $N_f = 1$ model provides an interesting test case. Since double occupancy of the f-level is then automatically suppressed, the $N_f = 1$ case is a one-particle problem, which can easily be solved by direct methods. Since the parameter $1/N_f = 1$, the $N_f = 1$ model is a stringent test. The results for $\Delta E - \varepsilon_f$ and n_f are shown in tables 1 and 2, respectively. These results are obtained for a semi-elliptical form of $V(\varepsilon)^2$

$$V(\varepsilon)^2 = 2V^2(B^2 - \varepsilon^2)^{1/2}/(\pi B^2). \tag{89}$$

For this energy-dependent $V(\varepsilon)$ we define

$$\tilde{\Delta} = N_f\pi V^2(\varepsilon_F). \tag{90}$$

The tables show that for $N_f = 1$ a calculation to order $(1/N_f)^0$ can be quite

TABLE 1

The energy $\Delta E - \varepsilon_f$ for different values of the f-level energy ε_f in a nondegenerate ($N_f = 1$) Anderson model. The calculations are performed to different orders in $1/N_f$ for the parameters $V = 1.5$ and $B = 6$ ($\tilde{\Delta} = 0.75$). The state $|E\varepsilon\varepsilon', 2\rangle$ has here been included in the $(1/N_f)^1$ calculation. All energies are in eV.

Basis set	$\Delta E - \varepsilon_f$				
	$\varepsilon_f = 2$	$\varepsilon_f = 0$	$\varepsilon_f = -1$	$\varepsilon_f = -2$	$\varepsilon_f = -4$
$(1/N_f)^0$	−0.263	−0.534	−0.054	−0.001	−0.000
$(1/N_f)^1$	−0.293	−0.714	−0.408	−0.291	−0.188
$(1/N_f)^2$	−0.294	−0.726	−0.416	−0.294	−0.189
Exact	−0.294	−0.726	−0.416	−0.294	−0.189

TABLE 2

The f-occupancy n_f for different values of ε_f in the nondegenerate Anderson model ($N_f = 1$). The parameters are $V = 1.5$ and $B = 6$ ($\tilde{\Delta} = 0.75$). All energies are in eV.

Basis set	n_f				
	$\varepsilon_f = 2$	$\varepsilon_f = 0$	$\varepsilon_f = -1$	$\varepsilon_f = -2$	$\varepsilon_f = -4$
$(1/N_f)^0$	0.065	0.283	0.813	0.996	1.000
$(1/N_f)^1$	0.083	0.487	0.833	0.919	0.967
$(1/N_f)^2$	0.084	0.497	0.822	0.916	0.967
Exact	0.084	0.500	0.822	0.916	0.967

inaccurate. This is in particular the case for $-\varepsilon_f \gg \tilde{\Delta}$, for which the $(1/N_f)^0$ results differ qualitatively from the exact results. The results of order $(1/N_f)^1$ are, however, accurate to within 3% and the results of order $(1/N_f)^2$ have errors which are smaller than 1%.

Table 3 shows results for $N_f = 14$ and for a finite U. If the system is close to the spin fluctuation limit (the f^0 weight is small), the $(1/N_f)^0$ calculation is not very accurate. The comparison of the $(1/N_f)^1$ and $(1/N_f)^2$ calculations, however, suggests that the $(1/N_f)^1$ calculation is quite accurate also in the spin fluctuation limit. The table illustrates that there is a strong asymmetry between the f^0 and f^2 weights in this limit, although the parameters are 'symmetric' ($2\varepsilon_f + U = 0$). The f^2 weight is a factor 5 larger than the f^0 weight for $\tilde{\Delta} = 0.75$. The reason for this has been discussed elsewhere (Gunnarsson and Schönhammer 1985a,b).

The description of ground-state properties in the $1/N_f$ expansion has also been extensively tested by Rasul and Hewson (1983, 1984a,b). They used a diagrammatic technique for obtaining a $1/N_f$ expansion (Rasul and Hewson 1984a), extending a formalism developed earlier for the $N_f = 2$ case (Keiter and Kimball 1971). A relation between the conduction band width in the Anderson model and the cut-off in the Bethe ansatz was deduced (Rasul and Hewson 1984a,b). This allowed them to compare the results of the $1/N_f$ expansion with the exact Bethe ansatz results. Some typical results are shown in fig. 3, where the relation between the static, $T = 0$ susceptibility χ and the f-occupancy is shown for $N_f = 6$ and $N_f = 8$. The figure illustrates that there is an excellent agreement between the expansion to order $(1/N_f)^1$ and the exact Bethe ansatz. Rasul and Hewson concluded that a calculation to order $(1/N_f)^1$ for χ and n_f is correct to within a few percent even for N_f as small

TABLE 3

The energy $\Delta E - \varepsilon_f$ and the f^0, f^1 and f^2 weights for different values of $\tilde{\Delta}$. The parameters are $\varepsilon_f = -2.5$, $U = 5$, $B = 6$ and $N_f = 14$. The states h in fig. 2 were not included.

Basis set	$\tilde{\Delta} = 0.75$				$\tilde{\Delta} = 3.0$			
	$\Delta E - \varepsilon_f$	f^0	f^1	f^2	$\Delta E - \varepsilon_f$	f^0	f^1	f^2
$(1/N_f)^0$	−0.221	0.005	0.945	0.050	−1.094	0.128	0.738	0.134
$(1/N_f)^1$	−0.247	0.010	0.938	0.052	−1.202	0.128	0.730	0.142
$(1/N_f)^2$	−0.249	0.011	0.937	0.052	−1.211	0.128	0.730	0.143

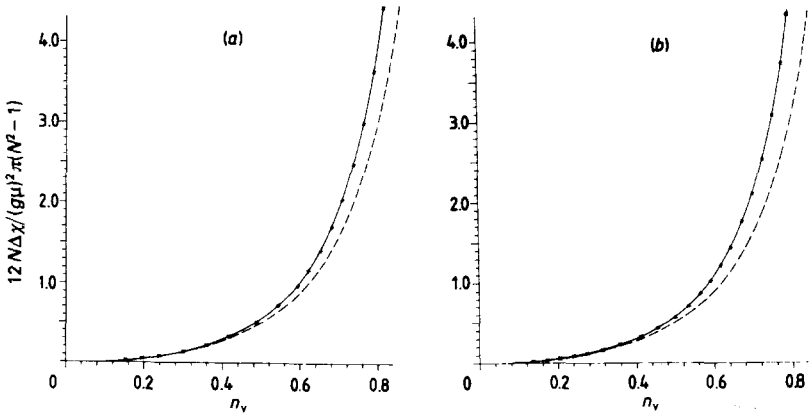

Fig. 3. The susceptibility χ as a function of the f-occupancy $n_v(=n_f)$ for $N=(N_f)=8$ (a) and 6(b). The full curve gives the exact results from the Bethe ansatz, the broken curve gives results of order $(1/N_f)^0$ and the crosses results of order $1/N_f$. The results are reproduced from Rasul and Hewson (1984b).

as 2. They further found that the $(1/N_f)^1$ result for the relation between χ and n_f is asymptotically correct as $\varepsilon_f \to \infty$ and $\varepsilon_f \to -\infty$.

It may seem surprising that the calculations to order $(1/N_f)^1$ or $(1/N_f)^2$ can give a good description even for $N_f = 1$ or $N_f = 2$. From fig. 2 it is clear that our calculations to these orders include the creation of one or two conduction electron–hole pairs relative to the unperturbed Fermi sea. It is, however, known that the introduction of a localized perturbation, such as the interaction with the 4f-level in the Anderson model, leads to the creation of an infinite number of electron–hole pairs, the so-called orthogonality catastrophe (Anderson 1967). It has however been known for some time that a fair description of the effects of the orthogonality catastrophe can be obtained by including one or two electron–hole pair excitations (Kotani and Toyozawa 1974a,b, Dow and Flynn 1980, Gunnarsson and Schönhammer 1982). This can be illustrated by studying a finite chain with N atoms (Gunnarsson and Schönhammer 1985a). As N is increased the local properties of the system are practically converged to their $N = \infty$ value before the states with two or more electron–hole pairs become important.

4.2. *Valence photoemission spectroscopy (PES)*

Since a Ce compound has n_f (~ 1) f-electrons and $N_f - n_f$ ($\sim N_f - 1$) f-holes, the weight of the f-level PES spectrum is of the order $1/N_f$ smaller than the weight of the BIS spectrum. In a $1/N_f$ type of treatment it is therefore convenient to treat the part of the f-spectrum below ε_F (PES) separately from the part above ε_F (BIS). This is naturally done in the 'intermediate-state' method.

For the f-level PES we use (18) and calculate

$$g_v^<(z) = \langle E_0(N)|\psi_v^+ \frac{1}{z - E_0(N) + H}\psi_v|E_0(N)\rangle. \tag{91}$$

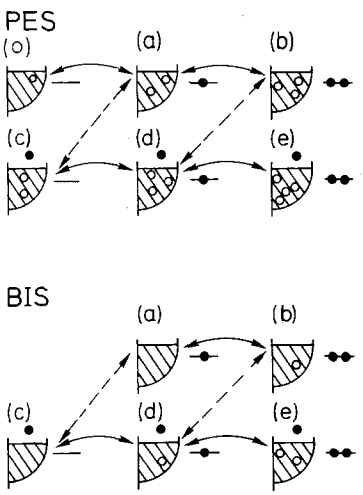

Fig. 4. Schematic representation of basis states used for valence PES and BIS. The notations are the same as in fig. 2.

The f-contribution to the PES is then given by

$$\rho_f^<(\varepsilon) = \sum_\nu \frac{1}{\pi} \mathrm{Im} g_\nu^<(\varepsilon - \mathrm{i}0) \equiv \frac{1}{\pi} \mathrm{Im} g_f^<(\varepsilon - \mathrm{i}0). \tag{92}$$

We first consider the $U = \infty$ case and work to lowest order in $1/N_f$. In this limit the ground state is expressed in the states $|0\rangle$ and $|\varepsilon\rangle$. Since $\psi_\nu|0\rangle = 0$, and

$$\psi_\nu|\varepsilon\rangle = \frac{1}{\sqrt{N_f}} \psi_{\varepsilon\nu}|0\rangle, \tag{93}$$

we introduce the basis states (0 in fig. 4)

$$|\varepsilon\nu\rangle = \psi_{\varepsilon\nu}|0\rangle. \tag{94}$$

These are the only states that overlap with $\psi_\nu|E_0(N)\rangle$ if the approximate ground state (75) is used. However, the states (a in fig. 4)

$$|\varepsilon\varepsilon'\nu; 1\rangle = \frac{1}{\sqrt{N_f - 1}} \sum_{\nu'(\neq\nu)} \psi_{\nu'}^+ \psi_{\varepsilon'\nu} \psi_{\varepsilon\nu}|0\rangle \tag{95}$$

couple to the states $|\varepsilon\nu\rangle$ with a strength $\sim\tilde{V}(\varepsilon)$ and they must therefore be included. The states (also a in fig. 4)

$$|\varepsilon\varepsilon'\nu; 2\rangle = \psi_\nu^+ \psi_{\varepsilon'\nu} \psi_{\varepsilon\nu}|0\rangle, \tag{96}$$

where the two holes have the same quantum number ν, have a coupling $\sim\tilde{V}(\varepsilon)/\sqrt{N_f}$ to $|\varepsilon\rangle$, and they are not needed to order $(1/N_f)^0$. The matrix elements are given by

$$\langle\varepsilon\varepsilon'\nu; 1|H|\varepsilon''\nu\rangle = \sqrt{1 - 1/N_f}\, \tilde{V}(\varepsilon')\delta(\varepsilon - \varepsilon''), \tag{97}$$

$$\langle\varepsilon\varepsilon'\nu, 2|H|\varepsilon''\nu\rangle = \sqrt{1/N_f}\, [\tilde{V}(\varepsilon')\,\delta(\varepsilon - \varepsilon'') - \tilde{V}(\varepsilon)\,\delta(\varepsilon' - \varepsilon'')]. \tag{98}$$

From (93) and (94) it follows that we need $\tilde{H}(z)^{-1}_{\varepsilon\nu,\varepsilon'\nu}$ where the matrix $\tilde{H}(z)$ defined in (53) has indices referring to the states (94) and (95). The matrix elements of $\tilde{H}$ in the

basis (94) and (95) are given by

$$\tilde{H}(\varepsilon, \varepsilon') = (z - \Delta E - \varepsilon)\,\delta(\varepsilon - \varepsilon'), \tag{99}$$

$$\tilde{H}(\varepsilon\varepsilon', \varepsilon_1\varepsilon_2) = (z - \Delta E + \varepsilon_f - \varepsilon - \varepsilon')\,\delta(\varepsilon - \varepsilon_1)\,\delta(\varepsilon' - \varepsilon_2), \tag{100}$$

$$\tilde{H}(\varepsilon\varepsilon', \varepsilon_2) \approx \tilde{V}(\varepsilon^1)\,\delta(\varepsilon - \varepsilon_2), \tag{101}$$

where we have dropped a factor $\sqrt{1 - 1/N_f}$ in eq. (101), since we are working to order $(1/N_f)^0$. For the inversion of $\tilde{H}$ it is convenient to use a block matrix form, with the elements $\tilde{H}_{11}$, $\tilde{H}_{12}$, $\tilde{H}_{21}$ and $\tilde{H}_{22}$, where, e.g., $\tilde{H}_{11}$ refers to $\tilde{H}(\varepsilon, \varepsilon')$ and $\hat{H}_{22}$ to $\tilde{H}(\varepsilon\varepsilon', \varepsilon_1\varepsilon_2)$. The matrix formula

$$(\tilde{H}^{-1})_{11} = (\tilde{H}_{11} - \tilde{H}_{12}\tilde{H}_{22}^{-1}\tilde{H}_{21})^{-1} \tag{102}$$

greatly simplifies the problem, since $\tilde{H}_{22}$ is diagonal and its inversion is trivial. Equation (102) leads to

$$(H(z))^{-1}_{\varepsilon,\varepsilon'} = \tilde{g}(z - \Delta E + \varepsilon_f - \varepsilon)\delta(\varepsilon - \varepsilon'), \tag{103}$$

where

$$\tilde{g}_v(z) = \frac{1}{z - \varepsilon_f - \tilde{\Gamma}(z)}, \tag{104}$$

with

$$\tilde{\Gamma}(z) = \int_{-B}^{0} \frac{\tilde{V}(\varepsilon)^2}{z - \varepsilon}\,\mathrm{d}\varepsilon. \tag{105}$$

Observe that the integration in (105) only extends to $\varepsilon_F = 0$. The remaining matrix elements of $\tilde{H}^{-1}$ are not needed, since they do not couple to $\psi_v|E_0(N)\rangle$. Combining (75), (91)–(94) and (103) we obtain (Gunnarsson and Schönhammer 1983b)

$$g_f^<(z) = A^2 \int_{-B}^{0} \mathrm{d}\varepsilon\, a(\varepsilon)^2\, \tilde{g}(z - \Delta E + \varepsilon_f - \varepsilon). \tag{106}$$

This expression is well-behaved for all energies and it does not have the 'infrared problems' appearing in the NCA (Müller-Hartmann 1984). An alternative way of deriving and analyzing the result (104)–(106) has been given by Allen (1985), who used a Fano-type language. The result (106) can easily be generalized to include spin-orbit splitting (Gunnarsson and Schönhammer 1983b).

We first analyze the structure of this lowest-order result. The function $\mathrm{Im}\,\tilde{g}(\varepsilon - \mathrm{i}0)$ has a continuum part for $-B \leqslant \varepsilon \leqslant 0$ due to the imaginary part of $\tilde{\Gamma}(\varepsilon - \mathrm{i}0)$. In addition $\tilde{g}(z)$ has a pole at $\varepsilon = \delta = \varepsilon_f - \Delta E$, since

$$\tilde{\Gamma}(\delta) = -\Delta E \tag{107}$$

as can be seen from eq. (80). The strength of this pole is

$$1\Big/\left(1 - \frac{\mathrm{d}\tilde{\Gamma}(z)}{\mathrm{d}z}\bigg|_{z=\delta}\right) = 1 - n_f, \tag{108}$$

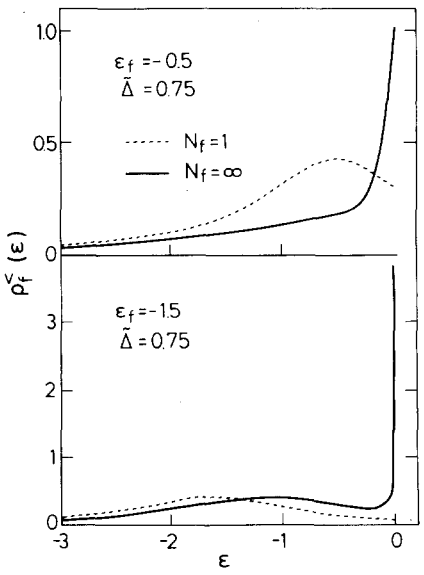

Fig. 5. The f-level PES spectrum for $N_f = \infty$ (full curve) and $N_f = 1$ (dashed curve). We have used a constant density of states with $\tilde{\Delta} = 0.75\,\text{eV}$ and the bottom of the band is at $-6\,\text{eV}$.

where we have used (82) and (83). Inserting this result in eq. (106) gives

$$\rho_f^<(\varepsilon) = \frac{1}{\pi}\text{Im}g^<(\varepsilon - \text{i}0) = A^2 a(\varepsilon)^2(1 - n_f) = \frac{(1 - n_f)^2\tilde{V}(\varepsilon)^2}{(\delta - \varepsilon)^2},$$

$$-\delta \leqslant \varepsilon \leqslant 0, \tag{109}$$

where we have used (83) and (87). For $\varepsilon \leqslant -\delta$ the continuum of $\text{Im}\tilde{g}(\varepsilon - \text{i}0)$ also contributes to $\text{Im}g^<$. In addition there can be a split-off state below the conduction band ($\varepsilon < -B$).

Equation (109) describes a sharp rise in the spectrum, determined by δ, as ε approaches $\varepsilon_F = 0$ from below. In fig. 5 this is illustrated by the $N_f = \infty$ curves, In section 4.3 we demonstrate that this rise is the tail of a peak at $\varepsilon \sim \delta$ on the BIS ($\varepsilon > 0$) side of the spectrum. This peak is the 'Kondo' peak discussed in section 3. To understand the origin of this feature we study the character of the corresponding final states. If we only consider the basis states (94) and (95) (order $(1/N_f)^0$ for $\rho_f^<(\varepsilon)$) the first energy variable ε in these states can be considered as a dummy index, since different values of ε are not mixed by the matrix elements (97). Thus we can perform a variational calculation for each value of ε and obtain a state

$$|\tilde{\varepsilon}\nu\rangle = \psi_{\varepsilon\nu}|E_0(N)\rangle, \tag{110}$$

which is identical to the ground-state except for a hole at ε (Gunnarsson and Schönhammer 1983b). This procedure provides all the lowest final states up to an energy δ above the lowest state. Since

$$|\langle\tilde{\varepsilon}\nu|\psi_\nu|E_0(N)\rangle|^2 = (1 - n_f)^2 a(\varepsilon)^2/N_f, \tag{111}$$

the states $|\tilde{\varepsilon}v\rangle$ contribute the weight $A^2a(\varepsilon)^2(1-n_f)$ in agreement with eq. (109). The factor $A^2a(\varepsilon)^2$ comes from the weight of $|\varepsilon\rangle$ in the initial state, i.e., from the distribution of holes in the initial state. This distribution is the reason for the steep rise in the spectrum close to ε_F.

Thus we arrive at the interpretation that the structure at $\varepsilon_F = 0$ corresponds to final states where the f-hole created in the photoemission process has been partly filled by a conduction electron close to ε_F, so that the final state has exactly as many f-electrons as the initial state. The shape of the spectrum close to $\varepsilon_F = 0$ and the large weight at ε_F result from many-body effects. This can be seen in fig. 5, which compares results for $N_f = \infty$ and $N_f = 1$. For $N_f = 1$ the model reduces to a one-particle problem and the spectrum shows no sign of a peak at ε_F if the f-level is well below ε_F. Integration of the 'pole contribution' (109) from $-B$ to 0 gives the weight $n_f(1-n_f)$. In the $U = \infty$ limit discussed here, this weight becomes very small for $n_f \approx 1$. It is interesting to compare the result (109) with the quasiparticle density of states $\Delta\rho(\varepsilon)$ in the local Fermi liquid description of de Châtel (1982)

$$\Delta\rho(\varepsilon) = (1-n_f)\left[\frac{\tilde{V}(\varepsilon)^2}{(\varepsilon-\delta)^2} - \frac{1}{\varepsilon-\delta}\frac{\partial\tilde{V}(\varepsilon)}{\partial\varepsilon}\right]. \tag{112}$$

For $\tilde{V}(\varepsilon) \equiv \tilde{V}^2$ constant, this density of states agrees with spectrum (109) apart from an additional (renormalization) factor $(1-n_f)$ in $\rho_f^<(\varepsilon)$.

We next consider the continuum contribution from $\mathrm{Im}\tilde{g}(\varepsilon - \mathrm{i}0)$. For simplicity we discuss $\tilde{V}(\varepsilon)^2 \equiv \tilde{V}^2 = \tilde{\Delta}/\pi$ constant and we consider the limit $\tilde{\Delta} \ll -\varepsilon_f \ll B$. Then

$$\varepsilon_f + \tilde{\Gamma}(\varepsilon_f - \mathrm{i}0) \approx \varepsilon_f + \mathrm{i}\tilde{\Delta}. \tag{113}$$

The function $\mathrm{Im}g(\varepsilon - \mathrm{i}0)$ then has a peak at ε_f with the half-width $\tilde{\Delta}$. Since $a(\varepsilon)^2$ has its maximum at $\varepsilon = 0$ and decays rapidly as ε is reduced, $\mathrm{Im}g^<(\varepsilon - \mathrm{i}0)$ also has a peak at roughly ε_f with the half-width $\tilde{\Delta}$. We may consider this as an 'ionization' peak corresponding to the removal of an f-electron. A (very narrow) peak would result at ε_f even if we only included the basis states $|\varepsilon v\rangle$ (94) with no f-electron. The inclusion of the states (95) gives this peak a broadening with the half-width $\tilde{\Delta}$. This result follows, since a conduction electron with energy $\varepsilon \sim \varepsilon_f$ can hop into the f-level. The probability that this happens in a given channel v is related to $\Delta = \pi V^2$. Since there are N_f such channels, we obtain the result $\tilde{\Delta} = N_f\Delta$ (Brenig and Schönhammer 1974). If we relax the condition $\tilde{\Delta} \ll -\varepsilon_f \ll B$, the peak at ε_f is shifted and distorted. In particular, it tends to merge with the structure at $\varepsilon_F = 0$ if $\tilde{\Delta} \gtrsim -\varepsilon_f$. This is illustrated in fig. 5a. The figure also illustrates the large difference between the $N_f = 1$ and $N_f = \infty$ cases.

It has sometimes been suggested that PES is in principle incapable of giving information about the low-lying excitations of a Kondo system, since "the high photon energy destroys the Kondo system. The comparison of eq. (109) and (112) shows that this is not correct. Actually, the large photon energy is a requirement for obtaining the result (109), since this result is based on the sudden approximation (see section 3.1). For a small photon energy we would have to study a three-particle Green's function, and the relation to the density of low-lying states is much less clear. In practice the study of the low-lying excitations by PES is greatly com-

plicated by two factors. Firstly the resolution which can presently be obtained is for many systems larger than the width of the Kondo resonance. Secondly, the additional prefactor $(1 - n_f)$ in (109) reduces the weight of this resonance. For systems with a large Kondo temperature δ, the Kondo resonance can, however, be clearly seen in PES (Allen et al. 1983, Patthey et al. 1985).

The most outstanding feature in fig. 5 is the large spectral density at $\varepsilon_F = 0$. To test the accuracy of the lowest-order theory, we compare with an exact Fermi-liquid relation (Langreth 1966, Haldane 1981, Martin 1982, Yoshimori and Zawadowski 1982) which relates $\rho_f^<(\varepsilon_F)$ to the f-occupancy

$$\rho_f^<(\varepsilon_F) = \frac{N_f^2}{\pi \tilde{\Delta}} \sin^2\left(\frac{\pi n_f}{N_f}\right), \tag{114}$$

where we have assumed that $\tilde{V}(\varepsilon)^2 \equiv \tilde{V}^2 = \tilde{\Delta}/\pi$ and that B is very large. In this limit the result (109) takes the form

$$\rho_f^<(\varepsilon_F) = \frac{\pi}{\tilde{\Delta}} n_f^2, \tag{115}$$

where we have used (85). In the limit $N_f \to \infty$ this expression agrees with the exact result (114). In fig. 6 the $(1/N_f)^0$ result (115) is compared with the exact result for finite N_f. For $N_f \geqslant 6$ the lowest-order result is correct to within 10%. Since the 'Kondo peak' does not appear in many approximate treatments, this peak is particularly sensitive to the approximations made. The rather good result for $N_f \geqslant 6$ in the lowest-order treatment therefore suggests that the $(1/N_f)^0$ treatment for $\rho_f^<(\varepsilon)$ is rather accurate for $N_f \geqslant 6$. On the other hand the figure also illustrates that the lowest-order treatment is insufficient for $N_f = 2$ and even more so for $N_f = 1$. In fig. 7 we therefore compare more accurate treatments for $N_f = 1$ with the exact result, which can easily be obtained for $N_f = 1$. The $N_f = \infty$ curve was obtained by using eqs. (104)–(106). This curve has a large 'Kondo peak' at $\varepsilon_F = 0$, which is absent in the exact solution. The shoulder seen at $\varepsilon_F = 0$ in the exact curve results from the cut-off of the PES spectrum at $\varepsilon_F = 0$ and from the broadening, and it is not due to a Kondo peak. Thus the 'Kondo peak' should gradually disappear in the approximate

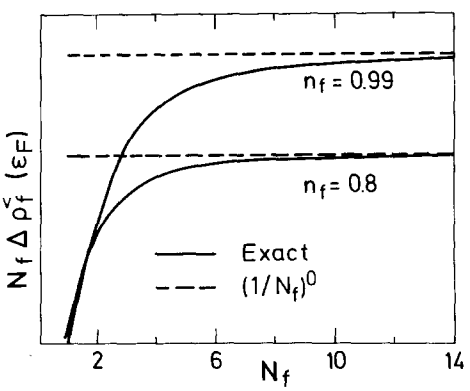

Fig. 6. The weight $\rho_f^<(\varepsilon_F)$ of the valence spectrum at the Fermi energy as a function of the degeneracy N_f. The exact result (full curve, eq. (114)) is compared with the $(1/N_f)^0$ result (dashed curve, eq. (115)) for the mixed valence ($n_f = 0.8$) and spin-fluctuation ($n_f = 0.99$) regimes.

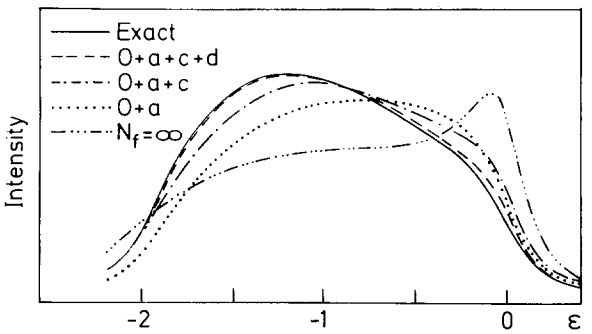

Fig. 7. The f-level PES spectrum for $N_f = 1$. The full line gives the exact result, and the $N_f = \infty$ curve (— ··· —) the result of eqs. (104)–(106). The remaining curves show the changes of the results as the states a,c and d in fig. 4 are included. The calculation including the states 0, a, c and d is of order $(1/N_f)^1$. The parameters are $\varepsilon_f = -0.6$ eV, $\tilde{\Delta} = 0.8$ eV and $B = 2$ eV and the form (89) for $V(\varepsilon)^2$ has been used. A Lorentzian broadening with the FWHM 0.3 eV has been introduced.

$N_f = 1$ solutions as we increase the accuracy in $1/N_f$. In the $N_f = \infty$ solution we included the states (95) but neglected the states (96). For $N_f = 1$, however, the states (95) do not contribute, since the requirement $\nu \neq \nu'$ in the definition requires $N_f \geqslant 2$. Thus the states (96) are the only ones of type a in fig. 4, which contribute for $N_f = 1$. The result using states (94) and (96) is shown by the dotted curve. The chain curve is calculated using also the states of type c in fig. 4, and for the dashed curve the states d are included. Since the double occupancy states do not enter for $N_f = 1$, the dashed curve is correct to order $(1/N_f)^{-1}$. This curve is in very good agreement with the exact result.

In this context it is interesting to compare with the noncrossing approximation (NCA) (eqs. (61) and (62)). In fig. 8 this theory is compared with the intermediate states method and the exact result for the same parameters as in fig. 7. The 'intermediate states' method of the order $(1/N_f)^1$ for $\rho_f^<(\varepsilon)$ gives substantially more accurate results, because $(1/N_f)^1$ contributions are not correctly treated in the NCA. The correct treatment to this order in $(1/N_f)$ would require the inclusion of vertex corrections in the NCA.

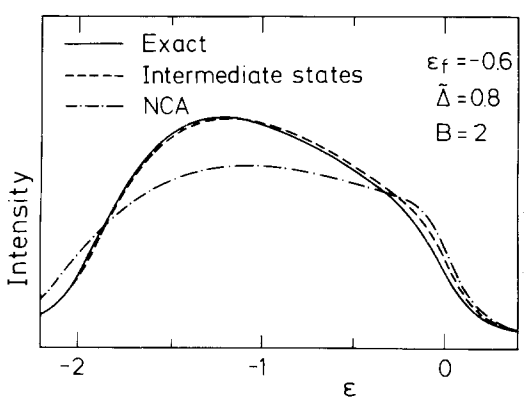

Fig. 8. The f-level PES spectrum for $N_f = 1$. The full curve gives the exact result, the dashed curve the $(1/N_f)^1$ result of the intermediate-state theory and the dashed–dotted curve the result of the NCA. The parameters are the same as in fig. 7.

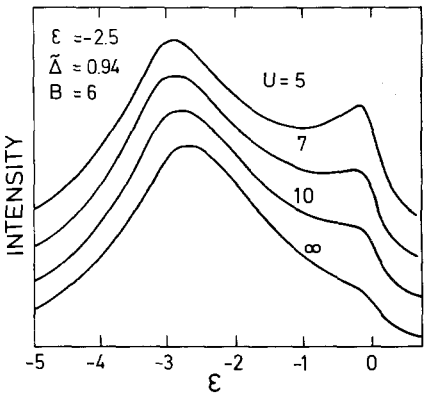

Fig. 9. The f-level PES spectrum as a function of U. The parameters are $\varepsilon_f = -2.5$, $\tilde{\Delta} = 0.94$ and $B = 6$. The form (89) was used for $V(\varepsilon)^2$. A Lorentzian broadening of 0.5 (FWHM) was introduced. All energies are in eV. The figure illustrates the sensitivity of the weight at $\varepsilon_F = 0$ to the value of U. Observe that the peak at $\sim\varepsilon_f = -2.5$ eV is not related to the bottom of the band at -6 eV.

We have so far considered the case $U = \infty$, since this case is particularly simple. There are, however, important quantitative and even qualitative changes when the finite value of U is taken into account. This is illustrated in fig. 9, where the spectrum is shown as a function of U. In particular close to $\varepsilon = 0$ the $U = 5$ and $U = \infty$ spectra differ qualitatively. The figure also illustrates that the spectrum can have a two-peak structure even if $V(\varepsilon)^2$ is structureless. In fig. 9 the bottom of the conduction band is at -6 eV far below the peak at $\varepsilon \sim -3$ eV. This peak is therefore *not* a split-off peak.

The shape of the spectrum for $U < \infty$ has been discussed in detail by Gunnarsson and Schönhammer (1985a). In the spin fluctuation limit and to lowest order in $1/N_f$ the dominating contribution for small ε is

$$\rho_f^<(\varepsilon) \approx A^4 a(\varepsilon)^2 \left(1 - \frac{\Delta E}{2\varepsilon_f + U - \Delta E}\right)^2, \tag{116}$$

where $Aa(\varepsilon)$ is the coefficient of the basis states $|\varepsilon\rangle$ in the ground state. Because of the factor $a(\varepsilon)^2$ this contribution decays on the energy scale of a Kondo energy and it corresponds to the contribution (109) obtained for the $U = \infty$ limit. In addition to this rapidly decaying term, the spectrum has a contribution

$$\rho_{f(1)}^<(\varepsilon) = A^4 \tilde{V}(\varepsilon)^2 \left[\int_{-B}^{0} d\varepsilon' \frac{a(\varepsilon')^2}{2\varepsilon_f + U - \Delta E - \varepsilon - \varepsilon'}\right]^2. \tag{117}$$

This term has no correspondence for $U = \infty$. The decay of this term is determined by the energy denominator in the integral and has an energy scale $2\varepsilon_f + U - \Delta E$, i.e. a few eV. Because of the prefactor $\tilde{V}(\varepsilon)^2$, this term is sensitive to the energy dependence of the conduction density of states and the hopping matrix elements. In the spin-fluctuation limit the integrated weight of eq. (116) becomes very small compared with the weight of eq. (117). Because of resolution problems, the sharp rise of (116) is hard to see experimentally in the spin-fluctuation limit. Since its weight is small the contribution (117) then dominates the broadened spectrum close to $\varepsilon = 0$.

The discussion so far has been based on the Anderson model eq. (8). In this model the conduction band and 4f Coulomb interaction U_{fd} is only included implicitly as a renormalization of ε_f and U, while all dynamical effects are neglected. For systems where the conduction band has a small (effective) band width, and/or the band filling is small, such dynamical effects can lead to additional satellites. This is the case for some 3d-elements and compounds (Kotani and Toyozawa 1974a) and for some chemisorption systems (Schönhammer and Gunnarsson 1977, 1978a,b, Gunnarsson and Schönhammer 1978, Fuggle et al. 1978). This has also been proposed as a possible mechanism for explaining the two peak structures seen in the f-level PES spectrum of Ce and several of its compounds (Liu and Ho 1982, Riseborough 1985, Nunez–Regueiro and Avignon 1985). The conduction band width of Ce and its intermetallics is, however, fairly large and the band filling is not very small. A large value of U_{fd} is therefore needed to obtain satellites with an appreciable weight, at least in the Liu–Ho model (Allen et al. 1986). For such values of U_{fd} the peak separation is, however, much larger than has been observed experimentally.

The effects of explicitly including U_{fd} has been studied by Takeshige et al. (1985) for Ce pnictides. In this treatment the f-level degeneracy was taken into account. Takeshige et al. (1985) calculated the ground state in a similar way as in section 4.1, except that they considered a magnetic state, which is more appropriate for the pnictides. They then used the 'intermediate-state' method for the calculation of the spectrum. This calculation also included the creation of an electron–hole pair, due to the f-conduction band Coulomb interaction. Although Takeshige et al. (1985) used a large value of $U_{fd}(=10\,\text{eV})$ they did not obtain any new satellites due to the U_{fd} term. The main effect of this new interaction was a broadening of the peaks and some transfer of weight away from the peak closest to ε_F (Takeshige et al. 1985).

4.3. *Bremsstrahlung isochromat spectroscopy (BIS)*

In BIS, or inverse photoemission, the sample is bombarded by electrons which make radiative transitions into lower-lying $(N+1)$-electron states. Here we study transitions into the f-level. Then the Green's function (Gunnarsson and Schönhammer 1983a) (eq. (20))

$$g_f^>(z) = \sum_\nu \langle E_0(N)|\psi_\nu \frac{1}{z + E_0(N) - H} \psi_\nu^+ |E_0(N)\rangle \tag{118}$$

is needed. First the case $U = \infty$ is studied. The integrated weight of the BIS spectrum is of the order N_f ($(1 - n_f)N_f$ for $U = \infty$) and to obtain results of the order $(1/N_f)^0$ for $\rho_f^>(\varepsilon) = \Sigma_\nu \rho_\nu^>(\varepsilon)$ we have to include states of the order $(1/N_f)^1$. For simplicity we here use a ground state of the order $(1/N_f)^0$ but use intermediate states of the order $(1/N_f)^1$, since it is then possible to obtain a closed expression. The intermediate states to order $(1/N_f)^1$ (a, c and d in fig. 4) are

$$|\nu\rangle = \psi_\nu^+ |0\rangle. \tag{119}$$

$$|E\nu\rangle = \psi_{E\nu}^+ |0\rangle, \tag{120}$$

$$|E\varepsilon\nu\rangle = \frac{1}{\sqrt{N_f}} \sum_{\nu'} \psi^+_{E\nu} \psi^+_{\nu'} \psi_{\varepsilon\nu'} |0\rangle. \tag{121}$$

Since we use a $(1/N_f)^0$-order ground state and consider $U = \infty$, it is sufficient to calculate the $\nu\nu$ element of the inverse of the matrix of $(z + E_0(N) - H)$ in the space (119)–(121). This is done in a similar way as for the PES spectrum, and eq. (102) is used twice. This leads to

$$g^>_f(z) = \frac{(1 - n_f)N_f}{z + \Delta E - \varepsilon_f - \mu(z)}, \tag{122}$$

where

$$\mu(z) = \int_0^{B'} \frac{V(E)^2}{z + \Delta E - E + \tilde{I}(-z - \Delta E + E + \varepsilon_f)} \, dE. \tag{123}$$

The integrand of (123) has a pole at $z = E$, as can be seen from eq. (107). Using (108) we find that the strength of the pole is $(1 - n_f)$. This leads to

$$\mathrm{Im}\,\mu(\varepsilon - i0) = (1 - n_f)\pi V(\varepsilon)^2, \qquad 0 \leqslant \varepsilon < \delta. \tag{124}$$

Since $\mathrm{Re}\mu(\varepsilon - i0) \sim (1/N_f)^1$, $\mathrm{Re}\mu(z)$ does not contribute to $\rho^>_f(\varepsilon)$ to order $(1/N_f)^0$ and is neglected there (Gunnarsson and Schönhammer 1983a,b). This leads to

$$\frac{1}{\pi}\mathrm{Im}g^>_f(\varepsilon - i0) = \frac{(1 - n_f)^2 V(\varepsilon)^2}{(\delta - \varepsilon)^2}, \qquad 0 \leqslant \varepsilon < \delta, \tag{125}$$

which joins smoothly to the PES result (109). This result is obtained by strictly expanding (122) and (123) in powers of $1/N_f$, while an evaluation of (122) and (123) as it stands leads to a weak unphysical pole slightly below $\varepsilon = 0$. A different type of anomaly appears in the NCA at $T = 0$. (Müller-Hartmann 1984, Kuramoto and Müller-Hartmann 1985) at $\varepsilon = 0$. Equation (125) describes a steep rise in the spectrum as $\varepsilon = \delta$ is approached from below. To describe the region $\varepsilon \sim \delta$ properly, we must include the imaginary part of $\mu(\varepsilon - i0)$ also in the denominator of (125). This results in a narrow peak at $\varepsilon \sim \delta$, with a width of the order (Gunnarsson and Schöhammer 1983b)

$$(1 - n_f)\pi V(\delta)^2 \approx \pi n_f \delta / N_f, \tag{126}$$

where we have used (85). A more accurate treatment of the range $\varepsilon \geqslant \delta$, however, requires the inclusion of the 'continuum part' of the integrand of (123) as well.

For a comparison with experiment it is crucial to take into account that $U < \infty$, since this leads to a second, f^2-like peak in the BIS spectrum. This can be done by using the $U < \infty$ ground state and using the intermediate states (b in fig. 4)

$$|\varepsilon\nu\rangle = \frac{1}{\sqrt{N_f - 1}} \sum_{\nu'(\neq\nu)} \psi^+_\nu \psi^+_{\nu'} \psi_{\varepsilon\nu'} |0\rangle. \tag{127}$$

The calculation now requires a numerical inversion of a matrix. The f^2 peak has a broadening of the order $2\Delta = 2\pi V(\varepsilon_f + U)^2$ (half-width), since the f^2 state can decay

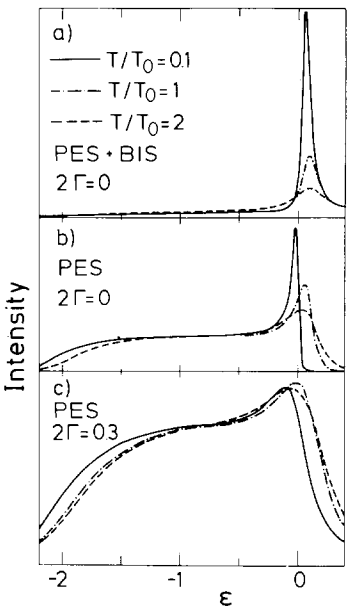

Fig. 10. The temperature dependence of the PES and BIS spectra in the NCA. Figure (a) shows the unbroadened PES + BIS spectrum and (b) shows the unbroadened PES spectrum. In (c) the broadened (FWHM = 0.3 eV) PES spectrum is shown. The parameters are $\varepsilon_f = -0.6$, $\tilde{\Delta} = 0.8$, $U = \infty$, $N_f = 6$ and $B = 2$. The form (89) was used for $V(\varepsilon)^2$. In (b) and (c) the total weight ($=n_f$) has been normalized to one to simplify a comparison of the shape of the PES spectrum for different T.

through the hopping of either of the two f-electrons into the conduction band. The f^2 peak also shows a tail towards higher energies. The reason is that the states (127) couple to the states $|\varepsilon\rangle$ (65) in the ground state, which have a distribution with a tail given by $a(\varepsilon)^2$ (Gunnarsson Schönhammer 1983b). In the experimental spectra multiplet effects and lifetime broadening, which are not included in the Hamiltonian (8), tend to dominate over the effects discussed above.

The discussion so far has been limited to $T = 0$. We now consider finite temperatures, using the NCA (Kuramoto 1983, Coleman 1984, Bickers et al. 1985, Cox 1985). In fig. 10a we show the valence spectrum PES + BIS for $T/T_0 = 0.1$, 1 and 2, where T_0 is a Kondo temperature as defined by Cox (1985). The spectrum shows a strong T-dependence both in terms of shape and weight. In fig. 10b we show the PES part of the spectrum. While there is still a strong T-dependence in the shape, the weight is now fairly T-independent. This is illustrated by fig. 10c, where we have introduced an instrumental broadening, so that the details of the shape are lost. The figure shows that the PES Kondo peak is shifted in energy as T is increased, but that it does not lose weight over this temperature range.

To understand the difference in weight between fig. 10a and 10b we use a sum rule valid for $U = \infty$ for the BIS spectrum

$$\frac{1}{\pi}\int \mathrm{Im} g_f^{>}(\varepsilon - \mathrm{i}0)\,\mathrm{d}\varepsilon = N_f(1 - n_f), \tag{128}$$

where the BIS weight for $U = \infty$ is primarily in the Kondo peak. Since n_f can have a strong temperature dependence it is obvious that the same is true for the BIS part of the weight. To understand the relative T-independence of the PES Kondo weight,

we first recall the interpretation of the Kondo peak for $T = 0$ below eq. (111). According to this interpretation the weight of the Kondo peak is related to the probability that a conduction electron close to ε_F fills the f-level, after the photoemission process, in such a way that the Kondo binding energy is gained. This probability is related to the f^0 weight of the *final* states and is not directly related to the character of the initial state. Thus weight close to the Fermi energy has been obtained using both a singlet and a nonsinglet ground state (Gunnarsson and Schönhammer 1983b). These arguments illustrate that even for magnetic initial states, which enter the calculation for $T > 0$, there is a mechanism which gives weight close to ε_F. The shift of the peak can be made plausible in terms of the energies of the initial states. At $T = 0$ the system is in a singlet state with the Kondo binding energy, while at $T > T_0$ the system is likely to be in an initial state without this binding energy. In both cases there are, however, final states which have the Kondo binding energy and therefore contribute to the Kondo peak.

For a finite U the f^2 weight in the initial state strongly influences the spectrum at ε_F. For this case there are presently no $T \neq 0$ calculations available. Since, however, the energy scale involved is of the order of eV for the new f^2-related features (117), we expect the temperature dependence to be weak. There has been an experimental attempt to observe temperatures effects in the PES spectrum for a Ce compound (Wieliczka et al. 1985). With the experimental resolution available no such effects could be observed for $CeSn_3$.

4.4. *XPS core level spectroscopy*

In the core level X-ray photoemission spectroscopy (XPS), a core electron is emitted. Thus we use eq. (17) with $\psi_i = \psi_c$, where ψ_c annihilates a core electron, and study

$$g_c(z) = \langle E_0(N)|\psi_c^+ \frac{1}{z - E_0(N) + H}\psi_c|E_0(N)\rangle. \tag{129}$$

We first consider the case $U = \infty$ and work to order $(1/N_f)^0$. Thus only the final state basis functions $\psi_c|0\rangle$ and $\psi_c|\varepsilon\rangle$ enter the calculation. The Green's function (129) can then be calculated using eq. (102) (Gunnarsson and Schönhammer 1983a,b). Alternatively, the present approximation can be mapped onto the so-called filled band model (Schönhammer and Gunnarsson 1978b) in the following way. To lowest order in $1/N_f$ the conduction states above ε_F do not enter the calculation. Thus the actual conduction band can be replaced by a band with a sharp cut-off at ε_F. Then the state $\psi_c|0\rangle$ corresponds to a completely filled conduction band. Since only the states $\psi_c|0\rangle$ and $\psi_c|\varepsilon\rangle$ are considered, the model can be mapped onto a nondegenerate ($N_f = 1$) model if $V(\varepsilon)$ is replaced by $\tilde{V}(\varepsilon) = \sqrt{N_f}V(\varepsilon)$. In this $N_f = 1$ model the matrix elements and the energies are the same as in the $N_f \neq 1$ model. The $N_f = 1$ filled band model has, however, only one hole and the calculation of the initial and final states represents two one-particle problems with different parameters ε_f and $\varepsilon_f - U_{fc}$, respectively. This calculation can easily be performed exactly (Schönhammer and Gunnarsson 1978b). The result is given by

$$\rho_c(\varepsilon) = \frac{1}{\pi}\mathrm{Im}g_c(\varepsilon - i0) = (1 - n_f)\left(\frac{U_{fc}}{\varepsilon - U_{fc}}\right)^2 \tilde{\rho}_f(\varepsilon - \Delta E + \varepsilon_f - U_{fc}), \tag{130}$$

where

$$\tilde{\rho}_f(\varepsilon) = \frac{1}{\pi}\mathrm{Im}\frac{1}{\varepsilon - i0 - \varepsilon_f + U_{fc} - \tilde{\Gamma}(\varepsilon - i0)}, \tag{131}$$

is the f density of states of the $N_f = 1$ filled band model in the presence of the core hole. In this limit the core spectrum is therefore related to the valence spectrum $\tilde{\rho}_f(\varepsilon)$. The multiplying factor $[U_{fc}/(\varepsilon - U_{fc})]^2$ changes the weights of the structures in $\tilde{\rho}_f(\varepsilon)$, but does not normally introduce new structures. Thus the structures in $\rho_c(\varepsilon)$ can be related to the features in $\tilde{\rho}_f(\varepsilon)$, which can be related to $\tilde{V}(\varepsilon)^2$ (Fuggle et al. 1987. Gunnarsson et al. 1985). For $U < \infty$ we allow double occupancy of the f-level. To lowest order in $1/N_f$ the calculation is then a two-hole problem. This problem can also be solved exactly using the properties of a separable perturbation (Schönhammer and Gunnarsson 1978b) or using eq. (102) and numerical inversion (Gunnarsson and Schönhammer 1983b).

To test the accuracy of the $1/N_f$ method, we have studied the $N_f = 1$ limit. In this limit the core spectrum can be calculated exactly numerically, even without assuming a filled band (Schönhammer and Gunnarsson 1977, 1978a) by solving a Nozières–deDominicis (1969) integral equation. In fig. 11a we show the exact

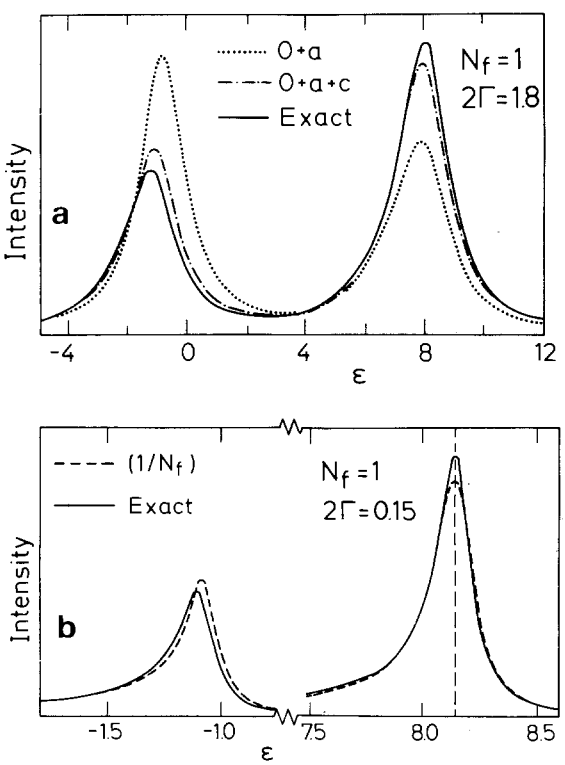

Fig. 11. The core level spectrum for $N_f = 1$, $\varepsilon_f = 0$, $\Delta = 1.5$ and $U_{fc} = 9$ using the form (89) with $B = 3$ for $V(\varepsilon)^2$. In (a) and (b) we have used a Lorentzian broadening (FWHM) of 1.8 and 0.15, respectively. All energies are in eV. In (a) the calculation to order $(1/N_f)^1$, using the states 0 + a + c + d in fig. 2, agrees with the exact result to within the plotting accuracy.

calculation with a realistic broadening of $2\Gamma = 1.8\,\text{eV}$ due to lifetime broadening and instrumental resolution. The dotted curve shows results to lowest order in $1/N_f$. While the peak positions are rather well described, the peak heights are off by a factor two. The inclusion of the states c in fig. 2, however, gives a rather good agreement with the exact result. The further introduction of the states d (order $(1/N_f)^1$) gives agreement with the exact result to within the plotting accuracy. For this reason we have reduced the broadening by an order of magnitude in fig. 11b, which shows that the $1/N_f$ calculation is still in a good agreement with the exact result. The exact unbroadened result has an 'infrared' singularity at threshold (~ 8.1), which is not present in the approximate result. This is probably the main reason why the leading peak is somewhat higher in the exact calculation even after broadening. Due to the infrared singularity the leading peak shows a clear asymmetry due to the excitation of (an infinite number of) electron–hole pairs (Nozières) and deDominicis 1969). Although the $(1/N_f)^1$ calculation includes excitations with at most one conduction electron, one f-electron and two holes it gives a good description of this asymmetry except very close to threshold. At threshold the approximate solution gives a delta-function, which, however, has an entirely negligible weight for parameters realistic for rare earth compounds.

The leading peak in fig. 11 corresponds to final states of mainly f^1 character, while the satellite corresponds to f^0-like states. Since the f-electrons give a particularly efficient screening of the core hole, the leading peak and the satellite are sometimes referred to as the 'well screened' and the 'poorly screened' peaks, respectively (Fuggle et al. 1980b). For the rare earth compounds the 'poorly screened' peak is assumed to correspond to final states where the core hole is screened by conduction electrons, since such a screening is implicitly included in the Hamiltonian (2) as a renormalization of U_{fc}. This mechanism for obtaining additional peaks in the core spectrum has been discussed for 3d-systems (Kotani and Toyozawa 1974a), rare earths (Kotani and Toyozawa 1974b) and chemisorption systems (Schönhammer and Gunnarsson 1977, 1978a). This mechanism is of particular interest if the creation of the core hole leads to a substantial change of the relative energies of the configurations involved (e.g. f^0 and f^1 for La compounds) and the coupling $\tilde{\Delta}$ between the configurations is not too strong. In such a case both the 'well' and 'poorly' screened peaks may have a nonnegligible weight. This is the case for the La compounds. For Ce compounds it is important to take f^2 configurations into account. The core spectrum then often has three peaks, corresponding to f^0, f^1 and f^2-like states. Since the initial state is typically of mainly f^1 character, we may refer to the f^1 and f^2 peaks as the 'poorly' and 'well screened' peaks, respectively. In the Ce compounds the parameters are usually such that the f^2 peak (shoulder) has a small but observable weight. Finally, one should note that the different configurations in some cases may mix so strongly that the language of 'poorly' and 'well screened' peaks becomes meaningless (Gunnarsson et al. 1985).

4.5. *X-ray absorption spectroscopy (XAS)*

There has been extensive experimental work on the $L_{II,III}$ edge in XAS, which involves the excitation of a 2p core electron into a continuum d-state. This

transition has been studied theoretically by Delley and Beck (1985), and below we essentially follow their treatment. The operator

$$T_L = \sum_d W_d \psi_d^+ \psi_c \tag{132}$$

is used to describe the excitation from a core level (c) to a conduction state of d-symmetry with respect to the impurity. The absorption probability of a photon with energy $\hbar\omega$ is then given by

$$\rho_{p\to d}(\hbar\omega) = \sum_n |\langle \widetilde{E_n(N+1)}| T_L | E_0(N)\rangle|^2 \delta(\widetilde{E_n(N+1)} - E_0(N) - \hbar\omega), \tag{133}$$

where $|\widetilde{E_n(N+1)}\rangle$ is a state with $N+1$ valence electrons in the presence of a core hole (indicated by $\sim$). Since the conduction electrons are treated as noninteracting and since we distinguish between conduction electrons of d- and f-symmetry (with respect to the impurity), the final states are written as

$$\psi_d^+ |\widetilde{E_n(N)}\rangle. \tag{134}$$

The spectrum is then given by

$$\rho_{p\to d}(\hbar\omega) = \sum_d W_d^2 \sum_n |\langle \widetilde{E_n(N)}|\psi_c | E_0(N)\rangle|^2 \delta(\widetilde{E_n(N)} + E_d - E_0(N) - \hbar\omega). \tag{135}$$

The XAS spectrum can then be expressed in terms of the XPS spectrum $\rho_c(\varepsilon)$

$$\rho_{p\to d}(\hbar\omega) = \int_0^\infty dE\, D(E)\rho_c(E - \hbar\omega), \tag{136}$$

where

$$D(E) = \sum_d W_d^2 \delta(E - E_d) \tag{137}$$

includes density of states and matrix element effects for the unoccupied d-states ($E_d > \varepsilon_F = 0$). In this approximation the $L_{II,III}$ spectrum is thus a convolution of the XPS spectrum with the function $D(E)$ (Delley and Beck 1985).

Recently, there have also been studies of the $M_{4,5}$ edge ($3d \to 4f$ transitions) (Fuggle et al. 1983a, Kaindl et al. 1984, Thole et al. 1985, van der Laan et al. 1986).

This spectroscopy has formal similarities with BIS, as an electron is added to the f-level. Physically the processes are, however, very different since in $3d \to 4f$ XAS the final states are calculated in the presence of a core hole. In the formalism this difference only enters as a shift of $\varepsilon_f \to \varepsilon_f - U_{fc}$ and we can use the same type of basis states as in BIS. If we work to lowest order in $1/N_f$ it is possible to obtain an analytical solution even if f^2 configurations are included (Gunnarsson and Schönhammer 1983b).

5. Comparison with experiment

In the introduction we referred to the 'discrepancy' between thermodynamic and spectroscopic estimates of n_f and Δ. In section 5.1 we therefore discuss how information about these quantities can be extracted from spectroscopies. We first consider a simplified model and then give numerical results for the Anderson model. In the following sections we compare with experiment for specific systems. Compounds of Ba and La, with essentially zero f-occupancy in the ground state, are studied in section 5.2. In section 5.3 we consider Ce compounds and in section 5.4 the Yb compounds. To study the Pr and Nd compounds, the model (8) should be generalized. These compounds are nevertheless briefly discussed in section 5.5 within the model (8).

5.1. *Determination of n_f and Δ from spectroscopies*

To simplify the discussion, we first consider the model (8) in the limit when the conduction band width B goes to zero (Gunnarsson and Schönhammer 1983b). This model has been used extensively by Fujimori (1983a,b,c). We assume that states with more than two f-electrons are suppressed by the large Coulomb potential U. In the $B = 0$ limit, the system then has only three basis states $|f^0\rangle$, $|f^1\rangle$ and $|f^2\rangle$, with 0, 1 and 2 f-electrons, respectively, and the corresponding number of holes. The energies of these configurations are schematically shown in fig. 12 ('no core hole'). For the core spectroscopies we are also interested in the energies in the presence of a core hole. The figure illustrates that in this case the f^2 configuration is the lowest one, and that the f^1 configuration is far below the f^0 configuration. This effect is described by the term (2) in the Hamiltonian, where $U_{fc} \sim 10$ eV describes how the f-level is pulled down by the core hole.

The ground state is given by

$$|E_0(N)\rangle = a_0|f^0\rangle + a_1|f^1\rangle + a_2|f^2\rangle. \tag{138}$$

We let the hopping matrix element V be negative. Then the coefficients a_0 and a_1 have the same sign, since the ground state is a bonding state. We now study core

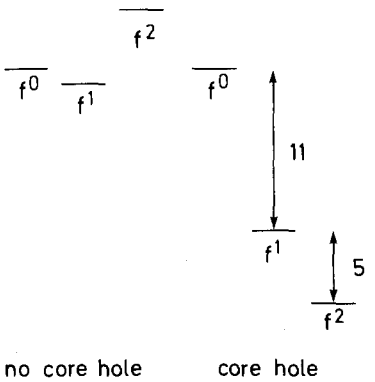

Fig. 12. Schematic representation of the energies of different configurations of a Ce impurity without and with a core hole. The configurations are labelled according to the number of f-electrons and typical energy differences (in eV) are shown.

level XPS. According to eq. (12) the final states, in the presence of a core hole, are needed. The model has only three basis states, and there are therefore three final states. Since the hybridization $N_f V^2$ is fairly small compared with the energy separation of the basis states, the mixing is moderate and the final states can be labelled by the configuration contributing most of the weight. Thus we have the final states

$$|\text{“}f^n\text{”}\rangle = c_0^{(n)}|f^0\rangle + c_1^{(n)}|f^1\rangle + c_2^{(n)}|f^2\rangle, \quad n = 0,1,2, \tag{139}$$

where $c_n^{(n)}$ is large. The weight of the peaks is now calculated from eq. (12)

$$p(f^n) = \left| \sum_{m=0}^{2} a_m c_m^{(n)} \right|^2 . \tag{140}$$

We first consider the f^2 peak. Since the final f^2 configuration is far below the f^0 configuration, we assume for a moment that the f^2-like final state is a linear combination of the f^1 and f^2 configurations, i.e. that $c_0^{(2)} \approx 0$. This gives the f^2 weight

$$p(f^2) \approx |a_1 c_1^{(2)} + a_2 c_2^{(2)}|^2 . \tag{141}$$

For the systems we are interested in $a_1 \approx 1$ and $c_2^{(2)} \approx 1$. The f^2 weight is then primarily determined by a_2 and $c_1^{(2)}$. As the coupling $N_f V^2$ between the configurations is increased both a_2 and $c_1^{(2)}$ increase. This leads to an increase of $p(f^2)$ in (141). These simple arguments remain qualitatively correct when the Anderson model with a finite band width is considered. This is illustrated in fig. 13 where the core spectrum is shown for different values of Δ. This figure illustrates how the weight of the f^2 peak in the core XPS spectrum can be used to estimate Δ.

In the same way we can calculate the weight of the f^0 peak. In this case we neglect

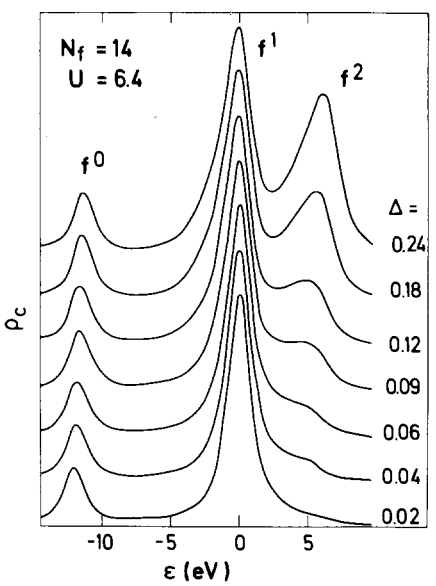

Fig. 13. The core level XPS spectrum as a function of Δ. The shape of $V(\varepsilon)^2$ was chosen to simulate a compound with a transition element and Δ refers to the maximum of $\pi V(\varepsilon)^2$. The average value of $V(\varepsilon)^2$ is $\Delta_{av} = 0.84\Delta$. For details about $V(\varepsilon)^2$ see fig. 6 in Gunnarsson and Schönhammer (1983b). The spectra are normalized to the height of the f^1 peak and a 1.8 eV (FWHM) Lorentzian broadening has been introduced.

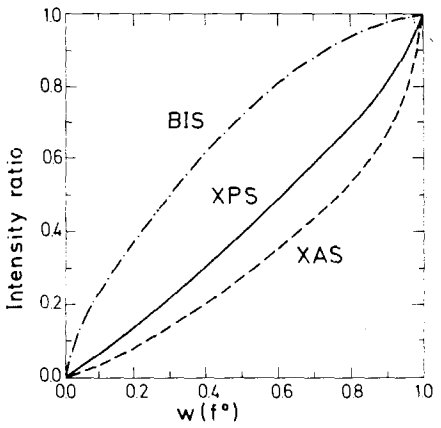

Fig. 14. The intensity ratio $p(f^0)/[p(f^0) + p(f^1) + p(f^2)]$ for the XPS spectrum (solid curve) and the ratio $p(f^1)/[p(f^1) + p(f^2)]$ for the 3d → 4fXAS (dashed curve) and BIS (dashed–dotted curve) spectrum as a function of the f^0 weight $w(f^0)$ in the initial state. The shape of $V(\varepsilon)^2$ is the same as in fig. 13, and $\Delta_{av} = 0.1$ eV.

the f^2 mixing into the f^0-like final state, i.e. $c_2^{(0)} \approx 0$. This leads to

$$p(f^0) \approx |a_0 c_0^{(0)} + a_1 c_1^{(0)}|^2. \tag{142}$$

Since the final "f^0" state is an anti-bonding state, the coefficients $c_0^{(0)}$ and $c_1^{(0)}$ have different signs. The two terms in (142) therefore also have different signs and the weight $p(f^0)$ of the f^0 peak is smaller than the f^0 weight $w(f^0) = a_0^2$ in the initial state. This is shown in fig. 14, which has been obtained for the finite band width Anderson model.

In 3d → 4f XAS and in BIS an f-electron is added to the system. Thus the initial f^0 and f^1 configurations couple to the final f^1 and f^2 configurations, respectively. The final f^0 configuration can be neglected in this case and we write the weight of the f^1 peak as

$$p(f^1) \approx |a_0 c_1^{(1)} + a_1 c_2^{(1)}|^2. \tag{143}$$

This shows that the initial state f^0 weight is related to the weight of the f^1 peak. In 3d → 4f XAS the f^1 configuration is above the f^2 configuration, and the "f^1" state is an antibonding state, while in BIS the ordering is the opposite and the "f^1"-like state is a bonding state. In XAS the terms in (143) therefore have opposite signs, while in BIS they have the same sign. Thus $p(f^1) < w(f^0)$ in XAS but $p(f^1) > w(f^0)$ in BIS. This is illustrated in fig. 14 for the finite band width Anderson model. For these parameters, $w(f^0) = 0.1$ leads to an f^1 peak which is about 4 times larger in BIS than in 3d → 4f XAS. This mixing effect of the 4f configurations therefore plays a crucial role when the spectra are interpreted.

5.2. *Ba and La compounds*

The Ba and La compounds are somewhat simpler than the Ce compounds, since the f-occupancy in the ground-state is very small, and since the f^2 configurations play a small role even in the final states. These systems have been studied extensively by Schneider et al. (1985).

Figure 15 shows theoretical and experimental results for the valence XPS and the

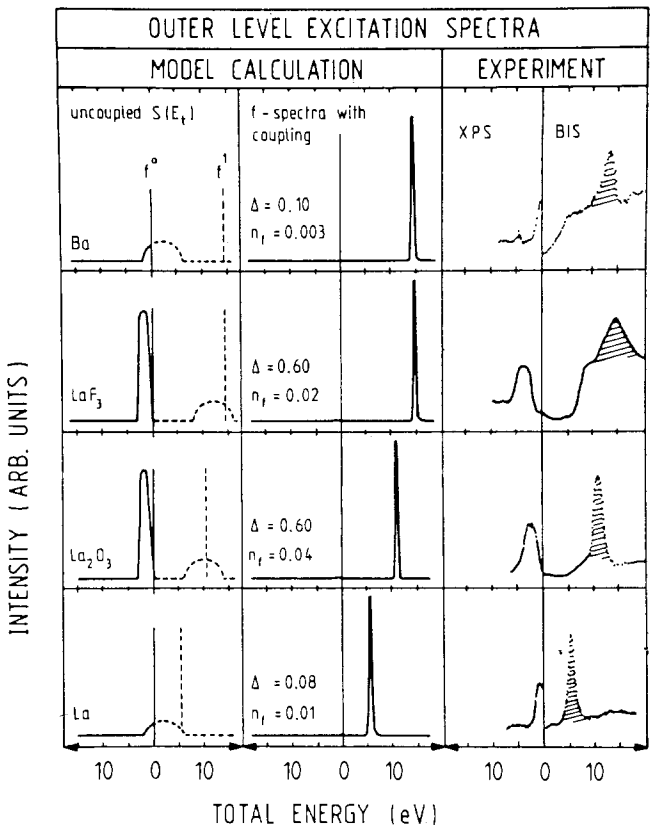

Fig. 15. Calculated and measured valence XPS and BIS spectra (Schneider et al. 1985, or references therein). To the left the assumed shape of $V(\varepsilon)^2$ and the position of the f-level (the dashed line denoted f^1) are shown. The values of n_f and Δ are also shown, where Δ is the maximum of $\pi V(\varepsilon)^2$. A Gaussian instrumental resolution of 0.4 eV (FWHM) was included in the calculations. In the experimental spectra the hatched areas show f-related structures. The figure is reproduced from Schneider et al. (1985).

BIS spectra. For Ba the f-level position is approximately given by an f-related peak in the BIS spectrum at about 14 eV. Since the f-level is so far above ε_F, the f-occupancy is very small and there is no detectable f-contribution to the valence PES spectrum. The situation is similar for the La compounds. Although the f-level tends to be lower than in Ba compounds, the coupling $\tilde{\Delta}$ is not strong enough to give an appreciable f-occupancy. The valence spectra therefore only have a BIS peak close to the f-level position.

Figure 16 shows the 3d XPS and the 3d electron energy loss spectroscopy (EELS) core spectra. The EELS spectra are taken at energies where $3d \rightarrow 4f$ transitions dominate. In Ba and La compounds the initial state is an almost pure f^0 configuration. Within the model discussed here, the center of gravity of the 3d XPS spectrum therefore approximately gives the energy of the f^0 configuration in the presence of the 3d core hole. In EELS, on the other hand, where an f-electron is

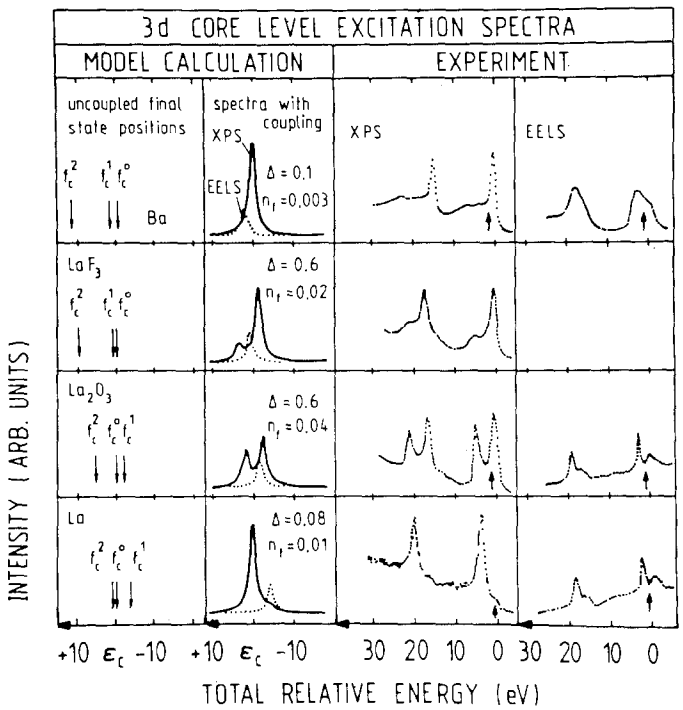

Fig. 16. Calculated and measured 3d XPS and 3d EELS spectra (Schneider et al. 1985, or references therein). The left part shows the energies of the different configurations in the absence of a coupling. The calculated spectra have a Lorentzian broadening of 1.2 eV (FWHM) to include lifetime broadening. The full curves show the XPS and the dotted curves the EELS spectra. The arrows show the center of gravity of the experimental EELS spectra. The figure is reproduced from Schneider et al. (1985).

added to the system, the center of gravity is approximately equal to the energy of the f^1 configuration in the presence of a core hole. The arrows in the experimental spectra show the center of gravity of the EELS spectra. A comparison with the XPS spectra, shows that the final state f^1 configuration moves down in energy compared with the f^0 configuration in going from Ba to La_2O_3 to La (Schneider et al. 1985). These experimental observations provide a good support for the assumptions about $\varepsilon_f - U_{fc}$ indicated to the left in fig. 16. The XPS spectra can now be understood in terms of the values assumed for $\varepsilon_f - U_{fc}$ and Δ (Schneider et al. 1985). For Ba the f^1 configuration is above the f^0 configuration in both the initial and final states. The coupling $\tilde{\Delta} = N_f \Delta \sim 1.4$ eV is not strong enough to lead to any appreciable mixing of the final f^0 and f^1 configurations. The theory therefore predicts essentially a Lorentzian peak corresponding to final states of mainly f^0 states. Experimentally one observes plasmon satellites and a peak asymmetry due to conduction electron–hole pair excitations (Ley et al. 1980, Schneider et al. 1985). Both these effects are neglected in the calculations in fig. 16. For LaF_3 the coupling $\tilde{\Delta} \sim 8$ eV is very large and there is a strong mixing of the final-state configurations. The f^0 and f^1 configurations therefore form essentially 'bonding' and 'antibonding' linear com-

binations. Both types couple to the initial state giving rise to two peaks in the XPS spectrum. In La_2O_3 the situation is similar, except that for La_2O_3 the ordering of the f^0 and f^1 configurations is changed when the core hole is created. This leads to a much larger weight in the satellite, as is shown by both the experimental and theoretical spectra. In La, finally, the final f^1 configuration is fairly far below (~ 4 eV) the f^0 configuration. Since the coupling is not very strong ($\bar{\Delta} \sim 1$ eV) almost all the weight is in the high-binding-energy peak. The corresponding final states are in this case of primarily f^0 character.

Figure 16 also shows calculations for the EELS spectrum (Schneider et al. 1985). In these calculations a $3d \rightarrow 4f$ transition is asumed to take place and multiplet effects are neglected. The formalism then becomes the same as for the $3d \rightarrow 4f$ XAS calculation. Multiplet effects are seen in the experimental EELS spectra, which therefore differ in shape from the theoretical spectra. Multiplet effects also influence the apparent relative positions of the peaks in different spectroscopies (Esteva et al. 1983).

The XPS core level spectrum of La is often fairly simple, with two features corresponding to f^0 and f^1 final states. If, however, the conduction band is broad, the f-level may not be pulled below the bottom of the band when the core hole is created. This corresponds to $U_{fc} - \varepsilon_f < B$. From eqs. (130) and (131) it can be seen that the hybridization between the f-level and the conduction states then can lead to additional structure. Fuggle et al. (1987) found that this is the case for LaAu and $LaAu_2$. In these cases the final state f-level falls in the large density of states derived from the Au d-band. The hybridization with the d-band is then so strong that the f^0 peak tends to be split into two peaks. The result is that the f^0 XPS peak in LaAu and $LaAu_2$ appears anomalously broad. Strong effects of structures in the density of states have also been observed in the core spectrum of CO chemisorbed on a Cu surface. In this case the density of states derived from the Cu d-band has such a strong variation that an additional peak appears in the core spectrum (Gunnarsson and Schönhammer 1978). Interesting effects are also observed in Th compounds. These compounds have essentially zero occupancy of the 5f level and they have some similarities to the La compounds. The value of U_{fc} is, however, smaller, and the f^0 and f^1 configurations are almost degenerate in the presence of a core hole. An analysis of the expressions (130) and (131) shows that the spectrum then becomes very sensitive to the shape of $V(\varepsilon)^2$. Depending on this shape it was found that the high-binding-energy peak may or may not be smeared out (Gunnarsson et al. 1985).

5.3. *Ce compounds*

In the last few years several groups have studied spectra of Ce compounds using Anderson like models (Gunnarsson and Schönhammer 1983a,b, 1985a,b,c, Fujimori 1983a,b,c, Fuggle et al. 1983a,b, Gunnarsson et al. 1983, Wuilloud et al. 1983, 1984, 1985, Hillebrecht et al. 1984, Delley and Beck 1984, 1985, Sakai et al. 1984, Bickers et al. 1985, Watanabe and Sakuma 1985, Takeshige et al. 1985, Kasuya et al. 1985, Kotani and Parlebas 1985, Kotani et al. 1985, Patthey et al. 1985, Allen et al. 1986). We will therefore not try to give an exhaustive review but rather present some

typical examples. The aim is to illustrate to what extent a generalized Anderson model can describe experiment and to discuss the main physical effects which emerge from these calculations.

In fig. 17 we show results for a typical mixed valence intermetallic, $CeNi_2$. The insert shows the valence PES spectrum taken at the photon energy $\hbar\omega = 112\,\text{eV}$. At this energy the spectrum is assumed to be primarily due to the conduction electrons. Thus we may write this spectrum as $\rho_{\text{cond}}(\varepsilon) = \rho(\varepsilon)\tau(\varepsilon)^2$, where $\rho(\varepsilon)$ is the conduction density of states and $\tau(\varepsilon)^2$ includes matrix element effects and effects due to the final states available. From (4)–(8) it follows that $V(\varepsilon)^2 = \rho(\varepsilon)W(\varepsilon)^2$, where $W(\varepsilon)$ is an appropriate average of the hopping matrix element $V_{k\alpha m}$. We now make the assumption that $W(\varepsilon)/\tau(\varepsilon)$ is independent of energy, which allows us to estimate the energy dependence $V(\varepsilon)^2$ from $\rho_{\text{cond}}(\varepsilon)$. This approximation may involve substantial errors and better estimates, for instance based on band calculations (Sakai et al. 1984, Monnier et al. 1986), are desirable. The full curve in the insert shows the $V(\varepsilon)^2$ used in these calculations after it has been broadened by the instrumental resolution.

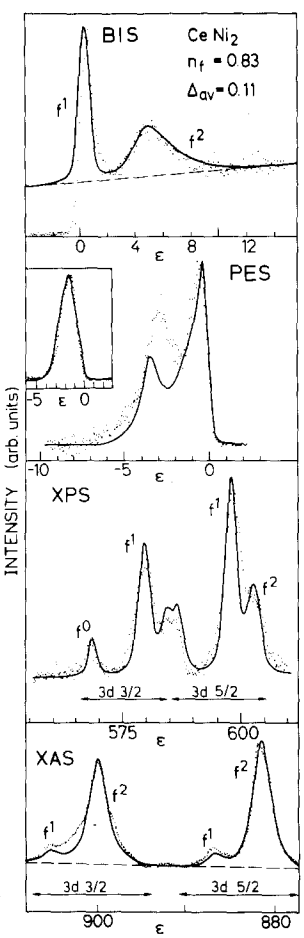

Fig. 17. The experimental (dots) and theoretical (full lines) 3d → 4f XAS, 3d XPS, 4f PES and BIS spectra of $CeNi_2$. The experimental XAS spectrum is from Fuggle et al. (1983a) and the XPS, PES and BIS spectra are from Allen et al. (1986). The insert shows the off-resonance ($\hbar\omega = 112\,\text{eV}$) spectrum (dots) and the (broadened) $V(\varepsilon)^2$ used in the calculations. The dashed curve in the BIS calculation shows the assumed background. The parameters are $U_{fc} = 10.5\,\text{eV}$ (XPS) and 11.0 eV (XAS), $U = 7.0\,\text{eV}$ (XAS, XPS and PES) and $U_{av} = 5.8\,\text{eV}$ (BIS). In the XPS spectrum ε is the kinetic energy of the emitted electron and in the other cases it is the binding energy.

The $V(\varepsilon)^2$ was chosen so that it agrees with the 112 eV spectrum after broadening. The absolute strength of $V(\varepsilon)^2$ is not determined in this procedure. This strength is represented by an average Δ_{av} of $\pi V(\varepsilon)^2$ over the occupied part of the conduction band. The f-level spin-orbit splitting is included.

The bottom part of fig. 17 shows the 3d → 4f XAS spectrum. The two components of the spectrum are due to transitions from the 3d 3/2 and 3d 5/2 levels, respectively. The relative weight of these components differ from the ideal 4:6 ratio, and they also have a somewhat different shape. This is due to the effects of intermediate coupling (Bonnelle et al. 1974, Thole et al. 1985). Each component shows an f^1 and an f^2 peak. Multiplet effects can clearly be seen in these peaks. In the calculations we have adjusted the relative weights of the 3d 3/2 and 3d 5/2 compounds to experiment. A weak background was also added as indicated. The relative weights of the f^1 and f^2 peaks result from the calculation. We have used a Lorentzian broadening (FWHM = 2.0 eV) to describe lifetime broadening and instrumental resolution.

Above the XAS spectrum the 3d core level XPS spectrum is shown. This spectrum also has a 3d 3/2 and a 3d 5/2 component, which partly overlap. Each component has an f^0, an f^1 and an f^2 feature. In the calculation we have assumed that the two components have the relative weights 4:6 and that they are separated by a spin-orbit splitting of 18.4 eV. A Lorentzian broadening of 1.4 eV (FWHM) was used to describe lifetime effects and a Gaussian broadening of 1.2 eV (FWHM) to take into account the instrumental resolution. This broadening gives a good description of the width of the f^0 peak (at 568 eV), which in the theory has a very small intrinsic broadening. The experimental f^1 and f^2 peaks are broader than the calculated ones. This is probably mainly due to multiplet effects, which are not included in the calculation. An inelastic background has been subtracted from the experimental data.

The f-level PES spectrum is shown above the 3d XPS spectrum. An inelastic background was subtracted from the experimental spectrum. Both the theoretical and experimental spectra show a pronounced two-peak structure. The calculated high binding energy peak is at a somewhat too low energy. This deviation from experiment could be reduced by using a $V(\varepsilon)^2$ which decays more rapidly for $\varepsilon \leqslant -2$ eV or by reducing the overall strength of $V(\varepsilon)^2$.

The BIS spectrum is shown in the top part of the figure. The experimental f^2 peak is quite broad. This is partly due to multiplet effects but lifetime broadening is probably also important. These effects are not included in the theory. To simulate the multiplet effects, we have performed a series of calculations where $U_i = U_0 + \varepsilon_i$ in the final state calculations. Since the f^2 peak position depends on U_i, we can choose ε_i so that the different f^2 peaks have a displacement to each other corresponding to the f^2 multiplet splitting. These spectra were added with the relative weights w_i, where ε_i and w_i were obtained from Lang et al. (1981). Thus the relative weight of the f^2 multiplets is an input to the calculation, while the relation between the f^1 and total f^2 weights is a result of the calculations. We have further, in addition to the instrumental Gaussian broadening, introduced a Lorentzian broadening

$$\Gamma(\varepsilon) = \Gamma_0 + \Gamma_1(\varepsilon - \varepsilon_F)^2. \tag{144}$$

The second term has a quadratic energy dependence and it is interpreted as a lifetime broadening. A broadening of this type is necessary to describe the width and the 'soft' shape of the f^2 peak. The first term is nonzero at $\varepsilon = 0$ and it is therefore not due to lifetime broadening. Its origin is an interesting issue. Such a broadening is needed to describe the f^1 peak. Finally we have added a background which, at least partly, is due to transitions into conduction states and to inelastic effects. Such effects are not included in the theory. In fig. 17 we have for simplicity assumed that the background is a straight line. This is the reason for the weight below $\varepsilon = 0$, where the BIS spectrum, apart from broadening effects, by definition is zero at $T = 0$.

Figure 17 illustrates that after multiplet, broadening and background effects have been added, the generalized Anderson model (8) can give a satisfactory description of the 3d–4f XAS, 3d XPS, 4f PES and BIS spectra. In fig. 17 slightly different values of U and U_{fc} were used for XPS, XAS and BIS to obtain the experimental f^1–f^2 peak separations. In all cases $V(\varepsilon)$, Δ_{av} and n_f were the same. Because of the different values of U we also varied ε_f slightly to obtain the same value of n_f for all spectroscopies.

We have here focussed on the relative weights of the peaks, i.e. the f^1 and f^2 peaks in XAS, f^0, f^1 and f^2 in XPS, the two peaks in PES and the f^1 and f^2 peaks in BIS. These weights are essentially determined by the overall strength Δ_{av} of $V(\varepsilon)^2$ and by the value of n_f. It is a strong support for the theory that so many relative weights can be rather well described by only two parameters. A comparison of 3d–4f XAS and BIS is particularly striking. Since both spectroscopies involve the transition of an electron into the 4f-level, the weight of the f^1 peak is in both spectroscopies related to the f^0 weight, $w(f^0)$, in the initial state. The figure illustrates, however, that the weight of the f^1 peak is very different in the two spectroscopies. The reason is that there is a nonnegligible mixing of the f^1 and f^2 configurations, which leads to a transfer of weight to the f^1 peak in BIS and to the f^2 peak in $3d \rightarrow 4f$ XAS. This was discussed in more detail in section 5.1. Although there are uncertainties in the comparison of the theoretical and experimental peak weights, fig. 17 shows that the theory gives a fair account for the dramatic difference between BIS and XAS for $CeNi_2$. Actually the theory exaggerates this difference. To obtain the proper weights in XAS the assumed value of n_f has to be reduced from 0.83 to 0.77.

The f-level PES spectrum of $CeNi_2$ has a pronounced two peak structure. The peak at $\varepsilon_F = 0$ has several contributions. As was discussed in section 4.2 below eq. (109) the $U = \infty$ spectrum has a 'Kondo peak' at $\varepsilon_F = 0$. Since the ground state of $CeNi_2$ has a substantial f^0 weight (~ 0.21), the Kondo peak has an appreciable weight. As discussed in the context of fig. 9 the weight of the peak close to $\varepsilon_F = 0$ is further enhanced when the finite value of U is taken into account. Finally there is a contribution to this peak which we may refer to as a hybridization contribution (Sakai et al. 1984, Gunnarsson and Schönhammer 1985a,b). This comes from the continuum part of $\tilde{g}$ in eqs. (104)–(106). The $\tilde{\Gamma}$ entering $\tilde{g}$ has a sharp cut-off at $\varepsilon = 0$, due to the large degeneracy, which gives rise to the 'pole contribution' (109) and the 'Kondo peak'. Apart from this cut-off, $\tilde{g}$ has the same structure as the f-level Green's function of a $N_f = 1$ (noninteracting) system with the hybridization $\tilde{V}(\varepsilon)$.

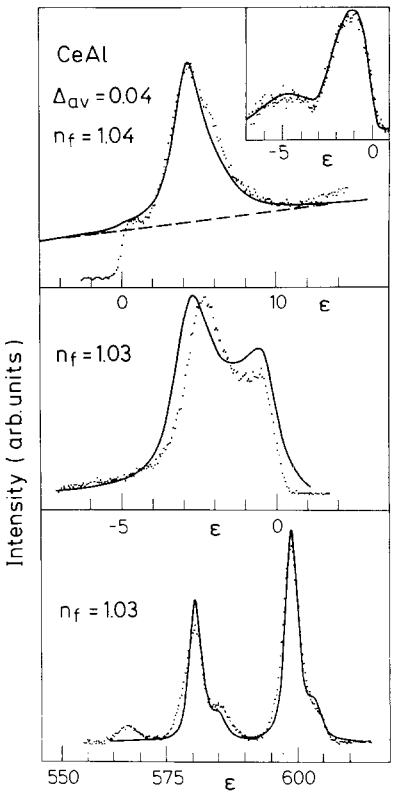

Fig. 18. The 3d XPS, 4f PES and BIS spectra of CeAl (Allen et al. 1986). The curves have the same meaning as in fig. 17. The parameters are $U_{fc} = 10.0\,\text{eV}$, $U = 6.7\,\text{eV}$ (XPS and PES) and $U_{av} = 6.5\,\text{eV}$ (BIS).

This hybridization can give rise to further structure. For $CeNi_2$ the f-level is located close to the peak of $V(\varepsilon)^2$. The peak in $\text{Im}\tilde{g}(\varepsilon - i0)$ that one might have expected at $\varepsilon_f = -1.6\,\text{eV}$ is therefore split into two peaks. One peak appears below the main weight of $V(\varepsilon)^2$ at roughly $\varepsilon \sim -3.5\,\text{eV}$ and one is shifted upwards towards $\varepsilon \sim 0$. The function $\tilde{g}$ is inserted in eq. (106) and the ε-integration is performed. Since $a(\varepsilon)^2$ is rather peaked at $\varepsilon = 0$, this integration only introduces some broadening. There is therefore a hybridization contribution to the peak close to $\varepsilon = 0$ in the spectrum. It is interesting that due to the strong hybridization the PES spectrum has a *minimum* close to ε_f and neither of the peaks is close to ε_f.

Figure 18 shows results for CeAl (Allen et al. 1986). For all the spectra the same values of n_f and Δ_{av} were used. For the BIS spectrum U was slightly reduced to give the appropriate position for the f^2 peak. The PES spectrum was given an additional Lorentzian broadening of 0.6 eV (FWHM), since the structures were otherwise too sharp compared with experiment. The source of this broadening is unclear, but it could conceivably be due to lattice effects or effects from the finite value of U_{fd} discussed by Takeshige et al. (1985). The f^0 weight in the ground state is very small (<0.01) and the Kondo peak has negligible weight. It should therefore not be very important that we assumed a singlet state in the calculations, although CeAl is magnetic. In spite of the unimportance of the Kondo peak CeAl has a substantial

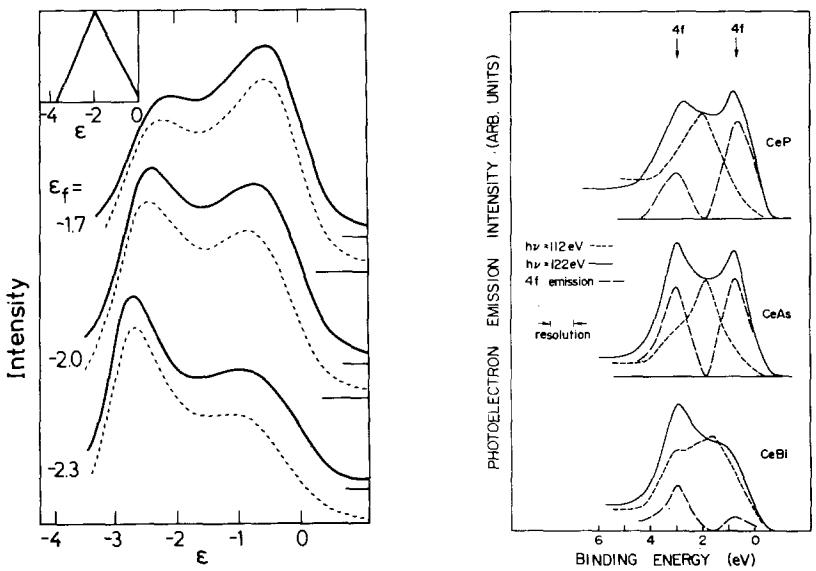

Fig. 19. Right: the experimental valence PES spectra of CeP, CeAs and CeBi at resonance ($\hbar\omega = 122$ eV, full curve) and off resonance ($\hbar\omega = 112$ eV, dashed curve) (Franciosi et al. 1981). Left: the calculated PES spectrum for different values of ε_f using the $V(\varepsilon)^2$ shown in the insert (Gunnarsson and Schönhammer 1985b). The full (dashed) curve shows results for $U = 6$ eV ($U = \infty$). The parameter $N_f \Delta_{av}$ was set to 0.7 eV.

weight close to $\varepsilon_F = 0$. This is primarily due to finite U effects, illustrating the importance of taking into account that $U < \infty$, and to hybridization effects.

In fig. 19 results for the valence PES spectra of the Ce pnictides are shown (Gunnarsson and Schönhammer 1985b). The off-resonance spectra of the pnictides show spectra with a peak at $\varepsilon \sim -2$ eV. For simplicity we have therefore used a simple triangular shape for $V(\varepsilon)^2$ as shown in the insert. The figure shows results for both $U = \infty$ and for a finite U. In this case the finite U effects have a small influence on the spectra. The weight of the 'Kondo peak' is also negligible. In these cases the hybridization effects dominate. The same conclusion was reached by Sakai et al. (1984).

Valence PES spectra for α- and γ-Ce are shown in fig. 20. There has been much interest in Ce, since measurements with a good resolution (~0.1 eV) seemed to indicate that the low binding energy peak is somewhat below ε_F in γ-Ce but not in α-Ce (Wieliczka et al. 1984). The work by Patthey et al. (1985) in fig. 20 represents an important progress, since their high resolution (~0.02 eV) spectra showed that there are actually two structures close to ε_F and that there is a transfer of weight away from the peak closest to ε_F in going from α- to γ-Ce. Patthey et al. (1985) demonstrated that these results can be understood if the spin-orbit splitting (0.28 eV) of the f-level is included in the formalism (Gunnarsson and Schönhammer 1983b). Patthey et al. (1985) found that the peaks are related to the 4f 5/2 and 4f 7/2 levels and that the relative weight of the 4f 5/2 level increases in going from γ-Ce to α-Ce. The importance of the spin-orbit splitting for the shape of a high-resolution

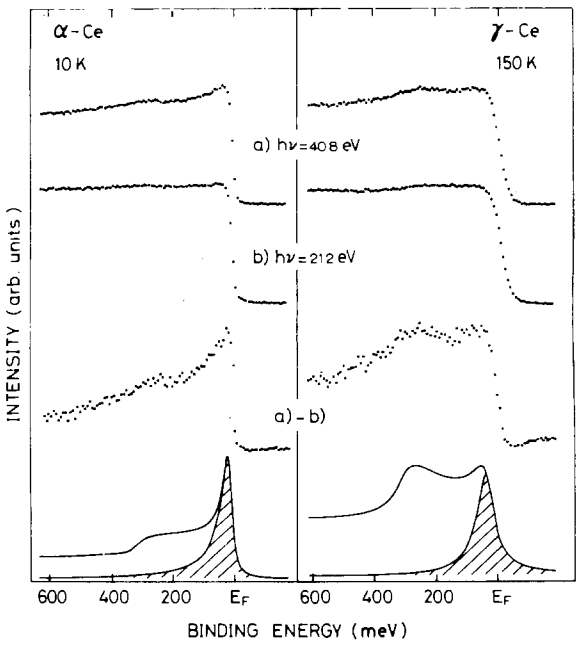

Fig. 20. Experimental (dots) and theoretical (full line) spectra of α- and γ-Ce. The experimental results were obtained for the photon energies 40.8 eV (a) and 21.2 eV (b). The difference (a – b) provides an estimate of the f-spectrum. The results are reproduced from Patthey et al. (1985).

spectrum was first shown by Bickers et al. (1985) and by Watanabe and Sakuma (1985).

5.4. *Yb compounds*

In the Yb compounds the f^{13} and f^{14} configurations play the same role as the f^1 and f^0 configurations in Ce compounds. It is therefore possible to map the Ce results onto the Yb compounds, by considering (the Yb) f-holes instead of (the Ce) f-electrons (Bickers et al. 1985, Jones and Wilkins 1985). An interesting difference is, however, that the spin-orbit splitting is much larger for Yb ($\Delta_{so} \approx 1.2$ eV) than for Ce ($\Delta_{so} \approx 0.28$ eV). This greatly improves the possibilities of seeing the effects of the spin-orbit splitting in the Yb spectra. As shown in fig. 21a, the calculated spectrum shows two spin-orbit induced peaks at $\sim\varepsilon_F \pm \Delta_{so}$ for appropriate parameters (Jones and Wilkins 1985). The spectrum changes shape in an interesting way as $\varepsilon_f \equiv E(f^{14}) - E(f^{13})$ becomes smaller than $\varepsilon_F + \Delta_{so}$ (fig. 21b), and the peak at $\varepsilon_F + \Delta_{so}$ becomes an antiresonance (Bickers et al. 1985).

Monnier et al. (1986) have studied YbP. They performed a band calculation in the LSD approximation. The band structure was parameterized in a linear combination of atomic orbital formalism. This allowed the extraction of the hopping matrix elements $V_{k\alpha m}$ between the 4f state and the non-f bands. These values of $V_{k\alpha m}$ were used in the Anderson model (1) and a $V(\varepsilon)^2$ was generated. The $V(\varepsilon)^2$ has similarities with the conduction density of states $\rho(\varepsilon)$, but it also has definite deviations from $\rho(\varepsilon)$. The value of ε_f was chosen so that the model calculation gave the same value of n_f as the band calculation. In this approach both $V(\varepsilon)^2$ and ε_f were therefore

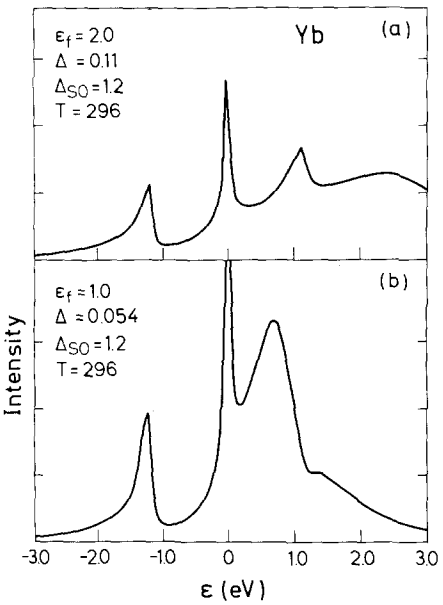

Fig. 21. The valence spectrum for Yb calculated in the NCA. The density of states was assumed to have a Lorentzian shape with the half-width $D = 3$. All energies are in eV. The results are reproduced from Jones and Wilkins (1985) and from Bickers et al. (1985).

obtained from first principles, and the only adjustable parameter was the value of U. Monnier et al. (1986) then calculated the PES and BIS spectra, considering the f^{12}, f^{13} and f^{14} configurations. With an appropriate instrumental broadening their BIS spectrum showed a bump centered at $\varepsilon \sim 0.22$ eV and with a width of 0.70 eV. Preliminary measurements (Baer et al. 1985) showed a similar feature centered at $\varepsilon \sim 0.65$ eV and with a width of ~ 1 eV. The deviation in the peak position was ascribed to the method for determining n_f and/or the position of the phosphorous p-bands in the calculation (Monnier et al. 1986). In general it is nontrivial to distinguish between the 'true' 4f-charge on an Yb atom and the $l = 3$ component of the overlapping charge densities from the neighbouring atoms. Monnier et al. (1986) therefore concluded that their method would tend to put the f-level at a too low energy. Furthermore, the LSD approximation may put the phosphorous p-bands at a too high energy, which would also lead to a too large f-occupancy (Monnier et al. 1986). Both effects could contribute to the deviation from experiment. For the PES spectrum Monnier et al. (1986) obtained peaks at $\varepsilon \approx -6.2$ eV and at $\varepsilon \approx 0$ eV. While the peak at $\varepsilon \approx -6.2$ eV has been observed experimentally, the peak at $\varepsilon \approx 0$ has a negligible weight (Baer et al. 1985). As for the BIS spectrum, this deviation could be ascribed to an overestimate of the f-charge (Monnier et al. 1986). Although the approach of Monnier et al. (1986) cannot fully describe the experimental data, their calculation of V_{kam} represents a promising attempt to obtain a first principles theory of Yb compounds.

5.5. *Pr and Nd compounds*

In La, Ba and Ce compounds the f^0 and/or f^1 configurations dominate. For Pr and Nd compounds configurations with more f electrons become important, and the

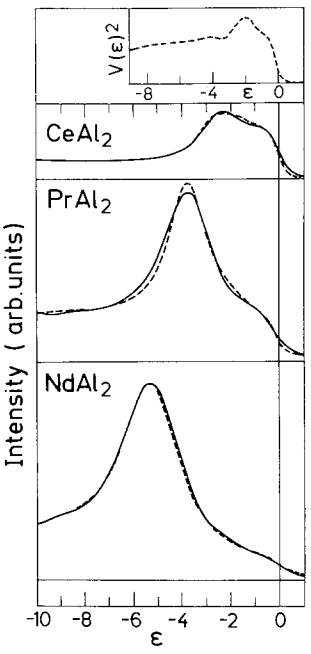

Fig. 22. Experimental (full curve) and theoretical (dashed curve) results for $CeAl_2$, $PrAl_2$ and $NdAl_2$. For Δ_{av} the values 0.032 eV ($CeAl_2$), 0.022 eV ($PrAl_2$) and 0.006 eV ($NdAl_2$) were used, and for ε_f the values -2.2 eV ($CeAl_2$), -3.5 eV ($PrAl_2$) and -5.1 eV ($NdAl_2$) were used. The experimental results are reproduced from Parks et al. (1984, 1985).

theory developed for Ce compounds is not automatically applicable. As a preliminary test one can, however, map the f^{n+1} (f^{n+2}) configuration of Pr(Nd) onto the f^n configuration of Ce and use the theory discussed before. In such an approach Pr and Nd only differs from Ce through a change of Δ_{av} and ε_f. This approach neglects that the prefactors of the matrix elements (e.g., $\sqrt{N_f}$) depend on the number of f-electrons. Furthermore, multiplet effects are then not appropriately included or neglected altogether as in the approach here. Finally we assume below that the ground state is a singlet although the Pr and Nd compounds are magnetic.

This kind of treatment has been applied to $Pr_{0.9}Th_{0.1}$, and $PrRu_2$ (Gunnarsson and Schönhammer 1985a) and to $PrAl_2$ and $NdAl_2$ (Allen et al. 1986). In fig. 22 we show results for $CeAl_2$, $PrAl_2$ and $NdAl_2$. The experimental results are from Parks et al. (1984, 1985) and the theoretical results from Allen et al. (1986). The shape of $V(\varepsilon)^2$ was estimated as described in section 5.3. The curve $V(\varepsilon)^2$, shown in the inset of fig. 22, has been broadened by the experimental resolution and an inelastic background has been added. It is in good agreement with experiment. In the calculated PES spectra an instrumental resolution (0.6 eV FWHM Gaussian) and an inelastic background have been included. In such an approach the peak at $\sim\varepsilon_f$ is too narrow for $PrAl_2$ and $NdAl_2$. The reason is probably the neglect of lifetime broadening effects in the theory. In the calculations we have therefore also introduced a lifetime broadening (eq. (144)) with $\Gamma_1 = 0.046\,\text{eV}^{-1}$. The calculated spectra are in good agreement with experiment, although the peak at ~ -3.8 eV in $PrAl_2$ is somewhat too narrow and the peak at ~ -2.5 eV in $CeAl_2$ is somewhat too broad. In particular, the low-binding-energy structures in $CeAl_2$ and $PrAl_2$ are well

described. These structures result from hybridization between the f-level and the conduction band and from effects due to the finite value of U. These structures are not associated with Kondo-like effects.

6. Concluding remarks

In this chapter different methods for calculating electron spectra of the Anderson impurity model have been presented. In particular, the recent development in terms of $1/N_f$ expansions was emphasized. It was demonstrated that for $T = 0$ there are now fairly accurate calculations available, even for small values of the degeneracy N_f. In particular it is possible to obtain a fair description of the so-called Kondo resonance.

The extension of the work described here to the Anderson lattice is an interesting but difficult problem. It would also be interesting to include more terms in the Anderson impurity model, describing for instance multiplet effects, Auger decay and the direct f–d Coulomb interaction. The determination of the parameters in the model from first principles is an important problem. Much progress has been made by Herbst et al. (1978) and by Herbst and Wilkins (1979) for U, U_{fc} and ε_f and there are promising attempts to estimate $V_{k\alpha m}$ from band structure calculations.

The spectra of the Anderson impurity model have been compared extensively with experimental results for many different lanthanide compounds. Some of this work was reviewed in section 5. It was shown that the model gives a surprisingly good description of the experimental results. In particular, it was shown that for a given compound essentially the same parameters can be used to describe the different spectroscopies. It was, however, also found that the neglected multiplet effects often are important and that there are broadening effects, which are not included in the model.

As mentioned in the introduction, an important issue has been the magnitude of the parameters in the Anderson model. The values of Δ and $|\varepsilon_f - \varepsilon_F|$ obtained from electron spectroscopies have usually been one or two orders of magnitude larger than most estimates based on thermodynamic measurements. Calculations for the Anderson model show, however, that for the mixed valence compounds, the 'spectroscopic' parameters lead to predictions for the thermodynamic properties, which are of the right order of magnitude (Gunnarsson and Schönhammer 1983b, 1985b, Gunnarsson et al. 1983). Although the spectroscopic parameters ($|\varepsilon_f - \varepsilon_F|$, $N_f\Delta$) are of the order eV, the model also leads to a small energy scale ('Kondo temperature') related to a narrow resonance at the Fermi energy, which is necessary for the understanding of the thermodynamic properties, such as the susceptibility and specific heat at low temperatures. Early work (Kuramoto and Müller-Hartmann 1981) on the width $\Gamma/2$ of the quasi-elastic peak in neutron scattering suggested that $\Gamma/2$ is proportional to Δ for $n_f \lesssim 0.6$, which was believed to be relevant for many Ce compounds. Since $\Gamma/2$ typically is in the meV range, this supported the belief that Δ is very small. More recent work, however, shows that the Kondo temperature provides the relevant energy scale for the peak width

(Kuramoto and Kojima 1984, Bickers et al. 1985, Gunnarsson and Schönhammer 1985d,e), making our present values of Δ consistent with the order of magnitude of $\Gamma/2$. This work also predicts an interesting fine structure in the line shape, due to the breaking up of the Kondo singlet (Kuramoto and Kojima 1984, Gunnarsson and Schönhammer 1985d,e), which appears to have been observed experimentally (Galera et al. 1985). The values of n_f obtained here are substantially larger than the older ones deduced from lattice parameter data. The estimates based on the lattice parameter assume that the contribution of the f-states to the cohesion can be neglected. This leads to an underestimate of n_f, which can be substantial for the present large values of Δ (Gunnarsson and Schönhammer 1983b). This mechanism enters in the so-called Kondo volume collapse model introduced by Allen and Martin (1982) to explain the γ–α transition of Ce.

Electron spectroscopies are particularly well suited for studies of high-energy excitations. Valence PES and BIS can in principle also give information about the low-energy excitations (compare eq. (109) and eq. (112)). The Kondo peak has, for instance, been seen in several Ce mixed valence compounds. For systems closer to the spin-fluctuation limit, the spectroscopic study of low-energy excitations is, however, in practice very difficult. This is partly due to experimental resolution problems and partly due to matrix element effects (see section 4.2), which in this limit greatly reduce the integrated weight of the Kondo peak in the one-particle spectrum. Nevertheless the electron spectroscopies can complement 'low-energy measurements', even for the study of low-energy excitations. With the presently available spectroscopic resolution the 'low-energy' experiments are superior in probing the quasiparticle density of states. The spectroscopic data, interpreted with a theoretical model, can, however, give information about the nature and origin of these low-energy excitations. For the Ce compounds the spectroscopic estimates of $|\varepsilon_f - \varepsilon_F|$ and Δ are inconsistent with the promotional model and similar models, while they provide a strong support for the interpretation of the large quasiparticle density of states at ε_F as a Kondo resonance.

7. Recent developments

Below we briefly review a few of the developments after this chapter had been submitted (February, 1986). There has been a substantial amount of work on the extension of the impurity model to a lattice model. Rice and Ueda (1985) and Fazekas and Brandow (1987) used a generalized Gutzwiller ansatz for the spin-degenarate Anderson lattice. Saso and Seino (1986) and Blankenbecler et al. (1987) used the Monte Carlo technique for studying a finite one-dimensional chain. Millis and Lee (1987) used the slave boson formalism for the large degeneracy Anderson lattice. A renormalization group calculation has also been performed for the two-impurity model by Jones and Varma (1987).

Gunnarsson and Schönhammer (1987) and Gunnarsson and Li (1987) have developed a formalism for resonance photoemission in the $1/N_f$ technique. The constant initial state (CIS) spectrum was studied. It was found that the CIS

spectrum is strongly influenced by interference effects between the intermediate f^2 and f^3 configurations, which are the important configurations after the $4d \rightarrow 4f$ excitation but before the Auger decay. This interference can explain the different CIS spectra for the 'Fermi energy peak' and the '2 eV peak' in resonance photoemission. Similar effects were also found to be important for the 4f CIS spectrum of UO_2 close to the resonance due to the $3d \rightarrow 5f$ transition (Gunnarsson et al. 1987).

Degiorgi et al. (1987) have studied the 3d core spectrum of YbP. They used the values for the hopping matrix elements determined earlier from a first-principle band structure calculation (Monnier et al. 1986). The agreement with experiment is good, providing important support for their method of calculating hopping matrix elements.

Appendix

In this appendix we briefly review some numerical methods for the ground-state calculations and for the calculations of the spectra.

For a 'small' basis set the ground-state calculation can be performed directly (see section 4.1). For a 'larger' basis set one can use a Chebyshev iterative method (Gunnarsson and Schönhammer 1985a) or Lanczos's method (Parlett 1980). The Green's function can be calculated using a 'folding' method (Gunnarsson and Schönhammer 1983b), a time-dependent method (Gunnarsson and Schönhammer, 1985a) or Lanczos's method (Parlett 1980, Haydock 1980). Here we describe the Lanczos or recursion method briefly.

In this method a new basis set is found, which tridiagonalizes H. The spectrum is then obtained from a continued fraction expansion. The first function in the new basis set is

$$|v_0\rangle = T|E_0(N)\rangle, \tag{A1}$$

where T is, e.g., the operator ψ_ν in eq. (52). Due to this choice, the spectrum is given by the element $[z - E_0(N) + H)^{-1}]_{00}$, when H is expressed in the new basis. The basis states are now generated by the formula

$$(H - E_0(N))|v_n\rangle = b_{n+1}|v_{n+1}\rangle + a_n|v_n\rangle + b_n|v_{n-1}\rangle, \tag{A2}$$

where $|v_{-1}\rangle = 0$. The requirement that $|v_n\rangle$ is orthogonal to $|v_{n+1}\rangle$ and $|v_{n-1}\rangle$ gives

$$a_n = \langle v_n|H - E_0(N)|v_n\rangle, \tag{A3}$$

$$b_{n+1}|v_{n+1}\rangle = (H - E_0(N))|v_n\rangle - a_n|v_n\rangle - b_n|v_{n-1}\rangle. \tag{A4}$$

and the requirement that $|v_{n+1}\rangle$ is normalized gives b_{n+1} and $|v_{n+1}\rangle$. In this way $H - E_0(N)$ is transformed to a tridiagonal form. Due to numerical rounding errors, the set $\{|v_n\rangle\}_{n=0}^{N}$ rapidly becomes linearly dependent as N is increased. This method can, nevertheless, provide accurate results for a few of the extreme eigenvalues and the corresponding eigenstates (Parlett 1980). In particular, for $|v_0\rangle = |0\rangle$ this method can be used to calculate the ground state. The element $[z - E_0(N) +$

$H)^{-1}]_{00}$, needed for the spectrum, can be obtained from a continued fraction expansion (Haydock, 1980).

$$[(z - E_0(N) + H)^{-1}]_{00} = 1/\{z + a_0 - b_1^2/[z + a_1 - b_2^2/(z - \cdots)]\}. \quad \text{(A5)}$$

Provided that z has a finite imaginary part, this provides an efficient method for evaluating the Green's functions discussed in section 4. The calculation of (A3) and (A4) is fast, since H is very sparse for the cases of interest here. Compared with the time-dependent method (Gunnarsson and Schönhammer 1985a), the numerical effort is essentially comparable but somewhat smaller in the Lanczos method. Both methods give identical results within the numerical accuracy.

References

Abrikosov, A.A., 1965, Physics **2**, 5.

Allen, J.W., 1985, J. Magn. & Magn. Mater. **52**, 135.

Allen, J.W., and R.M. Martin, 1982, Phys. Rev. Lett. **49**, 1106.

Allen, J.W., S.-J. Oh, I. Lindau, J.M. Lawrence, L.I. Johansson and S.B.M. Hagström, 1981, Phys. Rev. Lett. **46**, 1100.

Allen, J.W., S.-J. Oh, M.B. Maple and M.S. Torikachvili, 1983, Phys. Rev. B **28**, 5347.

Allen, J.W., S.-J. Oh, O. Gunnarsson, K. Schönhammer, M.B. Maple, M. Torikachvili and I. Lindau, 1986, Adv. Phys. **35**, 275.

Anderson, P.W., 1961, Phys. Rev. **124**, 41.

Anderson, P.W., 1967, Phys. Rev. Lett. **18**, 1049.

Anderson, P.W., 1982, Summary talk, in:Valence Fluctuations in Solids, eds L.M. Falicov, W. Hanke and M.B. Maple (North-Holland, Amsterdam) p. 451.

Baer, Y., E. Wuilloud, H.R. Ott and F. Hulliger, 1985, unpublished.

Barnes, S.E., 1976, J. Phys. F **6**, 1375.

Bickers, N.E., D.L. Cox and J.W. Wilkins, 1985, Phys. Rev. Lett. **54**, 230.

Blankenbecler, R., J.R. Fulco, W. Gill and D.J. Scalapino, 1987, Phys. Rev. Lett. **58**, 411.

Bonnelle, C., R.C. Karnatak and J. Sugar, 1974, Phys. Rev. A **9**, 1920.

Brandt, U., H. Keiter and F.S. Liu, 1985, Z. Phys. B **58**, 267.

Brenig, W., and K. Schönhammer, 1974, Z. Phys. B **267**, 201.

Coleman, P., 1984, Phys. Rev. B **29**, 3035.

Coleman, P., 1985, Modelling mixed valence systems using the generalized Anderson model, in: Proc. 8th Taniguchi Symposium, eds T. Kasuya and T. Saso (Springer, Berlin) p. 163.

Cox, D.L., 1985, Ph.D. Thesis, Cornell University.

Croft, M., J.H. Weaver, D.J. Peterman and A. Franciosi, 1981, Phys. Rev. Lett. **46**, 1104.

Czycholl, G., 1985, Phys. Rev. B **31**, 2867.

de Châtel, P.F., 1982, Solid State Commun. **41**, 853.

Degiorgi, L., T. Greber, F. Hullinger, R. Monnier, L. Schlabach and B.T. Thole, 1987, to be published.

Delley, B., and H. Beck, 1984, J. Phys. C **17**, 4971.

Delley, B., and H. Beck, 1985, J. Magn. & Magn. Mater. **47&48**, 269.

Dow, J.D., and C.P. Flynn, 1980, J. Phys. C **13**, 1341.

Esteva, J.M., R.C. Karnatak, J.C. Fuggle and G.A. Sawatzky, 1983, Phys. Rev. Lett. **50**, 910.

Fazekas, P., and B.H. Brandow, 1987, to be published.

Franciosi, A., J.H. Weaver, N. Mårtensson and M. Croft, 1981, Phys. Rev. B **24**, 3651.

Fuggle, J.C., E. Umbach, D. Menzel, K. Wandelt and C.R. Brundle, 1978, Solid State Commun. **27**, 65.

Fuggle, J.C., R. Lässer, O. Gunnarsson and K. Schönhammer, 1980a, Phys. Rev. Lett. **44**, 1090.

Fuggle, J.C., M. Campagna, Z. Zolnierek, R. Lässer and A. Platau, 1980b, Phys. Rev. Lett. **45**, 1597.

Fuggle, J.C., F.U. Hillebrecht, J.-M. Esteva, R.C. Karnatak, O. Gunnarsson and K. Schönhammer, 1983a, Phys. Rev. B **27**, 4637.

Fuggle, J.C., F.U. Hillebrecht, Z. Zolnierek, R. Lässer, Ch. Freiburg, O. Gunnarsson and K. Schönhammer, 1983b, Phys. Rev. B **27**, 7330.

Fuggle, J.C., G.A. Sawatzky, O. Gunnarsson and K. Schönhammer, 1987, to be published.

Fujimori, A., 1983a, Phys. Rev. B **27**, 3992.

Fujimori, A., 1983b, Phys. Rev. B **28**, 2281.

Fujimori, A., 1983c, Phys. Rev. B **28**, 4489.

Galera, R.M., D. Givord, J. Pierre, A.P. Murani, J. Schweizer, C. Vettier and K.R.A. Ziebeck, 1985, J. Magn. & Magn. Mater. **52**, 103.

Glötzel, D., 1978, J. Phys. F **8**, L163.

Grewe, N., 1982, Renormalized perturbation expansion for Green's functions of intermediate valence systems, in: Valence Instabilities, eds P. Wachter and H. Boppart (North-Holland, Amsterdam) p. 21.

Grewe, N., 1983a, Z. Phys. B **52**, 193.

Brewe, N., 1983b, Z. Phys. B **53**, 271.
Brewe, N., and H. Keiter, 1981, Phys. Rev. B **24**, 4420.
Gunnarsson, O., and T.C. Li, 1987, to be published.
Gunnarsson, O., and K. Schönhammer, 1978, Phys. Rev. Lett. **41**, 1608.
Gunnarsson, O., and K. Schönhammer, 1982, Phys. Rev. **26**, 2765.
Gunnarsson, O., and K. Schönhammer, 1983a, Phys. Rev. Lett. **50**, 604.
Gunnarsson, O., and K. Schönhammer, 1983b, Phys. Rev. B **28**, 4315.
Gunnarsson, O., and K. Schönhammer, 1985a, Phys. Rev. B **31**, 4815.
Gunnarsson, O., and K. Schönhammer, 1985b, Ground-state and spectroscopic properties of the finite U Anderson model, in: Proc. 8th Taniguchi Symposium, eds T. Kasuya and T. Saso (Springer, Berlin) p. 110.
Gunnarsson, O., and K. Schönhammer, 1985c, J. Magn. & Magn. Mater. **52**, 141.
Gunnarsson, O., and K. Schönhammer, 1985d, J. Magn. & Magn. Mater. **52**, 227.
Gunnarsson, O., and K. Schönhammer, 1985e, The frequency-dependent susceptibility in the Anderson model, in: Proc. 8th Taniguchi Symposium, eds T. Kasuya and T. Saso (Springer, Berlin) p. 100.
Gunnarsson, O., and K. Schönhammer, 1987, Intermediate valence spectroscopy, in: Giant Resonances in Atoms, Molecules and Solids, eds J.P. Connerade, J.-M. Esteva and R.C. Karnatak (Plenum, New York) p. 405.
Gunnarsson, O., K. Schönhammer, J.C. Fuggle, F.U. Hillebrecht, J.-M. Esteva, R.C. Karnatak and B. Hillebrand, 1983, Phys. Rev. B **28**, 7330.
Gunnarsson, O., K. Schönhammer, D.D. Sarma, F.U. Hillebrecht and M. Campagna, 1985, Phys. Rev. B **32**, 5499.
Gunnarsson, O., D.D. Sarma, F.U. Hillebrecht and K. Schönhammer, 1987, to be published.
Haldane, F.D.M., 1981, Scaling approach to impurity configurational fluctuations in metals, in: Valence Fluctuations in Solids, eds L.M. Falicov, W. Hanke and M.B. Maple (North-Holland, Amsterdam) p. 153.
Haydock, R., 1980, in: Solid State Physics, Vol. 35, eds H. Ehrenreich, D. Turnball and F. Seitz (Academic, New York) p. 215.
Hedin, L., and S. Lundqvist, 1969, in: Solid State Physics, Vol. 23, eds H. Ehrenreich, D. Turnbull and F. Seitz (Academic Press, New York) p. 1.
Herbst, J.F., and J.W. Wilkins, 1979, Phys. Rev. Lett. **43**, 1760.
Herbst, J.F., R.E. Watson and J.W. Wilkins, 1978, Phys. Rev. B **17**, 3089.
Hewson, A.C., 1966, Phys. Rev. **144**, 420.
Hillebrecht, F.U., J.C. Fuggle, G.A. Sawatzky, M. Campagna, O. Gunnarsson and K. Schönhammer, 1984, Phys. Rev. B **30**, 1777.
Hüfner, S., and P. Steiner, 1982, Z. Phys. B **46**, 37.
Iandelli, A., and A. Palenzona, 1979, Crystal chemistry of intermetallic compounds, in: Handbook on the Physics and Chemistry of Rare Earths, Vol. 3, eds K.A. Gschneidner Jr and L. Eyring (North-Holland, Amsterdam) p. 1.
Iangaki, S., 1979, Prog. Theor. Phys. **62**, 1441.
Johansson, B., 1974, J. Phys. F **4**, L 169.
Johansson, L.I., J.W. Allen, T. Gustafsson, I. Lindau and S.B.M. Hagström, 1978, Solid State Commun. **28**, 53.
Jones, B.A., and C.M. Varma, 1987, Phys. Rev. Lett. **58**, 843.
Jones, B.A., and J.W. Wilkins, 1985, Bull. Am. Phys. Soc. **30**, 637; private communication.
Jones, R.O., 1985, private communication.
Kaindl, G., G. Kalkowski, W.D. Brewer, B. Perscheid and F. Holtzberg, 1984, J. Appl. Phys. **55**, 1910.
Kasuya, T., O. Sakai, K. Takegahara and M. Takeshige, 1985, J. Magn. & Magn. Mater. **52**, 1.
Kawakami, N., and A. Okiji, 1981, Phys. Lett. A **86**, 483.
Keiter, H., and G. Czycholl, 1983, J. Magn. & Magn. Mater. **31**, 477.
Keiter, H., and J.C. Kimball, 1971, Int. J. Magn. **1**, 233.
Keiter, H., and G. Morandi, 1984, Phys. Rep. **109**, 227.
Koelling, D.D., 1982, Solid State Commun. **43**, 247.
Kohn, W., and L.J. Sham, 1965, Phys. Rev. **140**, A1133.
Kojima, H., Y. Kuramoto and M. Tachiki, 1984, Z. Phys. B **54**, 293.
Kotani, A., and J.C. Parlebas, 1985, J. Phys. (France) **46**, 77.
Kotani, A., and Y. Toyozawa, 1974a, J. Phys. Soc. Jpn. **37**, 563.
Kotani, A., and Y. Toyozawa, 1974b, J. Phys. Soc. Jpn. **37**, 912.
Kotani, A., H. Mizuta, T. Jo and J.C. Parlebas, 1985, Solid State Commun. **53**, 805.
Kuramoto, Y., 1983, Z. Phys. B **53**, 37.
Kuramoto, Y., and H. Kojima, 1984, Z. Phys. B **57**, 95.
Kuramoto, Y., and E. Müller-Hartmann, 1981, in: Valence Fluctuations in Solids, eds L.M. Falikov, W. Hanke and M.B. Maple (North-Holland, Amsterdam) p. 139.
Kuramoto, Y., and E. Müller-Hartmann, 1985, J. Magn. & Magn. Mater. **52**, 122.
Lacroix, C., 1981, J. Phys. F **11**, 2389.
Lang, J.K., Y. Baer and P.A. Cox, 1981, J. Phys. F **11**, 121.
Lang, N.D., and A.R. Williams, 1977, Phys. Rev. B **16**, 2408.
Langreth, D.C., 1966, Phys. Rev. **150**, 516.
Lawrence, J.M., P.S. Riseborough and R.D. Parks, 1981, Rep. Prog. Phys. **44**, 1.
Ley, L., N. Mårtensson and J. Azoulay, 1980, Phys. Rev. Lett. **45**, 1516.

Liu, S.H., and K.-M. Ho, 1982, Phys. Rev. B **26**, 7052.
Luttinger, J.M., 1961, Phys. Rev. **121**, 942.
Mårtensson, N., B. Reihl and R.D. Parks, 1982, Solid State Commun. **41**, 573.
Martin, R.M., 1982, Phys. Rev. Lett. **48**, 362.
Millis, A.J., and P.A. Lee, 1987, Phys. Rev. B **35**, 3394.
Monnier, R., L. Degiorgi and D.D. Koelling, 1986, Phys. Rev. Lett. **56**, 2744.
Müller-Hartmann, E., 1984, Z. Phys. B **57**, 281.
Norman, M.R., 1985, Phys. Rev. B **31**, 6261.
Norman, M.R., D.D. Koelling and A.J. Freeman, 1985, Phys. Rev. B **31**, 6251.
Nozières, P., and C.T. de Dominicis, 1969, Phys. Rev. **178**, 1097.
Nunez-Regueiro, M.D., and M. Avignon, 1985, Phys. Rev. Lett. **55**, 615.
Oh, S.-J., and S. Doniach, 1982, Phys. Rev. B **26**, 2085.
Parks, R.D., S. Raaen, M.L. den Boer, Y.-S. Chaug and G.P. Williams, 1984, private communication.
Parks, R.D., S. Raaen, M.L. den Boer, Y,-S. Chaug and G.P. Williams, 1985, J. Magn. & Magn. Mater. **47&48**, 163.
Parlett, B.N., 1980, The symmetric eigenvalue problem (Prentice, Englewood) p. 257.
Patthey, F., B. Delley, W.-D. Schneider and Y. Baer, 1985, Phys. Rev. Lett. **55**, 1518.
Platau, A., and S.-E. Karlsson, 1978, Phys. Rev. B **18**, 3820.
Podloucky, R., and D. Glötzel, 1983, Phys. Rev. B. **27**, 3390.
Ramakrishnan, T.V., 1982, Perturbative theory of mixed valence systems, in: Valence Fluctuations in Solids, eds L.M. Falicov, W. Hanke and M.B. Maple (North-Holland, Amsterdam) p. 13.
Ramakrishnan, T.V., and K. Sur, 1982, Phys. Rev. B **26**, 1798.
Rasul, J.W., and A.C. Hewson, 1983, J. Phys. C **16**, L933.
Rasul, J.W., and A.C. Hewson, 1984a, J. Phys. C **17**, 2555.
Rasul, J.W., and A.C. Hewson, 1984b, J. Phys. C **17**, 3337.
Read, N., 1985, J. Phys. C **18**, 2651.
Read, N., and D.M. Newns, 1983, J. Phys. C **16**, 3273.
Read, N., and D.M. Newns, 1984, Solid State Commun. **52**, 993.
Read, N., D.M. Newns and S. Doniach, 1984, Phys. Rev. B **30**, 3841.
Rice, T.M., and K. Ueda, 1985, Phys. Rev. Lett. **55**, 995.
Riseborough, P.S., 1985, J. Magn. & Magn. Mater. **47&48**, 271.
Sakai, O., H. Takahashi, M. Takeshige and T. Kasuya, 1984, Solid State Commun. **52**, 997.
Saso, T., and Y. Seino, 1986, J. Phys. Soc. Jpn. **55**, 3729.
Schlottmann, P., 1983, Phys. Rev. Lett. **50**, 1697.
Schneider, W.-D., B. Delley, E. Wuilloud, J.-M. Imer and Y. Baer, 1985, Phys. Rev. **32**, 6819.
Schönhammer, K., 1977, Solid State Commun. **22**, 51.
Schönhammer, K., and O. Gunnarsson, 1977, Solid State Commun. **23**, 691.
Schönhammer, K., and O. Gunnarsson, 1978a, Solid State Commun. **26**, 399.
Schönhammer, K., and O. Gunnarsson, 1978b, Z. Phys. B **30**, 297.
Schönhammer, K., and O. Gunnarsson, 1984, Phys. Rev. B **30**, 3141.
Skriver, H.L., 1981, Electronic transitions in praseodymium under pressure, in: Physics of Solids under High Pressure, eds J.S. Schilling and R.N. Shelton (North-Holland, Amsterdam) p. 276.
Suhl, H., 1965, Phys. Rev. **138**, A515.
Takeshige, M., O. Sakai and T. Kasuya, 1985, J. Magn. & Magn. Mater. **52**, 363.
Theumann, A., 1969, Phys. Rev. **178**, 978.
Thole, B.T., G. van der Laan, J.C. Fuggle, G.A. Sawatzky, R.C. Karnatak and J.-M. Esteva, 1985, Phys. Rev. B **32**, 5107.
van der Laan, G., B.T. Thole, G.A. Sawatzky, J.C. Fuggle, R. Karnatak, J.-M Esteva and B. Lengler, 1986, J. Phys. C **19**, 817.
Varma, C.M., and Y. Yafet, 1976, Phys. Rev. B **13**, 2950.
von Barth, U., and A.R. Williams, 1983, Applications of Density Functional Theory to Atoms, Molecules and Solids, in: Theory of the Inhomogeneous Electron Gas, eds S. Lundqvist and N.H. March (Plenum, New York) p. 189.
Vosko, S.H., L. Wilk and M. Nusair, 1980, Can. J. Phys. **58**, 1200.
Watanabe, T., and A. Sakuma, 1985, Phys. Rev. B **31**, 6320.
Wiegmann, P.B., 1980, Phys. Lett. A **80**, 163.
Wieliczka, D.M., C.G. Olson and D.W. Lynch, 1984, Phys. Rev. B **29**, 3028.
Wieliczka, D.M., D.W. Lynch and C.G. Olson, 1985, Bull. Am. Phys. Soc. **30**, 637.
Wuilloud, E., H.R. Moser, W.-D. Schneider and Y. Baer, 1983, Phys. Rev. B **28**, 7354.
Wuilloud, E., B. Delley, W.-D. Schneider and Y. Baer, 1984, Phys. Rev. Lett. **53**, 202.
Wuilloud, E., B. Delley, W.-D. Schneider and Y. Baer, 1985, J. Magn. & Magn. Mater. **47&48**, 197.
Yamada, K., 1975, Prog. Theor. Phys. **53**, 970.
Yoshimori, A., and A. Zawadowski, 1982, J. Phys. C **15**, 5241.
Yosida, K., and K. Yamada, 1975, Prog. Theor. Phys. **53**, 1286.
Zhang, F.C., and T.K. Lee, 1983, Phys. Rev. B **28**, 33.
Zhang, F.C., and T.K. Lee, 1984, Phys. Rev. B **30**, 1556.
Zlatic, V., B. Horvatic and D. Sokcevic, 1985, Z. Phys. B **59**, 151.
Zubarev, D.N., 1960, Sov. Phys. -Usp. **3**, 320.

Handbook on the Physics and Chemistry of Rare Earths, Vol. 10
edited by K.A. Gschneidner, Jr., L. Eyring and S. Hüfner

Chapter 65

LOCAL DENSITY SUPERCELL THEORY OF PHOTOEMISSION AND INVERSE PHOTOEMISSION SPECTRA

A.J. FREEMAN, B.I. MIN and M.R. NORMAN
Department of Physics and Astronomy, Northwestern University, Evanston, IL 60201, USA

and

Argonne National Laboratory Argonne, IL 60439, USA

Contents

List of symbols

PES	photoelectron spectroscopy		ground state
BIS	(bremsstrahlung isochromat spectroscopy) inverse photoelectron spectroscopy	$\tilde{\varepsilon}_f$	mean f-eigenvalue in the excited state
		ε_{eff}	effective binding energy of the 4f-electron
XAS	X-ray absorption spectroscopy	$E = E_{tot}$	total energy
XPS	X-ray photoelectron spectroscopy	ΔE	change of total energy
		n	number of f-electrons
DOS	density of states	vBH	von Barth–Hedin
E_F	Fermi energy	KS	Kohn–Sham
$N(E_F)$	DOS at E_F	WMT	warped muffin tin
r_{WS}	Wigner–Seitz radius	Δ_{ex}	exchange splitting
$\langle r \rangle$	expectation value of distance r	Δ_{so}	spin–orbit splitting
		Δ_-	4f PES excitation energy
U_{eff}	effective intra-atomic f–f Coulomb correlation energy	Δ_+	4f BIS excitation energy
		δ	relaxation energy shift
		ρ	charge density
LDA	local density approximation	I_{xc}	exchange–correlation integral
LSD	local spin density		
LMTO–ASA	linearized muffin-tin orbital – atomic sphere approximation	m	spin magnetic moment
		Q_l, N_l	number of electrons of angular momentum l.
FLAPW	full potential linearized augmented plane wave	S	Stoner enhancement factor
		U_{fd}	interaction between the 3d core hole and 4f-electrons
ΔSCF	difference of self-consistent total energies	B	bulk modulus
		j	total angular momentum quantum number
ε	one electron eigenvalue		
$\bar{\varepsilon}_f$	mean f-eigenvalue in the		

1. Introduction and experiment

As is clear from other chapters in this volume, the advent of highly sophisticated spectroscopic methods directed to the study of the electronic properties of the lanthanides has brought new excitement to the field. These methods, especially photoemission spectroscopy (PES), bremsstrahlung isochromat spectroscopy (BIS), and X-ray absorption spectroscopy (XAS) are now recognized as powerful tools to investigate various properties such as the 4f-energy position, the localized or delocalized nature of the f-band, valence configurations, the magnitude of the intra-atomic Coulomb correlation interactions, etc.

The first experimental evidence of a double-peaked structure due to f-emission in the valence band photoemission spectrum of a lanthanide was reported by Mårtensson et al. (1982) and Wieliczka et al. (1982) for Ce, by Franciosi et al. (1981) and Gudat et al. (1982) for the cerium pnictides. (The spectrum had been seen by other groups before, but was not realized as such.) The spectra of Ce exhibit a double-peak structure associated with the 4f-electrons, with a peak near E_F and another 2eV below E_F. The data for cerium pnictides indicated a peak about 3eV below E_F and one about 0.5eV below E_F. Moreover, the intensity ratio between the two peaks changed as one worked down the series (CeP, CeAs, CeSb, CeBi) with

CeP having the peak near E_F strongest and CeBi having the one 3 eV down the strongest.

Since these experiments give rise to a strong perturbation in the system, the observed results are obviously excited stated properties which include Coulomb correlation and core-hole relaxation effects. Hence, a comparison between theoretical ground state results and the observed excited state results is usually not possible, especially for localized electron excitations which are accompanied by strong relaxation effects. Thus it is quite clear that the eigenvalues from a ground state band structure calculation do not represent the observed energy positions of the localized f-electrons at all (Min et al. 1986a,e). Instead, the excitation process has to be modelled by calculating total energy changes between initial and final relaxed states in order to compare with experiment. Early on, Herbst et al. (1976) calculated the 4f excitation energies of the lanthanides by calculating total energy differences using the renormalized atom method. They assumed that the localized hole in PES is completely screened by the conduction electrons within a unit cell to maintain charge neutrality.

Actually, as we shall see, these PES experiments have given rise to interesting controversies about their origin. There appears to be only a small difference (in shape and peak position) between the spectra of γ-Ce and α-Ce. In contrast, the total density of states from band structure calculations show only one peak of f-character near E_F and another of s–d character 1.3 eV below E_F for both materials.

Many theoretical models have been proposed to interpret this anomalous two-peak structure in relation to the γ–α transition in Ce metal. Hüfner and Steiner (1982a,b) and also Mackintosh (1985) considered the different channels for the screening of the 4f excitations to suggest the importance of final state effects in the photoemission. Liu and Ho (1983) took into account the final state concept in emphasizing the large Coulomb correlation interaction between 4f-hole and the conduction electrons. Allen and Martin (1982), Martin (1982) and Levagna et al. (1983) used the concept of a Kondo lattice model (Doniach 1977) to successfully account for the thermodynamics of the γ α transition and interpreted the peak near E_F as a Kondo resonance peak. Gunnarsson and Schönhammer (G–S) (1983) reproduced the two-peak structure of Ce with the Anderson model by considering available final states. In some ways, the G–S explanation was seen as radically different from a screening model. The lower peak was ascribed to an $f^1 \rightarrow f^0$ transition, just as in the screening model (this is essential input into the G–S model). The peak near E_F, though, has been variously described as an f-hole screened by f-electrons (equivalent to the screening model) or as a manifestation of the Kondo resonance. The unclear nature of the interpretation is due to the many-body nature of the G–S solution which makes 'single-particle' interpretations difficult. The G–S model is described in detail in chapter 64 of this volume. Fujimori (1983) also discussed the photoemission spectra with the similar concept of hybridization using a cluster approach. All of these models assume the constancy of the number of f-electrons during the γ–α transition. Franciosi et al. (1981) interpreted their spectra for the Ce pnictides in terms of a screening model with the peak 3 eV down representing a d-screened f-photohole, and the one near E_F representing an f-photohole which delocalized due to p–f hybridization.

We, ourselves, have interpreted these spectra (Norman 1985, Norman et al. 1985a,b,c Min et al. 1986a,e) in terms of the screening model using first principles local-density supercell calculations. This work represents the essential aspect of this chapter.

The next important experimental discovery was the observation of the two-peak structure in Pr and Nd compounds by Parks et al. (1984) and Wieliczka et al. (1984b). Basically, one sees a similar spectrum as seen in a cerium compound, but displaced further below E_F (1 eV in the case of Pr and 3 eV in the case of Nd) with the peak separation remaining about the same. This observation lead Parks et al. (1984) to conclude that a Kondo interpretation of the peak near E_F is incorrect (such a resonance would be tied to E_F). In fact, the spectrum is most easily interpreted from the screening model point of view (see Norman et al. (1985b) and Hüfner (1986)). Modifications of the G–S model, however, seem to account for at least the Pr case (Gunnarsson and Schönhammer 1985).

Recently, a spin–orbit split structure was observed in the case of cerium for the peak near E_F by Patthey et al. (1985) which can be interpreted with a modified G–S model which includes spin–orbit effects. Inclusion of spin–orbit splitting in the screening model can also explain this spectrum (Norman 1986). Recently, a two-peak structure has been resolved in uranium compounds by Arko (1986). The data also seems to be consistent with a screening model interpretation. Finally, we need to emphasize that although the two-peak structure seen in all of these cases is considered to be an exotic effect, such structure is also seen in the case of nickel, where the peak away from E_F is actually a satellite below the nickel d-band. And, of course, this multiple peak structure is seen in core level spectroscopy all over the periodic table. As we shall see, the observation of such structure in the valence emission of f-electron compounds is merely a reflection of the localization of such electrons as compared to the other valence electrons.

2. Ground state properties

2.1. *Introduction*

As is apparent from previous volumes in this handbook, the lanthanides have been studied extensively during the last two decades (Elliot 1972, Gschneidner and Eyring 1978) because of their unique electronic and magnetic properties inherent to a partially occupied 4f-shell. The lanthanide series is usually divided into two groups, the light (La–Eu) and the heavy (Gd–Lu) lanthanide elements. In the gas phase, most lanthanide atoms have a divalent configuration $[4f^n(5d6s)^2]$ except for trivalent La, Ce, Gd, and Lu. In the solid, however, except for Eu and Yb, one 4f-electron is promoted to the conduction band resulting in a trivalent configuration $[4f^{n-1}(5d6s)^3]$. This indicates that the energy gained by adding one more bonding conduction electron is larger than the energy lost by promoting an f-electron to the conduction band. The exceptions, Eu and Yb, retain a divalent configuration even in the solid because a half- or completely-filled 4f-shell is strongly favored, also see

chapter 69 of this volume; this causes them to display anamalous behavior in many of their physical properties.

In the light lanthanides, the first element, La, is a superconductor with a dhcp structure. The second element, Ce, exhibits a number of phases with intriguing and different behavior from the other lanthanides, which is due to the presence of both localized and delocalized aspects of the 4f-electrons. As a result, Ce has been the focus of much research. The next materials, Pr and Nd, are normal trivalent lanthanides, while Pm is a radioactive element, which prevents a detailed study of this material. These three elements have the dhcp structure. Sm has a typical and complicated Sm-type structure and a trivalent configuration. The last element, divalent Eu, has a bcc structure.

All the heavy lanthanides except for divalent Yb, have a stable hcp structure and a stable trivalent configuration. The magnetic moment of Gd orders ferromagnetically below 293.2 K, while the others except for Yb and Lu, show complicated magnetic structures. The three elements, Tb, Dy, and Ho order their moments in the basal plane, either in a helical structure or ferromagnetically, and Er and Tm show c-axis ferrimagnetic structures. At low temperature, an antiphase-domain-type structure is observed in Tm with four layers having up spin and the next three having down spin.

Since the 4f-orbitals are located spatially far inside the shells of the 5d and 6s conduction electrons, the contribution of these 4f-electrons to the chemical properties is usually very small. The 5d and 6s conduction electrons are considered to be instrumental in determining the cohesive properties. Hence a number of properties in the lanthanide series, with the exception of Ce, Eu, and Yb, are similar due to their having the same trivalent conduction electron configurations. For example, the equilibrium Wigner–Seitz radii, r_{WS}, decrease slightly in a linear fashion in the lanthanide series (lanthanide-contraction). In Eu and Yb, the effect of one less bonding electron and the consequent increase in screening of the nuclear charge is to expand the system to have a larger lattice constant than those of the trivalent materials. In Ce, the f-electrons are somewhat delocalized and give rise to a bonding effect and a smaller lattice constant. The linear lanthanide contraction with increasing atomic number relates to the incomplete screening of the nuclear charge by the additional f-electrons.

Recently, Skriver (1983) investigated the ground state properties of the lanthanides within local density theory using the linearized muffin-tin orbital (LMTO) band structure method (Andersen 1975) and successfully reproduced the general trends found in the experimental Wigner–Seitz radii and bulk moduli in the series. Nugent et al. (1973) and Johansson and Rosengren (1975a) discussed the cohesive properties of the lanthanides by using an interpolation method based on the assumed smooth behavior of the heat of sublimation and the bonding energy in the lanthanide series, respectively. Herbst et al. (1978) obtained the cohesive properties of the lanthanides with the simpler renormalized atom method.

An interesting sequence, hcp, Sm-type, dhcp, fcc, is observed for the crystal structures in the trivalent elements of the lanthanide series with decreasing atomic number. A number of conjectures (Jayaraman 1978) have been put forward to

explain these changes in the crystal structure. Johansson and Rosengren (1975b) proposed that a parameter, v, which is the ratio of the Wigner–Seitz radius and the ionic radius, correlates with the stable crystal structure as a function of the atomic number or pressure. Since v decreases with decreasing atomic number, this variation of v can be related to a pressure induced effect. Duthie and Pettifor (1977) extended this idea in a microscopic manner to show that v is intimately related to the relative occupation of the s-, p-, and d-bands, and they established correlation between the crystal structure and the number of d-electrons.

In this section, the ground state properties of the lanthanides are studied with a first principles all-electron total energy band structure method. The LMTO method is employed within the local density (LDA) and local spin density (LSD) functional approximations (Hohenberg and Kohn 1964, Kohn and Sham 1965, Gunnarsson and Lundqvist 1976). The von Barth–Hedin (1972) interpolation formula is used for the exchange and correlation potential with the parameters of Hedin and Lundqvist (1971) and RPA scaling (Janak 1978).

2.2. *Ground state properties of the lanthanides*

2.2.1. *Localization of the f-electrons*

The f-electrons in the lanthanides except Ce show an atomic-like localized behavior. Ce occupies a special position in the lanthanide series due to the presence of both the localized and delocalized character of the 4f-electrons. There are three important phases, α-, β-, and γ-Ce, in the phase diagram. Fcc α-Ce is the most stable phase at low temperatures. The f-electron in α-Ce is considered to form an itinerant electron band and to play a significant role in the electronic properties, while the f-electrons in dhcp β-Ce and fcc γ-Ce are often thought to be localized, exhibiting a Curie–Weiss paramagnetic behavior, In this study, we investigate this 4f-localization.

A quantitative description of the degree of f-localization is based on the spatial extension of the f-orbital within the Wigner–Seitz atomic cell. We calculate the radial expectation values of the wave functions at the Fermi level obtained from the ground state charge density. These values characterize the average distance from the nuclei for each orbital. The radial expectation values, $\langle r_l \rangle$, of the s-, p-, d-, and f-electrons, normalized by the experimental Wigner–Seitz radius, are displayed in fig. 1. The fcc structure is assumed for all lanthanides (because it is expected to give properties which are similar to those of the experimentally observed close-packed structures), except for Eu where we take the bcc structure. The extension of the s, p, and d conduction band orbitals varies weakly across the series and ranges between 0.7 and 0.8 times the Wigner–Seitz radius. It is seen that $\langle r_s \rangle$ decreases with atomic number, while $\langle r_p \rangle$ increases and $\langle r_d \rangle$ is almost constant through the series. When compared with this behavior of the conduction band electrons, $\langle r_f \rangle$ shows a steeper decrease and its magnitude is much smaller than the values for the conduction electrons. This is strong evidence for the localization of the f-orbitals – localization which becomes stronger with increasing atomic number. Note that overall $\langle r_f \rangle$ decreases linearly except in the beginning of the series; these deviations from

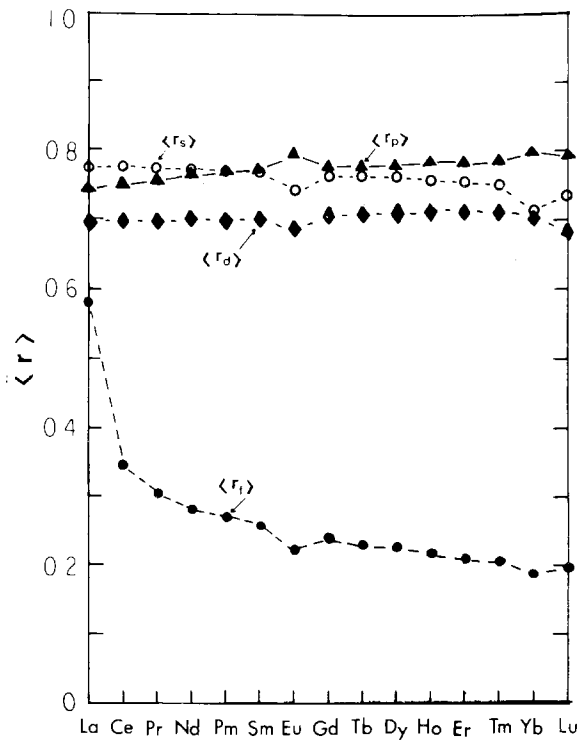

Fig. 1. Radial expectation values, $\langle r \rangle$, of the lanthanide for the wave functions at the Fermi level. (For Yb and Lu, we used the 4f wave functions at the center of gravity of the 4f density of states). The values are normalized by their Wigner–Seitz radii.

linearity are apparently due to the more delocalized nature of the f-electrons in these materials. Now since the f-band in La lies above the Fermi level, it naturally shows a delocalized nature. The deviation in Ce from the extrapolated value of a straight line amounts to 17%. We considered the γ-Ce phase in this case and hence $\langle r_f \rangle$ of α-Ce is expected to be even more extended. The deviation for Eu is attributed to the divalent configuration and to the anomalously large Wigner–Seitz radius in its experimentally observed bcc structure.

2.2.2. *Spin–orbit and magnetic exchange interactions*

Relativistic effects, especially the spin–orbit interaction, become important in the lanthanides due to their large atomic numbers. On the other hand, magnetic exchange interactions are also significant because of the large intra-atomic Coulomb correlation interaction of the 4f-electrons. In order to investigate the relative magnitude of the spin–orbit and magnetic exchange interactions, we have calculated the energy splittings, caused by these interactions, of the 4f-eigenvalues in the situation where we neglect all interatomic 4f-overlap, f–d hybridization and crystal field effects. When the 4f electrons are treated in a fully relativistic way, the spin–orbit splitting between the $4f_{5/2}$ and $4f_{7/2}$ levels is directly obtained. In order to obtain the exchange splitting of the 4f-levels, we treat the 4f-core electrons semirelativistically (Koelling and Harmon 1977) and force the spin magnetic moments to follow

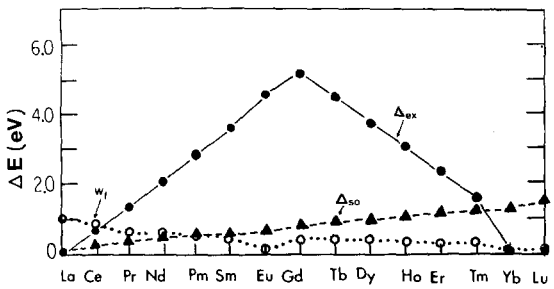

Fig. 2. The magnitude of the exchange and spin–orbit splittings for the lanthanide series. The 4f band width, W_f, is also provided for comparison.

the first Hund's rule. In the case of Tb, for example, seven out of eight 4f-electrons are put in the spin-up level and the remaining electron in the spin-down level. A ferromagnetic structure is assumed to be representative for the magnetic structure of the lanthanides.

The calculated spin–orbit and exchange splittings are provided in fig. 2. The 4f band width from the semirelativistic band structure calculations which treat the f-electrons as ordinary valence electrons are also compared with these splittings. The band width is chosen as the eigenvalue difference between Γ_2' and Γ_{25} at $\boldsymbol{k} = 0$. The spin–orbit splitting, Δ_{so}, increases monotonically through the series, from 0.34 eV for Ce to 1.52 eV for Lu; the 4f band width decreases with increasing atomic number, from 0.79 eV for Ce to 0.14 eV for Lu. Δ_{so} is larger than the band width beyond Pm, and hence the two spin–orbit components are separated in energy. Note, however, that the magnitude of the exchange splitting, Δ_{ex}, dominates over both the Δ_{so} and the band width for most lanthanides besides Ce. The values of Δ_{ex} increase to a maximum value (≈ 5 eV) at Gd (this value of Gd is consistent with the results by Harmon (1979) and Sticht and Kübler (1985)) and decrease to zero for the nonmagnetic metals Yb and Lu. The dominance of the magnetic exchange interaction over the band width of the 4f electrons series also provides evidence for the localized nature of the 4f-electrons in the lanthanide series.

The f-electron exchange–correlation integral, I_{xc}, from the relation $\Delta_{ex} = mI_{xc}$ (m denoting the spin magnetic moment) can be also evaluated. I_{xc} increases monotonically (from 0.67 eV for Ce to 0.79 eV for Tm) which indicates that no dramatic changes in the wave functions occur and that the magnetic moment, or the occupation of the up- and down-spin levels, is the most important factor in determining the energy of the levels. The conduction electrons are also polarized due to the exchange interaction between the localized spin of the f-electrons and the itinerant spin of the conduction electrons. The results show that the polarized conduction electrons are mainly d-electrons and s-electrons are hardly polarized at all. Note that the self-exchange interaction of the conduction electrons is not sufficient to magnetically polarize them; the Stoner factor, $I_{xc}N(E_F)$, of the conduction electrons alone is much less than one (for instance, $I_{xc}N(E_F) = 0.37$ in the case of Gd). The magnetic moments of the conduction electrons also exhibit the same behavior as Δ_{xc} and have a maximum polarization at Gd. The calculated values of conduction electron magnetization in Gd, 0.58 μ_B for the fcc and 0.70 μ_B for the hcp structure, are close to the experimental value of 0.63 μ_B (McEwen 1978, Roeland et al. 1975).

2.2.3. *Equilibrium atomic radii, bulk moduli, and cohesive energies*

Self-consistent paramagnetic total energy calculations are performed to study the ground state properties. In this case the 4f-electrons are treated as localized core states. Since the local density approximation is known to overestimate the extent of the 4f-orbitals, and hence the effects of interatomic hybridization and overlap, these terms in the matrix elements are neglected; the f-states are now atomic-like and in that respect can be called core-like. The fcc structure for the lanthanides are assumed, except for bcc Eu, because that is the simplest closed packed structure which approximates the real structure.

The calculated equilibrium Wigner–Seitz atomic radii, r_{WS}, are compared with the experimental values in fig. 3a. The agreement is quite satisfactory; the lanthanide contraction and the anomalous large lattice constants of Eu and Yb are well reproduced. In Eu and Yb, the divalent configuration leads to these large atomic

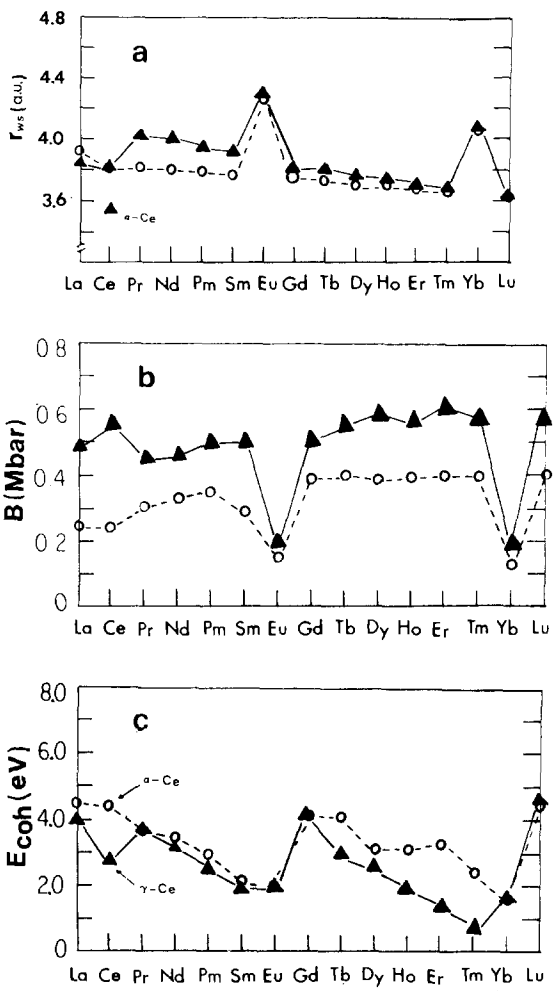

Fig. 3. Theoretical (▲) and experimental (○) values of (a) equilibrium Wigner–Seitz radii, (b) the bulk modulus and (c) cohesive energies. The experimental value for Pm is not available.

radii. The calculated r_{WS} values of the light lanthanides (Pr–Sm are slightly larger than experiment (4 to 5%), which apparently originates from an underestimation of bonding effects. This implies that the contribution to *the bonding from the 4f-electrons is not completely negligible* in the light lanthanide metals. It is interesting to contrast these results with results of LDA band structure calculations which include the interatomic hybridization and overlap of the 4f-electrons; in such a treatment, an overestimation of the 4f-bonding contributions and much smaller atomic radii are found. On the other hand, the calculated values of r_{WS} for the heavy lanthanides are close to the experimental values (with deviations of less than 2%). This result is consistent with the previous discussion that the f-localization becomes stronger with increasing atomic number in the series and gives clear evidence that the 4f-electrons in the heavy lanthanides are localized enough to be treated as core electrons and to have nonbonding character.

Next the bulk moduli of the lanthanides are investigated in the same way. The agreement between theory and experiment given in fig. 3b is less satisfactory than that for the atomic radii; this may originate from our choice of fcc structure which is different from the structures observed in the metals. The calculated values are overestimated by 30 to 40% compared with experiment, as was also found by Skriver (1983). However, both sets of calculations show similar general trends and a monotonic weak increase of the bulk moduli across the series (beside Eu and Yb). The dips appearing for Eu and Yb are again associated with their divalent nature. A spin-polarized calculation is expected to reduce this discrepancy, as in the case of the magnetic 3d transition metals (Moruzzi et al. 1978).

The cohesive energies (E_{coh}) of the lanthanides are considered and compared with experiment. The cohesive energy is a combined property in that it is the difference in energy of the solid and the free atom; hence it is a different quantity from the cases of atomic radii and bulk moduli. A correct description of the electronic structure of the free atom is thus a prerequisite in determining the cohesive energy. As reference atomic energies, a trivalent atomic configuration is taken for La, Ce, Gd, and Lu and a divalent atomic configuration for the others, which are the corresponding stable configurations in the atomic phases. The effect of spin-polarization for the heavy lanthanides is taken into account; here the energy shift from the ground state paramagnetic total energy is assumed to be independent of volume near the equilibrium lattice constant. This assumption is justified in the band structure calculation of Eu (Min et al. 1986d). The results of the spin-polarized calculation are indeed similar to those of the paramagnetic calculation except for a constant shift between the two total energy curves. The results displayed in fig. 3c predict the general trend well, especially the minimum at Eu and the maxima at Gd and Lu. However, in contrast to our expectation, the calculated values for the light lanthanides are closer to experiment than are those for the heavy lanthanides (Tb–Tm). We have seen that the 4f-electrons in the heavy lanthanides are sufficiently localized to be appropriately described by core-like states. Therefore, the anomalous results for the cohesive energy probably have to be attributed to errors in the description of the electronic structure of the free atoms in LDA.

2.2.4. *Crystal structures*

2.2.4.1. *Lu as a microcosm of the lanthanides.* The stable crystal structure of Lu at normal pressure is hcp as is also found for the other heavy trivalent rare-earth materials (Gd to Tm). A structural transition from this stable hcp to the Sm-type structure was observed (Liu 1975) in high-pressure ($P \approx 230$ kbar) X-ray diffraction experiments. This structural transition points out an interesting mechanism which might be operating and which also plays a role to explain the crystal structure sequence observed in the trivalent rare-earth series. A sequence of close-packed structures, hcp, Sm-type, dhcp, fcc, is observed with decreasing atomic number in the trivalent rare-earth series. There have been many conjectures to account for this phenomena (Jayaraman 1978). Duthie and Pettifor (1977) found a close relationship between the crystal structure and the occupancy of the 5d-band, using a canonical band structure method within the atomic sphere approximation. In their work the d-band occupancy, N_d, increases monotonically from right to left in the trivalent lanthanide series and determines the stable structure. This mechanism is similar to that which occurs in the d-band transition metals (Pettifor 1970) where a hcp–bcc–hcp–fcc structural sequence is found as the d-band occupancy increases. (At this point, it is important to note that the f-electrons in the lanthanides are believed to be completely localized and to play no significant role in determining the crystal structure. Among others who believe otherwise, see for example Langley (1982).) These concepts were extended by Skriver (1985) to obtain the stable structures under pressure in Lu and La based on a comparison of one-electron eigenvalue sums for different structres. He found a pressure induced structural transition in Lu and La corresponding to the crystal structures which appear in the rare-earth series. Unfortunately, Skriver obtained for Lu at ambient pressure, the stable Sm-type structure rather than the observed hcp structure.

The structural properties of Lu under pressure are investigated (Min et al. 1986c) with a self-consistent total energy approach for the hcp, Sm-type, double hcp (dhcp), and fcc structures. These structures are closely related through the sequence in which the hexagonal layers of the atoms are stacked (Beaudry and Gschneidner 1978). According to the ways of adding successive layers in the z-direction, it can be considered that hcp has 100% hexagonal character, Sm-type has 66.7% hexagonal and 33.3% cubic character, dhcp has 50% hexagonal and 50% cubic character, and fcc has 100% cubic character. Since all these structures are close-packed, the LMTO method can be used to calculate the total energy consistently.

Duthie and Pettifor (1977) found that structural transitions are not sensitive with respect to the axial values of c/a; hence, the ideal value ($c/a = 1.63$) for all the structures are assumed. Since it has been seen (Min et al. 1986e) that the 4f-electrons do not play an important role in the bonding, we treat the 4f-electrons as core in this study, which makes the calculations effectively fast. In fact, although the $4f_{7/2}$ level moves up toward the Fermi level with increasing pressure, it still lies deep enough in energy to maintain its localized nature (from 3.9 eV below E_F at $r_{WS} = 3.62$ a.u. to 3.1 eV below E_F at $r_{WS} = 3.3$ a.u.). Such a treatment is also justified

TABLE 1
Total energies E_{tot}, equilibrium Wigner–Seitz radii r_{WS}, bulk moduli B, and cohesive energies E_{coh} of hcp, Sm-type, dhcp, and fcc Lu. 4f-electrons are treated as core in this case.

	E_{tot} (Ry)	r_{WS} (a.u.)	B (Mbar)	E_{coh} (eV)
hcp	−29144.1464	3.65	0.63	4.76
Sm-type	−29144.1459	3.65	0.61	4.76
dhcp	−29144.1454	3.64	0.60	4.75
fcc	−29144.1433	3.64	0.59	4.72

by the fact that almost the same structural transition lattice point from hcp to fcc is obtained in both ways of treating the 4f-electrons, i.e., as either valence or core electrons ($r_{WS} = 3.33$ a.u. for 4f as valence and $r_{WS} = 3.32$ a.u. for 4f as core).

First, a number of the ground state properties of Lu are considered in different close-packed structures; the results are given in table 1. In agreement with experiment, hcp is the most stable structure with the Sm-type being the next most stable one. However, the energy differences between them are very small but just within the precision of the calculations. Note that, in all cases, their bulk moduli and cohesive energies are, for all purposes, identical. As an indication of the structural transitions with pressure, fig. 4 demonstrates total energy differences between the structures plotted with respect to the energy of the fcc phase. The first structural transition is from hcp to Sm-type followed by the Sm-type–dhcp–fcc sequence, which is exactly the same as occurs in the crystal structures when going from right to left in the trivalent lanthanide metals. Except for our obtaining correctly the ground state as hcp, these results are similar to those obtained by Skriver (1985); this is quite remarkable since our results are obtained from self-consistent all-electron total energy calculations in contrast to those from the non-self-consistent one-electron eigenvalue sums used by Skriver.

The predicted structural transition from hcp to Sm-type occurs at $r_{WS} = 3.48$ a.u. ($V/V_0 = 0.89$), which corresponds to the pressure $P \approx 110$ kbar. Compared with the observed transition pressure ($P \approx 230$ kbar) by Liu (1975) the theoretical value is smaller by a factor of two. Such a direct comparison may not be possible, however, since the experiment was done at the room temperature whereas our calculations

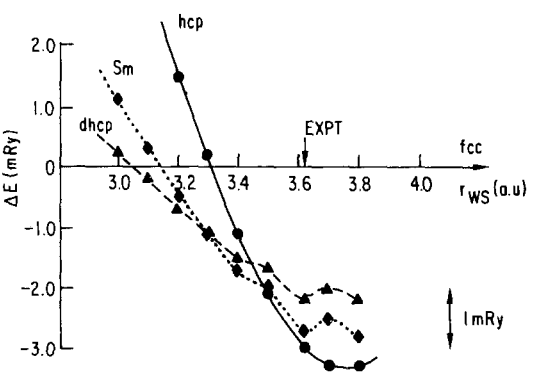

Fig. 4. Structural transitions between the four close-packed structures hcp, Sm-type, dhcp, and fcc. Total energy difference with respect to that of fcc are drawn as a function of Wigner–Seitz radius.

are for $T = 0$ K. The second structural transition from Sm-type to dhcp is predicted to occur at $r_{WS} = 3.3$ a.u. ($V/V_0 = 0.76$, $P = 325$ kbar), and the third one from dhcp to fcc at $r_{WS} = 3.05$ a.u. ($V/V_0 = 0.60$, $P = 925$ kbar).

It is of some interest that sp- to d-electron transfer occurs with applied pressure, since the d-band moves down in energy with respect to the sp-band. Generally speaking, the sp-electrons are more sensitive to pressure because of their large spatial extent. With applied pressure, the increase of the kinetic energy of the sp-electrons is much larger than that of the d-electrons. Therefore, the sp-band moves up with respect to the d-band with pressure. This change of d-occupancy is believed to determine the stable structure under pressure (Duthie and Pettifor 1977, McMahan and Young 1984). Figure 5 plots the occupation number of s-, p-, and d-electrons of Lu as a function of Wigner–Seitz radius and also shows the stable structures. One sees that the hcp structure is stable for the range of d-occupancy, $N_d < 1.52$, Sm-type for $1.52 < N_d < 1.65$, dhcp for $1.65 < N_d < 1.8$ and fcc for $N_d > 1.8$. This correlation between the stable structures and d-occupation number can be related to the crystal structure sequence as observed in the trivalent lanthanides metal series, as we will discuss in the next section.

2.2.4.2. *d-band occupancy versus crystal structure.* In order to investigate the relationship between the crystal structures observed in the lanthanide series and d-band occupancy, the calculated self-consistent s-, p-, and d-band occupancies are considered. As Skriver (1983) did, the hybridization between the conduction electrons is included (besides the f-electrons) in contrast to the case of Duthie and Pettifor (1977) who found this relationship using the unhybridized canonical band structure method. Fcc structures are assumed for all lanthanides but bcc Eu and the calculations are performed at the experimental lattice constants.

The resulting values plotted in fig. 6 are close to the values of Skriver (1983). The occupancy of the s- and p-bands increases linearly with atomic number and small discontinuities are found at Eu and Yb. In contrast to this behavior the d-band occupancy decreases with increasing atomic number (from 1.93 for La to 1.44 for Lu) and large dips are found at Eu and Yb due to their divalent configurations. The electron transfer from the sp- to the d-band with decreasing atomic number is

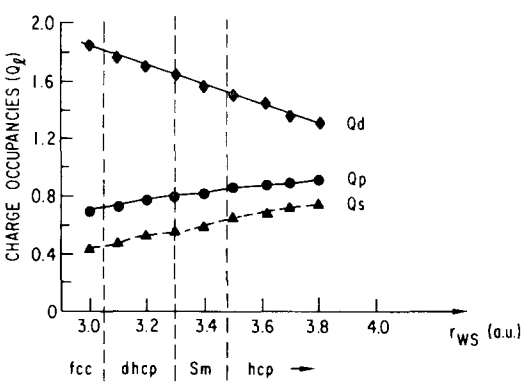

Fig. 5. Change of occupancies (s-, p- and d-character) with pressure. The corresponding ranges for the stable structures are indicated. 4f-electrons are treated as core in this case.

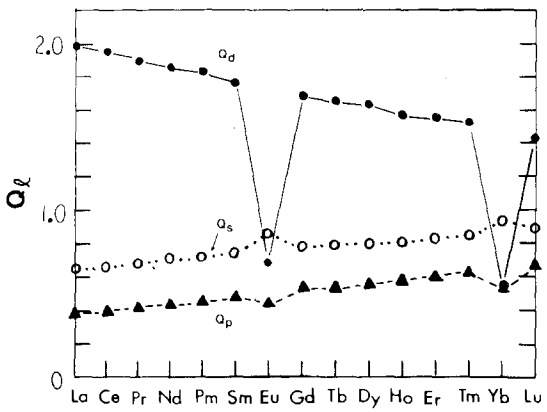

Fig. 6. Number of s-, p-, and d-electrons in the lanthanide metals.

similar to the pressure induced s–d electron transfer. (The electron transfer by pressure occurs because the s- and p-bands move up relative to the center of d-band.) This behavior is closely related to that of the $\langle r_f \rangle$ values discussed in section 2.2.1. Because $\langle r_f \rangle$ is the ionic core radius normalized by the Wigner–Seitz radius, the inverse of this value corresponds to the parameter v introduced by Johansson and Rosengren (1975b). Hence the decrease of $\langle r_f \rangle$ with atomic number implies that the interstitial region, in which the s- and p-bands are mainly occupied, increases as we move from La to Lu. Consequently, the kinetic energy of the s- and p-bands decreases and thus the s- and p-bands move down in energy with respect to the d-band and so increase their occupancies, consistent with fig. 6.

The relation between the observed structural sequence in the lanthanides and the d-band occupancy can be examined qualitatively using the above values of the number of occupied d-electrons. The study of the pressure-induced structural transition of Lu above (Min et al. 1986c) shows that the dependence of the d-band occupancy on the structure is small at the given lattice constant: the differences obtained between structures are only 0.02 or 0.03 electrons. Hence it is possible to relate, within a small uncertainty, the observed structures in the lanthanide metals with the absolute values of the d-band occupancy obtained in the fcc structure. From fig. 6, the resulting ranges of d-band occupancy (N_d) for the stable structures are: $N_d < 1.7$ for hcp and $1.75 < N_d < 1.8$ for Sm-type and $1.8 < N_d < 2.0$ for dhcp and $N_d > 2.0$ for the fcc structure. Compared with the ranges predicted by Duthie and Pettifor (1977), these values are somewhat reduced due to the inclusion of hybridization; for example Sm-type is stable for $\approx 1.7 < N_d < \approx 2.3$ in their work, compared with $1.75 < N_d < 1.8$ in this work.

2.3. *Ground state properties of Ce*

2.3.1. *Introduction*

Ce metal has unique properties compared with neighboring elements in the lanthanide series. It is generally believed that f-electrons in most of the lanthanide metals are located far inside the s and d conduction band orbitals and behave as

localized core electrons. However, f-electrons in Ce are much more extended and thus f–d hybridization and even f–f direct interactions between nearest neighbors are not small. As a result, Ce shows the intermediate behavior and exhibits both localized and delocalized (itinerant) properties which leads to many intriguing manifestations expected of Fermi liquid, mixed valence, and Kondo systems, etc. Thus, Ce shows either a magnetic or a superconducting phase depending upon temperature and pressure (Koskenmaki and Gschneidner 1978). Fcc α-Ce, which is the most stable phase at normal pressure, behaves as an enhanced Pauli paramagnetic metal, and becomes a superconductor below 50 mK at a pressure of 40 kbar. With increasing temperature, α-Ce transforms at ambient pressure to dhcp β-Ce at $T = 95$ K and to fcc γ-Ce at $T = 263$ K. Both of these phases show magnetic behavior in that their susceptibilities follow a Curie–Weiss law, which is taken to indicate that the f-electrons in β-Ce and γ-Ce are localized to form magnetic moments. Both phases probably show Kondo-like behavior (Koskenmaki and Gschneider (1978)). At higher pressure, α-Ce transforms to orthorhombic α′-Ce which is a superconductor with $T_c = 1.9$ K.

The most fascinating property of Ce metal is the occurrence of the γ–α isostructural (fcc to fcc) transition, which ends in a critical point (Ponyatovskii 1958, Jayaraman 1965) near 550 K and 18 kbar in analogy to the well-known liquid–gas phase transition. A large volume (a 17% decrease) and loss of magnetic moment follow in going from γ- to α-Ce. The γ–α transition was originally suggested (Zachariasen 1949, Pauling 1947, Coqblin and Blandin 1968, Ramirez and Falicov 1971) to be a valence transition in which a magnetic localized 4f-electron is partially promoted into the conduction band to form an intermediate valence (Lawrence et al. 1981) phase in α-Ce (promotional model). Various recent experiments, however, indicate that there is no appreciable change in the number of 4f-electrons at the γ–α transition, whereas the promotional model requires a change of about 50%. On the other hand, Gschneidner (1965) and Gustafson et al. (1969) proposed delocalization of the 4f-electrons into a band state. Johansson (1974b) extended this idea to point out, on the basis of empirical data, the possibility of a Mott-like transition in which the γ-phase is the low density insulator side of a Mott transition and that under pressure a localization–delocalization transition of the 4f-electron occurs with a concomitant loss of magnetic moment. These arguments appear to be consistent with most of the experimental measurements and, in fact, several band structure calculations (Glötzel 1978, Pickett et al. 1981, Podloucky and Glötzel 1983, Min et al. 1986b) show that the 4f-band in α-Ce is over one electron volt wide and that the number of f-electrons changes only slightly from γ to α in support of Johansson's Mott transition model.

An LDA band structure calculation is expected to yield a good description of the ground state properties of rather extended 4f-band Ce metal, provided it is carried out to self-consistency. Kmetko and Hill (1976) performed the first self-consistent APW band structure calculation for γ- and α-Ce and pointed out the increase in hybridization of the 4f-states with the conduction band with reduction of the atomic volume. Glötzel (1978) reported the cohesive and magnetic properties of fcc Ce obtained with the self-consistent relativistic LMTO method (Andersen 1975) and

found spin polarization to occur near the lattice constant of γ-Ce, which is related to the localization of the f-electrons. Pickett et al. (1981) performed self-consistent relativistic linearized APW band structure (Andersen 1975) calculations for both the α- and γ-phases of Ce metal which include the non-spherical potential as well as spin–orbit coupling by perturbation theory and discussed the electronic and magnetic properties of Ce metal. Podloucky and Glötzel (1983) studied the ground state cohesive properties and calculated Compton profiles of γ- and α-Ce using the LMTO method to confirm the evidence against the promotional model.

It has been reported (Probst and Wittig 1978) that α-Ce undergoes a phase transition at 40 kbar and room temperature and that the superconducting T_c jumps by a factor 40 up to 1.9 K. With greater pressure T_c decreases. The high pressure phase, α′-Ce, has an orthorhombic α-U structure, which is ascribed to the existence of itinerant f-bonding effects. Wittig (1973) speculated from this that α′-Ce is a 4f-band metal, in which delocalized f-band electrons hybridized with the conduction band are responsible for the high T_c of α′-Ce. However, the effects of f-electrons on the superconducting properties still appear to be in dispute.

In this section, we describe total energy band structure calculations undertaken to investigate the ground state properties of Ce (Min et al., 1986b) by employing both the full potential linearized APW (FLAPW) (Jansen and Freeman 1984) and the LMTO band structure methods within the local spin density functional approximation. The total energies of the paramagnetic and spin-polarized phases of Ce are used to discuss the energetics involved in the γ–α transition. In sections 2.3.2 and 2.3.3, the results of paramagnetic and spin-polarized band calculations are presented. The f-electron localization in the γ–α transition is presented in section 2.3.4, and discussion follows in section 2.3.5.

2.3.2. *Paramagnetic calculations*

The main features of the resulting band structures, densities of states and Fermi surface are close to those obtained previously by Pickett et al. (1981) The one difference in this calculation from that of Pickett et al. is the way the 5p-core electrons are treated. Min et al. (1986b) find that the 5p-electrons, which are located approximately 1 Ry below the conduction band, have a nonnegligible density outside the muffin-tin sphere, especially at smaller volumes (that is, at higher pressures). The interstitial 5p-contribution amounts to almost 0.3 electrons in the case of α-Ce ($r_{WS} = 3.54$ a.u.; r_{WS} is the Wigner–Seitz radius) and this has a strong effect on the total energy. Hence the 5p-electrons are treated in the same way as the valence electrons; the resulting band width is of almost 200 mRy for α-Ce. The effect of neglecting spin–orbit coupling of the 5p-band is small on the total energy because this band is completely filled and the 5p band contribution to the binding energy is much more important.

The total energy and band structure results (Min et al. 1986b) using the FLAPW method are given in fig. 7 and table 2 respectively. The angular momentum decomposed densities of states and occupied charges inside the muffin tin and interstitial are provided in table 2 as a function of Wigner–Seitz radius; the 4f-band widths are also given for comparison. As is seen in fig. 7, there is no evidence of any

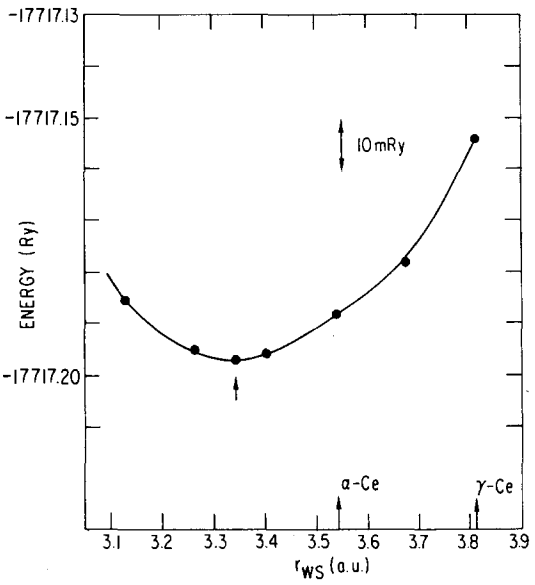

Fig. 7. FLAPW total energy results as a function of Wigner–Seitz radius.

first-order structural transition in the total energy curve and hence the γ–α phase transition apparently has a different origin. We notice, however, that with increasing pressure the number of 4f-electrons increases and the 4f-band broadens. The number of 4f-electrons increases because the relative positions of s- and p-bands move up and these electrons are converted to d- or f-bands. The change in the number of 4f-electrons, however, is small in going from γ-Ce to α-Ce. The band broadening effect is clearly seen in the 4f-band width, $W(4f)$, which is chosen as an eigenvalue difference of $\Gamma_{2'}$ and Γ_{25} at $\boldsymbol{k} = 0$. The values of $W(4f)$ are 0.78 for γ-Ce ($r_{WS} = 3.81$ a.u.) and 1.23 eV for α-Ce ($r_{WS} = 3.54$ a.u.). Due to this band broadening, the total density of states at the Fermi level, $N(E_F)$, decreases from 57.0 states/Ry for γ-Ce to 37.6 states/Ry for α-Ce. The Fermi level is located near the bottom of a large f-peak in all cases.

Our resulting cohesive energy (4.9 eV) is close to the experimental value (4.32 eV). For the energy of the atom, we use −17716.8397 Ry, which pertains to the LDA atomic ground-state configuration of $4f^{1.6}5d^{0.4}6s^2$. The equilibrium value of the Wigner–Seitz radius, $r^0_{WS} = 3.35$ a.u., however, is almost 5% smaller than the experimental value of α-Ce and the bulk modulus ($B = 0.56$ Mbar) is larger by a factor of three. The reduction in the equilibrium lattice constant is related to the overestimated contribution of the 4f bonding effect in the local density approximation which is common in the LDA description of localized bands. For example, calculations on Eu and Yb metals (Min et al. 1986d) in which the 4f-electrons are very localized, show that r^0_{WS}'s are almost 12% and 7% smaller, respectively, and the B's are almost 50% larger than the experimental values if the 4f-electrons are treated as ordinary valence bands. In contrast to Eu and Yb, the 4f-electrons in Ce are considered to be closer to the delocalized limit; nevertheless, even here the LDA

TABLE 2

Calculated FLAPW partial density of states at E_F inside the muffin tin sphere, $N_l(E_F)$, in the interstitial, $N^{int}(E_F)$ and total density of states, $N^{tot}(E_F)$, (in states/atom Ry). Partial charges inside the muffin tin sphere Q_l, in the interstitial, Q_{int}, the 4f band width $W(4f)$ and the total energy, E^{tot}, as a function of Wigner–Seitz atomic radius, r_{WS}[a.u.].

r_{WS}	$N_s(E_F)$	$N_P(E_F)$	$N_d(E_F)$	$N_f(E_F)$	$N_g(E_F)$	$N^{int}(E_F)$	$N^{tot}(E_F)$	Q_s	Q_p	Q_d	Q_f	Q_g	Q_{int}	$W(4f)$ [eV]	E^{tot} [Ry]
3.13	0.23	0.15	1.66	7.02	0.04	0.79	9.90	0.17	5.62	1.73	1.36	0.03	1.10	2.27	−17717.1852
3.27	0.99	0.29	2.61	11.96	0.07	1.76	17.68	0.21	5.72	1.73	1.28	0.02	1.03	2.00	−17717.1953
3.40	0.74	0.33	3.47	14.25	0.07	1.95	20.80	0.27	5.81	1.71	1.22	0.02	0.98	1.56	−17717.1957
3.54	1.48	0.62	6.37	25.27	0.10	3.75	37.58	0.31	5.86	1.65	1.19	0.02	0.98	1.23	−17717.1879
3.68	1.32	0.74	7.31	32.06	0.07	5.97	47.46	0.30	5.86	1.47	1.14	0.01	1.22	0.95	−17717.1782
3.81	1.52	0.82	8.82	41.13	0.10	4.62	57.00	0.41	5.96	1.60	1.18	0.01	0.84	0.78	−17717.1543

description is not adequate in reproducing the correct behavior of the lattice constant.

In order to investigate this effect in more detail, the following three cases for Ce are considered by employing the LMTO method. (1) The 4f-electrons are treated as ordinary valence band electrons; (2) one occupied 4f-electron is treated as belonging to the core still including the f-like radial functions in the description of the valence band, and (3) the one 4f-electron is treated as core suppressing f-hybridization in the valence band completely.

The overall results of the LMTO band structure calculations are found to be the same as those obtained with the FLAPW method: the shapes of their total energy curves are similar, aside from a 0.3 eV upward shift in the absolute energy for the LMTO cases. The equilibrium Wigner–Seitz radius is 3.37 a.u. in LMTO compared with 3.35 a.u. in FLAPW and the bulk modulus is 0.57 Mbar (LMTO) compared with 0.56 Mbar (FLAPW).

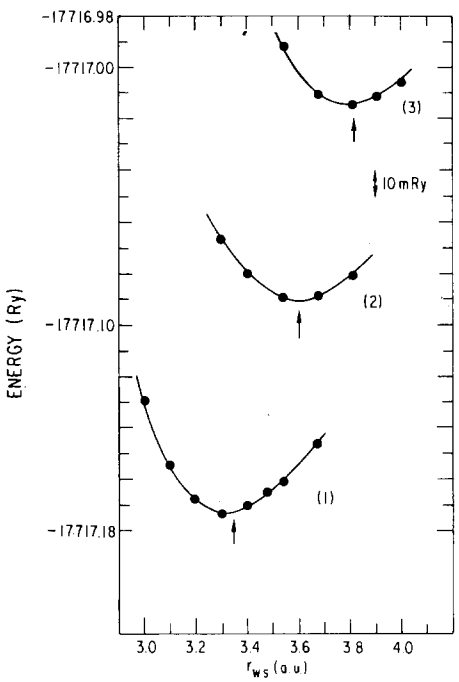

Fig. 8. LMTO total energy results for the three cases discussed in the text.

TABLE 3

Calculated LMTO equilibrium Wigner–Seitz atomic radius, r^0_{WS}, bulk modulus, B, and total energy E_{tot}, for the three cases discussed in the text.

Case	r^0_{WS}[a.u.]	B [Mbar]	E_{tot} [Ry]
1	3.34	0.69	−17717.172
2	3.61	0.52	−17717.090
3	3.82	0.56	−17717.015

The resulting total energy results for the three cases are displayed in fig. 8 with the corresponding values of r^0_{WS} and B, provided in table 3. In case (2), one still finds 0.4–0.7 f-valence electrons in addition to the one 4f core electron consistent with the result of case (1), in which 1.4–1.7 f-valence electrons are obtained. The total density of states in cases (2) and (3) are greatly reduced due to the loss of one f-valence electron. The equilibrium Wigner–Seitz radii are 3.35, 3.60, and 3.80 a.u., respectively for the three cases. It is interesting to note that r^0_{WS} of case (3) is close to that of experiment for γ-Ce and that r^0_{WS} of case (2) is close to that of experiment for α-Ce, (attributed to the bonding contribution of f-electrons). By treating the 4f-electrons as core in cases (2) and (3), one possibly mimics the localized properties of the f-electrons; the hybridization between f- and conduction electrons are neglected as well as the direct f–f hopping interaction between nearest neighbors. In fact, in a separate study, we found that the experimental lattice constants of the heavy lanthanide metals are well reproduced (within errors of less than 2%), if the f-electrons are considered to be completely localized. Hence the agreement of the calculated equilibrium lattice constant in case (3) and experiment for γ-Ce implies that the f-electrons in γ-Ce do not contribute much to the cohesive properties, that is, they are in the localized limit. In comparison, the experimental equilibrium lattice constant of α-Ce is located between the results of case (1) and case (2) (but closer to that of case (2)), which apparently originates from the existence of partial bonding effects due to f-electrons in α-Ce; f-electrons are more or less delocalized at this atomic volume. These results suggest that two competing effects (f-bonding and f-localization) determine the stable phase under given external conditions so as to give rise to the γ–α transition. The localized nature of the f-electrons can be also simulated by the inclusion of spin polarization – as will be discussed in the next section.

2.3.3. *Spin-polarized calculations*

Local spin density calculations were performed (Min et al. 1986b) with the LMTO method in order to investigate the magnetic behavior of Ce metal at large volumes. From the self-consistent paramagnetic charge density, they first obtained the intra-atomic exchange–correlation integral presented in table 4. The total density of states at E_F and angular momentum decomposed occupied charges are also given for comparison with the FLAPW results. The value of I_{xc} is almost constant, 0.42 eV (30 mRy), over the whole range of lattice constant, which indicates that I_{xc} is essentially a pressure independent parameter. From the product $(N(E_F)I_{xc})$, one can derive the Stoner enhancement factor, $S = [1 - \frac{1}{2}N(E_F)I_{xc}]^{-1}$; the calculations predict the occurrence of a ferromagnetic instability for values of r_{WS} larger than 3.74 a.u. This means that γ-Ce ($r_{WS} = 3.81$) is located just in the ferromagnetically ordered region, which is consistent with the result of Glötzel (1978). The Stoner enhancement factor of α-Ce is still large ($S = 5.6$) and so it behaves as a strongly exchange enhanced paramagnetic metal. (Recall that this is similar to the case Pd ($S = 4.5$)) (Watson-Yang et al. 1976, Janak 1977).

The total energies and magnetic moments obtained in the spin-polarized

TABLE 4

Calculated LMTO charges (by l values), Q_l, the total density of states at E_F, $N(E_F)$ (in states/atom Ry), intra-atomic exchange correlation integral, I_{xc}, Stoner enhancement factor, S, and the total energy E_{tot} – all versus Wigner–Seitz radius, r_{WS}.

r_{WS} [a.u.]	Q_s	Q_p	Q_d	Q_f	$N(E_F)$	I_{xc} [Ry]	$N(E_F)I_{xc}/2$	S	E_{tot} [Ry]
3.1	0.29	5.76	2.30	1.65	29.55	0.032	0.47	1.9	−17717.1542
3.2	0.34	5.82	2.27	1.57	31.44	0.031	0.49	2.0	−17717.1671
3.3	0.39	5.86	2.24	1.51	37.18	0.030	0.56	2.3	−17717.1727
3.4	0.44	5.90	2.20	1.46	39.25	0.031	0.60	2.5	−17717.1685
3.54	0.50	5.94	2.14	1.42	53.19	0.031	0.82	5.6	−17717.1609
3.68	0.55	5.97	2.08	1.40	59.64	0.031	0.91	11.1	−17717.1462
3.74	0.57	5.98	2.05	1.40	65.67	0.030	0.99	100.0	−17717.1367
3.81	0.59	5.99	2.03	1.39	66.24	0.030	1.01	−10.0	−17717.1259

TABLE 5
Spin-polarized LMTO results for the total energy, the 4f and total spin magnetic moment (in Bohr magnetons) and the spin-up and spin-down density of states in E_F (in states/Ry spin) – all as a function of Wigner–Seitz radius, r_{WS}.

r_{WS} [a.u.]	E_{tot} [Ry]	$m(4f)$ [μ_B]	m^{tot} [μ_B]	$(N(E_F)$ ↑	↓
3.74	−17717.1369	0.31	0.34	40.4	24.4
3.81	−17717.1269	0.80	0.90	50.1	17.4
3.9	−17717.1132	0.90	1.02	69.3	14.7
4.0	−17717.1009	1.03	1.16	64.3	13.3
4.1	−17717.0835	1.13	1.30	88.9	12.6
4.25	−17717.0643	1.21	1.40	80.7	10.0

calculations are given in table 5 and fig. 9. In agreement with the estimate of the Stoner instability, the total energy difference between para- and ferromagnetic structures plotted in fig. 10 shows that magnetic instability does occur for $R_{WS} \approx 3.7$ a.u. The total energy difference between two states is, however, small; about 1 mRy for γ-Ce ($r_{WS} = 3.81$). As is clear from fig. 9b, the spin only magnetic moments (4f and total) increase as one expands the volume; 4f-moments are fully polarized for the atomic radius larger than 4.5 a.u. Further, the band splitting in the spin-polarized calculation also supplies a value of I_{xc} from the relation: $\Delta E = E_\uparrow - E_\downarrow = mI_{xc}$, where m is the spin magnetic moment. With $m = 0.9$ and $\Delta E = 0.03$ Ry at $k = 0$ in the case of γ-Ce, we obtain $I_{xe} = 33$ mRy, which is consistent with the paramagnetic Stoner calculation ($I_{xc} = 30$ mRy).

Total energy calculations were performed at selected values of the lattice constants assuming the first kind of antiferromagnetic ordering in the fcc structure (Min et al. 1986b). The difference in total energy obtained for the antiferromagnetic state from that for the para- and ferromagnetic states is shown in fig. 10. The ferromagnetic phase is seen to be more stable than the antiferromagnetic phase. Note that the energy differences between the different magnetic phases are small, especially near the observed lattice constant of γ-Ce. At this lattice constant, the antiferromagnetic phase is more stable than the paramagnetic phase by 0.6 mRy (= 80 K) but lies above the ferromagnetic phase by 0.4 mRy. These results are consistent with observations for the magnetic behavior of γ-Ce, which has a disordered magnetic structure at room temperature. Apparently then, no long-range magnetic order exists due to the competition of the three phases at room temperature; however, local moments are formed so that the susceptibility follows a Curie–Weiss law. These predictions for γ-Ce are consistent with the general view that γ-Ce is located in the low-density (localized-f) side of Ce metal.

2.3.4. *Coulomb correlation and localization of f-electrons*

In contrast to the promotional model, Min et al. (1986b) found that the f-bands are broadened with pressure and that the number of f-electrons is constant. This result supports the localization and delocalization transition of the 4f-electrons. In agreement with Johansson's (1974b) arguments based on empirical data, calcu-

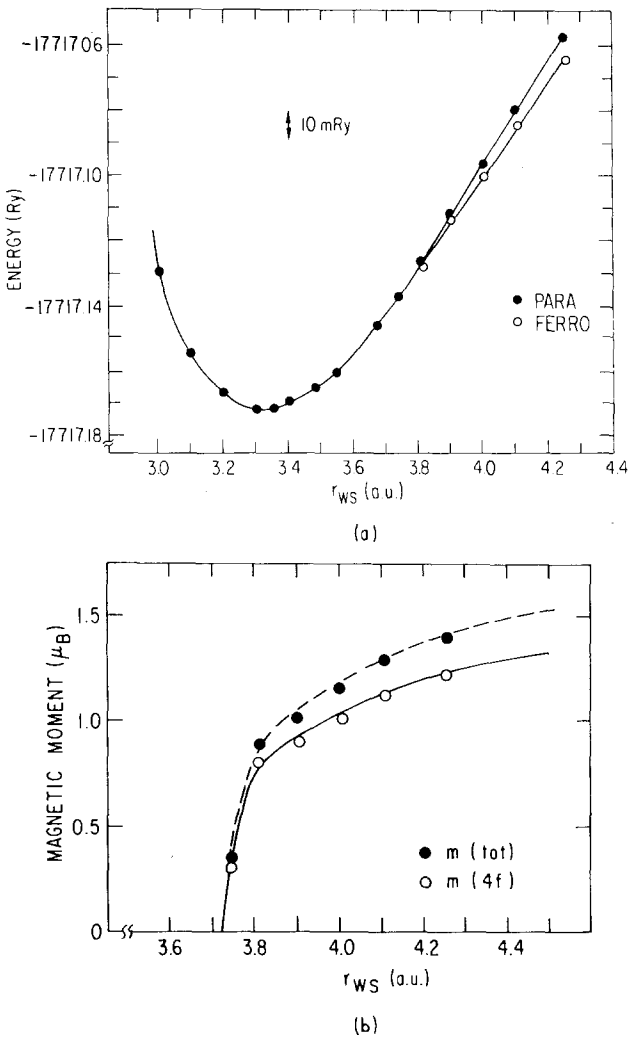

Fig. 9. (a) Paramagnetic and spin-polarized LMTO total energy results as a function of Wigner–Seitz radius; (b) the 4f and total spin magnetic moments as a function of Wigner–Seitz radius.

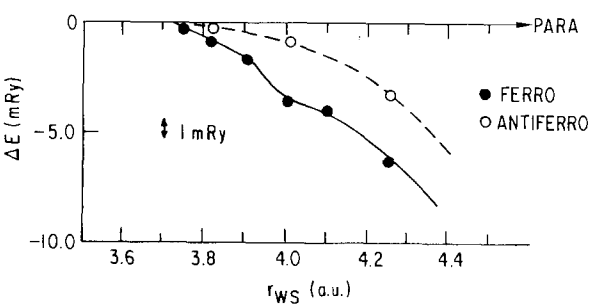

Fig. 10. LMTO total energy differences between the ferromagnetic and antiferromagnetic phases with respect to that of paramagnetic phase as a function of Wigner–Seitz radius.

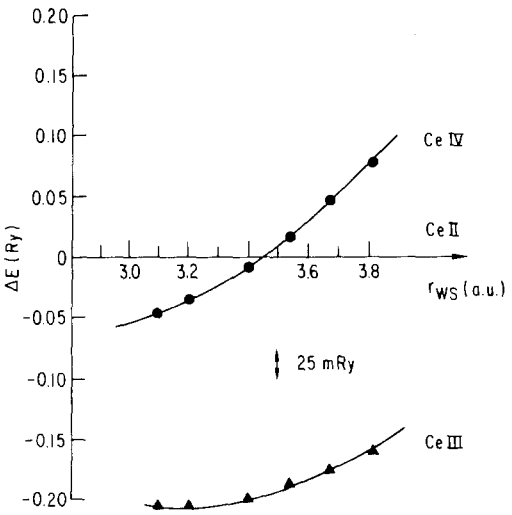

Fig. 11. LMTO total energy differences of the trivalent (III) and tetravalent (IV) phases of Ce relative to that of the divalent (II) phase as a function of Wigner–Seitz radius. The 4f-electrons are treated as core states.

lations with the number of 4f-electrons kept fixed in the core yield total energy differences between trivalent and tetravalent configurations which are too large for α-Ce metal to be a promotional type mixed-valent material. The total energies of three valence configurations, di-, tri-, and tetravalent are plotted as a function of Wigner–Seitz radius in fig. 11 by treating the f-electrons as core states. The trivalent configuration is lower in energy by about 2.4 eV than the tetra- or divalent configurations over the range of lattice constants considered and the divalent configuration is more stable than the tetravalent at the lattice constant of α-Ce ($r_{WS} = 3.54$ a.u.). The energy differences between tri- and tetravalent configurations amount to 3.2 eV for γ-Ce and 2.8 eV for α-Ce, which correspond to the localized 4f excitation energies in the photoemission experiment (Norman et al. 1984a, Min et al. 1986a). From these total energies, we can obtain the intra-atomic Coulomb correlation interaction parameter, U, by the relation: $U = E[f^0(5d\,6s\,6p)^4] + E[f^2(5d\,6s\,6p)^2] - 2E[f^1(5d\,6s\,6p)^3]$. The resulting values of U are found to vary weakly between 5.0 and 5.6 eV over the volume range considered and to decrease with pressure.

Compared with the bandwidth of 0.78 eV for γ-Ce and 1.23 eV for α-Ce, the value of the Coulomb correlation U, is much too large (even for α-Ce) for the 4f-band to delocalize, in the ordinary sense of the Hubbard model. Recently f-shell localization was discussed by Harrison (1984). He proposed the condition for localization of f-electrons, which is similar to the form obtained when an Anderson local moment forms in a degenerate band. Qualitatively, Harrison's localization condition can be written as

$$p \equiv \frac{2U}{\pi}\,\frac{1}{W(4f)}\sin^2\left(\frac{\pi n_f}{2J+1}\right) > 1, \tag{1}$$

where n_f is the number of occupied f-electrons ($n_f = 1$ for Ce) and J is the total

angular momentum of the f-shell. When spin–orbit coupling is included, the ground state of Ce has $J = 5/2$, which has six-fold degeneracy. If we apply this relation (eq. (1)) with values of the band width, W, and Coulomb correlation, U, considered above ($W = 1.23$ eV and $U = 5.4$ eV for α-Ce and $W = 0.78$ eV and $U = 5.5$ eV for γ-Ce), we obtain $p = 0.7$ for α-Ce and $p = 1.1$ for γ-Ce. Hence this result indicates α-Ce is in the region of delocalization. This result is consistent with the occurrence of f-band magnetism which was considered in section 2.3.3.

In order to investigate the degree of f-localization more quantitatively, we consider the spatial extent of the f-orbital within the Wigner–Seitz atomic cell. By calculating the radial expectation value, $\langle r \rangle$, of wave functions on the Fermi surface, the average distance of the valence electrons is obtained from the nucleus. The $\langle r \rangle$'s of 6s-, 5p-, 5d-, and 4f-orbitals normalized by the Wigner–Seitz radius are displayed in fig. 12 as a function of Wigner–Seitz radius. It is seen that $\langle r_f \rangle$ is much smaller than those of the other orbitals and thus shows clear evidence for the localized nature of the f-electrons. The spatial extent of the 6s and 5d (conduction band) orbitals is almost constant over the whole range of volume shown, while that of the 5p- and 4f-orbitals increase monotonically with decreasing lattice constant. As discussed in section 2.3.2, the 5p-electrons become greatly extended with pressure. However, $\langle r_f \rangle$ does not indicate any appreciable change between α- and γ-Ce (0.35 for γ-Ce and 0.37 for α-Ce). Note that if the f-electrons in γ-Ce are treated as core states, $\langle r_f \rangle$ is reduced to be 0.31. The dramatic change in the tail region of the 4f-orbitals between α-Ce and γ-Ce is seen when one calculates $\langle r^n \rangle$ values with higher n values (Picket et al. 1981).

2.3.5. *Discussion*

The calculation of the paramagnetic total energy does not show any dramatic features associated with the γ–α transition in Ce metal (Min et al. 1986b). One might expect that a spin-polarized calculation will reduce the f-bonding effect, as in the case of Am (Skriver et al. 1980) leading to some structure in the total energy curve. In fact, a magnetic instability is found close to the lattice constant of γ-Ce. The total energy difference between the para- and ferromagnetic phases is too small,

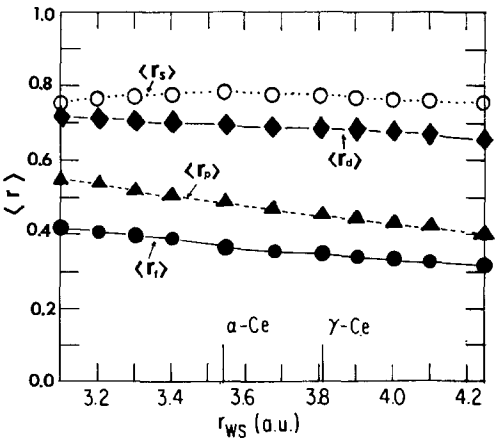

Fig. 12. The radial expectation values, $\langle r \rangle$, of the wave functions of each orbital on the Fermi surface. Each value is normalized to the respective Wigner–Seitz atomic radius.

however, to show clear evidence of a first order phase transition; only a small change of curvature can be seen in fig. 9. The transition pressure which can be obtained using a Maxwell construction in the total energy versus volume plot amounts to -120 kbar, which is of the same order of magnitude as Glötzel (1978) obtained from his pressure calculation. Compared with the experimental transition pressure ($P = -10$ kbar) at zero temperature, which is the extrapolated value from the γ–α phase line, the estimated transition pressure is larger by one order of magnitude. This large discrepancy implies that a spin-polarized calculation for Ce does not adequately describe the localization of the 4f-electrons, unlike the case of Am which has about six 5f-electrons in an almost half-filled band. The calculation (Min et al. 1986d) for bcc Eu, which has almost seven fully polarized 4f-electrons, shows a similar behavior; a spin-polarized calculation substantially improves the error in the lattice constant, but is still 5% off from experiment. When considering the 4f-electrons in Eu as core states, the equilibrium Wigner–Seitz radius is found to be 4.33 a.u., which is close to the experimental value ($r_{WS} = 4.29$ a.u.). This example indicates that the 4f-electrons in the heavy lanthanide metals are localized, so that the bonding effect of the 4f-electrons can be neglected. In Ce, however, the degree of hybridization of the 4f-electrons is smaller than predicted by LDA, but is not negligible (in fact, Ce metal under high pressure acts much like a 4f-band metal) to make a localization description difficult.

The actual volume collapse during the γ–α transition indicates that the electron–phonon interaction is an important factor. Hence it is expected that some anomaly will be seen in the phonon spectra, which is associated with a possible softening in the transition arising from the electronic contribution, as is discussed for La by Pickett et al. (1980). To our knowledge, no phonon spectra of α-Ce are available to date due to the difficulties of sample preparation. Once available, the comparison of phonon spectra in the various phases of Ce metal will yield crucial insights into the nature of the phase transition. We note that phonon data for γ-Ce shows evidence for a phonon softening which may be related to the $\gamma \rightarrow \alpha$ transformation (Stassis et al. 1979, 1982).

3. Excited state properties

3.1. *Introduction: model of the photoemission process*

The differential cross-section for the photoemission and its inverse process is given by (Doniach and Sondheimer 1974)

$$\frac{d^2\sigma}{d\omega\, d\varepsilon} = \sum_n |M_n|^2 |\langle n, N-1|\psi_c|0, N\rangle|^2 \delta(E_0(N) + \omega - E_n(N-1) - \varepsilon), \tag{2}$$

where the following symbols are used:

$\|0,N\rangle$:	initial ground state of the N-electron system,
$\|n,N-1\rangle$:	final eigenstate of the $N-1$ electron system,
$E_0(N), E_n(N-1)$:	corresponding total energies of these states,
ω:	energy of incident photon,

ε: energy of photoelectron,
ψ_c: annihilation operator for a 3d core level or a 4f-level,
M_n: matrix element describing all events from excitation to detection.

Many important contributions to the intensity are hidden in the matrix element M_n, which encompasses all the relaxation effects taking place while the photo-emitted electron moves towards the surface, the interactions taking place at the surface, and the actual detection process. The second matrix element $\langle n,N-1|\psi_c|0,N\rangle$ dictates the symmetry restrictions on the possible final states.

At present, a full theoretical description of the photoemission process within local density functional theory is not feasible. A major step in this direction was taken by Pendry in developing a lenghty successful scattering formalism (Hopkinson et al. 1980, Larsson 1982). Applications have been made to a number of systems (Redinger et al. 1985) but to date not on the materials of interest here (Rosina et al. 1986). As a result, we focus on the so-called three-step model for the photoemission process which has been widely used for the interpretation of experimental spectra as bulk bands.

The conceptual model followed is the simple three step process where a photon enters the solid causing a transition, the excited electron transports to the surface, and exits. It is assumed that relatively little of interest to a discussion of the excited state (two-peak) structure occurs in the transport so all attention is focussed on the transition. No consideration is given to resonance effects as they are assumed to be a modulation in the driving rate that will cancel out in the energetics. As will be discussed later, in the case that one restricts consideration solely to the two primary channels, one is basically studying the poorly screened and fully screened model (Fuggle et al. 1980) that has been used successfully to interpret the data for the lanthanides (Gudat et al. 1982).

In this model electrons with primarily s-, p- and d-character may be assumed to make transitions between states that are spatially extended over the crystal. In such cases, the change in potential upon excitation is negligible and the ground-state eigenvalues may then be used as a reasonable approximation to the change in the total energy. Identifying these eigenvalues with the excitation energies is the standard practice for a treatment of photoemission based on band theory. At the current level of sophistication, this treatment is adequate for those states. Such is not the case, however, for states involving f-orbitals, and it is the treatment of these localized states that introduces new aspects into the problem. These states with high f-orbital content have low mobility, so it is more appropriate to assume that the excitation is such a local one that in many cases it is essentially restricted to a single site. Thus the f-orbital transitions should be described in much the same way as are core excitations. (It should be noted, however, that this local nature is assumed as a consequence of the excitation process. It is not necessarily a property of the ground state.) The similarity of this situation to that of the 3d transition metals should be apparent.

The next two important hypothesis in the model are that the transition is *not sudden*: (i) The system is assumed to have time to relax before the exciting electron has left the system; and (ii) the screening can occur by several distinct temporally

selected channels. This set of hypotheses has been explored extensively for core-level excitations and has proven quite appropriate for the systematic interpretation of several complete series of transition-metal compounds (Veal and Paulikus 1983) and lanthanide metals (Herbst et al. 1977, Herbst and Watson 1979, Herbst and Wilkins 1982, Herbst 1982, 1983, also see chapter 68 of this volume). But of more direct applicability is the fact that hypothesis (i) is the basis of the rather successful renormalized-atom studies of the lanthanide-metal binding energies (Herbst et al. 1972, Herbst et al. 1976). Johansson (1974a, 1979) has pointed out that for energy considerations the time scale is sufficiently long to permit the successful use of thermodynamic analysis. These two treatments of the metals also assume an extremely local picture – not only the initial excitation but the final screening is assumed to occur on a single site. Their successes may be taken as some assurance that the perturbations caused by the excitation are quite local. This is useful to know since computational limitations restrict one to moderately local – although not site-local – perturbations. The fact that the Anderson–Hamiltonian-based model of Gunnarsson and Schönhammer (1983) is an impurity model also argues for this assumption (although it is possible in this model to adjust parameters to compensate for some nonlocality).

In using such a model without developing the full underlying formalism, the content of the results will be determined by one's skill in determining the possible excitation (screening) channels and the appropriate ways to represent them. On the other hand, it is an implicit assumption of this approach that a relatively standard band-theory treatment is an adequate description of the ground state. As discussed below this requires some justification in the case of the more localized systems.

3.2. *Method*

3.2.1. *Screening channels and their treatment*

If the photoemission excitation process is assumed to be local for an f-orbital because of its low mobility, an f-hole will be created which can be viewed initially as a single-site hole. The excitation process breaks the symmetry of the crystal in a very strong sense by creating an impurity-like excited atom. What will happen to this hole? Initially, it will move down far in energy (>7 eV) since this energy is simply the unrelaxed self-interaction of the electron (Perdew and Zunger 1981). Such a huge perturbation will cause a rapid rearrangement of the orbitals on that site (denoted as intra-atomic relaxation) and will shift the effective one-particle level upwards to lie about 7 eV below the original level. If the surrounding atoms do not react significantly to this perturbation, then this 7 eV level should be seen in the spectrum as the unscreened hole. Such an excitation is most likely to be seen in insulators, of course. On the other hand, metals may be expected to adjust to the presence of this localized positive hole through interatomic screening which will result in a further upward shift of the excitation level. The magnitude of this shift will depend very much on the spatial extent of the screening. If the hole were to be filled in reoccupation of an f-orbital, the site will return close to its ground state. In this case the resulting spectrum should closely reflect the initial state dispersion of the f-levels

and be given adequately by the ground state density of states obtained from a band calculation. This is the fully relaxed case. A competing process involves the filling of a 5d-level on the Ce hole site. Since the d-levels are quite extended ($\langle r \rangle > 2.5$ a.u. even for Ce atom), the screening is not complete and the resulting energy shift is not nearly as great as in the fully relaxed case. This is the poorly screened case whose simulation will be discussed below in more detail. Its accompanying peak is also the binding energy dealt with by the renormalized atom (Herbst et al. 1972, Herbst et al. 1976) and thermodynamic treatments (Johansson 1974a, 1979, also see chapter 69 of this volume) for the metals. Note that they refer to it as completely screened, implying complete screening on the same site. The characterization used here as poorly screened is not inconsistent with that requirement, since it merely requires that the screening charge be located at a further distance from the nucleus. Because this is a many-body process with substantial relaxation, it is necessary to calculate the excitation energy as a difference of total energies. Although quite straightforward in the renormalized-atom and thermodynamic approaches, some additional thought is required in the present case.

One's initial prejudice is that the poorly screened peak is the more complex and difficult peak to understand. In actuality, this is not the case as it can be attributed to a single excitation process. Surprisingly, it is the peak at E_F which presents greater conceptual difficulties. That peak can arise in one of several ways. It can come from a band-like transition since the occupied ground-state f density of states (DOS) is concentrated at E_F. This might be possible in the case of CeN and $CeRh_3$ and is extremely likely in such actinide materials as URh_3 and UIr_3. It can also come from a fully screened hole as mentioned above. This is more likely the case for CeP and CeSb. Both types of excitation are favored by stronger coupling of the f-orbitals so the dependence on 'itinerancy' will be the same: these channels will be favored in systems with higher itinerancy. There is also the question of whether the fully screened channel involves refilling the hole with the same f-orbital or with other f-orbitals. Both are possible. In a study of lanthanide trihalides, Rusic et al. (1983) performed transition state calculations on Ce molecules in which they explicitly prohibited repopulation of the excited orbital. In that case they found that the screening charge replaced the majority of the f-charge removed – a surprising result in view of the fact that the system is a molecule with only three ligands (halides) to provide the screening charge. It is not unreasonable therefore to assume that a nearly complete replacement of f-charge could occur in a metal even if the original orbital was not used. Fortunately, at the level of approximation being used, the particular choice will not matter since the excitation energetics of all these processes will be appropriately described using the ground DOS. When it does become significant, one has to make a greater effort to correctly model this channel.

3.2.2. *Supercell method*

It is apparent that this description of the excited state, which plays such a fundamental role in the photoemission process, brings one outside the realm (and validity) of density functional theory. Now, the construction of the excited final states breaks the translational symmetry of the crystal and so the atom on which the

localized hole is created forms an impurity in the system. Clearly Bloch's theorem, so crucial in simplifying the solution of the electronic structure problem in solids, is no longer valid. To retain Bloch's theorem, one introduces an (artificial) periodicity by approximating the geometry of the 'impurity' problem with a supercell approach (Zunger and Freeman 1977) in which a large cluster of host atoms plus a central impurity is repeated periodically in real space. The effect of the impurity–impurity interaction can be traced by utilizing larger and larger supercells. The results to be given later show that most of the electronic screening of the localized holes takes place in the central impurity site, which implies that the supercell method is an efficient approach to solving our specific impurity problems.

In solving the LDA equations for the localized core electrons, the interaction between these electrons on different sites can be safely neglected. As a result, the wave functions of these electrons are represented by atomic-like orbitals, which makes it straightforward to create a core hole in a given atom. The occupation of the 3d-level is simply reduced to nine on this site. The 4f-electrons can be treated in a similar way, although they do have some interatomic interaction. Ground state calculations show resulting absolute uncertainty of about 1 eV (relative uncertainties are much smaller!) and hence the approximation concerning the treatment of the hybridization of the localized electrons constitutes a major source of numerical error. These errors, however, still allow us to draw meaningful conclusions from our data given in the next section.

Two approaches have been followed for solving the local density equations for the impurity atom – a total energy method and a Slater transition state (Slater 1974) analysis. As is apparent from the fact that the calculation of the matrix elements needed to determine intensities is not feasible, we focus in both of these approaches on the energetics of the system. Total energies can be obtained with LDA methods whenever ψ_c pertains to a localized level, e.g., corresponding to electrons with a characteristic hopping time much longer than the duration of the photoemission process from the incoming of the photon to the escape of the photoelectron. This type of calculation is based on determining the change in total energy from separate self-consistent field calculations (ΔSCF approach). One thus calculates the total energy of the ground state and compares the result with the outcome of a total energy calculation in which we force a local level to be unoccupied. A theoretical justification of this latter procedure within density functional theory relies on the possibility of applying an external field to stabilize this one-hole configuration. This approach has been successfully applied to obtain ionization energies and core hole binding energies (Zunger and Freeman 1977, Gunnarsson and Lundqvist 1976, Williams and Lang 1978).

For the case of Ce and the other lanthanides, total energies are obtained using numerical algorithms based on the linearized muffin-tin orbital method in the atomic sphere approximation (LMTO–ASA) (Andersen 1975). Calculations for the ground state of Ce show (Min et al. 1986b) that the LMTO–ASA total energy results have a relative precision of about 0.07 eV as compared to the values obtained with our precise full potential linearized augmented plane wave (FLAPW) method (Jansen and Freeman 1984). (There is, of course, an absolute change in the energy

scale; in the case of Ce the LMTO–ASA results are higher by 0.4 eV.) The value of the relative precision just given is much smaller than the energy differences which we will discuss in the next sections, and consequently, the use of the LMTO–ASA method is justified.

In the alternate approach – used for the pnictide compounds – excitation energies are determined using a Slater (1974) transition state analysis. Here too one first notes that one generally cannot use the ground-state eigenvalues. Instead, one first considers the fully screened final state (the f-screened hole) which can be approximately described using the ground-state eigenvalues. The essential idea is that the screening charge is sufficiently close to the charge removed by the excitation that the energetics of the system is essentially that of the effective one-particle eigenvalue. More precisely, we use the idea that the occupation-number derivative of the total energy is this eigenvalue, $dE/dn = \varepsilon$, and ε is essentially unchanged because of the nature of the screening. Thus, the eigenvalue ε is equal to the integral of dE/dn for a change of one in the excitation charge which is just the change in total energy, i.e., it is the excitation energy. This also has the advantage of revealing more about what is happening in the system than does calculating the total energy of the initial and final states directly. The total-energy difference is written as

$$\Delta E = -\int_0^y (\delta E/\delta n)\mathrm{d}n = -\int_0^y e_f(n)\,\mathrm{d}n, \tag{3}$$

using the property of the local-density-approximation (LDA) functional that the eigenvalue is the occupation-number derivative of the total energy. Here y is the f-occupation in the ground state. This integral can be simply evaluated if one invokes the observation that the eigenvalue is to a good approximation a linear function of the occupation – a property that is satisfied by the f-orbitals in the Ce atom (Koelling 1981). As a result, the integral can be evaluated by taking an average of the end points,

$$\Delta E = -(\bar{e}_f + \tilde{e}_f)/2 \tag{4}$$

where $\bar{e}_f$ is the mean f-eigenvalue in the ground state and $\tilde{e}_f$ is the mean f-eigenvalue of the excited state.

3.3. *Ce-excited state properties*

In order to obtain excitation energies, a knowledge of the total energy of both the final state and the initial ground state is necessary. A detailed study of the electronic structure and total energy of the ground state of Ce and the α–γ phase transition were discussed in the previous section (see also Min et al. 1986b); here only the results of ground state calculations consistent with the choice of final state in the excited state calculations are presented in each table.

In general, the core electrons in solids are chemically not important. In materials with a large nuclear charge, however, this is not exactly true for the higher semi-core

electrons like the 5p's in Ce. The spatial extent of these electrons is large enough to cause a noticeable overlap with orbitals on neighboring atoms and to result in a nonnegligible band width. On the other hand, these electrons approach close enough to the nucleus for relativistic effects to be important. Both features affect the screening of the nucleus and hence the energy of the 4f-electrons. The programs used in this study do not treat valence electrons fully relativistically and therefore one had to make the choice of either treating the 5p-electrons like the other core electrons, (i.e., fully relativistically but without interatomic hybridization), or treating the 5p-electrons as valence including all overlap but neglecting spin–orbit coupling. The difference between these results is a measure of the uncertainty in the numerical data.

3.3.1. *3d core excitation energies*

First, final state calculations are performed for a 3d core hole in α-Ce in which the 4f-electrons are treated as normal band states, i.e., without fixing the number of 4f-electrons. Three different sizes for the supercell are considered; details are given in table 6. In these calculations, the lattice constant, a, is set equal to the experimental value for α-Ce and the 5p-electrons are treated as valence electrons. The results in table 7 clearly show that the screening of a 3d core hole takes place predominantly in the central cell. The integrated charge in the surrounding atoms (including the 4f-shell) in the larger clusters are close to that of the pure system and also the total energy hardly changes. There is a strong Coulomb attraction between the core-hole and the 4f-electrons and as a result the local 4f-level is pulled towards lower energy (Oh and Doniach 1982) and the 4f-occupancy of the central cell is increased by more than one. Consequently, the spatial extent of these levels is reduced and both the central 3d core hole and the 4f-electrons are completely localized within the impurity cell. The changes in total energy due to the interaction of the impurity with its neighbors are in the mRy range and hence these core level spectra are already obtained precisely from a one-atom 'supercell'.

The experimental 3d core level XPS spectra (Wuilloud et al. 1983) show a multiplet structure related to the coupling of the 3d core hole and the localized 4f-electrons. The energy splittings of these multiplets are smaller than the energy differences between 4f-occupancies, where Coulomb interactions play a larger role. Therefore, in the following, only differences in final state 4f-occupation are con-

TABLE 6
Description of the supercell calculations.

Size of supercell atoms	Basic lattice	Number of different types of atoms	Atom type	Number of atoms per type	Impurity–impurity distance in terms of lattice parameter
1	fcc	1	1	1	$a/\sqrt{2}$
4	simple cube	2	1	1	a
			2	3	
8	fcc	3	1	1	$\sqrt{2a}$
			2	6	
			3	1	

TABLE 7
Results of ΔSCF-supercell calculations for $3d_{3/2}$ core-hole excitations of α-Ce as a function of the size of the supercell. Q's denote angular momentum decomposed integrated charges inside the atomic sphere. The ground state results are provided for comparison.

Size	Atom type	Q_s	Q_p	Q_d	Q_f	Q_{tot}	E_{tot}	ΔE [Ry]	ΔE [eV]
1	1	0.47	5.92	1.78	2.83	11.0	−17651.7118	65.4495	890.5
4	1	0.49	5.94	1.81	2.85	11.8	−70803.1934	65.4518	890.5
	2	0.50	5.93	2.11	1.42	9.97			
8	1	0.49	5.94	1.80	2.84	11.06	−141671.8366	65.4538	890.5
	2	0.50	5.94	2.13	1.42	9.99			
	3	0.51	5.94	2.13	1.43	10.01			
Ground state	1	0.50	5.94	2.14	1.42	10.00	−17717.1613		

sidered and one has to keep in mind that the results represent some average of the available multiplet terms.

The number of 4f-electrons in the final state is easily controlled by treating these electrons as core electrons, neglecting 4f-hybridization, and by subsequently omitting the $l = 3$ basis functions on the central atom. Charge distributions and total energies as a function of supercell size are given in table 8 for a $3d_{3/2}$ core hole in the $4f^1$ final state configuration of γ-Ce. Almost all screening takes place in the impurity cell itself. This also shows the strong spatial localization of the 4f-orbitals, since the screening of more extended orbitals also includes neighboring atoms. The results in

TABLE 8
Results of ΔSCF-supercell calculations for a $3d_{3/2}$ core hole of γ-Ce for the $4f^1$ final state; symbols are as in table 7.

Size	Atom type	Q_s	Q_p	Q_d	Q_f	Q_{tot}	E_{tot}	ΔE [Ry]	ΔE [eV]
1	1	0.61	6.06	3.33	1.0	11.0	−17651.0462	65.9679	897.5
4	1	0.65	6.06	3.45	1.0	11.15	−70802.1015	65.9549	897.4
	2	0.59	6.05	2.30	1.0	9.95			
8	1	0.66	6.05	3.43	1.0	11.14	−141670.1659	65.9469	897.3
	2	0.61	6.05	2.32	1.0	9.97			
	3	0.62	6.05	2.35	1.0	10.02			
Ground state	1	0.61	6.05	2.33	1.0	10.0	−17717.0141		

table 8 pertain to γ-Ce, in which case the neglect of the 4f interatomic matrix elements has smaller effects than for α-Ce, due to the larger atomic spacing. It is also consistent with the fact that the 4f-electrons in γ-Ce are localized to such an extent that they are close to a Mott transition (Johansson 1974b). On the other hand, the peak positions in the 3d core-hole spectra for α-Ce and γ-Ce are similar and hence differences in the electronic structure are relatively small, as is also borne out by band structure calculations (Pickett et al. 1981, Podloucky and Glötzel 1983, Min et al. 1986b).

The theoretical results (Min et al. 1986a) for 3d core hole spectra and different final state 4f-configurations are given in table 9. Here only one atom 'supercells' have been employed, which is sufficient to obtain a precision better than 1eV, as shown above. For γ-Ce the results are compared with experimental results (Fuggle et al. 1983) where they are available. From these data it is derived that the energy difference is minimal when the number of 4f-electrons is approximately 2.5, which is consistent with the results of the first calculation in table 7.

The results in table 9 show that the experimental 3d core binding energies are about 5eV larger than our theoretical values. This number is larger than possible discrepancies due to the effects (Esteva et al. 1983) of selection rules.

A possible explanation for the absolute shift of the 3d core hole binding energies may be found in the LDA itself. Although the Hedin–Lundqvist (1971) form of the exchange and correlation potential produces good results for the valence electrons, it is questionable whether it describes a 3d core state with the same accuracy. In

TABLE 9

Comparison of ΔSCF results with experiment considering several $4f^n$ final states. The initial state is assumed to be $4f^1$. Results in parentheses pertain to calculations in which the 5p-electrons were treated as core electrons.

		Final states	ΔE [eV]	(ΔSCF)	ΔE [eV] (expt)	Difference [eV]
γ-Ce	$3d_{3/2}$	$4f^0$	910.5	(909.0)		
		$4f^1$	897.5	(896.6)	901.9 ± 0.4	4.2 (5.1)
		$4f^2$	891.2	(891.1)	896.4 ± 1.0	5.2 (5.3)
		$4f^3$	890.9	(891.7)		
	$3d_{5/2}$	$4f^0$	891.3	(889.7)		
		$4f^1$	878.3	(877.3)	883.7 ± 1.0	5.4 (6.4)
		$4f^2$	871.9	(871.8)	878.5 ± 1.0	6.6 (6.7)
		$4f^3$	871.6	(872.4)		
α-Ce	$3d_{3/2}$	$4f^0$	909.7			
		$4f^1$	897.0	(895.9)		
		$4f^2$	891.1	(891.0)		
		$4f^3$	891.2			
	$3d_{5/2}$	$4f^0$	890.5			
		$4f^1$	877.8	(876.7)		
		$4f^2$	871.9	(872.4)		
		$4f^3$	871.9			

order to test this hypothesis, 3d ionization energies for a Ce atom are calculated. Two different formula for the exchange and correlation potential are employed: the Hedin–Lundqvist form and the Kohn–Sham (1965) Gaspar (1954) form. The last one only includes the term with the one-third power of the density. The resulting ionization energies differ by 1.9eV, which is smaller than the differences we found between experiment and theory for the 3d core hole excitations. Though one cannot exclude the possibility that the difference resulting from using the Hedin–Lundqvist form in LDA or the exact exchange and correlation potential in density functional theory will be about 6eV, it is expected that this is probably not the case and that the absolute shift in our 3d core binding energies has, at least partly, another explanation like the effect of a charged environment.

In choosing the final states Min et al. (1986a) restricted themselves to neutral supercells. (The samples in the experiment are always grounded to achieve a macroscopic charge neutrality.) Locally, however, charge neutrality is determined by the difference between the time it takes the photoelectron to leave the sample and the time it takes an additional electron to enter the vicinity of the excited atom. In order to accurately describe the photoemission process one needs time-dependent theory, incorporating the dynamical effects of the screening electrons moving towards the d-hole. In our calculations we only consider final states, where the conduction electrons are in equilibrium with a certain number of f-electrons and a d-hole. Hence, another possible explanation of the absolute shift of the binding energies in table 9 is our approximation that we neglect these dynamical effects.

The difference in total energy between $d_{3/2}$-configurations and the corresponding $d_{5/2}$-states measures the strength of the spin–orbit interaction for the 3d-levels. The theoretical value, 19.3eV, overestimates the experimental value (18.0eV). By contrast, the separation of the 3d-eigenvalues in the ground state calculations is 18.8eV. The eigenvalues of the LDA equations do not represent excitation energies because of self-energy corrections which are needed to modify the LDA equations into Dyson's equations. The results show that the self-energy corrections to the $3d_{3/2}$-and $3d_{5/2}$-levels are similar. The spin–orbit splitting from the LDA eigenvalues is only 0.5eV smaller than that from the total-energy differences and both are about 1eV larger than the experimental value. The $3d_{3/2}$ LDA eigenvalue itself, however, is at 874.3eV for the α-Ce ground state. The excitation energy is 890.5eV (table 7), which results in a total self-energy correction of 16.2eV for the $3d_{3/2}$-level, which is much larger than the difference between the values for $3d_{3/2}$ and $3d_{5/2}$.

3.3.2. *4f excitation energies*

The peak positions of 4f valence band photoemission spectra are obtained in a similar way as in the case of 3d core hole spectra. Here too Min et al. (1986a) first studied the convergence with respect to cluster size and the results are given in table 10. Again it is found that an efficient screening of the localized 4f-hole and only a small effect of the size of the supercell occurs. The 4f-occupancy of the central (hole) site is treated as before.

In the first set of calculations, the 4f-electrons at the neighboring sites and the ground state were treated as ordinary band states. This is the major reason that the

TABLE 10

Results of ΔSCF-supercell calculations for 4f-excitations of α-Ce. Values in parentheses pertain to calculations in which the 5p-electrons are treated as valence-band electrons and included in the Q count.

Size	Atom type	Q_s	Q_p	Q_d	Q_f	Q_{tot}	E_{tot} [Ry]	ΔE [Ry]	ΔE[eV]
1	1	0.58	0.43	2.99	0.0	4.00	−17716.9751	0.3312	4.5
		(0.55)	(6.06)	(3.39)	(0.0)	(10.00)	(−17716.7852)	(0.3761)	(5.1)
4	1	0.60	0.26	3.14	0.0	4.01	−70868.8974	0.3278	4.5
	2	0.51	0.28	2.04	1.16	4.00			
8	1	0.60	0.27	3.11	0.0	3.97	−141738.1211	0.3293	4.5
	2	0.51	0.25	2.08	1.16	4.00			
	3	0.51	0.22	2.15	1.15	4.03			
Ground state	1	0.51	0.22	2.11	1.15	4.00	−17717.3063		
		(0.50)	(5.94)	(2.14)	(1.42)	(10.00)	(−17717.1613)		

calculated total energy difference (4.5eV) becomes too large compared with the experimental value (2eV). In addition, by neglecting the $l = 3$ basis functions on the central site the variational freedom of the s- and d-like bands was limited, and so the total energy will not reach its lowest value. Now a photoemission experiment is extremely fast and will see only distinct configurations of 4f-electrons, since they have a long hopping time on the time scale of photoemission experiments. Finally, in the local density approximation, the band width of the 4f-electrons is overestimated by an order of magnitude when treated with full hybridization and this results in too large an f-occupancy.

The solution to this problem is straightforward – force the occupation numbers to be integral. This procedure, which is followed next, is closer to the experimental situation as observed in photoemission experiments because the fluctuation of f-occupation is slow compared to the time scale of the measurement. The resulting values of the total energy are given in table 11 for γ-Ce and α-Ce. The 4f excitation energies, 2.4eV for γ-Ce and 1.9eV for α-Ce correspond to the 2eV peak in PES. The values given in parenthesies (3.3 and 2.8eV for γ- and α-Ce, respectively) are for the case where 5p-electrons are treated as valence band electrons. The agreement with experiment is good, since one has to keep in mind that the theoretical values have error bars of 1eV due to the numerical approximations discussed before.

In both 3d-core and 4f-valence photoemission spectra the size of the supercell turned out not to be an important parameter due to the extreme localization of the created hole. One might expect a qualitatively different situation in the BIS spectra, because the presence of the additional 4f electron forces the orbitals to be more delocalized. The results in table 12, however, show only a small effect; the energy difference between a large and a small cluster is only 0.1eV. Experimental BIS spectra show a broad line centered about 4eV above the Fermi level (Wuilloud et al. 1983) and the Min et al. (1986a) values are in qualitative agreement. The results are discussed in more detail in the next section.

3.3.3. *Discussion of results: f-band hybridization, number of f-electrons and* U_{eff}

In all band structure calculations describing elements in the left side of the periodic table one always faces the problem how to treat the extended semi core p-states. In pure Ce, the 5p-electrons are sufficiently delocalized to have a direct overlap and hence to form a band. This suggests treating them as valence electrons and using a larger basis to describe more rapid changes in the charge density in the interstitial region near the sphere boundaries. On the other hand, local density theory is known to overestimate the band width pertaining to such localized electrons, and hence it is possibly more realistic to neglect the hybridization of these semicore electrons by describing them as ordinary core states. We have performed most of the calculations for both situations in order to investigate the importance of the semicore 5p-electrons for the excitation spectra. Since the valence electrons are described in a semirelativistic approximation in our method, the neglect of spin–orbit coupling (which is not a severe approximation for a completely filled band) causes an absolute shift of 0.2 Ry between the total energies in the two cases. Since we are interested in relative ΔSCF energy differences, this absolute shift is unimportant.

TABLE 11

4f-electron removal energies resulting from our ΔSCF-supercell calculation. Values in parentheses are for the case where 5p-electrons are considered as valence-band electrons.

	Size	Atom type	Q_s	Q_p	Q_d	Q_f	Q_{tot}	E_{tot} [Ry]	ΔE [Ry]	ΔE [eV]
γ-Ce	1	1	0.65	0.51	2.84	0.0	4.0	−17716.9447	0.1768	2.4
			(0.61)	(6.06)	(3.33)	(0.0)	(10.0)	(−17716.7752)	(0.2389)	(3.3)
	8	1	0.69	0.43	3.00	0.0	4.13	−141736.7983	0.1737	2.4
		2	0.64	0.40	1.94	1.0	3.98			
		3	0.65	0.38	1.97	1.0	4.00			
		1	0.66	6.05	3.40	0.0	10.11	(−141735.8802)	(0.2326)	(3.2)
		2	0.61	6.05	2.32	1.0	9.98			
		3	0.62	6.05	2.34	1.0	10.01			
	Ground state	1	0.65	0.38	1.97	1.0	4.00	−17717.1215		
			(0.62)	(6.05)	(2.33)	(1.0)	(10.00)	(−17717.0141)		
α-Ce	1	1	0.58	0.43	2.99	0.0	4.00	−17716.9007	0.1387	1.9
			(0.55)	(6.06)	(3.39)	(0.0)	(10.00)	(−17716.7852)	(0.2086)	(2.8)
	Ground state	1	0.55	0.31	2.14	1.0	4.00	−17717.0394		
			(0.54)	(6.02)	(2.44)	(1.0)	(10.00)	(−17716.9938)		

TABLE 12
4f-electron addition energies. Symbols are as in table 11.

	Size	Atom type	Q_s	Q_p	Q_d	Q_f	Q_{tot}	E_{tot} [Ry]	ΔE [Ry]	ΔE [eV]
γ-Ce	1	1	0.60	0.21	1.18	2.0	4.0	−17716.8914	0.2301	3.1
			(0.58)	(6.00)	(1.42)	(2.0)	(10.00)	(−17716.8533)	(0.1608)	(2.2)
	8	1	0.59	0.30	1.15	2.0	4.04	−141736.7336	0.2389	3.2
		2	0.65	0.36	1.98	1.0	3.99			
		3	0.65	0.39	1.98	1.0	4.03			
		1	0.56	6.03	1.45	2.0	10.04	(−141735.9543)	(0.1585)	(2.2)
		2	0.63	6.04	2.32	1.0	9.99			
		3	0.62	6.05	2.34	1.0	10.01			
α-Ce	1	1	(0.48)	(5.95)	(1.57)	(2.0)	(10.0)	(17716.8036)	(0.1947)	(2.6)

The main effect of the hybridization of the 5p semicore levels is a slight delocalization of their orbitals. As a result, the atomic core is less well screened and the 4f-electrons experience a more attractive potential. Their energy eigenvalues drop to a lower value and the 4f-occupation increases. The results in table 9 show absolute changes in the 3d binding energies of at most 1 eV, which is consistent with our earlier estimates and is much smaller than the difference between the theoretical values and experiment. The effects on the 4f binding energies are also approximately 1 eV (see tables 10, 11, 12) and hence one can conclude that theoretical binding energies have an absolute error of about 1 eV due to numerical (LMTO) and theoretical (LDA) approximations.

The total energy $E(n)$ as a function of the number of 4f-electrons, n, can be parameterized as follows (Hirst 1970):

$$E(n) = E_0 + n\varepsilon_{\text{eff}} + \tfrac{1}{2}n(n-1)U_{\text{eff}}. \tag{5}$$

U_{eff} is an effective intra-atomic f–f Coulomb interaction energy and ε_{eff} is the effective binding energy of the 4f-electron. These are renormalized parameters which include all the effects of the conduction electrons. In the presence of a 3d core hole, the binding energy ε_{eff} is lower than its ground state value by an amount U_{fd}, which represents the effective interaction energy of the 4f-electron with the core hole.

The total energy results are fitted to the function given in eq. (5) and resulting ε_{eff} and U_{eff} are given in table 13, together with the value of n at which $E(n)$ is minimal. The effective intra-atomic f–f interaction U_{eff} is determined directly by the shape of the 4f-orbitals and also indirectly by the presence of the conduction electrons. The value of U_{eff} is independent of the treatment of the 5p-electrons and is the same for α-Ce and γ-Ce (one cannot attribute any meaning to differences of order 0.1 eV because of numerical approximations).

The value for U_{eff} agrees well with the experimental result (Baer et al. 1981) (around 6 eV). Since in the calculations only the f-occupation is fixed and the conduction electrons are allowed to relax completely, this indicates that the quasiparticles seen in the experiment are indeed f-electrons (or holes) dressed with a rapidly responding cloud of conduction electrons.

The average number of f-electrons, n, decreases from γ-Ce to α-Ce, which is in agreement with experiment. For the free-atom local density theory underestimates the 4f-occupancy, i.e., one finds 1.57 instead of 2. In the solid, the value of the number of 4f-electrons depends on the theoretical treatment of the 5p-semicore. Several factors play a role in determining the value of ε_{eff}. Neglecting the hybridization of these 5p-electrons makes them more localized and as a result the 4f-orbitals become more extended and less occupied. Hence, in addition to errors due to the local density approximation made in describing the 4f-electrons, the 4f occupation numbers and related binding energies are also indirectly affected by errors due to the local density description of the 5p-electrons. The effects on the binding energies are much larger than the effects on the energy U_{eff}.

The average number of 4f-electrons is related to the quasiparticle energy ε_{eff} by setting $\partial E(n)/\partial n = 0$ in eq. (5):

$$n = \tfrac{1}{2} - \varepsilon_{\text{eff}}/U_{\text{eff}}. \tag{6}$$

TABLE 13

Parameters in the equation: $E = E_0 + \varepsilon_{\text{eff}} + \frac{1}{2}n(n-1)U_{\text{eff}}$. η and ε_{eff} are number and effective level of 4f-electrons respectively. U_{eff} is the effective intra-atomic Coulomb correlation interaction of 4f-electrons. U_{fd} is an interaction between the 3d core hole and 4f-electrons.

		U_{eff}	ε_{eff}	U_{fd}	n
γ-Ce	Ground state				
	5p-valence	5.44	−3.24		1.10
	5p-core	5.54	−2.41		0.93
	$3d_{3/2}$ core hole				
	5p-valence	6.35	−12.86	−9.61	2.53
	5p-core	6.50	−12.24	−9.83	2.38
	$3d_{5/2}$ core hole				
	5p-valence	6.35	−12.90	−9.65	2.53
	5p-core	6.50	−12.24	−9.83	2.38
α-Ce	Ground state				
	5p-valence	5.43	−2.84		1.02
	$3d_{3/2}$ core hole				
	5p-valence	6.40	−12.54	−9.70	2.46
	$3d_{5/2}$ core hole				
	5p-valence	6.35	−12.52	−9.68	2.47
Ce atom	Ground state	4.53	−4.86		1.57
	$3d_{3/2}$ core hole	5.09	−12.99	−8.13	3.04
	$3d_{5/2}$ core hole	5.09	−12.97	−8.11	3.05

The results show that U_{eff} is the same for α-Ce and γ-Ce and hence that changes in the n are directly related to changes in ε_{eff}. Values of the 4f-occupation (Allen et al. 1983) derived from BIS experiments on the basis of the Gunnarsson–Schönhammer (1983) (G–S) model are 1.0 for γ-Ce and 0.85 for α-Ce. In our case, n is derived in a simple way by finding the minimum of the total energy curve and is different from the 4f-occupation number in the G–S model, which is the eigenvalue of a number operator in their model Hamiltonian. Since our basic quantities are total energies, a direct comparison of our results with the experimental spectra is more appropriate than is a comparison with the G–S values.

Photoemission results show the f^0 peak to be at 2.0 eV for both α-Ce and γ-Ce and an increasing intensity of the 4f-peak near the Fermi level in α-Ce. The BIS results show, in addition, that the intensity of the $4f^1$-peak in α-Ce has become (at least partially) more enhanced and is located slightly above the Fermi level. The center of the broad $4f^2$-peak is shifted to slightly higher energies in α-Ce. Accurate assignments of the experimental energy levels depend on the model one uses for the line shape; in table 14 some possibilities are presented which agree with the experimental spectra and which display the physics involved. In this way, Min et al. (1986a) derive ranges for the experimental values of the parameters ε_{eff}, U_{eff}, and n. Note that an overall change in the position of the $4f^2$-peak only affects U_{eff}. Also, the location of the $4f^0$-peak at 2.0 eV indicates that the absolute value of ε_{eff} has to be smaller than 2.0 eV, because $E(4f^0) = -\varepsilon_{\text{eff}} + E(4f^1)$.

TABLE 14
Possible experimental peak assignments in eV.

	α-Ce			γ-Ce		
$E(0)$	2.0	2.0	2.0	2.0	2.0	2.0
$E(1)$	0.1	0.3	0.3	0.1	0.0	0.0
$E(2)$	4.3	4.3	4.8	4.0	4.0	4.5
ε_{eff}	−1.9	−1.7	−1.7	−1.9	−2.0	−2.0
U_{eff}	6.1	5.7	6.2	5.8	6.0	6.5
n	0.81	0.80	0.77	0.83	0.83	0.81

The change in the experimental value of U_{eff} between α-Ce and γ-Ce depends on the choice of the position of the $4f^1$-level and is somewhere between 0.0 eV and 0.3 eV. The calculated values given in table 13 indicate a change of less than 0.1 eV, which is in fair agreement with experiment. The experimental value of ε_{eff} changes by 0.2 eV and again, given all error bars, is consistent with our change of 0.4 eV. The only large discrepancy is in the absolute value of ε_{eff}, which is about 1 eV too large in our theoretical treatment.

The discrepancy between the theoretical value of ε_{eff} and the experimental value indicates that in the theoretical treatment the potential for the 4f-electrons is too attractive. As a consequence, the position of the 4f-band with respect to the conduction band is too low and its occupancy is too large. Neglecting the hybridization of the 5p semicore electrons contracts the 5p-orbitals and yields a better screening of the nucleus. As a result, the 4f-electrons experience a less attractive potential and the binding energy becomes smaller as can be seen in table 9. Similarly, the decrease in lattice constant between γ-Ce and α-Ce increases the density of the conduction electrons near the nucleus and again the binding energy decreases. In the standard local density treatment for Ce the hybridization of the 4f-electrons is too strong and gives rise to an overestimated drop in energy of the single 4f bonding orbital. This effect, however, is already accounted for in table 13 since all hybridization of the 4f-electrons is neglected.

The ground state calculations (Min et al. 1986b) without direct 4f-hybridization and overlap yield an equilibrium lattice constant which is slightly larger than the value for γ-Ce, indicating that the 5d-bonds alone are not sufficiently strong. A direct 4f-contribution is needed. A standard local density calculation with full 4f-hybridization, however, gives a lattice constant which is about 6% smaller than the value for α-Ce. Hence, the 4f-contribution to the bonding is somewhere between zero and the LDA value. As a result one expects from a linear interpolation that the resulting value of ε_{eff} will be around −2.8 eV for γ-Ce, which is too strongly bound. Therefore, nonlinear effects are important and the details of the interactions between the f-electrons, the conduction electrons and the 5p core electrons are very subtle.

3.4. *Excited state properties of the other lanthanides*

As discussed above, excitations of the 4f-electrons as observed in PES and BIS are

accompanied by a strong relaxation of the system. Due to this relaxation, Koopman's theorem certainly does not hold (Slater 1974) for the LDA eigenvalues and so a comparison between theoretical ground state results and experiment is not possible. Hence, differences of the total energies of self-consistent calculations for the initial ground state and the final excited state (ΔSCF) are needed in order to predict the correct f-electron excitation energies as measured in PES and BIS experiments (Lang et al. 1981).

The charge density of the final state can be simulated in a supercell geometry (Zunger and Freeman 1977), which puts the 'impurity atom' with the 4f core hole in the center of a cluster of normal atoms with the ground state configuration. If one chooses the unit cell (supercell) large enough, one can minimize the intercellular impurity–impurity interaction and use an ordinary LDA band structure calculation to obtain a total energy of the excited state. In fact, in a study of localized 4f-excitations in Ce, Min et al. (1986a) have established that the dependence on the size of the supercell is not significant and that even a one-atom supercell is already sufficient for reasonable precision in the total energy as discussed in a previous section.

This idea is extended to the study of 4f-excitations in the lanthanide metals assuming them to have the fcc structure – except for Eu which is taken as bcc (Min et al. 1986e). Again, the 4f-electrons are treated as core-like and in this way mimic the localized nature of the excitation. The configurations are assumed as $f^n(5d\,6s)^m$ for the ground state, where $m = 2$ for Eu and Yb and $m = 3$ for the others, $f^{n-1}(5d\,6s)^{m+1}$ for PES, and $f^{n+1}(5d\,6s)^{m-1}$ for BIS final states. Hence, the localized hole or electron is assumed to be completely screened by conduction electrons as in the work of Herbst et al. (1976). The 4f PES excitation energy, Δ_-, is given by $\Delta_- = E[f^{n-1}(5d\,6s)^{m+1}] - E[f^n(5d\,6s)^m]$ and the 4f BIS excitation energy, Δ_+, is given by $\Delta_+ = E[f^{n+1}(5d\,6s)^{m-1}] - E[f^n(5d\,6s)^m]$. In fact, the experimental results show broadened f-PES or BIS peaks due to many effects, such as multiplet interactions, crystal field effects, spin–orbit interaction, many-body effects, energy resolution, etc. It is expected that our estimated values of Δ_- and Δ_+ correspond to the central positions of the observed broadened peaks.

The resulting values of the 4f-PES energy Δ_- are given in fig. 13a and are compared with the experimental values. The calculations were performed at the experimental lattice constants and the effects of Hund's rule are included in the spin-polarized calculation, as discussed in section 2.2.2, for the heavy lanthanides metals (Eu to Tm). The agreement is fairly good, considering the simplicity of the calculation and the assumption of the fcc structure; general trends are well reproduced even though some discrepancies are observed. Rather large differences (40 to 45%) are seen for Er and Tm. The small values of Δ_- for Eu and Yb are directly related to the existence of valence fluctuations (Lawrence et al. 1981) between the divalent and trivalent configurations which are observed in some of their compounds.

In the same way, the 4f-BIS energy Δ_+ of the localized 4f-electron are obtained. The corresponding theoretical and experimental values are compared in fig. 13b and one finds good agreement except for a few heavy lanthanide metals (Ho, Er, and

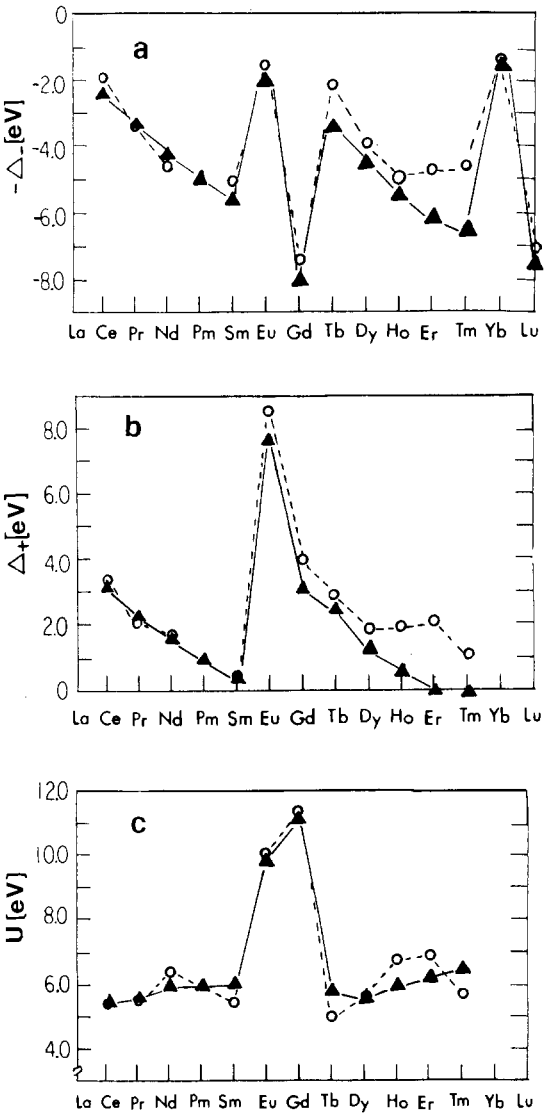

Fig. 13. Theoretical (▲) and experimental (○) values for (a) Δ_-, (b) Δ_+ and (c) the intra-atomic Coulomb correlation, U, for the lanthanide series.

Tm). The minimum for Sm and the maximum for Eu in Δ_+ are well reproduced. The small value of Δ_+ for Sm is again consistent with the observed valence fluctuations in some compounds of Sm. In Er and Tm, the calculated Δ_+'s are quite different from experiment and become slightly negative which indicates that the assumed ground state trivalent configurations for them are higher in energy than are the divalent configurations. The error in Δ_- and Δ_+ for these materials is apparently due to overestimations of 4f-occupancy in LDA. In fact, the LDA band structure calculations give 4f-occupancies (11.7 for Er and 12.7 for Tm) which are rather closer to the divalent configurations.

The energies, Δ_- and Δ_+, considered above, correspond to the peaks for localized 4f-excitations screened by the conduction electrons. Besides these peaks, there might occur an extra peak near the Fermi level in metals which have delocalized f-bands; this is the case in Ce which exhibits double peak structures (Wieliczka et al. 1984a, Wuilloud et al. 1983) in 4f-PES and BIS. The existence of this extra peak is determined by the relation of the PES process time to the f-electron hopping time. If the f-electrons are sufficiently delocalized (or strongly hybridized with the d-electrons), the 4f localized excitations are screened by the itinerant f-electrons so that the final state becomes close to the initial state and this results in a small excitation energy. The additional peaks (about 0.5eV below E_F), observed in recent PES experiments (Wieliczka et al. 1984b, Parks et al. 1984) for the light lanthanides (Pr, Nd) and their compounds, can be interpreted by this mechanism, which implies that f-electrons in these compounds are sufficiently delocalized so as to take part in the screening (further discussion will be in section 3.6).

From the results for Δ_- and Δ_+, one can estimate the intra-atomic Coulomb correlation interaction, U, by the relation $U = \Delta_- + \Delta_+$. Figure 13c provides estimated values of U compared with experiment. The agreement is better than for Δ_- or Δ_+ separately; apparently the errors are cancelled in the summation. The large U's of Eu and Gd are well predicted and they reflect the strong stability of the half-filled 4f-shell. Finally, these large values of the Coulomb correlation compared with the 4f-band width give additional strong evidence for the localized nature of the 4f-electrons.

To describe the localized 4f-excitations, it is pointed out that self-consistent total energy calculations are essential, since the eigenvalues in the LDA one-electron equation cannot account for the strong relaxation observed in the experiments. However, it is interesting to compare the results from ΔSCF total energy calculations and from LDA band structure eigenvalues for the 4f energy position in the ground state. Figure 14 gives the positions of the LDA 4f-levels with respect to E_F. Compared with Δ_- in fig. 13a one finds that the overall shape is similar except for an almost constant shift in energy. The differences between the two values correspond to the unrelaxed self-interaction and the relaxation–polarization self-energy term (Slater 1974) which comes from the perturbed relaxation of these levels. Hence this constant value of the energy differences implies that the response to the perturbation is similar in most lanthanide elements.

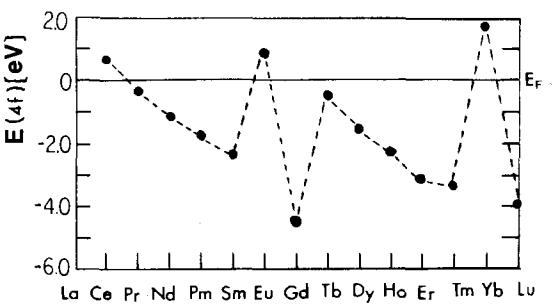

Fig. 14. Position of the LDA 4f-eigenvalues of the lanthanides with respect to the Fermi level.

3.5. *Ground and excited state properties of the Ce pnictides*

3.5.1. *Experimental observations*

Cerium pnictides offer three advantages for the study of the different screening channels: (1) they are computationally quite tractable as they crystallize in the rock-salt structure; (2) experimental data are available for the series; and (3) by considering the different pnictides one can examine a quite itinerant-electron system (CeN) or a fairly localized system (CeSb) with some variation in-between. With the exception of CeN, cerium pnictides all exhibit rather similar photoemission spectra (Baer et al. 1978, Franciosi et al. 1981). The pnictide p-states produce a rather broad peak about 2eV below E_F. On top of this are superimposed the two peaks derived from the f-orbital: one near E_F and the other 3eV below E_F. As one scans down the series from CeP to CeBi, the peak at the Fermi energy diminishes in intensity and the lower-energy peak grows in intensity in a manner consistent with the interpretation of increasing localization (Franciosi et al. 1981).

The CeN spectrum shows a different structure (Gudat et al. 1982). The nitrogen p-states produce a double-peak structure at about 3eV. The f-peak at E_F is strongly present but the lower f-peak is not observed. An f-orbital-derived peak is present at 1.2eV, but is thought to be surface related. Although included in table 15 for completeness, this structure will not be considered here. (The peak is probably due to surface vacancies (Norman et al. 1985c).)

3.5.2. *Calculational techniques*

The basic calculational techniques utilized by Norman (1985) and Norman et al. (1985a) are all well documented so this description is quite brief. All calculations were performed using a self-consistent linearized augmented-plane-wave (LAPW) method (Koelling and Arbman 1975). The warped muffin-tin (WMT) shape approximation was used. In this approximation, the potential is spherically averaged about

TABLE 15

Peak positions relative to the Fermi energy for the cerium pnictides. Peak B in CeN is a surface related property only included here for completeness since it is not discussed. Units are electron volts.

	CeN			CeP			CeSb		
Peak	expt[b]	expt[a]	theor	expt[c]	expt[a]	theor	expt[c]	expt[a]	theor
A	0.35	0.1	0.1	0.6	0.08	0.08	0.6	0.04	0.04
B	1.2	0.95							
C1	2.7	2.45	2.1						
C2	3.6	3.35	3.3	2.1	1.58	1.6	2.15	1.59	1.55
D				3.0	2.48	2.55	3.1	2.54	2.75
E	5.5	5.25	5.1						

[a] As discussed in the text, the experimental Fermi energy has been reassigned to match peak A to the theoretical value (theor).

[b] (Gudat et al. 1982).

[c] (Franciosi et al. 1981).

each atomic site (muffin tin) but is of general form elsewhere (interstitial region). Relativistic kinematics were included by performing all self-consistency iterations in the semi- (or scalar) relativistic approximation (Harmon and Koelling 1974) and then including the spin–orbit coupling (MacDonald et al. 1980) in the final analysis without further iteration. This procedure allowed Norman (1985) and Norman et al. (1985a) to carry out sufficient iterations (25–30) to achieve mRy convergence even for the f-levels. All calculations employed the local-density approximation (LDA) for the exchange–correlation functional. The functional was chosen to include only the exchange part ($\alpha = 2/3$), since the inclusion of correlation within LDA is thought to be inappropriate for f-orbital materials (Koelling 1982).

Densities of states (DOS) and partial densities of states were obtained using the relatively coarse mesh in k-space that was used in the self-consistency process: the data of the $\pi/4a$ cubic mesh (89 points in the irreducible wedge of the zone) were linearly interpolated to obtain the body-centered point of the subcube. With use of this body-centered point, the cube was then broken up into 12 tetrahedra and standard linear tetrahedron analyses were applied to determine the contribution of each of these tetrahedra. Clearly such an approach does not give state-of-the-art results for the density of states but, since all final results will be compared using a broadening factor, it is quite adequate.

3.5.3. *Ground state results*

The band densities of states for CeN, CeP, and CeSb are shown in fig. 15 (Norman et al. 1985a). In these plots, the zero of the energy scale has been set at E_F. As expected for such an isoelectronic sequence, the basic structure of the DOS for these materials is similar. There is a two-peaked structure from about -5eV up to just below E_F that results from the pnictide p-bands. There is also a broad Ce d-band DOS starting just about where the pnictide p-bands leave off and extending well above the scale of the plots. Just above E_F are the two spin–orbit split peaks resulting from the f-orbitals; they clearly appear as nearly localized levels. A significant feature is the tail that extends down in energy from the lower level across E_F. This is the major f-orbital occupation. One sees that this tail is very sharp in CeP and CeSb and that E_F falls in a region with rapidly rising density of states.

In CeN, not only do the sharp localized f-levels lie higher above E_F, but the tail is much broader. In fact, E_F in CeN falls in a region where the band DOS is relatively constant as opposed to CeP and CeSb. This will be an important feature to remember when discussing the experimental assignment of E_F. The reason for this difference is that the Ce–Ce separation in CeN is sufficiently close so that direct f–f interactions can become significant. In the other pnictides, the f-orbitals can only hybridize with the other conduction-band states – mainly the ligand p-orbitals. This difference between CeN and the rest of the pnictides also appears in the p-band manifold. In CeP and CeSb, unlike the case for CeN, the upper p-band DOS peak is much higher than is the lower peak. In CeP and CeSb, the f-orbitals interact strongly with the pnictide p-orbitals and repel them from the vicinity of E_F – an effect that compresses the bands. This effect occurs in addition to the diminished band width arising from the larger lattice constants (which shows up for the entire

TABLE 16

Selected band results for the cerium pnictides. The angular momentum decomposition is a single-site decomposition of the wave function within the muffin tins, not the LCAO decomposition. The radial charge density of the 4f-orbital at the muffine tin boundary and the valence band width ($E_F - E_{L_1}$) are tabulated here as they enter into the discussion of relative peak heights (section 3.7). Units are atomic units except the band width which is given in electron volts.

	CeN	CeP	CeSb
Lattice constant	9.493	11.15	12.1
Ce muffin-tin radius	2.737	3.025	3.025
Pnictide (X) radius	1.990	2.550	3.025
l-decomposition			
Ce-s	0.10	0.13	0.12
Ce-p	0.27	0.17	0.12
Ce-d	0.93	1.04	0.92
Ce-f	0.86	1.02	1.07
X-s	0.02	0.02	0.02
X-p	3.15	2.54	2.57
X-d	0.02	0.06	0.07
$\sigma_f(r)$	0.0326	0.0150	0.0104
Band width (eV)	4.76	3.99	3.68

manifold). Both the lattice constants and the valence band width are included in table 16, where it can be seen that the valence band of CeN is almost a full electron volt wider than the CeP and CeSb.

The charge decomposition given in table 16 for each of the pnictides shows that the major charge contributions come from the Ce d-, Ce f-, and pnictide p-orbitals. The pnictide s-states have been included in the core and thus do not appear in this valence-band tabulation. Because these numbers are determined by a decomposition within a muffin-tin sphere, the size of that sphere will influence the values obtained – especially for the Ce d- and pnictide p-charge. The Ce f-charge, however, should be much less affected as most of the f-orbital is contained within the mufftin-tin sphere. Here one sees another difference between the members of this series. CeSb has an f-charge of 1.07 which is just about one f-charge beyond what is found in LaSb (the f-charge in LaSb of 0.1 is mostly due to a single-site reanalysis of orbitals from other sites). This is consistent with the $L1_2$ structure Ce systems $CeSn_3$ (Koelling 1982), $CeRh_3$ and $CePd_3$ (Koelling 1984), where f–f interactions are not possible. CeN has a much lower f-charge of 0.86 which is more in line with the cubic Laves phases where direct f–f interactions do occur. Pickett and Klein (1983) have discussed the question of direct f–f interaction in CeN and concluded that it was of considerable significance. CeP is intermediate between the two extremes. The Ce–Ce separation is sufficiently large in CeP that direct f–f interaction is not expected.

Only features resulting from the band-to-band transitions or from the fully screened channel should be represented in the ground state results. Thus, from the

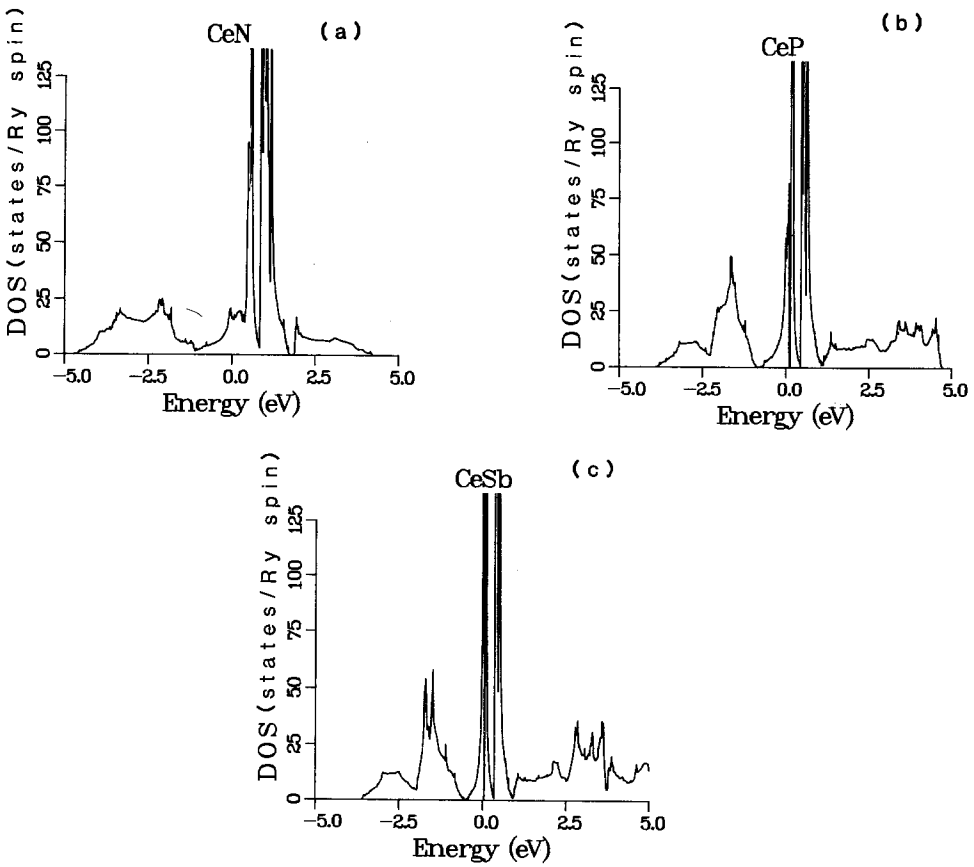

Fig. 15. Ground state band DOS (in states per Rydberg per spin) for CeN, CeP, and CeSb. The Fermi energy is at zero.

tabulation of the observed structures in table 15, only the subset consisting of the pnictide p-band emission (C) and the Ce f-state emission near the Fermi energy (A) should be compared to the DOS in fig. 15. It is necessary to first consider the emission at E_F to pin down the energy scale. It has been observed that E_F assigned in the experimental analysis in CeN is probably too high (Gudat et al. 1982). We expect that the error will be larger in CeP and CeSb for the following reasons. That assignment was based on a simple treatment of the edge shape that includes an assumption that the DOS at E_F is a constant over the range of the instrument broadening. Assuming that a fully screened transition should produce results much like the DOS cut off by E_F it is significant that the calculated DOS is rising rapidly in the vicinity of E_F (cf. figs. 15 and 16). If this is broadened by a reasonable instrument resolution function (0.2 eV wide), it is found that E_F should be nearly at the peak. This can be seen in fig. 17 where the broadened results are presented. An experimental test of this reassignment of the position of E_F should be undertaken since it is of interest to know if the fully screened peak represents a completely relaxed state. One strong supporting observation for the assignment of E_F is that the

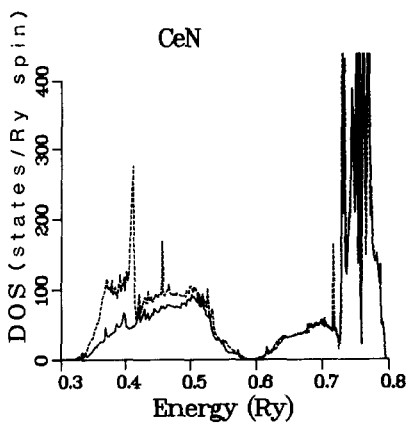

Fig. 16. Supercell DOS for CeN (in states per Rydberg per spin). The solid line is for the f-hole case. The dashed line is the result for the central site f-states back in (calculated using the f-hole supercell potential). The supercell Fermi energy is at 0.6821 Ry. In the cases of Ce and CeSb, the dashed curve replicates the solid curve except for a sharp peak below the valence band bottom.

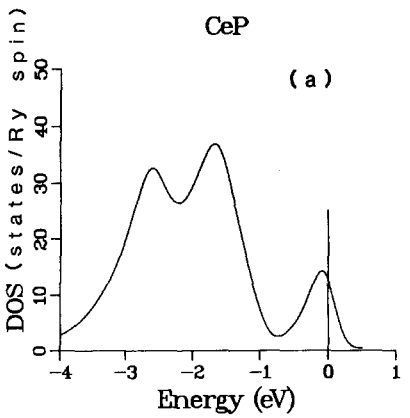

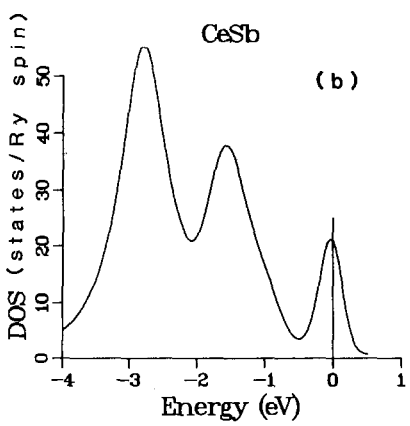

Fig. 17. Broadened DOS for (a) CeP and (b) CeSb (in states per Rydberg per spin). The Fermi energy is at zero. These were formed by taking the ground state DOS and the f-hole DOS and combining them in the manner described in the text (see section 3.5.5). In CeP, both f-peaks were enhanced by a factor of two relative to the p–d states in order to obtain better agreement with experiment.

pnictide p-band-derived peaks are then found to be in good general agreement with experiment. In CeP and CeSb, the two-peak structure seen in the bare DOS is not distinguishable when instrument and linewidth broadening are included. Thus there is only one peak (C) associated with the pnictide p-bands in these materials. In CeN, two peaks are still distinguishable even when broadening effects are included. The lower peak (C2) is seen to match rather well once the Fermi-energy correction has been applied. The experimental value of the upper peak (C1) lies 0.35eV below the band value. This difference probably relates to the fact that the band calculation shows f-hybridization into this peak as previously mentioned by Pickett and Klein (1983).

3.5.4. *The poorly screened peak*

Peak D in table 15 is attributed to the poorly screened f-hole channel. In CeP and CeSb it is observed 2.5eV below the fully screened peak, but in CeN it is not observed at all. This screening channel can be studied using supercell techniques to approximate the impurity-like problem arising from the presence of the f-hole. To induce the f-hole, one can simply remove from the basis set the variational freedom to represent a 4f-orbital on that site. Within the LAPW method, this is trivially done by placing the energy parameter for the $l = 3$ radial solution in the energy region of the 5f-orbital. Because the 5f-orbital is orthogonal to the 4f-orbital, there will be no possibility for the resultant basis set to resolve the 4f-solutions on that site. This 'impurity' atom is then studied by forming a supercell consisting of one such impurity together with three standard Ce atoms and their associated pnictides, i.e., the full cubic cell for the rock-salt structure with eight atoms per unit cell. The Ce atoms are then on a simple-cubic lattice so the impurity atoms are separated by one lattice constant. Fortunately, the f-hole turns out to be very local, so this separation should be adequate to reduce the impurity interactions to an acceptable level. It is necessary to proceed under this assumption in any case since expansion to larger supercells would be prohibitively expensive.

Much larger basis sets are required to achieve the same level of convergence for this eight-atom per-unit-cell–simple-cubic structure as for the rock-salt structured ground state. By iterating the system to self-consistency, the screening effects are incorporated into the model. The system is treated as a neutral solid. This is appropriate for a metallic system which is assumed to be in contact with a reservoir of electrons. Once self-consistency is achieved, one has established the nature of the screening charge and only determination of the excitation energy remains.

By definition, the relaxation energy shift δ being sought is the difference between the change in total energy of the system ΔE and the average occupied f-eigenvalue $\bar{e}_f$:

$$\Delta E = -\bar{e}_f + \delta = |\bar{e}_f| + \delta. \tag{17}$$

As discussed in section 3.2.2, the total energy difference is given by

$$\Delta E = -(\bar{e}_f + \tilde{e}_f)/2, \tag{8}$$

TABLE 17
Angular momentum decomposition inside the muffin tins for the supercell calculations. Ce(1) is the site with the hole, Ce(2) are the other three Ce sites, X(1) are the three (equivalent) pnictide sites, and X(2) the other inequivalent pnictide sites.

	CeN	CeP	CeSb
Ce(1)-s	0.11	0.15	0.14
Ce(1)-p	0.25	0.16	0.12
Ce(1)-d	1.43	1.73	1.76
Ce(1)-f	0.07	0.05	0.03
Ce(2)-s	0.10	0.13	0.12
Ce(2)-p	0.28	0.17	0.12
Ce(2)-d	0.96	1.05	0.98
Ce(2)-f	0.91	1.08	1.14
X(1)-s	0.02	0.03	0.03
X(1)-p	3.12	2.50	2.49
X(1)-d	0.03	0.08	0.09
X(2)-s	0.02	0.02	0.03
X(2)-p	3.11	2.50	2.52
X(2)-d	0.02	0.06	0.07

where $\bar{e}_f$ is the mean f-eigenvalue in the ground state and $\tilde{e}_f$ is the mean f-eigenvalue of the excited state. Thus

$$\delta = (\bar{e}_f - \tilde{e}_f)/2. \tag{9}$$

Note that since $\tilde{e}_f$ falls below $\bar{e}_f$, δ is a positive number consistent with the poorly screened state being a more excited state. If one were then to blindly view ΔE as the position of an f-level, it would appear more deeply bound.

The mean ground-state f-eigenvalue is taken to be at E_F for the transition state analysis. The eigenvalues for the excited state are found by performing a calculation with use of the supercell potential. The lack of dispersion found is an excellent demonstration that the f-hole is quite localized. Further, an examination of the charge decomposition in table 17 shows an approximate $f \rightarrow d$ transition. Most of a d-electron shows up on the central site after the loss of an f-electron, while the surrounding atoms are nearly unchanged. Because of the truncation of the d-orbital by the muffin-tin radius, that d-charge in the muffin-tin analysis probably corresponds to very nearly a full d-electron in an LCAO analysis of the wave function.

When these mean f-eigenvalues are inserted into the transition state analysis, the calculated peak position (D in table 15) agrees well with the experimentally observed peak for CeP. The calculated shift is somewhat too large for CeSb, as is expected from the fact that the supercell calculation has removed too much (≈ 1.07) f-charge. One can determine the size of the effect of removing too much f-charge by

a simple calculation based on the assumption of a linear dependence of the eigenvalues on occupation number. With use of this assumption to correct back to one f-electron of charge removed, the calculated peak would occur at 2.57eV, which is closer to the corrected experimental value (2.54eV) than is the result of the direct supercell calculation (2.75eV).

CeN again differs from CeP and CeSb. Because of the width of the valence band, the f-hole eigenvalues do not separate energetically from the valence band as they did for CeP and CeSb. The impurity site f-DOS is spread throughout the valence band and thus the f-orbitals are strongly hybridized with the pnictide p-states, as can be seen in fig. 16. Thus, the initial assumption of a well-defined hole is not realized and this channel should be extremely weak if at all present in CeN. If one were to persist and estimate the mean eigenvalue $\tilde{e}_f$ from the low-lying peak in fig. 16, the resultant transition state energy would fall in the vicinity of the upper p-band peak (C1). Finally, it should be observed that, as there is only 0.86 f-electron in the ground state (compared to 0.18 in LaN), a pure f-hole is not a reasonable possibility in this model anyway.

3.5.5. *Experimental spectra*

There is a huge variation in the relative intensity of the fully screened and the poorly screened f-peaks as one proceeds from CeP to CeBi (Franciosi et al. 1981). This must be considered an important part of the information available from the experimental spectra. Although possible in principle, we are not now in a position to calculate the intensity ratio. (The many-body matrix elements can be set up, but it will be necessary to approximate them to make their evaluation tractable.) Instead, it is possible to understand the variation of the ratio at least qualitatively. The fully screened peak, like a band transition, will be favored by itinerancy of the f-states. Thus, the fully screened peak at E_F will be strongest for the more itinerant f-systems and, conversely, the poorly screened peak will be favored by localized (immobile) f-states. This is because full relaxation is due to an f-electron hopping in to fill the hole.

A good indication of the 4f-orbital being able to couple with the surrounding orbitals is that it has significant density at the muffin-tin radius. Accordingly, the 4f radial density ($4\pi r^2\rho$) at the muffin-tin radius has been included in table 16. Clearly, this quantity is quite a bit larger for CeN than CeP or CeSb. It decreases monotonically as one scans down the pnictides as does the relative strength of the fully screened peak. The ratio of the poorly screened peak (D) to the fully screened peak (A) is actually dramatically dependent on the choice of pnictide ranging from under 1:2 for CeP to over 2:1 for CeBi. One suspects that this huge variation is caused by the increasing localization of the f-states in the heavier pnictides, which would imply a sharp dependence of the probability ratio on the hopping parameter.

To better understand the relation of the calculated results to the experimental data, it is useful to include, at least phenomenologically, such effects as instrument resolution, linewidth broadening, thermal broadening and transition strengths. To do so, techniques similar to that used for UIr_3 have been employed (Arko et al. 1983), but modified to include the poorly screened peak not present in that material.

The resultant model spectra are shown in fig. 17. Comparison of fig. 17 to the experimental results of Franciosi et al. (1981) shows a satisfactory resemblance. Several details of the various parameters used to produce fig. 17 are of interest. Both instrument resolution and linewidth broadening have been approximated as Gaussians. The instrument width was taken to be 0.2eV and the temperature to be room temperature (0.025eV). The linewidth broadening, assumed to arise primarily from Auger processes, increases as the square of the separation of the initial state from E_F. The coefficient was taken to be 0.05eV^{-1}. To the broadened ground state DOS was added a Lorentzian of width 0.4eV centered at the position of the d-screened f-hole given in table 15. The height of the Lorentzian was set at some arbitrary value.

In addition to the satisfying ability to reproduce the experimental data, there is one important point to be gleaned from fig. 16. In this calculation, the underlying Fermi energy is known and is shown in the figure. As noted above, it falls much closer to the peak than the assignment in the experimental references. This occurs because the DOS is rapidly increasing for all energies within the instrument width of E_F rather than being nearly constant. It is this observation that is the justification for the reassignment of E_F in table 15 with its resultant overall improvement in the agreement of theory and experiment. It would, however, be desirable for E_F to be determined experimentally (e.g., by overlayer deposition of a gold film), since it is of interest to know if the fully screened peak is completely relaxed or not.

3.6. *Excited state properties of PrSb and NdSb*

3.6.1. *Introduction and methods*

Parks et al. (1984) and Wieliczka et al. (1984b) noticed that the two-peak structure present in cerium systems also appeared in Pr and Nd systems, but the structures there were further removed from E_F. This seems to rule out a Kondo explanation for the upper peak since in that model such a feature is inherently tied to E_F. It is, therefore, of some interest to see whether our approach followed for the Ce compounds would explain the Pr and Nd pnictides in the same manner as it did the Ce pnictides. Comparison will be made with photoemission data on PrSb and NdSb (unfortunately, no resonance data exist).

As in the case of the Ce pnictides, the ground state of each compound was determined by performing a standard local-density band calculation using the self-consistent warped-muffin-tin, linearized augmented-plane-wave method in a semirelativistic approximation with a perturbative spin–orbit correction (Norman et al. 1985b). Since one expects the f-electrons to be localized in PrSb and NdSb, the f-electrons were treated as $j = 5/2$ states in an overlapping (nonfrozen) core model. A full exchange–correlation potential was used, the correlation part being that of von Barth and Hedin (vBH) (1972). Some calculations were also performed in an exchange-only, or Kohn–Sham (KS) potential. The results obtained will be contrasted with those for CeSb when treating the f-electrons as itinerant or localized in the ground state.

3.6.2. *Results*

Table 18 shows the calculated peak positions for PrSb and NdSb using a full exchange–correlation (vBH) potential compared to their experimental values. A represents the f-screened hole, B the main peak in the Sb valence band, C the shoulder in the Sb valence band, and D the d-screened hole. Also shown are the results for CeSb (using an exchange-only (KS) potential), where the f-electrons were treated as extended states in the ground state plus two new calculations where the f-electrons were treated as localized – one with a KS potential and the other with a vBH potential. The shoulder, peak C, is not seen in CeSb since it is masked by the screened-hole peak (D). The exp[a] columns represent shifting the experimental positions by a constant so that the Sb valence band (peak B) lines up with the theoretical prediction. This shift is 0.3 eV for PrSb and 0.0 eV for NdSb, indicating that there was probably a slightly incorrect experimental assignment of the Fermi energy for PrSb (the experimental resolution was 0.55 eV full width at half maximum). As can be seen, there is excellent agreement between experiment and theory for the two cases. The values for peak A constitute a prediction as to where an f-screened hole might be seen in these compounds if resonant photoemission is done to enhance that feature. It is quite possible, however, that the f-electrons are so localized in the ground state that the intensity of this feature might be too small to resolve.

As seen above, CeSb is a more difficult system. To probe further the limitation previously described and to explore the effect of using a local-orbital approach,

TABLE 18

Experimental and theoretical positions for the valence-band spectral peaks in CeSb, PrSb, and NdSb with respect to E_F[eV]. A is the f-screened f-hole, B the main Sb p-peak, C the Sb p-shoulder, and D the d-screened f-hole. KS stands for exchange-only and vBH for von Barth–Hedin exchange–correlation potentials.

	PrSb (local)			NdSb (local)	
Peak	expt[b]	expt[a]	theor (vBH)	expt[b]	theor (vBH)
A	?	?	−0.95	?	−2.95
B	−2.1	−1.8	−1.8	−1.9	−1.9
C	−3.4	−3.1	−2.9	−3.1	−3.1
D	−4.7	−4.4	−4.4	−5.7	−5.75

	CeSb (extended)			CeSb (local)		
Peak	expt[c]	expt[a]	theor (KS)	expt[c]	theor (vBH)	theor (KS)
A	−0.6	−0.05	−0.05	−0.6	−0.35	+0.10
B	−2.15	−1.6	−1.6	−2.15	−2.15	−2.15
D	−3.1	−2.55	−2.8	−3.1	−3.55	−3.1

[a] Values shifted such that the Sb peak B lines up.
[b] (Campagna et al. 1974).
[c] (Franciosi, et al. 1981).

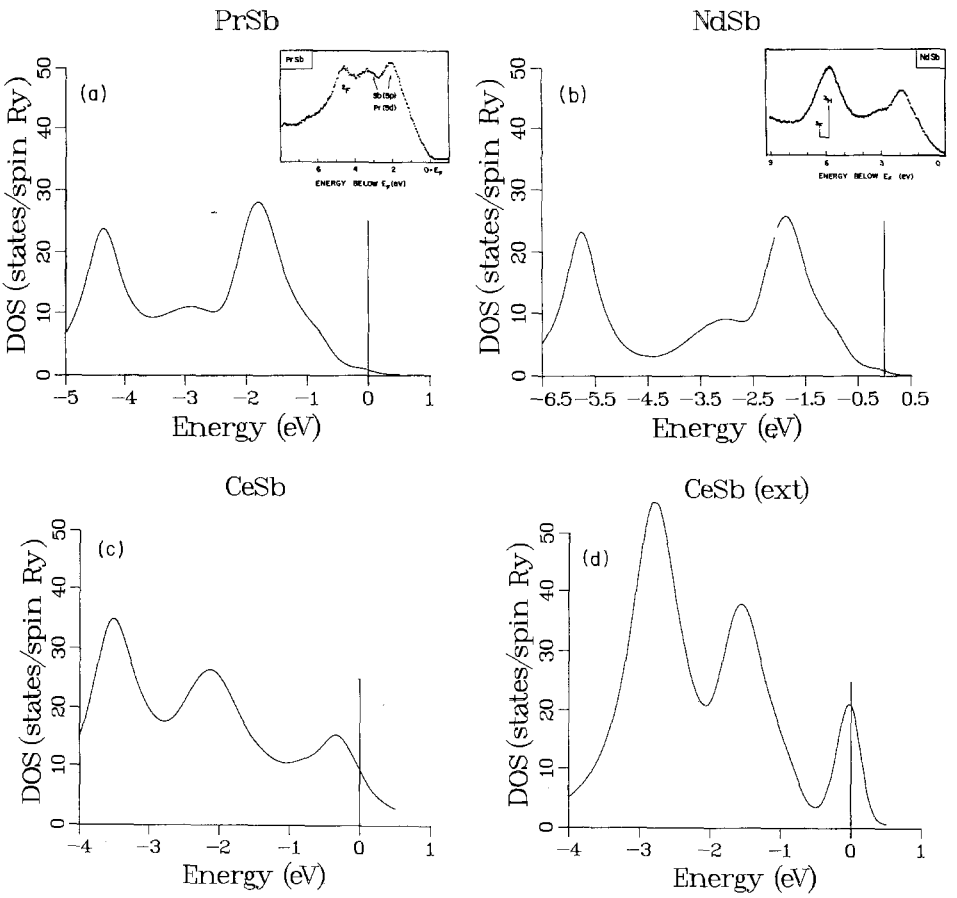

Fig. 18. The local f-spectra for PrSb, NdSb and CeSb, using a vBH potential. CeSb (ext) is the spectrum obtained when the f-electrons are treated as extended in the ground state using a KS potential.

CeSb calculations treating the f-electrons as localized in the ground state (with an occupation number of 1) were performed. The results are shown marked local in table 18. It is seen that in the local f-case, no shift is needed to get the valence-band peak B to line up but, for the vBH potential which worked well for PrSb and NdSb, there is an overshoot of 0.45eV for peak D and an undershoot of 0.25eV for peak A. In other words, the separation of the two f emission peaks overshoots by a full 0.7eV. The effect of reducing the correlation by using the KS potential is to shift both f emission features up to 0.45eV, yielding the same separation between the peaks with peak D lined up with experiment, but peak A above the Fermi energy.

In fig. 18, we show the vBH spectra for CeSb, PrSb, and NdSb with the f-states treated as local plus the CeSb spectrum with the f-electrons treated as extended. These spectra were formed by taking the calculated density of states and Gaussian broadening with an instrument broadening factor of 0.2eV, temperature broadening with $T = 0.025$eV, and including a lifetime broadening factor $a(e - E_F)^2$ where E_F is

the Fermi energy and a is set at $0.05\,eV^{-1}$. To this was added a Lorentzian of width 0.4 eV centered at the position of the d-screened hole for the local f CeSb spectrum (in the extended spectrum, of course, the ground state f-levels are hybridized with the other states and are thus already included). For the most part, the spectra agree rather nicely with experiment. The discrepancies are discussed in the next section.

3.6.3. *Discussion*

Several points need to be considered. First, it is necessary to analyze the trend in the f emission features as one proceeds from CeSb to PrSb to NdSb. One sees that the separation of the f emission features is not constant, but still does not vary too much (note that there is no correlation between the separation and atomic number). There is, however, a dramatic drop in the absolute positions of these peaks as one proceeds from CeSb to PrSb to NdSb, just as was observed by Parks et al. (1984) and by Wieliczka et al. (1984b). In fact, the positions of the calculated peaks are in the same general energy range as found by Parks et al. (1984) for a variety of Pr and Nd compounds. Theoretically, this result may be extremely important since this means that even for localized states, the local-density ground-state eigenvalues may have physical meaning as fully screened eigenvalues. This finding should not be hard to accept since the major error in local-density eigenvalues is the self-interaction error, and full screening should be equivalent to compensating for the self-interaction error.

Of course, full screening is equivalent to the f hole hopping off the site via coupling to the Sb p-states. In fact, this explains why Parks et al. (1984) see such a huge dispersion in the upper peaks (f-screened hole) in the various Pr and Nd compounds. If the f-screening electron originates from E_F, one would expect to see a sharp peak at E_F. Since this is not observed, the f-screening occurs via coupling to the ligand p-band (or d-band for the transition-metal ligands). Since such a band is wide and has its main weight a few electron volt below E_F, the resulting f-screened feature is smeared out (although it is energetically centered about the position of the ground-state f-eigenvalue). One can in fact see this if one attempts to simulate the excitation by using the model of Gunnarsson and Schönhammer (1983). In this model, one couples a localized f-level to a valence band of a desired shape via an Anderson Hamiltonian. One sees that by adjusting parameters, the f-screened feature can be pulled down below E_F resulting in a large smearing out of that feature. This model seems to simulate Pr spectra fairly well, but whether it will work as well for Nd systems where the f-screened feature is a full 3 eV below E_F remains to be determined.

Consider now the effect of choosing a particular potential. The effect of von Barth–Hedin correlation was seen to bring the f-levels down by 0.45 eV relative to the KS results for CeSb both in the ground and excited state. Other correlation potentials should yield similar results. This is exactly the same shift as was found for the unoccupied f-states in LaN (Norman et al. 1984b), and was also found for the ground-state calculations performed on PrSb. From table 18, we see that using the vBH potential yields good results in PrSb and NdSb for the peak-D to peak-B separation. One can contrast this to the case where the f-electrons are treated as

extended in the ground state. In that case, since if the f-levels dropped in energy, the f-occupation would go up resulting in an enormous Coulomb correlation effect (note that in the local calculations, the f-occupation is frozen). This has been verified for $CeSn_3$ where additional correlation had virtually no effect on the Fermi-surface topology (Norman and Koelling 1985). The result implies that the peak separation between the d- and f-screened holes would be larger with the inclusion of correlation since in the excited state, the occupation number is frozen at an integer value and thus the f-level will drop with inclusion of correlation. (As mentioned above, in the localized-f calculations, the peak separation remained the same.)

The final question to ask is the role and treatment of localized versus extended f-states. In CeN, it was necessary to treat the f-states as band states to get a specific heat in agreement with experiment, as well as to obtain a spectrum to agree with experimental photoemission data (Norman et al. 1985c). On the other hand, in PrSb and NdSb, it was completely necessary to treat the f-states as localized in the ground state to get peak A to separate significantly from the Fermi energy. As can be seen from table 18, it seems hard to choose whether the local or extended calculation gives better results in the case of CeSb. In favor of the extended-f-electron calculation is the fact that the f-peak separation overshoots experiment by a smaller value 0.25eV as compared to 0.7eV for the local calculation – although it must be remembered that the inclusion of correlation for the extended calculation would lead to a larger overshoot. In favor of the local f electron calculation is that the experimental Fermi energy need not be shifted to get the experimental and theoretical valence bands to line up – although this in turn should be tempered by the fact that, as can be seen in the figures, the theoretical E_F is closer to the centroid of peak A than the standard experimental assignment. The situation is further complicated by the fact that the itinerant f-calculations do not give precisely $\delta n_f = 1$. To shed some further light on this question, local f electron calculations were also performed for the ground state of CeP with f occupation numbers of 0.93 and 1.00. From the results obtained it appears that the extended calculation does a better job for CeP than does either of the two local calculations.

Finally, a comment is needed on the spectra themselves. To begin with, the relative height of the Lorentzian for the localized f-levels with respect to the Gaussian broadened DOS was simply set at some arbitrary value. It is of some importance to find a way to calculate such a value from first principles. Next, consider the valence-band shoulder, peak C; in NdSb, this shoulder agrees rather well with experiment, both in its small height and in its position; in PrSb, however, this shoulder differs by 0.2eV from experiment and the calculation shows that it is as weak as its NdSb counterpart, whereas experimentally the shoulder has a rather large intensity. This might indicate that the valence-band DOS and the (f) peak D should be broadened more than has been done, although this would probably smear out the shoulder completely. Again, resonance data and better resolution would be helpful in clarifying this part of the spectrum.

In conclusion, good agreement between experiment and theory for PrSb and NdSb gives substantial support to the screening mechanisms assumed in carrying out these calculations. It should be emphasized that these are unadjusted impurity-

like calculations using standard local-density potentials, which for localized excitations makes the good agreement with experiments even more remarkable. In fact, it seems that for localized levels, the local-density ground state eigenvalues have physical meaning as fully screened eigenvalues. Finally, it is interesting to note that the inclusion of full correlations (say, via vBH potentials) yields correct absolute positions for the f-peaks.

3.7. *Inverse photoemission of CeP*

3.7.1. *Introduction*

A similar two-peak structure is seen in the inverse photoemission (bremsstrahlung isochromat spectroscopy (BIS)) spectra of cerium (Land et al. 1981) and several of its compounds (Allen et al. 1983). (In a BIS experiment, one adds an electron to the system.) The first peak is just above E_F ($\approx$0.5eV) and is dominant in the more 'itinerant' cerium compounds. The second peak is located 4–5eV above the E_F and is due to localized $f^1 \rightarrow f^2$ transitions. The BIS spectrum in certain ways thus mirrors what is seen in the photoemission spectrum. With this in mind, it was decided to apply the techniques of the preceding sections to determine the inverse photoemission spectrum of CeP (Norman, 1985).

3.7.2. *Calculational procedure*

The use of supercell technique to calculate the photoemission spectra of cerium compounds has been extensively discussed above. A similar scheme can be used to calculate the inverse photoemission spectra. Here, a brief discussion of the supercell technique is given with emphasis on the changes needed to calculate the BIS spectra. Basically, one assumes that the f-states are itinerant in the ground state (this is not necessary for the technique per se, but it appears appropriate for the model to be explored). Norman (1985) thus performed a self-consistent band calculation using the LAPW method with a local-density exchange-only potential. The ground state should be equivalent to a 'fully relaxed' final state of the photoemission or inverse photoemission process, and thus the f-band partial DOS from the band calculations is used as an approximation for the peak near E_F. To describe the other peak, a band calculation was performed on a large unit cell (eight atoms for the cerium pnictides as opposed to two for the ground-state calculation). As described previously, the excited state for the photoemission was obtained by not allowing any f-occupation on the central cerium site. This simulates the f-hole. Although the f-hole is periodically repeated, the separation of f-holes is sufficiently large not to affect things very much. The system was then allowed to relax resulting in d-screening of the hole.

A similar procedure can be used to obtain the second peak in the BIS spectrum. Since this peak is supposedly due to a localized f bound state, this was simulated with the same supercell calculation as above but placing two f-electrons in the 'core' on the central site. In this way, the f-electrons are treated as site localized (i.e., they are not allowed to hybridize), but in all other ways they are treated normally (i.e., they were not frozen). In fact, these f-states were treated as $j = 5/2$ states in an

overlapping core model. Once self-consistency was achieved, the final iteration was re-run setting the $l = 3$ energy parameter back into the 4f energy region for the central site. This is done to see where the 'unoccupied' f-states lie in the new potential. The differences between these unoccupied eigenvalues and the supercell Fermi energy are taken, and the results divided by two. This yields the appropriate transition state values to be used in constructing the supercell contribution to the BIS spectrum.

3.7.3. *Results*

In fig. 19 the combined spectrum is shown. This is obtained by taking the unoccupied density of states from the band calculation and adding in the unoccupied f density of states inside the central muffin tin for the supercell (this latter is found as described in the last few sentences of the preceding section). A two-peak structure is seen with the peak at 0.4eV above the Fermi energy coming from the band calculation and the peak at 4.4eV coming from the supercell calculation. The state forming the peak near the Fermi energy are largely pure f with some d-admixture from both Ce and P sites. The states from the upper peak contain a good bit of hybridization with d-character on the Ce and P sites as well as p-character on the phosphorus sites, although only the f-character inside the central Ce muffin tin was used to construct the upper peak in fig. 19. In table 19 angular momentum decompositions of the charge for the band calculation and the supercell calculation are compared. On sees an enhancement of p-character inside the central Ce muffin tin. This is because the semicore Ce 5p-states have risen over 5eV in response to the now more repulsive core and have begun to hybridize more with the valence states. Significant depletion of d-character out of the central site is also seen as expected. There is a slight depletion of the p-character inside the nearest-neighbor phosphorus sites as well as f-character on the other cerium sites. Part of this effect is due to the fact that the electron filling factor for the valence states in the supercell has been reduced from 28 to 26 to accommodate two f-electrons in the 'core'. Also in table 19 are total charges inside and outside the muffin tins. As can be seen, there is a significant reduction of interstitial charge in the supercell.

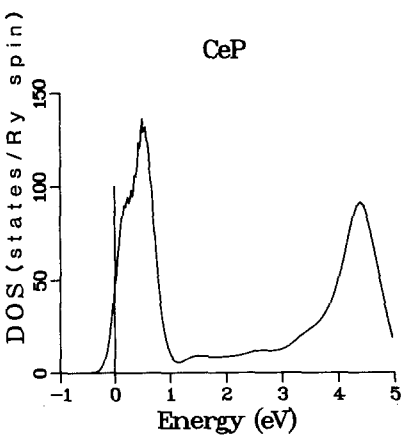

Fig. 19. Calculated BIS spectrum for CeP. This was formed by combining the unoccupied band density of states with the unoccupied f density of states for the supercell Ce central site as described in the text. The Fermi energy is at zero. A Gaussian broadening factor of 0.2eV was employed as well as a temperature factor of 0.025eV.

TABLE 19
Angular momentum charge decomposition inside the muffin-tin spheres as well as total charges for the band and the BIS supercell calculations. A lattice constant of 11.15a.u. and the muffin-tin radii of 3.025 (Ce) and 2.550 (P) were employed. Ce(1) is the modified Ce site, Ce(2) the other three equivalent Ce sites; P(1) are the three equivalent P sites which border Ce(1), and P(2) is the odd phosphorus site. The interstitial charge for the band calculation was multiplied by four since there are four formula units within the supercell.

		Band	Supercell
Ce(1)	s	0.13	0.10
	p	0.17	0.25
	d	1.04	0.54
	f	0.94	2.03
	total	56.15	56.69
Ce(2)	s	0.13	0.13
	p	0.17	0.18
	d	1.04	1.09
	f	0.94	0.89
	total	56.15	56.16
P(1)	p	2.53	2.49
	d	0.06	0.05
	total	14.37	14.39
P(2)	p	2.53	2.52
	d	0.06	0.07
	total	14.37	14.43
interstitial		9.92	9.23

3.7.4. *Discussion*

Setting two f-electrons in the core on the central site as well as depleting all other f-character out of this site is simply a device used to obtain the appropriate potential with which to analyze the unoccupied states. As such this method is very general. This device has been used to analyze the spectrum of a two-f-electron bound state on a cerium site, but one could easily simulate other many-body excitations (two-hole bound states, for example).

In principle, the full many-body matrix elements can be set up, but some way of approximating them must be found to make their evaluation tractable. The combined spectrum of fig. 19 was obtained by simply adding the two base spectra together. The result is to grossly exaggerate the feature at E_F. Recent BIS spectra for CeAs and CeSb (Hillebrecht et al. 1985) show no feature near E_F. The reason for this is that there is virtually no pnictide p-character above E_F which implies that f–p coupling in that energy region is extremely weak. Thus, one would expect to see at most a small bump near E_F in CeP if at all. This is in contrast to CeN where a large peak is seen near E_F as well as one about 5eV above E_F (Wuilloud et al. 1985). The intensity of the peak near E_F is understandable in CeN since this compound appears

to be an ordinary f-band metal which would imply a large probability for f-hopping. Of course, in a model theory such as that of Gunnarsson and Schönhammer (1983), intensity ratios come out naturally and the reader is referred to their chapter 64 in this volume to see how the ratio is dependent upon the various model parameters.

Although the effect of the spin–orbit interaction was included for the band peak, it was not for the supercell peak since the effect was thought to be too small to be worth the effort (the two f-electrons in the core used to construct the potential were treated as $j = 5/2$ states, though). Multiplet effects were also not taken into account. In principle, this can be done in the local-density formalism (von Barth 1979), but has not been applied to solids to the authors' knowledge. If multiplet effects turn out to be crucial for interpreting the BIS spectra of cerium pnictides, then an effort could be made to incorporate those effects into the calculation.

A discussion of the peaks themselves is now in order. The first peak represents the extra f electron hopping away and is thus located just above E_F. This peak will be strong in itinerant f-systems since the probability for f hopping will be greater. The second peak due to a two-f bound state is at 4.4 eV above E_F. This is encouraging since the experimental spectra indicate this peak at 4–5 eV for cerium metal (Land et al. 1981) and in the various compounds (Allen et al. 1983). The reason this peak is not higher is that the final energy is lowered by d-charge moving off the site in response to the extra f-electron (antiscreening). This is simply the mirror process of the d-screened f-hole discussed previously. The antiscreening can be seen by observing the difference in charges between the band and supercell calculations given in table 19 which shows significant depletion of central-site Ce d-character as well as interstitial charge. In fact, plots made of the difference in charge density between the two calculations inside the central Ce muffin tin show depletion of charge from 2 a.u. outwards. Plots of the radial wave functions also reveal that the supercell 4f-function drops off more rapidly in this region than does the corresponding band function, indicating more localization for the two-f bound state. The d-antiscreening, though, makes the $f^1 \rightarrow f^2$ excitation more extended than the corresponding $f^1 \rightarrow f^0$ photoemission process.

Acknowledgements

We are grateful to H.J.F. Jansen, D.D. Koelling, T. Oguchi, and Ling Ye for close collaboration. This work was supported by the Air Force Office of Scientific Research, the National Science Foundation, and the Department of Energy.

References

Allen, J.W., and R.M. Martin, 1982, Phys. Rev. Lett. **49**, 1106.

Allen, J.W., S.-J. Oh, M.B. Maple and M.S. Torikachvili, 1983, Phys. Rev. B **28**, 5347.

Andersen, O.K., 1975, Phys. Rev. B **12**, 3060.

Arko, A.J., 1986, private communication.

Arko, A.J., D.D. Koelling and B. Reihl, 1983, Phys. Rev. B **27**, 3955.

Baer, Y., R. Hauger, Ch. Zurcher, M. Campagna and G.K. Wertheim, 1978, Phys. Rev. B **18**, 4433.

Baer, Y., H.R. Ott, J.C. Fuggle and L.E. Delong,

1981, Phys. Rev. B **24**, 5384.
Beaudry, B.J., and K.A. Gschneidner Jr, 1978, in: Handbook on the Physics and Chemistry of Rare Earths, Vol. 1, eds K.A. Gschneidner Jr and L. Eyring (North-Holland, Amsterdam).
Campagna, M., E. Bucher, G.K. Wertheim, D.N.E. Buchanon and D.L. Longinotti, 1974, Proc. 11th Rare-Earth Conf., Traverse City, Michigan, eds J.M. Haschke and H.A. Eick (NTIS, Springfield, VA.).
Coqblin, B., and A. Blandin, 1968, Adv. Phys. **17**, 281.
Doniach, S., 1977, Physica B **91**, 231.
Doniach, S., and E.H. Sondheimer, 1974, Green's Functions for Solid-State Physicists (Benjamin, Reading, MA.).
Duthie, J.C., and D.G. Pettifor, 1977, Phys. Rev. Lett. **38**, 564.
Elliot, R.J., 1972, Magnetic Properties of the Rare Earth Metals (Plenum Press, London).
Esteva, J.-M., R.C. Karnatak, J.C. Fuggle and G.A. Sawatsky, 1983, Phys. Rev. Lett. **50**, 910.
Franciosi, A., J.H. Weaver, N. Mårtensson and M. Croft, 1981, Phys. Rev. B **24**, 3651.
Fuggle, J.C., M. Campagna, Z. Zolnierek, P. Lasser and A. Platau, 1980, Phys. Rev. Lett. **45**, 1597.
Fuggle, J.C., F.U. Hillebrecht, Z. Zolnierek, R. Lässer, Ch. Freiburg, O. Gunnarsson and K. Schönhammer, 1983, Phys. Rev. B **27**, 7330.
Fujimori, A., 1983, Phys. Rev. B **28**, 4489.
Gaspar, R., 1954, Acta Phys. Hung. **3**, 263.
Glötzel, D., 1978, J. Phys. F **8**, L163.
Gschneidner Jr, K.A., 1965, in: Rare Earth Research III, ed. L. Eyring (Gordon and Breach, New York).
Gschneidner Jr, K.A., and L. Eyring, eds, 1978, Handbook on the Physics and Chemistry of Rare Earths, Vol. 1 (North-Holland, Amsterdam).
Gudat, W., M. Iwan, R. Pinchaux and F. Hulliger, 1982, in:Valence Instabilities, eds P. Wachter and H. Boppart (North-Holland, Amsterdam) p. 249.
Gunnarsson, O., and B. I. Lundqvist, 1976, Phys. Rev. B **13**, 4274.
Gunnarsson, O., and K. Schönhammer, 1983a, Phys. Rev. B **28**, 4315.
Gunnarsson, O., and K. Schönhammer, 1983b, Phys. Rev. Lett. **50**, 604.
Gunnarsson, O., and K. Schönhammer, 1985, Phys. Rev. B **31**, 4815.
Gustafson, D.R., J.D. McNutt and L.O. Roelling, 1969, Phys. Rev. **183**, 435.
Harmon, B.N., 1979, J. Phys. C **5**, 65.
Harmon, B.N., and D.D. Koelling, 1974, J. Phys. C **7**, L210.
Harrison, W.A., 1984, Phys. Rev. B **29**, 2917.
Hedin, L., and B.I. Lundqvist, 1971, J. Phys. C **4**, 2064.
Herbst, J.F., 1982, Phys. Rev. Lett. **49**, 1586.
Herbst, J.F., 1983, Phys. Rev. B **28**, 4204.
Herbst, J.F., and R.E. Watson, 1979, Phys. Rev. B **20**, 2999.
Herbst, J.F., and J.W. Wilkins, 1982, Phys. Rev. B **26**, 1689.
Herbst, J.F., D.N. Lowy and R.E. Watson, 1972, Phys. Rev. B **6**, 1913.
Herbst, J.F., R.E. Watson and J.W. Wilkins, 1976, Phys. Rev. B **13**, 1439.
Herbst, J.F., R.E. Watson and Y. Baer, 1977, Phys. Rev. B **16**, 2447.
Herbst, J.F., R.E. Watson and J.W. Wilkins, 1978, Phys. Rev. B **17**, 3089.
Hillebrecht, F.U., W. Gudat, N. Mårtensson, D.D. Sarma and M. Campagna, 1985, J. Magn. & Magn. Mater. **47&48**, 221.
Hirst, L.L., 1970, Phys. Kondens. Mater. **11**, 255.
Hohenberg, P., and W. Kohn, 1964, Phys. Rev. **136**, B864.
Hopkinson, J.F.L., J.B. Pendry and D.J. Titterington, 1980, Comput. Phys. Commun. **19**, 69.
Hüfner, S., 1986, J. Phys. F **16**, L31.
Hüfner, S., and P. Steiner, 1982a, in: Valence Instabilities, eds P. Wachter and H. Boppart (North-Holland, Amsterdam) p. 263.
Hüfner, S., and P. Steiner, 1982b, Z. Phys. B **46**, 37.
Janak, J.F., 1977, Phys. Rev. B **16**, 255.
Janak, J.F., 1978, Solid State Commun. **25**, 53.
Jansen, H.J.F., and A.J. Freeman, 1984, Phys. Rev. B **30**, 561.
Jayaraman, A., 1965, Phys. Rev. **137**, A179.
Jayaraman, A., 1978, in: Handbook on the Physics and Chemistry of Rare Earths, Vol. 1, eds K.A. Gschneidner Jr and L. Eyring (North-Holland, Amsterdam) p. 707.
Johansson, B., 1974a, J. Phys. F **4**, L169.
Johansson, B., 1974b, Philos. Mag. **30**, 469.
Johansson, B., 1979, Phys. Rev. B **20**, 1315.
Johansson, B., and A. Rosengren, 1975a, Phys. Rev. B **11**, 1367.
Johansson, B., and A. Rosengren, 1975b, Phys. Rev. B **11**, 2836.
Kmetko, E.A., and H.H. Hill, 1976, J. Phys. F **6**, 1025.
Koelling, D.D., 1981, Rep. Prog. Phys. **44**, 149.
Koelling, D.D., 1982, Solid State Commun. **433**, 247.
Koelling, D.D., 1984, in: The Electronic Structure of Complex Systems, eds P. Phariseau and W.M. Temmerman (Plenum Press, New York).
Koelling, D.D., and G.D. Arbman, 1975, J. Phys. F **5**, 2041.
Koelling, D.D., and B.N. Harmon, 1977, J. Phys. C **10**, 3107.
Kohn, W., and L.J. Sham, 1965, Phys. Rev. **140**, A1133.
Koskenmaki, D.C., and K.A. Gschneidner Jr, 1978, in: Handbook on the Physics and Chemistry of Rare Earths, Vol. 1, eds K.A. Gschneidner Jr and L.R. Eyring (North-Holland, Amsterdam) p. 337.
Lang, J.K., Y. Baer and P.A. Cox, 1981, J. Phys.

F **11**, 121.
Langley, R.H., 1982, Phys. Status Solidi b **111**, 501.
Larsson, C.G., 1982, Ph.D. thesis, Chalmers University of Technology Gothenburg.
Lavagna, M., C. Lacroix and M. Cyrot, 1983, J. Phys. F **13**, 1007.
Lawrence, J.M., P.S. Riseborough and R.D. Parks, 1981, Rep. Prog. Phys. **44**, 1.
Liu, L., 1975, J. Phys. Chem. Solid **36**, 31.
Liu, S.H., and K.M. Ho, 1983, Phys. Rev. B **28**, 4220.
MacDonald, A.H., W.E. Pickett and D.D. Koelling, 1980, J. Phys. C **13**, 2675.
Mackintosh, A.R., 1985, Physica B **138**, 112.
Mårtensson, N., B. Reihl and R.D. Parks, 1982, Solid State Commun. **41**, 573.
Martin, R.M., 1982, Phys. Rev. Lett. **48**, 362.
McEwen, K.A., 1978, in: Handbook on the Physics and Chemistry of Rare Earths, Vol. 1, eds K.A. Gschneidner Jr and L. Eyring (North-Holland, Amsterdam) p. 411.
McMahan, A.K., and D.A. Young, 1984, Phys. Lett. A **105**, 129.
Min, B.I., H.J.F. Jansen, T. Oguchi and A.J. Freeman, 1986a, Phys. Rev. B **3**, 8005.
Min, B.I., H.J.F. Jansen, T. Oguchi and A.J. Freeman, 1986b, Phys. Rev. B **34**, 369.
Min, B.I., T. Oguchi, H.J.F. Jansen and A.J. Freeman, 1986c, Phys. Rev. B **34**, 654.
Min, B.I., H.J.F. Jansen, T. Oguchi and A.J. Freeman, 1986d, J. Magn. & Magn. Mater. **59**, 277.
Min, B.I., H.J.F. Jansen, T. Oguchi and A.J. Freeman, 1986e, J. Magn. & Magn. Mater. **61**, 139.
Moruzzi, V.L., J.F. Janak and A.R. Williams, 1978, Calculated Electronic Properties of Metals (Pergamon, New York).
Norman, M.R., 1985, Phys. Rev. B **31**, 6261.
Norman, M.R., 1986, unpublished.
Norman, M.R., and D.D. Koelling, 1985, Physica B **135**, 95.
Norman, M.R., D.D. Koelling, A.J. Freeman, H.J.F. Jansen, B.I. Min, T. Oguchi and Ling Ye, 1984a, Phys. Rev. Lett. **53**, 1673.
Norman, M.R., H.J.F. Jansen, D.D. Koelling and A.J. Freeman, 1984b, Solid State Commun. **52**, 739.
Norman, M.R., D.D. Koelling and A.J. Freeman, 1985a, Phys. Rev. B **31**, 6251.
Norman, M.R., D.D. Koelling and A.J. Freeman, 1985b, Phys. Rev. B **32**, 7748.
Norman, M.R., E. Wimmer and A.J. Freeman, 1985c, Phys. Rev. B **32**, 7830.
Nugent, L.J., J.L. Burnett and L.R. Morss, 1973, J. Chem. Thermodyn. **5**, 665.
Oh, S.-J., and S. Doniach, 1982, Phys. Rev. B **26**, 2085.
Parks, R.D., S. Raaen, M.L. den Boer and Y.-S. Chang, 1984, Phys. Rev. Lett. **52**, 2176.
Patthey, F.B., B. Delley, W.-D. Schneider and Y. Baer, 1985, Phys. Rev. Lett. **55**, 1518.
Pauling, L., 1947, J. Am. Chem. Soc. **69**, 542.
Perdew, J.P., and A. Zunger, 1981, Phys. Rev. B **23**, 5048.
Pettifor, D.G., 1970, J. Phys. C **3**, 367.
Pickett, W.E., and B.M. Klein, 1983, J. Less-Common Met. **93**, 219.
Pickett, W.E., A.J. Freeman and D.D. Koelling, 1980, Phys. Rev. B **22**, 2695.
Pickett, W.E., A.J. Freeman and D.D. Koelling, 1981, Phys. Rev. B **23**, 1266.
Podloucky, R., and D. Glötzel, 1983, Phys. Rev. B **27**, 3390.
Ponyatovskii, E., 1958, Sov. Phys.-Dokl. **3**, 498.
Probst, C., and J. Wittig, 1978, in: Handbook on the Physics and Chemistry of Rare Earths, Vol. 1, eds K.A. Gschneidner Jr and L.R. Eyring (North-Holland, Amsterdam) p. 749.
Ramirez, R., and L.M. Falicov, 1971, Phys. Rev. B **3**, 1225.
Redinger, J., P. Weinberger, E. Wimmer, A. Neckel and A.J. Freeman, 1985, Phys. Rev. B **32**, 6993.
Roeland, L.W., G.J. Cock, F.A. Muller, A.C. Moleman, K.A.M. McEwen, R.C. Jordan and D.W. Jones, 1975, J. Phys. F **5**, L233.
Rosina, G., E. Bertel, F.P. Netzer and J. Redinger, 1986, Phys. Rev. B **33**, 2364.
Rusic, B., G.L. Goodman and J. Berkowitz, 1983, J. Chem. Phys. **78**, 5443.
Skriver, H.L., 1983, in: Systematics and the Properties of the Lanthanides, ed. S.P. Sinha (Reidel, Dordrecht) p. 213.
Skriver, H.L., 1985, Phys. Rev. B **31**, 1909.
Skriver, H.L., O.K. Andersen and B. Johansson, 1980, Phys. Rev. Lett. **44**, 1230.
Slater, J.C., 1974, in: The Self-Consistent Field for Molecules and Solids, Vol. 4 (McGraw-Hill, New York).
Stassis, C., T. Gould, O.D. McMasters, K.A. Gschneidner Jr and R.M. Nicklow, 1979, Phys. Rev. B **19**, 5746.
Stassis, C., C.-K. Loong, O.C. McMasters and R.M. Nicklow, 1982, Phys. Rev. B **25**, 6485.
Sticht, J., and J. Kübler, 1985, Solid State Commun. **53**, 529.
Veal, B.W., and A.P. Paulikus, 1983, Phys. Rev. Lett. **51**, 1995.
von Barth, U., 1979, Phys. Rev. A **20**, 1693.
von Barth, U., and L. Hedin, 1972, J. Phys. C **5**, 1629.
Watson-Yang, T.J., B.N. Harmon and A.J. Freeman, 1976, J. Magn. & Magn. Mater. **2**, 334.
Wieliczka, D.M., J.H. Weaver, D.W. Lynch and C.G. Olson, 1982, Phys. Rev. B **26**, 6056.
Wieliczka, D.M., C.G. Olson and D.W. Lynch, 1984a, Phys. Rev. B **29**, 3028.
Wieliczka, D.M., C.G. Olson and D.W. Lynch, 1984b, Phys. Rev. Lett. **52**, 2180.
Williams, A.R., and N.D. Lang, 1978, Phys. Rev. Lett. **40**, 954.
Wittig, J., 1973, in: Festkorperprobleme, Vol. XIII, ed. H.J. Queisser (Vieweg, Braunschweig) p. 375.

Wuilloud, E., H.R. Moser, W.-D. Schneider and Y. Baer, 1983, Phys. Rev. B **28**, 7354.
Wuilloud, E., B. Delley, W.-D. Schneider and Y. Baer, 1985, J. Magn. & Magn. Mater. **47&48**, 197.
Zachariasen, W.H., 1949, (unpublished) quoted in: A.W. Lawson and T.Y. Tong, 1949, Phys. Rev. **76**, 301.
Zunger, A., and A.J. Freeman, 1977, Phys. Rev. B **16**, 2901.

Handbook on the Physics and Chemistry of Rare Earths, Vol. 10
edited by K.A. Gschneidner, Jr., L. Eyring and S. Hüfner

Chapter 66

PHOTOEMISSION OF Ce AND ITS COMPOUNDS

D.W. LYNCH
Department of Physics, Iowa State University, Ames Laboratory USDOE, Ames, Iowa 50011, USA

J.H. WEAVER
Department of Chemical Engineering and Materials Science, University of Minnesota, Minneapolis, Minnesota 55455, USA

Contents

List of symbols

μ	material-specific, frequency-dependent photon absorption coefficient	$c^+_{k,\sigma}$ and $c_{k,\sigma}$	creation and annihilation operators for a conduction electron of momentum k and spin σ
$E_i, \boldsymbol{k}_i$	electron energy and momentum for state Ψ_i	f^+_σ and f_σ	creation and annihilation operators for a localized 4f electron of spin σ
$\boldsymbol{p}_{if}$	dipole matrix element for initial state Ψ_i and final state Ψ_f	$V_{k,\sigma}$	hopping matrix element for a 4f electron and one-electron conduction band states
Λ	photoelectron mean free path		
Φ	sample work function		
E_B	binding energy, referred to the Fermi level, E_F	ε_f	localized 4f energy level
		δ, T_K	Kondo energy and temperature

1. Introduction

Valence band photoelectron spectroscopy seeks to elucidate fully the electronic structure of the sample under investigation by identifying bulk states, surface states, and, when appropriate, changes in these states due to chemisorption or reaction. This means more than determining just the distribution of states according to their binding energies (the density of states). With photoemission, particularly with synchrotron radiation photoemission, it is now possible to extract information about the nature of the electronic states themselves, including their spin and angular momentum character, their degree of localization or hybridization, their wave function symmetry, and the detailed energy band structure in the form of energy vs. momentum or $E(\boldsymbol{k})$. Information about the empty states can also be gained from angle integrated or angle resolved photoemission or through core level excitation spectra near threshold.

In investigations of Ce and its compounds, the fundamental question to be addressed concerns the degree to which the 4f electron can be treated by one-electron theory. Indeed, the 4f electron appears to exist in a highly correlated, localized state in some cases and a more band-like state in others. A closely related second question concerns the nature of the other electronic states and how they mix with the 4f states. Photoelectron spectroscopy does not always provide a simple or direct answer to these questions (ejection of an electron from a system perturbs the system), but photoemission does provide a great deal of insight.

At the time of this writing, there is a developing concensus on several of the controversial questions of interpretation for photoelectron spectra of the 4f and valence states of Ce and its compounds. We will address some of these questions in this chapter. Others are discussed elsewhere in this volume or in this series of volumes. It should be stated at the onset that 'the cerium question' is fundamental in solid state physics and this research area is advancing rapidly. As a result, we can expect ever greater understanding of 4f-related phenomena in the years to come.

Electronic structure studies of the 4f and valence electrons in Ce and its compounds bring to bear all the techniques of ultraviolet and soft X-ray photoelectron spectroscopy. We begin this review by describing those techniques, especially those utilizing synchrotron radiation as the photon source. We do this because the latter differ in many ways from X-ray photoelectron spectroscopy (XPS or ESCA) discussed earlier in this volume. We then illustrate some of them with data for CeF_3 where the interpretation is relatively straightforward. We then turn to α- and γ-Ce where the experimental results are far more complicated. As part of the interpretation of these Ce results, we review in section 4 the theoretical models for the 4f electron. We then survey photoelectron spectroscopy results for metallic and semiconducting Ce compounds, presenting results for La and Pr when possible to aid in the interpretation of the 4f character, and conclude with a discussion of Ce oxides and oxidation. Our discussion will include photoemission studies of the 4d core levels of Ce because these levels are usually within the range of excitation of the instrumentation used to obtain valence band spectra (binding energy ~ 100 eV) and because their spectra are complementary to direct valence band and 4f electron studies.

Valence band photoelectron spectroscopy results must not, of course, be viewed in isolation. In particular, bremsstrahlung isochromat spectroscopy (BIS) and X-ray photoelectron spectroscopy are complementary techniques. These and other spectroscopies are discussed elsewhere in this volume (chapters 62, 63, 70, 71 and 72) (see also Baer 1984). XPS core level results show a rich satellite structure which yields additional information, and valence band results resemble the density of states in delocalized electron systems. BIS spectra reveal the empty states which are not directly accessed by most other spectroscopies. Thus, a combination of BIS and either XPS or UPS provides spectroscopic coverage of the states on both sides of the Fermi level.

2. Valence band photoelectron spectroscopy

We outline below the simplest description of the photoemission process for a solid. More extensive presentations and reviews can be found elsewhere (Smith 1971, Eastman 1972, Feuerbacher et al. 1978, Cardona and Ley 1978, Ley and Cardona 1979, Williams et al. 1980, Smith and Himpsel 1982, Margaritondo and Weaver 1985). The more complicated (and more correct) formulations are mentioned at the end of this section. We do not describe instrumentation, but refer the reader to the more thorough discussions of photoelectron spectroscopy just referenced.

2.1. *The photoemission process*

The three-step model (Berglund and Spicer 1964a,b) divides the photoemission process into distinct parts: propagation of the photon into the solid with photo-excitation of an electron, propagation of the excited electron to the surface, and escape of the electron into the vacuum. We use this model for its conceptual simplicity, knowing that quantum mechanics requires a one-step model. Such a one-step model has been developed and, under appropriate limiting conditions, it reduces to the more conceptual model.

Assume that a radiation beam is incident on the flat surface of the sample as shown in fig. 1. The fraction of the incident flux which is reflected is given by R, the reflectance. R can be calculated from the Fresnel relations, and it depends on the angle of incidence, the state of polarization of the incident radiation, the dielectric function of the material, and the quality of the surface. A fraction $A = (1 - R)$ penetrates the surface and propagates into the material. For a given material, A will be larger for p-polarization and angles of incidence near the pseudo-Brewster angle. In general, the electromagnetic wave within the medium propagates as an inhomogeneous plane wave, and the flux falls as

$$I(z) = I(0)\exp(-\mu z) = I_0(1 - R)\exp(-\mu z), \tag{1}$$

where μ is the material-specific, frequency-dependent absorption coefficient and z is the depth normal to the surface, as shown in fig. 1. This expression is valid even at non-normal incidence. We ignore non-local optical effects because they have yet to

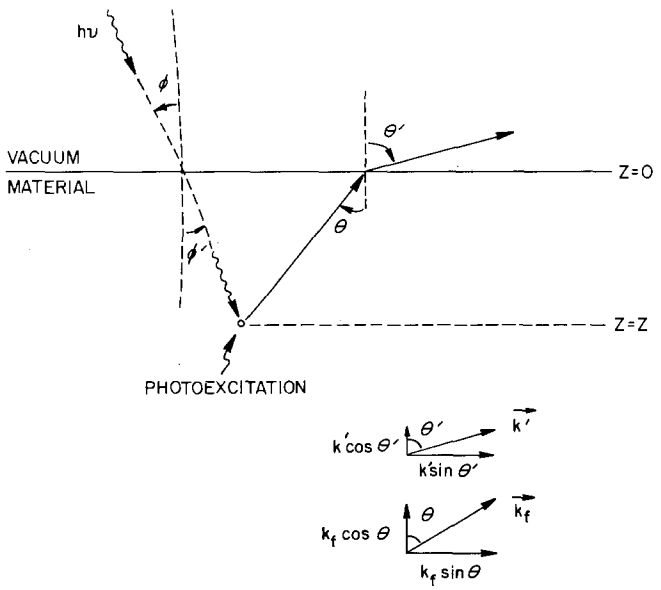

Fig. 1. Schematic of the photoemission three-step model. A photon of energy $h\nu$ is incident onto a sample and excites a photoelectron a distance z below the surface. The photoelectron has a finite probability of propagating to the surface and escaping into vacuum where it is detected. (The motion of the photoelectron need not be in the same plane as the photon propagation.) The inset below shows the photoelectron final state wave vector inside (k_f) and outside (k') the surface.

be observed in studies on Ce and its compounds. At a depth z, the number of photons of energy $h\nu$ which are absorbed in depth dz per unit time and area is

$$dN = -\mu I dz/h\nu. \tag{2}$$

Thus, 95% of the radiation is absorbed in a depth of $3\mu^{-1}$, which is typically ten to hundreds of ångstroms.

Quantum mechanically, the absorption coefficient results from the excitation of electrons from an initial state i to a final state f. If we consider these to be Bloch states described by energies and wave vectors $(E_i, \boldsymbol{k}_i)$ and $(E_f, \boldsymbol{k}_f)$, the absorption coefficient can be written as (Wooten 1972)

$$\mu(h\nu) = \frac{\pi e^2}{ncm\nu} \sum_{if} |\hat{e}\cdot \boldsymbol{p}_{if}|^2 \delta(E_f - E_i - h\nu) F(E_i)[1 - F(E_f)], \tag{3}$$

where $F(E)$ is the Fermi–Dirac distribution function, the factors F and $(1 - F)$ ensure that the initial state is occupied and the final state empty, n is the index of refraction, and the summation is over all initial and final states. $\boldsymbol{p}_{if}$ is the dipole matrix element defined by

$$\boldsymbol{p}_{if} = \int \Psi_f^* \boldsymbol{p} \Psi_i d^3 r, \tag{4}$$

where $\boldsymbol{p}$ is momentum operator. $\hat{e}$ is the polarization vector for the radiation. In eq.

(3) the refractive index is assumed known, but in reality it depends on frequency as much as the absorption coefficient does, and it should be calculated as well. For the Bloch states envisioned here and for $h\nu \lesssim 200$ eV, the integral vanishes unless $\boldsymbol{k}_i = \boldsymbol{k}_f$. Since the delta function requires $E_f = E_i + h\nu$, we can see that both momentum and energy are conserved. We have ignored spin since spin-polarized photoelectron spectroscopy has not yet been applied to Ce or its compounds. Note that the absorption process produces a spectrum which reflects ground *and* excited states of the system rather than just the ground state.

The second step in photoemission describes transport of the excited electron to the surface. With experimental resolution in the 0.1–0.4 eV range, scattering from phonons can be treated as elastic and we need consider only electron–electron and electron–plasmon scattering. Such scattering introduces a finite mean free path Λ for inelastic scattering. It is difficult to calculate the mean free path accurately since it depends on the details of the electronic structure of the material and the energy of the electron. For our purposes, we simply note that the variations of Λ from material to material generally do not exceed a factor of two. As a result a 'universal' curve is often used to describe the kinetic energy dependence of the mean free path, as shown in fig. 2 (Powell 1974, Lindau and Spicer 1974, Seah and Dench 1979, Leckey 1981). The general shape of the curve can be explained theoretically, and the magnitude has been adjusted to fit a large number of measurements on a variety of materials. The initial drop in Λ arises from the increase in the density of states into which the electron can scatter as the electron energy increases and from the increasing number of electrons which can cause the scattering when Fermi–Dirac statistics are considered. (We assume a metal, or energies larger than the band gap of a non-metal.) The subsequent rise is due to a reduction in the scattering matrix element. Note that for inhomogeneous samples the concept of a single mean free path loses its meaning.

We can see from fig. 2 that the surface sensitivity of photoelectron spectroscopy

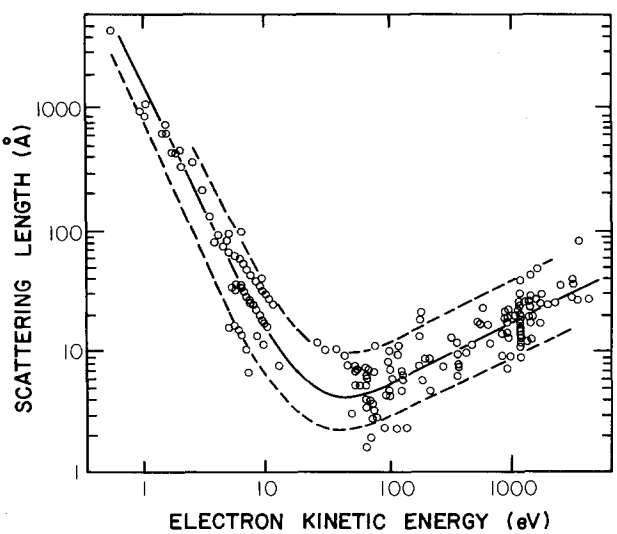

Fig. 2. The 'universal curve' showing the photoelectron scattering length or mean free path as a function of its kinetic energy. The circles correspond to results for the scattering lengths for different materials and show the spread in scattering length (Seah and Dench 1979). (The mean free path (see text) and scattering or attenuation length are not necessarily identical. See Powell (1985). However, for our purposes the difference is negligible.)

can be varied substantially. Indeed, by selecting the right photon energy, the photoelectrons may come predominantly from the first two layers of atoms at the surface. At the same time, one never detects photoelectrons from deep within the solid unless they have scattered inelastically and appear as part of the secondary, or scattered, electron background. This high degree of surface sensitivity is both an advantage and a disadvantage. On the one hand, we can extract information about surface and near-surface effects. On the other, small amounts of surface contamination can distort the photoelectron spectra or contribute new, contamination-derived features.

The probability that an electron excited at depth z below the surface can reach the surface without inelastic scattering is given by

$$\exp(-z/\Lambda \cos\theta), \tag{5}$$

where θ is the angle of the electron trajectory from the surface normal, shown in fig. 1. At the same time, inelastically scattered electrons also reach the surface and escape, but their spectrum is generally rather featureless. Hence, in a typical energy distribution curve or EDC there are structures associated with the primary, or unscattered, electrons superimposed on the background of secondaries.

The third photoemission step corresponds to the escape of the excited electron into the vacuum. The classical picture due to Fowler (1931) is used with the three-step model. The momentum of the excited electron is resolved into components parallel and perpendicular to the surface. The motion through the surface in the perpendicular direction is opposed by retarding forces whose action is described by

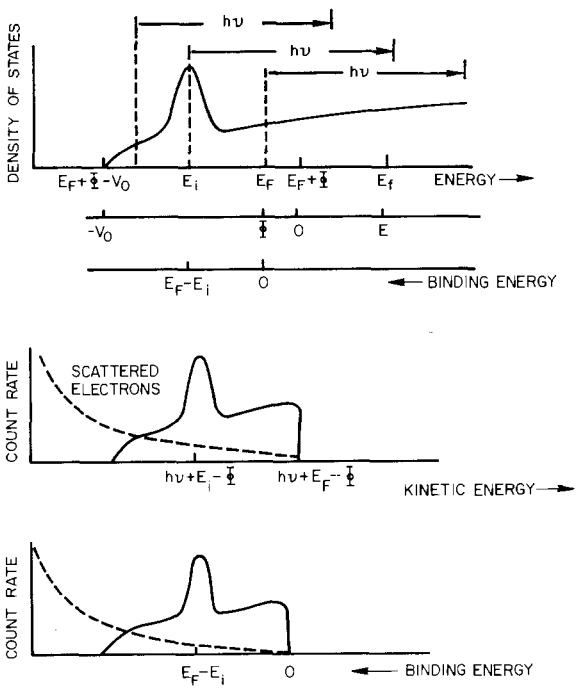

Fig. 3. Construction of an electron energy distribution curve (EDC) from a density of states. The top panel depicts a parabolic density of states with structure centered around E_i. For simplicity, we show photoexcitation of three initial state levels by a photon energy $h\nu$ with no account taken of dipole matrix element effects. E_F is the Fermi energy, V_0 is the inner potential, Φ is the work function, E_i is some initial energy, and E_f is some final energy reached by excitation of energy $h\nu$ from E_i. The center panel shows the distribution of escaping electrons as a function of their kinetic energy. The bottom panel is the same as the center panel except for a shift in the direction of the energy scale and its origin. A background of scattered electrons is shown to make the EDC resemble experimental spectra.

the work function, Φ. The electron will then escape if the normal component of the kinetic energy is large enough, namely,

$$\frac{\hbar^2 k_f^2}{2m^*} \sin^2\theta > V_0. \tag{6}$$

In this expression V_0 is the inner potential which is equal to the sum of the Fermi energy and the work function, i.e., the energy of the bottom of the conduction band of a metal measured from the vacuum level (see fig. 3). This leads to an escape cone defined by the largest value of θ satisfying eq. (6): for an electron energy of E_f inside the crystal, only those electrons travelling within a cone of half-angle θ_e oriented normal to the surface will escape, with

$$\theta_e \leqslant \cos^{-1}(V_0/(E_f + V_0))^{1/2}. \tag{7}$$

The electron will then emerge with kinetic energy $E = E_f - V_0$ and, because the normal component of momentum has been reduced, it appears refracted at the surface (see fig. 1). The fraction of excited electrons upon escape (ignoring transport to the surface) is the ratio of the solid angle of the escape cone to 4π, namely.

$$\begin{aligned} &0 \qquad\qquad\qquad , \quad E_f < E_F + \Phi \quad (E < 0), \\ &\tfrac{1}{2}[1 - \sqrt{V_0/(E_f + V_0)}], \quad E_f > E_F + \Phi \quad (E > 0), \end{aligned} \tag{8}$$

where the final state energies are measured inside (outside) the solid.

To determine the total electron yield, one forms the product of the three probabilities, one for each step, and integrates over the depth of excitation and the angle of escape. In principle, all of the emitted electrons can be collected by the energy analyzer, but this is never the case. Indeed, it is advantageous to vary the angular acceptance of the detector and perform angle resolved photoemission. In this case the integration over θ is reduced to one over the acceptance of the detector. In an energy distribution curve (EDC) an additional factor must be inserted to account for the fact that we detect only those electrons with a particular energy set by the energy analyzer.

A schematic EDC is shown in the center panel of fig. 3 where the ordinate is the count rate and the abscissa is the electron kinetic energy measured in vacuum. Generally, the abscissa is the binding energy, E_B, measured with respect to the Fermi energy of the sample with

$$E_B = h\nu - \Phi - E. \tag{9}$$

To the extent that the dipole matrix elements of eqs. (3) and (4) are constant, the EDC resembles a convolution of the empty and filled densities of the states with k-conservation assured (Berglund and Spicer 1964a). In general, the matrix elements will not be constant unless at least one of the bands is flat or the photon energy is very high. Because of the contributions of both initial and final states, a single EDC measured in the band structure regime (where dipole matrix elements are not constant) is difficult to interpret unambiguously, and most studies seek sets of EDCs taken at different photon energies. At very high photon energies such as those used in XPS, the experimental EDCs resemble the filled density of states since all of the final states are approximated as plane waves.

The lack of constancy of the dipole matrix elements, which depend on the individual states involved in the excitation, is an advantage rather than an impediment to interpreting the EDCs. Indeed, the matrix elements can now be calculated from first principles, although high accuracy is often difficult to achieve because of the oscillations in sign of the integrand of eq. (4). For fcc and bcc metals, this can be done relatively accurately, without recourse to numerical integration, by an approximation technique suitable for Bloch states (Smith and Mattheiss 1974, Traum and Smith 1974, Rowe and Smith 1974, Smith 1979, Benbow and Smith 1983). They demonstrate that for a single initial state band, $|\boldsymbol{p}_{if}|$ may change considerably as the wave vector $\boldsymbol{k}_i$ increases from zero to a value on the Brillouin zone boundary. In any case, for single crystals in certain orientations, many transitions may be forbidden because $\boldsymbol{p}_{if} = 0$.

Dipole matrix elements for core electrons in solids are reasonably well approximated by those calculated for free atoms, except near the thresholds of the core excitations (Cooper 1975, Manson 1978). For a particular core level, the photoexcitation cross section varies with photon energy in a way which makes it possible to select a photon energy to discriminate for, or against, a particular core electron (Eastman and Kuznietz 1971). Typical calculated free-atom one-electron cross sections for Ce (Yeh and Lindau 1985) are shown in fig. 4. In general, it may be said that the photoexcitation cross sections for s and p electrons increase from threshold, then decrease with increasing photon energy. In contrast, d and especially f electrons exhibit a delayed rise from threshold due to the $l(l+1)/r^2$ or centrifugal barrier term in the potential (Fano and Cooper 1968, Cooper 1975, Manson 1978). Atomic partial cross sections involving transitions from one subshell may also exhibit a zero

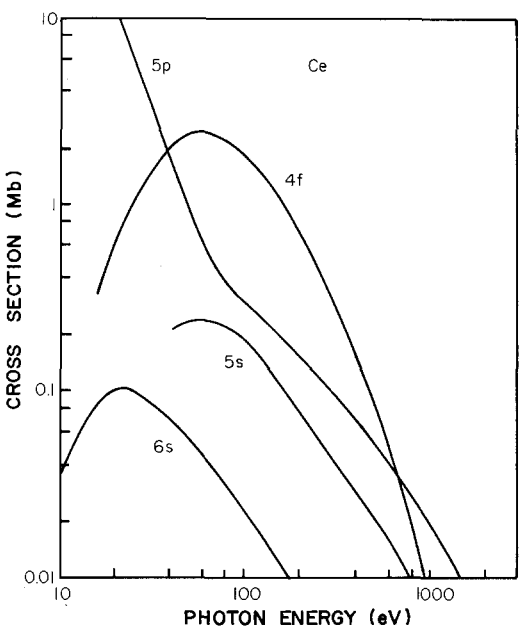

Fig. 4. Calculated photoionization cross sections for several atomic subshells in cerium as a function of photon energy (Yeh and Lindau 1985).

or Cooper minimum which is useful in suppressing background spectra from the electrons not under study. The delayed onset of the photoexcitation of 4f states will be particularly important in our discussion of Ce since it allows us to minimize or maximize 4f emission relative to overlapping valence band (s, p, d-derived) emission.

2.2. *CIS, CFS and yield spectroscopies*

The synchrotron radiation continuum makes it possible to measure EDCs at any photon energy. A set of them defines a surface in the space of emitted current, electron kinetic energy, and photon energy. In the early 1970s, when synchrotron radiation photoemission studies were first being undertaken, it was realized that this space could be explored in several useful ways (Lapeyre et al. 1974a,b). In the EDC mode described above, both initial states and final states change as the electron energy is scanned for fixed $h\nu$. In the constant initial state or CIS mode, the electron kinetic energy is scanned synchronously with the photon energy, as shown in fig. 5. In the constant final state or CFS mode, the desired final state energy is fixed and the photon energy is scanned. These CIS and CFS scans give spectra which are in some respects simpler to interpret than the EDCs and, together, they represent different sections through the photocurrent/electron-kinetic-energy/photon-energy

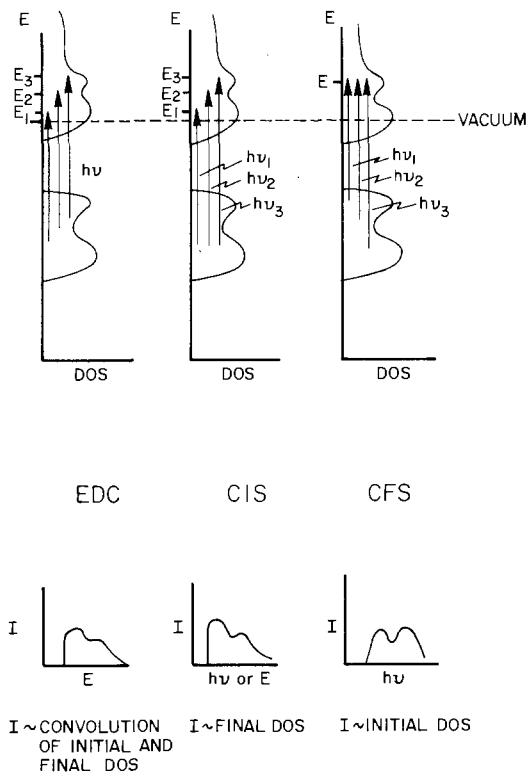

Fig. 5. The origin of energy distribution curves (EDCs), of constant initial state spectra (CISs), and constant final state spectra (CFSs). For the EDC, the photon energy is fixed and the electron energy is scanned. For the CIS, the photon and the electron energies are scanned synchronously. For the CFS, the electron energy is fixed while the photon energy is scanned. Matrix element and escape effects will distort all these spectra.

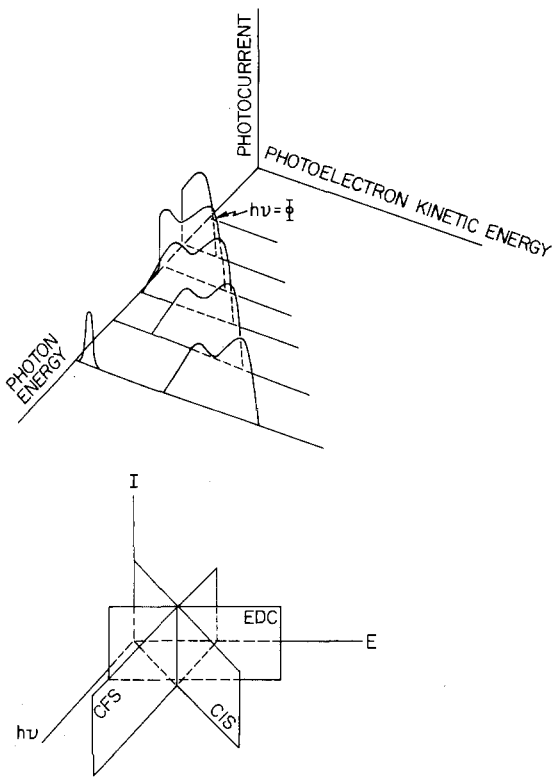

Fig. 6. The top portion shows a series of EDCs in the space of photon energy, electron kinetic energy, and photocurrent to show how the photoelectron spectra form a surface in this space. With increasing photon energy, we can excite electrons from states of increasing binding energy, including core levels, as depicted by the narrow structure at low kinetic energy in the EDC having the highest photon energy. The lower panel shows how EDCs, CISs, and CFSs are produced by the intersections of different planes with that surface.

space, as shown in fig. 6. All of the aforementioned photoelectron spectroscopies can be carried out with either valence band or core electrons.

There is an additional spectroscopy related to CFS spectroscopy called total yield spectroscopy (Gudat and Kunz 1972, Kunz 1979). This technique calls for a measurement of the inelastically scattered electrons as a function of incident photon energy. These electrons may represent over 90% of the total yield. They can be measured by collecting all photoelectrons with a positively biased collector or, in a more restricted sense, by setting an energy analyzer to collect secondary electrons within a band of energies that is very low in mean energy, typically a few eV. Experiments show that for a number of prototypical solids the yield spectrum is similar to the absorption coefficient. In particular, the positions of structures in the two spectra are the same and the relative strengths are quite close. The depth sampled is of the order of 100 Å because secondaries are emphasized. Yield spectra have proven to be quite useful for Ce and its compounds. They can be obtained easily in any photoelectron spectrometer using synchrotron radiation, while the photon absorption coefficient spectrum itself requires relatively difficult sample preparation methods.

2.3. *Resonance photoemission*

So far, we have described the photoelectron spectra as they are measured

experimentally. We have mentioned the dependence of the photoelectron excitation cross section on energy, and we have alluded to the possibility of a minimum in this cross section for certain transitions. In the study of rare earths, there is another phenomenon called resonance photoemission which has proven to be extremely useful in investigation of 4f related phenomena.

For any lanthanide with n 4f electrons, the $4d \rightarrow 4f$ transitions have unusual properties. (The $5d \rightarrow 5f$ transitions in the actinides and $p \rightarrow d$ transitions in the d-band metals are analogous.) We can write

$$h\nu + 4d^{10}\,4f^{n} \rightarrow 4d^{9}\,4f^{n+1}.$$

These transitions occur at a photon energy of about 100 eV for La with $n = 0$ and progress to higher energy at a rate of about 8 eV per increment in atomic number across the lanthanide series. Multiplet structures result from the 'residual' Coulomb and exchange interactions among the electrons in unfilled shells. For lanthanides the mean radii of the 4d hole and the 4f electrons are comparable, leading to very strong electrostatic and exchange interactions among the $(n + 1)$ 4f electrons and the 4d hole (Dehmer et al. 1971, Dehmer and Starace 1972, Starace 1972, Sugar 1972). The multiplet splitting of the final states is then very large, of the order of 10 eV. As a result, a few final states fall below threshold and others are pushed well above, where they autoionize by interaction with a continuum of ionization states and broaden. The resultant absorption (or yield) spectrum is characterized by a number of narrow lines followed by a structured continuum to higher energies. The number of lines depends on the value of n, as can be seen in fig. 7 where the optical absorption spectra for the trihalides of La and Ce are shown. These spectra can be calculated rather accurately by assuming that they arise from free tripositive ions, as shown in fig. 7. Spectra for metallic Ce, for CeF_3, and for Ce vapor are very similar (Wolff et al. 1976), as shown in fig. 8.

After the $4d \rightarrow 4f$ excitation, the excited state can decay in a number of ways, including

$$4d^{9}\,4f^{n+1}\,v^{m} \rightarrow 4d^{10}\,4f^{n-1}\,v^{m} + \varepsilon f, \qquad 4d^{9}\,4f^{n+1}\,v^{m} \rightarrow 4d^{10}\,4f^{n-1}\,v^{m-1} + \varepsilon l,$$

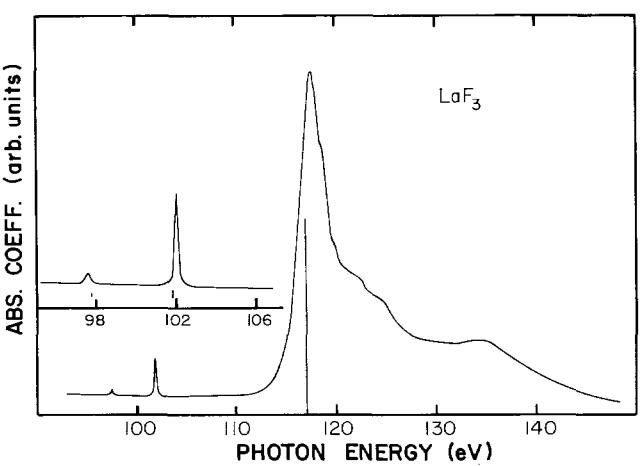

Fig. 7a. Photoabsorption spectra for the trifluoride of La in the region of the 4d–4f excitation (Olson and Lynch 1982). The vertical lines are the absorption lines calculated for the free tripositive lanthanide ion (Sugar 1972).

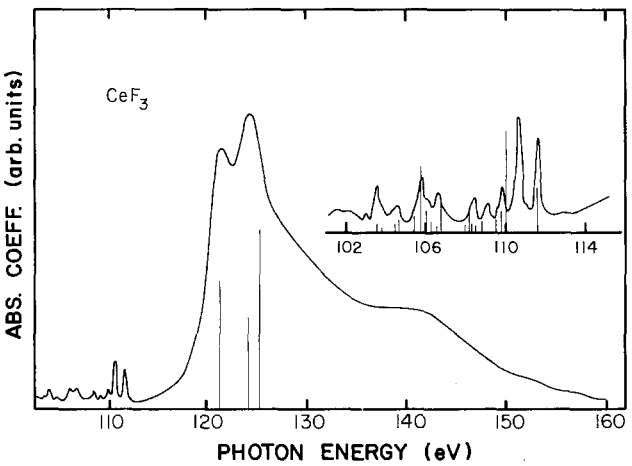

Fig. 7b. Photoabsorption spectra for the trifluoride of Ce in the region of the 4d–4f excitation (Olson and Lynch 1982). The vertical lines are the absorption lines calculated for the free tripositive lanthanide ion (Sugar 1972).

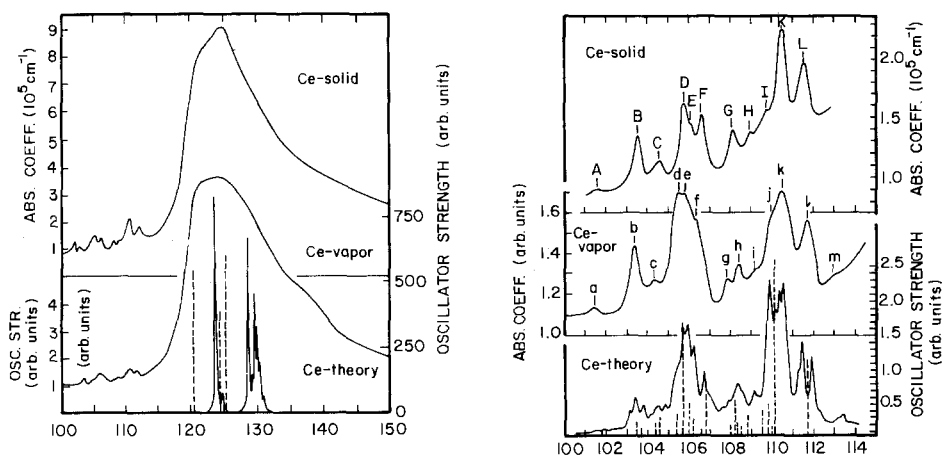

Fig. 8. Absorption spectra of γ-Ce and Ce vapor (Wolff et al. 1976), and calculated spectra. The dashed vertical lines indicate the positions and strengths of absorption lines for a free tripositive ion (Sugar 1972) and the solid lines are the result for calculations of a free neutral Ce atom (Wolff et al. 1976).

where v represents a valence electron and ε is the energy in the continuum of the emitted electron. The probability of each decay mode depends on the energy of the photon absorbed (Zangwill and Soven 1980, Zangwill 1982). In general, for photon energies in the region of the 'fine structure' (see fig. 7 or 8), the decay by emission of a 4f electron is the most probable. At higher energies, decay by emission of electrons with larger mean radii becomes more probable, as shown in fig. 9. Thus, 4f emission is enhanced by using a photon energy corresponding to one of the sharp peaks of the fine structure, while only a small energy difference in the exciting energy results in suppression of 4d → 4f transitions and little 4f emission is expected. Similar, but less dramatic, effects occur in the continuum part of the 4d → 4f excitation spectrum. The theoretical picture has been tested (Gerken et al. 1982) and has been found to

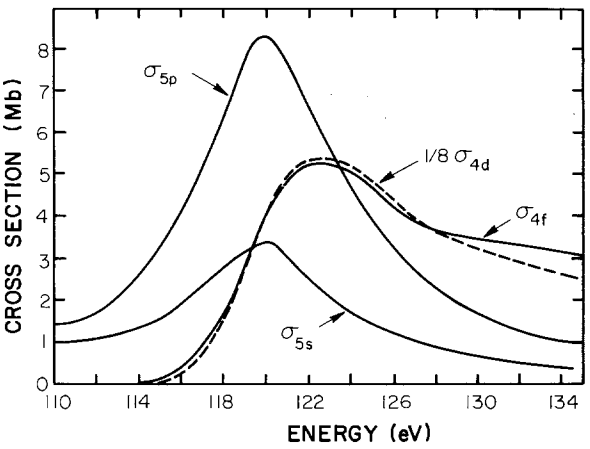

Fig. 9. Probability or cross section for resonant decay of the 4d–4f excitation in Ce by emission of a 4f, 5s, or 5p electron. The dashed line is the cross section for direct 4d emission. (After Zangwill and Soven 1980.)

be qualitatively correct, but some details which are important for Ce have not been confirmed, particularly the degree of overlap in excitation energy of the decays via the 4f and the 5f electrons (to be discussed below).

2.4. *Angle resolved photoemission*

Angle resolved photoemission (Pendry 1975, Plummer and Eberhardt 1982) differs from the above techniques in that electrons are analyzed only when they are emitted into a relatively small solid angle. The advantage is that an angle resolved EDC selects electrons with a small spread in momentum. The simplest and most easily interpreted angle resolved EDC is that which collects only electrons emitted normal to the surface. These electrons must have momenta along a particular direction in k-space to be emitted normal to the corresponding surface (e.g. $k \| [100]$ to be emitted from the (100) surface).

Angle resolved photoemission is best discussed with the aid of fig. 1. For a fixed angle of incidence and polarization, the probability of exciting an electron with a given initial state k_i to a final state of wave vector k_f is proportional to $|\hat{e}\cdot \boldsymbol{p}_{if}|^2$. If this electron propagates to the surface and escapes, the normal component of velocity will be reduced by those microscopic forces responsible for the work function. For a clean, well-defined crystalline surface, however, the parallel component of velocity or wave vector is unchanged as the electron passes through the surface. Once in vacuum, the escaping (free) electron has a wave vector k' and energy $\hbar^2 k'^2/2m$. An angle resolving detector determines the kinetic energy and the direction of propagation to get $k'_{\|}$ and $k'_{\perp}$ individually. If the other component of the (internal) final state wave vector can be found, and there are schemes for determining this (not needed for this chapter), one can map the band structure E vs. k for the material. To date, only γ-Ce has been examined with angle resolved photoemission.

Angle resolved photoemission can also be used to obtain symmetry information for the electronic states. Consider the situation shown in fig. 10 where the incident photon, the surface normal, and the detector axis define a plane. The angle of incidence and the angle of the detector axis may be arbitrary in this plane. If it

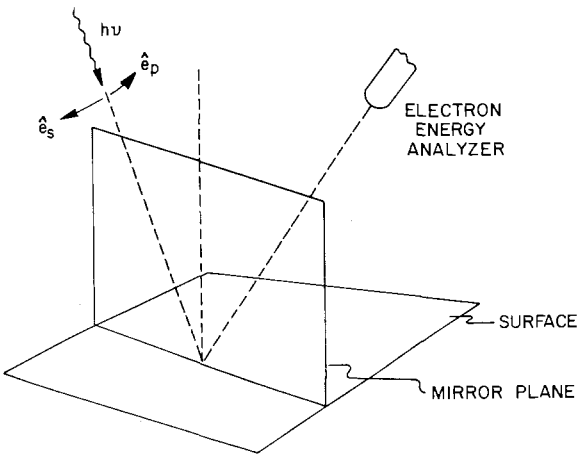

Fig. 10. Geometry for determining initial state symmetries with respect to the mirror plane of a sample by angle resolved photoemission. e_s and e_p denote the directions of polarization for the electric field vector as perpendicular or parallel to the plane of incidence.

coincides with a plane of mirror symmetry for the crystal, Hermanson (1977) and Jacobi et al. (1977) have shown that the symmetry of the electronic states involved in the photoemission process can be determined. In the limit of infinite angular resolution, the only final states which can be detected are those that are even with respect to reflection in the mirror plane. The odd states have a node in this plane, and therefore no amplitude. For the photoexcitation process to have non-zero probability, $\hat{e}\cdot\boldsymbol{p}_{if}$ in eq. (4) must not vanish. If Ψ_f is even, $\hat{e}\cdot\boldsymbol{p}\Psi_i$ must be even. If Ψ_i is even, then $\boldsymbol{p}\Psi_i$ is odd and if Ψ_i is odd, then $\boldsymbol{p}\Psi_i$ is even. $\hat{e}$, which is parallel to the electric field of the radiation, will be even with respect to reflection in the mirror plane for p-polarized radiation (fig. 10) and odd for s-polarization. Putting these together, the quantity $\hat{e}\cdot\boldsymbol{p}_{if}$ does not vanish for even initial states when s-polarization is used and for odd initial states when p-polarization is used. These selection rules have proven to be very useful. To employ them, the highly polarized continuum of synchrotron radiation is highly advantageous.

2.5. *Surface core level shifts*

It is well known that the binding energies of core electrons in atoms on the surface will differ from the corresponding energies of bulk atoms. This surface core level shift is a chemical shift and may be of either sign (Citrin et al. 1978, van der Veen et al. 1980, Citrin et al. 1983, Citrin and Wertheim 1983). The fact that valence band studies of Ce, especially those using resonance photoemission, involve photoelectron kinetic energies near those which give a minimum mean free path for inelastic scattering (fig. 2) suggests that surface contributions to the spectrum might range from minor to important. Since the 4f electrons of heavy rare earth metals resemble core electrons, there has been interest in their surface binding energy shifts. The surface binding energy shifts of all of the stable rare earths have been measured by Parks et al. (1982) and Gerken et al. (1982, 1985). The surface shifts for the heavy rare earths were found to be as large as 0.8 eV. They decrease as the atomic number decreases, extrapolating to about 0.3 eV for Ce, a splitting so small that it could not

be determined by the fitting procedure on the data for Ce. (The fits to the Ce data gave a surface 4f binding energy shift of 0.3 eV (Parks et al. 1982) and 0–0.4 eV (Gerken et al. 1985).) The significance of this result for the two-peaked structure of Ce (to be discussed in detail in section 3.2) is that it is a shift too small to account for the peaks themselves, but may play a role in any detailed line-shape analysis of surface sensitive spectra. A reliable fit to the shape of the Ce 4f contribution to the EDCs is not possible with the present state of the theories of their origin (see section 4).

A related problem occurs for studies of γ- and α-Ce which use films condensed onto substrates at different temperatures (Wieliczka et al. 1982, 1984). Schneider et al. (1983) studied films of Yb evaporated on substrates at different temperatures. The shapes of the 4f contributions to the EDCs, measured with a photon energy giving high surface sensitivity, varied with temperature. This was interpreted as arising from a variety of surface shifts, each corresponding to a different surface atom coordination. The relative distribution of coordination numbers depended on the substrate temperature, with lower-coordinated surface atoms favored for cold substrates. Although important for Yb with surface core level shifts of 0.51–0.86 eV, depending on coordination, this effect should be negligible for Ce. It is not large enough to lead to different line shapes measured at 40 K for films deposited at that temperature and films deposited at 300 K.

2.6. *Complications in photoemission*

The description we have given for photoemission is conceptually the simplest but there are a number of inadequacies in it. In the study of Ce and its compounds, some of these inadequacies become apparent. In the following we mention several of them.

First, photoemission does not occur in three temporally sequential steps. Since the mean free path for inelastic scattering may be only a few interatomic spacings, photoelectron transport to the surface and escape through it are part of one process. A quantum mechanically correct picture is to view an initial state consisting of a photon and a solid with N electrons which makes a transition to a final state consisting of a solid with $N - 1$ electrons plus an electron that is outside the solid. The formal treatment of photoemission as a one-step process was given relatively early and considered subsequently (Adawi 1964, Mahan 1970, Schaich and Aschroft 1970, 1971, Schaich 1978, Ashcroft 1978, Pendry 1976, 1978 Spanjaard et al. 1977, Maham 1978, Inglesfield 1983, Ambladh 1985, Bardyszewski and Hedin, 1985, Borstel 1985), but it has not been applied to many specific cases. Feibelman and Eastman (1974) recast a many-body form of it (Caroli et al. 1973) into a more transparent form and showed under what conditions the one-step picture reduced to the three-step picture (non-interacting electrons, long mean free path for inelastic scattering).

The second shortcoming of our treatment above, one that is very important for this chapter, is that the energy of the outgoing electron is related to the energy of the $(N - 1)$-electron final state, not to the energy of just one of the electrons in that state and not to the energy of any initial state electron. Thus, photoelectron spectroscopy

does not necessarily give a spectrum related simply to the initial (ground) state spectrum. Although the starting point is the ground state of the many-electron system, the final state may not be the ground state of the ionized system.

There are two approximations used to characterize the photoemission process and the role of the final state. In the adiabatic approximation, the photoelectron is removed very slowly so that the $N-1$ remaining electrons adjust to minimize the total energy at each stage of the process and the final state hole is left well screened. The final state would then be the ground state of the ionized system, and the apparent binding energy of the electron would be a minimum for this fully relaxed final state. This binding energy is smaller than that given by Koopmans' theorem since the latter is the energy of a ground state orbital assuming all other orbitals are frozen and cannot relax. This adiabatic photoionization may be the predominant process when the photoelectron kinetic energy is low. In contrast, if the photoelectron is removed with much greater velocity, then the sudden approximation may be more appropriate. Here the $N-1$ electrons have the same wave functions they had before photoexcitation. However, since they are not eigenfunctions of the new Hamiltonian, they must be expanded in terms of at least several of the new eigenfunctions. They represent linear combinations of many states of the $(N-1)$ electron system, all but one of which will be excited states. By conservation of energy, the outgoing photoelectrons will have a distribution of energies lower than in the adiabatic case. These will appear as contributions of the spectrum that come from initial state electrons of apparent higher binding energy than the adiabatic contribution.

These excited states are easily seen in the X-ray induced photoelectron spectra of atoms where they cause discrete peaks in the spectra at energies roughly corresponding to excitation energies of the atom – not the atom excited but the one of next-higher atomic number because the nucleus plus the inner shell hole in the final state can be approximated by the nucleus of the next atom in the periodic chart (the $Z+1$ or equivalent-cores approximation). An introductory discussion of final state effects with many references can be found in Carlson (1975). See also Martin and Shirley (1976a,b). Such satellites are found in the XPS spectra of molecules and solids as well. The crossover from adiabatic to sudden approximations was once thought to occur at energies several hundred eV above threshold (Carlson and Krause 1965), but a recent study suggested that the transition can be nearly complete by 10–20 eV (Stöhr et al. 1983).

To reiterate, a single core level can give rise to several features in XPS spectra, some at higher binding energy than the calculated binding energy of a Koopmans' theorem value and some at lower. There is a sum rule, in fact, which states that the intensity-weighted average of the energies of all the structures from one level will equal the Koopmans' theorem value (Lundqvist 1969, Hedin and Lundqvist 1969, Manne and Åberg 1970). Unfortunately, it is difficult to apply this rule because some structures, especially those which are broad, may be difficult to distinguish from the background of inelastically scattered electrons.

The difference between the adiabatic and sudden approximations is generally not important for valence band photoelectron spectroscopy of metals because a large

number of electrons respond to the presence of a hole, and each one may shift in energy by an immeasurably small amount. However, for a hole in a localized core level or the 4f shell of Ce, a smaller number of electrons may undergo measurable shifts in response to the potential of the newly created hole. This is important because it means that studies of the 4f electrons in Ce compounds do *not* provide the binding energies of the 4f states in the ground state of the system. Indeed, whenever the interaction energy of two electrons on one atomic site is of the order of a band width, the simple interpretation of the photoemission spectrum breaks down. With this reiteration of the cautionary words of the leading paragraphs of this chapter, we now turn to case studies.

3. Experimental results

3.1. *Cerium trihalides: systems with straightforward 4f character*

CeF_3 is an ionic insulator with a band gap of about 10 eV (Olson et al. 1978). Each tripositive Ce ion is surrounded by eleven fluorine ions (Huschke 1979) and is isolated from other Ce ions. Because the the neighboring F^- ions have closed shells, hybridization is expected to be extremely small. Since the Ce ion has lost three electrons, the 4f spectrum for CeF_3 should closely resemble that of a free ion.

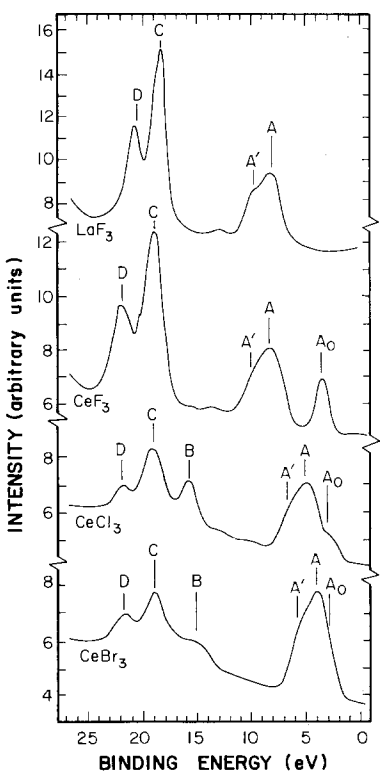

Fig. 11. Valence band photoemission for LaF_3, CeF_3, $CeCl_3$, and $CeBr_3$ (Sato 1976). The ordinates are in arbitrary units for each spectrum. Normalization to the common Ce 5p core level peaks (C and D) would allow a quantitative comparison of valence band spectra, denoted by A and A′. Feature A_0 reflects the 4f emission and is absent in LaF_3.

The first photoelectron study of CeF_3 was reported by Sato (1976). He used XPS to obtain valence band spectra of the trifluorides, trichlorides, and tribromides of both La and Ce. His spectra for LaF_3 and the Ce halides are shown in fig. 11. The resolution was about 1 eV, and the zero of energy is in the center of the band gap. The band with the structures labeled A and A′ is the valence band and is derived almost exclusively from the 2p, 3p, and 4p states of F, Cl, and Br, respectively. Since it is broader than the resolution of the spectra and contains structure, it shows the effects of valence band dispersion. Peak B arises from the Cl 3s and Br 4s states which broaden only slightly, if at all, into a band. The corresponding peak is not seen in CeF_3. Peaks C and D arise from the lanthanide 5p shallow core levels; they exhibit a spin-orbit splitting of 2.4 and 3.1 eV in La and Ce, respectively. The remaining peak, A_0, is not present in the La trihalides but is observed in the Ce trihalides because it is due to the Ce 4f electron. Peak A_0 falls in the band gap in CeF_3 but it overlaps with the valence band when the gap narrows with increasing halogen atomic number.

It is tempting to conclude that fig. 11 shows the positions of the 4f levels with respect to the valence bands, but it is not correct to do so. As discussed above, a photo-induced hole in the 4f level and a hole in the valence band do not give rise to identical responses of the system because relaxation or screening energies can be different. For these insulating systems, the screening is provided by remaining electrons in the subshell of the hole, by outer electrons on the ion in the case of the Ce 4f hole, and by electrons on neighboring ions. Unfortunately, the details of the screening processes in insulators such as CeF_3 are not well understood. An extensive study of relaxation around core holes in transition metal halides was carried out by Veal and Paulikas (1985) but their results can be applied only qualitatively to Ce halides.

Resonant photoemission provides important information about the degree of mixing of Ce 4f electrons with valence band states, and we will use this technique repeatedly throughout the following sections. In preparation for those discussions, it is important to understand the details of the absorption spectrum itself in the photon energy range 100–150 eV. Since CeF_3 is a nearly ideal case in which to examine the $d \rightarrow f$ resonance, we reproduce its absorption spectra in fig. 7. In general, the optical transitions in the $d \rightarrow f$ region are of the form

$$h\nu + 4d^{10}\,4f^{n} \rightarrow 4f^{9}\,4f^{n+1}$$

for all of the lanthanides. As described in the last section, the 4f electron and the 4d hole have comparable radii and there is a large multiplet splitting in the $4f^9\,4f^{n+1}$ configuration. The multiplet structures below the autoionization threshold remain sharp in the solid and they appear to be relatively insensitive to the environment of the lanthanide atom because of the small radii of the 4f and 4d electrons (fig. 7). Calculations have been carried out for these transitions for many of the rare earths in which the system was assumed to be a free tripositive ion (Starace 1972, Sugar 1972, Dehmer and Starace 1972). Although calculated Coulomb and exchange integrals gave poor agreement with experiment, there was a very successful fit to the spectra when these integrals were treated as fitting parameters.

The calculated multiplet absorption features for Ce are shown as dashed lines in fig. 8 where the heights of the lines indicate the calculated oscillator strengths. Only five fitting parameters were adjusted to yield a good fit for the positions and strengths of all of the sharp lines. The solid lines in fig. 8 are the result of a similar calculation for the free Ce atom. The region below the autoionization limit is fit very well by the free ion spectrum for both CeF_3 and metallic γ-Ce. After the calculations were done, the photoabsorption spectrum of atomic Ce was measured by Wolff et al. (1976). The spectrum for atomic Ce agrees very well with that for solid Ce in the region below the autoionization limit. At the same time, there were subtle differences in the details of the absorption spectra which are important for assessing changes in the degree of hybridization of the 4f electron.

There have been no theoretical treatments of the autoionization region of the $d \rightarrow f$ transition, but it is clear from the spectra for CeF_3 and metallic Ce that there are effects of the Ce environment in this region. Two mechanisms have been proposed to account for these high energy structures. One is that they arise from differences in the density of states into which autoionization takes place, and the other suggests that they could be near-edge absorption fine structure (Bianconi et al. 1985). For the latter, structure results from interference between the out-going final state wave function and wave function backscattered from neighboring nuclei, both being the result of photoexcitation ten or more eV above a threshold, in this case one of the strong lines.

3.2. α- *and* γ-*cerium*

One of the foremost goals of photoemission studies of metallic cerium has been to locate the 4f electron within the valence band or, more accurately, to investigate 4f-derived features in the photoemission spectra for correlation to ground state phenomena (see section 2.6). These studies were motivated by (and have subsequently been the source of motivation for) models which seek to elucidate the mechanism for the γ–α phase transition. In the mid-1970s, there were three models for the γ–α transition. The oldest, the promotion model (Pauling 1950, Zachariasen 1973), held that the 4f electrons were 'promoted' under pressure into the conduction band, i.e. the 4f occupancy in α-Ce was zero. The delocalization, or Mott transition, model (Johansson 1974) had the 4f wave functions, localized in the γ phase, overlapping with increasing pressure sufficiently to delocalize in the α phase. A hybridization model was proposed by Hill and Kmetko in 1975. The first and last of these models require that the 4f level be located near the Fermi level. Recent studies have shown the successes and limitations of these models. In this section and the next, we focus on experimental results pertaining to elemental α- and γ-Ce and to Ce clusters. In section 4 we review the theoretical picture for the Ce 4f, discussing in detail the many models which have been proposed for the phase transition in the context of the experimental results.

Early ultraviolet photoemission (Helms and Spicer 1972) and X-ray photoemission studies (Baer and Busch 1973, 1974, Pollak et al. 1976, Steiner et al. 1977, Baer and Zürcher, 1977, Crecelius et al. 1978) of metallic γ-cerium showed the difficulty of separating the 4f contribution from that of the '5d' and '6s' electrons

when single photon energies were used to probe the electronic states. These studies reported values for the 4f binding energy which ranged from 0.5 to 1.9 eV. In a study which used several photon energies (21.2, 40.8 and 1253.6 eV) to vary the 4f photoionization cross section, Platau and Karlsson (1978) reported that the 4f electron had an apparent binding energy of 1.9 eV. Lang et al. (1981) also obtained a binding energy of 1.9 eV by XPS measurements while Crecelius et al. (1978) obtained 1.8 eV. Baer et al. (1981) reported XPS and bremsstrahlung isochromat spectra which supported a conclusion based on synchrotron radiation studies that a second 4f feature appeared near the Fermi level (see below). At the time of most of this work, an apparent binding energy as large as 2 eV was not considered to be consistent with the promotion model or the hybridization model, but it was consistent with the Mott transition model for the phase transition. The possibility of two 4f-derived photoemission features sparked many stimulating discussions.

Synchrotron radiation with its tunable photon energy made it possible to vary more fully the relative photoionization cross section of the various valence band states. With synchrotron radiation, it also became possible to develop the technique of resonance photoemission for studies of the 4f states via the $4d \rightarrow 4f$ transitions. The first such study of γ-Ce using resonance photoemission was reported by Johansson et al. (1978) who again observed the 4f peak to be at 1.9 eV apparent binding energy. A second resonance photoemission study by Allen et al. (1981a,b) concluded that the 4f-derived peak had a binding energy of 2.2 eV for γ-Ce. The next two studies by Mårtensson et al. (1982) and Wieliczka et al. (1982) used several synchrotron radiation photoemission techniques to show unambiguously that the 4f contributions to the EDCs of *both* γ- and α-Ce consisted of *two* peaks, not one, making the interpretation of the spectra in terms of the earlier pictures of the electronic states of Ce less straightforward than expected.

The 4f contributions to the EDCs of γ-Ce were identified by these authors in two ways. One made use of the fact that the ratio of 4f to valence electron photoionization cross sections increased with $h\nu$ in the range from 20 to 90 eV (see fig. 4). Hence, comparison of spectra taken at 30 and 60 eV showed the growth of the 4f-derived emission. The resulting difference curves were obtained by normalizing the spectra at some energy in the valence band that contained little or no 4f character. The second method used resonance photoemission and compared spectra taken at energies on resonance ($\sim$120 eV) and off resonance ($\sim$115 eV, see fig. 8). These revealed the 4f contribution since the most likely decay mechanism involved 4f emission. Both techniques showed the existence of a two-peaked contribution from the 4f electrons in the spectrum of γ-Ce, as shown in fig. 12 (Wieliczka et al. 1982).

It should be noted that the observation of two 4f-derived peaks in Ce metal was preceded by the detection of such structure in the cerium pnictides CeP, CeAs, and CeBi, as will be discussed in section 5.2 (Franciosi et al. 1981). These two final state peaks were seen more easily in these semimetallic compounds than in Ce metal because they were not so well masked by contributions from other electrons.

The two photoemission techniques which were used to demonstrate the double-peak character of the 4f emission in the EDCs of γ-Ce were also brought to bear in studies of α-Ce. Temperature-dependent studies showed the very intriguing result

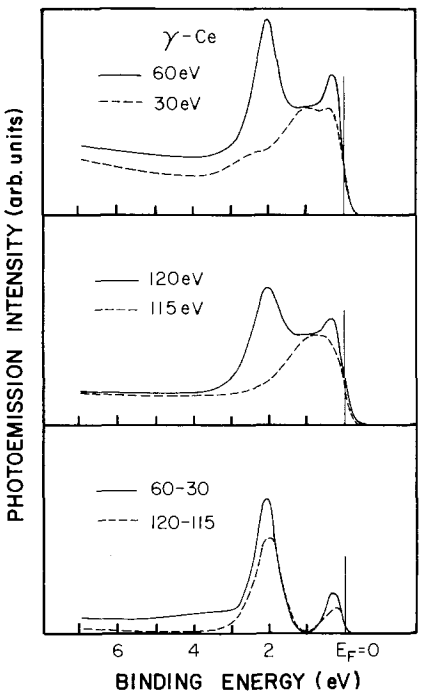

Fig. 12. Valence band photoemission for γ-Ce which highlights the 4f contribution. The top two panels show EDCs which have low 4f content (*hν* of 30 and 115 eV) and high 4f content (60 and 120 eV). The difference curves in the lowest panel clearly show two 4f-derived structures. (After Wieliczka et al. 1982.)

that differences in the EDCs between γ- and α-Ce were rather small. Parks et al. (1982) examined $Ce_{0.9}Th_{0.1}$ which, upon cooling, goes from the γ phase to the α phase without an intervening β phase. Their study had the advantage that spectra could be taken very close to each other in time at nearly the same temperature, even though they were not examining pure Ce phases. Wieliczka et al. (1982) used films of α-Ce produced by evaporation onto a 300 K substrate, then cooled to ca. 40 K to yield α-Ce, and films of α-Ce produced by evaporation onto cold substrates which were later warmed to 300 K to yield γ-Ce. The advantage was that the films were high-purity Ce and the disadvantage was that there were longer time intervals between studies of the two phases. To investigate the possibility of some β-phase contamination in the low-temperature studies of α-Ce, Wieliczka and Olson (1983) also examined the intermediate β-phase of Ce. They found that the EDCs for β-Ce closely resembled those for γ-Ce.

Figure 13 shows a comparison of the 4f contribution to the EDCs of γ- and α-Ce taken at photon energies which highlight the 4f emission (Wieliczka et al. 1982). The only change in the 4f spectrum due to the phase transition is a decrease in the strength of the component near 2 eV binding energy and an increase in the strength of the component near the Fermi level. No shift in binding energies was observed in these measurements. Similar conclusions were reached by Mårtensson et al. for $Ce_{0.9}Th_{0.1}$. Taken together, the experimental results convincingly argued for the existence of two 4f-derived features and demonstrated that the photoemission results were inconsistent with formal conversion from $4f^1$ to $4f^0$ upon entering the α-phase.

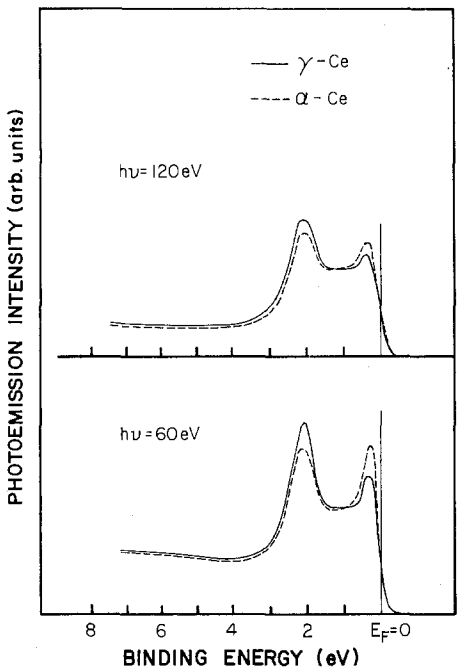

Fig. 13. Comparison of 4f emission in photoemission spectra of γ- and α-Ce. The 4f content of EDCs taken at both 60 and 120 eV is high, as shown in fig. 12. As shown, emission from the feature closer to E_F increases in the α phase while emission from the deeper feature diminishes. (After Wieliczka et al. 1982.)

The observation of the double-peaked structure motivated several theoretical attempts to model final state effects in this correlated electron system. In turn, the predictions provided the impetus for further experimental studies. In particular, Wieliczka et al (1984) undertook higher resolution measurements (0.12 eV) to determine whether or not the peak near the Fermi energy was really *at* the Fermi energy, as some theoretical models for the double-peak structure predicted. The results shown in fig. 14 reveal peaks in γ-Ce at 2.0 and 0.2 eV binding energy while

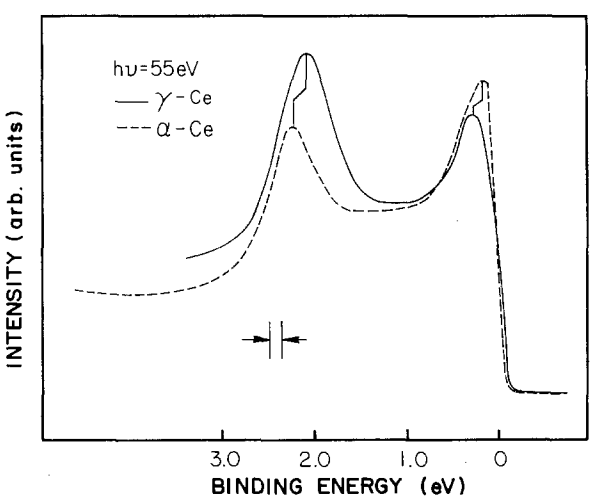

Fig. 14. Photoemission spectra of γ- and α-Ce taken at higher resolution than in fig. 13 to show the sharpening of the structure near E_F and the shifting of the deeper structure to higher binding energy for the α phase. (After Wieliczka et al. (1984.)

those in α-Ce appear at 2.1 and about 0.1 eV. The observed peak at 0.1 eV in α-Ce is believed to indicate that the actual position of the maximum is at the Fermi energy, shifted by the experimental instrument function. (Model convolution of a Gaussian function with the original spectrum consisting of a peak near the Fermi edge indicated that the peak must lie in the binding energy range of 0 to 0.05 eV. A peak as deep as 0.1 eV would be shifted by the instrument function to an energy detectably greater than that observed.) These results then showed that a 4f peak was not pinned to E_F and that the deeper of the two features shifted in energy during the phase transition.

Still higher resolution studies of evaporated films of γ-Ce and α-Ce were carried out very recently by Patthey et al. (1985). They used the inherently sharp He resonance lines at 21.2 and 40.8 eV and a very low pass energy in their electron energy analyzer to achieve an overall resolution of 20 meV. To reduce thermal broadening of the spectra of γ-Ce, they cooled their samples to 150 K. (The β phase should be the stable phase at this temperature, but its spectrum is similar to that of γ-Ce, based on lower energy resolution results of Wieliczka and Olson (1983).) The results of fig. 15 show that α-Ce has a structured peak at the Fermi level, while γ-Ce has a peak at the Fermi level and another peak about 350 meV lower. These two were unresolved in earlier measurements and they were ascribed to spin-orbit-split $4f_{5/2}$ and $4f_{7/2}$ levels (see later).

When temperature-dependent studies are performed, there is a question as to whether a shift in binding energy of a spectral feature might be due to simple temperature changes alone. We therefore note that typical temperature shifts of electronic levels are in the range of $1–10 \times 10^{-4}$ eV/K. This linear shift is valid to a temperature of the order of the Debye temperature, below which it smoothly reaches a zero shift at 0 K. Since the sign of the shift is usually negative, we can expect the

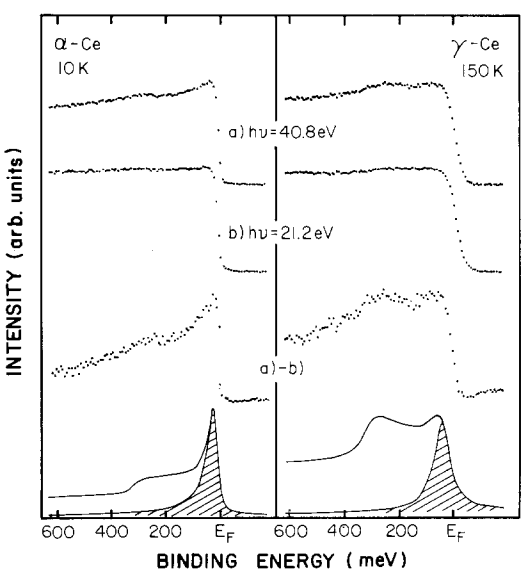

Fig. 15a. Photoemission spectra of γ- and α-Ce taken with 20 meV resolution for the valence bands within 600 meV of E_F. The upper two pairs of EDCs were taken at 21.2 and 40.8 eV at 10 K (left panel) and 150 K (right panel). The difference curve labelled a – b shows the 4f contribution. The bottom curves are calculated 4f contributions using the model of Gunnarsson and Schönhammer (1983b) (text section 4). The hatched region represents the contribution of the state consisting of a 4f electron and a valence hole to the system ground state. (After Patthey et al. 1985.)

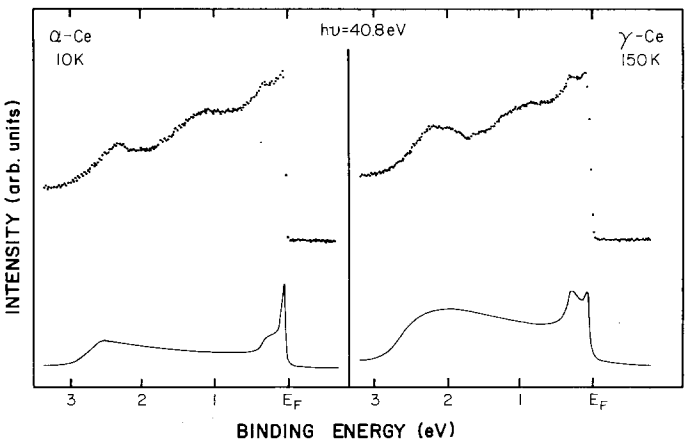

Fig. 15b. EDCs and calculations for γ- and α-Ce for a broader range of the valence band than shown in fig. 15a. The upper curves are the experimental data. (After Patthey et al. 1985.)

binding energy of a localized level to shift by as much as 0.2 eV upon cooling from 300 to 20 K. This may account for the shift of the deeper peak from 2.0 to 2.1 eV in Ce as one goes from γ- to α-Ce. In fact, since part of the temperature shift arises from thermal expansion, the reduction in the volume of α-Ce with respect to γ-Ce may account for a significant part of this shift. It is important to note, however, that the lower binding energy peak shifts in the opposite direction upon cooling, and we conclude that at least one of these two peaks shifts for a reason in addition to temperature change.

Wieliczka et al. (1984) undertook a photoemission study of evaporated films of La to determine the baseline or reference level of emission of 5d6s valence states when 4f levels are absent. As shown in fig. 16, the expected fall-off of the photoionization cross section was observed, but it was greater than anticipated. Indeed, the EDCs for La decreased in intensity by about a factor of 100 between 32 and 60 eV photon energy, but showed minimal changes in shape. This indicated that dipole matrix element effects are small at these photon energies corresponding to the density of states limit in angle integrated photoemission of the light rare earths. More important for Ce, the results suggest that at 60 eV most of the EDC intensity in Ce arises from the 4f electrons. This is so because the matrix element fall-off with energy depends on the 5d wave function radial distribution and this does not vary significantly for La and Ce. Hence, in the normalization procedure for comparing γ- and α-Ce, Wieliczka et al. (1982) subtracted some 4f contribution to both spectra. Similar comparative measurements were made by Parks et al. (1982) for $Ce_{0.9}Th_{0.1}$ and $La_{0.9}Th_{0.1}$, but the foregoing conclusions could not be drawn, apparently because of a spurious peak in the EDCs at higher photon energies.

Jensen and Wieliczka (1984) undertook the first angle resolved photoemission study of Ce to examine the details of the γ-Ce band structure and to distinguish 4f-derived features. The results are shown in fig. 17. By orienting the analyzer and photon beam in a (011) mirror plane of the (100) surface, they were able to vary the

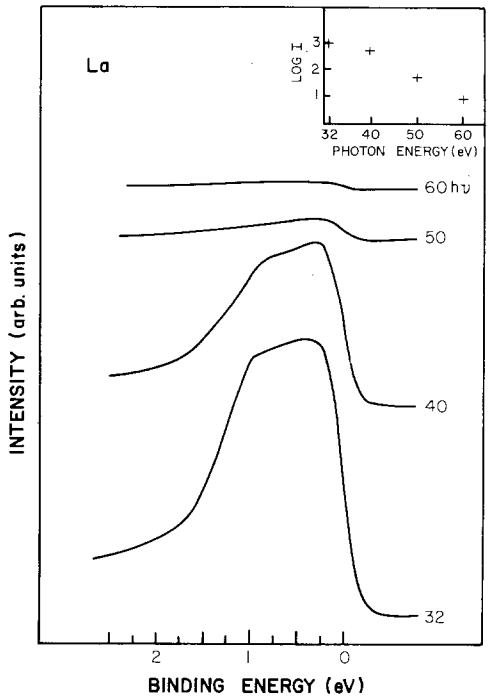

Fig. 16. Photoemission spectra for La which have been corrected for differences in incident photon flux for photon energies between 32 and 60 eV. The inset shows the peak height as a function of photon energy. Since there is no change in shape of the spectra, this height is proportional to the photoionization cross section. (After Wieliczka et al. 1984.)

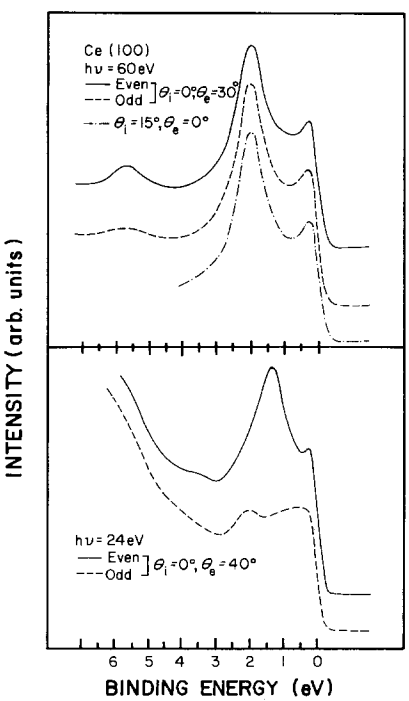

Fig. 17. Angle resolved EDCs for single crystal γ-Ce (100). θ_i is the angle of incidence for the photons and θ_e is the exit direction for detected photoelectrons, both measured from the (100) surface normal in a 110 mirror plane. Even and odd refer to the photon polarization defined in fig. 10. The lower panel shows EDCs from predominantly 5d-derived states and demonstrates the operation of the mirror plane polarization selection rules. The upper panel shows emission from states of higher 4f character for which selection rules are not obeyed. (After Jensen and Wieliczka 1984.)

polarization of the incident radiation by selecting different orthogonal, but equivalent, mirror planes. The spectra for the two polarizations are quite different at 24 eV, but they are nearly the same at 60 eV. At 24 eV they were exciting primarily valence electrons and, to a lesser extent, 4f electrons; at 60 eV they were exciting primarily 4f electrons. The initial state for emission from valence bands 0–2 eV below the Fermi level is expected to be even, according to band structure calculations (Pickett et al. 1981, Podloucky and Glötzel 1983), in agreement with the measured spectra. At 60 eV, the polarization anisotropy analogous to that at 24 eV is much less pronounced, even though the calculated 4f bands predict a specific symmetry. The 4f emission peak was also found not to disperse in energy as the parallel component of wave vector was changed. The authors concluded that Bloch states were not good zero-order descriptions of the 4f states since there appeared to be a lack of dispersion in the states and symmetry selection rules were violated. (Some small amount of anisotropy is consistent with the data, but it is small.) Further, Jensen and Wieliczka measured the dispersion of the non-4f bands at a photon energy of 24 eV and found that agreement with the calculated valence bands was not particularly good.

Rosina et al. (1985, 1986) recently reported angle resolved photoemission results from a (100) face of γ-Ce, using several discrete line sources with energies between 12 and 40 eV. They noted that the 4f-derived peaks did not vary with the angle of emission, i.e., their apparent initial state energies did not depend on wave vector. Significantly, they found evidence for 4f contribution to the EDCs at photon energies as low as 11.8 eV. Interband transitions involving 5d-derived states were observed to disperse, as expected from their own band structure calculations which extended to 22 eV above E_F, and polarization selection rules were obeyed.

Gerken et al. (1982) reported a study of resonance photoemission in several light rare earths which sought to determine the contribution of each process to the decay of the $4d^9 4f^{n+1}$ excited state, including ordinary Auger decay subsequent to the resonance process. They followed all possible core level emission and emission at 0.5 and 2 eV binding energy. After background subtraction and normalization of the spectra, they obtained the contribution of each decay process, as shown in fig. 18. (The units are arbitrary, but they are the same for each spectrum.) The decay channels which involve emission of electrons from states at 0.5 and 2 eV binding energy have the same magnitudes and shapes, implying the same mixture of 4f and valence electrons at both binding energies. The shapes were fitted to a Fano line shape and compared with the calculations of Zangwill and Soven (fig. 9) with good agreement observed. The fit to theory is not as good, however, for the 5s and 4d resonances since there are peak shifts of about 4 eV. The shape similarity of the 0.5 and 2 eV resonances led to the conclusion that both contained 4f character but the degree of the valence electron contribution could not be determined. Nevertheless, the fact that resonance photoemission and the use of the energy-dependent photoexcitation cross section below resonance both give the same 4f spectral shapes (fig. 12), coupled with the very small photoionization cross sections of the valence electrons of La in the 60 eV region, suggests that the valence electron contribution to the two peaks is rather small and that resonance decay via 4f electrons is much more probable than decay via valence electron emission.

Meyer et al. (1986) studied resonance photoemission from Ce vapor. The

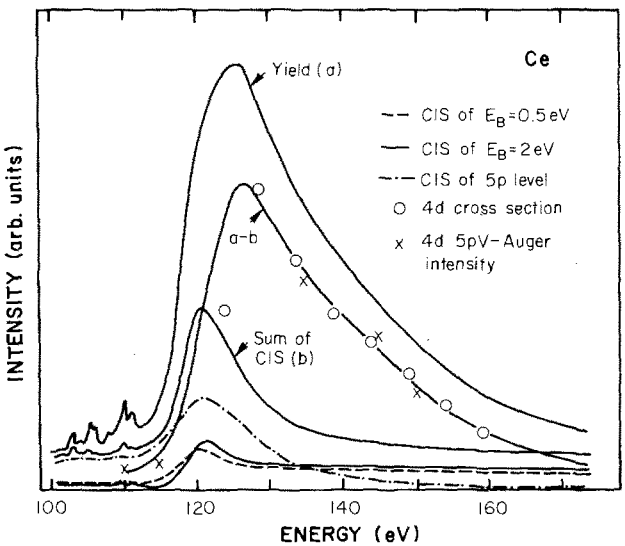

Fig. 18a. Measured partial photoionization cross sections for Ce in the 4d–4f excitation region. The lowest three curves are the partial cross sections for emission of an electron with 0.5 eV binding energy (dashed), with 2 eV binding energy (solid), and of a 5p core electron (dash–dot). Their sum is indicated by curve (b). The total yield is the top curve (labelled (a)) and the difference between curves (a) and (b) (labelled a–b) should represent the emission of 4d electrons. The open circles are the measured cross section for 4d emission, (×) correspond to the yield of 4d–5p valence Auger electrons. (After Gerken et al. 1982.)

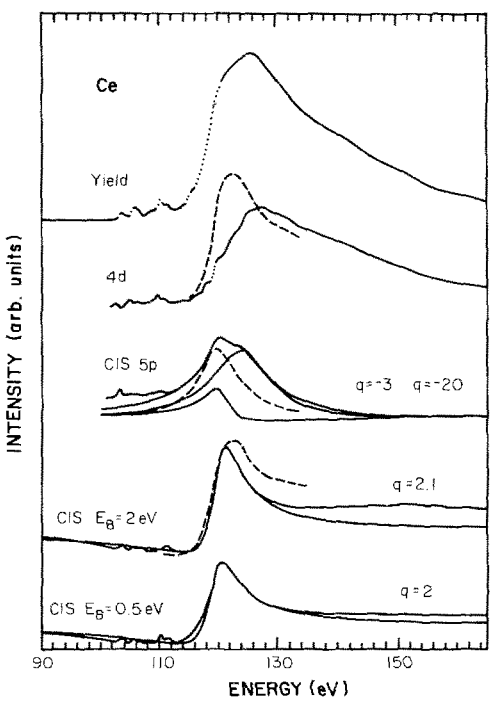

Fig. 18b. Fit of the partial cross sections from fig. 18a given by dots to Fano line shapes drawn solid and to the calculations of Zangwill and Soven (1980) drawn dashed. (After Gerken et al. 1982.)

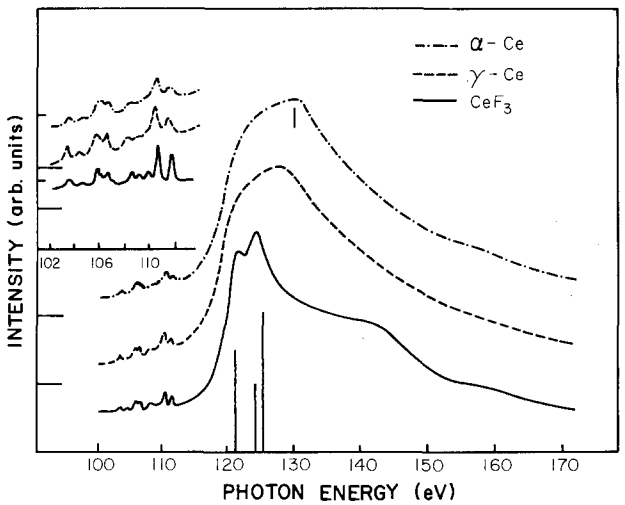

Fig. 19. Partial yield spectra of CeF_3, γ-Ce and α-Ce in the region of the 4d–4f excitation measured with electrons having 4 eV kinetic energy (Wieliczka et al. 1982). The vertical lines are for some of the prominent multiplet final states as in fig. 7.

measured partial cross sections generally resembled those calculated by Zangwill for the emission of 4d, 5s, and 5p electrons. They could separate the 4f emission from that of the 5d and 6s electron. The partial cross section for all these together gave a peak coincident with that of the experimental 5p partial cross section, not with the expected 4f partial cross section peak shown in fig. 9. The experimental peak was narrower on the high energy side than the calculated peak, the measured 5s peak was at the same position as the measured 4d peak, and the calculated 5s peak (fig. 9) was at the position of the 4d peak. From this, we conclude that agreement of the calculated partial yields with experiment is not yet quantitative.

Other photoemission measurements which have been made on Ce metal also refute the promotion model. The yield spectra for γ- and α-Ce are shown in fig. 19 for the region of 4d → 4f excitations (Wieliczka et al. 1982). As can be seen, there is very little difference in the spectra. Since we know that these transitions are very sensitive to the number of 4f electrons in the initial state (assuming integral values for the free ions on which the calculations have been carried out), we can say that this number has changed very little between γ- and α-Ce. If one 4f electron were lost, Ce would have a similar spectrum to La, as shown in fig. 7, although the spectrum would be shifted about 8 eV to higher energy due to the extra nuclear charge. Such a spectrum is, in fact, observed for heavily oxidized Ce (Wieliczka 1982).

Cerium and its compounds are not unique in displaying 4f-derived double-peaked structure in valence band EDCs. Intermetallic compounds of Pr and Nd were studied by Parks et al. (1982, 1984). Pr has a 4f peak at a binding energy of 3.6 eV, one that is well known from XPS studies. Wieliczka et al. (1984) examined Pr with synchrotron radiation and reported a second 4f-derived peak at 0.75 eV. Its width was large, 0.5–1 eV, and there was considerable amplitude at E_F. Parks et al. (1982, 1984a,b) brought out the corresponding structures in the intermetallics $PrRu_2$ and $PrPd_3$ by using resonance photoemission techniques (4f peaks at 1.5 and 3.5 eV in $PrRu_2$ and 2.2 and 4.8 in $PrPd_3$). They also showed a weaker feature in the corresponding Nd compounds (fig. 20) where both peaks are at larger binding

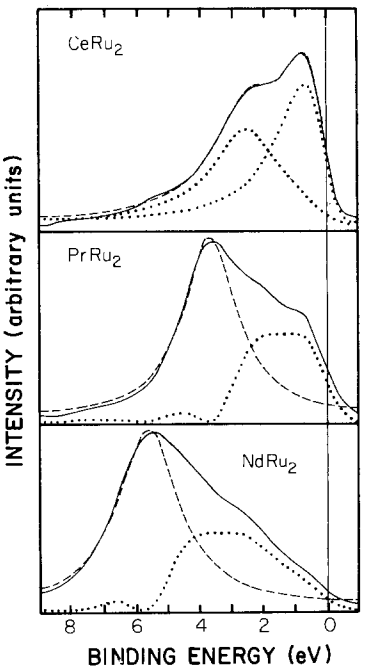

Fig. 20. 4f-derived contributions to the EDCs of $CeRu_2$, $PrRu_2$, and $NdRu_2$. The solid lines are the total 4f contribution since secondary and primary valence electron contributions have been removed through subtraction. The dashed and dotted lines represent the individual contributions obtained by fitting a Lorentzian to the structure at larger binding energy. (After Parks et al. 1984a,b.)

energies. The peak separations of some 2 eV are about the same as observed in the Pr intermetallics, Ce metal, and Ce intermetallic compounds and alloys.

3.3. *Cerium clusters*

The discussion of section 3.2 shows that photoemission spectra for α- and γ-Ce are not simple. In principle, the corresponding photoemission spectra for Ce vapor would be simpler than those of the metal because there are fewer valence electrons to respond to the photohole. Valence-electron photoemission measurements of Ce vapor have not as yet been carried out. Studies of small clusters of Ce metal have, however, been reported by Fujimori et al. (1985).

Cerium clusters can be prepared by the evaporation of Ce onto single-crystal Si surfaces when the coverage range is less than the equivalent of about 0.6 monolayers (Grioni et al. 1984a,b). The 4f contribution to the emission spectra can then be highlighted by measuring EDCs at 35 and 60 eV photon energies and taking the difference, as discussed above for Ce metal and shown for Ce/Si(111) in fig. 21. At low coverage, there is a single 4f-derived peak which is shifted 1.3 eV to higher binding energy with respect to the 2 eV peak in bulk Ce and is broader than that observed for bulk Ce. Corresponding binding energy shifts of localized levels in small clusters have been observed for non-4f levels in several metals, as summarized by Fujimori et al. (1985). The main feature of interest here is not the shift but rather that the 4f-derived structure near the Fermi energy is not observed for small clusters. Unfortunately, the structure and sizes of the clusters were not known, although the authors inferred that they were probably no larger than about 100 atoms (the spectra exhibited no Fermi level cutoff).

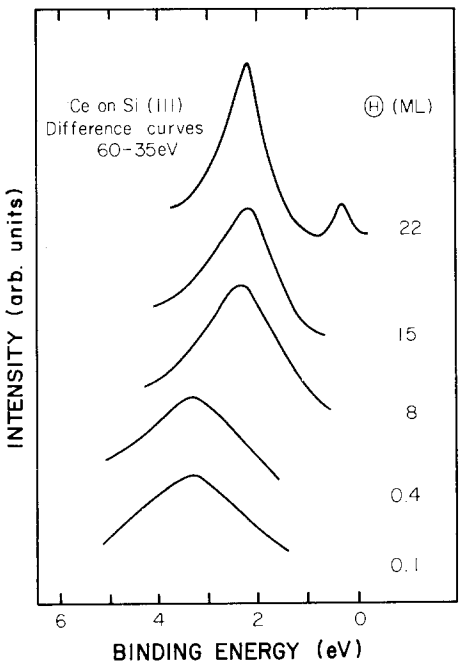

Fig. 21. Photoemission difference curves for Ce deposited onto Si(111) based on EDCs taken at 60 and 35 eV to highlight the changing 4f contribution. The curves for the two lowest coverages are for Ce clusters of small but unknown size. Those at higher coverage reflect increasingly pure Ce films with diminishing amounts of Si in solution. These results show that the 4f feature near E_F does not appear until the Ce matrix is extended. (After Fujimori et al. 1985.)

In the cluster, if the lattice parameter were larger than that of γ-Ce and/or if most of the atoms were atoms with fewer than full coordination, we would expect to observe γ-Ce-like emission but with less 4f-conduction electron hybridization and weaker 4f–5d Coulomb interaction. Significantly, in discussions of the double-peaked structure in metallic Ce (next section), when diminishing 4f conduction electron hybridization or 4f–5d Coulomb interaction have been considered, the structure nearer the Fermi level is the one that weakens. The observed behavior for Ce clusters then encourages further consideration of these parameters.

As the Ce coverage on Si(111) increases, the 4f-derived peak is observed to shift to the position of the peak in bulk Ce, although it remains broader. The second peak near the Fermi level does not appear until still larger coverages are attained. At these coverages the morphology of the material being sampled in the measurement is more complicated than at low coverage, and its details are even harder to surmise, but present modeling of the interface suggests that it is likely to be a solution of Si in a Ce matrix. It appears, however, that if the lattice parameter of the matrix is close to that of bulk γ-Ce, a fairly extensive volume of Ce is needed to produce bulk-like behavior, i.e. the 4f wave functions are extended or hybridized with rather extended wave functions. Likewise, modification of the lattice by Si in solid solution is sufficient to alter the 4f spectral signature of Ce metal.

Studies of the evolving Ce/GaAs(110) interface by Weaver et al. (1985) showed analogous slow convergence to Ce-like behavior. In this work, however, there was immediate reaction between Ce and GaAs, and the resultant phase showed the spectral signature of CeAs at low coverage. Interestingly, the size threshold for the double-featured 4f structure in the CeAs reaction products was much lower than for Ce itself

Results for Ce clusters grown by matrix isolation in films of solid Xe were reported by Wieliczka et al. (1986). They found that small amounts of evaporated Ce exhibited only a structureless valence band EDC. The deposition of additional Ce atoms resulted in an EDC with a peak at 2 eV binding energy and a weak structure at the Fermi level. The structure at E_F grew with respect to the 2 eV peak as the amount of deposited Ce increased. The many-body picture of the photoemission spectra for Ce thus requires a threshold size for Ce clusters before the model is applicable, but that threshold size is not yet known.

4. Theory of cerium 4f electron photoemission

The one-electron band model which has been used so successfully to interpret the photoelectron spectra of the valence bands of many metals clearly will not be satisfactory by itself to interpret the 4f spectra of Ce. Indeed, self-consistent band calculations for both γ- and α-Ce yield a 4f band about 1 eV wide which straddles the Fermi level (Glötzel 1978, Pickett et al. 1981, Podloucky and Glötzel, 1983). The filled portion extends only ~0.1 eV below the Fermi level and contains approximately one electron. It is hybridized with other states and is not a pure 4f band. The simple one-electron picture of photoemission based on these bands would predict a narrow 4f-derived peak at the Fermi level in both phases of Ce, and this is not observed. To describe adequately the photoemission spectra, we must then move beyond the one-electron picture. As discussed above, photoelectron spectra are *final state* spectra which reflect the initial states to a greater or lesser extent depending on the localization of the states themselves.

In the following we examine models for α- and γ-Ce which seek to explain the double structures observed in the 4f spectra. First, we consider satellite phenomena as they have been observed in a variety of systems, but then turn to the specific models which center around the Anderson Hamiltonian. Subsequent discussion examines other proposals.

Satellite lines often appear in the XPS spectra of core levels of free atoms and solids on either the high or low binding energy side of the main line. (The main line is often assumed to correspond to ionization of the core electron with no change in the states of other electrons or with a small relaxation shift.) Those on the high binding energy side have been called shake-up or shake-off structures (Carlson 1975, Wendin 1981) while those on the low energy side are termed shake-down. Shake-up or shake-off features correspond, respectively, to the system left in an excited or doubly ionized state, respectively, as a result of the presence of the photohole. (Excited or ionized here refers not to the ground state of the original system but to the lowest energy state of the system containing the photohole, i.e., the state reached if the photohole were produced adiabatically.) The sudden approximation leads to many states as possible final states, not just the ground state of the residual ion. The shake-up satellites are the result of a final ion with a core hole and a discrete excitation of a valence electron. The shake-off continuum arises from the core hole plus a valence electron that has been excited to the continuum. If the remaining electrons respond to the core hole by relaxing or polarizing around the hole, then

the photoelectron emerges with an increased kinetic energy. The result is a shake-down satellite on the low binding energy side of the main line. (These are not the only sources of satellite or multiple structures in XPS spectra.)

Several authors have shown that for rare earth core levels it is not always easy or meaningful to distinguish between main line and satellite features (Schönhammer and Gunnarsson 1977, 1978a,b, Fuggle et al. 1980). The analogy with core levels is introduced here to show that the response of the system to a single hole can give rise to a multiply-peaked spectrum and a similar effect *could* cause such structure in Ce and its compounds.

Hüfner and Steiner (1982) pointed out that inadequate screening of the photohole from a 4f state which was close to the Fermi level before excitation could produce a photoemission feature $\sim 2\,\text{eV}$ below E_F. Hüfner (1986) later showed that screening arguments, elaborated in following sections, could be used to explain the double-peaked 4f structures found in Ce, Pr, Nd, and their compounds. In each case, the peak at greater binding energy arose from a 4f hole screened by 5d electrons and the shallower peak arose from a 4f hole screened by a 4f electron (leaving a 5d hole at the Fermi level). The energy difference between these two is 2.0–2.5 eV and can be obtained from thermodynamic arguments. As has been shown by Johansson (1974) (and chapter 68 of this volume), thermodynamic arguments can be most useful in discussing many properties, including photoemission spectra which represent excited states. The Hüfner and Steiner interpretation has been further elaborated in Hüfner 1984, and Hüfner and Schlapbach (1986).

Since the Ce atom has only a single 4f electron and crystal field and spin-orbit splittings are small on the scale of 2 eV, the two-peaked structure is presumably a many-body effect involving the interaction of the 4f electron with other 4f electrons or with the valence electrons. The latter interaction has long been believed to be the origin of intermediate valence phenomena in Ce-based solids and the Kondo effect in many systems containing impurities with magnetic moments (Grüner and Zawadowski 1974, Robinson 1979, Lawrence et al. 1981, Brandt and Moschalkov 1984).

The first calculation of the 4f photoemission spectrum for Ce was reported by Herbst et al. 1972, 1976 (see also chapter 67 of this volume). They calculated the difference in energy between the ground state of the rare earth metal and the system with a 4f hole for all the rare earths. This was done by treating the 4f states as localized in each cell of the crystal and using approximately self-consistent bands for the valence electrons (Herbst et al., 1976). As a result, there was a hole at each atomic site in the final state. This gave poor agreement with the 4f XPS spectra of the rare earths (one peak for Ce was known at the time) because screening of the 4f hole was not included. Including screening by placing an extra valence electron at each site in the final state and allowing it to relax around the hole during the iterations to self-consistency gave very good agreement with binding energies from XPS spectra for all the rare earths. For Ce, the 4f binding energy was 1.9 eV. In their calculations, the final state giving rise to the peak at 1.9 eV involved a 4f hole which was screened as completely as possible by valence electrons, with primary screening from 5d electrons. Screening by a 4f electron by refilling the 4f hole was not considered.

When the two-peaked structures were unambiguously observed for Ce and many of its compounds, several theoretical approaches were taken to explain their origin. Most of these studies of valence and 4f photoemission in Ce began with the assumption that the 4f state was best described as localized. Authors disagreed, however, not only on which terms were important in the Hamiltonian, but also on whether the double-peaked structure was present in the ground state or not. Many began with the Anderson Hamiltonian in which the 4f system is treated as an impurity on one site of the system (the origin) which can be written as

$$H = \sum_{k,\sigma} E_k \, c^+_{k,\sigma} \, c_{k,\sigma} + E_f f^+_\sigma f_\sigma + U \sum_\sigma f^+_\sigma f_\sigma \, f^+_{-\sigma} f_{-\sigma} + \sum_{k,\sigma} (V_{k,\sigma} f^+_\sigma c_{k,\sigma} + \text{h.c.}) + \sum_{k,k',\sigma,\sigma'} U_{\sigma,\sigma'} c^+_{k,\sigma} \, c_{k',\sigma} f_\sigma f^+_{\sigma'}. \tag{10}$$

Here $c^+_{k,\sigma}$ and $c_{k,\sigma}$ are the creation and annihilation operators for a conduction electron of wave vector $\boldsymbol{k}$ and spin σ, and f^+_σ and f_σ are the corresponding operators for a localized (4f) electron on the single impurity-like site. The first two terms are for non-interacting conduction and 4f electrons. The third term represents the repulsion of two 4f electrons on the impurity site. As written, it omits the multiplet structure. The fourth term represents the hybridization between the 4f electron and the conduction electrons. $V_{k,\sigma}$ is often called a hopping matrix element and is the matrix element of the one-electron Hamiltonian for the system between a 4f and a conduction band state. The last term represents the Coulomb repulsion between a 4f electron and conduction electron or, written differently, the Coulomb attraction between a 4f hole and a conduction electron. (Strictly speaking, the last term in eq. (10) is an addition to the Anderson Hamiltonian. It was introduced by Falicov and Kimball (1969) in a Hamiltonian with no hybridization term.) By ignoring the third and last terms, this Hamiltonian reduces to a one-electron description which will give the band structure, $E(k)$, of the system for the coupled conduction and 4f states when all sites are allowed to have 4f electrons and these states become band states. One can extend this Hamiltonian by summing the second term over lattice sites, thereby locating a 4f electron on each lattice site. The 4f electrons on different sites do not interact by direct overlap to form a 4f band. Only 4f conduction band overlap is implied.

Allen and Martin (1982) and Lavagna et al. (1982, 1983) proposed that the γ–α transition in Ce was related to the Kondo effect. Since Kondo systems have densities of states with two peaks, one very close to the Fermi level and one below, this offered a possible explanation of the two peaks in the photoelectron spectra, assuming that the photoabsorption process would transfer the structure in the density of states to the emitted spectrum. Detailed calculations of a photoelectron spectrum were not, however, carried out. The Kondo (or Abrikosov–Suhl) resonance in the density of states can be obtained from the Anderson Hamiltonian in the limit $U \to \infty$ (Lacroix 1981). For a Fermi level in the center of a valence band of width $2D$ and a constant density of states coupled by a constant matrix element V to an N_f-fold degenerate localized level at energy ε_f below E_F, two peaks can arise in the density of states of the coupled system at low temperatures if ε_f is not too small. As

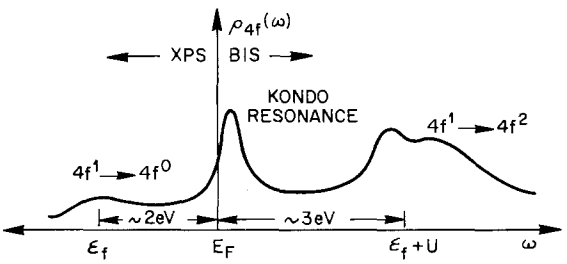

Fig. 22. Schematic representation of the Kondo picture of the spectral density of a Ce impurity in an electron gas. The region below E_F can be studied by photoemission and the region above E_F is accessible to BIS.

shown in fig. 22, one will be near ε_f. It will have a width $N_f\Delta$ and a height $1/(2\pi\Delta)$, with $\Delta = \pi V^2/2D$. The other will be very near the Fermi energy. Its height will be $1/\pi\Delta$ and its width will be kT_K where T_K is the Kondo temperature. (Low temperatures mean $T \ll T_K$.) The Kondo temperature here is approximately $T_K = (D\Delta)^{1/2} \exp(\pi(\varepsilon_f - E_F)/N_f\Delta)$. As T rises toward T_K, this peak weakens until it vanishes at T_K. For modeling α-Ce, T_K is of the order of 1000 K (Lavagna et al. 1982). Smaller values for T_K used in earlier discussions of thermodynamic properties call for a peak near the Fermi level of such a small strength and width that it would not be detectable in photoemission. Figure 22 actually shows a 4f spectral density for removal of a 4f electron, as in photoemission, in the region below E_F and for the addition of a 4f electron, as in BIS, in the region above E_F (see eq. (22) in chapter 64 of this volume). This function is what is calculated in the work to be described next.

A more extensive picture of the photoemission process in Ce which was based on the Anderson Hamiltonian (eq. 10)) was proposed by Gunnarsson and Schönhammer (1983a,b, 1985a,b) (see also chapter 64 of this volume). They initially assumed that the Coulomb interaction between the 4f hole and the conduction electron (the last term in eq. (10)) could be neglected, arguing that it might renormalize some parameters in their model but would not give rise to the basic physics of the spectrum. The hybridization term was therefore the key term in the Hamiltonian. It eliminated angular momentum as a good quantum number, making the ground state of Ce a combination of $4f^0$, $4f^1$, and $4f^2$ configurations, the latter two mixed with conduction band states, while the former is just a conduction band state ($4f^2$ states occur only if U is not infinite). The final states were similarly not eigenstates of angular momentum and were mixed 4f conduction band states. This Hamiltonian was used with variationally-determined singlet wave functions for a system resembling α-Ce. The valence band was simplified to one with an elliptical density of states. The degeneracy of the 4f level was considered, and was shown to be important. The valence photoelectron spectrum, the spectra of several core levels, and the $3d \rightarrow 4f$ X-ray absorption spectrum were calculated at $T = 0$ K using the sudden approximation. Rather good agreement with experiment was achieved with a hybridization matrix element about ten times larger than previously used in fitting other types of data for several Ce-based systems, of the order of 0.1 eV. (Not all authors define this matrix element the same way.) Despite the large hybridization matrix element, the model still allows a small Kondo energy, kT_K, for reconciliation with thermodynamic data. This model then was further employed to study a variety of spectra for other Ce compounds (Gunnarsson and Schönhammer 1983b; Fuggle

et al. 1983a,b, Gunnarsson et al. 1983, Hillebrecht et al. 1984). A pedagogical version of the calculations has been given by Allen, 1985b, and the reader is referred to chapter 64 in this volume by Gunnarsson and Schönhammer.

Imer and Wuilloud (1987) have developed a simplified version of the Gunnarsson–Schönhammer model and applied it to 4f valence band photoemission, 3d level XPS, electron energy loss spectra, and inverse photoemission (see also Wuilloud and Imer (1986) and chapter 62 of this volume). The ground state consists of a valence state, $|f^0\rangle$, at $E = 0$, and non-degenerate states $|4f^1\rangle$ and $|4f^2\rangle$ at E_f and $2E_f + U$, respectively. The states neighboring in energy are coupled by a single hybridization integral V. The valence state has no dispersion and can be represented by a single state instead of a band. The ground state energies and wave functions can be obtained by diagonalizing a 3×3 matrix. Final states are obtained from the same matrix (photoemission) or a different, but similar, one (core-level XPS, BIS, core-level electron energy loss spectra). The intensities of the lines in the spectra can be calculated from the coefficients in the wave functions. Broadening these into Lorentzians can give a remarkably good fit to measured spectra for a number of materials. The appearance of the spectra depends on the parameters E_f, U, and V (plus another parameter for coupling a core hole to the 4f states), and the model allows easy fitting to spectra. The resulting fit is not quite as good as that obtained with the full Gunnarsson–Schönhammer model.

In the Gunnarsson–Schönhammer picture of photoemission from α-Ce, the peak at the Fermi level can be viewed as arising from a 4f hole screened by 4f-like charge density (the hole is then a valence band hole) and the peak at 2 eV arises from a 4f hole screened by valence electrons. The apparent electron–hole attraction is provided by the hybridization term in the Hamiltonian rather than by a direct electron–hole Coulomb interaction. The peak at E_F is present only if the hybridization V is strong enough. Its integrated area is $n_f(1 - n_f)$, where n_f is the number of localized 4f electrons in the impurity site in the ground state. The peak at greater binding energy is due to a 4f photohole screened by 5d conduction electrons. It dominates the spectrum for weak hybridization.

The Gunnarsson–Schönhammer calculations show that the two peaks in the photoelectron spectrum do not give *direct* information about the location of the 4f level in the ground state. In the calculations, they found that a single bare 4f level placed at a binding energy of 1.1 eV gave rise to two peaks at the positions observed in photoelectron spectra, roughly zero and 2 eV binding energy with no structure at 1.1 eV. Figure 23 shows the calculated valence band photoelectron spectrum. Gunnarsson and Schönhammer (1983a,b) also calculated bremsstrahlung isochromat spectra with the same model, finding a 4f final state peak just above the Fermi level. These calculations illustrated that the observed spectral features for localized electronic systems do not give direct ground-state information. In later calculations, Gunnarsson and Schönhammer (1985a,b) allowed U to become finite and observed that the strength of the peak near the Fermi level increased due to mixing of 4f states in the final state. The effects of varying the hybridization strength and the shape of the conduction band density of states were also demonstrated. (In fig. 23, as the hybridization increases, the peak near the Fermi level grows at the

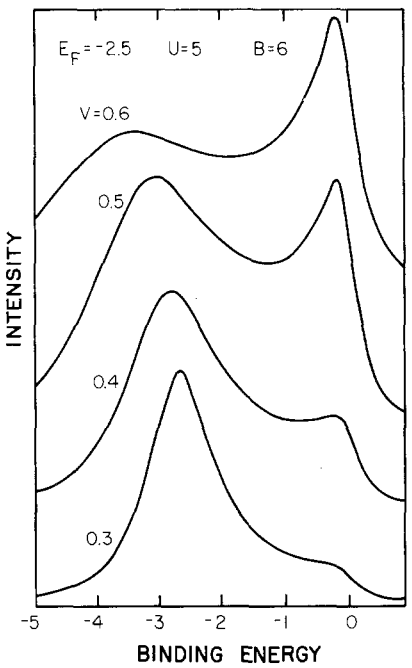

Fig. 23. Calculated 4f contribution to the EDC of α-Ce for different values of the hybridization matrix element, V. The bare 4f level was placed at a binding energy of 2.5 eV, the f–f repulsive interaction, U, was 5 eV, and the elliptical conduction band width was 6 eV with E_F at its center. The calculated spectra were convolved with a Lorentzian of full width at half maximum of 0.5 eV to simulate experimental broadening. (After Gunnarsson and Schönhammer 1985a,b.)

expense of the peak near the position of the bare 4f level, an effect seen in Ce at the phase transition.) The calculation was extended to model Pr where the 4f levels lie deeper and the less-bound experimentally observed peak is well below the Fermi energy. In order to obtain a peak below the Fermi level, rather than at it, a different conduction band density of states was used for Pr, one which peaked some 0.6 eV below E_F.

This model has been used by others (Zhang and Lee 1983, 1984, Grewe 1983, Sakai et al. 1984, Kuramoto and Kojima 1984, Kojima et al. 1984, Coleman 1984, Sakuma et al. 1985, Bickers et al. 1985, Sakuma et al. 1986), using different techniques for obtaining results from the Anderson Hamiltonian. In some cases, the 4f component of the ground state density of states was calculated but the photoelectron spectrum was not. Some of these authors also included spin-orbit splitting of the Ce 4f state (as did Gunnarsson and Schönhammer 1983b) and finite temperatures in some cases. Those who used a relatively small value of the hybridization matrix element obtained a peak in the density of states near the Fermi energy at low temperature which became negligibly small at room temperature. Although the width and strength of this peak are expected to be strongly temperature dependent, Gunnarsson and Schönhammer were able to reduce the expected temperature dependence by using a large hybridization matrix element (they calculated only for $T = 0$) also obtaining agreement with other spectroscopic results. Although the model used a non-magnetic ground state, it can be extended to magnetic ground states like those of α-Ce and Pr (Gunnarsson and Schönhammer 1985a,b). Note that

this model, and all others arising from the Anderson Hamiltonian, contain one or two fitting parameters, V and U, as well as the energy of the bare 4f state. However, once these are fit to one spectrum, they may be used to calculate other spectra and physical properties.

A recent application of the Gunnarsson–Schönhammer model has been the fitting of the high resolution photoemission spectra for γ- and α-Ce by Patthey et al. (1985). Both the data and the fit are shown in fig. 15. To obtain the fit they used for values of n_f, the ground state 4f occupancy obtained earlier from fitting to several types of spectra, 0.98 and 0.88 for γ- and α-Ce, respectively (Gunnarsson and Schönhammer 1983a,b). An elliptical density of states was assumed, the bare $4f_{5/2}$ level was placed 1.2 eV below E_F, and the spin-orbit splitting was taken to be 0.28 eV. The best-fit hybridization parameters were 0.082 and 0.105 eV for γ- and α-Ce, respectively. With these parameters, the model could be used to obtain a picture of the ground state. The spectrum of the part of the ground state which consisted of a 4f electron and a valence hole is shown convolved with a Lorentzian as the cross-hatched peak in fig. 15a. This is the part originating from the Kondo peak. It is found to be about 6 times greater in strength (integrated area) in α-Ce than in γ-Ce. However, with this fit to photoemission data, the authors obtained values for the hybridization parameters that were roughly twice as large as those obtained previously in fitting BIS and core excitation data, namely, 0.025 and 0.060 eV for γ- and α-Ce (Wuilloud et al. 1983). This calculation again illustrates the qualitative difference between a photoelectron spectrum and the ground state density of states in Ce. The peak near E_F in the calculated EDC arises from the Ce $4f_{5/2}$ states while the structure about 0.28 eV below E_F arises from the $4f_{7/2}$ states. The ground state should have very little $4f_{7/2}$ contribution since neutron scattering measurements indicate nearly pure $4f_{5/2}$ character (Stassis et al. 1978). The Ce $4f_{7/2}$ admixing is related entirely to the final state of the photoemission process. Its appearance below E_F in the spectrum is because a $4f_{7/2}$ final state is an excited state of the system. For further comments on this work, see Liu (1986) and Patthey et al. (1986).

Schneider et al. (1985) applied the Gunnarsson–Schönhammer model to XPS and BIS valence band spectra and XPS and electron energy loss spectra of 3d core levels for a large number of materials, including some with empty 4f levels just above the Fermi level, including Ba, La, LaF_3, La_2O_3, and CeO_2, as well as Ce (discussed above), $CeCo_2$, and CeN (both to be discussed later). For insulators or semiconductors, two elliptical bands were used, with a gap between them. The model gives good qualitative account of all the spectra. Allen et al. (1986) have done the same for many Ce-based intermetallics.

Other theoretical work has emphasized the role of the direct Coulomb interaction between the 4f hole and the valence electrons (rather than hybridization) in providing the double-peaked structure in the photoemission spectra of Ce. Liu and Ho (1982) calculated 4f photoemission spectra, omitting the hybridization term in the Hamiltonian and treating the Coulomb interaction between the 4f hole and the conduction electrons as the crucial term. Later, they investigated the effect of the hybridization term (Liu and Ho 1983). Kotani and Toyozawa (1974, 1979) studied the problem of the creation of a core hole in the presence of a partly-filled band.

They found that if the conduction band were not filled too far, the Coulomb potential of the hole could split a state from the conduction band and lower it below the band minimum. This state could be left empty or occupied during photoexcitation. The resulting two peaks in the photoelectron spectrum would have intensities proportional to the probability of filling or not filling the split-off state. This model was later expanded by Davis and Feldkamp (1979, 1980a,b). The two peaks, corresponding to the hole's being left screened or unscreened by a conduction electron, are not infinitely sharp but have tails to greater binding energy due to the possibility of exciting conduction electrons by arbitrarily small amounts.

Liu and Ho treated the 4f electron as a core electron, even though its energy places it in the filled part of the valence band. Parameters of their model included the conduction band width, its fractional occupancy, and the screened Coulomb interaction between the 4f hole and a conduction electron. The relative positions and strengths of the two peaks could be fitted by choosing reasonable values for these parameters for γ-Ce (α-Ce) of 4 eV (4 eV), 0.15 (0.20), and 3.0 eV (2.8 eV), respectively. In addition to two final state peaks, which appear as edges, there is a tail to higher binding energy on each edge which tends to fill in the region between the peaks. These tails arise from the primary excitation plus the creation of an electron–hole pair in the conduction electron system, i.e., they are shake-up excitations of the latter. Liu and Ho later extended this model, taking advantage of the fact that the energy of the screened peak relative to the Fermi level is also a free parameter such that the less bound peak need not be at the Fermi level to describe mixed valence properties of other Ce-based systems (Liu and Ho 1983). In this extension, the hybridization of the 4f electrons with conduction electrons was treated as a perturbation which led to fine structure on the photoemission peak located at, or near, the Fermi energy (see also Liu (1986) and Patthey et al. (1986a)). A subsequent investigation by Liu and Ho (1984) considered the formation of 4f bands via the hybridization term when each lattice site contained a 4f electron. The effect was to provide a strongly temperature dependent broadening, but one that is still small with respect to experimental resolution. Allen et al. (1986) have pointed out some difficulties in fitting the model of Liu and Ho to experimental data with reasonable parameters.

Nunez-Regueiro and Avignon (1985) examined the role of the f–d Coulomb interaction (last term in eq. (10)) without introducing hybridization. They were able to obtain a double-peaked structure related to the 4f contribution to the ground state density of states with the lower-energy peak not pinned to the Fermi level. Their model is then suitable for γ-Ce and Pr, as well as α-C. They suggest that more work is necessary before one can conclude whether the hybridization term or the f–d Coulomb interaction is the principal cause of the 4f structure observed in photoemission. Riseborough (1985, 1986) has also considered screening from the Coulomb attraction to be the more important effect. He finds that if hybridization is present, its primary effect is to make screening easier for the case where the 4f level is close to the bottom of the conduction band.

Another approach was taken by Norman et al. (1984, 1985a,b) (see chapter 65 in this volume). They treated the Ce crystal with a cluster model, using nineteen atoms

in an fcc cluster with an interatomic spacing which corresponded to that of α-Ce. In their calculations, they first determined the total ground state energy. They then placed a 4f hole on the central Ce site and recalculated the total energy, either allowing or forbidding the other cluster electrons to reoccupy the 4f hole. (In previous calculations, the 4f hole was not allowed to be reoccupied (Herbst et al. 1972, 1976, Liu and Ho 1982, 1983).) These two final states corresponded to a 4f hole screened by a 4f electron and by conduction electrons, respectively. Photoemission was thereby treated in an adiabatic sense with two types of screening. They found that in the latter case the screening was predominantly by 5d electrons. The energy difference between the two final states was 1.9 eV, in agreement with experiment and in agreement with the calculations for the 5d-screened 4f hole by Herbst et al. (1972, 1976). The initial 4f states were in the bottom of the 4f band within 0.1 eV of the Fermi level. These, and their subsequent calculations, give the energies of expected peaks in a photoelectron spectrum. Since wave functions are not calculated the intensities, even relative intensities, of peaks are not calculated.

Norman et al. performed additional calculations to test this last result. They used a supercell structure with one Ce site in the center that had a 4f hole. The energy differences between the poorly (5d)- and fully (4f)-screened 4f holes were 1.9 and 2.4 eV for α- and γ-Ce, respectively – close to the experimental results but in reverse order. They tentatively attributed this reversal to the use of the linear muffin-tin-orbital approximation and the atomic-sphere approximation.

Norman et al. indicated that their interpretation of the double-peak structure in Ce may be qualitatively similar to that of Gunnarsson and Schönhammer in that the fully screened final state is a 4f hole screened by a 4f electron and the poorly screened state at higher binding energy is a 4f hole screened primarily by 5d conduction electrons in both models. In the work of Liu and Ho, the 4f structures correspond to screening by a 5d electron and an unscreened 4f photohole. The positions of the bare 4f levels differ between the work of Gunnarsson and Schönhammer (~1 eV below the Fermi energy) and Norman et al. (4f band peaking above the Fermi level, but extending about 0.1 eV below), but this energy is not a measurable quantity in photoelectron spectroscopy.

The calculations of Norman et al. (1984, 1985a,b) have been extended by Min et al. (1986a) to include BIS and 3d core XPS spectra in addition to the 4f photoelectron spectra for both γ- and α-Ce. They again find two peaks in the photoelectron spectrum, corresponding to the 4f hole screened by 4f and by 5d electrons. In this work the 4f states were treated as extended (band) states at first. Doing so gave a splitting of 4.5 eV between the two peaks, traced to too large an occupancy in the 4f band. Forcing this to be near unity gave splittings of 2.4 and 1.9 eV for γ- and α-Ce, respectively. (The relative splittings are reversed with respect to experiment, but this discrepancy is within the errors of the calculation, as mentioned above.) Min et al. (1986b) extended these calculations to encompass the energetics of the γ–α phase transition.

Allen (1983) pointed out that hybridization of a localized level with a partially filled conduction band can give a double-peaked structure in the density of states. One such peak will be just above the Fermi energy and will give rise to a Kondo-

like system while the other will be deeper. Such a spectrum is implicit in the treatment of Gunnarsson and Schönhammer, but it was not presented because they continued all their calculations to final measurable spectra in which final state effects cause significant changes. This Kondo-like peak is not compatible with the 4f photoelectron spectra of Pr and Nd, unless final-state effects can move it below E_F.

Fujimori (1983a,b) interpreted the two α- and γ-Ce photoemission peaks with a model in which the 4f hole hybridizes with valence holes on ligands in a cluster surrounding the Ce atom or ion. (The ligand orbitals may have significant Ce 5d and 6s6p character.) Satellites on core level photoemission lines were interpreted in the same model, which was based on a non-degenerate 4f state. This model was later extended to CeN where mixing with Ce 5d states occurs together with mixing with N 2p ligand states (Fujimori and Weaver 1985a) and to metallic Ce (Fujimori 1983b) where mixing occurs only with Ce 5d states. For γ-Ce the ground state is taken to be a localized 4f electron and filled ligand orbitals. The final state is a linear combination of a 4f hole and a state with a symmetrized hole on the ligands with a 4f electron present. The latter component introduces screening of the 4f hole by 4f electrons. The sudden approximation treatment of photoemission yields a peak from each of the two components. Their separations and relative intensities are given in terms of two parameters, the initial energy separation of the two final states before hybridization and the hybridization strength. α-Ce is treated similarly, except that the ground state is now assumed to be a mixture of a state with no 4f electron and one with a 4f electron and a symmetrized ligand hole, i.e. a mixed valent state. The larger hybridization in the more compressed α-Ce lattice leads to the relative change in the strengths of the two peaks at the γ-α transition with little shift in peak positions, as observed. Fujimori and Weaver (1985b) discuss the γ–α phase transition in metallic Ce using this model. One difficulty, however, is the fact that the hybridization integrals appear as fitting parameters, and it is difficult to assess the significance of the resultant values, ~0.1–1.0 eV. A second difficulty that this model shares with some others is that it predicts two lines for the EDC which represent the two peaks in the spectrum, but the region between the two peaks also has significant 4f character.

The models discussed so far involve screening of the 4f hole, although they differ in the driving force of this screening. Other models have been proposed, but they have not been explored as extensively and they have not been applied to fitting of photoemission or other spectra. In the remaining paragraphs of this section, we will discuss these models.

Schlüter and Varma (1982) considered the self-energy of a 4f electron on a cerium atom in metallic Ce by using the local density approximation. They obtained two peaks for the 4f electron in the ground state of the system. They treated the 4f state with a simple variational radial wave function which was used to minimize the total energy of a free atom, keeping self-consistency with the other electronic states. This total energy had one minimum as a function of the variational parameter, which was a measure of the radial extent to the 4f wave function, and a fall-off for large values, which corresponded to extended radial wave functions. By placing the atom in a lattice of identical atoms, they showed that this fall-off could produce a second

minimum about 5 eV above the principal minimum when Wigner–Seitz radii characteristic of both γ- and α-Ce were used. This minimum corresponded to a radially extended f wave function with its maximum still within the Wigner–Seitz radius. This f wave function can be viewed as an admixture of 5f, 6f, ..., functions. The difference in energy between the states at the two minima arises from the difference in radii of core electrons, mostly the 5s and 5p which relax toward the nucleus as the f radial function becomes extended. Schlüter and Varma (1982, 1983) formulated a many-body picture of Ce in which the peak near 2 eV in γ-Ce was due to excitation from the normal 4f state and the peak near the Fermi level corresponded to excitation from the second minimum. In α-Ce, the peak at the Fermi level is taken to arise from the normal 4f state, with the second minimum available for a shake-up peak (the 2 eV peak). The observed splitting of about 2 eV is far less than the 5 eV calculated for the system energy difference. They ascribed this difference to the neglect of 4f correlations, some screening processes, and possibly a too-simple variational f wave function. Full numerical calculations were not carried out, but estimates of the requisite matrix elements were made which included the coupling of the f state to the 5s and 5p core electrons. Bringer (1983) was unable to find a second minimum in the system energy when he used non-hydrogenic wave functions.

Another suggestion for the origin of the double-peaked structure was made by Connerade (1983) on the basis of the radial wave function for 4f electrons on Ce^{+3} ions (Connerade 1978). Due to competition between the attractive central potential and the repulsive centripetal potential for 4f states, the effective radial potential has two minima. If the inner well is deep enough, the lower-energy eigenstates have wave functions inside the inner well, while higher eigenstates have wave functions with larger radii. For an inner well that is slightly less deep, there will be no bound states located inside the well. The crossover between extended lowest 4f states and 'collapsed' states occurs between the free ions Ba^{+} and Ba^{+2} in which the 4f state is normally empty. This collapse is very sensitive to the radial potential, and it is possible that for Ce the effect of neighboring atoms, or a photohole, could trigger the collapse or expansion of the 4f wave function. This idea has not been pursued further, although there is some similarity to the proposal of Schlüter and Varma.

Mackintosh (1985) emphasized the band-like nature of the 4f electrons in Ce without ignoring the localized part. The two peaks in Ce were assumed to arise from well-screened and poorly-screened final states, as in other models. The physical picture, however, is that upon the creation of a localized hole (which is not an eigenstate of the final-state Hamiltonian) the hole has a probability of diffusing away from the site, a probability which increases with increasing 4f band width. This diffusion leads to 4f screening of the original hole such that the final state is much like, for example, the d hole state in photoemission from transition metals. It gives a peak very close to the one-electron position of the 4f band state, namely, near the Fermi energy. The hole also has a finite probability of not diffusing before the photoemission process is over and in this case it is trapped, but generally screened by the more mobile (5d, 6sp) electrons. The final state produces the 2 eV peak. The peak near the Fermi level corresponds to an adiabatic excitation process while the

2 eV peak is closer to the sudden limit. There is evidence in the photoelectron EDCs that the deeper peak grows slightly in relative strength as the photon energy increases, the 'quicker' photoexcitation and faster photoelectron escape favoring the sudden process, but such a growth may arise from uncorrected experimental effects. Since the 4f band width is greater in α-Ce than in γ-Ce, the peak at the Fermi energy should be larger in the former phase, as observed. Mackintosh discussed the difficulty in applying this model to γ-Ce, for which a 4f band model would appear to be inappropriate, but concluded that the difficulties can, in principle, be overcome.

Eckardt and Fritsche (1986) carried out a calculation similar to that of Norman et al. (1984, 1985a,b). They modeled the solid with a free atom which had a non-integral number of 4f 5d electrons using values taken from a self-consistent band calculation. (The total number of 4f and 5d electrons was integral.) They calculated the energy of the system with a self-consistent field method, the atom having a hole screened by electrons. They ascribe the 2 eV peak to a final state consisting of a 4f hole screened by a 5d electron. The calculated peak was at 1.92 eV for γ-Ce and 1.57 eV for α-Ce. The peak near the Fermi energy was attributed to a 5d hole screened by a 4f electron (the 4f photohole was filled by a 5d electron from the Fermi level, resulting in 4f screening of the 4f hole). The binding energy of the second peak for both phases (0.24 eV) was obtained by a somewhat different calculation due to a numerical instability in the method originally used.

Riseborough (1986) re-examined the treatment of Liu and Ho and included both the hybridization term and the primary f–d Coulomb interaction. He found that if the f level is near the bottom of the conduction band, then the inclusion of the hybridization term makes it easier for the hole potential to split off a bound state from the band, as is necessary to explain the double-peak structure. Hybridization plays a less significant role for other locations of the f level. He emphasized that in this model the separation between the two peaks will be slightly larger than the width of the filled part of the conduction band and that the well-screened peak need not appear at the Fermi level. The model is thus compatible with the observation of similar peaks in Pr, Nd, and some of their compounds.

In summary, the current status of the theory is that the hybridization model based on the Anderson Hamiltonian can account for a variety of phenomena, including photoemission spectra, thermodynamic properties and some aspects of heavy-fermion behavior. An early limitation related to its inability to deal with magnetic systems like α-Ce and Pr has been resolved and, although relatively complex, the model may readily be applied to different systems. It has been used to address the γ–α phase transition in Ce, but in this context suffers from the limitation that band-structure effects due to 4f–4f overlap are neglected. These have been shown to be important for the ground-state properties. Band-structure models with screening include such overlap effects (while neglecting intra-ionic 4f repulsion) and allow first-principles calculations of the energies, though not yet the relative intensities, of the two principal 4f photoemission features. In the future, the relation between the various models will be further explored as a theory is developed which includes the relevant interactions and allows a detailed, quantitative comparison with experiment.

5. Compounds of cerium

In this section, we review the photoemission literature for Ce compounds, picking up where we left off in the discussion of Ce metal and clusters. We first consider metallic and semiconducting compounds of Ce and then turn to the insulating systems. The photoemission studies of these various Ce compounds have used most of the techniques discussed above in the context of Ce, including $h\nu$-dependent valence band studies, comparisons with corresponding La compounds, resonance photoemission, and CIS spectra in the resonance region.

The metallic Ce compounds exhibit a variety of properties which are related to their electronic states, including Kondo resistivity minima, intermediate valency, superconductivity, various types of magnetic ordering, and heavy fermion behavior (along with some of the properties previously mentioned). Some of these Ce compounds exhibit properties like those of Ce, including γ–α phase transitions (related to variations in composition if not to variations in temperature or pressure). Others resemble either γ-Ce or α-Ce.

5.1. *CeB_6*

CeB_6 is a metallic compound in which Ce is trivalent. At low temperature, its resistivity exhibits a Kondo-like minimum. Valence band and resonance photoemission spectra have been reported by Sugawara et al. (1982). For CeB_6 there was a peak at 2.5 eV binding energy which was ascribed to the Ce 4f states and another peak was observed at the Fermi energy. The feature at E_F exhibited a resonance photoemission behavior which was similar to that of the 2.5 eV peak, but the authors did not associate it with the f electron. PrB_6 and LaB_6 were also investigated for comparison, but they showed nothing at the Fermi level. As a result, the Fermi level peak in CeB_6 was not assigned to a band structure effect either. (PrB_6 does not show a Kondo effect, although Pr is trivalent, because the 4f level is too far below the Fermi level.)

Ikeda et al. (1985) calculated the photoemission spectra of CeB_6 and PrB_6 with a molecular orbital scheme fitted to band structure calculations. Account was taken of strong hybridization between the lanthanide 4f and the B 2p states, and screening effects were considered through hybridization matrix elements. For CeB_6, the bare 4f level was placed 4.5 eV below the Fermi level and gave little direct structure in the EDC. The only predicted peak was at 2.5 eV, at the upper edge of the B 2p-based bonding valence band. (There is also a higher energy part of the valence band based on antibonding B 2p states.) On the basis of this calculation, the peak near the Fermi level was not ascribed to be of definite 4f origin, although the analogy to experiments with α- and γ-Ce would favor such an interpretation.

5.2. *Ce chalcogenides and pnictides*

The Ce calcogenides are metallic and the Ce pnictides are semi-metallic materials which form in the rocksalt structure (Flahaut 1979, Hulliger 1979). CeN exhibits

mixed valence behavior; all the other compounds in these two series have stable trivalent Ce. CeS and CeP each have a collapsed volume state like that of α-Ce under high pressure. To the extent that the cerium chalcogenides are good metals, they could show screening effects similar to those of metallic Ce, but many of the experimental studies were made before current models were proposed, i.e., before 4f screening of a 4f hole was widely accepted. As of this writing, there is no evidence for a second 4f related feature for CeS, CeSe, or CeTe.

The photoemission spectra for the Ce chalcogenides have been reported by several authors using synchrotron radiation and resonance techniques (Gudat et al. 1981, Croft et al. 1981a,b, Weaver 1983). (See also chapter 67 of this Volume.) Those studies showed that the Ce 4f electron had an apparent binding energy in CeS of 2.4 eV (2.3 eV for CeSe and 2.5 eV for CeTe) and full width at half maximum of ~0.7 eV. These 4f-related emission features appear in a region of very low density of states between the narrow Ce 5d-derived states (occupied states with ~1.5 eV of E_F and empty states above E_F) and the p states derived from the chalcogen (~3.5 to 8.5 eV below E_F for CeS). The 4f structure in the EDCs showed dramatic resonance enhancement when the photon energy was swept through the 4d threshold. There was no experimental evidence that there was more than a single 4f peak. Comparison of the non-f-derived states with band calculations showed quite good agreement.

Attempts to establish the position and nature of the 4f state in the Ce pnictides have been far more complicated, and it was only relatively recently that there has been consensus. In part, this is because the 4f intensity was divided between two final states. It was in the Ce pnictides that the double-featured character of the 4f emission was first observed (Franciosi et al. 1981).

Early XPS work (Baer et al. 1978, Campagna et al. 1979) observed a 4f-derived feature in CeP at 0.4 eV. They suggested that this feature moved away from E_F and was Auger broadened with succession from CeP to CeAs and CeSb. Allen et al. (1981b) reported that CeBi had 4f-derived emission at 3.2 eV apparent binding energy based on resonance photoemission experiments. In their paper on CeS and CeP, Croft et al. (1981a,b) observed structure near E_F in CeP. They attributed this peak to 4f hybridized states, but this interpretation was later improved by Franciosi et al. (1981). Each of these studies was correct in its observation, namely that there was 4f emission near E_F for CeP, that it was harder to observe for CeAs and CeSb, but that it could be detected below the pnictogen-derived p bands for CeBi.

Franciosi et al. (1981) used direct and resonant photoemission to show that the 4f emission was divided into a feature near E_F and a feature below the pnictogen bands. Their data are shown in fig. 24. The feature near E_F appeared at 0.6 eV binding energy with a full width at half maximum of 0.6–0.7 eV. It neither moved nor broadened with succession from CeP to CeBi. The deeper structure appeared at 3.0–3.1 eV binding energy and had a full width at half maximum of approximately 1 eV. Significantly, the authors showed that the area ratio of the two features diminished by a factor of nearly ten on going from CeP to CeBi. It was this change in relative intensity that precluded observation in the earlier XPS studies.

A later report (Gudat et al. 1982) presented data for CeP, CeAs, CeSb, and CeBi,

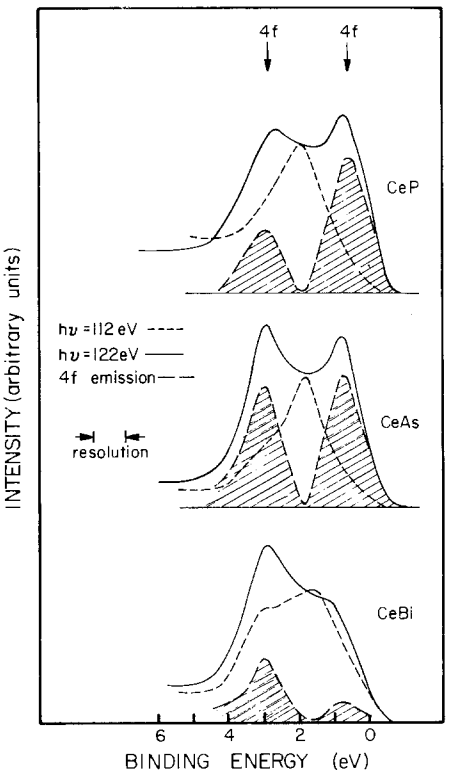

Fig. 24. Photoemission spectra for the cerium pnictides taken with photon energies on resonance (122 eV, solid) and off resonance (122 eV, dashed). Their difference is shown cross hatched. This technique makes it possible to highlight the 4f emission. Analogous results but with higher resolution were obtained by comparing spectra at 30 and 60 eV. As shown, the dominant feature is the one close to E_F for CeP but is the deeper feature for CeBi. (After Franciosi et al. 1981.)

using resonance photoemission and the dependence of the photoionization partial cross sections to isolate the 4f contributions. Angle-resolved photoemission was also employed to study the dispersion of the 4f peaks (they did not disperse).

It is now obvious that the results for the cerium pnictides resemble the spectra of metallic γ-Ce (fig. 12). The peak at deeper binding energy was originally assigned to a 4f hole screened by 5d electrons and the peak near the Fermi level to a 4f hole that partially delocalizes into p states on neighboring pnictides due to hybridization. An alternate way to stating the latter is that electrons from ligand 2p orbitals refill the Ce 4f photohole.

XPS spectra of the valence and 4f region of CeN have been reported by Baer and Zürcher (1977) and Baer et al. (1978). They showed a valence band composed of N 2p states with a peak at the Fermi energy, possibly extended to 2 or 3 eV binding energy which they assigned to the Ce 4f states. Later XPS spectra on films of CeN reproduced the spectra of the earlier work with single crystals (Wuilloud et al. 1985). Gudat et al. (1981) used resonance photoemission and partial yield (constant final state) spectroscopy to investigate the 4f electrons in CeN. They showed that CeN has N 2p-derived valence band peaks in the 2–4 eV region. Peaks from the Ce 4f levels were identified at 0.35 and 1.2 eV binding energy. (These peaks appeared unresolved in the early XPS measurements.) There was considerable overlap with structures from the Ce 5d states, which also showed resonant emission as discussed

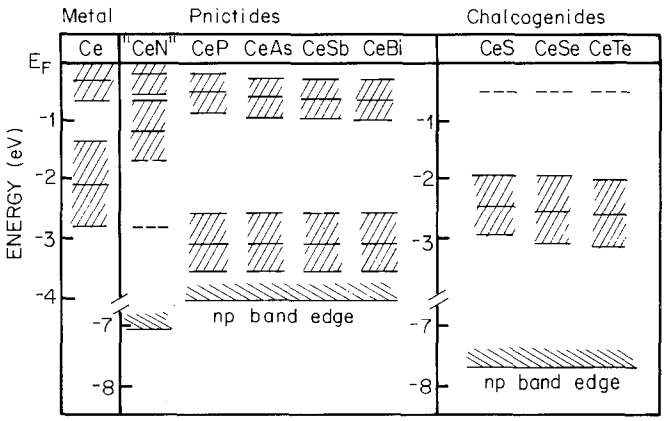

Fig. 25. Summary of the positions and widths of the Ce 4f contributions to the EDCs of Ce pnictides and chalcogenides (Gudat et al. 1982).

for Ce. The 1.2 eV peak was attributed to a stable 4f configuration for surface Ce atoms. A reasonably prominent peak at 2.6 eV binding energy was assigned to Ce 5d states because of its different resonance characteristics. At the time of this work, the peak near the Fermi level was assigned to the bulk 4f level, consonant with expectations for a valence-fluctuation material. The 1.2 eV peak assignment has been questioned recently. Calculations by Norman et al. (1985c) suggest that it is not simply a surface shift, but may arise from surface non-stoichiometry, as suggested also from additional experimental work (Schneider 1986).

A summary of the 4f contributions to the EDCs in Ce chalcogenides and pnictides is given in fig. 25, taken from the work of several authors. The pnictides all have two 4f-derived peaks separated by about 2.6 eV with the peak nearer the Fermi level increasing slightly in binding energy as the atomic number of the anion and the lattice parameter increase. The data also show that the 4f peak at lower binding energy decreases in strength as the atomic number of the anion increases, as in fig. 24. The chalcogenides all have 4f peaks near 2.5 eV binding energy. They exhibit weak structures at about 0.5 eV binding energy which show resonance enhancement which has been attributed by Gudat et al. to resonantly enhanced 5d emission. All the structures in both series overlap structures from the valence electrons from the other type of atoms, as well as from Ce 5d and 6s, p electrons.

Norman et al. (1984, 1985c) reinterpreted the double-peaked 4f structure in the Ce pnictides, except CeN, using a model and calculational methods discussed for Ce in section 4. They argued that the peak near the Fermi level is caused by a 4f photohole screened by 4f electrons and the deeper 4f peak by 4f holes poorly screened by Ce 5d or ligand electrons. The relative strengths of the peaks and their relative positions, as well as the structures in the valence bands based on the pnictide p states, were described well by the calculation. For these systems, it was concluded that the more itinerant the 4f electron, the stronger the peak near the Fermi level and the weaker the 4f peak at greater binding energy. The most itinerant 4f states occur in CeN and the least in CeBi. For CeN, the experimental

photoelectron spectra show a very different valence band from those of CeP and CeSb. The valence band is wider and the hybridization of the 4f and pnictide valence band states is much stronger in CeN. The 4f hole is less localized in both energy and space and does not give rise to a prominent peak 2 eV below the Fermi energy. Instead, the fully-screened peak just below the Fermi level is dominant in the 4f component of the spectrum.

Wuilloud et al. (1985) and Schneider et al. (1985) fitted their XPS and BIS spectra for CeN with the Gunnarsson–Schönhammer model, placing the bare Ce 4f level just above the elliptical N 2p valence band and at the bottom of an elliptical Ce 5d conduction band. The resultant hybridization parameter with both bands was relatively large, but the actual hybridization with the valence band was small, due to the relative placements of the unhybridized states. Hybridization with the Ce 5d band was larger, and this accounts for the large hybridization effects in CeN. The best fit of the Gunnarsson–Schönhammer model seemed incompatible with valence fluctuation behavior because the $4f^0$–$4f^1$ energy difference was about 1 eV, the hybridization with the conduction electrons was only about a tenth of this, and the mixing of the two configurations was weak. Baer et al. (1986) discussed new high-resolution UPS spectra for CeN in this context (Patthey et al. 1987b). In their fit of the new data to the Gunnarsson–Schönhammer model they included spin-orbit splitting. They found a localized 4f population of 0.82. This led to a rather large, but narrow, peak at the Fermi level, indicative of a metallic band. Significantly, states in this band were correlated electronic states, not those of a simple metallic band.

Sakai et al. (1985) calculated a band structure for CeSb which had a single 4f-derived peak in the density of states 2.34 eV below E_F. The self-energy correction, which included d–f Coulomb interactions and hybridization, caused a peak in the spectral density near the Fermi energy which arose from 4f states on Ce. The authors tentatively identified this spectral density feature with the observed structure near E_F.

Sakai et al. (1984, 1985) and Takeshige et al. (1985) used the previously calculated band structures for the Ce pnictides and added p–f hybridization, d–f hybridization, and d–f Coulomb interactions, keeping the Ce site 4f occupancy zero or unity (see also Kasuya et al. 1985). The d–f Coulomb interactions reduced the magnitude of the hybridization, which was the principal cause for the screening of the 4f photohole, and broadened the two peaks. Their results are shown in fig. 26, where the position of the bare f level was adjusted to give the right intensity ratio of the two 4f-derived peaks. They also carried out calculations on γ- and α-Ce with comparable agreement with experiment. In all cases their peaks were narrower than experimental peaks, although Auger lifetime broadening of the deeper peak will account for some of this. Fujimori (1983a,b, 1985) and Fujimori and Weaver (1985a,b) used a simpler version of a hybridization model to describe the Ce pnictide photoemission spectra.

5.3. *Compounds of Ce with transition and noble metals*

The 4f electrons for the intermetallic alloys of Ce have often been elusive in

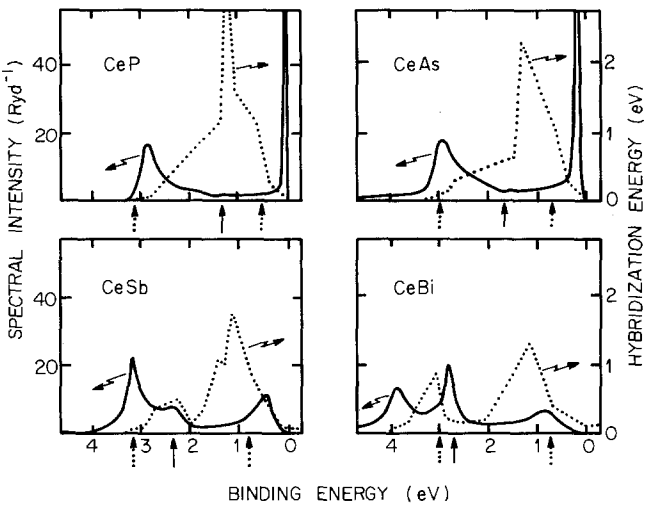

Fig. 26. Calculated 4f contribution and the energy dependent hybridization matrix element between Ce 4f and chalcogen p states for Ce chalcogenides. The 4f contribution is labeled spectral density and the matrix element is drawn dotted. (After Takeshige et al. 1985.)

photoemission because of the competing (overlapping) emission from states derived from the other metals. When these are transition metals, the 4f emission is dominated by the large number of d electrons with large photoionization cross sections.

$CePd_3$ is a mixed-valent intermetallic compound. Transport and neutron scattering measurements have characterized it as having a Kondo energy of 20 meV, close to the 17 meV ascribed to γ-Ce. XPS studies of $CePd_3$ did not show a spectral feature that could unambiguously be assigned to Ce 4f electrons, although accompanying BIS measurements suggested that there was some Ce 4f character near the Fermi energy (Baer et al. 1981). Resonance photoemission data by Allen et al. (1981b) showed a broad 4f-derived peak at a binding energy of about 0.9 eV. Allen et al. (1981b) subsequently reexamined $CePd_3$ but with similar results, namely a 4f-derived peak at 0.7–1.0 eV binding energy.

Peterman et al. (1982) made an extensive study of $CePd_3$, comparing results for $CePd_3$ to $LaPd_3$, $Ce(Ag_{0.3}Pd_{0.7})_3$, and $CeRh_3$. All of these compounds, except $CePd_3$, were believed to be integral valent with a trivalent lanthanide for all except $CeRh_3$. ($CeRh_3$ had been assigned a tetravalent Ce ion.) Comparison with $CeRh_3$ and $CePd_3$ calculations (Peterman et al. 1983) are much more important than these and led to different conclusions. Resonance photoemission indicated broad 4f-derived peaks in the EDCs near the Fermi energy in $CeRh_3$, $CePd_3$, and $Ce(Ag_{0.3}Pd_{0.7})_3$, the width being greater than that observed for many other Ce-based compounds. Comparison of the spectra of $LaPd_3$ and $CePd_3$ made the identification of the 4f contribution more certain, as shown in fig. 27. (A single, broad 4f peak at 0.9 eV binding was obtained again in a later resonance photoemission study by Peterman et al. 1983.) In the region of the Ce $4d \rightarrow 4f$

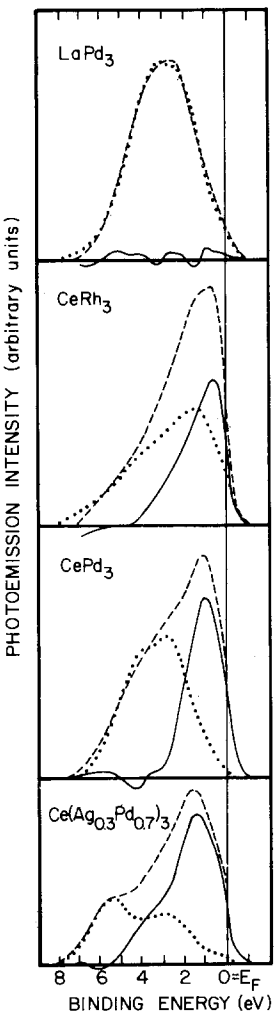

Fig. 27. Photoemission spectra for $CeRh_3$, $CePd_3$, and $Ce(Ag_{0.3}Pd_{0.7})_3$ taken on resonance (dashed) and off resonance (dotted). Their difference (solid) highlights the 4f contribution. The upper panel shows the corresponding spectra for $LaPd_3$ and demonstrates that the Pd 4d contributions have been adequately removed from the difference spectrum for the Ce compounds. (After Peterman et al. 1982.)

resonance, the Pd 4d photoexcitation cross section was very small because of the 4d Cooper minimum, and the Ce 4f could be most easily identified. Photoyield measurements showed fine structure indicative of trivalent Ce in the region below the $4d \rightarrow 4f$ resonance in $CePd_3$, in alloys of $CePd_3$ with Ag, and in $CeRh_3$. 1983 work by Peterman et al. concluded that there was no evidence for tetravalent $CeRh_3$. The conclusions from this work are that estimates of the valence from bulk measurements (such as lattice constants) can be in error, as in the case of $CeRh_3$, and that $CePd_3$ shows only a single 4f peak, a peak that is very broad when compared to that in either phase of Ce metal. This probably resutls from extensive 4f hybridization with valence electrons.

An interesting XPS study of $CePd_3$ containing up to one-half boron atom per formula unit was carried out by Wuilloud et al. (1984) along with BIS and electron

energy loss measurements. Adding boron to $CePd_3$ was believed to change the valence of Ce from mixed valent to nearly trivalent at $CePd_3B_{0.5}$. This study showed two peaks that were assigned to the Ce 4f electron in pure $CePd_3$, one near the Fermi energy and one at 1.3 eV binding energy. As boron was added, the lattice parameter increased and boron valence electrons were added. Both peaks ascribed to Ce 4f electrons were observed to broaden, and the rest of the valence band region, due to Pd 4d and B 2s states, changed shape. BIS measurements showed a loss in 4f character as the boron concentration increased. The BIS and core level XPS spectra were fitted with the model of Gunnarsson and Schönhammer. (BIS was not discussed in section 4, but is described in Gunnarsson and Schönhammer 1983b.) This fit showed that the 4f character decreased as boron was added, falling to zero at 0.5 B per formula unit. The hybridization between 4f and conduction electrons was 150 meV for all the samples, independent of boron concentration. Wuilloud et al. were also able to show that changes in the 4f occupation number correlated with the non-linear increase in lattice parameter as boron was added.

$LaPd_3$, $CePd_3$, $PrPd_3$, and $NdPd_3$ were studied by Parks et al. (1984a,b, 1985). (Pr and Nd exhibit stable $4f^2$ and $4f^3$ states, respectively.) Resonance photoemission was used to isolate the 4f contributions to the EDCs, and all of the materials except $LaPd_3$ were reported to have two 4f-derived peaks. In Pr and Nd, the peaks were broader and at greater binding energy than in $CePd_3$. In this study $CePd_3$ was shown to have 4f-derived peaks at binding energies of 1.3 and 3.9 eV, different from the energies reported in previous work. The corresponding peaks in $PrPd_3$ were at 2.3 and 4.8 eV, and those of $NdPd_3$ were at 3.5 and 5.8 eV. Each was about 1.3 eV wide, and the deeper peak became weaker as the atomic number of the rare earth increased. The peak near E_F was clearly not tied to the Fermi level but moved to higher binding energy along with the other peak as the atomic number increased. The separation between them remained roughly constant. (This depends on the analysis of line shapes, and has been questioned by Allen et al. 1986.) With increasing atomic number, the 4f level binding energy increased and the average radius of the wave function decreases, resulting in diminished hybridization. Parks et al. suggested that the screening model of Liu and Ho was appropriate since the Gunnarsson–Schönhammer model had not been applied to magnetic systems like Pr and Nd at that time. The diminished hybridization led to poorer screening of the 4f hole by 4f electrons since they come from the 4f component of valence electrons. This correlated with the observed decrease in relative strength of the peak nearer the Fermi energy as the atomic number of the lanthanide increased. The reported constant separation of the two peaks was evidence of the expected constant difference in energy for the two screening states.

$CeH_{2.1}$, $CeH_{2.4}$, $CeAl_2$, $CePd_3$, and $CeRu_2$ were studied by Peterman et al. (1983). Resonance photoemission was used to identify 4f features in the EDCs and photoyield spectroscopy was used to examine the multiplet fine structure associated with the Ce 4d core excitation. In addition, valence band photoemission spectra of $CeRu_2$ and $CeRh_3$ were compared with band structure results and with photoemission spectra from the analogous La-based compounds (noting that $LaRh_3$ and $CeRh_3$ have different structures). $CeRu_2$, which had traditionally been

considered to be tetravalent, exhibited one 4f-derived peak near the Fermi level and possibly a second one at about 2.5 eV. The conclusion drawn from this study, which included compounds spanning the entire traditional mixed valent range for Ce, was that the so-called mixed valent range in these compounds was accompanied by 4f delocalization and hybridization rather than 4f promotion.

Parks et al. (1984a,b, 1985) measured resonance photoemission spectra of $CeRu_2$, $PrRu_2$, and $NdRu_2$, as discussed earlier. Their data are shown in fig. 20. Kalkowski et al. (1985) used the same techniques on $CeIr_2$, $PrIr_2$, $NdIr_2$, $CeRh_2$, $PrRh_2$, and $NdRh_2$. Difference curves all showed two peaks which could be attributed to lanthanide 4f states. The two peaks had a constant separation of about 2.5 eV, and they moved to deeper binding energy as the atomic number of the lanthanide increased, as in the work of Parks et al. The peak nearer the Fermi energy weakened and broadened with increasing lanthanide atomic number. This peak also had a doublet structure which is not understood. It, and the 2.5 eV separation of the two peaks, may depend on the techniques used for background subtraction and peak stripping (see Allen et al. 1986).

The resonance photoemission spectra of $CeCo_2$, $CeRu_2$, and $CeIr_2$ were obtained by Allen et al. (1982a, 1983). All three compounds appeared to be tetravalent Ce systems with a collapsed volume. $CeRu_2$ was observed to have a 4f-derived peak at 2.5 eV and a stronger peak nearer the Fermi energy, originally assigned to 5d emission (Allen et al. 1981a, 1983) but later assigned to 4f emission on the basis of BIS measurements. $CeIr_2$ and $CeCo_2$ both resembled $CeRu_2$.

Schneider et al. (1985) measured the XPS and BIS spectra of $CeCo_2$ and used the Gunnarsson–Schönhammer model to fit them. The spectra include a contribution from the Co 3d electrons that the model does not treat adequately, but the principal features are described well. Both the hybridization parameter and its effect on the mixing are quite large. The calculated results are similar to those of α-Ce, not γ-Ce, in agreement with the collapsed volume nature of $CeCo_2$.

Sampathkumaran et al. (1985a,b) carried out valence band photoemission, resonance photoemission, and L_{III} absorption edge measurements on $LaRh_3B_2$, $CeRh_3B_2$, and $PrRh_3B_2$. These hexagonal materials had unusual magnetic properties in that the Ce-based compound ordered ferromagnetically, even though Ce was believed to be in a mixed valent state, while $PrRh_3B_2$ had a larger moment on the Pr ion and ordered ferromagnetically at a lower temperature. The valence band photoemission results showed that the Rh 4d band had a low density of states at the Fermi level, and the L_{III} edge measurements showed that Ce was trivalent. This helped explain the magnetic properties as arising from moments due to the 4f electrons on the lanthanide ions themselves. Resonance photoemission again showed two 4f-derived peaks, with the pair lying at greater binding energy in $PrRh_3B_2$ than in $CeRh_3B_2$ and with a relatively weaker intensity on the lanthanide tripalladides, as in the work of Parks et al. Sampathkumaran et al. suggested that the 4f hybridization with Rh 4d states was larger in $CeRh_4B_2$ than in similar compounds based on other lanthanides and this could explain why it has the highest Curie temperature.

Maple et al., (1985) performed a resonance photoemission study of $CeRh_3B_2$ and

$CeRu_3B_2$. The two 4f-derived peaks in $CeRh_3B_2$ were at the same energy as in the measurements of Sampathkumaran et al. but the relative intensities differed, probably because Maple et al. corrected for inelastically scattered electrons while Sampathkumaran et al. did not. $CeRu_3B_2$ also showed two 4f-derived peaks which were located nearer the Fermi energy than in the Rh-based compound and had relative intensities indicative of more Ce–Ru 4f–4d hybridization than Ce–Rh 4f–4d hybridization. Maple et al. argued that as the strength of the Ce 4f-derived peak near the Fermi level increased, magnetism would be suppressed, in contrast with Sampathkumaran et al. Unfortunately, Sampathkumaran et al. varied the hybridization by changing the lanthanide, while Maple et al. varied the transition metal.

Ce compounds with transition metal silicides also exhibit mixed behavior. Parks et al. (1983) studied $CeCu_2Si_2$, $CeAg_2Si_2$, $CeAu_2Si_2$, and $CePd_2Si$ by valence band and resonance photoemission. $CeCu_2Si_2$, is a Kondo system exhibiting heavy fermion behavior (see section 5.9) and is superconducting at low temperature. $CePd_2Si_2$ is also a Kondo system but it orders antiferromagnetically at low temperature. The other two compounds also order magnetically at low temperature, but they do not show Kondo behavior at higher temperature. The valence band EDCs showed features from the transition metal d electrons, with pronounced structure at the Fermi level for $CePd_2Si_2$. This structure arose from the Pd 4d states, as shown by similar measurements of $LaPd_2Si_2$. Resonance photoemission highlighted the Ce 4f-derived peaks at $\sim$2 eV and near the Fermi energy. These peaks changed position and relative strengths, ranging from 2.2 eV in $CePd_2Si_2$ to 2.6 eV in $CeAg_2Si_2$, with the 2 eV peak always the more intense but with a peak near the Fermi level which grew in relative strength as the other metal varied from Ag to Cu to Au to Pd. (This peak also varied from 0.25 to 0.6 eV in binding energy.) The authors suggested that the differences in the peak near E_F, which they assigned to 4f emission, resulted from differences in hybridization with the metal d states. Sampathkumaran et al. (1985c) studied $CeFe_2Si_2$, $CeCo_2Si_2$, and $CeNi_2Si_2$, which are mixed valent members of the same series of compounds. Difference spectra taken on and off resonance showed two 4f-derived peaks (2.4–2.6 and 0.5 eV), with relative intensities which depended on the transition metal. The intensity variations were attributed to differences in hybridization between Ce 4f and transition metal 3d electrons.

5.4. *Ce aluminides*

$CeAl_2$ is trivalent, orders magnetically at low temperatures, and is Kondo-like at higher temperatures. It has a collapsed-volume phase at higher pressures similar to that of α-Ce. Several photoemission studies of $CeAl_2$ have been reported.

The first photoemission studies used resonance photoemission to show a single Ce 4f-derived peak at 2.8 eV binding energy (Allen et al. 1981a,b). Simultaneously, Croft et al. (1981b) considered $CeAl_2$ and $LaAl_2$. They showed the Ce 4f peak to be at 2.55 eV binding energy with a full width at half maximum of 1.1 eV. Comparison with $LaAl_2$ showed that the valence bands of the two materials were nearly

identical, and they concluded that the 4f state did not hybridize significantly with the valence states in this traditionally-trivalent material. They further examined $Ce_{1-x}Sc_xAl_2$ and $Ce_{1-x}Y_xAl_2$ alloys to vary the lattice parameters by substitutional atomic replacements of up to 40% Ce. Interestingly, they found that the 4f-derived peak did not shift in energy when the lattice parameters changed. The authors argued that the large changes in the Kondo temperature brought about by the addition of Sc did not arise from the shift of the 4f level toward the Fermi level, but instead were consistent with subtle changes in 4f conduction electron hybridization. Unfortunately, this change in hybridization was too small to be directly observable in the photoelectron spectra. Note, however, that this assumed that the photoelectron spectral features were directly related to structures in the ground state.

Parks et al. (1984b, 1985) reported resonance photoemission studies of the dialuminides of La, Ce, Pr, and Nd. They found two 4f-derived peaks for $CeAl_2$ at 0.8 and 2.4 eV binding energy and two for $PrAl_2$ at 1.6 and 3.7 eV, as shown in fig. 28. Only one peak at 5.1 eV was found in $NdAl_2$. Since the peak nearer the Fermi level was considerably weaker in $PrAl_2$ than in $CeAl_2$, its absence in $NdAl_2$ was expected.

CeAl is antiferromagnetic at low temperatures and Ce is believed to be in a stable trivalent configuration. Resonance photoemission was used by Lawrence et al. (1982) to isolate the Ce 4f emission. They obtained a double-peaked difference spectrum with a larger peak at 2 eV binding energy and a weaker peak at 0.5 eV (fig. 29). They associated the deeper feature with the 4f state and attributed the weaker feature to decay via 5d emission of the 4d → 4f excitation which did not involve 4f states.

$CeAl_3$ has been described as an intermediate valence Kondo system with heavy-

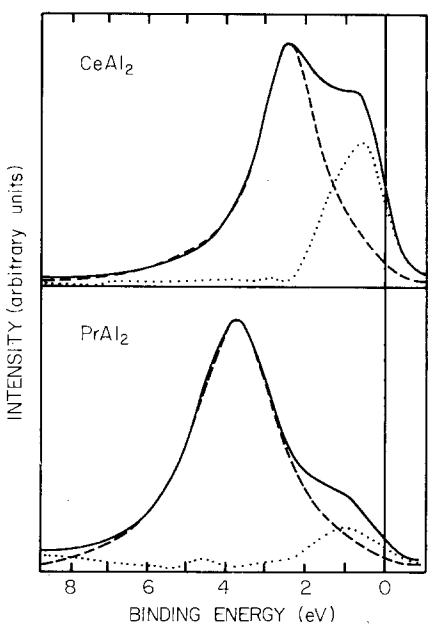

Fig. 28. On-resonance and off-resonance difference curves decomposed into two 4f contributions to the experimental spectra for $CeAl_2$ and $PrAl_2$ as in fig. 20 (Parks et al. 1985).

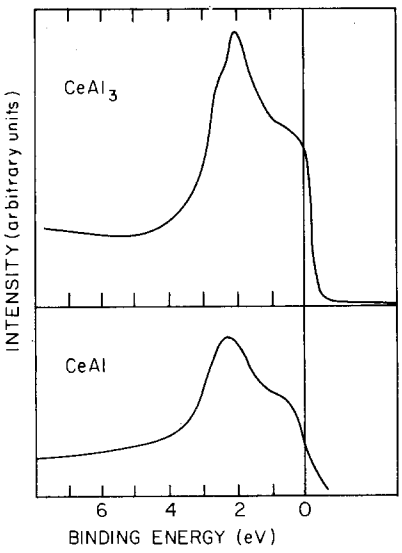

Fig. 29. On-resonance EDCs of $CeAl_3$ (Allen et al. 1982) and CeAl (Lawrence et al. 1982).

fermion behavior at low temperature (section 5.9). XPS measurements by Baer et al. (1981) and by Ott et al. (1981) showed a peak at the Fermi energy that was assigned to Ce 4f emission. Allen et al. (1982) reported resonance photoemission results obtained with a resolution of about 0.4 eV (fig. 29). They found a broad, 4f-derived peak at about 2 eV binding energy and a weaker peak at the Fermi level. They did not definitely assign the latter to the Ce 4f electrons. Higher resolution resonance photoemission measurements were carried out at low temperatures by Olson (1985) and Arko et al. (1984) to look for a narrowing of the 4f-derived peak near the Fermi level. The double-peaked structure was present, and closely resembled that of γ-Ce. The peak near E_F had a width of about 0.1 eV at 20 K but this was far wider than could be explained by the Gunnarsson–Schönhammer model for a material with a rather low Kondo temperature. At the same time, they felt that it might be possible to reconcile the experimental results and the Gunnarsson–Schönhammer theory by the inclusion of spin-orbit splitting and a more realistic band structure.

5.5. *$CeIn_3$ and $CeSn_3$*

$CeIn_3$ is a trivalent Ce compound which exhibits antiferromagnetism at low temperatures. Its photoemission spectra should thus resemble those of γ-Ce. Resonance photoemission spectra by Allen et al. (1981a,b) showed that this is the case. Indeed, for γ-Ce and $CeIn_3$ they reported peaks at 2.2 and 2.1 eV binding energy, respectively. Since the peak near the Fermi energy in γ-Ce was not identified in this relatively early work, the existence of a 4f-derived peak near the Fermi level in $CeIn_3$ is still uncertain.

$CeSn_3$ is a non-magnetic compound, and its Fermi surface indicates that the Ce 4f electrons form bands with very large effective masses. An XPS spectrum by Baer et

al. (1981) showed some intensity at the Fermi level which could be attributed to Ce 4f electrons. $CeSn_3$ was studied with valence band photoemission, resonance photoemission, and partial yield measurements on samples at 20 K and 300 K by Wieliczka and Olson (1983). The partial yield spectra in the region of $4d \rightarrow 4f$ excitations showed that $CeSn_3$ is trivalent at both temperatures. The EDCs showed two peaks at both temperatures, similar to those in metallic Ce and numerous compounds, in contrast to de Haas–van Alphen measurements which showed that this material exhibits a Ce 4f-based band at low temperatures. The observation of 4f-band characteristics in this material is not easily reconciled with the models used to describe 4f photoemission, except those of Norman et al. (1984, 1985a,b) and of Mackintosh (1985).

5.6. *$CeSi_2$*

$CeSi_2$ is a valence fluctuation compound. Valence band and resonance photoemission spectra were obtained by Lawrence et al. (1982), and the valence band spectra compared with those of $LaSi_2$. A 4f-derived peak was found at 2.5 eV binding energy. A peak at about 0.5 eV binding energy that appeared in resonance photoemission was ascribed to resonant emission of Ce 5d electrons, as for $CeAl_2$ reported in the same paper, but it was weaker in $CeSi_2$. CIS and CFS spectra in the region of Ce 4f excitation showed Ce to be trivalent. Weaver (1986) also undertook synchrotron radiation photoemission studies of $CeSi_2$, finding a sharp structure at the Fermi level and a deeper structure at 2.4 eV. Both features exhibited strong enhancement in resonance photoemission. Valence band studies at 20–30 eV showed that both were also clearly evident at low energy, despite the fact that the 4f cross section should be very low at these energies. Systematics of p–d bonding observed for other metal silicides (Weaver et al. 1984) did not provide compelling reason to associate these features with normal valence band structures.

Wuilloud et al. (1985) reported XPS and BIS measurements of $CeSi_2$ which showed a peak at the Fermi level that they assigned to Ce 4f emission. They argued that these states did not overlap significantly with the Si-derived valence band states in the spectrum. These authors used the Gunnarsson–Schönhammer model to fit their BIS and XPS spectrum, adjusting the location of the bare 4f state in the elliptical valence band.

Allen et al. (1986) recently presented new valence and 3d electron photoemission and BIS data for $CeSi_2$, $CeOs_2$, $CePd_3$, $CeCo_2$, and $CeNi_5$. They analyzed these data with the Gunnarsson–Schönhammer model, also reanalyzing existing data for $CeRu_2$, $CeNi_2$, $CeIr_2$, and CeAl. All these data can be fit in á consistent way with the model. The interpretation of some of the older data differs from that reported earlier, as summarized earlier in this chapter, but the systematic variations of the spectra of these compounds are now consistent with the variations of their other physical properties. Figure 30 shows the 4f photoelectron spectra of many of these compounds, arranged in order of increasing 4f valence electron hybridization. It is clear that as the hybridization increases, (more α-Ce-like) the peak near the Fermi level increases in relative strength.

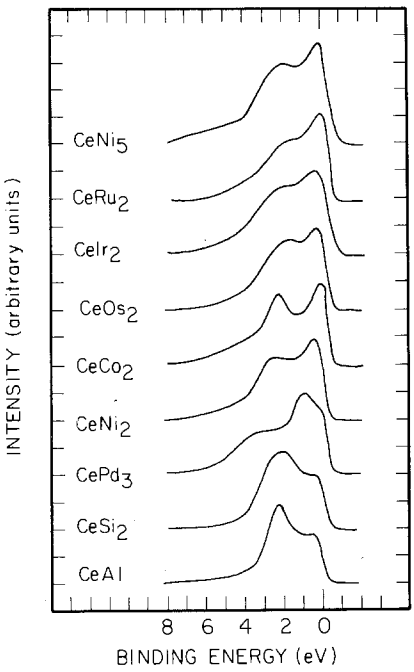

Fig. 30. 4f contribution to the photoelectron spectra of a series of Ce-based compounds. All these spectra were taken on the same instrument and the background of scattered electrons subtracted in the same fashion. These spectra are the difference between on-resonance and off-resonance spectra. They are ordered by increasing amount of 4f-valence electron hybridization from the bottom to the top (more γ-Ce-like to more α-like). (After Allen et al. 1986.)

5.7. *$CeCu_2$ and $CeCu_6$*

Soda et al. (1985) used resonance photoemission to study the Ce 4f states of $CeCu_2$ and $CeCu_6$, both of which are considered heavy fermion systems. In that work, they used resonance spectra to locate the 4f states of Ce. In $CeCu_2$, the Ce 4f contribution was reported at 2.0 eV binding energy, with a long tail to larger binding energy. There was also a weaker peak near the Fermi level. In $CeCu_6$, the Ce 4f emission appeared to contribute a peak at 2 eV, but this overlapped the broad Cu 3d-derived structure, the latter exhibiting a maximum at 4 eV. The authors argued that there was significant hybridization of the Ce 4f states with Cu 3d states, as all spectral features were resonantly enhanced. There was also evidence of a shoulder in $CeCu_6$ at about 0.5 eV which was not related to Cu emission. Despite this shoulder, the authors concluded that the double-peaked Ce 4f structure was absent in both compounds.

Olson et al. (1985) also used resonance photoemission to study $CeCu_6$. They reported structure at 1.75 eV and a weak peak at 0.5 eV, as shown in fig. 31. It may be that the reason that Olson et al. and Soda et al. observed different features can be attributed to the use of slightly different photon energies, to different normalization schemes, or to physical differences in the resonant decay processes after $4d \rightarrow 4f$ photoexcitation. In any case, the structure in $CeCu_6$ at 0.5 eV is very weak compared to that at 1.75 eV, and these authors were also reluctant to associate it with 4f emission.

More recently, Soda et al. (1986) (with communication by Ishii (1986)) repeated

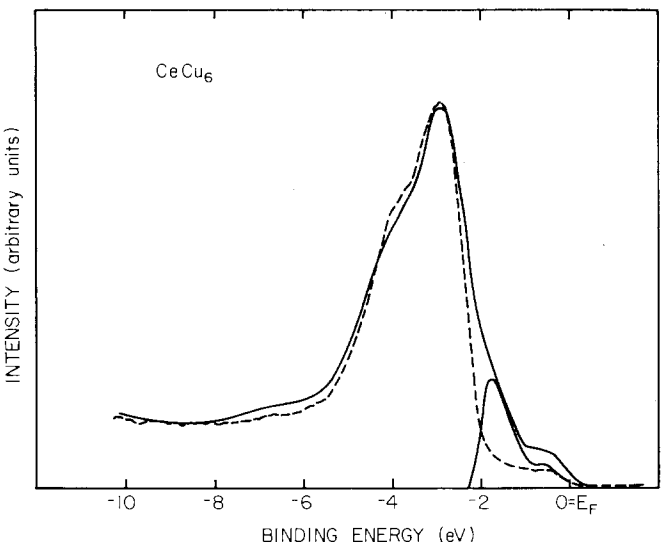

Fig. 31. On-resonance (solid) and off-resonance (dashed) EDCs for $CeCu_6$. The difference curve is shown within about 2 eV of E_F. (After Alson and Arko 1985.)

their measurements on $CeCu_6$ and on alloys $Ce_xLa_{1-x}Cu_6$. Their results on $CeCu_6$ resemble those of fig. 31. They used lower resolution, ~0.6 eV, but more careful and extensive spectrometer calibrations and background subtractions. They found a 4f-derived peak at 2.3 eV with a shoulder at 0.5 eV and another around 4 eV. The peak at lower binding energy, ~0.5 eV, was far weaker than that in the other heavy fermion systems, $CeAl_2$ and $CeCu_2Si_2$ (see section 5.9). The results for the alloys are interesting in that the entire difference curves (on-resonance minus off-resonance) decrease as x decreases from 1 to 0. Their difference curves extend to 8 eV binding energy and the structure between 2 and 4 eV also vanishes, demonstrating that considerable Ce 4f and Cu 3d hybridization occurs in this energy range. More recent higher resolution data (Patthey et al. 1987a) are shown in fig. 32. These will be discussed further in section 5.9.

5.8. *Cerium hydrides*

The hydrides of Ce, CeH_x, offer an interesting opportunity to vary the electronic distribution of the non-4f-derived states near the Fermi level. As discussed in detail by Peterman et al. (1981) (and references therein), there are changes in the Ce-derived s, p, d states due to increased hybridization with hydrogen. Hydrogen is absorbed into the fcc lattice and forms a stable CaF_2-structured hydride. At low hydrogen composition, $x \cong 2$, hydrogen occupies tetrahedral sites while at higher composition the octahedral sites are occupied as well. The hydrides with composition near CeH_2 are metallic while those close to $CeH_{2.9}$ are semiconducting. The transition from metallic to semiconducting results from the mixing of metal and hydrogen states and the lowering in energy of the new bonding states.

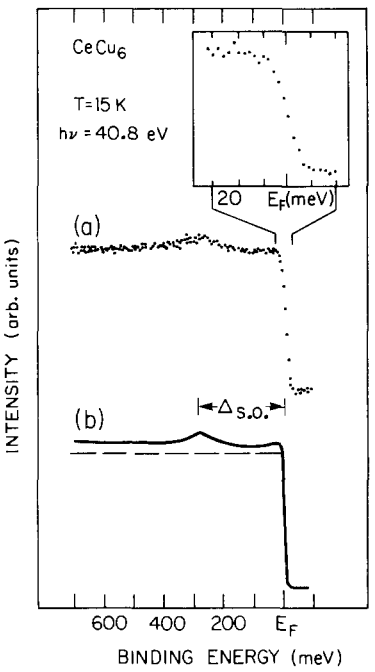

Fig. 32. High-resolution EDC of $CeCu_6$ near the Fermi energy. (a) experimental spectrum measured with a resolution of 20 meV. (b) Simulation of the spectrum using the Gunnarsson–Schönhammer model with spin-orbit splitting and a constant background (dashed) of valence states. The inset shows the Fermi edge measured with a resolution of 12 meV. (After Patthey et al. 1986b.)

Experimentally, it is now well-known that a strong bonding band due to these hybrid states is centered about 5.5 eV below the Fermi level for the dihydrides of the group III and group IV metals, including Ce (Weaver et al. 1979, 1981, Peterman et al. 1980, 1981).

Peterman et al. (1983) reported synchrotron radiation photoemission studies of cerium hydrides as part of their extensive study of metal–hydrogen systems. They showed that both $CeH_{2.1}$ and $CeH_{2.4}$ had a single 4f-derived peak at 2.0 eV and dominant hydrogen induced states centered at 5.5 eV binding energy. XPS measurements by Schlapbach and Osterwalder (1982) also showed this single 4f-derived peak in the EDC at 2 eV for both $CeH_{2.1}$ and $Ce_{2.9}$. The valence band density of states at the Fermi level in $CeH_{2.1}$ was reduced from that of γ-Ce and was zero in $CeH_{2.9}$, as discussed earlier by Peterman et al. (1981) for LaH_x. Fujimori and Tsuda (1982) performed XPS and valence band photoemission studies and found the 4f peak at 2 eV for $CeH_{2.45}$. Hydrides of La, Ce, and Pr were examined by Osterwalder (1985) using valence band photoemission and BIS. The single 4f peak was again observed at 2.0 eV for $CeH_{2.1}$ and $CeH_{2.95}$. In each of these systems, there appeared to be minimal interaction of the 4f with valence band states, as demonstrated by the insensitivity of the results to the modifications of the states near E_F. Likewise, the 4f emission was prominent in each case, showing no change in energy or full width.

5.9. *Heavy fermion systems*

A number of intermetallic compounds containing cerium or uranium are heavy-fermion systems (Stewart 1984, Fisk et al. 1986). The name arises from several low

temperature properties, notably electronic specific heats and magnetic susceptibilities like those of nearly free electron metals but with a very large apparent electron effective mass. A band picture of such materials would have a narrow Ce 4f or U 5f band centered just above the Fermi level with approximately one electron in states below E_F. Energy band calculations show that such a band would have an effective mass of ten to fifty times the free electron mass, but this is still well below what has been observed (Boring et al. 1985, Strange and Gyorffy 1985, Wang et al. 1985, Albers et al. 1985). Apparently, many f electrons are coupled in these systems to give large effective masses. Interestingly, some heavy fermion systems are superconducting at low temperatures, others are magnetic, while others are neither superconducting nor magnetic. Heavy fermion systems may be described phenomenologically by Fermi liquid theory, but a complete microscopic picture is not yet at hand (Varma 1985, Lee et al. 1986, Brandow 1986). Indeed, there is a great deal of exciting work being done in the area of heavy fermions, and we anticipate that the next few years will see major improvements in our understanding of these challenging systems.

If we take the naive view that the large mass arises from an excitation which is highly localized in energy and we treat it as coming from a parabolic tight-binding band located just above the Fermi level, than an effective mass of 100 at the bottom of this band would require a band width of about 4 meV. Moreover, as we have seen for the 4f electrons in Ce, the response of the system to the creation of a localized photohole is responsible for most of the features in the spectrum. Since the extremely heavy mass is a low temperature phenomenon caused by the coupling of f states, and the peak in the spectral density is extremely narrow, many of the experiments under way today seek features in the electronic structure that may be prerequisites for heavy-fermion behavior. Koelling et al. (1985) have argued, for example, that f coupling via hybridization with d electrons appears to be necessary for heavy fermion behavior. At the same time, preparations are under way for ultrahigh resolution studies of these systems in the low-temperature heavy-fermion state.

Prototypical heavy fermion systems are UBe_{13} or UPt_3. Photoemission studies have associated the uranium 5f contribution with the density of states in a narrow region at the Fermi level. This indicates only that there is a large density of states at E_F in a one-electron or band picture, subject to all of the interpretational problems of the 4f levels in Ce. Hence, photoemission shows the presence of a 5f photohole screened by conduction electrons that essentially reoccupy it during the photoemission process. All other many-body effects which give rise to the heavy-fermion ground state are broken by the photoemission process. Several other uranium-based heavy-fermion systems do not show an analogous narrow 5f-derived peak at the Fermi level.

The known or suspected Ce-based heavy fermion systems are $CeCu_2Si_2$, $CeAl_3$, $CeCu_2$, and $CeCu_6$. Low temperature photoelectron spectra have been measured for $CeAl_3$ and $CeCu_6$ with a resolution of about 0.13 eV by Olson (1985) and Arko et al. (1984) (see fig. 31). In both cases, the 4f component was identified by resonance photoemission or the dependence of the cross section on photon energy. It was found to be not very different from that of γ-Ce. Parks et al. (1983, 1984a,b) studied $CeCu_2Si_2$, $CeAu_2Si_2$, $CePd_2Si_2$, UBe_{13}, and UPt_3. Resonance photoemission re-

sults showed a strong f contribution for $CeCu_2Si_2$ at 2.5 eV and a weaker feature at 1 eV. Both $CeAg_2Si_2$ and $CeAu_2Si_2$ showed similar doublets with the structure near the Fermi level being more prominent in $CeAu_2Si_2$. For $CePd_2Si_2$ there was considerable strength from the Pd 4d states near the Fermi level, and a more elaborate data analysis procedure was needed. Difference curves using resonance techniques showed the peak at 2.5eV in $CeCu_2Si_2$ shifted to 2.8eV. As Cu was replaced by Au, and Pd, this peak grew weaker and it shifted to 2.5 eV for $CePd_2Si_2$. The weaker peak at 0.5 eV grew stronger as Cu was replaced by Au and Pd but weaker if Cu was replaced by Au. The peak at 0.5 eV was over half as high as the 2.5eV peak in $CePd_2Si_2$. All studies to date of Ce-based heavy fermion systems show considerable hybridization between the Ce 4f level and valence states on neighboring atoms of other types.

Photoelectron spectra of $CeCu_6$ are shown in figs. 31 and 32. Patthey et al. (1987a) used the Gunnarsson–Schönhammer model to fit their XPS spectrum of the 3d level, their BIS spectrum, and the spectrum of fig. 32. They found very little 4f conduction electron hybridization. The bare 4f level is at 1.2 eV below E_F, and mixing with the valence band is so weak that the effective number of localized 4f electrons is at least 0.995. This leads to a Kondo energy $\delta = kT_K$ of no more than 1 meV. Such a small value predicts too small a peak to be seen at E_F with 12 meV resolution, and indeed no peak is present. The peak 280 meV below E_F arises from the $j = \frac{7}{2}$ state, which is above E_F in the ground state. It appears as an excited final state of the system. There are several remaining problems in the fitting. One is that only a single 4f site has been considered, and this will not give rise to heavy Fermion behavior. However, the temperature of the measurement was too high for such collective behavior to have occurred. The second difficulty is that the fit used was for $T = 0$, really $T \leqslant T_K$, a condition not quite satisfied in the experiment. Finally, the Gunnarsson–Schönhammer model predicts two peaks (excluding spin-orbit effects), one at E_F (too weak to see in this case) and one at a binding energy slightly greater than 1.2 eV. The weak structure at 0.5 eV in fig. 31, apparently exhibiting 4f character, is left unexplained. It is possible that a more realistic picture of the band structure and 4f conduction band coupling could account for this peak structure.

5.10. *Ce oxides and oxidation*

There have been several interesting studies of the oxidation of metallic Ce and of the oxides Ce_2O_3 and CeO_2. These have been motivated, in part, by the belief that the oxides Ce_2O_3 and CeO_2 epitomize trivalent and tetravalent Ce, respectively, based on simple chemical arguments involving charge transfer and valence. Unfortunately, it has been found that ideal, well characterized single crystals are hard to prepare in suitable form for optical or photoemission studies. Indeed, X-ray and neutron diffraction studies have shown (Bevan 1955, Brauer et al. 1960, Bevan and Kordis 1964, Ray et al. 1975, Campserveux and Gerdanian 1978, Eyring 1979) that there are intermediate phases between these two oxides (Ce_7O_{12}, Ce_9O_{16}, $Ce_{10}O_{18}$, and $Ce_{11}O_{20}$). This indicates that there is substantial covalent bonding between cerium and oxygen. Further, these compounds are not merely non-stoichiometric Ce_2O_3 or CeO_2, unless the vacancies order, because their symmetries dif-

fer. (Ce_7O_{12} is rhombohedral, while the others listed are monoclinic or triclinic.) Clearly, the existence of these Ce–O phases complicates studies of the oxidation of Ce metal itself.

We begin this section with a description of the valence band, 4f, and 4d photoelectron spectra of what is believed to be stoichiometric CeO_2. We then conclude with a review of the oxidation of metallic Ce. As we will see, all oxidation studies have been carried out on polycrystalline, evaporated films in spite of the fact that chemisorption, precursor states, and oxidation rates depend on the crystallographic plane of the surface and the presence of grain boundaries or lower-dimensional defects. There remains, therefore, a great deal of work to be done with these complex systems before they are fully understood.

Optical absorption or total electron yield measurements have been performed on Ce, oxidized Ce, and evaporated films of CeO_2 in the region of the $4d \rightarrow 4f$ transitions (Zimkina et al. 1967, Fomichev et al. 1967, Haensel et al. 1970, Suzuki et al. 1975, Zimkina and Lyakhovskaya 1976, Hanyu et al. 1985). The results showed that the structures observed in this region are sensitive to the number of 4f electrons in the ground state, as could be inferred from our earlier discussion of $4d \rightarrow 4f$ resonance absorption. The spectra for both γ- and α-Ce show that there is one 4f electron in the ground state (fig. 19). Oxidation of Ce changes this gradually and eventually a spectrum similar to that for La appears, indicating tetravalent Ce with no 4f electrons (Wieliczka 1982). More recently, Hanyu et al. (1985) reported higher resolution studies of films of evaporated CeO_2 and reconfirmed that the spectrum of evaporated CeO_2 is that of tetravelent Ce ions for the $4d \rightarrow 4f$ transitions. They noted, however, a trace of the spectrum of trivalent Ce and attributed this to partial reduction of the oxide during evaporation or to a final state effect in the absorption process.

Photoemission studies of the valence bands of the cerium oxides are few in number. Orchard and Thornton (1977) performed XPS experiments to examine the valence band electrons of Ce and many other rare earth oxides. For CeO_2, they found peaks from the 5s and 5p electrons of Ce, the 2s and 2p of O, and the 2s of C impurities, but they observed no 4f electron contribution. The O 2p levels were shown to form the valence band, but the valence band shape was not discussed.

After a calculation of the band structure of CeO_2 by Koelling et al. (1983), Wuilloud et al. (1984, 1985) re-examined the valence band of CeO_2 by XPS with higher resolution than in the previous study and by BIS, XPS, and energy loss spectroscopy of the Ce 3d level. These authors noted that electron beams cause a partial reduction of CeO_2 to Ce_2O_3, which could be prevented by simultaneous exposure to a low partial pressure of oxygen, but that no such reduction was observed during the XPS measurements. The valence band EDC has peaks at 4 and 6 eV binding energy, in good agreement with the calculated density of states. (This brief review does not do justice to the work of Wuilloud et al. since they also used BIS to examine the region above the Fermi level where the 4f state is located and XPS to examine the 4d levels.) Koelling et al. concluded that, although there was significant covalent bonding in CeO_2, it was still valid to consider the Ce ion as tetravalent. Wuilloud et al. fitted their XPS and BIS spectra to the model of Gunnarsson and Schönhammer using the position of the bare 4f level and the 4f

valence band hybridization matrix elements with valence and conduction bands as parameters. They found the 4f peak in the spectral density to be in the band gap (present in BIS but not XPS) but with some 4f character mixed into the oxygen 2p valence bands. (See also Schneider et al. 1985.)

Allen (1985a) reported XPS and BIS measurements of both CeO_2 and Ce_2O_3. CeO_2 films were measured, then reduced to Ce_2O_3 by sputtering and heating. CeO_2 had no 4f-derived peak in the XPS spectrum but one grows at about 2 eV as reduction proceeds. CIS spectra of the 4d → 4f excitation show structure characteristic of trivalent Ce in Ce_2O_3, i.e., spectra like those of figs. 7b and 8. The oxygen 2p initial state also goes through a resonance at the energy of the peak in the Ce 4d resonance, but it is weak and without fine structure. CeO_2 has a similar oxygen 2p resonance and it is stronger and shifted to slightly higher energy than the one in Ce_2O_3. It could arise from partial reduction of the CeO_2.

Lenth et al. (1978) measured resonance photoemission spectra of the insulators cerium pentaphosphate, CeP_5O_{14}, and a mixed La–Gd pentaphosphate. This study was undertaken to learn more about the resonance photoemission process itself. The valence band was composed primarily of oxygen 2p states, and there is overlap with the Ce 4f level. The latter provides a single peak at 2 eV binding energy which undergoes a very pronounced resonance as the Ce 4d → 4f threshold is crossed. By using spectral features from atoms other than Ce for normalization, they were able to show that the $4d^94f^2$ excited state of the Ce tripositive ion has a probability of decaying by 4f emission to $4d^{10}4f^0 + \varepsilon f$ that is as high as 20% in the resonance region.

The first photoelectron study of the oxidation of γ-Ce was by Helms and Spicer (1972). They examined room temperature changes in the valence bands upon oxygen exposure, using photons of energy 11.7 eV or less. Large structures grew in the region between 4 and 9 eV binding energy as the oxygen exposure increased, but there were prominent structures in this region before oxygen exposure, indicating considerable oxidation of the as-prepared samples. Oxygen exposure induced a peak at 5 eV binding energy and another in the 6.5–8 eV range, the peak position of which varied with exposure. At the same time, the contribution of metallic Ce in the 0–2 eV region vanished with increasing oxygen exposure. Plots of the height of the 5 eV peak versus oxygen exposure showed logarithmic growth, which they interpreted as the formation of an oxide layer (Ce_2O_3) with subsequent diffusion of oxygen through that layer.

Platau et al. (1977) also studied the oxidation of Ce films at room temperature, using XPS to monitor the core levels of both Ce and O and XPS and UPS to follow valence band changes. The O 1s peak grew, almost without shifting, with increasing oxygen exposure up to 2000 L. The effect of 2 L exposure was easily detectable. A small peak which they attributed to physisorbed O was also present, and the limiting binding energy shift of the O 1s level for the oxide with respect to it was 2.7 eV to lower binding energy. After about 100 L exposure the oxide film was estimated to be 7 Å thick based on relative intensites of Ce core level peaks from the oxide and the underlying metal, using the universal curve (fig. 2) for escape lengths. The growth of the oxide with increasing exposure finally saturated, indicating that a

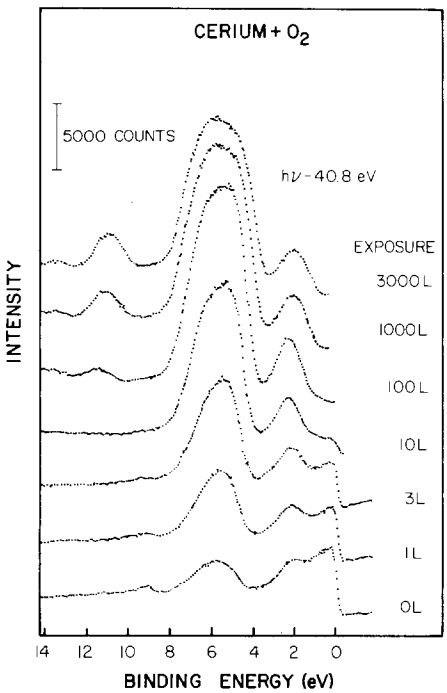

Fig. 33. EDCs of a Ce film taken at 40.8 eV as a function of oxygen exposure. 1 L corresponds to an exposure to 1×10^{-6} Torr of oxygen for 1 s (Platau and Karlsson 1978).

protective film of Ce_2O_3 had formed. Valence band spectra of the oxide were reported later by Platau and Karlsson (1978). They were similar in character to those of Helms and Spicer. These authors saw the loss of the Fermi edge of the metal as oxidation occurred, 100 L of oxygen being necessary for its complete loss, as shown in fig. 33. The structure between 4 and 8 eV is due to the valence band of the oxide and is derived primarily from 2p functions. The 11 eV peak reveals the O 2s level. The 2.4 eV peak corresponds to the Ce 4f level. This was not detected in earlier work because the photoionization cross section was too low at low photon energies. Its presence indicates that the oxide contains trivalent Ce and is probably Ce_2O_3 at the exposures shown.

Platau and Karlsson also exposed a film of oxidized Ce to 1000 L of oxygen at about 600°C. The 2 eV structure was greatly reduced. This was interpreted as the result of CeO_2 formation with a small Ce excess, i.e., the formation of oxides intermediate between Ce_2O_3 and CeO_2. They also concluded from escape length considerations that a 20 Å thick layer of Ce_2O_2 is not yet a protective layer, and oxidation continues through such a layer, in contrast to their previous estimates.

Paraline et al. (1980) and Koel et al. (1980) studied the oxidation of Ce by exposure to oxygen and water vapor, respectively. They used XPS and investigated films held at 120 K and 300 K. (At 120 K the samples were cleaned by sputtering without subsequent annealing. They may not have been the equilibrium-phase Ce and they were certainly disordered.) They studied only core levels and found no evidence for any physisorption or chemisorption of oxygen, based on an interpretation of the core level peaks different from that of Platau et al. Oxygen exposure at either

temperature produced Ce_2O_3 immediately until a thick layer was built up, after which a thin layer of CeO_2 formed (after ca. 50 L exposure). There was also evidence for OH, the result of reaction with residual water vapor in the vacuum chamber. Oxidation with water (actually D_2O) was somewhat different because Ce_2O_3 grew on the surface at 300 K, but there was no CeO_2. There was, however, a thin overlayer of OH on the oxide. At 120 K the water condensed as ice, and no oxidation took place. A thin layer of OH was found on the surface of the ice. They found that at 300 K the Ce_2O_3 layer exceeded 24 Å in thickness at only 20 L exposure to oxygen, a faster growth rate than that previously reported, but based on a different interpretation of some of the core level peaks.

Finally, Latta and Ronay (1984, 1986) and Ronay and Latta (1985) have reported remarkable effects of a thin overlayer of Ce on the oxidation of Nb. As shown by core-level XPS, Nb oxidizes slowly at low exposures to oxygen. The deposition of a few monolayers of Ce onto Nb promotes rapid oxidation of Nb at oxygen pressures for which the oxidation of Nb surfaces is negligible. They interpreted this in terms of the repeated valence change of Ce as follows. Ce_2O_3 donates both 4f electrons to an adsorbed oxygen atom. The O ion fills an oxygen vacancy in the Ce_2O_3 layer, converting it locally to CeO_2. Two electrons then tunnel from the Nb through the Nb_2O_5 layer below the Ce_2O_3 into the Ce_2O_3, converting $2CeO_2$ to Ce_2O_3 plus an oxygen ion which diffuses through the Nb_2O_5 to the Nb beneath. The rate-limiting step is diffusion of the oxygen ion for thinner Nb_2O_5 films, while for thicker films at later stages of oxidation it is electron tunneling through the Nb_2O_5.

6. Concluding remarks

In this chapter, we have considered the contributions that have been made by photoelectron spectroscopy to understanding the Ce problem. We have emphasized synchrotron radiation photoemission studies because of the advantages of that technique (section 2). We have shown that the features observed in photoemission spectra are related to the final state rather than the ground state. We have shown that very recent photoemission studies have shown that two 4f related features are observed, and we have discussed how these can be viewed based on the sophisticated models of many authors (sections 3 and 4). Finally, we reviewed the experimental situation for many Ce compounds, noting the significant progress that has been made in the last few years.

The issues relating to the Ce 4f electron are now understood, even though the answers to those issues continue to be controversial. Photoelectron spectroscopy has made major contributions to this understanding, and we can anticipate that equally impressive advances will be forthcoming in the near future.

Acknowledgments

It is a pleasure to thank C.G. Olson, D.M. Wieliczka, D.J. Peterman, A. Franciosi, A. Fujimori, S.H. Liu and K.-M. Ho for valuable interactions over several years.

Conversations with Y. Baer and W.-D. Schneider and correspondence with O. Gunnarsson and A.R. Mackintosh are gratefully acknowledged. K.A. Gschneidner, B.J. Beaudry, and O.D. McMasters were generous in both discussions and providing Ce samples for our work. D.W. Lynch was supported by the Ames Laboratory, USDOE, which is operated by Iowa State University under contract No. W-7405-eng-82. J.H. Weaver was supported by the National Science Foundation under DMR-82-16489 (Solid State Chemistry).

References

Adawi, I., 1964, Phys. Rev. **134**, A788.
Albers, R.C., A.M. Boring, P. Weinbergen and N.E. Christensen, 1985, Phys. Rev. B **32**, 7646.
Allen, J.W., 1985a, J. Magn. & Magn. Mater. **47&48**, 168.
Allen, J.W., 1985b, J. Magn. & Magn. Mater. **52**, 135.
Allen, J.W., and R.M. Martin, 1982, Phys. Rev. Lett. **49**, 1106.
Allen, J.W., S.-J. Oh, J. Lawrence, I. Lindau, L.I. Johansson and S.B. Hagström, 1981a, in:Valence Fluctuations in Solids, eds L.M. Falicov, W. Hanke and M.B. Maple (North-Holland, Amsterdam) p. 431.
Allen, J.W., S.-J. Oh, I. Lindau, J.M. Lawrence, L.I. Johansson and S.B.M. Hagström, 1981b, Phys. Rev. Lett. **46**, 110.
Allen, J.W., S.-J. Oh, I. Lindau, M.B. Maple, J.F. Suassuna and S.B. Hagström, 1982, Phys. Rev. B **26**, 445.
Allen, J.W., S.-J. Oh, M.B. Maple and M.S. Torikachvili, 1983, Phys. Rev. B **28**, 5347.
Allen, J.W., S.-J. Oh, O. Gunnarsson, K. Schönhammer, M.B. Maple, M.S. Torikachvili and I. Lindau, 1986, Adv. Phys. **35**, 275.
Ambladh, C.-O., 1985, Phys. Scr. **32**, 341.
Arko, A.J., C.G. Olson, D.M. Wieliczka, Z. Fisk and J.L. Smith, 1984, Phys. Rev. Lett. **53**, 2050.
Ashcroft, N.W., 1978, in: Photoemission and the Electronic Properties of Surfaces, eds B. Feuerbacher, B. Fitton and R.F. Willis (Wiley, New York).
Baer, Y., 1984, in: Handbook of the Physics and Chemistry of the Actinides, eds A.J. Freeman and G.H. Lander (North-Holland, Amsterdam) p. 271.
Baer, Y., and G. Busch, 1973, Phys. Rev. Lett. **31**, 35.
Baer, Y., and G. Busch, 1974, J. Electron Spectrosc. & Relat. Phenom. **5**, 611.
Baer, Y., and C. Zürcher, 1977, Phys. Rev. Lett. **39**, 596.
Baer, Y., B. Hauger, C. Zürcher, M. Campagna and G.K. Wertheim, 1978, Phys. Rev. B **18**, 4433.
Baer, Y., H.R. Ott, J.C. Fuggle and L.E. De Long, 1981, Phys. Rev. B **24**, 5384.
Baer, Y., F. Patthey, W.-D. Schneider and B. Delley, 1987, J. Magn. & Magn. Mater. **63&64**, 503.
Bardyszewski, W., and L. Heden, 1985, Phys. Scr. **32**, 439.
Benbow, R.L., and N.V. Smith, 1983, Phys. Rev. B **27**, 3144.
Berglund, C.N., and W.E. Spicer, 1964a, Phys. Rev. **136**, A1030.
Berglund, C.N., and W.E. Spicer, 1964b, Phys. Rev. **136**, A1044.
Bevan, D.J.M., 1955, J. Inorg. Nucl. Chem. **1**, 49.
Bevan, D.J.M., and J. Kordis, 1964, J. Inorg. Nucl. Chem. **26**, 1509.
Bianconi, A., L. Incoccia and S. Stipcich, eds, 1985, EXAFS and near edge structure, Springer Series in Chemical Physics, Vol. 27 (Springer-Verlag, Berlin).
Bickers, N.E., D.L. Cox and J.W. Wilkins, 1985, Phys. Rev. Lett. **54**, 230.
Boring, A.M., R.C. Albers, F.M. Mueller and D.D. Koelling, 1985, Physica B **130**, 171.
Borstel, G., 1985, Appl. Phys. A **38**, 193.
Brandow, B.H., 1986, Phys. Rev. B **33**, 215.
Brandt, N.B., and V.V. Moschalkov, 1984, Adv. Phys. **33**, 373.
Brauer, G., and K.A. Gingerich, 1960, J. Inorg. Nucl. Chem. **16**, 87.
Brauer, G., K.A. Gingerich and U. Holtschmidt, 1960, J. Inorg. Nucl. Chem. **16**, 77.
Bringer, A., 1983, Solid State Commun. **46**, 591.
Campagna, M., G.K. Wertheim and Y. Baer, 1979, in: Photoemission in Solids II, Case Studies, eds L. Ley and M. Cardona (Springer-Verlag, Berlin) p. 217.
Campserveux, J., and P. Gerdanian, 1978, J. Solid State Chem. **23**, 73.
Cardona, M., and L. Ley, eds, 1978, Photoemission in Solids, Vol. 1 (Springer-Verlag, Berlin).
Carlson, T.A., 1975, Photoelectron and Auger Spectroscopy (Plenum Press, New York).
Carlson, T.A., and M.O. Krause, 1965, Phys. Rev. **140**, A1057.
Caroli, C., D. Lederer-Rosenblatt, B. Roulet and D. St. James, 1975, Phys. Rev. B **8**, 4552.
Citrin, P.H., and G.K. Wertheim, 1983, Phys. Rev. B **27**, 3176.
Citrin, P.H., G.K. Wertheim and Y. Baer, 1978,

Phys. Rev. Lett. **41**, 1425.
Citrin, P.H., G.K. Wertheim and Y. Baer, 1983, Phys. Rev. B **27**, 3160.
Coleman, P., 1984, Phys. Rev. B **29**, 3035.
Connerade, J.P., 1978, Contemp. Phys. **19**, 415.
Connerade, J.P., 1983, J. Less-Common Met. **93**, 171.
Cooper, J.W., 1975, Photoionization of inner-shell electrons, in: Atomic Inner-Shell Processes, Vol. I, ed. B. Crasemann (Academic Press, New York).
Crecelius, G., G.K. Wertheim and N.D.E. Buchanan, 1978, Phys. Rev. B **18**, 6519.
Croft, M., A. Franciosi, J.H. Weaver and A. Jayaraman, 1981a, Phys. Rev. B **24**, 544.
Croft, M., J.H. Weaver, D.J. Peterman and A. Franciosi, 1981b, Phys. Rev. Lett. **46**, 1104.
Davis, L.C., and L.A. Feldkamp, 1979, J. Appl. Phys. **50**, 1944.
Davis, L.C., and L.A. Feldkamp, 1980a, Phys. Rev. B **22**, 3644.
Davis, L.C., and L.A. Feldkamp, 1980b, Phys. Rev. B **22**, 4994.
Dehmer, J.L., and A.F. Starace, 1972, Phys. Rev. B **5**, 1985.
Dehmer, J.L., A.F. Starace, U. Fano, J. Sugar and J.W. Cooper, 1971, Phys. Rev. Lett. **26**, 1521.
Eastman, D.E., 1972, Photoemission spectroscopy of metals, in: Techniques of Metal Research, Vol. VI, ed. E. Passaglia, part 1, p. 411.
Eastman, D.E., and M. Kuznietz, 1971, Phys. Rev. Lett. **26**, 846.
Eckhardt, H., and L. Fritsche, 1986, J. Phys. F **16**, 1731.
Eyring, L., 1979, in: Handbook on the Physics and Chemistry of Rare Earths, Vol. 3, eds K.A. Gschneidner Jr and L. Eyring (North-Holland, Amsterdam) p. 337.
Falicov, L.M., and J.C. Kimball, 1969, Phys. Rev. Lett. **22**, 997.
Fano, U., and J.W. Cooper, 1968, Rev. Mod. Phys. **40**, 441 (addendum in Rev. Mod. Phys. **41**, 724 (1969)).
Feibelman, P.J., and D.E. Eastman, 1974, Phys. Rev. B **10**, 4932.
Feuerbacher, B., B. Fitton and R.F. Willis, eds, 1978, Photoemission and the Electronic Properties of Surfaces (Wiley, New York).
Fisk, Z., H.R. Ott, T.M. Rice and J.L. Smith, 1986, Nature **320**, 124.
Flahaut, J., 1979, in: Handbook of the Physics and Chemistry of Rare Earths, Vol. 4, eds K.A. Gschneidner Jr and L. Eyring (North-Holland, Amsterdam) p. 1.
Fomichev, V.A., T.M. Zimkina, S.A. Grobovski and I.I. Zhukova, 1967, Sov. Phys.-Solid State **9**, 1163.
Fowler, R.H., 1931, Phys. Rev. B **38**, 45.
Franciosi, A., J.H. Weaver, N. Mårtensson and M. Croft, 1981, Phys. Rev. B **24**, 3651.
Fuggle, J.C., 1983, J. Less-Common Met. **93**, 159.
Fuggle, J.C., M. Campagna, Z. Zolnierek, R. Lässer and A. Platau, 1980, Phys. Rev. Lett. **45**, 1597.
Fuggle, J.C., U. Hillebrecht, J.-M. Esteva, R.C. Karnatak, O. Gunnarsson and K. Schönhammer, 1983a, Phys. Rev. B **27**, 4637.
Fuggle, J.C., F.U. Hillebrecht, Z. Zolnierek, R. Lässer, C. Freiburg, O. Gunnarsson and K. Schönhammer, 1983b, Phys. Rev. B **27**, 7330.
Fujimori, A., 1983a, Phys. Rev. B **27**, 3992.
Fujimori, A., 1983b, Phys. Rev. B **28**, 4489.
Fujimori, A., 1985, J. Magn. & Magn. Mater. **47&48**, 243.
Fujimori, A., and N. Tsuda, 1982, Phys. Status Solidi b **114**, K139.
Fujimori, A., and J.H. Weaver, 1985a, Phys. Rev. B **32**, 2422.
Fujimori, A., and J.H. Weaver, 1985b, Phys. Rev. B **31**, 6345.
Fujimori, A., M. Grioni, J.J. Joyce and J.H. Weaver, 1985, Phys. Rev. B **31**, 8291.
Gerken, F., J. Barth and C. Kunz, 1982, in: Proc. Int. Conf. on X-Ray and Atomic Inner-Shell Physics, A.I.P. Conf. Proc. **44**, ed. B. Crasemann (American Institute of Physics, New York) p. 602.
Gerken, F., A.S. Flodström, J. Barth, L.I. Johansson and C. Kunz, 1985, Phys. Scr. **32**, 43.
Glötzel, D., 1978, J. Phys. F **8**, L163.
Grewe, N., 1983, Z. Phys. B **52**, 193.
Grioni, M., J.J. Joyce, S.A. Chambers, D.G. O'Neill, M. del Giudice and J.H. Weaver, 1984a, Phys. Rev. Lett. **53**, 2331.
Grioni, M., J.J. Joyce, M. del Giudice, D.G. O'Neill and J.H. Weaver, 1984b, Phys. Rev. B **30**, 7370.
Grüner, G., and A. Zawdowski, 1974, Rep. Prog. Phys. **37**, 1497.
Gudat, W., and C. Kunz, 1972, Phys. Rev. Lett. **29**, 169.
Gudat, W., M. Campagna, R. Rosei, J.H. Weaver, W. Eberhardt, F. Hulliger and E. Kaldis, 1981, J. Appl. Phys. **52**, 2123.
Gudat, W., M. Iwan, R. Pinchaux and F. Hulliger, 1982, in: Valence Instabilities, eds P. Wachter and H. Boppart (North-Holland, Amsterdam) p. 249.
Gunnarsson, O., and K. Schönhammer, 1983a, Phys. Rev. Lett. **50**, 604.
Gunnarsson, O., and K. Schönhammer, 1983b, Phys. Rev. B **28**, 4315.
Gunnarsson, O., and K. Schönhammer, 1985a, Phys. Rev. B **31**, 4815.
Gunnarsson, O., and K. Schönhammer, 1985b, J. Magn. & Magn. Mater. **52**, 141.
Gunnarsson, O., K. Schönhammer, J.C. Fuggle, F.U. Hillebrecht, J.-M. Esteva, R.C. Karnatak and B. Hillebrand, 1983, Phys. Rev. B **28**, 7330.
Haensel, R., P. Rabe and B. Sonntag, 1970, Solid State Commun. **8**, 1845.
Hanyu, T., H. Ishii, M. Yanagihara, T. Kamada, K. Naito, S. Suzuki and T. Ishii, 1985, Solid

State Commun. **56**, 381.
Hedin, L., and S. Lundqvist, 1969, Solid State Phys. **23**, 1.
Helms, C.R., and W.E. Spicer, 1972, Appl. Phys. Lett. **21**, 237.
Herbst, J.F., D.N. Lowy and R.E. Watson, 1972, Phys. Rev. B **6**, 1913.
Herbst, J.F., R.E. Watson and J.W. Wilkins, 1976, Phys. Rev. B **13**, 1439.
Hermanson, J., 1977, Solid State Commun. **22**, 9.
Hill, H.H., and E.A. Kmetko, 1975, J. Phys. F **5**, 1119.
Hillebrecht, F.U., J.C. Fuggle, G.A. Sawatzky, M. Campagna, O. Gunnarsson and K. Schönhammer, 1984, Phys. Rev. B **30**, 1777.
Hüfner, S., 1984, Z. Phys. B **58**, 1.
Hüfner, S., 1986, J. Phys. F **16**, L31.
Hüfner, S., and L. Schlapbach, 1986, Z. Phys. B **64**, 417.
Hüfner, S., and P. Steiner, 1982a, Z. Phys. B **46**, 37.
Hüfner, S., and P. Steiner, 1982b, in: Valence Instabilities, eds P. Wachter and H. Boppart (North-Holland, Amsterdam) p. 263.
Hulliger, F., 1979, in: Handbook of the Physics and Chemistry of Rare Earths, eds K.A. Gschneidner Jr and L. Eyring (North-Holland, Amsterdam) p. 153.
Huschke, J.M., 1979, in: Handbook of the Physics and Chemistry of Rare Earths, Vol. 4, eds K.A. Gschneidner Jr and L. Eyring (North-Holland, Amsterdam) p. 89.
Ikeda, M., Y. Aoki and T. Kasuya, 1985, J. Magn. & Magn. Mater. **52**, 264.
Imer, J.-M., and E. Wuilloud, 1987, Z. Phys. B **66**, 153.
Inglesfield, J.E., 1983, J. Phys. C **16**, 403.
Ishii, T., 1986, private communication.
Jacobi, K., M. Scheffler, K. Kambe and F. Forstmann, 1977, Solid State Commun. **22**, 17.
Jensen, E., and D.M. Wieliczka, 1984, Phys. Rev. B **30**, 7340.
Johansson, B., 1974, Philos. Mag. **30**, 469.
Johansson, L.I., J.W. Allen, T. Gustafsson, I. Lindau and S.B.M. Hagström, 1978, Solid State Commun. **28**, 53.
Kalkowski, G., E.V. Sampathkumaran, C. Laubschat, M. Domke and G. Kaindl, 1985, Solid State Commun. **55**, 977.
Kasuya, T., O. Sakai, K. Takegahara and M. Takeshige, 1985, J. Magn. & Magn. Mater. **52**, 1.
Koel, B.E., G. Praline, H.I. Lee, J.M. White and R.L. Hance, 1980, J. Electron Spectrosc. & Relat. Phenom. **21**, 31.
Koelling, D.D., A.M. Boring and J.H. Wood, 1983, Solid State Commun. **47**, 227.
Koelling, D.D., B.D. Dunlap and G.W. Crabtree, 1985, Phys. Rev. B **31**, 4966.
Kojima, H., Y. Kuramoto and M. Tachiki, 1984, Z. Phys. B. **54**, 293.
Kotani, A., and Y. Toyozawa, 1974, J. Phys. Soc. Jpn. **37**, 912.
Kotani, A., and Y. Toyozawa, 1979, in: Synchrotron Radiation, ed. C. Kunz (Springer-Verlag, Berlin) ch. 4.
Kunz, C., 1979, in: Photoemission in Solids, Vol. 2, eds L. Ley and M. Cardona (Springer-Verlag, Berlin) p. 299.
Kuramoto, Y., and H. Kojima, 1984, Z. Phys. B **57**, 95.
Lacroix, C., 1981, J. Phys. F **11**, 2389.
Lang, J.K., Y. Baer and P.A. Cox, 1981, J. Phys. F **11**, 121.
Lapeyre, G.J., A.D. Baer, J. Hermanson, J. Anderson, J.A. Knapp and P.L. Gobby, 1974a, Solid State Commun. **15**, 1601.
Lapeyre, G.J., J. Anderson, P.L. Gobby and J.A. Knapp, 1974b, Phys. Rev. Lett. **33**, 1290.
Latta, E.-E., and M. Ronay, 1984, Phys. Rev. Lett. **53**, 948.
Latta, E.-E., and M. Ronay, 1986, J. Vac. Sci. Technol. A **4**, 1626.
Lavagna, M., C. Lacroix and M. Cyrot, 1982, Phys. Lett. A **90**, 210.
Lavagna, M., C. Lacroix and M. Cyrot, 1983, J. Phys. F **13**, 1007.
Lawrence, J.M., P.S. Riseborough and R.D. Parks, 1981, Rep. Prog. Phys. **44**, 1.
Lawrence, J.M., J.W. Allen, S.-J. Oh and I. Lindau, 1982, Phys. Rev. B **26**, 2362.
Leckey, R.C.G., 1981, Appl. Surf. Sci. **13**, 125.
Lee, P.A., T.M. Rice, J.W. Serene, L.J. Sham and J.W. Wilkins, 1986, Comments Cond. Mat. Phys. **12**, 99.
Lenth, W., F. Lutz, J. Barth, G. Kalkoffen and C. Kunz, 1978, Phys. Rev. Lett. **41**, 1185.
Ley, L., and M. Cardona, eds, 1979, Photoemission in Solids, Vol. 2 (Springer-Verlag, Berlin).
Lindau, I., and W.E. Spicer, 1974, J. Electron Spectrosc. & Relat. Phenom. **3**, 409.
Liu, S.H., 1986, Phys. Rev. Lett. **57**, 269.
Liu, S.H., and K.-M. Ho, 1982, Phys. Rev. B **26**, 7052.
Liu, S.H., and K.-M. Ho, 1983, Phys. Rev. B **27**, 4220.
Liu, S.H., and K.-M. Ho, 1984, Phys. Rev. B **30**, 3039.
Lundqvist, B.I., 1969, Phys. Kondens. Mater. **9**, 236.
Mackintosh, A.R., 1985, Physica B **139**, 112.
Mahan, G.D., 1970, Phys. Rev. B **2**, 4334.
Mahan, G.D., 1978, in: Electron and Ion Spectroscopy of Solids, eds L. Fiermans, J. Vennik and W. Dekeyser (Plenum Press, New York) p. 1.
Manne, R., and T. Ådberg, 1970, Chem. Phys. Lett. **7**, 282.
Manson, S.T., 1978, in: Photoemission in Solids I, eds M. Cardona and L. Ley (Springer-Verlag, Berlin) p. 135.
Maple, M.B., S.E. Lambert, M.S. Torikachvili, K.N. Yang, J.W. Allen, B.B. Pate and I. Lindau, 1985, J. Less-Common Met. **111**, 239.
Margaritondo, G., and J.H. Weaver, 1985, in: Methods of Experimental Physics: Surfaces,

eds M.G. Lagally and R.L. Park (Academic Press, New York) ch. 3.
Mårtensson, N., B. Reihl and R.D. Parks, 1982, Solid State Commun. **41**, 573.
Martin, R.L., and D.A. Shirley, 1976a, J. Chem. Phys. **64**, 3685.
Martin, R.L., and D.A. Shirley, 1976b, Phys. Rev. A **13**, 1475.
Meyer, M., T. Prescher, E. von Raven, M. Richter, E. Schmidt, B. Sonntag and H.-E. Wetzel, 1986, Z. Phys. D **3**, 347.
Min, B.I., H.J.F. Jansen, T. Oguchi and A.J. Freeman, 1986a, Phys. Rev. B **33**, 8005.
Min, B.I., H.J.F. Jansen, T. Oguchi and A.J. Freeman, 1986b, Phys. Rev. B **34**, 369.
Norman, M.R., D.D. Koelling, A.J. Freeman, J.J.F. Jansen, B.I. Min, T. Oguchi and L. Ye, 1984, Phys. Rev. Lett. **53**, 1673.
Norman, M.R., D.D. Koelling and A.J. Freeman, 1985a, Phys. Rev. B **31**, 6251.
Norman, M.R., D.D. Koelling and A.J. Freeman, 1985b, Physica B **130**, 61.
Norman, M.R., E. Wimmer and A.J. Freeman, 1985c, Phys. Rev. B **32**, 7830.
Nunez-Regueiro, M.D., and M. Avignon, 1985, Phys. Rev. Lett. **55**, 615.
Olson, C.G., 1985, unpublished.
Olson, C.G., and A.J. Arko, 1985, unpublished.
Olson, C.G., and D.W. Lynch, 1982, J. Opt. Soc. Am. **72**, 88.
Olson, C.G., M. Piacentini and D.W. Lynch, 1978, Phys. Rev. B **18**, 5740.
Olson, C.G., D.M. Wieliczka, A.J. Arko, Z. Fisk and J.L. Smith, 1985, Bull. Am. Phys. Soc. **30**, 515.
Orchard, A.F., and G. Thornton, 1977, J. Electron Spectrosc. & Relat. Phenom. **10**, 1.
Osterwalder, J., 1985, Z. Phys. B **61**, 113.
Ott, H.R., Y. Baer and K. Andres, 1981, in: Valence Fluctuations in Solids, eds L.M. Falicov, W. Hanke and M.B. Maple (North-Holland, Amsterdam) p. 297.
Parks, R.D., N. Mårtensson and B. Reihl, 1982, in: Valence Instabilities, eds P. Wachter and H. Boppart (North-Holland, Amsterdam) p. 239.
Parks, R.D., B. Reihl, N. Mårtensson and F. Steglich, 1983, Phys. Rev. B **27**, 6502.
Parks, R.D., M.L. den Boer, S. Raaen, J.L. Smith and G.P. Williams, 1984a, Phys. Rev. B **30**, 1580.
Parks, R.D., S. Raaen, M.L. den Boer, Y.-S. Chang and G.P. Williams, 1984b, Phys. Rev. Lett. **52**, 2176.
Parks, R.D., S. Raaen, M.L. den Boer, Y.-S. Chang and G.P. Williams, 1985, J. Magn. & Magn. Mater. **47&48**, 163.
Patthey, F., B. Delley, W.-D. Schneider and Y. Baer, 1985, Phys. Rev. Lett. **55**, 1518.
Patthey, F., B. Delley, W.-D. Schneider and Y. Baer, 1986, Phys. Rev. Lett. **57**, 270.
Patthey, F., W.-D. Schneider, Y. Baer and B. Delley, 1987a, Phys. Rev. B **35**, 5903.
Patthey, F., S. Cattarinussi, W.-D. Schneider, Y. Baer and B. Delley, 1987b, to be published.
Pauling, L., 1950, J. Chem. Phys. **18**, 145.
Pendry, J.R., 1975, J. Phys. C **8**, 2413.
Pendry, J.R., 1976, Surf. Sci. **57**, 679.
Pendry, J.R., 1978, in: Photoemission and the Electronic Properties of Surfaces, eds B. Feuerbacher, B. Fitton and R.F. Willis (Wiley, New York).
Peterman, D.J., D.T. Peterson and J.H. Weaver, 1980, J. Less-Common Met. **74**, 167.
Peterman, D.J., J.H. Weaver and D.T. Peterson, 1981, Phys. Rev. B **23**, 3903.
Peterman, D.J., J.H. Weaver and M. Croft, 1982, Phys. Rev. B **25**, 5530.
Peterman, D.J., J.H. Weaver, M. Croft and D.T. Peterson, 1983, Phys. Rev. B **27**, 808.
Pickett, W.E., A.J. Freeman and D.D. Koelling, 1981, Phys. Rev. B **23**, 1266.
Platau, A., and S.-E. Karlsson, 1978, Phys. Rev. B **18**, 3820.
Platau, A., L.I. Johansson, A.I. Hagström, S.-E. Karlsson and S.B.M. Hagström, 1977, Surf. Sci. **63**, 153.
Plummer, E.W., and W. Eberhardt, 1982, in: Advances in Chemical Physics, Vol. XLIV, eds I. Prigogine and S.A. Rice (Wiley, New York) p. 533.
Podloucky, R., and D. Glötzel, 1983, Phys. Rev. B **27**, 3390.
Pollak, R.A., S. Kowalczyk and R.W. Johnson, 1976, in: Valence Instabilities and Related Narrow-Band Phenomena, ed R.D. Parks (Plenum Press, New York) p. 463.
Powell, C.J., 1974, Surf. Sci. **44**, 29.
Powell, C.J., 1985, Surf. & Interface Anal. **7**, 256.
Praline, G., B.E. Koel, R.L. Hance, H.I. Lee and J.M. White, 1980, J. Electron Spectrosc. & Relat. Phenom. **21**, 17.
Ray, S.P., A.S. Nowick and D.E. Cox, 1975, J. Solid State Chem. **15**, 344.
Riseborough, P.S., 1985, Physica B **130**, 66.
Riseborough, P.S., 1986, Solid State Commun. **57**, 721.
Robinson, J.M., 1979, Phys. Rep. **51**, 1.
Ronay, M., and E.-E. Latta, 1985, Phys. Rev. B **32**, 5375.
Rosina, G., E. Bertel and F.P. Netzer, 1985, J. Less-Common Met. **111**, 285.
Rosina, G., E. Bertel, F.P. Netzer and J. Redinger, 1986, Phys. Rev. B **33**, 2364.
Rowe, J.E., and N.V. Smith, 1974, Phys. Rev. B **10**, 3207.
Sakai, O., H. Takahashi, M. Takeshige and T. Kasuya, 1984, Solid State Commun. **52**, 997.
Sakai, O., M. Takeshige, H. Harima, K. Otaki and T. Kasuya, 1985, J. Magn. & Magn. Mater. **52**, 18.
Sakuma, A., Y. Kuramoto, T. Watanabe and C. Horie, 1985, J. Magn. & Magn. Mater. **52**, 393.
Sakuma, A., Y. Kuramoto and T. Watanabe, 1986, Phys. Rev. B **34**, 2231.
Sampathkumaran, E.V., G. Kalkowski, C. Laubschat, G. Kaindl, M. Domke, G. Schmiester

and G. Wortmann, 1985a, J. Magn. & Magn. Mater. **47&48**, 212.
Sampathkumaran, E.V., G. Kaindl, C. Laubschat, W. Krone and G. Wortmann, 1985b, Phys. Rev. B **32**, 3185.
Sampathkumaran, E.V., G. Kalkowski, C. Laubschat, M. Domke and G. Kaindl, 1985c, Annu. Rep. BESSY, p. 112.
Sato, S., 1976, J. Phys. Soc. Jpn. **41**, 913.
Schaich, W.L., 1978, in: Photoemission in Solids, Vol. 1, eds M. Cardona and L. Ley (Springer-Verlag, Berlin) p. 105.
Schaich, W.L., and N.W. Ashcroft, 1970, Solid State Commun. **8**, 1959.
Schaich, W.L., and N.W. Ashcroft, 1971, Phys. Rev. B **3**, 2452.
Schlapbach, L., and J. Osterwalder, 1982, Solid State Commun. **42**, 271.
Schlüter, M., and C.M. Varma, 1982, in: Valence Instabilities, eds P. Wachter and H. Boppart (North-Holland, Amsterdam) p. 259.
Schlüter, M., and C.M. Varma, 1983, Helv. Phys. Acta **56**, 147.
Schneider, W.-D., 1986, private communication.
Schneider, W.-D., C. Laubschat and B. Reihl, 1983, Phys. Rev. B **27**, 6538.
Schneider, W.-D., B. Delley, E. Wuilloud, J.-M. Imer and Y. Baer, 1985, Phys. Rev. B **32**, 6819.
Schönhammer, K., and O. Gunnarsson, 1977, Solid State Commun. **23**, 691.
Schönhammer, K., and O. Gunnarsson, 1978a, Solid State Commun. **26**, 147.
Schönhammer, K., and O. Gunnarsson, 1978b, Solid State Commun. **26**, 399.
Schönhammer, K., and O. Gunnarsson, 1987, this volume, chapter 64.
Seah, M.P., and W.A. Dench, 1979, Surf. & Interface Anal. **1**, 2.
Smith, N.V., 1971, CRC Crit. Rev. Solid State & Mater. Sci. **2**, 45.
Smith, N.V., 1979, Phys. Rev. B **19**, 5019.
Smith, N.V., and F.J. Himpsel, 1982, in: Handbook on Synchrotron Radiation, Vol. 1, eds D.E. Eastman, Y. Farge and E.-E. Koch (North-Holland, Amsterdam) ch. 10.
Smith, N.V., and L.F. Mattheiss, 1974, Phys. Rev. B **9**, 1341.
Soda, K., S. Asaoka, T. Mori, M. Taniguchi, K. Naito, Y. Onuki, T. Komatsubara, T. Miyahara, S. Sato and T. Ishii, 1985, J. Magn. & Magn. Mater. **52**, 347.
Soda, K., T. Mori, M. Taniguchi, S. Asaoka, K. Naito, Y. Onuki, T. Komatsubara, T. Miyahara, S. Sato and T. Ishii, 1986, J. Phys. Soc. Jpn. **55**, 1709.
Spanjaard, D.D., D.W. Jepsen and P.M. Marcus, 1977, Phys. Rev. B **15**, 1728.
Starace, A.F., 1972, Phys. Rev. B **5**, 1773.
Stassis, C., C.-K. Loong, G.R. Kline, O.D. McMasters and K.A. Gschneidner Jr., 1978, J. Appl. Phys. **49**, 2113.
Steiner, P., H. Höchst and S. Hüfner, 1977, J. Phys. F **7**, L145.
Stewart, G.R., 1984, Rev. Mod. Phys. **56**, 755.
Stöhr, J., R. Jeager and J.J. Rehr, 1983, Phys. Rev. Lett. **51**, 821.
Strange, P., and B.L. Gyorffy, 1985, Physica B **130**, 41.
Sugar, J., 1972, Phys. Rev. B **5**, 1785.
Sugaware, H., A. Kakizaki, I. Nagakura, T. Ishii, T. Komatsubara and T. Kasuya, 1982, J. Phys. Soc. Jpn. **51**, 915.
Suzuki, S., T. Ishii and T. Sagawa, 1975, J. Phys. Soc. Jpn. **38**, 156.
Takeshige, M., O. Sakai and T. Kasuya, 1985, J. Magn. & Magn. Mater. **52**, 363.
Traum, M.M., and N.V. Smith, 1974, Phys. Rev. B **9**, 1353.
van der Veen, J.F., F.J. Himpsel and D.E. Eastman, 1980, Phys. Rev. Lett. **44**, 189 (erratum on p. 533).
Varma, C.M., 1985, Comments Solid State Phys. **11**, 221.
Veal, B.W., and A.P. Paulikas, 1985, Phys. Rev. B **31**, 5399.
Wang, C.S., H. Krakauer and W.E. Pickett, 1985, Physica B **135**, 34.
Weaver, J.H., 1983, J. Less-Common Met. **94**, 17.
Weaver, J.H., 1986, unpublished results for $CeSi_2$.
Weaver, J.H., D.T. Peterson and R.L. Benbow, 1979, Phys. Rev. B **20**, 5301.
Weaver, J.H., D.J. Peterman, D.T. Peterson and A. Franciosi, 1981, Phys. Rev. B **23**, 1692.
Weaver, J.H., A. Franciosi and V.L. Moruzzi, 1984, Phys. Rev. B **29**, 3293.
Weaver, J.H., M. Grioni, J.J. Joyce and M. del Giudice, 1985, Phys. Rev. B **31**, 5290.
Wendin, G., 1981, in: Structure and Bonding, Vol. 45 (Springer-Verlag, Berlin).
Wieliczka, D.M., 1982, Ph.D. thesis, Iowa State University.
Wieliczka, D.M., and C.G. Olson, 1983, unpublished.
Wieliczka, D.M., J.H. Weaver, D.W. Lynch and C.G. Olson, 1982, Phys. Rev. B **26**, 6056.
Wieliczka, D.M., C.G. Olson and D.W. Lynch, 1984, Phys. Rev. Lett. **52**, 2180.
Wieliczka, D.M., A. Franciosi, C. Caprile and C.G. Olson, 1986, Bull. Am. Phys. Soc. **31**, 498.
Williams, R.H., G.P. Srivastava and I.T. McGovern, 1980, Rep. Prog. Phys. **43**, 87.
Wolff, H.W., R. Bruhn, K. Radler and B. Sonntag, 1976, Phys. Lett. A **59**, 67.
Wooten, F., 1972, Optical Properties of Solids (Academic Press, New York).
Wuilloud, E., 1985, thesis, University of Neuchâtel.
Wuilloud, E., H.R. Moser, W.-D. Schneider and Y. Baer, 1983, Phys. Rev. B **28**, 7354.
Wuilloud, E., B. Delley, W.-D. Schneider and Y. Baer, 1984, Phys. Rev. Lett. **53**, 202.
Wuilloud, E., B. Delley, W.-D. Schneider and Y. Baer, 1985, J. Magn. & Magn. Mater. **47&48**,

197.
Yeh, J.J., and I. Lindau, 1985, At. Data & Nucl. Data Tables **32**, 1.
Zachariasen, H.W., 1973, J. Inorg. Nucl. Chem. **35**, 3487.
Zangwill, A., 1982, in: Atomic Physics, Vol. 8, eds I. Lindgren, A. Rosen and S. Svanberg (Plenum Press, New York) p. 339.
Zangwill, A., and P. Soven, 1980, Phys. Rev. Lett. **45**, 204.
Zhang, F.C., and T.K. Lee, 1983, Phys. Rev. B **28**, 33.
Zhang, F.C., and T.K. Lee, 1984, Phys. Rev. B **30**, 1556.
Zimkina, T.M., and I.I. Lyakhovskaya, 1976, Sov. Phys. Solid State **38**, 156.
Zimkina, T.M., V.A. Fomichev, S.A. Griborski and I.I. Zhukova, 1967, Sov. Phys. Solid State **9**, 1128.

Handbook on the Physics and Chemistry of Rare Earths, Vol. 10
edited by K.A. Gschneidner, Jr., L. Eyring and S. Hüfner

Chapter 67

PHOTOEMISSION IN CHALCOGENIDES

S. HÜFNER
Fachbereich Physik, Universität des Saarlandes, D-6600 Saarbrücken, Fed. Rep. Germany

Contents

1. Introduction

The chalcogenides of the lanthanides comprise the oxides (in addition to the sulfides, selenides and tellurides) and are, because of this fact, probably the most common and most accessible lanthanide compounds. They therefore have been studied by photoemission in considerable detail (Campagna et al. 1979, Campagna et al. 1976) and results are incorporated in many contributions at various places in this volume. Therefore, this brief chapter was chosen to present mostly only those examples which give specific and new information or information which is not equally apparent if studied in other systems.

2. Core and valence spectra of lanthanum and cerium oxides

Oxides are perhaps the most common compounds and therefore it is natural to use those of lanthanum and cerium for the description of the core and valence level photoemission spectra of lanthanide compounds. This seems especially appropriate because cerium oxide can occur in trivalent (Ce_2O_3) and tetravalent (CeO_2) forms, therefore giving rise to some quite interesting observations.

The energy level diagram in terms of which the core and valence spectra of La_2O_3

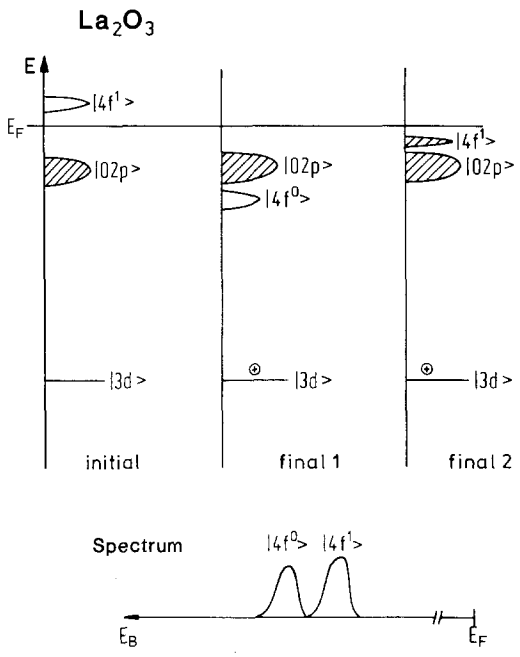

Fig. 1. A diagram illustrating the 3d core level photoemission in La_2O_3. In the ground state the O 2p band is the highest occupied state in La_2O_3, whereas the La 4f level is the lowest unoccupied state. Photoemission of a 3d electron can be simulated (approximately) by the addition of one nuclear charge. This lowers the La energy levels in such a way that now the 4f level is below the Fermi energy (as in Ce_2O_3). This 4f level can now either be empty ($|4f^0\rangle$ final state) or occupied by charge transfer from the O 2p band ($|4f^1\rangle$ final state), giving rise to two distinct energetically different final states (Kotani and Toyozawa 1973a, 1973b, 1974).

will be discussed is given in fig. 1 (Allen 1985b, Feldkamp and Davis 1979, Davis and Feldkamp 1981, Gunnarsson and Schönhammer 1983a,b, 1985, 1986, Kotani and Toyozawa 1974, Fujimori 1983a,b,c, Kotani and Toyozawa 1973a,b, Kotani and Jo 1986, Kotani et al. 1986). As an example of a core level here the 3d level is indicated. In the initial state the highest occupied level in La_2O_3 is the oxygen 2p level. The 4f level of lanthanum is not occupied. One is now interested in the result of photoemission out of the 3d level. Note that this photoemission of a 3d electron of lanthanum can, to a good approximation, be described by the addition of one nuclear charge to lanthanum making it similar to cerium. (This is the so-called $Z + 1$ approximation, see chapter 69 of this volume). This additional charge then 'pulls', so to speak, the total energy level scheme of the La ion and therefore also the 4f level to lower energies. In principle two possible final states can occur as is apparent from fig. 1. The first final state is one in which this 4f level, although it has been pulled below the Fermi level, remains unoccupied. One designates this final state by its 4f occupation, namely $|4f^0\rangle$. The second final state occurs if the total electronic valence configuration adopts a state similar to the one found in the initial state of Ce_2O_3. This means that one electron is transferred from the oxygen 2p band into the cerium 4f state, thus forming a $|4f^1\rangle$ configuration. This is obviously the ground state of the photoionized La ion giving the lowest energy and one designates it by the $|4f^1\rangle$ configuration.

Thus photoemission of the 3d levels of La_2O_3 results in two spin–orbit split doublets ($d_{3/2}$, $d_{5/2}$); one representative of the valence electron configuration $|4f^0\rangle$ and the other one representative of the valence electron configuration $|4f^1\rangle$, which has the smaller binding energy (nearer to the Fermi energy). These considerations

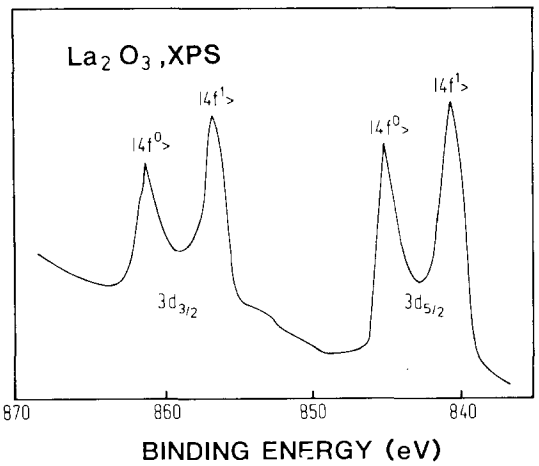

Fig. 2. An XPS spectrum of the 3d region in La_2O_3. Each component of the $3d_{3/2,5/2}$ multiplet shows a splitting due to the two different final states $|4f^0\rangle$ and $|4f^1\rangle$ (Schneider et al. 1985).

are borne out by the experimental spectra which are shown in fig. 2 and which clearly show the anticipated splitting of each of the spin–orbit split components of the 3d configuration into two lines (Schneider et al. 1985, Moser et al. 1984, Fuggle et al. 1980, Signorelli and Hayes 1973, Suzuki et al. 1974).

The question now arises about how far a theory, which is devised along the principles as outlined in fig. 1, can indeed describe actual spectra. The work of Kotani et al. (1985, 1986), Jo and Kotani (1985), Fujimori (1983b), Schneider et al. (1985) and Gunnarsson and Schönhammer (1983a,b, 1985) has shown that a surprising degree of agreement between theory and experiment can be achieved. The current theories (Kotani and Jo 1986, Gunnarsson and Schönhammer 1986, but not Fujimori 1983b) use the Anderson single-impurity Hamiltonian for the description of the 4f level, which should be a very good approximation because of the narrowness of the 4f band (level, state) in the solid. These calculations use in addition a core level, a filled valence band (oxygen 2p), a 4f level (as mentioned), a bandwidth for the valence band, a hybridization between the 4f electrons and the valence band, a 4f–4f Coulomb interaction and a Coulomb interaction between the core hole and the 4f electrons. A typical result as obtained for the $3d_{5/2}$ 'line' of La_2O_3 (Kotani and Jo 1986) is shown in fig. 3 with a full line. The comparison is made here with the experimental data of Fuggle et al. 1980 (dashed line; the intensities of the two curves have been adjusted). The numerical values for the parameters, as specified above, come out quite similar in the calculations of the different groups, giving confidence to the procedure employed. Fujimori 1983b, 1985, uses a slightly different approach in that he describes the valence electrons (oxygen 2p and lanthanide 4f) by a cluster approximation, getting, however, in the end, results similar to those of the other authors.

The important results from all these calculations is that they can simulate the experimental data only if they assume a hybridization between the f electrons and the valence band, which is much larger ($\sim$0.5 eV) than hitherto believed. For completeness we show in fig. 4 the combination of the valence band photoemission spectra of La_2O_3, which only gives the oxygen 2p level, and a BIS spectrum of that

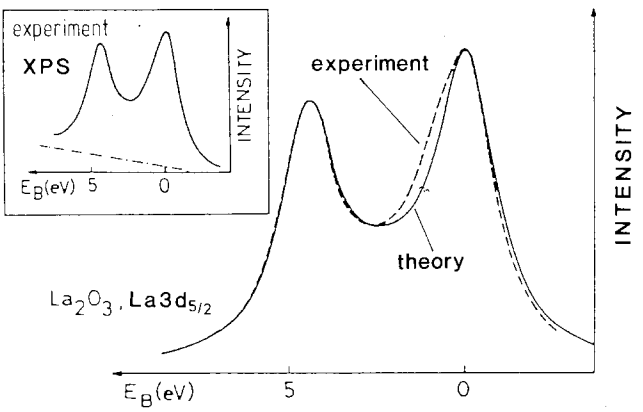

Fig. 3. A comparison (Kotani and Jo 1986) of the measured $3d_{5/2}$ spectrum (dashed curve) with that calculated (full curve) in La_2O_3. The insert shows the measured raw data (Fuggle et al. 1980) where the background is indicated by a dashed–dotted line.

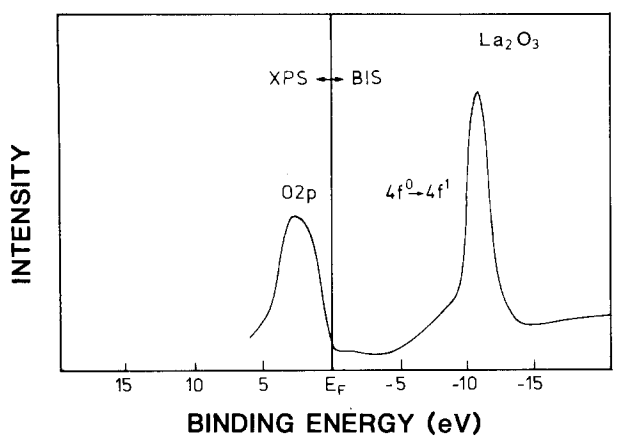

Fig. 4. A combination of an XPS and BIS spectrum of the valence/conduction band in La_2O_3 (Schneider et al. 1985). XPS measures the O2p valence band and BIS the lowest occupied state, via the $4f^0 \rightarrow 4f^1$ transition energy. (There is some inconsistency in the literature with respect to the classification of 4f spectra like that in fig. 3. We think that the most correct one is by assigning the transition energy, because this is the property actually measured. Whether one prefers to call this energy the $|4f^0\rangle$ state or the $|4f^1\rangle$ state is a matter of taste.)

same compound which gives the position of the 4f configuration in this oxide, or more rigorously the energy of the $4f^0 \rightarrow 4f^1$ excitation (Schneider et al. 1985).

The situation in Ce_2O_3 is very similar to the one just described for La_2O_3 except that the valence electron count in the 4f level has to be increased by one. This means for the 3d photoemission that now the two possible final states are $|4f^1\rangle$ and $|4f^2\rangle$ and this is evident in the experimental spectra as shown in fig. 5 (Allen 1985a). Figure 6 gives a combination of photoemission and BIS spectra for the valence band region and here one sees in order of increasing energy the oxygen 2p band, the $4f^1 \rightarrow 4f^0$ excitation energy in the valence 4f configuration and the $4f^1 \rightarrow 4f^2$ excitation in the conduction electron configuration (Allen 1985a). We prefer here to

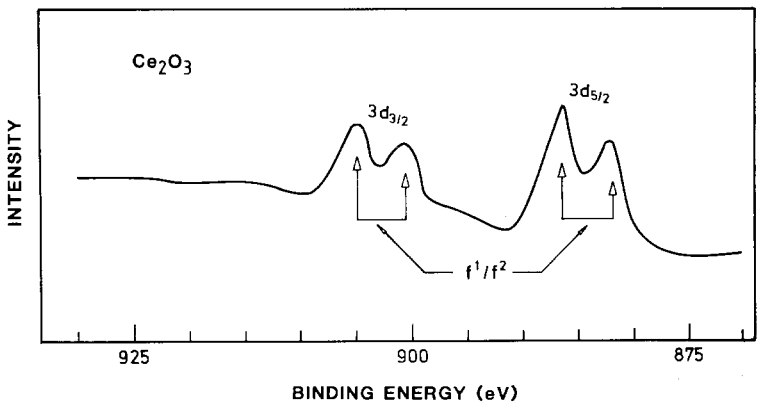

Fig. 5. The $3d_{3/2,5/2}$ spectrum (XPS) of Ce_2O_3 (Allen 1985a) showing a situation similar to the one found in La_2O_3. The energy separation between the $|4f^1\rangle$ and $|4f^2\rangle$ final states is small and therefore their mixing is strong. For that reason a classification f^1/f^2 has been chosen.

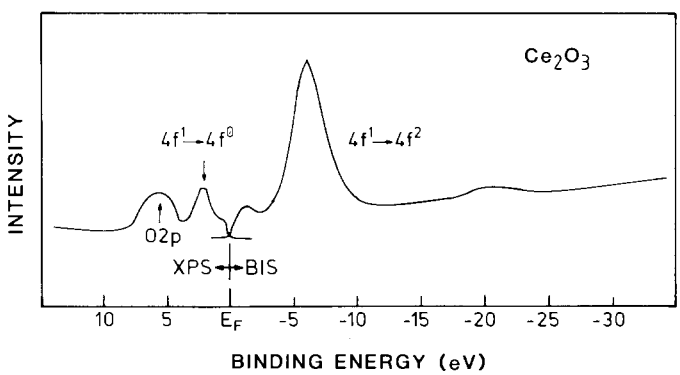

Fig. 6. The combination of an XPS and BIS spectrum of Ce_2O_3 (Allen 1985a). The $4f^1 \rightarrow 4f^0$ excitation energy is below the Fermi energy and the $4f^1 \rightarrow 4f^2$ energy above it.

describe spectral features by the corresponding excitation energies because some confusion has been produced if they are designated by their final or initial state configuration. Thus e.g., the 4f peak below the Fermi energy has been called intermittently the $4f^1$ or the $4f^0$ state, where clearly one label is the initial state, the other one the final state, and therefore the labelling with the process that produces it ($4f^1 \rightarrow 4f^0$ excitation) seems the least controversial one.

The situation in CeO_2 is not quite so simple and has to be described in more detail. In principle one could assume that the considerations which have been given for La_2O_3 should also apply to CeO_2 because CeO_2, at least nominally, has no 4f electron in the initial state. This is however, too simple a view. Because of the closeness of the $4f^0$ configuration and the oxygen 2p band in CeO_2 there is strong hybridization which results in some 4f character of the valence electrons even in the ground state (Fujimori 1983b, Koelling et al. 1983). This is indicated in the energy level diagram in fig. 7 by letting the Fermi energy 'touch' the $4f^1$ state. This diagram cannot, however, show correctly that due to the hybridization between the 4f

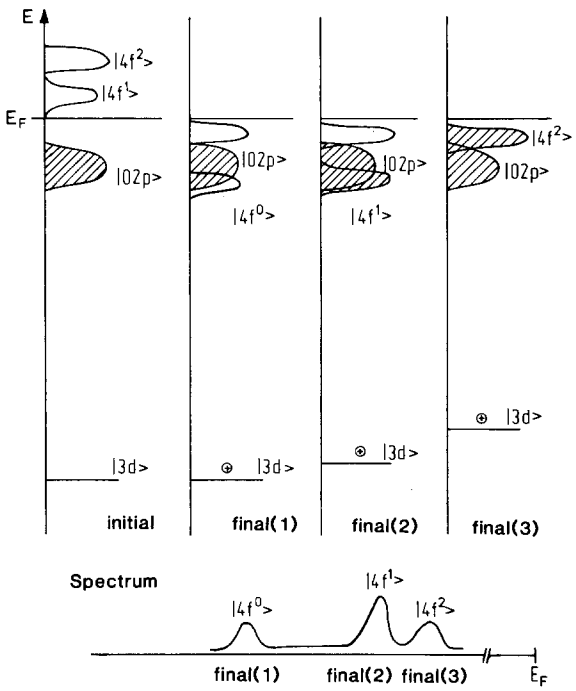

Fig. 7. A diagram for the analysis of the 3d core level XPS process in CeO_3 (Kotani and Toyozawa 1973a, 1973b, 1974). In order to demonstrate the O 2p–Ce 4f hybridization it was decided to let the Fermi energy intersect the 4f state, which is admittedly a crude picture because it could be wrong. However, we could find no other way to demonstrate the 4f character of the valence electron configuration in the ground state. In the final state the core can be simulated by an additional nuclear charge. The valence band can then accomodate a maximum of two 4f electrons. This makes possible three final states, $|4f^0\rangle$, $|4f^1\rangle$ and $|4f^2\rangle$.

electrons and the oxygen 2p electrons the 4f electron count is ~ 0.5 in the ground state of CeO_2. The $4f^2$ configuration is unoccupied in this compound. Naturally this diagram is slightly misleading although we are unable to construct another for the discussion of the situation. We emphasize again that in CeO_2 the mixing of the wavefunctions is between the oxygen 2p functions and the Ce 4f functions (Koelling et al. 1983) and that the energy of this hybridized state is what is generally called the oxygen 2p band, which is fully occupied. The first unoccupied state is the Ce 4f state, which is separated by ~ 3 eV from the oxygen 2p state and therefore CeO_2 is an insulator.

In principle three valence configurations are possible in the final state reached by a 3d photoelectron. Note that we describe the photoemission final state again by the addition of one nuclear charge to the cerium ion thus producing a core configuration which is close to the one of praseodymium. This 'pulls' the Ce valence electron configuration (and of course the other Ce electron levels above the 3d level) to lower energies and can lead to three different final states (Kotani and Jo 1986). One, which has no 4f occupancy, we call it $|4f^0\rangle$, one which has one 4f electron in

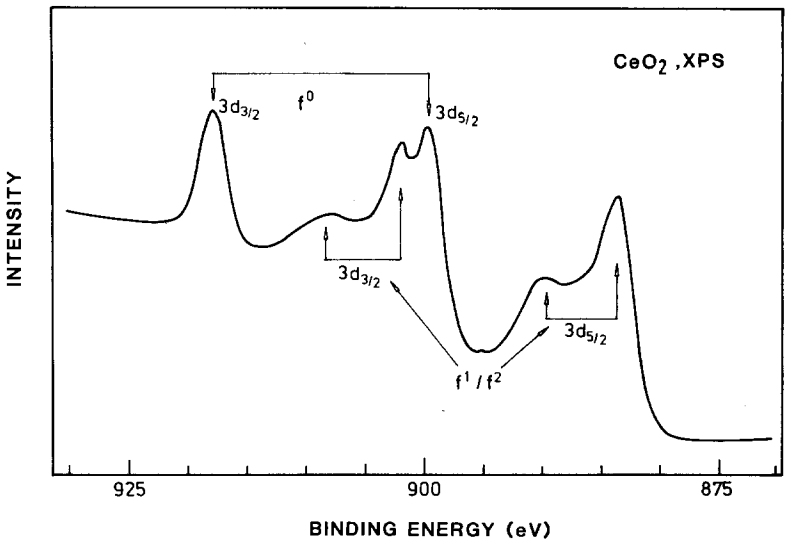

Fig. 8. A 3d core level spectrum of CeO_2 showing the three different final states for each of the 3d lines. As in the case of Ce_2O_3 the $|4f^1\rangle$ and $|4f^2\rangle$ final states are strongly mixed (Allen 1985a).

the valence electron configuration, $|4f^1\rangle$, and one, which is the ground state and has two 4f electrons in the valence state, $|4f^2\rangle$. This leads to the three-peak structure in the spin-orbit split 3d components observed in the spectra shown in fig. 8 (Allen 1985a). The two final state configurations $|4f^1\rangle$ and $|4f^2\rangle$ are strongly mixed and one author has reversed the order of these two final states depending on the mixing of the wavefunctions, which he gets out of his calculations (Fujimori 1983b). (For similar data see Schneider et al. 1985 and Borroughs et al. 1976). Spectra like that in fig. 8 reflect a final state, which has other valence electron occupations than the initial state.

In the spirit of the Kotani/Toyozawa/Gunnarsson/Schönhammer approach, which was shown to work well for the calculation of the core levels of La_2O_3, the core level spectra of CeO_2 have been calculated (Jo and Kotani 1985; see also Schneider et al. 1985, Fujimori 1985). Figure 9 shows the calculated spectrum for one of the $3d_{3/2,5/2}$ doublets and the inset gives a measured spectrum (Kotani and Jo 1986). The calculation clearly reproduces the three final states which can be read off the diagram in fig. 7. The inset shows a measured 3d spectrum of CeO_2 (similar to the one in fig. 8) and one can realize that the theory represents the experimental data quite well (Kotani and Jo 1986).

Finally fig. 10 gives again the combination of a photoemission and a BIS spectrum of CeO_2 and one can see that indeed the 4f configuration is situated just above the Fermi energy, thus reflecting the situation as sketched in fig. 7 and showing that the 4f level in CeO_2 is the lowest unoccupied level (Allen 1985a; see also Wuilloud et al. 1984).

Since the question of the 'valency' in CeO_2 has been discussed in the literature at

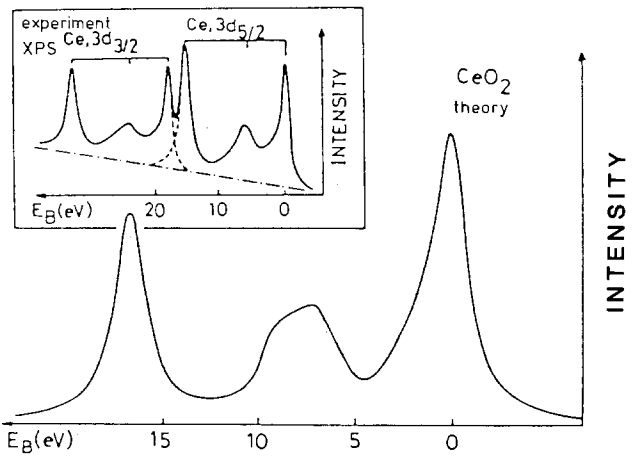

Fig. 9. A comparison (Kotani and Jo 1986) of the measured (inset, $3d_{3/2,5/2}$ doublet, Schneider et al. 1985) with the calculated $3d_{5/2}$ spectrum in CeO_2.

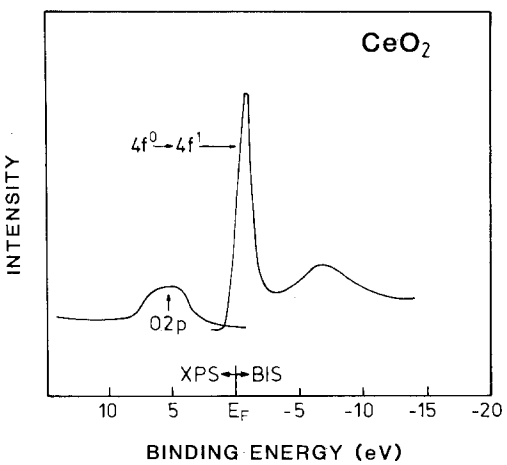

Fig. 10. A combination of the XPS and BIS spectrum of CeO_2 (Allen 1985a), similar data have been published by Wuilloud et al. (1984). The Fermi energy is in the gap between the O 2p band and the Ce 4f state, showing that CeO_2 is an insulator. There is, however, strong mixing between the O 2p and Ce 4f wavefunctions (Koelling et al. 1983).

some length, it seems appropriate to evaluate the foregoing data in more general terms. First of all, one has to realize that the term 'valence' is not very well defined and therefore the magnitude of the valence will depend on the method of its determination. Let us demonstrate what we mean by this statement. The data as in fig. 8 indicate, even without any sophisticated analysis, that the $|f^0\rangle$ component in the spectrum has a strength of $\sim 50\%$ of the total spectrum, which points to a state of $Ce^{3,5+}$ in CeO_2, or a valence of $v = 3.5$. Another high-energy measurement, namely, X-ray absorption leads to a higher valence, namely $v = 3.65$, where however the exact number depends somewhat on the method of data handling (J. Röhler, chapter 71, this volume). These numbers could also be interpreted by saying that there is a population of the 4f level of $4 - v$ in CeO_2. One can however attempt to measure this 4f population and thereby the valence of cerium in CeO_2 by measuring,

e.g., the susceptibility. This has been done, with the result that there is at most a population of 5% of the 4f state (Wachter 1982) which, if written in terms of valencies would mean $v = 3.95$.

Finally one may take the data in fig. 10 to analyze the valence. These spectra show, that CeO_2 is a wide gap semiconductor (or insulator) with a filled oxygen 2p band and an empty cerium 4f band which could be interpreted by saying that the valence of cerium in CeO_2 is $v = 4$ (because the oxygen 2p band is completely filled!). Note however, that while the experiment in fig. 10 is meant to determine energy levels that in fig. 8 determines primarily transition probabilities. These transition probabilities sense the nature of the wavefunctions of the states involved and therefore give, of course, a different picture, than the data of fig. 10. The two sets of data therefore do not contradict one another.

The spectrum in fig. 8 shows that there is strong mixing between the Ce 4f and the O 2p wavefunctions, meaning a considerable covalent bond and therefore the simple valence term, which is so convenient to describe most lanthanide compounds (with the exception of the mixed valent systems), loses some of its simplicity. This is emphasized by the band structure calculation of Koelling et al. (1983), which finds just that hybridization. However the question of the size of the 4f population, and therefore of the valence, as determined by these calculations, is also one of the choice of the spheres for the integration of the charges around the ions.

Using the charge analysis in the muffin-tin spheres one arrives at the following charge numbers for the valence bands Koelling et al. (1983):

metal (s, p, d, f)	:	1.41	(f: 0.47)
oxygen (2 atoms):		8.44	
total muffin tin	:	9.85	
interstitial	:	2.15	
Total	:	12.00	

These numbers lead to some interesting observations. The charge transfer away from the metal ion is much less than the 4 charges one would expect if CeO_2 were a truly tetravalent compound. The f-population comes out as ~ 0.5, close to the value estimated from the analysis of the 3d core level spectra. The charges on the oxygen ions is much less than the 12 expected for a truly ionic bond. And finally there is considerable charge which cannot be assigned to either ion, indicating again the strong covalent bond in CeO_2.

It has to be emphasized that these numbers can only be taken as a rough guide, because the charge analysis can also be performed in slightly different ways leading to different numbers, which does not, however, change the bulk of the argument.

The term valence has to be used with care if used for the description of the electronic properties in CeO_2. If it is employed to demonstrate the covalent bond in this compound it is a valid procedure and thus indicates the mixing of the cerium and oxygen wavefunctions. The sizable 4f population obtained in this description can, however, not be used to infer a large susceptibility for CeO_2 or even to deduce an occupation in the 4f band. This band, as demonstrated by the BIS data, is completely empty.

3. Mixed valent compounds: samarium sulfide and thulium selenide

Photoemission has played an important role in the past in obtaining a clearer picture of the so-called mixed valent phenomenon (Campagna et al. 1976). Mixed valent means that, contrary to the generally observed case, there are some lanthanide compounds in which the occupation number for the 4f configuration is not integral but takes a value markedly different from this integral value (Varma 1976, 1985, Wohlleben and Coles 1973, Lawrence et al. 1981). This situation can be visualized from the diagram in fig. 7. If in that diagram the Fermi energy is made to intersect the 4f band, the 4f count can be nonintegral. Using a more atomic approach to describe this case, one can say that for a compound for which this situation applies there is a fluctuation of an electron between the valence electron configuration provided, e.g., by the 5d electrons of the lanthanides and the 4f configuration, which in the time average amounts to a nonintegral occupation number of the 4f configuration.

In that definition the conduction electron wavefunction of the lanthanide electrons can be written as:

$$\sin\alpha|4f^n\rangle + \cos\alpha|4f^{n-1}\ 5d\rangle \qquad (\sin^2\alpha + \cos^2\alpha = 1).$$

This implies a metallic state for a mixed valent compound. Note that in CeO_2 the hybridization is between the Ce 4f wavefunction and the O 2p wavefunction, leading to an insulating state as demonstrated by the gap between the top of the valence band (O 2p) and the bottom of the conduction band (Ce 4f, fig. 10). Some authors have chosen to call CeO_2 a mixed valent compound because of the large Ce 4f–O 2p hybridization. Here, however, we want to stay with the general notation in which the mixed valent term is reserved for a metallic system, where the electrons fluctuate between the 4f and the 5d band of the lanthanide.

Some insight into the mixed valence problem can perhaps be obtained from figs. 11 and 12. Figure 11 gives the $4f^n \rightarrow 4f^{n-1}$ (Δ_-) excitation energies as measured by XPS and the $4f^n \rightarrow 4f^{n+1}$ (Δ_+) excitation energies as measured by BIS for the lanthanide metals which are trivalent, except for Eu and Yb which are divalent (Lang et al. 1981). These energies can be shifted somewhat by pressure or hybridization (or a combination of the two) and thus for Ce, Sm, Eu, Tm and Yb either one of Δ_+ or Δ_- can be brought to coincide (within the 4f bandwidth) with the Fermi energy, making a 4f–5d exchange possible and thereby leading to a mixed valent state.

Figure 12 gives the lattice constants for the sulfides, selenides and tellurides of the lanthanides (Campagna et al. 1976). These constants show a regular behaviour except for some deviations for Sm, Eu, Tm and Yb. The regular curves are for the 'normal' trivalent chalcogenides. The anomalous lattice constants occur for the divalent lanthanides, which due to the additional 4f electron have a larger ionic radius. Thus one sees that under normal conditions SmS, SmSe and SmTe are divalent (with respect to the Sm ion) but they can be driven into the mixed valent state by external pressure (Jayaraman et al. 1970).

The diagram in fig. 12 also shows the lattice constant of 'golden' SmS, a

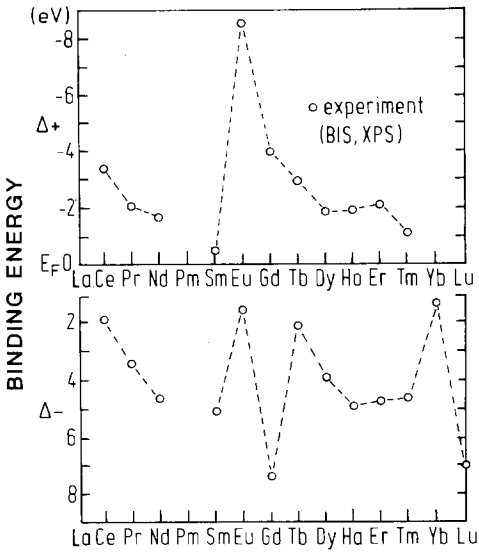

Fig. 11. Δ_- and Δ_+ (electron removal and electron addition energies) for the lanthanide metals (Lang et al. 1981).

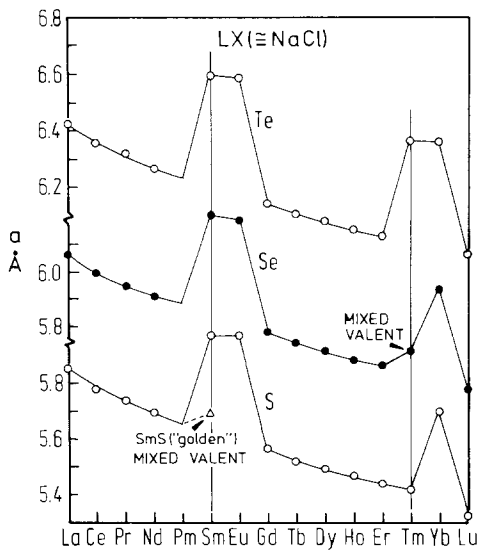

Fig. 12. The lattice constants of the sulfides, selenides and tellurides of the lanthanides (Campagna et al. 1976). For the trivalent compounds these lattice constants show a regular behaviour, and from the deviations the divalent ones and the mixed valent ones (TmSe and 'collapsed' SmS) are easily discernible.

modification of SmS which is produced by the application of external pressure. Since the lattice constant of 'golden' SmS is between that of trivalent and divalent SmS, one can read the degree of mixed valence (between Sm^{2+} and Sm^{3+}) from this diagram.

Similar observations can be obtained for the thulium chalcogenides. TmTe is obviously divalent. With increasing internal pressure (decreasing lattice constant), the tendency towards trivalency increases. This means that TmS is purely trivalent and TmSe is mixed valent as is evident from the magnitude of their lattice constants.

One of the first intermediate valent system studied by photoemission was the

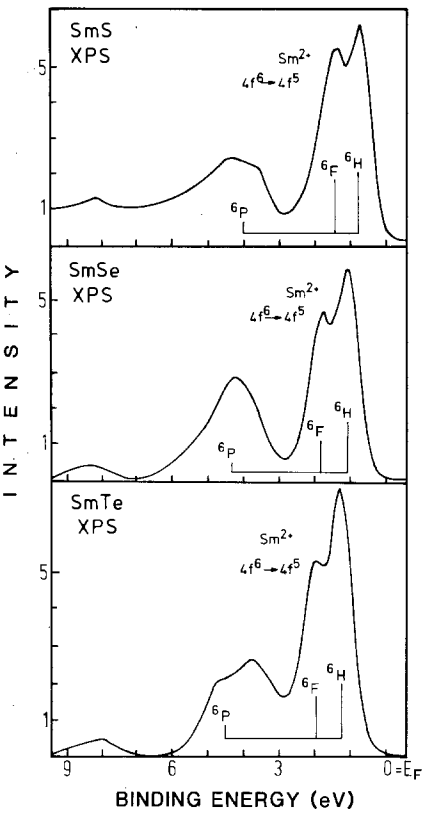

Fig. 13. The XPS spectra of SmS, SmSe and SmTe (all divalent). These spectra show predominantly the $4f^6 \rightarrow 4f^5$ final state structures (Campagna et al. 1976).

'golden' (collapsed) form of SmS. SmS is under normal conditions a (small gap) divalent semiconductor (see fig. 12). XPS spectra of SmS, SmSe and SmTe (all divalent) are shown in fig. 13. They give the final state structure resulting from the $f^6 \rightarrow f^5$ excitation and in addition the chalcogen valence band (Campagna et al. 1976).

By applying modest external pressure SmS can be driven into a first-order phase transition (Jayaraman et al. 1970) which results in the so-called metallic or 'golden' phase of SmS, in which SmS is in a mixed valent state.

Photoemission experiments under applied external pressure are difficult to perform. One can, however, simulate the external pressure by forming alloys with a reduced lattice constant which can be thought of as producing an internal pressure. This can, e.g., be achieved by substituting some of the Sm ions by Th ions. If 10% of the Sm ions are replaced by Th ions, the same sort of phase transition, which can be induced by external pressure, is observed.

The effect on the photoemission spectra of this phase transition can be seen by the series of spectra in fig. 14. The top panel gives again the spectrum of pure divalent SmS and this spectrum is dominated by the final state structure produced by the $f^6 \rightarrow f^5$ excitation. In order to evaluate the spectrum of mixed valent SmS produced

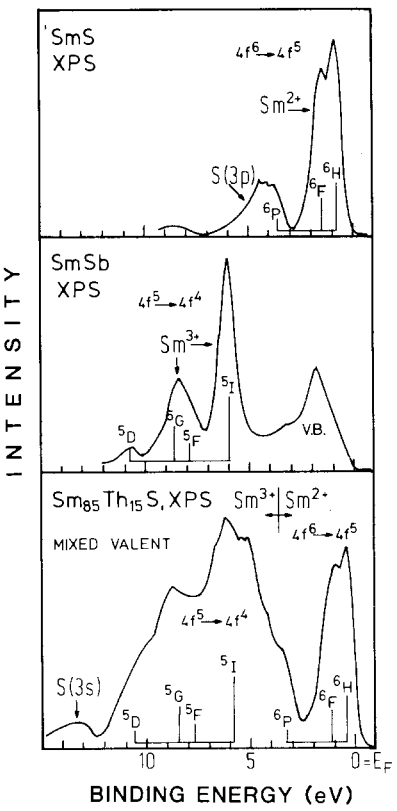

Fig. 14. The XPS spectra of SmS (divalent), SmSb (trivalent) and $Sm_{0.85}Th_{0.15}$ (mixed valent). The spectrum of the last compound contains the $4f^6 \rightarrow 4f^5$ and the $4f^5 \rightarrow 4f^4$ final state structure (Campagna et al. 1976).

by the doping of SmS with Th, the second panel gives the spectrum representative of Sm^{3+} which is, e.g., measured in SmSb. Here near the Fermi edge one observes the valence band which is mainly produced by the Sm 5d electrons and at larger binding energies one sees the 4f structure produced by the $f^5 \rightarrow f^4$ excitation. The bottom spectrum in fig. 14 is an XPS spectrum of a sample of mixed valent SmS, where the phase transition has been produced by replacing 15% of the Sm ions by Th ions leading to an alloy $Sm_{0.85}Th_{0.15}S$. It is immediately apparent that this spectrum contains a final state structure representative of the $f^6 \rightarrow f^5$ transition and the $f^5 \rightarrow f^4$ transition. This means that the initial state is a mixture of the f^6 and the f^5 configuration or, in other words, that the 4f band, narrow as it is, intersects the Fermi energy, leading to a nonintegral f occupation number (Pollak et al. 1974, Freeouf et al. 1974, Campagna et al. 1974).

A similar situation is encountered in TmSe. This compound is, however, thought to be mixed valent whereas TmTe is divalent and TmS is trivalent. An XPS photoemission spectrum of TmSe is shown in fig. 15. Here one sees both the final states of the $f^{13} \rightarrow f^{12}$ and of the $f^{12} \rightarrow f^{11}$ excitations (Campagna et al. 1974, 1976, Oh et al. 1984).

It is obvious from these data that a quantitative estimate of the valence in, e.g.,

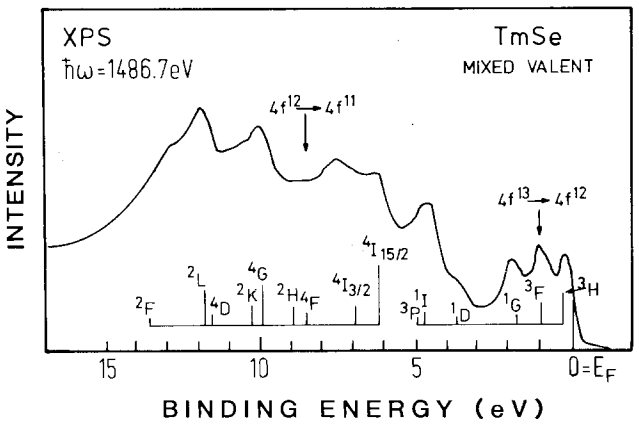

Fig. 15. The XPS spectrum of TmSe (mixed valent). The spectrum contains the $4f^{13} \rightarrow 4f^{12}$ (divalent and the $4f^{12} \rightarrow 4f^{11}$ (trivalent) final state structure (Campagna et al. 1976).

TmSe is not easy from photoemission spectra because it requires a careful background determination which is not always possible with great accuracy.

There is, however, a matter which further complicates the situation. Photoemission is a technique sensitive to only a few surface layers. In any solid the topmost surface layer can show an electronic structure different from that of the bulk. This must be determined before one can obtain a quantitative estimate of the degree of mixed valence.

As in the case of CeO_2 the question 'what kind of quantitative numbers can one extract from the photoemission spectra' must be addressed. In SmS the XPS data yield $v \approx 2.75$ (Campagna et al. 1976) a number which is slightly larger than that derived from other methods yielding $v = 2.60 \pm 0.10$ (Jayaraman et al. 1973, Coey et al. 1974, Holtzberg 1973). Similarly in TmSe the photoemission spectra yield $v = 2.62 \pm 0.15$ (Oh et al. 1984) again not in disagreement with the results from other experimental techniques yielding $v = 2.60 \pm 0.10$ (Launois et al. 1980, Holland-Moritz and Loewenhaupt 1979, Wertheim et al. 1980, Kaindl et al. 1982, Oh and Allen 1984).

A comprehensive discussion of the valencies derived from high-energy spectroscopy and other methods can be found in chapter 71 of this volume. Perhaps it is worthwhile to point out that the agreement or disagreement between the results from different techniques are not independent of the error bars that various experimenters 'dare' to attribute to the numbers derived from their experimental data. It is our impression that an uncertainty of ± 0.15 as given, e.g., by Oh et al. (1984) reflects very realistically the accuracy which can be achieved in that field, and leaves little room for spectacular disagreements. If however error bars are reduced by an order of magnitude, as some authors prefer to do, considerable discrepancies occur and can give rise to corresponding speculations.

4. Surface core level shifts in lanthanide chalcogenides

Ions in the surface of a solid have a different coordination number than those in

the bulk. Therefore the electronic structure of a surface is different from that of the bulk. Since the binding energy of the core levels of an ion depends also on the valence electron distribution of this ion, there can be a shift between the core levels of an ion in the bulk and those of the ion on the surface (surface core level shift) (Johansson 1979, Johansson and Mårtensson 1980, Rosengren and Johansson 1981).

The principle of the core level shifts can be demonstrated with the diagram in fig. 16. Note that for the purpose of the argument we shall consider the 4f electrons as core electrons which because of their localized nature, is a very reasonable approximation. Also it is assumed in what follows that the valence band is made up of the 5d electrons of the lanthanides, which again can serve only as an approximation, but a convenient one for the sake of the argument. In addition we note that in trivalent and divalent lanthanides the number of 5d electrons which make up the valence band is smaller than 5. Finally for simplicity a triangular density of states for the 5d electrons will be assumed.

One knows that in the surface layer the number of neighbours of each ion is reduced with respect to that in the bulk. This leads to a narrowing of the density of states in the surface because this is roughly proportional to the number of nearest neighbours. As can be seen in fig. 16 this then has the consequence that, if the number of valence electrons is assumed to be the same in the surface, as in the bulk, the bulk Fermi energy is at lower energies than that of the surface. Of course, in the sample these two Fermi energies have to coincide and this then means that the position of the core level of the surface is shifted to lower energies (higher binding energies!) than that of the bulk.

Measurements of this effect for a SmS, EuS and YbS are shown in fig. 17 (Martensson et al. 1982). They have been performed with a photon energy of 70 eV which brings out specifically the electronic properties of states in the surface layer because of the small escape depth of electrons with kinetic energies in that range. The separation of the bulk and the surface contribution to the spectra can be

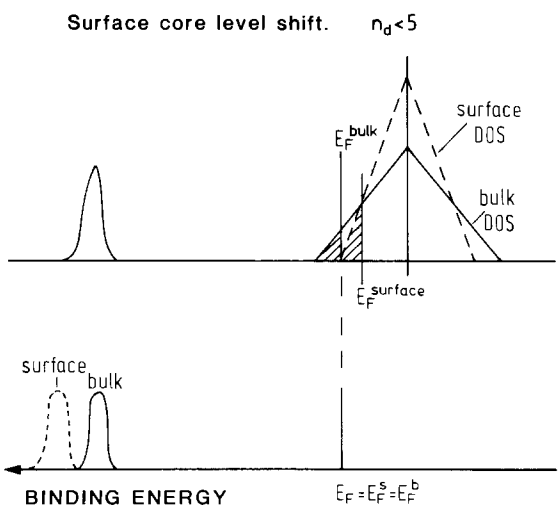

Fig. 16. Principles of the core level shift if the number of 5d conduction electrons is smaller than 5. The density of states is assumed to have a triangular shape and, in addition, in going from the bulk to the surface the number of conduction electrons remains constant.

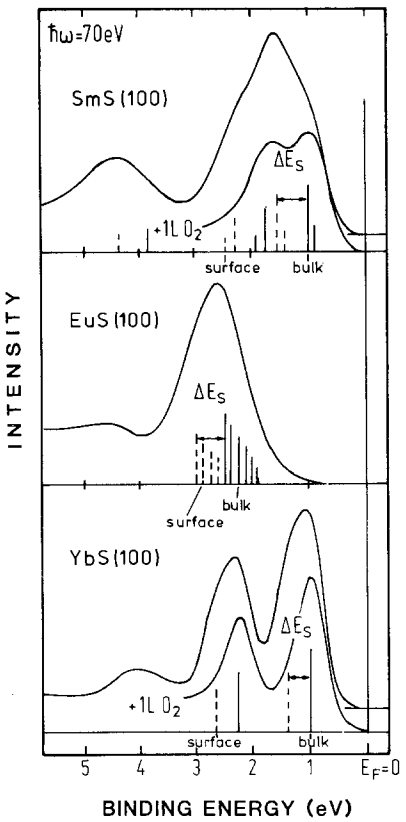

Fig. 17. The photoemission spectra of clean SmS, EuS and YbS and of oxygen exposed SmS and YbS. The latter samples give only small surface contributions to the total spectrum and can therefore be taken as being representative of the bulk. This allows the separation of bulk and surface contributions in the spectra from the clean samples. The final state multiplets are indicated: bulk = full lines, surface = dashed lines (Mårtensson et al. 1982).

performed by comparing the spectra of the clean samples with those from samples which have been exposed to a small dose of oxygen. This latter procedure tends to reduce strongly the surface contribution and therefore these spectra are more or less representative of the bulk sample. As can be seen from fig. 17 for all of the sulfides the bulk contribution to the spectra is nearer to the Fermi energy than the surface contribution. This is in agreement with the simple model which was indicated in fig. 16. The shift of the surface contribution with respect to the bulk contribution is of the order of 0.5 eV.

All the sulfides mentioned, namely SmS, EuS and YbS, are divalent in their ground state. The final state after ejection of one 4f electron is then in principle a trivalent configuration and the measured excitation energy can therefore be identified as the divalent to trivalent excitation energy ($\Delta E_{II,III}$). This is only an approximation to which small correction terms like an impurity solution term must be added. These excitation energies are plotted in fig. 18. The excitation energies for the elements between europium and ytterbium can be estimated from those measured for SmS, EuS and YbS and measurements obtained for the metals (Lang et al. 1981). These estimated values are given as full points in fig. 18. In addtion, this figure shows the bulk and the surface Fermi energy in the sense as defined in fig. 16. The

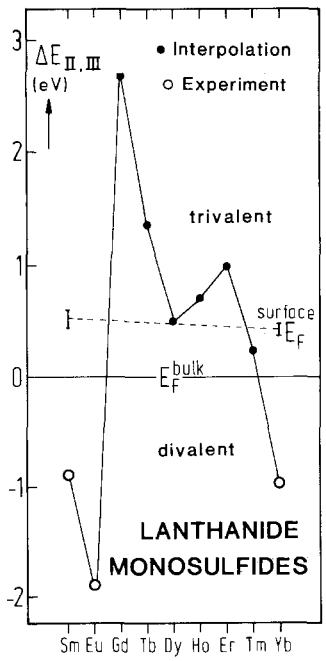

Fig. 18. The excitation energies from the divalent to the trivalent state ($\Delta E_{II,III}$) for some lanthanide sulfides (Mårtensson et al. 1982). The open points are from the data in fig. 16, the full points are interpolated using the data for the metals (Lang et al. 1981).

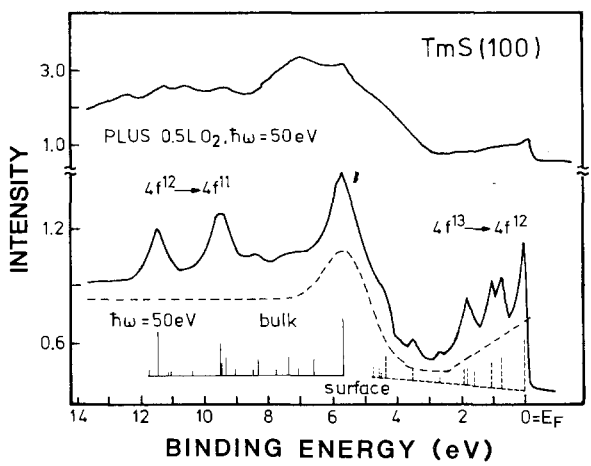

Fig. 19. The photoemission spectrum of clean and oxygen covered TmS (trivalent). The oxygen covered sample, is representative for the bulk, and the surface oxide (trivalent) shows only the $4f^{12} \rightarrow 4f^{11}$ final state structure, apart from emission from the 5d conduction band. The spectrum of the clean sample shows a $4f^{12} \rightarrow 4f^{11}$ final state structure from the bulk and an additional $4f^{13} \rightarrow 4f^{12}$ final state structure near the Fermi energy from the divalent surface structure. According to fig. 18, bulk TmS is trivalent but surface TmS divalent (Kaindl et al. 1982). The final state multiplets are indicated: bulk = full lines, surface = dashed lines.

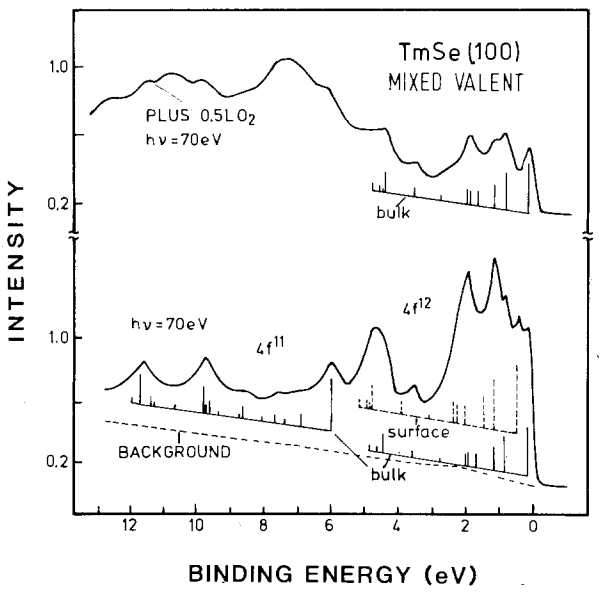

Fig. 20. The photoemission spectrum of clean and oxygen covered TmSe (mixed valent). The occurrence of a surface contribution can best be seen from the splitting of the peak next to the Fermi energy, which is absent in the oxygen covered sample (Kaindl et al. 1982).

data in fig. 18 indicate that for TmS (and perhaps for DyS) the surface layer has not the trivalent but the divalent configuration.

This is indeed borne out by the experimental findings as shown in fig. 19. Here in the energy range between 6 and 12 eV below the Fermi energy the signal from the trivalent bulk final state is observed. In addition, one sees the signal from the divalent surface contribution near the Fermi energy. This latter contribution can be quenched, as shown before, by a weak exposure of the sample to oxygen and the spectrum of such a sample is also shown in fig. 19 (Kaindl et al. 1982).

It is obvious that the surface contribution poses an additional difficulty for the determination of the valence in a mixed valent compound from photoemission data. A careful analysis of the spectrum of TmSe, which is mixed valent, is shown in fig. 20. In this material, of course, both the bulk and surface divalent contributions overlap and are, therefore, difficult to distinguish. The clearest sign of these two contributions is found in the splitting of the peak nearest the Fermi energy. Note that in TmS the separation between bulk and surface spectra was simple because there the bulk was trivalent whereas the surface was divalent. In fig. 20 the bulk contribution is indicated by the bar diagram with the full lines whereas the surface contribution, which is shifted to lower binding energy, is indicated by the dashed bar diagram. This latter contribution can be quenched by exposure of the sample to a slight amount of oxygen.

References

Allen, J.W., 1985a, J. Magn. & Magn. Mater. **47&48**, 168.

Allen, J.W., 1985b, J. Magn. & Magn. Mater. **52**, 135.

Burroughs, P., A. Hamnett, A.F. Orchard and G. Thornton, 1976, J. Chem. Soc. Dalton Trans. **17**, 1686.

Campagna, M., E. Bucher, G.K. Wertheim and L.D. Longinotti, 1974, Phys. Rev. Lett. **33**, 165.

Campagna, M., G.K. Wertheim and E. Bucher, 1976, Structure and Bonding **30**, 99.

Campagna, M., G.K. Wertheim and Y. Baer, 1979, in: Photoemission in Solids II, Topics in Applied Physics, Vol. 27 (Springer-Verlag, Berlin) p. 217.

Coey, J.M.D., G. Ghathak and F. Holtzberg, 1974, AIP Conf. Proc. **24**, 38.

Davis, L.C., and L.A. Feldkamp, 1981, Phys. Rev. B **23**, 6239.

Feldkamp, L.A., and L.C. Davis, 1979, Phys. Rev. Lett. **43**, 151.

Freeouf, J.L., D.E. Eastman, F. Holtzberg and J.B. Torrance, 1974, Phys. Rev. Lett. **33**, 161.

Fuggle, J.C., M. Campagna, Z. Zolnierek and R. Lässer, 1980, Phys. Rev. Lett. **45**, 1597.

Fujimori, A., 1983a, Phys. Rev. B **27**, 3992.

Fujimori, A., 1983b, Phys. Rev. B **28**, 2281.

Fujimori, A., 1983c, Phys. Rev. B **28**, 4489.

Fujimori, A., 1985, J. Magn. & Magn. Mater. **47&48**, 243.

Gunnarsson, O., and K. Schönhammer, 1983a, Phys. Rev. Lett. **50**, 604.

Gunnarsson, O., and K. Schönhammer, 1983b, Phys. Rev. B **28**, 4315.

Gunnarsson, O., and K. Schönhammer, 1985, Phys. Rev. B **31**, 4815.

Gunnarsson, O., and K. Schönhammer, 1986, J. Phys. Colloq. C **8**, No. 12, 47.

Holland-Moritz, E., and M. Loewenhaupt, 1979, J. Phys. Colloq. **40**, C5-359.

Holtzberg, F., 1973, AIP Conf. Proc. **18**, 478.

Jayaraman, A., V. Narayanamurti, E. Bucher and L.D. Longinotti, 1970, Phys. Rev. Lett. **35**, 1430.

Jayaraman, A., E. Bucher, P. Dernier and L.D. Longinotti, 1973, Phys. Rev. Lett. **31**, 700.

Jo, T., and A. Kotani, 1985, Solid State Commun. **54**, 451.

Johansson, B., 1979, Phys. Rev. B **19**, 6615.

Johansson, B., and N. Martensson, 1980, Phys. Rev. B **21**, 4427.

Kaindl, G., C. Laubschat, B. Reihl, R.A. Pollak, N. Martensson, F. Holtzberg and D.E. Eastman, 1982, Phys. Rev. B **26**, 1713.

Koelling, D.D., A.M. Boring and J.H. Wood, 1983, Solid State Commun. **47**, 227.

Kotani, A., and T. Jo, 1986, J. Phys. Colloq. C **8**, No. 12, 47.

Kotani, A., and Y. Toyozawa, 1973a, J. Phys. Soc. Jpn. **35**, 1073.

Kotani, A., and Y. Toyozawa, 1973b, J. Phys. Soc. Jpn. **35**, 1082.

Kotani, A., and Y. Toyozawa, 1974, J. Phys. Soc. Jpn. **37**, 912.

Kotani, A., H. Mizuta, T. Jo and J.C. Parlebas, 1985, Solid State Commun. **53**, 805.

Kotani, A., M. Okada and T. Jo, 1986, to be reported in 8th Intern. Conf. on Vacuum Ultraviolet Radiation Physics, Lund.

Lang, J.K., Y. Baer and P.A. Cox, 1981, J. Phys. F **11**, 121.

Launois, H., M. Raviso, E. Holland-Moritz, R. Pott and G. Wohlleben, 1980, Phys. Rev. Lett. **44**, 1271.

Lawrence, J.M., P.S. Riseborough and R.D. Parks, 1981, Rep. Prog. Phys. **44**, 1.

Martensson, N., B. Reihl, R.A. Pollak, F. Holtzberg and G. Kaindl, 1982, Phys. Rev. B **25**, 6522.

Moser, H.R., B. Delley, W.-D. Schneider and Y. Baer, 1984, Phys. Rev. B **29**, 2947.

Oh, S.-J., and J.W. Allen, 1984, Phys. Rev. B **29**, 589.

Oh, S.-J., J.W. Allen and I. Lindau, 1984, Phys. Rev. B **30**, 1937.

Pollak, R.A., F. Holtzberg, J.H. Freeouf and D.E. Eastman, 1974, Phys. Rev. Lett. **33**, 820.

Rosengren, A., and B. Johansson, 1981, Phys. Rev. B **23**, 3582.

Schneider, W.-D., B. Delley, E. Wuilloud, J.-M. Imer and Y. Baer, 1985, Phys. Rev. B **32**, 6819.

Signorelli, A.J., and R.G. Hayes, 1973, Phys. Rev. B **8**, 81.

Suzuki, S., T. Ishii and T. Sagawa, 1974, J. Phys. Soc. Jpn. **37**, 1334.

Varma, C.M., 1976, Rev. Mod. Phys. **48**, 219.

Varma, C.M., 1985, Comments Solid State Phys. **11**, 221.

Wachter, P., 1982, in: Valence Instabilities, eds P. Wachter and H. Boppart (North-Holland, Amsterdam) p. 145.

Wertheim, G.K., W. Eib, E. Kaldis and M. Campagna, 1980, Phys. Rev. B **22**, 6240.

Wohlleben, D.K., and B.R. Coles, 1973, in: Magnetism V, eds G.T. Rado and H. Suhl (Academic Press, New York).

Wuilloud, E., B. Delley, W.-D. Schneider and Y. Baer, 1984, Phys. Rev. Lett. **53**, 202.

Handbook on the Physics and Chemistry of Rare Earths, Vol. 10
edited by K.A. Gschneidner, Jr., L. Eyring and S. Hüfner

Chapter 68

CALCULATION OF 4f EXCITATION ENERGIES IN THE METALS AND RELEVANCE TO MIXED VALENCE SYSTEMS

J.F. HERBST
Physics Department, General Motors Research Laboratories, Warren, Michigan 48090–9055, USA

J.W. WILKINS
Laboratory of Atomic and Solid State Physics

and

The Materials Science Center, Cornell University, Ithaca, New York 14853–2501, USA

Contents

List of symbols

D	surface dipole energy
e	electron charge
$E_{ac}(4f^n)$	LS-average total energy of the $4f^n$ configuration

$E_{\text{corr}}[4f^n(5d,6s)^m]$	atomic correlation energy for the $4f^n(5d,6s)^m$ configuration
$E_{4f\text{HRC}}(4f^n)$	Hund-rule total energy correction for the $4f^n$ configuration
$E_{\text{metal}}[4f^n(5d,6s)^m]$	total energy of all electrons in a Wigner–Seitz sphere having n 4f electrons and valence m
$E_{\text{atom}}^{\text{RHF}}[4f^n(5d,6s)^m]$	RHF total energy of the $4f^n(5d,6s)^m$ atomic configuration
$E_{\text{band}}^{\text{RHF}}[4f^n(5d,6s)^m]$	RHF band total energy of the $4f^n(5d,6s)^m$ metallic configuration
$E_{\text{ion}}^{\text{RHF}}[4f^n(5d,6s)^{m-1}]$	RHF total energy of the $4f^n(5d,6s)^{m-1}$ ion
$E_{\text{metal}}^{\text{RHF}}[4f^n(5d,6s)^m]$	RHF total energy of the $4f^n(5d,6s)^m$ metallic configuration with the 4f electrons in the Hund-rule ground multiplet
$F^k(4f,4f)$	effective 4f–4f Coulomb integral
$G^k(4f,4f)$	effective 4f–4f exchange integral
$\hbar$	Planck's constant (divided by 2π)
H_A	Anderson Hamiltonian
J	total angular momentum
k_B	Boltzmann's constant
L	total orbital angular momentum
m	valence (number of 5d, 6s conduction electrons)
M_L	component of orbital angular momentum
M_S	component of spin angular momentum
N_f	f-orbital degeneracy factor
P	pressure
q	wave vector
RHF	relativistic Hartree–Fock
$R^k(nlj,n'l'j')$	RHF electrostatic integral for the nlj and $n'l'j'$ subshells
$R^k(nl,n'l')$	j,j' average of $R^k(nlj,n'l'j')$
r_{WS}	Wigner–Seitz radius
S	total spin angular momentum
T_K	Kondo temperature
$U(4f^n)$	effective 4f–4f Coulomb interaction energy for the $4f^n$ configuration; or, the energy separation between the $4f^n$ and $4f^{n+1}$ levels
U_ε	one-electron analog of $U(4f^n)$
V	volume
V_{kf}	4f conduction electron hybridization matrix element
W_{4fj}	4fj bandwidth
W_{5d}	5d bandwidth
Z	atomic number
Γ	4f hybridization width
$\delta E(\text{atom})$	difference of $E_{\text{atom}}^{\text{RHF}}$ between two configurations
$\delta E(\text{atom} \rightarrow \text{band})$	difference of $(E_{\text{band}}^{\text{RHF}} - E_{\text{atom}}^{\text{RHF}})$ between two configurations
$\delta E(\text{Hund})$	difference of $E_{4f\,\text{HRC}}$ between two 4f configurations
$\delta(nl)$	splitting of 4f-screened and conduction-electron-screened nl excitation energies
$\Delta(nl\text{sat})$	excitation energy of an nl core electron with the nl hole screened by a 4f electron
$\Delta_I(4f)$	4f intraatomic relaxation energy
$\Delta_S(\text{atomic})$	atomic estimate of 4f screening energy
$\Delta_S(\text{band})$	band estimate of 4f screening energy
$\Delta_-(4f\,\text{ion})$	$4f^n \rightarrow 4f^{n-1}$ excitation energy in the absence of screening
$\Delta_-(4f^n \rightarrow 4f^{n-1})$	energy required to excite a 4f electron from the $4f^n$ shell into the conduction bands at the Fermi level
$\Delta_-(4f^n\varepsilon;nl)$	excitation energy of an nl core electron in a metal having 4f occupancy n_f
$\Delta_+(4f^n \rightarrow 4f^{n+1})$	energy required to convert a Fermi level conduction electron into a 4f electron at a $4f^n$ site
$\varepsilon_{5d_{\text{min}}}$	energy of the 5d-band minimum

$\varepsilon_{5d_{max}}$	energy of the 5d-band maximum
ε_{4fj}^{atom}	RHF atomic 4fj eigenvalue
ε_{4fj}	4fj one-electron eigenvalue in the metal
ε_F	Fermi energy
ε_{Γ_1}	energy of the 6s-band minimum
λ	multiplet spin–orbit parameter
ζ_{4f}	4f one-electron spin–orbit parameter
ξ(ion)	correlation energy difference between a $4f^n$ atom and the $4f^{n-1}$ ion
$\xi_{\pm}(4f^n \rightarrow 4f^{n\pm1})$	free atom correlation energy difference between $4f^{n\pm1}$ and $4f^n$ configurations
$\rho(nl)$	replicate splitting of the nl core shell
$\sigma(nl)$	shift in $4f^{n+1}$ level due to an nl core hole
ω	frequency

1. Introduction

To a large extent the opulent diversity of electronic and magnetic properties manifested by lanthanide materials arises from the existence of an open shell of atomic-like 4f electrons. A number of challenging theoretical problems accompanies the panoply of physical phenomena, not only for the exotic mixed valence systems but for comparitively simpler materials such as the metals as well. In this chapter we treat one of these issues, the calculation of 4f electron excitation energies in the lanthanide metals. Measurement of the excitation energies is one of the principal achievements of the high-energy spectroscopies which form the subject of the present volume.

Figure 1 serves to introduce a central aspect of the problem. Shown are the charge densities of the 4f shell and the shells exterior to it in the $4f^5\,5d^2\,6s$ configuration of

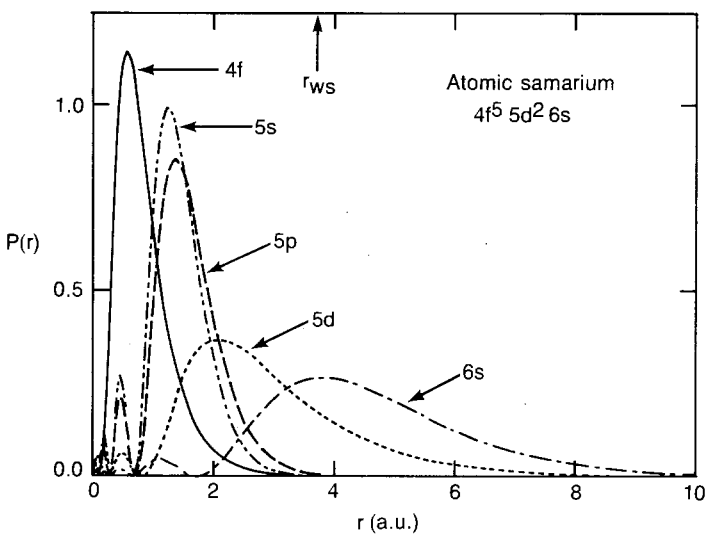

Fig. 1. Charge densities $P(r)$ [$\int_0^\infty P(r)\,dr \equiv 1$] of the $4f_{5/2}$, $5s_{1/2}$, $5p_{1/2}$, $5d_{3/2}$, and $6s_{1/2}$ shells from relativistic Hartree–Fock calculations for the $4f^5\,5d^2\,6s$ configuration of atomic samarium.

atomic samarium. Although the atomic Sm ground state is $4f^6\,6s^2(^7F_0)$ (Martin et al. 1974), the $4f^5\,5d^2\,6s$ excited configuration corresponds most closely to the electron distribution in samarium metal. When such atoms coalesce to form the solid, whose Wigner–Seitz radius r_{WS} is indicated in the figure, it is clear that the 5d and 6s wave functions will heavily overlap; their interaction generates the conduction bands. In contrast, the atomic 4f electrons are quite localized. Confined within the closed 5s and 5p core shells, the 4f charge is quite small at r_{WS}, and its localized atomic character is essentially retained in the metallic state.

Calculation of a 4f excitation energy (for example, the energy required to remove a 4f electron, as in a photoemission event) thus requires an *atomic* treatment of the 4f electrons in concert with a *band* description of the 5d–6s conduction electrons, two fundamentally disparate approximations. One-electron eigenvalues from conventional band theory are *a priori* inadequate for estimating the 4f excitation energies since they do not incorporate intraatomic or extraatomic relaxation effects. Electrons in the vicinity of a localized hole are significantly perturbed, and the alteration of their wave functions vitiates identification of the one-electron energy with the removal energy. In other terms, the effective 4f–4f Coulomb interaction energy is large compared to the 4f level width, so that the band picture does not apply and 4f excitation energies must be obtained from total energy differences between appropriate initial and final states rather than from single-particle eigenvalues.

As we describe below, the renormalized atom (RA) method (Watson et al. 1970, Hodges et al. 1972) offers a means both for combining the atomic and band approximations and for obtaining the requisite total energies. RA techniques were first applied to the problem of 4f excitation energies in a non-relativistic treatment (Herbst et al. 1972) and then in a relativistic version (Herbst et al. 1976a, 1978). The present review concentrates on relativistic results. In chapter 69 Johansson describes a qualitatively different approach relying on the use of a Born–Haber cycle coupled with thermochemical information which is the only other systematic investigation of 4f promotion energies.

2. Calculational scheme

We are concerned specifically with two 4f excitation energies in the lanthanide metals: (i) the energy $\Delta_-(4f^n \rightarrow 4f^{n-1})$ required to excite a 4f electron from an occupied $4f^n$ shell into the conduction bands at the Fermi level ε_F, and (ii) the energy $\Delta_+(4f^n \rightarrow 4f^{n+1})$ needed to convert a Fermi level conduction electron into a localized 4f at a metallic site already having n 4f electrons present. In effective one-particle language, $\Delta_-(4f^n \rightarrow 4f^{n-1})$ is the energy of an occupied 4f level below ε_F, and $\Delta_+(4f^n \rightarrow 4f^{n+1})$ is the energy of an unoccupied 4f level above ε_F when the ground state configuration is $4f^n$. Figure 2 illustrates these quantities. Since binding energies from high-energy spectroscopies such as X-ray photoemission (XPS) and bremsstrahlung isochromat spectroscopy (BIS) are generally reported relative to ε_F, these definitions are convenient. As indicated in fig. 2, the sum

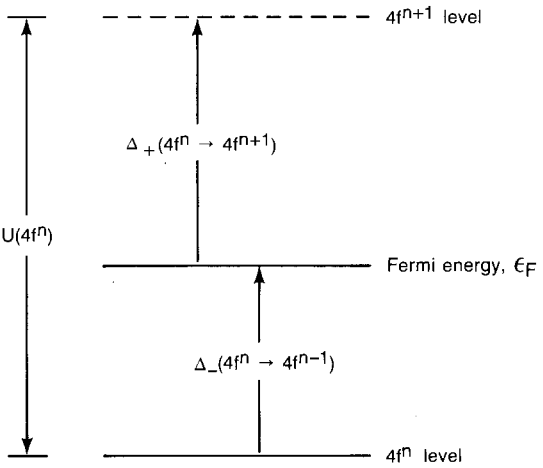

Fig. 2. Effective energy level diagram defining $\Delta_-(4f^n \rightarrow 4f^{n-1})$, $\Delta_+(4f^n \rightarrow 4f^{n+1})$, and $U(4f^n)$. The $4f^n$ ground state configuration is assumed, so that both $\Delta_-(4f^n \rightarrow 4f^{n-1})$ and $\Delta_+(4f^n \rightarrow 4f^{n+1})$ are positive quantities. If the ground state configuration were $4f^{n-1}$, a similar diagram could be drawn with a new $\Delta_-(4f^{n-1} \rightarrow 4f^{n-2})$, $\Delta_+(4f^{n-1} \rightarrow 4f^n) = -\Delta_-(4f^n \rightarrow 4f^{n-1})$, and $U(4f^{n-1}) = \Delta_-(4f^{n-1} \rightarrow 4f^{n-2}) + \Delta_+(4f^{n-1} \rightarrow 4f^n)$.

$$U(4f^n) \equiv \Delta_-(4f^n \rightarrow 4f^{n-1}) + \Delta_+(4f^n \rightarrow 4f^{n+1}) \tag{1}$$

is the energy separation between the filled and empty 4f levels, and it may also be interpreted as the Coulomb interaction energy between two 4f electrons at the same metallic site (see sections 3 and 4).

The excitation energies are written as total energy differences:

$$\Delta_\pm(4f^n \rightarrow 4f^{n\pm1}) = E_{\text{metal}}[4f^{n\pm1}(5d, 6s)^{m\pm1}] - E_{\text{metal}}[4f^n(5d, 6s)^m]. \tag{2}$$

E_{metal} represents the total energy of all the electrons in a Wigner–Seitz (WS) sphere of the metal having the indicated electron configuration, and m is the valence or the number of (5d, 6s) conduction electrons in the initial state.

Equation (2) embodies two principal approximations. First, we have replaced the problem of a $4f^{n-1}$ or $4f^{n+1}$ impurity in a rare earth metal host by the more tractable question of determining the difference in total energy per cell of two metals, one with the initial state $4f^n(5d, 6s)^m$ configuration at every site and the other having the $4f^{n\pm1}(5d, 6s)^{m+1}$ final state configuration in each unit cell. This simplification is quite plausible for localized electrons, whose excitation is primarily a single-site process.

Second, we assume charge neutrality of all configurations, modifying in particular the number of conduction electrons in the final state to compensate the change in 4f occupancy. Neutral final states are appropriate to the XPS and BIS measurements with which we will compare results. This approximation is consistent with the first assumption of ignoring variations in intercellular contributions to the 4f excitation energies, and it provides a physically reasonable, well-defined means for describing the conduction electron response to the localized $4f^{n\pm1}$ impurity. In the case of $\Delta_-(4f^n \rightarrow 4f^{n-1})$, corresponding to 4f electron removal, we have designated the assumption of neutral final states the *complete screening approximation* (Herbst et al. 1976a) since an additional unit conduction electron charge is confined to the neutral excited cell. We assess the impact of that approximation in section 5 by examining

the zero-screening limit in which no additional screening charge is present in the final state cell.

Our insistence on neutral final states may seem surprising given the conventional description of photoemission (see, for example, Gadzuk 1978) in which the many-body states are considered to have definite electron number N. In that view the XPS final state is the product of a high-energy plane wave and an $(N-1)$-electron many-body state. Core electron ejection reduces N to $N-1$, the number of valence electrons in the WS cell surrounding the depleted core is unchanged, and that cell has unit positive charge.

In extended systems, however, the many-body states are characterized by a constant electrochemical potential (and an indefinite number of electrons). There are two independent reasons for this: (i) in an XPS experiment the sample is grounded so that electrons can flow into it and compensate the ejected ones, and (ii) the Coulomb forces in metallic systems move any excess charge to the surface. The second reason (which follows from Poisson's equation) couples with the first to insure charge neutrality of the sample. Since our final states are by construction translationally invariant (the 4f number in every cell is the same), this implies in turn that every WS cell in the final state must be electrically neutral. In particular, a photoionized cell having one fewer core electron must contain an additional valence, or conduction, electron.

What makes the neutral final state or complete screening condition approximate rather than exact is the time required for the system to respond to the core excitation (the various time scales are discussed by Gadzuk (1978)). In this work we are concerned only with the excitation energy, the threshold for absorption. Since the threshold corresponds to a long-time process (in the sense of a Fourier transform of a correlation function), the actual dynamics of complete screening will have negligible effect on the threshold energy but will affect the lineshape.

2.1. *Relativistic Hartree–Fock total energies*

To derive the total energies entering $\Delta_\pm$ we perform relativistic Hartree–Fock (RHF) computations, and eq. (2) becomes

$$\Delta_\pm(4f^n \to 4f^{n\pm1}) = \xi_\pm(4f^n \to 4f^{n\pm1}) + E^{\mathrm{RHF}}_{\mathrm{metal}}[4f^{n\pm1}(5d,6s)^{m\mp1}] - E^{\mathrm{RHF}}_{\mathrm{metal}}[4f^n(5d,6s)^m], \tag{3}$$

where $E^{\mathrm{RHF}}_{\mathrm{metal}}$ now denotes the total RHF energy per cell. Since the Hartree–Fock approximation is employed, we introduce the correlation energy difference terms $\xi_\pm$ which serve to approximately correct the RHF excitation energies for correlation effects; the use of atomic spectral data to estimate these terms is described in section 2.3.

Our procedure for deriving $E^{\mathrm{RHF}}_{\mathrm{metal}}$ is comprised of four major steps. First, we perform RHF computations for the $4f^n 5d^{m-1} 6s$ *atomic* configurations most closely approaching those of the initial and final states in the metal. Solutions are obtained within the average of LS configuration scheme (Lindgren and Rosén 1974) which averages the L, S, M_L, and M_S quantum numbers of the open shells. A complete, self-consistent calculation is carried out for each configuration.

Second, the RA method is used to construct band potentials for the metals. The atomic wave functions are truncated at r_{WS} and normalized to unity within the WS sphere by a simple rescaling which preserves wave function shape for $r \leqslant r_{WS}$; only the 5d and 6s wave functions are significantly affected by this process (cf. fig. 1). Recomputation of the RHF potentials with the truncated wave functions yields l-dependent crystal potentials. For any given configuration the 6s-band minimum ε_{Γ_1} and the extrema of the 5d bands are calculated by imposing WS-type boundary conditions on the large components of the wave functions obtained from integration of the RHF equations. That is, the 5d and 6s RHF equations are solved for wave functions over a range of energies ε. The value of ε ($\varepsilon_{5d_{min}}$ or ε_{Γ_1}) for which the large component has zero radial derivative at r_{WS} specifies the minimum of the corresponding band; the ε ($\varepsilon_{5d_{max}}$) for which the large component of a 5d wave function is zero at r_{WS} determines the maximum of the 5d band. 5d–6s hybridization is not included; we do not expect it to have any substantial impact on total band energy differences.

Third, the band calculations are iterated to self-consistency in the following way. The 5d and 6s occupation numbers are allowed to become non-integral, and a parabolic 6s-band and a rectangular 5d-band density of states are assumed. The Fermi energy is determined by filling the bands to the appropriate conduction electron occupancy. 5d and 6s wave functions are then computed at average energies in the occupied bands, and the 5d and 6s crystal potentials are reconstructed with these average wave functions. Band extrema are again determined and the procedure repeated until ε_{Γ_1} and the 5d-band extrema have converged to within 0.003 eV.

Finally, the total RHF band energy per cell, E_{band}^{RHF}, is calculated. E_{band}^{RHF} is defined by the standard atomic expressions but is computed with the renormalized wave functions, including the self-consistent average 5d and 6s conduction band wave functions and occupation numbers. E_{band}^{RHF} differs from E_{metal}^{RHF} of eq. (3) only by the exclusion of the Hund-rule correction for the 4f electrons discussed in section 2.2.

Although the detailed conduction band structure of the rare-earth metals is intricate and fascinating (Liu 1978), our simplified treatment of it for the purpose of deriving 4f excitation energies is motivated by computational viability. The E_{band}^{RHF} terms are on the order of 10^5 eV while $\Delta_{\pm}$ are of order 1 eV. It is essential, therefore, that the same well-controlled algorithm be applied in calculating both the initial and final state total energies since their *difference* is of interest.

2.2. *Hund's rules and multiplet theory*

It is well known (e.g., Elliott 1972) that to excellent first approximation the 4f electrons in the ground configurations of the metals are in the Hund-rule states (i.e., maximum S, maximum L consistent with that S, and $J = L \pm S$ for $n \gtrless 7$). Aside from relatively small conduction electron polarization contributions and crystal field effects which are more important for the lighter elements, the magnetic moments of the metals agree reasonably well with those specified by the Hund-rule quantum numbers of the 4f shell (Rhyne 1972, McEwen 1978). Our RHF calculations are done in the LS-average scheme, however, so that E_{band}^{RHF} for the initial states must be corrected to properly describe the Hund-rule 4f states. Since the atomic 4f wave

function character is preserved in the metal by the RA method, the correction is readily determined via non-relativistic (NR) Condon–Slater–Racah atomic multiplet theory (see, e.g., Slater 1960a). The LS multiplets for f^n configurations and their energies expressed in terms of electrostatic integrals have been tabulated by Nielson and Koster (1963), and the average of configuration energies are given by Slater (1960b), among other sources.

Justification for employing the NR multiplet energy expressions lies in the fact that the RHF electrostatic integrals $R^k(nlj, n'l'j')$ calculated in the *LS*-average scheme for the 4f (as well as the 5d and 6s) electrons of the lanthanides are not very dependent on j and j'. If this independence were exact, then the relativistically correct multiplet expressions would reduce to their NR analogs because the RHF equations reduce to the NRHF forms when the velocity of light is taken to be infinite. The complications of jj coupling are circumvented by averaging the $R^k(nlj, n'l'j')$ over the values of j and j' to yield an effective $R^k(nl, n'l')$ which is then used in the NR multiplet expressions.

We include the 4f spin–orbit contribution to each total energy by calculating the expectation value of $\lambda \boldsymbol{L}\cdot\boldsymbol{S}$ for the Hund-rule multiplet, where λ is given (Blume et al. 1964) by

$$\lambda = \pm\, \xi_{4f}/2S \quad (n \gtrless 7). \tag{4}$$

ξ_{4f} is obtained from the RHF one-electron eigenvalues:

$$\xi_{4f} = \tfrac{2}{7}(\varepsilon_{4f_{7/2}} - \varepsilon_{4f_{5/2}}), \tag{5}$$

and we find

$$\langle \lambda \boldsymbol{L}\cdot\boldsymbol{S}\rangle = -\tfrac{1}{7}(\varepsilon_{4f_{7/2}} - \varepsilon_{4f_{5/2}}) \begin{cases} L+1 & n < 7 \\ L & n \gtrless 7. \end{cases} \tag{6}$$

To illustrate these procedures we take the $4f^2$ configuration relevant to Pr metal as an example. The average of LS configuration energy is (Slater 1960b)

$$E_{ac}(4f^2) = F^0(4f,4f) - \tfrac{4}{195}F^2(4f,4f) - \tfrac{2}{143}F^4(4f,4f) - \tfrac{100}{5577}F^6(4f,4f), \tag{7}$$

and the electrostatic energy of the $^3H_4$ Hund-rule ground multiplet is (Nielson and Koster 1963)

$$E_{gnd}[4f^2(^3H)] = F^0(4f,4f) - \tfrac{1}{9}F^2(4f,4f) - \tfrac{17}{363}F^4(4f,4f) - \tfrac{25}{14157}F^6(4f,4f). \tag{8}$$

For $F^2(4f,4f)$ we use the following multiplicity-weighted average:

$$\begin{aligned} F^2(4f,4f) = {} & \tfrac{6}{14}\left[\tfrac{6}{14}F^2(4f_{5/2},4f_{5/2}) + \tfrac{8}{14}F^2(4f_{5/2},4f_{7/2})\right] \\ & + \tfrac{8}{14}\left[\tfrac{6}{14}G^2(4f_{5/2},4f_{7/2}) + \tfrac{8}{14}F^2(4f_{7/2},4f_{7/2})\right]. \end{aligned} \tag{9}$$

The renormalized RHF integrals on the right side are all 12.0 ± 0.1 eV for $Pr(4f^2)$. $F^4(4f,4f)$ and $F^6(4f,4f)$ are similarly obtained. (The greatest disparity among RHF electrostatic integrals corresponding to the same NR quantity occurs for the $F^2(4fj, 4fj')$ of the heaviest elements. The largest of these integrals are 17.3 ± 0.3 eV, so that the left side of eq. (9) or its analogs for $F^4(4f,4f)$ and $F^6(4f,4f)$ does not

depart appreciably from any of the individual terms on the right.) The spin–orbit contribution (zero in the configurational average) is

$$\langle 4f^2(^3H_4)|\lambda \boldsymbol{L}\cdot\boldsymbol{S}|4f^2(^3H_4)\rangle = -\tfrac{6}{7}(\varepsilon_{4f_{7/2}} - \varepsilon_{4f_{5/2}}) \tag{10}$$

for the Hund-rule multiplet. The resultant correction to the LS-average total energy is thus

$$\begin{aligned} E_{4f\,HRC}(4f^2) &\equiv E_{gnd}[4f^2(^3H)] - E_{ac}(4f^2) + \langle 4f^2(^3H_4)|\lambda \boldsymbol{L}\cdot\boldsymbol{S}|4f^2(^3H_4)\rangle \\ &= -\tfrac{53}{585}F^2(4f,4f) - \tfrac{155}{4719}F^4(4f,4f) + \tfrac{2975}{184041}F^6(4f,4f) \\ &\quad -\tfrac{6}{7}(\varepsilon_{4f_{7/2}} - \varepsilon_{4f_{5/2}}) \\ &= -1.5\,\text{eV}. \end{aligned} \tag{11}$$

Although miniscule in comparison with E^{RHF}_{band}, $E_{4f\,HRC}$ is on the same 1 eV scale as $\Delta_{\pm}$.

In eq. (3) E^{RHF}_{metal} for the initial states includes the 4f Hund-rule correction:

$$E^{RHF}_{metal}[4f^n(5d,6s)^m] \equiv E^{RHF}_{band}[4f^n(5d,6s)^m] + E_{4f\,HRC}(4f^n), \tag{12}$$

and we will focus on results in which the 4f final states are given by Hund's rules as well. We emphasize, however, that the ability to use atomic multiplet theory is a distinct advantage of our method since it clearly allows derivation of excitation energies corresponding to *any* set of initial and final 4f states, not only those specified by Hund's rules.

2.3. *Correlation energy corrections* $\xi_{\pm}$

Although the trends differ, departures of calculated *atomic* excitation energies from the values determined by spectroscopic measurements are on the order of eV for the 3d electrons of the iron series elements whether the calculations are of the NRHF (Watson 1960), RHF (Kagawa 1975), or local spin-density functional (Harris and Jones 1978) variety. Departures of equal magnitude (i.e., on the same scale as $\Delta_{\pm}$) occur for the atomic 4f electrons of the lanthanide row. Figure 3 displays RHF 4f binding energies for the ground states of the lanthanide atoms together with estimated spectroscopic values and the few available direct photoemission measurements, and it can be seen that the discrepancies, or the correlation energy differences, range from $\sim$1 to $\sim$4 eV. For $\Delta_{\pm}$ the issue of correlation effects is exacerbated both by the metallic environment as well as by the fact that not only a change in 4f number but a concomitant change in conduction electron (chiefly 5d) occupancy is involved. In the absence of any accurate theoretical procedure for calculating such effects, we exploit atomic spectral information to estimate them.

Specifically, the free atom transition corresponding to $\Delta_+(4f^n \to 4f^{n+1})$ for the trivalent metals is $4f^n\,5d^2\,6s \to 4f^{n+1}\,5d\,6s$, and we use the associated correlation energy difference $\xi_+(4f^n \to 4f^{n+1})$ as an additive correlation correction to $\Delta_+(4f^n \to 4f^{n+1})$ (cf. eq. (3)). $\xi_+(4f^n \to 4f^{n+1})$ is defined by

$$\begin{aligned} \xi_+(4f^n \to 4f^{n+1}) &\equiv E_{corr}(4f^{n+1}\,5d\,6s) - E_{corr}(4f^n\,5d^2\,6s) \\ &\equiv [E(4f^{n+1}\,5d\,6s) - E(4f^n\,5d^2\,6s)]_{expt} \\ &\quad - [E(4f^{n+1}\,5d\,6s) - E(4f^n\,5d\,6s)]^{RHF}_{atom\ gnd}, \end{aligned} \tag{13}$$

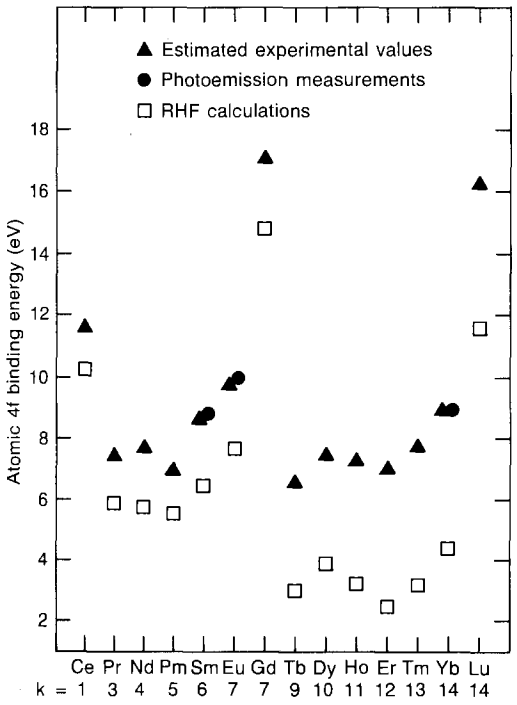

Fig. 3. 4f electron binding energies for the ground states of lanthanide *atoms*. Triangles are estimated experimental values derived by combining the known ionization potentials (Martin et al. 1974) with estimates of the ion spectral term energies (Brewer 1971b). Circles represent the results of direct photoemission measurements on Sm, Eu, and Yb vapors (Lee et al. 1977). Squares denote calculations of atom → (4f ion) total energy differences, multiplet theory having been used to correct the *LS*-average results to correspond to the Hund-rule terms (Herbst et al. 1978). k is the number of 4f electrons in the atomic ground state; it is equal to the metallic ground state 4f occupancy n for La, Ce, Eu, Gd, Yb, and Lu, but $k = n + 1$ for the other elements.

where the first term in square brackets is obtained from available spectral data (Martin et al. 1978, Brewer 1971a). The second term in square brackets is derived from our RHF calculations for the same transition, with multiplet theory (cf. section 2.2) serving to place the 4f, 5d, and 6s electrons into the appropriate ground states.

Except for divalent Eu and Yb, the atomic transition corresponding to $\Delta_-(4f^n \to 4f^{n-1})$ is $4f^n\,5d^2\,6s \to 4f^{n-1}\,5d^3\,6s$ for which, unfortunately, no reliable spectral information exists. We are consequently compelled to use the data for the $4f^n\,5d\,6s \to 4f^{n-1}\,5d^2\,6s$ transition involving the same number of 4f electrons but corresponding to the preceding element in the periodic table. That is, we approximate $\xi_-(4f^n \to 4f^{n-1})$ by

$$\begin{aligned}\xi_-(4f^n \to 4f^{n-1}) &\equiv E_{\text{corr}}(4f^{n-1}\,5d^3\,6s) - E_{\text{corr}}(4f^n\,5d^2\,6s)\\ &\sim E_{\text{corr}}(4f^{n-1}\,5d^2\,6s) - E_{\text{corr}}(4f^n\,5d\,6s)\\ &= -\xi_+(4f^{n-1} \to 4f^n). \qquad (14)\end{aligned}$$

$\xi_-(4f^8 \to 4f^7)$ for the $4f^8\,5d^2\,6s \to 4f^7\,5d^3\,6s$ transition relevant to $\Delta_-(4f^8 \to 4f^7)$ of Tb, for example, is thus taken to be the correlation energy difference $[-\xi_+(4f^7 \to 4f^8)]$ for the $4f^8\,5d\,6s \to 4f^7\,5d^2\,6s$ transition in Gd. Since the localized atomic character of the 4f electrons is maintained in the metals, our assumption of common atomic and metallic correlation effects as embodied in the $\xi_\pm$ terms of eq. (3) is quite reasonable. Introduction of the necessary approximation represented by eq. (14), however, leads to a greater uncertainty, perhaps as large as 1 eV, in ξ_- and hence in our Δ_- results for the heavier elements.

TABLE 1
Ground state atomic and metallic electron configurations (omitting the closed $1s^2 \ldots 4d^{10}\,5s^2\,5p^6$ xenon-like core), crystal structures, and Wigner–Seitz radii r_{WS} of the lanthanide elements.

Element	Atomic configuration	Metallic configuration	Crystal structure	r_{WS} (a.u.)
La	$5d\,6s^2$	$(5d, 6s)^3$	dhcp	3.92
Ce	$4f\,5d\,6s^2$	$4f(5d, 6s)^3$	fcc	3.81
Pr	$4f^3\,6s^2$	$4f^2(5d, 6s)^3$	dhcp	3.82
Nd	$4f^4\,6s^2$	$4f^3(5d, 6s)^3$	dhcp	3.80
Pm	$4f^5\,6s^2$	$4f^4(5d, 6s)^3$	dhcp	3.78
Sm	$4f^6\,6s^2$	$4f^5(5d, 6s)^3$	rhomb	3.77
Eu	$4f^7\,6s^2$	$4f^7(5d, 6s)^2$	bcc	4.26
Gd	$4f^7\,5d\,6s^2$	$4f^7(5d, 6s)^3$	hcp	3.76
Tb	$4f^9\,6s^2$	$4f^8(5d, 6s)^3$	hcp	3.72
Dy	$4f^{10}\,6s^2$	$4f^9(5d, 6s)^3$	hcp	3.70
Ho	$4f^{11}\,6s^2$	$4f^{10}(5d, 6s)^3$	hcp	3.69
Er	$4f^{12}\,6s^2$	$4f^{11}(5d, 6s)^3$	hcp	3.67
Tm	$4f^{13}\,6s^2$	$4f^{12}(5d, 6s)^3$	hcp	3.65
Yb	$4f^{14}\,6s^2$	$4f^{14}(5d, 6s)^2$	fcc	4.05
Lu	$4f^{14}\,5d\,6s^2$	$4f^{14}(5d, 6s)^3$	hcp	3.62

3. Results for the metals

Table 1 lists the ground state atomic and metallic configurations of the lanthanide elements, the crystal structures of the metals, and the Wigner–Seitz radii used here which were computed from the lâttice constants given by Beaudry and Gschneidner (1978). A 4f → valence electron conversion occurs on formation of the metals Pr–Sm and Tb–Tm; i.e., those metals have one fewer 4f (and one more valence) electron than the corresponding atoms. This change in 4f number has a marked influence on the atom → solid shifts of core level binding energies in those elements, as calculations based on the techniques described here have shown (Herbst 1982, 1983). The atomic and metallic 4f occupancies of La, Ce, Eu, Gd, Yb, and Lu are the same. It is clear that the trivalent metals display the lanthanide contraction, their r_{WS} values decreasing generally through the series. As the atomic number Z increases, the addition of another 4f electron does not completely screen the larger nuclear charge, and the lattice contracts.

3.1. *Conduction band structure*

Results of our calculations for the metals are summarized in fig. 4, which shows the extent of the 5d bands, the Fermi level ε_F, and the 6s-band minimum ε_{Γ_1}. Table 2 enumerates ε_{Γ_1}, the 5d-band minimum $\varepsilon_{5d_{min}}$ and maximum $\varepsilon_{5d_{max}}$, the 5d bandwidth W_{5d}, ε_F, and n_{6s}, the number of 6s electrons in the occupied bands (the 5d occupancy is equal to $m - n_{6s}$, where m is the valence). We note that the energy zero is the crystal zero, which is the bulk metal analog of the vacuum zero and differs from the latter by the surface dipole term D as defined by Seitz (1940). Put another

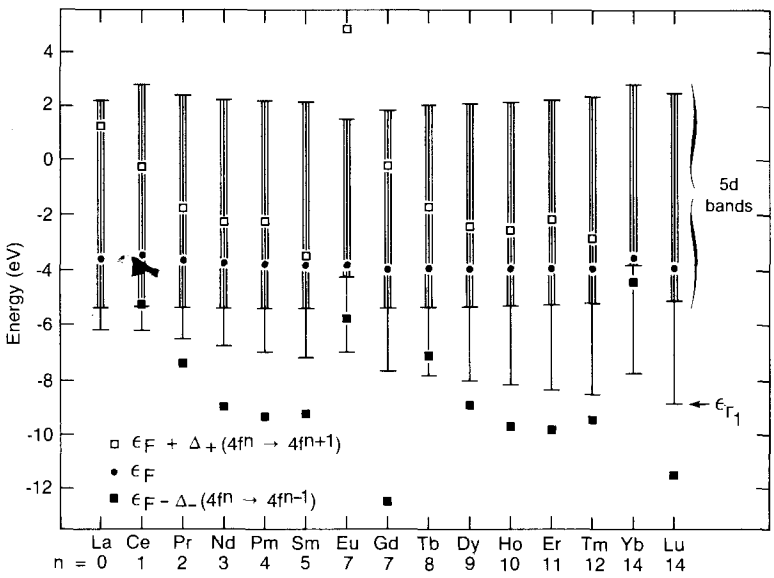

Fig. 4. Conduction band limits, Fermi levels, and 4f excitation energies calculated for the lanthanide metals.

TABLE 2

Band parameters from our calculations for the metallic ground states. ε_{Γ_1} is the 6s-band minimum, $\varepsilon_{5d_{min}}$ and $\varepsilon_{5d_{max}}$ the minimum and maximum of the 5d bands as determined by imposition of Wigner–Seitz boundary conditions, W_{5d} the 5d bandwidth, ε_F the Fermi energy, and n_{6s} the 6s electron occupancy. All energies in eV.

Metal	ε_{Γ_1}	$\varepsilon_{5d_{min}}$	$\varepsilon_{5d_{max}}$	W_{5d}	ε_F	n_{6s}
La	−6.2	−5.3	2.2	7.6	−3.6	0.7
Ce	−6.2	−5.3	2.8	8.1	−3.5	0.7
Pr	−6.5	−5.4	2.4	7.8	−3.6	0.8
Nd	−6.8	−5.4	2.2	7.6	−3.7	0.8
Pm	−7.0	−5.4	2.2	7.6	−3.8	0.9
Sm	−7.2	−5.4	2.2	7.5	−3.8	0.9
Eu	−7.0	−4.2	1.5	5.8	−3.8	1.2
Gd	−7.7	−5.4	1.9	7.2	−4.0	1.1
Tb	−7.8	−5.3	2.0	7.4	−3.9	1.1
Dy	−8.0	−5.3	2.1	7.4	−3.9	1.2
Ho	−8.2	−5.3	2.2	7.4	−3.9	1.2
Er	−8.3	−5.2	2.2	7.5	−3.9	1.3
Tm	−8.5	−5.2	2.4	7.5	−3.9	1.3
Yb	−7.7	−3.8	2.8	6.6	−3.5	1.6
Lu	−8.8	−5.1	2.5	7.6	−3.9	1.5

way, the crystal zero is the electrostatic potential on the boundary of a WS cell; as Bardeen (1936) emphasizes, this definition implies $D = 0$ if the electron distribution in a WS sphere at the surface of a metal is the same as that of an interior WS sphere.

We find that the 5d bands are 7–8 eV wide for the trivalent metals and somewhat narrower, 6–7 eV, for divalent Eu and Yb. The 4f complements of Eu and Yb are larger by one than trivalency would imply (a consequence of the energetic favorability of a half-filled or filled 4f shell), and the relatively smaller effective nuclear charge is responsible for larger lattice constants and correspondingly narrower 5d bands. Our 5d bandwidths are in reasonable agreement with those of conventional band structure calculations (see the review by Liu (1978)), even though the methods of potential construction are quite different.

Figure 4 and table 2 indicate that ε_{Γ_1} progressively decreases across the row, a corollary effect of the lanthanide contraction, while the 5d bands occupy roughly the same energy region. The decline in ε_{Γ_1} is accompanied by an increase in the 6s-band occupation number n_{6s}, as the final column of table 2 shows. Except for Yb, all the n_{6s} values are near unity and are thus consistent with our choice of the input $4f^n 5d^{m-1} 6s$ atomic configurations having a single 6s electron.

The small (0.5 eV) variation of the Fermi levels and the similarity of the gross band structures suggest that the work functions of the lanthanide metals have no strong dependence on Z. Indeed, available measured work functions for polycrystalline Ce, Nd, Sm, Eu, Gd, Er, and Yb are all 3.0 ± 0.5 eV (Hölzl and Schulte 1979). This experimental fact in conjunction with our ε_F values implies that the surface dipole energy also varies slowly with Z and that $D \sim 1$ eV (relative to the crystal zero).

3.2. *4f levels*

$\Delta_\pm$ results corresponding to the Hund-rule initial and final 4f states, the lowest excitation energies, are included in fig. 4 as effective single-particle quantities (cf. fig. 2). Except for europium most of the empty 4f levels (Δ_+) lie within the unoccupied 5d bands, while the majority of the filled 4f levels (Δ_-) are below the conduction bands. Certainly the most significant feature of the results, however, is that Δ_- is smallest for Ce, Eu, and Yb, and Δ_+ is least for Sm and Tm. The minimal excitation energies imply that valence transitions involving $4f \longleftrightarrow$ conduction electron conversion (generated by pressure and temperature changes, for example, or by compound formation) will be most probable for these elements. The observation of mixed valence behavior in materials such as $CePd_3$, SmS, EuTe, TmSe, and $YbAl_2$ containing only these five lanthanides lends ample credence to the implication (for reviews of mixed valence phenomena see Campagna et al. (1976), Parks (1977), Lawrence et al. (1981), Falicov et al. (1981), Wachter and Boppart (1982), Müller-Hartmann et al. (1985), Kasuya and Saso (1985)). Study of the lattice constant variation of the 4f levels for several of the metals reveals fascinating pressure-induced valence transitions (section 7).

Solid state vs. atomic contributions to the excitation energies can be analyzed by

separating $\Delta_\pm$ as defined by eq. (3) into four components:

$$\begin{aligned}\Delta_\pm(4f^n \to 4f^{n\pm1}) &= \xi_\pm(4f^n \to 4f^{n\pm1}) \\ &\quad + \{E^{\mathrm{RHF}}_{\mathrm{atom}}[4f^{n\pm1}(5d,6s)^{m\mp1}] - E^{\mathrm{RHF}}_{\mathrm{atom}}[4f^n(5d,6s)^m]\} \\ &\quad + [E_{4f\,\mathrm{HRC}}(4f^{n\pm1}) - E_{4f\,\mathrm{HRC}}(4f^n)] \\ &\quad + \langle\{E^{\mathrm{RHF}}_{\mathrm{band}}[4f^{n\pm1}(5d,6s)^{m\pm1}] - E^{\mathrm{RHF}}_{\mathrm{atom}}[4f^{n\pm1}(5d,6s)^{m\mp1}]\} \\ &\quad - \{E^{\mathrm{RHF}}_{\mathrm{band}}[4f^n(5d,6s)^m] - E^{\mathrm{RHF}}_{\mathrm{atom}}[4f^n(5d,6s)^m]\}\rangle \\ &\equiv \xi_\pm + \delta E(\mathrm{atom}) + \delta E(\mathrm{Hund}) + \delta E(\mathrm{atom} \to \mathrm{band}). \end{aligned} \tag{15}$$

δE(atom) is the difference between the initial and final state atomic total energies, $E^{\mathrm{RHF}}_{\mathrm{atom}}$, from our LS-average RHF computations, and δE(Hund) represents the net energy change due to placing the 4f electrons of the initial and final states into the appropriate Hund-rule multiplets (cf. section 2.2). δE(atom → band) is the difference in atom → band energy reduction between the initial and final states which results from the self-consistent band calculations for the 5d and 6s conduction electrons. These components of Δ_+ and Δ_- are listed in table 3 and table 4, respectively.

For the present review we have repeated our earlier calculations, incorporating improved convergence procedures for the band computations and exploiting the more recent spectral data of Martin et al. (1978) to estimate the $\xi_\pm$ corrections. The largest departures from our original relativistic work (Herbst et al. 1976a, 1978) are increases of 0.5 eV in Δ_+ for Gd and Δ_- for Er, and 0.3 eV in Δ_- for Ho. All other changes in the entries of tables 2–4 are at most 0.2 eV. In tables 3 and 4 we also include $\Delta_\pm$ results for promethium as well as for other 4f excitations in Sm, Eu, Tm, and Yb pertinent to mixed-valent systems.

From tables 3 and 4 it is apparent that the correlation energy corrections $\xi_\pm$ are significant, and their signs (cf. the first lines of eqs. (13) and (14)) indicate that

TABLE 3

Components of $\Delta_+(4f^n \to 4f^{n+1})$ as defined by eq. (15). Both initial and final 4f states are specified by Hund's rules. All energies in eV.

Metal	Transition	ξ_+	δE(atom)	δE(Hund)	δE(atom → band)	Δ_+
La	$4f^0 \to 4f^1$	−1.0	3.3	−0.1	2.6	4.9
Ce	$4f^1 \to 4f^2$	−1.0	2.6	−1.1	2.7	3.2
Pr	$4f^2 \to 4f^3$	−1.1	2.0	−1.7	2.7	1.9
Nd	$4f^3 \to 4f^4$	−1.6	1.5	−1.1	2.7	1.5
Pm	$4f^4 \to 4f^5$	−1.6	1.0	−0.6	2.7	1.6
Sm	$4f^5 \to 4f^6$	−1.9	0.7	−1.2	2.7	0.3
	$4f^6 \to 4f^7$	−3.1	5.6	−1.8	3.2	4.0
Eu	$4f^7 \to 4f^8$	−3.4	5.6	3.9	2.5	8.6
Gd	$4f^7 \to 4f^8$	−3.3	0.2	4.1	2.8	3.7
Tb	$4f^8 \to 4f^9$	−3.2	+0.0	2.6	2.8	2.2
Dy	$4f^9 \to 4f^{10}$	−2.9	−0.1	1.7	2.9	1.5
Ho	$4f^{10} \to 4f^{11}$	−3.6	−0.2	2.3	2.9	1.4
Er	$4f^{11} \to 4f^{12}$	−3.9	−0.2	2.9	2.9	1.8
Tm	$4f^{12} \to 4f^{13}$	−3.8	−0.2	2.1	3.0	1.1
	$4f^{13} \to 4f^{14}$	−3.5	6.1	0.6	3.1	6.4

TABLE 4
Components of $\Delta_-(4f^n \rightarrow 4f^{n-1})$ as defined by eq. (15). Both initial and final 4f states are specified by Hund's rules. All energies in eV.

Metal	Transition	ξ_-	δE(atom)	δE(Hund)	δE(atom → band)	Δ_-
Ce	$4f^1 \rightarrow 4f^0$	1.0	2.6	0.2	−1.9	1.8
Pr	$4f^2 \rightarrow 4f^1$	1.0	3.3	1.3	−1.8	3.8
Nd	$4f^3 \rightarrow 4f^2$	1.1	3.9	2.0	−1.8	5.2
Pm	$4f^4 \rightarrow 4f^3$	1.6	4.4	1.4	−1.8	5.5
Sm	$4f^5 \rightarrow 4f^4$	1.6	4.9	0.8	−1.8	5.4
Eu	$4f^7 \rightarrow 4f^6$	1.9	−0.4	2.3	−1.8	1.9
	$4f^6 \rightarrow 4f^5$	1.9	5.3	1.5	−0.8	7.9
Gd	$4f^7 \rightarrow 4f^6$	1.9	5.6	2.7	−1.7	8.5
Tb	$4f^8 \rightarrow 4f^7$	3.3	5.9	−4.3	−1.8	3.2
Dy	$4f^9 \rightarrow 4f^8$	3.2	6.2	−2.7	−1.8	4.9
Ho	$4f^{10} \rightarrow 4f^9$	2.9	6.4	−1.7	−1.8	5.8
Er	$4f^{11} \rightarrow 4f^{10}$	3.6	6.5	−2.4	−1.8	5.9
Tm	$4f^{12} \rightarrow 4f^{11}$	3.9	6.6	−3.2	−1.8	5.5
Yb	$4f^{14} \rightarrow 4f^{13}$	3.5	0.2	−0.7	−2.1	0.9
	$4f^{13} \rightarrow 4f^{12}$	3.8	6.7	−2.3	−0.9	7.4
Lu	$4f^{14} \rightarrow 4f^{13}$	3.5	6.7	−0.8	−1.9	7.6

correlation is more important in the configuration having one more 4f and one fewer 5d electron. The magnitude of $\xi_\pm$ is larger in the second half of the series. When the 4f number is less than or equal to 7 all 4f spins are parallel in the Hund-rule state, but for $n > 7$ both majority and minority spins are present and correlation effects are more substantial.

The positive (negative) signs of the δE(atom → band) components of Δ_+ (Δ_-) simply mean that the energy lowering arising from conduction band formation is greater for the configuration with more conduction electrons, which is the initial state for Δ_+ and the final state for Δ_-. Tables 3 and 4 show that the sum $\xi_\pm + \delta E$(atom → band), whose terms are of opposite sign, displays much smaller variation through the series (−1.0 to 1.7 eV, and −0.9 to 2.9 eV, respectively) than does δE(atom) + δE(Hund), the sum of the atomic RHF terms alone (−0.5 to 9.5 eV, and −0.5 to 8.3 eV, respectively). The trend in the latter combination is qualitatively similar to that of $\Delta_\pm$, but the correlation ($\xi_\pm$) and band contributions (δE(atom → band)) produce quantitative differences. For more tightly bound core electrons such as the 3d states the atomic terms dominate the excitation energy (Herbst and Wilkins 1979a).

4. Comparison with experiment

4.1. *Metals*

Systematic XPS and BIS investigations of all the rare earth metals (excepting radioactive Pm) have been conducted by Baer and co-workers (Baer and Lang 1979, Lang and Baer 1980, Lang et al. 1979, 1981). The structures in the spectra reflect

transitions between the Hund-rule $4f^n$ state and the accessible multiplets of the final $4f^{n-1}$ (XPS) and $4f^{n+1}$ (BIS) configurations. It has been demonstrated (Cox 1975, Cox et al. 1981) that the relative intensities of the structures observed in both kinds of spectra are approximated well by the squares of the fractional parentage coefficients, which appear in expansions of the $4f^{n\pm1}$ states in terms of those belonging to $4f^n$. (The work of Cox assumed *LS* coupling; more recently Gerken (1983) has computed relative intensities as well as final state energy separations in intermediate coupling for XPS, obtaining somewhat improved results for the heavier metals.) Lang et al. (1979, 1981) used these coefficients, together with final state splittings estimated from ultraviolet absorption data on lanthanide ions, to identify the observed lines unambiguously.

In general the structures of minimal excitation energy (relative to ε_F) correspond to the Hund-rule $4f^{n\pm1}$ final states, and fig. 5 compares those measured levels with our $\Delta_\pm$ calculations. The qualitative agreement between theory and experiment is excellent; in particular, both sets of results indicate 4f levels nearest the Fermi energy in Ce, Sm, Eu, Tm, and Yb. Quantitatively, the largest departures of the calculated from the measured values are ~ 1 eV and occur for Δ_- of the heavier elements. We believe they arise primarily from the approximation for the correlation terms specified by eq. (14), i.e., $\xi_- \sim -\xi_+$. In the second half of the series the atomic correlation energy differences ξ_+ are greater (cf. table 3), and we expect the uncertainty associated with that approximation to be greater also.

Aside from Δ_- for Ce, Yb and Δ_+ for Eu, the calculated Δ_+ (Δ_-) values are all lower (higher) than experiment. Lang et al. (1979, 1981) have speculated that our

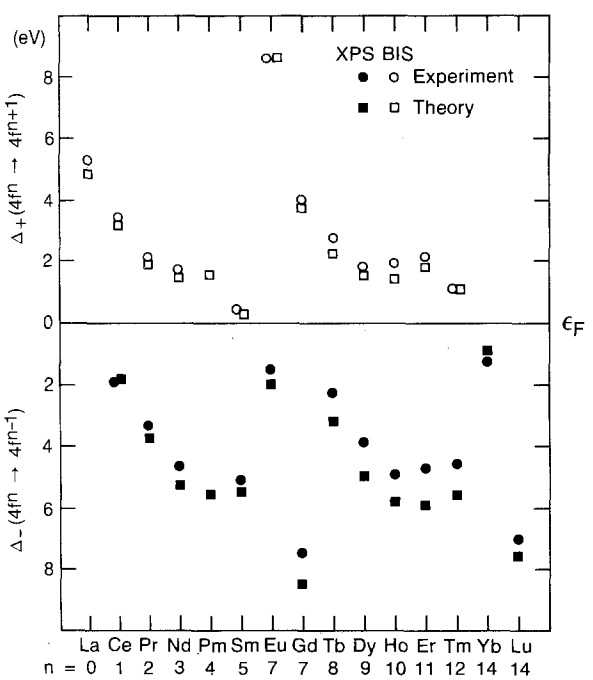

Fig. 5. Comparison of $\Delta_+(4f^n \rightarrow 4f^{n+1})$ and $\Delta_-(4f^n \rightarrow 4f^{n-1})$ calculated for the Hund-rule initial and final 4f states with the minimal excitation energies measured by XPS (filled levels) and BIS (empty levels) for the lanthanide metals. The experimental values are those of Lang et al. (1981) with the exception of Δ_- for Ce, which was taken from the work of Platau and Karlsson (1978) and Johansson et al. (1978).

simplified conduction band structure and the placement of ε_F in it are at least partially responsible for these systematic shifts. In our opinion some of the shifts may be attributed to the approximate band structure insofar as it neglects 5d–6s hybridization. This opinion is motivated by the following consideration. The 5d bands are less than half-filled, and the inclusion of hybridization will lower the total energy more for the states which have more conduction electrons. Since the initial state of Δ_+ and the final state of Δ_- have one more band electron (cf. eq. (3)), this energy reduction will *increase* Δ_+ and *decrease* Δ_- relative to the results in fig. 5, i.e., in a direction toward the measurements in each case. We expect such effects to be a few tenths of an eV at most, however, on the order of the departures in the first half of the series but small compared to the uncertainties introduced by eq. (14) for the heavier metals.

4.1.1. *Multiplet splittings*

We emphasize that the placement of the excitation energies relative to ε_F depends upon a $\Delta_\pm$ calculation for some specific 4f final state, such as the Hund-rule term. The energies of the other final states with respect to that level can be predicted by multiplet theory (e.g., Gerken 1983) and the relative intensities by the coefficients of fractional parentage. Some of the final state energetics can be straightforwardly understood, and we consider two sets of examples.

First, the XPS spectra of Yb and Lu ($4f^{14}$ initial states) consist of two structures belonging to the spin–orbit-split $^2F_{5/2}$ and $^2F_{7/2}$ final states, the only ones possible. The line separations observed by Lang et al. (1981) are 1.3 eV (Yb) and 1.5 eV (Lu). Each splitting can be estimated by the difference $\varepsilon_{4f_{7/2}} - \varepsilon_{4f_{5/2}}$ of the $4f_{5/2}$ and $4f_{7/2}$ eigenvalues from our calculations for the $4f^{13}$ final state configurations. We find separations of 1.6 eV (Yb) and 1.8 eV (Lu) which are in reasonable accord with the experimental values.

Second, while the Hund-rule XPS final states for the heavier elements correspond to the photoejection of a minority-spin 4f electron from the over-half-filled 4f shell, many of the peaks at higher binding energies involve excitation of a majority-spin 4f electron. The most intense of these lines correspond to spin $S - 1$, where S is the spin of the $4f^{n-1}$ Hund-rule ground state, and maximum possible L. They are the ^{6}I, ^{5}L, ^{4}M, ^{3}M, and ^{2}L states for Tb, Dy, Ho, Er, and Tm, respectively. Use of the 4f shell electrostatic integrals from our final state calculations (scaled by a factor of 0.8 to roughly account for correlation effects) and the multiplet expressions of Nielson and Koster (1963) yields splittings between these states and the Hund-rule levels which agree quite well with the observed separations (Baer and Busch 1974).

We should also note that the method of fractional parentage is a purely atomic procedure and hence an approximation for the metal in view of hybridization between f and conduction electrons. Furthermore, for mixed-valent systems (i.e., with more than one 4f configuration in the ground state) the approach may be seriously in error and one may need extensions of the method of Gunnarsson and Schönhammer (1983a,b) so far developed only for Ce impurities.

4.1.2. *Coulomb term U*

Combination of the XPS and BIS measurements for each element in fig. 5

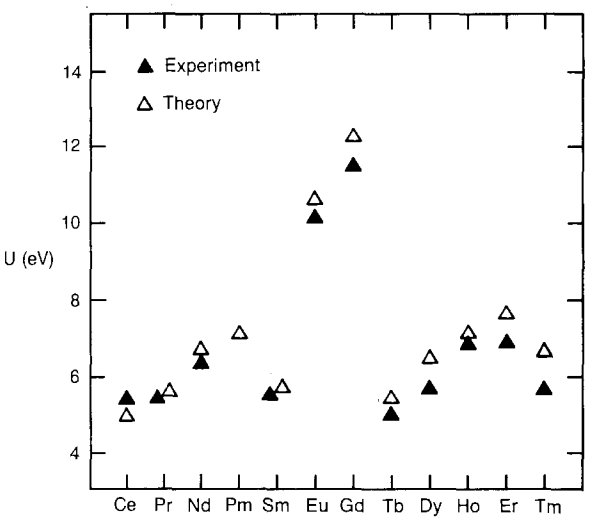

Fig. 6. Experimental and theoretical values of the 4f–4f Coulomb interaction energy $U = \Delta_- + \Delta_+$ (from the results of fig. 5).

provides a direct experimental determination of the separation between the occupied and unoccupied 4f levels, which is the 4f–4f Coulomb interaction energy U as specified by eq. (1). Figure 6 shows that the experimental and theoretical results for the metals are in very satisfactory accord. U varies in the 5–8 eV range except for the ~10 to ~12 eV values for Eu and Gd, respectively, which reflect the particular stability of their half-filled, spherically symmetric 4f shells. These rather large Coulomb energies are directly linked to the spatial localization of the 4f electrons. For the more extended 3d states of the transition metals $U \sim 2$ eV (Herring 1966, Hüfner and Wertheim 1973). The 5f electrons of the actinides exhibit intermediate behavior, U varying from ~2 eV at the beginning of the series to ~5 eV for the elements of higher atomic number (Johansson 1975, Herbst et al. 1976b).

4.1.3. *4f level widths*

Lang et al. (1981) estimated 4f linewidths from their spectra, finding that the XPS widths showed an overall decline through the series while the BIS widths displayed no consistent trend. Those authors remark that the major contributions to the observed widths are lifetime broadening due to photon or Auger decay and many-body effects; phonon broadening can be neglected for such heavy elements. Our calculations permit a simple, one-electron estimate of the intrinsic 4f widths via imposition of WS boundary conditions on the initial state 4f wave functions. Figure 7 presents the widths $W_{4f_{7/2}}$ obtained from the energies at which the $4f_{7/2}$ wave functions have zero value or zero derivative at r_{WS}. $W_{4f_{7/2}}$ decreases monotonically through the series, varying from 0.32 eV (Ce) to 0.04 eV (Lu). The variation is qualitatively similar to that of the estimated XPS widths (also included in fig. 7), with the $W_{4f_{7/2}}$ values approximately half as large.

4.1.4. *Inadequacy of one-electron results*

We stressed in section 1 that the one-electron approximation is fundamentally incapable of accurately predicting the excitation energies of localized states, and in

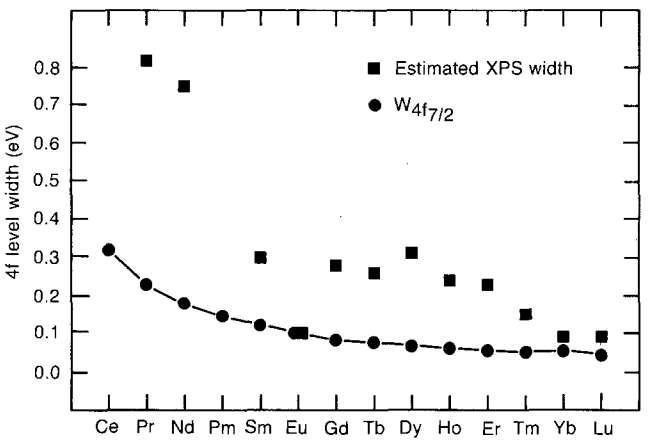

Fig. 7. One-electron 4f level widths $W_{4f_{7/2}}$ obtained from the energies at which the initial state $4f_{7/2}$ wave functions have zero value or zero derivative at r_{WS} (filled circles). (These widths differ insignificantly from those calculated with the $4f_{5/2}$ wave functions.) The squares represent estimates of the XPS 4f full widths at half maximum (Lang et al. 1981).

this section the point is explicitly demonstrated for the 4f electrons. As the one-electron analog of $\Delta_-(4f^n \rightarrow 4f^{n-1})$ we use the LS-average $4f_{7/2}$ eigenvalue relative to the Fermi level in the initial $4f^n$ configuration and modify it to correspond to the Hund-rule state by the addition of $(2/n)E_{4f\,HRC}(4f^n)$, where $E_{4f\,HRC}(4f^n)$ is the total energy correction described in section 2.2:

$$[\varepsilon_F - \varepsilon_{4f_{7/2}}]_{4f^n} = \varepsilon_F - \varepsilon_{4f_{7/2}} + (2/n)E_{4f\,HRC}(4f^n). \tag{16}$$

$\varepsilon_{4f_{7/2}}$ is computed in our self-consistent band calculations and is always smaller in magnitude than $\varepsilon_{4f_{5/2}}$. Similarly, rewriting eq. (2) as

$$-\Delta_+(4f^n \rightarrow 4f^{n+1}) = E_{metal}[4f^n(5d,6s)^m] - E_{metal}[4f^{n+1}(5d,6s)^{m-1}], \tag{17}$$

we infer that the one-electron cognate of $-\Delta_+(4f^n \rightarrow 4f^{n+1})$ can be taken to be

$$[\varepsilon_F - \varepsilon_{4f_{7/2}}]_{4f^{n+1}} \equiv \varepsilon_F - \varepsilon_{4f_{7/2}} + [2/(n+1)]E_{4f\,HRC}(4f^{n+1}), \tag{18}$$

which is the Hund-rule-corrected $4f_{7/2}$ eigenvalue relative to ε_F in the $4f^{n+1}$ metallic configuration.

Figures 8 and 9 show that the one-electron excitation energies grossly depart from $\Delta_\pm$ and, hence, experiment. $[\varepsilon_F - \varepsilon_{4f_{7/2}}]_{4f^n}$ exceeds Δ_- by as much as 10 eV (fig. 8), while $-[\varepsilon_F - \varepsilon_{4f_{7/2}}]_{4f^{n+1}}$ underestimates Δ_+ by amounts as great as 9 eV (fig. 9) and, even more strikingly, fails to yield the proper sign for most of the metals.

A large part of the disparity between $\Delta_\pm$ and their one-electron analogs may be attributed to the intraatomic relaxation (or intraatomic screening) which accompanies the creation of a 4f hole. This can be seen from the following RHF-only considerations. A measure of the energy associated with such relaxation in the $4f^n$ atomic configuration is

$$\Delta_I(4f) \equiv -\varepsilon^{atom}_{4f_{7/2}}(4f^n) - \{E^{RHF}_{ion}[4f^{n-1}(5d,6s)^m] - E^{RHF}_{atom}[4f^n(5d,6s)^m]\}_{gnd}. \tag{19}$$

Here $-\varepsilon^{atom}_{4f_{7/2}}(4f^n)$ is the 4f one-electron removal energy computed in the $4f^n$ state, and the term in wavy brackets is the atom → (4f ion) total energy difference result for

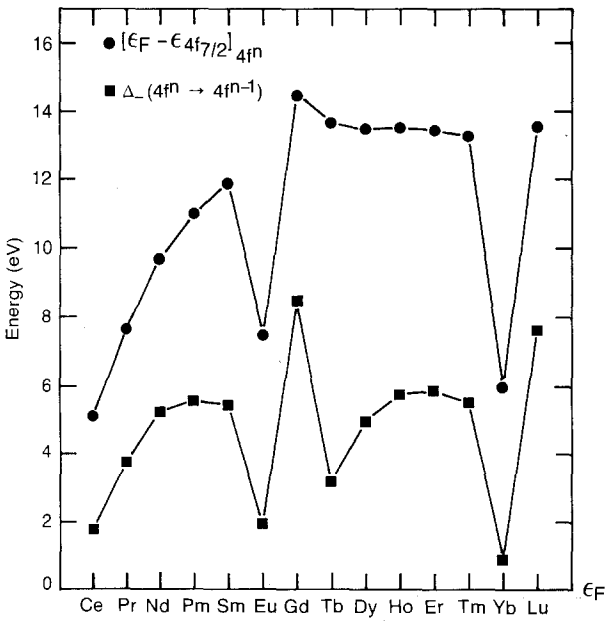

Fig. 8. $\Delta_-(4f^n \rightarrow 4f^{n-1})$ and its one-electron analog, $[\varepsilon_F - \varepsilon_{4f_{7/2}}]_{4f^n}$.

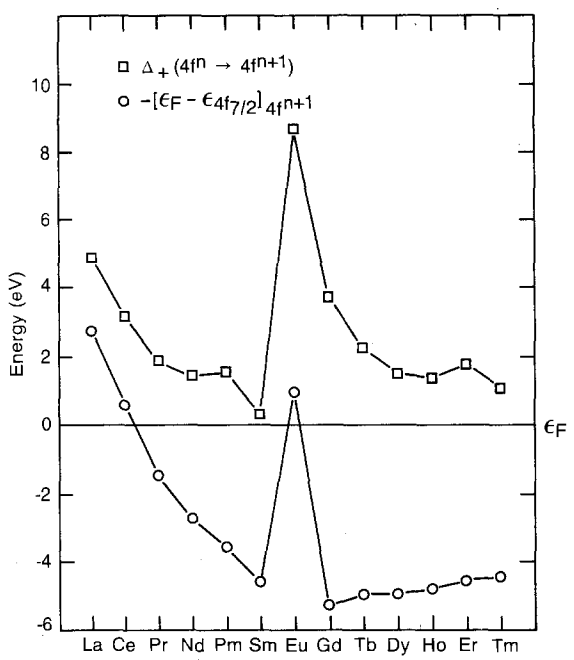

Fig. 9. $\Delta_+(4f^n \rightarrow 4f^{n+1})$ and its one-electron analog, $-[\varepsilon_F - \varepsilon_{4f_{7/2}}]_{4f^{n+1}}$

the same quantity (again including the Hund-rule ground-state corrections for each). $\Delta_I(4f)$ would be negligible if there were no readjustment of the remaining atomic wave functions in the presence of the 4f hole, i.e., if Koopmans' theorem (Koopmans 1933) applied. The corresponding energy for the $4f^{n+1}$ configuration is

$$\Delta_I^+(4f) \equiv -\varepsilon_{4f\,7/2}^{atom}(4f^{n+1}) - \{E_{ion}^{RHF}[4f^n(5d,6s)^{m-1}] - E_{atom}^{RHF}[4f^{n+1}(5d,6s)^{m-1}]\}_{gnd}. \quad (20)$$

To make specific contact with the metallic results we define by $\tilde{\Delta}_\pm(4f^n \to 4f^{n\pm1})$ the RHF-only versions of $\Delta_\pm$, the tilde signifying neglect of the $\xi_\pm$ correlation energy contributions. Figure 10 compares $\Delta_I(4f)$ to

$$[\varepsilon_F - \varepsilon_{4f\,7/2}]_{4f^n} - \tilde{\Delta}_-(4f^n \to 4f^{n-1}),$$

and $\Delta_I^+(4f)$ is displayed with

$$\tilde{\Delta}_+(4f^n \to 4f^{n+1}) - \{-[\varepsilon_F - \varepsilon_{4f\,7/2}]_{4f^{n+1}}\}$$

in fig. 11. It is clear from these figures that the intraatomic relaxation energies track the difference between the metallic one-electron and total energy results quite well in each case, even though the individual quantities vary substantially through the series. This circumstance also obtains for deeper core states whose greater localization involves greater intraatomic screening. For example, we found that $\Delta_I(3d)$ ranges from 20 to 34 eV across the row, but for each metal this energy departs by at most $\sim$1 eV from the difference between the one-electron and total-energy calculations of the 3d excitation energy (Herbst and Wilkins 1979a).

Single-particle estimates of the Coulomb interaction term U can be made at two levels of sophistication. At the simpler level U is approximated by the $F^0(4f,4f)$

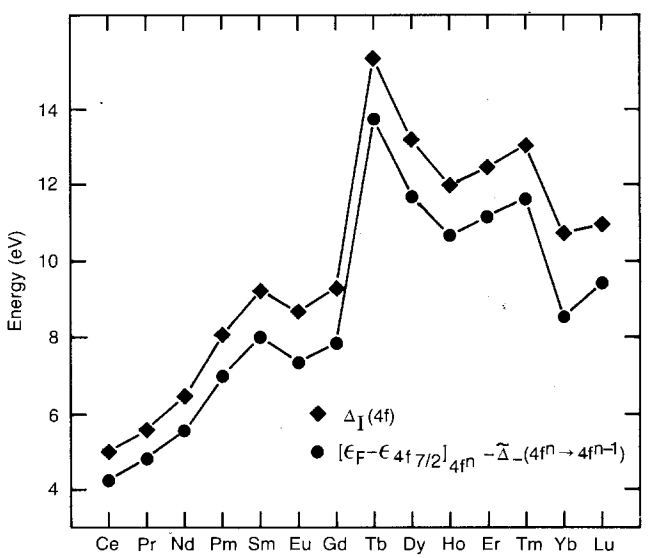

Fig. 10. Comparison of the intraatomic relaxation energy $\Delta_I(4f)$ with the difference between the one-electron and RHF-only total energy results for the $4f^n \to 4f^{n-1}$ excitation energy.

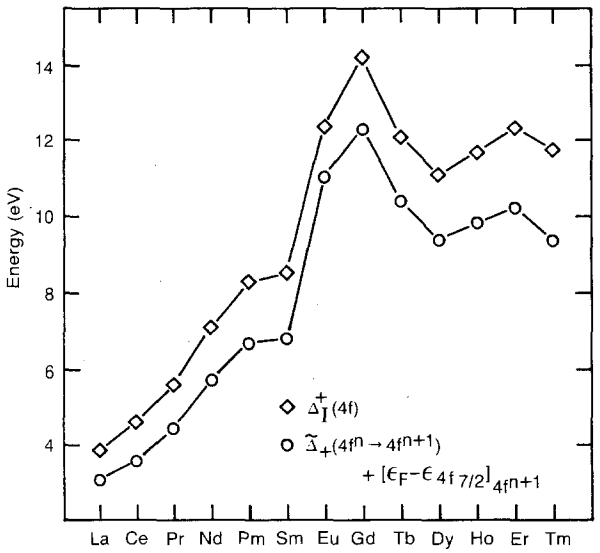

Fig. 11. Comparison of the intra-atomic relaxation energy Δ_I^+ (4f) with the difference of the RHF-only total energy and one-electron results for the $4f^n \rightarrow 4f^{n+1}$ excitation energy.

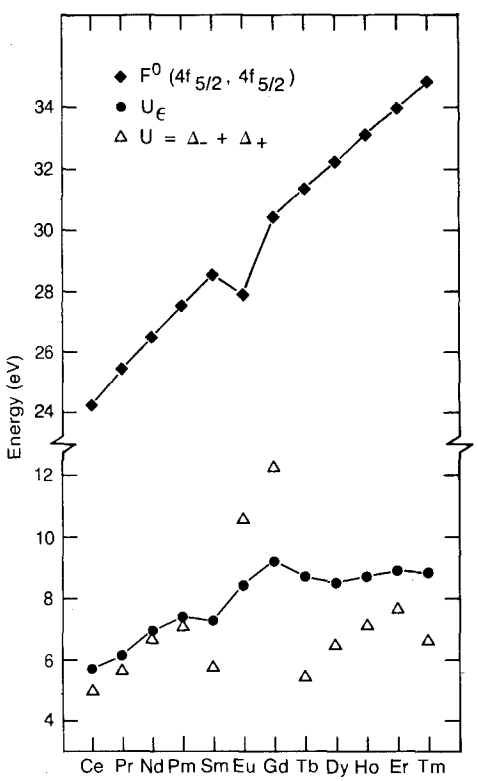

Fig. 12. Coulomb interaction energy $U = \Delta_- + \Delta_+$ and two single-particle estimates of it.

electrostatic integral, a direct atomic measure of the unscreened Coulomb interaction between two 4f electrons. Values of $F^0(4f_{5/2}, 4f_{5/2})$ from our RHF computations are included in fig. 12. They range from 24 eV (Ce) to 35 eV (Tm) and are roughly a factor of five larger than the U results from the $\Delta_\pm$ calculations which are also shown in the figure. The one-electron analogs of $\Delta_\pm$ defined in eqs. (16) and (18) afford a second-level estimate embodying some of the solid state effects:

$$U_\varepsilon \equiv [\varepsilon_F - \varepsilon_{4f\,7/2}]_{4f^n} - [\varepsilon_F - \varepsilon_{4f\,7/2}]_{4f^{n+1}}. \tag{21}$$

Figure 12 indicates that U_ε is on the order of $U = \Delta_- + \Delta_+$ (and experiment). Despite the fact that the components of eq. (21) deviate considerably from $\Delta_\pm$ (cf. figs. 8 and 9), extensive cancellation occurs in their sum. That is, the screening and relaxation effects producing the significant departures of $\Delta_\pm$ from their one-electron cognates are much less evident in the *separation* of the filled and empty 4f levels, which determines U. Although U_ε does not reproduce the detailed variation through the series, the results in fig. 12 show that one-electron energies from band structure calculations in which the 4f occupancy is constrained to appropriate values should provide reasonable estimates of U.

Another example of the use of constrained occupancies to estimate many-body parameters is provided by the recent calculation of Δ_- for Ce by Norman et al. (1984). For a supercell containing as many as eight atoms they computed the total energy difference between a system with one atom in the supercell having an empty 4f shell (screened predominantly by 5d electrons) and a system with all the atoms in the supercell having the same unit 4f occupancy. The energy difference of 2.4 eV they obtain agrees well with our renormalized atom result $\Delta_- \cong 1.8$ eV (table 4), thus validating our approximation scheme.

4.2. *Other systems*

The overall variation of the 4f excitation energies through the series of lanthanide metals characterizes other lanthanide systems as well. Figure 13 compares 4f binding energies measured via photoemission on a variety of materials with our $\Delta_-(4f^n \rightarrow 4f^{n-1})$ results for the metals. In each case the binding energy observed for the same 4f transition described by Δ_- is given. For example, the symbol for the fluctuating valence compound SmB_6 represents the Sm^{3+} binding energy whose analog is $\Delta_-(4f^5 \rightarrow 4f^4)$ for Sm metal. An Sm^{2+} peak also occurs in SmB_6 close below ε_F, and its cognate for the metal is (cf. table 3)

$$\Delta_-(4f^6 \rightarrow 4f^5) = -\Delta_+(4f^5 \rightarrow 4f^6) = -0.3\,\text{eV},$$

which is not included in fig. 13 for simplicity. Measured values for metallic (e.g., RSb) and semiconducting (e.g., EuS) systems having stable as well as mixed valences are included in fig. 13. It is clear that the chemical shifts of the 4f levels are at worst only moderate, $\lesssim 2$ eV, indicating grossly similar screening effects for these systems. In insulators the 4f electrons are generally much more strongly bound since mobile screening charge is unavailable. The same is true for the atomic 4f states, as comparison of the experimental points in fig. 3 with those in fig. 5 and fig. 13 shows.

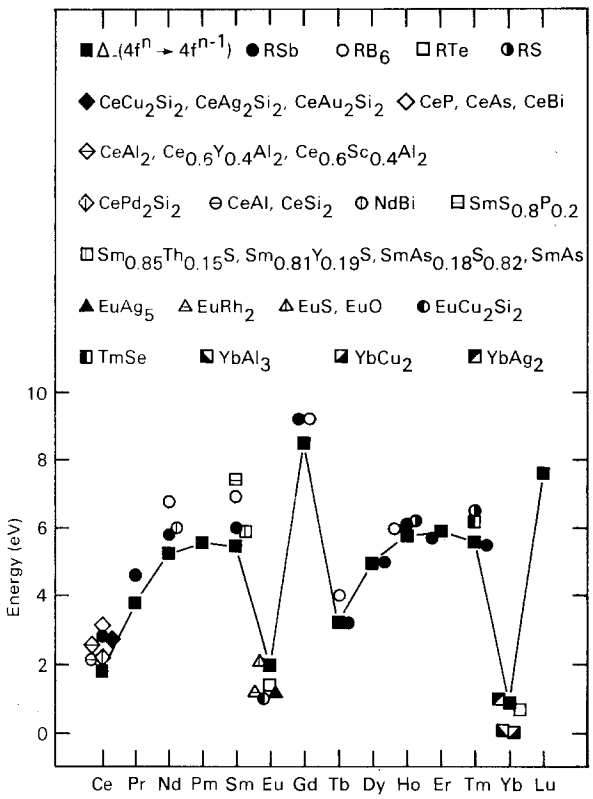

Fig. 13. Comparison of $\Delta_-(4f^n \rightarrow 4f^{n-1})$ calculated for the metals and photoemission measurements of the same 4f excitation energies in various rare earth (R) materials. The data are from the following sources. RSb, RTe, $Sm_{0.85}Th_{0.15}S$, $Sm_{0.81}Y_{0.19}S$, $SmAs_{0.18}S_{0.82}$, SmAs: Campagna et al. (1976). RB_6, NdBi, EuS, EuO, HoS: Campagna et al. (1979). $CeCu_2Si_2$, $CeAg_2Si_2$, $CeAu_2Si_2$, $CePd_2Si_2$: Parks et al. (1983). CeP, CeAs, CeBi: Franciosi et al. (1981). $CeAl_2$. $Ce_{0.6}Y_{0.4}Al_2$, $Ce_{0.6}Sc_{0.4}Al_2$: Croft et al. (1981). CeAl, $CeSi_2$:. Lawrence et al. (1982). $SmS_{0.8}P_{0.2}$: Krill et al. (1980). $EuAg_5$, $EuRh_2$: Schneider et al. (1983). $EuCu_2Si_2$, $YbAl_3$: Buschow et al. (1977). $YbAg_2$, $YbCu_2$: Wertheim (1979).

We saw in section 4.1.2 that combination of XPS and BIS data for the metals furnishes experimental values for the Coulomb term U. In the mixed valence systems fingerprints of the two relevant 4f configurations can often be discerned in a single spectrum, providing a more direct determination. Figure 14 compares the values of U obtained from the XPS spectra of the fluctuating valence systems included in fig. 13 as well as estimates derived by Hillebrecht et al. (1984) from BIS measurements on a variety of cerium intermetallic compounds. For Eu and Yb the theoretical values are based on the $4f^6$ and $4f^{13}$ configurations, respectively, which are appropriate for comparison with the experimental values given (note that the U value for Eu in figs. 6 and 12 is based on the $4f^7$ configuration). In particular, we have

$$U(4f^6) \equiv \Delta_-(4f^6 \rightarrow 4f^5) + \Delta_+(4f^6 \rightarrow 4f^7)$$
$$= \Delta_-(4f^6 \rightarrow 4f^5) - \Delta_-(4f^7 \rightarrow 4f^6) \cong 6.0\,\text{eV} \tag{22}$$

for Eu and

$$U(4f^{13}) \equiv \Delta_-(4f^{13} \rightarrow 4f^{12}) + \Delta_+(4f^{13} \rightarrow 4f^{14})$$
$$= \Delta_-(4f^{13} \rightarrow 4f^{12}) - \Delta_-(4f^{14} \rightarrow 4f^{13}) \cong 5.3\,\text{eV} \tag{23}$$

for Yb using table 3.

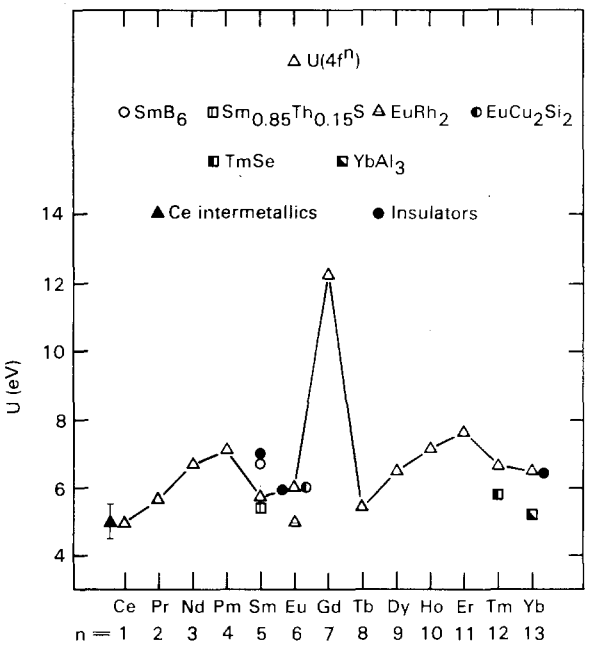

Fig. 14. Coulomb term $U(4f^n)$ calculated for the rare earth metals and experimental values for (i) mixed valence systems also included in fig. 13, (ii) cerium intermetallic compounds (Hillebrecht et al. 1984), and (iii) rare earth insulators (Hüfner and Wertheim 1973).

Figure 14 also contains U estimates obtained by Hüfner and Wertheim (1973) from XPS data on *insulators*, and it is evident that they compare as favorably with our results for the metals as do the measurements on the mixed-valence materials. This may at first seem surprising since the individual 4f binding energies for metals and insulators can differ significantly. Rewriting $U(4f^n)$ defined by eq. (1) in the form

$$U(4f^n) = \Delta_-(4f^n \rightarrow 4f^{n-1}) - \Delta_-(4f^{n+1} \rightarrow 4f^n), \tag{24}$$

as was done specifically in eqs. (22) and (23), we emphasize that U can be considered the *difference* of two 4f binding energies. Therefore, insofar as the screening and relaxation effects are similar for the two excitations, which is a plausible approximation for the localized 4f electrons, their energy *difference* will be insensitive to chemical environment.

5. Screening energetics

In calculating $\Delta_\pm(4f^n \rightarrow 4f^{n\pm1})$ we assumed neutral final (as well as initial) states. Here the impact of that assumption on $\Delta_-(4f^n \rightarrow 4f^{n-1})$ is assessed via calculations in which the final state contains *no* additional screening charge after 4f electron removal. That is, each final state atomic site has net unit positive charge in this zero screening limit. We designate the corresponding 4f excitation energy as $\Delta_-(4f\,\text{ion})$; its definition is analogous to eq. (3) for $\Delta_-(4f^n \rightarrow 4f^{n-1})$:

$$\Delta_-(4f\,\text{ion}) \equiv \xi(\text{ion}) + E^{\text{RHF}}_{\text{metal}}[4f^{n-1}(5d,6s)^m] - E^{\text{RHF}}_{\text{metal}}[4f^n(5d,6s)^m]. \tag{25}$$

The initial states of eq. (3) and eq. (25) are identical, but the absence of the screening charge in the final state of Δ_-(4f ion) leads to a different correlation energy contribution and a more important change in the RHF final state total energy.

5.1. *Determination of Δ_-(4f ion) and comparison with $\Delta_-(4f^n \rightarrow 4f^{n-1})$*

We again exploit atomic spectral information (Brewer 1971a,b, Martin et al. 1978) and ionization potentials (Martin et al. 1974) to estimate the correlation energy difference ξ(ion) for the $4f^n 5d^{m-1} 6s(\text{atom}) \rightarrow 4f^{n-1} 5d^{m-1} 6s(\text{ion})$ transition corresponding to Δ_-(4f ion). The measured ionization potential is the splitting between the free atom and free ion ground states, and the spectroscopic data provide the splittings between the ground states of the $4f^n 5d^{m-1} 6s$ and $4f^{n-1} 5d^{m-1} 6s$ configurations relevant to Δ_-(4f ion) and those defining the ionization potential. As a specific example, the ionization potential for neodymium is the ground state energy difference for the $4f^4 6s^2(\text{atom}) \rightarrow 4f^4 6s(\text{ion})$ transition. The spectral data furnish the splittings for the atomic $4f^4 6s^2 \rightarrow 4f^3 5d^2 6s$ and ionic $4f^4 6s \rightarrow 4f^2 5d^2 6s$ transitions, so that the $4f^3 5d^2 6s(\text{atom}) \rightarrow 4f^2 5d^2 6s(\text{ion})$ ground state energy difference can be obtained. Coupling this experimental information with our RHF calculations for the $4f^n 5d^{m-1} 6s$ and $4f^{n-1} 5d^{m-1} 6s$ configurations, we find ξ(ion):

$$\begin{aligned}\xi(\text{ion}) &\equiv E_{\text{corr}}(4f^{n-1} 5d^{m-1} 6s) - E_{\text{corr}}(4f^n 5d^{m-1} 6s) \\ &= [E(4f^{n-1} 5d^{m-1} 6s) - E(4f^n 5d^{m-1} 6s)]_{\text{expt}} \\ &\quad - [E(4f^{n-1} 5d^{m-1} 6s) - E(4f^n 5d^{m-1} 6s)]_{\text{gnd}}^{\text{RHF}}. \end{aligned} \tag{26}$$

Values of ξ(ion) are included in table 5. Comparing them with ξ_- of table 4 we see that

TABLE 5

Correlation energy differences ξ(ion), 4f excitation energies Δ_-(4f ion) calculated for ionized (unscreened) final states, and screening energy estimates Δ_s(band) and Δ_s(atom). The initial states are the ground metallic configurations. All energies in eV.

Metal	ξ(ion)	Δ_-(4f ion)	Δ_s(band)	Δ_s(atom)
Ce	1.9	6.8	4.0	5.0
Pr	1.6	8.5	4.1	5.0
Nd	1.9	10.3	4.2	4.9
Pm	2.5	10.7	4.2	4.9
Sm	2.8	10.9	4.2	4.8
Eu	2.6	7.2	4.5	3.8
Gd	2.7	13.8	4.4	4.6
Tb	4.9	9.2	4.4	4.6
Dy	4.6	10.8	4.4	4.5
Ho	4.2	11.6	4.5	4.4
Er	4.8	11.5	4.5	4.3
Tm	5.4	11.6	4.5	4.2
Yb	4.3	6.3	4.6	3.2
Lu	4.3	13.1	4.6	4.0

$$-1.6\,\text{eV} \leqslant [\xi_- - \xi(\text{ion})] \leqslant -0.6\,\text{eV}. \tag{27}$$

Now ξ(ion) is a measure of the correlation accompanying the excitation of a 4f electron alone, while ξ_- represents the correlation associated with $4f \rightarrow 5d$ conversion. The bracketed quantity in the above expression is thus an estimate of the correlation energy associated with the additional conduction electron which is present in the neutral (completely screened) final state of $\Delta_-(4f^n \rightarrow 4f^{n-1})$ and absent in the ionic (unscreened) final state of Δ_-(4f ion).

We calculate the total RHF energy of the ionized metallic final state, the second term on the right side of eq. (25), by the methods described in section 2.1. RHF computations are performed for the $4f^{n-1}\,5d^{m-1}\,6s$ free ions, renormalized atom crystal potentials are constructed, and self-consistent band calculations are carried out. Normalization of the wave functions to the WS sphere ensures that the final state cell has charge $+1|e|$. The $\boldsymbol{q} = 0$ component of the full crystal potential, which arises from the charge of the other WS cells, is not included in the total energy since our intent is to compare to the completely screened limit where no such term appears (each cell in that case being neutral). Multiplet theory is again employed to place the 4f electrons into their Hund-rule states..

Figure 15 compares Δ_-(4f ion), whose values are also listed in table 5, with $\Delta_-(4f^n \rightarrow 4f^{n-1})$. The screening charge present in the final state of $\Delta_-(4f^n \rightarrow 4f^{n-1})$ reduces the 4f binding energy by 5–6 eV across the series. Since the $\Delta_-(4f^n \rightarrow 4f^{n-1})$ results are in excellent agreement with photoemission measurements on this energy scale (cf. fig. 5), we infer that the experimental situation does in fact correspond closely to the completely screened limit, as we argued in section 2. Furthermore, the departures between $\Delta_-(4f^n \rightarrow 4f^{n-1})$ and Δ_-(4f ion) in fig. 15 are similar to those

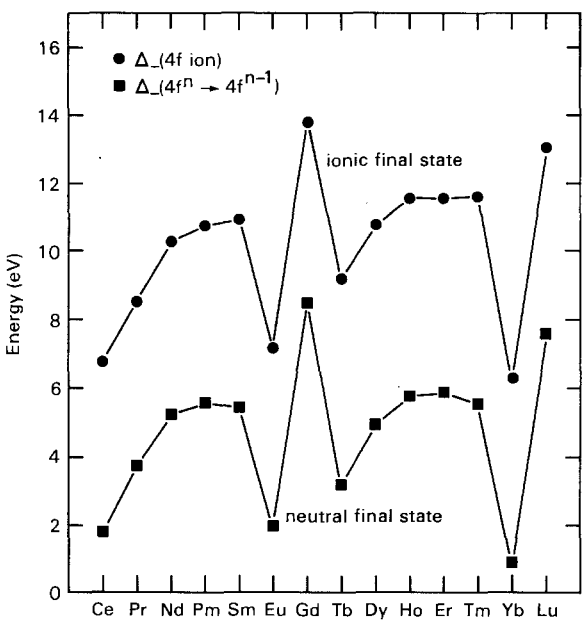

Fig. 15. Comparison of Δ_-(4f ion), the 4f excitation energy calculated for unscreened final states, with $\Delta_-(4f^n \rightarrow 4f^{n-1})$. For both quantities the initial states are the ground metallic configurations.

between $\Delta_-(4f^n \rightarrow 4f^{n-1})$ and its one-electron analog in fig. 8; the two sets of findings are consistent since neither the one-electron results nor Δ_-(4f ion) include screening effects.

5.2. *Alternate screening energy estimates*

Simpler approximations for the screening energy are afforded by neglecting the correlation energy changes and using the RHF terms alone. For the metals we rewrite eq. (3) and eq. (25) as

$$\Delta_-(4f^n \rightarrow 4f^{n-1}) \equiv \xi_-(4f^n \rightarrow 4f^{n-1}) + \tilde{\Delta}_-(4f^n \rightarrow 4f^{n-1}), \tag{28}$$

$$\Delta_-(4f\ \text{ion}) \equiv \xi(\text{ion}) + \tilde{\Delta}_-(4f\ \text{ion}), \tag{29}$$

where the tildes signify RHF-only total energy differences. An RHF estimate of the screening energy associated with the additional conduction electron is then

$$\begin{aligned}\Delta_s(\text{band}) &\equiv \tilde{\Delta}_-(4f\ \text{ion}) - \tilde{\Delta}_-(4f^n \rightarrow f^{n-1}) \\ &= E^{\text{RHF}}_{\text{metal}}[4f^{n-1}(5d, 6s)^m] - E^{\text{RHF}}_{\text{metal}}[4f^{n-1}(5d, 6s)^{m+1}].\end{aligned} \tag{30}$$

The atomic analog of this energy is

$$\Delta_s(\text{atom}) \equiv E^{\text{RHF}}_{\text{ion}}(4f^{n-1}\,5d^{m-1}\,6s) - E^{\text{RHF}}_{\text{atom}}(4f^{n-1}\,5d^m\,6s), \tag{31}$$

the *LS*-average total energy difference between the free ion and free atom final states involved in $\Delta_-(4f^n \rightarrow 4f^{n-1})$ and Δ_-(4f ion). Both Δ_s(band) and Δ_s(atom) are generally in the 4–5 eV range, as table 5 indicates.

These screening energies are quantitatively similar to those we have found in corresponding investigations of 2p (Herbst and Wilkins 1982), 3d (Herbst and Wilkins 1979a), 5s (Herbst et al. 1977), and 5p (Herbst 1984) core level excitations in the rare earth metals. Comparable values have also been obtained for core electron excitations in the 3d transition metals via two distinct calculational approaches (Watson et al. 1976, Williams and Lang 1978). An approximate 4–6 eV screening energy accompanying core electron removal is characteristic of metallic systems in general.

6. Connection between parameters in the Anderson model and $\Delta_\pm$

A central feature of our $\Delta_\pm$ calculations is that each transition is confined to a Wigner–Seitz cell. Accordingly, one might expect the calculated values to be relevant to dilute magnetic alloys, provided the radius of the WS cell used in a given calculation is appropriate to that of a magnetic impurity in a particular host. (This proviso is non-trivial since excitation of an f electron may form an ion, albeit screened, whose size differs from that of the initial ion.) $\Delta_\pm$ might also be relevant to more concentrated systems, including the mixed valent or heavy fermion materials. In the best characterized of these Ce or Yb is the lanthanide constituent, and this discussion is confined to such systems.

Two contrasting properties illustrate the problem faced in deducing the para-

meters of the Anderson model: (i) XPS and BIS measure excitation energies $\Delta_{\pm}$ on the scale of eV, while (ii) the strongly-enhanced Pauli-like magnetic susceptibility suggests a characteristic excitation energy on the meV scale. The recent resolution of this paradox will be described below.

To begin we write the Anderson Hamiltonian (Anderson 1961) as

$$H_A = \sum_{k\sigma} \varepsilon_k c^\dagger_{k\sigma} c_{k\sigma} + \sum_{\sigma} \varepsilon_f f^\dagger_\sigma f_\sigma + U n_{f\uparrow} n_{f\downarrow} + \sum_{k\sigma} V_{kf} (c^\dagger_{k\sigma} f_\sigma + f^\dagger_\sigma c_{k\sigma}). \tag{32}$$

The first term represents the conduction band, the second and third describe a single, localized, non-degenerate f orbital, and the last term represents hybridization between the f orbital and the conduction band. An f electron may only hybridize with a conduction state having the same point symmetry as the f orbital, and so in writing H_A we implicitly restrict the f_σ operators to act on states of the same point symmetry. We may make the following identifications:

$$\Delta_- (f^n \to f^{n-1}) \longleftrightarrow -\varepsilon_f, \qquad \Delta_+ (f^n \to f^{n+1}) \longleftrightarrow \varepsilon_f + U; \tag{33}$$

these obviously preserve the relation

$$U = \Delta_- + \Delta_+ . \tag{34}$$

In the limit $V_{kf} \to 0$ the Anderson parameters ε_f and U can be related to ground state energy differences of various f configurations.

Experimental information pertinent to our discussion is presented in fig. 16, which shows combined XPS/BIS spectra for $CeRu_2$ (Allen et al. 1983). The data contain two expected features and a surprising one. The expected characteristics are the $\Delta_- = -\varepsilon_f$ peak in the XPS spectrum and the $\Delta_+ = \varepsilon_f + U$ structure, broadened by

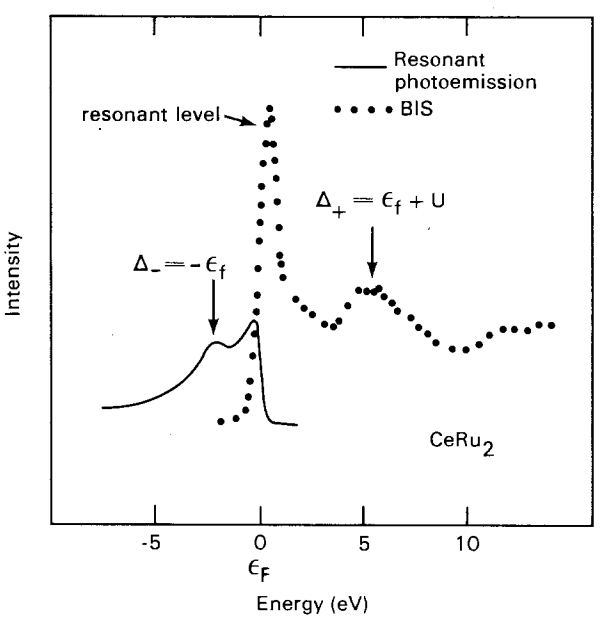

Fig. 16. Combined resonant photoemission and BIS spectra of $CeRu_2$ (adapted from Allen et al. (1983)).

the multiplet splitting of the f^2 final state, in the BIS spectrum. The surprising feature is the resolution-limited peak just above the Fermi energy. From work based on analyses of H_A (e.g., Gunnarsson and Schönhammer 1983a,b) we know this peak is a many-body resonance (designated the Kondo resonance by some authors and the Abrikosov–Suhl resonance by others) in the f-projected density of states. The peak occurs at energy

$$\hbar\omega \simeq k_B T_K \sim \varepsilon_F \exp(-\pi|\varepsilon_f|/N_f\Gamma), \tag{35}$$

where $\Gamma(=\pi\rho|V_{kf}|^2, \rho$ the density per spin of conduction electron states at the Fermi level) is the hybridization width of the f state. Note that the expression (35) for the Kondo temperature T_K includes the N_f-fold degeneracy of the cerium f orbital. (N_f can range from 14 to 6, to 2, depending on the strength of the spin–orbit and crystal field splittings, respectively). The magnitude of the Kondo resonance increases as $N_f\Gamma/|\varepsilon_f|$ increases (or, equivalently, as the weight of the A_- peak decreases). In our opinion the peak of 4f character observed near the Fermi level in photoemission measurements on Ce and $Ce_{0.9}Th_{0.1}$ (Martensson et al. 1982, Wieliczka et al. 1982, 1984) can also be identified as such a many-body structure.

This resonance at $\sim k_B T_K$ provides a partial explanation for the surprising temperature dependence of equilibrium and transport properties of dilute alloys and mixed-valent systems. The important conclusion emerging from the relevant theory (Bickers et al. 1985, Allen et al. 1986) is that the low-temperature susceptibility and specific heat reflect a greatly enhanced density of states proportional to $1/T_K$, *not* $1/\varepsilon_F$. Since these arguments are based on solution of the single-impurity Anderson model, they cannot be expected to apply *a priori* to concentrated systems. Nonetheless, for temperatures $T > T_K$ the single-impurity results, scaled by the number of impurities, seem to work for most properties. The most prominent deviation at low temperatures occurs for the resistivity, which Bloch's theorem forces to zero whereas the single-impurity result saturates (Lee et al. 1986).

The essential point we wish to convey is that the Anderson Hamiltonian H_A, with one set of parameters (ε_f, U, and V_{kf}) is capable of explaining the high energy ($\sim$1 eV) excitation properties measured by XPS and BIS as well as the low energy ($\sim$0.01 eV) equilibrium properties in dilute and concentrated Ce and Yb materials.

Finally, following Haldane (1977a,b), we point out that H_A does not permit the local conduction electron environment to completely adjust to a change in f occupancy, an effect which we have built into our $A_\pm$ calculations. To do so one can add a screening Hamiltonian to H_A of the form

$$H_{scr} = \sum_i \varepsilon_i c_i^\dagger c_i + \sum_\sigma n_{f\sigma} \sum_{ij} V_{ij} c_i^\dagger c_j. \tag{36}$$

Here the subscript i refers to conduction electrons having point symmetry *different* from that of the localized f state and V_{ij} is a Coulomb-type matrix element coupling these conduction electrons with the f states. This additional Hamiltonian accounts (at least imperfectly) for the redistribution of conduction electron charge due to a change in f occupancy. If we wished to impose charge neutrality (within a WS cell, for example) we could adjust the value of V_{ii} to do this. In the work of Haldane (1977a,b) the same idea is incorporated by imposing the Friedel sum rule.

We consider the influence of H_{scr} on $\Delta_{\pm}$ in two stages; in all this we suppose $V_{kf} = 0$. First, from the diagonal piece of the second term of H_{scr} we see that

$$\varepsilon_f \to \varepsilon_f + \sum_i V_{ii}\langle n_i\rangle,$$

which, since $V_{ii} > 0$, means that the effective single-particle f level is higher in energy (that is, closer to the Fermi level) than in the absence of H_{scr}. This result parallels the effect of the additional screening electron in our Δ_- calculations (section 5). Second, in XPS the transition is to a fully relaxed final state in which the conduction electrons have relaxed to the f hole. A traditional way to calculate this is to replace H_{scr} by a set of bosons (representing the particle–hole excitations in the conduction electron gas) which are linearly coupled to n_f. In any event, one finds a positive shift energy $\Delta\varepsilon$ which is equal to the coupling divided by the frequency. Combining these two aspects we see that

$$\Delta_-(f^n \to f^{n-1}) = -\left(\varepsilon_f + \sum_i V_{ii}\langle n_i\rangle - \Delta\varepsilon\right),$$

$$\Delta_+(f^n \to f^{n+1}) = \varepsilon_f + U + \sum_i V_{ii}\langle n_i\rangle - \Delta\varepsilon, \tag{37}$$

and the relation (34) for U is still retained. On the basis of calculations for the electron gas $\Sigma_i V_{ii}\langle n_i\rangle$ and $\Delta\varepsilon$ are comparable. Hence, H_A remains a reasonable model.

7. Lattice constant variation of 4f levels: pressure-induced valence transitions

As we remarked in section 3.2, the proximity of a 4f level to the Fermi level in many of the metals introduces the possibility of altering the 4f number (equivalently, the valence) by means such as pressure and temperature changes, alloying, and compound formation. To examine pressure effects we have performed calculations of relevant 4f excitation energies $\Delta_+(4f^n \to 4f^{n+1})$ as functions of Wigner–Seitz radius r_{WS} for Ce, Sm, Er, and Yb metals (Herbst and Wilkins 1984). An integral change in 4f occupancy is signalled by a sign change in Δ_+ (cf. eqs. (2), (3)), and the corresponding transition pressure is estimated by a Maxwell construction using $E^{RHF}_{metal}[4f^{n+1}(5d, 6s)^{m-1}]$ and $\{E^{RHF}_{metal}[4f^n(5d, 6s)^m] - \xi_+\}$ expressed as functions of atomic volume. We find that the 4f occupancy increases at elevated pressures, with transitions to states of larger 4f number first occurring in the megabar range.

Results for two cerium 4f levels, $\Delta_+(4f^0 \to 4f^1)(= -\Delta_-(4f^1 \to 4f^0))$ and $\Delta_+(4f^1 \to 4f^2)$, are displayed in fig. 17. Throughout the entire r_{WS} range investigated $\Delta_+(4f^0 \to 4f^1)$ is negative, implying that the trivalent $4f^1$ configuration is always stable with respect to the tetravalent $4f^0$ state. This finding is consistent with band structure calculations (Pickett et al. 1981) and with photoemission (Martensson et al. 1982, Wieliczka et al. 1982, 1984), muon spin rotation (Wehr et al. 1981), positron annihilation (Gustafson et al. 1969), and Compton scattering (Felsteiner et al. 1979, Kornstädt et al. 1980) measurements, all of which indicate little or no change in 4f occupancy through the $\gamma \to \alpha$ transition. The relative

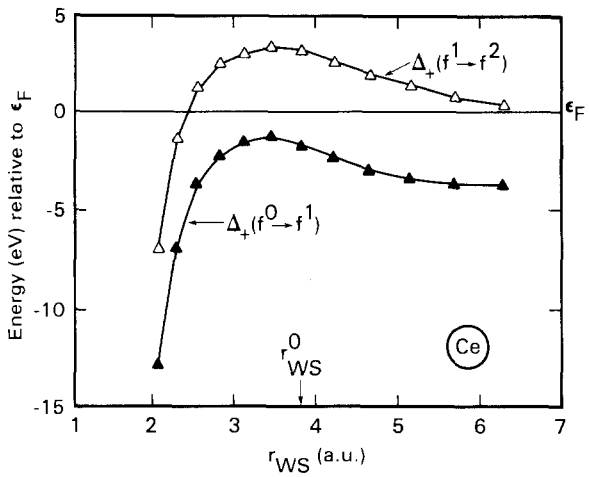

Fig. 17. Calculated 4f excitation energies $\Delta_+(4f^0 \rightarrow 4f^1)$ and $4_+(4f^1 \rightarrow 4f^2)$ for cerium metal. The sign change of Δ_+ $(4f^1 \rightarrow 4f^2)$ near $r_{WS} = 2.4$ a.u. indicates a $4f^1 \rightarrow 4f^2$ transition for pressure $P \sim 6$ Mbar.

instability of the tetravalent configuration also supports, at least indirectly, the suggestion (Bauchspiess et al. 1981, Wohlleben and Röhler 1984) that no completely tetravalent metallic cerium compounds exist.

In fig. 17 the sign change of $\Delta_+(4f^1 \rightarrow 4f^2)$ for $r_{WS} \sim 2.4$ a.u. signals a $4f^1 \rightarrow 4f^2$ transition which we estimate to occur at a pressure $P \sim 6$ Mbar. At that radius the 4f level width, again determined by imposing WS-type boundary conditions on the 4f wave functions as was done in section 4.1.3, is $W_{4f_{7/2}} \sim 7$ eV. This value is considerably larger than $W_{4f_{7/2}} \sim 0.3$ eV at the equilibrium radius (cf. fig. 7) and on the order of $U \equiv \Delta_+(4f^1 \rightarrow 4f^2) - \Delta_+(4f^0 \rightarrow 4f^1) \sim 5$ eV evident from fig. 17. Hence, 4f band formation is probably involved, and the transition may be more complicated than a first-order change between $4f^1$ and $4f^2$ configurations. We nevertheless expect the 4f population to *increase* in this pressure regime.

Figure 18 summarizes our calculations for ytterbium and samarium, two other elements which also form mixed-valent materials. The curves of $\Delta_+(4f^{13} \rightarrow 4f^{14})$ for Yb and $\Delta_+(4f^5 \rightarrow 4f^6)$ for Sm are similar, each crossing ε_F twice. For Yb (fig. 18(a)) a $2+ \rightarrow 3+$ transition near $r_{WS} = 3.9$ a.u. $< r^0_{WS} = 4.1$ a.u. is indicated, and the corresponding pressure is $P \sim 90$ kbar. Johansson and Rosengren (1975) earlier predicted $P \sim 140$ kbar, and measurements of the L_{III} absorption edge in ytterbium metal as a function of pressure have established that such a transition does occur, although over a broad pressure range beginning near $P = 40$ kbar (Syassen et al. 1982). In addition, fig. 18(a) shows that $\Delta_+(4f^{13} \rightarrow 4f^{14})$ returns to negative values for $r_{WS} \lesssim 2.5$ a.u., signifying reentrance to the $4f^{14}(2+)$ state for $P \gtrsim 3$ Mbar. At the crossover radius $W_{4f_{7/2}} \lesssim 3$ eV, making it likely that the transition is between integrally occupied $4f^{13}$ and $4f^{14}$ configurations.

As r_{WS} decreases from large values in samarium (fig. 18(b)), a divalent $\rightarrow$ trivalent transition is predicted for $r_{WS} \sim 4.0$ a.u., which is only slightly greater than the equilibrium WS radius $r^0_{WS} = 3.8$ a.u. XPS evidence of a divalent component at the surface of Sm metal (Wertheim and Campagna 1977, Wertheim and Crecelius 1978, Wertheim 1979, Allen et al. 1978, 1980) as well as other theoretical work (Johansson

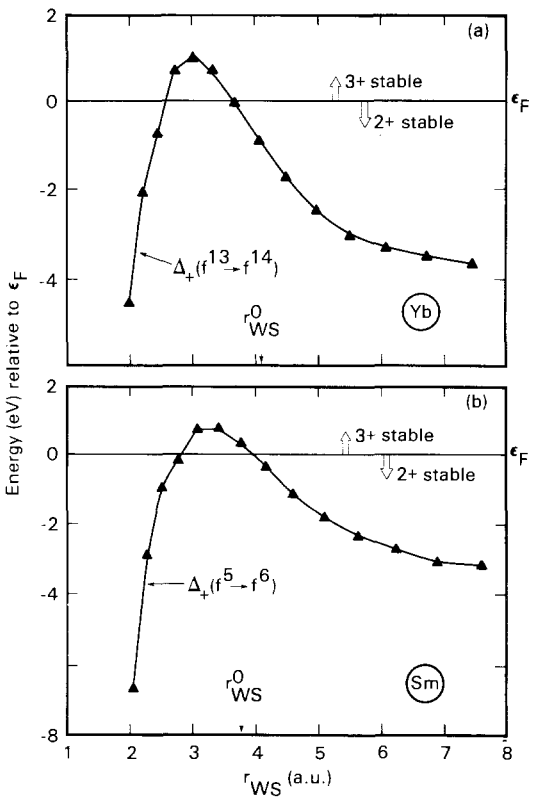

Fig. 18. (a) $\Delta_+(4f^{13} \rightarrow 4f^{14})$ for ytterbium metal. The sign changes for $r_{WS} \sim 3.9$ a.u. and $r_{WS} \sim 2.5$ a.u. correspond to $4f^{14} \rightarrow 4f^{13}$ ($P \sim 90$ kbar) and $4f^{13} \rightarrow 4f^{14}$ ($P \sim 3$ Mbar) transitions, respectively. (b) $\Delta_+(4f^5 \rightarrow 4f^6)$ for samarium metal. The zero-crossing near $r_{WS} = 4.0$ a.u. corresponds to a $4f^6 \rightarrow 4f^5$ transition which occurs for a $\lesssim 8\%$ expansion of the equilibrium lattice (Herbst and Wilkins 1981), while that for $r_{WS} \sim 2.8$ a.u. signals reentry to the $4f^6$ configuration for $P \sim 1$ Mbar.

1979) provide some indication that a bulk valence change may in fact occur under pressure. Contact with experimental information on Sm fluctuating valence systems can also be made. First, SmS transforms from a divalent ($4f^6$) semiconductor to a fluctuating valence ($4f^5 \longleftrightarrow 4f^6$) metal at a pressure of 6.5 kbar. Second, in $Sm_{1-x}R_xS$ alloys with R = Y, Gd, Th, the $4f^6$ levels have been observed to move nearer the Fermi energy with increasing x, i.e., with decreasing lattice constant (Wertheim et al. 1978). Both sets of observations broadly correspond with the rise of $\Delta_+(4f^5 \rightarrow 4f^6)$ as r_{WS} passes through r^0_{WS} from above in fig. 18(b). The correspondence does not always hold, however, since substitution of calcium (2+) in SmS also contracts the lattice but the $4f^6$ levels move further away from ε_F with increasing Ca concentration. This example illustrates the danger of applying calculations done for metallic systems, where the pressure is isotropic, to insulating systems where chemical bonds can produce significant level shifts.

In fig. 18(b) $\Delta_+(4f^5 \rightarrow 4f^6)$ reaches a maximum and again becomes negative for $r_{WS} \sim 2.8$ a.u., indicating that samarium metal reenters the divalent ($4f^6$) configuration for $P \sim 1$ Mbar. Since the 4f width at that juncture is ~ 2 eV while $U \sim 5$ eV, it is likely that a genuine 4f band has not yet developed.

From the Ce, Sm, and Yb calculations we infer that the 4f occupation number n in the rare earth metals becomes progressively enhanced at megabar pressures. With

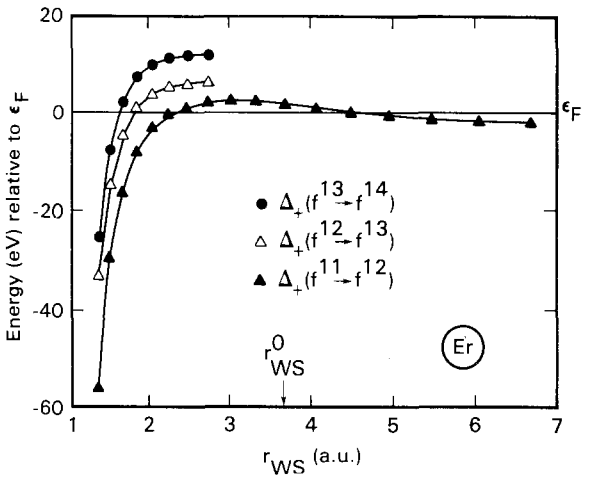

Fig. 19. 4f excitation energies calculated for erbium metal. For $r_{WS} < r^0_{WS}$ the sign changes in $\Delta_+(4f^{11} \to 4f^{12})$, $\Delta_+(4f^{12} \to 4f^{13})$, and $\Delta_+(4f^{13} \to 4f^{14})$ are associated with $4f^{11} \to 4f^{12}$($P \sim 6$ Mbar), $4f^{12} \to 4f^{13}$($P \sim 40$ Mbar), and $4f^{13} \to 4f^{14}$ ($P \sim 80$ Mbar) transitions, respectively. The zero of $\Delta_+(4f^{11} \to 4f^{12})$ near $r_{WS} = 4.6$ a.u. corresponds to a $2+ \to 3+$ valence change connected with formation of the $3+(4f^{11})$ equilibrium metal from $2+(4f^{12})$ Er atoms.

sufficient compression we expect n to approach 4 and 8 in cerium and samarium, respectively, and in general $n \to Z - 54$ for a lanthanide metal of atomic number Z. A fascinating corollary of this expectation is the possibility that erbium ($Z - 54 = 14$) may undergo a metal → insulator transition by filling its 4f shell. The three erbium 4f levels relevant to this possibility are shown in fig. 19. At successively smaller WS radii $\Delta_+(4f^{11} \to 4f^{12})$, $\Delta_+(4f^{12} \to 4f^{13})$, and ultimately $\Delta_+(4f^{13} \to 4f^{14})$ become negative. These sign changes imply $4f^{11} \to 4f^{12}$, $4f^{12} \to 4f^{13}$, and $4f^{13} \to 4f^{14}$ transitions for pressures of ~6, ~40, and ~80 Mbar, respectively. Since hybridization effects are neglected in our calculations, however, we emphasize that it is uncertain whether a gap will separate the 4f from the higher-lying bands and generate an insulating state as $n \to 14$.

The pressure-induced enhancement of the 4f occupancy predicted by our calculations is a manifestation of the proclivity for bands of lower angular momentum l to increase in energy relative to bands of higher l under compression. McMahan and Albers (1982) have noted that this behavior fundamentally reflects the different volume (V) dependences of the one-electron kinetic energy ($\sim V^{-2/3}$) and potential energy ($\sim V^{-1/3}$), which favor the population of states having lower kinetic energy (higher l) as V diminishes. Those authors investigated such behavior in the form of 4s → 3d conversion, predicting a metal → insulator transition in nickel at 340 Mbar. Our work demonstrates that a similar trend is operative for the 4f states of the rare earth metals.

8. Replicate core levels

Spectroscopic measurements of materials having either an inhomogeneous (e.g., Sm_3S_4, Eu_3O_4) or homogeneous (e.g., CeN, SmB_6, $EuPd_2Si_2$, TmSe, $YbCu_2Si_2$) distribution of two distinct 4f shells often reveal *two* sets of structures, or replicas,

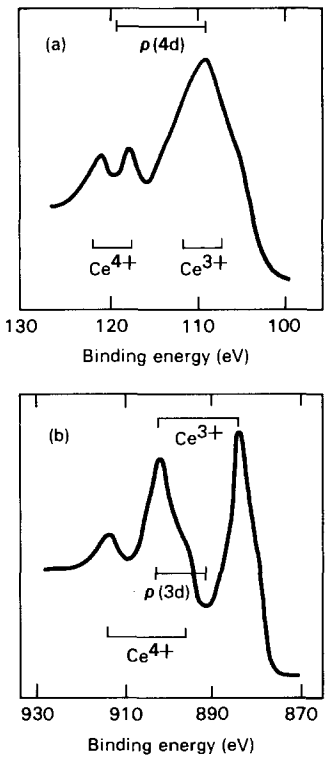

Fig. 20. X-ray photoemission spectra of CeN in the Ce 4d (a) and 3d (b) regions (adapted from Baer and Zürcher (1977)). $\rho(3d)$ and $\rho(4d)$ denote the replicate splittings.

associated with a given core level. The spectrum belonging to the higher valence ($4f^{n_f}$) configuration always has higher binding energy than the spectrum belonging to the lower valence ($4f^{n_f+1}$) configuration; the smaller effective nuclear charge in the latter case is responsible for the decreased binding. Observation of such replicate spectra indicates that the two 4f configurations are present in the ground state.

Examples of 3d and 4d replicas are shown in the XPS spectra of fig. 20 for the mixed valence compound CeN. The energy distribution curve for each core level is comprised of two pairs of spin–orbit-split $d_{3/2}$ and $d_{5/2}$ peaks, with the pair corresponding to the $4+$ ($4f^0$) state occurring at a binding energy larger than that for the pair associated with the $3+$ ($4f^1$) configuration. We define the replicate splitting, the energy separation of the spin–orbit-split structures, as $\rho(nl)$ for each nl core level. Figure 20 shows that $\rho(3d) \simeq 11\,eV$ and $\rho(4d) \sim 10\,eV$ for CeN. The 3d structures in fig. 20(b) overlap since the 3d spin–orbit splitting ($\sim 18\,eV$) is larger than $\rho(3d)$. Such replicate spectra are particularly useful for mixed-valent Ce systems since direct observation of the two 4f configurations is obscured by both the fact that one of the relevant configurations is $4f^0$ and also that the 4f spectrum is often difficult to distinguish from the valence band emission.

We obtain theoretical estimates of $\rho(nl)$ in the following way. The calculational scheme we have developed for the 4f levels is used to compute the excitation energy $\tilde{A}_-(4f^{n_f}; nl)$ of a core electron having quantum numbers nl in a lanthanide metal

with 4f occupancy n_f:

$$\tilde{\Delta}_-(4f^{n_f}; nl) \equiv E^{RHF}_{metal}[(nl \text{ hole})4f^{n_f}(5d, 6s)^{m+1}] - E^{RHF}_{metal}[4f^{n_f}(5d, 6s)^m]. \quad (38)$$

Here the tilde denotes neglect of both correlation effects and multiplet interactions between the nl hole and the open shells; m is the valence corresponding to n_f. The 4f electrons in both terms on the right side of eq. (38) are once more placed into the Hund-rule states via multiplet theory. Since the RHF computations are done in the average of LS configuration mode, $\tilde{\Delta}_-(4f^{n_f}; nl)$ represents the degeneracy-weighted average excitation energy of the $j = l \pm \frac{1}{2}$ levels when $l \neq 0$ and the average of the two levels split by the 4f exchange field when $l = 0$. Calculations of 3d excitation energies based on eq. (38) deviate from the binding energies measured for the metals by no more than ~ 2 eV (Herbst and Wilkins 1979a). The replicate splitting is given by the difference of the nl excitation energies calculated for the two relevant 4f occupation numbers:

$$\rho(nl) \equiv \tilde{\Delta}_-(4f^{n_f}; nl) - \tilde{\Delta}_-(4f^{n_f+1}; nl). \quad (39)$$

Table 6 lists splittings calculated for the 2p, 3d, 4d, 5s, and 5p levels of Ce, Sm, Eu, Tm, and Yb metals. We find that $\rho(nl) \sim 8$–10 eV for the 2p, 3d, and 4d states while the splittings for the 5s and 5p electrons are significantly smaller, 3–5 eV. This contrast stems from the fact that the core states (5s, 5p) whose charge is *exterior* to the 4f shell are more effectively shielded from the nucleus as n_f increases than those states (2p, 3d, 4d) *interior* to the 4f shell. Put another way, all core level binding energies are reduced when $n_f \to n_f + 1$ (i.e., all $\rho(nl)$ defined by eq. (39) are positive), but the reduction is greater for those core states more spatially localized than the 4f electrons.

The 2p, 3d, and 4d replicate splittings we have derived for the metals depart by at most ~ 2 eV from those measured by XPS and X-ray absorption on a variety of mixed valence systems (Herbst and Wilkins 1979b, 1982). Some experimental information is also available for the 5p levels. Campagna et al. (1979) noted that the XPS 5p binding energy is ~ 2 eV smaller in SmTe (3+ Sm ions) than in SmSb (2+ Sm ions). Franciosi et al. (1983) investigated Si–Sm interfaces and monitored the 5p emission as a $2+ \to 3+$ transition occurred with increasing overlayer thickness; their spectra indicate a replicate splitting of $\lesssim 2$ eV. Although somewhat less than $\rho(5p) = 3.0$ eV in table 6 for Sm, both results are significantly smaller than the

TABLE 6

Replicate splittings of the 2p, 3d, 4d, 5s, and 5p core levels calculated for the five lanthanide metals which form mixed-valent materials characterized by the indicated 4f configurations. All splittings in eV.

Metal	4f configurations	ρ(2p)	ρ(3d)	ρ(4d)	ρ(5s)	ρ(5p)
Ce	$4f^0, 4f^1$	9.0	10.3	7.8	3.6	2.8
Sm	$4f^5, 4f^6$	8.2	9.3	7.8	3.9	3.0
Eu	$4f^6, 4f^7$	8.5	9.6	7.8	4.1	3.2
Tm	$4f^{12}, 4f^{13}$	8.3	9.3	8.0	4.6	3.7
Yb	$4f^{13}, 4f^{14}$	8.6	9.5	8.3	4.7	3.7

splittings for the deeper core levels. In a resonant XPS study of the fluctuating valence compound TmSe, Oh et al. (1984) observed a $\gtrsim 3\,\mathrm{eV}$ splitting of the Tm 5p levels which is in good accord with the 3.7 eV value we find. Despite having been calculated for the pure metals, the $\rho(nl)$ entries of table 6 provide reasonable estimates for other systems since each splitting is a *difference* of excitation energies. Changes in chemical environment may shift the individual binding energies, but only a differential chemical shift, which we expect to be much smaller, can influence $\rho(nl)$.

An identity exists between $\rho(nl)$ and the energy lowering of the $4f^{n_f+1}$ level in the presence of an nl core hole, a connection we have investigated explicitly for the 2p (Herbst and Wilkins 1982) and 5p (Herbst 1984) levels. Neglecting correlation effects for simplicity (the following relations also hold if they are included), we specify the position of the $4f^{n_f+1}$ level relative to ε_F (cf. eq. (3)) by

$$\tilde{\Delta}_+(4f^{n_f} \to 4f^{n_f+1}) \equiv E^{\mathrm{RHF}}_{\mathrm{metal}}[4f^{n_f+1}(5d,6s)^{m-1}] - E^{\mathrm{RHF}}_{\mathrm{metal}}[4f^{n_f}(5d,6s)^m]. \tag{40}$$

If an nl core hole is present this energy becomes

$$\begin{aligned}\tilde{\Delta}_+(4f^{n_f} \to 4f^{n_f+1};\ nl\ \text{hole}) \equiv{}& E^{\mathrm{RHF}}_{\mathrm{metal}}[(nl\,\text{hole})4f^{n_f+1}(5d,6s)^m] \\ &- E^{\mathrm{RHF}}_{\mathrm{metal}}[(nl\,\text{hole})4f^{n_f}(5d,6s)^{m+1}].\end{aligned} \tag{41}$$

The core hole consequently changes the $4f^{n_f+1}$ level position by an amount

$$\begin{aligned}\tilde{\sigma}(nl) &\equiv \tilde{\Delta}_+(4f^{n_f} \to 4f^{n_f+1}) - \tilde{\Delta}_+(4f^{n_f} \to 4f^{n_f+1};\ nl\ \text{hole}) \\ &= \{E^{\mathrm{RHF}}_{\mathrm{metal}}[(nl\ \text{hole})4f^{n_f}(5d,6s)^{m+1}] - E^{\mathrm{RHF}}_{\mathrm{metal}}[4f^{n_f}(5d,6s)^m]\} \\ &\quad - \{E^{\mathrm{RHF}}_{\mathrm{metal}}[(nl\ \text{hole})4f^{n_f+1}(5d,6s)^m] - E^{\mathrm{RHF}}_{\mathrm{metal}}[4f^{n_f+1}(5d,6s)^{m-1}]\} \\ &\equiv \rho(nl),\end{aligned} \tag{42}$$

where the last line follows from eqs. (38) and (39). Hence, the replicate splitting of the nl core hole in the presence of $4f^{n_f}$ and $4f^{n_f+1}$ configurations is equal to the energy by which removal of an nl core electron lowers the $4f^{n_f+1}$ level.

Core state spectra of lanthanide systems may feature satellite structures which correspond to screening of the core hole by 4f rather than by conduction electrons (Wertheim and Campagna 1978, Crecelius et al. 1978, Herbst et al. 1980). In our scheme the excitation energy of such a satellite is

$$\tilde{\Delta}(nl\ \text{sat}) \equiv E^{\mathrm{RHF}}_{\mathrm{metal}}[(nl\ \text{hole})4f^{n_f+1}(5d,6s)^m] - E^{\mathrm{RHF}}_{\mathrm{metal}}[4f^{n_f}(5d,6s)^m], \tag{43}$$

and its separation $\tilde{\delta}(nl)$ from the conduction-electron-screened line is

$$\tilde{\delta}(nl) \equiv \tilde{\Delta}(nl\ \text{sat}) - \tilde{\Delta}_-(4f^{n_f};\ nl). \tag{44}$$

These definitions imply that

$$\tilde{\Delta}_+(4f^{n_f} \to 4f^{n_f+1}) = \tilde{\Delta}(nl\ \text{sat}) - \tilde{\Delta}_-(4f^{n_f+1};nl) \tag{45}$$

and

$$\rho(nl) = \tilde{\sigma}(nl) = \tilde{\Delta}_+(4f^{n_f} \to 4f^{n_f+1}) - \tilde{\delta}(nl). \tag{46}$$

Now in mixed valence systems ambiguity may arise regarding distinction between a conduction-electron-screened core line corresponding to the $4f^{n_f+1}$ configuration and the satellite associated with the $4f^{n_f}$ configuration. We have suggested (Herbst and Wilkins 1982) that a BIS determination of $\Delta_+(4f^{n_f} \rightarrow 4f^{n_f+1})$ in addition to measurement of the *nl* core spectrum can be used with eqs. (45) and (46) to resolve the ambiguity.

In the case of cerium alloys such a complete study exists (Fuggle et al. 1983, Gunnarsson et al. 1983, Gunnarsson and Schönhammer, cf. chapter 64). The approach of Gunnarsson and Schönhammer (1983 a,b) has been used to fit the XPS/BIS and core XPS spectra of many Ce compounds. With essentially constant values of Δ_+, $\Delta_-[=U-\Delta_+]$, $\rho(nl)$, and $\delta(nl)[=\Delta_+-\rho]$, it is possible to achieve very good fits and hence determine Γ (called Δ by Gunnarsson and Schönhammer) and the relative amounts of f^0, f^1, and f^2 in the ground state. The most striking result is that the f occupancy of the ground state always exceeds 0.8, in rough consistency with our fig. 17 illustrating the difficulty of reducing $\Delta_-(f^1 \rightarrow f^0)$ below an eV. While Γ lies in the range 30 to 250 meV, a typical value is 0.1 eV. Perhaps it is fitting to close with this observation: the only serious problem remaining for 4f excitations in the lanthanides is a first-principles approach to the calculation of the hybridization matrix element. It is nonetheless satisfying that we can fit the spectra with only that adjustable parameter.

Acknowledgements

Much of the research described in this review developed from initial work done in collaboration with R.E. Watson, whose enthusiasm and insights we gratefully acknowledge. We are also indebted to both Bengt I. Lundqvist for initially stimulating our interest in the lanthanides and Ingvar Lindgren for providing the relativistic atomic code as well as indispensable advice regarding its use. It has been our distinct pleasure to constructively interact with many colleagues actively involved with experiments in this area, and we especially thank D. Wohlleben, G.K. Wertheim, S.P. Kowalczyk, M.B. Maple, M. Campagna, Y. Baer, and J.W. Allen. One of us (JWW) gratefully acknowledges the NSF through the Materials Science Center at Cornell for the support of all work in this area.

References

Allen, J.W., L.I. Johansson, R.S. Bauer, I. Lindau and S.B.M. Hagström, 1978, Phys. Rev. Lett. **41**, 1499.

Allen, J.W., L.I. Johansson, I. Lindau and S.B.M. Hagström, 1980, Phys. Rev. B **21**, 1335.

Allen, J.W., S.-J. Oh, M.B. Maple and M.S. Torikachvili, 1983, Phys. Rev. B **28**, 5347.

Allen, J.W., M.B. Maple and J.W. Wilkins, 1987, to appear in Rev. Mod. Phys.

Anderson, P.W., 1961, Phys. Rev. **124**, 41.

Baer, Y., and G. Busch, 1974, J. Electron Spectrosc. & Relat. Phenom. **5**, 611.

Baer, Y., and J.K. Lang, 1979, J. Appl. Phys. **50**, 7485.

Baer, Y., and Ch. Zürcher, 1977, Phys. Rev. Lett. **39**, 956.

Bardeen, J., 1936, Phys. Rev. **49**, 654.

Bauchspiess, K.R., W. Boksch, E. Holland-Moritz, H. Launois, R. Pott and D. Wohlleben,

1981, L_{III} absorption edges of Ce and Yb intermediate valence compounds: Non-existence of tetravalent cerium compounds, in: Valence Fluctuations in Solids, eds L.M. Falicov, W. Hanke and M.B. Maple (North-Holland, Amsterdam) p. 417.
Beaudry, B.J., and K.A. Gschneidner Jr, 1978, Preparation and basic properties of the rare earth metals, in: Handbook on the Physics and Chemistry of Rare Earths, Vol. 1, eds K.A. Gschneidner Jr and L. Eyring (North-Holland, Amsterdam) ch. 2, p. 216.
Bickers, N.E., D.L. Cox and J.W. Wilkins, 1985, Phys. Rev. Lett. **54**, 230.
Blume, M., A.J. Freeman and R.E. Watson, 1964, Phys. Rev. **134**, A320.
Brewer, L., 1971a, J. Opt. Soc. Am. **61**, 1101.
Brewer, L., 1971b, J. Opt. Soc. Am. **61**, 1666.
Buschow, K.H.J., M. Campagna and G.K. Wertheim, 1977, Solid State Commun. **24**, 253.
Campagna, M., G.K. Wertheim and E. Bucher, 1976, Structure and Bonding **30**, 99.
Campagna, M., G.K. Wertheim and Y. Baer, 1979, Unfilled inner shells: Rare earths and their compounds, in: Photoemission in Solids II, Topics in Applied Physics, Vol. 27, eds L. Ley and M. Cardona (Springer, Berlin) ch. 4.
Cox, P.A., 1975, Structure and Bonding **24**, 59.
Cox, P.A., J.K. Lang and Y. Baer, 1981, J. Phys. F **11**, 113.
Crecelius, G., G.K. Wertheim and D.N.E. Buchanan, 1978, Phys. Rev. B **18**, 6519.
Croft, M., J.H. Weaver, D.J. Peterman and A. Franciosi, 1981, Phys. Rev. Lett. **46**, 1104.
Elliott, R.J., 1972, Introduction to the magnetic properties of rare earth metals, in: Magnetic Properties of Rare Earth Metals, ed. R.J. Elliott (Plenum, London) ch. 1.
Falicov, L.M., W. Hanke and M.B. Maple, eds, 1981, Valence Fluctuations in Solids (North-Holland, Amsterdam).
Felsteiner, J., M. Heilper and K.-F. Berggren, 1979, Solid State Commun. **32**, 343.
Franciosi, A., J.H. Weaver, N. Mårtensson and M. Croft, 1981, Phys. Rev. B **24**, 3651.
Franciosi, A., J.H. Weaver, P. Perfetti, A.D. Katnani and G. Margaritondo, 1983, Solid State Commun. **47**, 427.
Fuggle, J.C., F.U. Hillebrecht, Z. Zolnierek, R. Lässer, Ch. Freiburg, O. Gunnarsson and K. Schönhammer, 1983, Phys. Rev. B **27**, 7330.
Gadzuk, J.W., 1978, Many-body effects in photoemission, in: Photoemission and the Electronic Properties of Surfaces, eds B. Feuerbacher, B. Fitton and R.F. Willis (Wiley, New York) ch. 5.
Gerken, F., 1983, J. Phys. F **13**, 703.
Gunnarsson, O., and K. Schönhammer, 1983a, Phys. Rev. Lett. **50**, 604.
Gunnarsson, O., and K. Schönhammer, 1983b, Phys. Rev. B **28**, 4315.
Gunnarsson, O., K. Schönhammer, J.C. Fuggle, F.U. Hillebrecht, J.-M. Esteva, R.C. Karnatak and B. Hillebrand, 1983, Phys. Rev. B **28**, 7330.
Gustafson, D.R., J.D. McNutt and L.O. Roellig, 1969, Phys. Rev. **183**, 435.
Haldane, F.D.M., 1977a, Phys. Rev. B **15**, 281.
Haldane, F.D.M., 1977b, Phys. Rev. B **15**, 2477.
Harris, J., and R.O. Jones, 1978, J. Chem. Phys. **68**, 3316.
Herbst, J.F., 1982, Phys. Rev. Lett. **49**, 1586.
Herbst, J.F., 1983, Phys. Rev. B **28**, 4204.
Herbst, J.F., 1984, Phys. Rev. B **30**, 3020.
Herbst, J.F., and J.W. Wilkins, 1979a, Phys. Rev. B **20**, 2999.
Herbst, J.F., and J.W. Wilkins, 1979b, Phys. Rev. Lett. **43**, 1760.
Herbst, J.F., and J.W. Wilkins, 1981, Phys. Rev. B **24**, 1679.
Herbst, J.F., and J.W. Wilkins, 1982, Phys. Rev. B **26**, 1689.
Herbst, J.F., and J.W. Wilkins, 1984, Phys. Rev. B **29**, 5992.
Herbst, J.F., D.N. Lowy and R.E. Watson, 1972, Phys. Rev. B **6**, 1913.
Herbst, J.F., R.E. Watson and J.W. Wilkins, 1976a, Phys. Rev. B **13**, 1439.
Herbst, J.F., R.E. Watson and I. Lindgren, 1976b, Phys. Rev. B **14**, 3625.
Herbst, J.F., R.E. Watson and Y. Baer, 1977, Phys. Rev. B **16**, 2447.
Herbst, J.F., R.E. Watson and J.W. Wilkins, 1978, Phys. Rev. B **17**, 3089.
Herbst, J.F., J.M. Burkstrand and J.W. Wilkins, 1980, Phys. Rev. B **22**, 531.
Herring, C., 1966, Exchange interactions among itinerant electrons, in: Magnetism, Vol. IV, eds G.T. Rado and H. Suhl (Academic, New York) ch. IX.
Hillebrecht, F.U., J.C. Fuggle, G.A. Sawatzky, M. Campagna, O. Gunnarsson and K. Schönhammer, 1984, Phys. Rev. B **30**, 1777.
Hodges, L., R.E. Watson and H. Ehrenreich, 1972, Phys. Rev. B **5**, 3953.
Hölzl, J., and F.K. Schulte, 1979, Work function of metals, in: Solid Surface Physics, ed. G. Höhler (Springer, Berlin) p. 1.
Hüfner, S., and G.K. Wertheim, 1973, Phys. Rev. B **7**, 5086.
Johansson, B., 1975, Phys. Rev. B **11**, 2740.
Johansson, B., 1979, Phys. Rev. B **19**, 6615.
Johansson, B., and A. Rosengren, 1975, Phys. Rev. B **11**, 2836.
Johansson, L.I., J.W. Allen, T. Gustafsson, I. Lindau and S.B.M. Hagström, 1978, Solid State Commun. **28**, 53.
Kagawa, T., 1975, Phys. Rev. A **12**, 2245.
Kasuya, T., and T. Saso, 1985, Theory of Heavy Fermions and Valence Fluctuations (Springer-Verlag, Berlin).
Koopmans, T.H., 1933, Physica **1**, 104.
Kornstädt, U., R. Lässer and B. Lengeler, 1980, Phys. Rev. B **21**, 1898.
Krill, G., J.P. Senateur and A. Amamou, 1980, J. Phys. F **10**, 1889.

Lang, J.K., and Y. Baer, 1980, J. Magn. & Magn. Mater. **15–18**, 1227.
Lang, J.K., Y. Baer and P.A. Cox, 1979, Phys. Rev. Lett. **42**, 74.
Lang, J.K., Y. Baer and P.A. Cox, 1981, J. Phys. F **11**, 121.
Lawrence, J.M., P.S. Riseborough and R.D. Parks, 1981, Rep. Prog. Phys. **44**, 1.
Lawrence, J.M., J.W. Allen, S.-J. Oh and I. Lindau, 1982, Phys. Rev. B **26**, 2362.
Lee, P.A., T.M. Rice, J.W. Serene, L.J. Sham and J.W. Wilkins, 1986, Comments Con. Mat. Phys. **12**, 99.
Lee, S.-T., S. Süzer, E. Matthias, R.A. Rosenberg and D.A. Shirley, 1977, J. Chem. Phys. **66**, 2496.
Lindgren, I., and A. Rosén, 1974, Case Studies At. Phys. **4**, 93.
Liu, S.H., 1978, Electronic structure of rare earth metals, in: Handbook on the Physics and Chemistry of Rare Earths, Vol. 1, eds K.A. Gschneidner Jr and L. Eyring (North-Holland, Amsterdam) ch. 3.
Martensson, N., B. Reihl and R.D. Parks, 1982, Solid State Commun. **41**, 573.
Martin, W.C., L. Hagan, J. Reader and J. Sugar, 1974, J. Phys. & Chem. Ref. Data **3**, 771.
Martin, W.C., R. Zalubas and L. Hagan, 1978, Atomic Energy Levels – The Rare Earth Elements (U.S. GPO, Washington, D.C.).
McEwen, K.A., 1978, Magnetic and transport properties of the rare earths, in: Handbook on the Physics and Chemistry of Rare Earths, Vol. 1, eds K.A. Gschneidner Jr and L. Eyring (North-Holland, Amsterdam) ch. 6.
McMahan, A.K., and R.C. Albers, 1982, Phys. Rev. Lett. **49**, 1198.
Müller-Hartmann, E., B. Roden and D. Wohlleben, 1985, Proc. 4th Int. Conf. on Valence Fluctuations, J. Magn. & Magn. Mater. **47&48**.
Nielson, C.W., and G.F. Koster, 1963, Spectroscopic Coefficients for the p^n, d^n and f^n configurations (MIT, Cambridge).
Norman, M.R., D.D. Koelling, A.J. Freeman, H.J.F. Jansen, B.I. Min, T. Oguchi and Ling Ye, 1984, Phys. Rev. Lett. **53**, 1673.
Oh, S.-J., J.W. Allen and I. Lindau, 1984, Phys. Rev. B **30**, 1937.
Parks, R.D., 1977, Valence Instabilities and Related Narrow-Band Phenomena (Plenum, New York).
Parks, R.D., B. Reihl, N. Martensson and F. Steglich, 1983, Phys. Rev. B **27**, 6052.
Pickett, W.E., A.J. Freeman and D.D. Koelling, 1981, Phys. Rev. B **23**, 1266.
Platau, A., and S.-E. Karlsson, 1978, Phys. Rev. B **18**, 3820.
Rhyne, J.J., 1972, Bulk magnetic properties of the rare earth metals, in: Magnetic Properties of Rare Earth Metals, ed. R.J. Elliott (Plenum, London) ch. 4.
Schneider, W.-D., C. Laubschat, G. Kalkowski, J. Haase and A. Puschmann, 1983, Phys. Rev. B **28**, 2017.
Seitz, F., 1940, The Modern Theory of Solids (McGraw-Hill, New York) ch. XI.
Slater, J.C., 1960a, Quantum Theory of Atomic Structure, Vols. I and II (McGraw-Hill, New York).
Slater, J.C., 1960b, Quantum Theory of Atomic Structure, Vol. I (McGraw-Hill, New York) p. 324.
Syassen, K., G. Wortmann, J. Feldhaus, K.H. Frank and G. Kaindl, 1982, Phys. Rev. B **26**, 4745.
Wachter, P., and H. Boppart, eds, 1982, Valence Instabilities (North-Holland, Amsterdam).
Watson, R.E., 1960, Phys. Rev. **118**, 1036.
Watson, R.E., H. Ehrenreich and L. Hodges, 1970, Phys. Rev. Lett. **24**, 829.
Watson, R.E., M.L. Perlman and J.F. Herbst, 1976, Phys. Rev. B **13**, 2358.
Wehr, H., K. Knorr, F.N. Gygax, A. Schenck and W. Studer, 1981, Phys. Rev. B **24**, 4041.
Wertheim, G.K., 1979, J. Electron Spectrosc. & Relat. Phenom. **15**, 5.
Wertheim, G.K., and M. Campagna, 1977, Chem. Phys. Lett. **47**, 182.
Wertheim, G.K., and M. Campagna, 1978, Solid State Commun. **26**, 553.
Wertheim, G.K., and G. Crecelius, 1978, Phys. Rev. Lett. **40**, 813.
Wertheim, G.K., I. Nowik and M. Campagna, 1978, Z. Phys. B **29**, 193.
Wieliczka, D.M., J.H. Weaver, D.W. Lynch and C.G. Olson, 1982, Phys. Rev. B **26**, 7056.
Wieliczka, D.M., C.G. Olson and D.W. Lynch, 1984, Phys. Rev. B **29**, 3028.
Williams, A.R., and N.D. Lang, 1978, Phys. Rev. Lett. **40**, 954.
Wohlleben, D., and J. Röhler, 1984, J. Appl. Phys. **55**, 1904.

Handbook on the Physics and Chemistry of Rare Earths, Vol. 10
edited by K.A. Gschneidner, Jr., L. Eyring and S. Hüfner

Chapter 69

THERMODYNAMIC ASPECTS OF 4f LEVELS IN METALS AND COMPOUNDS

Börje JOHANSSON
Center for Materials Science, Los Alamos National Laboratory, Los Alamos, New Mexico 87545, USA

and

*Condensed Matter Theory Group, Department of Physics, Box 530, Uppsala University, S-751 21 Uppsala, Sweden**

Nils MÅRTENSSON
Department of Physics, Box 530, Uppsala University, S-751 21 Uppsala, Sweden

Contents

List of symbols

A	atomic number
A_{mol}	surface area of one mol of atoms
BIS	bremsstrahlung isochromat spectroscopy

* Permanent address

D	ionization energy difference
$D\varepsilon^{\text{comp}}(\text{f} \rightarrow \varepsilon_{\text{F}})$	generalized 4f binding energy shift. (The difference between the XPS 4f binding energy in a compound and the energy for a bulk valence change in the pure metal (to a higher valence))
$D\varepsilon^{\text{comp}}(\varepsilon_{\text{F}} \rightarrow \text{f})$	generalized unoccupied 4f level shift. (The difference between the BIS 4f energy position in a compound and the energy for a bulk valence change in the pure metal (to a lower valence))
$\Delta E_{\text{I,II}}$	energy difference between the divalent and monovalent metal states
$\Delta E_{\text{II,III}}$	energy difference between the trivalent and divalent metal states
$\Delta E_{\text{III,IV}}$	energy difference between the tetravalent and trivalent metal states
$\Delta E_{\text{II,III}}^{\text{cluster}}$	energy difference between the trivalent cluster and divalent cluster
$\Delta E_{\text{II,III}}^{\text{surf}}$	energy difference between a completely trivalent system and one with a trivalent bulk and a divalent surface
$\Delta E_{\text{II,III}}^{\text{comp,surf}}$	energy difference between the trivalent and divalent states at the surface of a compound
$\Delta\varepsilon^{\text{comp}}(\text{f} \rightarrow \varepsilon_{\text{F}})$	chemical shift of the 4f level (4f position in a compound relative to the 4f position in the pure metal)
$\Delta\varepsilon^{\text{comp}}(\varepsilon_{\text{F}} \rightarrow \text{f})$	chemical shift of the unoccupied 4f level
ΔE_{S}	surface shift of the 4f level in the pure metal
$\Delta E_{\text{S}}^{\text{comp}}$	compound surface shift. Shift of the surface 4f level relative to the bulk for a compound
$\Delta(\Delta E_{\text{S}})$	difference between the compound surface shift and the pure metal surface shift
$\Delta E_{\text{S}}^{\text{BIS}}$	unoccupied 4f level energy shift between a surface and a bulk atom
$\Delta H^{\text{comp}}(\text{II})$	heat of formation of a divalent compound
$\Delta H^{\text{comp}}(\text{III})$	heat of formation of a trivalent compound
$\Delta(n)$	correction term due to change of Racah parameters between element A and $A+1$
ΔE^1	change of the Racah parameter E^1 between atom A and $A+1$
E^0, E^1, E^3	Racah parameters
$E_{\text{coh,surf}}$	surface cohesive energy
E_{coh}	cohesive energy
$E_{\text{IV}}^{\text{imp}}(\text{III})$	restricted heat of solution of a tetravalent impurity in a trivalent lanthanide metal host
$E_{\text{IV,thermo}}^{\text{imp}}(\text{III})$	thermodynamical heat of solution of a tetravalent impurity in a trivalent lanthanide metal host
$E_{\text{III}}^{\text{imp}}(\text{II})$	restricted heat of solution of a trivalent impurity in a divalent lanthanide metal host
$E_{\text{II}}^{\text{imp}}(\text{III})$	restricted heat of solution of a divalent impurity in a trivalent lanthanide metal host
$E_{\text{III}}^{\text{imp,surf}}(\text{II})$	heat of solution for a surface substitutional trivalent impurity in a divalent system
$E_{\text{II}_{\text{comp}}}^{\text{imp}}(\text{II comp})$	'trivalent molecular impurity' solution energy in a divalent compound
$E_{\text{II}}^{\text{interf}}(\text{III})$	interfacial energy between a divalent layer and a trivalent bulk
$E_{\text{f}\rightarrow\text{d}}^{\text{atom}}$	atomic excitation energy from $f^{n+1}s^2$ to $f^n ds^2$
$\varepsilon(\text{f} \rightarrow \varepsilon_{\text{F}})$	4f binding energy relative to the Fermi energy
ε_{F}	Fermi energy
$\varepsilon^{\text{surf}}(\text{f} \rightarrow \varepsilon_{\text{F}})$	energy position of the 4f level relative to the Fermi energy for a surface atom
$\varepsilon^{\text{comp}}(\text{f} \rightarrow \varepsilon_{\text{F}})$	energy position of the 4f level relative to the Fermi energy in a compound
$\varepsilon(\varepsilon_{\text{F}} \rightarrow \text{f})$	energy position of the unoccupied 4f level relative to the Fermi energy
EXAFS	extended X-ray absorption fine structure
F^{S}	Helmholtz surface free energy
γ	surface tension in the solid phase
γ_{L}	surface tension in the liquid phase
γ_{M}	molar surface tension
I_4	fourth ionization energy
$I_4^{\text{XPS}}(\varepsilon_{\text{F}})$	$\varepsilon(\text{f} \rightarrow \varepsilon_{\text{F}})$ for a trivalent lanthanide metal
UPS	ultraviolet photoelectron spectroscopy
U_{M}^{S}	molar surface energy

U_{II}^{S}	molar surface energy of a divalent metal
U_{III}^{S}	molar surface energy of a trivalent metal
U_f	Racah parameter
XPS	X-ray photoelectron spectroscopy

1. Introduction

Recently quite a number of basic studies have been devoted to lanthanide metals and lanthanide compounds. There are several reasons for this. For instance, the discovery of the *mixed valence phenomenon* has created a wide-spread interest in the fundamental electronic structure of 4f materials (see for example Parks 1977, Falicov et al. 1981, Wachter and Boppart 1982, Müller-Hartmann et al. 1985). More recently, the discovery of the so-called *heavy fermion superconductors* (Steglich et al. 1979, Fisk et al. 1986) has drawn further attention to the properties of the 4f and 5f shells. A lot of research will still be necessary before a detailed understanding of these physical phenomena will be obtained (Lee et al. 1986). Another important reason for the present development in lanthanide research is that high-quality samples are now available (Gschneidner 1984).

Photoelectron spectroscopy is an experimental method which has gained wide-spread popularity since it monitors the electronic structure in a relatively direct way. Furthermore, the recent dramatic increase of surface physics and surface chemistry studies have accentuated the interest in the technique, since the experimentally observed photoelectrons originate essentially only from the topmost surface layer and a few layers beneath the surface of the crystal. The surface sensitivity of this technique, however, also causes experimental problems for lanthanide systems due to the high chemical reactivity of these materials. Therefore it is only relatively recently that photoelectron spectroscopy has become widely applied to lanthanide based systems (Baer and Busch 1974, Campagna et al. 1976, 1979); also see the following chapters in this volume: Baer and Schneider chapter 62, Campagna and Hillebrecht chapter 63, Lynch and Weaver chapter 66, and Hüfner chapter 67. The most detailed information concerning the electron structure of solids is obtained from single crystal systems. Using angular resolved photoemission in connection with oriented single crystal surfaces it is possible to map the bulk and surface electronic band structure. Furthermore it is only for single crystal surfaces that a well-defined surface crystallographic structure can be achieved. Polycrystalline samples will instead give a distribution of different surface orientations. There are, however, considerable experimental difficulties connected with the cleaning procedure of single crystal surfaces of the lanthanide metals. Such experiments are therefore still rare, but one can expect an increased number of single-crystal studies in the near future.

The photoemission of electrons from a 4f shell often gives rise to a rather strong signal and to an easily recognizable pattern in the spectrum, which has stimulated the experimental work in this area. The 4f levels are clearly seen in X-ray photoelectron spectroscopy (XPS) where photon energies of 1254 and 1487 eV are generally used. It is only for the light lanthanides that the 4f emission can sometimes

be difficult to separate from other contributions to the photoemission intensity. Using tunable synchrotron radiation it is however possible to selectively enhance the 4f emission in such a way that the 4f's are clearly visible also for the light lanthanides. Most synchrotron radiation studies have been performed with photon energies between 50–200 eV. An important difference between using high and low photon energies is that this leads to significantly different surface sensitivities. The mean free path of photoelectrons has a minimum at around 50–100 eV and increases towards higher kinetic energies. Therefore, when low photon energies are used an extreme surface sensitivity can be obtained with as much as 50% of the photoemission intensity coming from the outermost surface layer. In XPS experiments, on the other hand, the corresponding fraction is of the order of 15%, permitting fundamental investigations of the bulk electronic structure.

The present focussing of interest to this type of spectroscopy for lanthanide materials has undoubtedly led to some duplication of work. As an example we mention the numerous studies of the ytterbium metal. At least ten published papers have reported the photoelectron valence band spectrum of this element. However, in an early stage of development of a research technique, such as the present photoelectron spectroscopy in connection with highly chemically reactive materials, such duplication might be quite useful.

Also the inverse technique to photoelectron spectroscopy, which is used to study the unoccupied electron states, has become more and more frequently applied to lanthanide systems. This spectroscopy is commonly referred to as inverse photoemission or BIS (bremsstrahlung isochromat spectroscopy). The name inverse photoemission is generally used when studying low-energy photons whereas the name BIS is used for experiments in the X-ray regime (most commonly 1487 eV). It might be that BIS has its most advantages when applied to f electron systems. In the 4f systems the unoccupied valence states (i.e. those relatively close to the Fermi energy) are of primary interest and also here processes involving the f shell

$$f^n + e \rightarrow f^{n+1} + h\nu \tag{1}$$

are dominating the spectra and have typical fingerprint features. Hence also this spectroscopy can be used for valence assignments. The comments above concerning the surface sensitivity of photoelectron spectroscopy also applies to this technique. The present development of experimental equipments suggests that BIS will become a rather common spectroscopy in a relatively near future.

This flourishing experimental activity has created a need to understand the observed phenomena from a theoretical point of view. The observed fingerprint pattern of the $f^n \rightarrow f^{n-1}$ photoelectron process has been well explained by the fractional parentage method (Cox 1975, Beatham et al. 1979, Gerken 1983). Similarly, the intensity distribution for the inverse process, $f^n \rightarrow f^{n+1}$ is also well accounted for by the same method (Lang et al. 1981, chapter 62 by Baer and Schneider in this volume). In the present chapter we will, however, turn most of the attention to the *energy position* of the 4f level in rare-earth materials. Firstly, we will discuss the pure elements where both the occupied and unoccupied f states will be treated. Secondly, as one of the simplest examples of a chemical shift we

will consider surface induced shifts of the 4f level. In contrast to other elements in the Periodic Table, surface shifts, or more generally chemically induced shifts, may in the case of certain favourable lanthanide systems give rise to radically *different ground states* than for the reference system (i.e., the bulk of the pure metal), namely, a change of the valence configuration. Such changes are accompanied by most dramatic effects, both physically and chemically. This possibility of valence changes and drastic electronic structure modifications gives an extra dimension to the photoelectron studies of 4f materials and is probably one of the main reasons why photoemission experiments on lanthanide systems have become so popular. This circumstance might also explain why in this area there is an unusually strong and healthy interaction between chemists and physicists, since traditionally the occurrence of different valences has been a central issue within chemistry, while the electronic structure and its effect on physical properties like resistivity and magnetic susceptibility has attracted the attention of physicists.

2. Energy position of the 4f level in the lanthanide metals

The lanthanide elements, characterized by the gradual filling of the 4f shell, have during the last two decades or so been rather extensively studied by various spectroscopic methods. This is true both for the free atoms and ions (Martin et al. 1978) as well as for the metallic state (Baer and Busch 1974, Campagna et al. 1976, 1979). Also reliable thermochemical data for the pure metals have been accumulated, like for example their heats of vaporization (cohesive energy at zero temperature) (Habermann and Daane 1964). Since these measurements all involve energy differences between different states of the lanthanide atoms (ions), it seems possible to interrelate the various data to each other and from this gain further understanding of the electronic structure of the lanthanides.

In this section we will focus our attention to photoemission results for the lanthanide metals. The 4f positions for the lanthanide metals have been determined by Lang, Baer and Cox (1981) using XPS. As will be apparent later on, these measurements have reached a level of accuracy and internal consistency that they now can be trustfully employed for theoretical considerations. What we especially have in mind is the energy position of the 4f level relative to the Fermi energy.

In the pure metallic state the open 4f electron shell retains an integral occupation number and gives rise to a well-defined localized magnetic moment. The electronic structure of the f shell in the free ion or atom remains essentially intact when the metallic state is formed. Thus there are two types of electronic states in the lanthanide metals; (a) a normal conduction band state of (sd) type and (b) a localized f state. Because of its localized nature the energy position of the 4f level cannot be obtained from a conventional band-structure calculation (Freeman 1972). Then in order to go beyond the inappropriate one-particle scheme the following picture of the position of the 4f level relative to the Fermi energy appears to be more adequate (Rosengren and Johansson 1976, Johansson and Rosengren 1976): namely, (for the case of a *trivalent* metal) that it is the *energy difference* between, on one

hand, a trivalent metallic host with *one* of its lanthanide ions in the tetravalent ionic state, and on the other hand, the perfect crystal composed of only trivalent lanthanide ions. Thus in the excited state one of the 4f electrons of a particular ion has been promoted to the conduction band leaving behind a tetravalent ion at that site. This new ionic state is assumed to be in its ground state. This means in particular that we consider only the *lowest multiplet level* of the 4f final state configuration. This restriction will be made throughout this chapter. We also assume that all the atomic crystallographic positions remain identical to those of the unexcited crystal. Also the original conduction electrons plus the extra excited one are assumed to be in a completely relaxed state relative to the new ionic configuration of the whole crystal. This means that the excited state is composed of a tetravalent impurity placed in a trivalent metallic host. Therefore, hypothetically, this excited state may be reached by the following two-step process. First the trivalent atomic site is converted to a tetravalent atomic site (as it should be in a tetravalent environment, i.e., if the whole metal was made tetravalent) costing an energy $\Delta E_{\mathrm{III,IV}}$. Thereafter this tetravalent cell is left free to adjust itself electronically to the trivalent environment (with the condition that the atoms are frozen to their initial positions), involving the energy $E_{\mathrm{IV}}^{\mathrm{imp}}(\mathrm{III})$. Thus the 4f excitation energy, $\varepsilon(\mathrm{f} \rightarrow \varepsilon_{\mathrm{F}})$, ($\varepsilon_{\mathrm{F}}$ = Fermi energy), can be written

$$\varepsilon(\mathrm{f} \rightarrow \varepsilon_{\mathrm{F}}) = \Delta E_{\mathrm{III,IV}} + E_{\mathrm{IV}}^{\mathrm{imp}}(\mathrm{III}). \tag{2}$$

In this chapter we will, to begin with, concentrate on the first part of this process, $\Delta E_{\mathrm{III,IV}}$, since this turns out to give by far the most important contribution to the excitation energy. However, we will later argue that the solution energy of the impurity, $E_{\mathrm{IV}}^{\mathrm{imp}}(\mathrm{III})$, is also of great significance.

In the above picture for the energy position of the 4f level the atomic positions were kept frozen during the excitation, which is appropriate for optical transitions (this is often referred to as a vertical transition). However, in certain situations, like for instance for stability considerations, it might be more appropriate to consider a thermodynamical excitation, $\varepsilon(\mathrm{f} \rightarrow \varepsilon_{\mathrm{F}})_{\mathrm{thermo}}$, where also the atomic positions in the final state are allowed to relax. This state is obtained by letting the impurity term in eq. (2) be replaced by the thermodynamical one, $E_{\mathrm{IV,thermo}}^{\mathrm{imp}}(\mathrm{III})$. This has the advantage that in principle it might be obtained from independent thermodynamical measurements. The quantity $\varepsilon(\mathrm{f} \rightarrow \varepsilon_{\mathrm{F}})_{\mathrm{thermo}}$ is obviously a lower limit to the actual optical excitation energy.

In the photoionization process one electron is totally removed from the system. If this electron happens to originate from a $4f^n$ configuration, then, because of the localized character of the 4f orbitals, the photoionized atom will be left with an $n-1$ occupation of its 4f shell. Therefore if the metal is trivalent the photoionized site will have a tetravalent ionic configuration, giving rise to a charge imbalance in the system. Since photoexcitation is a vertical process the atoms remain fixed to the positions they had in the moment when the X-ray quantum excites the system. Furthermore, since the photoionization takes place in a metallic system, the valence electrons will immediately respond to the $+e$ charge on the ionized site and screen this charged site as well as possible. Assuming that the main line observed in the

photoelectron spectrum indeed corresponds to this electronically completely relaxed state, this line corresponds to a final state where all the valence electrons are in their ground states relative to the $(N-1)$ trivalent, $4f^n$, ions and the one tetravalent, $4f^{n-1}$, ion (N = total number of lanthanide atoms in the system). The total number of lanthanide valence electrons in this final state is $3N$. If this final state is compared with the one used in the definition of $\varepsilon(f \rightarrow \varepsilon_F)$ in eq. (2), i.e., the one with a tetravalent impurity, we find that the only difference is that in eq. (2) the impurity final state has $3N+1$ valence electrons and is obviously a neutral system. Therefore a removal of *one* electron from this impurity final state will give the *same final state* as visualized above for the photoionization $4f^n \rightarrow 4f^{n-1}$ process, provided this electron is taken from the Fermi level, i.e., so that this ionized $+e$ charged state is in its lowest electronic configuration. In the actual photoelectron spectroscopy measurements for the trivalent metal, the measured Fermi level corresponds to an ionic configuration where *all* the atoms have the trivalent $4f^n$ configuration. Thus the experimentally measured Fermi level is not exactly the same as the Fermi level for the impurity system (composed of $N-1$ trivalent f^n atoms and one tetravalent f^{n-1} atom). However their difference is of the order of $1/N$ and for a macroscopic system they become practically identical. Therefore by relating the energy position of the $4f^n \rightarrow 4f^{n-1}$ line to the Fermi level in the photoelectron spectrum, this energy will, to the order of $1/N$, be identical to the energy expression given in eq. (2).

The picture of a charge neutral site in the final state for the $f^n \rightarrow f^{n-1}$ photoelectronic ionization was early advocated by Herbst and coworkers (Herbst et al. 1972, 1976, 1978). This was also the picture used in the thermochemical treatment of the 4f levels in the lanthanides by Johansson (1974a). A more careful examination of this complete screening picture for the lanthanides was later performed by Johansson (1979), where the impurity aspects were stressed. This type of thermochemical treatment of core electron ionizations has been generalized to include all the metallic elements in the periodic table (Johansson and Mårtensson 1980). Also de Châtel and de Boer (1981) performed a thermodynamical treatment of the 4f photoelectron ionization for some of the lanthanides, where the impurity term was included. Similarily, two-core hole final states as obtained in Auger decay processes have been considered by means of a thermodynamical approach (Mårtensson et al. 1984). Even three- and four-hole states have been treated within the complete screening picture (Johansson et al. 1983, Mårtensson et al. 1984). In all these cases good agreement with experimental data has been obtained, strongly supporting the correctness of the complete screening picture of core level ionizations in metallic systems.

Above the description of the position of the 4f level relative to the Fermi energy was given for a trivalent metal. However, the same type of arguments of course also applies to a divalent metal and the only necessary modification in eq. (2) is simply that III is replaced by II and IV by III. Thus $\Delta E_{II,III}$ is the energy difference between the trivalent and divalent metallic states of the particular element in question. For a divalent lanthanide metal the energy position of the occupied 4f level relative to the Fermi level is therefore given by

$$\varepsilon(f \rightarrow \varepsilon_F) = \Delta E_{II,III} + E_{III}^{imp}(II). \tag{2'}$$

Bremsstrahlung isochromat spectroscopy (BIS), was utilized by Lang et al. (1981) to

study also the unoccupied 4f levels (residing above the Fermi level) for the lanthanide metals. Again the complete screening picture should be applicable for the $f^n + e \rightarrow f^{n+1}$ process. By the same reasoning as above, the measured line position relative to the Fermi level can, to the order fo $1/N$, be related to a similar expression as in eq. (2). Now the situation corresponds to an electron being taken from the Fermi level and injected into the f shell of a specific ion, i.e., exactly the reverse of eq. (2). Evidently, in this case the metallic site is converted into a site with a *lower* integral valence state. The completely screened and relaxed model gives the energy position of the unoccupied 4f level relative to the Fermi energy (for a trivalent metal)

$$\varepsilon(\varepsilon_F \rightarrow f) = -\Delta E_{II,III} + E_{II}^{imp}(III). \tag{3}$$

The minus sign originates from the particular way $\Delta E_{II,III}$ was defined above. $E_{II}^{imp}(III)$ is the solution energy of the appropriate divalent impurity in the trivalent host. Again, obviously, the impurity term is not the thermodynamical one, but rather a restricted quantity where the atomic positions remain fixed in the electron capture process. Naturally, also here a thermodynamical impurity energy will give a lower limit to the vertical excitation energy in eq. (3).

With the given theoretical description of the energy position of the 4f level it is clear that the energies necessary for a *complete valence change of the whole system* play a most central role, i.e., the energies $\Delta E_{II,III}$ and $\Delta E_{III,IV}$. Fortunately, it turns out to be possible to obtain accurate numbers for these quantities. The accuracy for $\Delta E_{II,III}$ is in fact about ± 0.05 eV, which is more accurate than the experimental accuracy of ± 0.2 eV for the XPS and BIS experiments. For the energy positions of the occupied f levels in the trivalent lanthanide metals, where the theoretical expression involves a transition from a trivalent site to a tetravalent one, i.e. $\Delta E_{III,IV}$, the uncertainty in the absolute value is considerably larger than for $\Delta E_{II,III}$. However, in this case, after having fixed the position of the f level for one element (as a tie-point), the relative uncertainty for the neighbouring elements is again small. Therefore in the theoretical treatment of the f electron excitation energy the dominating contribution can be obtained with a high accuracy and good internal consistency.

As a final comment we want to emphasize that the numbers which will be derived in the following two sections for $\Delta E_{II,III}$ and $\Delta E_{III,IV}$ can be obtained from just a few 'canonical' values. These are the free atomic excitations $f^{n+1}s^2 \rightarrow f^n ds^2$ and $f^n ds^2 \rightarrow f^{n-1} d^2 s^2$ and the regular values of the cohesive energy of di-, tri- and tetravalent metals (the II A–IV A elements of the Periodic Table). Thus, for example, in a trivalent metal, the position of the occupied f level relative to the Fermi energy, ε_F, is essentially the energy of the atomic reaction $f^n ds^2 \rightarrow f^{n-1} d^2 s^2$ renormalized by about 2 eV (Johansson 1974a).

3. Energy difference between the divalent and trivalent metallic states of the lanthanide elements

Since we want to study total energy differences between different metallic valence states it is natural that we should consider cohesive energies. In fig. 1 we give

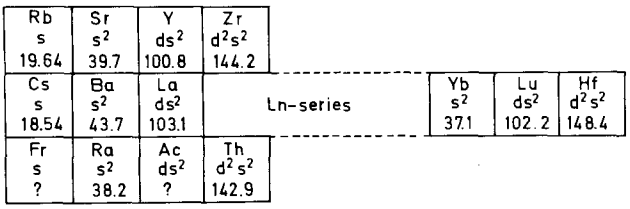

Fig. 1. Cohesive energies (Brewer 1975) for some elements relevant to the lanthanide elements (kcal/mol).

cohesive energies (Brewer 1975) for some elements relevant for the present study. From this figure it is immediately clear that mono-, di-, tri- and tetravalent metals have cohesive energies of about 20, 40, 100 and 145 kcal/mol, respectively. (Such a regular behaviour of the cohesive energy in the Periodic Table is not limited to just these elements but has a much wider applicability (Gschneidner 1964).) This regularity together with experimental atomic spectroscopic levels could in fact have been used to give results practically identical to those we will now derive in a somewhat different way. We choose, however, this different route in order to make a more direct contact with experimental thermochemical data and to achieve as accurate values as presently possible.

As free atoms most of the lanthanides have a divalent atomic configuration, $4f^{n+1}\,6s^2$. (Here and in the following the 4f electrons will be considered as core electrons.) Only lanthanum, cerium, gadolinium and lutetium are different in this respect holding a trivalent configuration; $4f^0\,5d\,6s^2$, $4f^1\,5d\,6s^2$, $4f^7\,5d\,6s^2$ and $4f^{14}\,5d\,6s^2$, respectively. However, as is well known, in the metallic phase most of the lanthanides are found in a trivalent $4f^n$ configuration. There is a simple explanation to this, based on the non-bonding property of the localized f electrons and the property that II A and III A elements have a cohesive energy of about 40 and 100 kcal/mol, respectively. This means that in the case of a divalent metal a promotion of one f electron for each lanthanide atom in the system to the bonding metallic (5d 6s) state gives an additional binding energy of about $100 - 40 = 60$ kcal/mol. However, this gain of binding energy must be balanced against the energy required to excite the f electron to the 5d orbital. From atomic spectroscopic levels (Martin et al. 1978) it is then immediately clear that it is only for europium and ytterbium that this promotion energy is more costly than the gain of binding energy, i.e., the energy for the atomic reaction $f^{n+1}\,s^2 \rightarrow f^n\,ds^2$ is larger than 60 kcal/mol. This is the fundamental reason why Eu and Yb are divalent metals in contrast to all the other lanthanides. Note that we here only compare total energies and do not invoke a single-particle picture with a level crossing.

A tetravalent metal (IV A-type) has a cohesive energy of about 145 kcal/mol (compare fig. 1). Thus if a trivalent lanthanide metal is made tetravalent by promoting one f electron of every atom into the conduction band, a binding energy of about $145 - 100 = 45$ kcal/mol is gained. However, for all the lanthanide elements the promotion energy of the f electron is much too high to make such a transition energetically favourable (Johansson 1974b, 1977a, 1978b). That is why none of the lanthanides is found in a tetravalent metallic state. This means in

particular that the non-magnetic, so-called α-like, cerium systems do not involve a tetravalent $4f^0$ configuration. Therefore the rather common way to refer to these systems as intermediate valence (IV) systems can be very misleading, unless the meaning of IV is clarified. Clearly the properties of α-like cerium are not comparable to the electronic structure of the IV state found in some systems involving samarium, europium, thulium and ytterbium. Only in compounds with strongly electronegative elements like oxygen and fluorine does one find that a few of the lanthanide elements can attain a tetravalent configuration.

We will now derive the energy difference between the divalent and trivalent metallic states of the same lanthanide element. The cohesive energies of barium, europium and ytterbium are known experimentally (Brewer 1975). Therefore, a smooth interpolation between these values gives an accurate estimate of the (hypothetical) divalent metallic cohesive energy for the rest of the lanthanides relative to their $f^{n+1}s^2$ atomic states. As is immediately clear from fig. 2(a) the difference between such an interpolated value and the one actually measured gives directly $\Delta E_{II,III}$ for most of the lanthanides. Only for La, Ce and Gd do we have to take into account the atomic excitation $E(f^n ds^2 \rightarrow f^{n+1} s^2)$ before we can obtain $\Delta E_{II,III}$. This is illustrated in fig. 2(b). To give a comprehensive survey we show in fig. 3 the experimental cohesive energy (Brewer 1975) for all the lanthanides relative to the divalent atomic configuration $f^{n+1}s^2$. The difference between this value and the smoothly interpolated divalent cohesive energy curve in fig. 3 gives immediately $-\Delta E_{II,III}$ for most of the lanthanides. The experimental cohesive energies are generally determined with an accuracy better than 1 kcal/mol and they are listed in the first column of table 1. This accuracy means that the derived values of $\Delta E_{II,III}$ also should have a precision of about 1 kcal/mol or 0.05 eV/atom. (Unfortunately there is at present no thermochemical data available for the highly radioactive element promethium.) It is only for europium and ytterbium that a different procedure must be utilized to obtain $\Delta E_{II,III}$. This has been discussed

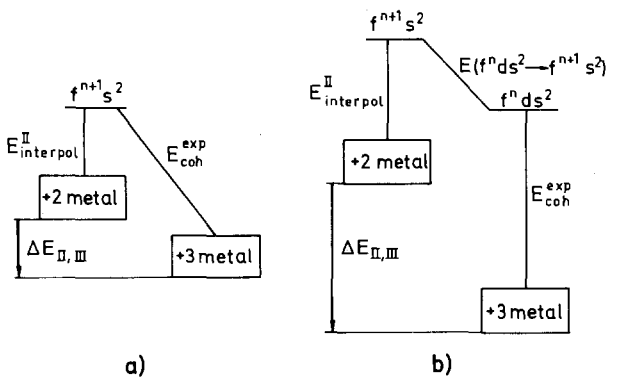

Fig. 2. Illustration of the energy difference between the trivalent and divalent states of the trivalent lanthanide metals, $\Delta E_{II,III}$. For a lanthanide with a divalent atomic ground state configuration this is the difference between the interpolated divalent cohesive energy $E^{II}_{interpol}$ and the experimental cohesive energy E^{exp}_{coh} (a). For a lanthanide with a trivalent atomic configuration, the atomic excitation, $E(f^n ds^2 \rightarrow f^{n+1} s^2)$, has to be included before $\Delta E_{II,III}$ is obtained (b).

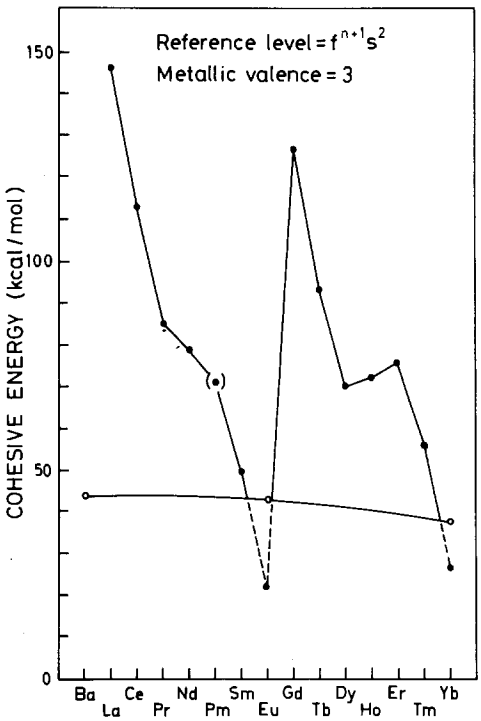

Fig. 3. Cohesive energy of the lanthanide elements as measured relative to their lowest divalent configuration, $f^{n+1}s^2$ (filled circles). For europium and ytterbium the filled circles correspond to their hypothetical trivalent metallic state. The open circles refer to the divalent metals and the smooth line gives interpolated cohesive energies for the lanthanides in their hypothetical divalent metallic state (relative to their divalent atomic configuration).

TABLE 1

Experimental data for the cohesive energies (Brewer 1975) E_{coh}, for the lanthanide elements. Derived values for $-\Delta E_{II,III}$ and $\Delta E_{III,IV}$ as described in the main text. The experimental BIS and XPS data for the 4f levels are also listed. (All energies are given in eV.)

	E_{coh}	$-\Delta E_{II,III}$	BIS experiments[a]	$\Delta E_{III,IV}$	XPS experiments[a]
La	4.47(4)	4.47	5.31(20)		
Ce	4.31(2)	3.01	3.46(20)	1.95	1.9(2)[b]
Pr	3.70(2)	1.82	2.14(20)	3.51	3.33(20)
Nd	3.41(2)	1.53	1.72(20)	4.80	4.65(20)
Pm				5.07	
Sm	2.14(2)	0.27	0.46(20)		5.07(20)
Eu	1.857(9)	−0.9	8.63(20)[c]	6.38	1.50(20)[d]
Gd	4.14(2)	3.67	4.04(20)	7.7	7.44(20)
Tb	4.05(2)	2.26	2.76(20)	2.49	2.23(20)
Dy	3.046(4)	1.30	1.81(20)	4.08	3.86(20)
Ho	3.137(13)	1.43	1.93(20)	5.16	4.89(20)
Er	3.289(4)	1.62	2.15(20)	4.99	4.70(20)
Tm	2.42(4)	0.78	1.10(20)	4.75	4.57(20)
Yb	1.61(4)	−0.5		5.69	1.27(20)[d]
Lu	4.434(9)			7.15	7.02(20)

[a] Lang et al. (1981).

[b] Platau and Karlsson (1978).

[c] The BIS experiment for Eu is related to $|\Delta E_{I,II}|$, see text.

[d] Note that the XPS experimental values for Eu and Yb should be compared with $|\Delta E_{II,III}|$.

by Gschneidner (1969), who for example, compares the heat of formation of $EuCl_3$, in which compound Eu has clearly become trivalent, with that of its neighbour element, $GdCl_3$. The formation of $EuCl_3$ can be thought of as taking place in two steps in which the divalent europium metal is first transformed to the trivalent metal and only then the trichloride is formed. For the latter process, the heat of formation of $EuCl_3$ should be very similar to that of $GdCl_3$. Therefore, the difference in the experimental values of the heat of formation for $EuCl_3$ and $GdCl_3$ corresponds directly to $\Delta E_{II,III}$(Eu). Naturally the experimental heat of formation of other compounds where Eu is trivalent can be used for the same purpose. The same type of procedure can also be applied to Yb. A somewhat different method, but still closely related to the one used by Gschneidner, was applied by Johansson and Rosengren (1975b). The most consistent value for $\Delta E_{II,III}$ appears to be 21 and 11 kcal/mol for Eu and Yb, respectively (Johansson and Munck 1985). In the second column of table 1 the derived values for $-\Delta E_{II,III}$ have been collected.

Since none of the lanthanides forms a tetravalent metal, it is somewhat more difficult to obtain accurate values for $\Delta E_{III,IV}$. However, from fig. 1 it is quite clear that cerium as a tetravalent metal should have a cohesive energy close to 145 kcal/mol relative to its tetravalent atomic state d^2s^2. For the tetravalent element after lutetium in the Periodic Table, i.e. hafnium, the experimental cohesive energy is 148.4 kcal/mol (Brewer 1975). Therefore all the lanthanides should in their hypothetical tetravalent metallic state have a cohesive energy of about 145–148 kcal/mol relative to the proper tetravalent atomic state. This means that if the atomic excitations $f^n ds^2 \rightarrow f^{n-1} d^2 s^2$ were known for the lanthanides we could easily obtain accurate values for $\Delta E_{III,IV}$. However, since these tetravalent levels are very high in energy, they have not yet been identified among the spectroscopic levels. (In fact for most of the lanthanides the $f^{n-1} d^2 s^2$ level is above the first ionization potential.) Still, even if this atomic excitation was known for only one element, there are reliable methods available from which the $f^n ds^2 \rightarrow f^{n-1} d^2 s^2$ excitation energies for the rest of the lanthanides could be estimated. This was actually the procedure employed by Johansson (1974a) to derive $\Delta E_{III,IV}$. Here we will review a somewhat different approach to obtain as accurate values for $\Delta E_{III,IV}$ as possible (Johansson 1979). This is a generalization of methods applied in accurate estimations of atomic spectroscopic data.

4. Energy difference between the trivalent and tetravalent metallic states of the lanthanide elements

In the previous section the energy difference $\Delta E_{II,III}$ for the lanthanide metals was derived from the experimental cohesive energies. Here it will be shown that these data can be used directly to give $\Delta E_{III,IV}$ through the series, provided that this value is known for at least one of the elements. The method to be used is well known in atomic spectroscopy and is called the "horizontal analysis" method. Originally this method was applied to the 3d series (Catalán et al. 1954, Racah 1954), but more recently it has been used for the lanthanide atoms by Jørgensen (1962). A more

refined and a more extensive treatment has been given by Vander Sluis and Nugent (1974), again for the lanthanides.

The basis is that the f^{n-1}–f^n difference can be expressed as (Jørgensen 1962)

$$U_f - (n-1)E^0 - g(S_{n-1} - S_n + \tfrac{1}{2})E^1 + y((L,U)_{n-1}, (L,U)_n)E^3, \tag{4}$$

where U_f, E^0, E^1 and E^3 are known as the Racah parameters and the coefficients in eq. (4) depend on certain group quantum numbers (Martin 1972). (For brevity the spin-orbit term has been neglected in eq. (4). In the analysis to follow this term, however, has been accounted for.) The Racah parameters are assumed to be equal for the two configurations f^n and f^{n-1}. Therefore, if the Racah parameters are known for all the lanthanides and the f^{n-1}–f^n difference is known for one element, then the expression in eq. (4) can be used to give an estimation of the f^{n-1}–f^n difference for the rest of the lanthanides.

An alternative method of making predictions, due originally to Racah (for a review see Martin (1972)) is also available and is known as the 'vertical analysis' method. This can simply be stated as follows: a plot of, for example, the following atomic promotion energies for the same element $f^{n+1}s^2 \rightarrow f^n ds^2$, $f^{n+1}s \rightarrow f^n ds$ and $f^{n+1} \rightarrow f^n d$ through the lanthanide series will give three essentially parallel curves. Therefore if one of the mentioned excitations is known for all the elements, the other two may be obtained by a vertical displacement of this curve (Brewer 1971). We should observe that the Racah method applies for the $f^n \rightarrow f^{n-1}$ excitation for the same element, but at different ionization stages. However, for the present problem we want to compare the excitation $f^n \rightarrow f^{n-1}$ for neighbouring elements, i.e. Ln(A, $f^n \rightarrow f^{n-1}$) and Ln($A+1$, $f^n \rightarrow f^{n-1}$), where A is the atomic number. If the Racah parameters E^1 and E^3 were the same for Ln(A) and Ln($A+1$) we would again expect a parallel behaviour of this $f^n \rightarrow f^{n-1}$ excitation energy (when plotted as a function of n) except for a possible (but relatively small) linear deviation, i.e.,

$$\mathrm{Ln}(A+1, f^n \rightarrow f^{n-1}) = E_0 + \mathrm{Ln}(A, f^n \rightarrow f^{n-1}) + K(n-1), \tag{5}$$

where E_0 and K are constants. However, it is certainly true that the Racah parameters for the f^n and f^{n-1} configurations are not exactly equal for Ln(A) and Ln($A+1$). Therefore there should be a correction $\Delta(n)$ to eq. (5) and we write

$$\mathrm{Ln}(A+1, f^n \rightarrow f^{n-1}) = E_0 + \mathrm{Ln}(A, f^n \rightarrow f^{n-1}) + \Delta(n) + K(n-1), \tag{6}$$

where $\Delta(n=1)$ is defined to be zero.

Provided the f^n configuration maintains its atomic properties in the metallic state it is obvious that we can generalize eq. (6) to a metallic situation and obtain the energy difference between the trivalent and tetravalent metallic states, $\Delta E_{III,IV}$, for the lanthanides from the following relation:

$$\Delta E_{III,IV}(A+1, f^n \rightarrow f^{n-1}) = E_0' + \Delta E_{II,III}(A, f^n \rightarrow f^{n-1}) + \Delta(n) + B(n-1), \tag{7}$$

where E_0' and B are constants. In this relation $\Delta E_{II,III}$ is already known as a function of the atomic number (section 3). Then it remains to determine the value of the constants E_0' and B, and the function $\Delta(n)$. In order to do that we need first of all to know the value of $\Delta E_{III,IV}$ for one of the lanthanide elements. From the

regularities in the cohesive energies of the metallic elements this quantity was found to be about 48 kcal/mol in the case of cerium (Johansson 1977a). In a study of the heat of formation of tetravalent cerium compounds (Johansson, 1978b), i.e., from a determination of the deviation between the experimental value and the one expected for tetravalent metallic cerium, $\Delta E_{\mathrm{III,IV}}$ was found to be about 40 kcal/mol. From this we choose 45 kcal/mol as a relatively appropriate value. An error in this value will give the same vertical displacement of all the other lanthanide $\Delta E_{\mathrm{III,IV}}$ values. Since

$$\Delta E_{\mathrm{II,III}}(\mathrm{La}) = -103\ \mathrm{kcal/mol},$$

and since $\Delta E_{\mathrm{II,III}}(\mathrm{La})$ and $\Delta E_{\mathrm{III,IV}}(\mathrm{Ce})$ both corresponds to $n = 1$ we immediately obtain $E_0' = 148$ kcal/mol. Furthermore we will neglect the possible influence by the linear correction term $B(n-1)$. Since the $\Delta E_{\mathrm{II,III}}(n)$ function is known (compare fig. 3 and table 1), it only remains to determine $\Delta(n)$ in order to obtain $\Delta E_{\mathrm{III,IV}}$ throughout the lanthanide series.

In order to find appropriate values for the $\Delta(n)$ correction we have in fig. 4 plotted the difference between the atomic LnIV($A+1$, $f^n \rightarrow f^{n-1}$ s) and LnIII(A, $f^n \rightarrow f^{n-1}$ s) excitation energies. Considering the scale in the figure, it is true that the difference between these excitation energies is essentially constant. (This property has in fact been utilized in estimations of atomic spectroscopic levels and is often referred to as a constant system difference (SD) change). However, upon this large constant difference, there is a small but significant variation. This variation undoubtedly has as its origin the change of the Racah parameters in going from LnIII(A) to LnIV($A+1$). If the excitation energies themselves are given by the expression in eq. (4) then their difference must again be given by eq. (4) only that the Racah parameters for this difference are given by their change, i.e. ΔE^1 and ΔE^3. Therefore, also the difference between the excitations LnIV($A+1$, $f^n \rightarrow f^{n-1}$ s) and LnIII(A, $f^n \rightarrow f^{n-1}$ s) will show the same familiar zigzag behaviour (compare fig. 3) as the excitation energies themselves, only at a much smaller scale. Realizing this we arrive at the "interpolated" values, shown as open circles in fig. 4 (Johansson 1979). From this figure we immediately obtain the dependence of n for the function $\Delta(n)$ ($\Delta(1)$ is put equal to zero.) Note, however, that the total variation in $\Delta(n)$ is only

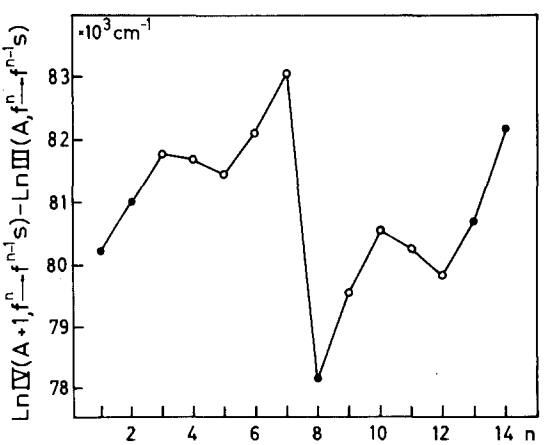

Fig. 4. Difference between the free atomic excitations LnIV($A+1$, $f^n \rightarrow f^{n-1}$s) and LnIII (A,$f^n \rightarrow f^{n-1}$s) as a function of the number of f electrons, n. Filled circles are experimental values and open circles are 'interpolated' values as described in the text. The variation of this difference relative to the $n = 1$ case gives the $\Delta(n)$ function.

$5 \times 10^3\,\mathrm{cm}^{-1}$ (0.6 eV). From this we are now in a position to obtain $\Delta E_{\mathrm{III,IV}}$ for all the lanthanides. The derived values are collected in the fourth column of table 1.

5. Comparison with XPS and BIS experiments for the lanthanide elements

The calculated $\Delta E_{\mathrm{III,IV}}$ values, which include the $\Delta(n)$ correction, are plotted as filled circles in fig. 5. In this figure also the experimental XPS data (Lang et al. 1981) for the position of the 4f level relative to the Fermi energy have been included. For cerium metal the data by Platau and Karlsson (1978) has been used. It is immediately clear that the $\Delta E_{\mathrm{III,IV}}$ values reproduce the XPS results exceedingly well. For completeness these experimental values are also tabulated in table 1 (last column). Thus the valence change energy, $\Delta E_{\mathrm{III,IV}}$, accounts in a most satisfactory way for the main part of the measured f electron binding energies. The difference is that the f electron binding energies refer to a local valence change, while $\Delta E_{\mathrm{III,IV}}$ is a global valence change of the system.

In fig. 6 we plot the difference between the experimental XPS values and $\Delta E_{\mathrm{III,IV}}$. Considering the quoted accuracy of the experimental data (± 0.2 eV) the obtained rather smooth and almost constant behaviour of the difference demonstrates that the neglected linear term $B(n-1)$ in eq. (7) has little importance. In section 6 we will return to the remaining discrepancy between the experimental data and the $\Delta E_{\mathrm{III,IV}}$ values.

The data point for Yb in figs. 5 and 6 refers to an estimated XPS binding energy for the f^{13} level in hypothetically trivalent Yb. This estimation is based on the fourth

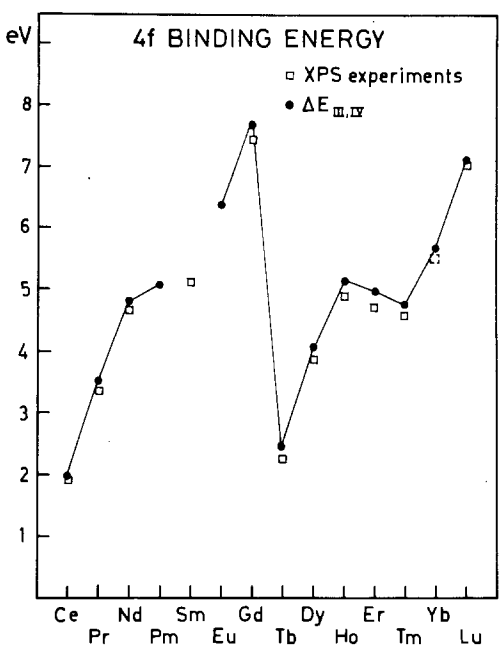

Fig. 5. Experimental XPS data (Lang et al. 1981) for the position of the 4f level relative to the Fermi energy. For cerium the data point by Platau and Karlsson (1978) is used. These experimental data are denoted by open squares. The filled circles are the calculated values for $\Delta E_{\mathrm{III,IV}}$ (Johansson 1979) (including the $\Delta(n)$ correction). For ytterbium the dotted square is used to show that this is not an experimental value but is derived from its fourth ionization energy, as described in section 8.

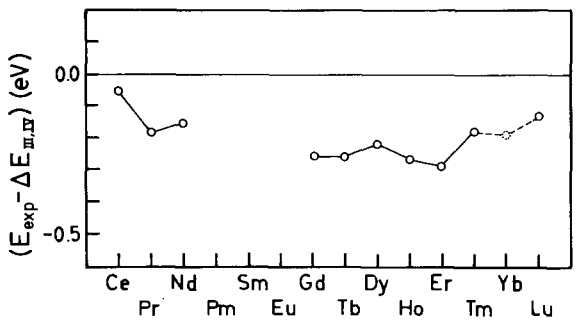

Fig. 6. Difference between experimental XPS data, E_{exp}, and $\Delta E_{III,IV}$ for the position of the 4f level relative to the Fermi energy. The dotted circle for ytterbium is used to show that it is not based on direct experimental data but is derived from the fourth ionization potential (section 8).

ionization energy of the free Yb(+3) ion (see section 8). The deviation for Yb in fig. 6 is close to that for Tm and Lu, which shows that the estimated value is accurate.

From the consistency of the difference between the experimental values and $\Delta E_{III,IV}$ it is possible to estimate rather accurately the XPS binding energy of the f^6 level in hypothetically trivalent europium metal. The value one obtains is 6.1 ± 0.2 eV. This value might be useful for considerations of chemical shifts in compounds where Eu is trivalent. For promethium the corresponding XPS binding energy can also be estimated and is found to be 4.9 ± 0.2 eV.

In fig. 7 and in table 1 we compare the experimental BIS data (Lang et al. 1981) for the lanthanides with the $-\Delta E_{II,III}$ values derived in section 3. Also the general

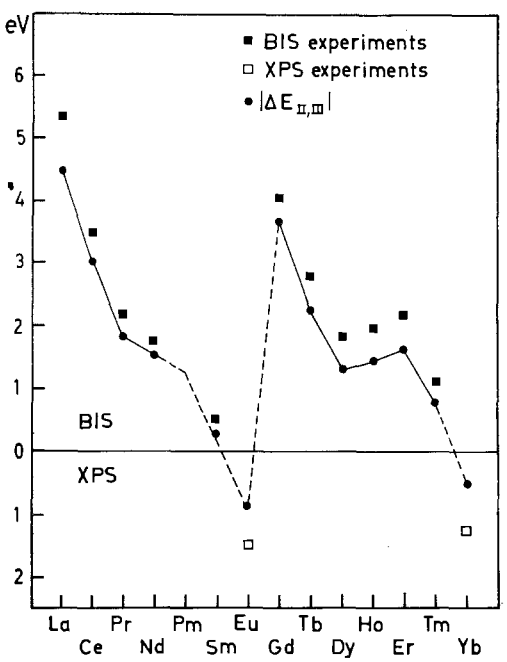

Fig. 7. Filled squares are the BIS data (Lang et al. 1981) for the unoccupied 4f levels for the lanthanide metals. The filled circles are the derived values for $\Delta E_{II,III}$ (Johansson 1979). Similarly, the open squares are XPS data for europium and ytterbium (Lang et al. 1981). Note that the upper part of the figure refers to BIS experiments, and that the lower part corresponds to XPS experiments.

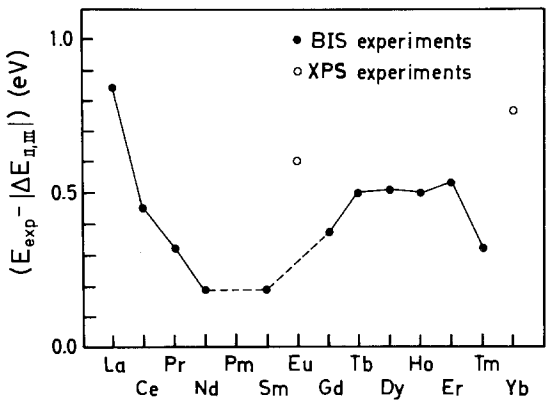

Fig. 8. Difference between on one hand the experimental BIS data for the trivalent lanthanides and the XPS data for the divalent metals europium and ytterbium and on the other the derived values of $|\Delta E_{II,III}|$. Filled circles correspond to the BIS case and open circles to the XPS case.

features of the BIS data are certainly well reproduced by $-\Delta E_{II,III}$. (In the work by Johansson (1979) a comparison was made with *preliminary* BIS data and there a large deviation could, for instance, be noticed for dysprosium. However, the final published experimental data give a much better agreement and consistency with theory). The uncertainties in the $\Delta E_{II,III}$ values are generally of the order of ± 0.05 eV. Therefore it is clear from fig. 7 that there are quite substantial deviations between the BIS data and the $\Delta E_{II,III}$ values, in fact greater than between the XPS data and $\Delta E_{III,IV}$ for the trivalent metals. In addition to this the sign of the deviation is different for the XPS data than for the BIS data.

In fig. 8 we plot the difference between the BIS experiments and the $-\Delta E_{II,III}$ values. The slightly irregular behaviour is unexpected, because even if there are deviations, these should vary smoothly through the series. However, it should be kept in mind that the experimental uncertainties are of the order of ± 0.2 eV. A comparison with fig. 6 therefore suggests that the experimental XPS data are internally more consistent than the experimental BIS data.

The finding that the $\Delta E_{III,IV}$ values reproduce the XPS data quite well but that $-\Delta E_{II,III}$ deviates more substantially from the BIS data might lead one to suspect that these two types of experiments are not directly comparable. However, in fig. 7 we have also included the XPS data for the two divalent metals europium and ytterbium and also here we note a most substantial deviation between experiment and $\Delta E_{II,III}$. These deviations are also included in fig. 8 and are in fact even somewhat larger than the deviations from the BIS data. From this we conclude that it is rather the fact that we are dealing with a divalent → trivalent or a trivalent → divalent transition instead of a trivalent → tetravalent transformation that causes the difference between the BIS and XPS results and not the experimental technique. We will return to this point in the following section.

Recent UPS data (Nilsson et al. 1985) suggest that the f^{14} binding energy in ytterbium metal is 1.17 eV rather than the value 1.27 eV used in figs. 7 and 8. Accepting this value, the difference between $\Delta E_{II,III}$(Yb) and experiment becomes more similar to the corresponding difference for Eu.

For the divalent metal europium, the BIS experiment involves a transition to a monovalent state. Therefore the complete screening picture implies that we should

study the quantity $-\Delta E_{\mathrm{I,II}}$, i.e., the energy difference between the divalent and monovalent metal. This may be obtained from the following steps of reaction:

$$\Delta E_{\mathrm{I,II}} = (+1 \text{ metal}) \rightarrow \mathrm{f}^{n+2}\mathrm{s} \text{ atom} \rightarrow \mathrm{f}^{n+1}\mathrm{s}^2 \text{ atom} \rightarrow (+2 \text{ metal}). \quad (8)$$

The first step corresponds to the cohesive energy of a monovalent metal, and should accordingly be about 20 kcal/mol (compare fig. 1). The last reaction in eq. (8) is the experimental divalent cohesive energy. For the reaction involving the two atomic states there are no experimental data available. However, the atomic excitation has been estimated to be about (Johansson 1979)

$$E(\mathrm{f}^8\mathrm{s} \rightarrow \mathrm{f}^7\mathrm{s}^2) = -7.6 \pm 0.5 \text{ eV}.$$

Thus one obtains $-\Delta E_{\mathrm{I,II}} = 8.6 \pm 0.5$ eV which should be compared with the experimental BIS value 8.63 ± 0.2 eV (Lang et al. 1981).

The same arguments can be applied to barium metal. Again considering the quantity $-\Delta E_{\mathrm{I,II}}$ one finds that the unoccupied 4f level should be situated at about 5.3 eV above the Fermi level. In this case experiments give a position of about 10 eV above the Fermi level (Kanski and Nilsson 1981), i.e., a huge deviation from the theoretical value. This shows that the 4f orbital in barium must be far more extended than for the lanthanides and therefore very sensitive to changes in the (sd) valence electron density distribution. Thus the 4f electron in barium metal cannot be treated as a core electron and therefore the approach outlined above is no longer applicable.

This large deviation for barium suggests that also the somewhat anomalous 4f position in lanthanum has a similar origin although much less pronounced. (Compare the deviation from the $-\Delta E_{\mathrm{II,III}}$ value shown in fig. 8). Thus it appears that the 4f orbital has not quite become completely core-like in lanthanum metal. However, for instance for the La^{1+} ion the localization of the 4f orbital should be more complete.

Experiments have shown that there are divalent atoms present at the surface layer of samarium metal (Wertheim and Crecelius 1978, Allen et al. 1978). Therefore, in the BIS experiments there should also be some spectral contribution from a transition to a monovalent samarium ion at the surface. From the complete screening model, the position of the f^7 level (again using eq. (8) and estimated atomic spectroscopic data) should be at about 4.1 ± 0.4 eV above the Fermi energy.

6. The impurity term

In this section we will turn to the remaining discrepancies between $\Delta E_{\mathrm{III,IV}}$ and the XPS data as well as $-\Delta E_{\mathrm{II,III}}$ and the BIS data. For example it seems quite significant that the sign of the deviations for the trivalent metals is different for the XPS data than for the BIS data. In section 2 we derived a theoretical expression for the position of the f level relative to the Fermi level. Up to now we have, however, neglected the so-called impurity term, E^{imp}.

Since a completely theoretical treatment of the energy term, E^{imp}, is not yet feasible (at least not with an accuracy appropriate to the present problem), we turn

instead to possible experimental information for the heat of solution of impurities. Thereby one is, however, referring to a thermodynamical energy, while the one required for the experimental situation in XPS or BIS is a restricted impurity term (see section 2). The thermodynamical value E^{imp}_{thermo} will always be a limiting value and gives a lower bound to E^{imp}. The quantity we are looking for in connection with the XPS experiments is the restricted solution energy of a tetravalent impurity in a trivalent host. The corresponding thermodynamical quantity is in fact something that can be determined experimentally for related systems. However, we are not aware of any such experiments for systems relevant in the present context. On the other hand it is known that thorium forms solid solutions with the lanthanide metals for all concentrations. This would imply that $E^{imp}_{IV,thermo}$ (III) is negative. Further, over this complete range of solid solubility there is no predominant tendency to formation of well-defined compounds. This must mean that even though $E^{imp}_{Th,thermo}$ (Ln) is negative, its magnitude should be comparatively small. Similar conclusions can be drawn from the binary phase diagrams between lanthanide metals and zirconium (Gschneidner 1980). With this experimental background, it still seems possible to state with some confidence that $E^{imp}_{IV,thermo}$ (III) in general will be negative, although only slightly so. If we add this effect to $\Delta E_{III,IV}$ the agreement with XPS data would obviously improve (fig. 6). Whether this impurity effect will show a slight variation with the lanthanide element or not is presently a too difficult question to answer. Such a dependence could in fact have masked the small linear correction term $B(n-1)$ discussed in connection with eq. (7).

By applying the same ideas to the BIS experiments, we then deal with a divalent impurity in a trivalent host. Similarly, the XPS experiments for europium and ytterbium involve a trivalent impurity in a divalent host. Experimentally it is known that alkaline-earth metals and trivalent lanthanide metals do not form any solid solutions. This means that $E^{imp}_{II,thermo}$ (III) and $E^{imp}_{III,thermo}$ (II) are positive. Therefore the $|\Delta E_{II,III}|$ curve in fig. 7 should be subject to a correction upwards for the theoretical BIS values and downwards for the theoretical XPS values when the effect of the impurity term is included. Apparently this would improve on the agreement with experiments. Using the Miedema semi-empirical method (Miedema 1976) for the present situation one finds that E^{imp} here might be of the order of 0.5 eV. This correction is in fact of the right magnitude to give a good agreement for most of the lanthanides (compare fig. 8).

Thus it is clear that the impurity term, although generally small compared to the energy differences $\Delta E_{II,III}$ and $\Delta E_{III,IV}$, gives a significant contribution to the $\varepsilon(f \rightarrow \varepsilon_F)$ and $\varepsilon(\varepsilon_F \rightarrow f)$ excitation energies. From the theoretical point of view it is obvious that the required *restricted* impurity energies in the expressions (2), (2′) and (3) for the f-electron excitation process are simple entities compared with the true thermodynamical ones. Therefore theoretical calculations for heats of solutions of impurities should first be applied to the present type of situations (XPS or BIS), before calculations are attempted for the much more difficult cases with completely relaxed impurities (thermodynamical limit).

It is tempting, however, to neglect the difference between E^{imp} and E^{imp}_{thermo}. Thereby the possibility opens up to use XPS and BIS experiments to *derive thermochemical*

data on a quantitative level. The thermodynamical treatment of the f-level position in the pure metals presented in section 2 can be generalized to alloys and compounds (see section 11), whereby the chemical shift of the 4f level relative to the pure metal can be expressed in terms of various thermodynamical entities. This was successfully applied by Steiner et al. (1981) to core level shifts for other types of metal atoms than lanthanides. Another case was the use of the Pd core level shifts for a derivation of the heat of formation of $Pd_{1-x}Ag_x$. Also here a most satisfactory agreement with thermochemical data was obtained (Steiner and Hüfner 1981a). This suggests that an identification of E^{imp} with $E^{\mathrm{imp}}_{\mathrm{thermo}}$ is a good approximation. It should also be remembered that when one considers chemical shifts a restricted impurity term enters twice and with opposite signs. Therefore there will at least be a partial cancellation of errors.

7. Assessments of the thermodynamical model

With the picture of the main XPS line (i.e. deconvoluted for asymmetries) for the position of the 4f level relative to the Fermi level as corresponding to a final state where the valence electrons have fully relaxed relative to the f-ionized site, the formal expression in eq. (2) is accurate. In the actual numerical evaluation of the two contributions in this expression it turns out that the energy difference $\Delta E_{\mathrm{III,IV}}$ is dominating, and that the impurity term plays only a secondary role. In an assessment of the achieved results presented in the previous sections, it is therefore important to critically examine the accuracy of $\Delta E_{\mathrm{III,IV}}$ and $\Delta E_{\mathrm{II,III}}$.

From atomic spectroscopy it has been noted that when comparing various excitations of the type $f^n \rightarrow f^{n-1}$ (by vertical or horizontal analysis), there might be a slight discontinuity for the $f^1 \rightarrow f^0$ excitation relative to the other excitation energies ($n > 1$) (Vander Sluis and Nugent 1972, Johansson and Rosengren 1975a). This is a bit unfortunate since we use cerium as the tie-point element for the $\Delta E_{\mathrm{III,IV}}$ estimations, and here we just meet this $f^1 \rightarrow f^0$ case. However, it is only for cerium that the $\Delta E_{\mathrm{III,IV}}$ value is known with a reasonable accuracy so there is no other choice. In fig. 6 the deviation for cerium is slightly different than for the other elements, which might be due to this discontinuity for the $f^1 \rightarrow f^0$ case relative to the $f^{n+1} \rightarrow f^n$ energies for the rest of the lanthanides.

Another inaccuracy is found in the correction term $\Delta(n)$, which had to be estimated for many of the lanthanides (fig. 4). The estimations are somewhat more accurate for the heavier ($n > 7$) lanthanides than for the lighter elements. (However, the deviations between $\Delta E_{\mathrm{III,IV}}$ and XPS measurements shown in fig. 6 seem to behave smoothly.) If these two types of uncertainties could be avoided it might be that the so-refined values for $\Delta E_{\mathrm{III,IV}}$ will show a nearly constant shift relative to the XPS experiments. However, it must be stressed that this discussion is presently rather academic, since neither of these inaccuracies are greater than the XPS experimental uncertainty (± 0.2 eV). If the accuracy of experiments improves in the future, hopefully experimental values of $\Delta(n)$ for all the lanthanides will have become available from atomic spectroscopy, so that more accurate $\Delta E_{\mathrm{III,IV}}$ values are at our

disposal. Finally, the value of the constant E_0' in eq. (7) is a bit uncertain, but a small change in this constant will only result in a small rigid displacement of the $\Delta E_{\mathrm{III,IV}}$ curve relative to the experimental values.

Another uncertainty, which was not discussed in sections 3–6, is the possibility of a change of the f-state Racah parameters when going from the free atom to the solid (both having the same valence state). However, from careful considerations of the cohesive energy through the trivalent lanthanide series no such effect could be discerned within the experimental accuracy (Johansson and Munck 1985). Therefore, this possible energy change of the f-level position could not exceed 0.05 eV. The same upper limit should also be expected for the divalent as well as the tetravalent metallic cases. Therefore, for quantities like $\Delta E_{\mathrm{II,III}}$ and $\Delta E_{\mathrm{III,IV}}$, where a subtraction is made, this possible effect will be totally negligible.

8. Fourth ionization energies of the lanthanides

The first three ionization energies for most of the lanthanides are known with a reasonable accuracy (Martin et al. 1978). This is no longer true for the fourth ionization energy, I_4. Presently it is only for the elements Ce, Pr, Tb, Yb and Lu that I_4 is known with an accuracy better than 0.1 eV. Some years ago interpolation methods had suggested that the I_4 values for the other elements could be fairly well estimated (Martin et al. 1974). This is still true, but the more recent experimental fourth ionization value for Tb (Spector and Sugar 1976), was found to be outside the error limit for the previous estimated value. Therefore in general, the estimated values of I_4 are now ascribed an uncertainty of about ± 0.7 eV. The reason for this can in fact be traced back to the assumption of a constant difference between the system difference (SD) values for different ionization stages, which was used in the estimation of the fourth ionization energy. As we have seen in section 4 for the excitations of interest in the present context, this assumption holds only with an accuracy of about ± 0.6 eV. In fact, the deviation from a constant SD value was the basis for the $\Delta(n)$ corrections to $\Delta E_{\mathrm{III,IV}}$. The availability of accurate experimental XPS data makes it possible to estimate new improved values for the fourth ionization energy (Johansson 1979). Since the accuracy of the XPS measurements is about ± 0.2 eV, the derived I_4 values should have a comparable accuracy.

The fact that the XPS measurements for trivalent metals can be used for such a purpose is not so surprising since they really involve an ionization of a trivalent ion to a tetravalent one. In order to make the estimations we will study the ionization energy difference D given by

$$D = I_4 - I_4^{\mathrm{XPS}}(\varepsilon_{\mathrm{F}}). \tag{9}$$

Here I_4 is the ionization energy of the LnIV species and $I_4^{\mathrm{XPS}}(\varepsilon_{\mathrm{F}})$ is the XPS result for the position of the f level relative to the Fermi energy. Since I_4 is rather accurately known for Pr, Tb and Lu we will use the values of D(Pr), D(Tb) and D(Lu) for a smooth interpolation through the series. Obviously the quantity D should vary smoothly through the series and we are therefore in the favourable position that we know its value in the beginning, in the middle, and at the end of the series. This

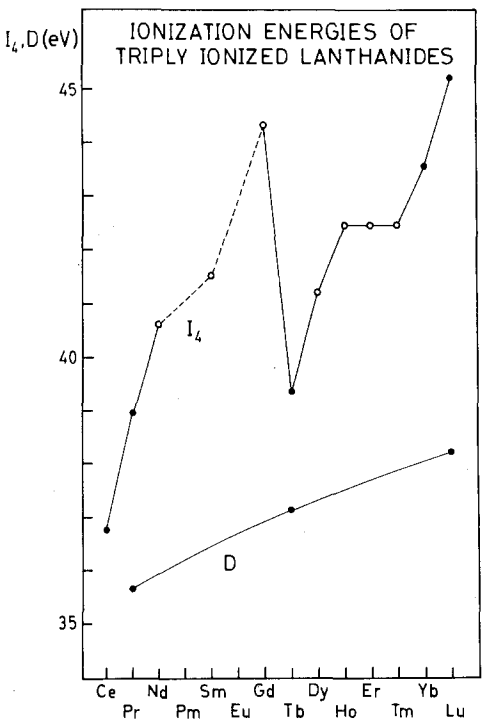

Fig. 9. Estimation of the fourth ionization energy of the lanthanides. Filled circles correspond to experimental values (Martin et al. 1978). The smooth curve is the interpolated D function discussed in the text.

permits an accurate interpolation. The interpolated smooth D curve is shown in fig. 9. From this interpolated curve we can now use eq. (9) to derive I_4 for the other lanthanides. The obtained values are shown as open circles in fig. 9. For completeness we also include in fig. 9 the experimental I_4 values for Ce and Yb.

For Eu and Yb we naturally lack XPS data for the trivalent state. The same is of course also true for Pm but for other reasons. In the case of Yb we may use the relation (9) in a reversed way, i.e., use the experimental value of I_4(Yb) to predict the XPS value for the 4f excitation in the hypothetical trivalent Yb metal. From this we immediately find

$$I_4^{\mathrm{XPS}}(\varepsilon_{\mathrm{F}})_{\mathrm{Yb(III\ metal)}} = 5.5 \pm 0.2\,\mathrm{eV}.$$

This value was used in figs. 5 and 6 where a comparison with the calculated $\Delta E_{\mathrm{III,IV}}$(Yb) was made.

In table 2 we compare the so-derived ionization energies with previous estimates. As can be seen all the new values are within the error limits of the earlier estimations.

In the previous section we estimated XPS binding energies for Pm and hypothetical trivalent Eu from the calculated values of $\Delta E_{\mathrm{III,IV}}$. From relation (9) one can from this easily obtain I_4(Pm) = 41.1 eV and I_4(Eu) = 42.8 eV. These values are in good agreement with the earlier estimations of 41.1 ± 0.6 eV and 42.7 ± 0.6 eV (Martin et al. 1978). This demonstrates that there is a good internal consistency between various types of spectroscopic data for the lanthanides.

TABLE 2
Derived values of the fourth ionization energy for the lanthanide elements by use of XPS data from the metallic state. For comparison earlier estimations are given in the last column. (All energies are given in eV).

	Exp. values (ref. a)	Estimated values from XPS data (ref. b)	Earlier estimations (ref. a)
Ce	36.758(5)		
Pr	38.98(2)		
Nd		40.6(2)	40.4(4)
Pm			41.1(6)
Sm		41.5(2)	41.4(7)
Eu			42.7(6)
Gd		44.4(2)	44.0(7)
Tb	39.37(10)		
Dy		41.2(2)	41.4(4)
Ho		42.4(2)	42.5(6)
Er		42.4(2)	42.7(4)
Tm		42.5(2)	42.7(4)
Yb	43.56(10)		
Lu	45.250(25)		

[a] Martin et al. (1978).
[b] Johansson (1979). The values have been slightly modified in accordance with the published XPS data (Lang et al. 1981).

9. Valence state at the surface of the lanthanide metals

From high-resolution X-ray photoemission spectra (XPS) for metallic samarium it was concluded that either the bulk or surface of samarium could very well be in an intermediate valence state (Wertheim and Campagna 1977). However, since the trivalent metallic state of samarium is favoured relative to the (hypothetically) divalent metallic state of samarium by about 6 kcal/mol and since the bulk properties of samarium fit very nicely to the other trivalent rare-earth metals as well as to intra-rare-earth alloys (Johansson and Rosengren 1975a) the bulk interpretation appeared to be rather unlikely. Instead it seemed more plausible that the conditions at the surface might be such that the divalent state is more favoured there than it is in the bulk (Johansson 1978a). This was confirmed in the XPS measurements on samarium by Wertheim and Crecelius (1978). In these experiments the XPS data were studied as a function of the electron take-off angle with the substrate surface. From the observed angular dependence it could be concluded that the divalent component of the spectrum originates from atoms in the surface layer. By employing synchrotron radiation, Allen et al. (1978) performed most surface-sensitive photoemission measurements and arrived at the same conclusion in a somewhat more direct way.

A characteristic feature of a surface is the incomplete atomic coordination which gives rise to a surface-tension force perpendicular to the surface. The surface tension

γ_L has been experimentally determined for a substantial part of the elemental metals in their liquid phase (for a review, see Allen (1972)). Furthermore, in many cases, its temperature dependence has also been measured. These data extrapolated to lower temperatures, provide estimates of γ for elemental solids. The surface tension is numerically related to the Helmholtz surface free energy F^s as follows:

$$\gamma = F^s/A, \tag{10}$$

where A is the surface area. In the theoretical treatment Skapski (1948, 1956) found it more convenient to discuss the molar surface tensions, i.e., the values referred to a surface occupied (in a mono-atomic layer) by 1 mol of atoms. The molar surface tension γ_M is thus defined by $\gamma_M = A_{mol}\gamma$, where A_{mol} is the surface area of 1 mol of atoms. By using a nearest-neighbour broken-atomic-bond model, Skapski derived for a closed-packed metal, that at zero temperature the molar surface energy U^S_M can be related to the cohesive energy E_{coh} in the following way:

$$U^S_M \cong 0.25 E_{coh}. \tag{11}$$

To arrive at this relation Skapski made the simplifying assumption that the bond energies of surface and bulk atoms are equal. Evans (1974) has criticized the main initial assumption, namely, that the total energy of the metal is due to pair-wise bonds between the atoms. However, for the present purpose, it is more important that *empirically* the simple expression given above has been found to hold with a quite reasonable degree of accuracy, and it is in this sense relation (11) will be applied below. In doing this a coefficient 0.20 rather than 0.25 will be used in eq. (11), since this has been found to better account for the known experimental data (Allen 1972, Lucas 1973). Thus we may give the following picture. It takes about $0.20 E_{coh}$ to bring a metal atom from the bulk solid to the surface (while enlarging the surface area correspondingly) and then it costs another $0.80 E_{coh}$ to remove the atom from the surface to infinity (while decreasing the surface area).

For a trivalent lanthanide metal the cohesive energy is about 103 kcal/mol relative to the proper trivalent atomic state (Johansson and Munck 1985). For a divalent metal such as (hypothetical) divalent samarium the cohesive energy relative to the divalent atomic configuration should be close to that of europium, i.e. 42.8 kcal/mol (Brewer 1975, Nugent et al. 1973, Johansson and Rosengren 1975b). However, the measured cohesive energy for samarium is 49.3 kcal/mol. Since the atomic configuration of samarium is divalent, $f^6 s^2$, this experimental value tells us firstly that metallic samarium is trivalent and secondly that the energy difference between the trivalent metallic state and the (hypothetically) divalent metallic state, $\Delta E_{II,III}$ is $43 - 49 = -6$ kcal/mol. Thus 6 kcal/mol is the energy margin by which samarium in the bulk phase maintains its trivalent character.

From the observed *empirical* relation for the molar surface energy $U^S_M = 0.20 E_{coh}$, we can state that by taking a bulk atom in trivalent samarium and bringing it to the surface (and thereby enlarging the surface appropriately as well as keeping the atom in the trivalent state) we lose the energy, $0.20 \times 103 \cong 21$ kcal/mol. Similarly, the same process in hypothetical divalent samarium or in europium will cost about $0.20 \times 43 \cong 9$ kcal/mol. Thus in a *relative sense we gain energy in the divalent case*

as compared to the trivalent one, the gain being about $21 - 9 = 12$ kcal/mol. If we compare this relative gain with the energy margin by which samarium is a trivalent metal, we note that it is certainly large enough to convert the surface atoms of samarium into the divalent state.

From their experimental results Wertheim and Crecelius (1978) concluded that the valence state at the surface was of an intermediate type, the formal valency being about 2.6. This would indicate that the energy actually gained in having a divalent surface is close to 6 kcal/mol. From the numbers above this is not unrealistic. Still, as pointed out by Wertheim and Crecelius, the experimental result may also be interpreted as if the surface is totally divalent but that due to surface roughness the orientation of the sample surface may vary from one small region to another, thereby invalidating the analysis which gave rise to the intermediate valence state interpretation. However, the experiments by Allen et al. (1978) also seemed to point towards a mixed valence state at the surface. From more recent BIS measurements the position of the unoccupied 4f level (corresponding to a divalent final state) in bulk samarium was found to be 0.46 eV (11 kcal/mol) above the Fermi energy (Lang et al. 1981). If we interpret this experiment as actually creating a divalent samarium atom in a trivalent host, we find that the solution energy of a divalent samarium impurity in trivalent samarium is $11 - 6 = 5$ kcal/mol (note its positive value). By applying Miedema's semi-empirical scheme (Miedema 1976) to this situation a higher value is obtained but with the same sign. At the surface the corresponding solution energy would be somewhat reduced, and by applying the same kind of arguments as those used in eq. (11) we can estimate the 'surface solution energy' to be about $0.8 \times 5 \cong 4$ kcal/mol. Thus the above 'energy gain' at the surface of about 12 kcal/mol is reduced to about $12 - 4 = 8$ kcal/mol when we account for the impurity effect. However, this gain is just about equal to the energy required to transform trivalent samarium into a divalent metallic state. Admittedly, the derivation of the impurity effect is somewhat crude, but at least it serves to illustrate that the conditions at the surface of metallic samarium might be such that a mixed valence cannot be completely ruled out.

However, later work showed that the binding energy of the surface divalent $4f^6$ level is 0.77 ± 0.25 eV relative to the Fermi level (Lang and Baer 1979), which is in good agreement with the value of 0.65 eV reported by Allen et al. (1980). This 4f binding energy seems to be too large for having a mixed valence situation at the surface and instead indicates a totally divalent surface or possibly an inhomogeneous valence state at the surface. Also electron energy loss spectroscopy studies show that samarium has a divalent surface (Strasser et al. 1982, Netzer and Matthew 1986). Recent careful UPS experiments (Gerken et al. 1985) showed no surface shift of the trivalent $4f^5$ level, from which it was concluded that there was less than 10% trivalent atoms at the samarium surface. Thus the present picture of the samarium surface is that there is a totally divalent surface layer on top of a trivalent bulk metal. Later in this section we will return to some of the problems which are encountered in a theoretical treatment of a divalent surface on a trivalent bulk. The complications mainly arise from the interfacial interaction between the topmost layer and those beneath.

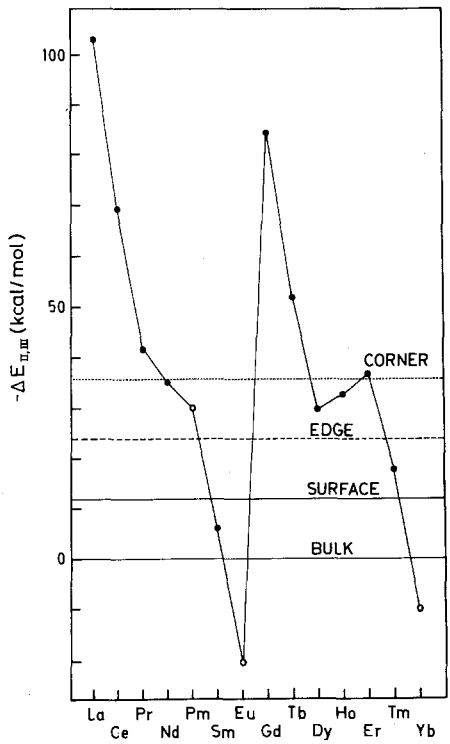

Fig. 10. Energy difference $-\Delta E_{II,III}$ between the divalent and trivalent states of the lanthanide metals. For Eu and Yb open dots are used to denote that for these elements the $-\Delta E_{II,III}$ values are not directly obtained from experimental cohesive energies, compare section 3. The open dot for Pm is used to show that this is an estimated data point. For those elements where $-\Delta E_{II,III}$ falls below the critical line labelled 'surface', the surface will be divalent (Johansson 1979). The critical values for divalent edges and corners are also indicated.

The fact that for samarium the surface has a different valence than the bulk suggests that there might be other lanthanide metals with a similar surface valence change. For almost all of the lanthanides we know very accurately the energy difference between the divalent and trivalent bulk states (section 3). In fig. 10 we plot these numbers and compare them with the 'energy gain' 12 kcal/mol (for clarity we disregard for the moment the interfacial interaction problem), i.e. the gain for the surface situation relative to the bulk. As can be immediately noted, the surface layer will remain trivalent for all the trivalent lanthanide metals except samarium. Not even for thulium should there be a divalent surface. This is confirmed by the experimental results on thulium obtained by Johansson et al. (1981). (However, also see below.)

If instead of a surface we consider atoms at a perfect edge of a single crystal, say with 90° between the cutting planes, it seems reasonable that the molar edge energy should be something like $U_M^{edge} = 2 \times 0.20 E_{coh}$. The reason for the factor of 2 is that at the edge two planes meet instead of just one as in the case of a surface. The energy gain would in this situation be about $2 \times 12 = 24$ kcal/mol (again disregarding the 'interface' interactions). From fig. 10 we notice that in this case thulium actually might show a valence change. Finally for a 'corner atom' the corresponding energy gain would be about $3 \times 12 = 36$ kcal/mol. From fig. 10 we now find that several of the lanthanide metals might show divalent behaviour at the corners of a single crystal. Naturally these critical energy numbers (24 and 36 kcal/mol, respectively)

should not be taken too literally, but rather they represent a trend. Interestingly enough, in a recent work by Domke et al. (1986) divalency for a heavily distorted thulium surface has been observed, confirming the general trend of the surface stability expressed by fig. 10.

For the heavier actinide metals it has in recent years become increasingly clear that in many respects they behave like the rare-earth elements (Brooks et al. 1984). Therefore it is just as meaningful to discuss also these elements in terms of valence as it is for the lanthanides. Experimental crystallographic work by Noé and Peterson (1976) indicated that californium might be a mixed-valence metal. That this is not unreasonable could also be derived (Johansson 1977b) from the relevant atomic spectroscopic levels for californium (Worden and Conway 1970) (i.e. the $5f^9 6d7s^2$ level relative to the ground state $5f^{10} 7s^2$). However, the experimental determination of the heat of sublimation of californium made by Ward et al. (1979) gave $\Delta H^0_{298} = -46.9$ kcal/mol. Since this value is numerically larger than -43 kcal/mol (typical for a divalent metal) it certainly indicates that californium is a trivalent metal and casts serious doubts on the validity of the observations of a bulk intermediate valence state by Noé and Peterson. This is especially so since the experiment by Ward et al. was performed on a 2 mg sample, while Noé and Peterson used much smaller samples (weighing less than 10 μg). However, undoubtedly the divalent metallic state of californium will be quite close in energy to the trivalent state. In fact it is perhaps even closer than for samarium metal. Therefore, as is clear from the discussion given above for samarium, it is most likely that the surface layer of californium is completely divalent. This means that even for thin films it cannot be excluded that californium will be divalent. In the X-ray powder diffraction study by Noé and Peterson a lot of surface area might have been scanned. Thus, their observations of a purely divalent, a purely trivalent as well as of a mixed-valence state might to a large extent originate from surface properties of californium. The apparent contradiction between the experiment by Ward et al. on the one hand and the experiments by Noé and Peterson on the other, could then find its explanation in that Ward et al. were investigating a truly bulk sample, while Noé and Peterson were working on a microscale. Since experiments on californium necessarily must be performed on small samples, this indicates that caution must be taken so that real bulk properties are being studied.

Also americium metal behaves as a trivalent lanthanide metal. The UPS and XPS data for an evaporated americium film (Naegele et al. 1984) show clearly that the 5f emission is totally withdrawn from the Fermi level, just as the 4f emission is well separated from the Fermi energy in the lanthanides. Attempts to fit in detail the UPS spectrum with calculated 5f spectra indicate that there is a substantial fraction of divalent americium atoms at the surface (Zangwill 1984, Johansson 1984, Mårtensson et al. 1987). Since the heat of sublimation for americium numerically is as high as $\Delta H^0_{298} = -67.9$ kcal/mol (Ward et al. 1976) this is rather surprising. The reason for the appearance of divalency might therefore be that the preparation method for the film does not give rise to a smooth planar surface but rather to an uneven and less well characterized surface.

As pointed out by Wertheim et al. (1978a) the surface valence of lanthanide

systems in general may be anticipated to be lower (or rather have a tendency to be lower) than that of the bulk. This is fully consistent with the picture outlined above. A trivalent lanthanide atom always forms stronger bonds than the corresponding divalent atom. Therefore the loss of bonding in forming a surface will always be larger for the trivalent case than for the divalent one and thus the lower valence will become somewhat favoured at the surface relative to the bulk. This means that experimental results, obtained from a surface-sensitive technique such as XPS, must be carefully analyzed before a specific structure of the spectrum can be said to originate from the bulk or the surface, respectively.

The energy comparison between the situation when the trivalent bulk metal is covered by a divalent layer and when both surface and bulk are trivalent is in fact rather complicated. Here we would like to consider this in a more careful way than the simple treatment given above. Let us start from the completely trivalent case. First we remove the surface layer, but in such a way that external boundary conditions are imposed on the remaining system so that *all* the remaining atoms behave as in a bulk system, and thereafter the removed layer is put into the bulk. The energy gained is the surface energy $U^{\mathrm{S}}_{\mathrm{III}}$. Thereafter a macroscopic part of the system is made divalent, involving the energy $-\Delta E_{\mathrm{II,III}}$. Then a surface layer is created for the divalent system which costs the surface energy $U^{\mathrm{S}}_{\mathrm{II}}$. After this the divalent surface layer is removed in such a way that it leaves behind itself a system with such boundary conditions that it is totally bulk-like. In the next step this divalent surface layer is put on top of the prepared trivalent system (i.e., a trivalent metal with such boundary conditions that it is totally bulk-like). Finally the divalent layer and trivalent bulk are left free to relax relative to each other. The last processes involve an interaction energy, $E^{\mathrm{interf}}_{\mathrm{II}}(\mathrm{III})$. Thus the energy difference between a totally trivalent system (i.e. with a trivalent surface) and one with a trivalent bulk and a divalent surface becomes

$$\Delta E^{\mathrm{surf}}_{\mathrm{II,III}} = -U^{\mathrm{S}}_{\mathrm{II}} + U^{\mathrm{S}}_{\mathrm{III}} + \Delta E_{\mathrm{II,III}} + E^{\mathrm{interf}}_{\mathrm{II}}(\mathrm{III}). \tag{12}$$

Assuming, again for simplicity, that $U^{\mathrm{S}}_{\mathrm{M}} \simeq 0.2 E_{\mathrm{coh}}$, in analogy to eq. (11), we obtain

$$\Delta E^{\mathrm{surf}}_{\mathrm{II,III}} = -0.2\ (E^{\mathrm{coh}}_{\mathrm{II}} - E^{\mathrm{coh}}_{\mathrm{III}}) + \Delta E_{\mathrm{II,III}} + E^{\mathrm{interf}}_{\mathrm{II}}(\mathrm{III}). \tag{13}$$

However $\Delta E_{\mathrm{II,III}}$ can be written as (compare fig. 2 or see next section fig. 11 and eqs. (17)–(18))

$$\Delta E_{\mathrm{II,III}} = E^{\mathrm{coh}}_{\mathrm{II}} + E^{\mathrm{atom}}_{\mathrm{f}\to\mathrm{d}} - E^{\mathrm{coh}}_{\mathrm{III}}, \tag{14}$$

where $E^{\mathrm{atom}}_{\mathrm{f}\to\mathrm{d}}$ is an atomic excitation energy from $\mathrm{f}^{n+1}\mathrm{s}^2$ to a proper $\mathrm{f}^n\mathrm{ds}^2$ configuration. Combining (13) and (14) we arrive at

$$\Delta E^{\mathrm{surf}}_{\mathrm{II,III}} = -0.8(E^{\mathrm{coh}}_{\mathrm{III}} - E^{\mathrm{coh}}_{\mathrm{II}}) + E^{\mathrm{atom}}_{\mathrm{f}\to\mathrm{d}} + E^{\mathrm{interf}}_{\mathrm{II}}(\mathrm{III}). \tag{15}$$

Assuming first that the energy difference between having a divalent layer on top of a divalent bulk and a divalent layer on top of a trivalent bulk is negligible, i.e., $E^{\mathrm{interf}}_{\mathrm{II}}(\mathrm{III}) \simeq 0$, then

$$\begin{aligned}\Delta E^{\mathrm{surf}}_{\mathrm{II,III}} &= -0.8(E^{\mathrm{coh}}_{\mathrm{III}} - E^{\mathrm{coh}}_{\mathrm{II}}) + E^{\mathrm{atom}}_{\mathrm{f}\to\mathrm{d}} \\ &= \Delta E_{\mathrm{II,III}} + 0.2(E^{\mathrm{coh}}_{\mathrm{III}} - E^{\mathrm{coh}}_{\mathrm{II}}).\end{aligned} \tag{16}$$

This expression is equivalent to the verbal description given in the early part of this section. This simplified formula shows that at the surface the energy balance is such that it favours a divalent surface by about 12 kcal/mol relative to the energy balance in the bulk.

However, there are some serious problems involved in the reduction of eq. (12) to eq. (16). First of all it neglects the fact that the divalent atoms are considerably larger than the trivalent atoms. This means that in order to cover a given surface area the required number of divalent atoms is less than for a trivalent coverage (a reduction β of about 25%). At first sight this certainly seems to favour a divalent surface. However, the trivalent second layer below the surface will thereby have less neighbours in the outermost divalent layer than for the situation with a trivalent surface layer. The average number of missing (broken) bonds with the uppermost divalent layer will in fact correspond to the difference in number of atoms covering the surface with a trivalent and a divalent configuration, respectively. Thus these two effects tends to partially cancel each other. In an explicit calculation, using a simple pair bonding model (Rosengren and Johansson 1982), this partial cancellation was in fact demonstrated. For a given surface which is covered by N_3 trivalent atoms, the number of divalent atoms covering the same surface will be βN_3, ($\beta < 1$). Thus when βN_3 trivalent atoms are made divalent at the surface and $(1-\beta)N_3$ trivalent atoms are brought into the second layer and thereby becomes more bulk-like, there will in the bonding between the surface layer and second layer on the average only be $K\beta N_3$ bonds (K is some proportionality constant) instead of KN_3 bonds, i.e. the reduction of the number of bonds is $K(1-\beta)N_3$. Thus, effectively, $(1-\beta)N_3$ atoms in the second layer are therefore still surface atoms (in the sense that the energy contribution from the second layer to the total energy is reduced by an amount approximately equal to the surface energy of $(1-\beta)N_3$ atoms). Since the expression in eq. (16) refers to an energy per atom, it can be directly applied to this situation. Thus eq. (16) is a better approximation for the energy difference (12) than what one at first would expect.

Therefore it has to be realized that the way the interfacial interaction term E_{II}^{interf}(III) was defined, it also contains contributions where some of the atoms are changing valence. This makes it a difficult quantity to evaluate with precision. Another difficult problem concerns the geometry of the divalent surface relative to the underlying trivalent layer. Because of the volume difference there must be serious matching problems. This raises for example the question whether there will be a buckling of the divalent surface layer (Rosengren and Johansson 1982) or if there instead will be island formation but still with an almost complete coverage of the underlying trivalent layer. Apparently, future experimental structure determinations of the samarium surface will be extremely important before a deeper insight into the energetics, governing the samarium surface conditions, can be developed.

Thus in comparison with the surface formed by a simple termination of a bulk trivalent material into vacuum, the real surface of samarium involves a tremendous reconstruction, namely, both a valence change and most likely a geometrical transformation. The obtained surface should be expected to be heavily dependent on the mode of preparation. As regards to surface properties samarium is a most exclusive element in the Periodic Table.

A different type of experiments for studying the coordination number dependence of the lanthanide valence was performed by Lübcke et al. (1986). They isolated Pr, Nd and Sm clusters in solid argon and monitored the valence state by means of L_{III} absorption thresholds, which change markedly upon a valence change. The average size of the clusters could be determined for some of the Sm/Ar matrices by investigation of the extended X-ray absorption fine structure (EXAFS). As a function of cluster size an abrupt change of the average valence was observed. The critical number of atoms in the cluster, S_c, for this valence change was determined to be 5 and 13 ± 3 for Nd and Sm, respectively. In the case of Sm, the surface atoms of the cluster are expected to remain divalent, independent of the cluster size. For Nd, however, it is more likely that all of the atoms in the cluster change valence from 2+ to 3+ simultaneously when the cluster size increases. By applying the simple pair bonding model introduced by Rosengren and Johansson (1982), Lübcke et al. (1986) could quite well account for the critical cluster size from considerations of the energy balance between the trivalent and divalent cluster, $\Delta E_{II,III}^{cluster}$.

10. Surface shift of the 4f level

The energy position of the 4f level depends on the chemical environment of the particular lanthanide atom from which the 4f electron is ionized (chemical shift). Since the environment for a surface atom is different than for a bulk atom, one expects a shifted 4f level binding energy for a surface atom relative to a bulk atom. This will here be referred to as a *surface shift* of the 4f level. Due to its surface sensitivity the photoelectron spectroscopy technique is well suited for studies of these shifts.

Already long ago the existence of surface core-level shifts (among which the shift of the 4f levels in the lanthanides is just a special case) was anticipated. However, it is only relatively recently that these shifts have been verified experimentally and have been studied in a more systematic way (for reviews see Johansson and Mårtensson 1983, Citrin and Wertheim 1983 and Spanjaard et al. 1985). For this development to take place the improvement of the experimental resolution has been an absolute necessity, since the magnitude of the surface shifts are small, generally less than 0.5 eV, making the separation between the surface signal and the more intense bulk signal most difficult. The increased availability of tunable photon energy sources (synchrotron radiation) has been extremely valuable for the development of this field. By variation of the photon energy, the experiments can be performed with a varying degree of surface sensitivity, which is most helpful in the identification of the surface signal (Tran Minh Duc et al. 1979).

The fact that the surface-shifted core-level signals originate exclusively from atoms in the topmost surface layer(s), make them attractive in studies of problems within surface and interface physics. Thus, they might become useful in investigations of catalytic activity, corrosion resistance, surface and grain boundary segregation in alloys, just to mention a few possibilities. At the present stage of development we believe that they already now can be fruitfully applied, like for example in connection with surface segregation.

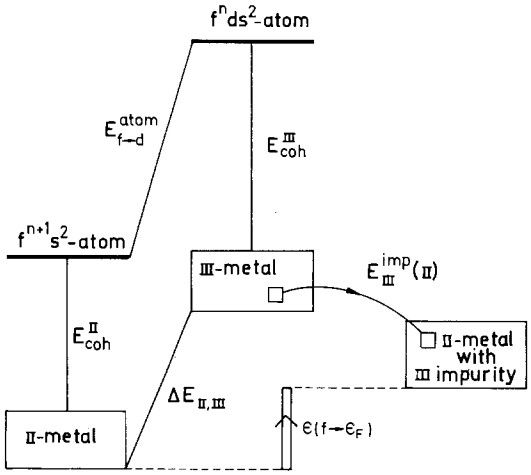

Fig. 11. Diagram showing the connection between $\varepsilon(f \to \varepsilon_F)$ on one hand and $\Delta E_{II,III}$ and E^{imp}_{III} (II) on the other. An extension of the cycle to the free atoms is also included.

For the treatment to follow it is useful to reconsider the position of the 4f level in the bulk metal (say for a divalent lanthanide). The illustration in fig. 11 shows that our earlier expression (compare the 'inner' Born–Haber cycle in the figure)

$$\varepsilon(f \to \varepsilon_F) = \Delta E_{II,III} + E^{imp}_{III}(II) \tag{17}$$

can be rewritten in a more complicated way (see the 'outer' Born–Haber cycle in fig. 11):

$$\varepsilon(f \to \varepsilon_F) = E^{II}_{coh} + E^{atom}_{f\to d} - E^{III}_{coh} + E^{imp}_{III}(II), \tag{18}$$

where $E^{imp}_{III}(II)$ is (as before) the heat of solution of a substitutional trivalent metallic impurity atom (f^n) into the divalent (f^{n+1}) host metal.

This decomposition of the position of the bulk 4f level can be immediately repeated for a surface atom. Thereby one arrives at the following surface 4f level binding energy (Johansson and Mårtensson 1980, 1983):

$$\varepsilon^{surf}(f \to \varepsilon_F) = E^{II}_{coh,surf} + E^{atom}_{f\to d} - E^{III}_{coh,surf} + E^{imp,surf}_{III}(II). \tag{19}$$

Here we have introduced the surface cohesive energy, $E_{coh,surf}$, both for the original divalent metal and for the hypothetical trivalent metal. (With the surface cohesive energy is meant the energy gained when a free atom is brought to the metal surface (the metal and the free atom having the same valence), while enlarging the surface area correspondingly.) In eq. (19) there is also a surface substitutional impurity energy, $E^{imp,surf}_{III}(II)$. This is the solution energy for bringing a surface atom of the (hypothetical) trivalent metal into the divalent metal surface layer.

By combining eqs. (18) and (19) the 4f level energy shift between the surface and the bulk, ΔE_S, is found to be

$$\Delta E_S = \varepsilon^{surf}(f \to \varepsilon_F) - \varepsilon^{bulk}(f \to \varepsilon_F) = E^{III}_{coh} - E^{III}_{coh,surf} - (E^{II}_{coh} - E^{II}_{coh,surf}) - (E^{imp}_{III}(II) - E^{imp,surf}_{III}(II)). \tag{20}$$

Since the difference $E_{coh} - E_{coh,surf}$ is just the surface energy, U_M^S, we obtain

$$\Delta E_S = U_{III}^S - U_{II}^S - (E_{III}^{imp}(II) - E_{III}^{imp,surf}(II)). \tag{21}$$

Thus there is a direct connection between the surface 4f level shift and surface energies, modified only by the difference in heat of solution for a bulk and a surface substitutional trivalent impurity.

The expression (21) for the surface 4f level shift can be interpreted as the energy difference between having the trivalent metal atom impurity in a substitutional surface position or in a substitutional bulk position. This is illustrated in fig. 12, which, in fact, could have been used directly to give the above expression for the surface shift. From this it becomes immediately clear that ΔE_S is nothing but the *surface segregation energy* of a trivalent impurity (compare the lowest figure in fig. 12) (Johansson and Mårtensson 1980, Rosengren and Johansson 1981). Due to experimental difficulties, this technologically important quantity has not been measured thermochemically, not even for more general systems than the lanthanides. It follows that experimentally determined surface 4f level shifts indirectly provide us with segregation data not available otherwise. However, it must also be kept in mind that the photoemission process is vertical. Thus the measured surface shift is not exactly the thermodynamical surface segregation energy, but rather corresponds to the segregation energy for a 'restricted' impurity in the sense that the atomic positions of the surroundings to the impurity have not relaxed. From a theoretical point of view this segregation energy is a much more tractable quantity to handle than the truely thermodynamical one. It is, however, likely that the difference between the thermodynamical segregation energy and the restricted one obtained from the surface shift is only marginal.

In order to quantitatively calculate the surface 4f level shift, we will introduce some approximations. As in the previous section we use the empirical relation for the surface energy

$$U_M^S \simeq 0.2 E_{coh}. \tag{22}$$

Furthermore, it seems plausible that, at least approximately, the impurity term should obey a similar type of relation, i.e.,

$$E_{III}^{imp,surf}(II) \simeq 0.8 E_{III}^{imp}(II). \tag{23}$$

With these approximations the following expression for the surface 4f level shift is obtained:

$$\Delta E_S \simeq 0.2(E_{coh}^{III} - E_{coh}^{II} - E_{III}^{imp}(II)). \tag{24}$$

In most applications of this formula the impurity term has been neglected, and we then finally obtain a simple but approximate relation for the surface shift (Johansson and Mårtensson 1980)

$$\Delta E_S \simeq 0.2(E_{coh}^{III} - E_{coh}^{II}). \tag{25}$$

This expression can of course be trivially generalized to a trivalent lanthanide metal.

Experimentally, the surface shifts of the 4f level for the lanthanides have been thoroughly studied by Gerken et al. (1985), so that experimental shifts are now

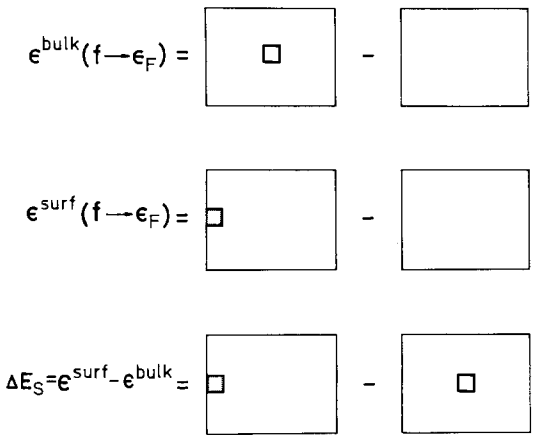

Fig. 12. Illustration of the correspondence between the surface 4f level shift, ΔE_S, and the surface heat of segregation of the final state impurity.

available for practically all the elements in the series. Of special interest is also the work by Kaindl et al. (1983) where the surface shifts of both the 4f and 5p levels in Yb and Lu were determined. These are up to now the only cases where for the same element more than one core-level has been investigated with respect to surface shifts. Within the experimental uncertainties, identical shifts were found for the two levels. For lanthanum, with no occupation of the 4f level, the surface shift of the 5p level has been measured to be 0.48(7) eV (Nilsson et al. 1985).

In the absence of reliable data for the lanthanide surface energies, we use eq. (25) for the calculation of the surface shifts. Due to the practically constant cohesive properties throughout the series, the shift values for Yb and Lu should be appropriate for the whole series, at least to a first-order approximation. A comparison between the theoretical values and the experimental data is made in fig. 13. As can be seen, the agreement is fairly good, but there are clear systematic deviations for the heavier elements.

From the data in fig. 13 we note that the surface shift is about 0.5 eV for the earlier trivalent elements, but reaches values of the order of 0.7 eV for the heavier trivalent elements. It is also clear that the 5p shift for lanthanum appears to be consistent with the 4f shift for the lighter lanthanides. The shift for the divalent

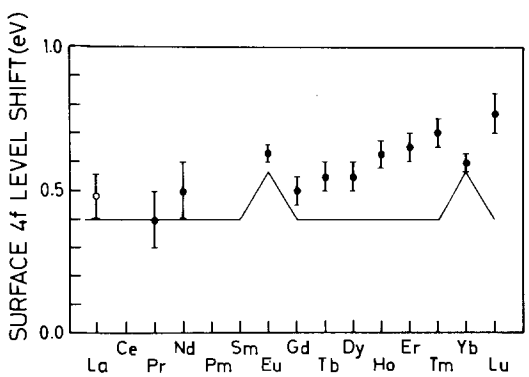

Fig. 13. Calculated (solid line) (Johansson and Mårtensson 1983) and experimental (data points with error bars) (Gerken et al. 1985) surface shifts of the 4f level in the lanthanide metals. For lanthanum the surface shift of the 5p level is shown (Nilsson et al. 1985).

TABLE 3
Experimental surface 4f and 5p level shifts for the lanthanide elements (in eV). All data refer to polycrystalline samples.

	4f	5p		4f	5p
La		0.48(7)[a]	Tb	0.55(5)[c]	
Ce	⩽0.4(1)[b]		Dy	0.55(5)[c]	
Pr	0.4(1)[c]		Ho	0.63(5)[c]	
Nd	0.5(1)[c]		Er	0.65(5)[c]	
Pm			Tm	0.70(5)[c]	
Sm			Yb	0.62(3)[d], 0.60(3)[c,e]	0.60(5)[d]
Eu	0.60(5)[d], 0.63(3)[c]			0.56(3)[e], 0.51(8)[f]	0.56(5)[a]
Gd	0.50(5)[c]		Lu	0.77(5)[c], 0.83(10)[d]	0.74(10)[d]

[a] Nilsson et al. (1985).
[b] Parks et al. (1982).
[c] Gerken et al. (1985).
[d] Kaindl et al. (1983).
[e] Alvarado et al. (1980).
[f] Schneider et al. (1983).

metals, Eu and Yb, appears to be more constant throughout the series, and agrees quite well with theory. For completeness we list in table 3 the experimental data for the surface 4f and 5p level shifts.

The main difference in the electronic structure of the light and the heavy lanthanide elements is the number of 5d electrons. Energy band calculations give for lanthanum $n_d = 2.0$ and for lutetium $n_d = 1.4$ (Skriver 1983). For hafnium the number of d-electrons is 2.3, i.e. about one more than in lutetium. Thus, as regards the number of d-electrons, lanthanum is intermediate between lutetium and hafnium. Assuming that the d-electrons are mainly responsible for the surface energies, one obtains, according to eq. (21), that the lanthanum surface shift should be somewhere between that of lutetium and hafnium (Gerken et al. 1985). Since experimentally the surface shift is 0.77(5) eV for lutetium and 0.42(4) eV for hafnium (Nyholm and Schmidt-May 1984), this gives a reasonable explanation for the smaller surface shift for the lighter lanthanides as compared to the heavier ones. For the divalent lanthanide elements the number of d-electrons relative to the number of s-electrons is probably too low for the assumption about a dominating d-contribution to the surface energy to be valid. Therefore, for the divalent elements there will not necessarily be a corresponding variation with the atomic number as for the trivalent lanthanides.

Also the unoccupied 4f levels will be shifted at the surface. For a trivalent metal the surface shift, ΔE_S^{BIS}, takes (in the simplest approximation) the form

$$\Delta E_S^{BIS} = 0.2(E_{coh}^{II} - E_{coh}^{III}), \tag{26}$$

i.e., equal in magnitude but opposite in sign to the surface shift of the occupied 4f level for a divalent metal. From the measured bulk unoccupied 4f level in samarium, 0.46 eV, a surface shift of -0.6 eV (which is the negative of the surface shift of the occupied 4f level in europium) implies that the unoccupied level lies below the Fermi level, i.e., a clearly unstable situation. This means that the samarium metal is unstable against a surface valence change, a fact which was discussed in the previous section.

At the divalent surface layer of samarium the $4f^6$ level is measured to have a binding energy of 0.77 ± 0.25 eV (Lang and Baer 1979). Allen et al. (1980) find a binding energy of 0.65 eV. This corresponds to a $4f^6 \rightarrow 4f^5 \varepsilon_F$ excitation, compare section 2. In the bulk the BIS experiment, as just mentioned, gives a position of 0.46 eV for the $4f^5 \varepsilon_F \rightarrow 4f^6$ reaction. Thus the XPS and BIS experiments imply a surface 4f level shift of the f^6 level of about $0.5 + 0.7 = 1.2$ eV towards higher binding energies (notice that we here consider a shift between an *unoccupied* f^6 bulk level and an *occupied* f^6 surface level). This surface shift is about a factor of 2 larger than the surface shifts measured for the other lanthanides. There is, however, a distinct difference between the present case of samarium and a normal type of surface core-level shift, namely that for the samarium surface there is a macroscopic number of atoms which have turned over into the divalent state. Therefore the surface $f^6 \rightarrow f^5$ transition (XPS) occurs in an environment which is very different from that of a bulk samarium atom on which the $f^5 \rightarrow f^6$ transition (BIS) takes place. Thus, rather than to show a normal value for the surface 4f level shift (i.e. of about 0.5–0.6 eV), which would have given an f^6 level close to the Fermi energy and a possibility for a homogeneously mixed valence state, the observed shift indicates that the transition at the samarium surface is of a first-order type.

Rosengren and Johansson (1982) studied this question using a simple pair-bonding model and showed that the reason for the somewhat unexpected high binding energy of the f^6 level at the surface originated from the fact that the whole samarium surface is transformed to a divalent layer. From the following *Gedanken* experiment additional support can be given to this explanation. Namely, we first assume that Sm as a whole is a divalent metal. For europium the measured binding energy of the $4f^7$ level is 1.5 eV. Since $\Delta E_{II,III}(Eu)$ is 0.9 eV it follows that $E_{III}^{imp}(II)(Eu)$ is 0.6 eV. For samarium $\Delta E_{II,III}$ is -0.27 eV. The same value as for europium should be expected for $E_{III}^{imp}(II)(Sm)$. Thus for hypothetically divalent samarium we derive $\varepsilon(f \rightarrow \varepsilon_F) = 0.33$ eV. This result is by itself remarkable since it means that the divalent samarium metal is *stable locally*. Thus the valence change in samarium is of a collective type, since the single sites in divalent samarium are by themselves locally stable against a valence change. With this binding energy in the bulk for hypothetically divalent samarium metal, and with the assumption of an equal surface 4f level shift in divalent samarium as in europium (i.e. 0.6 eV), we find $\varepsilon^{surf}(f \rightarrow \varepsilon_F) = 0.93$ eV for hypothetical divalent samarium metal. The surface layer of this system should be rather similar to the one for the real samarium surface, except that in the latter case the divalent surface layer interacts with the trivalent layers beneath the surface. Thus the derived value for the surface f^6 level position in hypothetical divalent samarium should be somewhat higher than for the true samarium system. The observed value of about 0.7 eV confirms this, and shows that it is the total reconstruction to divalency at the surface which gives rise to such a high binding energy for the 4f level. Again this supports the picture that the surface of samarium is completely divalent.

The expected close neighbourhood of the divalent surface state for thulium can also be inferred from available experimental data. For samarium the measured shift between the unoccupied bulk f^6 level and the occupied surface f^6 level is about

1.2 eV (see above). Since the unoccupied bulk f^{13} level in thulium is at 1.1 eV above the Fermi energy (Lang et al. 1981) the expected similarity of the shifts for samarium and thulium gives that for a *reconstructed* completely divalent thulium surface on top of a trivalent bulk, the f^{13} level should be 0.1 eV below the Fermi level and thus be stable in the divalent state. As seen above for divalent samarium metal, this is a necessary but not a sufficient condition for the stability of a divalent thulium surface. Thus a divalent thulium surface layer is locally stable against a valence change, but cooperative effects make this divalent state globally unstable. Still, it strongly indicates that the divalent surface state must be almost stable in the thulium metal. A monolayer (or less) of thulium on an ytterbium crystal is a system where thulium may attain a divalent state (Rosengren and Johansson 1982). Experimentally this situation might, however, be difficult to realize since trivalent thulium droplets might be formed instead.

From a study of the 4f surface shifts for ytterbium, Schneider et al. (1983) were able to draw conclusions about the temperature dependence of the microstructure of evaporated Yb surfaces. At low substrate temperatures, due to the low mobility of the Yb atoms, nucleation is enhanced, leading to island formation and an increase in surface roughness. Thereby, the 4f surface signals become dominated by contributions from surface atoms with a relatively low coordination number (7). The corresponding surface shift is measured to be as high as 0.86(5) eV. Thus the absolute 4f binding energy for such surface atoms is 2.03(7) eV. Since $\Delta E_{\mathrm{II,III}}$ (Yb) = 0.5 eV and $\Delta E_{\mathrm{II,III}}$ (Tm) = −0.78 eV, a corresponding geometrical configuration for *hypothetical* divalent thulium metal would give a surface 4f binding energy of 2.03 − (0.5 + 0.78) = 0.75 eV. This surface binding energy is almost comparable to the value obtained above in the *Gedanken* experiment for hypothetical divalent samarium metal (0.93 eV). Thus it appears quite possible that thulium surface atoms with a low coordination number would attain a stable divalent f^{13} configuration. The observation of a divalent signal for a distorted thulium surface shows that this is actually the case (Domke et al. 1986). This surface was obtained in the same way as the ytterbium surface with the high surface 4f level shift, i.e., evaporated on a cold substrate. In these experiments the divalent thulium 4f binding energy was found to be 0.5 eV. For samarium the actually measured surface divalent 4f binding energy was about 0.7 eV (see above), i.e., a lowering of 0.2 eV relative to the derived value for the hypothetical completely divalent samarium metal. Thus a similar reduction of 0.75 − 0.5 = 0.25 eV is observed for the real thulium surface relative to the distorted and hypothetical completely divalent thulium metal. This suggests that the divalent signal originates from divalent atoms, which within the surface layer are surrounded by other divalent surface atoms and by trivalent atoms in the layers beneath the surface. From the pair-bonding calculations by Rosengren and Johansson (1982) it can be shown that when a divalent surface on top of a trivalent bulk is just stable, then the surface 4f binding energy is 0.4 eV. Thus the measured divalent surface 4f binding energy of 0.5 eV for thulium, indicates that the divalent low coordination surface configuration is stable relative to a fully trivalent state by $\approx$0.1 eV. This also means that none of the other lanthanides (like Dy or Nd) could be divalent for this type of surface geometry.

Presently no direct BIS experiments have been performed in order to identify a

surface shift of the unoccupied 4f level. However, in their photoemission experiments on single crystal Gd(0001) Himpsel and Reihl (1983) recorded the spectrum of secondary electrons. There, a double peak structure is observed around 4 eV above the Fermi level. One possible interpretation is that these two peaks correspond to a surface f^8 and a bulk f^8 final-state configuration separated by at least 0.5 eV (the surface peak being closest to the Fermi level). The simplified formulas in eqs. (25) and (26) suggest that the surface shift of the unoccupied level in a trivalent metal is about equal in magnitude but opposite in sign to the surface shift of the occupied level in a divalent metal. Thus one would expect a surface shift in Gd of about -0.6 eV. This is consistent with an interpretation of the double peak in the secondary electron spectrum as a genuine surface shift of an unoccupied 4f level.

11. Energy positions of 4f levels in metallic lanthanide compounds

By forming alloys and compounds of the lanthanide metals the properties of these elements can be modified significantly. For the light lanthanides (especially Ce), which have the most extended 4f orbitals, different environments lead to different degrees of hybridization of the 4f states. In those Ce compounds which have a small 4f-ligand hybridization one finds γ-like behaviour with localized 4f-moments, while it is observed that a large 4f-ligand hybridization leads to α-like behaviour with loss of magnetism (e.g. see the following chapters in this volume: 64 of Gunnarsson and Schönhammer, 63 of Campagna and Hillebrecht, and 70 of Hillebrecht and Campagna). However, also in systems with completely localized 4f states the properties of these can vary considerably between different compounds. As a particularly dramatic example of this we note the occurrence of mixed-valence states in certain compounds of Sm, Eu, Tm and Yb (e.g., Parks 1977, Falicov et al. 1981, Wachter and Boppart 1982, Müller–Hartmann et al. 1985).

The (electropositive) lanthanide metal atoms form strong bonds with the more electronegative metal atoms at the end of each d-transition series. In these cases it is natural to expect that the strength of the bonds change differently for different valence states of the lanthanide metal atoms relative to the corresponding bonds in the pure metals. Therefore, the *energy balance between the valence states becomes modified in compounds.* In several intermetallics of this kind, the divalent lanthanide metals Eu and Yb thereby become mixed-valent or trivalent due to the relative increase of the bond strength for the trivalent state as compared to the divalent state. In other cases as for instance in certain compounds with p-electron elements the trivalent Sm and Tm metals become mixed-valent or even divalent, i.e., in direct contrast to the situation for the lanthanide compounds with the late transition metals. It is thus of considerable importance to understand the mechanisms which cause these dramatic changes.

At first we consider how $\Delta E_{\mathrm{II,III}}$ and $\Delta E_{\mathrm{III,IV}}$ are modified in alloys and compounds. For simplicity we restrict the discussion to the energy difference between the divalent and trivalent forms of a lanthanide metal compound. The corresponding equations for the energy difference between the trivalent and tetravalent states and between the divalent and monovalent states, respectively, are easily written down in

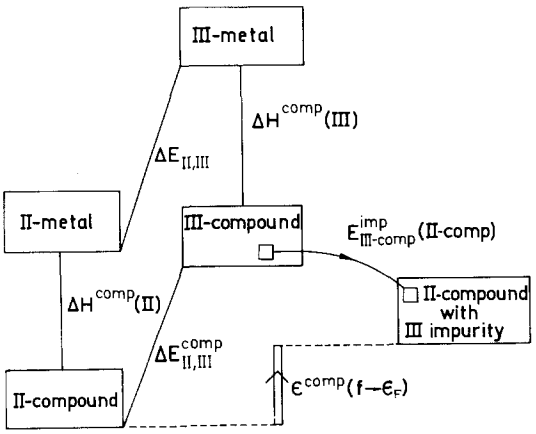

Fig. 14. Diagram relating the energy difference between the divalent and trivalent states of a lanthanide compound, $\Delta E^{comp}_{II,III}$ to $\Delta E_{II,III}$ for the metal (left-hand side). On the right-hand side the diagram shows the connection to the energy position of the 4f level, relative to the Fermi energy, $\varepsilon^{comp}(f \rightarrow \varepsilon_F)$.

analogy with these. In the left part of fig. 14 we show how the previous derivation of $\Delta E_{II,III}$ (section 3) can be extended to a compound. Compared to the derivation for the pure metals in fig. 2 it is now necessary to take into account the fact that the divalent and trivalent modifications of the metal form bonds in the compound which are of different strengths. On one side of the cycle we have to add an additional step which connects the divalent compound to the divalent metal. We denote the associated heat of formation ΔH^{comp}(II). Similarly, on the other side of the cycle we have to connect the trivalent form of the compound to the trivalent metal which is described by the heat of formation ΔH^{comp}(III). We thus obtain for the energy difference between the trivalent and divalent states of the compound

$$\Delta E^{comp}_{II,III} = \Delta E_{II,III} + \Delta H^{comp}(III) - \Delta H^{comp}(II). \quad (27)$$

From eq. (27) we immediately obtain a criterion for a valence transition in a compound. For an initially divalent metal we see that the compound becomes trivalent when the difference in the heat of formation, ΔH^{comp}(II) − ΔH^{comp}(III), becomes larger than $\Delta E_{II,III}$ (note that ΔH^{comp} is negative for a stable compound). This difference in the heats of formation expresses the difference in the bonding strengths between the divalent and trivalent configuration with the ligands. Similarly we find that a necessary condition for homogeneous mixed valence is that the right-hand side of eq. (27) is close to zero. From eq. (27) it is thus possible to predict the valence state of any compound for which the necessary ΔH values are known. The problem, however, is that at most one of the heats of formation in eq. (27) can be a direct experimental quantity, since for each compound the heat of formation is of course only known for the stable valence state. Furthermore, it is only in cases where the compound and the pure lanthanide metal have the same valence state that the ΔH^{comp} value in eq. (27) is the quantity which is obtained directly from a calorimetric measurement. If the valence states are different the measured value must be corrected by the valence change energy, $\Delta E_{II,III}$, before the quantity ΔH^{comp} is obtained. As will become clear in section 13 the energy separation between various valence states, expressed by eq. (27), is a situation where most important information can be obtained from photoemission and inverse photoemission data.

As an example of how this stability criterion can be used we consider Eu, which is a divalent metal. In section 3, $\Delta E_{II,III}$(Eu) was ascribed a value of 21 kcal/mol. Therefore, in order to find trivalent Eu in a certain type of compound, the heat of formation of this compound formed from pure hypothetically trivalent Eu metal and the other component must numerically be at least 21 kcal/mol Eu larger (more negative ΔH^{comp}) than the heat of formation for the divalent compound formed from divalent Eu metal. Similarly we find that mixed valence can occur when the heat of formation difference is close to 21 kcal/mol Eu.

This approach was applied to predict the valence state for a large number of Eu (Miedema 1976) and Yb (de Boer et al. 1979) intermetallic systems. A semi-empirical scheme was then used to obtain the quantities ΔH^{comp}(II) and ΔH^{comp}(III). The result of this analysis for Eu intermetallics is shown in fig. 15. In this figure the valence state of a large number of Eu intermetallic compounds is plotted against the calculated heat of formation difference, ΔH^{comp}(II) − ΔH^{comp}(III), for the compounds. It is seen that there is a critical value for the valence transition around 21 kcal/mol Eu, which in fact just corresponds to the value of $\Delta E_{II,III}$ for Eu metal. Considering the accuracy of $\Delta E_{II,III}$ and the calculated ΔH^{comp} values, this perfect agreement must be considered to be somewhat fortuitous. However, the analysis shows that the separation between divalent and trivalent compounds is well described by the Miedema semiempirical scheme.

Also for Yb (de Boer et al. 1979) a most satisfactory account for the valence state of different intermetallic compounds was obtained. de Boer et al. (1979) also extended their treatment to discuss the possible existence of tetravalent Ce intermetallic systems. However, in this case, using the same scheme as for Eu and Yb, it was not possible to reproduce the separation between γ- and α-like Ce compounds as a transition from trivalent (f^1) to tetravalent (f^0) Ce. This demonstrated, in full agreement with many other later observations, that the 4f electron cannot always be treated as completely core-like, i.e. the Ce 4f electron is not always chemically inert. As a further example of valence investigations, a simple extension of eq. (27) has been used to determine the stabilities of various valence states for lanthanide- and actinide-halides and oxides (Johansson 1978b). Again a good agreement with the experimental data was obtained.

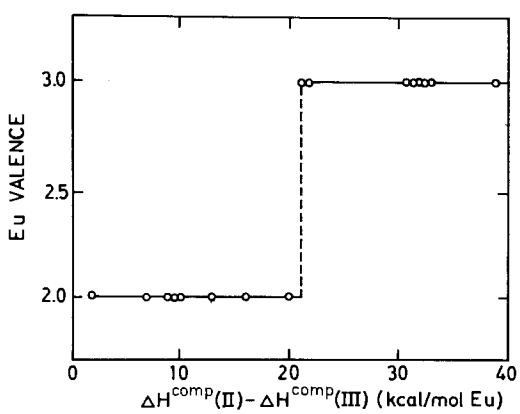

Fig. 15. Diagram showing the Eu valence state in a number of intermetallic compounds as a function of the calculated heat of formation difference ΔH^{comp}(II) $-\Delta H^{comp}$(III) (after Miedema 1976). Compared to the original analysis an extra data point for $EuRe_2$ (39 kcal/mol Eu) has been included whereas the somewhat uncertain data point for $EuPt_2$ has been omitted. Furthermore, compared to Miedema's original analysis a slightly different value for $\Delta E_{II,III}$ is used (21 kcal/mol).

Equation (27) refers to a *valence transition of the whole lattice*, i.e., every lanthanide atom in the system makes the valence change. In contrast, in the case of an f-emission (or f-addition) process by photoelectron spectroscopy (or BIS) only the valence of *one* lanthanide atom is changed, while the surrounding lattice remains undisturbed. As an example we first consider the photoemission process in a divalent lanthanide alloy which brings one of the 2+ ions into a 3+ state. General expressions for chemical shifts in alloys have been derived which have proven to describe the situation well (Johansson and Mårtensson 1980, Steiner et al. 1981). Applying these expressions to the present system we obtain for the f-ionization energy relative to the Fermi level;

$$\varepsilon^{\text{alloy}}(\text{f} \rightarrow \varepsilon_{\text{F}}) = \Delta E_{\text{II,III}} + E_{\text{III}}(\text{II alloy}) - E_{\text{II}}(\text{II alloy}). \tag{28}$$

In analogy to the discussion leading to eqs. (2) and (2′) we have obtained the expression in eq. (28) by considering the following steps. Firstly one divalent lanthanide atomic site in the alloy is decoupled from the rest of the system in such a way that it behaves as in a purely divalent metal. This process then corresponds to the solution energy of a divalent lanthanide metal atom into the divalent alloy, E_{II}(II alloy). This divalent lanthanide metal site is then converted to a trivalent site, as it should be in a fully relaxed trivalent metallic environment, a process which requires an energy $\Delta E_{\text{II,III}}$. Finally, this trivalent site is left free to adjust itself electronically to the alloy, which defines the solution energy of a trivalent impurity in the otherwise divalent alloy, E_{III}(II alloy). As was discussed in section 6 the solution energy E_{III}(II alloy) refers to a situation where there is no lattice relaxation. However, in practical situations this quantity is generally substituted by the thermodynamical analogue $E_{\text{III,thermo}}$(II alloy).

In many situations the lanthanide metals form intermetallic compounds with well-defined structures. In such cases the expression in eq. (28) is a less practical decomposition of the 4f binding energy. The derivation of a more appropriate expression for the binding energy in a divalent compound is demonstrated in fig. 14. It is convenient to consider a process where *one* lanthanide atom plus a corresponding fraction of the other atoms in the lattice (e.g., one Eu and two Pd atoms in an $EuPd_2$ compound) are removed from the system. This molecular unit is thereafter split up into its metallic constituents with the lanthanide metal in its divalent state. These two steps correspond to the heat of formation of the divalent compound (per lanthanide atom), ΔH^{comp}(II). Thereafter the divalent metal is made trivalent which requires the energy $\Delta E_{\text{II,III}}$. When we dissolve the trivalent metal atom back into the lattice in order to form the final state configuration in the 4f photoelectron ionization process, we do this in two steps. Firstly we bring together one formula unit of the trivalent compound (as it would appear in an infinite system of the trivalent compound) which then defines the energy ΔH^{comp}(III). Secondly we bring this whole unit back into the original lattice. This last step is associated with a 'molecular impurity' energy which we denote $E^{\text{imp}}_{\text{IIIcomp}}$(II comp). This is thus the solution energy of one formula unit of the trivalent compound (containing just one lanthanide atom) in the corresponding divalent compound. Instead of (28) we obtain in this way the following expression for the 4f binding energy:

$$\varepsilon^{\text{comp}}(\text{f} \rightarrow \varepsilon_{\text{F}}) = -\Delta H^{\text{comp}}(\text{II}) + \Delta E_{\text{II,III}} + \Delta H^{\text{comp}}(\text{III}) + E^{\text{imp}}_{\text{III comp}}(\text{II comp}). \quad (29)$$

Here the important point is that the final-state level is reached by a decomposition such that in the intermediate step $\Delta H^{\text{comp}}(\text{III})$ corresponds to a thermodynamical process with full lattice relaxation. In this way it becomes possible to use eq. (27) and rewrite eq. (29) in the following way:

$$\varepsilon^{\text{comp}}(\text{f} \rightarrow \varepsilon_{\text{F}}) = \Delta E^{\text{comp}}_{\text{II,III}} + E^{\text{imp}}_{\text{III comp}}(\text{II comp}). \quad (30)$$

Thereby the expression for the f binding energy has a form completely analogous to the expression for the pure metals, compare eq. (2′), where the first term expresses a complete valence change of the whole system. As for the metals the impurity energy is of the restricted type, which means that the trivalent impurity and its environment retain the geometry given by the initial lattice. Also here, however, it is a reasonable approximation to use the corresponding thermodynamical 'molecular impurity' term.

It is of interest to relate the 4f position in the compound to the 4f position in the metal. This is commonly referred to as *the chemical shift* of the 4f level and we will denote this quantity by $\Delta\varepsilon^{\text{comp}}(\text{f} \rightarrow \varepsilon_{\text{f}})$. Combining eq. (29) with eq. (2′) we find that the 4f level shift can be expressed as

$$\begin{aligned}\Delta\varepsilon^{\text{comp}}(\text{f} \rightarrow \varepsilon_{\text{F}}) &= \varepsilon^{\text{comp}}(\text{f} \rightarrow \varepsilon_{\text{F}}) - \varepsilon(\text{f} \rightarrow \varepsilon_{\text{F}}) \\ &= \Delta H^{\text{comp}}(\text{III}) - \Delta H^{\text{comp}}(\text{II}) \\ &\quad + E^{\text{imp}}_{\text{III comp}}(\text{II comp}) - E^{\text{imp}}_{\text{III}}(\text{II}). \end{aligned} \quad (31)$$

Here it should be noted that the impurity energies enter twice and with opposite signs. Therefore, the errors introduced by using a thermodynamical impurity energy to approximate the restricted one tend to cancel each other when one considers chemical shifts.

For the BIS process in an initially trivalent compound, using a similar derivation as above, we get the following expression for the position of the unoccupied f level relative to the Fermi energy:

$$\varepsilon^{\text{comp}}(\varepsilon_{\text{F}} \rightarrow \text{f}) = -\Delta H^{\text{comp}}(\text{III}) - \Delta E_{\text{II,III}} + \Delta H^{\text{comp}}(\text{II}) + E^{\text{imp}}_{\text{II comp}}(\text{III comp}). \quad (32)$$

Combining this with eq. (27) we arrive at

$$\varepsilon^{\text{comp}}(\varepsilon_{\text{F}} \rightarrow \text{f}) = -\Delta E^{\text{comp}}_{\text{II,III}} + E^{\text{imp}}_{\text{II comp}}(\text{III comp}), \quad (33)$$

which is completely analogous to eq. (3) for the pure elements. One can also write down a chemical shift expression for the unoccupied 4f level:

$$\begin{aligned}\Delta\varepsilon^{\text{comp}}(\varepsilon_{\text{F}} \rightarrow \text{f}) &= \varepsilon^{\text{comp}}(\varepsilon_{\text{F}} \rightarrow \text{f}) - \varepsilon(\varepsilon_{\text{F}} \rightarrow \text{f}) \\ &= -\Delta H^{\text{comp}}(\text{III}) + \Delta H^{\text{comp}}(\text{II}) \\ &\quad + E^{\text{imp}}_{\text{II comp}}(\text{III comp}) - E^{\text{imp}}_{\text{II}}(\text{III}). \end{aligned} \quad (34)$$

From this derivation we observe that similar expressions are obtained for the electron emission and electron addition processes. With respect to eqs. (30) and (33) we note that the molecular impurity terms, $E^{\text{imp}}_{\text{III comp}}(\text{II comp})$ and $E^{\text{imp}}_{\text{II comp}}(\text{III comp})$,

can be expected to be quite small in many types of compounds. This is especially the case for compounds which are dilute in the content of lanthanide metal, since thereby the lanthanide atoms will mainly be surrounded by atoms of the opposite kind. For compounds, and in particular for dilute compounds, the measured 4f positions will thus according to eqs. (30) and (33) often be a good approximation to $\Delta E^{\mathrm{comp}}_{\mathrm{II,III}}$. Therefore in this connection it becomes natural to consider also the following type of *generalized shift* expressions, $D\varepsilon^{\mathrm{comp}}(\mathrm{f} \rightarrow \varepsilon_{\mathrm{F}})$:

$$\begin{aligned} D\varepsilon^{\mathrm{comp}}(\mathrm{f} \rightarrow \varepsilon_{\mathrm{F}}) &= \varepsilon^{\mathrm{comp}}(\mathrm{f} \rightarrow \varepsilon_{\mathrm{F}}) - \Delta E_{\mathrm{II,III}} \\ &= \Delta H^{\mathrm{comp}}(\mathrm{III}) - \Delta H^{\mathrm{comp}}(\mathrm{II}) + E_{\mathrm{III\,comp}}(\mathrm{II\,comp}), \end{aligned} \tag{35}$$

and $D\varepsilon^{\mathrm{comp}}(\varepsilon_{\mathrm{F}} \rightarrow \mathrm{f})$,

$$\begin{aligned} D\varepsilon^{\mathrm{comp}}(\varepsilon_{\mathrm{F}} \rightarrow \mathrm{f}) &= \varepsilon^{\mathrm{comp}}(\varepsilon_{\mathrm{F}} \rightarrow \mathrm{f}) + \Delta E_{\mathrm{II,III}} \\ &= -\Delta H^{\mathrm{comp}}(\mathrm{III}) + \Delta H^{\mathrm{comp}}(\mathrm{II}) + E_{\mathrm{II\,comp}}(\mathrm{III\,comp}) \end{aligned} \tag{36}$$

for photoemission and BIS, respectively. In these generalized shift expressions the energy positions of the 4f levels in the compounds are related to the energy difference $\Delta E_{\mathrm{II,III}}$ for the pure metals instead of to the spectroscopic 4f positions. It is seen from these equations that, apart from the 'molecular impurity' terms, the generalized photoemission and BIS shifts are the same but with opposite signs. For regular heat of mixing curves between the divalent and trivalent compounds, the terms $E_{\mathrm{III\,comp}}(\mathrm{II\,comp})$ and $E_{\mathrm{II\,comp}}(\mathrm{III\,comp})$ will have the same sign and most often they will also be of similar magnitudes. These terms will thus tend to remove the direct correspondence between the generalized photoemission and BIS shifts, $D\varepsilon^{\mathrm{comp}}(\mathrm{f} \rightarrow \varepsilon_{\mathrm{F}})$ and $D\varepsilon^{\mathrm{comp}}(\varepsilon_{\mathrm{F}} \rightarrow \mathrm{f})$, respectively. However, it was noted above that these impurity terms are often quite small and therefore they can in many applications be disregarded. The situation for the 'normal' chemical shifts $\Delta\varepsilon^{\mathrm{comp}}(\mathrm{f} \rightarrow \varepsilon_{\mathrm{F}})$ and $\Delta\varepsilon^{\mathrm{comp}}(\varepsilon_{\mathrm{F}} \rightarrow \mathrm{f})$ is somewhat different due to the relative importance of the terms $E^{\mathrm{imp}}_{\mathrm{III}}(\mathrm{II})$ and $E^{\mathrm{imp}}_{\mathrm{II}}(\mathrm{III})$, see section 6.

Laubschat et al. (1986) have investigated the relationship between measured 4f positions and the stability of different valence states for a number of lanthanide compounds (see also Laubschat (1984)). Particularly interesting are the results for the lanthanide dialuminides, $\mathrm{LnAl_2}$, for which both photoemission and BIS experiments were performed. In the divalent compound $\mathrm{EuAl_2}$ these authors located the bulk 4f position at 0.45 eV. This should be compared to the 4f binding energy in Eu metal which is 1.50 eV (Lang et al. 1981). The chemical shift of the 4f position, $\Delta\varepsilon^{\mathrm{comp}}(\mathrm{f} \rightarrow \varepsilon_{\mathrm{F}})$, is thus -1.05 eV in this compound, i.e. a most substantial shift. Considering instead the generalized shift expression $D\varepsilon^{\mathrm{comp}}(\mathrm{f} \rightarrow \varepsilon_{\mathrm{F}})$ in eq. (35) and using table 1 for $\Delta E_{\mathrm{II,III}}$, a shift of $0.45 - 0.9 = -0.45$ eV is obtained. For the trivalent compound $\mathrm{GdAl_2}$, Laubschat et al. (1986) investigated in a corresponding way the BIS 4f position. This level was located at 4.2 eV above the Fermi energy in the compound, compared to the experimental position in the pure metal of 4.04 eV (Lang et al. 1981). The chemical shift of the unoccupied 4f level is thus 0.16 eV in $\mathrm{GdAl_2}$. The generalized shift $D\varepsilon^{\mathrm{comp}}(\varepsilon_{\mathrm{F}} \rightarrow \mathrm{f})$ in $\mathrm{GdAl_2}$ is instead $4.2 - 3.67 = 0.5$ eV.

From this it can be seen that the generalized shifts $D\varepsilon^{\mathrm{comp}}$ for the two cases are very similar in magnitude and of opposite signs. This gives strong support for the

correctness of the assumption that the molecular impurity terms in eqs. (35) and (36) are small and that it is a reasonable approximation to neglect these terms for the lanthanide dialuminides. The directly measured chemical shifts, $\Delta\varepsilon^{\text{comp}}(\text{f} \rightarrow \varepsilon_{\text{F}})$ for $EuAl_2$ and $\Delta\varepsilon^{\text{comp}}(\varepsilon_{\text{F}} \rightarrow \text{f})$ for $GdAl_2$ are, however, quite different from each other. This demonstrates the importance of the impurity terms $E_{\text{III}}^{\text{imp}}(\text{II})$ and $E_{\text{II}}^{\text{imp}}(\text{III})$ in the pure Eu and Gd metals, respectively. The different magnitudes for the chemical photoelectron shift in $EuAl_2$ and the BIS shift in $GdAl_2$ are mainly caused by the impurity terms for the pure metals.

The close correspondence between the 4f positions and the stability energies between different valence states for lanthanide compounds will be further discussed in section 13.

12. Surface shifts of 4f levels in lanthanide metal compounds

As for the pure lanthanide metals it is necessary to treat the 4f properties at the surface of a compound separately. As a matter of fact the difference between bulk and surface is in many cases even more accentuated in compounds than in the pure metals. This is so since for a compound not only the structure but also the composition can be different in the surface region as compared to the bulk.

We start by considering how the derivation of the bulk 4f binding energy for a compound (section 11) is modified for a surface layer. As for the bulk we can proceed step by step to obtain the corresponding surface expressions. To start with we formally rewrite eq. (27) as

$$\Delta E_{\text{II,III}}^{\text{comp,surf}} = \Delta E_{\text{II,III}}^{\text{surf}} + \Delta H^{\text{comp,surf}}(\text{III}) - \Delta H^{\text{comp,surf}}(\text{II}), \tag{37}$$

where $\Delta E_{\text{II,III}}^{\text{comp,surf}}$ denotes the energy difference between the trivalent and divalent states at the surface of the compound. Note, however, that in this case it will be necessary to treat separately various, different situations. The heat of formation of a surface layer, $\Delta H^{\text{comp,surf}}$, will for instance depend on the underlying bulk valence state. This could be included by an interface term as in eq. (12) for the pure metals. There are also other effects which will influence $\Delta E_{\text{II,III}}^{\text{comp,surf}}$. One is the already mentioned possibility that the composition and structure at the surface might be different than in the bulk. Furthermore, a surface valence transition might alter the equilibrium composition at the surface and also this effect would have to be included in a full treatment of $\Delta E_{\text{II,III}}^{\text{comp,surf}}$. These and other effects add up to a situation which is even more complicated than for the pure lanthanide metals. However, instead of discussing formal expressions which cover all these different situations we will for the sake of transparency neglect these effects and instead make a number of simplifying assumptions already from the beginning. This will be done in such a way that we can see more directly how surface and bulk properties are related to each other. To do this we will try to relate the surface terms in eq. (37) to the corresponding bulk terms.

Considering the expression in eq. (37) we first of all note that it was already discussed in section 9 how for the pure metals $\Delta E_{\text{II,III}}^{\text{surf}}$ can be related to $\Delta E_{\text{II,III}}$. The remaining two terms in eq. (37) are the heats of formation of the compounds at the

surface. Due to the reduced coordination at the surface these energies will be related to the bulk values by some factor α which is smaller than one. If we for simplicity assume that α is the same for the divalent and trivalent compounds we obtain

$$\Delta E_{\mathrm{II,III}}^{\mathrm{comp,surf}} = \Delta E_{\mathrm{II,III}}^{\mathrm{surf}} + \alpha(\Delta H^{\mathrm{comp}}(\mathrm{III}) - \Delta H^{\mathrm{comp}}(\mathrm{II})). \tag{38}$$

This equation can now be used to estimate the valence state at the surface of a lanthanide compound. In section 11 we performed an analysis of the bulk valence of different Eu compounds on the basis of Miedema's (1976) scheme. It is now interesting to investigate what the same kind of analysis gives for the surface. At first we note that for bulk Eu metal the energy difference between the trivalent and divalent states, $\Delta E_{\mathrm{II,III}}$, is 21 kcal/mol. At the surface the divalent configuration is according to eq. (16) further stabilized by about $0.2(103 - 43) = 12$ kcal/mol. Accordingly, the stability of the divalent configuration at the surface of Eu metal, $\Delta E_{\mathrm{II,III}}^{\mathrm{surf}}(\mathrm{Eu})$, becomes $21 + 12 = 33$ kcal/mol. This stability energy should now be compared to the difference in heat of formation of the divalent and trivalent surface compounds. In eq. (38) we express this difference as a reduction factor α times the corresponding heat of formation difference for the bulk. From fig. 15 we notice that the maximum value of $\Delta H^{\mathrm{comp}}(\mathrm{II}) - \Delta H^{\mathrm{comp}}(\mathrm{III})$ that is calculated for any Eu compound within Miedema's (1976) scheme is around 39 kcal/mol (for $EuRe_2$). To obtain an estimation of the corresponding difference for the surface, $\Delta H^{\mathrm{comp,surf}}(\mathrm{III}) - \Delta H^{\mathrm{comp,surf}}(\mathrm{II})$, the same reduction factor $\alpha = 0.8$ is used as in section 10 for the pure metals. Thereby a maximum difference of $0.8 \times 39 = 31$ kcal/mol is obtained. We immediately see that this energy is smaller than what is required for a transition to a trivalent surface, 33 kcal/mol. Therefore according to eq. (38) the surfaces of europium compounds are predicted to be divalent. Only for $EuRe_2$ do we find a close neighbourhood to a trivalent surface.

For the sake of completeness it should be pointed out that we have presented a rather simplified analysis for the surface valence stabilities. Even within the framework of Miedema's model it would be possible to refine the given treatment considerably (see, e.g., Nilsson et al. 1985). Within Miedema's scheme it would even be possible to estimate certain aspects of the presently neglected details of the interface term since ternary systems can be handled, i.e., the bonding interaction between a divalent surface layer and a trivalent bulk can be treated in some depth. There is, however, a more fundamental reason why the result for Eu-compound surfaces, based on eq. (38) should be used with some caution. In a detailed analysis it would for each compound be necessary to consider what surface structure and surface composition gives the lowest total energy. Thus it is possible to imagine a situation in a Eu compound where at the surface there will be a dramatic enrichment of the second non-lanthanide component. Thereby only a few Eu bonds are broken in the surface region. For such a surface the conclusions above could therefore very well be altered. However, the trivalent Eu compounds which have so far been investigated by photoemission, i.e. $EuPd_3$ and $EuPd_5$ (Murgai et al. 1982), do indeed show a divalent europium surface, which is in complete agreement with the predictions above. Thus, unless a drastic reconstruction of some kind has taken place at the surface, it seems possible to state that all europium compounds, except possibly $EuRe_2$, will be divalent at the surface.

Surface valence transitions from a trivalent bulk to a divalent surface have been observed also in a number of other trivalent compounds such as $YbAu_2$ (Wertheim et al. 1978a), TmS (Kaindl et al. 1982b, Mårtensson et al. 1982b), $SmAl_2$ (Kaindl et al. 1983, Laubschat et al. 1986) and $YbPd_3$ (Domke et al. 1985). Divalent surface layers have furthermore been identified in several mixed divalent–trivalent compounds such as SmB_6 (Allen et al. 1980), $YbAl_2$ (Kaindl et al. 1982a), $EuPd_2Si_2$ (Mårtensson et al. 1982a), TmSe (Kaindl et al. 1982b), $Tm_{1-x}Y_xSe$ (Mårtensson et al. 1982e), $Sm_{1-x}Y_xS$ (Reihl et al. 1982) and YbPd (Domke et al. 1985).

The photoemission 4f energy position for the surface of a lanthanide compound can in analogy with eq. (29) be expressed as

$$\varepsilon^{\text{comp,surf}}(\text{f} \rightarrow \varepsilon_\text{F}) = \Delta E^{\text{surf}}_{\text{II,III}} + \Delta H^{\text{comp,surf}}(\text{III}) - \Delta H^{\text{comp,surf}}(\text{II}) + E^{\text{imp,surf}}_{\text{III comp}}(\text{II comp}). \tag{39}$$

An expression for the surface shift, $\Delta E^{\text{comp}}_\text{S}$, i.e., the difference in 4f energies between the surface and the bulk of the compound can be obtained by combining eqs. (29) and (39). Before writing this expression down we make the simplifying assumption that all the cohesive energies, heats of formation and impurity energies for the surface can be obtained by multiplying the corresponding bulk quantities by one and the same factor α ($\alpha < 1$). In this way we obtain for the compound surface shift

$$\Delta E^{\text{comp}}_\text{S} = \varepsilon^{\text{comp,surf}}(\text{f} \rightarrow \varepsilon_\text{F}) - \varepsilon^{\text{comp}}(\text{f} \rightarrow \varepsilon_\text{F}) = \Delta E^{\text{surf}}_{\text{II,III}} - \Delta E_{\text{II,III}} + (\alpha - 1)(\Delta H^{\text{comp}}(\text{III}) - \Delta H^{\text{comp}}(\text{II}) + E^{\text{imp}}_{\text{III comp}}(\text{II comp})). \tag{40}$$

Based on the discussion in section 10 it is also possible to rewrite the expressions for the surface shift in the pure lanthanide metals in a similar way, namely,

$$\Delta E_\text{S} = \Delta E^{\text{surf}}_{\text{II,III}} - \Delta E_{\text{II,III}} + (\alpha - 1)E^{\text{imp}}_{\text{III}}(\text{II}). \tag{41}$$

An interesting quantity in this connection is the difference in measured surface shift between the compound and the pure metal, $\Delta(\Delta E_\text{S})$. By combining eqs. (40) and (41) we obtain the following expression for the difference in surface shift:

$$\Delta(\Delta E_\text{S}) = \Delta E^{\text{comp}}_\text{S} - \Delta E_\text{S} = (\alpha - 1)(\Delta H^{\text{comp}}(\text{III}) - \Delta H^{\text{comp}}(\text{II}) + E^{\text{imp}}_{\text{III comp}}(\text{II comp}) - E^{\text{imp}}_{\text{III}}(\text{II})). \tag{42}$$

The expression within the parenthesis is immediately recognized as the *bulk* chemical shift of the 4f position in the photoemission experiment, $\Delta\varepsilon^{\text{comp}}_\text{B}$ (compare eq. (31)). We thus end up with the simple result (Mårtensson et al. 1982a, Johansson et al. 1982, Murgai et al. 1982, Kaindl et al. 1983, Laubschat et al. 1986)

$$\Delta(\Delta E_\text{S}) = (\alpha - 1)\ \Delta\varepsilon^{\text{comp}}_\text{B}. \tag{43}$$

This equation can also be expressed as a relationship between the chemical shift of the 4f level at the surface in the compound and at the surface in the metal, $\Delta\varepsilon^{\text{comp}}_\text{S}$, and the corresponding shift in the bulk, $\Delta\varepsilon^{\text{comp}}_\text{B}$;

$$\Delta\varepsilon^{\text{comp}}_\text{S} = \alpha\Delta\varepsilon^{\text{comp}}_\text{B} \tag{44}$$

This simple relation shows that the surface 4f energy position undergoes a shift which is numerically smaller than the bulk shift. One can thus set up simple rules for

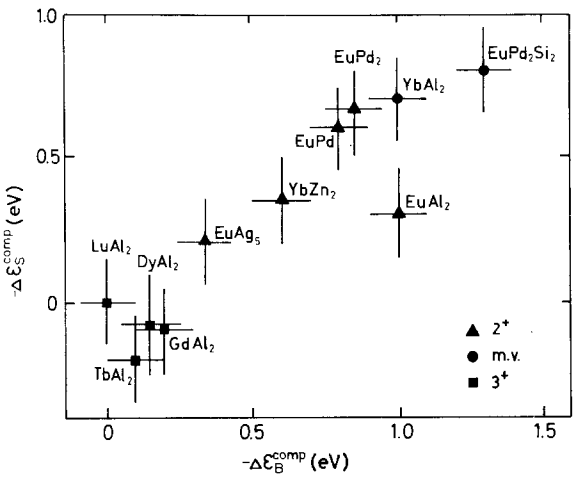

Fig. 16. Diagram showing the relationship between the chemical shift of the bulk 4f level, $\Delta\varepsilon_B^{comp}$, and the shift of the surface 4f level, $\Delta\varepsilon_S^{comp}$, for a number of lanthanide compounds. The points are denoted according to whether the compounds are divalent (2+), mixed-valent (m.v.) or trivalent (3+). (Data from Schneider et al. (1983) and Laubschat et al. (1986).)

the behaviour of the surface shifts in lanthanide systems. In all the pure lanthanide metals the surface 4f position is shifted to higher energies relative to the bulk position. For a compound in which the bulk 4f level shifts towards the Fermi level, the surface 4f level will shift in the same direction but with a reduced amount. Thus in such a compound there will be a larger surface shift (ΔE_S^{comp}) than for the pure metal (ΔE_S). A shift of the bulk 4f level towards higher binding energies will by the same argument lead to a smaller shift for the surface 4f level. In this case the surface shift for the compound will be smaller than in the pure metal.

Kaindl et al. (1983) and Laubschat et al. (1986) discussed for a number of lanthanide compounds the behaviour of the 4f surface shifts. In fig. 16 the shift of the surface 4f level, $\Delta\varepsilon_S^{comp}$, in each compound is plotted against the corresponding bulk 4f shifts, $\Delta\varepsilon_B^{comp}$. In the figure two groups of data points can be distinguished. To the left there are a number of points obtained from 4f spectra of trivalent lanthanide dialuminides. These compounds show small shifts of the bulk as well as of the surface 4f levels. On the right-hand side of the figure there are a set of data points corresponding to divalent or mixed-valent Eu and Yb compounds. These compounds show larger shifts both for the bulk and for the surface. As can be seen from the figure there is to a first approximation a linear relationship between the shift of the surface and the bulk 4f levels. It is furthermore seen that the surface 4f level shifts are less than for the bulk, in full agreement with eq. (44). There have also been measurements for con pounds with shifts in the opposite direction. Mårtensson et al. (1982c) studied the 4f spectra in several trivalent lanthanide antimonides. The spectra from ErSb and LuSb are shown in fig. 17. The 4f levels in these antimonides are shifted by 1.10–1.15 eV towards higher binding energies relative to the bulk positions in the pure metals. Furthermore, the spectra reveal no sign at all of a separate surface 4f signal. Considering the experimental widths of the 4f features it could be concluded that the surface shifts must be small (at most a few tenths of an eV) for these compounds. This is again consistent with eq. (44) in so far that a large positive shift of the bulk 4f levels, $\Delta\varepsilon_B^{comp}$, should lead to a reduced shift of the surface component and thus to a reduced surface shift, $\Delta\varepsilon_S^{comp}$. However, since the

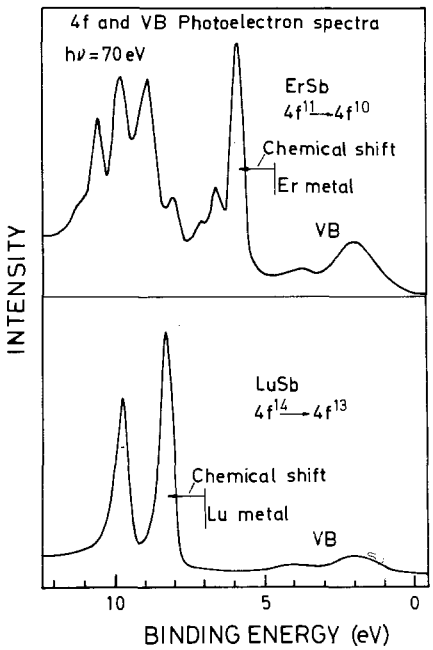

Fig. 17. Photoelectron spectra of the trivalent compounds ErSb and LuSb (after Mårtensson et al. 1982c). The 4f energy positions for the pure metals (Lang et al. 1981) are inserted for comparison.

surface shifts could not be resolved there is still a large uncertainty in the positions of the surface 4f peaks and therefore none of these points have been included in fig. 16.

Kaindl et al. (1983) and Laubschat et al. (1986) obtained from their analysis of surface vs. bulk 4f shifts a value of α of the order of 0.7 (compare fig. 16). However, as can be seen from fig. 16, there are a few data points which behave significantly differently. The assumption of a fixed value of α for all the different compounds is thus clearly an oversimplification. This means that a detailed knowledge about the structure and composition at the surface is required. From broken bond arguments one would expect α to be about 0.8, which is the number that was used earlier in connection with the pure metals. However, if the composition of the surface layer is different from the bulk this factor will be modified (Johansson et al. 1982, Nilsson et al. 1985 and Laubschat et al. 1986). To see what happens in such a situation let us consider a compound in which the bulk 4f level is shifted towards the Fermi level, i.e. a negative chemical shift $\Delta\varepsilon_B^{comp}$. If the surface region is enriched in the lanthanide metal this means that the surface lanthanide atoms experience a situation which is intermediate between the perfect (non-segregated) surface of the compound and the surface of the pure metal. This corresponds to a numerically reduced shift of the surface 4f energy level relative to the pure metal surface 4f energy and thus effectively a smaller α. Since thereby $(1 - \alpha)$ increases we find from eq. (43) that this kind of segregation will lead to a larger surface shift, ΔE_S^{comp}, of the 4f level in the compound than in the pure metal. In an analogous way a depletion of the lanthanide content in the surface layer leads to a reduced surface shift in the compound (provided that $\Delta\varepsilon_B^{comp}$ is negative).

The most extreme case for segregation would be a lanthanide system in which the lanthanide component segregates to form a complete monolayer at the surface. We now assume that the interatomic bonding is mainly determined by the nearest-neighbour interaction and that we can divide the number of bonds for an atom approximately equal between bonds within the layer, bonds to the layer above and bonds to the layer below. In the segregated case each lanthanide atom at the surface experiences the effects of the atoms of the opposite kind only from the layer below the surface. One would thus obtain a shift of the compound surface peak relative to the pure metal surface peak, which is only $\frac{1}{3}$ of the shift of the bulk. For such an extremely segregated case one could thus obtain effective α values as low as of the order of 0.3. The other extreme case is that the surface becomes totally covered by the non-lanthanide component of the system. This might lead to a situation where no influence of a surface on the 4f binding energy can be measured, i.e., in practice all the lanthanide atoms have become bulk-like. This may for example be the reason why no surface shift could be identified for the lanthanide antimonides (compare above).

In general the surface shift will of course depend on the details of the surface structure of the compound. One can visualize various situations where the lanthanide bonds are more or less affected by the surface, leading to different shifts. (This was for example clearly demonstrated by the variation of the surface shift for evaporated ytterbium metal as a function of the deposition temperature (Schneider et al. 1983)). However, the basic parameters which determine the shifts are known and measurements of the surface shifts can thus give important information on the structure and composition of surfaces of lanthanide compounds.

Related to the discussion in the present section is also the increasing number of studies of the properties of very thin lanthanide layers deposited on metals and semiconductors. The valence state and 4f positions of such systems can be treated in a completely analogous way as above for compound surfaces (Nilsson et al. 1985, Fujimori et al. 1986). Similar treatments have also been presented for non-lanthanide systems (Steiner and Hüfner 1981b, Egelhoff 1983, Wertheim 1986). Structurally well-characterized lanthanide overlayers on single crystal surfaces can for instance be used as most valuable model systems for studying concentration- and structure-dependent surface properties of lanthanide compounds. Such investigations have for example been performed for Sm on Cu(100) and Al(100) (Fäldt and Meyers 1984a,b), Yb on Al(100) (Nyholm et al. 1984) and Yb on Ni (110) (Chorkendorff et al. 1985b). There has also been a particular interest in the properties of lanthanide metals on semiconductor surfaces (e.g. Rossi et al. 1983, Grioni et al. 1984, Franciosi et al. 1984, Grioni et al. 1985, Chorkendorff et al. 1985a, Rossi et al. 1985 and Fujimori et al. 1986). This is related to the importance of the formation of Schottky barriers at metal–semiconductor interfaces. Fujimori et al. (1986) have in this connection discussed the thermodynamical aspects of rare-earth metal–semiconductor interfacial reactions. They demonstrated that already the variation of lanthanide valences could be used to give important information on thermodynamical quantities related to these interfaces. For example at ultra-low coverages of lanthanide metals on Si(111) it has been observed that Sm is divalent

(Franciosi et al. 1984) and Tm is trivalent (Fujimori et al. 1986). This observation alone defines a relatively narrow range for the difference in adsorption energies for the divalent and trivalent states of the lanthanide atoms. In the future, accurate experimental recordings of the energy positions of 4f levels by photoelectron spectroscopy and BIS for this type of systems should be most valuable. Thereby the quantification of important thermodynamical parameters for the interfacial interaction could be facilitated.

13. Stability of 4f configurations of lanthanide compounds studied by photoelectron spectroscopy and BIS

As a demonstration of the effects of compound formation Murgai et al. (1982) showed how the Eu 4f photoemission spectrum changes as the europium valence is brought from Eu^{2+} in EuPd and $EuPd_2$ through mixed-valence in $EuPd_2Si_2$ to Eu^{3+} in $EuPd_3$ and $EuPd_5$. The spectra from this investigation are shown in fig. 18. In the Eu 4f spectra, Eu^{2+} atoms give rise to characteristic features in the energy region 0–3 eV below the Fermi level, whereas the Eu^{3+} intensity is to be found in the energy region 6–10 eV. The europium valence can thus be determined by investigating the presence of the characteristic Eu^{2+} and Eu^{3+} 4f emission features. Furthermore, as discussed in the previous sections the absolute energy position of the Eu^{2+} 4f level gives direct information about the relative stabilities of the divalent and trivalent europium states.

The measurements by Murgai et al. (1982) were performed with synchrotron radiation using a photon energy of 120 eV. This leads to a considerable surface sensitivity of the measurements with an information depth of only a few atomic layers. In the present systems this photon energy has also the particular advantage that it is close to the Cooper minimum for the Pd 4d emission. This means that in the photoemission spectrum there is an almost total dominance of the Eu 4f states in the valence band energy region.

The spectrum from EuPd is shown in greater detail in fig. 19. From this figure it can be seen how the Eu 4f spectrum can be decomposed into two peaks (each peak consisting of several closely spaced multiplet lines) separated by about 0.8 eV. The peak closest to the Fermi level was identified as due to the bulk 4f emission, while the structure at higher binding energies originates from a few Å thick surface layer. The higher binding energy of the surface peak in EuPd as well as in $EuPd_2$ implies that there is a higher stability of the divalent state in the surface region as compared to the bulk.

In $EuPd_2Si_2$ it is observed that the Eu^{2+} bulk and surface emission features are both shifted towards E_F relative to their positions in EuPd (fig. 18). Analyzing the bulk 4f emission spectrum, one finds in this case that the lowest-lying multiplet line is located in the vicinity of the Fermi level. A small $Eu(4f^7) \rightarrow Eu(4f^6)$ excitation energy implies that the Eu^{2+} and Eu^{3+} configurations are essentially degenerate in energy, and therefore the necessary condition for homogeneous mixed-valence is fulfilled. The mixed-valent character of this system is then established in the

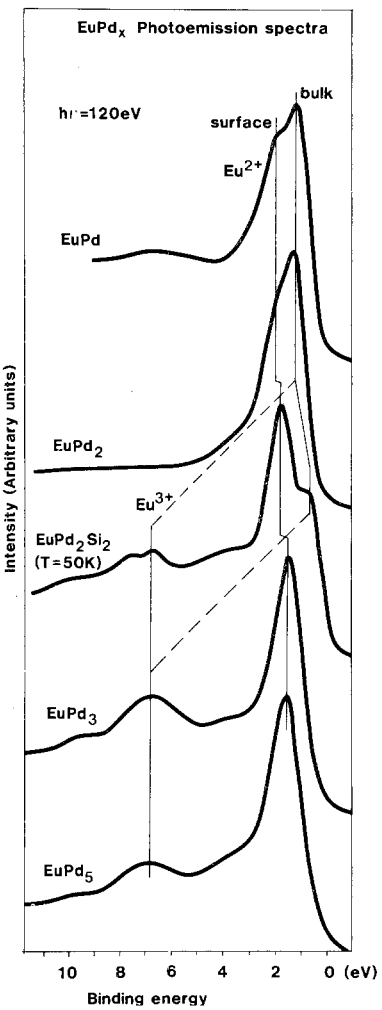

Fig. 18. Eu 4f photoelectron spectra from the divalent compounds EuPd and $EuPd_2$, the mixed-valent compound $EuPd_2Si_2$ and the trivalent compounds $EuPd_3$ and $EuPd_5$ (Murgai et al. 1982). The spectra are almost totally dominated by the Eu 4f emission due to a Cooper minimum in the Pd 4d intensity.

spectrum by the simultaneous appearance of Eu^{3+} emission features at around 6–10 eV binding energies.

The main divalent intensity for $EuPd_2Si_2$ is still located at about 2 eV (peak position) from the Fermi level. The surface origin of this feature could be shown by performing temperature-dependent measurements (Mårtensson et al. 1982a). $EuPd_2Si_2$ undergoes a valence transition from $Eu^{2.2+}$ at room temperature to $Eu^{2.9+}$ at low temperatures ($\lesssim 100$ K). It was found that the intensity of the Eu^{2+} feature closest to the Fermi level and the Eu^{3+} intensity vary in accordance with the effective bulk valence, whereas the intensity of the 2 eV feature stays practically the same during the transition. This implies that the 2 eV peak originates from a surface stabilized divalent layer. The surface shift thus generates a divalent surface layer on top of the mixed-valent bulk compound. The same effect has been seen in a number of other mixed-valent systems (see section 12) and it seems possible to conclude that the surface of a mixed divalent and trivalent compound is always divalent.

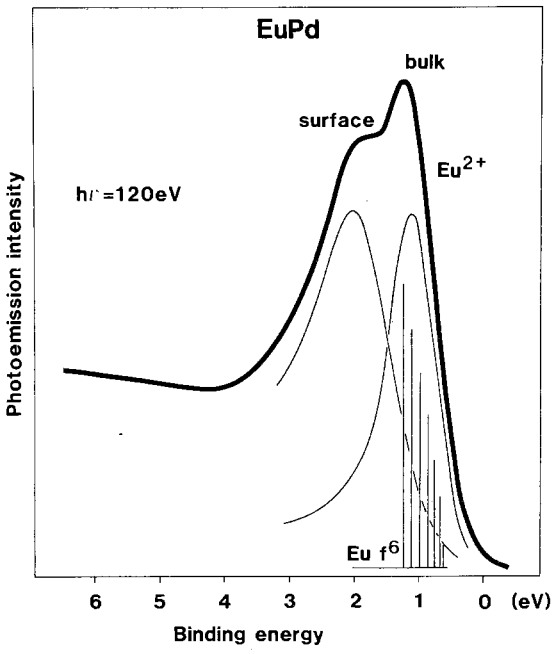

Fig. 19. Bulk and surface 4f emission features in divalent EuPd (Murgai et al. 1982).

As the Pd concentration is further increased in the series of compounds one can from fig. 18 observe for $EuPd_3$ and $EuPd_5$ how the bulk 4f intensity close to the Fermi level becomes completely transferred to the Eu^{3+} emission region; i.e. the bulk samples have attained a completely trivalent state. The spectrum of $EuPd_3$ is also shown in greater detail in fig. 20. Although the effects of the alloying are sufficient to bring the bulk to an integral valent Eu^{3+} state it is seen that the surface europium atoms still remain divalent. The decreased divalent surface 4f binding energy as a function of Pd content shows, however, that the energy difference between the two valence states at the surface is reduced.

This example with Eu and Pd demonstrates first of all how the valence state of a lanthanide can be determined by the presence of the well separated Ln^{2+} and Ln^{3+} emission features. For the mixed-valent compound it is furthermore possible to establish the degree of valence mixture from the relative intensities of the two emission features. The relative stabilities of the divalent and trivalent configurations are also revealed by the position of the divalent photoemission features in the different compounds. Therefore one can determine for each compound by how much the divalent configuration is stabilized by the surface.

Complementary information for the $EuPd_x$ systems has been obtained by BIS experiments (Laubschat et al. 1984, Mårtensson et al. 1985). As explained in the previous sections, this technique can for example be used to estimate $\Delta E^{\text{comp}}_{II,III}$ for the trivalent compounds $EuPd_3$ and $EuPd_5$. The BIS data of $EuPd_3$ are shown in fig. 21. In this spectrum we observe the dominating $f^6 \rightarrow f^7$ contribution close to the Fermi level, showing that there is only a small stability of the trivalent configuration. Here we will, however, first consider the spectral feature identified at 10.0eV above the Fermi level which Mårtensson et al. interpreted as due to an

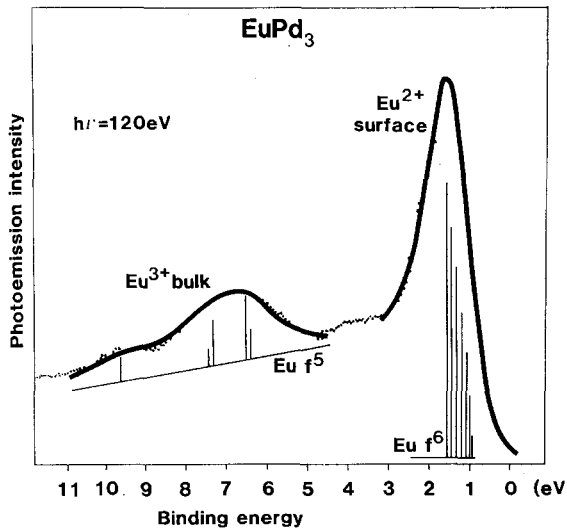

Fig. 20. Bulk and surface 4f emission features in trivalent $EuPd_3$ (Murgai et al. 1982).

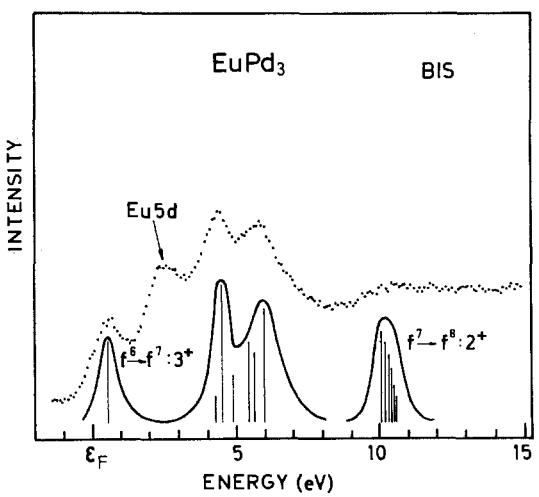

Fig. 21. Bremsstrahlung isochromat spectrum (BIS) from the trivalent compound $EuPd_3$ recorded at $h\nu = 1487\,eV$. The weak $f^7 \rightarrow f^8$ feature at 10 eV has been interpreted as due to a divalent surface layer. (After Mårtensson et al. 1985.)

$Eu(4f^7) \rightarrow Eu(4f^8)$ transition in the divalent surface layer. Strong support for this interpretation was given by the fact that the 10 eV feature disappeared upon adsorption of oxygen, a process which is known to remove the divalent layer at the surface. It is interesting to investigate in some detail the energy position of this feature. Using Miedema's (1976) scheme for the thermodynamic quantities in eq. (34) one obtains a calculated chemical shift $\Delta\varepsilon_B^{comp}(\varepsilon_F \rightarrow f)$ of 1.9 eV between the 4f BIS position in the bulk of hypothetically divalent $EuPd_3$ and the bulk of Eu metal. Since for $EuPd_3$ we are in reality considering a surface layer, this shift relative to the surface of Eu metal should be reduced by a factor α according to eq. (44). With $\alpha = 0.8$ this leads to a calculated shift $\Delta\varepsilon_S^{comp}(\varepsilon_F \rightarrow f)$ of 1.5 eV. To obtain the absolute value in $EuPd_3$ we first note that the experimental 4f BIS position in bulk Eu metal is 8.63 eV (Lang et al. 1981). The surface 4f position should, however, be

shifted somewhat from this position. Using an expression analogous to eq. (26) for the BIS process a surface shift of -0.15 eV is predicted for Eu metal. This gives an estimated surface 4f position in the metal of 8.5 eV. Adding to this the calculated chemical shift of the surface component we obtain $8.5 + 1.5 = 10.0$ eV for the $4f^7 \rightarrow 4f^8$ position at the surface of $EuPd_3$, which is in perfect agreement with the experimental position. Although this very good agreement must be considered to be somewhat fortuitous it gives good support for the given interpretation.

In section 11 we derived expressions for $\Delta E^{comp}_{II,III}$ and $\Delta E^{comp}_{III,IV}$ in compounds. If we consider the expression for $\Delta E^{comp}_{II,III}$ in eq. (27) we first of all note that the $\Delta E_{II,III}$ values for the pure metals are accurately known from section 3. However, the required heats of formation, ΔH^{comp}, are often insufficiently known. For example, it is clear that only one of the required ΔH^{comp} values can be a direct experimental quantity. However, from the chemical similarity of different lanthanides it can be safely assumed that the energy terms $\Delta H^{comp}(III)$ and $\Delta H^{comp}(II)$ for a certain type of compound will vary smoothly over the lanthanide series. There will only be a continuous variation due to the lanthanide contraction. Therefore, if the heats of formation are known for a few lanthanide systems of a certain type it is possible to obtain the remaining values in the series by interpolation. The ΔH^{comp} values used in eq. (27) are thus most often interpolated quantities. In particular, this regularity in the compound formation also implies that if $\Delta E^{comp}_{II,III}$ is known only for a few members of a series of Ln–X compounds, then the $\Delta E^{comp}_{II,III}$ energies can be derived accurately also for the remaining Ln–X compounds.

The same kind of systematic behaviour can be anticipated for the 4f positions $\varepsilon^{comp}(f \rightarrow \varepsilon_F)$ and $\varepsilon^{comp}(\varepsilon_F \rightarrow f)$ seen in photoemission and BIS, respectively. Furthermore, as discussed in section 11 these spectroscopic positions are in many cases nearly the same as the corresponding energies for changing the valence state of the whole lattice, especially for compounds which are dilute in the lanthanide component. This therefore provides a method for studying the stabilities of a whole series of lanthanide compounds based on spectroscopic measurements on only a few members of the series.

Laubschat et al. (1986) used this approach to discuss the bulk and surface valence states of the LnPd and $LnPd_3$ compounds. In EuPd which is a divalent compound the bulk 4f position was found at 0.6 eV (Murgai et al. 1982), compare fig. 19. YbPd, which has been found to be mixed-valent, gives rise to both divalent and trivalent emission features (Domke et al. 1985). The energy of the divalent bulk 4f feature was determined to be 0.1 eV in this compound. The generalized shifts, $D\varepsilon^{comp}(f \rightarrow \varepsilon_F)$, eq. (35), for these two compounds are thus $0.6 - 0.9 = -0.3$ eV for EuPd and $0.1 - 0.5 = -0.4$ eV for YbPd, respectively. Thus the shifts are seen to be nearly the same for the two compounds. Since this $D\varepsilon^{comp}$ shift should be a smoothly varying function of the atomic number in the lanthanide series the 4f positions can be determined also for the other LnPd compounds by interpolation and extrapolation in the series of compounds. In fig. 22 the $-\Delta E_{II,III}$ values (see table 1) for the lanthanide metals are plotted. In this figure a new Fermi level ε_F^B can now be drawn which is determined by the generalized shifts, $D\varepsilon^{comp}$, for EuPd and YbPd. This is the Fermi level relative to which the 4f positions for the LnPd compounds should be referred. From this diagram the valence stability of all the LnPd compounds can be

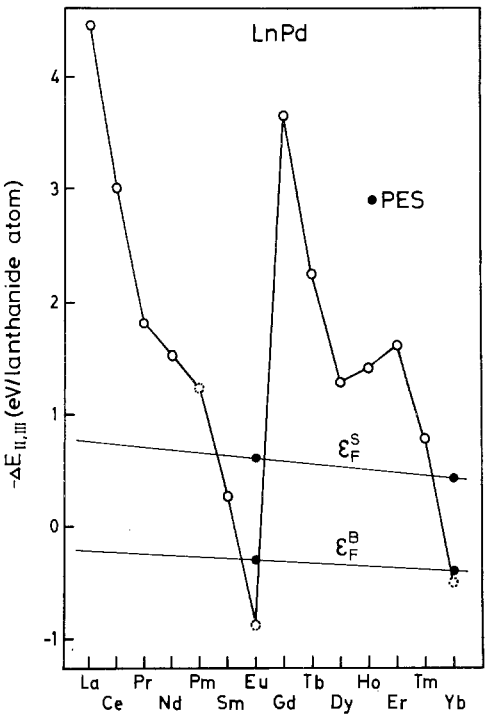

Fig. 22. Constructed stability diagram for the LnPd compounds (after Laubschat et al. 1986). PES denotes photoelectron spectroscopy. For further explanation, see the text.

predicted. It can be seen that in fact all the lanthanides except Eu and Yb form trivalent LnPd compounds.

The stability diagram for the surface valence states of the LnPd compounds was constructed in a completely analogous manner. The surface 4f binding energies were measured to be 1.5 eV in EuPd (Murgai et al. 1982) and 0.9 eV in YbPd (Domke et al. 1985). This implies generalized shifts of $1.5 - 0.9 = 0.6$ eV and $0.9 - 0.5 = 0.4$ eV for Eu and Yb, respectively, relative to the metallic $\Delta E_{II,III}$ values. These shifts now define the Fermi level ε_F^S for the surface 4f positions of the LnPd compounds (fig. 22). As a result of this analysis it can be seen that a divalent surface is predicted in SmPd. For the other LnPd compounds, however, trivalent surfaces will be found.

In a similar analysis, Laubschat et al. (1986) discussed the relative stabilities of the divalent and trivalent configurations of the $LnPd_3$ compounds. The difference is in this case that all the bulk compounds are trivalent. The analysis was therefore based on BIS results for $EuPd_3$ and $YbPd_3$ (Laubschat et al. 1984). In $EuPd_3$ the $4f^6 \rightarrow 4f^7$ transition has been located at 0.67(5) eV while the $4f^{13} \rightarrow 4f^{14}$ transition in $YbPd_3$ has an energy of 0.93(5) eV. This gives generalized shifts, $D\varepsilon^{comp}(\varepsilon_F \rightarrow f)$, of $0.67 + 0.9 = 1.6$ eV and $0.93 + 0.5 = 1.4$ eV for $EuPd_3$ and $YbPd_3$, respectively. Based on these shifts the Fermi level which corresponds to the bulk of the $LnPd_3$ compounds has been inserted in the stability diagram in fig. 23. This diagram shows clearly why all lanthanides form trivalent $LnPd_3$ compounds. The surface layers for $EuPd_3$ and $YbPd_3$, on the other hand, have been found to be divalent and a

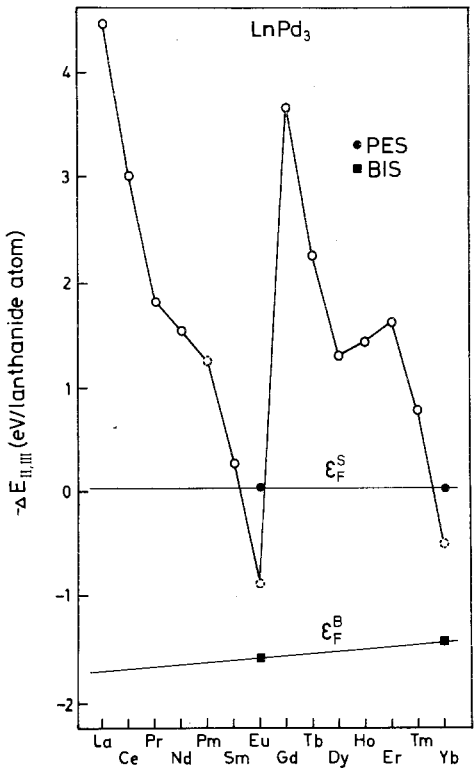

Fig. 23. Constructed stability diagram for the $LnPd_3$ compounds (after Laubschat et al. 1986). PES denotes photoelectron spectroscopy and BIS denotes bremsstrahlung isochromat spectroscopy. For further explanation, see the text.

discussion of the surface valence stability could consequently be based on photoemission measurements for these compounds. These energies are measured to be 0.93 eV for $EuPd_3$ (Murgai et al. 1982) and 0.53 eV for $YbPd_3$ (Domke et al. 1985), i.e. in both cases very close to the $\Delta E_{II,III}$ values themselves. From the so constructed stability diagram in fig. 23 it can be seen that in this series of compounds only Eu and Yb form divalent surfaces. $SmPd_3$ is predicted to be trivalent also at the surface, in contrast to the situation in Sm metal and SmPd. This prediction for $SmPd_3$ is supported by XPS measurements for the 3d core levels in $SmPd_3$ which show no sign of divalent Sm atoms (Hillebrecht and Fuggle 1982).

Using a combination of photoemission and BIS, Laubschat et al. (1986) furthermore obtained a coherent picture of the relative stabilities of the divalent and trivalent configurations in the bulk and at the surface of the lanthanide dialuminides. This is an interesting series of isostructural compounds where $EuAl_2$ is divalent, $YbAl_2$ mixed-valent and where the remaining compounds are trivalent. The stability diagram in fig. 24 was constructed from the measured bulk and surface 4f levels in divalent $EuAl_2$ and mixed valent $YbAl_2$. From this diagram it can be seen that all the other lanthanide dialuminides are trivalent in the bulk. It is, however, seen that a divalent surface state is predicted for $SmAl_2$. Such a surface valence transition has in fact also been observed for this compound (Laubschat et al. 1986).

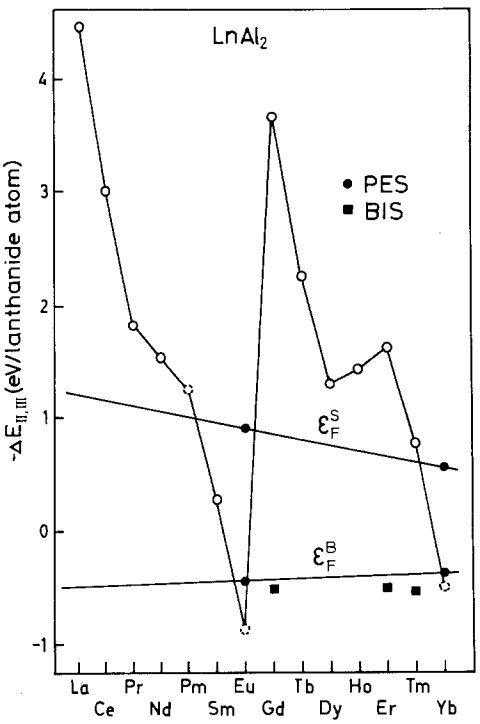

Fig. 24. Constructed stability diagram for the $LnAl_2$ compounds (after Laubschat et al. 1986). PES denotes photoelectron spectroscopy and BIS denotes bremsstrahlung isochromat spectroscopy. For further explanation, see the text.

For the trivalent $LnAl_2$ compounds similar information on $\Delta E_{II,III}^{comp}$ can, in accordance with eq. (34), be derived from BIS measurements. The BIS spectra for $GdAl_2$, $ErAl_2$ and $TmAl_2$ were therefore also investigated (see fig. 25). These measurements yield $\varepsilon^{comp}(\varepsilon_F \rightarrow f)$ transition energies of 4.2, 2.1 and 1.3 eV, respectively. These energies define additional points for the bulk Fermi level (ε_F^B in fig. 24). These points are marked by filled squares and it is interesting to note that they fall close to the ε_F^B line which was previously derived from the photoemission measurements for $EuAl_2$ and $YbAl_2$. This proves experimentally that for the $LnAl_2$ systems the measured XPS and BIS 4f positions closely correspond to the $\Delta E_{II,III}^{comp}$ stability energies.

Mårtensson et al. (1982b) investigated in the same way by photoemission the energy relationship between the divalent and trivalent configurations of the lanthanide monosulphides. The analysis was based on measured 4f positions for the divalent compounds SmS, EuS and YbS. The spectrum from YbS is shown in fig. 26 and reveals both bulk and surface-related 4f levels. Also in SmS a surface shift of the 4f spectrum could be resolved, while for EuS, the large number of closely spaced 4f-multiplet levels prevents a unique resolution of the bulk and surface emission features, which makes the determined EuS 4f energies somewhat less accurate.

The measured bulk 4f positions for the divalent compounds SmS, EuS, and YbS are 0.91 eV, 1.9(2) eV and 0.98 eV, respectively, which gives generalized shifts, $D\varepsilon^{comp}$, of 1.18 eV for SmS, 1.0 eV for EuS, and 0.48 eV for YbS. Using these shifts the

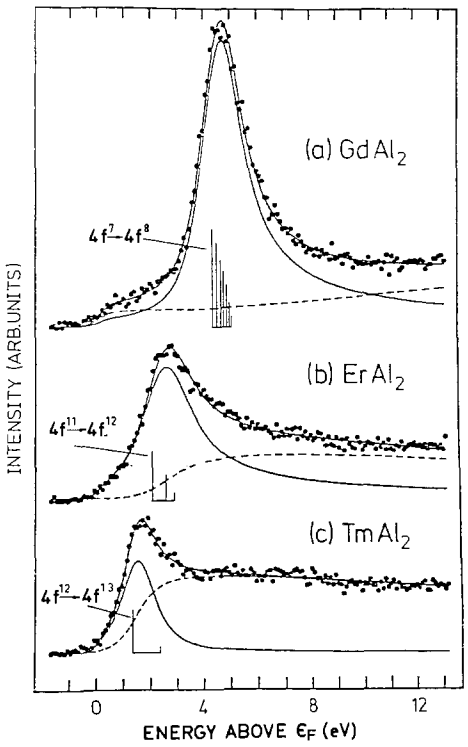

Fig. 25. Bremsstrahlung isochromat spectra (BIS) from the trivalent compounds $GdAl_2$, $ErAl_2$ and $TmAl_2$ (after Laubschat et al. 1986).

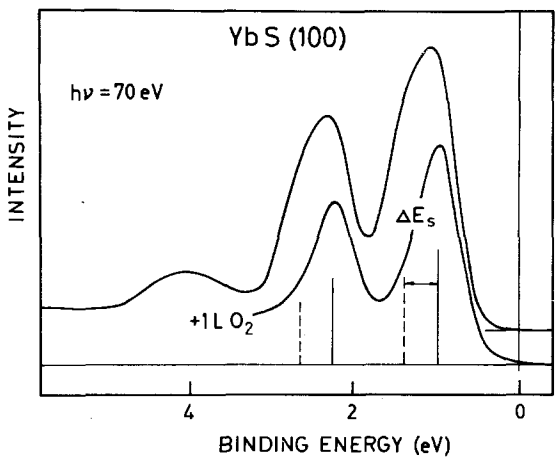

Fig. 26. Yb 4f photoelectron spectrum from a cleaved (100) surface of the divalent compound YbS. The spectrum shows both bulk (solid bars) and surface (broken bars) 4f levels. Oxygen exposure (one Langmuir) is seen to remove the characteristic surface feature. (After Mårtensson et al. 1982b.)

stability diagram in fig. 27 was constructed. From this diagram it is seen that all the other lanthanides give interpolated 4f positions on the trivalent side of the Fermi level. However, for TmS, an interpolated 4f position of only 0.2 eV above the Fermi level is obtained.

The Fermi level (ε_F^S) for the surface valence stabilities are obtained from the measured surface 4f positions in YbS, 1.4 eV and SmS 1.45 eV. For TmS we now find

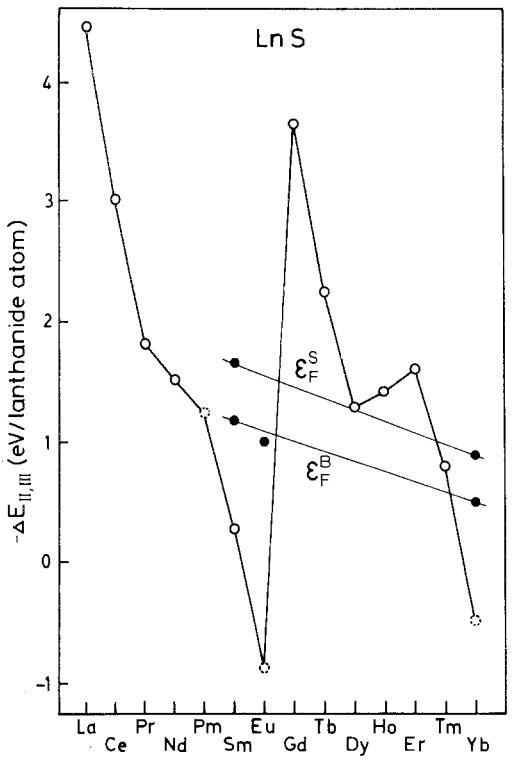

Fig. 27. Formally constructed stability diagram for the lanthanide monosulphides. The diagram is obtained from the Fermi level referenced data for the semiconducting compounds SmS, EuS and YbS (Mårtensson et al. 1982b). Complications due to the non-metallic character of the divalent monosulphides, as for instance incomplete screening, are discussed in the text.

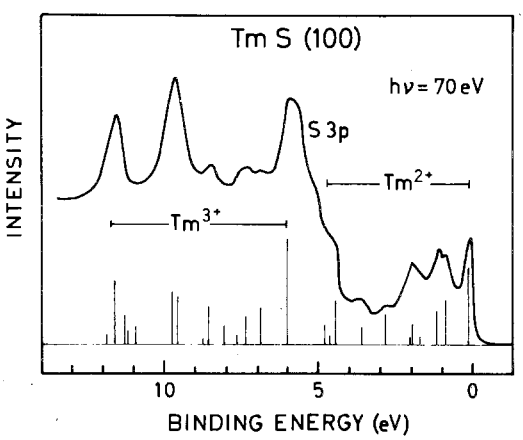

Fig. 28. Tm 4f photoelectron spectrum from a cleaved (100) surface of TmS. Both divalent and trivalent 4f features are seen in the spectrum. (After Mårtensson et al. 1982b.)

that a divalent surface is predicted. Divalent multiplets were also observed in the TmS spectrum (see fig. 28) and we can now conclude that the surface in TmS is divalent, but that the bulk is trivalent. This agrees well with the detailed analysis of the TmS spectrum performed by Kaindl et al. (1982b). We also note that the position of the lowest-lying multiplet line ($^3H_6$) in the Tm^{2+} spectrum is 0.15 eV in

good agreement with the interpolated value for the surface 4f position (0.19 eV). For DyS, the interpolated 4f position corresponds to a very small stability for the trivalent configuration. Also for this compound the UPS spectrum was recorded and no divalent signature was found.

In connection with the construction of the stability diagram for the lanthanide monosulphides in fig. 27, based on spectroscopically determined 4f positions, it should be pointed out that the divalent compounds used for the analysis are not metallic. Firstly, this might lead to experimental difficulties due to calibration problems. Secondly, the whole concept of comparing Fermi level referenced 4f binding energies to valence transition energies is based on the assumption of complete screening in the photoemission process in the sense that there is no energy associated with the hole left behind when providing the screening electron. This assumption is justified only for metals. It is therefore most interesting to note that the measured bulk and surface 4f energies for YbS are completely consistent with the observed bulk and surface valence states and 4f level positions of TmS, which is trivalent and therefore metallic. Although the surface of TmS is divalent and therefore non-metallic it seems most reasonable that it anyway experiences a complete screening, since this atomically thin surface layer sits on top of a metallic bulk. However, in the photoelectron spectrum for SmS a large binding energy of the 4f level relative to the Fermi level is found (Wertheim et al. 1978b, Brocksch et al. 1982), whereas it is known (for instance from pressure experiments) that $\Delta E_{II,III}^{SmS}$ must be very small. This shows that for SmS the spectroscopic 4f position is not directly related to the valence transition energy. (Therefore the diagram in fig. 27 should not be used as a stability diagram in the same way as for the previously discussed intermetallic compounds. This is also the reason why no extrapolation to the light lanthanides has been made in fig. 27).

Photoelectron spectroscopy has also been used to study the relative stabilities of the trivalent and tetravalent configurations of different lanthanide compounds. This is of particular interest in connection with discussions of the 4f properties in Ce systems. Mårtensson et al. (1982c) investigated in a systematic manner the photoemission spectra from NdSb, GdSb, ErSb and LuSb, in which compounds the Ln atoms all have a trivalent configuration. The spectra for ErSb and LuSb are shown in fig. 17 and they were recorded at a photon energy of 70 eV. At this energy the spectra are dominated by the lanthanide 4f contribution. The 4f emission features are sharp and no sign of a surface shift was observed. Considering the widths of the observed levels this implies that any surface shift must be small. The multiplet patterns are identical to the ones in the spectra from the pure metals, and the characteristic energy shifts between the antimonides and the elemental metals could be determined with high accuracy. These chemical shifts are summarized in fig. 29. It is clear that they fall close to a straight line with essentially a constant shift of about 1.1 eV throughout the lanthanide series. Additional chemical shifts can be obtained from early XPS measurements on the rare earth antimonides by Campagna et al. (1976). These spectra yield chemical shifts in the range 0.9–1.2 eV for another six trivalent antimonides, i.e., within the experimental errors they fall on the line drawn in fig. 29.

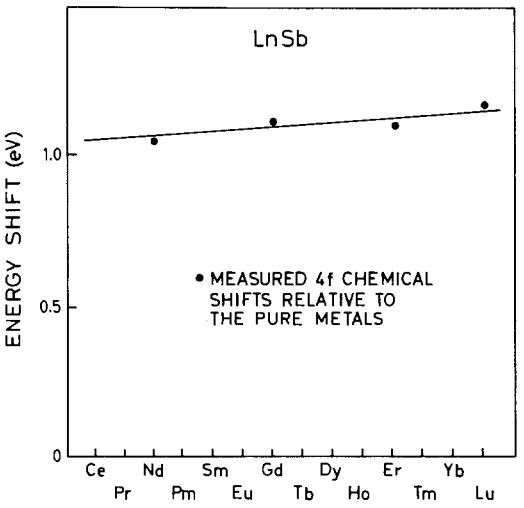

Fig. 29. Chemical shift of the 4f level in the lanthanide antimonides relative to the pure metals (Mårtensson et al. 1982c).

The observed regularity of the antimonide shifts was used to discuss the interpretation of the photoemission spectra of Ce metal and the Ce pnictides. A complication in the case of these Ce systems is that experimentally one observes *two* 4f related photoemission features. These two 4f signals were first observed by Franciosi et al. (1981) in spectra from Ce pnictides and shortly after by Mårtensson et al. (1982d) for $Ce_{0.9}Th_{0.1}$, and Wieliczka et al. (1982) for evaporated Ce films. The interpretation of these two features was controversial and it was proposed that the characteristic 4f chemical shifts could be used to add information on this problem (see also Freeman et al. chapter 65, this volume). One of the controversies concerned the identification of the $4f^0$ final state in the Ce spectra. This corresponds to a $4f^1 \rightarrow 4f^0$ process with 5d-screening in complete analogy with the 4f emission process in the heavier lanthanides. By extrapolation in fig. 29 Mårtensson et al. (1982c) obtained under these assumptions a shift of 1.0 eV between CeSb and Ce metal.

Figure 30 shows the photoemission spectrum of γ-$Ce_{0.9}Th_{0.1}$, recorded at $h\nu = 50$ eV (Mårtensson et al. 1982d). (The 10% Th is added to stabilize the FCC phase and has no significant influence on the Ce 4f spectrum.) The two 4f related features are clearly seen at this photon energy. The pnictide spectra (CeP, CeAs and CeBi) show the same type of two peak structure (Franciosi et al. 1981). The spectrum from CeSb was unfortunately not measured but since CeAs and CeBi show their two 4f features at practically identical positions (0.6 eV and 3.0–3.1 eV), the same positions will certainly be found in CeSb (As is located above and Bi below Sb in the Periodic Table). These anticipated 4f spectral positions for CeSb are marked by vertical bars in fig. 30. In the figure it is also indicated how these energy positions should be modified by the previously extrapolated antimonide chemical shift of 1.0 eV. From fig. 30 it is immediately clear that only the most bound features in Ce and CeSb are related by this energy shift. Therefore it is the 2 eV peak in γ-$Ce_{0.9}Th_{0.1}$ which shows the same characteristic displacement as shown above for

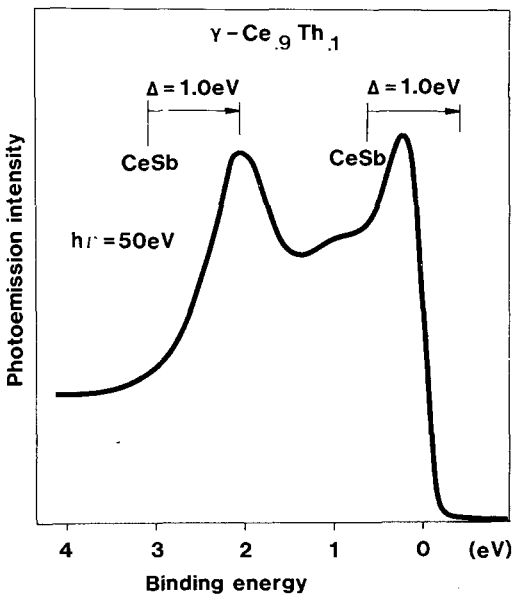

Fig. 30. Spectrum of γ-$Ce_{0.9}Th_{0.1}$, recorded at 50 eV photon energy (Mårtensson et al. 1982d). The energies of the 4f related features in CeSb (see text) are marked at 3.05 eV and 0.6 eV. The arrows show how these spectral features in CeSb should be displaced according to the extrapolated Ce 4f shift from fig. 29 (Mårtensson et al. 1982c).

the other lanthanide antimonides. Based on this regularity it was concluded that the 2 eV feature in γ-Ce (as well as the 3 eV feature in CeAs, CeSb and CeBi) corresponds to a process, which in analogy with the other lanthanides produces a d-screened $4f^0$ final-state configuration ($Ce(4f^1) \rightarrow Ce(4f^0)$ transition).

This approach was also used by Mårtensson et al. (1982c) to discuss the energy separation between the tetravalent and trivalent states of CeP. At 100 kbar CeP undergoes an isostructural phase transition with a large volume collapse of $\sim 8\%$. This transition was interpreted as due to a promotion of the 4f electron into the 5d conduction band (Jayaraman et al. 1976). Such an interpretation requires a relatively low value for the $\Delta E^{CeP}_{III,IV}$ transition energy. Previous XPS results for CeP identified a 4f peak at 0.4 eV and therefore seemed to provide strong support for the promotional model (Baer et al. 1978). However, Franciosi et al. (1981) showed that there is an additional 4f derived spectral feature at ~ 3 eV below ε_F in CeP. Before concluding anything about the valence transition in CeP it was therefore necessary to determine what spectral feature corresponds to the $4f^1(ds)^3 \rightarrow 4f^0(ds)^4$ transition. In this case it was possible to utilize the fact that Baer et al. (1978) measured the 4f binding energy in GdP to be 0.6 eV higher than in Gd metal. As discussed above the $4f^1 \rightarrow 4f^0$ process in γ-Ce requires an energy of about 2 eV. With the most reasonable assumption that the shifts in the phosphides show the same type of element dependence as the antimonides in fig. 29 it could be concluded that actually the 3 eV feature in the CeP spectrum corresponds to this process. With the close correspondence between the measured binding energy $\varepsilon^{comp}(f \rightarrow \varepsilon_F)$ and the valence change energy $\Delta E^{CeP}_{III,IV}$ it is clear that this identification of the 3 eV signal casts serious doubts on the interpretation that the pressure-induced phase transition in CeP corresponds to a 4f promotion. Instead it seems to suggest that the transition is

related to the γ–α transition in Ce metal, for which practically no change in the 4f count is observed.

Acknowledgment

The authors would like to express their gratitude to The Swedish Natural Science Research Council for partial support.

References

Allen, B.C., 1972, in: Liquid Metals Chemistry and Physics, ed. S.Z. Beer (Dekker, New York) p. 161.
Allen, J.W., L.I. Johansson, R.S. Bauer, I. Lindau and S.B.M. Hagström, 1978, Phys. Rev. Lett. **41**, 1499.
Allen, J.W., L.I. Johansson, I. Lindau and S.B.M. Hagström, 1980, Phys. Rev. B **21**, 1335.
Alvarado, S.F., M. Campagna and W. Gudat, 1980, J. Electron Spectrosc. & Relat. Phenom. **18**, 43.
Baer, Y., and G. Busch, 1974, J. Electron Spectrosc. & Relat. Phenom. **5**, 611.
Baer, Y., R. Hauger, Ch. Zürcher, M. Campagna and G.K. Wertheim, 1978, Phys. Rev. B **18**, 4433.
Beatham, N., P.A. Cox, A.F. Orchard and I.P. Grant, 1979, Chem. Phys. Lett. **63**, 69.
Brewer, L., 1971, J. Opt. Soc. Am. **61**, 1101.
Brewer, L., 1975, Rep. LBL-3720 (Lawrence Berkeley Laboratory, Berkeley).
Brocksch, H.-J., D. Tománek and K.H. Benneman, 1982, Valence Instabilities, eds P. Wachter and H. Boppart (North-Holland, Amsterdam) p. 291.
Brooks, M.S.S., H.L. Skriver and B. Johansson, 1984, Handbook on the Physics and Chemistry of the Actinides, Vol. 1, eds G.H. Lander and A.J. Freeman (North-Holland, Amsterdam) p. 153.
Campagna, M., G.K. Wertheim and E. Bucher, 1976, Structure and Bonding **30**, 99.
Campagna, M., G.K. Wertheim and Y. Baer, 1979, Top. Appl. Phys. **27**, 217.
Catalán, M.A., F. Rohrlich and A.G. Shenstone, 1954, Proc. R. Soc. London Ser. A **221**, 421.
Chorkendorff, I., J. Kofoed and J. Onsgaard, 1985a, Surf. Sci. **152/153**, 749.
Chorkendorff, I., J. Onsgaard, J. Schmidt-May and R. Nyholm, 1985b, Surf. Sci. **160**, 587.
Citrin, P.H., and G.K. Wertheim, 1983, Phys. Rev. B **27**, 3176.
Cox, P.A., 1975, Structure and Bonding **24**, 59.
de Boer, F.R., W.H. Dijkman, W.C.M. Mattens and A.R. Miedema, 1979, J. Less-Common Met. **64**, 241.
de Châtel, P.F., and F.R. de Boer, 1981, in: Valence Fluctuations in Solids, eds L.M. Falicov, W. Hanke and M.B. Maple (North-Holland, Amsterdam) p. 377.
Domke, M., C. Laubschat, E.V. Sampathkumaran, M. Prietsch, T. Mandel and G. Kaindl, 1985, Phys. Rev. B **32**, 8002.
Domke, M., C. Laubschat, M. Prietsch, T. Mandel, G. Kaindl and W.-D. Schneider, 1986, Phys. Rev. Lett. **56**, 1287.
Egelhoff Jr, W.F., 1983, Phys. Rev. Lett. **50**, 587.
Evans, R., 1974, J. Phys. C **7**, 2808.
Fäldt, Å., and H.P. Myers, 1984a, Phys. Rev. Lett. **52**, 1315.
Fäldt, Å., and H.P. Myers, 1984b, Phys. Rev. B **[illegible]**, 5481.
Falicov, L.M., W. Hanke and M.B. Maple, eds, 1981, in: Valence Fluctuations in Solids (North-Holland, Amsterdam).
Fisk, Z., H.R. Ott, T.M. Rice and J.L. Smith, 1986, Nature **320**, 124.
Franciosi, A., J.H. Weaver, N. Mårtensson and M. Croft, 1981, Phys. Rev. B **24**, 3651.
Franciosi, A., P. Perfetti, A.D. Katnani, J.H. Weaver and G. Margaritondo, 1984, Phys. Rev. B **29**, 5611.
Freeman, A.J., 1972, in: Magnetic Properties of the Rare Earth Metals, ed. R.J. Elliott (Plenum, New York) p. 245.
Fujimori, A., M. Grioni and J.H. Weaver, 1986, Phys. Rev. B **33**, 726.
Gerken, F., 1983, J. Phys. F **13**, 703.
Gerken, F., A.S. Flodström, J. Barth, L.I. Johansson and C. Kunz, 1985, Phys. Scr. **32**, 43.
Grioni, M., J.J. Joyce, S.A. Chambers, D.G. O'Neill, M. del Giudice and J.H. Weaver, 1984, Phys. Rev. Lett. **53**, 2331.
Grioni, M., J.J. Joyce and J.H. Weaver, 1985, Phys. Rev. B **32**, 962.
Gschneidner Jr, K.A., 1964, Solid State Phys. **16**, 275.
Gschneidner Jr, K.A., 1969, J. Less-Common Met. **17**,13.
Gschneidner Jr, K.A., 1980, Science and Technology of Rare Earth Materials, eds E.C. Subbarao and W.E. Wallace (Academic Press, New York) p. 51.

Gschneidner Jr, K.A., 1984, J. Less-Common Met. **100**, 1.
Habermann, C.E., and H.A. Daane, 1964, J. Chem. Phys. **41**, 2818.
Herbst, J.F., D.N. Lowy and R.E. Watson, 1972, Phys. Rev. B **6**, 1913.
Herbst, J.F., R.E. Watson and J.W. Wilkins, 1976, Phys. Rev. B **13**, 1439.
Herbst, J.F., R.E. Watson and J.W. Wilkins, 1978, Phys. Rev. B **17**, 3089.
Hillebrecht, F.U., and J.C. Fuggle, 1982, Phys. Rev. B **25**, 3550.
Himpsel, F.J., and B. Reihl, 1983, Phys. Rev. B **28**, 574.
Jayaraman, A., W. Lowe, L.D. Longinotti and E. Bucher, 1976, Phys. Rev. Lett. **36**, 366.
Johansson, B., 1974a, J. Phys. F, L169.
Johansson, B., 1974b, Philos. Mag. **30**, 469.
Johansson, B., 1977a, J. Phys. F **7**, 877.
Johansson, B., 1977b, in: Proc. 2nd Int. Conf. Electronic Structure of the Actinides, eds J. Mulak, W. Suski and R. Troć (Polish Academy of Science, Wroclaw) p. 49.
Johansson, B., 1978a, Inst. Phys. Conf. Ser. No. 37, ch. 3, p. 39.
Johansson, B., 1978b, J. Phys. & Chem. Solids **39**, 467.
Johansson, B., 1979, Phys. Rev. B **20**, 1315.
Johansson, B., 1984, Phys. Rev. B **30**, 3533.
Johansson, B., and N. Mårtensson, 1980, Phys. Rev. B **21**, 4427.
Johansson, B., and N. Mårtensson, 1983, Helv. Phys. Acta **56**, 405.
Johansson, B., and P. Munck, 1985, J. Less-Common Met. **100**, 49.
Johansson, B., and A. Rosengren, 1975a, Phys. Rev. B **11**, 1367.
Johansson, B., and A. Rosengren, 1975b, Phys. Rev. B **11**, 2836.
Johansson, B., and A. Rosengren, 1976, Phys. Rev. B **14**, 361.
Johansson, B., H. Ludvigsen and O. Keski-Rahkonen, 1983, Phys. Rev. B **28**, 3622.
Johansson, L.I., J.W. Allen and I. Lindau, 1981, Phys. Lett. A **86**, 442.
Johansson, L.I., A. Flodström, S.-E. Hörnström, B. Johansson, J. Barth and F. Gerken, 1982, Solid State Commun. **41**, 427.
Jørgensen, C.K., 1962, Mol. Phys. **5**, 271.
Kaindl, G., B. Reihl, D.E. Eastman, R.A. Pollak, N. Mårtensson, B. Barbara, T. Penney and T.S. Plaskett, 1982a, Solid State Commun. **41**, 157.
Kaindl, G., C. Laubschat, B. Reihl, R.A. Pollak, N. Mårtensson, F. Holtzberg and D.E. Eastman, 1982b, Phys. Rev. B **26**, 1713.
Kaindl, G., W.-D. Schneider, C. Laubschat, B. Reihl and N. Mårtensson, 1983, Surf. Sci. **126**, 105.
Kanski, J., and P.O. Nilsson, 1981, J. Phys. F **11**, 1859.
Lang, J.K., and Y. Baer, 1979, Solid State Commun. **31**, 945.
Lang, J.K., Y. Baer and P.A. Cox, 1981, J. Phys. F **11**, 121.
Laubschat, C., 1984, Ph.D. thesis, Freie Universität Berlin, unpublished.
Laubschat, C., G. Kaindl, E.V. Sampathkumaran and W.-D. Schneider, 1984, Solid State Commun. **49**, 339.
Laubschat, C., G. Kaindl, W.-D. Schneider, B. Reihl and N. Mårtensson, 1986, Phys. Rev. B **33**, 6675.
Lee, P.A., T.M. Rice, J.W. Serene, L.J. Sham and J.W. Wilkins, 1986, Comments Cond. Matter Phys. **12**, 99.
Lübcke, M., B. Sonntag, W. Niemann and P. Rabe, 1986, Phys. Rev. B **34**, 5184.
Lucas, A.A., 1973, in: Collective Properties of Physical Systems, eds B. Lundqvist, S. Lundqvist and V. Runnström-Reio (Academic Press, New York) p. 169.
Mårtensson, N., B. Reihl, W.-D. Schneider, V. Murgai, L.C. Gupta and R.D. Parks, 1982a, Phys. Rev. B **25**, 1446.
Mårtensson, N., B. Reihl, R.A. Pollak, F. Holtzberg and G. Kaindl, 1982b, Phys. Rev. B **25**, 6522.
Mårtensson, N., B. Reihl and F. Holtzberg, 1982c, in: Valence Instabilities, eds P. Wachter and H. Boppart (North-Holland, Amsterdam) p. 303.
Mårtensson, N., B. Reihl and R.D. Parks, 1982d, Solid State Commun. **41**, 573.
Mårtensson, N., B. Reihl, R.A. Pollak, F. Holtzberg, G. Kaindl and D.E. Eastman, 1982e, Phys. Rev. B **26**, 648.
Mårtensson, N., P. Hedegård and B. Johansson, 1984a, Phys. Scr. **29**, 154.
Mårtensson, N., R. Nyholm and B. Johansson, 1984b, Phys. Rev. B **30**, 2245.
Mårtensson, N., F.U. Hillebrecht and D.D. Sarma, 1985, Surf. Sci. **152/153**, 733.
Mårtensson, N., B. Johansson and J.R. Naegele, 1987, Phys. Rev. B **35**, 1437.
Martin, W.C., 1972, Opt. Pura & Apl. **5**, 181.
Martin, W.C., L. Hagan, J. Reader and J. Sugar, 1974, J. Phys. Chem. Ref. Data **3**, 771.
Martin, W.C., R. Zalubas and L. Hagan, 1978, Atomic Energy Levels – The Rare-Earth Elements, Natl. Bur. Stand., Ref. Data Ser. **60**, U.S. GPO, Washington D.C.
Miedema, A.R., 1976, J. Less-Common Met. **46**, 67.
Müller-Hartmann, E., B. Roden and D. Wohlleben, 1985, Proc. Int. Conf. Valence Fluctuations (North-Holland, Amsterdam).
Murgai, V., L.C. Gupta, R.D. Parks, N. Mårtensson and B. Reihl, 1982, in: Valence Instabilities, eds P. Wachter and H. Boppart (North-Holland, Amsterdam) p. 299.
Naegele, J.R., L. Manes, J.C. Spirlet and W. Müller, 1984, Phys. Rev. Lett. **52**, 1834.
Netzer, F.P., and J.A.D. Matthew, 1986, Rep. Prog. Phys. **49**, 1986.
Nilsson, A., N. Mårtensson, J. Hedman, B. Eriksson, R. Bergman and U. Gelius, 1985, Surf. Sci, **162**, 51.

Noé, M., and J.R. Peterson, 1976, in: Transplutonium Elements, eds W. Müller and R. Lindner (North-Holland, Amsterdam) p. 69.
Nugent, L.J., J.L. Burnett and L.R. Morss, 1973, J. Chem. Thermodyn. **5**, 665.
Nyholm, R., and J. Schmidt-May, 1984, J. Phys. C **17**, L113.
Nyholm, R., I. Chorkendorff and J. Schmidt-May, 1984, Surf. Sci. **143**, 177.
Parks, R.D., 1977, Valence Instabilities and Related Narrow-Band Phenomena (Plenum Press, New York).
Parks, R.D., N. Mårtensson and B. Reihl, 1982, in: Valence Instabilities, eds P. Wachter and H. Boppart (North-Holland, Amsterdam) p. 239.
Platau, A., and S.E. Karlsson, 1978, Phys. Rev. **18**, 3820.
Racah, G., 1954, Bull. Res. Com. Isr. **3**, 290.
Reihl, B., F. Holtzberg, R.A. Pollak, G. Hollinger, G. Kaindl and N. Mårtensson, 1982, in: Valence Instabilities, eds P. Wachter and H. Boppart (North-Holland, Amsterdam) p. 287.
Rosengren, A., and B. Johansson, 1976, Phys. Rev. B **13**, 1468.
Rosengren, A., and B. Johansson, 1981, Phys. Rev. B **23**, 3852.
Rosengren, A., and B. Johansson, 1982, Phys. Rev. B **26**, 3068.
Rossi, G., J. Nogami, I. Lindau, L. Braicovich, I. Abbati, U. del Perrnino and S. Nannarone, 1983, J. Vac. Sci. & Technol. A **1**, 781.
Rossi, G., J. Nogami, I. Lindau and J.J. Yeh, 1985, Surf. Sci. **152/153**, 1247.
Schneider, W.-D., C. Laubschat and B. Reihl, 1983a, Phys. Rev. B **27**, 6538.
Schneider, W.-D., C. Laubschat, G. Kalkowski, J. Haase and A. Puschmann, 1983b, Phys. Rev. B **28**, 2017.
Skapski, A.S., 1948, J. Chem. Phys. **16**, 389.
Skapski, A.S., 1956, Acta Metall. **4**, 576.
Skriver, H.L., 1983, in: Systematics and the Properties of the Lanthanides, ed. S.P. Sinha (Reidel, Dordrecht) p. 213.
Spanjaard, D., C. Guillot, M.C. Desjonquères, G. Tréglia and J. Lecante, 1985, Surf. Sci. Rep. **5**, 1.
Spector, N., and J. Sugar, 1976, J. Opt. Soc. Am. **66**, 436.
Steglich, F., J. Aarts, C.B. Bredl, W. Lieke, D. Meschede, W. Franz and H. Schäfer, 1979, Phys. Rev. Lett. **43**, 1892.
Steiner, P., and S. Hüfner, 1981a, Solid State Commun. **37**, 79.
Steiner, P., and S. Hüfner, 1981b, Solid State Commun. **37**, 279.
Steiner, P., S. Hüfner, N. Mårtensson and B. Johansson, 1981, Solid State Commun. **37**, 73.
Strasser, G., E. Bertel, J.A.D. Matthew and F.P. Netzer, 1982, in: Valence Instabilities, eds P. Wachter and H. Boppart (North-Holland, Amsterdam) p. 169.
Tran Minh Duc, C. Guillot, Y. Lassailly, J. Leconte, Y. Jugnet and J.C. Vedrine, 1979, Phys. Rev. Lett. **43**, 789.
van der Sluis, K.L., and L.J. Nugent, 1972, Phys. Rev. A **6**, 86.
van der Sluis, K.L., and L.J. Nugent, 1974, J. Opt. Soc. Am. **64**, 687.
Wachter, P., and H. Boppart, eds, 1982, Valence Instabilities (North-Holland, Amsterdam).
Ward, J.W., P.D. Kleinschmidt and R.G. Haire, 1979, J. Phys. (France) C **4**, 233.
Wertheim, G.K., 1986, Appl. Phys. A **41**, 75.
Wertheim, G.K., and M. Campagna, 1977, Chem. Phys. Lett. **47**, 182.
Wertheim, G.K., and G. Crecelius, 1978, Phys. Rev. Lett. **40**, 813.
Wertheim, G.K., J.H. Wernick and G. Crecelius, 1978a, Phys. Rev. B **18**, 875.
Wertheim, G.K., I. Nowik and M. Campagna, 1978b, Z. Phys. B **29**, 193.
Wieliczka, D., J.H. Weaver, D.W. Lynch and C.G. Olson, 1982, Phys. Rev. B **26**, 7056.
Worden, E.F., and J.G. Conway, 1970, J. Opt. Soc. Am. **60**, 1144.
Zangwill, A., 1984, (private communication).

Handbook on the Physics and Chemistry of Rare Earths, Vol. 10
edited by K.A. Gschneidner, Jr., L. Eyring and S. Hüfner

Chapter 70

BREMSSTRAHLUNG ISOCHROMAT SPECTROSCOPY OF ALLOYS AND MIXED VALENT COMPOUNDS

F.U. HILLEBRECHT*
Institut für Festkörperforschung der KFA Jülich, D-5170 Jülich, Fed. Rep. Germany

M. CAMPAGNA
Institut für Festkörperforschung der KFA Jülich, D-5170 Jülich, Fed. Rep. Germany

and

II. Physikalisches Institut der Universität zu Köln, 5000 Köln 41, Fed. Rep. Germany

Contents

List of symbols

BIS	bremsstrahlung isochromat spectroscopy
Δ	average hybridization between 4f and extended states
Δ_-	first ionization energy of $4f^n$ state
Δ_+	electron affinity of $4f^n$ state
DOS	density of states
E_F	Fermi energy
m_{eff}	electronic specific heat coefficient
n_f	average 4f occupancy, or f-count
σ	cross section for photoemission in BIS
U	average Coulomb correlation energy between two 4f electrons
XPS	X-ray photoemission spectroscopy
Z	nuclear charge

*Present address: Max-Planck Institut für Festkörperforschung, 7000 Stuttgart 80, Fed. Rep. Germany

1. Introduction

Because of the large Coulomb and exchange interaction the 4f electrons largely retain their atomic nature even in solids. This large correlation energy U which plays a central role in the physics of the lanthanides, ensures that the 4f electrons are usually localized, and that fluctuations of the type $2f^n \rightarrow f^{n+1} + f^{n-1}$ do not occur. As far as is presently known, except for the Ce compounds, lanthanides where despite the large U two different f-configurations are present in the ground state (Campagna et al. 1976) – the so-called homogeneously mixed valent compounds – are known to exhibit in X-ray 4f photoemission spectra multiplets of *two* final states with relative amplitudes closely related to the mixing amplitudes of the two initial-state configurations. U can then be experimentally determined directly from the energy separation between the centroids of these two multiplets (Campagna et al. 1974); its magnitude has been found to be in agreement with early theoretical predictions (Herbst et al. 1972). U can also be determined in the case of stable, f^n-configuration compounds (Lang et al. 1979b, 1981). In such a case one uses photons to excite an electron from the 4f level to the continuum, so that in photoemission one measures the ionization energy Δ_- of the $4f^n$ state. Inversely, to obtain the affinity energy Δ_+ of the $4f^{n+1}$ state one can irradiate with electrons the same solid, so that a transition $4f^n \rightarrow 4f^{n+1}$ may take place and hence $U = \Delta_- + \Delta_+$. This is the idea of the inverse photoemission experiment: the sample is irradiated with electrons and one detects the emitted photons. The technique of keeping the photon energy fixed in the soft X-ray regime while scanning the energy of the incident electrons is called *bremsstrahlung isochromat spectroscopy*, abbreviated BIS. The energy of the emitted photon is given by the kinetic energy of the incoming electrons, increased by the work function of the spectrometer minus the energy of the final state. In a metal the valence band is cut by the Fermi level E_F, and the photons with the highest energy are those emitted when the incident electrons make transitions into states immediately above E_F. For metallic systems one has therefore a good reference in the energy scale because E_F appears as a sharp cut-off in the spectrum. The transition probability is given by the product of the appropriate matrix element and the density of final states. For incident electron energies of $\sim$1500 eV, variations of the density of *initial* states can be neglected. Also the *matrix element* for initial and *final* states located in the energy up to 20 eV above E_F is not expected to change due to a change of the initial state in BIS. Consequently, the probability for emission of a photon is largely determined by the density of final states, weighted by a transition probability (see fig. 1). The first experimental spectra of the unoccupied states of La and Ce metals obtained in this way were published by Liefeld et al. (1974) and Chamberlain et al. (1974). In fig. 2 we show a typical example of combined XPS–BIS data for Gd, allowing easily the identification of the f-related structure and hence the determination of U, which is 10.5 eV for Gd (Lang et al. 1981).

In many compounds, especially intermetallic compounds with 4d or 5d elements the photoemission cross section for the ligand states is comparable or even higher than the 4f cross section. Lanthanides do not form many intermetallic compounds with transition metals having nearly empty d-bands ('early' transition metals). In

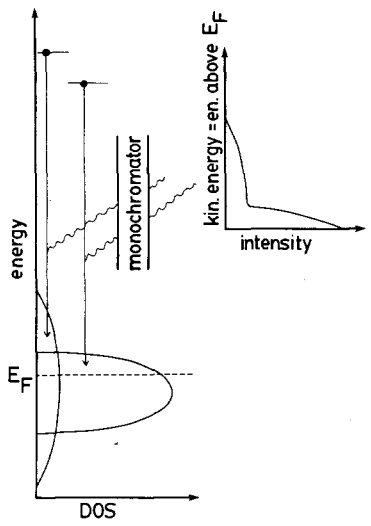

Fig. 1. Probing the unoccupied states by bremsstrahlung isochromat spectroscopy (BIS). The number of emitted photons is proportional to the density of final states (DOS) weighted by a transition matrix element.

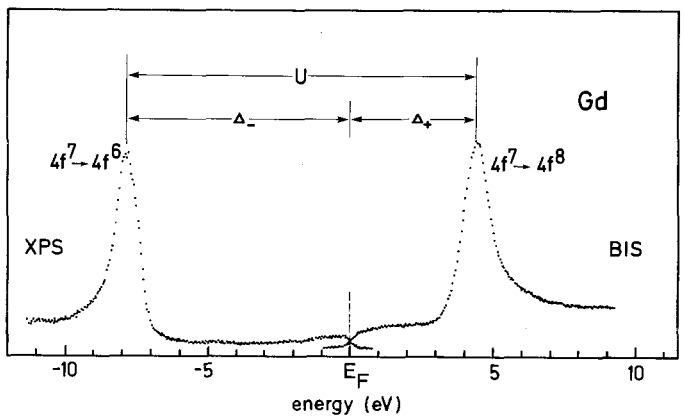

Fig. 2. XPS and BIS spectra of GD (Lang et al. 1981). The sum of the 4f ionization potential Δ and the 4f electron affinity Δ_+ is equal to the 4f intrashell Coulomb correlation energy U.

contrast, when the d-band is substantially filled ('late' transition metals), the contribution of these empty states to the BIS spectrum above E_F is obviously small. We recall that in these cases resonant photoemission spectroscopy with synchrotron radiation at high resolution is the most appropriate technique for studying such occupied states. BIS will in contrast easily allow the identification of the empty f-states.

In summary the questions to be answered by studying the unoccupied states of integral and mixed-valent lanthanide compounds by BIS concern:

(i) magnitude of the 4f Coulomb correlation energy U and its variation upon compound formation;

(ii) changes of the electronic structure and especially of the f-signature due to f–d or f–p hybridization upon transition to mixed-valent or heavy-fermion behaviour;

comparison with f-counts, n_f, known from other experiments as well as with results of single-particle and many-body theories.

2. Inverse photoemission in the soft X-ray regime

2.1. *The technique*

The spectrometers presently used for BIS are combined instruments originally built for X-ray photoemission spectroscopy (XPS). For high-resolution XPS Johann-type crystal monochromators equipped with quartz single crystals are widely used. The best resolution achieved is about 0.25 eV (Gelius et al. 1984), however 0.5 to 0.7 eV is more common. Any XPS instrument equipped with a monochromator can readily be modified to perform BIS. One has to add an electron gun to the measuring chamber, and to introduce a detector at the entrance slit of the monochromator, which acts as the exit slit in BIS. Figure 8 of chapter 63 (this volume) shows schematically the apparatus built in Jülich (Fuggle et al. 1979, Hillebrecht 1983c). The electron gun is a Pierce-type gun, designed to yield a well-defined beam while operating in the space-charge limit. The apparatus of Lang and Baer (1979a) is equipped with a spherical Pierce gun producing a circular spot, whereas the design of Hillebrecht (1987) uses a cylindrical gun producing an elongated spot, matched to the imaging properties of the multicrystal Johann-type monochromator (see fig. 8 of chapter 63). The detector consists of a photocathode (CsI) and a channeltron, which detects the low-energy secondary electrons ejected from the photocathode by the X-ray photons. To obtain a small energetic spread of the electron beam, a BaO dispenser cathode is used which yields a sufficient current at 1000°C operating temperature and a thermal broadening of less than 200 meV.

The *probing depth* of the BIS experiment is about the same as for XPS of valence levels. The limiting factor is the electron mean-free-path of the incident electrons, which at 1500 eV is 20 to 30 Å. This is why the BIS experiment is more bulk sensitive than inverse photoemission in the UV regime. However, as in XPS, it is still extremely important to maintain atomically clean sample surfaces which can be monitored by scanning the O and C (ls) core lines in the XPS mode. The high flux of electrons needed in the BIS experiment can create a problem when measuring reactive materials such as the lanthanides since a portion of the electrons will be reflected from the sample, impinge on the walls of the vacuum vessel and lead to desorption. A procedure useful in this case is irradiation of the sample until outgassing of both sample and vacuum vessel are negligible. The changes seen in the BIS spectra due to oxidation are clearly discernible, and in many cases the degree of sample cleanliness can be inferred from the BIS spectrum without having to change to the XPS mode. As an example we present in fig. 3 a series of BIS spectra of La with increasing contamination by the residual gas in the measuring chamber (1×10^{-10} Torr) over a period of 10 h. The BIS $4f^1$ final state, which is located at 5.4 eV above E_F in La, broadens upon oxidation on the high-energy side. This is caused by the appearance of a $4f^1$ final state shifted to higher energy by 1.6 eV with

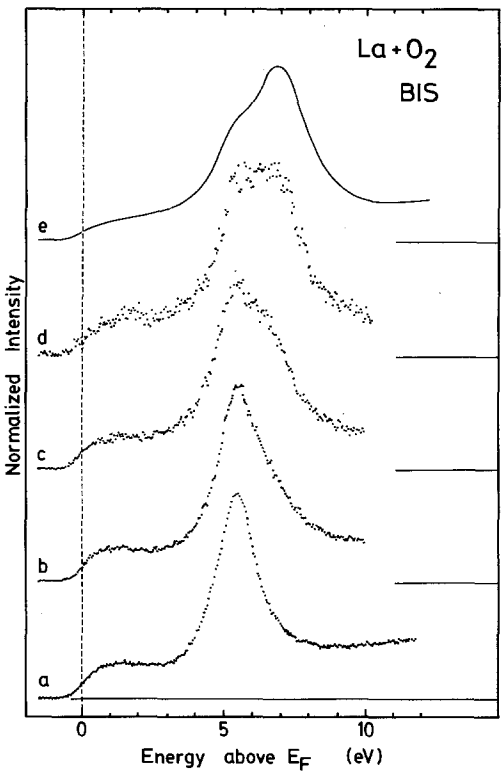

Fig. 3. Oxygen contamination of lanthanide surfaces causes a shift of the BIS 4f derived signal. Sample cleanliness can often be assessed without the use of XPS. Spectrum (e) corresponds to approximately one monolayer exposure of O_2.

respect to E_F. At the same time the relative intensity of the underlying 5d-states decreases. We see in fig. 3 the effect of approximately 1 monolayer of oxygen: although O interacts primarily with the 5d6s electron states of La, the BIS 4f derived feature is seen to be a very sensitive indicator of the presence of oxygen (or of other contaminants).

2.2. *Cross sections for photoemission and inverse photoemission*

Inverse photoemission is the time-reversed process of the photoemission process. The cross section for inverse photoemission is a strong function of the kinetic energy of the incoming electrons in an analogous way as the photoemission cross section depends on photon energy. Calculations show that the Au 4f/5d ratio of the photoemission cross section increases by 5 orders of magnitude between 25 and 500 eV final-state energy (Manson and Cooper 1968, Manson 1978). The experimentally determined variation of such ratio is not quite as big, but still a significant effect. In fig. 4 inverse photoemission spectra of Gd are shown for different initial-state energies, i.e., different kinetic energies of the incoming electrons (Fauster and Himpsel 1984, Lang et al. 1981). At 28 eV the 4f structure located at 4.3 eV above E_F has a size comparable to features originating from critical points in the one-electron band structure of noble metals (van der Marel et al. 1984). At 1487 eV the 4f/5d ratio

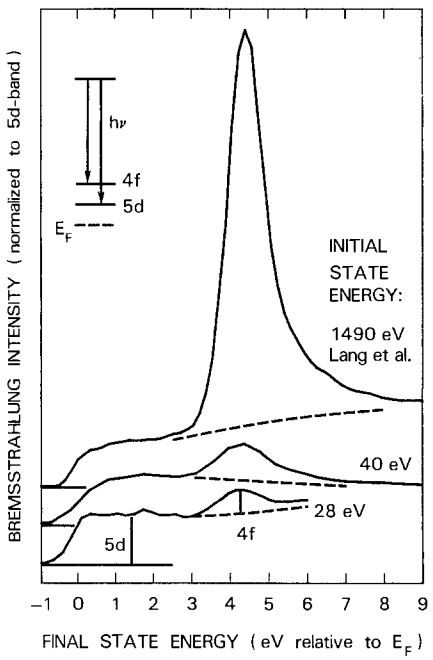

Fig. 4. In Gd the 4f BIS cross section increases dramatically with respect to the 5d/6s cross section for incident electron energies from 20 up to 1490 eV (Fauster and Himpsel 1984, Lang et al. 1981).

is about 20. This confirms that a photon energy of 1487 eV is very favourable for observing the 4f states of most of the lanthanides and their compounds.

Next we consider the 4f cross-section variation through the lanthanide series in BIS, in analogy to the 4f photoionization as calculated by Scofield (1976). As can be seen from fig. 5, σ scales linearly with the atomic number Z for Ce, Pr and Nd, making a linear extrapolation to La meaningful. The rise in the cross section with Z is caused by the lanthanide contraction, resulting in a higher amplitude of the 4f wavefunction in the vicinity of the nucleus. From La through Gd, this rise exceeds the loss due to the increasing occupation of the 4f states. For Tm, with only one or two 4f holes, the total σ is of comparable size as for La with 14 holes!

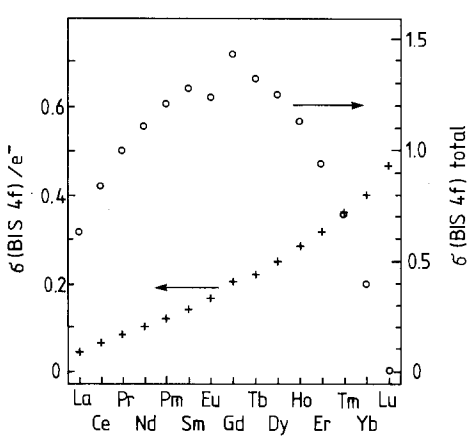

Fig. 5. Cross section for the 4f shell in BIS, normalized to the Cls XPS cross section (Scofield 1976). Crosses represent the cross section per electron state (left scale), circles the total cross section (right scale). For the total cross sections of Tm and Yb metals trivalent configurations have been assumed; for divalent configurations the total cross sections for Tm^{2+} and Yb^{2+} are 0.35 and 0, respectively.

3. BIS spectra of the lanthanide metals and compounds with stable 4f configurations

3.1. *Lanthanide metals*

Lang et al. (1981) have studied all the lanthanide metals by XPS and BIS. Their results have been discussed in chapter 62 of this book, so that we refer the reader to this chapter for the original data. As in core photoionization of metals also in BIS involving 4f levels the final state must be viewed as (anti-)screened (neutrality within the Wigner–Seitz cell). (Anti-)screening can be reached via conduction electron (hole) states. An indication of the width of the 5d6s conduction states can be inferred from self-consistent calculations, which give a 5d width of about 8 to 10 eV (Pickett et al. 1980, 1981, Glötzel and Podloucky 1980) or from BIS data for Yb metal, see fig. 15.

3.2. *La compounds*

Figure 6 shows the occupied and empty valence states of a series of ordered La–Ni compounds (Hillebrecht et al. 1984). Ni d-band filling increases with La concentration, as seen from the drop of intensity at E_F, indicating a reduced total density of states (DOS) near E_F. Also the decreased intensity of the well-known 6eV two-hole final state (Hüfner and Wertheim 1975, Fuggle et al. 1983) as well as the disappearance of the core-hole satellite structure (Hillebrecht et al. 1983a) are signs of d-band filling. The BIS $4f^1$ final state is seen superimposed on a background signal due to La 5d6sp states. The Pauling electronegativities of Ni and La are 1.8 and 1.1, indicating a possible charge transfer from La to Ni. This would naively imply a somewhat more positive La in the compounds leading to an increased 4f binding energy, in contrast to the observations.

Band-structure calculations for Ln–Ni_5 compounds by Malik et al. (1982) indicate that the DOS at E_F is only reduced by 20% from the original value for Ni. This seemed to be confirmed by values of the coefficient of the electronic specific heat (Takeshita et al. 1980). Figure 7 shows a more detailed comparison of $LaNi_5$ XPS–BIS data with a calculation by Cabus (1983). The small unoccupied part of the Ni d-band at E_F is not seen in the spectra, primarily because of the low instrumental resolution of 0.7 eV. In contrast we note also that the calculated DOS shows a split-off peak at 1.8eV above E_F, mainly of La 5d character, in accordance with experiment.

3.3. *Lanthanide–Pd_3 compounds*

A number of lanthanide compounds with Pd, Sn, and In crystallize in the Cu_3Au structure. These compounds have been extensively studied because most of them are fairly easy to prepare by congruent solidification from the melt, sometimes even as single crystals. In addition the simple structure makes it possible to perform self-consistent band-structure calculations (König 1983). In fig. 8 XPS and BIS data are shown for YPd_3 (Hillebrecht et al. 1983b). Again the reduced intensity at E_F

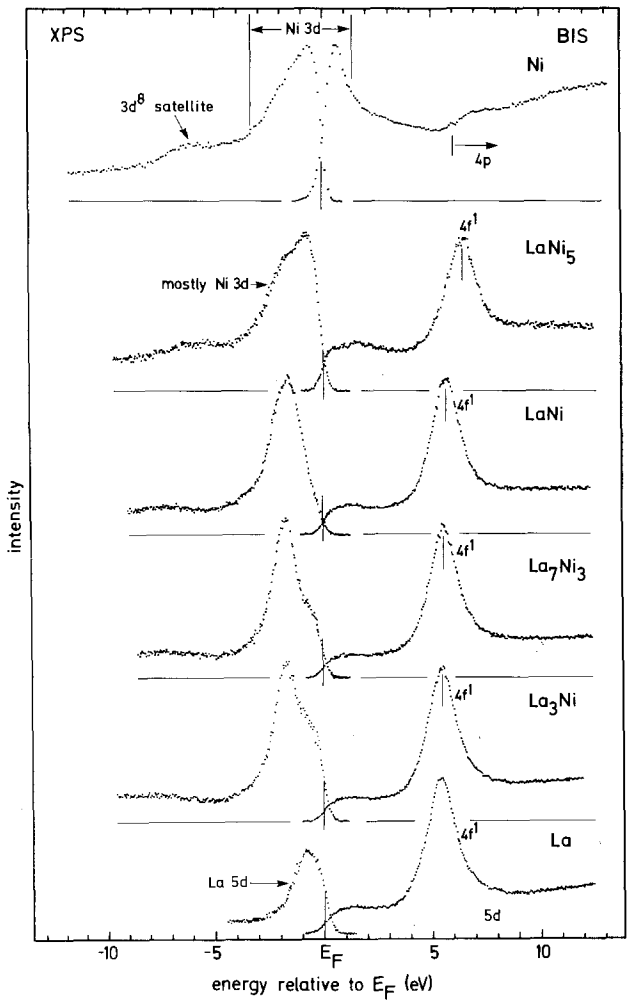

Fig. 6. Occupied and unoccupied states of La, Ni and La–Ni intermetallic compounds as seen by XPS/BIS. There is no evidence of the empty part of the Ni 3d band in the compounds. The XPS and BIS data have been normalized to constant peak height (except for La).

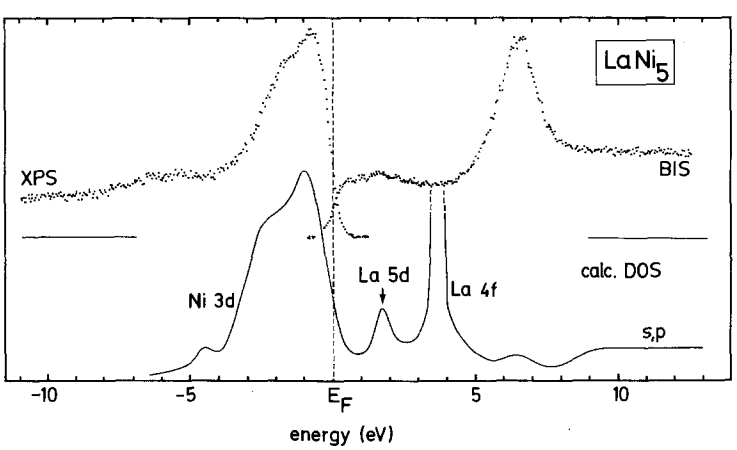

Fig. 7. Comparison of a calculated density of states (DOS) (Cabus 1983) and the experimental result for $LaNi_5$. Although the Ni d-band is cut by E_F, the BIS spectrum does not show a peak at E_F. The structure at 1.8eV is a split-off d-band state (Hillebrecht et al. 1983b). The position of the f-states is calculated significantly lower (3.8eV) than found in experiment (6.5eV).

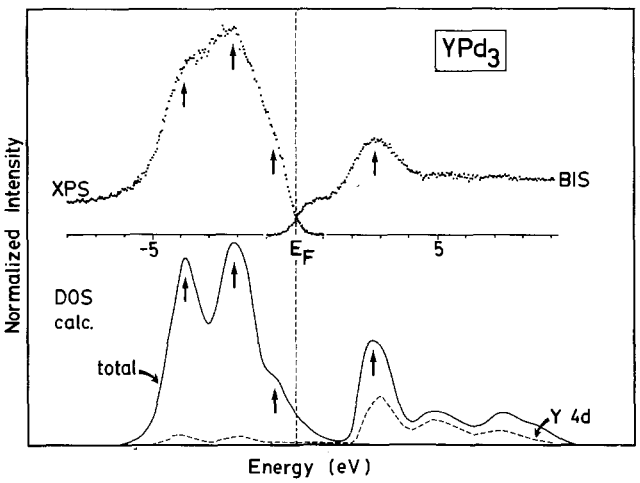

Fig. 8. Experimental and calculated valence states of YPd_3 (König 1983, Hillebrecht et al. 1983b). The structure at 2.8eV is mostly due to Y 4d states.

compared to Pd metals is a sign of filling of the Pd d-band, which extends down to 5eV below E_F. Above E_F, the BIS spectrum of YPd_3 shows a peak at 2.8eV, superimposed on an otherwise structureless spectrum, a quite different empty DOS from the one of metallic Y (Speier et al. 1984). The XPS/BIS data for YPd_3 are in good agreement with the results of the calculations.

In fig. 9 the BIS spectra of several Ln–Pd_3 compounds are shown, where the split-off d-band state is visible in the range 2.8 to 3eV above E_F. These results indicate that compound formation can lead to new structures in the density of states making the 4f derived feature somewhat more difficult to be identified.

4. BIS spectra of compounds with fluctuating 4f configuration

4.1. *Sm, Eu, Tm and Yb compounds*

We have seen in chapter 63 of this book that when *surface effects* are taken into account the determination of the f-count with so-called low-energy probes (e.g. lattice constant, susceptibility, Mössbauer, etc.) for mixed-valent compounds of Sm, Eu, Tm and Yb is in reasonable agreement with determinations of n_f from XPS or XAS data.

In fig. 10 we show a BIS spectrum for divalent, semiconducting SmS (Oh and Allen 1984). The BIS spectrum of divalent Sm should be analogous to that of trivalent Eu ($4f^5$ initial-state configuration). The agreement with calculated $f^5 \rightarrow f^6$ multiplet spectra is however poor, and more work is needed to establish experimentally whether all the features seen in the spectrum are 4f related. Oxidation yields Sm_2O_3 (trivalent Sm). The shape of the BIS spectrum of oxidized SmS is again only in fair agreement with that of trivalent Sm metal.

As an example for a Eu intermetallic compound we show in fig. 11 the occupied and unoccupied valence states for $EuPd_3$ (Mårtensson et al. 1985). Small structures

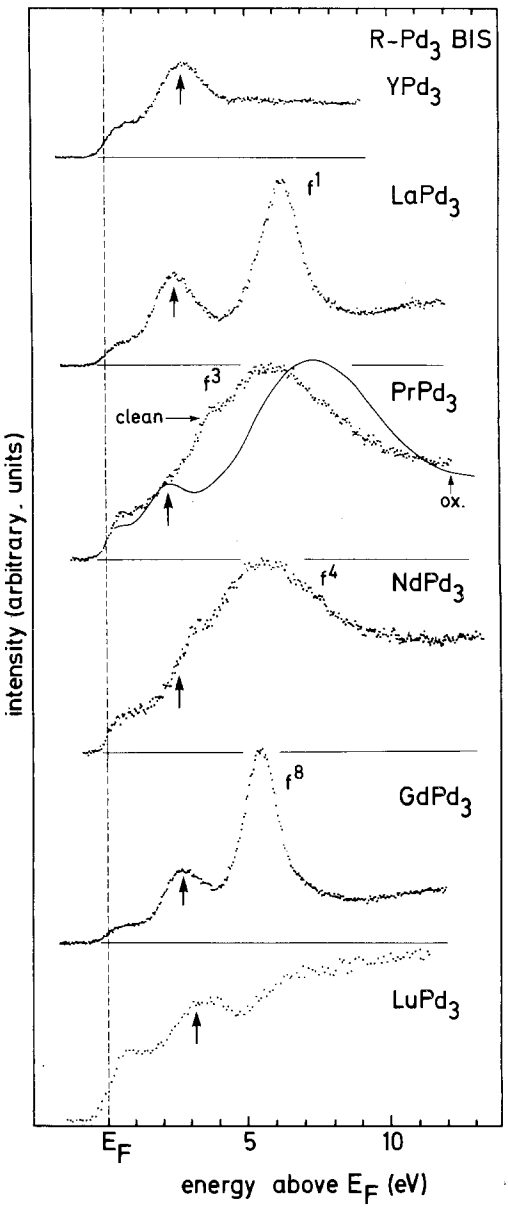

Fig. 9. BIS spectra for some lanthanide–Pd_3 compounds, showing the split-off d-band state (see arrow). Contamination by residual gases in the spectrometer shifts and broadens the 4f-state by about 2 eV in RPd_3 and the d-band state becomes visible (see full line, $PrPd_3$). Data for $LuPd_3$ are from Laubschat et al. (1984).

below E_F, which can be identified by comparison to $LaPd_3$ or by resonant photoemission, are due to Eu 4f states as indicated. Several 4f related structures are more clearly seen above E_F, besides the peak at 2.5 eV due to a split-off d-band state. The f^8 final-state assignment can be made because exposure to a small dose of oxygen reduces the divalent contribution in both the XPS core level spectra as well as the peak at 10.5 eV in the BIS spectrum as shown in fig. 12. A similar surface effect as for $EuPd_3$ is observed in trivalent $EuNi_5$, see fig. 13. The divalent

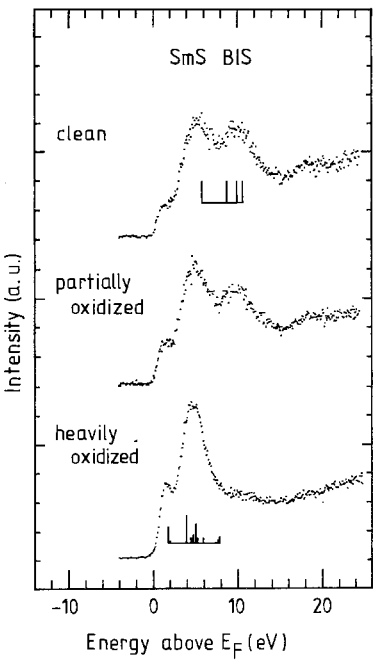

Fig. 10. BIS spectra for semiconducting SmS which, upon oxidation, forms a trivalent Sm oxide, Sm_2O_3 (Oh and Allen 1984).

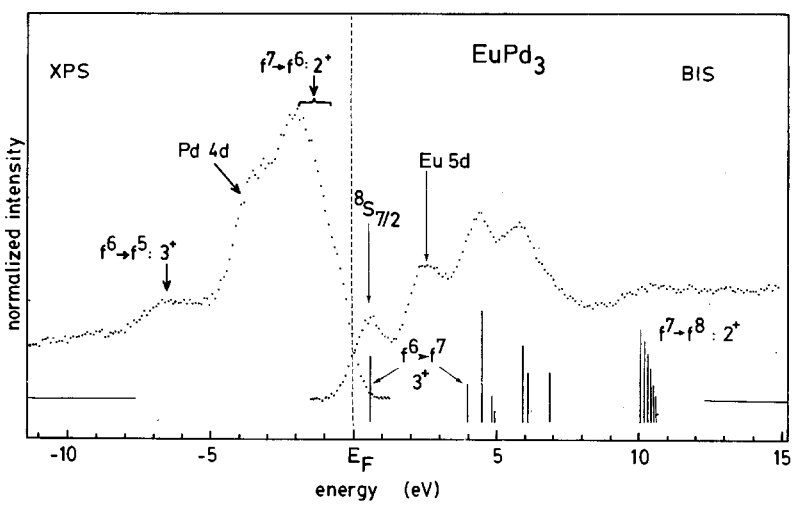

Fig. 11. XPS–BIS data for $EuPd_3$ (Mårtensson et al. 1985).

contribution also appears at 10.5 eV, as for $EuPd_3$, but has more intensity. This again scales with the related intensities in the photoemission spectra.

The valence changes in $EuPd_2Si_2$ or $EuCu_2Si_2$ upon temperature have not yet been studied by BIS and remain an interesting topic for future investigation.

In fig. 14 the results of Oh and Allen (1984) for TmSe are shown. The BIS structure around 4 eV, peak B, is also found in YS and is attributed to s–d

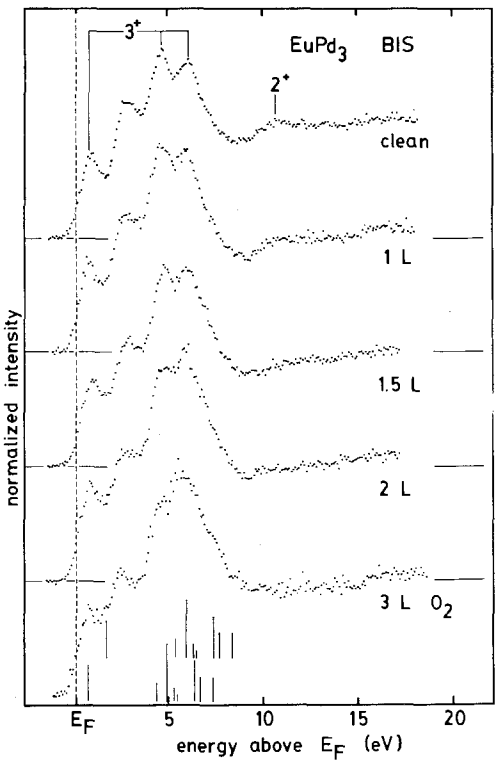

Fig. 12. Effect of oxygen exposure on the XPS/BIS data of $EuPd_3$, indicating the quenching of the f^8 final-state signal.

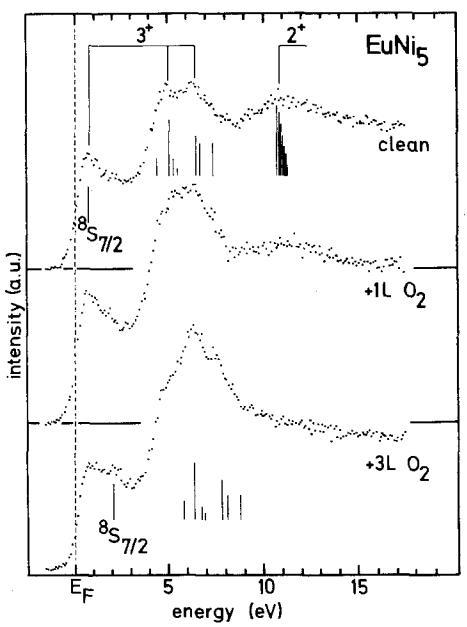

Fig. 13. BIS of trivalent $EuNi_5$, showing a strong (~30%) divalent signal due to a surface valence transition (Mårtensson et al. 1985).

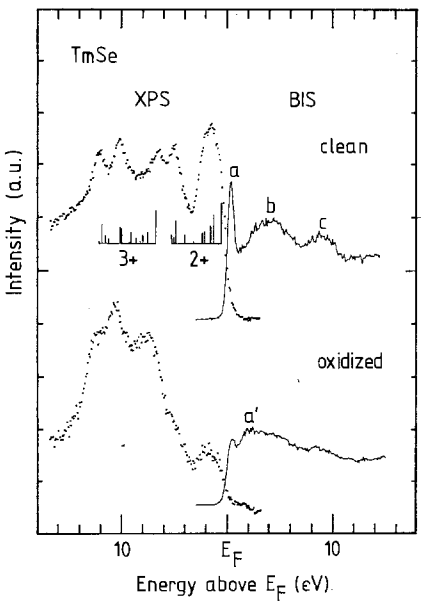

Fig. 14. XPS and BIS of homogeneously mixed valent TmSe (Oh and Allen 1984). Oxidation quenches the 2^+ contribution both in XPS and BIS.

conduction states. The peaks A and C are then associated with f^{12} to f^{13} and f^{13} to f^{14} transitions.

In fig. 15 BIS data are shown for Yb and some Yb compounds. $(Yb_{1-x}Y_x)CuAl$ is a mixed-valent compound (Mattens et al. 1979), and one finds the $4f^{14}$ final state in the BIS spectrum practically *pinned at* E_F in contrast to trivalent to $YbRh_{2.5}$ and $YbPd_3$ (Laubschat et al. 1984), where the f^{14} final state is distinctly *above* E_F.

So far the only BIS study of a valence change with temperature has been performed on $YbAl_2$ by Oh et al. (1985). At 80 K, Yb is divalent in this material, but the valency increases to about 2.5 as the temperature is raised to 800 K, as deduced from systematics of lattice constant and magnetic susceptibility. We recall that the changes (Oh et al. 1985) observed in XPS are consistent with a change of valence upon temperature. The BIS spectra of $YbAl_2$ shown in fig. 16 indicate qualitatively a similar behaviour, i.e., an increase of the $4f^{14}$ final state which is a measure of the valency with temperature.

4.2. *The novel view of the Ce 4f level width*

Ce intermetallic compounds, in which the local moment of the 4f electron is quenched and in which the volume of the Ce ion is similar to that of γ (α)-Ce are called γ (α)-type materials (e.g. $CePd_3$). The first published BIS spectrum of an α-type material was the spectrum of $CePd_3$, by Baer et al. (1981) shown in fig. 17. Also shown are data for γ-Ce and for the heavy-fermion compounds $CeAl_3$ and $CeSn_3$. In these spectra the $4f^2$ final state can be easily identified because it appears with similar energy and shape as in γ-Ce. The BIS spectrum of $CePd_3$ also contains a $4f^2$ signature, shifted however from E_F by about 1.1 eV compared to γ-Ce. In addition it shows two more peaks at 0.45 and 2.25 eV. The peak at 0.45 eV above E_F, whose

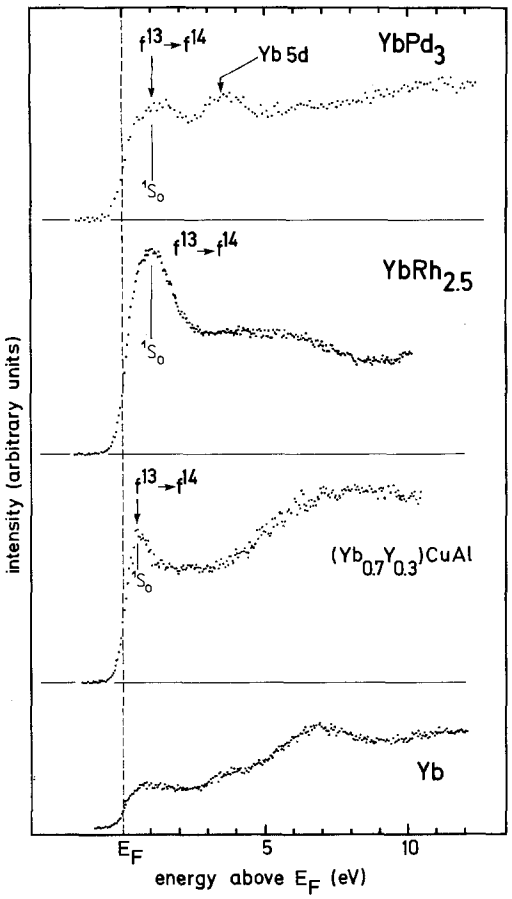

Fig. 15. BIS of Yb and Yb intermetallic compounds. Note the occurrence of a $4f^{14}$ signal at or just above E_F, indicating a $4f^{13}$ configuration in the initial state. For mixed-valent YbYCuAl, the peak is pinned at E_F. For $YbRh_{2.5}$ and $YbPd_3$ the peak is removed from E_F, indicating a trivalent ($4f^{13}$) ground state. (Data for $YbPd_3$ from Laubschat et al. (1984); for Yb from Lang et al. (1981).)

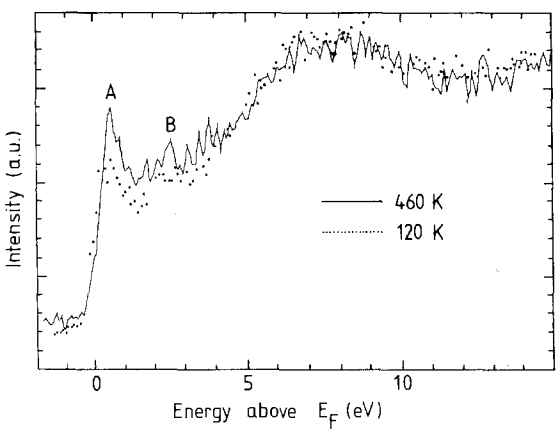

Fig. 16. BIS of $YbAl_2$ at 460 and 120 K (Oh et al. 1985). At low temperatures peak A, due to a $4f^{13} \rightarrow 4f^{14}$ transition, is smaller than at higher temperatures, indicating a valence change upon temperature.

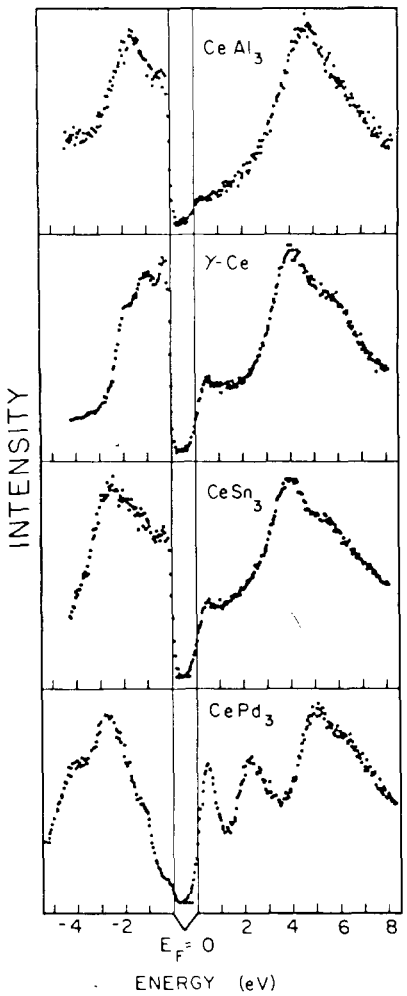

Fig. 17. BIS and XPS data for γ-Ce and Ce intermetallics (Baer et al. 1981).

position can only be determined within the experimental resolution, was assigned to a $4f^1$ final state. The peak at 2.25 eV is due to a split-off d-state, as discussed in section 3.3 (Hillebrecht et al. 1983b).

In figs. 18 through 25 we show a collection of systematic XPS–BIS data of Ce compounds (Hillebrecht et al. 1984). Details are given in the figure captions. Data for γ- and α-Ce (fig. 25) and $CePd_3$ are also compared with calculations in figs. 26 and 27. The valence band data confirm the introductory remark concerning the difficulty of detecting 4f-related features of Ce in XPS spectra. This is especially true when they are energetically located in the d-band region of the ligand (see figs. 18, 20 and 23). Only the use of resonant photoemission with synchrotron radiation allows the 4f features to be identified (see figs. 22 and 24). In contrast BIS at high energy is very suitable for this purpose. The empty 4f-states can easily be identified because of their characteristic spectral shape, see figs. 18, 20 and 21. We see in figs.

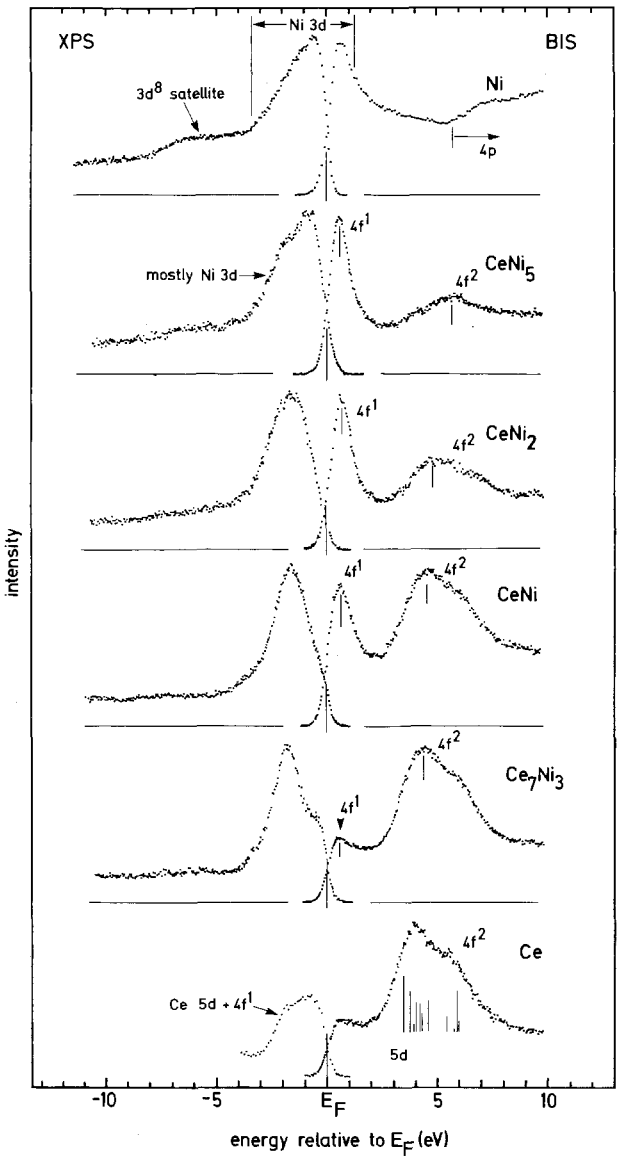

Fig. 18. XPS and BIS spectra of Ce–Ni intermetallic compounds; also shown for comparison are data for the metals. Comparison to La–Ni compounds (fig. 6) shows that the peak located at E_F in the BIS spectra of Ce–Ni compounds is entirely due to a $4f^1$ final state. XPS and BIS are independently normalized.

18 or 20 that the transition to a nonmagnetic Ce ground state in $CeNi_5$ or $CePd_3$ starting from γ-Ce is accompanied by the appearance of a $4f^1$ final state pinned at E_F, a clear indication of a transition to a strong mixing of the type $(5d6s)^3 4f^1 \longleftrightarrow (5d6s)^4 4f^0$ in the ground state. The experimental demonstration that the peak at E_F in the mixed valent cases is 4f related is best illustrated in fig. 19: the $4f^1$ final state disappears upon oxidation and the $4f^2$ broadens and loses its characteristic multiplet structure. It can be seen that the Coulomb correlation U is essentially unchanged for magnetic and nonmagnetic compounds since the $4f^2$ final state is

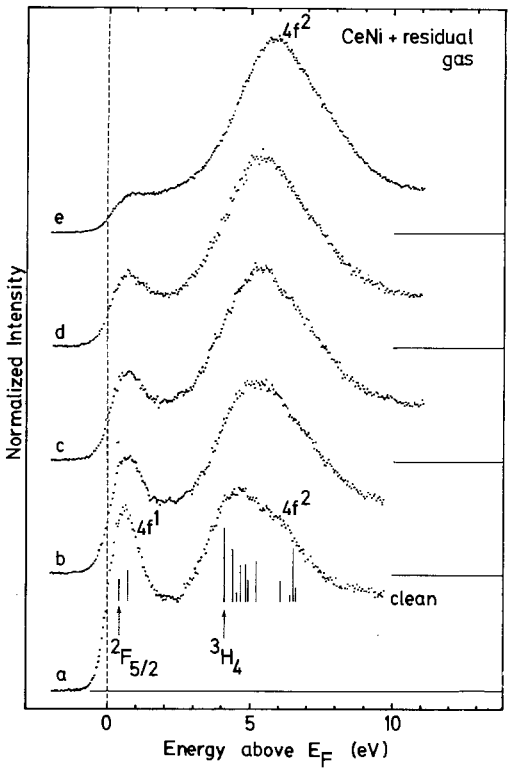

Fig. 19. Influence of residual gases in the spectrometer chamber on the CeNi BIS spectrum. Spectrum (e) corresponds to maximum oxygen dose of 12L (IL = 10^{-6} Torr s).

always 4 to 5 eV above E_F, while the f^1 state is below or at E_F. The large U value makes a single-particle band structure approach inappropriate for describing the physics of both γ- and α-type Ce materials, see figs. 24. 25 and 26.

According to the above findings we see that the BIS spectra of Ce intermetallic compounds can be classified in two groups: those exhibiting only a $4f^2$ final state and characterizing materials having γ-like behaviour, and those characterizing the α-like materials whose spectra show a pronounced $4f^1$ final state pinned at E_F.

In table 1 the relative $4f^1$ intensities are given, together with some other numerical results from the BIS spectra. For comparison also f-counts derived from XPS as well as from low-energy experiments are indicated. The apparent discrepancies between intensities of f^0-related structures, $I(f^0)$, which in the simplest picture yield the f-occupancy $n_f = [1 - I(f^0)]$, obtained with different high-energy spectroscopies show unambiguously that *dynamical* effects caused by measuring process influence the intensity distribution over the various final states. This is a consequence of the hybridization Δ between 4f and band states, which determines spectral features in both 'high-' and 'low-energy' experiments. The weights in the spectra can only be explained by a value of the hybridization Δ significantly larger than the traditionally accepted order of magnitude of 10 meV. This finding can be considered as the main contribution of spectroscopic studies towards a quantitative understanding of the properties of Ce compounds.

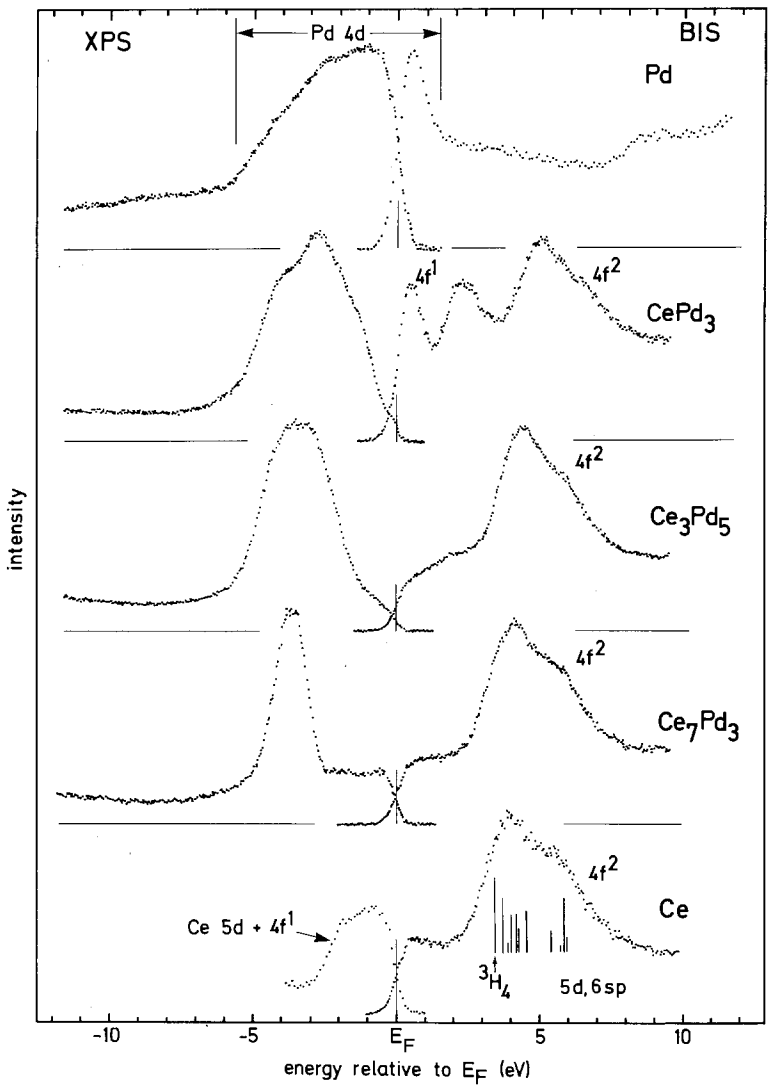

Fig. 20. XPS–BIS data for Ce–Pd compounds. XPS and BIS spectra are independently normalized.

4.3. *Comparison with model calculations*

Gunnarsson and Schönhammer (1983a,b,c, 1985a,b; see also chapter 64 in this volume) proposed a description of Ce spectroscopic data in terms of an Anderson impurity model, which allows to extract the crucial parameters, i.e., the 4f conduction band hybridization Δ and the 4f occupancy n_f from spectroscopic data. The *justification* for using a single-impurity Anderson Hamiltonian comes from spectroscopic data like the BIS data discussed here or photoemission and absorption data discussed in other chapters of this book. The fact that Δ increases, e.g., for Ce–Ni

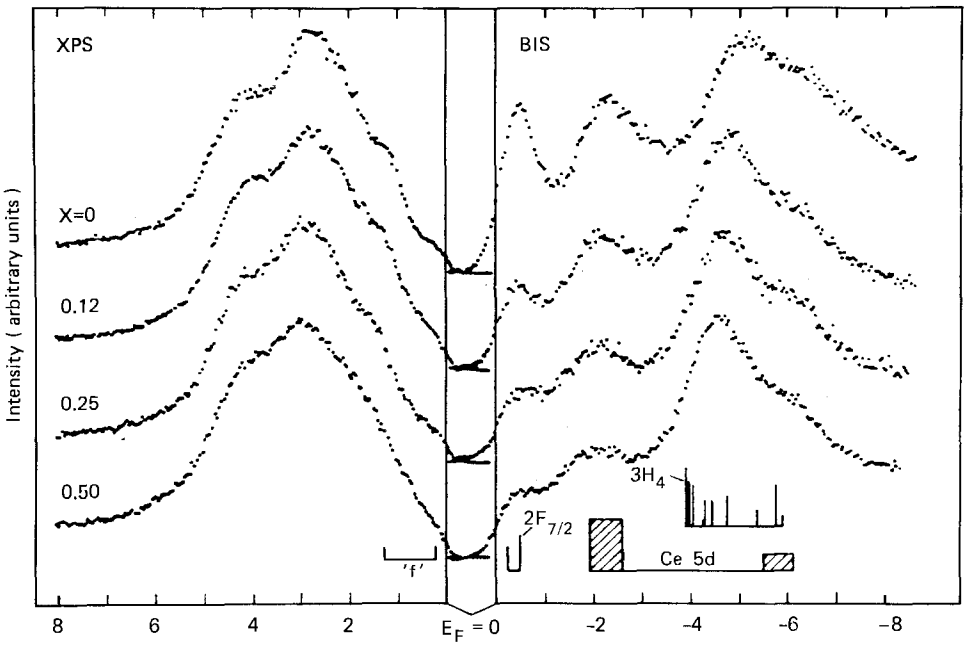

Fig. 21. XPS and BIS data for $CePd_3$ with increasing amounts of B dissolved in the lattice (Wuilloud et al. 1984b).

compounds with increasing Ni content and increasing Ce–Ce separation shows that direct 4f overlap is *not* the driving mechanism for the 4f charge fluctuation. In fig. 28 a set of BIS spectra for fixed $\Delta = 120$ meV and ground state f-occupancies as parameter are shown. The calculation shows a $4f^1$ final state at E_F whose intensity is significantly *larger* than the ground state $4f^0$ contribution. In analogy to the XPS case the comparison with experimental spectra allows one to determine n_f and provides a kind of internal self-consistency check for the model calculation. Indeed one set of values of the parameters Δ, n_f, and U gives a reasonable description of both XPS and BIS data for a given material. When the multiplet structure and spin–orbit coupling is included the agreement with experiment is further improved, see fig. 29 for the cases of $CeRu_2$ and $CeNi_2$. The mixing width Δ, used as a parameter in the calculation, is largely responsible for the variation of the $4f^1$-amplitude in the spectrum for *constant* ground-state occupation of the f^0- and f^1-configurations, see fig. 30. The transfer of spectral weight upon variation of Δ is a nice illustration of the influence of dynamical effects on spectroscopic properties of Ce systems.

4.4. *Initial-state hybridization and final-state screening, heavy-fermion systems*

The excitement about many Ce and U compounds came about because of their unusual physical behaviour due to 'heavy electrons' as originally found by Andres et al. (1975) and Steglich et al. (1979). As we mentioned in chapter 63, core-level

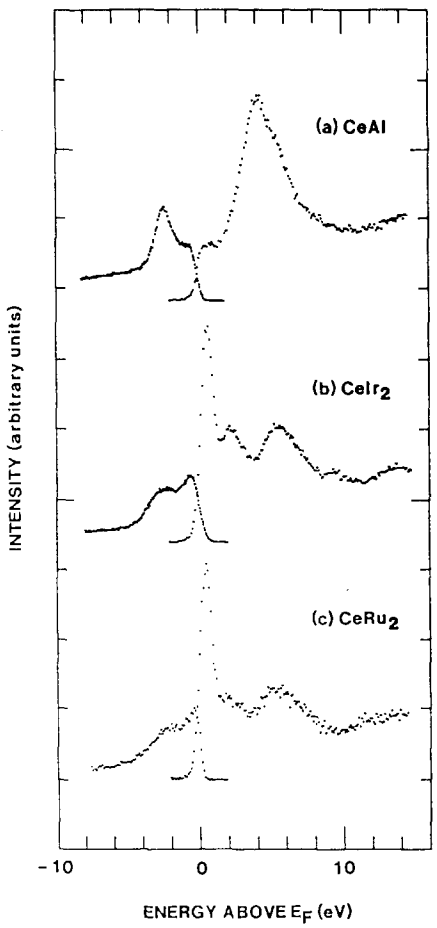

Fig. 22. UPS and BIS data for CeAl, $CeIr_2$, and $CeRu_2$ (Allen et al. 1983). The data for the occupied states have been obtained by resonant photoemission using 122 eV photons.

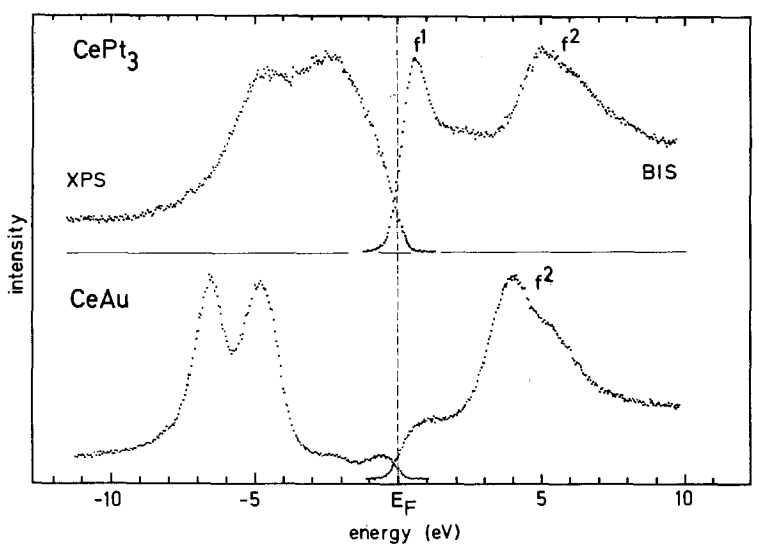

Fig. 23. XPS/BIS data for $CePt_3$ and CeAu.

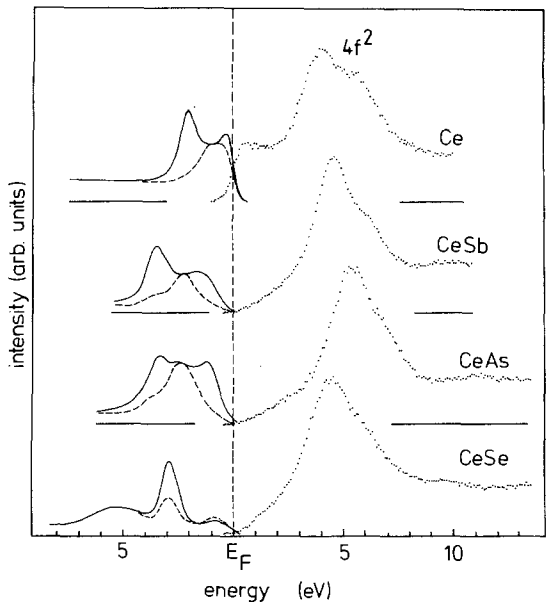

Fig. 24. Resonant photoemission and BIS spectra of γ-Ce, CeSb, CeAs, and CeSe (Gudat et al. 1982a,b, Hillebrecht et al. 1985).

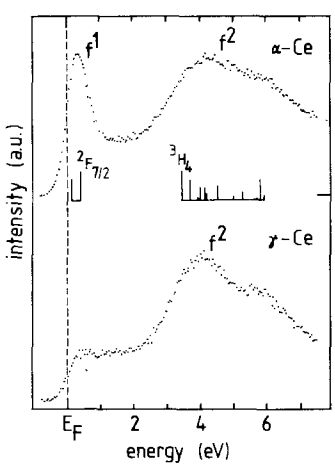

Fig. 25. BIS spectra for γ- and α-Ce (Wuilloud et al. 1983). The α-phase was prepared by evaporation onto a substrate held at low temperature (80 K).

spectroscopy had to be extended to an investigation of the unoccupied states by BIS in order to obtain a confirmation of the role of empty states in determining core-level lineshapes as suggested, e.g., by Fuggle et al. (1980). We conclude the review of experimental data by comparing XPS/BIS data of strongly mixed valent, non-magnetic $CeCo_2$ (superconducting, below $T_C = 1$ K) and the heavy-fermion compound $CeCu_6$ (fig. 31), as well as insulating CeO_2, mixed valent CeN and heavy fermion $CeSi_2$ (Yashima et al. 1982) (fig. 32). These data confirm the universal features of the mixed-valence problem in Ce systems, of which the heavy-fermion aspect is just one special case. In the cases of strong mixed valence the f^1 spectral feature in photoemission is clearly seen by XPS only in CeN and $CeSi_2$; the use of resonant photoemission allows its observation in the presence of transition metal ligands, e.g. in $CeCo_2$.

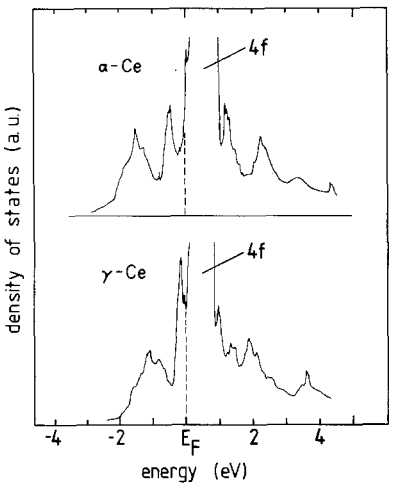

Fig. 26. Calculated density of states for γ- and α-Ce (Pickett et al. 1981).

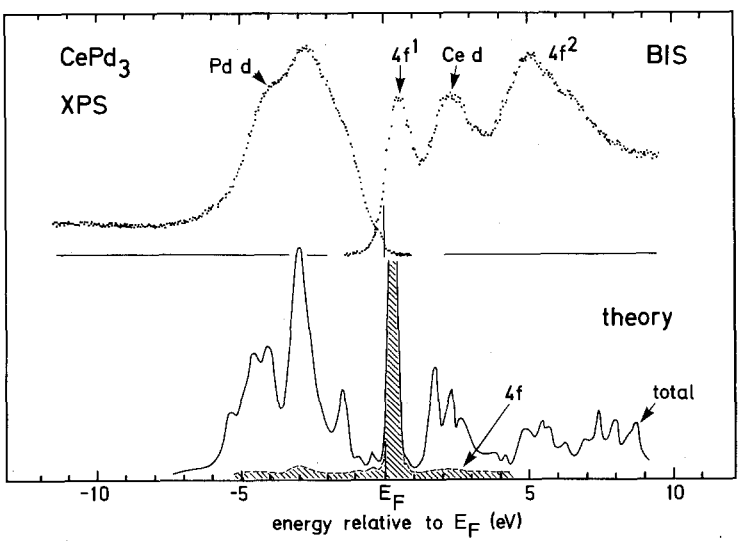

Fig. 27. Experimental and calculated valence band density of states for $CePd_3$ (Ackermann 1984).

The absence of f-related features *at* E_F in XPS and BIS in *insulating* compounds, e.g. CeO_2, see fig. 32, is a nice illustration of the role of initial-state hybridization of 4f levels in determining final-state spectral features, especially in core-level photoemission and X-ray absorption spectroscopy.

5. Summary and outlook

The study of the unoccupied states of lanthanides and their compounds by Bremsstrahlung Isochromat Spectroscopy has been used only fairly recently in

TABLE 1

Fraction of $4f^0$ related features normalized to total intensity from different spectroscopic experiments. Also given is a crude characterization of the magnetic behaviour, as well as $4f^0$ amplitudes obtained from low-energy experiments; the 4f-occupancy n_f is given by $n_f = 1 - f^0$. Abbreviations are: P = Pauli paramagnetic; F = ferromagnetic; C – W = Curie–Weiss behaviour; N = nonlinear susceptibility over the entire temperature range studied.

	Magnetic behaviour	f^0 (%) low-E exp.	XAS	f^0 (%) XPS	BIS
γ-Ce	C–W	5	2	–	2–7
α-Ce	P	67		5	22
$CeAl_3$				–	–
$CeCo_2$	P			10	66–52
$CeCo_5$	F			7	61–56
Ce_7Ni_3	C–W			–	3–13
CeNi	P	30		2	21–22
$CeNi_2$	N		11	6	44–42
$CeNi_5$	C–W		8	12	62–54
$CeCu_6$				–	–
$CeRu_2$				12	64–52
Ce_7Pd_3				–	–
Ce_3Pd_5			–	–	–
$CePd_3$	N		6	5	29
$CeSn_3$	C–W	14	–	–	2–7
$CePt_3$				10	21–23
CeAu			–	–	–

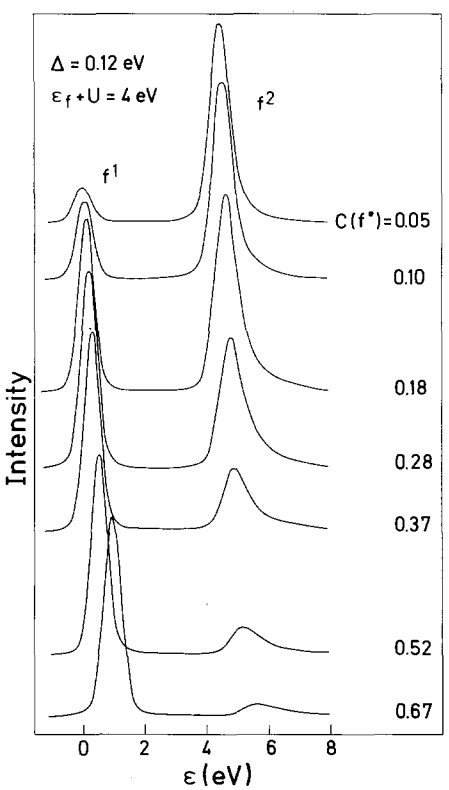

Fig. 28. BIS spectra for 4f signature in Ce and Ce compounds calculated by Gunnarsson and Schönhammer (1983a,b) using the extended Anderson impurity Hamiltonian.

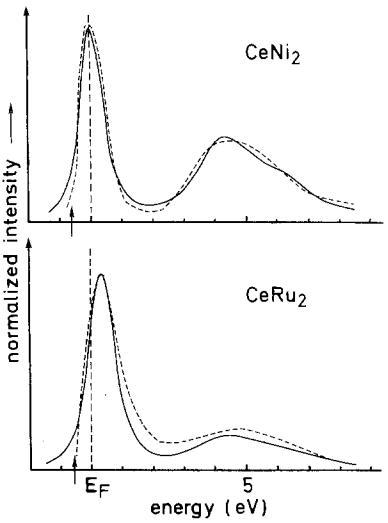

Fig. 29. Simulation of multiplet splitting in the model calculation, compared to experimental results (dashed) for $CeNi_2$ and $CeRu_2$.

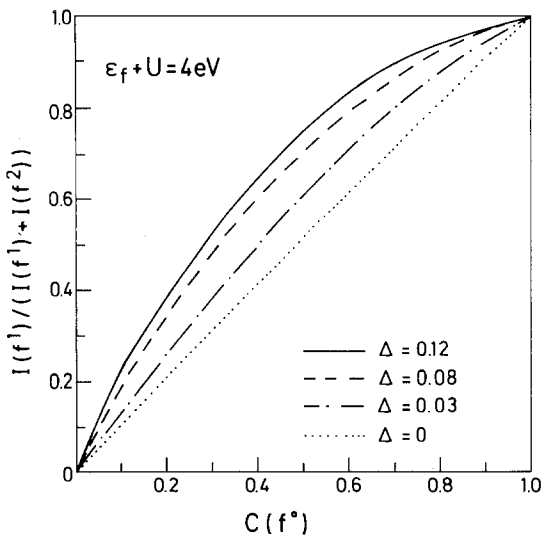

Fig. 30. Intensity of f^1 final state in BIS, normalized to total f intensity, over f^0 contribution in the ground state, derived from spectra calculated with the Anderson impurity model (Gunnarsson and Schönhammer 1983a,b).

comparison to other spectroscopic techniques. Nevertheless, the data available today are complete enough to allow some general conclusions. First of all, the unoccupied 4f states can easily be observed in BIS spectra of lanthanides and their compounds because of their large cross section and distinct shapes. If the non-4f or ligand states yield structures of comparable intensity in the unoccupied DOS, comparison to analog compounds containing different lanthanides still allows identification of the relevant 4f features. To isolate the 4f features one can also make use of the fact that the presence of oxygen affects the 4f states more strongly than states of other subshells. Because of the small probing depth of BIS, surface-induced effects can be present and have to be separated from the bulk spectral features. The

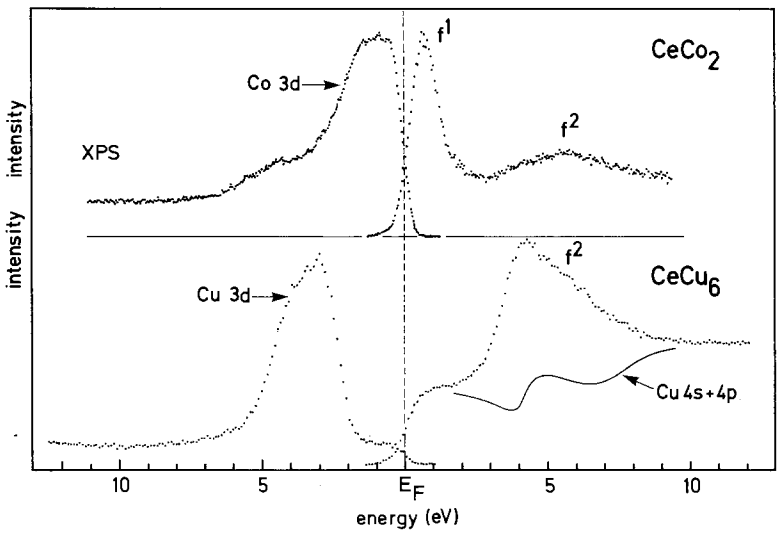

Fig. 31. XPS and BIS valence band data for mixed valent, superconducting $CeCo_2$ and the heavy fermion compound $CeCu_6$ (see also Patthey et al. 1986). The BIS spectrum of pure Cu (Van der Marel et al. 1983) is indicated for comparison.

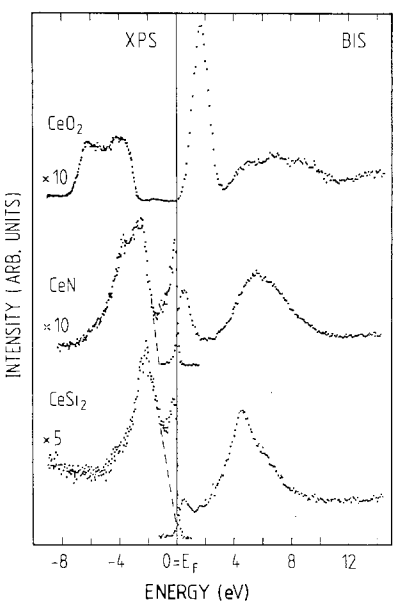

Fig. 32. XPS/BIS valence band density of states for insulating CeO_2, mixed valent CeN, and heavy fermion $CeSi_2$ (Wuilloud et al. 1984a, 1985).

unoccupied 4f states can be well described by atomic multiplet theory, and the 4f intrashell Coulomb correlation energy U is of the order of 5 to 10 eV in agreement with theoretical calculations. The Coulomb correlation energy is not changed significantly by compound formation. Consequently, the loss of magnetism for some Ce compounds cannot be attributed to a Mott transition. For mixed valent compounds final states are observed which originate from the two configurations

present in the ground state. For many cases – i.e., most compounds of Sm, Eu, and Tm – the intensity ratio of the final states is a good measure for the average f occupancy in the ground state, as determined either from other spectroscopies or from "low-energy" experiments. For nonmagnetic Ce compounds the average 4f occupancy determined *purely* from the intensity ratios observed in BIS does not agree with results from other experiments. This was one of the findings which demonstrated the importance of hybridization for the spectroscopic as well as low-energy properties of Ce compounds. The discrepancy can be resolved by a large coupling or hybridization between the localized 4f state and the extended states of the solid. Calculations based on the single-impurity Anderson Hamiltonian which allow for such a large hybridization have been performed by Gunnarsson and Schönhammer (chapter 64, this volume), and can model the experimental spectra of very diverse materials, as shown in figs. 31 and 32. In this sense one can say that the Ce problem from the point of view of spectroscopy has been solved. The *apparent* discrepancies between various spectroscopic results, especially with regard to f occupancy, are removed by taking into account dynamical effects which are caused by the large hybridization. Recently, also examples of Yb compounds have been found for which a sizeable hybridization is required to explain the data (Oh et al. 1987). Based on hybridization and 4f occupancy as determined from spectroscopic data, it is possible to estimate the Kondo temperature which in turn determines the low-energy properties, e.g. susceptibility. Such estimates yield at least a rough agreement with experimental results (Gunnarsson et al. 1983c, Allen et al. 1986). It appears then that it may be possible to describe *all* the phenomena displayed by lanthanide compounds – mixed valence, heavy Fermion behaviour, Kondo effect, etc. – within one single theory, with the hybridization being the determining factor for the physical properties of the material. The observation of the "Kondo resonance" at the Fermi level, which has been achieved by ultraviolet photoemission in some favourable cases for the occupied portion below E_F (see chapter 62, this volume) would make the spectroscopic evidence for this picture complete, however a resolution of ~ 10 meV in inverse photoemission or BIS is difficult if not impossible to achieve.

References

Ackermann, B., 1984, unpublished.

Allen, J.W., S.J. Oh, M.B. Maple and M.S. Torikachvili, 1983, Phys. Rev. B **28**, 5347.

Allen, J.W., S.-J. Oh, O. Gunnarsson, K. Schönhammer, M.B. Maple and M.S. Torikachvili, 1986, Adv. Phys. **35**, 275.

Andres, K., J.E. Graebner and H.R. Ott, 1975, Phys. Rev. Lett. **35**, 1779.

Baer, Y., H.R. Ott, J.C. Fuggle and L.E. De Long, 1981, Phys. Rev. B **24**, 5384.

Cabus, S., 1983, unpublished.

Campagna, M., E. Bucher, G.K. Wertheim, D.N.E. Buchanan, L.D. Longinotti, 1974, Phys. Rev. Lett. **32**, 885.

Campagna, M., E. Bucher and G.K. Wertheim, 1976, Structure and Bonding (Springer-Verlag, Berlin) p. 99.

Chamberlain, M.B., A.F. Burr and R.J. Liefeld, 1974, Phys. Rev. A **9**, 663.

Fauster, Th., and F.J. Himpsel, 1984, Phys. Rev. B **30**, 1874.

Fuggle, J.C., H. Hanning, J. Keppels and Z. Zolnierek, 1979, unpublished.

Fuggle, J.C., M. Campagna, Z. Zolnierek, R. Lässer and A. Platau, 1980, Phys. Rev. Lett. **45**, 1597.

Fuggle, J.C., F.U. Hillebrecht, R. Zeller, Z. Zolnierek, P.A. Bennett and Ch. Freiburg, 1983,

Phys. Rev. B **27**, 2145.
Gelius, U., L. Asplund, E. Basilier, S. Hedman, K. Helenelund and K. Siegbahn, 1984, Nucl. Instr. & Methods (B1) **1**, 85.
Glötzel, D., and R. Podloucky, 1980, Physica B **102**, 348.
Gudat, W., R. Rosei, J.H. Weaver, E. Kaldis and F. Hulliger, 1982a, Solid State Commun. **41**, 37.
Gudat, W., M. Iwan, R. Pinchaux and F. Hulliger, 1982b, in: Valence Instabilities, eds P. Wachter and H. Boppart (North-Holland, Amsterdam) p. 249.
Gunnarsson, O., and K. Schönhammer, 1983a, Phys. Rev. Lett. **50**, 604.
Gunnarsson, O., and K. Schönhammer, 1983b, Phys. Rev. B **28**, 4315.
Gunnarsson, O., and K. Schönhammer, 1985a, J. Magn. & Magn. Mater. **47&48**, 266.
Gunnarsson, O., and K. Schönhammer, 1985b, Phys. Rev. B **31**, 4815.
Gunnarsson, O., K. Schönhammer, J.C. Fuggle, F.U. Hillebrecht, J.-M. Esteva, R.C. Karnatak and B. Hillebrand, 1983c, Phys. Rev. B **28**, 7330.
Herbst, J.F., N.D. Lowy and R.E. Watson, 1972, Phys. Rev. B **6**, 1913.
Hillebrecht, F.U., 1983c, Ph.D. thesis, University of Cologne, 1983, published as report no. Jül 1928, KFA Jülich 1984 (can be obtained from author).
Hillebrecht, F.U., J.C. Fuggle, P.A. Bennett, Z. Zolnierek and Ch. Freiburg, 1983a, Phys. Rev. B **27**, 2179.
Hillebrecht, F.U., J.C. Fuggle, G.A. Sawatzky and R. Zeller, 1983b, Phys. Rev. Lett. **51**, 1187.
Hillebrecht, F.U., J.C. Fuggle, G.A. Sawatzky, M. Campagna, O. Gunnarsson and K. Schönhammer, 1984, Phys. Rev. B **30**, 1777.
Hillebrecht, F.U., W. Gudat, N. Mårtensson, D.D. Sarma and M. Campagna, 1985, J. Magn. & Magn. Mater. **47&48**, 221.
Hillebrecht, F.U., K. Keppels and R. Otto, 1987, Rev. Sci. Instrum. **58**, 776.
Hüfner, S., and G.K. Wertheim, 1975, Phys. Lett. A **51**, 299.
König, C., 1983, Z. Phys. B **50**, 33.
Lang, J.K., and Y. Baer, 1979a, Rev. Sci. Instrum. **50**, 221.
Lang, J.K., and Y. Baer, 1979b, Solid State Commun. **31**, 945.
Lang, J.K., Y. Baer and P.A. Cox, 1981, J. Phys. F **11**, 121.
Laubschat, C., G. Kaindl, E.V. Sampathkumaran, W.-D. Schneider, 1984, Solid State Commun. **49**, 339.
Liefeld, R.J., A.E. Burr, M.B. Chamberlain, 1974, Phys. Rev. A **9**, 316.
Malik, S.K., F.J. Arlinghaus and W.E. Wallace, 1982, Phys. Rev. B **25**, 6488.
Manson, S.T., 1978, in: Photoemission in Solids, Vol. 1, eds M. Cardona, and L. Ley (Springer-Verlag, Berlin) ch. III, p. 135.
Manson, S.T., and J.W. Cooper, 1968, Phys. Rev. **165**, 126.
Mårtensson, N., F.U. Hillebrecht and D.D. Sarma, 1985, Surf. Sci **152/153**, 733.
Mattens, W.C.M., P.F. de Châtel, A.C. Moleman and F.R. de Boer, 1979, Physica B **96**, 138.
Oh, S.-J., and J.W. Allen, 1984, Phys. Rev. B **29**, 589.
Oh, S.-J., J.W. Allen, M.S. Torikachvili and M.B. Maple, 1985, J. Magn. & Magn. Mater. **52**, 183.
Oh, S.-J., S. Suga, A. Kakizaki, M. Taniguchi, T. Ishii, J.-S. Kang, J.W. Allen, O. Gunnarsson, N. Christensen, A. Fujimori, T. Suzuki, T. Kasuya, K. Schönhammer, M.S. Torikachvili and M.B. Maple, 1987, submitted to Phys. Rev. Lett.
Patthey, F., W.-D. Schneider, Y. Baer and B. Delley, 1986, Phys. Rev. B **34**, 2967.
Pickett, W.E., A.J. Freeman and D.D. Koelling, 1980, Phys. Rev. B **22**, 2695.
Pickett, W.E., A.J. Freeman and D.D. Koelling, 1981, Phys. Rev. B **23**, 1266.
Scofield, J.H., 1976, J. Electron Spectrosc. & Relat. Phenom. **8**, 129.
Speier, W., J.C. Fuggle, R. Zeller, B. Ackermann, K. Szot, F.U. Hillebrecht and M. Campagna, 1984, Phys. Rev. B **30**, 6921.
Steglich, F., J. Aarts, C.B. Bredl, W. Lieke, D. Meschede, W. Franz and H. Schäfer, 1979, Phys. Rev. Lett. **43**, 1892.
Takeshita, T., K.A. Gschneidner Jr, D.K. Thomas and O.D. McMasters, 1980, Phys. Rev. B **21**, 5636.
van der Marel, D., G.A. Sawatzky, R. Zeller, F.U. Hillebrecht and J.C. Fuggle, 1984, Solid State Commun. **50**, 47.
Wuilloud, E., H.R. Moser, W.-D. Schneider and Y. Baer, 1983, Phys. Rev. B **28**, 7354.
Wuilloud, E., B. Delley, W.-D. Schneider and Y. Baer, 1984a, Phys. Rev. Lett. **53**, 202.
Wuilloud, E., W.-D. Schneider, B. Delley, Y. Baer and F. Hulliger, 1984b, J. Phys. C **17**, 4799.
Wuilloud, E., B. Delley, W.-D. Schneider and Y. Baer, 1985, J. Magn. & Magn. Mater. **47&48**, 197.
Yashima, H., H. Mori, T. Satoh and H. Kohn, 1982, Solid State Commun. **43**, 193.

Handbook on the Physics and Chemistry of Rare Earths, Vol. 10
edited by K.A. Gschneidner, Jr., L. Eyring and S. Hüfner

Chapter 71

X-RAY ABSORPTION AND EMISSION SPECTRA

Jürgen RÖHLER
II. Physikalisches Institut, Universität zu Köln, Zülpicherstr. 77, 5000 Köln 41, Fed. Rep. Germany

Contents

List of symbols

K	1s core level
L_I	2s core level
L_{II}	$2p_{1/2}$ core level
L_{III}	$2p_{3/2}$ core level
M_I	3s core level
M_{II}	$3p_{1/2}$ core level
M_{III}	$3p_{3/2}$ core level
M_{IV}	$3d_{3/2}$ core level
M_V	$3d_{5/2}$ core level
N_{IV}	$4d_{3/2}$ core level
N_V	$4d_{5/2}$ core level
N_{VI}	$4f_{5/2}$ core level
N_{VII}	$4f_{7/2}$ core level
O_I	5s core level
O_{II}	$5p_{1/2}$ core level
O_{III}	$5p_{3/2}$ core level
O_{IV}	$5d_{3/2}$ valence electron level
O_V	$5d_{5/2}$ valence electron level
FWHM	full width at half maximum
m	number of 5d6s conduction electrons
n	number of 4f electrons
R	metallic radius
S	Mössbauer isomer shift
T_n	lifetime of the valence state with n 4f electrons
T_{n+1}	lifetime of the valence state with $n+1$ 4f electrons
T_t	transition time between the two states of different valence
v	fractional valence
v_v	fractional valence obtained from the linear interpolation of the lattice parameters
V_n	$4f^n$ reference volume
V_{n+1}	$4f^{n+1}$ reference volume
μ	linear absorption coefficient
μd	absorption
ν	population of the higher valence state
Γ	total natural core level width
Γ_A	Auger width
Γ_C	Coster–Kronig width
Γ_R	radiative width
σ	absorption cross section
Δ_{kl}	effective 2p binding energy shift upon 4f configurational change

1. Introduction

X-ray absorption and emission spectroscopy is a field with a distinguished history. At the beginning, i.e., from 1913 to the early thirties, these spectroscopies were dedicated to a systematic exploration of the atomic structure in the context of the periodic system of the elements. The intense work of numerous spectroscopists, which contributed prominently to the foundations of modern atomic physics and to the development of quantum theory, was reviewed in the classical books 'Spektroskopie der Röntgenstrahlen' by M. Siegbahn (1913) and 'X-Rays in Theory and Experiment' by Compton and Allison (1935).

The lanthanides were investigated through X-ray spectroscopy since Malmer (1915) measured the La, Ce, Pr, Nd $K_{\alpha,\beta}$ emission lines and de Broglie (1916) and

Wagner (1916) recorded the La, Ce, Nd, Tm, Yb and Lu K absorption edges. These data contributed to the completion of the original Moseley diagram, which had established the nuclear charge Z as the basic ordering scheme of the elements up to Ag ($Z = 47$). The measurement of the L absorption in Cs, Ba, La, Ce, Pr, Nd (Hertz 1920) resulted in the detection of internal screening doublets (L_I and L_{II}). Bohr and Coster (1922) summarized the K, L, M, N, and O absorption levels (from experimental absorption and emission data) in Moseley's diagram up to $Z = 92$. They found strong irregularities at $Z = 57$(La) and $Z = 71$(Lu). These irregularities confirmed the number of 4f electrons to be 14 ($4l + 2$, $l = 3$; according to Pauli's principle) and thus verified that the lanthanides are completed at Lu. The X-ray absorption transitions from inner shells into incompletely filled outer shells were expected to exhibit sharp lines (Pauli 1926), in analogy to optical transitions. Such intense (so-called white lines) were first observed in $2p_{1/2} - 5d(L_{II})$ and $2p_{3/2} - 5d(L_{III})$ excitations of lanthanides in various aqueous solutions (fig. la, b). The expected strong lines in transitions from $3d(M_{IV,V})$ or $4d(N_{IV,V})$ inner shell levels into the partially filled 4f shell were detected later (Lindberg 1931, Rule 1945, Zimkina et al. 1967, Fomichev et al. 1967).

The task of X-ray spectroscopy in clarifying the atomic structure of the elements was for the most part accomplished in the mid-thirties. Since then its even more voluminous task has been to trace modifications of the atomic shell configurations and of their energetics by the chemical bonding in molecules and solids. In absorption spectroscopy these chemical effects can be detected by chemical shifts and by new fine structures in the absorption line or edge and in the near edge region ($E - E_{edge} \leqslant 30\,eV$). The existence of such chemical effects has been known since the beginning of X-ray spectroscopy. They were interpreted by Kossel (1920) to originate from the specific chemical oxidation state, valence, or type of chemical bonding in the substance under investigation. A chemical fine structure in the absorption spectrum of a lanthanide molecule was observed 35 eV above the white lines at the L_{III} edge of Ce in $Ce(NO_3)_3 \cdot H_2O$ (Hertz 1920) and the L_{III} edges of R in $R_2(SO_4)_3$ + aq. (R = Pr, Nd, Sm, Eu, Dy, Ho) (Nishina 1925). However, at that early time only minor efforts were made to clarify such chemical effects quantitatively, since e.g. lanthanide chemistry was then just at its beginning. The experiments were performed with ill-defined chlorides, oxides and aqueous solutions, which gave variations of the spectra with the quality of the samples, apart from those due to varying states of the spectrometers.

Systematic and detailed studies of chemical effects on the X-ray absorption fine structure (predominantly in $L_{II,III}$ absorption in chemically well-characterized lanthanide compounds) first began in earnest in the early fifties. These investigations were mainly concerned with:

(i) The measurements of the L energy positions and of the chemical shifts between the $L_{II,III}$ maxima and the onset of the absorption lines in the trivalent sesquioxides R_2O_3 (R = La–Nd, Sm–Lu). These shifts ($5 \pm 2\,eV$) indicate that the so-called white lines in all R_2O_3 exhibit a similar shape and width (Sakellaridis 1953, 1954, Callon 1955, Allais 1942, Barrère 1947, Kushwaha et al. 1974, Vainshtein et al. 1962, 1963a, Ovsyannikova et al. 1967).

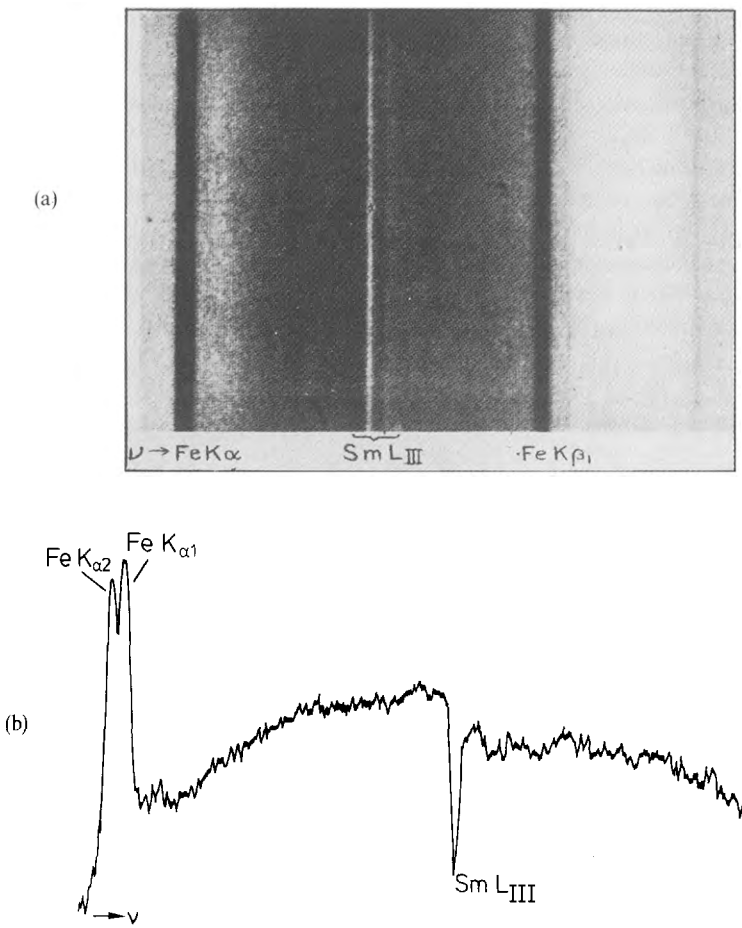

Fig. 1. (a) Reproduction of a historic spectrogram of the Sm L_{III} absorption line in $Sm_2(SO_4)_2$ + aq. The dark Fe $K_{\alpha,\beta}$ fluorescence lines serve as calibration marks for the energy scale. The energy increases from the left to the right (adapted from Nishina 1925). (b) Photometric curve of the spectrogram in fig. 1a. The narrow spike at the L_{III} absorption threshold corresponds to the 'white line' in (a). Noise masks the absorption fine structure at the high-energy side (EXAFS) of the spectrum. Note that the photometric curve exhibits the transmitted intensity, not the absorption μd (adapted from Nishina 1925).

(ii) The measurement of chemical shifts between the metallic-like hexaborides (RB_6) and the trivalent sesquioxides (R_2O_3). The $L_{II,III}$ absorption spectra of the divalent Eu- and Yb-hexaborides were found to be shifted by about −8 eV from the energy positions of the trivalent references Eu_2O_3 and Yb_2O_3, respectively (cf. fig. 2). The most prominent result of this systematic exploration of the oxidation states

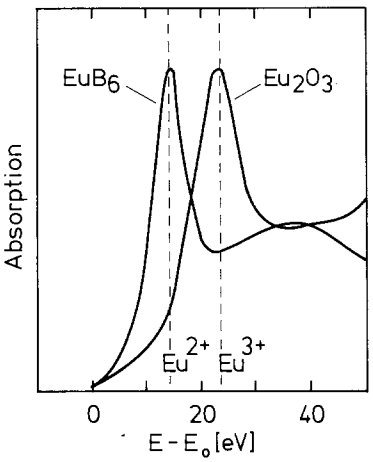

Fig. 2. L_{III} absorption lines of Eu in divalent EuB_6 and trivalent Eu_2O_3 (photometric recordings, adapted from Vainshtein et al. 1965a,b). The absorption maximum of Eu_2O_3 is shifted by $\cong 8$ eV to higher energies with respect to the absorption maximum of EuB_6. This shift is a signature of a configurational change from the divalent ($4f^7 6s^2$) to the trivalent ($4f^6 5d^1 6s^2$) Eu configurations.

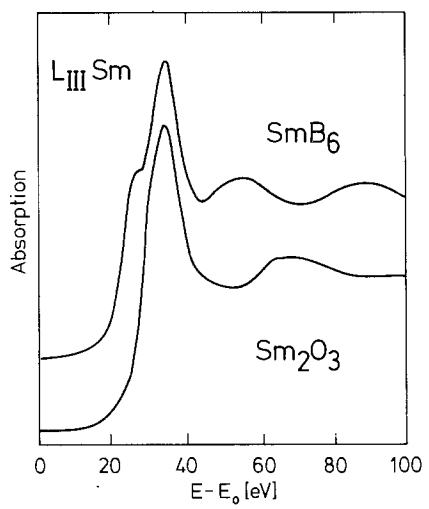

Fig. 3. L_{III} absorption spectra of Sm in trivalent Sm_2O_3 (lower spectrum) and in mixed valent SmB_6 (upper spectrum). The absorption maxima in both compounds are observed at identical energies. SmB_6, however, exhibits a significant shoulder at about -8 eV displaced from the maximum of the trivalent absorption line (adapted from Vainshtein et al. (1965a)). The second absorption line indicates the presence of divalent Sm in SmB_6 ($v = 2.65 \pm 0.05$). The valence number v is obtained from a weighted superposition of two single-shaped L_{III} absorption spectra displaced by $\cong 8$ eV (Vainshtein et al. 1965b).

in RB_6 through L absorption was the discovery of the homogeneously mixed valent state in SmB_6 (cf. fig. 3; Vainshtein et al. 1965a,b). Troneva et al. (1958) and Vainshtein et al. (1962) recorded the L_{III} absorption spectra of nominally tetravalent Ce in CeO_2 and of trivalent Ce in CeB_6. Surprisingly CeO_2 was found to exhibit a double peaked white line (cf. section 14) which is shifted by about $+3$ eV from the maximum of the L_{III} absorption in CeB_6 and Ce_2O_3 (Vainshtein et al. 1965a).

(iii) The measurement of L_{III} chemical shifts and fine structures (cf. fig. 4) in various R-chalcogenides (Eu-oxides, Eu-sulfides: Finkel'shtein et al. (1974); La-sulfides and selenides, La-, Pr-tellurides, Pr-selenides: Vainshtein et al. (1967a)). Further experiments were dedicated to the L absorption in RF_3 and ROF (Vainshtein et al. 1963a, Ovsyannikova et al. 1967), in RCl_3 (Agarwal et al. 1971a,b), in R-carbides and phosphides (Ovsyannikova et al. 1964, Vainshtein et al. 1967a,

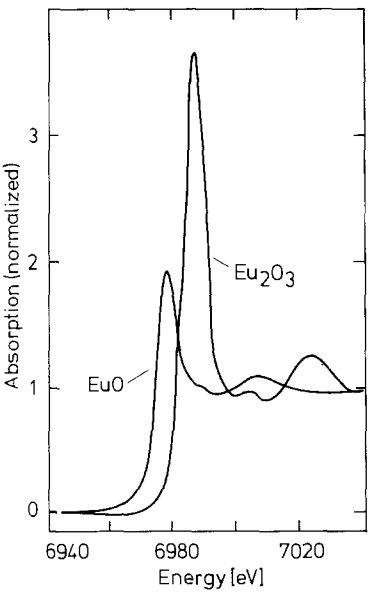

Fig. 4. Normalized L_{III} absorption spectra of Eu in divalent EuO and trivalent Eu_2O_3 (adapted from Ravot et al. 1981). The data are recorded with a double crystal spectrometer and synchrotron radiation. The amplitude of the absorption line in Eu_2O_3 turns out to be about 1.9 times larger than that of EuO and that of Eu_2O_3 in fig. 2. The discrepancy between the two Eu_2O_3 absorption lines presumably is due to saturation effects in the spectograms of Vainshtein et al. (1965a,b) (cf. section 5).

Vickery et al. 1959), in La- and Ce- hydrides (Vainshtein et al. 1963b), in intermetallic R compounds containing Si, Ge, Mg, Be, Al (Nemnonov and Klyushin 1958, Vainshtein et al. 1967b) and in other compounds.

The experimental work on X-ray absorption and emission spectra of the lanthanides and its compounds, performed until 1975, has been summarized e.g. in: 'Handbuch der Anorganischen Chemie' (Gmelin 1976). In this chapter we focus on the experimental work, published after 1975.

Most of the L spectra, measured during the early period of X-ray spectroscopy were recorded with energy dispersive spectrometers on photographic films. In many respects the gross spectral features recorded with this type of spectrometers match those recorded with today's state-of-the-art spectrometers. Large chemical shifts can be traced from such data, e.g., the significant shifts of about 8 eV in the $L_{III,II}$ spectra of lanthanide materials with different valence states. Accurate measurements of *amplitudes* and *lineshapes*, however, are best performed with modern double crystal monochromators and with the use of synchrotron radiation (cf. section 5).

When synchrotron radiation became available in the seventies, X-ray absorption spectroscopy took a jump in the volume of data taken and in their precision. These sources made absorption measurements in the soft X-ray region (M absorption in the lanthanides) and in the X-ray UV (N absorption in the lanthanides) much more easily accessible. At the same time, interest in information about solid state physics and chemistry of the lanthanides intensified with the discovery of valence fluctuations or homogeneously mixed valence. Accordingly the bulk part of this chapter is dedicated to a review of modern X-ray absorption spectroscopy of lanthanides, in particular of mixed valent materials, using synchrotron radiation.

2. X-ray emission in lanthanide solid state research

The energies of X-ray emission lines and absorption edges in the past have been extensively used for the determination of the atomic energy levels (Siegbahn, M., 1931, Bearden and Burr 1967). Since the energies of the X-ray emission lines provide accurate data for the determination of the atomic levels only on a relative scale, in most cases the energies of the well-defined L_{III} edges were chosen as the fundamental reference. To establish the absolute scale of the lanthanide atomic energy levels, Bearden and Burr (1967) used the L photoemission data of Bergvall and Hagström (1959). These data (L_I, L_{II}, L_{III} thresholds) have been taken on the trivalent sesquioxides R_2O_3 (R = La, Nd, Sm–Lu), tetravalent CeO_2 and mixed valent Pr_6O_{11}. Accordingly atomic energy levels in lanthanide systems with nominally different valence states deviate up to about +8 eV from the numbers tabulated by Bearden and Burr (1967).

Compared to X-ray absorption only minor efforts went into the application of X-ray emission spectroscopy to solid state or chemical problems in the lanthanides. This might be due to the fact that usually X-ray emission lines are superimposed on a set of weakly resolved and often undefined satellite lines. Accordingly chemical shifts from X-ray emission can be unambiguously related to the chemical oxidation state in only a few cases. Most of the few X-ray emission experiments dedicated to the exploration of the electronic configurations and of the chemistry of the lanthanides, analyze inner shell transitions, i.e., radiative transitions from levels inside the Xe core. Lee et al. (1974) used the shifts of the $K_{\alpha 1\alpha 2}(L_{II,III} \rightarrow K)$, $K_{\beta 1\beta 3}(M_{II,III} \rightarrow K)$ and $K_{\beta 2\beta 4}$ ($N_{II,III} \rightarrow K$) emission lines upon 4f-configurational change for the exploration of the valence state in Yb and Pr compounds. Sumbaev (1978) reviews an extensive work on K emission shifts covering all lanthanides (except La and Pm). The shifts were measured with respect to the $K_{\alpha,\beta}$ energies of unambiguously trivalent oxides or halides. The review of Sumbaev (1978) includes a theoretical analysis of the chemically induced K-emission shifts. Table 1 summarizes valences extracted from K-emission shifts.

The high energies of the $K_{\alpha,\beta}$ lines (33–35 keV) favor the K-emission spectroscopy for use in high-pressure experiments. Hard X-rays easily penetrate most of the high pressure window or anvil materials. The pressure dependence of the $K_{\alpha,\beta}$ emission line shifts was measured in Ce, SmS (Shaburov et al. 1974) and in $CeNi_5$, $CeCo_2$ (Shaburov et al. 1981) up to 12 kbar.

Tsutsumi et al. (1982) tried to identify the mixed valent state of SmB_6 through $L_{\gamma 1}(N_{IV} \rightarrow L_{II})$ emission shifts. Di- and trivalent stable reference systems, however, exhibit nearly identical $L_{\gamma 1}$ emission energies. Vo Chiong Ki et al. (1984) found chemical shifts of about 2 eV between the $L_{\alpha 1}(M_V \rightarrow L_{III})$, $L_{\beta 1}(M_{IV} \rightarrow L_{II})$ and $L_{\beta 2}(N_V \rightarrow L_{III})$ emission lines of di- and trivalent Eu- and Yb- fluorides and chlorides.

So-called resonant emission lines have been observed in the $M_\alpha(N_{VI,VII} \rightarrow M_V)$ and $M_\beta(N_{VI} \rightarrow M_{IV})$ X-ray emission from most of the elemental lanthanides and the lanthanide sesquioxides upon primary (incident electron beam) excitation (Stewardson and Wilson, 1956, Fisher and Baun 1967, Bonelle 1968, Bonelle and

TABLE 1

Valences derived from $K_{\alpha,\beta}$-emission shifts. The data published until 1979 are adapted from the review of Sumbaev (1978) [ref. 1], Lee et al. (1974) [ref. 2], and Shaburov et al. (1974) [ref. 6]. Data published after 1979 are from Sovestnov et al. (1981a) [ref. 3], Sovestnov et al. (1981b) [ref. 4], and Shaburov et al. (1981) [ref. 5].

Cerium	x	v	T[K]	p[kbar]	Ref.
γ-Ce		3.05	300	0	1
		3.0 –3.06 ± 0.02	300–950	0	3
		3.0 –3.34 ± 0.03	300	0–12	6
α-Ce		3.25–3.30	77	0	1
$CeCo_2$		3.32 ± 0.02	300–1000	0	3
		3.40 ± 0.08	300	12	3
Ce_3Co_7		3.40 ± 0.02	300	0	3
$CeCo_5$		3.41 ± 0.03–3.31 ± 0.02	77–1000	0	3
Ce_2Co_{17}		3.44 ± 0.04–3.42 ± 0.02	77–1000	0	3
$Ce(Co_{1-x}Cu_x)_5$	0–1	3.40 ± 0.03–3.00 ± 0.03	77	0	5
	0–1	3.38 ± 0.03–3.00 ± 0.03	300	0	5
	0–1	3.30 ± 0.03–3.00 ± 0.03	1000	0	5
	0.6	3.15 ± 0.03–3.08 ± 0.03	77–1000	0	5
	0.4	3.28 ± 0.03–3.15 ± 0.03	77–1000	0	5
	0.2	3.38 ± 0.03–3.22 ± 0.03	77–1000	0	5
	0	3.40 ± 0.03–3.33 ± 0.03	77–1000	0	5
CeF_4		4	300	0	1
CeNi		3.15 ± 0.02– 3.0	77–1000	0	3
$CeNi_2$		3.20 ± 0.02–3.10 ± 0.02	77–1000	0	3
$CeNi_3$		3.29 ± 0.02	300	0	3
Ce_3Ni_7		3.35 ± 0.02	300	0	3
$CeNi_5$		3.38 ± 0.03–3.35 ± 0.03	77–1000	0	3
		3.38 ± 0.1	300	0	3
$Ce(Ni_{1-x}Cu_x)_5$	0–1	3.40 ± 0.03–3.00 ± 0.03	77	0	5
	0–1	3.40 ± 0.03–3.00 ± 0.03	300	0	5
	0–1	3.40 ± 0.03–3.00 ± 0.03	1000	0	5
	0–1	3.42 ± 0.08–3.00 ± 0.08	300	12	5
	0.4	3.22 ± 0.03–3.05 ± 0.03	77–1000	0	5
	0.3	3.35 ± 0.03–3.15 ± 0.03	77–1000	0	5
	0.2	3.38 ± 0.03–3.29 ± 0.03	77–1000	0	5
	0	3.38 ± 0.03	77–1000	0	5
CeO_2		<4	300	0	1
		3.83 ± 0.03	77–1000	0	3
$Ce(SO_4)_{aq.}$		<4	300	0	1

Praseodymium	x	v	T[K]	p[kbar]	Ref.
Pr		3	300	0	1
$PrCl_2$		3	300	0	1
$Pr_{1-x}(Nd)_xCl_2$	'few percent'	2.5	300	0	1

TABLE 1 (cont.)

Praseodymium	x	v	T[K]	p[kbar]	Ref.
PrO_2		$\ll 4$	300	0	1
		3.4	300	0	2
Rb_3PrF_7		4	300	0	1
$PrFeO_3$		3.1	300	0	2
Pr_6O_{11}		3.25	300	0	2
$CsPrF_5$		3.4	300	0	2
$CePrF_6$		3.4	300	0	2
PrC_2		3	300	0	2

Neodymium	x	v	T [K]	p [kbar]	Ref.
Nd		3	300	0	1
NdS		3	300	0	1
$NdCl_2$		2	300	0	1
$Rb_3NdF_{6.5}$		(3.1)	300	0	1
$Cs_3NdF_{6.5}$		(3.1)	300	0	1

Samarium	x	v	T [K]	p [kbar]	Ref.
Sm		3	300	0	1
$SmCl_2$		2	300	0	1
SmS		2	300	0	1
		2–2.62 ± 0.03	300	0–12	6
$Sm_{1-x}R_xS$	$x > x_{cr}$				
	R = La	2.29	300	0	4
	R = Ce	2.44 ± 0.03	300	0	4
	R = Pr	2.59 ± 0.03	300	0	4
	R = Nd	2.60 ± 0.03	300	0	4
	R = Sm	2.59 ± 0.03	300	$> p_{cr}$	4
	R = Eu	2.18 ± 0.03	300	0	4
	R = Gd	2.59 ± 0.03	300	0	4
	R = Tb	2.67 ± 0.03	300	0	4
	R = Dy	2.60 ± 0.03	300	0	4
	R = Ho	2.67 ± 0.03	300	0	4
	R = Er	2.56 ± 0.03	300	0	4
	R = Tm	2.55 ± 0.03	300	0	4
	R = Yb	2.16 ± 0.03	300	0	4
	R = Lu	2.40 ± 0.03	300	0	4
	idem but $x \ll x_{cr}$	2.00 ± 0.05	300		4
$Sm_{1-x}Gd_xS$	0.2	2.65	300	0	1
$Sm_{1-x}Nd_xS$	0.4	2.65	300	0	1

TABLE 1 (cont.)

Europium	x	v	T [K]	p [kbar]	Ref.
Eu		2	300	0	1
EuF_2		2	300	0	1
Gadolinium	x	v	T [K]	p [kbar]	Ref.
Gd		3	300	0	1
$GdCl_2$		3	300	0	1
GdS		3	300	0	1
Terbium	x	v	T [K]	p [kbar]	Ref.
Tb		3	300	0	1
TbO_2		4	300	0	1
$Tb_{0.66}Dy_{0.33}Cl_2$		3	300	0	1
$Tb_{0.66}Sm_{0.33}Cl_2$		3	300	0	1
$Tb_2(C_2O_4)_3$		4	300	0	1
Dysprosium	x	v	T[K]	p [kbar]	Ref.
Dy		3	300	0	1
$DyCl_2$		2	300	0	1
$Rb_3DyF_{6.5}$		(3.1) indefinite	300	0	1
Holmium	x	v	T [K]	p [kbar]	Ref.
Ho		3	300	0	1
$HoCl_2$		2	300	0	1
Erbium	x	v	T [K]	p [kbar]	Ref.
Er		3	300	0	1
$ErCl_2$		3	300	0	1
Thulium	x	v	T [K]	p [kbar]	Ref.
Tm		3	300	0	1
$TmCl_2$		2	300	0	1
TmTe		2	300	0	1
TmSe		'mixed state'	300	0	1

TABLE 1 (cont.)

Ytterbium	x	v	T [K]	p [kbar]	Ref.
Yb		2	300	0	1
$YbCl_2$		2	300	0	1
$YbSO_4$		2	300	0	2
Lutetium	x	v	T [K]	p [kbar]	Ref.
Lu		3	300	0	1

Karnatak 1971, Chamberlain et al. 1974, Motais et al. 1981, Mariot and Karnatak 1974). The rather sharp resonant M_α, M_β emission lines occur at the same energies as the principal M_V and M_{IV} absorption lines (cf. fig. 6c and section 4.3). They may be considered to be the X-ray analogies to the well-known optical resonance lines. The electron excited X-ray emission spectra vary sensitively with the kinetic energy of the incident electrons. In addition self-absorption effects and the geometry of the experimental set-up may sensitively alter the intensities and lineshapes of the X-ray emission. Accordingly quantitative information, e.g., on the number of 4f electrons in the lanthanide material under investigation, have not been obtained from such spectra. Aita et al. (1986) compared electron excited and X-ray excited M_α, M_β emission spectra of stable Sm metal and mixed valent SmB_6 with each other. For both types of excitations each spectrum of SmB_6 was found to exhibit similar characteristic features as the corresponding spectra of Sm metal. The X-ray excited spectra of both samples did not exhibit the resonant emission lines observed by electron excitation.

$M_\varepsilon(O_V \rightarrow M_{III})$ X-ray emission from electron excited elemental Eu and Gd was registered by Mariot et al. (1974). The M_ε emission intensity from Gd was found to be five times larger than that from Eu. This finding is in qualitative agreement with the result of band-structure calculations (Freeman 1971, McGuire 1972), which confirm that the density of occupied 5d states should be large in Gd and small in Eu.

3. X-ray absorption versus photoemission

The synchrotron light sources, high resolution spectrometers and modern detection and data acquisition techniques have brought back old absorption spectroscopies into the physics and chemistry of the lanthanides. High quality absorption data from all core levels are available today and are compared with the corresponding X-ray photoemission (XPS) data, which have been collected since the sixties. The final goal of both X-ray absorption and X-ray photoemission spectroscopists is to obtain information about the ground state of the solid. A large part of this volume is dedicated to experimental and theoretical aspects of photoemission from the

lanthanides. Below we shall address the particular advantages of X-ray absorption over X-ray photoemission in obtaining the desired ground-state information.

The spectra from X-ray absorption turn out to be less complicated than those from XPS. This distinction between XPS and X-ray absorption can be explained by the dipole selection rules, which select only a small set of states from the spectral distribution of states excited upon creation of the core hole. XPS probes a much larger manifold of such final-state multiplets, which appear in relatively broad spectra. The relative intensities in the final-state multiplets of X-ray absorption spectra are moreover well defined through the dipole selection rules. Therefore X-ray absorption spectra exhibit a more transparent signature of the atom in the ground state of the solid.

Deep core level X-ray absorption in the lanthanides (cf. section 4) is understood in the so-called one electron picture (as far as the *transition* is concerned). Satellite structures due to many-electron and final-state effects are found to be insignificant. On the other hand, XPS spectra may exhibit considerable shake intensities, whose interpretation usually needs a set of parameters not determined directly through the experiment at hand or by other experiments. For instance, the much simpler final-state configurations in X-ray absorption have been experimentally demonstrated with 3d-XPS and $M_{IV,V}$ absorption in intermetallic Ce compounds (Fuggle et al. 1983). The $M_{IV,V}$ absorption spectra of Ce in α-type mixed valent $CeNi_2$, $CeNi_5$, $CePd_3$ exhibit only two final-state multiplets, $3d^9 4f^2$ and $3d^9 4f^1$. Admittedly the absence of significant final-state and many-electron effects in the deep core X-ray absorption is still a matter of controversy (cf. e.g., chapter 62 of this volume). The 3d-XPS spectra on the other hand exhibit *three* final-state multiplets, $3d^9 4f^2$, $3d^9 4f^1$ and $3d^9 4f^0$. The reason for the difference seems to lie in different screening processes in X-ray absorption and in XPS, respectively. In $M_{IV,V}$ absorption the core hole is completely screened through the 3d photoelectron. In 3d-XPS the screening of the core hole is much more complicated. Detailed understanding of the dynamics of screening in XPS is a prerequisite of the correct final-state assignment.

X-ray absorption experiments (in transmission geometry) unambiguously probe the bulk properties of the sample. On the other hand, XPS is a method sensitive in both bulk *and* surface. It is often impossible and otherwise difficult to discriminate quantitatively between photoemission from the surface on the one hand and from the bulk on the other hand, where the local states are in general different.

Very importantly absorption data of high quality can be routinely obtained from dilute lanthanides (0.1 atomic percent) in compounds or alloys, using electron or fluorescence yield detection techniques, while X-ray photoemission spectroscopies are restricted to the investigation of concentrated systems.

High pressure has proven to be an extremely powerful variable for the study of electronic phenomena in the solid state. Modern solid state models can be tested by their ability to account for the phenomena seen as function of pressure. Since the pioneering high-pressure studies in the optical region, the term 'pressure tuning' (Drickamer 1982) describes the experimentally controlled volume dependence of electronic levels. Pressure in the lanthanides induces mixed valence or valence transitions, induces 'heavy fermion' supraconductivity; in other words high pressure

may create a new ground state of the system with fundamentally different magnetic, electrical and chemical properties. The pressurizing environment of course does not allow for photoemission. On the other hand X-ray absorption experiments in the L region of the lanthanides (5.4–10 keV) can be performed at high pressures at ambient and low temperatures (Röhler et al. 1983b). High pressure X-ray absorption spectroscopy therefore extends 'pressure tuning' to innershell levels, e.g. the 4f levels. We focus in sections 9–14 on the discussion of data from X-ray absorption high-pressure experiments.

Altogether there are many good reasons why X-ray absorption should be considered as one of the most powerful experimental tools among the many high-energy solid state spectroscopies available today. Therefore it seems unavoidable that the theoretical literature concerned with such spectra will soon catch up in volume with the presently much more voluminous literature on the theory of photoemission.

4. The choice of the most appropriate core level

For the observation of sharp and *well-defined* final-state configurations one is concerned with two problems: (i) the need of sharp core levels, and (ii) the need of final-state configurations, which can be related to the unexcited ground-state configuration in a straightforward manner. In this paragraph we treat these two issues, discussing the choice of the most appropriate core holes for X-ray absorption spectroscopy as a tool in lanthanide solid state research.

Since the core level width causes a spectral broadening, which interferes with a clearly resolved level structure of the final-state configuration of interest, core levels with small inverse lifetimes Γ should be selected. Figures 5a and 5b (adapted from Keski-Rahkonen and Krause (1974) display calculated total and partial natural widths of a single hole in the elements $40 < Z < 80$. The total widths are determined solely by decay rates of a single hole in a given level and contain no contribution from other possible sources such as broadening by the presence of multiplets in atoms with partially filled shells. Radiative, Auger, and Coster–Kronig processes compete in filling a hole in a given level. The total natural width is given by $\Gamma = \Gamma_R + \Gamma_A + \Gamma_C$, where Γ_R is the radiative width, Γ_A is the Auger width and Γ_C is the Coster–Kronig width.

In the lanthanides ($57 \leqslant Z \leqslant 71$) the total natural widths of the K, L, M and N levels increase more or less monotonously with the atomic number Z. The K levels exhibit the largest total widths in the range from about 14 eV (La, $Z = 57$) to about 33 eV (Lu, $Z = 71$). These widths are predominantly due to strong radiative decay processes. All levels with principal quantum number $n > 1$ exhibit smaller total natural widths. Here essentially Auger and Coster–Kronig processes determine the total natural widths, which range from a few electron volts to about 12 eV. Most interestingly, holes in the highest angular momentum subshells ($2p_{3/2}$, $3d_{5/2}$) exhibit relatively small total natural widths due to the strongly reduced transition rates of Coster–Kronig processes: 2–5 eV (L_{III}, La–Lu) and 0.9–1.3 eV (M_V, La–Lu).

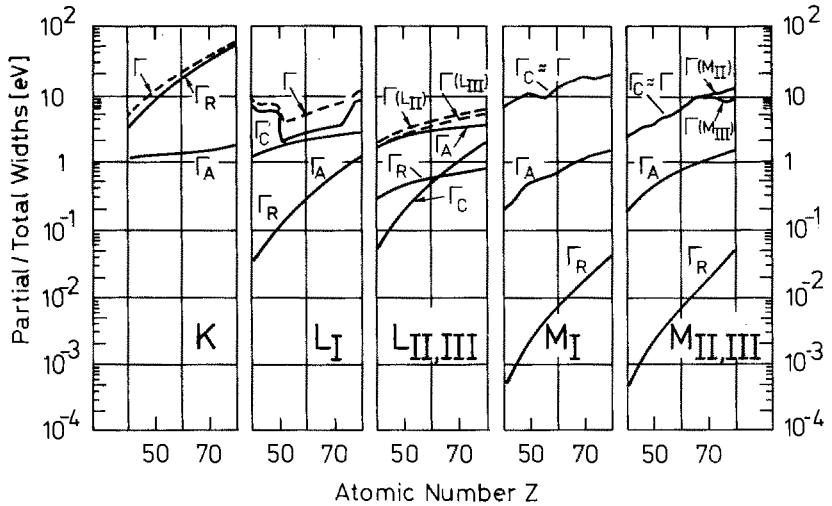

Fig. 5a. Calculated total natural widths Γ and partial natural widths Γ_R (inverse lifetime of the radiative decays), Γ_A (inverse lifetime of the Auger processes) and Γ_C (inverse lifetime of the Coster–Kronig processes) of K, L_I, $L_{II,III}$, M_I and $M_{II,III}$ levels for $Z = 40$–80 (from Keski-Rahkonen and Krause 1974).

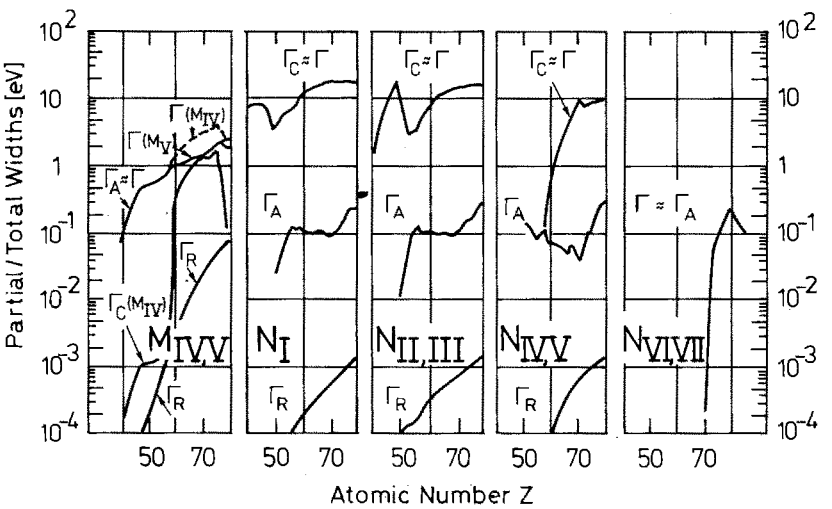

Fig. 5b. Calculated total natural widths Γ and partial natural widths Γ_R (inverse lifetime of the radiative decays), Γ_A (inverse lifetime of the Auger processes) and Γ_C (inverse lifetime of the Coster–Kronig processes) of $M_{IV,V}$, N_I, $N_{II,III}$, $N_{IV,V}$ and $N_{VI,VII}$ levels for $Z = 40$–80 (from Keski-Rahkonen and Krause 1974).

In figs. 6a–6c we reproduce core level absorption spectra of cerium (K, L_I, $L_{II,III}$, M_{III}, $M_{IV,V}$, $N_{IV,V}$). It is clearly visible that excitations into the uncompletely filled 4f shell ($M_{IV,V}$, $N_{IV,V}$) or 5d shell (M_{II}, $L_{II,III}$) cause pronounced spikes at the absorption thresholds (indicated by the dashed mark). On the other hand, excitations from 1s (K) and 2s (L_I) core levels into local p-type band states or np ($n > 6$) continuum states result merely in broad and rather structureless absorption spectra.

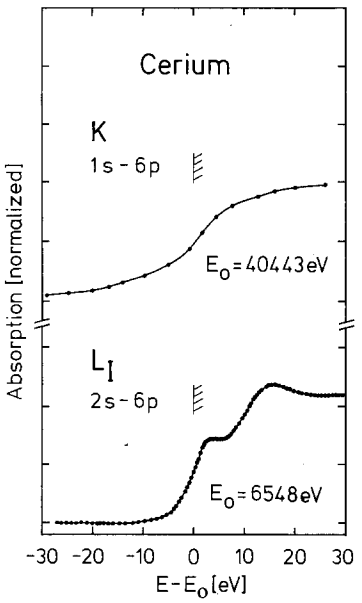

Fig. 6a. Absorption spectra with s–p symmetry (K, L_1) from elemental γ-cerium. The lines connecting the data points are guides for the eye. The inflection points of the spectra are calibrated with energies of the absorption thresholds (dashed mark) tabulated by Bearden and Burr (1967). The data of the K absorption are published by courtesy of Bedzyk et al. (1986).

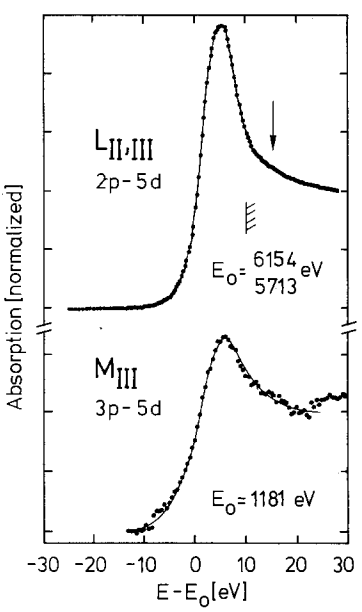

Fig. 6b. Absorption spectra with p–d symmetry ($L_{II,III}$, M_{III}) in elemental γ-cerium. The lines connecting the data points are guides for the eye. The dashed marks indicate the absorption thresholds tabulated by Bearden and Burr (1967). The L_{II} spectrum is not shown. It is found to be identical with the L_{III} spectrum. L_{III}: from Röhler (1984), M_{III}: adapted from Kaindl et al. (1984, 1985). The energy scale of the L_{III} spectrum is calibrated in respect to the first Cu–K maximum (8991.1 eV). The dashed mark indicates the threshold of tetravalent Ce. The energy calibration of the M_{III} spectrum is accurate within ±3 eV; the tabulated position of the M_{III} threshold is 1185 eV.

The *two* incompletely filled atomic-like shells of the lanthanides, namely the 4f shell (which is a core electron orbital) and the 5d shell (which is a valence electron orbital), are of particular interest in solid state physics. For instance many of the challenging anomalies of the lanthanides, e.g. mixed valence, are connected with the hybridization of 4f and 5d states. d- and p-type absorption spectroscopies are

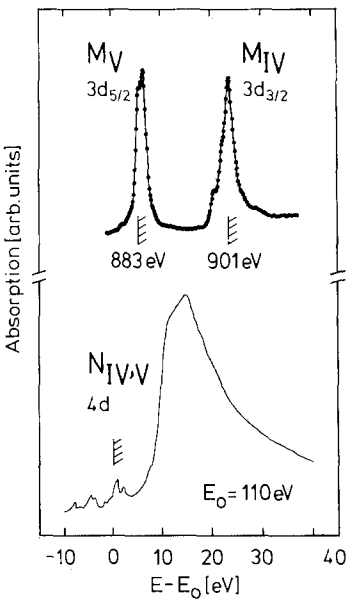

Fig. 6c. Absorption spectra with d–f symmetry $M_{IV,V}$, $N_{IV,V}$ in elemental γ-cerium. The dashed marks indicate the absorption edges tabulated by Bearden and Burr (1967). The $N_{IV,V}$ data are adapted from Wolff et al. (1976), the $M_{IV,V}$ data from Kaindl et al. (1985) (calculated oscillator strengths of the final state multiplets are omitted for reasons of clarity). The shallow core level $N_{IV,V}$ spectrum exhibits the characteristic 'giant resonance' above the threshold and $4d^9 4f^2$ mutiplet at threshold. The $N_{IV,V}$ multiplet splitting is masked by the large 4d–4f exchange splitting.

experimental methods examining the unoccupied 4f and 5d states according to the dipole $\Delta l = \pm 1$ selection rule.

The unoccupied states in the lanthanides can be reached by transitions from *deep* or *shallow* core levels. Following Wendin (1983), deep core levels are states in completely filled main shells, i.e. in the K, L and M levels. Levels in the incompletely filled main shells (N, O) are labelled as shallow core levels (except 5d, which is a valence electron level). The impact of this classification becomes clear by inspection of the strongly different types of absorption spectra, observed upon excitation of M and N core levels (fig. 6c). $N_{IV,V}$ and $M_{IV,V}$ spectra turn out to be completely different, although the d electrons from the *shallow* $N_{IV,V}$ levels ($4d \rightarrow nf, n \geqslant 4$) reach 4f states as the photoelectrons from *deep* core $M_{IV,V}$ levels ($3d \rightarrow nf, n \geqslant 4$). Each of the $M_{IV,V}$ spectra exhibits a set of discrete narrow lines. The $N_{IV,V}$ spectra on the other hand are dominated by a broad 'giant resonance' above threshold (cf. the strong line in fig. 6c). It exhibits only a weak and extended discrete line spectrum at threshold.

Comparing two *deep* core level spectra of identical symmetry (L_{III} and M_{III}) with each other, we do not observe striking differences. Apart from the different linewidths these spectra are quite similar.

In deep core level absorption spectroscopies the overlap of the core level wavefunction with the wavefunction of the excited state is of little or no importance. Deep core levels may be regarded as classical charge distributions, completely screened by the inner shells and the photoelectron. Most of the deep core level spectra can therefore be described neglecting many-electron processes. The large spatial overlap of the shallow 4d wavefunction with the 4f wavefunctions, however, favors relaxation processes of the excited atom involving spectacular many-electron effects as the 'giant resonances'. The correlation of these exotic final-state structures

to the ground state is difficult and controversal. Their theoretical explanation is of actual interest in atomic physics, rather than in solid state physics.

Accordingly spectra with minimized lifetime broadening and final states, largely unaffected by complicated many-electron effects, occur in $L_{III,II}(2p \rightarrow 4f\underline{5d})$ and $M_{IV,V}(3d \rightarrow \underline{4f})$ absorption.

4.1. *s → p transitions* (K, L_I)

Most of the lanthanide ($Z = 57$–60, 62–70) K absorption thresholds were determined by de Broglie (1916), Wagner (1916), M. Siegbahn and Jönsson (1919), Carbrera (1923) and others already in the pioneering period of X-ray absorption spectroscopy. K absorption as a tool in chemical analysis verified the existence of promethium ($Z = 61$) in the mineral monazite (Brunetti 1927). Manescu (1944) resolved weak fine structures up to about 30 eV above the K absorption limit in more or less purely trivalent R_2O_3 (R = Eu–Er, Yb, Lu). The K absorption discontinuities in some of the elemental lanthanides (Tb–Er) were recorded by Fairchild (1975) using synchrotron radiation (fig. 7). The K absorption discontinuity in Ce was measured by Bedzyk et al. (1986), cf. fig. 6a. All K-absorption spectra of the lanthanides exhibit a similar smooth energy dependence, due to the large total natural widths of the 1s core hole. The large spectral broadening wipes out nearly all the fine structure in the absorption discontinuity, which is expected from the excitations into p-type band states. Even chemical shifts are hard to extract. So K absorption is of rather limited value for practical applications of the physics and chemistry of the lanthanides.

On the other hand, K absorption spectra are useful for an accurate determination of the Z dependence of the 1s total natural widths, because the inverse core hole lifetime is much larger than the fine structure that has p symmetry above the

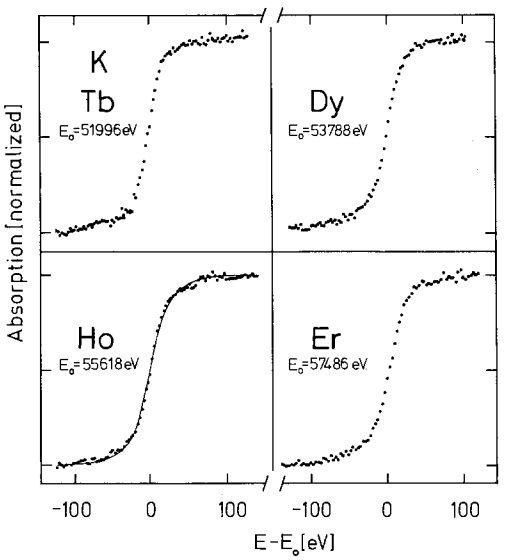

Fig. 7. K absorption spectra of elemental Tb, Dy, Ho and Er (adapted from Fairchild (1975)). The line connecting the holmium K absorption data represents an arctan fit with $\Gamma = 31$ eV. The inflection points of the spectra are calibrated at the E_0 values tabulated by Bearden and Burr (1967).

Fermi level. In a coarse approximation the p-level distribution can be assumed to correspond to that of a Fermi gas of free electrons, or even simpler, to that of a rectangular shaped distribution of equally spaced states (Richtmyer et al. 1934). Assuming equal transition probabilities and a Lorentzian lifetime broadening, the K absorption coefficient follows an arctan curve as a function of energy (cf. fig. 7, Ho):

$$\mu(E) = C\,\{\tfrac{1}{2} - (1/\pi)\arctan((E_0 - E)/\tfrac{1}{2}\Gamma)\}. \tag{1}$$

Here C denotes a constant, E the photon energy, E_0 the absorption limit and Γ the total natural core level width.

Accordingly the lifetime broadening can be directly read from the width of the arctan-shaped absorption discontinuity. K core level widths have been determined from experimental spectra through an arctan fit by Fairchild (1975). These numbers fit well to the empirical law for the Z dependence ($Z > 40$) of K widths, obtained by Leisi et al. (1961): $\Gamma(\mathrm{K}) = 1.73\,Z^{3.93}\,10^{-6}[\mathrm{eV}]$.

Comparison of K and L_I absorption spectra (cf. fig. 6a), which both involve s–p transitions, demonstrates similar smooth variations of the absorption coefficient with energy. In the L_I spectrum, however, fine structures can be resolved much more clearly than in the K spectrum ($\Gamma = 14\,\mathrm{eV}$), due to the considerably smaller total width of the L_I core hole ($\cong 5\,\mathrm{eV}$). The spectral shape of the L_I spectra in all lanthanide metals exhibits a stair-case-like rise of the absorption at threshold. A weak minimum is located at about 20 eV above the onset (figs. 6a). The fine structure of the L_I spectra reflects sensitively local s- and p-type band states and their modifications through different types of chemical bonding or crystal symmetries (Lengeler and Zeller 1984).

4.2. *p → d transitions* (L_{II}, L_{III}, M_{III})

The L_{III} and L_{II} absorption lines of La–Lu occur at about 5.5–10.3 keV. The $2p_{1/2}(L_{II})$–$2p_{3/2}(L_{III})$ multiplet splittings reach from 400 eV (La) to 1100 eV (Lu). The strong absorption lines at the $L_{II,III}$ thresholds have been known since the beginnings of lanthanide research in insulating salts and aqueous solutions (figs. 1 and 2). Just as in insulating systems, $L_{II,III}$ spectra of lanthanides in the gaseous phase, in metals, in intermetallic compounds semiconductors and dilute solutions exhibit such spikes at the absorption threshold. The exceptions reported by Agarwal et al. (1971a), Agarwal and Agarwal (1978) in the L_{III} absorption of Ho, $HoCl_3$ and Ho_2O_3 turned out to be artificial (cf. e.g. Wong et al. (1984)).

X-ray absorption of lanthanide 2p core levels probes the unoccupied atomic-like 5d states. Hence the occurrence of such intense absorption lines at the $L_{II,III}$ thresholds. By comparison, the spectral shapes of the L_{II} and L_{III} lines are found to be nearly identical. The L_{II} amplitudes (normalized to the continuum absorption), however, systematically turn out to be up to 50% larger in R_2O_3 and RF_3 (Feldhaus 1982, Wong et al. 1984, Okusawa et al. 1978) and to be about 5% smaller in the metals (Materlik et al. 1983a) than the corresponding L_{III} amplitudes. The slightly different L_{II}, L_{III} transition matrix elements cannot account for the observed strong discrepancies. Most likely the L_{II}/L_{III} amplitude ratio reproduces different final-state

multiplets *and* the effect of the Δj selection rule. Since the ratio of the absorption cross sections $\sigma(2p_{3/2} \rightarrow nd)/\sigma(2p_{1/2} \rightarrow nd)$ is near the statistical number of two, L_{III} spectra exhibit a better signal/noise ratio.

Thorough inspection of the $2p \rightarrow 5d$ transitions in solids reveals, apart from shifts upon 4f configurational change, a large manifold of spectral shapes and intensities. The correlation between line intensities and chemical shifts is one of the issues in section 8.3.1. Most of the lanthanides have single $L_{II,III}$ lines, exhibiting weak fine structures. Clearly double-peaked spectra are observed in inhomogeneously and homogeneously mixed valent systems with Ce, Pr, Nd, Sm, Eu, Tb, Tm and Yb. Figure 6b (top) displays the L_{III} absorption line of elemental γ-Ce. The weak shoulder at high energies (arrow) was found to be typical for all γ-Ce systems, indicating weak (5%) mixed valence (sections 12, 13).

Figure 6b (bottom) reproduces the M_{III} ($3p_{3/2} \rightarrow 5d$) spectrum of γ-Ce. As the L_{III} spectrum (top) the M_{III} absorption exhibits the characteristic absorption line of lanthanide $p \rightarrow d$ transitions. In M_{III} absorption Coster–Kronig transitions strongly increase the total lifetime broadening of the final states. Therefore mixed valent states can be only qualitatively traced from M_{III} spectra (Kaindl et al. 1984).

4.3. *$d \rightarrow f$ transitions ($M_{IV,V}$, $N_{IV,V}$)*

The absorption of the $M_{IV,V}$ and $N_{IV,V}$ transitions are located in the soft X-ray range ($\simeq$800–1700 eV) and in the ultraviolet ($\simeq$98–205 eV), respectively. In the early period of X-ray spectroscopy, such absorption measurements, in particular those in the ultraviolet, were hampered by the low intensities emitted from conventional X-ray sources, by the difficulty of preparing thin ($\simeq$ 100 Å) uncontaminated samples of defined thickness, and by the involved detection systems. Meanwhile most of these experimental problems have been overcome through the availability of intense and tunable synchrotron sources, the concomitant improvements of the detection systems (e.g., total electron yield detectors) and through developments of appropriate ultra high vacuum preparation techniques. Nevertheless, because of possible intrinsic surface effects, the question of whether one measures bulk properties remains a drawback here.

4.3.1. *$M_{IV,V}$ absorption*

The $M_{IV,V}$ absorption lines of R_2O_3, various trivalent R salts and some 'tetravalent' R oxides were determined by Lindberg (1931), Rule (1945), Zandy (1952), Lee et al. (1952), Stewardson and Wilson (1956), Fischer and Baun (1967), Bonelle et al. (1974) and Kaindl et al. (1984). Compared to the $L_{III,II}$ spectra, the multiplet splitting of the $3d_{3/2}$ and $3d_{5/2}$ core levels is much smaller (only about 15–45 eV), but much larger than the final state multiplets ($\simeq$10 eV). The $M_{IV,V}$ spectra exhibit rather sharp $3d^9\,4f^{n+1}$ multiplet structures consisting of several resolvable lines. Each of this final state multiplet through the number, intensities and positions of lines may serve as a characteristic fingerprint of the 4f ground state. The atomic $M_{IV,V}$ absorption multiplets of some lanthanides were first calculated by Sugar (1972a,b), Demekhin and Shelkovich (1974), Piacentini et al. (1974). The very intense $M_{IV,V}$ absorption

lines rise from a more or less straight background and are not distorted by a strong absorption edge as L absorption lines. Due to the high cross section of the $3d^{10}4f^n \rightarrow 3d^9 4f^{n+1}$ transitions the continuum absorption is nearly indistinguishable from the background.

The $M_{IV,V}$ absorption in the lanthanide elements has been investigated systematically only recently by Thole et al. (1985). Earlier measurements are from Bonelle and Karnatak (1971), Bonelle et al. (1972) who recorded the $M_{IV,V}$ absorption spectra of Eu, Gd, Dy. Ottewell et al. (1973) traced those of γ-Ce and mixed α/β-Ce, and Combley et al. (1968) those of Yb. Total electron yield recordings of γ-Ce, α-type Ce compounds, mixed valent Eu, Sm and Tm compounds were performed by Kaindl et al. (1984). Thole et al. (1985) present calculations of the total $3d^9 4f^{n*}$ final-state multiplets together with the Δj dipole rule filtered multiplets of all lanthanides. Adjusting the 3d spin–orbit splitting and taking into account the 3d lifetime broadening, except for Sm, Thole et al. (1985) find good agreement with their own recordings from the elements and with those of Kaindl et al. (1984) from R oxides. Anomalies in the Sm 3d absorption also were observed by Aita et al. (1986). From the latter measurements the $M_{IV,V}$ absorption spectrum in mixed valent SmB_6 surprisingly turned out to be identical with that in Sm metal and Sm_2O_3.

4.3.2. *$N_{IV,V}$ absorption*

The $N_{IV,V}$ absorption spectrum (100–150 eV) of metallic Ce is displayed in fig. 6c on the same relative energy scale as the $M_{IV,V}$ absorption. The $N_{IV,V}$ absorption of Ce was recorded in the solid and in the vapor and found to be nearly identical (Wolff et al. (1976), the spectrum from the vapor is omitted). The N_{IV}–N_V spin–orbit splitting reaches from 3.5 to 9.2 eV (Ce–Lu), much smaller than the $4d^9\ 4f^{n+1}$ exchange splitting. Hence the 4d absorption exhibits only one spectral feature. The other lanthanide $N_{IV,V}$ spectra, except Lu, have similar spectral features as that of Ce: a weak discrete line spectrum at the $N_{IV,V}$ absorption threshold and a rather broad and prominent maximum ('giant resonance') at about 20 eV above E_0 (Zimkina et al. 1967, Fomichev et al. 1967, Radtke 1976). The discrete fine structure at threshold is understood in terms of $4d^{10}4f \rightarrow 4d^9 4f^{n+1}$ transitions. In contrast to the deep core 3d absorption, the exchange interaction between the photoelectron and the *shallow* 4d core hole is so strong that the multiplet extends into the far continuum and shifts some levels about 20 eV beyond the threshold (Dehmer et al. 1972, Dehmer and Starace 1972, Sugar 1972b) interfering with the direct continuum excitation. The 'giant resonance' is due to complicated many-electron processes on shallow core level excitation. Tracy (1977), Connerade and Tracy (1977), Mansfield and Connerade (1976) recorded and analyzed 'giant resonances' the shallow 5p core level absorption ($O_{II,III}$) in lanthanide vapors. The absorption cross sections of the 'giant resonances' vary systematically with Z (Zimkina and Gribovskii 1971). The largest cross sections are observed at the beginning and in the middle of the series. For Dy–Lu the 'giant resonance' decreases and vanishes together with the discrete fine structure at the completely filled 4f shell (Yb^{2+}, Lu).

The discrete part of the $N_{IV,V}$ final-state multiplet has been recorded in γ-Ce, α-type Ce intermetallics, in tri- and 'tetravalent' Ce insulators (Haensel et al. 1970,

Hanyu et al. 1985, Kalkowski et al 1985b). At this time, however, it is not possible to extract quantitatively valence numbers from such spectra. Due to the complicated many-electron effects the shallow core level spectroscopies are the least reliable techniques for valence measurements.

5. Experimental aspects of X-ray absorption spectroscopy

Modern synchrotron light sources deliver intense and collimated photons from the visible to the hard X-ray region of up to 100 keV. Appropiate crystal or grating monochromators, completely covering the region of 1s to 5p absorption (50000 eV–20 eV) are accessible to the experimentalist in many synchrotron radiation laboratories. The spectrometer resolution $\Delta E/E$ is in the order of 10^{-4}, i.e., the spectrometer caused broadening of the absorption spectra is small or, in the worst cases, comparable to the core hole lifetime caused broadening of the spectral lines. When optimized experimental conditions exist, the absorption spectra of the lanthanides can be recorded without significant broadening or distortion due to the resolving power of the monochromators. Gudat and Kunz (1979) reviewed typical experimental arrangements for the spectroscopies in the X-ray ultraviolet and the soft X-ray region developed for instrumentation of the synchrotron radiation laboratories. Modern instrumentation for X-ray spectrometers for synchrotron radiation is, e.g., described in the 'Handbook on Synchrotron Radiation' (Koch 1983) and in 'Synchrotron Radiation Research' (Winick and Doniach 1980). Sandström (1957) and Blochin (1964) addressed the experimental technique of spectrometers equipped with X-ray tubes and the problems associated with data processing from photographic recording.

The measurement of the absorption coefficient $\mu(E)$ is usually performed through comparison of the incident intensity I_0 with I, the intensity transmitted by an absorber of thickness d

$$\mu(E) = (1/d)\ln(I_0/I). \tag{2}$$

In most cases the exact absorber thickness d is unknown and then merely the 'absorption' $\mu d = \ln(I_0/I)$ [arbitrary units] is determined.

Today soft X-ray absorption spectra (M, N) are routinely recorded by the detection of the total electron yield which is proportional to the absorption coefficient (Bothe 1926). The detection of the total electron yield is advantegeous over the detection of the transmitted intensities through thin (100–3000 Å) foils or evaporized layers. Since the spectra are recorded directly from the bulk material, investigations of compounds and dilute alloys are feasible. Experimental problems arise from the surface sensitivity of the method and saturation effects, which are not well understood up to now.

X-ray absorption spectroscopy in lanthanide solid state physics is used predominantly for the identification of atomic configurations which appear as atomic final-state multiplets (in $M_{IV,V}$, $N_{IV,V}$ absorption) or atomic-like line spectra (in M_{III}, $L_{III,II}$ absorption). The configurations are identified from a distribution of *intensities*

at characteristic energies. It is well known that the precise spectroscopic measurement of absolute intensities, even of relative intensities, is a delicate experimental task. In the following we briefly address the most important error sources which alter the experimental intensities of the absorption lines.

In transmission geometry falsifications of the 'true' intensities or intensity ratios are due to the 'thickness effect' (Parrat et al. 1957, Heald 1983, Heald and Stern 1977, Stern and Kim 1981, Goulon et al. 1982), pin-holes in the absorption foils, 'harmonics' in the monochromized X-ray beam, nonlinearities in the detection systems and finally to spectrometer broadening. All these types of experimental errors result in dampened, distorted lines with wrong intensities. These errors may be avoided with the use of state-of-the-art equipment. However, they can be only partially overcome in experiments carried out with conventional laboratory set-ups. Not surprisingly then the quality of the spectra is different from laboratory to laboratory due to the above listed experimental problems. The strongly different amplitudes of the L_{III} absorption of Eu in Eu_2O_3 displayed in figs. 2 and 4 may serve as an example.

X-ray tubes emit characteristic lines superimposed on the bremsstrahlung continuum. These lines are routinely used for the calibration of the energy axis (± 0.5 eV in the L- region) according to the tabulated numbers of emission lines (Bearden and Burr 1967). Spectrometers in synchrotron labs are usually calibrated from the tabulated position of an adjacent absorption edge. Since the calibration point in absorption edges is not unambiguously defined (inflection point maxima) the absolute energy scale in such spectrometers is usually certain within ± 2 eV. Chemical shifts, i.e. shifts in respect with a reference, however, may be recorded with high precision (± 0.1 eV) tracing simultaneously the sample together with the reference absorber and a third detection system in line. Hence the energy scale E–E_0 of most of the (high pressure) spectra, displayed in this chapter refers to a reference sample.

6. Concepts of $L_{II,III}$ absorption in the lanthanides

The absorption of X-rays by excitation of lanthanide 2p electrons is a simple and sensitive probe of the unoccupied lanthanide 5d states. In the following we treat the L absorption as a single-particle process. Possible many-electron effects are addressed in section 8.2, and in discussing the L absorption in $EuPdP_2$ (section 10.3), Ce (section 12) and CeO_2 (section 14). The experimental evidence for many electron effects in L absorption will turn out that they are insignificant.

According to the dipole selection rules, photoexcitation of a core electron with angular momentum l probes the $l \pm 1$ components of the final state. In the $L_{II,III}$ absorption processes $l - 1$ transitions ($2p \rightarrow 6s$) can be neglected. Their probability is less than 3% of the $l + 1$ ($2p \rightarrow 5d$) transition probability (cf., e.g., Barinski and Nefedow 1969). The contribution of quadrupolar transitions to the absorption coefficient can also be neglected. Quadrupolar transitions turn out to be important only in the higher Z elements (in $L_{II,III}$ absorption for $Z > 70$). Calculated ratios of quadrupolar to dipole transitions for K and L absorption are given in table 2 (Müller and Wilkins 1984).

TABLE 2
Average ratio of the electric-quadrupole to electric-dipole transition probabilities over states up to 40eV above E_F for different core levels (adapted from Müller and Wilkins 1984).

Element	K (1s)	L_I (2s)	$L_{II,III}$ (2p)
$_{13}$Al	0.012	0.004	0.001
$_{29}$Cu	0.058	0.026	0.010
$_{47}$Ag	0.152	0.073	0.029
$_{70}$Yb	0.314	0.194	0.063
$_{79}$Au	0.397	0.270	0.084

$L_{III,II}$ absorption probes the $4f^{n+1}(5d\,6s)^{m-1}$ and $4f^n(5d\,6s)^m$ configurations through the detection of $2p^5\,(5d\,6s)^m$ and $2p^5\,(5d\,6s)^{m+1}$ final-state configurations. The conduction electron configurations are no more purely atomic as the 4f configurations, due to the significant overlap of the 5d and the 6s orbitals with the neighboring atoms. However, they certainly may not be thought as devoid of all configurational correlations. In both configurations they show the effects of different effective charges and are sensitive to the existence of two different atomic volumes and to the symmetry of the environment. Most of the $L_{III,II}$ spectra exhibit more or less broad lines superimposed with weak fine structures. Exchange splittings of the L final states are small and masked by the relatively large lifetime broadening of the core level. Well-split states are caused by the much stronger crystalline or ligand field interaction induced from the overlap of the 5d states with the neighboring atoms. The distribution of experimentally observed final states, filtered out through the selection rules from the total final state multiplet in a crystal, mostly appears as a single and asymmetric line with a width of typical '5d bandwidths' of about 5–8 eV (corrected for lifetime effects). However these widths are not identical with the ordinary single-particle band density of states. Because calculations of such $2p^5$ (V)* final state configurations (V denote the lanthanide valence electron configuration in a crystal or ligand field) have not been performed up to now (although these type of calculations seems to be feasible at least for ionic and covalent compounds), we introduce a phenomenological concept of atomic-like spectral densities (or local density of outer valence states).

6.1. *The atomic approach*

We write the oscillator strength f of a discrete atomic nl–$n'l'$ transition as

$$f(nl\text{–}n'l') = \frac{2m_e(E_{n'l'} - E_{nl})}{3\hbar^2} \frac{l'}{2(l+1)} [R(nl, n'l')]^2. \tag{3}$$

Here n, l denote the quantum numbers of the core state and n', l' of the final state where $l' = l + 1$ only. $E_{n'l'} - E_{nl}$ is the excitation energy from the core state to the final state, m_e is the electron mass, and $R(nl, n'l')$ is the radial matrix element.

f measures the strength of individual lines in a Rydberg series. The linear absorption coefficient $\mu(E)$ can be expressed (in c.g.s. units) through the differential

oscillator strength (spectral density) $df/d\varepsilon$ as

$$\mu(E) = \frac{2\pi^2 e^2}{m_e c} N \frac{df}{d\varepsilon} = A \sum_i df_i/d\varepsilon_i, \tag{4}$$

$N \equiv$ number of absorbing atoms per unit cell. A is a constant, E = photon energy, $d\varepsilon_i$ = energy increment at i, i = number of accessible states with dipole symmetry.

It is useful to treat the atomic absorption below the ionization (discrete line spectrum) and the continuum absorption above the ionization threshold separately. The arctan expression in eq. (1), experimentally confirmed through the K spectra, is a good approximation for the continuum absorption. The atomic absorption lines may be interpreted through optical multiplets using the '$Z + 1$' approximation. The validity of this approximation has been successfully demonstrated in numerous cases of K and L spectra, first by Parrat (1939) in the K absorption of gaseous Ar. Here the optically determined np Rydberg series ($n \geqslant 4$) of K ($Z = 19$; '$Z + 1$') nicely fits the atomic absorption lines of $2s \rightarrow 4p$ (K) X-ray excitation of Ar ('Z'). The $Z + 1$ potential accounts for the creation of the deep core hole. The inflection point of the arctan shaped continuum absorption is located at the series limit, i.e. the first ionization potential.

The L absorption spectra in lanthanide vapors may be interpreted through this type of approximation. Figure 8 models an atomic L_{III} absorption spectrum through a superposition of a lifetime broadened distribution of atomic oscillator strengths and an arctan shaped continous absorption. Due to the relatively large core hole

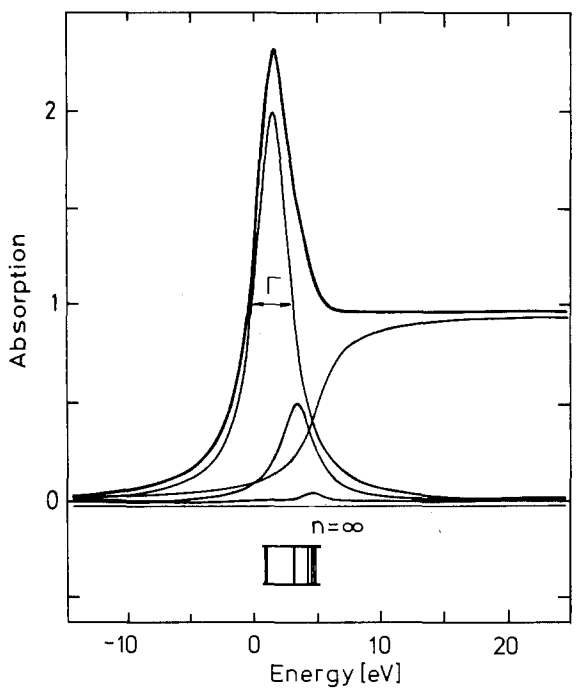

Fig. 8. Lanthanide L_{III} absorption constructed from a superposition of $2p_{3/2}$–nd ($n = 5 \rightarrow \infty$) atomic absorption lines and an arctan curve representing the continuous absorption. The onset of the continuous absorption is fixed at the series limit ($n = \infty$) of the underlying optical spectrum. Γ indicates the total L_{III} core level width (3 eV). The resulting spectral shape matches that of the L_{III} absorption in lanthanide vapors (fig. 10a).

broadening ($\Gamma = 3$ eV) lines other than the $n = 5$ line of the (schematical) Rydberg series cannot be resolved. Obviously the spectral density of the first state describes the main part of the spectrum. The $n \to \infty$ states only broaden the absorption line asymmetrically at high energies. The onset of the transitions into the continuum states is located about 6 eV ($Z + 1$ ionization potential) above the position of the first state.

The effective charge seen in the excitation of atoms in molecules is different from the $Z + 1$ approximation. This is observed due to the charge transfer from or to the neighboring atoms caused by the chemical binding power. Barinski and Nefedow (1969) extend the '$Z + 1$ approximation' to a concept of 'effective charges' describing rather successfully K and L absorption spectra in molecules, ionic and covalent crystals. The concept of 'effective charge' replaces the optical series through an *atomic-like* distribution of spectral densities. Assuming a hydrogen-like potential, the spectral densities are parameterized by η, an 'effective charge' acting on the photoelectron in the open 5d orbital, and n^*, the 'effective quantum numbers' of the 2p–*n*d final state. Vainshtein et al. (1962) applied this semiquantitative formalism to the analysis of the oxidation state in some RB_6 from the *intensities* of the atomic-like absorption. Due to the rather structureless $L_{II,III}$ absorption lines η and n^* are hard to extract from the experimental data. However, the formalism of Barinskii and Nefedow (1969) is useful to understand the existing correlations between the total line intensities and charge transfers from or onto the lanthanide outer valence electron orbitals (cf. section 8.3.1).

6.2. *The X-ray exciton*

The X-ray excitation process frequently is analyzed in terms of an excitonic electron hole pair (e.g. Cauchois and Mott 1949). The excitonic approach to X-ray absorption spectra accounts for the fact that the excited state is a hydrogen-like bound state. The X-ray exciton is different from the well-known optical excitons. In the latter cases the ejected electron polarizes a macroscopic fraction of the crystalline volume because the lifetime of optical excitations is in the order of 10^{-12} s. The lifetime of the excited deep core level state, however, is in the order of 10^{-15}–10^{-16} s, much too short to probe more than the direct vicinity of excited atom. Following Haken and Schottky (1958) the distance r between the ejected electron and core hole of an excited atom for $\varepsilon = 1$ turns out to be $r \propto [\hbar/(2m^*\omega)]^{1/2}$. Here m^* denotes the effective mass of the ejected electron, ω is the phonon frequency and ε is the dielectric constant. A numerical estimate yields $r \ll 10$ Å. Thus the information obtainable in an L_{III} spectrum of the solid is very local; the measurement probes essentially the 5d state of the absorbing atom as modified from the atomic 5d states by its immediate neighbors only. It is not suited to give information about extended Bloch states. On the other hand it is well suited to extract information about local correlations within the 5d conduction electrons, whose proper treatment is at the heart of the difficulty of the theory of narrow band materials and about chemical binding effects.

6.3. *The band structure approach*

Müller and Wilkins (1984) developed a band structure approach calculating the core level absorption spectra of the 4d and 3d (Müller et al. 1982) elements. The same technique has been applied to the calculation of the L_{III} and L_I absorption in Gd up to photon energies of 80eV above E_F (cf. fig. 9). The theoretical absorption coefficients (solid line) fit to the experimental data (dots) of the absorption 'edges', the near edge regions and the extended absorption fine structures (Materlik et al. 1983a). Here we are predominantly interested in the theoretical concept for the calculation of the absorption 'edges' ($0 \leqslant E \leqslant 20$eV). Müller and Wilkins (1984) treat the L absorption in Gd as a single-particle process. Many-body effects turn out to be negligible except for high kinetic energies of the photoelectron (cf. the dashed lines in fig. 9). The absorption spectra are factorized into an 'atomic-like' and a 'solid state' contribution. The solid state contribution is proportional to the distribution of spectral densities obtained from the angular momentum projected *band states*. The band states have been calculated using a periodic muffin-tin (ground-state) potential. The local nature of the X-ray excitation (cf. the X-ray exciton) is treated as the so-called single sphere (impurity) problem. A *single* muffin-tin (ground-state) potential confined in a sphere of the Wigner–Seitz radius is embedded in a constant potential. Thus the atomic-like spectral densities are obtained from core excitations into muffin-tin orbitals in a free electron metal. Broadening the spectral density with a Lorentzian (sum of the inverse lifetimes of the core level and the excited electron) and further convoluting it with a Gaussian, the theoretical absorption coefficient fits to the experimental L_{III} and L_I data of Gd.

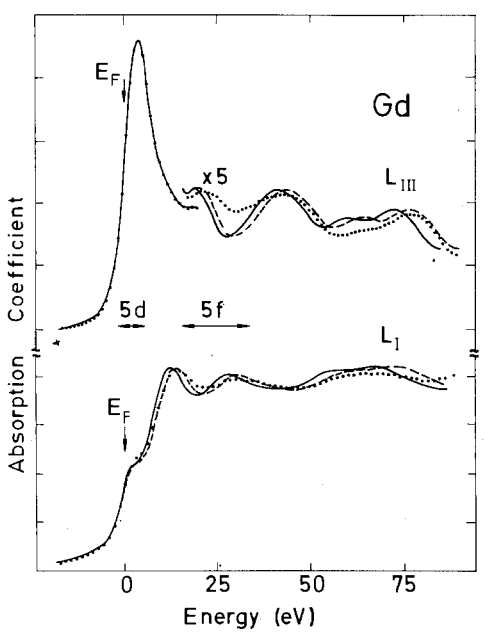

Fig. 9. Experimental (dotted lines) L_{III} and L_I absorption of Gd (Materlik et al. 1983a) together with spectra calculated from the band structure approach of Müller and Wilkins (1984) (solid lines). The dashed lines represent the calculated spectra obtained by rescaling the energy axis by 1.05 (L_{III}) and 1.07 (L_I). The two spectra are lined up at the inflection points of the absorption 'edges', labelled E_F.

In the L_I spectrum the maximum at about 12 eV and the shoulder at the threshold are found to reflect the p-projected density of states in the band structure of the conduction electrons. The L_I spectra give experimental evidence for the well-known fact, that in metals the outer p-symmetrical orbitals are *strongly* hybridized with the outer s- and d-symmetrical orbitals. The coincidence of the maximum in the L_{III} spectra and the valley ('hybridization valley') in the absorption structure of the L_I spectra (fig. 9) is interpreted by Müller and Wilkins (1984) through a phase shift of π between the 2p–5d (L_{III}) and 2s–6p (L_I) transition matrix elements, calculated from wavefunctions normalized within the muffin-tin radius of the Wigner–Seitz cell. This finding might be helpful for the identification of mixed valent states in L_I spectra in connection with the analysis of double-peaked L_{III} spectra. Since mixed valent L_{III} spectra exhibit two high densities of empty 5d states, one expects that mixed valent L_I spectra exhibit a double staircase feature split by about 8 eV. Therefore a systematic comparison of $L_{III,II}$ and L_I spectra might be useful discerning the atomic-like $L_{III,II}$ absorption from adjacent near edge resonances.

The band structure approach has of course its limitations in principle and these limitations can be to some extent detected in practice. For instance it did not yield agreement between theory and experiment with regard to the high energy ($E \simeq 10$ eV) peak in the double peaked $L_{III,II}$ absorption spectra of mixed valent cerium (Lengeler et al. 1983a,b; cf. sections 12, 13, 14). Domashevskaya et al. (1984) attempted to calculate the double peaked L_{III} spectrum of TmSe through a band structure approach, however, they only obtained a single-peaked spectrum in between the two integral valent reference spectra. These negative results constitute a significant breakdown of the band structure approach for mixed valent materials.

7. L absorption in the elemental lanthanides

It is instructive to compare X-ray absorption of the elements in the gaseous state with the absorption in the condensed metallic state. L_{III} and L_I spectra of Ce, Sm, Gd and Er were recorded by Materlik et al. (1983b) (cf. figs. 10a and 10b) in both states. The L_{III} spectra turn out to be similar in that they exhibit sharp absorption lines at thresholds in both aggregates. On condensation Sm and Er undergo a valence transition from the divalent gas to the trivalent crystal while Ce and Gd are trivalent in both states. The gas to solid valence transitions of Sm and Er can be clearly read from the large shifts ($\simeq 8$ eV) of the 2p core level binding energies. These shifts are found to be nearly identical in L_{III} and L_I absorption (cf. section 7.3 and chapters 68 and 69 in this volume). The spectral shapes of the L_I spectra from the absorption in the gas and in the solid, however, turn out to be significantly different. We first discuss the L_{III} spectra in the gas.

7.1. *L absorption in lanthanide vapors*

Consider the L_{III} spectrum of Gd. We first restrict ourselves to the analysis of its spectral *shape*. The significant large atomic to solid state binding energy shifts,

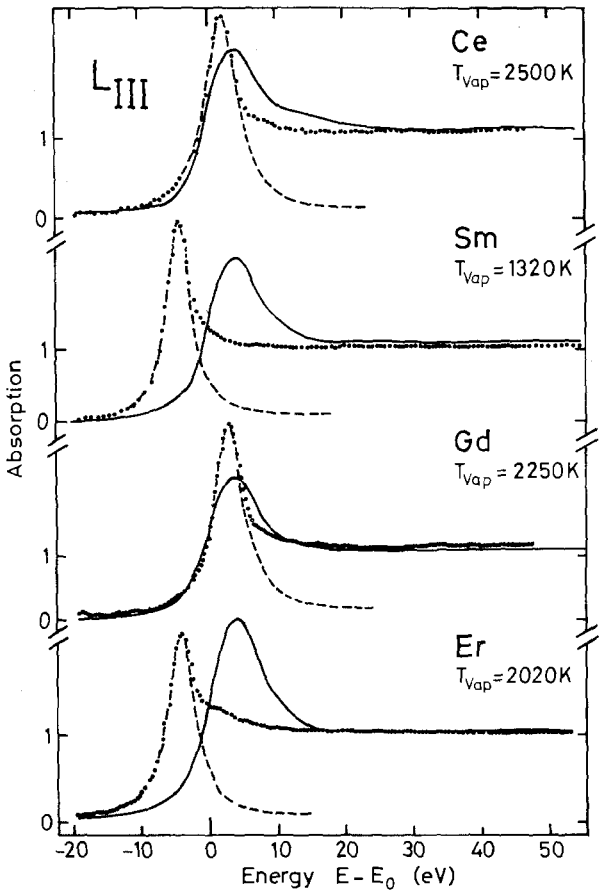

Fig. 10a. L_{III} absorption spectra of Ce, Sm, Gd and Er in the vapor state at T_{Vap} (dotted lines) and in the solid state at ambient temperature (solid lines). The Lorentzian profiles (dashed lines) represent fits to the 2p–5d absorption line (vapor state). The deviation of the experimental curve from the Lorentzian indicates transitions into *n*d ($n = \infty$) states (adapted from Materlik et al. 1983b).

observed in Sm and Er, also expected in Pr, Nd, Dy, Ho, Tm, will be treated further below. The spectrum in the gaseous state (dots in fig. 10a) exhibits a pronounced peak followed by a rather structureless continuous absorption. The absorption line can be fitted with a single Lorentzian of about 4.5 eV (FWHM) as indicated through the dashed line in fig. 10a. It corresponds to the one-electron transition $2p^6_{3/2}4f^7(5d^16s^2) \rightarrow 2p^5_{3/2}4f^7(5d^26s^2)$. The deconvolution of the atomic L_{III} absorption spectra is qualitatively demonstrated in fig. 8. There the slightly asymmetric shape at high energies is attributed to transitions into the series of bound *n*d states.

The experimental linewidth and shape of the atomic absorption line in the gas clearly demonstrates the absence of many-body effects. The observed width (FWHM $\cong$ 4.5 eV) is in good agreement with the calculated number for the total natural linewidth from Keski-Rahkonen (1974) ($\cong$3 eV, cf. fig. 5a) taking into account the $E^{-7/2}$ (Fano and Cooper 1968) dependence of the atomic spectral density. This observation clearly demonstrates that many-electron effects, which could also cause an asymmetric lineshape, do not contribute to the decay of the core

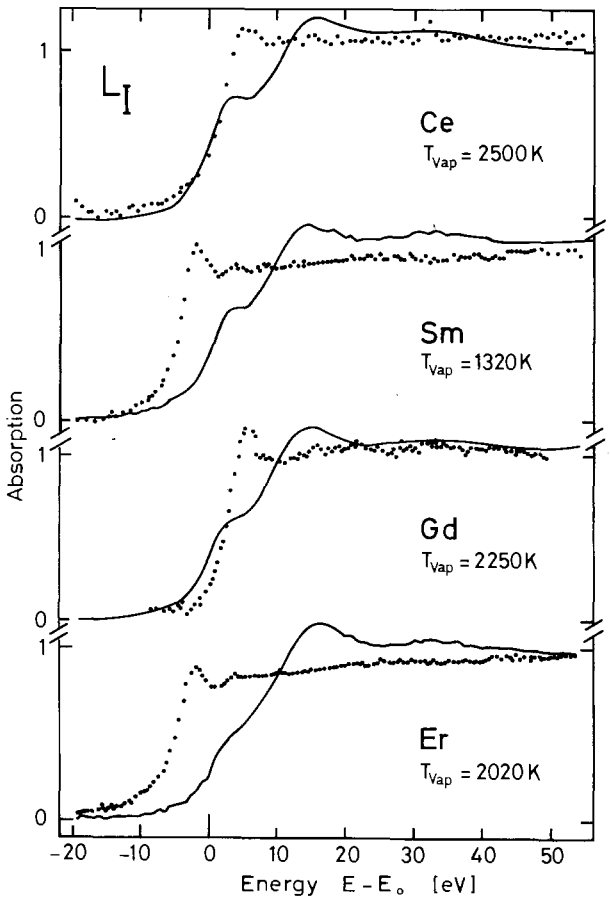

Fig. 10b. L_I absorption spectra of Ce, Sm; Gd and Er in the vapor state (dotted lines) at T_{Vap} and in the solid state (solid lines) at ambient temperature. The small absorption line observed in the vapor state is attributed to 2s–6p transitions (adapted from Materlik et al. 1983b).

hole in the gas. This finding is in contrast to the interpretation of lanthanide $L_{II,III}$ spectra in terms of 'giant resonances' (Bianconi et al. 1982). 'Giant resonances', resulting from many-electron processes, are known from the shallow 4d, 5p core level spectra (cf. the $N_{IV,V}$ spectrum in fig. 6c and the corresponding discussion in section 4).

The L_I spectra from the gas can be understood in the same manner. Here the atomic resonances corresponding to the one-electron transition $2s^2\,4f^7\,5d^1\,6p^0\,6s^2 \rightarrow 2s^1\,4f^7\,5d^1\,6p^1\,6s^2$ are very weak due to the smaller oscillator strengths of the s–p transitions. Nevertheless they are discernible from the absorption edge. Upon condensation into the metallic state, the L_1 spectra lose their atomic character completely (solid line in fig. 10b). The L_1 absorption in the solid state is e.g. described through the band structure approach (cf. section 6.3).

7.2. *L_{III} absorption in lanthanide metals*

Upon condensation from the atomic vapors into the metallic crystals, the L_{III} lines

do not vanish as one might most naively expect from the formation of a 5d band with free conduction electrons. Instead the atomic absorption line remains largely intact; it is merely broadened, and acquires a somewhat distorted, asymmetrical shape. This observation indicates that the 5d states conserve strongly their atomic character upon condensation. However, the overlap of the 5d wavefunctions with neighboring atoms (the chemical binding) causes a characteristic variation of the atomic spectral shape.

Interpretations of the lanthanide L_{III} absorption lines in the framework of many-body theories (Mahan 1974, Nozières and De Dominicis 1969) seem to be less appropriate by the inspection of the experimental data from both aggregates, the vapor and the solid state.

L_{III} absorption spectra of elemental Ce, Pr, Eu, Gd, Tb and Yb recorded by the author at ambient pressure and temperature are displayed in fig. 11. Measurements of the L_{III} absorption in the heavy elemental lanthanides (Sm and Gd–Lu) were performed by Materlik et al. (1983a). Feldhaus (1982) recorded the L_{III} absorption in Eu metal. γ-Ce and α-Ce (77 K, 0 kbar) and La were measured by Lengeler et al. (1983a, 1983b), Lengeler and Zeller (1984). All these recordings were taken with modern equipment allowing a precise determination of the lineshapes and amplitudes. The ratio of the absorption maximum to the absorption jump, measured relative to the background before the threshold, was found to be $2.3 \pm 5\%$ in Sm (2.04 by Kushwaha et al. (1974) from a photographic recording) and in the trivalent heavy (hcp) lanthanides, while it is considerably smaller ($\simeq 1.9$) for the divalent element Yb, crystallizing in the fcc structure. Divalent Eu, on the other hand, exhibits a normalized amplitude of 2.08 ± 0.01 (Röhler 1986b). The significantly smaller amplitudes determined in Ce and Tm by Bianconi et al. (1981), in Eu by Finkel'shtein et al. (1974) indicate strong experimentally caused nonlinearities presumably due to the sample preparation techniques. The L_{III} binding energy measurements in Tb and Tm–Lu by Padalia et al. (1974) exhibit similar strongly dampened amplitudes and therefore result in line positions deviating nonsystematically from those tabulated by Bearden and Burr (1967). Padalia et al. (1974) attribute small bumps at the onset of the absorption line to be quadrupolar transitions into unoccupied 4f states. The quadrupolar transition probabilities, however, are very weak (cf. table 2) and the observation of these transitions could not be reproduced in recordings with a properly defined background.

7.3. *The distribution of atomic-like spectral densities and the atomic volume*

Figure 11 (left-hand side) displays the normalized L_{III} absorption spectra of elemental Ce, Pr, Gd, Tb and Yb together with the spectrum of Eu (dashed line) plotted as reference. The positions are aligned at E_0 defined by the intersection points of the extrapolated high-energy absorption with the leading edge of the absorption lines. Apparently the divalent elements Eu and Yb exhibit distinctly narrower absorption lines than the trivalent elements. Consider the absorption lines of the trivalent elements Pr, Gd and Tb. Notwithstanding the different crystalline structures dhcp (Pr) and hcp (Gd, Tb), the width (measured at the average of the

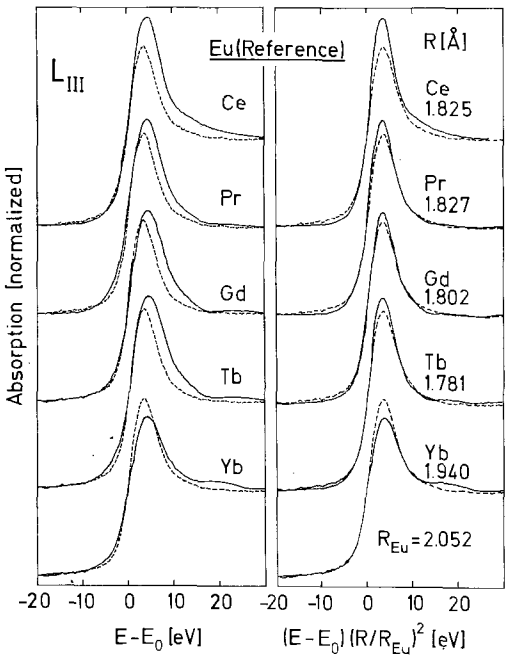

Fig. 11. (*Left-hand side*) L_{III} absorption spectra of Ce, Pr, Gd, Tb and Yb (solid lines) ligned up with the L_{III} absorption spectrum of Eu (dashed lines) at E_0. E_0 defines intersection of the atomic-like absorption lines with the average absorption at high energies. (*Right-hand side*) The same spectra as on the left side, however, the energy axis is scaled with $(R/R_{Eu})^2$. R denotes the metallic radii in Å, R_{Eu} is the metallic radius of europium from Matthias et al. (1967).

high-energy absorption, $\mu d = 1$) increases with the lanthanide contraction. Seemingly this width of the L_{III} absorption lines varies with the atomic volume (or the Wigner–Seitz radius) of the lanthanide atoms. The spectrum of mixed valent γ-Ce exhibits a shoulder at high energies and therefore deviates from the systematics.

Figure 11 (right-hand side) plots the same spectra of Ce, Pr, Gd, Tb and Yb on the energy scale E–E_0 factorized by $(R/R_{Eu})^2$. Again the Eu reference spectra are indicated by dashed lines. R denotes the metallic radii (equivalent to the Wigner–Seitz radii), $R_{Eu} = 2.052$ Å is the metallic radius of Eu. Using the metallic radii from Matthias et al. (1967) this rescaling aligns the spectra of the trivalent elements and of divalent Yb with the linewidth ($\mu d = 1$) of Eu. Clearly the amplitudes remain unchanged. The observed scaling behavior of the widths (at $\mu d = 1$) may be understood from the kinetic energy of free electron states in a given volume. Assumed that the empty 5d states are projected free electron states inside a sphere with the metallic radius R. Then a change of the relative volume rescales the energy dependence of the density of states with $(V/V_0)^{2/3} \equiv (R/R_{Eu})^2$ (cf. section 6.3 and Müller and Wilkins (1984), Albers et al. (1985)). Surprisingly the scaling procedure works already using the ground-state volumes. Since we ignored the volume effect on the energy dependence of the 2p–5d transition matrix element, we do not expect coinciding amplitudes. However, the relative widths (at $\mu d = 1$) may be taken as a relative measure of different Wigner–Seitz volumes in different valence states, at least in good metals. In homogeneously mixed valent systems these widths are in general different in the two valence states, also. This means that the Thomas–Fermi kinetic energy of the 5d electrons depends on the individual valence states and is translationally invariant in compounds only on time scales larger than the longest

lifetimes T_n or T_{n+1}. At shorter time scales, the homogeneously mixed valent material is better viewed as an alloy; in fact the L_{III} experiment can only probe this alloy aspect (cf. section 8). In most mixed valent spectra the individual widths can be disentangled from the other spectroscopic parameters (cf. eq. (7)). Correlations of these numbers with, e.g., the fractional valence will be addressed in section 12.

8. Mixed valence in lanthanide solid state physics

Since 1970 or so lanthanide mixed valence has moved into the centre of interest of fundamental solid state research. The increasing amount of the experimental and the theoretical work in this field is, e.g., documented in the 'Proceedings of the International Conferences on Valence Fluctuations' (Parks 1977, Falicov et al. 1981, Wachter and Boppart 1982, Müller-Hartmann et al. 1985).

X-ray absorption spectroscopies, i.e. $M_{IV,V}$ and $L_{II,III}$ absorption are routinely used in the physics of mixed valence for the identification of the atomic configurations and the measurement of their relative fractions. In particular L_{III} absorption has acquired an increasingly important role in this field. At the same time the complexity of the mixed valence problem stimulated also much basic theoretical and experimental work on the X-ray processes in the lanthanides. In the following we shall first outline our basic concept of mixed valence in lanthanide solids. For more details of this concept we refer to Wohlleben and Coles (1973) and Wohlleben (1984a, 1984b). We then give a general description of the information obtainable on mixed valence by L_{III} absorption.

8.1. *Homogeneous mixed valence*

In mixed valence materials macroscopic and microscopic measurements indicate the coexistence of two adjacent valence states of the lanthanide atom. There are two types of such solids. In one the two valence states occur on crystallographically distinguishable sites (inhomogeneously mixed valence). The main interest is in the other type, where the lanthanide atoms occupy only sites with identical point symmetry (homogeneously mixed valence). Such solids are certain intermetallic compounds and related sufficiently dilute lanthanide alloys and certain elements.

The focus of interest in homogeneously mixed valence is the 4f electron delocalization. In normal lanthanide solids (which have by definition integral lanthanide valence), the number of inner 4f electrons is integral. Moreover the 4f electrons then remain completely localized on a given lanthanide atom as all other inner core electrons; there is no 4f band formation. The outer 5d6s valence electrons are delocalized conduction electrons (Wannier states of the solid).

In a homogeneous mixed valent material an electron must temporarily leave the 4f shell. After the valence transition from 4^{n+1} to $4f^n$ it occupies one of the Wannier states of the outer 5d6s shell on the atom in question. It may get there in more than one intermediate step, but it must end up in the valence electron shell of the *same atom* because of local charge neutrality, at least in a metal. In the reverse transition

this or another electron will come back to the 4f shell. Thus in homogeneously mixed valent materials the 4f electron is effectively delocalized.

A rather successful description of the dynamics of 4f electron delocalization is in terms of valence fluctuations. The coexistence of two valence states on a single site implies average fractional valence of each lanthanide atom. Unless stated otherwise, by an integral valence state we mean the state of an *electrically neutral configuration* of a lanthanide atom. This state compromises several subconfigurations: that of the inner Xe core [Xe], that of the inner 4f shell ($4f^n$) and that of the outer 5d6s shell $(5d6s)^m$. n is the number of f electrons and m counts the electrons in the (5d6s) shell (valence electrons). The dynamics of a valence fluctuating atom is described through three timescales: the transition time T_t between the two states of different valence (an effective tunneling time) and the lifetimes T_n and T_{n+1} in the two valence states with n and $n+1$ 4f electrons. The transition time has a lower limit of about 10^{-15} s, given by the inverse conduction electron bandwidth. In ordinary valence fluctuators the lifetimes are of the order 10^{-13} s, but they can reach 10^{-11} s at low temperatures in the so-called heavy fermion systems. The atomic correlations within the two valence states become the more important the longer the lifetimes T_{n+1} and T_n are compared to the transition time T_t. Long lifetimes T_{n+1} and T_n compared to the transition time are therefore a necessary prerequisite for the validity of the concept of valence fluctuations.

Because of the long lifetimes T_{n+1} and T_n the 4f delocalization is characterized by slower timescales than that of all other partially filled atomic (s, p and d) shells. The effective f bandwidth, which may be identified with the lifetime widths $\hbar/T_n$ and $\hbar/T_{n+1}$, is e.g. at least one order of magnitude smaller than the bandwidths of delocalizing d shells; in the extreme case of so-called heavy fermion systems, the effective 4f bandwidth is of order 1 meV.

Accordingly we define fractional valence by the time-averaged ratio of the occupation probabilities of the two integral valence states. If the population of the higher valence state is v, the fractional valence is defined by

$$v = v_1 + v, \tag{5}$$

v_1 is the valence of the lower integral valence state. This definition of fractional valence rests on the assumption that there are two and only two atomic valence configurations with finite amplitude in the ground and excited states of the solid, such as $[Xe]4f^{n+1}\,5d^1\,6s^2$ and $[Xe]4f^n\,5d^2\,6s^2$, with a one-to-one correspondence in the number of inner 4f and outer 5d6s electrons. In principle it is possible to have a more complicated situation, for instance, three configurations like $[Xe]4f^{n+1}\,5d^0\,6s^2$, $[Xe]4f^n\,5d^0\,6p^1\,6s^1$ and $[Xe]4f^n\,5d^1\,6s^2$. Optical spectroscopies and thermodynamic data (Brewer 1971) suggest that in Eu and Yb these three configurations are close in energy (within 2 eV) in neutral atoms. Note that while all three atomic configurations differ with respect to the valence electron configurations, two have the same 4f shell configurations. In such a case the definition of fractional valence via configurational ratios becomes more complicated. So far there is no clear experimental evidence for such a situation, but the possibility should be kept in mind.

A thorough understanding of homogeneously mixed valent lanthanide solids

promises control over the general problem of narrow band solids which is also encountered in actinide and transition metals. This problem is theoretically very difficult; single electron band theory, e.g., seems to be inadequate. Hence the intense experimental and theoretical activity in lanthanide mixed valent solids.

8.2. *X-ray absorption in mixed valent systems*

As pointed out in section 4, X-ray absorption spectroscopies with d–f symmetry ($M_{IV,V}$, $N_{IV,V}$) prove directly the inner 4f configurations; while those with p–d symmetry ($L_{II,III}$, M_{III}) probe the outer valence electron configurations. $M_{IV,V}$ absorption exhibits rather sharp final-state multiplets which may serve as fingerprints of the 4f configurations. The atomic final state multiplets of the $M_{IV,V}$ spectra reproduce unambiguously the localized nature of the 4f configurations, i.e., the solid state exhibits well-defined atomic configurations. If delocalization effects in the solid state occur, the $M_{IV,V}$ absorption spectroscopies observe them through a second (atomic) 4f final-state *multiplet*. In other words: $M_{IV,V}$ absorption spectra prove directly, that 4f delocalization in the lanthanides is synonymous with the coexistence of *two 4f configurations*. Even strong 4f delocalization is unable to break up the individual Hund-rule correlations within the two 4f configurations. Accordingly the mixing ratio of the two 4f configurations and their adjacent valence electron configurations is considered to be a key parameter for understanding 4f delocalization phenomena. Hence the strong activity in the field of spectroscopic valence measurements through X-ray absorption. Table 3 summarizes most of the numbers obtained up to now from L_{III} absorption.

The application of $M_{IV,V}$ absorption to valence measurements is still at its infancy at this time, although first studies were started already in 1973 by Ottewell et al. (1973) and recently continued by Kaindl et al. (1983b, 1984) and by van der Laan et al. (1986). Analytic procedures for the extraction of the 4f occupation numbers from two complicated and superimposed $M_{IV,V}$ final-state multiplets require the existence of reliable theoretical calculations of their intensities and positions in each valence state, which are available only recently (Thole et al. 1985). In addition the special experimental problems of $M_{IV,V}$ absorption, e.g., saturation effects and surface shifts diminish drastically the potential of $M_{IV,V}$ absorption as a tool for high-precision valence determinations.

In $L_{II,III}$ absorption there is no more detailed information on the state of the 4f shell as in the $3d^9 4f^{n+1}$, $3d^9 4f^n$ final-state multiplets as in $M_{IV,V}$ absorption. Identification of the different 4f configurations involved in the mixed valent state can only be done *indirectly* by identifying the corresponding two outer valence electron configurations at characteristic binding energies. The individual $L_{III,II}$ line intensities may be obtained from a straightforward integration procedure (section 8.3.). By the relative strength of the two peaks, L_{III} absorption measures the ratio of the two lifetimes T_n and T_{n+1} or the degree of fractional valence. This valence measurement was the original motivation for L_{III} absorption measurements on mixed valent materials, and is still the most important one. The L_{III} method turned out to be in general superior to all other measurements of the fractional valence. The main

TABLE 3

L_{III} valence summary for lanthanide systems with instable lanthanide atoms. In those cases where valence numbers were not given, we list estimates in parentheses (see section 8.3). M/R under column x means 'matrix to lanthanide ratio'.

Lanthanum	x	v	T [K]	p [kbar]	Ref.
$LaAl_2$		3	300	0	1
		2.9	300	0	75
$LaCu_2Si_2$		3	300	0	1
LaF_3		(3)	300	0	2a
		3	300	0	1
$LaGe_2$		(3)	300	0	35a
$LaNi_5$		(3)	300	0	45
$LaNi_2Ge_2$		3	300	0	1
$LaNi_2Si_2$		3	300	0	1
La_2O_3		(3)	300	0	2a
$LaPd_3$		3	300	0	1
		(2.88)	300	0	3a
		(3)	300	0	45
$LaPO_4$		(3)	300	0	2a
$LaRu_2$		(3)	300	0	45
LaSb		(3)	300	0	2a
$LaSi_2$		(3)	300	0	35

Cerium	x	v	T [K]	p [kbar]	Ref.
Ce		3.03–3.32	300	0–120	42
γ-Ce		(3.03)	300	0	41a
		3	300	0	33a
α-Ce		(3.2)	77	0	41a
$(Ce_{0.05}\underline{Zr})B_{12}$		3.0	300	0	70a
PdCe 2%		(3.37)	300	0	41a
ScCe 4.5%		(3.20)	300	0	41a
YCe 3.7%		(3.06)	300	0	41a
YbCe 4.6%		(3)	300	0	41
$Ce_{0.17}La_{0.83}$		3.01	300	0	31
$Ce_{0.12}Sc_{0.88}$		3.08	300	0	31
$Ce_{0.17}Th_{0.87}$		3.16	300	0	60
$Ce_{0.15}Y_{0.85}$		3.01	300	0	31
Ce in 1N H_2SO_2 solution		$3^+/4^+$	300	0	82
Ce in 6N $HClO_4$ solution		$3^+/4^+$	300	0	82
Ce in H_2O acidified with HNO_3		3	300	0	82

TABLE 3 (cont.)

Cerium	x	v	T [K]	p [kbar]	Ref.
$CeAl_2$		3.0	300	0	1, 26
		3.038 ± 0.002–3.042 ± 0.002	300–9	0	4
		3.02–3.26	300	0–120	75, 20
		>3.00	300	0	35
	amorphous	3.0	300	0	61
$Ce_{1-x}Sc_xAl_2$		3	300	0	26
		3.07	300	0	26
$CeAl_3$		$3.091 \pm 0.002 - 3.094 \pm 0.002$	300–9	0	4
$CeAu_2Si_2$		3	300	0	31
$CeBe_{13}$		3.10 ± 0.05	300	0	5a
		3.04	300	0	8
		3.04–3.39	300	0–160	77
$CeCd_3$		3.0	300	0	31
$Ce_{24}Co_{11}$		3.08	300	0	31
$CeCo_2$		3.27 ± 0.05	300	0	1
		3.32	300	0	31
		4	300	0	53a, 72
$CeCo_5$		3.20 ± 0.05	300	0	5a
		3.29 ± 0.01	300	0	26
		3.29	300	0	31
Ce_2Co_{17}		3.29	300	0	31
$CeCo_2Ge_2$		3.09	300	0	31
$CeCo_2Si_2$		3.19	300	0	31
		3.15 ± 0.02	300	0	55
		3.18 ± 0.02	300	0	62
$CeCu_2$		3	300	0	31
$CeCu_5$		3	300	0	31
$CeCu_6$		3.118 ± 0.002–3.115 ± 0.002	300–9	0	4
$CeCu_2Ge_2$		3.01	300	0	31
$CeCu_2Si_2$		3	300	0	1
		3.03	300	0	8
		3	300	0	33
		3.07	300	0	31
		3.066 ± 0.002–3.068 ± 0.002	300–15	0	4a
		3.105 ± 0.002–3.115 ± 0.002	300–9	0	4b
		$\leqslant 3.02$	300	0	55
		3.054 ± 0.02–3.394 ± 0.03	300	0–200	78a
$(Ce_{1-x}Th_x)Cu_2Si_2$	0	3.08	300	0	60
	0.6	3.03	300	0	60
CeF_4		3.85 ± 0.06	300	0	1a
		3.87 ± 0.03	300	0	sect. 14
$CeFe_2$		3.30 ± 0.05	300	0	1
		3.27	300	0	31
Ce_2Fe_{17}		3.28	300	0	31

TABLE 3 (cont.)

Cerium	x	v	T [K]	p [kbar]	Ref.
$Ce(Fe_{1-x}Mn_x)$	0.25	3.24	300	0	31
	0.5	3.18	300	0	31
$CeFe_2Ge_2$		3.05	300	0	31
$CeFe_2Si_2$		3.18	300	0	31
		3.21 ± 0.02	300	0	55
		3.18 ± 0.02	300	0	62
$CeGe_2$		3	300	0	35
$CeIn_3$		3.02	300	0	1
CeInAu		3	300	0	1
		3.03	300	0	8a
$CeInAu_2$		3	300	0	1
		3.05	300	0	8b
$CeIr_2$		3.23 ± 0.05	300	0	1
		3.2	300	0	35
$Ce(Ir_xPt_{1-x})_2$	1	3.24 ± 0.01	300	0	74
	0.8	3.215 ± 0.01	300	0	74
	0.7	3.22 ± 0.01	300	0	74
	0.5	3.18 ± 0.01	300	0	74
	0	3.095 ± 0.01	300	0	74
$CeMn_2Ge_2$		3.01	300	0	31
$CeMn_2Si_2$		3.13	300	0	31
CeN		(–)	300	0	41b
Ce_7Ni_3		3.03	300	0	31
CeNi		3.06	300	0	31
$CeNi_2$		3.26 ± 0.05	300	0	1
		3.25 ± 0.05	300	0	5a
		3.20	300	0	31
$CeNi_3$		3.27	300	0	31
Ce_3Ni_7		3.28	300	0	31
$CeNi_5$		3.32 ± 0.05	300	0	1
		3.20 ± 0.05	300	0	5a
		3.29	300	0	31
		3.15	300	0	59
$Ce_{0.1}R_{0.9}Ni_5$	R = La	3.13	300	0	59
	Ce	3.15	300	0	59
	Pr	3.14	300	0	59
	Gd	3.15	300	0	59
	Er	3.15	300	0	59
	Lu	3.16	300	0	59
$CeNi_2Ge_2$		3.07 ± 0.02	300	0	8
		3.06	300	0	31
$CeNi_2Si_2$		3.20 ± 0.02	300	0	1
		3.15	300	0	31
		3.17 ± 0.02	300	0	55
		3.15 ± 0.02	300	0	62

TABLE 3 (cont.)

Cerium	x	v	T [K]	p [kbar]	Ref.
$(Ce_{1-x}Th_x)Cu_2Si_2$	0	3.19	300	0	60
	0.58	<3.19	300	0	60
$CeNO_3$		3	300	0	2
CeO_2		3.65 ± 0.06	300	0	1a
		3.32 ± 0.05	300	0	1
		4	300	0	5a
		3.50	300	0	27
		3.85 ± 0.05	300	0–260	81, sect. 14.2
$CeOs_2$		3.24	300	0	75
$CeOs_2Si_2$		3.08	300	0	31
$CePb_3$		3.21	300	0	1b
$CePd_2Si_2$		3.01	300	0	31
		3.0	300	0	35a
$Ce(Pd_{1-x}Ag_x)_3$	1.0	3.00 ± 0.02	300	0	31
	0.2	3.08 ± 0.02	300	0	32
	0.13	3.00	300	0	52
	0.09	3.01	300	0	52
	0.05	3.06	300	0	52
$CePd_3$		3.16 ± 0.02	300	0	32
		3.15 ± 0.05	300	0	5
		3.10	300	0	52
		3.17	300	0	26
		3.23 ± 0.05	300	0	1
		3.29 ± 0.05	23	0	1
	amorphous	3.29	300	0	61
		3.17	300	0	61
$Ce_{1-x}La_xPd_3$	0.0	3.17	300	0	26
	0.4	3.23	300	0	26
	0.75	3.09	300	0	26
$Ce_{1-x}Y_xPd_3$	0.0	3.17	300	0	26
	0.1	3.22 ± 0.02	300	0	32
	0.2	3.23 ± 0.02	300	0	32
	0.25	3.22 ± 0.02	300	0	32
	0.4	3.28 ± 0.02	300	0	32
		3.29	300	0	26
	0.78	3.32 ± 0.02	300	0	32
$Ce_{1-x}Th_xPd_3$	0.0	3.17	300	0	26
	0.4	3.10	300	0	26
$CePO_4$		(3)	300	0	2a
$CePt_2Si_2$		3.0	300	0	31
$CeRh_2$		3.24 ± 0.02	300	0	8
$CeRh_2Si_2$		3.02	300	0	31
		3.0	300	0	35a
		(3.05)	25–300	0	54

TABLE 3 (cont.)

Cerium	x	v	T [K]	p [kbar]	Ref.
$Ce(Pd_{1-x}Rh_x)_3$	0.05	3.13	300	0	52
	0.1	3.20 ± 0.02	300	0	32
	0.116	3.17	300	0	52
	0.16	3.19	300	0	52
	0.20	3.20	300	0	52
	0.25	3.21	300	0	52
	0.30	3.21	300	0	52
	0.35	3.28 ± 0.02	300	0	32
	0.40	3.21	300	0	52
	0.6	3.27 ± 0.02	300	0	32
$CeRh_3$		3.29 ± 0.05	300	0	1
		3.21	300	0	52
		3.15 ± 0.05	300	0	5a
		3.27 ± 0.02	300	0	32
$CeRu_2$		3.30	300	0	8
$CeRu_2Si_2$		3.03	300	0	31
		3.0	300	0	35a
$CeRu_4B_4$		3.20 ± 0.05	300	0	5
CeSb		3	300	0	7
$CeSb_{0.05}Te_{0.95}$		3	300	0	7
CeSe		3	300	0	7
$CeSi_2$		3.05	300	0	35
$CeSn_3$		3	300	0	1
		3.02	300	0	8
$Ce(SO_4)_2$		(3.9)	300	0	2a
		3.85	300	0	cf. sect. 14
CeTe		3	300	0	7
Ce_3Te_4		3	300	0	7
$CeZn_2$		3.01	300	0	31
Praseodymium	x	v	T [K]	p [kbar]	Ref.
Ar/Pr	M/R = 580:1	2.42	5	0	10
Kr/Pr	580:1	2.40	5	0	10
$(Pr_x\underline{Zr})B_{12}$	0.01	3.0	300	0	70
	0.045	3.0	300	0	70
	0.15	3.0	300	0	70
Pd<u>Pr</u> 3%		3.10	300	0	23
Pd<u>Pr</u> 1.4%		3.10	300	0	23
$PrAl_2Ga_2$		3	300	0	48a
$PrCo_2$		3	300	0	1
$PrCo_5$		(3)	300	0	45
$PrCu_2Ge_2$		3.00	300	0	40
		3	300	0	48

TABLE 3 (cont.)

Praseodymium	x	v	T [K]	p [kbar]	Ref.
$PrCu_2Si_2$		3	300	0	48
$PrGe_2$		3	300	0	35
$PrIr_2$		3	300	0	35
$PrNi_2$		(3)	300	0	45
$PrNi_5$		(3)	300	0	45
Pr_2O_3		3	300	0	1
Pr_6O_{11}		3.17 ± 0.05	300	0	1
PrO_2		3.40	300	0	27
$PrPd_3$		(3)	300	0	45
$PrRu_2$		(3)	300	0	45
$PrSi_2$		3.00	300	0	35

Neodymium	x	v	T [K]	p [kbar]	Ref.
Ar/Nd	M/R = 940:1–180:1	2.33–3.0	5	0	10

Samarium	x	v	T [K]	p [kbar]	Ref.
$SmAl_2$		3.0	300	0	9
		3.0	300	0	36
Ar/Sm	M/R = 440:1–6:1	2.0–2.8	5	0	10
Kr/Sm	M/R = 135:1–3.5:1	2.0–2.8	5	0	10
SmB_6		2.6–2.53	300–4.2	0	24
		2.6–2.81	300	0–100	80
$Sm_{1-x}Ba_xB_6$	0–0.9	2.57–3.0	300	0	57
$Sm_{1-x}Ca_xB_6$	0–1.0	2.53–2.72	300	0	57
$Sm_{0.1}Dy_{0.9}B_6$		2.42	300	0	57
$Sm_{1-x}Eu_xB_6$	0–0.9	2.53–3.0	300	0	57
$Sm_{1-x}Gd_xB_6$	0–0.9	2.53–2.34	300	0	57
$Sm_{1-x}La_xB_6$	0–0.75	2.6–2.30	300	0	28
	0.25	2.44–2.35	300–4.2	0	24
	0–0.70	2.53–2.36	300	0	57
$Sm_{1-x}Sr_xB_6$	0–0.72	2.6–2.8	300	0	28
$Sm_{1-x}Yb_xB_6$	0–0.88	2.6–2.95	300	0	28
	0.9	2.85	300	0	57
$Sm_{1-x}Y_xB_6$	0–0.82	2.6–2.30	300	0	28
$Sm_{1-x}Th_xB_6$	0–0.88	2.6–2.25	300	0	28
Sm_4Bi_3		(2.2)	300	0	49a
$SmCu_2Ge_2$		3.0	300	0	37
		3.0	300	0	40
SmO		2.0	10	0	11, 6

TABLE 3 (cont.)

Samarium	x	v	T [K]	p [kbar]	Ref.
$SmO_{0.07}S_{0.93}$		2.55	10	0	11
Sm_2O_3		3.0	300	0	85, 7
SmS		2	300	0	7
		2.10 ± 0.02–2.90 ± 0.02	300	0–72	12, sect. 9.1
		2.12 ± 0.05–2.42 ± 0.05	300	0–7.5	13
		2	300	0	37
			300	0	51
		2.1	300	0	76
$Sm_{1-x}As_xS$	0.04	2.25	300	0	76
	0.25	2.60	300	0	76
$Sm_{1-x}Sc_xS$	0.09	2.30	300	0	81
	0.14	2.63	300	0	81
	0.19	2.82	300	0	81
	0.24	2.61	300	0	81
	0.29	2.49	300	0	81
$Sm_{1-x}P_xS$	0.1	2.6	300	0	76
	0.3	2.75	300	0	76
$Sm_{1-x}Pr_xS_{1-x}Se_x$		2.04–2.10	300	0	14
$Sm_{1-x}Gd_xS$	0.14	2.32	25–300	0	44
	0.18	2.20–2.50	44–300	0	7a
	0.18	2.30–2.60	44–300	0	7b
	0.18	2.32–2.58	25–300	0	44
$Sm_{0.75}Y_{0.25}S$		2.40 ± 0.04	77	0	15
		2.53 ± 0.04	300	0	15
$Sm_{0.8}Y_{0.2}S$		2.22 ± 0.05–2.53 ± 0.05	77–300	0	15
Sm_2S_3		3	300	0	51
Sm_3S_4		2.62	300	0	51
SmSb		3	300	0	6
SmSe		2.18 ± 0.03–2.58 ± 0.03	300	0–55	sect. 9
SmTe		>2.0	300	0	7

Europium	x	v	T [K]	p [kbar]	Ref.
Eu		2.03 ± 0.03–2.64 ± 0.02	300	0–340	16
		2	300	0	79, 83, 50a
$EuAl_2$		>2.0	300	0	9
		2.0	300	0	36
$EuAl_2Ga_2$		2	300	0	48a
$EuAg_{2-x}Co_xSi_2$	0.0	2.0	300	0	22
	0.6	2.05 ± 0.02	300	0	22
	1.0	2.06 ± 0.02	300	0	22
	1.4	2.13 ± 0.02	300	0	22
	1.6	2.42 ± 0.02	300	0	22
	1.8	2.82 ± 0.02	300	0	22
	2.0	3.00 ± 0.02	300	0	22
EuC		2	300	0	79

TABLE 3 (cont.)

Europium	x	v	T [K]	p [kbar]	Ref.
EuC_2		2	300	0	79
EuC_6		2	300	0	79, 82
$EuCl_3$		3	300	0	79
$EuCo_2As_2$		2.055 ± 0.05	300	0	46a
$EuCo_2P_2$		2	300	0	29
$EuCu_2Ge_2$		2	300	0	37, 40, 49
		2.17 ± 0.01	300	0	46a
		2.11 ± 0.04	300	0	1
$EuCu_2Si_2$		2.6–2.76	300–20	0	17, sect. 10.1
		2.4	300	0	22
		2.6–2.8	300–77	0	49
$Eu_{0.07}Y_{0.93}Cu_2Si_2$		2.65–2.80	6–300	0	18, sect. 10.1
$EuCuSi_3$		2.0	300	0	43
$EuCu_{1.5}Si_{2.5}$		2.2	300	0	43
$EuCu_{2.25}Si_{1.75}$		2.55	300	0	43
EuF_2		2	300	0	79
EuF_3		3	300	0	37
$EuFe_2Si_2$		2.94 ± 0.02	300	0	22
$EuNi_2Si_2$		2.9	300	0	21
$EuNi_2P_2$		2.6	77–300	0	29
		2.58 ± 0.05–2.43 ± 0.05	15–300	0	58
EuO		2.09–2.40	300	0–300	19
		2	300	0	7
		(2.08)	300	0	51
Eu_2O_3		3	300	0	7, 51, 79a
Eu_3O_4		2.65 ± 0.05	300	0	51
$Eu_{0.95}Sm_{0.05}O$		2.0	300	0	7
$Eu_{0.92}Sm_{0.08}O$		2.0	300	0	7
Eu_2O_2S		(2.9)	300	0	51
$EuPd_3$		3	300	0	56
		2.95	300	0	76
		3	300	0	79
$EuPd_3B$	0.25	2.95	300	0	76
	0.5	2.6 ± 0.1	95–300	0	56
	0.5	2.6	300	0	76
	0.75	2.6	300	0	76
	1.0	2.4 ± 0.1	95–300	0	56
		2.5	300	0	76
$EuPd_3Be_{0.5}$		2.95	300	0	76
$EuPd_3Si_{0.25}$		2.95	300	0	76
$EuPd_2Ge_2$		2	300	0	30
		2.10 ± 0.01	300	0	46a
		2.05 ± 0.01–2.07 ± 0.01	300	0	46c

TABLE 3 (cont.)

Europium	x	v	T [K]	p [kbar]	Ref.
$EuPd_2Si_2$		2.19–2.60	300	0–29	12
		2.36–2.70	300–20	0	17
		2.30–2.70	300–120	0	30
		2.29 ± 0.03–2.72 ± 0.03	300–15	0	58a
		2.33–2.76	300–77	0	63
$EuPd_2P_2$		2.15 ± 0.05	300	0	25
		2.15 ± 0.01	300	0	46a
		2.11 ± 0.01	300	0	46b
		2.17 ± 0.03–2.46 ± 0.03	300	0–170	sect. 10.3
$Eu_{0.05}Y_{0.95}Pd_2P_2$		2.20 ± 0.01	300	0	46a
$EuRu_2Si_2$		3.0	300	0	30
EuS		2	300	0	51
α-Eu_2S_3		2.66 ± 0.02	300	0	51
$Eu_2S_{3.81}$		2.77 ± 0.02	300	0	51
Eu_3S_4		2.63 ± 0.02	300	0	51
EuTe		2.0	300	0	7
$Eu_{0.5}Yb_{0.5}Te$		>2.0	18 and 300	0	7

Terbium	x	v	T [K]	p [kbar]	Ref.
$(Tb_{0.05}Zr)B_{12}$		3.0	300	0	70
$TbAl_2$		3.0	300	0	36
$TbCu_2Ge_2$		3.0	300	0	36
		3.0	300	0	36, 40
$TbCu_2Si_2$		3.0	300	0	36, 40
$TbMn_2$		3.0	300	0	36, 37
TbO_2		3.7	300	0	27

Thulium	x	v	T [K]	p [kbar]	Ref.
$TmAl_2$		3	300	0	38, 36
$TmCu_2Si_2$		3	300	0	38
$TmCu_2Ge_2$		3	300	0	36, 40
$TmGa_2$		3	300	0	38
$TmMn_2$		3	300	0	38
TmNi		3	300	0	38
$TmNi_2$		3	300	0	38
$TmNi_3$		3	300	0	38
$TmNi_5$		3	300	0	38

TABLE 3 (cont.)

Thulium	x	v	T [K]	p [kbar]	Ref.
Tm_2Ni_{17}		3	300		38
TmS		<3.00	300		34
$Tm_{1-x}La_xS$	0	3.00 ± 0.02	300		64
	0.15	3.00 ± 0.03	300		64
	0.30	2.95 ± 0.03	300		64
	0.75	2.90 ± 0.03	300		64
	0.90	2.88 ± 0.03	300		64
TmSe		2.58 ± 0.07	300–10		34
		2.6	300		65
		2.665 ± 0.005–2.675	300–30		67
		2.65 ± 0.02	300		1
		2.66–2.77	300		12a, sect. 9.2
$Tm_xLa_{1-x}Se$	0.03	2.735 ± 0.005–2.63	300–30		67
	0.05	2.72 ± 0.02	300		1
	0.1	2.760 ± 0.005–2.727	300–30		67
$Tm_xYb_{1-x}Se$	0.43	2.45 ± 0.05	300		66
$Tm_xY_{1-x}Se$	0.05	2.62 ± 0.005–2.54	300–30		67
	0.1	$2.635 \pm 0.005 - 2.57$	300–30		67
	0.2	2.64 ± 0.005	300		67
	0.25	2.654 ± 0.005–2.57	300–30		67
$TmMn_2$		3	300		36,37
TmTe		>2.00	300		34

Ytterbium	x	v	T [K]	p [kbar]	Ref.
Yb		2.0 ± 0.03–2.92 ± 0.08	300	0–330	13,21
			300	0–58	sect. 11.2
$YbAl_2$		2.3–2.6	300	0–30	12
$YbAl_2$		2.4 ± 0.05	300	0	1
$YbAl_2Ga_2$		2	300	0	48a
YbCuAl		2.95 ± 0.05	300	0	1
$YbCu_2Ge_2$		2	300	0	40,49
$YbCu_2Si_2$		2.90 ± 0.05	300	0	1
		(2.8)	300	0	49
YbInAu		2.18 ± 0.05	300	0	1
$YbInAu_2$		2.68 ± 0.05	300	0	1
YbInPd		2.50 ± 0.05	300	0	1
$YbNi_2Ge_2$		2.80 ± 0.05	300	0	1
Yb_2O_3		3.0	300	0	1
$YbPb_3$		2.15	300	0	1
YbPd		2.807 ± 0.002–2.822 ± 0.002	10–300	0	71

TABLE 3 (cont.)

Ytterbium	x	v	T[K]	p[kbar]	Ref.
$YbPd_2Si_2$		2.89 ± 0.08–2.82 ± 0.08	300–16	0	73
$YbPt_2$		(2.0)	300	0	49
Yb_2S_3		3	300	0	51
Yb_3S_4		2.66 ± 0.02	300	0	51
YbS		(2.15)	300	0	51
		2.08 ± 0.03–2.52 ± 0.03	300	0–300	69
Yb_4Sb_3		2.66	300	0	68
YbSe		2	300	0	1
$YbZn_{2-x}Cu_xP_2$	0	2.35	300	0	1
	0.25	2.58	300	0	1
	0.50	2.74	300	0	1
	0.75	2.89	300	0	1
	1	3.00	300	0	1
$YbZn_{2-x}Cu_xAs_2$	0	2.14	300	0	1
	0.25	2.35	300	0	1
	0.50	2.53	300	0	1

References and comments for table 3

1. Bauchspiess et al. (1981), Bauchspiess (1982)
   (a) Valence analysis from a superposition of two split lines with proper consideration of the chemical shift with respect to metallic Ce systems.
   (b) Sample presumably oxidized (CeO_2). Valence is estimated to be close to three.
2. Bianconi et al. (1985)
   (a) The La compounds are labelled to be f^0 systems.
3. Marcelli et al. (1985), Bianconi et al. (1984a)
   (a) The significant intensity at the low-energy side of the spectrum is assigned to be a 12% contribution of a La ($4f^1$)–Pd($4d^8$) final-state configuration.
4. Klug et al. (1985), Klug (1986)
   (a) Nonsuperconducting sample.
   (b) Superconducting sample.
5. Krill et al. (1981a)
   (a) Valences are derived from the L_{II} spectra.
   (b) The main peak of the double bumped spectrum is believed to originate from a $4f^1$ shake-down satellite (60%).
6. Krill et al. (1981b)
7. Ravot et al. (1981)
   (a) Valence was determined from a superposition of two SmTe spectra shifted by 7.5 eV.
   (b) Valence was determined from a superposition of two Gaussians shifted by 7.5 eV.
8. Wohlleben and Röhler (1984)
   (a) Revisited data from ref. 1.
   (b) Data from J.P. Kappler and J. Röhler.
9. Jhans and Croft (1985)
10. Niemann et al. (1985), Lübcke et al. (1986), Niemann (1985), Lübcke (1985)
11. Krill et al. (1982)
12. Röhler et al. (1982)
    (a) Revisited data, cf. section 9.2.

References and comments for table 3 (cont.)

13. Frank et al. (1982), Syassen et al. (1981) (1982)
14. Smirnov et al. (1982)
15. Boyce et al. (1981), Martin et al. (1980)
16. Röhler (1986b)
17. Röhler (1985a)
    18% and 11% minority phases in $EuCu_2Si_2$ and $EuPd_2Si_2$, respectively.
18. Bittins et al. (1985)
19. Röhler et al. (1984b)
20. Röhler et al. (1983a)
21. Wortmann et al. (1982)
22. Samsonova et al. (1982)
23. Slebarski et al. (1985)
24. Tarascon et al. (1980b)
25. Sampathkumaran et al. (1985a)
26. Croft et al. (1984)
27. Dexpert et al. (1987)
28. Tarascon et al. (1980a)
29. Nagarajan et al. (1981a)
30. Nagarajan et al. (1981b)
31. Neifeld et al. (1985)
    Valence are partially read from figures.
32. Beaurepaire et al. (1984)
33. Bianconi et al. (1982)
    (a) Strongly dampened amplitude ($A_{max} = 1.45$), presumably due to an inappropriate absorber thickness.
34. Launois et al. (1980)
35. Lawrence et al. (1984)
    (a) Valence analysis was not performed in detail. Indicated numbers are estimates from us.
36. Prabhawalkar and Padalia (1982b)
37. Hatwar (1981) Ph. D. Thesis, Indian Institute of Technology, Bombay (unpublished), after ref. 36.
38. Prabhawalkar et al. (1983)
39. Prabhawalkar and Padalia (1982a)
40. Padalia et al. (1983)
41. Lengeler et al. (1983a,b)
    (a) The changes in the white line at the γ–α transition are believed to have nothing to do with changes in 4f count.
    (b) Double-peaked spectra. No valence estimate from us, because chemical shift with respect to Ce metal is not indicated.
42. Röhler et al. (1984a), Röhler (1984) and ref. 8.
43. Levin et al. (1984)
44. Godart et al. (1983b)
45. Raaen et al. (1983a)
46. Wortmann et al. (1986)
    Valence numbers given in the table are not corrected for weak Eu_2O_3 contaminations which have been determined from the corresponding Mössbauer data. A correction procedure would decrease the valences only by a few percent.
    (a) Spectra recorded in transmission geometry.
    (b) Absorption determined from the fluorescent yield from bulk material.
    (c) Absorption determined from the fluoresence yield at different orientations of the crystal.
47. Parks et al. (1983)
48. Ghatikar et al. (1981)
    (a) Valences are determined from the analysis of edge positions with respect to edge positions of

References and comments for table 3 (cont.)

stable reference compounds.

49. Hatwar et al. (1980)
    (a) Spectral shapes are strongly distorted, presumably due to nonlinear detection technique. No quantitative analysis of the data was performed.
50. Finkel'shtein et al. (1974)
    (a) Strongly dampened amplitude, presumably due to wrong absorber thickness.
51. Efmerova et al. (1976)
52. Parks et al. (1983)
53. Rao et al. (1981)
    (a) The spectral features of these works have been not observed by other authors.
54. Godart et al. (1983a)
55. Levin et al. (1981)
56. Darshan et al. (1984)
57. Finkel'shtein et al. (1981)
58. Wortmann et al. (1985)
    (a) The sample exhibits 20% relative satellite intensity (nearly divalent) at 20 K, 40% at 160 K (from Mössbauer isomer shift).
59. Raaen and Parks (1983b)
60. Neifeld and Croft (1985)
61. Croft et al. (1985)
62. Sampathkumaran et al. (1985b)
63. Kemly et al. (1985)
64. Smirnov et al. (1985)
65. Bianconi et al. (1982)
66. Suryanarayanan et al. (1985)
67. Haen et al. (1985)
68. Ochiai et al. (1985)
69. Syassen (1986)
70. Weidner et al. (1985a)
    (a) Ce presumably was not homogeneously solved in the Zr matrix.
71. Pott et al. (1985)
72. Sarode et al. (1982), idem ref. 53.
    The spectral shapes of these work have not been observed by other authors.
73. Frank (1984), Sampathkumaran et al. (1984)
74. Weidner et al. (1985b)
75. Röhler (unpublished data)
76. Krill et al. (1985)
77. Röhler et al. (1983b)
78. Röhler et al. (1987), Klug (1986)
    (a) Nonsuperconducting sample at ambient pressure.
79. Feldhaus (1982)
    (a) K absorption of oxygen has been recorded also.
80. Garg et al. (1986)
    For 3 to 33% Sc the sample segregates macroscopically into the 'black' and 'golden' phases.
81. Röhler et al. (1985)
82. Sham (1983)
    The binding energies of the trivalent and tetravalent lines were not determined with respect to the binding energy of the metal. Presumably the line assigned to be 3^+ is the low-energy line of the tetravalent double line feature, cf. section 14, fig. 36.
83. Kaindl et al. (1983a)
84. Röhler (1986a)
85. Blokhin et al. (1966)

reasons are: (i) The L_{III} valence measurements can be performed equally on all lanthanide atoms which show mixed valence (La, Ce, Pr, Sm, Eu, Tb, Tm and Yb). (ii) It can be performed at all concentrations of mixed valent atoms, in compounds, in concentrated alloys and in dilute alloys down to concentrations of order 1%. (iii) It can be applied at all temperatures. (iv) It can be applied at high pressures (so far up to 350 kbar). (v) It is a bulk measurement, surface valence shifts can be neglected.

In addition to the valence other important information from L_{III} absorption is beginning to emerge, e.g., on the average radial extension of the excited 5d wavefunction, linked to the atomic volume or the metallic (Wigner–Seitz) radius. Hence it seems to be possible to link $L_{III,II}$ data with independent macroscopic measurements such as unit cell volume, bulk modulus, shear modulus (cf. Röhler 1984). The pressure-dependent L_{III} spectra are especially informative. Not only is it possible to tune the system through a continuous variation of the binding energies of order eV; one can also study the binding energy shifts in structural phase transitions. Important correlations can be established between the binding energies and the unit cell volumes measured, e.g., by X-ray diffraction under pressure or by the extended absorption fine structure in the X-ray absorption measurement itself (Keulerz et al. 1986).

Finally, a few words are necessary with respect to the distinguishability of homogeneously and inhomogeneously mixed valent materials. In the L_{III} absorption experiment, the lifetime of the final-state configuration is in the order of 10^{-16} s. Since this lifetime is much shorter than that of the valence states, L_{III} absorption cannot give any direct information about the effective f bandwidth. This is true for all high-energy photoabsorption and emission techniques discussed in this volume. In particular, one cannot distinguish between a static and a dynamic mixture (inhomogeneously and homogeneously mixed valence) from one double-peaked spectrum alone. However, the energetics of homogeneously mixed valent materials change considerably when the effective f bandwidth crosses the energy of the optical phonons. Thus, if the 4f bandwidth can be tuned through this energy range, for instance by changing pressure (volume), one observes a characteristic change of the chemical bonding energies of the two valence states as function of volume. In this way, L_{III} absorption can provide important information about the dynamics of the mixed valent state indirectly. Otherwise homogeneous and inhomogeneous mixtures can only be distinguished by neutron, Raman and hyperfine spectroscopies.

8.3. *The measurement of valence from L_{III} absorption*

In a neutral integral valent atom in the gas phase the L_{III} transition energy (also called the 2p core hole binding energy) measures the difference between the energies of two sets of very complicated many-body states. These energy differences are well-known experimental numbers (cf. e.g. Bearden and Burr (1967)). In an atom in the same valence state in the solid, the L_{III} absorption event apparently proceeds between the same two well-known initial and final correlated states as in the gas. In first approximation the solid formation merely shifts the energies of these final correlated states as in the gas. This results in the so-called chemical shifts of the

absorption spectra, which amount to a few eV (cf. e.g. Faessler 1955, Nagel and Baun 1974).

A valence change by one shifts the 2p binding energy by 7 to 10 eV. This shift is considerably larger than the chemical shifts at fixed valence. It is also larger than the inverse core hole lifetime (3 eV) and the inverse lifetime of the 5d Wannier states of the solid (4–8 eV). Mixed valent systems exhibit two superimposed L_{III} spectra. The two individual atomic-like absorption lines are located near the energies of the two individual integral valent states. This finding may be interpreted as a direct experimental confirmation of the principle of linear superposition of configurational states, which is a very successful tool of theoretical chemistry of which the concept of valence is a special version. This principle goes an important step beyond the linear superposition of single-electron quantum states used, e.g., in band structure theory.

8.3.1. *Chemical shifts*

The L_{III} spectra provide measurements of one set of chemical effects for each valence state separately. This aspect is probably at least as important as the measurement of the fractional valence; its utilization is however in its infancy at this time. The first such effect is that the chemical binding energy to the solid must be larger in the higher valence state, in which the number of valence electrons is larger by one. Secondly, since the L_{III} transition is from the chemically inert 2p state to the chemically binding 5d state mainly, it can provide information about the distribution of the 5d amplitude over the ligands of the lanthanide atom with its chemical binding partners. The ligand electronegativity and coordination number effects predominantly vary the intensity of the absorption lines (normalized to the continuum absorption). The shifts of the positions (e.g. the inflection point with respect to the inflection point of the metal) are comparatively small. Wong et al. (1984) investigated systematically the amplitudes of the $L_{III,II}$ absorption lines in R_2O_3 and RF_3. In the fluorides both absorption lines are higher than the corresponding ones in the oxide. In the fluorides each R ion is coordinated by $9\,F^-$ ions, in the oxides each R ion by $7\,O^=$ ions; the electronegativities differ by 0.6. Prabhawalkar and Padalia (1982a,b) studied the chemical shifts in the lanthanide–gallium intermetallics RGa_2. The chemical shifts of the lanthanide L_{III} absorption lines and the gallium K spectra exhibit a linear relationship with the effective charges calculated from the partial ionic character of the chemical bonds according to K. Siegbahn's (1970) method.

Figure 12 illustrates the effect of different types of chemical bonds, coordination and of valence changes in the L_{III} spectra of some Pr compounds. Pr metal and the semi-metals PrBi, PrSb, PrCu are trivalent. Pr_6O_{11} is an insulating mixed valent compound with about 20% tetravalent Pr ions. The main discrepancy among the trivalent spectra are the shapes and the amplitudes of the absorption lines. Note that the shifts determined from the intersection points with respect to the intersection point of Pr metal turn out to be small. The trivalent absorption in insulating Pr_6O_{11} rises already at the onset of the absorption in the element. The dominant trivalent line, however, is shifted by about +3 eV from that of the element which may be assigned to the transition from a metal to an insulator. Both the tri- and tetravalent ions exhibit split absorption lines shifted by $\Delta_{kl} \cong 9$ eV. Actual splittings

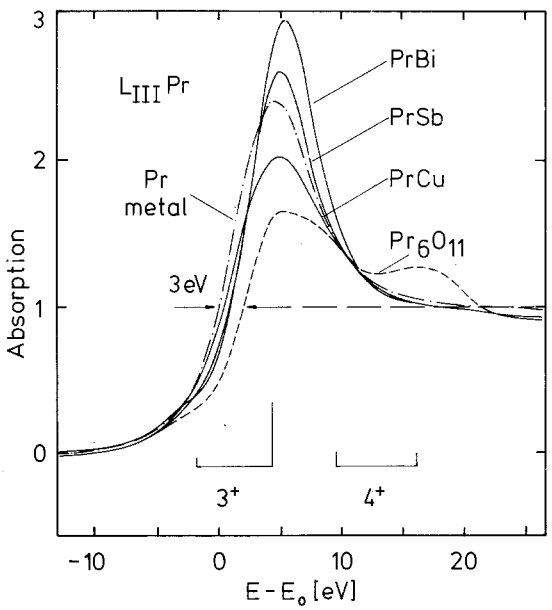

Fig. 12. Demonstration of typical chemical shifts in lanthanide L_{III} absorption. The energy calibration of the spectra recorded from the Pr absorption in the compounds is accurate within ± 0.2 eV with respect to E_0 fixed at the intersection point of the high-energy absorption with the absorption line in (dhcp) Pr metal (dashed–dotted line). The intersection point shifts to higher energies with decreasing metallic character of the compounds. The maxima of the prominent main lines, however, remain unshifted, just as the onsets of the lines. PrCu crystallizes in orthorhombic FeB structure ($a = 7.343$ Å, $b = 4.584$ Å, $c = 5.604$ Å). The semi-metals PrSb, PrBi have fcc (NaCl) structure ($a = 6.366$ and 6.463 Å, respectively). Pr_6O_{11} is a nonstoichiometric modification of nominally tetravalent PrO_2 (fluorite type, CaF_2). The bar diagram indicates ligand-field-split absorption lines for both, the tri- and tetravalent valence states in Pr_6O_{11} (cf. section 14).

of the 5d amplitude can be observed in other covalent or ionic solids, e.g. the 'tetravalent' Ce-, and Tb-oxides (cf. section 14) and in some metals, also.

Bianconi et al. (1984b) recorded the L absorption of *both*, R and Pd in RPd_3 (R = La, Nd). These experiments are in particular instructive, since they promise to yield detailed information on the role of chemical bonding. A clearly split Pd L_{III} absorption line is present in $LaPd_3$ on one hand, however it is absent in $NdPd_3$, on the other hand. The split L_{III} line of Pd in $LaPd_3$ is correlated to the split line in the La L_{III} absorption. Bianconi et al. (1984b) assign them to a ligand field caused splitting (La)$4f^0$–(Pd)$4d^9$ and (La)$4f^1$–(Pd)$4d^8$.

The information about local binding energies, line intensities, 5d crystal field splittings and 5d bandwidths will become essential in the future, once one wishes to obtain quantitative control over why certain materials are mixed valent and why the value of the fractional valence is what one measures. At this time, however, the methods of quantitative extraction of chemical binding energies and the theory of the mixed valent state are insufficiently developed to make use of this information contained in the L_{III} spectra. Accordingly, in the following we shall address this aspect only occasionally.

It is however obvious from the above, that extraction of numbers for the fractional valence has to be done with careful consideration of the various chemical effects contained in the spectra. For instance, a double-peaked spectral shape alone cannot be taken as an unambiguous signature of the mixed valent state, since splittings can also be produced by crystal field effects or by the formation of metal–ion ligands. Therefore we state as a rule that the proper spectroscopic analysis of L_{III} absorption in potentially mixed valent materials should be based on both, the measurement of the transition energy with respect to those in well-characterized isomorphous integral valent materials *and* the detailed analysis of the double-peaked spectra, i.e. their intensities, splittings and linewidths.

8.3.2. *Experimental problems of the valence measurement*

Various analytical procedures are applied to extract valence numbers from L_{III} spectra. They are based on a deconvolution of two superimposed and shifted single-peaked sub-spectra taken either from experimental or from numerical reference spectra. Within $\Delta v = \pm 0.1$ the different techniques yield the same results on identical spectra. An estimate of the absolute and relative uncertainties may be obtained from table 3. It lists the valence numbers from most of the $L_{III,II}$ spectra published from 1975 until 1986. These numbers have been worked out by more than ten different laboratories. Obviously the numbers extracted from identical systems agree fairly well in spite of the fact that they have been obtained with the use of quite different deconvolution techniques. Large systematic deviations (>0.1) from the average numbers (where available) should be attributed to different experimental results rather than to the specific valence determination procedure.

Some error sources, which give rise to falsified intensities or strongly distorted lineshapes were addressed in section 5. In the following we shall discuss those error sources which are of particular importance for the valence measurements.

The mixed valent system may be considered to be an alloy of $4f^{n+1}$ and $4f^n$ atoms. At nearly integral valences one of the two 4f atoms is very dilute; in midst of the mixed valent regime both, the $4f^n$ and the $4f^{n+1}$ atoms, are 'concentrated'. Small concentrations of $4f^{n+1}$ in a majority of the $4f^n$ atoms only modify the absorption onset (foot) of the prominent line and hence are difficult to resolve (the 'Yb case'). Small $4f^n$ concentrations in a majority of $4f^{n+1}$ atoms (the 'Ce case'), however, form a clearly resolved line sitting on the high-energy background. Accordingly the L_{III} detection limit for minority $4f^{n+1}$ atoms is higher ($\geqslant 10\%$) than that for minority $4f^n$ atoms ($\geqslant 1\%$).

Inappropriate absorber thicknesses (cf. section 5) have an effect on the line intensities and hence on the valences also. They may be responsible for an 'offset' in the valence scale and for nonlinearities on drastic (>0.2) valence shifts. Efmerova et al. (1976) studied the effect of different individual thicknesses in a series of exactly defined mixtures of trivalent Eu_2O_3 with divalent EuS (EuS replaces EuO which exhibits a weak trivalent contribution). Figure 13 plots the L_{III} numbers (solid lines connecting the open circles) obtained at different Eu^{2+} concentrations (right-hand side) versus the absorber thickness m_{opt}. $m_{opt} = 1$ denotes the thickness ($m = 6$–8 mg/cm^2) optimized for the maximum contrast of the line absorption at the continuum

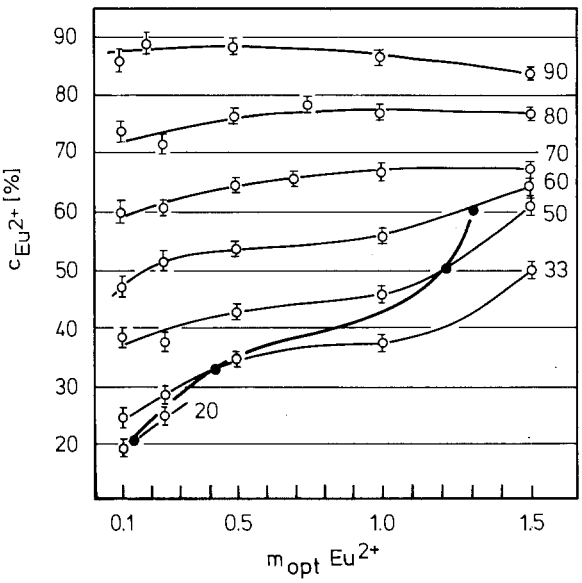

Fig. 13. Determination of the concentration of divalent EuS in a defined mixture of EuS and Eu_2O_3 through L_{III} absorption versus the absorber thicknesses m_{opt}. The solid lines connecting the L_{III} data points (open circles) represent the thickness dependence of the L_{III} numbers at given concentrations (90, 80, 70, 60, 50 and 33%). The thick solid line connecting the solid circles at 20, 33, 50 and 60% at the intersection points of the nominal with the L_{III} concentrations indicates the proper absorber thickness for 20–60% Eu^{2+} (adapted from Efmerova et al. 1976).

threshold (Blockin 1957). The L_{III} numbers behave nonlinearly with the absorber thickness at all concentrations. Due to the asymmetrical background of the L_{III} lines no simple saturation behavior is observed, instead it is a complicated nonlinearity. Apparently this nonlinearity for small divalent ($4f^{n+1}$) concentrations is more drastic than for small trivalent ($4f^n$) concentrations. Such plot is useful for selecting the appropriate absorber thickness in a distinct concentration range (thick solid line connecting the solid dots) because there is no universal thickness for the whole concentration range. The use of thin absorbers ($m_{opt} < 0.5$) diminishes the nonlinearity at a fixed absorber thickness but does not remove them. Figure 13 demonstrates that the proper absorber thickness is crucial for the absolute and relative precision of the valence measurements. It must be added, however, that fig. 13 was obtained from the investigation of a model substance exhibiting an extraordinarily large ratio of di- and trivalent L_{III} amplitudes $A: A_3/A_2 = 1.9$ (cf. fig. 4). In most other cases (e.g. isostructural intermetallics) the amplitude ratio is much smaller, reducing but not eliminating this type of thickness effect. Precise L_{III} valence measurements therefore should be founded on a systematic study of the particular thickness effects of the system under investigation. If necessary, such a study should be used for the linearization of the extracted valences.

Another source for different experimental results may be the enormous sensitivity of the L_{III} absorption to the local chemistry of the absorbing lanthanide atom. Crystalline defects or small amounts of other phases below the detection limit of the usual structural analysis or other measurements might explain different valence numbers from nominally identical materials. Most of the L_{III} measurements were performed on finely ground polycrystalline material. Even the few materials available as single crystals were powdered in order to prepare the required thin absorption foils (about 10 μm thick). Clearly this procedure may induce defects and imperfections which may alter the elastic and electronic properties. In particular powdered

crystals (mostly single crystals) of R-pnictides and R-chalcogenides, are found to exhibit slightly different L absorption spectra, depending on the preparation techniques. Wortmann et al. (1986) compared spectra from fine powders recorded through the usual transmission geometry with spectra from bulk material recorded through the detection of the fluorescence yield. The discrepancy between the valences obtained from these recordings was found to be only 0.04 (cf. section 10.3).

8.3.3. *Superposition of two experimental reference spectra*

The simplest method to obtain a valence number from a $L_{III,II}$ absorption spectrum is to read it from a superposition of two spectra taken from isomorphous integral valent reference systems shifted by about 8 eV. A linear background, extrapolated from the absorption before the edge, is subtracted from the spectra. The effect of different sample thicknesses is eliminated by normalizing the absorption at high energies to $\mu d = 1$. The valence is then

$$v = m - 1 + I_n/(I_n + I_{n+1}). \tag{6}$$

Here I_n and I_{n+1} are the relative fractions of the normalized absorption jumps in the $4f^n$ and $4f^{n+1}$ reference spectra and m is the number of outer valence electrons. This procedure was applied e.g. by Launois et al. (1980), Martin et al. (1980), Ravot et al. (1981) to extract the valence from the L_{III} spectra of mixed valent lanthanide chalcogenides. Figure 14 reproduces the spectra of mixed valent TmSe together with its (isostructural) references TmS (nominally 3^+) and TmTe (nominally 2^+). Divalent Tm in TmTe exhibits a smaller and narrower line than trivalent Tm in

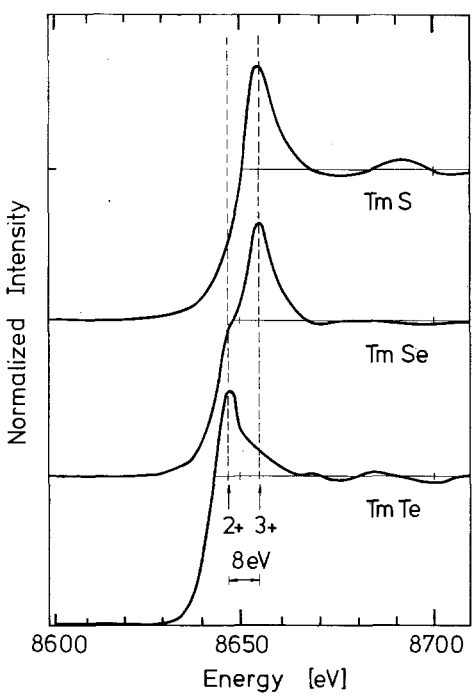

Fig. 14. L_{III} absorption of Tm in nominally divalent TmTe, mixed valent TmSe and nominally trivalent TmS (adapted from Launois et al. (1980)).

TmS. As in the elements (cf. section 7.3.) also in these compounds the relative linewidths turn out to be signatures of the $4f^{n+1}$ $(5d6s)^{m-1}$ and $4f^n$ $(5d6s)^n$ configurations, apart from their characteristic binding energies. Therefore superpositions of identical reference spectra do not reproduce properly a mixed valent spectra. Appropriate reference systems for both, $4f^{n+1}(5d6s)^{m-1}$ and $4f^n$ $(5d6s)^m$ configurations, however, are not always available. For instance, there are no purely tetravalent Ce, Pr or Tb intermetallic solids. In addition the spectra of nominally integral valent reference compounds frequently reveal a coexisting fraction of the other valence state, e.g. about 10% Tm^{3+} in TmTe (fig. 14). This problem will be addressed in much more detail in section 9 (R-chalcogenides), section 10.3. ($EuPd_2P_2$) and section 14 (CeO_2).

To extract valence numbers from L_{III} spectra without the use of reference spectra, various numerical procedures have been developed.

8.3.4. *Numerical deconvolution of a mixed valent L_{III} spectrum*

The simplest numerical descriptions model the asymmetric line spectra from two symmetric Lorentzian, Gaussian profiles (or convolutions of both) and rectangular step functions located at the center of the adjacent line profiles. Frequently the Gaussian contribution to a broadened Lorentzian (Vogt-profile) is attributed to the spectrometer resolution. Typical spectrometer resolutions, however, are about 2–3 times smaller than the total core level widths and therefore cannot account for Gaussians of about 5 eV. Realistically the Gaussian contribution models the distribution of spectral densities. Therefore it is more sound to decompose the experimental spectra numerically into the distinct atomic-like (line) and the solid state (continuous) absorption according to the atomic approach discussed in sections 6.1 and 7. In the following we address the procedure described by Röhler (1985a).

Figure 15 displays the L_{III} absorption of Eu in mixed valent $EuPd_2Si_2$ at 175 K. Using a least squares fitting procedure the following expression is fitted to the normalized experimental spectrum:

$$
\begin{aligned}
F(E) = {} & B_0 + B_1 E + (\tfrac{1}{2}\Gamma)^2 A_k \sum_i \frac{\mathrm{d}f_i}{[E - (E_k + \mathrm{i}\varepsilon_k)]^2 + (\Gamma/2)^2} \\
& + (\tfrac{1}{2}\Gamma)^2 A_l \sum_j \frac{\mathrm{d}f_j}{[E - (E_l + \mathrm{i}\varepsilon_l)]^2 + (\Gamma/2)^2} \\
& + \frac{A_k \varepsilon_k}{A_k \varepsilon_k + A_l \varepsilon_l \sum_j \mathrm{d}f_j / \sum_j \mathrm{d}f_i} \left\{ \tfrac{1}{2} + \frac{1}{\pi} \arctan \left[\frac{E - (E_k + \delta)}{\Gamma/2} \right] \right\} \\
& + \left(1 - \frac{A_l \varepsilon_l}{A_k \varepsilon_k + A_l \varepsilon_l \sum_j \mathrm{d}f_j / \sum_i \mathrm{d}f_i} \right) \left\{ \tfrac{1}{2} + \frac{1}{\pi} \arctan \left[\frac{E - (E_l + \delta)}{\Gamma/2} \right] \right\}. \qquad (7)
\end{aligned}
$$

Equation (7) decomposes into three parts: (i) the background absorption, (ii) two atomic-like absorptions, (iii) two continuous absorptions and the prescription for the

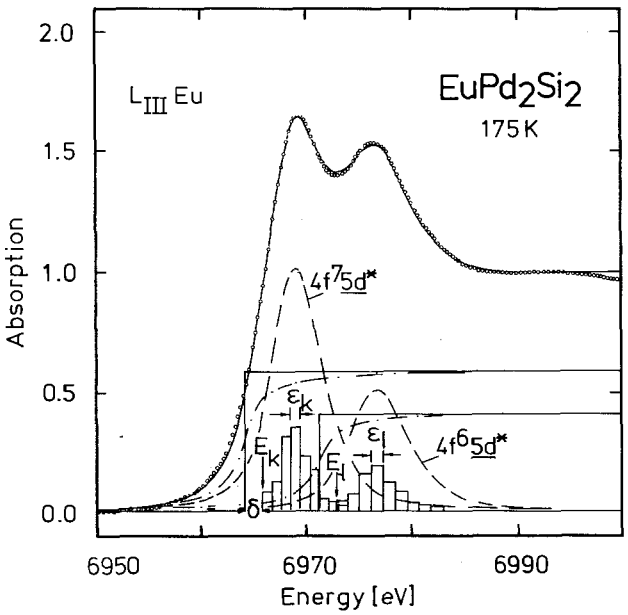

Fig. 15. Deconvolution of the L_{III} absorption of Eu in mixed valent $EuPd_2Si_2$ at 175 K according to the analysis described in the text. The valence $v = 2.42 \pm 0.01, E_1 = 6972.98$ eV, $E_k = 6965.85$ eV, $\varepsilon_k = 0.9$ eV, $\varepsilon_1 = 1.1$ eV, $\delta = -1.6$ eV, $\Gamma = 3$ eV (Röhler 1985a).

normalization of the atomic-like absorptions with respect to the continuous absorption. E denotes the photon energy. B_0 and B_1 are the coefficients of a linear background.

The two atomic-like absorption lines are described through Lorentzian profiles broadening the differential oscillator strengths $df_i(2p\text{–}[4f^n]5d)$ and df_j $(2p\text{–}[4f^{n+1}]5d)$ by the inverse $2p_{3/2}$ core-hole lifetime $\Gamma \equiv$ FWHM. df_i and df_j are equally spaced distributed by ε_i and ε_k, respectively, and split by $E_l - E_k$. Here E_l and E_k denote the corresponding lowest lying states. A_k and A_l are factors of the amplitudes. The effective 2p binding energy shift upon 4f configurational change, Δ_{kl}, is best defined through the distance between the centers of gravities from the atomic-like absorption.

The lifetime broadened step functions (arctan) describe the dipole allowed transitions into the continuum. The onset of the continuum states with respect to the onset of atomic-like states is shifted by δ. δ may range from 0 to a number in the order of the first ionization potential (~ 7 eV) (cf. section 6.1.). In metals δ is chosen to be close to the first atomic-like states.

The L_{III} spectrum of Eu in $EuPd_2Si_2$ exhibits two clearly resolved lines whose individual intensities vary drastically with temperature or pressure induced valence changes. This spectrum may serve as an example for a rather reliable determination of the individual lineshapes and linewidths. Here the atomic-like absorption lines for reasons of simplicity are assumed to exhibit the same shape. The spectral densities $df_i/d\varepsilon_k$ and $df_j/d\varepsilon_l$, however, are clearly different: $\varepsilon_l > \varepsilon_k$. In other words, the trivalent ($4f^6\,\underline{5d}^*$) absorption line turns out to be broader by $\varepsilon_l/\varepsilon_k = 1.22$ than the divalent ($4f^7\,\underline{5d}^*$) line (the asterisk denotes the excited state). The corresponding

factor found from the analysis of the L_{III} absorption in the stable elements Eu^{2+} and Gd^{3+} is 1.29 (cf. section 7.3).

The two valence states in a homogeneously mixed valent solid occur in the same local environments, i.e., they have the same local coordination numbers, local symmetry and type of chemical bonding. It is therefore a good approximation to normalize the intensities of the two atomic-like absorption lines in eq. (7) equally to their adjacent continuum absorption, provided the transition matrix elements and their energy dependences are not too much different. Accordingly eq. (6) determines the valence.

Practically we operate with 5 independent parameters: A_k, A_l, ε_k, ε_l, E_l. $E_k - E_l$ is brought into coincidence with the theoretically calculated numbers (Vlasov and Farberovich 1982, cf. also chapters 68 and 69 in this volume). The df_i and df_j and δ are determined once (say at $p = 0$) and then remain fixed. Γ enters from the tabulated values.

According to experience fine structures refer to crystalline or ligand field splittings. Such splittings increase up to about 6 eV in the ionic 'tetravalent' Ce, Pr and Tb compounds and are clearly resolved in such cases. Splittings of the excited 5d states occur also in the ligand field of metallic bonds, however, here they are smaller (3–4 eV) than in the ionic compounds. Due to the relatively large core-level widths of 3–4 eV, these splittings are hard to resolve, but they may be still traced from the 1st or 2nd absorption derivative (provided the data are of an excellent quality). A clearly split distribution of the tetravalent 2p–5d spectral density in a metal is

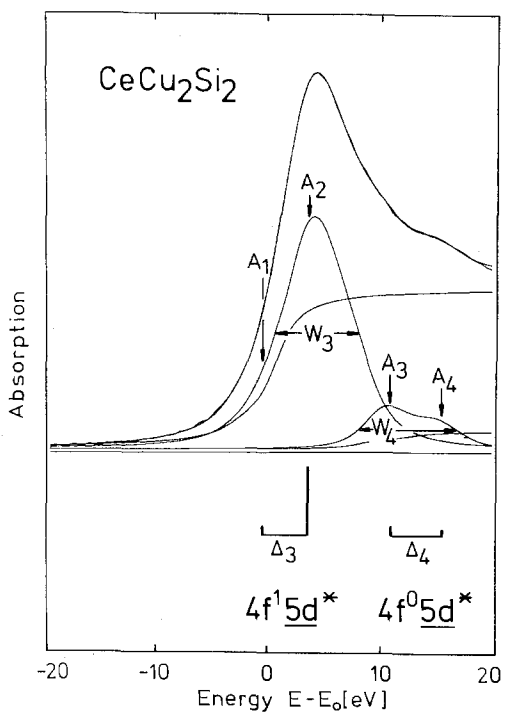

Fig. 16. Deconvolution of the L_{III} absorption of Ce in (superconducting) $CeCu_2Si_2$ at ambient temperature. The bar diagram indicates the positions and intensities of the ligand field split $2p_{3/2}$–$4f^1\,5d$ (Ce^{3+}) and $2p_{3/2}$–$4f^0\,5d$ (Ce^{4+}) spectral densities (see text).

observed in α-Ce at low temperatures (cf. section 12.1, fig. 29b). Carrying out a careful lineshape and linewidth analysis, it turns out that most of the absorption lines in Ce intermetallics are split. The valence then is best determined from a modification of eq. (7), including two sets of split spectral densities. Figure 16 exhibits the deconvolution of the L_{III} absorption in $CeCu_2Si_2$. Here Δ_3 and Δ_4 denote the ligand field splittings in each valence states, A_1, A_2 and A_3, A_4 are the adjacent amplitudes. W_3 and W_4 denote the total widths of the tri- and tetravalent absorption lines (Klug 1986). The bar diagrams indicate the relative intensities within each valence electron configuration (cf. section 13).

9. L_{III} absorption in the R-monochalcogenides

The R-monochalcogenides (see e.g. Methfessel and Mattis (1968) containing the potentially mixed valent elements La, Ce, Pr, Sm, Eu, Tm and Yb are the most intensively investigated semiconducting (semimetallic) compounds among the valence fluctuating materials. In particular the discovery of the pressure induced first-order semiconductor–(semi-) metal transition in SmS, which is an incomplete valence transition ($4f^5\,5d^1\,6s^2$–$4f^6\,5d^0\,6s^2$), opened a new chapter in the research of mixed valent lanthanide materials. We shall address the L_{III} absorption studies on the Sm chalcogenides in section 9.1. TmSe attracted special theoretical and experimental interest because it is one of the unstable lanthanide compounds exhibiting magnetic ordering and strongly mixed valence; the L_{III} absorption in TmSe will be discussed in section 9.2. Apart from the Sm-chalcogenides and TmSe, EuO and YbS are the only monochalcogenides which have been studied through L_{III} absorption in detail. As expected from the volume anomalies, L_{III} absoption in the Eu- and Yb-chalcogenides at ambient pressure and temperature indicates Eu and Yb to be in nearly divalent. The observed deviations from the integral divalent state (up to 10%) depend on the stoichiometry of the samples, as most of the macroscopic properties also do. So far the problem of these deviations has not been studied systematically. Optical reflectivity measurements at high pressures (Syassen 1984) gave evidence that EuO (Zimmer et al. 1984) and YbS (Syassen et al. 1985) undergo second-order semiconductor–metal transitions at about 130 and 100 kbar, respectively. As in the Sm-chalcogenides these transitions are accompanied by softening of the lattice and are expected to be valence transitions, also. The L_{III} absorption in EuO under high pressure up to 310 kbar (Röhler et al. 1985) indicates a relative valence change by $\Delta v = 0.37$ from 2.09 ± 0.02 to 2.46 at the highest applied pressure. An S-shaped dependence of the valence on pressure with an inflection point at about 80 kbar seems to be the signature of the semiconductor–metal transition in the valence–pressure relationship. However the transition occurs at a lower transition pressure than expected from the optical reflectivity. In YbS L_{III} absorption under high pressure (Syassen 1986) yields a valence shift of $\Delta v = 0.45$ between 0 and 300 kbar. The inflection point of the S-shaped valence increase is found to coincide approximately with the softening of the lattice and the onset of metallic reflectivity at about 100 kbar. As in EuO the L_{III} absorption in YbS indicates a nonintegral

valence at ambient pressure ($v = 2.08 \pm 0.03$); in both compounds transitions into the stable trivalent lanthanide configurations are not observed.

9.1. *Sm-monochalcogenides*

SmS is the best studied monochalcogenide. L_{III} absorption spectra of Sm in SmS have been recorded from its black (semiconducting) and its golden (semi-metallic) phase, the latter being induced by pressure, chemical alloying and temperature (cf. table 3). Figure 17 shows the pressure dependence of valence in stoichiometric SmS together with typical high pressure L_{III} absorption spectra (Röhler et al. 1982). The volume collapse at 6.5 kbar is associated with a drastic valence shift. At ambient pressure the valence of the sample is found to be nonintegral: $v_{0\,kbar} = 2.10 \pm 0.02$. The same observation has been made in the high-pressure experiment (0–7.5 kbar) of Frank et al. (1982): $v_{0\,kbar} = 2.12 \pm 0.05$ and by Ravot et al. (1981). Just after the phase transition the valence is found to be 2.57 ± 0.02 in good agreement with the numbers from $K_{\alpha,\beta}$ emission ($v = 2.62 \pm 0.03$, cf. table 1) and Mössbauer isomer shift ($v = 2.62 \pm 0.08$, Coey et al. (1976)). However, the valence number v_v, obtained from

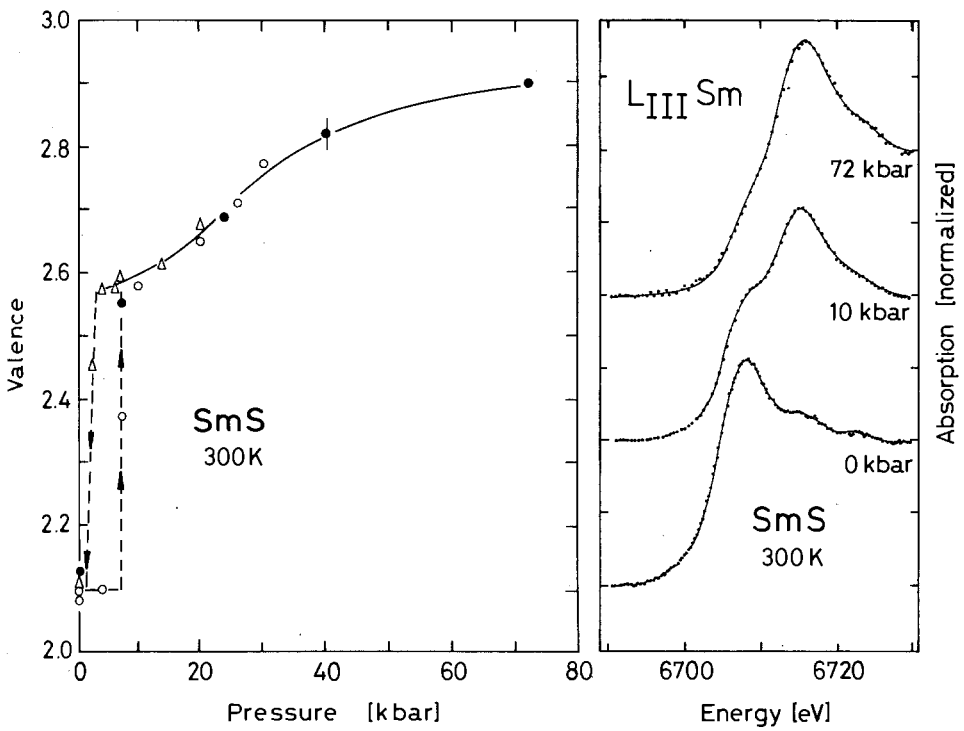

Fig. 17. (*Left-hand side*) The valence of SmS as a function of pressure up to 72 kbar at ambient temperature (Röhler et al. 1982). Open and closed symbols indicate data from different runs. Dots are measured at increasing pressures, triangles at decreasing pressures. (*Right-hand side*) L_{III} absorption edges of Sm in SmS at 0, 10 and 72 kbar at ambient temperature. The lines connecting the data points are fits from an analytical superposition of two L_{III} resonances with adjacent continuum functions (section 8.3).

the linear interpolation of the lattice parameters (Vegard's rule, $v_v = 2.77 \pm 0.06$, Maple and Wohlleben (1971)) is 15% too large with respect to the numbers extracted from the various spectroscopic measurements. A nonlinear interpolation (cf. e.g. Wohlleben (1984a)) brings the valence from the lattice parameter into coincidence with the average of the spectroscopically determined valence numbers. At pressures above the first-order transition ($p > 6.5$ kbar) the valence changes nonlinearly to $v \simeq 2.9$ at 72 kbar with an inflection point near 22 kbar. The valence at the inflection point is $v \simeq 2.7$ (fig. 17). In this pressure range Keller et al. (1979) observe an abnormally large pressure derivative of the bulk modulus. From high-pressure resistivity measurements Lapierre et al. (1981) find a transition from semi-metallic to metallic behavior at 20 kbar. The pressure dependence of valence in SmS above the first-order transition seems to behave similarly to the pressure dependence of valence of Sm in SmB_6 (Röhler et al. 1985). The valence of SmB_6 ($v_{p=0} = 2.6$) increases nonlinearly to $v = 2.81$ at 100 kbar with an inflection point at about 55 kbar. Near this pressure Beille et al. (1983) observe a transition from semi-metallic behavior to metallic behavior as observed by Lapierre et al. (1981) in SmS at $\simeq$20 kbar. Both compounds, SmS and SmB_6, exhibit unambiguous metallic resistivity behavior only at $v \geqslant 2.7$.

Figure 18 (adapted from Boyce et al. (1981)) displays the temperature induced valence shift of Sm in $Sm_{0.8}Y_{0.2}S$ (chemically stabilized 'golden' phase at ambient temperature) between 300 and 77 K. Cooling down the sample expands and

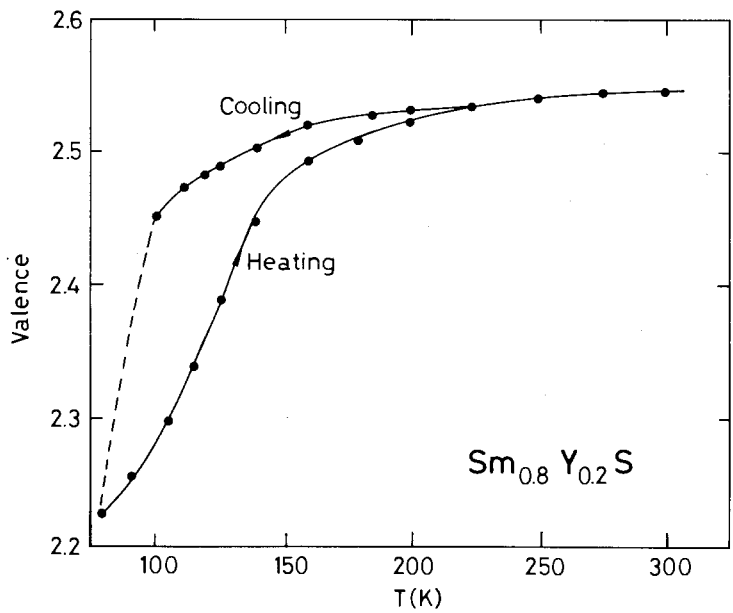

Fig. 18. The valence of Sm in $Sm_{0.8}Y_{0.2}S$ between 77 and 300 K at ambient pressure. 20 at % Y stabilizes the strongly intermediate valent state of Sm ($v \cong 2.6$) at high temperatures. At $T < 150$ K the system transforms into the semiconducting (black phase). The semiconducting phase turns out to be mixed valent also (adapted from Boyce et al. 1981).

transforms it into the 'black' phase with $v \simeq 2.2$ at 77 K. Heating transforms it back into the golden phase. The large hysteresis confirms the well-known first-order transition. Low temperature L_{III} absorption studies on alloyed SmS have been performed by Godart et al. (1983b) also (cf. table 3). Within the uncertainties discussed in section 8.3.2 their results are in good agreement with those of Boyce et al. (1981) and with the numbers from the $K_{\alpha,\beta}$ shifts (cf. table 1). The same number has been observed from the L_{III} absorption in dilute Sm in rare gas matrices (Niemann et al. 1985) on change of the metal concentration.

Independent of the conditions inducing the valence transition (pressure, temperature or chemical alloying) the valence numbers observed just after the first-order transition, converge to $v = 2.6 \pm 0.05$. The theoretical answer to why just the ratio 3/2 of the two valence state populations stabilizes SmS at low volumes might be obtained in the framework of the thermodynamics of valence fluctuations (see e.g. Wohlleben (1984a,b)).

A continuous valence transition of Sm in SmSe is expected from the equation of state and from the resistivity vs pressure data (Jayaraman et al. 1970, Jayaraman 1979). High-pressure L_{III} absorption data of Sm in SmSe were reported by Ingalls et al. (1980) and Tranquada et al. (1984). However, no valence numbers were extracted from the spectra. Figure 19a displays high-pressure L_{III} absorption data of Sm in SmSe up to 55 kbar, recorded from the author. The pressure dependence of the valence extracted from the deconvolution of the spectra in fig. 19a is plotted in fig. 19b. The zero-pressure spectrum has a prominent divalent absorption line but exhibits already a remarkably strong trivalent contribution. As in the spectra of SmS we notice a weak bump at about 6 eV split off the trivalent absorption line. The position of this bump turns out to be nearly independent on pressure. We attribute it to a 'chemical splitting' of the trivalent absorption line due to the formation of samarium (5d)–selenide (4p) ligands. Such splittings are expected from the R (5d)–Se(4p) gap in the energy level diagrams based on optical investigations. Crystal field splittings of the 5d states (t_{2g}–e_g) from optical studies are found to be much smaller (1–2 eV) and are below the L_{III} detection limit due to the larger $2p_{3/2}$ core level width. In the valence determination procedure the R(5d)–Se(4p) ligand field splitting of the spectral densities should be taken into account in both final-state configurations. The splitting of the divalent line cannot be resolved from the spectra, because the trivalent line superimposes the divalent lines. We therefore extract the valence numbers from the integration of identically split lines (6 eV) with a constant intensity ratio (10:1) of bonding and antibonding spectral densities. The valence $v = 2.18 \pm 0.02$ is independent of pressure up to about 25 kbar. The expected continous valence shift begins with a rather steep onset at about 28 kbar. The valence then increases monotonously up to $v = 2.58$ at 55 kbar. We expect the valence vs pressure to flatten at higher pressures as has been observed in SmS.

9.2. *Tm-chalcogenides*

The valence of Tm in Tm_xSe has been deduced from the lattice constants, the effective magnetic moment μ_{eff}, photoemission spectra, M_V and L_{III} absorption. The valence shifts linearly with x ($x > 0.87$) according to the volume–valence

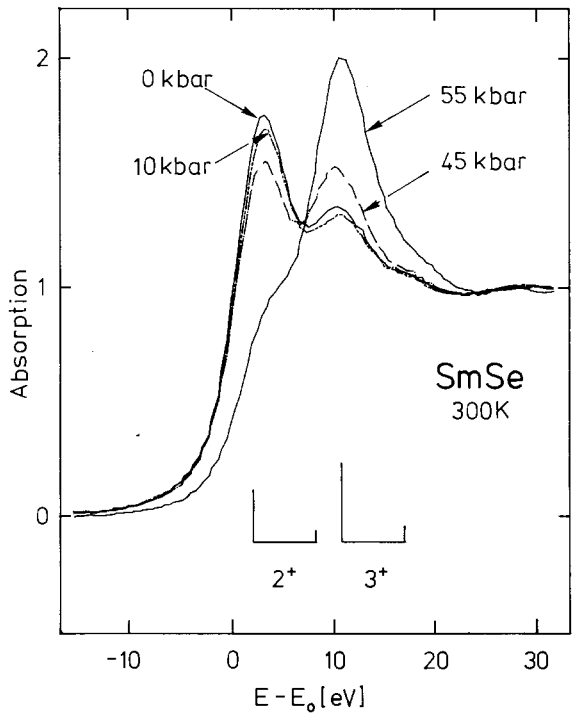

Fig. 19a. L_{III} absorption spectra of Sm in SmSe at various pressures (300 K). The bar diagram indicates the relative intensities of the split di- and trivalent absorption lines at 55 kbar. Note the distinctly different linewidths of the di- and trivalent lines at 45 kbar (dashed line).

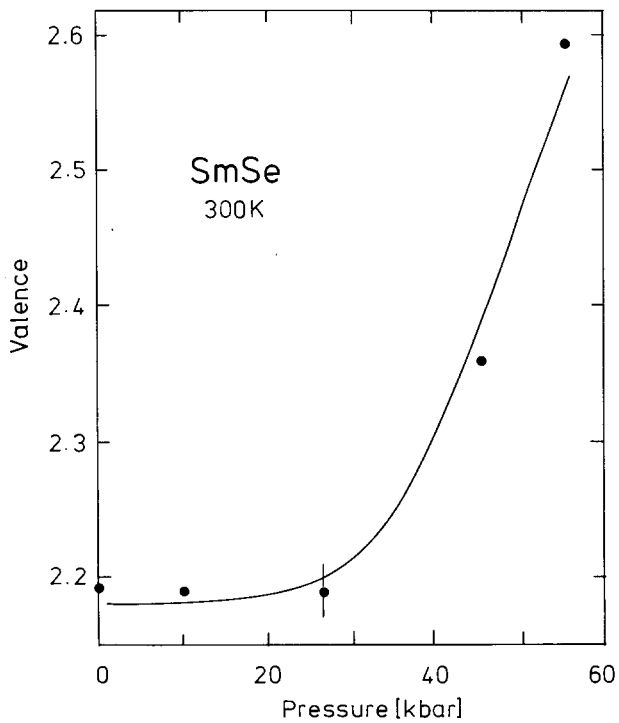

Fig. 19b. The valence of Sm in SmSe as a function of pressure.

relationship from a Vegard-type interpolation of stable di- and trivalent reference volumina

$$V_V(v) = (1 - v)V_{n+1} + vV_n \tag{8}$$

(here V_{n+1} and V_n are the $4f^{n+1}$ and $4f^n$ reference volumes, respectively; v is the population of the higher valence state). Crystals with $x = 0.83$–0.87 are found to be trivalent. When increasing x towards the stoichiometric composition $Tm_{1.00}Se$, Tm becomes mixed valent in TmSe; for $x = 1$ an average valence number $v_v = 2.75$ is obtained from the lattice parameters (see e.g. Batlogg et al. (1976)). Figure 14 (section 8.3.3) shows the L_{III} absorption spectrum of nearly stoichiometric TmSe ($a = 5.711 \pm 0.003$ Å) together with nominally divalent TmTe (bottom) and nominally trivalent TmS (top) (adapted from Launois et al. 1980). The shift between the di- and trivalent absorption maxima of the reference compounds is 8 eV. Launois et al. (1980) extract from the superposition of either the spectra of TmS and TmTe or two shifted ErSe spectra the valence of TmSe to be $v = 2.58 \pm 0.07$. Between 300 and 10 K the valence remains constant within 1%. Haen et al. (1985) extract from the L_{III} absorption in a stoichiometric sample ($a = 5.713 \pm 0.001$ Å) $v = 2.665$; v is found to be nearly temperature independent down to 40 K, also. The valence determination through a numerical deconvolution technique by Haen et al. (1985) may explain the higher precision of their data and the small discrepancy to the valence number of Launois et al. (1980). The valence numbers from L_{III} absorption agree well with the valence numbers obtained from the magnetic susceptibility at high temperatures and the valence numbers extracted from a XPS study (Wertheim et al. 1980); however, both are by 0.1–0.15 lower than the number v_v from the Vegard method. These numbers can be brought into coincidence using the following simple version of a more general nonlinear volume–valence relationship (Wohlleben, 1984a):

$$V(v) = \frac{q_{n+1} + v}{(1 - v)q_{n+1}/V_{n+1} + q_n/V_n}, \tag{9}$$

q_{n+1}, q_n are the integral valences with the adjacent unit cells V_n, V_{n+1}. This expression applies in environments of the lanthanide atom which suppress the breathing motion of the lanthanide atom from V_{n+1} to V_n and back. For instance if T_{n+1}^{-1} and $T_n^{-1} > \omega_D$, where ω_D is the Debye frequency, the valence fluctuation is fast compared to the relevant phonon frequencies. This condition is not fulfilled in TmSe. However, since $(1 - v)/v$ in TmSe is near 2/3, the lattice symmetry may prevent breathing motion, although it is permitted by T_{n+1}^{-1} and $T_n^{-1} > \omega_D$.

Valence numbers of Tm_xSe extracted from M_V absorption data (Kalkowski et al. 1985a, Kaindl et al. 1985) are found to coincide with v_v according to eq. (8). The origin of the discrepancy between the valence determination from L_{III} absorption, magnetic susceptibility and XPS on one hand and M_V absorption on the other hand, is not clear at this time. Probably it is due to the special experimental problems of M absorption (cf. sections 4.3.1 and 5).

The application of pressure shifts (Röhler et al. 1982) the valence of a nearly stoichiometric TmSe ($a = 5.691$ Å) towards the trivalent state (figs. 20, 21). The

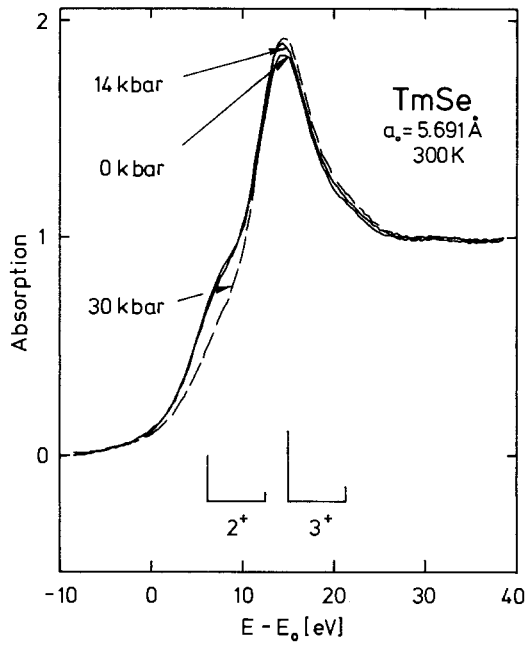

Fig. 20. L_{III} absorption spectra of Tm in TmSe at various pressures. The bar diagram indicates the relative intensities of the split di- and trivalent absorption lines at 0 kbar.

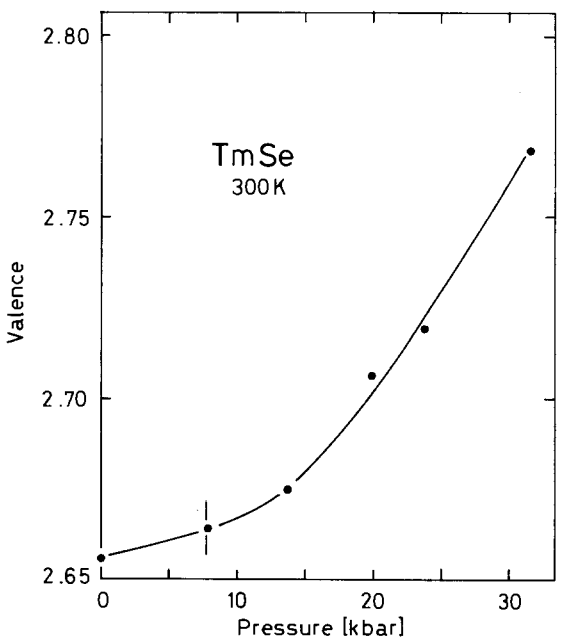

Fig. 21. The valence of Tm in TmSe (a_0 = 5.691 Å) as a function of pressure at 300 K.

stable trivalent state, however is not reached at 30 kbar in contrast to valence determinations from high pressure lattice parameter data through the linear Vegard interpolation (cf. e.g. Vettier et al. (1980)).

The temperature dependence (10–300 K) of the valence in $Y_{1-x}Tm_xSe$ and $La_{1-x}Tm_xSe$ down to concentrations of 5 and 3 at % was measured by Haen et al. (1985) through L_{III} absorption. In both alloys and at all concentrations the valence decreases on cooling. Clearly the thermal contraction (i.e. volume arguments) cannot explain this observation.

10. L_{III} absorption in lanthanide intermetallics with $ThCr_2Si_2$ structure

The lanthanide intermetallic compounds RB_2X_2 (B = transition metal, X = Si, Ge, P, ...) crystallizing in the $ThCr_2Si_2$ structure are of special importance in the physics of valence fluctuations. Apparently the $ThCr_2Si_2$ structure favors the occurrence of mixed valence. For instance, three of the potentially mixed valent lanthanides series actually were found to be mixed valent in the RCu_2Si_2 from the volume anomalies, specific heat, electrical resistivity, magnetic susceptibility and various spectroscopic techniques: $EuCu_2Si_2$, $YbCu_2Si_2$ and $CeCu_2Si_2$ (see e.g. Bauminger et al. (1973), Sales and Wohlleben (1975), Sales and Viswanathan (1976)). L_{III} absorption measurements of $EuCu_2Si_2$ and of dilute Eu in YCu_2Si_2 will be addressed in section 10.1; the possible relationship between the mixed valent state in $CeCu_2Si_2$ and the 'heavy fermion' properties is one of the issues of section 13. Among the RPd_2Si_2 compounds $EuPd_2Si_2$ is of special importance. It exhibits the largest temperature induced valence shift between 4.2 K and 300 K ever observed in an Eu compound ($\Delta v \simeq 0.4$) (cf. table 3).

The body-centered tetragonal $ThCr_2Si_2$ structure is a ternary derivative of the $BaAl_4$ structure. Most of the known ternary lanthanide transition metal silicides, germanides, pnictides (RB_2X_2) crystallize in the $ThCr_2Si_2$ structure (cf. Parthé and Chabot 1984), others in the $CaBe_2Ge_2$ structure which is another variation of the $ThCr_2Si_2$ structure. It is difficult to obtain single-phased crystals of mixed valent RB_2X_2 compounds. Polymorphism of different $BaAl_4$ type derivative structures has been frequently observed. The interplay between the polymorphism and the mixed valent states is a fascinating problem. In most cases the lanthanide atoms in the various polymorphous structures exhibit different valences. For instance, the Mössbauer spectra of $EuCu_2Si_2$ and $EuPd_2Si_2$ reveal the existence of a second mixed valent phase (close to divalence) through a more or less intense line occurring in addition to the main absorption line. The intensity and position of this so-called satellite line depend sensitively on the exact stoichiometry, the thermal treatment, and changing the valence of the main phase. Moreover the fractions of these mixed valent satellite phases are temperature and pressure dependent. In contrast to valence determination by Mössbauer spectroscopy (which unfortunately is restricted to Eu systems), L_{III} absorption is unable to resolve the valence of the individual phases. It measures only an average valence number. Comparative studies of the Mössbauer isomer shift and L_{III} valences are the issues of section 10.2.

Studies on the interplay between structures, chemical bonding and lanthanide mixed valence are in their infancy. The obvious stability of RB_2X_2 mixed valent compounds with B = Cu, Pd may be explained from arguments of quantum chemistry (Hoffmann and Zheng 1985). The $ThCr_2Si_2$ structure consists of B_2X_2 layers interspersed with lanthanide layers. The bonding between lanthanide and B_2X_2 layers appears largely ionic. Therefore the charge partitioning may be written as A^{2+} and $B_2X_2^{2-}$. In the $B_2X_2^{2-}$ layers there is indication not only of covalent B–X bonding but also of some metal–metal B–B bonding. The X–X contact within a layer is large. The X–X contact *between the two layers* is of particular importance for the stabilization of the lanthanide mixed valent states. This contact is found to be tunable, i.e. the interatomic distance between the X atoms sitting on the *c*-axis (d_{X-X}) is the primary geometric variable in this structure. The tuning is provided by the choice of the transition metal. Depending on whether the transition metal B is on the left-hand side or on the right-hand side of the periodic table diatomic X–X bonds are broken or made. Lanthanide mixed valence states mostly occur in RB_2X_2 compounds with Ni, Cu or Pd as transition metals, i.e., at strong X–X bonds (cf. table 3).

10.1. *L_{III} absorption of concentrated and dilute Eu*

Mixed valence is usually investigated in intermetallic compounds where the lanthanide atoms are arranged in high concentration in a translationally invariant lattice. Mixed valence however occurs also in dilute lanthanide impurities in an otherwise normal matrix. L_{III} measurements were applied on dilute Ce, Pr, Nd, Sm,

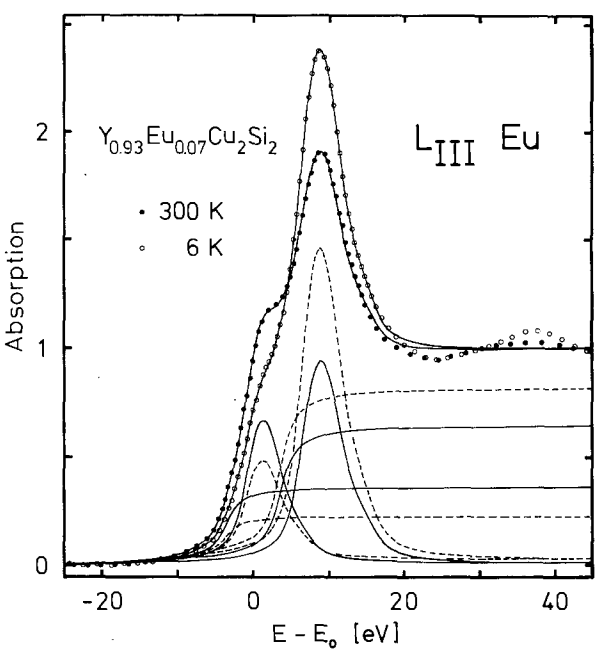

Fig. 22. L_{III} absorption of dilute Europium ($x = 0.07$) in $Y_{1-x}Eu_x$ Cu_2Si_2 at 6 K and 300 K (Bittins et al. 1985). The solid lines connecting the data points are fits to eq. (7). Deconvolutions of the fits are indicated by dashed (300 K) and solid lines (6 K).

Tm and Eu in various matrices (cf. table 3). As an example we discuss a comparative study of the physical properties of dilute and concentrated Eu in YCu_2Si_2. Bittins et al. (1985) performed an extended investigation on the resistivity, thermopower, thermal conductivity, magnetic susceptibility (0–12 kbar) and magnetization at various Eu concentrations (x = 3, 7, 10, 100 at.%). The temperature dependence of the L_{III} absorption (6–300 K) was recorded from the x = 7% sample (fig. 22). Figure 23 displays the temperature dependence of the L_{III} valences for dilute (7%) Eu in YCu_2Si_2 and $EuCu_2Si_2$ (x = 1) together with the Mössbauer isomer shift (main line) of several concentrated and dilute samples. The macroscopic measurements show that the physical properties of dilute alloys and the compounds are similar. The temperature dependences of the valence extracted from the L_{III} absorption for $x = 0.07$ and 1 (thick solid lines in fig. 23) are also similar, like the temperature dependences of the Mössbauer isomer shift. The relative valence shifts (300–20 K) are $\Delta v = 0.16$ for the concentrated sample and $\Delta v = 0.15$ for the dilute sample ($x = 0.07$). The valence number of the dilute sample at 300 K is by +0.05 larger than that of the concentrated sample, in agreement with the tendency observed from the Mössbauer isomer shift. The minority phases cannot account for this discrepancy since they occur at nearly the same positions and have equal intensities in both samples. It seems that the slightly different nonlinearities, observed in the temperature dependences of the L_{III} valences, correspond to the minor deviations between compound and dilute alloy found in the temperature dependences of the thermopower and resistivity.

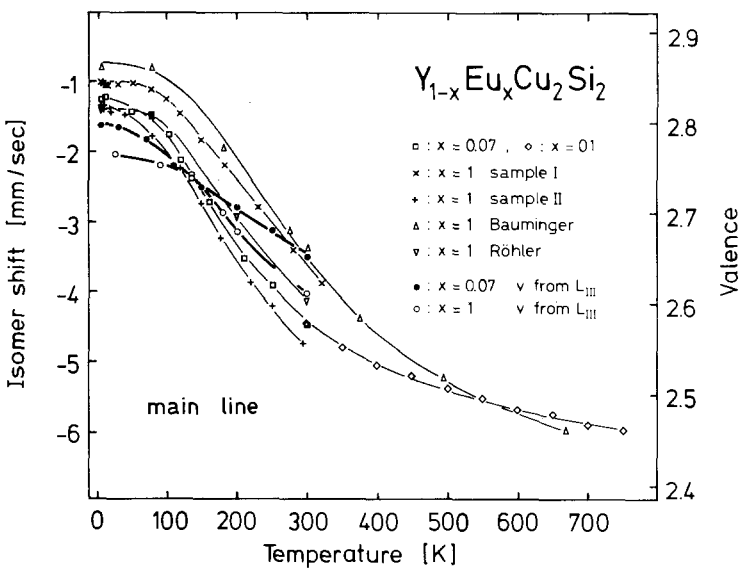

Fig. 23. Temperature dependence of the valence of dilute and concentrated Eu in $Y_{1-x}Eu_xCu_2Si_2$ from L_{III} absorption and Mössbauer isomer shift. The parameters used for the valence calibration of the Mössbauer isomer shift (^{151}Eu, relative to SmF_3) are S_{23} = 13 mm/s and S_3 = +1 mm/s (adapted from Bittins et al. 1985).

10.2. *L_{III} valence versus valence from Mössbauer isomer shift*

Both methods, deep core level X-ray absorption spectroscopy and the recoil free nuclear γ resonance are selective probes of the atomic valence states in the solid. The Mössbauer nucleus detects the s-electron density of the electronic ground state with a hyperfine interaction strength of the order of 10^{-8} eV. Deep core level X-ray absorption probes the electronic state of the atom through creation of an (excited) electronic final-state configuration. The Coulomb interaction strength of the electron–hole pair (in the single-electron picture) is in the order of several eV. Comparison of valence numbers obtained from both methods therefore is instructive. For instance, complementary use of both methods for valence measurements promises to reveal the possible systematic errors to each of the two methods. The comparative studies performed so far were concentrated on Eu systems due to the high resolving power and the large f-factor of the ^{151}Eu Mössbauer resonance. Generally valences from Mössbauer isomer shift and from L_{III} absorption were found to be in rather good agreement (cf. e.g. fig. 23), confirming the absence of significant L_{III} final-state effects. A quantitative agreement is also obtained from L_{III} absorption and Mössbauer isomer shift in SmS under high pressure and as function of stoichiometry (cf. section 9.1).

Both methods, Mössbauer effect and L_{III} absorption probe the fractional valence indirectly through the different screening of the $4f^{n+1}$ and $4f^n$ electrons on the 5s6s and 5d electrons, respectively. The high energy X-ray excitation is a fast measurement and resolves the individual configurations; the Mössbauer effect is a slow measurement and measures the average of the two configurations. Therefore the Mössbauer valence measurement needs a calibration of the valence scale from appropriate $4f^{n+1}$ and $4f^n$ reference values S_{n+1} and S_n, respectively (as the valence measurement from lattice parameters). As discussed previously, the Vegard-type valence measurement from the lattice parameters and the corresponding 'ansatz' for the isomer shift analysis $v_{ME} = (S - S_{n+1})/(S_n - S_{n+1})$ are rather coarse approximations. For more accurate valence determinations from the Mössbauer isomer shift one should take into account the distinctly different f-factors of the Mössbauer resonance of the two valence states. Kemly et al. (1985) and Wortmann et al. (1985) observe more or less linear relationships between the isomer shift S and the valence from L_{III} absorption in $EuPd_2Si_2$ between 4 and 300 K. Röhler (1985a) observed in the same compound a significantly nonlinear relationship similarly to the 'sagging curve' behavior, observed in the volume–valence relationship (cf. eq. (9)). Such a nonlinear isomer shift–valence relationship is also obtained from fig. 23 ($EuCu_2Si_2$). The reason of the discrepancy between the plots of Kemly et al. (1985), Wortmann et al. (1985) on one hand and Röhler (1985a) on the other hand is not clear at the time. Since falsifications of the relative L_{III} intensities due to temperature induced final-state effects can be definitely excluded, the discrepancy between the experimental results might originate from different choices of the spectroscopic parameters deconvoluting the L_{III} spectra. As discussed previously in sections 7.2 and 8.3.4 the trivalent line should be fitted with a larger linewidth than the divalent line.

10.3. $EuPd_2P_2$

The RPd_2P_2 series is different from the RPd_2Si_2 and RCu_2Si_2 series with respect to their stability throughout the lanthanide series. $TmPd_2P_2$ cannot be obtained under the preperation conditions of RPd_2P_2 (R = La–Er). $LuPd_2P_2$ does not exist. $EuPd_2P_2$ and $YbPd_2P_2$ exhibit positive volume anomalies (Jeitschko and Hoffmann 1983). It seems that the RPd_2P_2 crystals tend to stabilize the divalent lanthanide configurations, at least at the end of the series. Obviously $ErPd_2P_2$ is the last compound which can be prepared with a stable trivalent lanthanide atom. Jeitschko and Hoffmann (1983) claim that the relatively small volume anomaly ($\Delta V = 2.5$ Å^3 per formula unit) of $EuPd_2P_2$ indicates a mixed valent state between Eu^{2+} and Eu^{3+}. However, it is problematic to extract valence numbers exclusively from volume data. For instance the difference between stable di- and trivalent $ThCr_2Si_2$ primitive cells, $V_{23} = V_2 - V_3$, is not a universal number. The volume anomaly of, e.g., nearly divalent EuO ($v = 2.03$) is only 50% of the volume anomaly of EuS ($v = 2$). With the upper limit $V_{23} = 9$ Å^3 one obtains $v_v = 2.72$ for $EuPd_2P_2$ using a Vegard-type interpolation. From the more realistic nonlinear interpolation (sagging curve, cf. eq. (9)) we would then expect the 'true' valence to be smaller by about 0.1–0.2; i.e. the conservative valence estimate from the volume data would be $v \cong 2.6$. The lower limit may be obtained assuming ionic bonds between the Eu^{2+} atom and the $Pd_2P_2^{2-}$ layer: $V_{23} = 2.3$ Å^3 (from the ionic radii). This number is close to the observed volume anomaly and hence $EuPd_2P_2$ would be divalent.

The magnetic susceptibility between 300 and 4.2 K exhibits an effective magnetic moment $\mu_{eff} = (8 \pm 0.2)\mu_B$, corresponding to the pure Eu^{2+} ($^8S_{7/2}$) ground state with a negative Curie–Weiss temperature of $\Theta_P = -30$ K. Both, magnetic susceptibility and the magnetic hyperfine splitting in the Mössbauer spectrum indicate magnetic ordering of the Eu ions ($T_N \cong 20$ K). The ESR signal from the Eu ions has a linewidth of 800 Oe at 77 K. The Mössbauer isomer shift is found to be temperature-independent at $S = -9.73 \pm 0.05$ mm/s (Sampathkumaran et al. 1984). The full magnetic moment and the Mössbauer data indicate a divalent or nearly divalent state of Eu in $EuPd_2P_2$ confirming the volume anomaly V_{23} to be close to the lower limit. We would like to mention that magnetic ordering in Eu systems may coexist with a mixed valent state and therefore should not be considered as the signature of a stable divalent state. The coexistence of magnetic ordering and mixed valence has been unambiguously demonstrated in the high pressure phases of Eu metal (cf. section 11.1) and in $Eu(Au_xPd_{1-x})_2Si_2$ (Segre et al. 1982).

The spectroscopic determination of the valence through L_{III} absorption indicates a nominal valence of 2.15 ± 0.075 (Sampathkumaran et al. 1985a), slightly larger than the number expected from the magnetic susceptibility, and confirming the lower estimate of the volume anomaly. Wortmann et al. (1986) discusses possible trivalent sample contaminations from the powdering procedure to explain the L_{III} result. The valence of bulk polycrystalline material extracted from the total fluorescence yield turns out to be smaller by 0.04 (depending on the geometry) than the valence of powdered samples. Correcting the data for trivalent contaminations from Eu_2O_3 (as determined from Mössbauer spectroscopy), Wortmann et al. (1986) find $v = 2.1$.

Sampathkumaran et al. (1985a) attribute the intensity of the high-energy peak in the L_{III} spectrum of $EuPd_2P_2$ to a final-state configuration interaction effect (shake up) and therefore claim that the high-energy peak does not measure the average occupation of the trivalent $4f^6(5d6s)^3$ configuration in the ground state. This objection is based: (i) on the magnetic data, (ii) the 'divalent' Mössbauer isomer shift S and its normal pressure derivative at 4.2 K and (iii) on 3d, 4d and valence band photoemission spectra.

(i) The valence number $v = 2.1$ reconciles with the effective magnetic moment within the scatter of the susceptibility data (300–4.2 K) of Sampathkumaran et al. (1984). For an improved accuracy of the magnetic valence measurement one needs high temperature data at $T \gg 300$ K.

(ii) It is well known that the systematics of the Mössbauer isomer shifts yields no absolute scale for valence determinations. The Mössbauer isomer shifts for divalent Eu scatter between -7.9 mm/s and about -18 mm/s. The pressure derivative of the Mössbauer isomer shift at 4.2 K is not a signature of mixed valent behavior. Even in strongly mixed valent materials as $EuCu_2Si_2$ and $EuPd_2Si_2$ $\partial S/\partial p$ at 4.2 K is close to the 'normal' numbers (cf. Röhler 1979, Schmiester et al. 1982).

(iii) The 3d photoemission data (Wertheim et al. 1985) exhibit 15% Eu^{3+} components in the spectrum. No Eu^{3+} components were extracted from the 4d photoemission and the valence band spectrum. Probably they are below the detection limits of these spectroscopies. The final-state shake up intensity in the Eu 3d spectrum poses a problem. Following the current theories of many-electron effects on photoexcitation of core levels (see e.g. Kotani and Toyozawa (1979)), the creation of a core hole in metallic materials with hybridized 4f states induces 'shake down' processes, i.e. components of the $3d^94f^8$ multiplet in Eu spectra. However, the divalent Gd^{2+} ($4f^8$) configuration does not exist in solids. Thus the 'shake down' probability in Eu is close to zero. The same argument applies to the discussion of probable 'shake' effects in absorption. Instead 3d photoemission exhibits 'shake up' intensities ($3d^94f^6$). We conclude that the photoemission data from $EuPd_2P_2$ add another puzzle to the problems of photoemission in mixed valent lanthanide systems.

Unlike Sampathkumaran et al. (1985) we feel that the high-energy intensity in the L_{III} spectrum of $EuPd_2P_2$ is not attributable to final-state effects. Apparently Eu in $EuPd_2P_2$ is strongly bound (covalent or ionic) to the Pd_2P_2 layers. Even if the 4f electrons participate in the chemical bonding, the high-energy intensity cannot be explained in the framework of the current many-electron theories. Assuming the final-state effect to be true, its intensity is expected to increase with the degree of covalency. Wortmann et al. (1986) compared accurately the Mössbauer isomer shift (which is a measure of the degree of covalency) and the trivalent L_{III} intensities in series of nominally divalent Eu compounds. With the increasing degree of covalency (i.e. more negative ^{151}Eu isomer shift numbers), the trivalent L_{III} intensities were found to *decrease*, just the opposite trend as expected from covalency dependent 'shake up' processes.

It is conceivable, that a strong ligand field splits the spectral density of the $2p$–$4f^75d$ excitation (as discussed e.g. in sections 9 and 14). However, even in the clearly

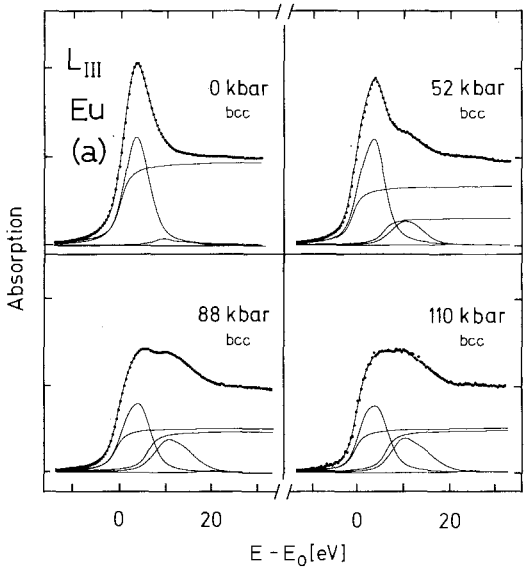

Fig. 26a. L_{III} absorption spectra of Eu in elemental Eu at various pressures in the crystallographic bcc phase (Röhler 1986b).

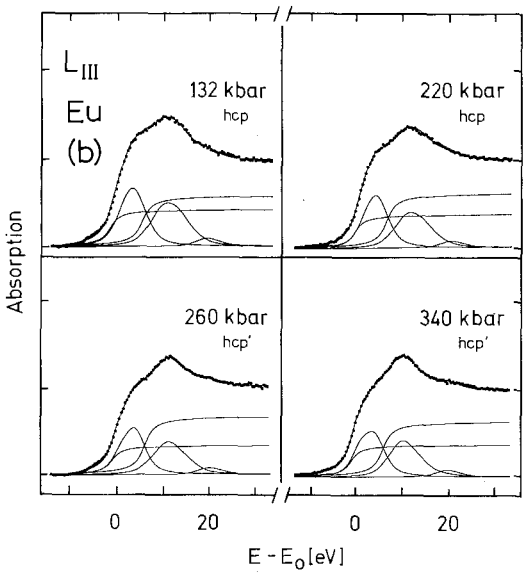

Fig. 26b. L_{III} absorption spectra of Eu in elemental Eu at various pressures in the crystallographic hcp phases (Röhler 1986b).

are used to monitor the phase transitions. At pressures $p > 200$ kbar the valence turns out to be independent of pressure and 'saturates' at $v = 2.64$. In contrast to the known theoretical calculations Eu does not reach the trivalent state at the highest applied pressure ($p = 340$ kbar). The energetics of the valence saturation was analyzed by Röhler (1985b) through a thermodynamical approach: in terms of volume and valence dependent free energies, including a valence dependent elastic (segregational) energy and an energy due to configurational mixing. It turns out that low volumes ($V/V_0 < 0.5$) drastically favor the latter term, minimizing the total

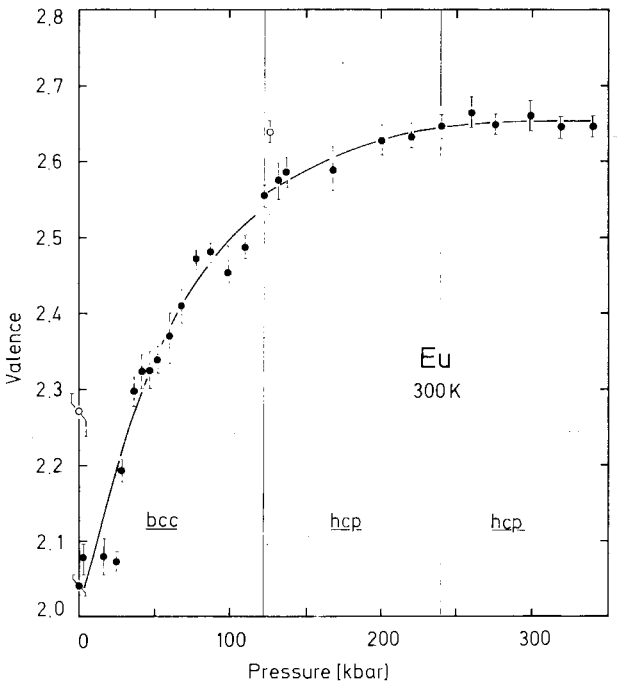

Fig. 27. The valence of Eu as a function of pressure at 300 K (Röhler 1986b).

energy at $v = 2.6$. The fit of this thermodynamical model to the observed high-pressure valence indicates that the nonmagnetic $^7F_0$ Hund-rule $4f^6$ ground state does not contribute to the configurational mixing, however its excited magnetic states $^7F_1$ and in particular $^7F_2$ do. This finding may qualitatively explain the *coexistence of mixed valence and of magnetic ordering* in Eu at high pressures. Magnetic ordering in Eu at high pressures was observed by Bundy and Dunn (1981) from resistivity data, and by Farrell and Taylor (1987) from the ^{151}Eu Mössbauer magnetic hyperfine splitting. According to the thermodynamical analysis of Röhler (1985b) the effective 4f bandwidth in the valence saturation phase is estimated to be about 0.1 eV at 125 kbar.

11.2. *Yb under high pressure*

Fcc ytterbium at atmospheric pressure and room temperature is a metal. With the application of pressure Yb becomes a semi-metal and then a semiconductor. The semiconducting fcc phase transforms into a metallic bcc phase at about 40 kbar (Jayaraman 1978), while Divakar et al. (1984) give 33 kbar. The relative volume change is about 3%. Another structural phase transformation (bcc–hcp) occurs at 260–309 kbar (cf. Takemura and Syassen 1985). Similar to europium the p–V isotherm of the adjacent trivalent reference element lutetium is found to intersect that of Yb at about 200 kbar (at 300 K). Syassen et al. (1981, 1982) measured the L_{III} absorption in Yb under high pressure up to 340 kbar with a conventional laboratory spectrometer. Divalent Yb clearly transforms into a mixed valent state at 40 kbar

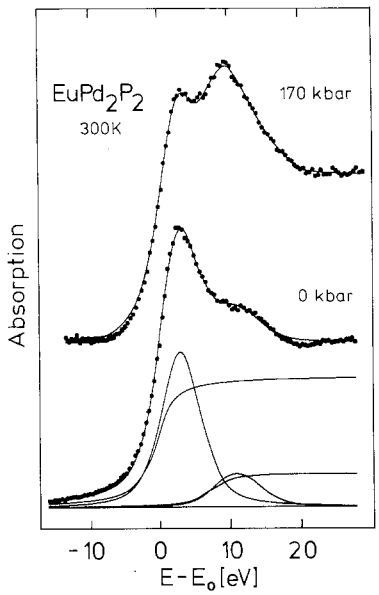

Fig. 24. L_{III} absorption of Eu in $EuPd_2P_2$ at ambient pressure and 170 kbar. A contribution of 8% trivalent Eu_2O_3 was subtracted from the original data.

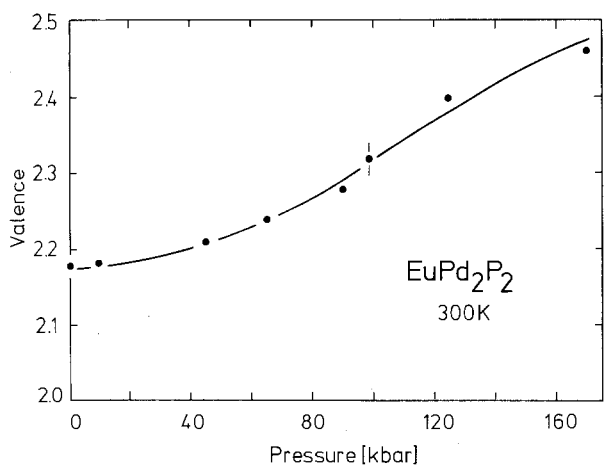

Fig. 25. The valence of Eu in $EuPd_2P_2$ as a function of pressure at ambient temperature.

ionic Ce compounds this splitting is distinctly smaller than the $\Delta_{kl} = 7.7$ eV found in $EuPd_2P_2$. Such a large splitting accounts for a 2p binding energy shift on 4f configurational change. Summarizing we find that the 'archetypal' case study of $EuPd_2P_2$ is far from giving conclusive evidence on significant final state effects in the L_{III} absorption of heavy lanthanides.

Figure 24 displays the L_{III} absorption of Eu in $EuPd_2P_2$ (300 K) at ambient pressure and 170 kbar. The valence vs pressure is nonlinear for 0–170 kbar (fig. 25) and has an inflection point at about 100 kbar. Compared to the pressure dependence of valence, e.g., in the ternary intermetallic compound $EuPd_2Si_2$ (cf. table 3) we observe a much weaker pressure dependence of valence, which compares with

that of EuO undergoing a semiconductor–metal transition at 130 kbar (cf. section 9).

11. L_{III} absorption in the divalent lanthanides under high pressure

Eu and Yb are the only lanthanide elements which keep their divalent atomic configurations of the gas phase, $4f^7\,5d^0\,6s^2$ and $4f^{14}\,5d^0\,6s^2$, upon condensation into the crystalline state.

High pressure is expected to destabilize the divalent metallic configurations of elemental Eu and Yb and to transform them into a stable trivalent state. Johansson and Rosengren (1976) predicted the mixed valent transition pressure regime of Eu to start at about 180 kbar and to range up to 350 kbar. From a similar type of calculation (Johansson and Rosengren 1975, 1976) Yb was expected to become trivalent at about 130 kbar. For a discussion of the pressure induced valence changes in these elements see, e.g., Jayaraman (1978).

The magnetic and thermal anomalies of Eu and Yb, observed already at ambient pressure, stimulated experimental and theoretical efforts to verify the presence of both configurations $4f^{n+1}$ and $4f^n$ ($n = 6$ for Eu and 13 for Yb). The $L_{II,III}$ absorption lines of both divalent elements exhibit the characteristic shift of about -8 eV with respect to the trivalent sesquioxides. Normalizing the energy scales (E–E_0) with respect to identical atomic volumes, the lineshapes at high energies turn out to deviate insignificantly from the elemental trivalent references (cf. section 7). Therefore from L_{III} absorption possible mixed valent states of Eu and Yb at ambient pressures are expected to be close to 2, if they exist at all. The $M_{IV,V}$ absorption of Eu indicates a similarly insignificantly small deviation from the theoretical divalent final state multiplet (Thole et al. 1985). High pressure L_{III} absorption experiments proved that both divalent elements, Eu and Yb, transformed into mixed valence but at low pressures, far below the calculated transition pressures in the 100 kbar range.

11.1. *Eu under high pressure*

Eu at ambient pressure crystallizes in the bcc structure; the bulk modulus is $B_0 = 117$ kbar. At 125 kbar the bcc structure collapses into the hcp structure ($\Delta V/V = 4\%$) and transforms between 180 and 240 kbar into a related hcp structure (hcp′). Surprisingly the high-pressure volume of Eu intersects the corresponding high-pressure volume of stable trivalent Gd at $p \geqslant 200$ kbar (cf. e.g. Takemura and Syassen (1985) and references therein). Figure 26 displays typical L_{III} absorption spectra of elemental Eu in its various crystallographic phases at high pressure: (a) bcc phase, (b) hcp and hcp′ phases (Röhler 1986b). The solid line connecting the data points represents a fit according eq. (6). The valence numbers obtained from these fits are reproduced in fig. 27 as a function of pressure. Already at low pressures ($p \leqslant 30$ kbar) elemental Eu exhibits mixed valence. Lowering the volume the valence increases and reaches $v = 2.55$ at the bcc–hcp phase boundary. The L_{III} lineshapes in the various crystallographic phases obviously differ from each other and therefore

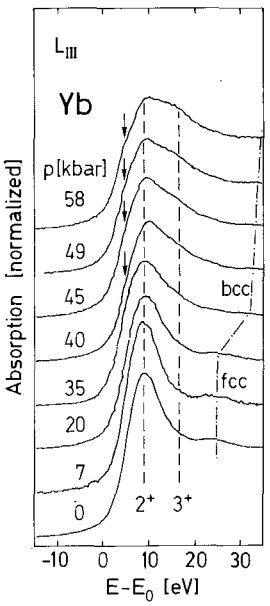

Fig. 28. L_{III} absorption of Yb as a function of pressure at 300 K in elemental Yb below and above the fcc–bcc phase transition at about 30 kbar.

($v = 2.2 \pm 0.05$) reaching $v = 2.5$ above 100 kbar. A single data point in the hcp phase at 340 kbar is interpreted to indicate a trivalent or nearly trivalent state in elemental Yb. However, due to the scatter of the data points at high pressures, this experiment does not yield reliable valence numbers at $p > 200$ kbar. Therefore it is still an experimentally unanswered question whether the valence of Yb saturates at high pressures as the valences of Ce and Eu do. Figure 28 displays the high pressure L_{III} absorption of Yb (recorded by the author) in the vicinity of the fcc–bcc phase transformation (0–58 kbar). The transition (at 35 kbar) may be clearly monitored from the shift of the change of the near edge structure at $E - E_0 > 25$ eV. Low pressures ($p \geqslant 7$ kbar) only broaden the absorption line at the high-energy side of the maximum ('volume broadening', cf. section 7.3). The 'trivalent line' however, can be already discerned from the prominent line at $p \geqslant 20$ kbar, below the nominal fcc–bcc transition pressure. The 'divalent line' in the bcc phase exhibits a shoulder at the absorption onset (arrows). A similar fine structure has been detected in the high-pressure bcc phase of Eu (cf. fig. 26a, 52 kbar).

12. The cerium problem viewed from L_{III} absorption

Cerium exhibits the most complicated T–p phase diagram of the lanthanides (cf. e.g. Koskenmaki and Gschneidner (1978)). The intriguing and different behavior of elemental cerium in its various phases and of cerium in a large manifold of compounds, concentrated and dilute alloys exhibiting fascinating deviations from the 'normal' solid state, stimulated intensive spectroscopic investigations through X-ray spectroscopies. Cerium is frequently considered to be an exceptional case among

the lanthanides due to the apparently stronger hybridization between the 4f and the conduction electrons at the beginning of the lanthanide series. The fascinating anomalies of cerium usually are attributed to a transition from a localized to a delocalized 4f state. Zachariassen and Pauling suggested the isostructural γ–α transition of Ce metal to originate from the promotion of the $4f^1$ electron into the tetravalent conduction electron configuration, hence changing the valence from three to four. A partial valence transition from 3.06 to only about 3.69 in the γ–α transition was suggested by Gschneidner Jr and Smoluchowski (1963) on the basis of volume and magnetic data. In a thermodynamical approach Johansson (1974) attributed this transition to be a Mott transition resulting in a 1 eV wide 4f band.

L_{III} absorption spectra of Ce intermetallic compounds were published by Bauchspiess et al. (1981). γ-type compounds exhibit strong trivalent absorption lines and a more or less pronounced shoulder at high energies, indicating already the presence of tetravalent cerium. α-type compounds can be clearly distinguished spectroscopically from the γ-type compounds through a characteristic double-peaked shape (for the discussion of CeO_2 cf. section 14). According to these spectra cerium in metals occurs never in completely trivalent or tetravalent states; it apparently always occurs in two types of mixed valent states. The valence of γ-type Ce is $3 < v \leqslant 3.14$ and the valence of α-type is Ce $3.14 \leqslant v < 3.3$–3.4 (cf. Wohlleben 1982, Wohlleben and Röhler 1984).

12.1. *L_{III} absorption in elemental Ce under high pressure*

L_{III} absorption spectra of elemental cerium under high pressure and at room temperature were recorded by Röhler et al. (1984a), Röhler (1984), under high pressures *and* low temperatures by Keulerz et al. (1986). Along the room temperature isotherm (fig. 29a) Ce transforms at 8 kbar into the α-phase, at 51 kbar into the superconducting α'-phase and at 112 kbar into the tetragonal phase. Along the 6 kbar isobar (fig. 29b) Ce transforms at about 150 K into the α-phase. Figure 29a displays the L_{III} spectra of γ-Ce (0 kbar), α-Ce (9, 24, 42 kbar), α'-Ce (61 kbar) and tetragonal Ce (120 kbar) at 300 K, fig. 29b shows the L_{III} absorption in the edge and near edge region of elemental Ce at 6 kbar between 300 K and 5 K. The spectra have a double-peaked shape in the α- and α'-phases. The two absorption lines are assigned to the final-state configurations $2p^5 4f^1 \underline{5d}^*$ and $2p^5 4f^0 \underline{5d}^*$, according to a $3^+/4^+$ mixed valent state. The valence along the room temperature isotherm changes from 3.03 to 3.32 with jumps by $+10\%$ each in the γ–α and α'-tetragonal transitions and with a clear reversal by about -3% near the α–α' transition. Across the entire α'-phase the valence remains pressure independent (fig. 30).

The splitting of the two distinct lines in γ-type spectra is slightly larger (8–9 eV) than in mixed valent ($2^+/3^+$) Sm, Eu, Tm and Yb intermetallics. The L_{III} absorption lines in α-type Ce systems are relatively broad and have weak total intensities.

Parks et al. (1983) find from their analysis of the L_{III} absorption in intermetallic compounds that the linewidth W_3 of the low-energy line ($4f^1 \underline{5d}$) is larger than the width W_4 of the high-energy line ($4f^0 \underline{5d}$). Beaurepaire et al. (1984) fit to the α-type absorption spectra in $Ce(Pd_x T_{1-x})_3$ (T = Ag, Rh) and $Ce_x Y_{1-x} Pd_3$ two lines

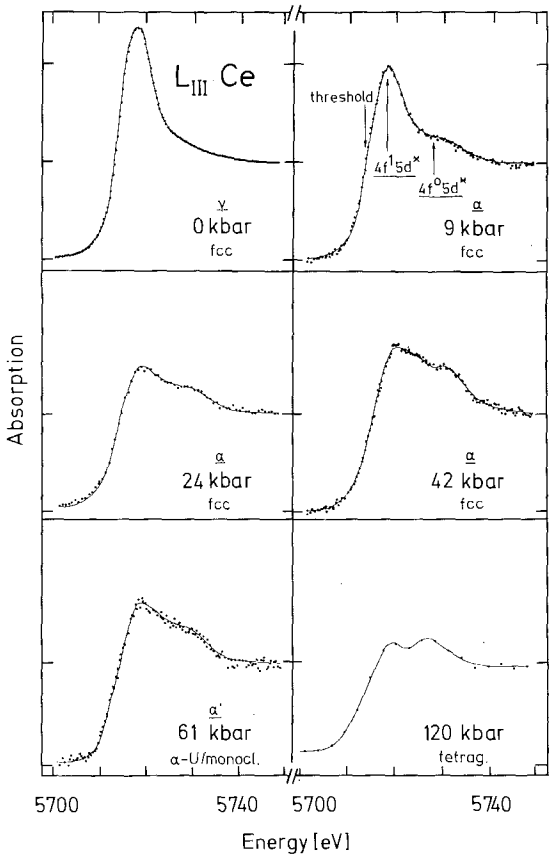

Fig. 29a. L_{III} absorption of elemental cerium in γ-Ce, α-Ce, α'-Ce and tetragonal Ce at ambient temperature (adapted from Röhler 1984).

exhibiting linewidth ratio $W_3/W_4 = 1.8$–2.4. From the discussion of the relationship between the metallic radii and the radial extension of the 5d wavefunction (section 7.3), we expect $W_4 > W_3$. We stated in section 7.3 that relatively large linewidths correspond to the configurations of the higher valence state and vice versa. It is clearly visible from fig. 29b (spectrum at 5 K) that the tetravalent line is larger than the trivalent line and in addition 'chemically' split as discussed in section 8 (cf. fig. 16). Taking properly into account this splitting, one obtains a reasonable linewidth ratio $W_3/W_4 =$ p.7 according to the volume arguments.

It is still a matter of controversy whether the XPS theories complementarily might apply to the analysis of L absorption (cf. section 3). If they apply, do shake effects falsify the L_{III} valence numbers as in XPS? Raaen and Parks (1985) and Raaen et al. (1983) address the linewidth problem discussing the experimental evidence of possible many-electron effects in Ce L_{III} absorption spectra. For this purpose they discern fine structures at the leading edge of trivalent absorption line in RPd_3 (R = La, Pr, Nd) and RNi_5 (R = La, Pr, Nd, Sm) from the prominent line intensities subtracting the spectra from its corresponding Gd isomorphs. Aligning the spectra at the absorption maxima, the intensities of such fine structure are found to be

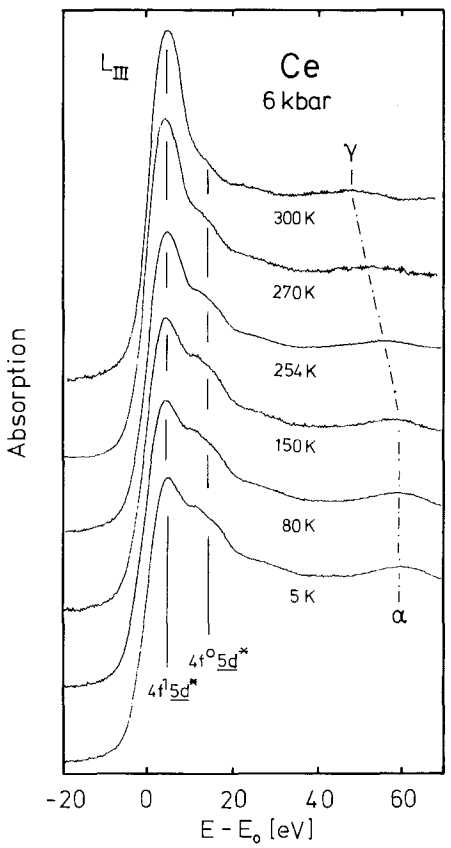

Fig. 29b. L_{III} absorption of elemental cerium at the temperature induced γ–α transition along the 6 kbar isobar from 300 K to 5 K. As is clearly visible the tetravalent line ($4f^0\underline{5d}^*$) of α-Ce is split (Keulerz et al. 1986).

$>12\%$ and to decrease with increasing Z. They vanish in the Sm spectra. These weak lines are interpreted to be $4f^{n+2}$ shake down satellites as the lines observed closest to E_F in 3d photoemission (cf. chapter 62). According to the approach of Gunnarsson and Schönhammer (1983) for mixed valent X-ray photoemmission spectra (cf. chapter 64), the probability for shake processes on photoexcitation of instable 4f systems is proportional to the 4f conduction electron hybridization Δ. Δ is expected to decrease with the lanthanide contraction and hence also the shake intensities. Raaen and Parks (1985) calculate the error occurring in a valence determination procedure assuming such final-state effects to be $\Delta v = 0.006$. A similar analysis was performed by Bianconi et al. (1984) and Marcelli et al. (1985) analyzing a fine structure in RPd_3 (R = La, Ce, Pr, Nd) and $CeCu_2Si_2$ from the absorption derivatives.

In addition to the information on the valence state the L_{III} *absorption of Ce as function of volume* yields distinct information on the final-state problem. If the 4f conduction electron hybridization strength would be volume-dependent, the 'shake up' intensity at the leading edge of the trivalent absorption line should increase with pressure. The 2p binding energy shift of the hypothetical divalent 'shake up' from

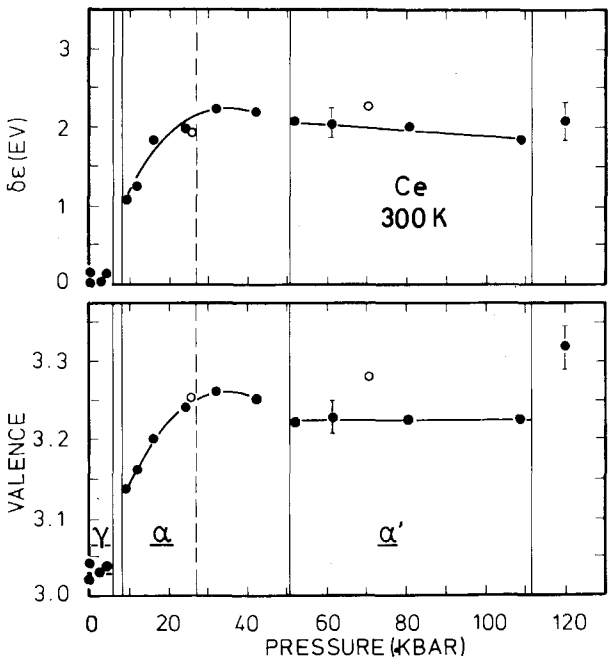

Fig. 30. The pressure induced shift of the center of gravity of the L_{III} absorption lines of Ce metal (top) (the shift between $Ce^{3+}(4f^1)$ and $Ce^{4+}(4f^0)$ is about 10 eV); the valence of Ce as function of pressure obtained from the ratio of the intensities of the tri- and tetravalent lines (bottom) (pressure increasing (●) and decreasing (○)) (Röhler et al. 1984a).

the trivalent final state would be about −4 eV. An increasing 'shake up' intensity with decreasing volume therefore should shift the onset of the absorption (threshold in fig. 29a) to lower energies. Figure 31 displays the pressure dependence of the position of the threshold and of the tri- and tetravalent maxima. It turns out that the threshold energy depends only weakly on pressure and is slightly shifted towards *high* energies. From the 'shake up' hypothesis one expects just the opposite tendency.

12.2. *Valence saturation in intermetallic Ce compounds and dilute alloys*

Ce intermetallics, concentrated and dilute alloys exhibit similar electronic properties as elemental Ce in its various phases. Analogous to the external pressure in the element, 'chemical pressure' induces transitions from magnetic γ-type to nonmagnetic α-type Ce systems. The L_{III} absorption spectra of Ce in these systems may serve as a fingerprint of the specific electronic state, i.e., double-peaked spectra with $v \geqslant 3.14$ indicate nonmagnetic α-Ce. As in Ce metal under high pressure the valence in dilute and concentrated alloys and in compounds saturates at low atomic Ce volumes, i.e., the valence does not exceed 3.4 (cf. table 3). In analogy to the 2^+–3^+ valence transitions, the tetravalent absorption spectrum would be expected to exhibit a shift of the center of gravity of the atomic part by about + 7 eV above the γ-type spectra. No such tetravalent spectrum of Ce in metals was ever observed. (The L_{III} spectra of Ce in the nominally tetravalent insulators will be discussed in section 14). Lengeler et al. (1983a) measured the L_{III} absorption of dilute Ce in Pd, Y, Sc and Yb, while they did not extract valence numbers from these spectra. It is obvious by inspection that dilute Ce impurities behave just like Ce in compounds.

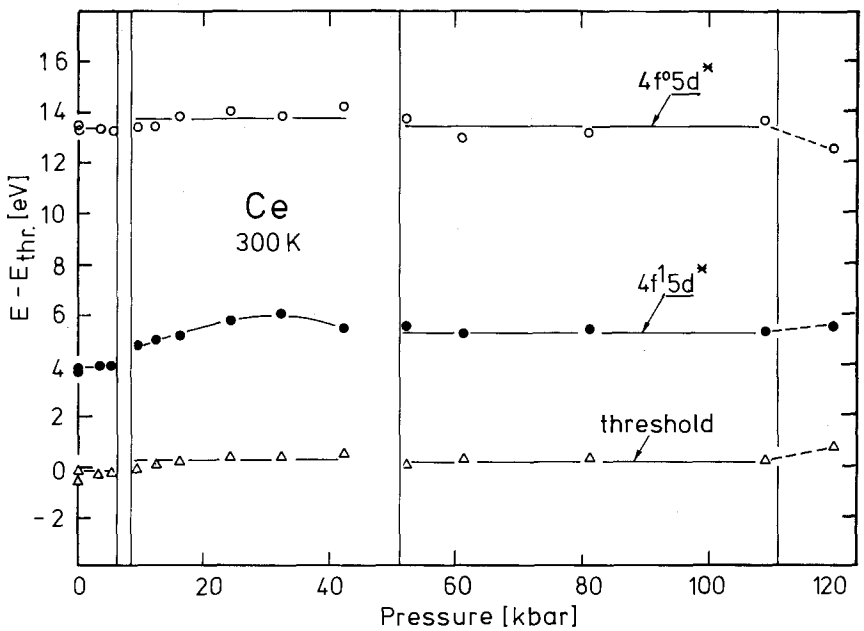

Fig. 31. Positions of the L_{III} threshold, the maxima of the (trivalent) low-energy and the (tetravalent) high-energy absorption in elemental Ce vs pressure (cf. fig. 29a).

They exhibit valences between 3 and 3.4. Beaurepaire et al. (1984) and Parks et al. (1983) studied the L_{III} absorption in $Ce(Pd_{1-x}T_x)_3$ (T = Ag, Rh, Y). The volume dependence of the Ce valence in these alloys is found to be similar to the valence–volume relationship measured in Ce metal under high pressure (Röhler 1985a). At small volumes the valence is pinned at about 3.3.

An analysis of the valence saturation of Ce metals at low volumes in the framework of the thermodynamics of valence fluctuations is given by Röhler et al. (1984a), Wohlleben and Röhler (1984) and Wohlleben (1984b).

13. L_{III} absorption of Ce in 'heavy fermion' Ce systems

The Ce intermetallics $CeCu_2Si_2$, $CeCu_6$, $CeAl_3$ exhibit an anomalously large specific heat coefficient of order $\gamma = 1$ J/mole/K^2; i.e., γ is up to two orders of magnitudes larger than in normal metals. These materials are usually considered to be trivalent. Investigations of the L_{III} absorption of Ce at low temperatures in these 'heavy fermion' materials were performed by Klug et al. (1985). The L_{III} absorption in $CeCu_2Si_2$ (nonsuperconducting at ambient pressure) under high pressure up to 200 kbar was recorded by Röhler et al. (1987).

13.1. *L_{III} absorption of Ce in $CeAl_3$, $CeCu_6$, $CeCu_2Si_2$*

Figure 32 (right-hand side) displays the Ce L_{III} absorption spectra of $CeCu_2Si_2$

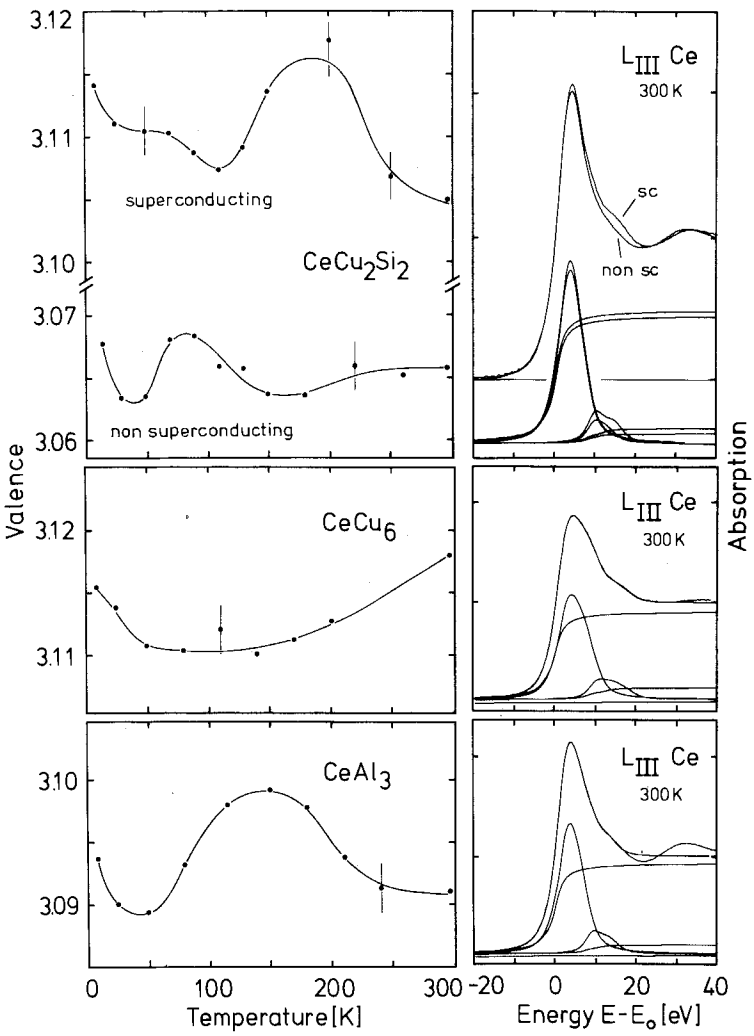

Fig. 32. Valences vs temperature of Ce in the 'heavy fermion' systems $CeCu_2Si_2$ (superconducting and nonsuperconducting samples), $CeCu_6$ and $CeAl_3$ together with the L_{III} absorption spectra at 300 K (adapted from Klug 1986).

(superconducting and nonsuperconducting sample), $CeCu_6$ and $CeAl_3$ at ambient pressure. The presence of tetravalent Ce is clearly visible from the spectra. Ce heavy fermion materials are not purely trivalent but mixed valent. From the deconvolution of the spectra one obtains valence numbers between 3.065 and 3.12. The valence numbers of superconducting $CeCu_2Si_2$ and $CeCu_6$ are close to $v = 3.14$, i.e., close to the crossover from γ- to α-Ce. Figure 32 (left-hand side) shows the temperature dependences of the valences between 300 K and helium temperature. Note the zoomed valence scales. Within $\Delta v = 0.01$ the valences remain temperature independent. Due to the excellent statistics of the spectra and the precision of the fits (cf. section 15), relatively small valence changes could be resolved. The temperature

dependences of the valences exhibit characteristic nonlinearities. They reflect the different crystal field schemes of the $4f^1$ Hund-rule ground states. The observed temperature dependence of the valence may be related, e.g., to the resistivity anomalies (Klug 1986, Klug et al. 1985).

13.2. *L_{III} absorption of Ce in $CeCu_2Si_2$ under high pressure*

L_{III} absorption spectra of Ce in $CeCu_2Si_2$ (nonsuperconducting at ambient pressure) at pressures up to 200 kbar are displayed in fig. 33. The spectra are similar to the high-pressure spectra of elemental cerium, displayed in figs. 29a,b. Apparently the transition to α- or α′-type cerium is shifted to higher pressures than in elemental cerium. The valence vs pressure is shown in fig. 34. It increases with increasing p and seems to saturate at about $v = 3.4$ for $p > 150$ kbar. At 38 kbar

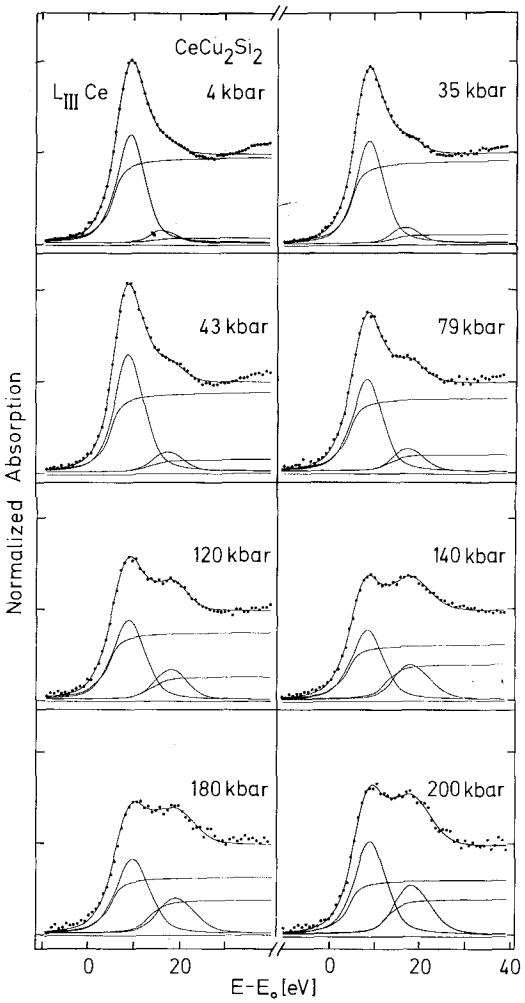

Fig. 33. L_{III} absorption of Ce in $CeCu_2Si_2$ (nonsuperconducting at $p = 0$ kbar) at high pressures. Lines connecting the data points are fits according to fig. 16 (Röhler et al. 1987).

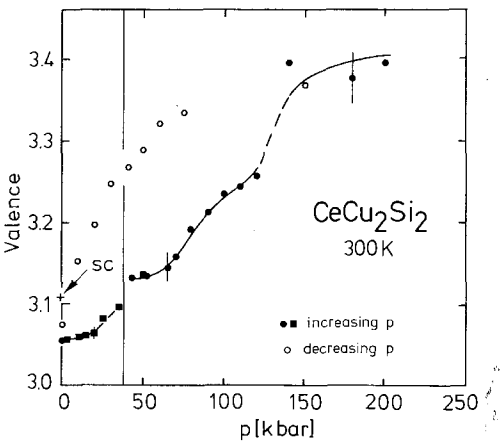

Fig. 34. The valence of Ce in $CeCu_2Si_2$ (non-superconducting at ambient pressure) as function of pressure. The cross at ambient pressure indicates the valence of the superconducting sample shown in fig. 32 (top). A first-order valence transition occurs at 38 kbar (vertical line).

(vertical line) one observes a first-order valence transition. The cross in fig. 34 indicates the valence of the superconducting sample shown in fig. 33. Hence the nonstoichiometry of the superconducting sample (excess copper) seems to cause an internal pressure of about 38 kbar shifting the valence into a two-phase region around the pressure of the first-order valence transition. Most interestingly the pressure dependence of the superconducting transition temperature T_c (Jaccard et al. 1985) exhibits a steep increase from about 0.8 K to 2.2 K between 20 and 35 kbar. This increase of T_c with pressure is comparable to the superconducting transition temperature vs pressure in Ce metal at the α–α' phase border line (Probst and Wittig 1978). The interplay between the mixed valent states, biphased structural features and the occurrence (or suppression) of superconductivity is a fascinating phenomenon. Braun et al. (1983) observed polymorphism for $LaIr_2Si_2$ between a high-temperature phase of a $CaBe_2Ge_2$ structure and a low-temperature phase of the $ThCr_2Si_2$ structure. The high-temperature modification exhibits superconductivity, while the low-temperature modification is nonsuperconducting. One may speculate whether the valence transition in $CeCu_2Si_2$ at 38 kbar is associated with a structural change into another derivate of the $BaAl_4$ structure (cf. section 10).

Figure 35 shows the individual linewidths W_3, W_4 of the L_{III} absorption in $CeCu_2Si_2$ as obtained from the spectra, exhibited in fig. 33 (cf. also fig. 16). The linewidths are pressure (volume) dependent as expected from the relationship of atomic volume and spectral density (section 7.3.). W_4 exhibits a larger pressure derivative than W_3. Plotting W_3, W_4 vs the occupation number v of the tetravalent state, we find a correlation of the linewidth differences $W_4 - W_3$ and the fractional valence. The derivative $\partial(W_4 - W_3)/\partial v = 8.6 \pm 1$ eV. This number seems to be a universal number in Ce systems. It has been found in elemental cerium under high pressure and Ce $(Pd_{1-x}T_x)_3$ (T = Ag, Rh, Y) also. From the L_{III} spectra in $2^+/3^+$ mixed valent materials (Pr, Sm, Eu) one extracts 2.6 eV (cf. e.g. Röhler et al. (1983a), Lübcke (1985)). At the time there is no sound interpretation of these empirical relationships between valence and L_{III} linewidths.

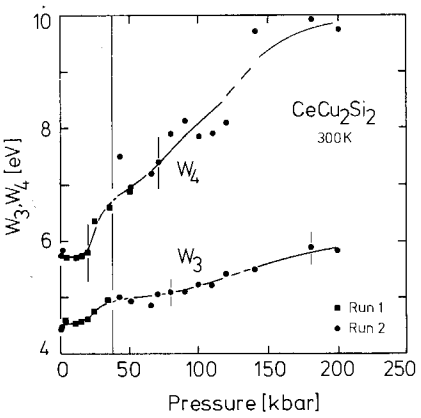

Fig. 35. Ce L_{III} linewidths W_3, W_4 in $CeCu_2Si_2$ (fig. 34) vs pressure.

14. Is CeO_2 tetravalent?

Stoichiometric CeO_2 crystallizes in the CaF_2 structure with $a = 5.411$ Å. Single crystals are colorless, polycrystalline powders exhibit a pale yellowish color. Small oxygen deficiencies ($>1\%$) change the color to black (Meyer 1903). Non-stoichiometric CeO_2 ('α-phases') have a defect CaF_2 lattice with larger unit cells than stoichiometric crystals. For instance the lattice parameter a is by 0.2% larger in a dark $CeO_{1.995}$ single crystal than in CeO_2. The magnetism of CeO_2 for decades was a matter of controversy in the lanthanide magneto-chemistry. Since chemically tetravalent Ce has an empty 4f shell ($4f^0[^1S_0]$), CeO_2 is expected to exhibit diamagnetic behavior as other $4f^0$ systems, e.g. La_2O_3. The experimental results of the static susceptibility, however, indicate weak temperature-independent paramagnetism between 4 and 300 K. The measurements of the molar magnetic susceptibility converge to a minimum at $\chi = 12.9 \times 10^{-6}$ [emu/mole] in samples with upgraded purity (Klemm and Hartlapp 1948). Serres (1935) and Wachter (1982) report slightly larger numbers ($(22 \pm 4) \times 10^{-6}$ and 25×10^{-6}[emu/mole], respectively). From optical transmission data Wachter (1982) claims the upper limit of Ce^{3+} ions in CeO_2 to be 5%. The technical importance of CeO_2 stimulated intensive investigations of its physical and chemical properties. Not one of the numerous experimental studies (either macroscopical or microscopical) proves unambiguously the existence of fully tetravelent CeO_2. Oxygen deficiencies and the corresponding defect structure may account for the presence of trivalent Ce ions in the black nonstoichiometric crystals. However, why is La_2O_3 truely diamagnetic but stoichiometric CeO_2 not? Which mechanism might account for the surprisingly high chemical sensitivity of ionic bonds in a highly symmetrycal crystal? We expect the answer to these questions to come from a thorough investigation of possible Ce valence instabilities in CeO_2 rather than in the search for the 'ideal' crystal. Hence our efforts to tackle the problem of mixed valence in the insulating compound CeO_2.

$K_{\alpha,\beta}$ emission line shifts (cf. table 1) and L_{III} absorption data from different laboratories (cf. table 3) indicate mixed valence in CeO_2. Comparing the L_{III}

absorption of metallic-like CeB_6 and CeO_2, Troneva et al. (1958) found four atomic-like lines in CeO_2. Blockin and Kuznetsov (1966) assign these lines to transitions into trivalent and tetravalent valence states.

14.1. *L_{III} absorption in 'tetravalent' Ce insulators*

Figure 36 displays the L_{III} absorption spectra of Ce in some of the nominally tetravalent insulating compounds: CeO_2, $Ce(SO_4)_2$ and CeF_4. These spectra were recorded simultaneously with the L_{III} absorption of metallic γ-Ce, using three detection systems in line. Their atomic-like absorption exhibits two prominent lines at high energies (labelled C and D) and two much weaker lines at low energies (labelled A and B). Line B is not resolved in $Ce(SO_4)_2$ and CeF_4. Their existence, however, is clearly confirmed by the analysis of the individual linewidths and by comparison with CeO_2. The splitting A–B is about 5eV and the splitting C–D is about 6eV. B is split from C by about 3eV. Analyzing CeO_2, Troneva et al. (1958) assigned the lines A and B to be quadrupolar $(l+2)$ transitions $2p_{3/2} \rightarrow 4f^0$ and the lines B and C to be dipolar ($l+1$ and $l-1$) transitions $2p_{3/2} \rightarrow 5d$ and $2p_{3/2} \rightarrow 6s$, respectively. The onset of the continuum was located at high energies near the position of line D. However, by reasons of the small 2p quadrupolar transitions probabilities (cf. table 2) and the small spectral density of 2p–6s transitions, this assignment cannot be maintained.

Blockin and Kuznetsov (1966) recorded the L_{III} absorption in stoichiometric Ce_2O_3 and CeO_2. The prominent absorption line in trivalent Ce_2O_3 occurs at the

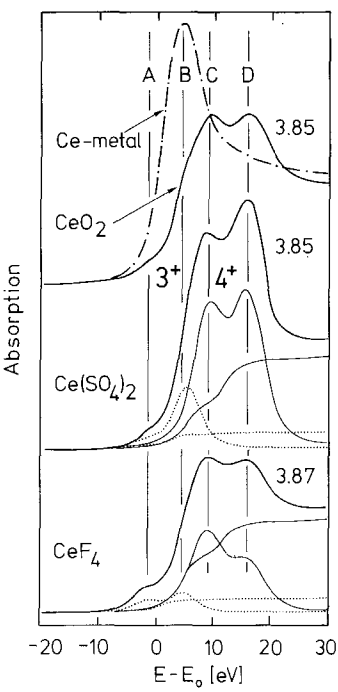

Fig. 36. L_{III} absorption of Ce in 'tetravalent' Ce insulators together with the L_{III} absorption in elemental Ce (simultaneous recording). A and B denote the positions of the two trivalent absorption lines, C and D the positions of the tetravalent absorption lines. The valence from the intensity ratios of the two subspectra is indicated at the right-hand side. The staircase-like lines represent the continuous absorption (see text).

position of line B in CeO_2. The recordings from nonstoichiometric $CeO_{1.75}$ (stabilized with La_2O_3) exhibit a strong intensity at the trivalent position B (Ce_2O_3) and a prominent peak at the tetravalent position C (and a weaker line at D). The concentration ratio of tri- and tetravalent Ce ions traced from these recordings is found to correspond approximately to the degree of reduction in CeO_2.

Neglecting the weak lines A and B, the double-peaked shape of the line absorption in CeO_2 seems to be similar to the atomic-like absorption in α-Ce metals. Analogous to the valence determination in the α-Ce intermetallics Bauchspiess et al. (1981) first assigned the two prominent lines C and D to transitions $2p_{3/2} \rightarrow [4f^1]$ $(5d6s)^3$ and $2p_{3/2} \rightarrow [4f^0]$ $(5d6s)^4$, respectively, and found $v = 3.32$. This analysis did not take into account the different positions of the two prominent lines in metallic and insulating Ce systems. Taking properly into account the position of CeO_2 with respect to the binding energy of trivalent (or nearly trivalent) Ce reference systems (e.g. Ce metal or Ce_2O_3), it suggests itself to assign the lines A *and* B to trivalent Ce and the lines C *and* D to tetravalent Ce. Then the valence of Ce in the "tetravalent" insulators turns out to be close to 4, but not to be 4, namely $v(CeO_2) = 3.65 \pm 0.06$ and $v(CeF_4) = 3.85 \pm 0.06$ (Wohlleben et al. 1981, Bauchspiess, 1982). Also see comments in chapter 62, sections 6.2.2 to 6.2.4 of this volume.

We do not know the exact positions of the continuum thresholds with respect to the positions of each of the two double lines. The somewhat arbitrary choice of the threshold positions is an additional source of systematical errors concerning the accuracy of the valence determination. Depending whether the atomic-like absorption is assumed to interfere with the continuum background or assumed to rise only far below a steep continuum threshold, the valence numbers range from 3.65 to 3.9, respectively.

The nominally tetravalent stoichiometric dioxides with Pr and Tb exhibit similar L_{III} absorption spectra as CeO_2 (Karnatak et al. 1985, 1987).

14.2. *L_{III} absorption of Ce in CeO_2 under high pressure*

The L_{III} absorption of Ce in CeO_2 was investigated at high pressures up to 260 kbar (Röhler 1986a; fig. 37). Figure 37 shows high-pressure L_{III} spectra of Ce in CeO_2 at 20 and 225 kbar. High pressure shifts the lines C and D monotonously to high energies, however at different rates. As a result the splitting of the lines C and D decreases by -2.4 ± 0.3 meV/kbar. At the same time the lines are broadened. The relative intensities remain largely unaffected and the valence is found to be pressure-independent within $\Delta v = \pm 0.05$. The L_{III} absorption spectra of Ce in CeO_2 have been calculated by Delley and Beck (1985) and Jo and Kotani (1985) based on different theoretical models. Delley and Beck assign the line B to the $4f^2 5d$ 'shake up', C to $4f^1 5d$ and D to $4f^0 5d$ final-state configurations, analogous to the assignment of the metallic α-type 3d-XPS spectra. If this assignment really would apply to the L_{III} spectra also, one expects the intensity of line B to increase with decreasing volume (cf. the discussion of final state effects in Ce metal, section 12). This pressure effect is not observed.

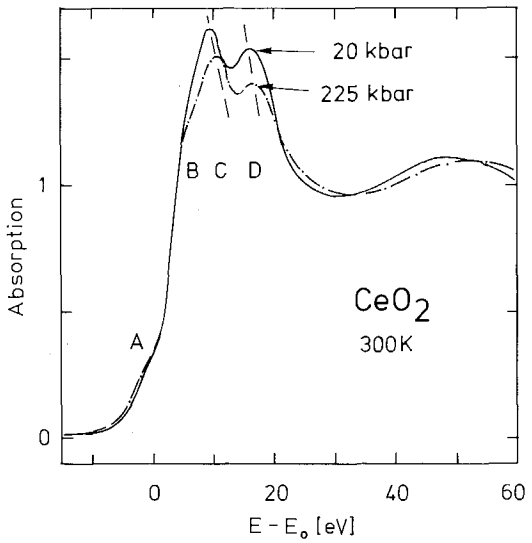

Fig. 37. L_{III} absorption of Ce in CeO_2 at 20 (solid line) and 225 kbar (dashed–dotted line). A and B denote the trivalent absorption lines, C and D the tetravalent lines. At increasing pressure, C and D shift at different rates to high energies. The valence remains pressures-independent.

15. Concluding remarks

X-ray absorption has been developed into a standard tool in the physics and chemistry of the lanthanides. The traditional absorption spectroscopies, rediscovered through the recent developments in synchrotron radiation research, and the fascinating properties of lanthanide mixed valence systems, stimulated a large variety of experimental work, which we could document in this chapter only incompletely. In contrast to the apparent intensity in the experimental work, the theory of X-ray absorption is still undeveloped. We feel that theoretical treatment of the X-ray absorption problem in lanthanide mixed valent materials is needed urgently for two problems: (i) the analysis of chemical shifts in the deep core level spectroscopies with final-state configurations involving outer valence electrons; (ii) the analysis of deep core level absorption in homogeneously mixed valent materials. At this time most of the theoretical work is concerned with the various photoemission techniques and many theoreticians and experimentalists claim the solution of the theoretical problems arising in X-ray absorption is easily transferable from the concepts of photoemission. It is a puzzling fact that important findings from L_{III} absorption such as the valence saturation in α-cerium and Ce intermetallics was not generally accepted until the much more complicated photoemission spectra could be theoretically understood. Clarification of the problem of all high-energy spectroscopies, namely, to which extent and under which detailed conditions valence fluctuations (or the dynamics of the 4f delocalization) interferes with the dynamics of the core hole screening is a pre-requisite for the safe measurements of ground-state properties, which are the focus of the physical interest. We feel that meanwhile there is an overwhelming experimental evidence for such perturbations in L_{III} absorption to be negligible. This observation could be a challenge for the theory of X-ray absorption, also.

Acknowledgements

The author wishes to thank D. Wohlleben for his help during the preparation of the article. He is also indebted to many colleagues for experimental contributions to this work and valuable discussions. In particular J.P. Kappler, K. Keulerz and J. Klug have been closely involved with many experimental aspects of these studies. Finally he gratefully acknowledges the support of the Synchrotron radiation laboratories, Hamburger Synchrotronstrahlungslabor (HASYLAB) and LURE (Orsay). This work was partly supported by Sonderforschungsbereich 125 of the Deutsche Forschungsgemeinschaft and by the Commission of the European Community.

References

Agarwal, B.K., and B.R.K. Agarwal, 1978, J. Phys. C **11**, 4223.
Agarwal, B.R.K., L.P. Verma and B.K. Agarwal, 1971a, Lett. Nuovo Cimento **1**, 781.
Agarwal, B.R.K., L.P. Verma and B.K. Agarwal, 1971b, Lett. Nuovo Cimento **2**, 581.
Aita, O., T. Watanabe, Y. Fujimoto and K. Tsutsumi, 1982, J. Phys. Soc. Jpn. **51**, 483.
Aita, O., K. Ichikawa, M. Okusawa and K. Tsutsumi, 1986, Phys. Rev. B **34**, 8230.
Albers, R.C., A.K. McMahan and J.E. Müller, 1985, Phys. Rev. B **31**, 3435.
Allais, M.L., 1942, Cah. Phys. **7**, 13.
Azaroff, L.V., and D.M. Pease, 1974, X-ray absorption spectra, in: X-Ray Spectroscopy, ed. L.V. Azaroff (McGraw-Hill, New York) p. 284.
Baerden, J.A., and A.F. Burr, 1967, Rev. Mod. Phys. **39**, 125.
Barinski, R.I., and W.I. Nefedow, 1969, Röntgenspektroskopische Bestimmung der Atomladungen in Molekülen [German translation of the 1st Ed. 1966, Moscow] (Verlag Chemie, Weinheim).
Barrère, G., 1947, J. Phys. Radium **8**, 72.
Batlogg, B., E. Kaldis, A. Schlegel and P. Wachter, 1976, Phys. Rev. B **14**, 5503.
Bauchspiess, K.R., 1982, Diplomarbeit Universität Köln (unpublished).
Bauchspiess, K.R., W. Boksch, E. Holland-Moritz, H. Launois, R. Pott and D. Wohlleben, 1981, in: Valence Fluctuations in Solids, eds L.M. Falicov, W. Hanke and M.B. Maple (North-Holland, Amsterdam) p. 417.
Bauminger, E.R., D. Froindlich, I. Nowik, S. Ofer, I. Felner and I. Mayer, 1973, Phys. Rev. Lett. **30**, 1053.
Beaurepaire, E., G. Krill, J.P. Kappler and J. Röhler, 1984, Solid State Commun. **49**, 65.
Beaurepaire, E., J.P. Kappler and G. Krill, 1986, Solid State Commun. **57**, 145.
Bedzyk, M.J., G. Materlik and J. Hrdy, 1986, unpublished.
Beille, J., M.B. Maple, J. Wittig, Z. Fisk and L.E. Delong, 1983, Phys. Rev. B **28**, 7397.
Bergvall, P., and S. Hagström, 1960, Ark. Fys. **17**, 61.
Bianconi, A., S. Modesti, M. Campagna, K. Fischer and S. Stizza, 1981, J. Phys. C **14**, 4737.
Bianconi, A., M. Campagna and S. Tizza, 1982, Phys. Rev. B **25**, 2477.
Bianconi, A., A. Marcelli, I. Davoli and S. Stizza, 1984a, in:X84 Proc. Int. Conf. X-Ray and Inner Shell Processes in Atoms, Molecules and Solids (Leipzig), eds A. Meisel and J. Finster, p. 403.
Bianconi, A., A. Marcelli, I. Davoli, S. Stizza and M. Campagna, 1984b, Solid State Commun. **49**, 409.
Bianconi, A., A. Marcelli, M. Tomellini and I. Davoli, 1985, J. Magn. & Magn. Mater. **47&48**, 209.
Bittins, B., K. Keulerz, A. Scherzberg, J.P. Sanchez, W. Boksch, H.F. Braun, J. Röhler, H. Schneider, P. Weidner and D. Wohlleben, 1985, Z. Phys. B **62**, 21.
Blochin, M.A., 1957, Physik der Röntgenstrahlen [German translation of the 2nd Ed.] (VEB Verlag Technik, Berlin).
Blochin, M.A., 1964, Methoden der Röntgenspektralanalyse [German translation] (Verlag Otto Sager, München) pp. 214–283.
Blockin, S.M., and F.A. Kuznetsov, 1966, Theor. & Exp. Chem. Acad. Sci. Ukr. SSR **2**, 321.
Blockin, S.M., E.E. Vainshtein and V.M. Bertenev, 1966, Sov. Phys. Solid State **7**, 2870.
Bohr, N., and D. Coster, 1922, Z. Phys. **12**, 342.
Bonelle, C., 1968, in: Soft X-Ray Band Spectra, ed. D.J. Fabian (Academic Press, New York) p. 163.
Bonelle, C., and R.C. Karnatak, 1971, J. Phys. (France) Coll. C4, Suppl. **10**, C4-230.
Bonelle, C., R.C. Karnatak and C.K. Jørgensen, 1972, Chem. Phys. Lett. **14**, 145.

Bonelle, C., R.C. Karnatak and J. Sugar, 1974, Phys. Rev. A **9**, 1920.
Bothe, W., 1926, Absorption und Zerstreuung von Röntgenstrahlen, in: Handbuch der Physik, Vol. XXIII, eds H. Geiger and K. Scheel (Julius Springer, Berlin), p. 349.
Boyce, J.B., R.M. Martin, J.W. Allen and F. Holtzberg, 1981, in: Valence Fluctuations in Solids, eds L.M. Falicov, W. Hanke and M.B. Maple (North-Holland, Amsterdam) p. 427.
Braun, H.F., N. Engel and E. Parthé, 1983, Phys. Rev. B **28**, 1389.
Brewer, L., 1971, J. Opt. Soc. Am. **61**, 1101.
Brunetti, R., 1927, Z. Anorg. Allg. Chem. **160**, 237.
Bundy, F.P., and K.J. Dunn, 1981, Phys. Rev. B **24**, 4136.
Callon, P., 1955, Comptes Rendus Acad. Sci. Paris **240**, 615.
Carbrera, J., 1923, Comptes Rendus Acad. Sci. Paris **176**, 740.
Chamberlain, M.B., A.F. Burr and R.J. Liefield, 1974, Phys. Rev. B **9**, 663.
Coey, J.M.D., S.K. Ghatak, M. Avignon and F. Holtzberg, 1976, Phys. Rev. B **14**, 3744.
Combley, F.H., E.A. Stewardson and J.E. Wilson, 1968, J. Phys. B **1**, 120.
Compton, A.H., and S.K. Allison, 1935, X-Rays in Theory and Experiment, 2nd Ed. (D. van Nostrand Company, Princeton).
Connerade, J.P., and D.H. Tracy, 1977, J. Phys. B **10**, L235.
Croft, M., R. Neifeld, C.U. Segre, S. Raaen and R.D. Parks, 1984, Phys. Rev. B **30**, 4164.
Croft, M., F. Lu, M.E. Mekler, A. Zolandz, G. Hall and E.G. Spencer, 1985, J. Magn. & Magn. Mater. **47&48**, 36.
Darshan, B., B.D. Padalia, R. Nagarajan, S.K. Dhar, S.K. Malik and R. Vijayaraghavan, 1984, Phys. Rev. B **30**, 4031.
de Broglie, M., 1916, Comptes Rendus Acad. Sci. Paris **163**, 87.
Dehmer, J.L., and A.F. Starace, 1972, Phys. Rev. B **5**, 1792.
Dehmer, J.L., A.F. Starace, U. Fano, J. Sugar and J.W. Cooper, 1971, Phys. Rev. Lett. **26**, 1521.
Delley, B., and H. Beck, 1985, J. Magn. & Magn. Mater. **47&48**, 269.
Demekhin, V.F., and T.V. Shelkovich, 1974, Sov. Phys.-Solid State **16**, 659.
Dexpert, H., R.C. Karnatak, J.M. Esteva, M. Gasgnier, P.E. Caro and L. Albert, 1987, Phys. Rev. B (in press).
Divakar, C., M. Mohan and A.K. Singh, 1984, J. Appl. Phys. **56**, 2337.
Domashevskaya, E.P., E.V. Farberovich, G.P. Nishnikova and S.V. Vlasov, 1984, Int. Conf. X-Ray and Inner Shell Processes in Atoms, Molecules and Solids, Aug. 20–24 1984, Leipzig, Abstracts Part I, 117 (unpublished).
Drickhamer, H.G., 1982, Int. Rev. Phys. Chem. **2**, 171.
Efmerova, N.N., L.D. Finkel'shtein, N.I. Samsonova and S.A. Nemnonov, 1976, Izv. Akad. Nauk SSSR Ser. Fiz. **40**, 420.
Faessler, A., 1955, Röntgenspektrum und Bindungszustand, in: Landolt-Börnstein, Bd. I, Teil 4, ed. K.H. Hellwege (Springer, Berlin) p. 842.
Fairchild, R.W., 1975, Ph.D. Thesis Cornell University, unpublished.
Falicov, L.M., W. Hanke and M.B. Maple, eds, 1981, Valence Fluctuations in Solids (North-Holland, Amsterdam).
Fano, U., and J.W. Cooper, 1968, Rev. Mod. Phys. **40**, 441.
Farrell, J.N., and R.D. Taylor, 1987, Phys. Rev. Lett. **58**, 2487.
Feldhaus, J., 1982, Dissertation Freie Universität Berlin (unpublished).
Finkel'shtein, L.D., S.A. Nemnonov, N.N. Efremova, A.A. Samokhalov, V.G. Bamburov, M.I. Simonova, N.N. Loshkareva and N.N Lobachevskaya, 1974, Izv. Akad. Nauk SSSR Ser. Fiz. **38**, 654.
Finkel'shtein, L.D., N.N. Efremova, E.S. Konovalova and Yu.B. Paderno, 1981, Sov. Phys.-Solid State **23**, 2015.
Fischer, D.W., and W.L. Baun, 1967, J. Appl. Phys. **38**, 4830.
Fomichev, V.A., T.M. Zimkina, S.A. Gribovskii and I.I. Zhukova, 1967, Sov. Phys.-Solid State **9**, 1163.
Frank, K.H., 1984, Dissertation Freie Universität Berlin (unpublished).
Frank, K.H., G. Kaindl, J. Feldhaus, G. Wortmann, W. Krone, G. Materlik and H. Bach, 1982, in: Valence Instabilities, eds P. Wachter and H. Boppart (North-Holland, Amsterdam) p. 189 and Interner Bericht DESY F41 HASYLAB 85-12 Nov. 1985.
Freeman, A.J., 1972, in: Magnetic Properties of Rare Earth Metals, ed. R.J. Elliot (Plenum Press, London) p. 245.
Fuggle, J.C., F.U. Hillebrecht, J.-M. Esteva, R.C. Karnatak, O. Gunnarsson and K. Schönhammer, 1983, Phys. Rev. B **27**, 4637.
Garg, K.B., D. Norman and R.P. Beeken, 1986, Phys. Status Solidi a **96**, 301.
Gauchois, Y., and N.F. Mott, 1949, Philos. Mag. **10**, 1260.
Gautier, F., J.P. Kappler, G. Krill and E. Beaurepaire, 1983, internal report:: 6emes Journees de la R.C.P. 520 sur les composes de terres rares et actinides a valence anormale, Strasbourg les 6 et 7 octobre 1983, 115.
Ghatikar, M.N., T.K. Hatwar, B.D. Padalia, E.V. Sampathkumaran, L.C. Gupta and R. Vijayaraghavan, 1981, Phys. Status Solidi b **106**, K89.
Gmelin, 1976, Handbuch der Anorganischen Chemie, System **39**, Main B **4** (Springer-Verlag, Berlin) pp. 334–420.
Godart, C., L.C. Gupta and M.F. Ravet-Krill, 1983a, J. Less-Common Met. **94**, 187.

Godart, C., J.C. Achard, G. Krill and M.F. Ravet-Krill, 1983b, J. Less-Common Met. **94**, 177.
Goulon, J., C. Goulon-Ginet, R. Cortes and J.M. Dubois, 1982, J. Phys. (France) **43**, 539.
Gschneidner Jr, K.A., and R. Smoluchowski, 1963, J. Less-Common Met. **5**, 374.
Gunnarsson, O., and K. Schönhammer, 1983, Phys. Rev. B **28**, 4315.
Haen, P., F. Lapierre, J.M. Mignot, J.P. Kappler, G. Krill and M.F. Ravet, 1985, J. Magn. & Magn. Mater. **47&48**, 490.
Haensel, P., P. Rabe and B. Sonntag, 1970, Solid State Commun. **8**, 1845.
Haken, H., and W. Schottky, 1958, Z. Phys. Chem. Neue Folge **16**, 218.
Hanyu, T., T. Miyahra, T. Kamada, H. Ishii, M. Yanagihara, H. Kato, K. Naito, S. Suzuki and T. Ishii, 1985, J. Magn. & Magn. Mater. **52**, 193.
Hatwar, T.K., 1981, Ph.D. Thesis, Indian Institute of Technology, Bombay (unpublished), cited after Ref. 36 in table 3.
Hatwar, T.K., R.M. Nayak, B.D. Padalia, N.N. Ghatikar, E.V. Sampathkumaran, L.C. Gupta and R. Vijayaraghavan, 1980, Solid State Commun. **34**, 617.
Heald, S.M., 1983, Springer Series in Chemical Physics **27**, 98.
Heald, S.M., and E.A. Stern, 1977, Phys. Rev. B **16**, 5549.
Herbst, J.F., 1985, J. Magn. & Magn. Mater. **47&48**, 238.
Hertz, G., 1920, Z. Phys. **3**, 19.
Hoffmann, R., and C. Zheng, 1985, J. Phys. Chem. **89**. 4175.
Ichikawa, K., A. Nisawa and K. Tsutsumi, 1986, Phys. Rev. B **34**, 6690.
Ingalls, R., J.M. Tranquada, J.E. Withmore, E.D. Crozier and A.J. Seary, 1980, in: EXAFS Spectroscopy: Techniques and Applications, eds B.K. Teo and D.J. Jay (Plenum, New York).
Jaccard, D., J.M. Mignot, B. Bellarbi, A. Benoit, H.F. Braun and J. Sierro, 1985, J. Magn. & Magn. Mater. **47&48**, 23.
Jayaraman, A., 1979, Valence changes in compounds, in: Handbook on the Physics and Chemistry of Rare Earths, Vol. 2, eds K.A. Gschneidner Jr and L. Eyring (North-Holland, Amsterdam) p. 575.
Jayaraman, A., V. Narayanamurti, E. Bucher and R.G. Maines, 1970, Phys. Rev. Lett. **25**, 1430.
Jeitschko, W., and W.K. Hoffmann, 1983, J. Less-Common Met. **95**, 317.
Jhans, J., and M. Croft, 1985, J. Magn. & Magn. Mater. **47&48**, 203.
Jo, T., and A. Kotani, 1985a, Solid State Commun. **54**, 451.
Jo, T., and A. Kotani, 1985b, J. Magn. & Magn. Mater. **52**, 396.
Johansson, B., 1974, Philos. Mag. **30**, 469.
Johansson, B., and A. Rosengren, 1975, Phys. Rev. B **11**, 2836.
Johansson, B., and A. Rosengren, 1976, Phys. Rev. B **14**, 361.
Kaindl, G., J. Feldhaus, U. Ladewig and K.H. Frank, 1983a, Phys. Rev. Lett. **50**, 123.
Kaindl, G., W.D. Brewer, G. Kalkowski and F. Holtzberg, 1983b, Phys. Rev. Lett. **54**, 2056.
Kaindl, G., G. Kalkowski, W.D. Brewer, B. Perscheid and F. Holtzberg, 1984, J. Appl. Phys. **55**, 1910.
Kaindl, G., G. Kalkowski, W.D. Brewer, E.V. Sampathkumaran, F. Holtzberg and A. Schach von Wittenau, 1985, J. Magn. & Magn. Mater. **47&48**, 181.
Kalkowski, G., W.O. Breuer, G. Kaindl and F. Holtzberg, 1985a, J. Magn. & Magn. Mater. **47&48**, 215.
Kalkowski, G., C. Laubschat, W.D. Brewer, E.V. Sampathkumaran, M. Domke and G. Kaindl, 1985b, Phys. Rev. B **32**, 2717.
Karnatak, R.C., M. Gasgnier, H. Dexpert, J.-M. Esteva, P.E. Caro and L. Albert, 1985, J. Less-Common Met. **110**, 377.
Karnatak, R.C., J. Esteva, H. Dexpert, M. Gasgnier, P.E. Caro and L. Albert, 1987, Phys. Rev. B (to be published).
Keller, R., G. Güntherodt, W.B. Holzapfel, M. Dietrich and F. Holtzberg, 1979, Solid State Commun. **9**, 753.
Kemly, E., M. Croft, V. Murgai, L.C. Gupta, C. Godart, R.D. Parks and C.U. Segre, 1985, J. Magn. & Magn. Mater. **47&48**, 403.
Keski-Rahkonen, and M.O. Krause, 1974, At. Data & Nucl. Data **14**, 139.
Keulerz, K., J. Röhler, J.P. Kappler, U. Murek and J. Klug, 1986, Jahresbericht 1986 HASYLAB am Deutschen Elektronen-Synchrotron, p. 305 (unpublished).
Klemm, W., and G. Hartlapp, 1948, Z. Anorg. Allg. Chemie **37**, 256.
Klug, J., 1986, Diplomarbeit Universität Köln (unpublished).
Klug, J., J. Röhler, K. Keulerz and J.P. Kappler, 1985, Jahresbericht 1985 HASYLAB am Deutschen Elektronen-Synchrotron, p. 184 (unpublished).
Koch, E.E., ed., 1983, Handbook on Synchrotron Radiation, Vol. 1a,b (North-Holland, Amsterdam).
Koskenmaki, D.C., and K.A. Gschneidner Jr, 1978, Cerium, in: Handbook on the Physics and Chemistry of Rare Earths, Vol. 1 (North-Holland, Amsterdam) p. 337.
Kossel, W., 1920, Z. Phys. **1**, 119.
Kotani, A., and Y. Toyozawa, 1979, Theoretical aspects of inner level spectroscopy, in: Synchrotron Radiation, Topics in Current Physics, Vol. 10, ed. C. Kunz (Springer, Berlin) p. 214.
Krill, G., J.P. Kappler, A. Meyer, L. Abadli and M.F. Ravet, 1981a, in: Valence Fluctuations in Solids, eds L.M. Falicov, W. Hanke and M.B.

Maple (North-Holland, Amsterdam) p. 435; idem: G. Krill, J.P. Kappler, A. Meyer, L. Abadli and M.F. Ravet, 1981, J. Phys. F **1713**.
Krill, G., M.F. Ravet, J.P. Kappler, L. Abadli and J.M. Léger, 1981b, Solid State Commun. **33**, 351.
Krill, G., J.P. Kappler, J. Röhler, M.F. Ravet, J.M. Léger and F. Gautier, 1982, in: Valence Instabilities, eds P. Wachter and H. Boppart (North-Holland, Amsterdam) p. 155.
Krill, G., J.P. Kappler, M.F. Ravet, C. Godart and J.P. Sénateur, 1985, J. Magn. & Magn. Mater. **47&48**, 190.
Kushwaha, M.S., B.D. Shrivastava and V.S. Dubey, 1974, Phys. Status Solidi b **64**, 65.
Lapierre, F., M. Ribault, F. Holtzberg and J. Flouquet, 1981, Solid State Commun. **40**, 347.
Launois, H., M. Rawiso, E. Holland-Moritz, R. Pott and D. Wohlleben, 1980, Phys. Rev. Lett. **44**, 1271.
Lawrence, J.M., M.L. den Boer, R.D. Parks and J.L. Smith, 1984, Phys. Rev. B **29**, 568.
Lee, P.A., E.A. Stewardson and J.E. Wilson, 1952, Proc. Phys. Soc. A **65**, 983.
Lee, P.L., F. Boehm and P. Vogel, 1974, Phys. Rev. A **9**, 614.
Leisi, H.J., J.H. Brunner, C.F. Perdrisat and P. Scherrer, 1961, Helv. Phys. Acta **34**, 161.
Lengeler, B., and R. Zeller, 1984, internal report DESY Hamburg SR 84-14.
Lengeler, B., J.E. Müller and G. Materlik, 1983a, Springer Series in Chem. Phys. **27**, 151.
Lengeler, B., G. Materlik and J.E. Müller, 1983b, Phys. Rev. B **28**, 2276.
Levin, E.M., R.V. Lutsiv, L.D. Finkel'shtein, N.D. Samsonova and R.I. Yasnitskii, 1981, Sov. Phys.-Solid State **23**, 1403.
Levin, E.M., I.N. Stets', O.I. Bodak and B.D. Oniskovets, 1984, Sov. Phys.-Solid State **26**, 1424.
Lindberg, E., 1931, Nova Acta Regiae Soc. Sci. Upsaliensis **7** no. 7, 1.
Lübcke, M., 1985, Dissertation Universität Hamburg (unpublished) and Interner Bericht HASYLAB 85–13 Dez. 1985.
Lübcke, M., B. Sonntag, W. Niemann and P. Rabe, 1986, Phys. Rev. B **34**, 5184.
Mahan, G.D., 1974, Many-body effects on x-ray spectra of metals, in: Solid State Phys. Vol. **29**, eds H. Ehrenreich, F. Seitz and D. Turnbull (Academic, New York) p. 75.
Malmer, I., 1915, Dissertation University Lund (unpublished).
Manescu, I., 1944, Compt. Rend. **218**, 454.
Mansfield, M.W.D., and J.P. Connerade, 1976, Proc. R. Soc. London Ser. A **352**, 125.
Maple, M.B., and D. Wohlleben, 1971, Phys. Rev. Lett. **27**, 511.
Marcelli, A., A. Bianconi, I. Davoli and S. Stizza, 1984, Springer Proc. Phys. **2**, 52.
Marcelli, A., A. Bianconi, I. Davoli and S. Stizza, 1985, J. Magn. & Magn. Mater. **47&48**, 206.
Mariot, J.-M., and R.C. Karnatak, 1974, J. Phys. F **4**, L233.
Mariot, J.-M., R.C. Karnatak and C. Bonelle, 1974, J. Phys. & Chem. Solids **35**, 657.
Martin, R.M., J.B. Boyce, J.W. Allen and F. Holtzberg, 1980, Phys. Rev. Lett., 1275.
Materlik, G., J.E. Müller and J.W. Wilkins, 1983a, Phys. Rev. Lett. **50**, 267.
Materlik, G., B. Sonntag and M. Tausch, 1983b, Phys. Rev. Lett. **51**, 1300.
Matthias, B.T., W.H. Zachariasen, G.W. Webb and J.J. Engelhardt, 1967, Phys. Rev. Lett. **18**, 781.
Methfessel, S., and D.C. Mattis, 1968, Magnetic semiconductors, in: Handbuch der Physik Bd. **18**, ed. S. Flügge (Springer-Verlag, Berlin) p. 1.
Meyer, R.J., 1903, Z. Anorg. Chem. **37**, 378.
Motais, P., E. Belin and C. Bonelle, 1981, J. Phys. F **11**, L169.
Müller, J.E., and J.W. Wilkins, 1984, Phys. Rev. B **29**, 4331.
Müller, J.E., O. Jepsen and J.W. Wilkins, 1982, Solid State Commun. **42**, 365.
Müller-Hartmann, E., B. Roden and D. Wohlleben, eds, 1985, Proc. 4th Int. Conf. Valence Fluctuations, reprint from J. Magn. & Magn. Mater. **47&48** (North-Holland, Amsterdam).
Nagarajan, R., E.V. Sampathkumaran, L.C. Gupta, R. Vijayaraghavan, V. Prabhawalkar, Bhaktdarshan and B.D. Padalia, 1981a, Phys. Lett. A **84**, 275.
Nagarajan, R., E.V. Sampathkumaran, L.C. Gupta and R. Vijayaraghavan, 1981b, Phys. Lett. A **81**, 397.
Nagel, D.J., and W.L. Baun, 1974, Bonding effects in x-ray spectra, in: X-Ray Spectroscopy, ed. L.V. Azaroff (McGraw-Hill, New York) p. 445.
Neifeld, R.A., and M. Croft, 1985, J. Magn. & Magn. Mater. **47&48**, 36.
Neifeld, R.A., M. Croft, R. Mihalisin, C.U. Segre, M. Madigan, M.S. Torikachvili, M.B. Maple and L.E. DeLong, 1985, Phys. Rev. B **32**, 6928.
Nemnonov, S.A., and V.V. Klyushin, 1958, Phys. Met. & Metallorg. USSR **6**, 183.
Niemann, W., M. Lübcke, W. Malzfeldt, P. Rabe and R. Haensel, 1985, J. Magn. & Magn. Mater. **47&48**, 462.
Nishina, Y., 1925, Philos. Mag. **49**, 521.
Nozières, P., and L.T. De Dominicis, 1969, Phys. Rev. **178**, 1097.
Ochiai, A., S. Nakai, A. Oyamada, T. Suzuki and T. Kasuya, 1985, J. Magn. & Magn. Mater. **47&48**, 570.
Okusawa, M., Y. Iwasaki, K. Tsutsumi, M. Aono and S. Kawai, 1978, J. Appl. Phys. Jpn. **17**, 161.
Ottewell, D., E.A. Steewardson and J.E. Wilson, 1973, J. Phys. B **6**, 2184.
Ovsyannikova, I.A., E.E. Vainshtein and G.V. Samsonov, 1964, Phys. Met. & Metallorg. USSR **18**, 153.
Ovsyannikova, I.A., S.S. Batsanov, L.I. Nasonova, L.R. Batsanova and E.A. Nekrasova, 1967, Bull. Acad. Sci. USSR, Phys. Ser. **31**, 936.

Padalia, B.D., S.N. Gupta, V.P. Vijayavargiya and B.C. Tripathi, 1974, J. Phys. F **4**, 938.
Padalia, B.D., T.K. Hatwar and M.N. Ghatikar, 1983, J. Phys. C **16**, 1537.
Parks, R.D., ed., 1977, Valence Instabilities and Related Narrow-Band Phenomena (Plenum Press, New York).
Parks, R.D., S. Raaen, M.L. den Boer, V. Murgai and T. Mihalisin, 1983, Phys. Rev. B **28**, 3556.
Parrat, L.G., 1939, Phys. Rev. **56**, 295.
Parrat, L.G., C.F. Hempstead and E.L. Jossem, 1957, Phys. Rev. **105**, 1228.
Parthé, E., and B. Chabot, 1984, in: Handbook on the Physics and Chemistry of Rare Earths, Vol. 6, eds K.A. Gschneidner Jr and L. Eyring (North-Holland, Amsterdam).
Pauli, W., 1926, Quantentheorie, in: Handbuch der Physik, Vol. XXIII, eds H. Geiger and K. Scheel (Julius Springer, Berlin) p. 198.
Piacentini, R., J. Smith and D.W. Lynch, 1974, in: Proc. 4th Int. Conf. Vacuum Ultraviolet Radiation Physics, Hamburg, 1974, p. 255.
Pott, R., W. Boksch, G. Leson, B. Politt, H. Schmidt, A. Freimuth, K. Keulerz, J. Langen, G. Neumann, F. Oster, J. Röhler, U. Walter, P. Weidner and D. Wohlleben, 1985, Phys. Rev. Lett. **54**, 481.
Prabhawalkar, V., and B.D. Padalia, 1982a, Phys. Status Solidi b **110**, 659.
Prabhawalkar, V., and B.D. Padalia, 1982b, Phys. Status Solidi b **110**, 357.
Prabhawalkar, V., B.D. Padalia, L.C. Gupta, E.V. Sampathkumaran and R. Vijayaraghavan, 1983, J. Less-Common Met. **91**, 271.
Probst, C., and J. Wittig, 1978, in: Handbook on the Physics and Chemistry of Rare Earths, Vol. I, eds K.A. Gschneidner Jr and L. Eyring (North-Holland, Amsterdam) p. 749.
Raaen, S., and R.D. Parks, 1983, Solid State Commun. **48**, 199.
Raaen, S., and R.D. Parks, 1985, J. Magn. & Magn. Mater. **47&48**, 200.
Raaen, S., M.L. den Boer, V. Murgai and R.D. Parks, 1983, Phys. Rev. B **27**, 5139.
Radtke, E., 1976, J. Phys. B **12**, L71, L77.
Rao, C.N.R., D.D. Sarma, P.R. Sarode, R. Vijayaraghavan, S.K. Dhar and S.K. Malik, 1981, J. Phys. C **14**, L451.
Ravot, D., C. Godart, J.C. Achard and P. Lagarde, 1981, in: Valence Fluctuations in Solids, eds L.M. Falicov, W. Hanke and M.B. Maple (North-Holland, Amsterdam) p. 423.
Richtmyer, F.K., S.W. Barnes and E. Ramberg, 1934, Phys. Rev. **46**, 843.
Röhler, J., 1979, Diploma Thesis, Ruhr Universität Bochum (unpublished).
Röhler, J., 1984, Springer Proc. Phys. **2**, 379.
Röhler, J., 1985a, J. Magn. & Magn. Mater. **47&48**, 175.
Röhler, J., 1985b, Dissertation Universität zu Köln (unpublished).
Röhler, J., 1986a, Verhandlungen der Deutschen Physikalischen Gesellschaft (Frühjahrstagung Freudenstadt 1986) p. 1249 (unpublished).
Röhler, J., 1986b, Physica B **144**, 27.
Röhler, J., 1987, (unpublished).
Röhler, J., G. Krill, J.P. Kappler, M.F. Ravet and D. Wohlleben, 1982, in: Valence Instabilities, eds P. Wachter and H. Boppart (North-Holland, Amsterdam) p. 215.
Röhler, J., G. Krill, J.P. Kappler and M.F. Ravet, 1983a, Springer Series in Chem. Phys. **27**, 213.
Röhler, J., J.P. Kappler and G. Krill, 1983b, Nucl. Instrum. & Methods Phys. Res. **208**, 647.
Röhler, J., D. Wohlleben, J.P. Kappler and G. Krill, 1984a, Phys. Lett. A **103**, 220.
Röhler, J., K. Keulerz, E. Dartyge, A. Fontaine, A. Jucha and D. Sayers, 1984b, Springer Proc. Phys. **2**, 385.
Röhler, J., K. Keulerz, J.P. Kappler and G. Krill, 1985, Rapport d'Activité LURE 1984/1985 (unpublished).
Röhler, J., K. Keulerz and J. Klug, 1987, to be published.
Rule, K.C., 1945, Phys. Rev. **68**, 246.
Sakellaridis, P., 1953, Comptes Rendus Acad. Sci. Paris **236**, 1014, 1244, 1547.
Sakellaridis, P., 1954, Comptes Rendus Acad. Sci. Paris **238**, 2296.
Sales, B.C., and R. Viswanathan, 1976, J. Low Temp. Phys. **23**, 449.
Sales, B.C., and D. Wohlleben, 1975, Phys. Rev. Lett. **35**, 1240.
Sampathkumaran, E.V., K.H. Frank, G. Kalkowski, G. Kaindl, M. Domke and G. Wortmann, 1984a, Phys. Rev. B **29**, 5702.
Sampathkumaran, E.V., B. Perscheid and G. Kaindl, 1984b, Solid State Commun. **51**, 701.
Sampathkumaran, E.V., G. Kaindl, W. Krone, B. Perscheid and R. Vijayaraghavan, 1985a, Phys. Rev. Lett. **54**, 1067.
Sampathkumaran, E.V., G. Kalkowski, C. Laubschat, G. Kaindl, M. Domke, G. Schmiester and G. Wortmann, 1985b, J. Magn. & Magn. Mater. **47&48**, 212.
Samsonova, N.D., L.D. Finkel'shtein and E.M. Levin, 1982, Sov. Phys.-Solid State **24**, 2116.
Sandström, A.E., 1957, Experimental methods of x-ray spectroscopy: ordinary wavelenghts, in: Encyclopedia of Physics, Vol. XXX, ed. S. Flügge (Springer, Berlin) p. 78.
Sarode, P.R., D.D. Sarma, R. Vijayaraghavan, S.K. Malik and C.N.R. Rao, 1982, J. Phys. C **15**, 6655 and Erratum (unpublished).
Schmiester, G., B. Perscheid, G. Kaindl and J. Zurkovsky, 1982, in: Valence Instabilities, eds P. Wachter and H. Boppart (North-Holland, Amsterdam) p. 219.
Segre, C.U., M. Croft, J.A. Hodges, V. Murgai, L.C. Gupta and R.D. Parks, 1982, Phys. Rev. Lett. **49**, 1947.
Serres, A., 1935, J. Phys. Radium **6**, 336.
Shaburov, V.A., A.E. Sovestnov and O.I. Sumbaev, 1974, Phys. Lett. A **49**, 83.
Shaburov, V.A., A.E. Sovestnov, I.A. Markova,

E.M. Savitskii, O.D. Chistyakov and T.M. Shkatova, 1981, Sov. Phys.-Solid State **23**, 1437.
Sham, T.K., 1983, J. Chem. Phys. **79**, 1116.
Siegbahn, K., 1970, Philos. Trans. R. Soc. London A **268**, 33.
Siegbahn, M., 1931, Spektroskopie der Röntgenstrahlen, 2nd Ed. (Julius Springer, Berlin) sections IV, V, VI.
Siegbahn, M., and E. Jönsson, 1919, Z. Phys. **20**, 251.
Slebarski, A., D. Wohlleben, P. Weidner, J. Röhler and A. Freimuth, 1985, J. Magn. & Magn. Mater. **47&48**, 595.
Smirnov, I.A., I.P. Akimchenko, T.T. Dedegkaev, A.V. Golubkov, E.V. Goncharova, N.N. Efremova, T.B. Zhukova, V.S. Oskotskii, L.D. Finkelstein, S.G. Shulman, N. Stepanov and N.F. Kartenko, 1982, in: Valence Instabilities, eds P. Wachter and H. Boppart (North-Holland, Amsterdam) p. 113.
Smirnov, I.A., A.V. Golubkov, V.M. Sergeeva, V. Buttaev, T.B. Zhukova, L.D. Finkelstein and N.N. Efremova, 1985, J. Magn. & Magn. Mater. **47&48**, 485.
Sovestnov, A.E., V.A. Shaburov, I.A. Markova, E.M. Savitskii, O.D. Chistyakov and T.M. Shkatova, 1981a, Sov. Phys.-Solid State **23**, 1652.
Sovestnov, A.E., V.A. Shaburov and K.I. Kozlov, 1981b, Sov. Phys.-Solid State **23**, 2009.
Stern, A., and K. Kim, 1981, Phys. Rev. B **23**, 3781.
Stewardson, E.A., and J.E. Wilson, 1956, Proc. Phys. Soc. A **65**, 668.
Sugar, J., 1972a, Phys. Rev. B **5**, 1785.
Sugar, J., 1972b, Phys. Rev. A **6**, 1764.
Sumbaev, O.I., 1978, Sov. Phys.-Usp. **21**, 141.
Suryanarayanan, R., H. Bach, O. Gorochov, G. Schmiester, K. Westerholt and G. Kaindl, 1985, J. Magn. & Magn. Mater. **47&48**, 487.
Suzuki, S., T. Miyahara, T. Hanyu, H. Ishii, M. Yanagihara, T. Kamada, K. Naito, H. Kato and T. Ishii, 1985, J. Magn. & Magn. Mater. **52**, 458.
Syassen, K., 1984, J. Phys. Coll. (France) C 8, suppl. 11, **45**, C8-132.
Syassen, K., 1986, Physica B **139&140**, 277; G. Schmiester and K. Syassen, unpublished work.
Syassen, K., G. Wortmann, J. Feldhaus, K.H. Frank and G. Kaindl, 1981, in: Physics of Solids under High Pressure, eds J.S. Schilling and R.N. Shelton (North-Holland, Amsterdam) p. 319.
Syassen, K., G. Wortmann, J. Feldhaus, K.H. Frank and G. Kaindl, 1982, Phys. Rev. B **26**, 4775.
Syassen, K., H. Winzen, H.G. Zimmer, H. Tups and J.M. Leger, 1985, Phys. Rev. B **32**, 8246.
Takemura, K., and K. Syassen, 1985, J. Phys. F **15**, 543.
Tarascon, J.M., Y. Isikawa, B. Chevalier, J. Etourneau, P. Hagenmuller and M. Kasaya, 1980a, J. Phys. (France) **41**, 1135.
Tarascon, J.M., Y. Isikawa, B. Chevalier, J. Etourneau, P. Hagenmuller and M. Kasaya, 1980b, J. Phys. (France) **41**, 1141.
Thole, B.T., G. van der Laan, J.C. Fuggle, G.A. Sawatzky, R.C. Karnatak and J.M. Esteva, 1985, Phys. Rev. B **32**, 5107.
Tracy, D.H., 1977, Proc. R. Soc. London Ser. A **357**, 485.
Tranquada, J.M., R. Ingalls and E.D. Crozier, 1984, Springer Proc. Phys. **2**, 374.
Troneva, N.V., I.D. Marchikova and I.B. Borovskiy, 1958, Fiz. Met. & Metalloved. **6**, 141.
Tsutsumi, K., O. Aita and T. Watanabe, 1982, Phys. Rev. B **25**, 5415.
Vainshtein, E.E., I.B. Staryi, S.M. Blokhin and Yu.B. Paderno, 1962, Zh. Strukt. Khim. **3**, 200.
Vainshtein, E.E., I.B. Staryi and M.N. Bril', 1963a, Dokl. Akad. Nauk SSSR **151**, No. 6, 1360.
Vainshtein, E.E., M.N. Bril', I.B. Staryi and M.E. Kost, 1963b, Dokl. Akad. Nauk SSSR **151**, 120.
Vainshtein, E.E., S.M. Blokhin, M.N. Bril, I.B. Staryi and Yu.B. Paderno, 1965a, Rus. J. Inorg. Chem. **10**, 64.
Vainshtein, E.E., S.M. Blokhin and Yu.B. Paderno, 1965b, Sov. Phys.-Solid State **6**, 2318.
Vainshtein, E.E., M.N. Bril, I.B. Staryi and E.I. Yarembash, 1967a, Izv. Akad. Nauk SSSR, Neorg. Mater. **3**, 1685.
Vainshtein, E.E., M.N. Bril, I.B. Staryi, E.I. Gladyshevskii, P.I. Kripyakevich, 1967b, Inorg. Mater. USSR **3**, 566.
van der Laan, G., J.C. Fuggle, M.P. van Dijk, A.J. Burggraaf, J.-M. Esteva and R. Karnatak, 1986, J. Phys. & Chem. Solids **47**, 413.
Vettier, C., J. Flouquet, J.M. Mignot and F. Holtzberg, 1980, J. Magn. & Magn. Mater. **15–18**, 987.
Vickery, R.C., R. Sedlacek and A. Ruben, 1959, J. Chem. Soc., p. 505.
Vlasov, S.V., and O.V. Farberovich, 1982, Sov. Phys.-Solid State **24**, 536.
Vo Chiong Ki, Yu., V. Zatseva, N.A. Kulagin, L.P. Podus and A.F. Sirenko, 1984, Sov. Phys.-Solid State **26**, 2119.
Wachter, P., 1982, in: Valence Instabilities, eds P. Wachter and H. Boppart (North-Holland, Amsterdam) p. 145.
Wachter, P., and H. Boppart, eds, 1982, Valence Instabilities (North-Holland, Amsterdam).
Wagner, E., 1916, II. Sitzungsberichte der bayerischen Akademie der Wissenschaften, Math.-Physik. Kl. **31**.
Weidner, P., A. Freimuth, K. Keulerz, B. Politt, B. Roden, J. Röhler and D. Wohlleben, 1985a, J. Magn. & Magn. Mater. **47&48**, 599.
Weidner, P., K. Keulerz, R. Löhe, B. Roden, J. Röhler, B. Wittershagen and D. Wohlleben, 1985b, J. Magn. & Magn. Mater. **47&48**, 75.
Wendin, G., 1983, Springer Series in Chem. Phys. **27**, 29.
Wertheim, G.K., W. Eib, E. Kaldis and M. Cam-

pagna, 1980, Phys. Rev. B **22**, 1910.
Wertheim, G.K., E.V. Sampathkumaran, C. Laubschat and G. Kaindl, 1985, Phys. Rev. B **31**, 6836.
Winick, H., and S. Doniach, eds, 1980, Synchrotron Radiation Research (Plenum Press, New York) pp. 353–385.
Wohlleben, D., 1982, in: Valence Fluctuations in Solids, eds L.M. Falicov, W. Hanke and M.B. Maple (North-Holland, Amsterdam) p. 1.
Wohlleben, D., 1984a, in: Physics and Chemistry of Electrons and Ions in Condensed Matter, eds J.V. Acrivos, A.D. Yoffe and N.F. Mott (Reidel, Dordrecht) p. 85.
Wohlleben, D., 1984b, in: Moment Formation in Solids, ed. W.J.L. Buyers (Reidel, Dordrecht) p. 171.
Wohlleben, D., and B.R. Coles, 1973, in: Magnetism, Vol. V (Academic Prss, New York) p. 3.
Wohlleben, D., and J. Röhler, 1984, J. Appl. Phys. **55**, 1904.
Wohlleben, D., J. Röhler, R. Pott, G. Neumann and E. Holland-Moritz, 1981, in: Valence Instabilities, eds P. Wachter and H. Boppart (North-Holland, Amsterdam) p. 141.
Wolff, H.W., R. Bruhn, K. Radler and B. Sonntag, 1976, Phys. Lett. A **59**, 67.
Wong, J., Scott, H. Lawson and K.J. Rao, 1984, Springer Proc. Phys. **2**, 49.
Wortmann, G., K. Syassen, K.H. Frank, J. Feldhaus and G. Kaindl, 1982, in: Valence Instabilities, eds P. Wachter and H. Boppart (North-Holland, Amsterdam) p. 159.
Wortmann, G., K.H. Frank, E.V. Sampathkumaran, B. Perscheid, G. Schmiester and G. Kaindl, 1985, J. Magn. & Magn. Mater. **49**, 325.
Wortmann, G., W. Krone, E.V. Sampathkumaran and G. Kaindl, 1986, Hyperfine Interactions **28**, 581.
Zandy, H.F., 1952, Proc. Phys. Soc. A **65**, 1015.
Zimkina, T.M., and S.A. Gribovskii, 1971, J. Phys. Coll. (France) C4, suppl. 10, **32**, C4-282.
Zimkina, T.M., V.A. Fomichev, S.A. Gribovskii and I.I. Zhukova, 1967, Sov. Phys.-Solid State **9**, 1128.
Zimmer, H.G., K. Takemura, K. Syassen and K. Fischer, 1984, Phys. Rev. B **29**, 2350.

Handbook on the Physics and Chemistry of Rare Earths, Vol. 10
edited by K.A. Gschneidner, Jr., L. Eyring and S. Hüfner

Chapter 72

INELASTIC ELECTRON SCATTERING MEASUREMENTS

F.P. NETZER
Institut für Physikalische Chemie, Universität Innsbruck, A-6020 Innsbruck, Austria

J.A.D. MATTHEW
Department of Physics, University of York, Heslington, York YO15DD, England

Contents

List of symbols

A	spin asymmetry parameter	δE	energy resolution of electron spectrometer
AES	Auger electron spectroscopy	$\varepsilon(q,\Delta E)$	dielectric response function
BIS	bremsstrahlung isochromat spectroscopy	$\varepsilon_1, \varepsilon_2$	real, imaginary parts of the dielectric function
CEELS	core electron energy loss spectroscopy	$\mathrm{Im}(-1/\varepsilon)$	dielectric loss function
(C)TEM	(conventional) transmission electron microscopy	$\dfrac{\mathrm{d}f(q,\Delta E)}{\mathrm{d}(\Delta E)}$	generalised oscillator strength
EELS	electron energy loss spectroscopy	i (f)	initial (final) states
E_p	primary electron energy	$\boldsymbol{k},\boldsymbol{k}'$	incident (scattered) electron wave vector
ΔE	electron loss energy	λ	inelastic mean free path

LEED	low energy electron diffraction	STEM	scanning transmission electron microscopy
n	effective free electron density	$S(q, \Delta E)$	form factor for inelastic scattering
N	number of electrons per atom	$d\sigma/d\Omega$, $d\sigma/d(\Delta E)$	differential scattering cross sections
n_{eff}	effective number of electrons per atom contributing to the loss intensity up to a given loss energy ΔE	θ	electron scattering angle
		θ_E	characteristic loss angle – a measure of the angular breadth of the loss profile
$N(E)$	energy distribution of emitted electrons	θ_0	angular aperture of spectrometer
ω_p	bulk plasmon frequency	$U = (E_p/\Delta E)$	reduced electron primary energy
P_0	spin polarisation		
$\boldsymbol{q}$	momentum transfer	v	electron velocity
r_c	core orbital radius	XAS	X-ray absorption spectroscopy
$\langle r_{nl} \rangle$	expectation value of r for nl orbital	XPS	X-ray photoelectron spectroscopy
SAM	scanning Auger microscopy		
SEM	scanning electron microscopy		

1. Introduction

The inelastic scattering of electrons provides a powerful technique for characterising both the chemical composition and electronic environment of materials; the energy loss ΔE suffered by an incident electron (energy E_p) directly defines a fundamental bulk or surface excitation in the solid. Experiments may be carried out either in the *transmission mode*, in which fast electrons ($50 \lesssim E_p \lesssim 300$ keV) pass through thin films (~ 100 nm) in an electron microscope while undergoing mainly bulk excitations, or in *reflection mode*, in which slower electrons $20\,\text{eV} \lesssim E_p \lesssim 2$ keV suffer both electron loss and backscattering from the surface. Here the effective sampling depth is directly dependent on E_p, varying from one or two layers to 2–3 nm at higher incident energies, and both bulk and surface excitations will be prominent. Inelastic scattering processes involve two main types of electronic excitation:

(a) Low-energy excitation of valence electrons, which may be collective in character (plasmons) or one-electron transitions. All materials have losses in the $0 < \Delta E < 20$ eV range, and so such loss data provide rather detailed fingerprints of electronic environment rather than element specific excitation energies.

(b) Higher-energy core excitations, which may at least schematically be regarded as one-electron excitations. These transitions occur in energy regions characteristic of particular atomic species and can carry information both on elemental concentration and electronic environment.

In reflection geometry it is possible to investigate energy losses ΔE comparable to the primary energy E_p, and under these circumstances exchange interaction between incident and target electrons becomes important leading to a widening of the range of possible excitations through the relaxing of strict selection rules.

Transmission electron energy loss spectroscopy has its origins in the 1940s through pioneering experiments by Ruthemann (1941), Hillier and Baker (1944) and others, but it was in the 1970s that the technique became widely established, and electron energy loss facilities are now standard attachments to electron microscopes. Amongst numerous reviews extolling the virtues and defining the limitations of the technique those by Raether (1965), Daniels et al. (1970), Colliex et al. (1976a), Schnatterly (1979), Raether (1980), Egerton (1984a,b), Leapman (1982), Colliex (1984) and Colliex et al. (1985) have proved particularly helpful to us. In addition Egerton and Egerton (1983) have produced a useful bibliography, while Ahn and Krivanek (1982) and Zaluzec (1981) have established reference libraries of spectra.

Modern reflection electron energy loss spectroscopy has its origins in work by Powell (1960), Robins and Swan (1960) and Best (1962), while Gerlach et al. (1970) and Gerlach and Du Charme (1972) showed that core ionisation could be studied in reflection. Surprisingly there is no comprehensive review of this field as far as electronic excitations are concerned, but the article by Froitzheim (1977) may be a useful starting point.

The lanthanide elements and their compounds have a number of properties that are particularly attractive for application of electron energy loss spectroscopy (EELS). The conduction band electrons in the metals are mixed s–d in character as in the lower part of the transition metal series, and the monitoring of both one-electron transitions and plasmons by EELS is a convenient indicator of changes in outer electronic structure in such metals, alloys and compounds. The partially filled 4f shells show strong atomic-like correlation even although the electrons are bound by only a few eV, and core excitations may reach localised atomic-like states. By appropriate variation of E_p EELS reveals a richness in excited state structure that remains hidden from other spectroscopies such as X-ray absorption. Electrons may also cause vibrational excitation (Ibach and Mills 1982), but no such experiments have as yet been carried out on rare earth systems.

In this review we consider how EELS complements other high-energy spectroscopies in elucidating the electronic properties of rare earths and their compounds. Section 2 reviews the interaction of electrons with matter, while section 3 surveys the experimental techniques of transmission and reflection EELS. Section 4 considers excitation of the outer electrons in rare earth metals and their compounds; one-electron and plasmon losses show both continuation of bulk properties to the surface and modified surface environment. Section 5 looks at core excitations, which emphasise atomic rather than band-like properties, while section 6 suggests new applications of EELS which will enhance understanding of the idiosyncracies of rare earth systems that keep the rare earth community both intrigued and employed.

Finally, before embarking on a study of electron energy loss spectroscopy (EELS but sometimes just ELS) it is important not to be too confused by various nearly equivalent acronyms that are used in the literature. CEELS (core electron energy loss spectroscopy) is similar to ILS (ionisation loss spectroscopy), although in the rare earths we shall see that excitation dominates rather than ionisation. AREELS stands for angle resolved EELS, which is equivalent to ILEED (inelastic low-energy electron diffraction); REELS (reflection EELS) and SEELS (slow EELS) – see Nassiopoulos and Cazaux (1985) – refer to electron loss involving reflection of

electrons of intermediate energy, while LEELS (low-energy EELS) and HREELS (high-resolution EELS) tend to be associated with vibrational loss spectroscopy.

2. The interaction of electrons with matter

The inelastic scattering of electrons by atoms or solids may be dealt with in two basic regimes according to whether or not the velocity of the incident electron, v, is large compared to the orbital speed of the electron(s) being excited. In the former case ('fast' electrons) the first Born approximation is valid, Bethe (1930, 1932, 1933) theory may be applied, and the differential cross section for scattering depends directly on the momentum transferred in the collision. In the latter case the incident energy is not much greater than the binding energy of the electrons being excited, and a much more complicated pattern of interaction emerges (Celotta and Huebner 1979, Kuppermann et al. 1968); however, in this 'slow' regime selection rules for excitation break down and important new scattering channels appear. The ideas inherent in the Bethe formalism survive reasonably intact in the intermediate energy regime between 'fast' and 'slow', and the Born–Bethe approximation forms a good basis for the interpretation of most (but as we shall see not all) EELS experiments on solids.

2.1. *Born–Bethe predictions*

Since Bethe's incisive analysis of the interaction of fast electrons with atoms, many useful reviews of its applications have appeared – see Inokuti (1971), Inokuti et al. (1978), Bonham (1979), Leapman (1982) and Inokuti and Manson (1984) – but it is important to summarise the main results here.

Let us first consider the interaction of a fast electron of energy $E_p = \frac{1}{2}k^2 = \frac{1}{2}v^2$ (in the formulae in this review we shall adopt Hartree atomic units, setting relative to SI units $e = \hbar = m_e = 4\pi\varepsilon_0 = 1$; the atomic unit of energy is then 27.2 eV, the unit of distance the Bohr radius 0.0529 nm); $\boldsymbol{k}$ is the incident wave vector, v the velocity. If the electron loses energy ΔE in being scattered into a final state of wave vector $\boldsymbol{k}'$ the momentum transfer (fig. 1d)

$$\boldsymbol{q} = \boldsymbol{k} - \boldsymbol{k}', \tag{1}$$

and for small angles of scattering

$$q^2 = k^2(\theta^2 + \theta_E^2), \tag{2}$$

where $\theta_E = \Delta E/2E_p$; $q_{min} = k\theta_E = \Delta E/\sqrt{2E_p}$ is the minimum momentum transfer for a given ΔE and its direction is parallel to $\boldsymbol{k}$. Table 1 gives the minimum ($\theta = 0$) momentum transfer for typical ΔE and E_p values occurring in EELS as well as the corresponding θ_E values.

First Born theory leads to a differential scattering cross section for loss ΔE,

$$d\sigma = 4\left(\frac{k'}{k}\right)\frac{1}{q^4}S(\boldsymbol{q},\Delta E)\,d\Omega, \tag{3}$$

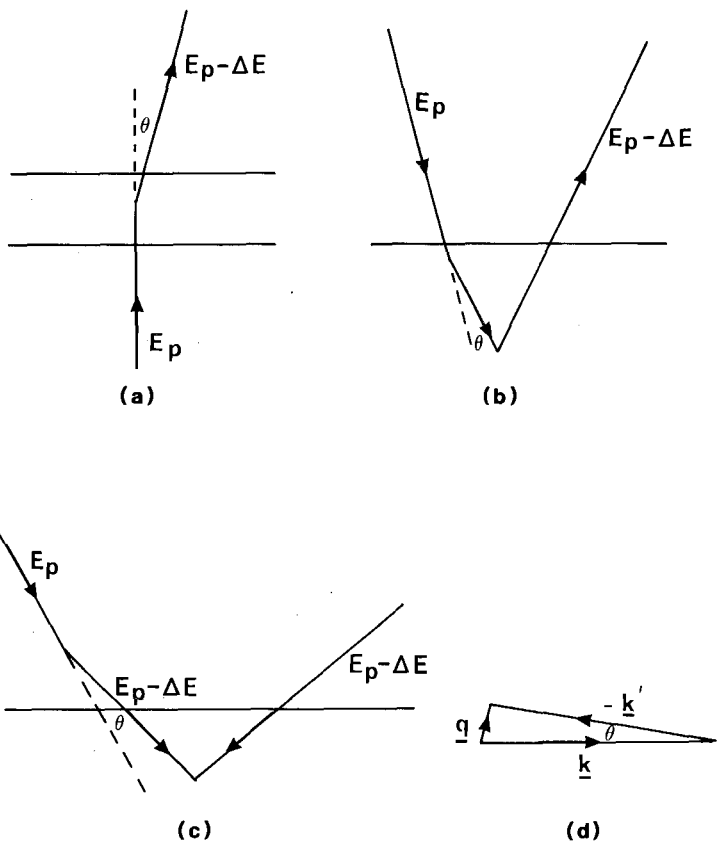

Fig. 1. Schematic diagram of: (a) transmission electron energy loss; (b) reflection electron energy loss; (c) excitation outside the surface in reflection electron energy loss; (d) momentum conservation in the energy loss process.

where $S(\boldsymbol{q}, \Delta E)$ is called the form factor for inelastic scattering in the system. For an N-electron atom or solid, $S(\boldsymbol{q}, \Delta E)$ takes the form of the square of the modulus of a matrix element between the initial state i and the final state f of excitation energy ΔE,

$$S(\boldsymbol{q}, \Delta E) = \left| \langle \mathrm{f} | \sum_{j=1}^{N} \exp(\mathrm{i}\boldsymbol{q} \cdot \boldsymbol{r}_j) | \mathrm{i} \rangle \right|^2, \tag{4}$$

with $\boldsymbol{r}_j$ the position operator of the jth electron. For transitions to continuum states $S(\boldsymbol{q}, \Delta E)\,\mathrm{d}(\Delta E)$ corresponds to the form factor for final states in the excitation energy range

$$\Delta E \rightarrow \Delta E + \mathrm{d}(\Delta E).$$

The merit of eq. (3) is its partitioning of the cross section into two parts. The term $4(k'/k)(1/q^4)$ is the Rutherford cross section for the scattering of one free electron by another at rest, so that $S(\boldsymbol{q}, \Delta E)$ represents the ratio of scattering from a system with electronic structure to the idealised 'structureless' electron case; it is a property of

TABLE 1

q_{min} and θ_E values for rare earth losses in reflection ($E_p = 100, 200, 2000$eV) and transmission ($E_p = 100000$eV) modes. The losses 4, 14, 40, 150 and 900eV are typical one-electron, bulk plasmon, 5p, 4d and 3d loss energies.

E_p(eV)	ΔE(eV)	q_{min}(Å^{-1})	θ_E(degrees)
100	4	0.10	1.1
	14	0.35	4.0
200	4	0.05	0.6
	14	0.18	2.0
	40	0.72	5.7
2000	4	0.02	0.06
	14	0.08	0.20
	40	0.23	0.57
	150	0.86	2.1
	900	5.16	12.9
100000	4	0.003	0.001
	14	0.011	0.004
	40	0.032	0.01
	150	0.12	0.04
	900	0.73	0.26

the scattering target, is a function of momentum transfer, and is independent of the incident velocity. Alternatively $d\sigma/d\Omega$ may be rewritten in terms of the generalised oscillator strength

$$\frac{df(q,\Delta E)}{d(\Delta E)} = \frac{2\Delta E}{q^2} S(\boldsymbol{q}, \Delta E). \tag{5}$$

The advantage of this reformulation is that in the limit $q \to 0$, i.e., expanding $\exp(i\boldsymbol{q}\cdot\boldsymbol{r}_j)$ in eq. (4) and taking the leading non-zero term, $df(q,\Delta E)/d(\Delta E)$ corresponds to the dipole oscillator strength encountered in photoabsorption.

For small angles of scattering θ the differential scattering cross section into continuum states of excitation energy ΔE is now

$$\frac{d^2\sigma}{d(\Delta E)d\Omega} = \frac{2}{v^2 \Delta E} \frac{1}{(\theta^2 + \theta_E^2)} \frac{df(q,\Delta E)}{d(\Delta E)}. \tag{6}$$

For dipole allowed transitions $df/d(\Delta E)$ is approximately constant over a reasonable range of q, so that the angle dependence of the cross section goes as $(\theta^2 + \theta_E^2)^{-1}$ and as θ^{-2} over a substantial angular range beyond θ_E.

2.2. *Core excitations in solids*

Core electrons in solids are basically atomic-like, and it is possible to take over the atomic theory directly, to give the differential cross section for excitation to a discrete state

$$\frac{d\sigma}{d\Omega} = \frac{4}{v^2} \frac{1}{(\theta^2 + \theta_E^2)} \frac{1}{q^2} |\langle f| \exp(i\boldsymbol{q}\cdot\boldsymbol{r}) |i\rangle|^2, \tag{7}$$

where a one-electron approximation has been adopted in evaluating the form factor. Since initial and final states are orthogonal the leading term is

$$\frac{d\sigma}{d\Omega} = \frac{4}{v^2} \frac{1}{\theta^2 + \theta_E^2} \frac{|\langle f|\boldsymbol{q}\cdot\boldsymbol{r}|i\rangle|^2}{q^2}, \tag{8}$$

emphasising the direct connection to the dipole matrix elements involved in X-ray absorption.

For dipole forbidden transitions, e.g., from a p core state to a 4f final state, higher-order terms in the exponential expansion lead to a finite contribution to the cross section. This is in general small unless $q \sim 1/r_c$, where r_c is the core orbital radius, but such conditions may be satisfied both in transmission and reflection geometry (Schnatterly 1979, Grunes and Leapman 1980, Ludeke and Koma 1975), and will be of importance in rare earth electron loss spectroscopy. Thus even within the Born–Bethe regime monopole, quadrupole and octopole transitions may be prominent.

2.3. *Dielectric formulation*

It is not so obvious how well Born–Bethe ideas are satisfied in describing excitations in solids with their extended band states. However, the structure of the basic result (eq. (3)) with the partitioning into a Rutherford cross section and a form factor depending on momentum transfer remains intact. All that is required is for the differential oscillator strength to be reinterpreted in terms of a response function for the system $\varepsilon(q, \Delta E)$, the Fourier transform of the space/time dielectric response $\varepsilon(\boldsymbol{r}, t)$.

The generalised oscillator strength now takes the form

$$\frac{df(q, \Delta E)}{d(\Delta E)} = \frac{2\Delta E \, \mathrm{Im}(-1/\varepsilon(q, \Delta E))}{\pi \omega_p^2}, \tag{9}$$

where $\omega_p = \sqrt{4\pi n}$ with n the effective electron density in the solid, and $\mathrm{Im}(-1/\varepsilon)$ is termed the bulk dielectric loss function; the expression may be modified to take account of anisotropy where appropriate. This result may be obtained by a number of different routes (Schnatterly 1979, Raether 1980), but the fact that $d^2\sigma/[d(\Delta E)\, d\Omega]$ should be proportional to $\mathrm{Im}(-1/\varepsilon(q,\Delta E))$ may be seen from the classical argument as given by Froitzheim (1977). The moving electron interacts with the electrons in the solid by long-range Coulomb forces; the space and time dependent response of these electrons produces a polarisation field characterised by a dielectric function $\varepsilon = \varepsilon_1 + i\varepsilon_2$ containing both real (refractive) and imaginary (damping) components. Looking at a particular Fourier component of the field, its amplitude will be reduced in the solid by a factor $1/\varepsilon$, its energy density by $|1/\varepsilon|^2$. As the field moves through the system its energy dissipation will be proportional to ε_2

so that

$$\left(\frac{d^2\sigma}{d(\Delta E)\,d\Omega}\right)_{\text{bulk}} \propto \frac{\varepsilon_2}{\varepsilon_1^2+\varepsilon_2^2} \propto \text{Im}\left(-\frac{1}{\varepsilon(q,\Delta E)}\right). \tag{10}$$

However, another possibility exists. The electron may lose energy even although it is outside the solid. Here there will be image screening, which reduces the field by a factor $1/(\varepsilon+1)$ leading to energy loss

$$\left(\frac{d^2\sigma}{d(\Delta E)\,d\Omega}\right)_{\text{surface}} \propto \frac{\varepsilon_2}{(\varepsilon_1+1)^2+\varepsilon_2^2} \propto \text{Im}\left(-\frac{1}{\varepsilon(q,\Delta E)+1}\right). \tag{11}$$

In transmission experiments the relative importance of bulk and surface loss components will be a function of film thickness, but bulk response will generally dominate. In reflection geometry the bulk/surface balance depends sensitively on incident energy and angle and the mean free path for inelastic loss within the solid, but at low E_p ($\lesssim 200$ eV) the contributions are likely to be comparable, with surface response becoming increasingly important near glancing incidence.

It must be emphasised that the surface dielectric response has nothing to do with intrinsic surface properties of the material – it is just a sensing of bulk properties from outside the surface. Features in the loss spectrum additional to those associated with $\varepsilon(q,\Delta E)$ may appear under highly surface-sensitive experimental conditions, and these are associated with different electronic properties in the surface region.

In all practical circumstances the characteristic angle θ_E that controls the angular profile near $\theta = 0$ (table 1) is quite small, and in reflection geometry the small angle loss must be accompanied by an elastic reflection in order for the electron to be detected in the spectrometer (fig. 1). Elastic backscattering is much more probable than the inelastic process, and furthermore the elastic momentum transfer is taken up by the whole crystal.

2.4. *What do we measure?*

So far we have outlined the physics of single inelastic scattering, but in condensed matter multiple inelastic scattering may occur; in transmission its importance is governed by the ratio of the inelastic mean free path for all electronic excitations to the sample thickness d, and well-established correction procedures (Swyt and Leapman 1982) may be applied to separate the single-scattering component. In reflection, the inelastic mean free path and the angle of incidence mainly determine the surface sensitivity of the experiment; λ varies with energy as E_p^x ($x \sim 0.5$–0.8) for $E_p \gtrsim 100$ eV, ranging from one to two layers ($E_p \sim 50$ eV) to about 1 nm ($E_p \sim 1000$ eV). There are, however, considerable material variations and there are some suggestions that the mean free path of rare earth metals is particularly low at low primary energies. Quantitative isolation of the single-scattering component is now more difficult, although identification of the single-loss features is generally easy.

In either transmission or reflection geometry inelastically scattered electrons are

sampled at a finite angular aperture θ_0 at an angle θ to the beam direction (in transmission) or with respect to the specular or a LEED beam direction (in reflection). At $\theta = 0$ the relation between the single-scattering intensity and $\varepsilon(q, \Delta E)$ depends on whether θ_0 is less than or greater than θ_E,

$$I_{\text{bulk}} \propto \frac{\theta_0^2}{\Delta E^2} \operatorname{Im}\left(-\frac{1}{\varepsilon(q_{\min}, \Delta E)}\right), \qquad \theta_0 \ll \theta_E, \tag{12}$$

while following Ritchie (1957) and Ibach and Mills (1982),

$$I_{\text{surface}} \propto \frac{\theta_0^2}{\Delta E^3} \operatorname{Im}\left(-\frac{1}{\varepsilon(q_{\min}, \Delta E) + 1}\right), \qquad \theta_0 \ll \theta_E. \tag{13}$$

At high E_p (as in transmission loss) $q_{\min} \sim 0$; ε then corresponds to the function sensed in optical transmission and reflection experiments; at lower E_p (in reflection) the minimum momentum transfer is not so negligible (table 1), but in most cases $q \sim 0$ when $\theta = 0$. In transmission EELS $\theta_0 < \theta_E$ is satisfied in some applications and in general the isolation of $\varepsilon(q, \Delta E)$ from experimental measurement is very direct, as discussed by Raether (1980) and Daniels et al. (1970).

In reflection geometry θ_0 may be greater or less than θ_E for different loss features; this effect combined with other complications at low E_p makes it more difficult to determine the dielectric function precisely, even though the main features in the spectrum will have good correspondence with peaks in $\operatorname{Im}(-1/\varepsilon)$ and $\operatorname{Im}(-1/(\varepsilon + 1))$, and additional peaks associated with events at the surface.

2.5. *The physics in the dielectric function*

Under typical scattering conditions the intensity of electron scattering may, with one degree of precision or another, be related to the bulk dielectric function $\varepsilon(q, \Delta E)$ with possible additional spectral structure due to genuine surface effects in reflection mode. In the $q \to 0$ limit the bulk and surface dielectric functions take the form

$$\operatorname{Im}\left(-\frac{1}{\varepsilon(0, \Delta E)}\right) = \frac{\varepsilon_2}{\varepsilon_1^2 + \varepsilon_2^2},$$

$$\operatorname{Im}\left(-\frac{1}{\varepsilon(0, \Delta E) + 1}\right) = \frac{\varepsilon_2}{(\varepsilon_1 + 1)^2 + \varepsilon_2^2}. \tag{14}$$

The dielectric components ε_1 and ε_2 now correspond exactly to the constants observed in photon spectroscopy, but electron loss may give very different emphasis from an optical absorption or reflection experiment. If ε_2 is low, the dominant bulk feature will be a bulk plasmon ($\varepsilon_1 = 0$) loss, which for a free electron gas (electron density n) occurs at energy $\omega_p = \sqrt{4\pi n}$. On the other hand if ε_1 is reasonably large ($> \varepsilon_2$) and not varying rapidly with ΔE, $\operatorname{Im}(-1/\varepsilon)$ reflects structure in ε_2. One-electron transitions, e.g., of interband-type will then be emphasised. This is exactly what occurs for core losses where at high ΔE, $\varepsilon_1 \sim 1$, ε_2 is small and $\operatorname{Im}(-1/\varepsilon) \approx \varepsilon_2$. This implies that the atomistic analysis discussed in section 2.3 is perfectly consistent with the dielectric formulation. In some cases ε_1 and ε_2 vary together leading to

plasmon–interband coupling which affects both the shape and intensity of loss features (Powell 1969, 1976, 1982).

Insights into which electrons in the solid are contributing to which features can be gained by examining the differential oscillator strength $\mathrm{d}f(0,\Delta E)/\mathrm{d}(\Delta E)$. Integrating with respect to ΔE gives

$$n_{\mathrm{eff}} = \int_0^{\Delta E} \frac{\mathrm{d}f(0,\Delta E')}{\mathrm{d}(\Delta E')}\mathrm{d}(\Delta E'), \tag{15}$$

where n_{eff} goes to N, the number of electrons per atom as $\Delta E \to \infty$ (the Thomas–Reiche–Kuhn sum rule). Probing $\mathrm{Im}(-1/\varepsilon(q,\Delta E))$ at finite q gives information on plasmon dispersion (Raether 1980), band dispersion (Bringans 1981), or on monopole, quadrupole and octopole responses, whose analysis again simplifies for the case of core excitation.

2.6. *Beyond Born–Bethe*

As E_p approaches ΔE the incident and target electrons move at similar speed, and so the simplicity of the Born–Bethe analysis collapses with no longer a simple functional dependence of cross section on momentum transfer. This regime has been widely studied in the gas phase (Kuppermann et al. 1968, Celotta and Huebner 1979), but is less well-understood in condensed matter. Total inelastic cross sections for dipole processes build up from threshold ($E_p = \Delta E$) to a maximum at a few times threshold, while for $U = (E_p/\Delta E) \approx 10$ the cross section falls slowly with increasing E_p as Born–Bethe predicts. Monopole and quadrupole cross sections peak closer to threshold, and fall off more rapidly with energy at high E_p (see, for example, Chutijian and Cartwright (1981)). Near threshold the exchange between the incoming electron and the target electron assumes great importance. It is then possible to change the spin of the target, e.g., from a singlet (no net spin) to a triplet state, transitions which are not allowed in the simplest Born–Bethe approach. Now total cross sections peak very close to threshold (you need a large collision time to facilitate the interchange) and fall off very rapidly as E_p increases. However, at high angles of scattering transitions involving change of spin have cross sections much higher than transitions involving no spin change. A combination of energy and angle dependence of loss intensities can therefore be used to identify transitions involving spin change. In addition such energy loss processes may show spin dependence (Mauri et al. 1984).

If the target has a macroscopically well-defined spin in relation to the incoming electron, e.g. for a ferromagnet, spin polarised electron energy loss spectroscopy gives information on magnetic excitations; it is possible to control the spin of the incident electron (Kirschner et al. 1984), measure the spin polarisation of the scattered electrons (Hopster et al. 1984) or both (Kirschner 1985a,b), and so determine the amplitudes of various direct and exchange processes, e.g., in Stoner excitations on Ni(001) or amorphous ferromagnetic glasses. Recent experiments on Gd(0001)

will be discussed in section 4, while general aspects of spin polarised electron scattering have been recently reviewed by Kirschner (1985b) and Siegmann et al. (1984).

3. Experimental set-up

Every electron energy loss experiment requires three components: a source of electrons, a target system and a spectrometer unit for analysing the energy and the momentum of scattered electrons. Depending on the geometry of the experiment the various components have to be arranged in different ways, and particular designs have been developed for transmission and reflection EELS. Apart from the different geometrical arrangement of electron source, target and electron energy analyser in transmission and reflection mode, the primary energy E_p of the incoming electrons forms the major difference between the two experimental set-ups. In reflection EELS the primary energy ranges from a few eV to several keV, in accord with the desired depth sensitivity, whereas in transmission electron loss E_p is of the order of several tens of keV up to MeV, in certain special cases. High E_p's are necessary in transmission mode to ensure weak interaction of electrons with matter and therefore the penetration through (thin slices of) the probing material.

High-energy electrons are readily available in electron microscopes of the conventional transmission (CTEM) or of the scanning transmission type (STEM). Electron energy loss experiments in transmission are therefore often combined with an electron microscope arrangement, with the additional advantage that the chemical specifity of core ionisation edges as seen in EELS provides a popular tool for chemical microanalysis. In a TEM electrons from the gun of the microscope are focussed onto a specimen area whose size and position can be controlled, and which can be imaged using the normal electron optical system of the microscope. The spectrometer section is placed after the specimen – a thin section of the material to be examined – to analyse the transmitted electrons. The most general way to characterise the interactions between the electrons and the specimen is to measure the momentum changes suffered by the electrons as they pass through the sample, that is, by measuring both the angle of scattering and the change in energy. In practice it is often sufficient to collect all the transmitted electrons within a cone around the incident beam direction and to analyse those for their energy loss. This destroys the momentum information, but allows simpler spectrometer designs, particularly if only chemical information is required.

Electron energy analysers attached to electron microscopes may be of the magnetic or the electrostatic deflector type (Schnatterly 1979, Joy 1979), but a simple magnetic prism attached to a STEM seems to offer the greatest capability (Crewe et al. 1971). A resolution of the order of 1 eV is possible with magnetic spectrometers (Leapman 1979), but even a 5–10 eV resolution is often adequate to detect core edges for chemical microanalysis purposes. To achieve resolutions better than 1 eV it is necessary to decelerate the electrons before entering the analyser section, as the inherent resolution of deflector type analysers is a function of the

electron kinetic energy (Daniels et al. 1970, Schnatterly 1979).

The electron gun in a CTEM is usually equipped with a heated W filament yielding electrons of thermal breadth 0.5–1 eV. Field emission guns in STEM have higher brightness and may have reduced energy spreads, as small as 0.2 eV. For high resolution studies, however, an electron monochromator is required in addition to a high resolution analyser. Transmission electron loss spectrometers with high energy ($\delta E < 100$ meV) and momentum resolution have been designed, e.g. by Daniels et al. (1970), Ritsko) et al. (1974) and Fink and coworkers (Pflüger et al. 1984), among others. Figure 2(a) shows a schematic diagram of the spectrometer of Daniels et al. (1970), which has a quoted energy resolution of 50 meV and angular resolution of 0.3 mrad.

Transmission EELS facilities in combination with electron microscopes provide, as mentioned above, convenient tools for chemical microanalysis. There is a vast amount of literature on this subject, and key reviews include those of Colliex et al. (1976a), Silcox (1979), Leapman (1979, 1982) and Egerton (1981, 1984a,b). A particularly interesting feature of EELS in a STEM is the possibility of energy selective imaging (Leapman 1979, Egerton 1984a). This can be achieved by using the electron spectrometer as a filter in order to obtain electron microscope images from electrons which have suffered a chosen range of energy loss. Both core ionisation edges of a particular element and collective valence excitations may be used for that purpose. It is also worth noting in this context that, in reflection geometry in scanning electron microscopes (SEM), images of slow electrons having incurred

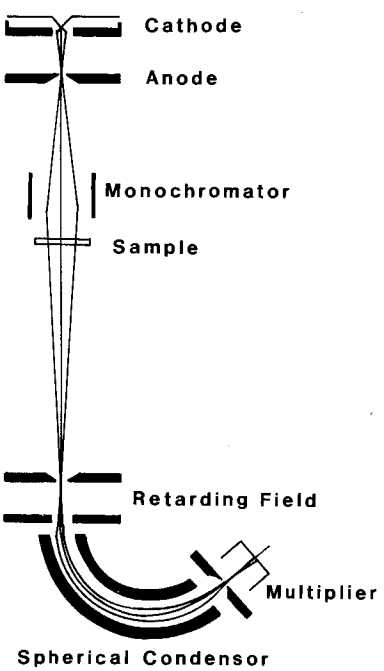

Fig. 2a. Scheme of a spectrometer with electrostatic analyser for energy losses of transmitted electrons (Daniels et al. 1970).

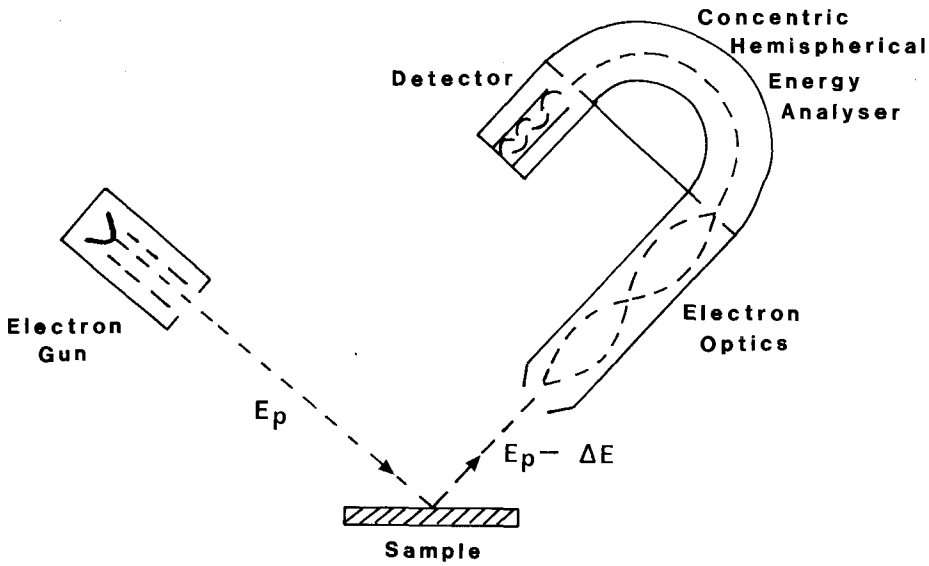

Fig. 2b. Schematics of an EELS experiment in reflection geometry.

plasmon losses have been obtained (Ichinokawa et al. 1981, Bevolo 1985a,b, El Gomati and Matthew 1987).

Reflection EELS is suited to study the outermost layers of a solid sample, and is therefore inherently a surface technique. Accordingly, vacuum requirements and sample preparation techniques have to match the stringent standards of modern surface science. For investigations of reactive materials, as to be considered in the present article, the spectrometer should be housed in ultrahigh vacuum (UHV) environment of the order of 1×10^{-10} Torr or better, and the sample surfaces have to be carefully prepared and characterised in situ. UHV compatible electron guns yielding electron currents up to $\sim 10^{-6}$ A/mm^2 at energies from several eV to the keV range are relatively cheap standard equipment, and energy dispersive analysers are commercially available because of the wide use of electron spectroscopic techniques in the study of solid surfaces. In principle, any electron energy analyser as used for Auger electron spectroscopy or photoelectron spectroscopy can be used in reflection EELS, but those equipped with pulse counting detectors are certainly favoured. The latter instruments yield the energy distribution of analysed electrons in form of $N(E)$ curves, but spectra in differentiated $dN(E)/dE$ or even doubly differentiated $d^2N(E)/dE^2$ form are also frequently recorded, particularly in spectrometers with analog detection. The most common energy analysers are of the cylindrical mirror or of the spherical sector type, but retarding field analysers are also employed because of their compatibility with low-energy electron diffraction devices (Prutton 1983, Riviere 1983). Figure 2(b) shows the schematics of an EELS experiment in reflection geometry with a concentric hemispherical energy analyser as used in the authors' laboratory. A combined resolution of 0.3–0.5 eV as measured on the elastically reflected beam is readily achievable over the whole energy range with a conventional electron gun and a spherical sector analyser, but for higher

resolution monochromatisation of primary electrons is again necessary. Some experimental aspects of high-resolution reflection EELS have been described by Froitzheim (1977), and for details on electron spectrometer and monochromator design see, e.g., Roy and Carette (1977).

In transmission EELS the specimens are confined to very thin slices of the material or thin edges of crushed powders. In the case of rare earths this restricts samples to evaporated thin films. Due to the high reactivity of the rare earths, oxide, hydroxide or hydride phases pose serious problems in the conventional vacua of many transmission spectrometers. More flexibility in the nature of samples is possible in reflection EELS. Evaporated thin films, foils or massive bulk samples can all be readily investigated, but the sample surfaces have to be cleaned thoroughly by often tedious procedures. Some surface cleaning and preparation techniques of rare earth materials have been compiled by Netzer and Bertel (1982), and more recently by Netzer and Matthew (1986).

4. Valence and conduction band excitations

Excitations of the valence/conduction band electrons of rare earth elemental solids and their compounds must be seen in the general context of their outer electronic structure. The metals have non-free-electron-like conduction bands (Liu 1978) with the 6s–5d mixing varying systematically through the series for the trivalents, and the divalent metals having less 5d character – see Duthie and Pettifor (1977) and Skriver (1983). Highly localised 4f states of low binding energy (Freeman 1980, Campagna et al. 1979) show strong intrashell correlation and are largely decoupled from the conduction/valence bands. In bulk metals from La to Lu there is one less 4f electron than in the free atom in all apart from Ce, Eu, Gd, Yb and Lu, but the energy balance that makes 4f promotion favourable in the bulk may change at the surface due to changes in coordination number. Hence Johansson (1979) suggests that Sm is likely to be divalent ($4f^6$) at the surface rather than trivalent $4f^5$). In compound formation it is possible for a given element to have more than one valence state (i.e. different 4f occupation numbers), or have states of intermediate valence as in rare earth intermetallic compounds in the lower part of the rare earth series (La to Pr), where the lowest energy state may be an admixture of basis states of different 4f counts. The 4f electrons do not usually take part in the bonding, but CeO_2 is something of a test case on that question, as will be discussed later in this review. Let us now see how some of these valence/conduction electron properties are illuminated by inelastic electron scattering experiments.

4.1. *Metals*

Following early transmission electron energy loss work by Bakulin et al. (1971), Daniels et al. (1970) and Zashkvara et al. (1972) and Brousseau–Lahaye et al. (1974, 1975), Colliex et al. (1976b) made a comprehensive study of heavy rare earth metals; their results for terbium metal are shown in fig. 3a. The raw loss spectrum is

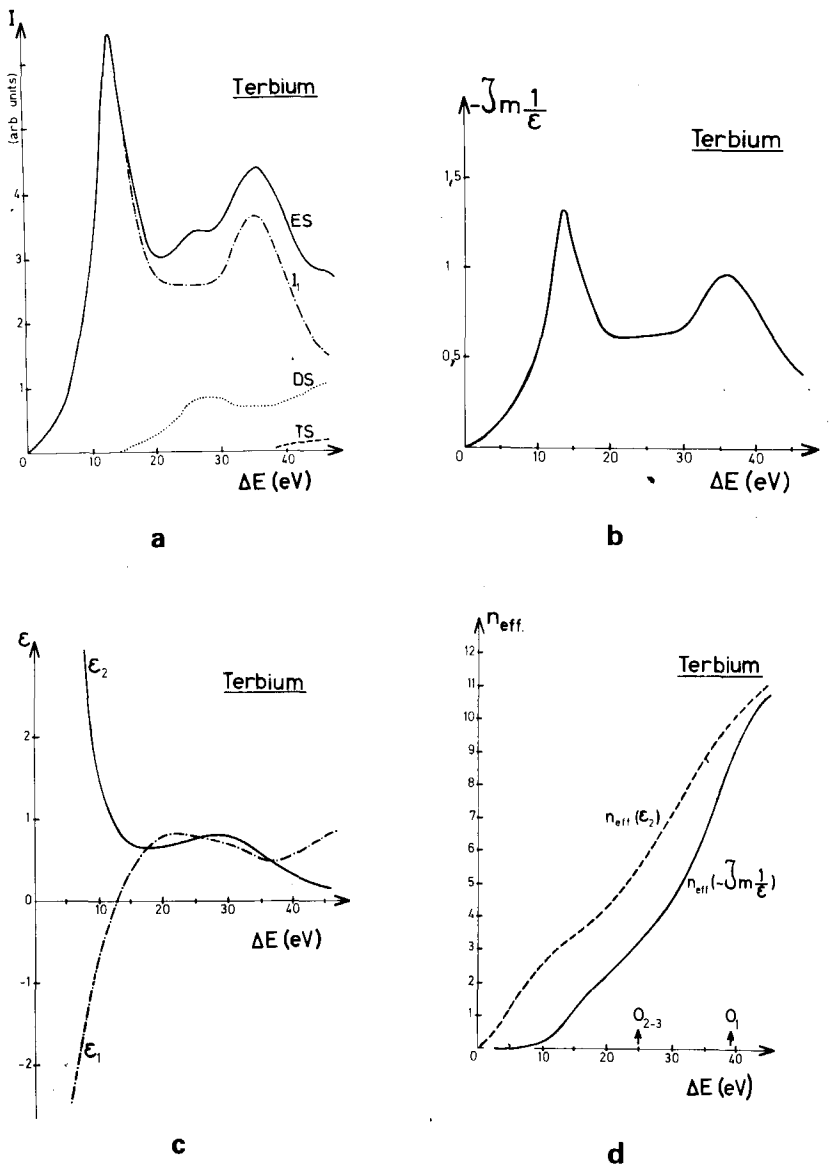

Fig. 3. Transmission electron energy loss spectrum of Tb metal (after Colliex et al. 1976b): (a) uncorrected loss spectrum; (b) $\mathrm{Im}(-1/\varepsilon)$; (c) $\varepsilon_1(\Delta E)$ and $\varepsilon_2(\Delta E)$; (d) $n_{\mathrm{eff}}(\Delta E)$.

corrected for instrumental aperture effects as well as multiple scattering to give $\mathrm{Im}(-1/\varepsilon(0,\Delta E))$ (fig. 3b), which undergoes a Kramers–Kronig transform (Daniels et al. 1970) to give ε_1 and ε_2 (fig. 3c). A well-defined bulk plasmon (peak in $\mathrm{Im}(-1/\varepsilon)$, $\varepsilon_1 = 0$) appears at $\Delta E_{\mathrm{BP}} = 13.3\,\mathrm{eV}$ with ε_1 and ε_2 behaving qualitatively in free-

electron fashion at low ΔE; the surface plasmon (peak in $\mathrm{Im}(-1/(\varepsilon+1))$, $\varepsilon_1 = -1$) would be around 9 eV, close to $1/\sqrt{2}$ times the bulk value as in free electron theory. Cukier et al. (1980) obtain similar results for Sc, Y, Gd and Dy metals with the further refinement of a small surface loss correction. The ΔE_{BP} values observed are generally between 1 and 3 eV higher than the free electron values $\Delta E_{BP} = \sqrt{4\pi n}$ a.u. ($n = 3$ electrons per atom for trivalent metals, $n = 2$ for divalent Yb and Eu) reflecting the influence of interband transitions associated with d electrons. Such electron microscope studies are typically carried out at energy resolution ~ 1 eV, so that the technique cannot compete with optical resolution for $0 < \Delta E < 5$ eV, where interband effects might be expected.

Converting the loss function to a differential oscillator strength according to eq. (9) and integrating with respect to ΔE given $n_{\mathrm{eff}}(\Delta E)$, fig. (3d). In Tb n_{eff} remains low, to just below the plasmon loss and builds up to a value $n_{\mathrm{eff}} \approx 3$ by the 5p threshold, a good indication that 4f electrons of binding energies 2.3 and 7–10 eV (Campagna et al. 1979) are playing little part in loss events at this stage. This is consistent with the fact that systems of similar conduction band structure Sc and Y (Brousseau-Lahaye et al. 1975), but without 4f electrons, show like behaviour. This apparent 'inactivity' of the 4f electrons may be understood in terms of the small spatial extension of the filled 4f orbitals relative to the outer electrons (table 2), which leads to small overlap with states above the Fermi level; the 4f oscillator strength will then be spread over a wide range of continuum energies. In contrast the 5p oscillator strength is largely dissipated in the strong 35 eV resonance loss as evidenced by the rapid rise of n_{eff} from near 3 to 9 between the 5p and 5s thresholds.

In reflection geometry surface cleanliness is at a premium, and experiments must

TABLE 2

The expectation values of r and r^{-1} for various orbitals of Gd showing that the 4f state has a similar spatial scale to 4s, 4p and 4d, but very different from the valence orbitals. $\langle r_{nl}^{-1} \rangle$ may be multiplied by $q_{\min}$ values from table 1 to give an estimate of the possible importance of non-dipole transitions. Theoretical values are from McLean and McLean (1981). Gd values are typical of the whole rare earth series.

Gd $4f^7 5d 6s^2$		
Orbital nl	$\langle r_{nl} \rangle$ Å	$\langle r_{nl}^{-1} \rangle$ Å^{-1}
3d	0.117	10.21
4s	0.310	4.48
4p	0.318	4.29
4d	0.338	3.89
4f	0.416	3.04
5s	0.764	1.69
5p	0.858	11.51
5d	1.296	1.00
6s	2.427	0.51

be carried out in good UHV with regular cleanliness monitoring by Auger electron spectroscopy (Netzer and Matthew 1986). A study of the reflection energy loss spectroscopy of polycrystalline rare earth metals La to Lu has been carried out by Netzer et al. (1985a), and the results (fig. 4) are consistent with investigations on individual systems by Onsgaard et al. (1980a,b, 1983), Bertel et al. (1981, 1982a) and Bloch et al. (1984). The energy resolution is now significantly higher than in the transmission studies, and some finer features may be revealed.

For $E_p \sim 1\,\text{keV}$ bulk plasmon and 5p peaks are again intense, and the difference in valence of Eu and Yb is clearly demonstrated. In the lower rare earths (Ce to Nd) the surface plasmon ($\Delta E \sim 8\,\text{eV}$) is now prominent; these peaks become bigger than the bulk plasmon if E_p is lowered to 250 eV, and decrease rapidly on exposure to oxygen (Strasser et al. 1985b). La shows a somewhat different pattern with a three-peak structure in the plasmon region. In addition an energy loss at $\Delta E = 3$–$4\,\text{eV}$ builds up in intensity through the series – these features are particularly accentuated at low E_p (higher surface sensitivity), an effect that is partly due to the size of the spectrometer aperture θ_0 in relation to θ_E (eq. (12)), the angle that controls the angular distribution of the differential cross section. Although these low-energy losses occur in the region of interband transitions they do not correlate well with peaks in $\text{Im}(-1/\varepsilon)$ or $\text{Im}(-1/(\varepsilon+1))$ as inferred from optical constants compiled by Weaver et al. (1981). Sensitivity to oxygen exposure suggests that they may be surface features. Since the surfaces are clean, this would imply an intrinsic surface excitation. However, it must be remembered that Auger spectroscopy is not capable of detecting hydrogen at the surface, and these features may in part be associated with that element. An account of the effects of hydrogen exposure is given in section 4.3. Amid this general pattern Sm behaves anomalously (Bertel et al. 1982b); under very clean conditions (fig. 5) the spectrum at $E_p = 100\,\text{eV}$ is dominated by lower-energy collective excitations, different in character from a conventional surface plasmon and reflecting the fact that the surface layer is divalent as predicted by Johansson (1979). Such behaviour is consistent with the picture built up from photoemission by Wertheim and Crecelius (1978), Lang and Baer (1979), Allen et al. (1980) and Gerken et al. (1982a).

The main peak in the 5p loss region shifts from 27.5 eV (La) to 42 eV (Lu), and decreases relatively in intensity through the series – see Netzer et al. (1985b). Strictly speaking this is a core excitation, but we treat it here for two reasons: (1) the intensities of these peaks are comparable to those of valence losses, and (2) ε_1 shows significant variation in this region (fig. 3c) so that the loss profile may not be controlled only by ε_2.

Onsgaard et al. (1983) have shown that the position of the main 5p peak in Tm is not closely related to peaks in the empty d density of states above E_F, where there is the right symmetry for dipole transitions, and it is clear that Coulomb and exchange effects due to the 5p core hole control the resonance. As in $3p \rightarrow 3d$ transitions in the lower part of the first transition series (Sc, V) the 5d wave function undergoes spatial collapse in the presence of the 5p core hole. Strong 5p–5d overlap leads to large exchange splitting, which drives the main dipole allowed component to high energy, well above the 5p ionisation thresholds, as shown in fig. 4. Spin–orbit splitting

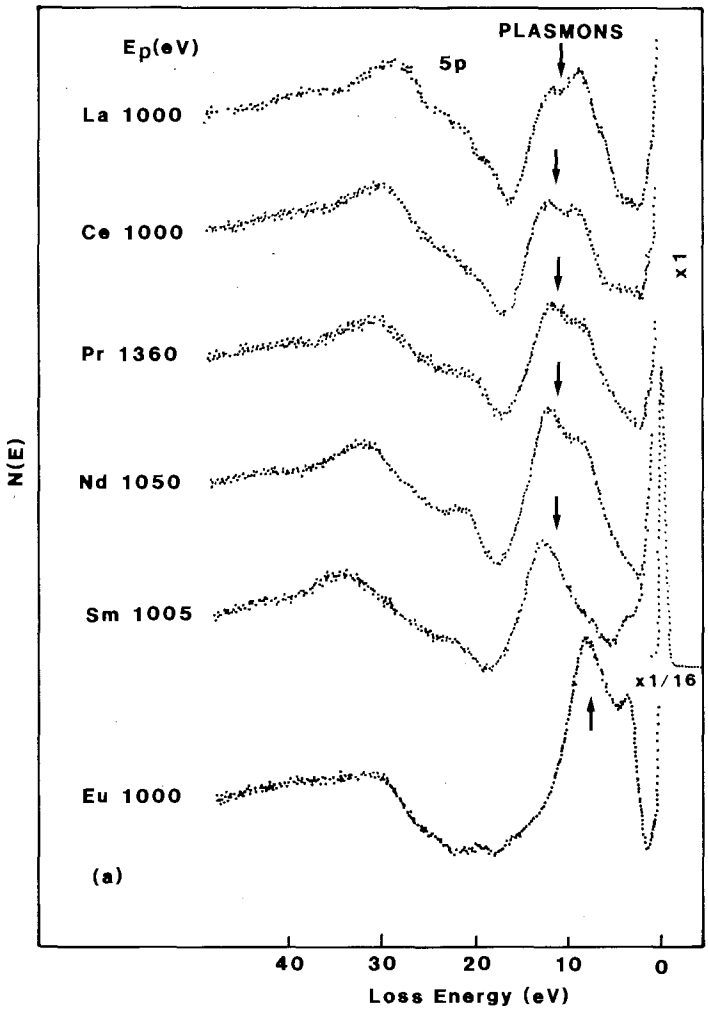

Fig. 4. Electron energy loss spectra in $N(E)$ form for clean rare earth metals La–Lu (Pm excepted) with $E_p \sim 1$ keV. Predictions of bulk plasmon energies based on a free electron model are shown by arrows (Netzer et al. 1985a).

increases with increasing atomic number, and there is a gradual shift in oscillator strength from being mainly concentrated above $5p_{1/2}$ (La) to being distributed more evenly between two main features. The losses in Eu and Yb have distinctive shapes, an effect probably due to the smaller amount of d character in the initial state. Such 5p resonances also occur in free atoms of the higher rare earths (Sm or above), but for the lower members of the series the resonance does not develop fully due to 5d–6s configurational interaction as discussed by Connerade and Tracy (1977). In solid state environments such inhibition does not occur, and it is at the bottom of the lanthanide series that most intense losses are seen. However, the fact that ε_1 varies

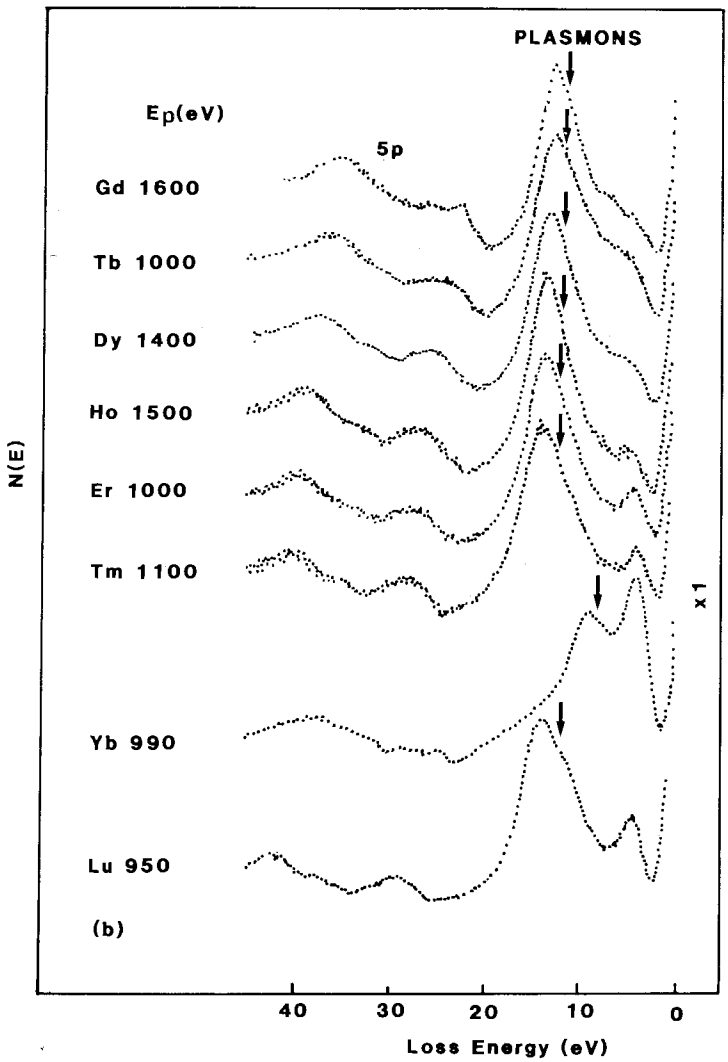

Fig. 4. (cont.).

significantly in the energy region of the loss shows that this is not a purely atomic phenomenon, but one fuelled by collective response.

4.2. *Oxides and oxidation*

Transmission electron energy loss spectroscopy has been applied to rare earth oxides by Colliex et al. (1976b), Cukier et al. (1980), Brown et al. (1984), Colliex et al. (1985) and by Gasgnier and Brown (1986), while the spatial resolution of the electron microscope has been exploited in studying oxide segregation by Dexpert et al. (1980). The main qualitative differences between metal and trivalent oxide EELS spectra in the valence region is the establishment of an energy gap of order 4 eV, and

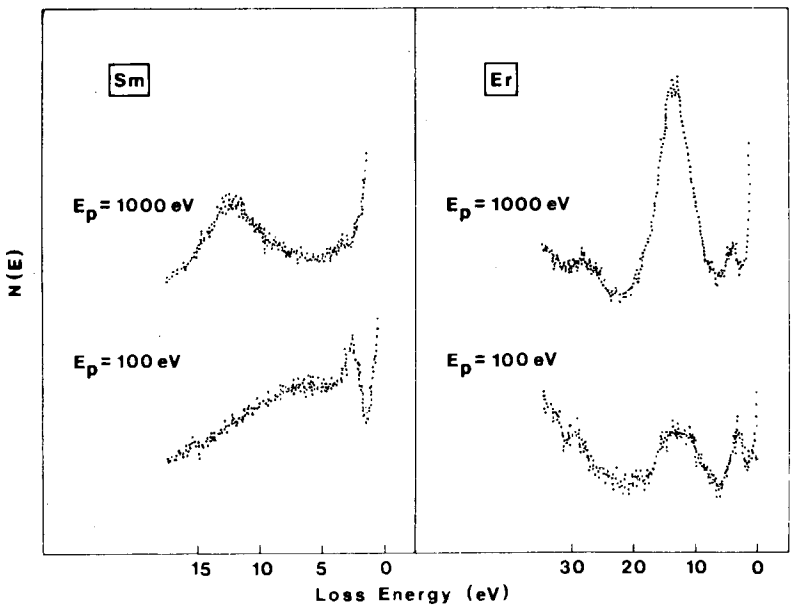

Fig. 5. Comparison of electron energy loss spectra in $N(E)$ form for clean Sm and Er metals at $E_p \sim 1$ keV and 100 eV (Bertel et al. 1982b). Note the anomalous energy dependence in the plasmon region in Sm, an effect associated with surface divalency.

the shift of the bulk plasmon by 1.5–2 eV to higher energy, reflecting the higher available density of polarisable electrons (mainly O 2p). At the energy resolution of these experiments there is no discernible structure at the band edge in the trivalent oxides, just a steady build-up of loss intensity beyond the edge, but in CeO_2 a sharp peak between 4 and 5 eV is found both in transmission (Gasgnier and Brown 1986) and in reflection by Bloch et al. (1984) and Strasser et al. (1985b).

Reflection EELS is an excellent monitor of changes in surface electronic structure, and so one can plot the progress of oxidation at the surfaces of highly reactive clean rare earth metals, a subject previously reviewed in this series by Netzer and Bertel (1982). Variation of incident primary energy and/or angle provides differential depth sampling. The oxidation of Ce, as studied by Strasser et al. (1985b), is shown in fig. 6. There are already substantial changes in the spectrum at 1 L exposure; the 3 eV peak moves to lower energy and steadily decreases in intensity, the surface plasmon at 8 eV declines rapidly, and the shift of the bulk plasmon evolves steadily; at 100 L the trivalent sesquioxide Ce_2O_3 is dominant, at which stage La, Gd (Netzer et al. 1985a) and Er (Bertel et al. 1981) behave similarly. However, if Ce undergoes large exposure and is maintained in an O_2 partial pressure of 10^{-8} Torr the 4.5 eV loss characteristic of CeO_2 appears. This feature is believed to be due to excitonic transitions from the valence band to a localised 4f state. There is agreement that the 4f electrons in CeO_2 hybridise with O 2p both in the ground state and excited states, although the precise mechanism continues to be controversial (Wuilloud et al. 1984,

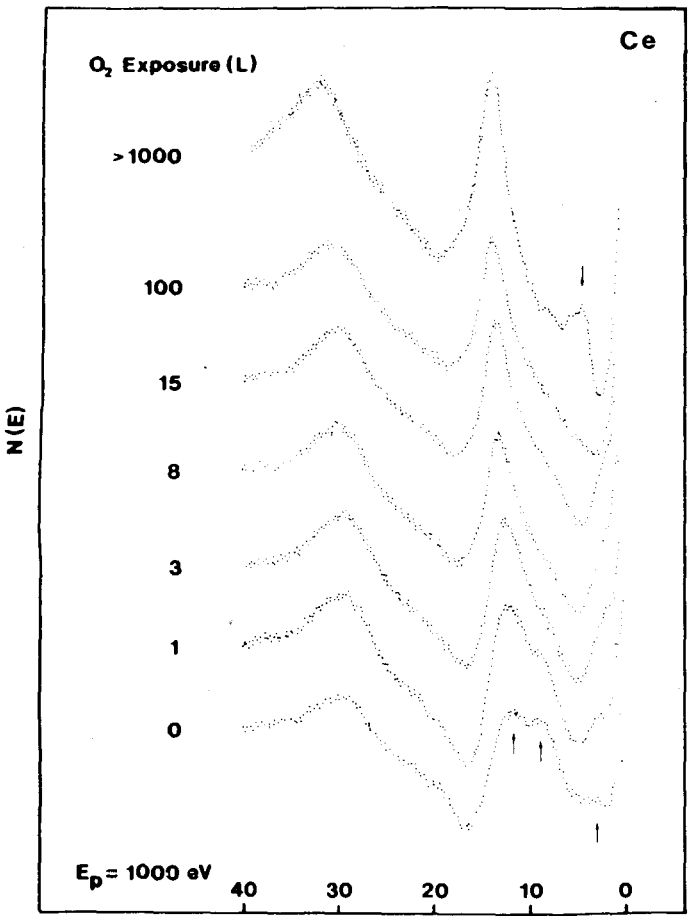

Fig. 6. Electron energy loss spectra of polycrystalline Ce film surfaces exposed to various amounts of oxygen for $E_p = 1000\,eV$ (Strasser et al. 1985b).

Fujimori 1984), but transitions to a localised higher state of partial 4f character may have reasonable oscillator strength.

In Yb (Bertel et al. 1982a) the divalent metal plasmon ($\Delta E \sim 9\,eV$) and the trivalent oxide plasmon ($\Delta E \sim 15\,eV$) are well separated, and it is possible to observe coexistence of the two for exposures of 2–10 L O_2. This suggests island oxide growth in accord with XPS evidence (Padalia et al. 1977). There is conflict between the work function data of Strasser et al. (1983a) and Takakuwa et al. (1984), but there was evidence of H precoverage in the latter study, so that the differences are likely to be due to hydroxylation accompanying oxidation (Netzer and Bertel 1982).

Interaction of clean metal surfaces with water vapour leads to molecular dissociation followed by hydroxylation as well as oxidation. Valence EELS spectra of Strasser et al. (1985b) on Ce and La reveal a characteristic OH excitation at 11 eV, accompanying trivalent oxide losses; the absence of the CeO_2 4.5 eV fingerprint after

gross exposure to water vapour is in accord with results of core spectroscopies (Strasser and Netzer 1984).

4.3. *Hydrides and interaction with hydrogen*

The loss experiments of Colliex et al. (1976b) showed that the main bulk plasmon of the higher rare earth dihydrides occurs at energies greater than for the corresponding clean metal, but due to limited energy resolution it was not possible to say anything about the interesting optical loss region ($0 < \Delta E < 4\,\text{eV}$). The bulk optical data of Weaver et al. (1979) reveal a sharp plasmon at 1.5–1.8 eV accompanied by a broader feature in $\text{Im}(-1/\varepsilon)$ of mixed interband/plasmon character in trivalent dihydrides RH_x ($0 < x \lesssim 2$, R = Sc, Y, Lu). In these compounds hydrogen atoms occupy interstitial tetrahedral sites in the fcc metal lattice, and the 'extra' plasmon occurs near an absorption edge associated with the onset of transitions to anti-bonding H states. When $x \gtrsim 2$ octahedral site occupation is involved, interband absorption sets in at lower energy, and the dihydride-like plasmon weakens.

Considering the technological potential of hydrogen–rare earth systems remarkably little work has been carried out on the reaction of hydrogen with clean well-characterised metal surfaces. Early EELS experiments by Bertel et al. (1981) on H reacting with polycrystalline Er showed that large exposures were required to build up hydride bulk losses at $\Delta E \sim 15\,\text{eV}$ in the immediate surface region, but it was not clear whether H was rapidly diffusing into the bulk, thereby evading the surface probe. Recently a more detailed EELS and UPS study of the interaction of H_2 with single crystal Ce(001) has been carried out by Rosina et al. (1986) using a high energy resolution ($\sim 0.3\,\text{eV}$) and angular resolution ($\theta_0 \sim 1°$) VG ADES 400 spectrometer set at specular geometry (fig. 7). At $E_p = 103\,\text{eV}$ the clean Ce losses are dominated by the surface plasmon ($\Delta E \simeq 8\,\text{eV}$) with additional contributions from the bulk plasmon ($\Delta E \simeq 12.5\,\text{eV}$) and the widely observed one-electron loss feature around 4 eV. At an exposure of 600 L H_2 (note the relatively large dose) the dihydride-like loss fingerprint (1.6 eV and 3.4 eV) is well-established, and at $E_p = 1000\,\text{eV}$ is even more prominent than at $E_p = 103\,\text{eV}$. At the higher primary energy two important changes occur: (a) the sampling depth increases from two layers to more than 1 nm, (b) finite aperture sampling of the loss profile would lead to a decrease in intensity of the low-energy hydride losses relative to the higher-energy losses *if* the hydride distribution were homogeneous.

The relative increase in intensity of the 1.6 eV peak at higher E_p is therefore evidence of a hydride phase increasing in H concentration with depth. The system is disordered, consistent with random occupation of tetrahedral sites, and a CeH_x ($x < 2$) stoichiometry. Heating to 550°C leads to partial H desorption, but at lower temperatures a different hydride phase may become established with possible octahedral sites occupation near the surface.

Recently Bevolo (1985b) has exploited the high spatial resolution inherent in electron beam excitation to create electron energy loss images in reflection geometry of hydrogenated scandium and gadolinium surfaces. The characteristic plasmon

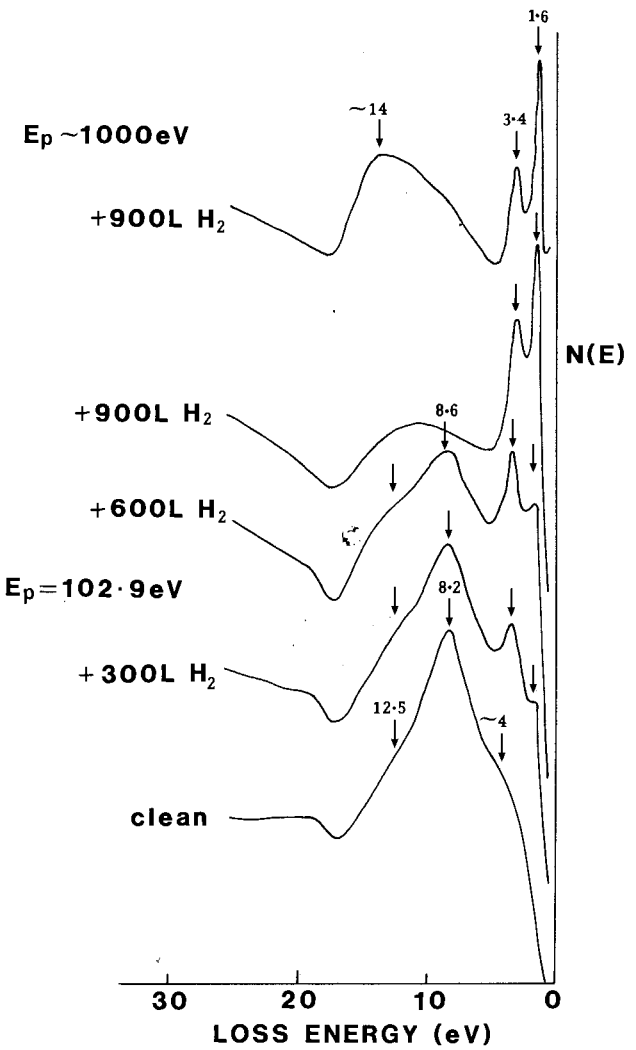

Fig. 7. Electron energy loss spectra of single-crystal Ce(001) exposed to varying H_2 exposures. In the main sequence $E_p \simeq 100\,eV$, but for large exposures $E_p \simeq 1\,keV$ is shown for comparison. Note the enhancement of the 1.6 eV hydride plasmon loss at high primary energy (Rosina et al. 1986).

losses of a rare earth metal with traces of H and of a nearly stoichometric hydride are clearly distinguishable (~3 eV shift); for the case of Gd (fig. 8c) differencing the spectometer signals at $E_1 = 1988\,eV$ and $E_2 = 1993\,eV$ gives brightness corresponding to the GdH_2 phase. It is then possible to correlate a conventional scanning electron microscope (SEM) image, which emphasises surface topography, with a scanning Auger microscope (SAM) image and the electron energy loss microscopy image. The loss technique gives contrast superior to SAM under these conditions; with spatial resolution of the order of 0.1 μm readily available loss imaging has considerable potential for understanding complex inhomogeneous surfaces of technological interest.

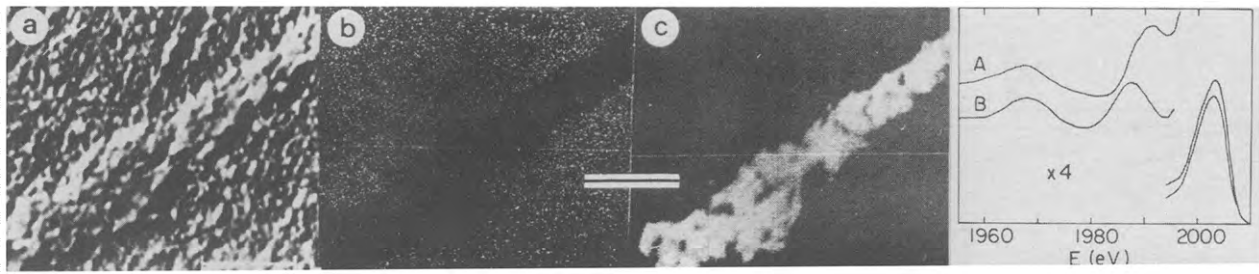

Fig. 8. Comparison of various images of a hydrogenated gadolinium surface: (a) SEM image; (b) SAM image of same area (GdH_2 dark); (c) Reflection electron energy loss microscopy (REELM) image of the same area (GdH_2 bright) based on the adjacent electron energy loss spectra of (A) Gd(H) and (B) GdH_2. The difference of the electron loss signals at $E_1 = 1988$ eV and $E_2 = 1993$ eV defines the brightness of the image. The bar is 10 μm.

4.4. *Yb/Al* (110)

It is possible to use valence losses not only to study the reaction of gases with rare earth metals, but also to examine metal–metal interactions. Onsgaard et al. (1984) have recently studied the growth of Yb on Al (110). Figure 9a shows the evolution of the EELS spectrum as a function of Yb coverage for $E_p = 126\,eV$. Initially the surface is characterised by bulk and surface Al plasmons (15.1 eV and 10.6 eV, respectively) accompanied by a weak interband transition, but losses corresponding to the bulk plasmon of divalent Yb metal ($\Delta E = 8.6\,eV$) and the one-electron transition ($\Delta E = 4.2\,eV$) grow steadily with coverage. Figure 9b gives the loss energy as a function of primary energy at fixed Yb coverage (3.5 monolayers). At high primary energy $E_p = 1200\,eV$ (probing more deeply) bulk Al losses tend to be dominant, while at low incident energy ($E_p \sim 90\,eV$) the one electron Yb excitation at 4.2 eV is accompanied by a plasmon loss intermediate in energy between those of bulk Al and bulk Yb. Raising the temperature to 45°C (or 70°C) promotes interdiffusion of Yb and Al resulting in a sharp reduction in the 4.2 eV loss and the emergence of a plasmon loss at an energy consistent with a valence of Yb intermediate between 2 and 3 in the resulting YbAl alloy.

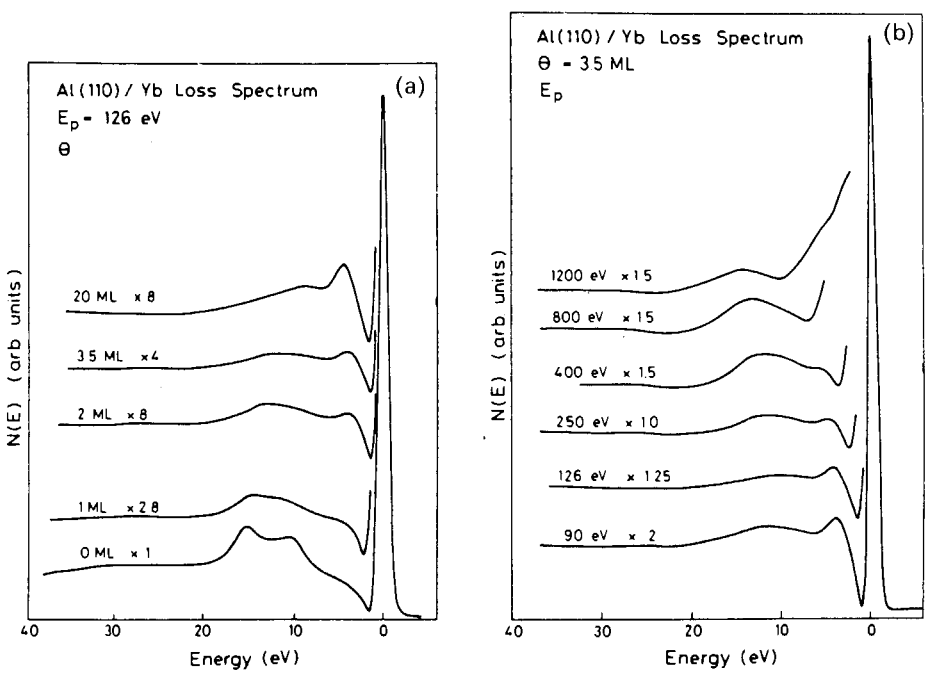

Fig. 9. Electron energy loss spectra of Yb/Al(110): (a) for various Yb thicknesses θ at fixed primary energy $E_p = 126\,eV$; (b) for fixed Yb thickness ($\theta \simeq 3.5$ monolayers) at various E_p. Work of Onsgaard et al. (1984).

4.5. *Other compounds*

In more complex solids such as rare earth vanadates (investigated in transmission by Tonomura et al. (1978)) or $LaCoO_3$ as examined in reflection loss by Richter et al. (1980), the plasmon energy is controlled by the electronic structure of the group accompanying the rare earth ion, but the 5p resonance loss of the rare earth ion continues to be prominent. In La_2S_2 and Sm_2S_3 (Balabanova et al. 1983) the bulk plasmon positions as observed in transmission loss are consistent with values inferred from UV reflectance data (Zhuze et al. 1980), but the energy values (15.9 eV and 17.3 eV respectively) are well above what is expected from a free electron plasmon model.

4.6. *Spin polarised inelastic scattering*

Weller and Alvarado (1985) carried out the first spin polarised electron energy loss experiment on the rare earths with a view to isolating spin dependent 5d → 4f transitions in clean ferromagnetic Gd metal. Electrons incident with polarisation P_0 ($25.5 < E_p < 63.5$ eV) show different scattering intensities for spin orientation parallel ($I_{\uparrow\uparrow}$) and anti-parallel ($I_{\uparrow\downarrow}$) to the magnetisation direction. The spin asymmetry

$$A = \frac{1}{P_0} \frac{I_{\uparrow\uparrow} - I_{\uparrow\downarrow}}{I_{\uparrow\uparrow} + I_{\uparrow\downarrow}}$$

may contain spin-sensitive information about both elastic and inelastic scattering. It might be expected that such experiments would emphasise inelastic exchange scattering from the 5d electrons with net moment in the direction of magnetisation to empty 4f states with spin exclusively opposite to the magnetisation direction; this would lead to preferential inelastic scattering of electrons in the minority spin direction (negative A). In practice a sharp positive asymmetry anomaly is observed at the expected energy $\Delta E = 4.5$ eV (fig. 10). This is interpreted as evidence of the dominance of a direct dipole allowed loss in which minority carriers near E_F are excited into empty 4f states of the same spin; this process occurs preferentially when the spin of the incident direction is parallel to the magnetisation direction (singlet scattering). The observed 5d → 4f polarisation is superimposed on a broad inelastic background with the spin asymmetry tending to correlate with the spin dependence of elastically scattered electrons at an energy equal to the energy of the incident energy, less than the loss energy (loss-diffraction dominant). This is in contrast to the case of Stoner excitations in transition metals and amorphous alloys (Kirschner et al. 1984, Hopster et al. 1984), where spin dependence in inelastic exchange processes involving spin flip controls the observed asymmetry or polarisation. However, these pioneering experiments by Weller and Alvarado point the way to a fuller understanding of surface magnetic excitations in rare earths and their compounds. Experiments incorporating both polarised electron sources and polarisation detection (Kirschner 1985a) will give further insight, while studies on amorphous alloys containing rare earths will eliminate complications due to diffraction.

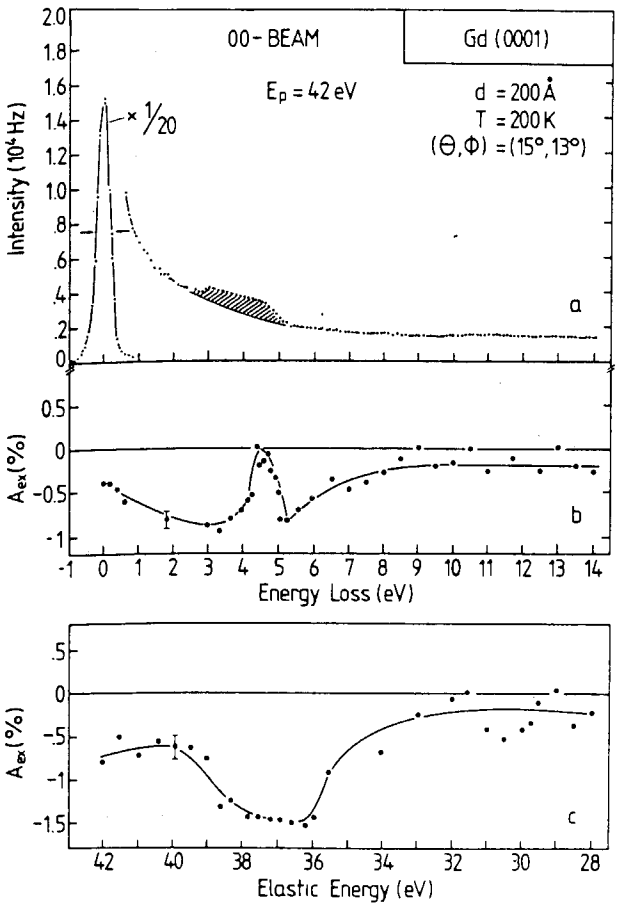

Fig. 10. Spin polarised electron energy loss of (00) beam of Gd(0001); primary energy $E_p = 42$ eV, angle of incidence of electron beam $\theta = 15°$, azimuthal angle $\phi = 13°$ (Weller and Alvarado 1985): (a) the spin-averaged loss intensity versus loss energy, (b) the exchange asymmetry A_{ex} versus loss energy, (c) the scattering asymetry of elastically diffracted electrons (SPLEED) of primary energy $E_p - \Delta E$. The peak at $\Delta E = 4.5$ eV is associated with 5d–4f transitions.

5. Core level excitations

Core level excitations in the rare earths are distinguished by strongly localised phenomena. This was manifested first by the existence of so-called 'white lines' in early X-ray absorption spectra (XAS), which occurred at the edges of 2p, 3d or 4d ionisation of the lanthanides. The term 'white line' comes from the days when photographic plates were used to record photoabsorption in transmission. When absorption in the sample was very strong and no radiation was transmitted through the sample a white line was observed on the film. 'White lines' became therefore a synonym for very strong absorption. Strong absorption near an ionisation edge is normally an indication of excitation of a core electron into localised final states. Particularly strong absorption was observed at the 4d edges of the rare earths (Zimkina et al. 1967, Fomichev et al. 1967), and the corresponding spectral features were honoured by the name 'giant resonances'. Optical excitation of d core electrons reaches final states of predominantly f character, as the matrix elements of $d \rightarrow f$

transitions exceed by far those of $d \rightarrow p$ transitions (Fano and Cooper 1968). The localised, empty 4f states of the lanthanides provide particularly good candidates for final states of d core excitations: as evident from table 2 the spatial extent of the 4f states is similar to that of 4d core states. The overlap of initial-state and final-state wave functions is therefore large, and the resulting high oscillator strength warrants high spectral intensity in the experiments. However, not only 4f final states are characterised by localised excitations of high oscillator strength; 5d final states may also become localised in the presence of p core holes. This is evidenced by the strong absorption edges in $L_{2,3}$ X-ray absorption spectra (see e.g. Röhler 1987) and by the 5p and 4p resonance phenomena discussed in the present article (sections 4.1 and 5.3).

The localised character of these core excitations suggests that theoretical description in terms of atomic-like ideas may be appropriate even in the solid state. This was proposed originally by Zimkina et al. (1967) for the 4d excitations, and then supported by the calculations of Dehmer et al. (1971). An experimental proof was obtained by comparing XAS of atoms and solids. Wolff et al. (1976) recorded 4d XAS for gaseous and solid Ce and observed identical spectra, and Radtke (1979, 1980) extended this comparison to several other lanthanide elements. In all cases the spectra corresponding to the same 4f occupation showed identical structures in the gas phase and in the solid. The 3d excitation structures have also been treated successfully within the framework of an atomistic multiplet picture (Sugar 1972b, Thole et al. 1985), and we have argued recently that the same may be true for p core excitations (Netzer et al. 1985b).

Due to the availability of synchrotron radiation as a tunable X-ray source the study of inner-shell excitations by photons has become very popular in recent times. However, excitation by electron beams also has particular advantages to offer. It is worthwhile at this point to discuss briefly various aspects of inner-shell excitations by photon and electron beams. Such a comparison has been made by Utlaut (1981), and we summarise here the important implications. The following points for comparison will be of interest here:

(1) photoabsorption cross sections versus differential electron energy loss cross sections;
(2) specific brightness of the sources;
(3) size of the beams;
(4) beam induced damage.

Photoabsorption cross sections of inner-shell excitations are several orders of magnitude greater than electron energy loss cross sections in the zero-momentum transfer limit. Therefore, to be competitive with photoabsorption spectroscopy electron beam spectroscopy needs more incident electrons to record a spectrum with given signal to noise ratio. On the other hand, the brightness of storage ring sources is several orders of magnitude lower than the brightness that can be achieved with electron sources. Furthermore, monochromatisation of the primary photon beam leads to additional brightness reduction, whereas electron sources are sufficiently monochromatic (for the purpose of inner-shell excitation studies). With electron

beams spatial resolution of <10 nm is easily achievable, but focussing photon beams to <1000 nm is a difficult task. If spatial resolution is required, electron beam excitation is therefore to be preferred, but for obtaining spatially averaged information photon beams may be better. An important difference between photon and electron excitation is, of course, the possibility of finite momentum transfer in the latter process. In addition, if the electron loss experiment is performed in reflection geometry, the exciting electron beam energy can be varied over a wide energy range, and excitations involving exchange processes may be possible at lower incident energies. This has been mentioned in section 2, and will be further emphasised in the following subsections. In general, photon beams should produce less damage per inner-shell excitation than electrons, because other excitations besides the one of interest can occur in electron loss. However, this depends on the exact mechanism of damage, and in some cases the damage may be equal for the two excitation modes. In any case, radiation damage should not pose serious problems in the system of interest here.

In the following subsections electron excitation from inner-shell states will be considered in some detail: we present first the basic principles of excitations from inner d, p and s shells by inelastic electron scattering (sections 5.1–5.3), and discuss then possibilities of the EELS technique to determine the valence in rare earth systems by core level excitation (section 5.4). Frequently, comparison between electron impact and photon excitation will be made, and similarities and differences of the two excitation modes will be emphasised.

5.1. *The 4d excitations*

The pioneering XAS experiments of Zimkina et al. (1967), Fomichev et al. (1967) and Haensel et al. (1970) revealed a series of complicated peaks near the 4d ionisation threshold of the lanthanides and intense resonances, which extend up to 5–20 eV into the continuum. These excitations were ascribed to atomic-like $4d^{10}4f^n \rightarrow 4d^9 4f^{n+1}$ transitions, and the first theoretical description was provided by Dehmer et al. (1971), Sugar (1972a) and Dehmer and Starace (1972) within the framework of conventional atomic theory. The lanthanides show this complicated structure because the unfilled 4f shell is collapsed, and therefore not subject to large interaction with the environment, and because of the large electrostatic interaction between the 4f and the 4d shell. The resulting large exchange interaction splits the $4d^9 4f^{n+1}$ final-state configuration and raises some multiplets up to 20 eV above the configuration average, thus driving them far into the continuum; autoionisation to $4d^9 4f^n \varepsilon f$ configurations then broadens the high-energy levels.

The parameterised calculations of the $4d^9 4f^{n+1}$ energy levels of Sugar (1972a) were able to describe the experimental spectra and their fine structure in a satisfying way, but the theoretical classification of the giant resonance at the beginning of the rare earth series (e.g. the ^1P channel in La) later stimulated controversy. At the beginning of the lanthanide series the 4f wave function is not yet fully collapsed, and term-dependent 4f wave-function contraction in excited configurations may be effective, to use the terminology of Lucatorto et al. (1982). Dehmer and Starace (1972)

predicted the energy and shape of the ^1P resonance in atomic La by combining spectroscopic theory with the theory of multilevel multichannel ionisation (Fano 1961). Accordingly, the giant resonance in La should be due to the $4d^94f^1\ ^1P$ state, which is shifted to above the $4d^9$ threshold by the strong exchange interaction. However, subsequent Hartree–Fock calculations by Hansen et al. (1975) placed the $4d^94f^1\ ^1P$ term below the ionisation limit. Wendin (1976), therefore, preferred a many-body description in terms of a 4f-like collective continuum resonance: continuum wave functions become resonantly localised with large amplitude in the inner well of the effective 4f potential, thus taking over most of the transition strength. This picture is essentially equivalent to a single-channel 'shape resonance' as discussed by Connerade (1983). Zangwill and Soven (1980) presented a calculation of the giant resonance in Ce in a time-dependent local density approximation: in this model the 4d shell is polarised, setting up a damped dipole oscillation. At resonance the induced inner field is at maximum, and the response of the outer shells is also driven to a maximum. Thus, the total ionisation cross section and partial ionisation cross sections (Gerken et al. 1982b) could be explained in a natural way, and the connection with Fano's theory of autoionisation (Fano 1961) of the $4d^94f^{n+1}$ state into different decay channels is also readily made. This approach emphasises the multichannel character of the resonances.

At the end of the rare earth series the attractive Coulomb potential of the 4d hole is strong enough to pull all the excited states of the $4d^94f^{n+1}$ configuration below the ionisation limit, and all the excitations may be classified as transitions to discrete $4d^94f^{n+1}$ states. The spectral profiles are well described by Beutler–Fano profiles resulting from the interference between the discrete transition $4d^{10}4f^n \rightarrow 4d^94f^{n+1}$ and various direct recombination channels (Radtke 1979, Johansson et al. 1980, Gerken et al. 1982b, Schmidt-May et al. 1984). On the other hand, Connerade and Pantelouris (1984) were able to fit the experimental data of the giant $4d \rightarrow f$ resonance in Gd and GdF_3 vapour using a simple single-channel description of the main shape resonance (Connerade 1984), thereby neglecting interchannel coupling. It appears that further theoretical work is still needed to clarify whether single-channel theories or autoionisation involving interchannel coupling gives a better description of the 4d spectra of the rare earths.

After this brief introduction into the nature of optical 4d excitations let us proceed by considering electron-excited processes. 4d excitations of rare earths in electron loss have been recorded first by Trebbia and Colliex (1973) in transmission of 75 keV electrons. The specimens were thin metal foils prepared by evaporation in a different preparation chamber. As vacuum conditions in both preparation and spectrometer chambers were not better than 10^{-6} Torr the samples were most likely in various forms of oxidised metals. Because of the atomic-like nature of the 4d excitations and their consequent insensitivity to the chemical environment, these experimental shortcomings should not seriously affect the major spectral features*,

*Note that this is true only in cases where no valence change takes place upon oxidation. In Eu, for example, the data of Trebbia and Colliex (1973) are more characteristic of the trivalent oxide ($4f^6$ initial state) than of the divalent metal ($4f^7$) (Netzer et al. 1984).

and reasonable agreement with XAS has been obtained. Borovskii and Komarov (1976) were first to investigate the influence of the electron primary energy E_p on the characteristic loss spectra of reflected electrons on several rare earth metals (Gd, Tb, Dy, Ho); additional spectral structures were observed near the 4d ionisation thresholds at low incident energy. These authors suggested changes in selection rules and dependence of transition probabilities upon energy as possible causes for these effects, but the rather poor quality of the experimental data precluded more detailed analysis.

A comprehensive investigation of core excitations in electron loss of all stable rare earth metals has been performed over the last five years in our laboratory (see Netzer (1985) for a bibliography), and 4d spectra for 14 clean lanthanide elements from La to Lu, with Yb_2O_3 included along with the clean metal are presented in fig. 11. Two sets of experimental data are included, one at medium-high $E_p(\gtrsim 1.5\,\text{keV})$, the other at an energy close to threshold (generally about 300 eV) such that the resulting losses avoid Auger emission and intense non-linear secondary backgrounds. The spectra were taken at an overall resolution of 0.5–0.7 eV over the whole range of primary energies; sample surfaces were prepared under stringent UHV conditions, while surface cleanliness was monitored and checked by Auger spectroscopy (Riviere et al. 1985). At the higher incident energies the overall shape of the loss profiles in fig. 11 agree well with modern XAS data (e.g. Olson and Lynch 1982), but some differences are noticed in the finer details. At low E_p's new structures appear and pronounced changes in relative intensities are observed.

It is useful to begin the discussion with Lu and Yb (fig. 11 (m) and (n)) where only weak $4d_{5/2}$ and $4d_{3/2}$ ionisation edges are found. There the 4f shell is filled and no 4d → 4f resonance is possible. Yb_2O_3, however, has a $4d^{10}4f^{13}$ ground state and can support transitions of the type $4d^{10}4f^{13} \rightarrow 4d^{9}4f^{14}$ (fig. 11 (m)). At medium-high energy only $^2F_{7/2} \rightarrow {}^2D_{5/2}$ transitions at 181 eV are dipole-allowed, and the sharp resonance agrees well with the Fano profile found by Johansson et al. (1980) and Schmidt-May et al. (1984) in measuring the total yield and the resonant enhancement in 4f yield as a function of photon energy. At lower primary energy ($E_p = 405\,\text{eV}$) the dipole-forbidden transition $^2F_{7/2} \rightarrow {}^2D_{3/2}$ ($\Delta J = 2$) gains significant intensity. The spectral profile of this system is particularly simple because the 4f shell is filled in the final state and multiplet splitting does not occur. The optically forbidden $^2D_{3/2}$ state is therefore unambiguously identified.

Next we investigate the $4d^{10}4f^{0}$ ($^1S_0$) → $4d^{9}4f^{1}$ transitions in La. Figure 12 gives a more detailed account of the 4d core EELS of La for a range of incident energies, and compares the loss spectra with XAS. In the inset the ratios of the heights of various sharp peaks to the height of the main resonance are plotted against E_p. The electron loss spectrum at the highest primary energy is markedly different from the photon absorption spectrum in the region of the sharp peaks, but agrees well in the broad resonance: the peak at 105.3 eV has no correspondence in the optical spectrum and the peak at 101.7 eV shows enhanced intensity in electron energy loss. If E_p is lowered, new structures appear and increase in intensity.

Dipole selection rules confine optical excitation to the $^1P_1$ channel (the main resonance) with the $^3D_1$ at 101.7 eV and the $^3P_1$ at 97.2 eV weakly allowed. The

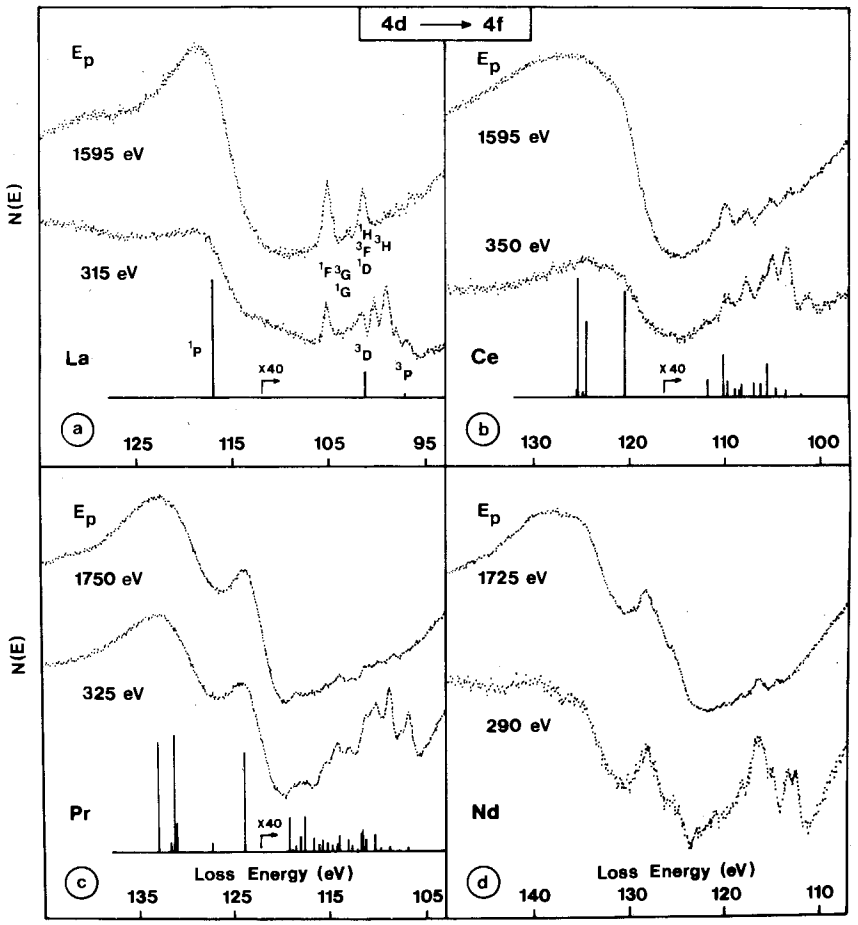

Fig. 11. The 4d → 4f core electron energy loss spectra of the lanthanides. Spectra are shown for two primary energies E_p. The theoretical relative intensities of electric dipole transitions of Sugar (1972a) are shown where available (Strasser et al. 1985a).

systematic deviations between EELS and XAS may be explained by breakdown of dipole selection rules in two stages:

(1) At intermediate energies ($E_p \gtrsim 1$ keV) a restricted set of additional singlet excitations is weakly allowed according to selection rules previously suggested by Goddard et al. (1971).

(2) At low energies ($E_p \lesssim 500$ eV) triplet excitations give rise to many new components in the spectrum. Multiplet analysis by Netzer et al. (1983a) confirmed that the peak at ~102 eV is ^{1}H, approximately degenerate with ^{3}D, and the feature at ~105 eV a ^{1}F multiplet. The selective deviation from strict dipole rules at intermediate primary energies has been interpreted in terms of the symmetry rules of Goddard et al. (1971), which predict that in dominantly forward scattering ΔL can be 1, 3 or 5. Thus ^{1}H and ^{1}F transitions have intensities rather greater than $^3P_1$ and

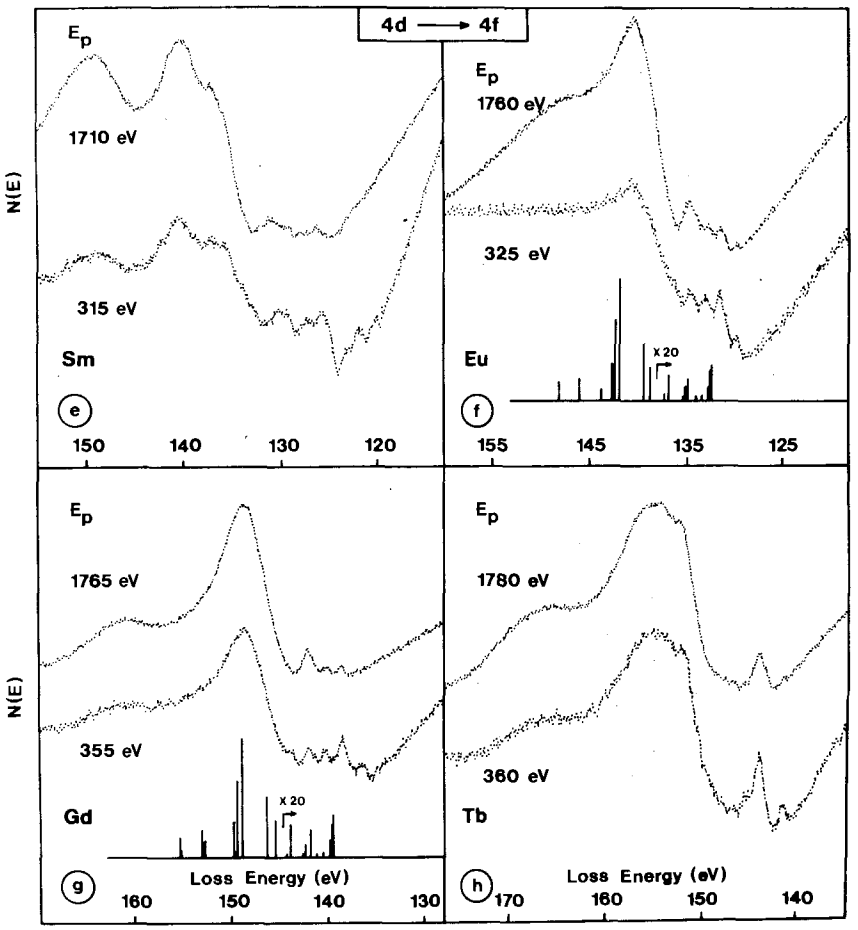

Fig. 11. (cont.)

$^3D_1$, which depend on weak spin–orbit effects for their intensity. As the primary energy is lowered the cross sections for exchange scattering become appreciable, and all triplet final states ^3F, ^3G and ^3H in addition to the optical ^3P and ^3D are allowed. Furthermore, the symmetry-forbidden singlet states ^1D and ^1G which may also be observed as forward scattering becomes less dominant. Note that the greatest intensity gain at low E_p is seen for the peak at 99 eV, which is associated with the ^3H state; this is the state with the highest J multiplicity, and we will come back to this point in the next paragraph. The term-dependent Hartree–Fock calculations of the $4d^9 4f^1$ multiplets of La by Clark and Lucatorto (1983) confirmed this interpretation, and very good agreement between experimental peak positions and multiplet calculations was obtained (Netzer et al. 1983a). It should be mentioned here that the data in fig. 12, the EELS spectra of La and their E_p dependence, have been reproduced exactly in a different laboratory by Moser et al. (1984), and the experimental facts are therefore very well established.

Although the final-state multiplets for $4d^{10}4f^{12}$ $(^3H_6) \rightarrow 4d^9 4f^{13}$ transitions in

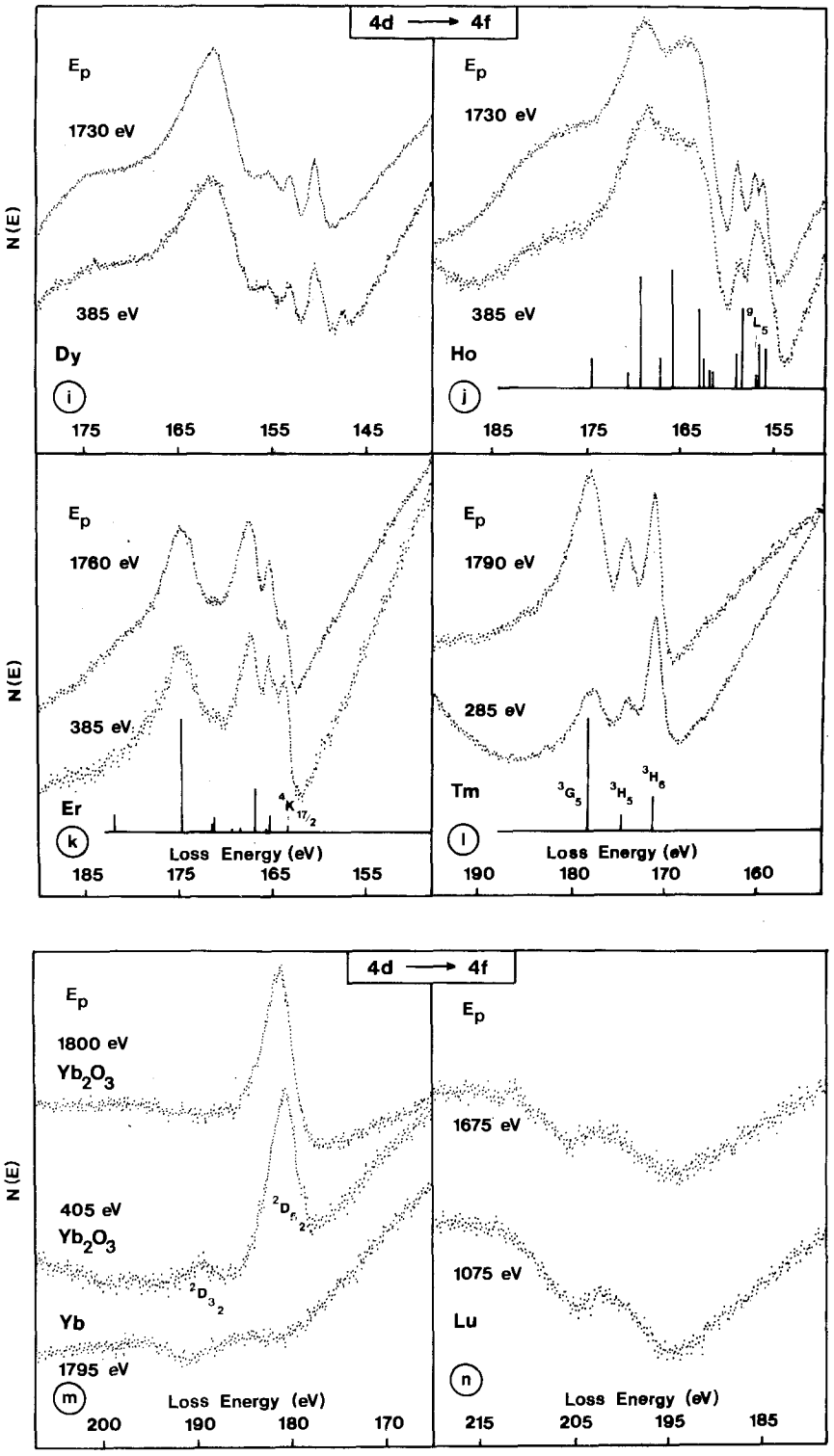
4d → 4f
E_p
1730 eV
385 eV
Dy
(i)
175 165 155 145
E_p
1730 eV
385 eV
Ho
(j)
185 175 165 155
9L5
N(E)
E_p
1760 eV
385 eV
Er
(k)
4K17/2
Loss Energy (eV)
185 175 165 155
E_p
1790 eV
285 eV
Tm
(l)
3G5
3H5
3H6
Loss Energy (eV)
190 180 170 160
4d → 4f
E_p
1800 eV
Yb2O3
405 eV
Yb2O3
Yb
1795 eV
(m)
2D5/2
2D3/2
Loss Energy (eV)
200 190 180 170
E_p
1675 eV
1075 eV
Lu
(n)
Loss Energy (eV)
215 205 195 185

Fig. 11. (cont.)

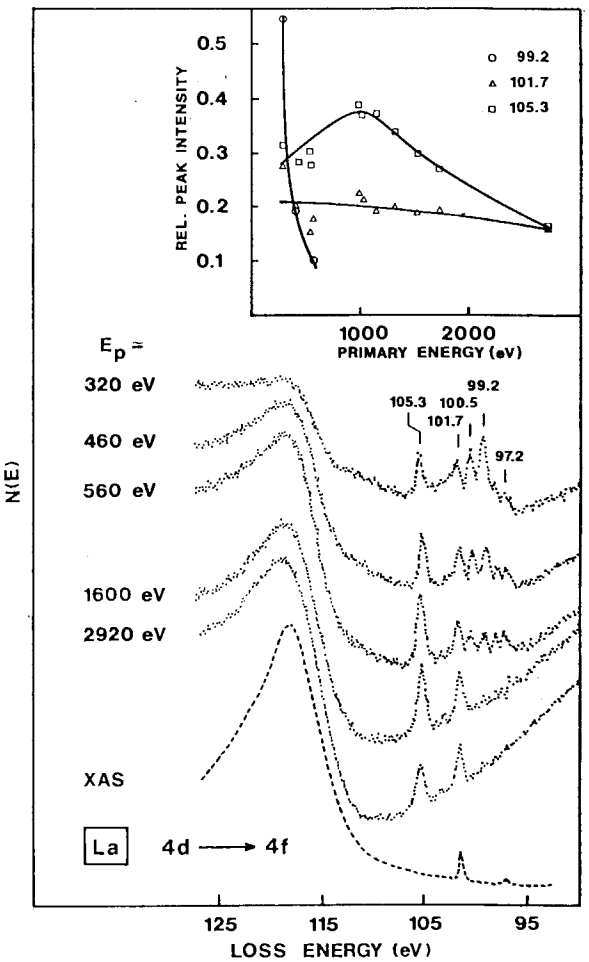

Fig. 12. The 4d → 4f excitations of La in EELS for various E_p. An XAS spectrum is shown for comparison (Rabe 1974) (Netzer et al. 1983a).

Tm (fig. 11 (l)) are identical with those of La the 4d excitation spectrum is now very different. Firstly spin–orbit interaction is now much stronger than in La, and, in addition, the initial state is now of high total angular momentum ($^3H_6$), so that the dipole-allowed transitions are low in relative energy rather than high as in La. Scaling the multiplet analysis of Larkins (1977) for the $4d^9 4f^{13}$ configuration of Yb, so that the $^3G_5$–$^3H_6$ splitting of Tm is reproduced, gives a complicated multiplet structure (Netzer et al. 1984), but only $^3G_5$, $^3H_5$ and $^3H_6$ are dipole active. At $E_p = 1.79$ keV the electron loss spectrum of Tm metal (fig. 11(l)) agrees well with the XAS spectrum of TmF_3 as recorded by Olson and Lynch (1982). When E_p is lowered to 285 eV no new spectral features appear, in sharp contrast to the case of La, but there is a marked increase of the $^3H_6 \rightarrow {}^3H_6$ intensity relative to the other transitions. Optically forbidden multiplet states are expected to occur close in energy to the strong dipole transitions and in the high-energy loss region (Larkins 1977), where they are in competition with the inelastic tails on the main losses and a

complicated background; therefore they may be difficult to detect. As in La the biggest gain in intensity is observed for the highest J final state, i.e. the state with the highest multiplicity, but here the transition is already dipole-allowed. This trend may be condensed into a so-called 'highest J rule': for slow electron impact all excitation restrictions into final states break down, and the multiplet state with the highest degeneracy $2J + 1$ may win the competition for the greatest intensity. Although without firm theoretical foundation this tentative 'highest J rule' seems to be fulfilled for the whole rare earth series.

We have so far discussed only the simplest 4d excitation systems, but the trend through the rare earth series may be assessed following the simple parentage ideas of Sugar (1972a). Because the 4d–4f interaction is strong relative to the 4f–4f interaction, going from La ($4d^9 4f^1$) to Ce ($4d^9 4f^2$), Pr ($4d^9 4f^3$) etc. by successively adding 4f electrons leads to multiplets having well-defined $4d^9 4f^1$ ^1P parentage. For example, in Pr at 1.75 keV (fig. 11 (c)) the main resonance is split into a number of multiplet components of ^1P parentage, and the loss spectrum generally agrees well with the XAS spectrum of Pr (Hagemann et al. 1976) with the exception of some differences in relative intensities below 120 eV as expected from experience in La. When E_p is lowered to 325 eV it is the low-energy multiplets, which have stronger ^3H parentage, that gain most in intensity.

At the other end of the lanthanide series it is possible to use the Tm $4d^9 4f^{13}$ multiplets as the parent structure, and then successively add 4f holes. The Er $4d^{10}4f^{11} \rightarrow 4d^9 4f^{12}$ transitions resemble the Tm spectrum with weak additional splittings well resolved in the lower part of the spectrum (fig. 11 (k)). At lower E_p the highly degenerate $^4K_{17/2}$ multiplet at lowest energy gains appreciable intensity in relation to the higher energy states, in accord with the postulates of the 'highest J rule'.

In the middle of the rare earth series (Eu–Dy) d–f parentage ideas tend to break down, oscillator strengths are more widely spread and, although distinctive changes close to threshold occur, the effects are less spectacular.

We have seen that the 4d excitations of the lanthanides have well-defined multiplet structure, which is characteristic of the 4f population. 4d excitations therefore provide very characteristic fingerprints of the f count. This can be used to monitor the valence of rare earth atoms in compound systems, and valence changes during surface reactions have been followed by reflection EELS, taking advantage of the inherent surface sensitivity of the method. In section 5.4 some illustrative examples of valence monitoring by EELS will be discussed.

5.2. *The 3d excitations*

As for 4d excitations, 3d excitations may also be described as atomic-like transitions of the type $3d^{10}4f^n \rightarrow 3d^9 4f^{n+1}$ (Sugar 1972b). There are, however, important differences between 4d and 3d: the spin–orbit interaction is dominant in 3d excitations and the exchange interaction is reduced. As a result the $3d^9 4f^{n+1}$ multiplets are separated into two groups of structures, which may be loosely associated with $3d_{5/2}$ and $3d_{3/2}$ hole states; the multiplet splitting within each group

of states is much smaller than in the 4d case. Nevertheless some ideas of 4d will survive as we shall see below.

Early XAS results at the 3d edges include those of Fischer and Baun (1967), Sugar (1972b) and Bonnelle et al. (1974). In the work of Sugar (1972b) an atomistic interpretation of the spectra of La, Er and Tm in terms of $3d^9 4f^{n+1}$ final states has been proposed. High-quality 3d XAS data for all the rare earth metals together with a full $3d^9 4f^{n+1}$ multiplet calculation in intermediate coupling has been reported recently by Thole et al. (1985). The use of 3d XAS in valence monitoring of complex rare earth systems has been discussed by Fuggle et al. (1983) and Kaindl et al. (1984), and some mention of this will be made later in this section.

The profiles and line widths of $3d \rightarrow 4f$ transitions in XAS have been investigated by Connerade and Karnatak (1981) and Karnatak et al. (1981). The $3d^9 4f^1\ {}^1P_1$ line of La and the $3d_{5/2}$ line in oxidised Yb^{3+} was found to be well represented by Beutler–Fano profiles, indicative of autoionisation involving direct recombination processes. The resonant enhancement of rare earth 4f photoionisation for photon energies at the rare earth 3d absorption edge was then observed accordingly by Allen et al. (1984), and the first observation of 3d direct recombination electron emission in Ce, due to the decay $3d^9 4f^2 \rightarrow 3d^{10} 4f^0 + \varepsilon l$, has been reported by Matthew et al. (1984). The decay of the $3d^9 4f^1$ excited state of La has also been investigated in X-ray absorption and emission by Motais et al. (1984). The deviations from statistical weighting of the spin–orbit split 3d photoionisation cross sections of La have been attributed to the exchange coupling between the components of spin–orbit split subshells (Wendin 1984).

The 3d electron energy loss profiles at higher incident energies (fig. 13) show in general remarkable agreement with the XAS spectra of Thole et al. (1985), but some extra intensity is noted in EELS at the lower-energy side of the main peaks, particularly in the first members of the rare earth series. Reduction of the primary energies then yields intense satellites in that energy region.

Primary energy-dependent EELS satellites in 3d excitations spectra of La and Ce have been noted first by Kanski and Nilsson (1979) and Kanski and Wendin (1981), and were ascribed to dynamical screening effects of an intermediate $3d^9 4f^{n+2}$ state, in the manner of a post-collision interaction. The higher-resolution spectra of La and Ce recorded by Matthew et al. (1983) (see fig. 13(a) and (b)) and the comprehensive multiplet analysis of Esteva et al. (1983) for the $3d^9 4f^1$ states of La, however, suggested a different interpretation in terms of multiplet effects. The intermediate coupling calculations of Esteva et al. (1983) have shown that the main ${}^3D_1(3d_{5/2})$ and ${}^1P_1(3d_{3/2})$ dipole allowed multiplets occur at energies high relative to the configurational average, while high J states tend to have lower energies. In fact, the higher J components tend to cluster at the low-energy side of the optically allowed states, and this is exactly the region where energy-dependent features are observed in EELS. Matthew et al. (1983) have therefore associated the energy dependence in 3d EELS spectra to progressive breakdown of the optical selection rules with decreasing energy of the exciting beam. The extra breadth of the non-dipole features compared to the sharp optical peaks in La (fig. 13(a)) reflects the range of multiplets involved, as predicted by Esteva et al. (1983).

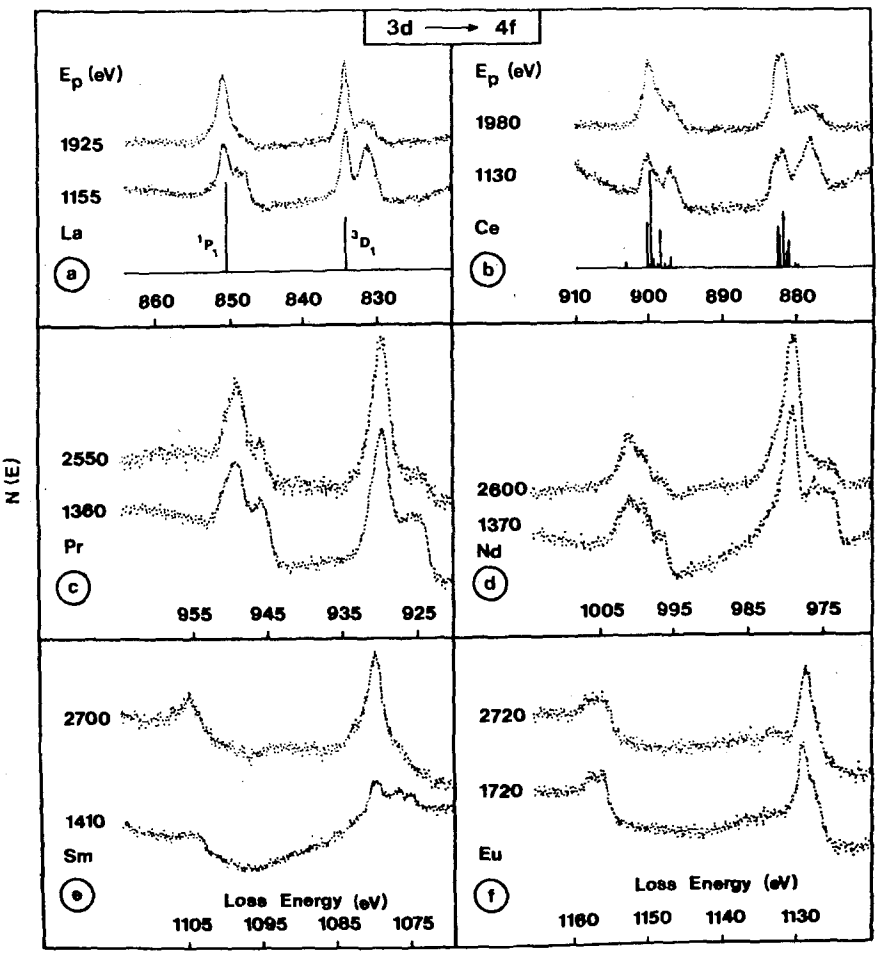

Fig. 13. The 3d → 4f electron energy loss spectra of elements La–Lu. Spectra are shown for E_p in excess of 2000 eV and for E_p close to threshold. The theoretical electric dipole intensities of Bonnelle et al. (1974) and Sugar (1972b) are shown where available (Strasser et al. 1985a).

Already in Ce (fig. 13(b)) there is large number of multiplets having $^1P_1$ and $^3D_1$ parentage and therefore significant dipole oscillator strength, but the same pattern as in La emerges with the enhancement of dipole forbidden excitations on the low-energy side of the dipole transitions as E_p is reduced. Through the first half of the rare earth series the main dipole contributions broaden as the dipole strength spreads in the same manner as in the 4d case, but low-energy transitions are still relatively enhanced as selection rules are relaxed.

As before, Lu (fig. 13(n)) and Yb metal show no resonance loss, while Yb_2O_3 (fig. 13(m)) has a sharp $3d_{5/2}(^2D_{5/2})$ loss at higher E_p with the $3d_{3/2}$ loss developing as E_p is lowered. Tm has three dipole-allowed $(3d_{5/2})^9 4f^{13}$ final states ($^1H_5$, $^3G_5$ and $^3H_6$) and one $(3d_{3/2})^9 4f^{13}$ state ($^3H_5$). Inspection of the $3d^9 4f^{13}$ multiplets of Yb as calculated by Larkins (1977) gives guidance on the relative positions of the dipole-

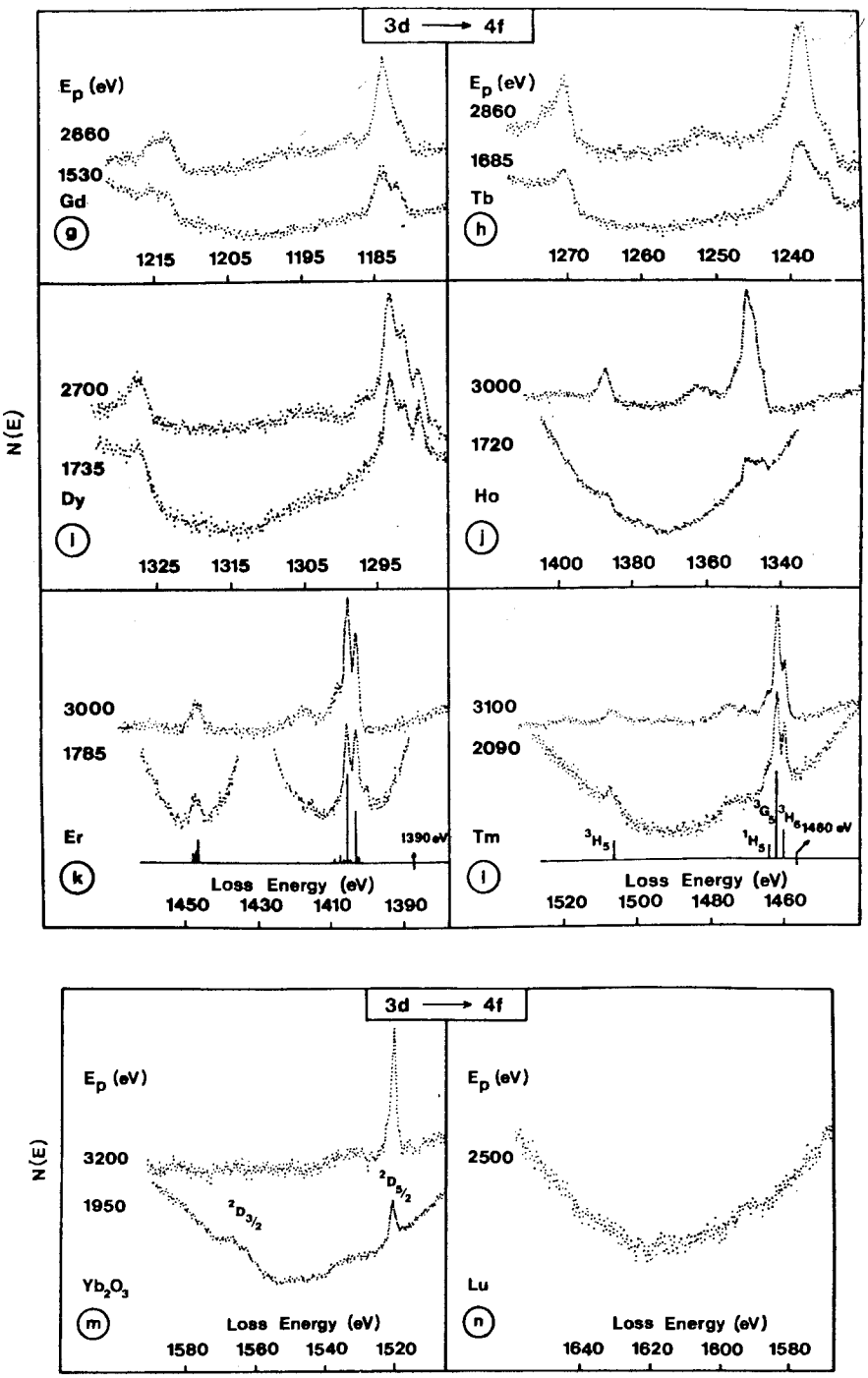
3d → 4f
N(E)
Ep (eV)
2860
1530
Gd
g
1215 1205 1195 1185
Ep (eV)
2860
1685
Tb
h
1270 1260 1250 1240
2700
1735
Dy
i
1325 1315 1305 1295
3000
1720
Ho
j
1400 1380 1360 1340
3000
1785
Er
1390 eV
k
Loss Energy (eV)
1450 1430 1410 1390
3100
2090
Tm
3H5
1G4 3H6 1460 eV
1H5
l
Loss Energy (eV)
1520 1500 1480 1460
3d → 4f
N(E)
Ep (eV)
3200
1950
2D5/2
2D3/2
Yb2O3
m
Loss Energy (eV)
1580 1560 1540 1520
Ep (eV)
2500
Lu
n
Loss Energy (eV)
1640 1620 1600 1580

Fig. 13. (cont.)

forbidden final states. As for 4d excitation $^3H_6$ lies low in energy, and gains relatively in intensity as E_p is reduced. In 3d excitation the tentative rule of high final J values being favored at low E_p therefore gains further support.

The final states reached in XAS or EELS excitations are identical to the f screened final state in XPS, e.g. $3d^94f^{n+1}$ (see Fuggle (1982) for a discussion of screening effects in XPS). As reported by Esteva et al. (1983) there is a difference in energy of the order of 2–3 eV between the f screened state in the XPS spectrum of La and the corresponding 3d XAS peak. The multiplet analysis of the $3d^94f^1$ final state revealed that the discrepancy may be understood by considering the different selection rules of the two processes. Whereas in XAS only transitions into dipole-allowed multiplet states are possible, all multiplet states may be populated in the screening process. In EELS both dipole and non-dipole multiplet states may be excited as discussed above, and a combination of EELS and XPS may allow the symmetry of the final-state screening orbitals in XPS to be determined. Moser et al. (1984) have exploited these ideas and have compared 3d XPS and EELS of La. They found the low-energy XPS satellite to coincide with the center of gravity of the loss structure. The f-screened $3d^94f^1$ final state character of the low-energy 3d XPS satellite has thus been confirmed. This relation between XPS and EELS final states has been discussed recently in some detail by Schneider et al. (1985).

5.3. *The 4p and 4s excitations*

In contrast to 3d and 4d levels 4p and 4s core levels have received less attention up to now either from EELS or from other core level spectroscopies. The case of 4p excitation is complicated by breakdown of the one-electron approximation for 4p core holes, which in this part of the Periodic Table may decay by $4p^{-1} \longleftrightarrow 4d^{-2}\varepsilon f$ giant Coster–Kronig coupling, leading to broad ill-defined peaks in photoemission (Wendin 1981). In the rare earths (except Yb) such processes are allowed for $4p_{1/2}$ holes but not for $4p_{3/2}$. In electron loss the unstable $4p_{1/2}^{-1}$ excitations lead to ill-defined structure in the corresponding energy region, but sharp peaks are observed near the $4p_{3/2}$ ionisation threshold (Strasser et al. 1984).

Representative examples of loss structures for 4p excitations in lanthanides are shown in fig. 14, both at high and lower incident energies. Sharp loss features are seen at excitation energies close to the $4p_{3/2}$ binding energies with some broad structures at higher energy. The intensities of the loss structures are much weaker than the intensities of 4d or 3d loss peaks and they depend on atomic number with a progressive decline in intensity of 4p losses through the lanthanide series. Yb and Lu metal have no loss peaks, the onset of the $4p_{3/2}$ channel being signalled only by a change of background gradient, but Yb_2O_3 shows a small peak (Netzer et al. 1985b). The influence of the primary electron energy is seen best in La, where a sharp loss feature on the low-energy side of the main loss grows in intensity as E_p drops from 1.5 keV to 470 eV (fig. 14(a)). In Pr (fig. 14(b)) the losses are somewhat broader, but the enhancement of a low-energy satellite at low E_p is still very marked. Nd (fig. 14(c)) shows more modest changes, and there are no clearly discernible shape variations with primary energy in the upper half of the lanthanide series, as in the case of Ho, for example (fig. 14(d)).

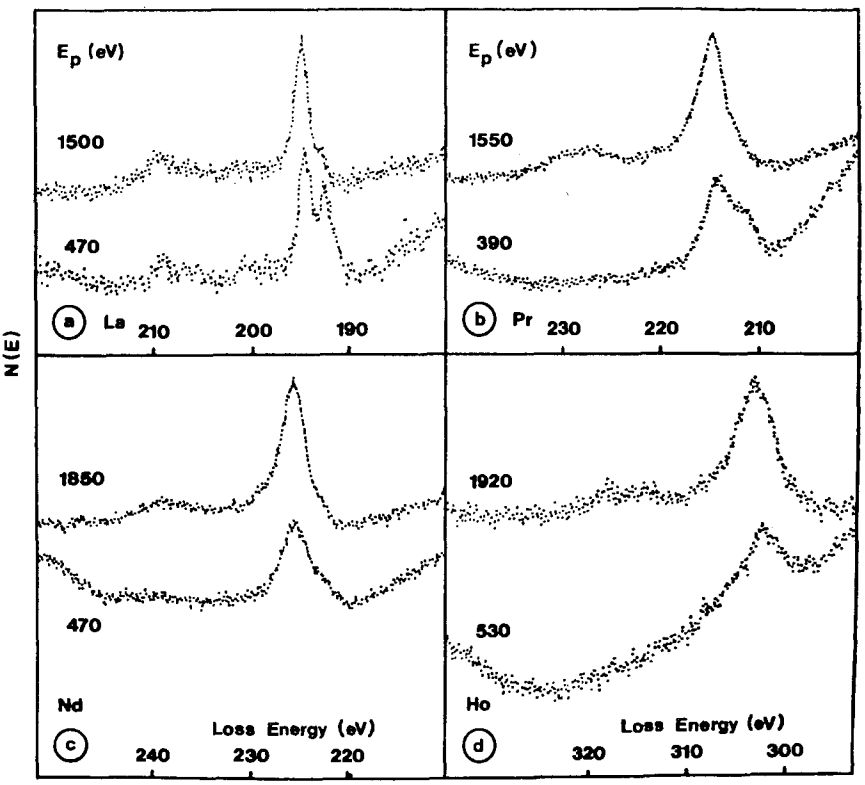

Fig. 14. 4p electron energy loss spectra of La, Pr, Nd and Ho at high and low primary energies (Netzer et al. 1985b).

In view of the many-body effects in the region of the $4p_{1/2}^{-1}$ excitations, we confine discussion here to the $4p_{3/2}$ excitations. An atomic-like interpretation of the $4p_{3/2}$ resonances is justified by the relatively symmetric shape of the loss peaks and by the fact that some occur at energies well below corresponding $4p_{3/2}$ XPS energies. In accordance with the ideas of Strasser et al. (1984) 4p–5d excitations will dominate at very high primary energy. Although exchange coupling between a 4p hole and an excited 5d electron will be smaller than for 5p–5d coupling, it may still give rise to similar correlation effects, but at energies closer to the $4p_{3/2}$ binding energies than in the case of 5p (see section 4.1). In that respect 4p relates to 5p excitation in the same manner as 3d to 4d excitation. On the other hand, the 4p and 4f radial charge distribution are similar in spatial extent (table 2). This means that quadrupole p–f matrix elements may be large under the experimental conditions of reflection EELS, where substantial momentum transfer is possible. Therefore, $4p \rightarrow 4f$ excitations may also be important. The absence of 4p loss resonances in Yb and Lu metal would be consistent with such an interpretation, but oxidised Yb, where $p \rightarrow f$ transitions are possible, has only a very weak loss.

Strasser et al. (1984) have discussed non-dipole effects in 4p EELS in La and Ce in terms of non-dipole 4p–5d multiplets as in the 3d–4f case. Alternative interpretations

might involve 4p → 4f *transitions at energies lower than* 4p → 5d, increasing in intensity as primary energy decreases and momentum transfer increases. Or yet again 4p → 4f transitions might completely dominate with the strongest peak corresponding to singlet excitations and the lower-energy peaks to the excitation of triplets.

Preliminary experiments on the 4p X-ray absorption spectrum of Ce (Matthew et al. 1987) show an absorption peak several eV *above* the $4p_{3/2}$ binding energy, in contrast to the main EELS structure which lies below. However, a weaker EELS peak is present in the same region as in the XAS experiment suggesting that this indeed may be the 4p → 5d transition with non-dipole-allowed 4p → 4f transitions responsible for the main features in the ELLS spectrum.

EELS excitations at energies close to the 4s binding energies are presented in fig.

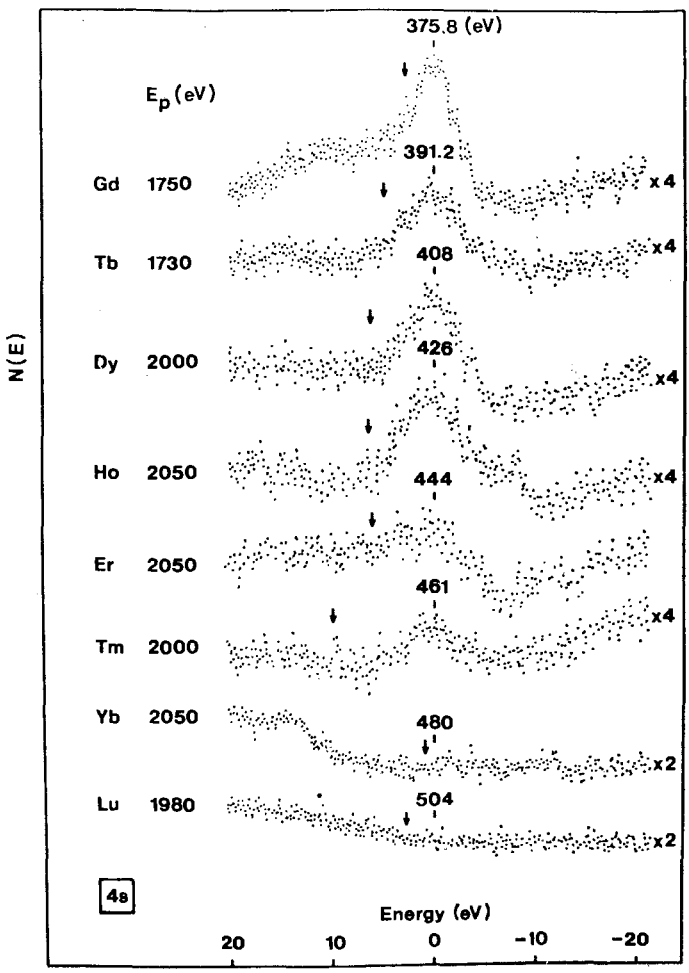

Fig. 15. 4s electron energy losses for the second half of the lanthanide series (Gd–Lu) for incident energies E_p of 1.7–2 keV. Arrows indicate known 4s XPS energies (Netzer et al. 1985b).

15 for the second half of the lanthanide series. Again distinctive peaks are seen rather than ionisation edges, but the peak intensities are generally much lower than in the 4p case; the peak intensities become even weaker for Er and Tm, while for Yb and Lu no loss feature may be discerned. The single-peak structures do not change appreciably as the primary energies are lowered. The presence of relatively sharp 4s losses is somewhat surprising, and it would appear that Coulomb coupling between hole and excited electron is operating here also. There are no strong reasons for p-like electrons in the conduction band to be localised, and so non-dipole-allowed $4s \rightarrow 4f$ transitions may be important. The large 4s–4f coupling apparent in XPS (McFeely et al. 1974) would likewise be strong for such transitions, and might explain the anomalously low excitation energies (with respect to 4s XPS binding energies) found in EELS of the higher rare earths and the virtual absence of losses in Yb and Lu. Again, XAS experiments are needed to clarify the issue.

5.4. *Valence monitoring by CEELS*

The valence of rare earth atoms in complex rare earth compounds has been a matter of considerable controversy in recent years, which was partly due to the different meaning associated with the term valence. It is appropriate in this context to return to the original chemist's definition, which states that valence has to be related to the number of bonds in which a particular atom is involved. In that sense Ce_2O_3, for example, is trivalent and CeO_2 is strictly tetravalent. Accordingly, the rare earth metals are mostly trivalent providing three 5d6s derived valence electrons per atom for the bonding, with the exception of Eu and Yb which are divalent. The strongly localised atomic-like 4f electrons act essentially as spectators to the bonding in most cases. However, in some systems a valence change may be introduced by physical or chemical changes of the environment. Then, a configuration change takes place, of the type $4f^n\,(5d6s)^m \longleftrightarrow 4f^{n-1}\,(5d6s)^{m+1}$; that is, a localised 4f electron becomes delocalised into valence states, or vice versa. If the two configurations are energetically degenerate, the ground state of the system may actually fluctuate between these two configurations, and unusual physical properties will result. This class of solids is designated best as 'inter-configuration fluctuation (ICF)' compounds. These compounds are also often called 'mixed valence' compounds, but Fuggle (1982) has worried about 'the almost audible protest of nineteenth century chemists at the misuse of the word valence', which seems to have reached him from their graves. In any case, 'valence fluctuating' compounds are known for Ce, Sm, Eu, Tm and Yb, and these elements are also found in more than one stable valence in simpler compounds.

The population of the 4f shell, the so-called f count, as a measure of valence may be determined by core level spectroscopies, as mentioned in several chapters of this volume. This is possible because the core hole created in the particular spectroscopic process couples to the partially filled 4f shell, thus providing characteristic spectral fingerprints of 4f configurations. However, the interesting compounds at the beginning of the rare earth series may have a delicate balance of different initial-state configurations, which can be altered in the final state by the suddenly switched on

core hole potential. In the atomistic argument of Connerade (1983) the creation of a core vacancy changes the shape of the effective 4f potential thus effecting the 4f wave function at the verge of 4f wave function collapse. In practice, the apparent 4f count is then influenced by final-state configurational mixing effects, and their theoretical assessment is necessary to derive meaningful evidence of the initial state. Such a theory has been proposed by Gunnarsson and Schönhammer for XAS of the 3d levels of Ce compounds (Fuggle et al. 1983, Gunnarsson and Schönhammer 1987), and this approach has been extended to the case of core electron energy loss spectroscopy (CEELS) by Schneider et al. (1985). In contrast, 3d XAS of the heavier rare earths with their more localised 4f states have been interpreted in a straightforward way in terms of initial-state valences without explicit consideration of final-state effects (Kaindl et al. 1983, 1984).

The f-count determination of ICF compounds at the beginning of the rare earth series in CEELS is therefore hampered by final-state effects as in other core level spectroscopies. In comparison to XAS CEELS shows further complications as a result of more complicated final-state multiplet structure (Strasser et al. 1983b, Hillebrecht et al. 1986). However, Schneider et al. (1985) have included recently analysis of 3d CEELS of La and Ce compounds with fractional f occupation into the many-body formalism of an Anderson impurity model. The agreement of relative energy positions between calculated and measured spectra was encouraging, but in order to assess fully the consequences of initial-state mixing in the final state, multiplet splitting has to be included into the many-body formalism.

In the context of this presentation we will be much more mundane and investigate only changes between integral valences as they occur in the course of surface reactions. We emphasise thus the surface sensitivity of CEELS as opposed to the more bulk oriented sensitivity of XAS. Oxidation reactions provide most illustrative examples, and the oxidation of Yb, Eu and Ce will be considered here. As mentioned before the characteristic multiplet structure of 4d excitations is particularly well suited as fingerprint of the 4f count. But also 3d and 4p excitation profiles exhibit changes that correlate with changes of the f count.

The oxidation of Yb from divalent metal ($4f^{14}$) to trivalent Yb_2O_3 ($4f^{13}$) is accompanied by the creation of a vacancy in the 4f shell. The turning-on of the giant $4d \rightarrow 4f$ resonance in Yb can therefore be followed during the oxidation process (Johansson et al. 1980, Bertel et al. 1982a), and provides a unique monitor of the formation of Yb^{3+}. The appearance of the 4d resonance in Yb_2O_3 and its absence in metallic Yb is shown here in fig. 11 of section 5.1, and it has been used by Bertel et al. (1982a) to investigate the surface oxidation of Yb. In that work the intensity of the 4d resonance as a function of oxygen exposure was compared to the oxygen uptake curve as measured in Auger spectroscopy; in combination with valence EELS and work function measurements a consistent picture of an island growth mechanism of the oxide phase could be derived. It is interesting to note that in the surface reaction with sulfur Yb remains in its divalent state, and no 4d resonance is observed (Strasser 1983, Netzer et al. 1983b).

The valence change at the surface of Eu metal upon exposure to oxygen pressures of 10^{-7} Torr was demonstrated first by CEELS (Strasser et al. 1982), and confirmed

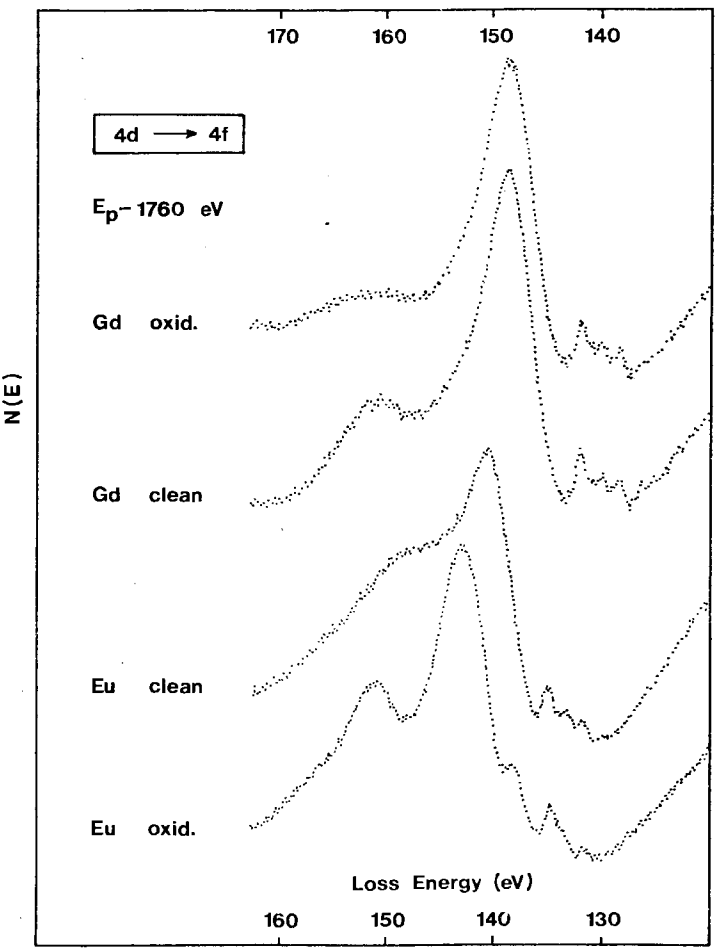

Fig. 16. 4d → 4f giant resonances of clean Gd and Eu and corresponding spectra of the oxidised surfaces. Upper energy scale: Gd; lower energy scale: Eu (Strasser et al. 1982).

by resonant photoemission (Barth et al. 1983). Figure 16 shows 4d excitation profiles of clean and oxidised Eu, compared to those of clean and oxidised Gd. In Gd the 4d excitation curves remain virtually unchanged between metal and oxide, consistent with the atomic-like nature of these exitations. In Eu, however, pronounced changes are observed upon oxidation: the main resonance shifts by 2.5 eV to higher excitation energy, and the preresonance fine structure is markedly different. The spectrum becomes similar to that of divalent Sm in the gas phase (Radtke 1980), and manifests the dominant contribution of trivalent Eu in the oxide phase.

The oxidation of Ce is a particularly interesting case. Not only do trivalent Ce_2O_3 and tetravalent CeO_2 oxide phases exist, but also the nature of the 4f state in CeO_2 has been a matter of fierce discussion (see Strasser and Netzer (1984), Wuilloud et al. (1984), and the related comments by Fujimori (1984) and Wuilloud et al. (1984)). 4d

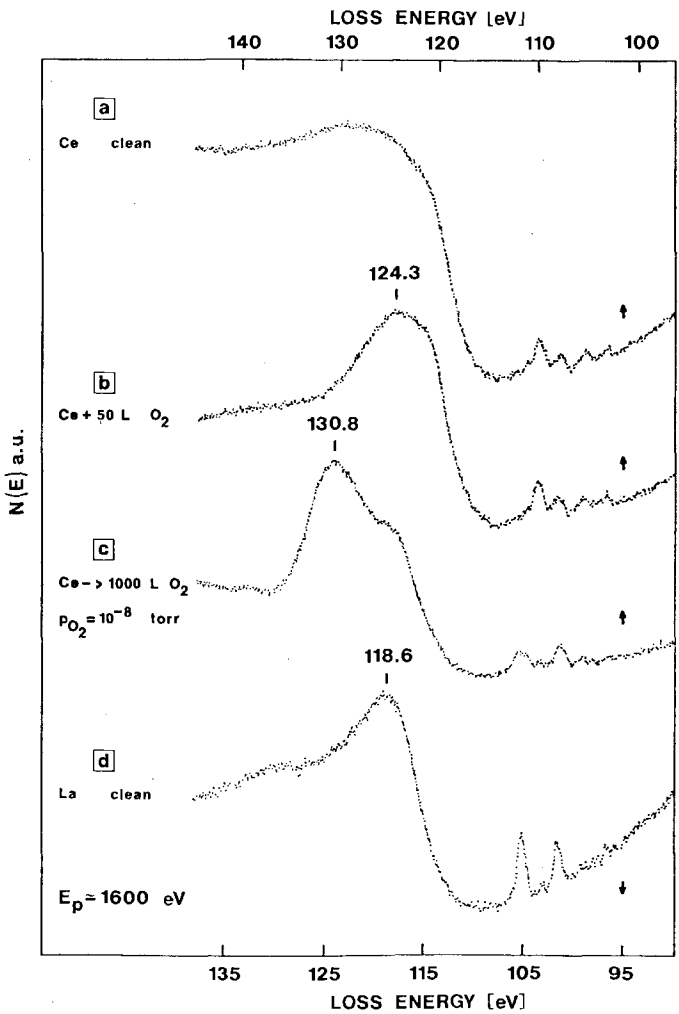

Fig. 17. Electron loss spectra of 4d excitations of clean γ-Ce and of oxidised Ce. For comparison, a La spectrum shifted by 6.5 eV to higher loss energy is included (Strasser and Netzer 1984).

CEELS of clean Ce metal and of Ce exposed to oxygen are shown in fig. 17, together with an appropriately shifted spectrum of La metal for comparison. Upon mild oxidation (50 L O_2) the oxidised spectrum (b) resembles closely the clean metal spectrum (a) in accord with the formation of trivalent Ce surface oxide. After exposing the surface to large amounts of O_2 (> 1000 L) and maintaining a stationary oxygen pressure in the spectrometer chamber important changes are observed (spectrum (c)). The main resonance shifts by 6.5 eV to higher energy and the complicated preresonance multiplet structure reduces essentially to a doublet structure. Comparison with the La spectrum (d) leaves little doubt that a CeO_2-like surface oxide phase with a dominant $4f^0$ ground-state configuration has been

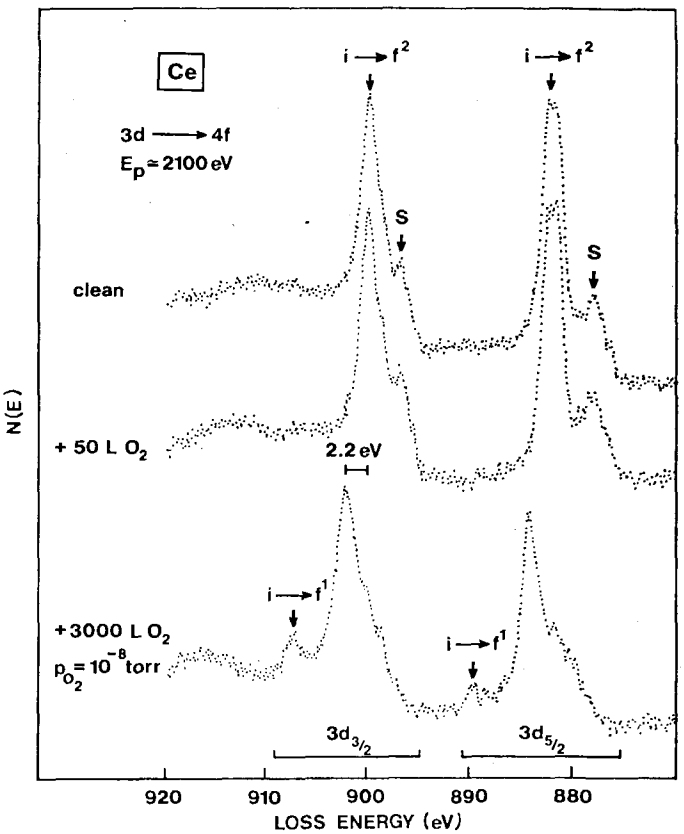

Fig. 18. Electron loss spectra of 3d excitations of clean and oxidised Ce (Strasser and Netzer 1984).

formed. The presence of empty localised 4f states in CeO_2 has been confirmed recently by Wuilloud et al. (1984) in XPS and BIS experiments.

Spectral changes of 3d CEELS between Ce metal and CeO_2 have been observed by Netzer and Strasser (1984), Bloch et al. (1984) and Wuilloud et al. (1984). Strasser and Netzer (1984) and Bloch et al. (1984) also reported characteristic differences in the 4p spectra. Figure 18 reproduces the 3d CEELS results of Strasser and Netzer obtained during surface oxidation of Ce. The spectra of clean and mildly oxidised Ce are identical, but the spectrum of heavily oxidised Ce (bottom spectrum of fig. 18) shows a shift of 2.2 eV of the main peaks and extra features at 5 eV to the higher energy of the main losses as a consequence of the valence change. The structures at the low-energy side of the main peaks, labelled S in fig. 18, are due to dipole-forbidden multiplets and have no relevance here. The low-intensity higher-energy features were associated by Strasser and Netzer (1984) with transitions into $4d^9 4f^2$ final states in analogy to the XAS analysis of Ce intermetallic compounds (Fuggle et al. 1983). However, Wuilloud et al. (1984) have suggested that the situation may actually be reversed – the main peaks carrying mainly f^1 and the satellites mainly f^2

character – but have also pointed out that f^1–f^2 configurational mixing impedes an unambiguous assignment. In any case, the valence change of Ce atoms during oxidation is well reflected in electron loss of core levels, and this technique complements in a useful way reaction studies at Ce surfaces (Strasser et al. 1985b).

In concluding we mention that CEELS at the 3p core edges of Sm shows a 6 eV peak shift between divalent and trivalent configurations (Chen et al. 1982). This is in contrast to the 3d and 4d excitation profiles where the differences between different valence states of Sm are not very significant (Allen et al. 1980, Chen et al. 1982, Netzer et al. 1983b). Chen et al. (1982) have explained this by the different final states for d and p core excitations. The increase in energy from $4f^6$ to $4f^7$ due to enhanced Coulomb repulsion is nearly balanced by the decrease in energy from $4f^6$ to $4f^7$ due to the particular strong Hund's rule coupling in the half-filled shell, thus leading to nearly identical spectra for $d \rightarrow f$ excitations. In $p \rightarrow d$ excitations divalent and trivalent Sm configurations involve $4f^5$ and $4f^6$ final states, and the electron repulsion is not offset by the now reduced correlation energy; significantly different p excitation energies therefore result.

6. Conclusions and future possibilities

The special properties of rare earth metals and their compounds manifest themselves in some interesting electron energy loss phenomena. In the valence region the low energy ($\Delta E \sim 3$–4 eV) one-electron transitions merit further study both by theory and experiment, while the surface divalency of Sm metal shows up in an anomalous plasmon-like excitation. The core region reveals a rich variety of quasi-atomic excitations with particularly strong resonance losses associated with $5p \rightarrow 5d$ and $4d \rightarrow 4f$ transitions. These phenomena lead on the one hand to convenient surface valence monitors and on the other to non-dipole excitations unseen by other spectroscopies.

What of the future? These properties have largely been investigated on metals and simple compounds, but in the next phase of development the insights gained thus far can be exploited in studying the role of rare earths in complex systems of potential technological interest. A major advantage of EELS over photoelectron spectroscopy is its potential for high spatial resolution. Although loss imaging in transmission EELS is well established, imaging in reflection geometry is relatively new, and has not had the investment of effort and expertise that has gone into Scanning Auger Microscopy (SAM). The availability of sharp loss features in rare earths, bearing unambiguous valence and environmental information, suggests that EELS imaging may be particularly effective in this field.

Some progress has been made in exploiting electron energy loss fine structure (EELFS) above core edges to give local geometry and bond lengths (De Crescenzi 1985). Here the cross sections for transitions into continuum states well above a core edge are modulated by weak reflection of the continuum final-state wave function from nearby atoms as in EXAFS (extended X-ray absorption fine structure). The technique may be applied either in transmission (bulk geometry) or in reflection

(near surface geometry). Applications to transition metal atom systems have met with some success, and investigations above the main d core excitations in the rare earths may prove fruitful.

Another technique in an early stage of development – spin polarised electron energy loss spectroscopy (SPEELS) – is expected to have particularly strong impact on rare earth surface science. In electron spectrometers with good temperature control of the sample the technique should unfold a wealth of interesting magnetic phases at surfaces and in ultra thin films on substrates.

Although photon spectroscopies, particularly those using synchrotrons, have many advantages, a monoenergetic electron beam is analogous to a white radiation source (the poor man's synchrotron) and is sufficiently cheap for the experimenter to have one in his own laboratory. This will ensure that EELS will play an important role in the characterisation of rare earth materials in the next decade.

Acknowledgments

We have pleasure in acknowledging stimulating discussions with E. Bertel, G. Strasser and J.C. Riviere in formulating our understanding of electron energy loss processes in the rare earths, and we thank Professor O.S. Heavens for critical reading of the manuscript. The scientific programme that has sustained our interest in the field has been supported by the Fonds zur Förderung der Wissenschaftlichen Forschung of Austria and the UK Science and Engineering Research Council.

References

Ahn, C.C., and O.L. Krivanek, 1982, A library of electron loss spectra at 1 eV resolution obtainable from Center for Solid State Science (Arizona State University).

Allen, J.W., L.I. Johansson, I. Lindau and S.B. Hagström, 1980, Phys. Rev. B **21**, 1335.

Allen, J.W., S.J. Oh, I. Lindau and L.I. Johansson, 1984, Phys. Rev. B **29**, 5927.

Bakulin, E.A., L.A. Balabanova, E.V. Stepin and V.V. Shcherbinina, 1971, Sov. Phys.-Solid State **13**, 189.

Balabanova, L.A., V.P. Zhuze, Ostroumova and S.G. Shul'man, 1983, Sov. Phys.-Solid State **25**, 971.

Barth, J., F. Gerken, J. Schmidt-May, A. Flodström and L.I. Johansson, 1983, Chem. Phys. Lett. **96**, 532.

Bertel, E., F.P. Netzer and J.A.D. Matthew, 1981, Surf. Sci. **103**, 1.

Bertel, E., G. Strasser, F.P. Netzer and J.A.D. Matthew, 1982a, Surf. Sci. **118**, 387.

Bertel, E., G. Strasser, F.P. Netzer and J.A.D. Matthew, 1982b, Phys. Rev. B **25**, 3374.

Best, P.E., 1962, Proc. Phys. Soc. (London) **79**, 133.

Bethe, H., 1930, Ann. Phys. **5**, 325.

Bethe, H., 1932, Z. Phys. **76**, 293.

Bethe, H., 1933, in: Handbuch der Physik, Vol. 24-1, eds H. Geiger and K. Scheel (Springer, Berlin) p. 273.

Bevolo, A.J., 1985a, J. Vac. Sci. & Technol. A **3**, 1312.

Bevolo, A.J., 1985b, S.E.M. PART IV, 1441.

Bloch, J., N. Shamir, M.H. Minz and U. Atzmony, 1984, Phys. Rev. B **30**, 2462.

Bonham, R.A., 1979, High-energy electron impact spectroscopy, in: Electron Spectroscopy, Vol. 3, eds C.R. Brundle and A.D. Baker (Academic Press, London) ch. 3.

Bonnelle, C., R.C. Karnatak and J. Sugar, 1974, Phys. Rev. A **9**, 1920.

Borovskii, I.B., and E.Y. Komarov, 1976, Sov. Phys.-Dokl. **21**, 735.

Bringans, R.D., 1981, J. Phys. C: Solid State Phys. **14**, 1053.

Brousseau-Lahaye, B., F. Frandon, C. Colliex, P. Trebbia and M. Casgnier, 1974, Energy loss spectra and optical constants of rare earth metals, hydrides and oxides between 5 and 200 eV, in: Vacuum UV Radiation Physics, eds E.

Koch, R. Haensel and C. Kunz (Perg non-Vieweg, Braunschweig) p. 622.
Brousseau-Lahaye, B., C. Colliex, J. Fran on, M. Gasgnier and P. Trebbia, 1975, Pi ys. Status Solidi b **69**, 257.
Brown, L.M., C. Colliex and M. Gasgnier, 1984, J. Phys. (France) **45**, C2-433.
Campagna, M., G.K. Wertheim and Y. Baer, 1979, Unfilled inner shells: rare earths and their compounds, in: Photoemission in Solids II, eds L. Ley and M. Cardona (Springer, Berlin) ch. 4.
Celotta, R.J., and R.H. Huebner, 1979, Electron impact spectroscopy, in: Electron Spectroscopy, Vol. 3, eds C.R. Brundle and A.D. Baker (Academic Press, London) ch. 2.
Chen, C.M., A.E. Meixner, M. Schluter, C.M. Varma and P.H. Schmidt, 1982, Phys. Rev. B **25**, 2036.
Chutijian, A., and D.C. Cartwright, 1981, Phys. Rev. A **23**, 2178.
Clark, C.W., and T.B. Lucatorto, 1983, private communication.
Colliex, C., 1984, in: Advances in Optical and Electron Microscopy, Vol. 9, eds R. Barer and V.E. Coslett (Academic Press, London) p. 65.
Colliex, C., V.E. Coslett, R.O. Leapman and P. Trebbia, 1976a, Ultramicroscopy **1**, 301.
Colliex, C., M. Gasgnier and P.Trebbia, 1976b, J. Phys. **37**, 397.
Colliex, C., T. Manoubi, M. Gasgnier and L.M. Brown, 1985, S.E.M. PART II, 489.
Connerade, J.P., 1983, J. Less-Common Met. **93**, 171.
Connerade, J.P., 1984, J. Phys. B **17**, L165.
Connerade, J.P., and R.C. Karnatak, 1981, J. Phys. F. **11**, 1539.
Connerade, J.P., and M. Pantelouris, 1984, J. Phys. B **17**, L173.
Connerade, J.P., and D.H. Tracy, 1977, J. Phys. B **10**, L235.
Crewe, A.V., M. Isaacson and D. Johnson, 1971, Rev. Sci. Instrum. **42**, 411.
Cukier, M., B. Gauthe and C. Wehenkel, 1980, J. Phys. **41**, 603.
Daniels, J., 1971, Opt. Commun. **3**, 13.
Daniels, J., C. v. Festenberg, H. Raether and D. Zeppenfeld, 1970, Optical constants of solids by electron spectroscopy, in: Springer Tracts in Modern Physics, Vol. 54, ed. G. Höhler (Springer, Berlin).
De Crescenzi, M., 1985, Surf. Sci. **162**, 838.
Dehmer, J.L., and A.F. Starace, 1972, Phys. Rev. B **5**, 1792.
Dehmer, J.L., A.F. Starace, U. Fano, J. Sugar and J.W. Cooper, 1971, Phys. Rev. Lett. **26**, 1521.
Dexpert, H., S.J. Pennycock and L.M. Brown, 1980, Inst. Phys. Conf. Ser. No. 52, 339.
Duthie, J.C., and D.G. Pettifor, 1977, Phys. Rev. Lett. **38**, 564.
Egerton, R.F., 1981, Applications of energy-loss microanalysis, in: Analytical Electron Microscopy, ed. R.H. Geiss (San Francisco Press) p. 154.
Egerton, R.F., 1984a, J. Phys. (France) **45**, C2-423.
Egerton, R.F., 1984b, Quantitative microanalysis by electron energy-loss spectroscopy: the current status, in: Scanning Electron Microscopy II (AMF O'Hare, Chicago) p. 505.
Egerton, R.F., and M. Egerton, 1983, An electron energy-loss bibliography, in: Scanning Electron Microscopy (AMF O'Hare, Chicago) p. 119.
El Gomati, M.M., and J.A.D. Matthew, 1987, J. Micros. **147** (2).
Esteva, J.M., R.C. Karnatak, J.C. Fuggle and G.A. Sawatzky, 1983, Phys. Rev. Lett. **50**, 910.
Fano, U., 1961, Phys. Rev. **124**, 1866.
Fano, U., and J.W. Cooper, 1968, Rev. Mod. Phys. **40**, 441.
Fischer, D.W., and W.L. Baun, 1967, J. Appl. Phys. **38**, 4830.
Fomichev, V.A., T.M. Zimkina, S.A. Gribovski and I.I. Zhukova, 1967, Sov. Phys.-Solid State **9**, 1163.
Freeman, A.J., 1980, Physica B **102**, 3.
Froitzheim, H., 1977, Electron energy loss spectroscopy, in: Electron Spectroscopy for Surface Analysis, ed. H. Ibach (Springer, Berlin) ch. 6.
Fuggle, J.C., 1982, Configuration interaction and screening in core-level spectroscopy of solids, in: X-Ray and Atomic Inner-Shell Physics, ed. B. Crasemann, AIP Conf. Proc. **94**, p. 661.
Fuggle, J.C., F.U. Hillebrecht, J.M. Esteva, R.C. Karnatak, O. Gunnarsson and K. Schönhammer, 1983, Phys. Rev. B **27**, 4637.
Fujimori, A., 1984, Phys. Rev. Lett. **53**, 2518.
Gasgnier, M., and L.M. Brown, 1986, Proc. S.F.M.E. (Soc. Franc. Microsc. Elect.) Strasbourg 1985 (to be published).
Gerken, F., J. Barth, R. Kammerer, L.I. Johansson and A. Flodström, 1982a, Surf. Sci. **117**, 468.
Gerken, F., J. Barth and C. Kunz, 1982b, Partial photoionisation cross-sections of rare earth metals in the region of the 4d resonance, in: X-Ray and Atomic Inner-Shell Physics, ed. B. Crasemann, AIP Conf. Proc. 94, p. 602.
Gerlach, R.L., and A.R. DuCharme, 1972, Phys. Rev. A **6**, 1892.
Gerlach, R.L., J.E. Houston and R.L. Park, 1970, Appl. Phys. Lett. **16**, 179.
Goddard III, W.A., D.L. Huestis, D.C. Cartwright and S. Trajmar, 1971, Chem. Phys. Lett. **11**, 329.
Grunes, L.A., and R.D. Leapman, 1980, Phys. Rev. B **22**, 3778.
Gunnarsson, O., and K. Schönhammer, 1987, this volume, ch. 64.
Haensel, R., P. Rabe and B. Sonntag, 1970, Solid State Commun. **8**, 1845.
Hagemann, H.J., W. Gudat and C. Kunz, 1976, Phys. Status Solidi b **74**, 507.
Hansen, J.E., A.W. Fliflet and H.P. Kelly, 1975, J. Phys. B **8**, L127.
Hillebrecht, F.U., G. Strasser and F.P. Netzer, 1986, J. Phys. F **16**, 937.

Hillier, J., and R.F. Baker, 1944, J. Appl. Phys. **15**, 663.
Hopster, H.R., R. Raue and R. Clauberg, 1984, Phys. Rev. Lett. **53**, 695.
Ibach, H., and D.L. Mills, 1982, Electron Energy Loss Spectroscopy and Surface Vibrations (Academic Press, London).
Ichinokawa, T., C. Le Gressus, A. Mogani, F. Pellerin and D. Massignon, 1981, Surf. Sci. **111**, L675.
Inokuti, M., 1971, Rev. Mod. Phys. **43**, 297.
Inokuti, M., and S.T. Manson, 1984, Cross sections for inelastic scattering of electrons by atoms, in: Electron Beam Interactions with Solids for Microscopy, Microanalysis and Microlithography, eds D.F. Kyser, H. Niedrig, D.E. Newburg, and R. Shimizu (SEM Inc., AMF O'Hare, Chicago) p. 1.
Inokuti, M., Y. Itikawa and J.E. Turner, 1978, Rev. Mod. Phys. **50**, 23.
Johansson, B., 1979, Phys. Rev. B **19**, 6615.
Johansson, L.I., J.W. Allen, I. Lindau, M.H. Hecht and S.B. Hagström, 1980, Phys. Rev. B **21**, 1408.
Joy, D.C., 1979, The basic principles of electron energy loss spectroscopy, in: Introduction to Analytical Electron Microscopy, eds J.J. Hren, J.I. Goldstein and D.C. Joy (Plenum Press, New York) ch. 7.
Kaindl, G., W.D. Brewer, G. Kalkowski and F. Holtzberg, 1983, Phys. Rev. Lett. **51**, 2056.
Kaindl, G., G. Kalkowski, W.D. Brewer, B. Perscheid and F. Holtzberg, 1984, J. Appl. Phys. **55**, 1910.
Kanski, J., and P.O. Nilsson, 1979, Phys. Rev. Lett. **43**, 1185.
Kanski, J., and G. Wendin, 1981, Phys. Rev. B **24**, 4977.
Karnatak, R.C., J.M. Esteva and J.P. Connerade, 1981, J. Phys. B **14**, 4747.
Kirschner, J., 1985a, Phys. Rev. Lett. **55**, 973.
Kirschner, J., 1985b, Polarised electrons at surfaces, in: Springer Tracts in Modern Physics, Vol. 106, ed. G. Höhler (Springer, Berlin).
Kirschner, J., D. Rebenstorff and H. Ibach, 1984, Phys. Rev. Lett. **53**, 698.
Kuppermann, A., J.K. Rice and S. Trajmar, 1968, J. Phys. Chem. **72**, 3894.
Lang, J.K., and Y. Baer, 1979, Solid State Commun. **31**, 94.
Larkins, F.P., 1977, At. Data & Nucl. Data Tables **20**, 311.
Leapman, R.D., 1979, Ultramicroscopy **3**, 413.
Leapman, R.D., 1982, Electron energy loss microspectroscopy and the characterisation of solids, in: Electron Beam Interactions with Solids for Microscopy, Microanalysis and Microlithography, eds D.F. Kyser, H. Niedrig, D.E. Newburg and R. Shimizu (SEM Inc., AMF O'Hare, Chicago) p. 217.
Liu, S.H., 1978, Electronic structure of rare earth metals, in: Handbook on the Physics and Chemistry of Rare Earths, Vol. 1, eds K.A. Gschneidner Jr and L. Eyring (North-Holland, Amsterdam) ch. 3.
Lucatorto, T.B., T.J. McIlrath, W.T. Hill III and C.W. Clark, 1982, The 4d-photoabsorption of Ba, Ba^+ and Ba^{++}: a view of shell collapse vs. contraction, in: X-Ray and Atomic Inner-Shell Physics, ed. B. Crasemann, AIP Conf. Proc. 94, p. 584.
Ludecke, R., and A. Koma, 1975, Phys. Rev. Lett. **34**, 817.
Matthew, J.A.D., G. Strasser and F.P. Netzer, 1983, Phys. Rev. B **27**, 5839.
Matthew, J.A.D., G. Strasser and F.P. Netzer, 1984, Phys. Rev. B **30**, 4975.
Matthew, J.A.D., F.P. Netzer, C.W. Clark and J.F. Morar, 1987, Europhys. Lett., in press.
Mauri, D., R. Allenspach and M. Landolt, 1984, Phys. Rev. Lett. **52**, 152.
McFeely, F.R., S.P. Kowalczyk, L. Ley and D.A. Shirley, 1974, Phys. Lett. A **49**, 301.
McLean, A.D., and R.S. McLean, 1981, At. Data & Nucl. Data Tables **26**, 197.
Moser, H.R., B. Delley, W.D. Schneider and Y. Baer, 1984, Phys. Rev. B **29**, 2947.
Motais, P., E. Belin and C. Bonnelle, 1984, Phys. Rev. B **30**, 4399.
Nassiopoulos, A.G., and J. Cazaux, 1985, Surf. Sci. **149**, 313.
Nassiopoulos, A.G., and J. Cazaux, 1986, Surf. Sci. **165**, 203.
Netzer, F.P., 1985, J. Vac. Sci. & Technol. A **3**, 1496.
Netzer, F.P., and E. Bertel, 1982, Adsorption and catalysis on rare earth surfaces, in: Handbook on the Physics and Chemistry of Rare Earths, Vol. 5, eds K.A. Gschneidner Jr and L. Eyring (North-Holland, Amsterdam) ch. 43.
Netzer, F.P., and J.A.D. Matthew, 1986, Rep. Prog. Phys. **49**, 621.
Netzer, F.P., G. Strasser and J.A.D. Matthew, 1983a, Phys. Rev. Lett. **51**, 211.
Netzer, F.P., G. Strasser and J.A.D. Matthew, 1983b, Solid State Commun. **45**, 171.
Netzer, F.P., G. Strasser and J.A.D. Matthew, 1984, Core level resonances in the rare earths monitored by electron energy loss specroscopy, in: Science with Soft X Rays, eds F.J. Himpsel and R.W. Klaffky, Proc. SPIE 447, p. 34.
Netzer, F.P., G. Strasser, G. Rosina and J.A.D. Matthew, 1985a, Surf. Sci. **152/153**, 757.
Netzer, F.P., G. Strasser, G. Rosina and J.A.D. Matthew, 1985b, J. Phys. F. **15**, 753.
Olson, C.G., and D.W. Lynch, 1982, J. Opt. Soc. Am. **72**, 88.
Onsgaard, J., S. Tougaard, P. Morgen and F. Ryborg, 1980a, in: Proc. 4th Int. Conf. Solid Surfaces, Cannes 1980, Vol. 2, eds D.A. Degras and M. Costa (Soc. Franc. du Vide, Paris) p. 1361.
Onsgaard, J., S. Tougaard, P. Morgen and F. Ryborg, 1980b, J. Electron Spectrosc. & Relat. Phenom. **18**, 29.
Onsgaard, J., I. Chorkendorff and O. Sørensen, 1983, Phys. Scr. T **4**, 169.
Onsgaard, J., I. Chorkendorff, O. Ellegaard and O. Sørensen, 1984, Surf. Sci. **138**, 148.

Padalia, B.D., W.C. Lang, P.R. Norris, L.M. Watson and D.J. Fabian, 1977, Proc. R. Soc. London Ser. A **354**, 269.
Pflüger, J., J. Fink, W. Weber, K.P. Bohnen and G. Crecelius, 1984, Phys. Rev. B **30**, 1155.
Powell, C.J., 1960, Proc. Phys. Soc. (London) **76**, 593.
Powell, C.J., 1969, J. Opt. Soc. Am. **59**, 738.
Powell, C.J., 1976, Rev. Mod. Phys. **48**, 33.
Powell, C.J., 1982, Inelastic scattering of electrons in solids, in: Electron Beam Interactions with Solids for Microscopy, Microanalysis and Microlithography, eds D.F. Kyser, H. Niedrig, D.E. Newburg and R. Shimizu (SEM Inc., AMF O'Hare, Chicago) p. 19.
Prutton, M., 1983, Surface Physics (Clarendon, Oxford).
Rabe, P., 1974, Ph.D. Thesis, University of Hamburg, W-Germany.
Radtke, E.-R., 1979, J. Phys. B **12**, L71.
Radtke, E.-R., 1980, Ph.D. Thesis, University of Bonn, W-Germany.
Raether, H., 1965, Solid state excitations by electrons, in: Springer Tracts in Modern Physics, Vol. 38, ed. G. Höhler (Springer, Berlin).
Raether, H., 1980, Excitation of plasmons and interband transitions by electrons, in: Springer Tracts in Modern Physics, Vol. 88, ed. G. Höhler (Springer, Berlin).
Richter, L., S.D. Bader and M.B. Brodsky, 1980, Phys. Rev. B **22**, 3059.
Ritchie, R.H., 1957, Phys. Rev. **106**, 874.
Ritsko, J.J., S.E. Schnatterly and P.C. Gibbons, 1974, Phys. Rev. B **10**, 5017.
Riviere, J.C., 1983, Instrumentation, in: Practical Surface Analysis by Auger and X-ray Photoelectron Spectroscopy, eds D. Briggs and M.P. Seah (Wiley, Chichester) ch. 2.
Riviere, J.C., F.P. Netzer, G. Rosina, G. Strasster and J.A.D. Matthew, 1985, J. Electron Spectrosc. & Relat. Phenom. **36**, 331.
Robins, J.L., and J.B. Swan, 1960, Proc. Phys. Soc. (London) **76**, 857.
Röhler, J., 1987, this volume, ch. 71.
Rosina, G., E. Bertel and F.P. Netzer, 1986, Phys. Rev. B **34**, 5746.
Roy, D., and J.D. Carette, 1977, Design of electron spectrometers for surface analysis, in: Electron Spectroscopy for Surface Analysis, ed. H. Ibach (Springer, Berlin) ch. 2.
Ruthemann, G., 1941, Naturwissenschaften **29**, 648.
Ryzhkov, M.V., V.A. Gubanov, Y.A. Teterin and A.S. Baev, 1985, Z. Phys. B **59**, 1.
Schmidt-May, J., F. Gerken, R. Nyholm and L.C. Davis, 1984, Phys. Rev. B **30**, 5560.
Schnatterly, S.E., 1979, Inelastic electron scattering spectroscopy, in: Solid State Physics, Vol. 34, eds F. Seitz and D. Turnbull (Academic Press, New York) p. 275.
Schneider, W.D., B. Delley, E. Wuilloud, J.M. Imer and Y. Baer, 1985, Phys. Rev. B **32**, 6819.
Siegmann, H.C., F. Meier, M. Erdubak and M. Landolt, 1984, Adv. Electr. Electr. Phys. **62**, 1.
Silcox, J., 1979, Ultramicroscopy **3**, 409.
Skriver, H.L., 1983, Electronic structure and cohesion in the rare earth metals, in: Systematics and the Properties of the Lanthanides, ed. S.P. Sinha (Reidel, Dordrecht) p. 213.
Strasser, G., 1983, Ph.D. Thesis, University of Innsbruck, Austria.
Strasser, G., and F.P. Netzer, 1984, J. Vac. Sci. & Technol. A **2**, 826.
Strasser, G., E. Bertel, J.A.D. Matthew and F.P. Netzer, 1982, Valence changes at rare earth metal surfaces monitored by EELS, in: Valence Instabilities, eds P. Wachter and H. Boppart (North-Holland, Amsterdam) p. 169.
Strasser, G., E. Bertel and F.P. Netzer, 1983a, J. Catalysis **79**, 420.
Strasser, G., F.U. Hillebrecht and F.P. Netzer, 1983b, J. Phys. F **13**, L223.
Strasser, G., F.P. Netzer and J.A.D. Matthew, 1984, Solid State Commun. **49**, 817.
Strasser, G., G. Rosina, J.A.D. Matthew and F.P. Netzer, 1985a, J. Phys. F **15**, 739.
Strasser, G., G. Rosina, E. Bertel and F.P. Netzer, 1985b, Surf. Sci. **152/153**, 765.
Sugar, J., 1972a, Phys. Rev. B **5**, 1785.
Sugar, J., 1972b, Phys. Rev. A **6**, 1764.
Swyt, C.R., and R.D. Leapman, 1982, Scanning Electron Microscopy (SEM Inc., AMF O'Hare, Chicago) p. 73.
Takakuwa, Y., S. Suzuki, T. Yokotsuta and T. Sagawa, 1984, J. Phys. Soc. Jpn. **53**, 687.
Thole, B.T., G. van der Laan, J.C. Fuggle, G.A. Sawatzky, R.C. Karnatak and J.-M. Esteva, 1985, Phys. Rev. B **32**, 5107.
Tonomura, A., J. Endo, H. Yamamoto and K. Usami, 1978, J. Phys. Soc. Jpn. **45**, 1684.
Trebbia, P., and C. Colliex, 1973, Phys. Status Solidi b **58**, 523.
Utlaut, M., 1981, A comparison of electron and photon beams for obtaining inner shell spectra, in: EXAFS Spectroscopy, eds B.K. Teo and D.C. Joy (Plenum, New York) ch. 20.
Weaver, J.H., D.T. Peterson and R.L. Benbow, 1979, Phys. Rev. B **20**, 5301.
Weaver, J.H., C. Krafka, D.W. Lynch and E.E. Koch, 1981, Physics Data **18**, 2.
Weller, D., and S.F. Alvarado, 1985, Z. Phys. B **58**, 261.
Wendin, G., 1976, J. Phys. B **9**, L297.
Wendin, G., 1981, Photoelectron spectra, Structure and Bonding 45 (Springer, Berlin).
Wendin, G., 1984, Phys. Rev. Lett. **53**, 724.
Wertheim, G.K., and G. Crecelius, 1978, Phys. Rev. Lett. **40**, 813.
Wolff, H.W., R. Bruhn, K. Radler and B. Sonntag, 1976, Phys. Lett. A **59**, 67.
Wuilloud, E., B. Delley, W.D. Schneider and Y. Baer, 1984, Phys. Rev. Lett. **53**, 202, 2519.
Zaluzec, N.J., 1981, A reference library of electron energy loss spectra, in: Analytical Electron Microscopy, ed. R.H. Geiss (San Francisco Press, San Francisco) p. 193.

Zangwill, A., and P. Soven, 1980, Phys. Rev. Lett. **45**, 204.
Zashkvara, V.V., E.V. Tsveiman, M.I. Korsunskii and V.S. Red'kin, 1972, Sov. Phys.-Solid State **14**, 1564.
Zhuze, V.P., M.G. Karin, D.P. Lurkirskii, V.M. Sergeeva and A.L. Shelykh, 1980, Sov. Phys.-Solid State **22**, 1558.
Zimkina, T.M., V.A. Fomichev, S.A. Gribovskii and I.I. Zhukova, 1967, Sov. Phys.-Solid State **9**, 1128.

SUBJECT INDEX